12ο ΔΙΕΘΝΕΣ ΣΥΝΕΔΡΙΟ
ΤΗΣ ΕΛΛΗΝΙΚΗΣ ΓΕΩΛΟΓΙΚΗΣ ΕΤΑΙΡΙΑΣ

ΠΛΑΝΗΤΗΣ ΓΗ:
Γεωλογικές Διεργασίες και Βιώσιμη Ανάπτυξη

12th INTERNATIONAL CONGRESS
OF THE GEOLOGICAL SOCIETY OF GREECE

PLANET EARTH:
Geological Processes and Sustainable Development

ΠΑΤΡΑ / PATRAS 2010

12ο ΔΙΕΘΝΕΣ ΣΥΝΕΔΡΙΟ
ΤΗΣ ΕΛΛΗΝΙΚΗΣ ΓΕΩΛΟΓΙΚΗΣ ΕΤΑΙΡΙΑΣ

ΠΛΑΝΗΤΗΣ ΓΗ:
Γεωλογικές Διεργασίες και Βιώσιμη Ανάπτυξη

Υπό την Αιγίδα του
Υπουργείου Περιβάλλοντος, Ενέργειας και Κλιματικής Αλλαγής

12th INTERNATIONAL CONGRESS
OF THE GEOLOGICAL SOCIETY OF GREECE

PLANET EARTH:
Geological Processes and Sustainable Development

Under the Aegis of the
Ministry of Environment, Energy and Climate Change

ΠΡΑΚΤΙΚΑ / PROCEEDINGS

ΕΠΙΜΕΛΕΙΑ ΕΚΔΟΣΗΣ	EDITORS
Γ. ΚΟΥΚΗΣ *Πανεπιστήμιο Πατρών*	G. KOUKIS *University of Patras*
Α. ΖΕΛΗΛΙΔΗΣ *Πανεπιστήμιο Πατρών*	A. ZELILIDIS *University of Patras*
Ι. ΚΟΥΚΟΥΒΕΛΑΣ *Πανεπιστήμιο Πατρών*	I. KOUKOUVELAS *University of Patras*
Γ. ΠΑΠΑΘΕΟΔΩΡΟΥ *Πανεπιστήμιο Πατρών*	G. PAPATHEODOROU *University of Patras*
Μ. ΓΕΡΑΓΑ *Πανεπιστήμιο Πατρών*	M. GERAGA *University of Patras*
Β. ΖΥΓΟΥΡΗ *Πανεπιστήμιο Πατρών*	V. ZYGOURI *University of Patras*

PATRAS, May 2010

ΟΡΓΑΝΩΤΙΚΗ ΕΠΙΤΡΟΠΗ 12ου ΔΙΕΘΝΟΥΣ ΣΥΝΕΔΡΙΟΥ

❖

ΠΡΟΕΔΡΟΣ
Γεώργιος ΚΟΥΚΗΣ, Καθηγητής Πανεπιστημίου Πατρών

ΑΝΤΙΠΡΟΕΔΡΟΣ
Αβραάμ ΖΕΛΗΛΙΔΗΣ, Καθηγητής Πανεπιστημίου Πατρών

ΓΕΝΙΚΟΣ ΓΡΑΜΜΑΤΕΑΣ
Ιωάννης ΚΟΥΚΟΥΒΕΛΑΣ, Αν. Καθηγητής Πανεπιστημίου Πατρών

ΕΙΔΙΚΟΣ ΓΡΑΜΜΑΤΕΑΣ
Γεώργιος ΠΑΠΑΘΕΟΔΩΡΟΥ, Αν. Καθηγητής Πανεπιστημίου Πατρών

ΤΑΜΙΑΣ
Μαρία ΓΕΡΑΓΑ, Λέκτορας Πανεπιστημίου Πατρών

ΜΕΛΗ
Νικόλαος ΚΟΝΤΟΠΟΥΛΟΣ, Καθηγητής Πανεπιστημίου Πατρών

Νικόλαος ΛΑΜΠΡΑΚΗΣ, Καθηγητής Πανεπιστημίου Πατρών

Νικόλαος ΣΑΜΠΑΤΑΚΑΚΗΣ, Αν. Καθηγητής Πανεπιστημίου Πατρών

Ευθύμιος ΣΩΚΟΣ, Επ. Καθηγητής Πανεπιστημίου Πατρών

Δημήτριος ΠΑΠΟΥΛΗΣ, Λέκτορας Πανεπιστημίου Πατρών

Μιχαήλ ΣΤΑΜΑΤΑΚΗΣ, Καθηγητής Εθνικού και Καποδιστριακού
Πανεπιστημίου Αθηνών

Απόστολος ΑΛΕΞΟΠΟΥΛΟΣ, Καθηγητής Εθνικού και Καποδιστριακού Πανεπι-
στημίου Αθηνών, Πρόεδρος Ε.Γ.Ε.

Κωνσταντίνος ΠΑΠΑΒΑΣΙΛΕΙΟΥ, Αν. Καθηγητής Εθνικού και Καποδιστριακού
Πανεπιστημίου Αθηνών, Γενικός Δ/ντής Ι.Γ.Μ.Ε.

Κωνσταντίνος ΜΑΚΡΟΠΟΥΛΟΣ, Καθηγητής Εθνικού και Καποδιστριακού
Πανεπιστημίου Αθηνών, Δ/ντής Γεωδυναμικού Ινστιτούτου Ε.Α.Α.

Εμμανουήλ ΜΑΝΟΥΤΣΟΓΛΟΥ, Αν. Καθηγητής Πολυτεχνείου Κρήτης

Σπυρίδων ΠΑΥΛΙΔΗΣ, Καθηγητής Αριστοτελείου Πανεπιστημίου Θεσσαλονίκης

Κωνσταντίνος ΠΑΠΑΚΩΝΣΤΑΝΤΙΝΟΥ, Πρόεδρος ΕΛ.ΚΕ.Θ.Ε.

Γραμματεία Συνεδρίου
Συνέδρα
Ηρ. Πολυτεχνείου 92, 26442 Πάτρα • Τηλ.: 2610 432.200 • Fax: 2610 430.884
URL: www.synedra.gr • E-mail: synedra@synedra.gr

ORGANIZING COMMITTEE OF THE 12th INTERNATIONAL CONGRESS

◈

PRESIDENT
George KOUKIS, Professor, University of Patras

VICE-PRESIDENT
Abraham ZELILIDIS, Professor, University of Patras

GENERAL SECRETARY
Ioannis KOUKOUVELAS, Assoc. Professor, University of Patras

EXECUTIVE SECRETARY
George PAPATHEODOROU, Assoc. Professor, University of Patras

TREASURER
Maria GERAGA, Lecturer, University of Patras

MEMBERS
Nikolaos KONTOPOULOS, Professor, University of Patras

Nikolaos LAMBRAKIS, Professor, University of Patras

Nikolaos SABATAKAKIS, Assoc. Professor, University of Patras

Eythimios SOKOS, Assist. Professor, University of Patras

Dimitrios PAPOULIS, Lecturer, University of Patras

Michael STAMATAKIS, Professor, National and Kapodistrian
University of Athens

Apostolos ALEXOPOULOS, Professor, National and Kapodistrian University of Athens.
President of G.S.G.

Constantinos PAPAVASSILEIOU, Assoc. Professor, National and Kapodistrian University of
Athens, Gen. Director of I.G.M.E.

Konstantinos MAKROPOULOS, Professor, National and Kapodistrian University of Athens,
Director of Institute of Geodynamics, N.O.A.

Emmanouil MANOUTSOGLOU, Assoc. Professor, Technical University of Crete

Spyridon PAVLIDES, Professor, Aristotle University of Thessaloniki

Konstantinos PAPACONSTANTINOU, President of H.C.M.R.

Congress Secretariat
Synedra
Iroon Polytechneiou 92, GR 26442 Patras • Ph.: +302610 432.200 • Fax: +302610 430.884
URL: www.synedra.gr • E-mail: synedra@synedra.gr

SPONSORS
OF THE 12th INTERNATIONAL CONGRESS OF THE GEOLOGICAL SOCIETY OF GREECE

◈

Under the Aegis of the
MINISTRY OF ENVIRONMENT, ENERGY AND CLIMATE CHANGE

and the Contribution of the
DEPARTMENT OF GEOLOGY, UNIVERSITY OF PATRAS
INSTITUTE OF GEOLOGY AND MINERAL EXPLORATION
GEOTECHNICAL CHAMBER OF GREECE

JOHN S. LATSIS, PUBLIC BENEFIT FOUNDATION

UNIVERSITY OF PATRAS

EARTHQUAKE PLANNING AND PROTECTION ORGANIZATION

AKTOR S.A.

EMBELIA S.A.

HELLENIC QUARRIES S.A..

CONSULTING ENGINEERING COMPANY (OTM) S.A.

GEFYRA S.A.

GENERAL CONSULTING LTD "ISTRIA"

GREEK MINING ENTERPRISES ASSOCIATION

DELFI-DISTOMON BAUXITE S.A.

GEOMECHANIKI S.A.

TITAN CEMENT COMPANY S.A.

EDAFOS ENGINEERING CONSULTANTS S.A.

GEOSCOPIO S.A.

The Organizing Committee of the 12th International Congress of the Geological Society of Greece expresses its grateful thanks to the above Foundations, Institutes, Organizations, Construction and Consulting Companies for their substantial support.

ΕΠΙΣΤΗΜΟΝΙΚΗ ΕΠΙΤΡΟΠΗ – SCIENTIFIC COMMITTEE

◈

Η Οργανωτική Επιτροπή ευχαριστεί θερμά τους κριτές για τη συμβολή τους στην κρίση όλων των εργασιών. Κάθε εργασία κρίθηκε από δύο κριτές για την από-κτηση Πρακτικών υψηλού επιστημονικού επιπέδου. Η Οργανωτική Επιτροπή δεν έχει ευθύνη για το περιεχόμενο και τις απόψεις που εκφράζονται στις εργασίες από τους συγγραφείς.

The Organizing Committee expresses sincere thanks to the reviewers for their contribution in evaluating and approving of the submitted papers. Each paper has passed through two reviewers, producing Proceedings of high scientific level. The Organizing Committee is not responsible for the content and the views expressed by the authors in the papers.

Alexopoulos A., Alexopoulos I., Alexouli A., Anagnostou C., Antonarakou A., Argyraki A., Avramidis P., Bersezio R., Bogdanov K., Caputo R., Christanis K., Christaras B., Christidis G., Depountis N., Drakatos G., Dresnier Th. Drinia H., Economou G., Fassoulas C., Ferentinos G., Fermeli G., Filippidis A., Fountoulis I. Frey M.L., Gaki – Papanastassiou K., Ganas A., Georgakopoulos A., Geraga M., Godelitsas A., Hatzipanagiotou K., Iliopoulos I., Ioakim C., Kalavrouziotis I., Kaleris V., Kallergis G., Kamberis E., Karakaisis G.F., Karakitsios V., Karastathis V., Karipi S., Katagas C., Kati M., Katsonopoulou D., Kilias A., Kiratzi A., Kitsou D., Kokkalas S., Kollaman H., Kondopoulou D., Konispoliatis N., Konstantinou C., Kontopoulos N., Koroneos A., Koukis G., Koukouvelas I., Lambrakis N., Laskou M., Lekkas E., Loupasakis C., Lykousis V., Magganas A., Manoutsoglou E., Marinos P.V., Markopoulos Th., Migiros G., Mladenova Th., Mountrakis D., Mposkos E., Mylonakis G., Nakov R., Nikolaou N., Oprsal I., Papadimitriou E., Papadimitriou P., Papadopoulos T., Papaioannou Ch., Papamarinopoulos S., Papanastassiou D., Papanikolaou D., Papatheodorou G., Papazachos C.B., Papoulis D., Paraskevopoulos P., Parcharidis I., Pavlides S., Pavlopoulos A., Pe – Piper G., Perdikakis V., Perrakis M., Perraki Th., Petalas C., Pomoni – Papaioannou F., Pomonis P., Ritolo S., Rokka A., Rondoyanni Th., Roumelioti Z., Rozos D., Ruiz – Ortiz P.A., Sabatakakis N., Sachpazi M., Sakellariou D., Scordilis Em., Seifert Th., Skarpelis N., Skias S., Sokos E., Soulios G., Soupios P., Stamatakis M., Stamatelopoulou - Seymour K., Stamatis G., Stiros S., Stournaras G., Syrides G., Theodorou G., Theodosiou I., Torok A., Tranos M., Triantafyllou M.V., Tsapanos T.M., Tselentis G-A., Tsiambaos G., Tsikouras B., Tsipoura – Vlahou M., Tsirambides A., Tsokas G., Tsolis–Katagas P., Tsombos P., Tsourlos P., Tucker M.E., Tulipano L., Tzanis A., Varnavas S., Vavelidis M., Voudouris K., Voulgaris N., Xypolias P., Zagana E., Zambetakis – Lekkas A., Zelilidis A., Zouros N., Zygouri V.

ΔΟΜΗ ΤΩΝ ΠΡΑΚΤΙΚΩΝ / SCHEME OF THE PROCEEDINGS

ΤΑ ΣΥΝΕΔΡΙΑ ΤΗΣ Ε.Γ.Ε.

1o ΔΙΗΜΕΡΟ, ΑΘΗΝΑ, 1983, Δελτίο XVII
2o ΔΙΗΜΕΡΟ, ΑΘΗΝΑ, 1984, Δελτίο XIX
3o ΣΥΝΕΔΡΙΟ, ΑΘΗΝΑ, 1986, Δελτίο XX
4o ΣΥΝΕΔΡΙΟ, ΑΘΗΝΑ, 1988, Δελτίο XXIII
5o ΣΥΝΕΔΡΙΟ, ΘΕΣΣΑΛΟΝΙΚΗ, 1990, Δελτίο XXV
6o ΣΥΝΕΔΡΙΟ, ΑΘΗΝΑ, 1992, Δελτίο XXVIII
7o ΣΥΝΕΔΡΙΟ, ΘΕΣΣΑΛΟΝΙΚΗ, 1994, Δελτίο XXX
8o ΣΥΝΕΔΡΙΟ, ΠΑΤΡΑ, 1998, Δελτίο XXXII
9o ΣΥΝΕΔΡΙΟ, ΑΘΗΝΑ, 2001, Δελτίο XXXIV
10o ΣΥΝΕΔΡΙΟ, ΘΕΣΣΑΛΟΝΙΚΗ, 2004, Δελτίο XXXVI
11o ΣΥΝΕΔΡΙΟ, ΑΘΗΝΑ, 2007, Δελτίο XXXX

❖

THE CONGRESSES OF G.S.G.

1st MEETING, ATHENS, 1983, Bull. XVII
2nd MEETING, ATHENS, 1984, Bull. XIX
3rd CONGRESS, ATHENS, 1986, Bull. XX
4th CONGRESS, ATHENS, 1988, Bull. XXIII
5th CONGRESS, THESSALONIKI, 1990, Bull. XXV
6th CONGRESS, ATHENS, 1992, Bull. XXVIII
7th CONGRESS, THESSALONIKI, 1994, Bull. XXX
8th CONGRESS, PATRAS, 1998, Bull. XXXII
9th CONGRESS, ATHENS, 2001, Bull. XXXIV
10th CONGRESS, THESSALONIKI, 2004, Bull. XXXVI
11th CONGRESS, ATHENS, 2007, Bull. XXXX

ΠΡΟΛΟΓΟΣ

◈

Η Γη είναι ένας πλανήτης με συνεχή και δυναμική εξέλιξη στην ιστορία του. Η γνώση και κατανόηση από τον άνθρωπο της εξέλιξης αυτής είναι μεγάλης σημασίας για τον εντοπισμό, την εκμετάλλευση και τη χρήση των φυσικών πόρων, καθώς και για την ανάδειξη και αντιμετώπιση των περιβαλλοντικών προκλήσεων-προβλημάτων από τη χρήση των πόρων αυτών.

Η περιβαλλοντική αυτή διάσταση απαιτεί μια ολοκληρωμένη, πολυ-επιστημονική θεώρηση του Πλανήτη, που θα περιλαμβάνει τη μελέτη όλων των παραγόντων, όπως της λιθόσφαιρας, της υδρόσφαιρας, της ατμόσφαιρας και της βιόσφαιρας, οι οποίοι συνδέονται μεταξύ τους σε πολύ σημαντικά συστήματα. Τα συστήματα αυτά απαιτούν τη συνεργασία, χωρίς σύνορα και περιορισμούς, των φυσικών επιστημών, όπως η Γεωλογία, η Βιολογία, η Χημεία και η Φυσική. Έτσι μόνο θα κατανοήσουμε τον Πλανήτη μας, θα αναδείξουμε τα περιβαλλοντικά προβλήματα και θα δημιουργήσουμε ενημερωμένες-ευαισθητοποιημένες κοινωνίες, οι οποίες θα μπορούν να αποφασίσουν για το παρόν και το μέλλον του.

Σήμερα είναι γεγονός ότι υπάρχει μια εμπεριστατωμένη άποψη σχετικά με την εξελικτική πορεία της Γης στη διάρκεια των 4,6 δισεκατομμυρίων ετών της ύπαρξής της. Παράλληλα αποτελεί κοινή συνείδηση ότι η ισορροπία του πλανήτη από την καθημερινή πίεση των έξι (6) περίπου δισεκατομμυρίων ανθρώπων που φιλοξενούνται σε αυτόν, είναι πλέον εύθραυστη. Ειδικότερα όσον αφορά στις Γεωεπιστήμες, υπάρχει σοβαρή γνώση σχετικά με τις **Γεωλογικές Διεργασίες**, που έχουν λάβει χώρα στα πλαίσια της ιστορίας αυτής με τη δημιουργία των ορέων και των ωκεανών, τους σεισμούς, την ηφαιστειακή δραστηριότητα, καθώς και την εκδήλωση εξωγενών φαινομένων, όπως οι κατολισθήσεις, οι πλημμύρες, οι ξηρασίες, τα τσουνάμι.

Όσον αφορά στη **Βιώσιμη Ανάπτυξη**, είναι γνωστό ότι τις τελευταίες δεκαετίες η τεχνολογική εξέλιξη και η πληθυσμιακή έκρηξη επέβαλαν μια αλόγιστη και χωρίς σχεδιασμό υπερεκμετάλλευση των φυσικών πόρων, με αποτέλεσμα την υποβάθμιση του περιβάλλοντος για πρώτη φορά στην ιστορία του Πλανήτη μας.

Έτσι, μερικά από τα ερωτήματα που τίθενται επιτακτικά και αναμένουν απαντήσεις από την επιστημονική κοινότητα, δεδομένου ότι εκφράζουν την αγωνία όλης της ανθρωπότητας, είναι τα εξής: α) Οι ανθρώπινες δραστηριότητες έχουν προκαλέσει πράγματι επικίνδυνες τροποποιήσεις του περιβάλλοντος και μάλιστα μη αναστρέψιμες ή οι κλιματικές μεταβολές που παρατηρούνται σήμερα αποτελούν φυσικές διακυμάνσεις; β) Ειδικότερα η βιομηχανική ανάπτυξη και η υπερκατανάλωση ενεργειακών πρώτων υλών αποτελούν κίνδυνο για το περιβάλλον ή θεωρούνται μηδαμινής επίδρασης σε σχέση με τις ηφαιστειακές εκρήξεις και τις αλλαγές των ρευμάτων στους ωκεανούς, οι οποίες προκαλούν δραματικές αλλαγές στο περιβάλλον;

γ) Είναι ακόμα δυνατή μια Βιώσιμη Ανάπτυξη και εάν ναι, ποιο είναι το είδος αυτής στα όρια αντοχής και αποδοχής του πλανήτη μας;

Στα παραπάνω ερωτήματα και προβληματισμούς η επιστήμη της Γεωλογίας έχει να προσφέρει πολλά, δεδομένου ότι οι φυσικές διεργασίες κατά τη διάρκεια της εξέλιξης της Γης έχουν καταγραφεί στους εδαφικούς και βραχώδεις γεωλογικούς σχηματισμούς, χωρίς επηρεασμούς από τις παρεμβάσεις του ανθρώπου. Έτσι οι ανθρώπινες παρεμβάσεις της σύγχρονης εποχής μπορούν να διαχωριστούν και να επισημανθούν, ώστε να αντιμετωπιστούν σωστά. Γενικότερα, η γνώση και κατανόηση της εξέλιξης της Γης μέσα από τις φυσικές διεργασίες μπορούν να συμβάλουν στην αποτύπωση των ρυθμών αλλαγής της Γης στο γεωλογικό χρόνο. Επιπλέον οι ρυθμοί αλλαγής και οι διεργασίες, που είναι υπεύθυνες για αυτούς, μπορούν παράλληλα να αποτελούν δείκτες πρόγνωσης για την πορεία του πλανήτη στο μέλλον. Με άλλα λόγια, το παρελθόν και γενικότερα η γεωλογική ιστορία του Πλανήτη μπορεί να αποτελέσει το «κλειδί» για το παρόν και το μέλλον αυτού.

Συμπερασματικά, η συμβολή της Γεωλογίας και γενικότερα των Φυσικών Επιστημών στην κοινωνία μας είναι πολύ σημαντική για τη γνώση της εξέλιξης της Γης, την έρευνα και αξιολόγηση των φυσικών πόρων, την εκτίμηση των περιβαλλοντικών επιπτώσεων λόγω εκμετάλλευσης των πόρων αυτών, καθώς και την πρόγνωση-αντιμετώπιση των διάφορων φυσικών επικινδυνοτήτων από γεωλογικές διεργασίες και καταστροφικά καιρικά φαινόμενα.

Το 12ο Διεθνές Συνέδριο της Ελληνικής Γεωλογικής Εταιρίας με τίτλο **«Πλανήτης Γη: Γεωλογικές Διεργασίες και Βιώσιμη Ανάπτυξη»** διοργανώνεται από το Τμήμα Γεωλογίας του Πανεπιστημίου Πατρών και πραγματοποιείται στο Συνεδριακό και Πολιτιστικό Κέντρο του Πανεπιστημίου από τις 19 έως 22 Μαΐου 2010. Το Δελτίο της Ελληνικής Γεωλογικής Εταιρίας περιλαμβάνει τα Πρακτικά του Συνεδρίου σε πέντε (5) τόμους των 2.992 σελίδων συνολικά. Οι τόμοι αυτοί καλύπτουν όλο το φάσμα των Γεωεπιστημών σε θέματα της βασικής και εφαρμοσμένης έρευνας. Στα πρακτικά περιλαμβάνονται 267 συνολικά εργασίες από 605 συγγραφείς, όλες στην Αγγλική γλώσσα, δίνοντας έτσι τη δυνατότητα διεθνούς προβολής και χρήσης του επιστημονικού Δελτίου της Εταιρίας. Οι επίσημες γλώσσες του Συνεδρίου είναι η Ελληνική και η Αγγλική.

Στο Συνέδριο υπάρχει σημαντικός αριθμός εργασιών από τον ευρύτερο γεωγραφικό μας χώρο, έχουν δε δηλώσει συμμετοχή πολλοί αξιόλογοι επιστήμονες από την Ελλάδα και το εξωτερικό, καθώς και νέοι ερευνητές και φοιτητές.

Όλες οι εργασίες που δημοσιεύονται, υπεβλήθησαν σε επιστημονική κρίση από εξωτερικούς κριτές, ακολουθώντας τη διαδικασία που είναι διεθνώς καθιερωμένη στα επιστημονικά περιοδικά. Πολλοί αναγνωρισμένοι επιστήμονες, Έλληνες και ξένοι, όλων των ειδικοτήτων, συμμετείχαν στη διαδικασία αυτή. Εκ μέρους της Οργανωτικής Επιτροπής τους ευχαριστώ για τη συμμετοχή και τη συμβολή τους με το σοβαρό έργο που προσέφεραν στην απόκτηση Πρακτικών υψηλού επιπέδου.

Οι επιστημονικές εργασίες εντάχθηκαν σε επιμέρους θεματικές ενότητες, στις οποίες διαχωρίστηκαν τα Πρακτικά και αποτέλεσαν αντικείμενο στις αντίστοιχες Συνεδρίες. Τα κείμενα των ειδικών και προσκεκλημένων ομιλιών, που καλύπτουν το ευρύτερο αντικείμενο της κάθε ενότητας και παρουσιάζουν υψηλού επιπέδου θεώρηση σχετικά με την υφιστάμενη γνώση, τις νέες απόψεις και τάσεις της έρευνας, αποτέλεσαν ιδιαίτερη ενότητα.

Στο Συνέδριο αυτό δίνεται ιδιαίτερη έμφαση στις Γεωλογικές Διεργασίες και τη Βιώσιμη Ανάπτυξη. Όπως αναφέρθηκε διεξοδικά παραπάνω, η κατανόηση της εξέλιξης του πλανήτη Γη μέσα από τις γεωλογικές διεργασίες επιτρέπει στον άνθρωπο να αξιολογήσει τις διάφορες δραστηριότητές του, όπως την αναζήτηση, εκμετάλλευση και χρήση των φυσικών πόρων, καθώς και την κατασκευή διαφόρων έργων υποδομής, χωρίς να προκαλεί επικίνδυνες μεταβολές στο φυσικό και το ανθρωπογενές περιβάλλον. Έτσι μόνο μπορεί να εξασφαλιστεί η Βιώσιμη Ανάπτυξη και να προβλεφθεί η πορεία του Πλανήτη.

Η έγκαιρη εκτύπωση και παράδοση των τόμων του Συνεδρίου στους συνέδρους και στην επιστημονική κοινότητα, καθώς και η γενικότερη οργάνωση του Συνεδρίου γίνεται με την οικονομική στήριξη πολλών φορέων, δημόσιων και ιδιωτικών. Εκφράζονται θερμές ευχαριστίες στο Υπουργείο Περιβάλλοντος, Ενέργειας και Κλιματικής Αλλαγής, που έθεσε το Συνέδριο υπό την αιγίδα του, καθώς και στο Τμήμα Γεωλογίας του Πανεπιστημίου Πατρών, το Ι.Γ.Μ.Ε., και το ΓΕΩΤ.Ε.Ε. Θερμές ευχαριστίες εκφράζονται επίσης στο Κοινωφελές Ίδρυμα Ιωάννη Σ. Λάτση, το Πανεπιστήμιο Πατρών, αλλά και σε ιδιωτικές Τεχνικές και Μελετητικές Εταιρίες, που με τόση προθυμία ανταποκρίθηκαν στην πρόσκλησή μας.

Τέλος, θα ήθελα να εκφράσω τις προσωπικές μου ευχαριστίες στους συναδέλφους της Οργανωτικής Επιτροπής για την αμέριστη βοήθειά τους και την άριστη συνεργασία στη συλλογική αυτή προσπάθεια, καθώς και στο Γραφείο Οργάνωσης Συνεδρίων «Συνέδρα», όπως επίσης στους φοιτητές του Τμήματος Γεωλογίας, που αγκάλιασαν και βοήθησαν στην οργάνωση του Συνεδρίου με απαράμιλλο ζήλο.

Πάτρα, 14 Απριλίου 2010

Γεώργιος Χρ. Κούκης
Πρόεδρος
της Οργανωτικής Επιτροπής

PROLOGUE

Earth is a dynamic Planet that has been continuously changing and evolving throughout its whole history. Knowledge and understanding of the evolution processes is of crucial importance not only to explore and take advantage of the natural recourses that our planet provides, but also to access the degree of environmental impacts that the exploitation of these causes.

This environmental aspect demands to consider a comprehensive and multi-scientific view of our Planet, which involves the study of lithosphere, hydrosphere, biosphere and atmosphere. All the above are closely connected together to form very important and complex natural systems, which need the close cooperation of all sciences involved, such as Geology, Biology, Chemistry and Physics. This is the most effective way to understand our Planet, to consider the environmental problems and enforce societies to become informed and conscious of its present and future.

Nowadays an almost complete and comprehensive knowledge about the evolution of Earth during the 4.6 billion years of its age has been gained. In parallel, it is common sense that our Planet's equilibrium is fragile due to environmental pressures that human causes, since Earth's population exceeds 6 billion people.

In the field of Geo-Sciences, in special, there has been gained sufficient experience about the **Geological Processes** that have been taken place during Earth's history and are evident in the formation of mountains and oceans, by the manifestation of earthquakes, by volcanic activity, as well as in natural phenomena as landslides, floods, droughts and tsunamis.

Concerning **Sustainable Development**, it is well known that during the last decades technological evolution and population growth have imposed an unreasonable and sometimes without design overconsumption of natural resources, which leads to gradual degradation of the environment for the first time in our Planet's history.

Thus, some of the "hot" questions that have been arisen and need to be answered by the Scientific Community, since they express the concern of the whole humanity, are: a) Human activities have indeed caused dangerous and non-reversible modifications of the environment or present climatic changes are a result of normal and natural fluctuations? b) Industrial development and overconsumption of natural recourses are a "red flag" for the environment or they can be considered as of minor effect when compared with volcanic eruptions and changes in the regime of ocean current circulation, which cause dramatic environmental changes? c) Is Sustainable Development still achievable and, if yes, in which form and within our Planet's bearing thresholds?

In the above questions Scientific Community can offer a lot, regarding that natural processes

during Earth's evolution have been imprinted on soil and rock geological formations, without any influence by human activities. Present human actions can be clearly distinguished and identified in order to be treated in the right way. The deep knowledge and understanding of Earth's evolution though natural processes can contribute to imprint the rates of Earth's changes through geological time. The changing rates and the processes responsible for them also contribute to obtain indices to predict similar phenomena for the future. In other words the Past and, generally, the geological history of our Planet is the "key" for the Present and Future.

In conclusion, the contribution of Geology and generally of Natural Sciences in our society is very important to understand Earth's evolution, to assist the research and assessment of natural resources, as well as to estimate the environmental impacts from their exploitation. Furthermore, they can provide solutions to the direction of the prevention and confrontation of natural hazards that are triggered by Geological Processes and catastrophic climatic events.

The 12th International Congress of the Geological Society of Greece entitled **"Planet Earth: Geological Processes & Sustainable Development"** is organized by the Department of Geology of the University of Patras in Greece and is held at the Conference and Cultural Center of the University between the 19th and 22nd of May 2010. The *Bulletin of the Geological Society of Greece* includes the Congress's Proceedings in 5 Volumes of 2.992 pages. These volumes cover the whole spectrum of Geo-Sciences in themes of basic and applied research. They include 267 research papers by 605 authors, all written in English making them easily accessible and promoted internationally. Official languages of the Congress are Greek and English. Many renowned scientists from Greece and abroad participate, covering scientific issues from our broad geographic region, as well as new researchers and students.

All submitted papers were reviewed by external reviewers, following the procedure that is established in scientific magazines. Many renowned scientists, Greek and foreigners, of all specialties, participated in this process. On behalf of the Organizing Committee I would like to thank them for their participation and contribution to acquire Proceedings of high quality.

The research papers were included in specific thematic units to which the Proceedings were divided and covered each Congress's session. Special and Keynote lectures about currently acquired knowledge, new insights and modern research trends for each area of interest comprised a special thematic unit.

This Congress focuses on Geological Processes and Sustainable Development. As it was mentioned above, the understanding of Earth's evolution though geological processes allows human to assess his activities, such as investigation and exploitation of natural resources and construction of Infrastructure Works, without causing serious and dangerous damages to the natural and human environment. This is the only way to secure sustainable development and forecast Earth's future.

The on-time production and delivering of the proceedings to the participants and scientific community, as well as the organization of the Congress is sponsored by many public and pri-

vate Organizations, Services and Companies. I would like to express my special thanks to the Ministry of Environment, Energy and Climate Change, which held the Congress under its aegis, as well as to the Department of Geology of the University of Patras, the Institute of Geology and Mineral Exploration (I.G.M.E.) and the Geotechnical Chamber of Greece for their contribution to organize this Congress. Special thanks are also expressed to the Public Benefit Foundation "John S. Latsis", to the University of Patras and to many private technical and consulting companies which willingly accepted our invitation.

Finally, I would like to personally thank the colleagues of the Organizing Committee for their generous help, support and cooperation to this teamwork, the Congress Organizing firm "*Synedra*", as well as the students of the Department of Geology for their precious contribution.

Patras, 14 of April 2010

George Ch. Koukis
President
of the Organizing Committee

ΠΕΡΙΕΧΟΜΕΝΑ / CONTENTS

◈

ΤΟΜΟΣ 1 / VOLUME 1

Εναρκτήρια Ομιλία / Opening Lectures
Κεντρικές και Θεματικές Ομιλίες / Special and Keynote Lectures
Γενική και Τεκτονική Γεωλογία / General and Structural Geology
Νεοτεκτονική και Γεωμορφολογία / Neotectonics and Geomorphology

---

ΕΝΑΡΚΤΗΡΙΑ ΟΜΙΛΙΑ / OPENING LECTURE

ΚΕΝΤΡΙΚΕΣ ΟΜΙΛΙΕΣ / SPECIAL LECTURES

ΘΕΜΑΤΙΚΕΣ ΟΜΙΛΙΕΣ / KEYNOTE LECTURES

ΓΕΝΙΚΗ ΚΑΙ ΤΕΚΤΟΝΙΚΗ ΓΕΩΛΟΓΙΑ / GENERAL AND STRUCTURAL GEOLOGY

ΝΕΟΤΕΚΤΟΝΙΚΗ ΚΑΙ ΓΕΩΜΟΡΦΟΛΟΓΙΑ / NEOTECTONICS AND GEOMORPHOLOGY

◈

ΤΟΜΟΣ 2 / VOLUME 2
Παλαιοντολογία, Στρωματογραφία και Ιζηματολογία /
Palaeontology, Stratigraphy and Sedimentology
Γεωαρχαιολογία / Geoarchaeology
Γεώτοποι / Geosites
Διδακτική των Γεωεπιστημών / Teaching Earth Sciences
Θαλάσσια Γεωλογία και Ωκεανογραφία / Marine Geology and Oceanography

---

ΠΑΛΑΙΟΝΤΟΛΟΓΙΑ, ΣΤΡΩΜΑΤΟΓΡΑΦΙΑ ΚΑΙ ΙΖΗΜΑΤΟΛΟΓΙΑ / PALAEONTOLOGY, STRATIGRAPHY AND SEDIMENTOLOGY

ΓΕΩΑΡΧΑΙΟΛΟΓΙΑ / GEOARCHAEOLOGY

ΓΕΩΤΟΠΟΙ / GEOSITES

ΔΙΔΑΚΤΙΚΗ ΤΩΝ ΓΕΩΕΠΙΣΤΗΜΩΝ / TEACHING EARTH SCIENCES

ΘΑΛΑΣΣΙΑ ΓΕΩΛΟΓΙΑ ΚΑΙ ΩΚΕΑΝΟΓΡΑΦΙΑ / MARINE GEOLOGY AND OCEANOGRAPHY

❖

ΤΟΜΟΣ 3 / VOLUME 3
Τεχνική Γεωλογία και Γεωτεχνική Μηχανική /
Engineering geology and Geotechnical Engineering
Φυσικές Καταστροφές / Natural Hazards
Αστική Γεωλογία / Urban Geology
Γ.Σ.Π. στις Γεωεπιστήμες / GIS in Earth Sciences

_____

ΤΕΧΝΙΚΗ ΓΕΩΛΟΓΙΑ ΚΑΙ ΓΕΩΤΕΧΝΙΚΗ ΜΗΧΑΝΙΚΗ /
ENGINEERING GEOLOGY AND GEOTECHNICAL ENGINEERING

ΦΥΣΙΚΕΣ ΚΑΤΑΣΤΡΟΦΕΣ / NATURAL HAZARDS

ΑΣΤΙΚΗ ΓΕΩΛΟΓΙΑ / URBAN GEOLOGY

Γ.Σ.Π. ΣΤΙΣ ΓΕΩΕΠΙΣΤΗΜΕΣ / G.I.S. IN EARTH SCIENCES

ΓΕΩΦΥΣΙΚΗ / GEOPHYSICS

ΣΕΙΣΜΟΛΟΓΙΑ / SEISMOLOGY

ΤΟΜΟΣ 5 / VOLUME 5

Ενεργειακές Πρώτες Ύλες και Γεωθερμία / Energy resources and Geothermics
Γεωχημεία και Κοιτασματολογία / Geochemistry and Ore Deposit Geology
Βιομηχανικά Ορυκτά και Πετρώματα / Industrial Minerals and Rocks
Ορυκτολογία και Πετρολογία / Mineralogy and Petrology

ΕΝΕΡΓΕΙΑΚΕΣ ΠΡΩΤΕΣ ΥΛΕΣ ΚΑΙ ΓΕΩΘΕΡΜΙΑ / ENERGY RESOURCES AND GEOTHERMICS

ΓΕΩΧΗΜΕΙΑ ΚΑΙ ΚΟΙΤΑΣΜΑΤΟΛΟΓΙΑ / GEOCHEMISTRY AND ORE DEPOSIT GEOLOGY

ΒΙΟΜΗΧΑΝΙΚΑ ΟΡΥΚΤΑ ΚΑΙ ΠΕΤΡΩΜΑΤΑ / INDUSTRIAL MINERALS AND ROCKS

ΟΡΥΚΤΟΛΟΓΙΑ ΚΑΙ ΠΕΤΡΟΛΟΓΙΑ / MINERALOGY AND PETROLOGY

12ο ΔΙΕΘΝΕΣ ΣΥΝΕΔΡΙΟ ΤΗΣ ΕΛΛΗΝΙΚΗΣ ΓΕΩΛΟΓΙΚΗΣ ΕΤΑΙΡΙΑΣ
ΠΛΑΝΗΤΗΣ ΓΗ: Γεωλογικές Διεργασίες και Βιώσιμη Ανάπτυξη

12th INTERNATIONAL CONGRESS OF THE GEOLOGICAL SOCIETY OF GREECE
PLANET EARTH: Geological Processes and Sustainable Development

❖

ΥΔΡΟΓΕΩΛΟΓΙΑ ΚΑΙ ΥΔΡΟΛΟΓΙΑ
HYDROGEOLOGY AND HYDROLOGY

COULD WATER CO-MANAGEMENT CONTRIBUTE TO PEACE, IN MIDDLE EAST?

Christaras B.[1]

[1] University of Thessaloniki, School of Geology, Lab. of Engineering Geology & Hydrogeology, 54124 Thessaloniki, christar@geo.auth.gr

Abstract

Water is the most precious resource in the Middle East, more important even than oil, given that while the citizens represent the 5% of the total world population, the Middle East & North Africa (MENA) region contains only 0.9% of global water resources (World Bank, 1996, Allan, 1999). For this reason, almost all conflicts, in Middle East, are mainly related to shared-water resources.

Historically, water was very often used as military tool or for religious purposes, Conflicts, for water management, were known from ancient years, till to the recent time. But also in our days, by 2010, the water deficit (difference between water supply and demand) is estimated to be at around 1 billion cubic meters, explaining the importance of the water to the joint futures of Palestinians, Jordanians, and Israelis.

For managing the water demand, various projects were proposed or already performed related to deep aquifers pumping, brackish-groundwater reverse-osmosis desalination, sea water desalinization, water transfer using canal or pipeline systems and dam construction. Nevertheless, it is important to understand that Peace can be possible in Middle East only if a rational and fair co-management of water resources could be real.

Key words: *Water-conflicts, water and peace, Middle-East.*

1. Introduction

North Africa and the Middle East constitute the driest region in the world. Annually, it has 355 billion cubic meters of renewable water resources, compared with 5,379 billion cubic meters in North America, 4,184 billion cubic meters in sub-Saharan Africa, and 9,985 billon cubic meters in Asia (Fisher & Askari, 2001).

Although water covers 71% of the Earth's surface, 98%, of it, is sea water, improper to be used for dinging, irrigation or even for most industrial purposes. Ground water and surface water in watercourses, rivers and lakes, account for the greater part of the planet's reserves of fresh water together with the polar ice caps and glaciers. The annual average flow of ground and surface water for the whole of the emergent lands (or "continental water") is estimated at 40,000 billion cubic metres. The arid and semi-arid zones contribute only 2% to this flow. Thus fewer than ten countries share 60% of the world's natural water resources; these are, in descending order, Brazil, Russia, China, Canada, Indonesia, the United States, India, Colombia and Congo (Sironneau, 1996).
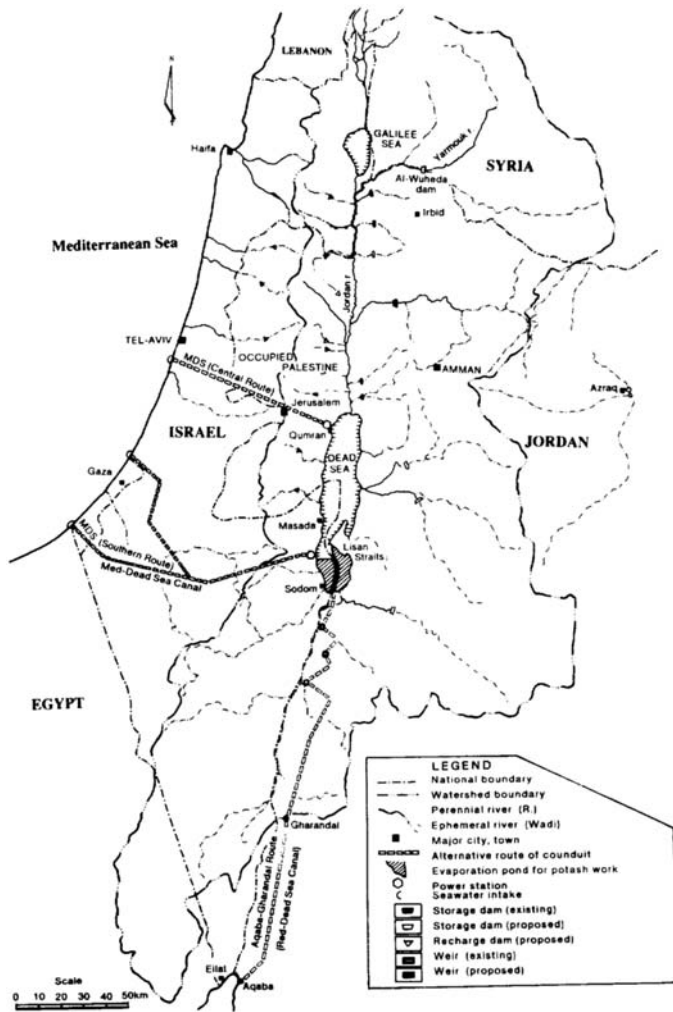
Fig. 1: Middle East water conflict area (Murakami, 1995).

2. Water use in Middle east

Water is the most precious resource in the Middle East, more important even than oil, given that while the citizens represent the 5% of the total world population, the Middle East & North Africa (MENA) region contains only 0.9% of global water resources (World Bank, 1996, Allan, 1999). For this reason, almost all conflicts, in Middle East, are mainly related to shared-water resources (Fig. 1).

By 2010, the water deficit (difference between water supply and demand) is estimated to be at around 1 billion cubic meters, explaining the importance of the water to the joint futures of Palestinians, Jordanians, and Israelis. Forty percent of Israel's water supply comes from aquifers beneath **Gaza Strip** and the **West Bank** [consisting of a) **Yarkon-Tanninim Aquifer** which supplies, annually, Israel with about 340×10^6 m^3 of water and Palestinians with about 20×10^6 m^3, 2) **Nablus-Gilboa Aquifer** which supplies, annually, Israel with about 115×10^6 m^3 and 3) **The Eastern Aquifer** which supplies, annually, about 40×10^6 m^3 and about 60×10^6 m^3 to the Palestinians, according to H. Gvirtman*:*

http://www.biu.ac.il/SOC/besa/publications/maps /map3.jpg]. About 25 percent comes from the Sea of Galilee, which helps to explain why Israelis balked when Syria insisted on giving up control of the shoreline as well as the entire Golan Heights—often called the "water tower of the Middle East"—as the price of peace (Smith, 2000).

3. Some historical data on water conflicts

Historically, water was very often used as military tool or for religious purposes, Conflicts, for water management, were known from ancient years, even from 3000 BC, when Ancient Sumerian legend recounted the deeds of the deity Ea, who punished humanity for its sins by inflicting the Earth with a six-day storm (Hatami and Gleick 1994). In 2500-2400 BC, a Lagash-Umma Border Dispute was performed, related to the divert of water from Lagash region to boundary canals, drying up boundary ditches to deprive Umma of water (Hatami and Gleick 1994). In 1790 BC, the Code of Hammurabi for the State of Sumer - Hammurabi listed several laws pertaining to irrigation management and water theft (Hatami and Gleick 1994). Later, in 1720-1684 BC, a grandson of Hammurabi dammed the Tigris river, for preventing the retreat of rebels who declared the independence of Babylon. (Hatami and Gleick 1994). In 1300 BC, according to the Old Testament, God sent heavy rainfall in the mountains, and the Kishon River overflowed the plain and immobilized or destroyed Sisera's technologically superior forces, for supporting Barak's army to defeat Sisera and his "nine hundred chariots of iron", on the fabled Plains of Esdraelon. (Bible, KJV). In 1200 BC, in Egypt, during the parting of the Red Sea, when Moses and the retreating Jews found themselves trapped between the Pharoah's army and the Red Sea, Moses miraculously divided the waters of the Red Sea, allowing his people to escape. The waters closed behind them and cut off the Egyptian who were following them (Hatami and Gleick 1994). In 720-705 BC, after a successful campaign against the Halidians of Armenia, Sargon II of Assyria destroyed their intricate irrigation network and flooded their land (Hatami and Gleick 1994). In 705-682 BC, in quelling rebellious Assyrians in 695 B.C., Sennacherib razes Babylon and diverts one of the principal irrigation canals so that its waters wash over the ruins (Hatami and Gleick 1994).

But also during more recent periods, starting just after the 2nd World War, water became the main reason of conflict in the area (Gleick, 2008), as follows: 1948: Arab forces cut of West Jerusalem's water supply in first Arab-Israeli war, 1951: irrigation of Jordan valley, by Jordans, 1953: water transfer from the sea of Galilee, by Israel, 1955: the Al-Wahda dam was project was proposed but the construction started in 2003, 1964: the headwaters of the Dan River on the Jordan River were bombed at Tell El-Qadi, 1965: failed attack by the Al-Fatah on the diversion pumps for the Israeli National Water Carrier, with new attacks during 1965-66, 1967: Israel destroyed the Arab diversion works on the Jordan River headwaters, and occupied Golan Heights, as well as West Bank (Gleick 1993, Wolf 1995, 1997) which consist the main aquifers in Middle East, 1969: Israel led two raids to destroy the newly-built East Ghor Canal, 1974: Iraq threatened to bomb the al-Thawra dam in Syria, alleging that the dam had reduced the flow of Euphrates River water to Iraq, 1975: Iraq-Syria both-sides clams about the water flow of Euphrates River water, 1982: Israel cut off the water supply of Beirut, 1983: an explosives-laden Hezbollah's truck disguised as a water delivery vehicle destroyed a barracks in a U.S. military compound, 1990: The flow of the Euphrates was interrupted for a month as Turkey finished construction of the Ataturk Dam. Syria and Iraq considered that action not as a developing project in a big waterless area but as a weapon of war, 1991: during the Gulf War, Iraq destroyed much of Kuwait's desalination capacity, 1993: From 1993 till present, the water supplies of the southern Shiite Muslims' areas of Iraq, were drained, creating sanitation problems to the people, 2001: Palestinians destroyed water supply pipelines to West Bank settlement of Yitzhar and Kibbutz Kisufim, 2004: the United States
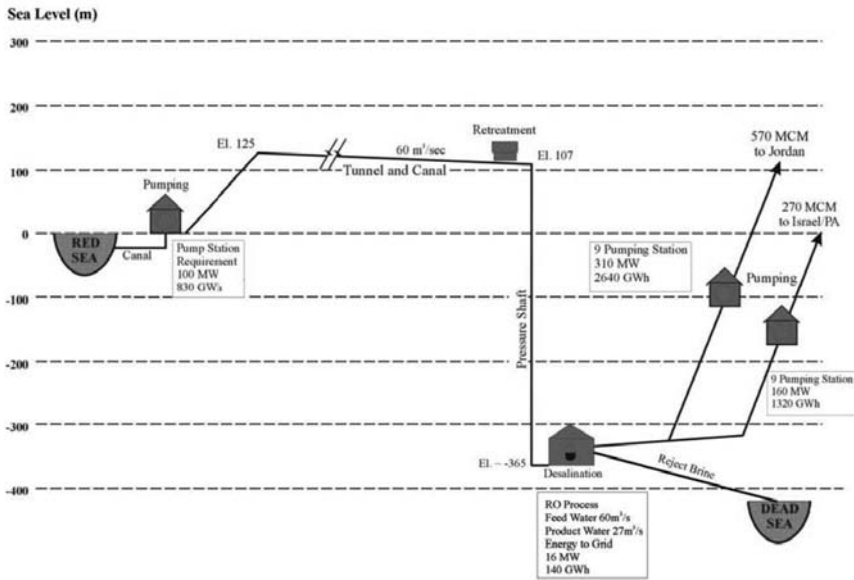
Fig. 2: Schematic presentation of the Red Sea – Dead Sea water transfer project (Beyth, 2007).

halted two water development projects as punishment to the Palestinian Authority for their failure to find those responsible for a deadly attack on a U.S. diplomatic convoy in October 2003, **2006**: Hezbollah rockets damaged a wastewater treatment plant in Israel. The Lebanese government estimated that Israeli attacks damaged water systems throughout southern Lebanon, including tanks, pipes, pumping stations, and facilities along the Litani River (Science 2006).

As populations increased, water became scarcer, aggravating regional tensions. The Lebanese had accused Israel of having designs on the waters of the River Litani, and Syria accused it of being reluctant to withdraw from the banks of the Sea of Galilee, the source of up to 30% of Israel's water. Israelis in the West Bank use four times more water than their Palestinian neighbours although the three principle underground aquifers, of Palestine, are found largely in the West Bank, as already mentioned above, in the chapter 2.

4. Water co-management for peace

For managing the water demand, various projects were proposed or already performed related to deep aquifers pumping, brackish-groundwater reverse-osmosis desalination, sea water desalinization, water transfer using canal or pipeline systems (eg. the Mediterranean-Dead Sea canal [MDSC], and Dead Sea-Red Sea canal [RSDSC], called peace valley, Fig. 1, 2) and Euphrates basins development by a series of dams and diversion tunnels for water supplying the countries of the Arabian peninsula.

Desalination is an interesting method which could mostly solve the water demand. In this framework, Israel has already started to embark on a desalination project consisting of a Seawater Reverse Osmosis Plant, with a capacity to desalinate about 100 million cubic meters (MCM). On the other hand, the Palestinian population requires at least an additional 30 to 40 MCM per year. This can only be obtained with desalination, and plans have already been drawn but any desalinated water provided to the Palestinians has to come from plants on the Israeli coast, as the West Bank has no ac-

cess to the Mediterranean Sea. Desalination will also be needed to supply the Palestinians of the Gaza Strip, where the aquifers are saline, started having high concentration of nitrates.

According to Michael Beyth (2007), the idea to study the MDSC for the generation of electricity was revived and thoroughly studied as a result of the 1973 energy crisis and the search for alternative energy sources. The goal of that project was to produce 800 MW during peak hours. The Red Sea – Dead Sea Canal was considered in the mid-1990s and re-considered in 2007 (Beyth, 2007, Fig. 2); it is the only of the system MDSC- RSDSC which is currently under consideration. The main goals of this project are a) desalination of 2000 MCM to produce 800–850 MCM with 20 to 300 mg/l TDS, annually and b) the Dead Sea (DS) level restoration at around 400 meters below sea level (mbsl).

Concerning surface waters, three important rivers, Euphrates (2,330 km), Tigris (1,718 km) and Jordan, consist the main water resources of the area. The primary users, of the Jordan River water (Fig. 1), are Israel and Jordan. Between them, the Jordan River system has been extensively exploited satisfying about half of their combined water demand. The other interested countries are Lebanon and Syria who satisfy only 5% of their water demand.

The Euphrates, which is the longest Tran boundary river in western Asia, has been developed since 4000 B.C. Several ancient civilizations in Mesopotamia were supported by basin irrigation from the Tigris and Euphrates Rivers. Owing to the extremely arid climate, however, the farm lands on the Mesopotamian alluvials have suffered from salt accumulation and water logging problems since 3000 B.C., during the Sumerian age. That ancient civilization disappeared with the abandonment of irrigation-canal systems. The washing out of accumulated salts, or leaching as it is called, can be carried out only with an efficient procedure.

In order to use and control Euphrates rivers water, large dams were constructed, the more famous of which, is the Ataturk dam (Murakami, 1995). The Tigris-Euphrates basin lies primarily in three countries-Turkey, Syria, and Iraq. Both the Tigris and Euphrates rivers rise in the mountains of southern Turkey and flow south-eastwards, the Euphrates crossing Syria into Iraq and the Tigris flowing directly into Iraq from Turkey. In southern Iraq the Tigris and the Euphrates unite to form the Shatt al-Arab, which in turn flows into the Arabian Gulf.

In order to find out an acceptable base for peace, numerous final status and peace plans have been advanced to settle the Israeli-Palestinian conflict. What is needed at first is not peace talks, but real peace actions related to land, water, security and a place to call your own. The peace process cannot be abandoned; however, Israelis and Palestinians need peace, the Middle East needs peace between Israel and the Palestinians.

It is necessary to adopt that a fair water co-management is probably the only first step toward to a permanent peace, because development creates peace.

5. Conclusions-Results

According to the above analysis, it is almost obvious that peace in Middle East is possible, only if a fair water co-management is established in the area. Several projects were elaborated during the last years proposing solutions mainly related to sea-water or brackish water desalination and transfer, between the Mediterranean Sea and Dead Sea as well as Red Sea and Dead sea, by constructing specific canals. The international scientific society could contribute to the peace, by providing or promoting ideas in this field, having in mind that, the Middle East is not only bombs and fanaticism but it is also a place where wonderful people, with dreams and hopes about democracy and peace, live there.

6. References

Allan, T., 1999. Israel and water in the framework of the Arab-Israeli conflict. *Conf. on Water and the Arab-Israeli conflict*, Centre of Law at Bir Zeit University.

Beyth, M., 2007. The Red Sea and Mediterranean-Dead Sea canal project. Desalination (Elsevier Ed.), 214, pp. 364-370.

Darwish, A., 2003. Analysis: Middle East water wars., BBC News/Middle East/Analysis: Middle East water wars., Friday, 30/5/2003, 16:40 GMT 17:40 UK., *in* http://news.bbc.co.uk/2/hi/middle_east/2949768.stm.

Eitzen, E.M. and E.T. Takafuji, 1997. Eitzen, E.M. and E.T. Takafuji. 1997. Historical Overview of Biological Warfare. In Textbook of Military Medicine, Medical Aspects of Chemical and Biological Warfare. Published by the Office of The Surgeon General, Department of the Army, USA. pp. 415-424.

Fisher F. and Askari H., 2001. Optimal water management in the Middle East and other regions. *Finance and Development* (quarterly magazine of IMF), 38, no. 3, pp. 1-7.

Gleick, P.H., 1993. Water and conflict: Fresh water resources and international security. *International Security* 18, Vol. 1, pp. 79-112.

Gleick, P.H., 2008. Water conflict chronology, Data from the Pacific Institute for Studies in Development, Environment, and Security database on Water and Conflict (Water Brief) 11/10/08.

Ha'aretz. 1999. Sharon unveils desalination plan. *Ha'aretz*, 3 Feb 99.

Hatami and Gleick 1994. Chronology of Conflict over Water in the Legends, Myths, and History of the Ancient Middle East. In "Water, war, and peace in the Middle East." *Environment*, 36, pp.6-on. Heldref Publishers, Washington.

Murakami M., 1995. Managing Water for Peace in the Middle East: Alternative Strategies. United Nations University Press TOKYO - NEW YORK – PARIS, 319p.

Sironneau, J., 1996: Water: a new strategic issue for the world, Ed. Economica, Paris, 1996, pp. 5 & 15.

Smith, D., 2000. Water in MI. *National Geographic*, July 14, 2000.

Science 2006. Tallying Mideast damage. *Science*, Vol. 313, Issue 5793, p. 1549.

World Bank Report 1996. From Scarcity to Security: Averting a Water Crisis in the Middle East and North Africa.

UNESCO' Report 2002. Water is not just a commodity, but a common public good, World Summit on Sustainable Development (WSSD) in Johannesburg (www.unesco.org/water).

UNESCO' Report N°2006-14 (2006). Water: a crisis of governance says second UN World Water Development Report. UNESCOPRESS, Press Release N°2006-14, www.unesco.org/en/ev.php-URL_ID=32057&URL_DO=DO_TOPIC&URL_SECTION=201.html.

Wolf, A.T., 1995. Hydropolitics along the Jordan River: Scarce Water and its Impact on the Arab-Israeli Conflict. United Nations University Press, Tokyo, Japan.

Wolf, A. T., 1997. 'Water wars' and water reality: Conflict and cooperation along international waterways. NATO Advanced Research Workshop on Environmental Change, Adaptation, and Human Security. Budapest, Hungary. 9-12 October.

World Bank Report 1996. From Scarcity to Security: Averting a Water Crisis in the Middle East and North Africa.

TOWARDS A NEW PROCEDURE TO SET UP GROUNDWATER THRESHOLD VALUES IN ACCORDANCE WITH THE PREVISIONS OF THE EC DIRECTIVE 2006/118: A CASE STUDY FROM ACHAIA AND CORINTHIA (GREECE)

Christoforidou P.[1], Panagopoulos A.[2], Voudouris K.[3]

[1] *Chemical Engineering, MSc, Thessaloniki, Greece, parthena@bio.auth.gr*

[2] *Land Reclamation Institute, National Agricultural Research Foundation, Sindos, 574 00, Thessaloniki, Greece, panagopoulosa@gmail.com*

[3] *Laboratory of Engineering Geology and Hydrogeology, Department of Geology, Aristotle University, 541 24 Thessaloniki, Greece, kvoudour@geo.auth.gr*

Abstract

The EU Water Framework and Groundwater Directives stipulate that EU member states have to assess groundwater chemical status by the use of groundwater threshold values derived for the protection of dependent ecosystems and human health. In the EU's 6th FP BRIDGE project "Background cRiteria for the IDentification of Groundwater thrEsholds", a methodology for the derivation of threshold values (TV) for groundwater bodies is proposed. Threshold values are quality standards for polluting substances in groundwater that need to be formulated by the Member States for the status assessment of groundwater bodies. These values represent the concentration of a pollutant that cannot be exceeded in order to protect both the environment and human health. The proposed method derives groundwater threshold values based on environmental objectives for groundwater "itself" as a receptor, using relevant reference criteria such as natural background levels, drinking and irrigation water standards. This methodology is tested on seven districts in Greece (two of them are analyzed in this paper). Concentrations of major ions, ammonium and data of electrical conductivity were examined. After a pre-selection on databases with groundwater samples the natural background level is determined as the 90- and 97.7 percentile.

Key words: Greece, groundwater, natural background level, threshold value, European groundwater directive, chemical status.

1. Introduction

Greece is a country which mainly depends on groundwater resources for its water supply. The types of aquifers that dominate are karst aquifers and coarse grained Neogene and Quaternary deposits (porous aquifers). The dominant hydrochemical type of groundwater in Greece is the one of Ca–Mg–HCO_3 representing freshwater of recent infiltration (Daskalaki and Voudouris, 2007).

The major water consumer is agriculture (86%), with irrigated areas rapidly increasing in the last decades. Nitrate pollution due to agricultural activities (pesticides, fertilizers, etc), as well as due to existing cesspools used for untreated domestic effluent, has become a pressing and important problem nowadays. Sea intrusion is a second groundwater quality problem in Greece, mainly faced by

overexploited coastal aquifers (Daskalaki and Voudouris, 2007).

According to the European groundwater directive, '*Member States should, where possible, use statistical procedures, provided they comply with international standards and contribute to the comparability of results of monitoring between Member States over long periods'*. The main aim of BRIDGE project was to develop a methodology for setting up threshold values (TV) for groundwater, based on scientific principles.

Natural background levels and environmental quality standards or drinking water standards derived from (eco)toxicological tests etc., may be established by scientific methods (Edmunds et al., 2003; WHO, 2006). BRIDGE methodology uses for the derivation of threshold values (TV), natural background levels (NBL) and environmental quality standards (EQS) for 1) dependent aquatic ecosystems, and 2) groundwater "itself". In the latter case groundwater is protected as an ecosystem "itself" or as a source of water supply for human consumption for the protection of human health. Since little is known about water quality needs of groundwater ecosystems, surface water quality standards (EQS) or drinking water standards (DWS) may be chosen (Müller et al., 2006).

The derivation of groundwater threshold values based on environmental objectives for terrestrial ecosystems was not considered specifically, as also little is known about environmental quality standards for these. In general, drinking water standards as reference values for groundwater "itself" and irrigation standards were used.

The aim of the present work is to derive and evaluate the threshold values by means of the methodology described in WP3 of Bridge Project, enriched with some additional criteria. After a pre-selection on a database the natural background level is determined as the 90th and 97.7th percentile; both options are offered to decision makers, depending on the particularities of each study area. The threshold values are calculated by comparing the natural background level with a reference value, which is dependent on the receptor.

2. Geological setting

NW Achaia

The Glafkos basin aquifer system is located in the southwestern part of Greece (Peloponnese). Unconsolidated alluvial sediments with silty and clayey intercalations are dispersed throughout the Glafkos basin, especially in the coastal area (Fig. 1). The aquifers of the alternating coarse-grained alluvial beds may be regarded as one unified aquifer system (Lambrakis et al., 1997). The presence of silts and clays implies the occurrence of artesian conditions in the coastal part of the aquifer. Groundwater recharge takes place mainly by seepage through the riverbed and direct infiltration during rainfall. Based on borehole data analyses the depth of boreholes ranges between 40-140 m below mean sea level (Voudouris, 1995).

In the coastal part of this aquifer system seawater intrusion is evidenced due to overexploitation combined with prolonged dry periods. The waters are of various hydrochemical types: $Ca-Mg-HCO_3$ (freshwater of recent infiltration), $Na-HCO_3$ (this type indicates ion-exchange phenomena and characterizes a transition zone) and $Na-Cl$ (typical brackish water in which the ions Na^+ and Cl^- dominate).

Coastal Corinthia

The area, named Vocha plain, is located at the northeastern part of the Corinthia Prefecture and covers an area of 65 km^2. It is characterized by ongoing urbanization, tourism development and inten-
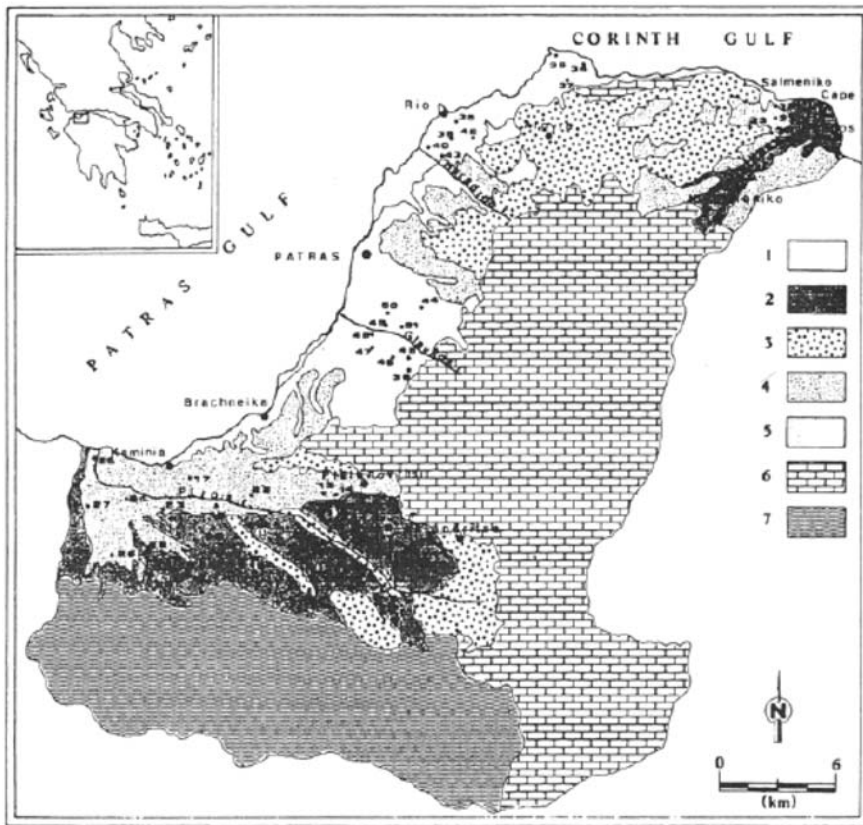
Fig. 1: Geological map of NW Achaia (Voudouris et al., 1997). 1. Recent alluvial deposits, 2. Terrestrial fluvial sediments, 3. Old alluvial deposits, 4. Clays, marls and sands, 5. Clays, siltstones, marls and silts with gravels, 6. Limestones, 7. Flysch.

sive agriculture that have considerable environmental impact, predominantly in the groundwater (Voudouris, 2006).

The area is formed of recent unconsolidated material consisting of sands, pebbles, breccias and fine clay to silty sand deposits (Fig. 2). The thickness of the plain's deposits varies from 30 m to 70 m, whilst along the fluvio-torrential deposits of the river Asopos exceeds 100 m. As a result of their origin the deposits are characterized by high degree of heterogeneity and anisotropy.

Within the alluvial deposits, successive confined or semi-confined aquifers and a superimposed phreatic aquifer exist. Their spatial extent is limited and on a regional scale they may be assumed to form a uniform aquifer system (Koumantakis et al., 1999). Mean groundwater level is 0.5-3 m below ground surface (b.g.s.) in the coastal area and 15-20 m b.g.s. inland, at the southern part of the study area. Highest levels are recorded in April or May and lowest in October.

Based on previous investigations (Voudouris et al., 2000; Panagopoulos et al., 2001), groundwater are of various hydrochemical types: $Ca-HCO_3$ is the dominant water type and is apparent adjacent to the main recharge zones of the aquifer system along the southern and especially the southwestern part of the studied area. $Na-HCO_3$ type, as well $Na-SO_4$ and $Na-Cl$ types, which are apparent far
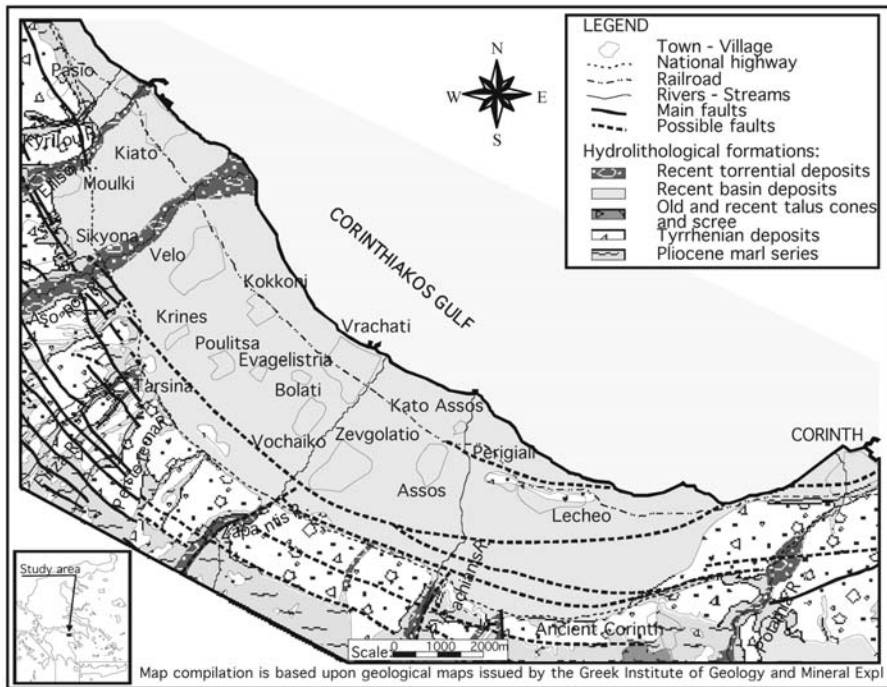
Fig. 2: Hydrolithological map of the northern coastal zone of Corinthia (Panagopoulos et al., 2002).

from the freshwater recharge zones, denote excessive mixing and ion exchange processes and saline water intrusion.

3. Methods

3.1 General

Estimation of natural background levels (NBL)

Natural background levels (NBL) play a key role as they are the starting point for the derivation of threshold values (TV). The methodology applied adopts a simplified pre-selection method, which uses the 90th or 97.7th percentile of a carefully selected dataset. The selection of the 90th or 97.7th percentile depends on the quantity and quality of the available data (Müller et al., 2006; Hinsby & Condesso de Melo, 2006).

When a large dataset is available (>60 points) the 97.7th percentile is preferred. In cases of smaller datasets or when human impact cannot be excluded the 90th percentile is recommended (Müller et al., 2006). The method may be applied if no national methodology exists or data do not allow for derivation of natural background levels by more advanced methods using environmental tracers, oxidation capacity or other pollution indicators etc.

Pre-selection criteria exclude (Müller et al., 2006).

- • Samples with ionic balance error (IBE)>10% (it is the minimum requirement for the quality of groundwater analyses):

Σ: sum of the concentrations of the ions in meq/l.

- Samples from unknown depth, samples that cannot be classified in any of the known aquifer types.
- Samples from hydrothermal aquifers.
- Data from salty aquifers (NaCl content of more than 1,000 mg/l) (coastal or influenced by evaporites). These particular conditions are not identified in the typology and should be examined separately.
- Samples with nitrate concentration >10 mg/l as they indicate human impact. The maximum admissible concentration (MAC) for the nitrates is 50 mg/l, as set in the European Directive for water intended for human consumption (EU Directive 98/83).
- Samples with ion concentration>Reference values (REF) as they indicate significant anthropogenic impact.

Data from anaerobic aquifers (DO<1 mg/l) should be studied separately, because in anaerobic conditions possible de-nitrification occurs in presence of carbon or pyrites (Griffionen et al., 2008). This may lead to inaccurate view about the actual concentration of nitrates, so additional pre-selection criteria should be used if possible. As in very few cases measurements of dissolved oxygen existed, an effort was made to implement a method proposed by Griffionen et al. (2008). This method is known as the oxidation capacity method (OXC). The use of OXC provides insight when nitrate reduction in association with pyrite oxidation is a relevant process. It is applied in fresh water samples (Cl$^-$<200 mg/l), with OXC=7[SO$_4^{2-}$] + 5[NO$_3^-$].

Where: OXC is the oxidation capacity in meq/l and the concentration of species is in mmol/l.

The values of 7 and 5 represent the amount of electrons transferred when NO$_3^-$ reduces to N$_2$ or SO$_4^-$ reduces to FeS$_2$, respectively. Samples having [OXC]>2 meq/l are removed as they indicate anthropogenic influence.

Threshold values (TV) derivation

Preliminary methodology

The preliminary methodology suggests deriving threshold values based on the following three scenarios:

<u>Case 1:</u> NBL/REF≥1/3 → TV=(NBL+REF)/2
<u>Case 2:</u> NBL/REF<1/3 →TV=2xNBL
<u>Case 3:</u> NBL/REF≥ 1 →TV=NBL

Case 2 was removed from the final proposed method, as it led to small threshold values, difficult to be achieved and implemented in practice (Pauwels et al., 2007).

Final methodology

The methodology finally applied included only the following two scenarios:
<u>Case 1:</u> NBL/REF<1 →TV=(NBL+REF)/2
<u>Case 2:</u> NBL/REF≥1 →TV=NBL

According to the European groundwater directive, any significant and sustained upward pollution
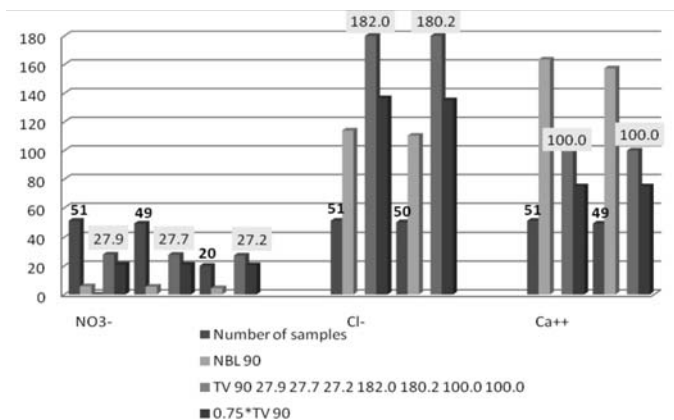
Fig. 3: Considered number of samples and corresponding values derived, NW Achaia basin. Varying number of considered samples relate to successive exclusion criteria applied on datasets as explained in the methodology section.

trend will have to be reversed when reaching 75% of the EU-wide groundwater quality standards and/or threshold values.

Pollutants for TV derivation

The pollutants considered for TV derivation were concentrations of major ions Ca^{2+}, Mg^{2+}, Na^+, K^+, HCO_3^-, SO_4^{2-}, Cl^-, NO_3^-, NH_4^+ and also electric conductivity (EC) values, that are often available in Greece. The reference values (REF) used were drinking water standards (DWS) (EU Directive 80/778 and EU Directive 98/83) and irrigation standards (Panoras & Ilias, 1999). The standards considered relate to the most crucial for public health and the dominant water use in Greece, respectively.

Selection of the reference quality standards

The considered receptor should be defined (linked surface waters, dependent terrestrial ecosystems or groundwater 'itself'-groundwater protected against pollution on its own right) (EU Directive 2006/118). In the study areas considered in this paper, groundwater 'itself' is selected.

3.2 Data analysis

NW Achaia

The methodology was applied to 51 samples collected in May 1992 (Voudouris, 1995). As the number of samples is small (N<60), NBL 90 is selected and therefore TV 90 derived. There were no sample exclusions based on the ionic balance error (IBE >10%) and the salinity ($[Na^+]$+$[Cl^-]$>1000 mg/l) criteria. TV's for nitrates were derived with the typical methodology (without taking into consideration possible anaerobic samples in datasets), as well as with the OXC method. 29 samples were additionally excluded when applying the OXC method.

Calculated TV's with both methods differ little with one another. TV 90 for nitrates was ~27 mg/l. High TV's of Ca^{2+} are attributed to the presence of $CaCO_3$ in the basin's sediments, the extensive outcrop of limestones upstream and the influence imposed by the hydrochemical character of groundwater recharge water. Also saline intrusion in the coastal aquifers results in high TV's of Na^+ and Cl^- ions. In figure 3 concentrations of NO_3^-, Cl^-, Ca^{2+} ions are presented in relation to the number of samples derived when applying the pre-selection criteria.
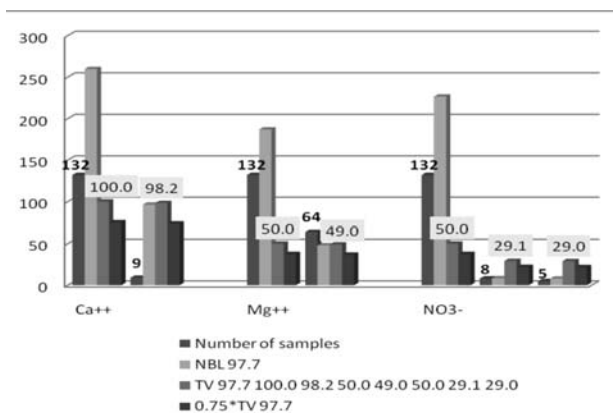
Fig. 4: Considered number of samples and corresponding values derived, coastal Corinthia basin-sampling period May 1997. Varying number of considered samples relate to successive exclusion criteria applied on datasets as explained in the methodology section.
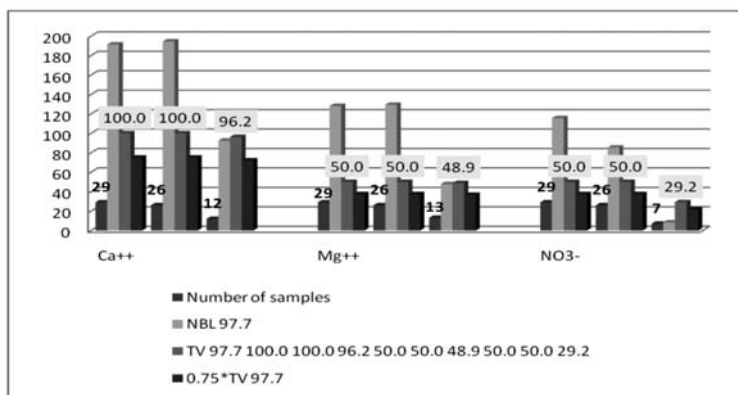
Fig. 5: Considered number of samples and corresponding values derived, coastal Corinthia basin-sampling period October 1997. Varying number of considered samples relate to successive exclusion criteria applied on datasets as explained in the methodology section.

Coastal Corinthia

A network of boreholes and wells distributed over the studied region was sampled in May 1997, October 1997 and May 1998, and 132, 29 and 69 samples were taken respectively. In all cases TV's for nitrates were derived with the OXC method as well. The values occurred differed a little from the conventional methodology. From the overview of the available data, it is expected that groundwater resources of coastal Corinthia are heavily polluted. This fact, along with the adequate number of samples available (>60), lead to the use of P97.7 for the estimations of NBL and TV's, as a less stringent approach. Average value of 7.0<pH<8.0 indicates slightly alkaline environment, while high conductivities are related to saline intrusion. Saline intrusion also results in increased values of Na^+ and Cl^- concentrations. Ca^{2+} and Mg^{2+} ions also exhibit high concentrations along the main freshwater recharge zones (south and especially southwestern edge of the basin), and this is attributed to the origin of freshwater recharge and also to the high $CaCO_3$ content of the aquifer matrix. This is illustrated in figures 4, 5 and 6 for the three sampling periods. Moderate to high K^+ ion concentrations are attributed to mixed-type fertilizers that contain nitrogen, potassium and phosphate (Voudouris et al, 2000). A great number of septic tanks which receive domestic wastewater, and in-
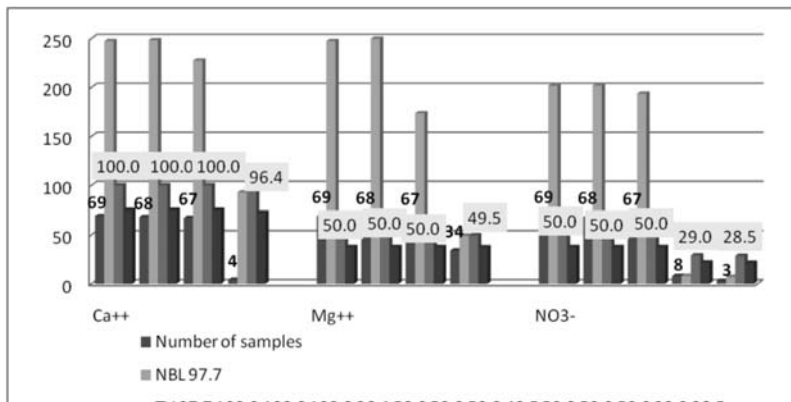
Fig. 6: Considered number of samples and corresponding values derived, coastal Corinthia basin-sampling period May 1998. Varying number of considered samples relate to successive exclusion criteria applied on datasets as explained in the methodology section.
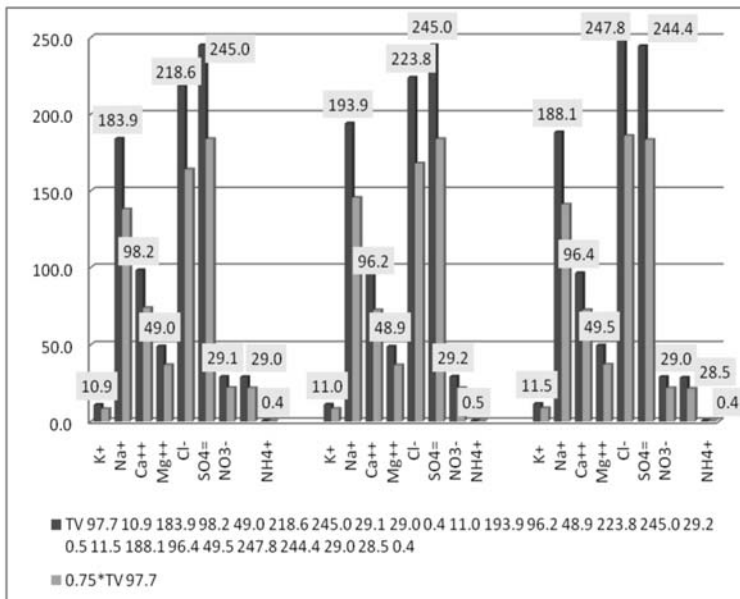
Fig. 7: Derived values for selected parameters over the 3 considered sampling periods, coastal Corinthia basin. Varying number of considered samples relate to successive exclusion criteria applied on datasets as explained in the methodology section.

tensified agricultural activities drive nitrates' concentrations to high levels. Occasional NH_4^+ ion increased concentrations are recorded and attributed to organic matter fission.

As far as Ca^{2+}, Mg^{2+}, SO_4^{2-} and NH_4^+ ions are concerned, TV's are too close to the limit values of drinking water. For nitrates TV is close to 29 mg/l. Figure 7 is representative of these facts and of course indicative of the significant degradation in groundwater's quality.

4. Conclusions-Results

P.90.0 yields small values closer to the median approach, while P97.7 provides higher values that are easier to comply with. Alternatively, where possible threshold values for NO_3^- were derived using the OXC method. It was concluded that the calculated values differed a little from those derived employing the standard methodology.

P.90.0 proved to be a better approach towards establishing values that opt for environmental protection. On the other hand, P.97.7 would be an option for cases of heavily polluted groundwater bodies that is more realistic in terms of goals to be accomplished (reach values below the assigned TV). Overall, the proposed methodology provided reasonable results. It suggests a good measure of evolving pollution in a specific groundwater body, prior to reaching any used reference value that indicates in most cases an alarming and prohibitive for use condition, (e.g. the use of 50.0 mg/l for nitrates as set in the European Directive for water intended for human consumption).

Application of the presented methodology is a dynamic process combining scientific methods, monitoring data, practical experience and of course socio-economic impacts. Finally, given a groundwater body where a broad set of quality and quantity data is available, the option for NBL's estimation is to apply scientifically sound methods (e.g. hydrochemical simulations, component separation by concentration separation analysis). Clearly, the procedure described only accounts for substances which occur naturally, whereas for substances that are purely synthetic with no natural sources, the NBL should be set to zero (Pauwels et al., 2007).

In conclusion, the proposed methodology offers a great degree of freedom to member states to design and implement environmental protection policies that have a sound scientific basis and on the same time achieve a balance between the environment and the socio-economic welfare of a region. In contrast to the conventional approaches employed so far, this is methodology brings forward an entirely new philosophy that sets higher, reliable and more comprehensive standards to environmental protection and safeguard of aquifer systems.

5. Acknowledgments

6. References

Daskalaki P., Voudouris K., 2007. Groundwater quality of porous aquifers in Greece: a synoptic view, *Environmental Geology*, 54, 505-513.

Edmunds WM., Shand P., Hart P., Ward RS., 2003. The natural (baseline) quality of groundwater: a UK pilot study, *Sci. Total Environ.*, 310, 25-35.

EC Directive 2000/60/EC of the European Parliament and of the Council of 23 October 2000 establishing a framework for Community action in the field of water policy. *Official J. Eur. Communities* L 327:1–72.

EC Directive 2006/118/EC of the European Parliament and of the Council of 12 December 2006 on the

protection of groundwater against pollution and deterioration. *Official J. Eur. Union,* L 372:19–31.

EC Directive 98/83/EC, On the quality of water intended for human consumption, *Official Journal of the European Communities*, L 330, 32-54.

Hinsby K., Condesso de Melo MT., 2006. Application and evaluation of a proposed methodology for derivation of groundwater threshold values: a case study summary report, www.wfd-bridge.net.

Griffionen J., Passier H., Klein J., 2008. Comparison of selection methods to deduce natural background levels for groundwater units, *Environ. Sci. Technol.*, 42, 4863-9.

Koumantakis, J., Panagopoulos, A., Voudouris, K., Stavropoulos, X., 1999. *Hydrogeological study of groundwater artificial recharge of the northern coastal and sub-hilly zone of Corinthia Prefecture*. Final report (in Greek).

Lambrakis, N., Voudouris, K., Tiniakos, L., Kallergis, G., 1997. Impacts of simultaneous action of drought and overpumping on Quaternary aquifers of Glafkos basin (Patras region, western Greece). *Environmental Geology*, 29 (3/4), 209-216.

Müller D., Blum A., Hart A., Hookey J., Kunkel R., Scheidleder A., Tomlin C., Wendland F., 2006. *Bridge Project*, Deliverable 18: Final proposal for a methodology to set out groundwater threshold values in Europe.

Panagopoulos A., 1995. A methodology for groundwater resources management of a typical alluvial aquifer system in Greece, *PhD Dissertation*, The University of Birmingham, UK.

Panagopoulos, A., Voudouris, K., Hionidi, M., Koumantakis, J., 2002. Irrational water resources management impacts on the coastal aquifer system of Corinthia. *Proceedings of the 6th International conference Protection and Restoration of the Environment, Vol. 1*, 419-426, Skiathos.

Panagopoulos A., Voudouris K., Koumantakis J., Hionidi M., 2001. Groundwater evolution of the northern Corinthian region coastal aquifer system, as indicated by Hydrochemistry, *Proceedings of the 9th International conference of the Geological Society of Greece, Vol. XXXIV*, No. 5, 1991–1997, Athens.

Panoras A, Ilias A., 1999. Irrigation with treated domestic effluent, 175 p (in Greek).

Pauwels H., Muller D., Griffionen J., Hinsby K., Melo T., Brower R., 2007. *Bridge Project*, Publishable final activity report.

Voudouris K., 1995. Hydrogeological conditions in northwestern part of Achaia. *PhD thesis*, Department of Geology, University of Patras (in Greek).

Voudouris, K., Lambrakis, N., Papatheodorou, G., Daskalaki, P., 1997. An application of factor analysis for the study of the hydrogeological conditions in Plio-Pleistocene aquifers of NW Achaia (NW Peloponnesus, Greece). *Mathematical Geology*, Vol. 29, No 1, 1997, 43-59.

Voudouris, K., Panagopoulos A., Koumantakis J., 2000. Multivariate statistical analysis in the assessment of hydrochemistry of the northern Corinthia Prefecture alluvial aquifer system (Peloponnese, Greece). *Natural Resources Research*, Vol. 9, No 2, 135-143.

Voudouris K., Panagopoulos A., Koumantakis I., 2004. Nitrate pollution in the coastal aquifer system of the Corinthia Prefecture (Greece), *Global Nest: the Int. Journal*, Vol. 6, No 1, 31-38.

Voudouris, K. 2006. Groundwater Balance and Safe Yield of the coastal aquifer system in North Eastern Corinthia, Greece. *Applied Geography*, Volume 26, 291-311.

World Health Organization (WHO), 2006. Guidelines for drinking-water quality.

ENVIRONMENTAL MANAGEMENT OF MINE WATER, CONSIDERING EUROPEAN WATER LEGISLATION. CASE STUDY OF MEGALOPOLIS MINES

Dimitrakopoulos D.[1] ,Vassiliou E.[2], Tsangaratos P.[2], Ilia I.[2]

[1]*Public Power Corporation (PPC-DMAOR/DEI),Kifisou & Dirachiou 89,Athens, Greece*

ddimitrakopoulos@gmail.com

[2]*National Technical University of Athens, School of Mining and Metallurgical Engineering, Laboratory of Engineering Geology and Hydrogeology,*

elvas@metal.ntua.gr, ptsag@metal.ntua.gr, gilia@metal.ntua.gr

Abstract

Mining activities causes many environmental problems to the surrounding areas, as other industrial activities do also. However mine water pollution, is considered a tough task to handle, as it requires specific regulations, quite distinct from those applicable to most other industrial processes. Even though there are several federal laws and regulations in Greece and in the European Union that influences the mining industry and mine water management, still certain factors complicates their implementation. The aim of this paper is to present a brief description of mining legislation in European Union and in Greece and also the efforts of Public Power Corporation (DEI), to integrate the Directive 2000/60/EC and Greek legislation in mining sector. The study is focused in Megalopolis open pit and in its surrounding, where lignite exploitation takes place and management of mine water is implemented. The outcomes of this effort are evaluated, considering the specific environmental conditions of the surrounding area and suggestions and methods, for mine water management, are proposed.

Key words: *mine water, management, water legislation, open pit, Megalopolis, pollution.*

1. Introduction

In mining industry, operations must meet standards that underlie federal and state laws which deal with the protection of the environment as a whole and especially surface and ground water from contamination. Until recently, mining in European Continent has been excluded from the scope of major environmental directives or has reserved a certain freedom for interpretation. Although the polluted ground and surface water has long been subject to legislative framework, mine water pollution has not been confronted equally.

Changes in European mining policy have been initiated as a result of the pressure from the public arena and its willingness to bring forward policy proposals involving environmental issues. A research project ERMITE (Environmental Regulation of Mine Waters in the European Union), was funded by the EU in order to provide guidelines for developing specific European legislation concerning water management in the mine sector. The general aim of the framework was to protect the water resources environment (rivers, lakes, coastal waters, and ground-

water), preventing pollution and setting control mechanisms for all pollution sources, ensuring sustainable management of natural resources and methods of detergent techniques.

Mine Water, was adopted by ERMITE to be referred as water which is in mined ground (including waste rock/tailings depositories) and/or which is now flowing from mined ground into adjoining water bodies (such as streams, wetlands, lakes, aquifers and oceans). It defined the potential impacts of mining activity on water environment, at various phases of the mining cycle (ERMITE, 2004a). In many cases, mine water could create massive contaminating events due to high concentrations of specific chemical elements, and thus appropriate measures should be implemented.

Mining activity in Greece has a very long history, as it's revealed by many cases of systematic exploiting of natural resources in Ancient Greece. The silver mines of Lavrio and the famous marble of Naxos are examples, which helped the establishment of the various Greek city states. Nowadays, the most significant mining exploitation in Greece is exerted by Public Power Corporation (DEI), which produces about $60*10^6$ tn of lignite annually excavating $360*10^6$ m^3 of waste material. At the present time, DEI (DEI) focuses the development of mining activity in Ptolemaida, Amynteo, Florina and Megalopolis. At the same time new lignite deposits have been discovered for exploitation in Drama and in Elassona. On average 1.7 m^3 of water per tn of lignite is pumped for dewatering and protection of the mines from groundwater and surface water. In some mines, this ratio increases to 2.5 m^3 water/tn of lignite.

The above mining activity is performed in accordance to national environmental legislation framework, which includes numerous modifications and replacements of previous rules, laws and instructions (Tsangaratos et al, 2008). This appears to be one of the drawbacks of development that extractive industry has to handle (Kavalopoulos, 2006). Moreover, as a Member State of EU, Greece must follow European Communities legislation, which takes precedence over national legal provisions. The European Community legislation includes treaties, as primary legislation, regulations, directives and decisions, as secondary legislation. The objectives of the Directives are to be achieved within a certain time-limit while leaving the national authorities the choice of form and means to be used (Hamor, 2004).

The aim of this paper is to present a brief description of the new perception which mine water management receives through European Union and the efforts of DEI to integrate the Directives 2000/60/EC, 2009/90/EC, 2008/105/EC and the Greek legislation considering mining activity. A case study of Megalopolis lignite mines is presented, were an actual mine water management program has been initiated under certain legislation framework.

2. Mining legislation in European Union

Mining activity was excluded from the Integrated Pollution Prevention and Control (IDEI) **Directive (96/61/EC)** and the **Seveso II Directive (96/82/EC),** yet introduced in the **Environmental Impact Assessment Directive (97/11/EC)**. The **Waste Framework Directive (75/442/EEC)** stated that mining waste would be excluded where they are already covered by other legislation. In addition, the **Water Framework Directive (WFD) (2000/60/EC)** applies to mining activities in a generic sense but there is no specific water legislation addressing the requirements of this sector (Amezaga and Younger, 2004).

The current framework (**Directive 2006/21/EC** on the management of waste from extractive industries, in accordance with **Directive 2000/60/EC**) implies that certain measures should be

Table 1. Main legislation framework in European Union concerning mining and water.

- **Directive 2006/21/EC** of the European Parliament and of the Council of 15 March 2006 on the management of waste from extractive industries and amending Directive 2004/35/EC - Statement by the European Parliament, the Council and the Commission.

- **Directive 2003/105/EC** of the European Parliament and of the Council of 16 December 2003 amending Council Directive 96/82/EC on the control of major-accident hazards involving dangerous substances.

- **Council Directive 96/61/EC** of 24 September 1996 concerning integrated pollution prevention and control.

- **Directive 2000/60/EC** of the European Parliament and of the Council of 23 October 2000 establishing a framework for Community action in the field of water policy.

- **Directive 2004/35/CE** of the European Parliament and of the Council of 21 April 2004 on environmental liability with regard to the prevention and remedying of environmental damage.

- **Council Directive 75/442/EEC** of 15 July 1975 on waste, in use for waste of extractive industry which are not included in Directive **2006/21/EC**.

- **Council Directive 92/32/EEC** of 30 April 1992 amending for the seventh time Directive **67/548/EEC** on the approximation of the laws, regulations and administrative provisions relating to the classification, packaging and labelling of dangerous substances.

- **Council Directive 85/337/EEC** of 27 June 1985 on the assessment of the effects of certain public and private projects on the environment.

- **Directive 2001/42/EC** of the European Parliament and of the Council of 27 June 2001 on the assessment of the effects of certain plans and programmes on the environment.

- **Directive 2003/4/EC** of the European Parliament and of the Council of 28 January 2003 on public access to environmental information and repealing Council Directive **90/313/EEC**.

taken by the extractive industries in order to prevent soil and water contamination. In particular, these measures should present a waste management plan that would prevent or reduce the disposal of waste and the negative impact of them, encourage waste recovery through recycling, re-use or reclaiming and finally to encourage the short and long-term safe disposal of waste. Concerning water resources, they should evaluate the quantities and the quality of the pumped water, minimize surface and groundwater contamination, and finally treat the contaminated water before discharging. The main mining and water legislation framework in EU is shown in Table 1.

3. Mining legislative framework and water policy in Greece

Mining legislation in Greece, although it prevents irrational mining, is responsible for a weak environmental performance. There are numerous federal laws and regulations that influence Greek mining industry (Table 2). However, four laws, concerning environmental matters, are prominent for Greek mining industry, Code of Mining and Quarrying Works (CMQW), L. 998/1979, L. 1650/1980 and Interministerial Decree 69269/5387/1990.

Table 2. Main Mining and water legislation in Greece.

- **Law and Decree-law which adapt EU directives in the Greek legislation**
- **D.L. 51/2007** (FEK 54/A'/8.3.2007) Determination of measures and procedures for the holistic protection and management of water resources in accordance of Directive 2000/60/EC
- **L 3199/2003** (FEK 280/A'/9.12.2003) Protection and management of water resources – according with the Directive 2000/60/EC
  - **Decisions regarding disposal limits of mine water which concern certain mining companies**
  - **Decisions regarding disposal limits of liquid effluents applied in prefecture level**
  - **Procedure for Environmental Permitting**
- **Joint Ministerial Decision (KYA) 126880/2007** (FEK 435/B'/29.3.2007)
- **KYA 37111/2021/2003** (FEK 1391/B'/29.9.2003)
- **KYA 13727/724/2003** (FEK 1087/B'/5.8.2003)
- **KYA 11014/703/F104/2003** (FEK 332/B'/20.3.2003)
- **KYA 25535/3281/2002** (FEK 1463/B'/20.11.2002)
- **KYA 15393/2332/2002** (FEK 1022/B'/5.8.2002)
- **Law 3010/2002** (FEK 91/A'/25.4.2002) reconciliation of 1650/1986 with 97/11/EC and 96/61/EC
- **KYA 69269/5387/1990** (FEK 678/B'/25.10.1990)
- **Law 1650/1986** (FEK 160/A'/16.10.1986) On Protection of the Environment

Concerning environmental issues, the CMQW states that mining and quarrying works should be performed in a way that environmental damage, should be restricted to the minimum extent. It also defines that mining firms are obligated to implement mitigation measures for adverse impacts. For this purpose, mining enterprises have to co-operate with the governmental agencies as well as Prefecture and Local authorities, especially for the after-use planning of mine sites. The involvement of many authorities, agencies and institutions (Ministry of Environment, Physical Planning and Public Works, Ministry of Agriculture, Ministry of Development, Prefecture agencies, Greek Mines Inspectorate) that appear to be responsible for the environmental issues in Greece, could be accused in some extent for weak environmental protection performance. They lead to delays in the environmental permitting procedure, operational problems and declaration of mining works (Kaliampakos and Damigos 2000).

The main features of the current legal framework concerning mining activities in Greece are the following:

(a) Environmental protection is covered by general environmental rules,

(b) Land-use rules govern whether land is available for mining activity,

(c) An environmental impact assessment study is always required in order to proceed to mine development,

(d) Reclamation of mined land is obligatory; however, the reclamation requirements are only qualitatively defined,

(e) Reclamation bonds (namely letter of credits) are being used in order to ensure that mining companies will perform the required reclamation works.

As already discussed although the concept of mine water management is newly introduced in the European legislation, Greece still does not have specific legislation for mine water. There is limited reference, in mine water considering it as industrial effluent, in order to prevent and minimize the potential pollution of the adjoining water bodies. Nevertheless, many efforts for the determination of the environmental terms in mines with specific obligations concerning the mining exploitations are done through the Joint Ministerial Decisions (KYA).

4. Case Study of Megalopolis lignite mines

In Megalopolis, three lignite open pit mines operate today, Xoremi, Marathousa and Kiparissia, whereas Thoknia lignite mine has recently finished its activity (1994). A power plant for the compulsion of lignite and generation of electricity is also located in this area. Four are the significant characteristics of the area (Fig.1):

— Alfios River flows near all the mines and several diversions of its riverbed were made, for the protection and proper operation of the mines.
— Waste and by-products of the desulfurization plant gradually fill the remnant void of Thoknia open pit mine, where a ''lake'' has been created also.
— A poor aquifer exists in the area of Thoknia, below the lignite layers in the neogene sediments.
— In the carbonate rocks, which form the basement and the surrounding mountains of the mines, a karstic system exists. Three karstic aquifers of great importance have been defined there.

Under the scope of mining exploitation in Megalopolis, DEI is obliged to obtain an exploitation license from the competent Ministry (YPEXODE). This license shall be accompanied by an order of adoption environmental terms, as described in the relevant KYA num. YPEXODE/GDP/DPS/rel.100532/200/23.1.2004. In this particular KYA, the obligations of DEI and measures taken for the management and protection of waters are as follows:

1. The pluvial water that is pumped from surface ponds in the mine undergoes relevant treatment before discharging in surface recipients.

2. All diversion works of surface waters to Alfios River are kept free from sediment and vegetation, in order to ensure discharge capacity of the river.

3. The groundwater pumped from the mines, is used to cover the industrial needs of DEI. In case there is quantitative adequacy and appropriate quality, it is available to cover water supply or irrigation needs of the region.

4. The total water balance in the immediate and wider range of intervention is determined with accuracy. The impacts on the hydrological balance of the region are investigated, giving emphasis on the river system of the region. The above are included in a hydro-
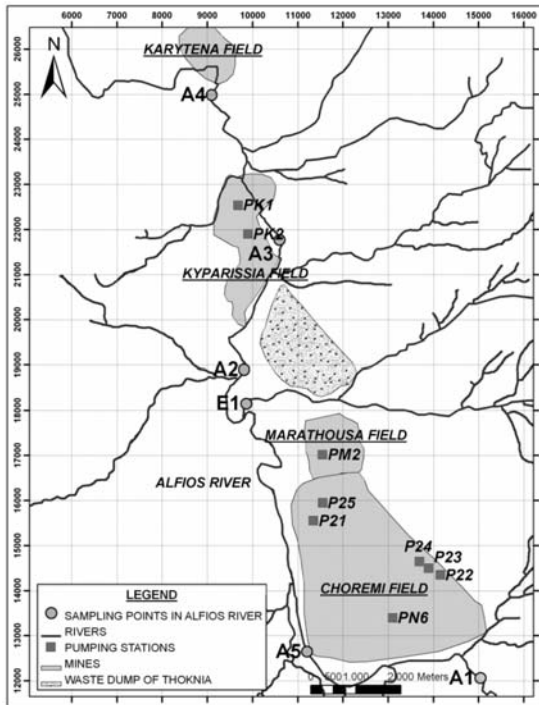
Fig. 1: Map of sampling points in Megalopolis mines.

geological report, which is submitted to the authorities.

5. The quality of water discharged in Alfios River is monitored and pH, temperature and conductivity are measured on continuous basis. Measurements of the concentrations of pendulous and dissolved particles, as well as trace elements As, Cd, Pb, Zn, Cr, Hg, Ni, V and Cu, are done once per three months, according to the specific KYA. Moreover, the liquid wastes of the mining activity undergo biological treatment for the purpose of reuse.

6. The water level and pumping rate of ground water is recorded on continuous basis.

5. Evaluating the mine water management

The management of mine water during and after the exploitation is of great importance for the mining companies and the local societies (Dimitrakopoulos D., 1996, Modis K., 2009). DEI is obliged to carry out several chemical analyses and to present them in annual reports.

In Megalopolis mine, the measurements described above were plotted in diagrams, and statistical analysis was done in order to evaluate them (Fig.2, 3, 4).

PH and electrical conductivity (EC) are within the acceptable limits, in accordance with the environmental terms (EC 2000μS/cm and pH 7.5-8.5). The total dissolved solids (TDS) appeared with particularly high values, in samples taken from the sumps (Fig. 2). The particular high values of Molybdenum (upper limit 75ppb) observed in A2, A3, and A4 of Alfios River are attributed to the chemical composition of lignite (Fig. 3). The concentrations of sulphide SO_4^{-2} are found to be within the acceptable potable limits, with an exception of the A3 during 2004, which, however, seems to decrease, reaching in 2006 the acceptable limits (Dimitrakopoulos et al., 2007).
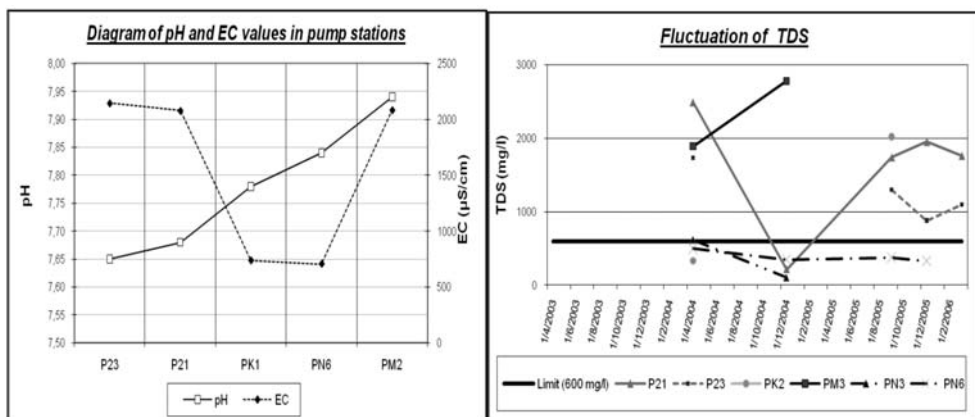
Fig. 2: Diagrams of average values of pH and EC in Megalopolis and the fluctuation of TDS for the period 2003-2006.
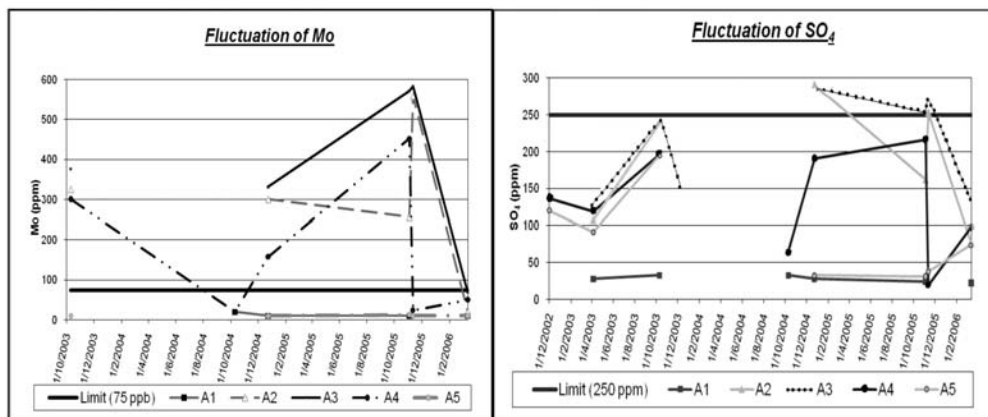
Fig. 3: Diagrams of Mo values and SO_4^{-2} in Alfios River.

In Figure 4, the statistical analysis is presented, in which the results are interesting. The maximum average value in pH was measured in Alfios River but this value isn't above the limits for potable use. The high pH value (alkaline environment) does not help the dissolution of cations from the geological formations or the waste dump. As a consequence the water of Alfios River is generally of good quality. The lower mean values, of parameters under investigation, are observed in the karstic aquifer. This is a strong indication that it has not been affected by mining activity and generally is of good quality. The water of the ponds and the ground water in the waste dump area of Thoknia, are the most degrading and present the higher values in E.C., TDS, SO_4^{-2}, Mo (fig. 4). These high values are not reflected in the samples from the deep aquifer below the dump, the karstic aquifer or Alfios River. The conclusion from this analysis is that the mining activities have not affected the main water resources of the area. The increased concentrations of Mo in Alfios are due to the fact that it is part of the geochemical texture of lignite in Megalopolis and it is highly soluble. All the others chemical elements which are increased, come from the urban and agricultural activities in the area. Main part for the increased values of Ca^{2+} and Mg^{2+} has the geological formations (carbonic) in Megalopolis (Waterchem, 2007).

Sample ID		pH	EC _S/cm	TDS mg/l	Ca ppm	Mg ppm	SO₄ ppm	Mn ppb	Ba ppb	Mo ppb
RIVERS	MIN	7,64	250,00	180,00	6,40	4,65	19,50	2,00	24,00	2,08
	MAX	8,42	1300,00	1010,00	229,00	25,10	573,00	64,00	70,30	583,00
	AVERAGE	8,04	638,04	415,87	94,04	14,43	134,67	11,90	46,87	242,74
PONDS I-II IN THOKNIA	MIN	6,90	840,00	570,00	118,00	10,90	308,00	2,00	50,80	730,00
	MAX	8,00	4370,00	3120,00	684,00	64,30	1807,00	2154,00	113,00	11110,00
	AVERAGE	7,58	2113,85	1733,85	350,77	34,31	1050,77	434,42	86,25	4487,3
PONDS IN OTHER MINES	MIN	6,85	430,00	102,00	5,80	1,49	82,00	2,00	18,00	5,00
	MAX	11,00	3660,00	2810,00	580,00	129,00	1650,00	2090,00	205,00	547,00
	AVERAGE	7,77	1815,72	1273,90	299,71	52,59	728,00	472,50	80,90	104,96
KARSTIC AQUIFERS	MIN	7,65	380,00	230,00	75,00	8,39	16,10	2,20	20,00	10,00
	MAX	8,10	550,00	330,00	87,80	17,00	37,30	112,00	65,30	12,60
	AVERAGE	7,99	487,00	293,33	81,88	14,45	29,58	46,90	34,40	10,98
DEEP AQUIFER IN THOKNIA	MIN	7,20	570,00	360,00	34,80	12,10	4,90	4,10	52,40	5,00
	MAX	8,10	1130,00	730,00	210,00	20,00	228,00	538,00	503,00	32,50
	AVERAGE	7,63	882,00	582,00	148,68	15,97	97,86	158,07	209,12	18,78
GROUNDWATER ARROUND WASTE DUMP	MIN	6,60	540,00	450,00	11,80	11,60	0,39	59,00	0,12	5,00
	MAX	8,90	2940,00	1710,00	506,00	91,70	1181,00	5082,00	884,00	97,70
	AVERAGE	7,65	1504,11	950,77	186,71	29,44	180,94	687,04	242,73	31,64
GROUNDWATER IN WASTE DUMP	MIN	6,41	870,00	580,00	115,00	0,30	86,70	14,00	4,00	5,00
	MAX	9,40	4980,00	3200,00	1030,00	167,00	2080,00	4792,00	250,00	5800,00
	AVERAGE	7,46	2587,91	1959,80	459,94	73,22	1224,23	772,51	39,94	616,94

The maximum average value

Minimum average value

Fig. 4: Statistical analysis of sampling in Megalopolis (Waterchem 2007).

Besides the obligations of DEI and the measures described above, the company participated in three European Research Programs (Minwater, Interwatpol, Waterchem). In these the impact of mining activity in the aquatic environment was investigated and various methods, for the management and the protection of surface and groundwater, were proposed (Dimitrakopoulos D., 1998, Stefouli M., 2005). During these Research Projects, the geochemical modeling PhreeqC was applied in Megalopolis in order to investigate the quality of mixed waters from the karstic aquifer, Alfios River and the mine water from Thoknia area (Vassiliou et al., 2008). The result of the investigation verified that there is no remarkable influence of the dumping area to the quality of Alfios River and karstic aquifer.

6. Conclusions

- In Megalopolis lignite mines, a coordinated attempt to monitor and control the quality of groundwater and surface waters, with regularly water table measurements and samplings, is made, beyond the obligatory measurements suggested by the relevant KYA.
- According to the relevant KYA, DEI has planned scheduled water table measurements in order to control the water balance of the area
- In the area of Megalopolis there is intensive mining activity. However the water quality of Alfios River and karstic aquifer, which are the main water bodies of the area, is generally good. This is attributed to the implementation of the process, which follows the relative legislation framework.
- The legislation framework concerning the management of water in Greece appears to

have certain gaps, since there is not specific legislation for treatment and management of mine water. The lawmaking of the relevant KYA, applied to each Prefecture does not solve the problem.

5. References

Amezaga, J., Younger L., 2004. ERMITE: supporting European policy making on mine wastes and waters. In *Proceedings of Mine Water 2004*., Newcastle upon Tyne, UK. University of Newcastle upon Tyne, 19-23 September, Vol 2, 41- 46.

Dimitrakopoulos, D., Vassiliou, E., Founda, M., 2007. Impacts of mining activities on water resources to Megalopolis lignite area, *EGU General Assembly*, Vienna., Austria, 15-20 April. ,

Dimitrakopoulos D, Voight, R., 1996 "Postmining water management problems in Ptolemais-Amynteon Lignite district, Macedonia, Greece". *Proceedings of the Geocongress, Grundwasser und Rohstoffgewinnung*, Freiberg, Germany, pp 49–54.

Dimitrakopoulos, D., Koumantakis, J., Poutios, G., Heliadis, K., 1998: Methods of artificial recharge in areas with open pit exploitations. Case of South field Open Pit, West Macedonia, Greece. *5th International SWEMP*, Ankara, Turkey.

ERMITE Consortium, 2004. "Mining Impacts on the Fresh Water Environment: Technical and Managerial Guidelines for Catchment-Focused Remediation". In: Younger PL, Wolkersdorfer C (eds). *Mine Water and the Environment*, Suppl. Issue 1. Berlin: Springer.

Hamor, T., 2004. Sustainable Mining in the European Union: The Legislative Aspect. *Environmental Management*, 33, 252-261.

Kaliampakos, D., Damigos, D., 2000. Mining Regulation in Greece: Perspectives on its Environmental Performance, *Proceedings V International Conference on Clean Technologies for the Mining Industry*, Santiago, Chile, 9-13 May, 271-277.

Modis, K., Vatalis, K., Papantonopoulos, G., Sachanidis, Ch. 2009 Uncertainty management of a hydrogeological data set in a greek lignite basin, using BME Published online: 13/1/2009 in *Stochastic Environmental Research and Risk Assessment* DOI 10.1007/s00477-008-0298-3 Publisher Springer-Verlag Berlin / Heidelberg.

Kavalopoulos, C., 2006. "Extractive activity in Greece: importance, opportunities, challenges, problems", 3rd European Workshop: *Mining and Environment*, Patra, Greece, 1-3 June.

Stefouli, M., Dimitrakopoulos, D., Papadimitrakis, J. Charou, E., 2005: Monitoring and assessing internal waters (lakes) using operational space born data, field measurements and numerical models. EWRA European water 9/10/2005, pp.25-33, E.W. Publications.

Tsangaratos, P., Vassiliou, E., Grigorakou, E., Rozos, D., 2008. Environmental management of Mine Water in Greece and in the European Union, *International Conference Geology and Water Management: Resources, Risks and Regulations*, Athens.

Vassiliou, E., Founda, M., Dimitrakopoulos, D., 2008. The water quality of Alfios River and the effects on it from the mining activities, in the area of Megalopolis. Estimating the quality of the river system by Phreeqc modeling, *EGU General Assembly*, Vienna, Austria, 13 -18 April.

WATERCHEM: Optimization of Mine Water Discharge by Monitoring and Modelling of Geochemical Processes and Development of Measures to Protect Aquifers and Active Mining Areas from Mine Water Contamination. Financed by RFCS, Research Fund For Coal and Steel. Contract: No RFC-CR-03006 (10/2003-2/2007), 3rd, 4th, 5th, 6th, final technical reports by DEI, Project leader D. Dimitrakopoulos.

HYDROGEOLOGICAL ASSESSMENT OF GROUNDWATER DEGRADATION AT THE EASTERN NESTOS RIVER DELTA, N.E. GREECE.

Gkiougkis I.[1], Mwila, G.[2], Pliakas F.[3], Kallioras A.[4], and Diamantis I.[5]

[1] *Democritus University of Thrace, Department of Civil Engineering, Laboratory of Engineering Geology, 67100 Xanthi, Greece, jgiougis@civil.duth.gr*

[2] *Technical University of Darmstadt, Institute of Applied Geosciences, Hydrogeology Group, 64287 Darmstadt, Germany, gbmwila@yahoo.com*

[3] *Democritus University of Thrace, Department of Civil Engineering, Laboratory of Engineering Geology, 67100 Xanthi, Greece, fpliakas@civil.duth.gr*

[4] *Technical University of Darmstadt, Institute of Applied Geosciences, Hydrogeology Group, 64287 Darmstadt, Germany, kallioras@geo.tu-darmstadt.de*

[5] *Democritus University of Thrace, Department of Civil Engineering, Laboratory of Engineering Geology, 67100 Xanthi, Greece, jdiam@civil.duth.gr*

Abstract

This paper deals with the hydrogeological study of the evolution of groundwater salinisation - degradation at the eastern Nestos River Delta. Relevant field works including in-situ measurements of groundwater level, pH, Specific Electrical Conductivity (SEC) and temperature took place in the years 2008 and 2009. Groundwater samples were also collected for chemical analysis at the Engineering Geology Laboratory of the Department of Civil Engineering of D.U.Th. (July of 2009). Important conclusions regarding the progress of the groundwater degradation at the study area were drawn based on the analysis of all the available data and the elaboration of the designed piezometric maps and the various maps showing the distribution of SEC, Chloride, SAR (Sodium Absorption Ratio) and Revelle coefficient values. Some managerial suggestions for the confrontation of the seawater intrusion regime of the study area are also included.

Key words: coastal aquifers, seawater intrusion, groundwater quality, N.E. Greece.

1. Introduction

Seawater intrusion is a widespread environmental phenomenon which takes place in most coastal aquifers, especially those which are located within the Mediterranean coastal zone. This is mainly due to the climatological conditions, which are related to hot and dry summers, as well as due to the extensive farming and other anthropogenic activities occurring at the coastal zone. Greece is one of the most affected countries of the Mediterranean region, partially due to the fact that farming and agriculture is a core element of the national economy (hence large amounts of groundwater are being extracted every year) and on the other hand the long shoreline of the country does not enhance the application of countermeasure techniques (high financial costs). Once seawater has intruded the coastal aquifer and the pumping conditions continue to take place extensively, the hydraulic regime
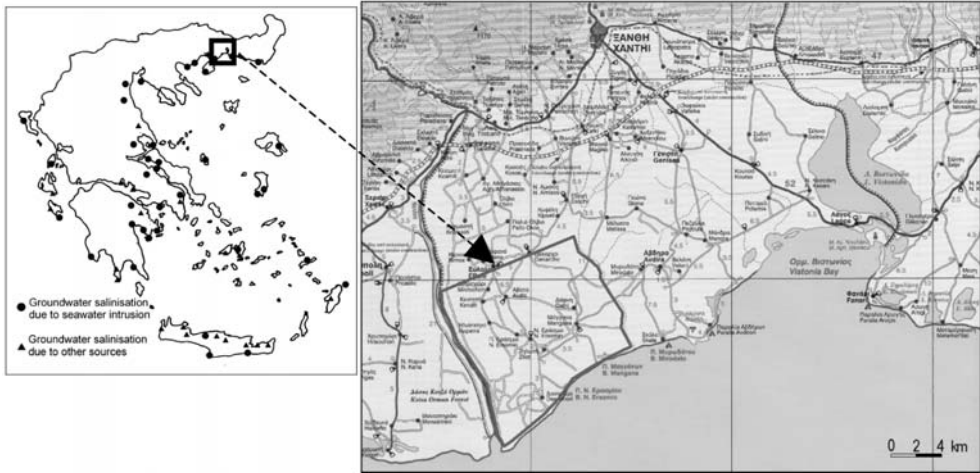
Fig. 1: Areas of groundwater salinization in Greece (modified map of the Ministry of Agriculture) and location of the study area (Gkiougkis, 2009; Kallioras, et al., 2006).

may be altered in such a manner so that it may produce active seawater intrusion. This is the case where the rehabilitation of the groundwater resources qualitative regime is rather not feasible (Gaaloul et al., 2008).

Seawater encroachment appears within the majority of the coastal aquifers in Greece, which are under hydrogeological investigation, and is responsible for their qualitative degradation (Fig. 1). Today, all scientific evidences lead to the conclusion that the encroachment of seawater into coastal aquifers is a phenomenon that regards the majority of the coastal area of northern Greece, including the coastal area of Eastern Macedonia and Thrace (Kallioras et al. 2006).

The construction of several drainage works and the increasing use of irrigation water in the east delta plain of the River Nestos, have resulted in seawater intrusion and related deterioration of the groundwater quality (Gkiougkis, 2009, Daskalopoulos, 2007, Sakkas et al., 1998, Pliakas et al., 2001). This paper deals with the study of hydrogeological and hydrochemical characteristics of the coastal aquifer system of the eastern delta area of the Nestos River, with the aim of contributing to the understanding of processes which lead to groundwater quality degradation due to over pumping of groundwater for irrigation from the unconfined coastal aquifer.

2. Geomorphological and geological framework, hydrogeology

The study area is located south of the city of Xanthi in the prefecture of Xanthi, N.E. Greece. It is bounded to the west by the Nestos River and to the south by the Aegean Sea (Fig. 1). The morphology of the region is characterised by a very low relief and shallow pits, to the S and SE, forming small ponds, which are part of the eastern Nestos delta wetlands. The geomorphology of the study area is characterised as being generally flat, with elevation of a few meters above sea level throughout the entire study site. The most important surface water body of the area is River Nestos located to the west of the study area. It is also the one of the main sources of freshwater recharge for the coastal unconfined aquifer, as it flows through the area from the north-northwest to the south-southeast into the Thracean Sea. Laspias stream is located across the eastern side of the study area

where the degraded industrial and sewage treatment effluents are discharged. Northerly, at a distance of approximately 2km, a drainage trench is located, which after draining the northerly irrigated land, conveys water into the Laspias stream.

The main agricultural activity is cultivation of corn and cotton which is done by irrigation with groundwater from the coastal aquifer. Main crops are maize (occupying more than 50% of the land under cultivation), cereals, trefoil, sugar beet, garden products, industrial tomato, cotton and tobacco. The intensive agricultural activities in combination with the irrational use of fertilizers and insecticides have resulted in severe problems such as soil degradation, exhaustion of the aquifers potential and increase of the salt concentrations in the shallow aquifers particularly in the coastal areas.

The study area is located in a recent sedimentary delta environment of a thickness of some tens of meters created by the Nestos deposits. These alternate sand, clay and silt layering deposits, resulting from a wide range of structural and depositional processes, produce a heterogeneous geological environment. It is worth mentioning the presence of organic clay at some points due to the delta marshes. The evolution of the east part of the delta under flooding conditions has been instrumental in forming low potential aquifers in the study area (Gkiougkis, 2009; Mwila, 2009).

There is a geological study which has included the necessary relative research works such as test drillings, piezometers and geophysical exploration and the study of the well geologic logs of the study area. It was concluded that at the north side of the study area, alternate clay and mostly sand layering extend down to the depth of 30 m. A marly layer of 50 m thickness comes in between. Below the depth of 80 m, the same clay and sand layers extend again (Pliakas, et al., 2001, Sakkas, et al., 1998).

The east delta plain extends to 176.4 km^2, from which the 106.63 km^2 are cultivated (only 60%), while the coastal saline uncultivated lands extend to 45 km^2. Considering the hydrological data of Nestos Delta plain (mean annual rainfall for the period 1965 - 1996: 546.9 mm, infiltration approximately: 15%), the annual infiltration for the 131.4 km^2 area (176.4 - 45 = 131.4) is estimated at 10.8×10^6 m^3. The irrigated lands extend to 89,893 km^2, while the 35 km^2 of them meet irrigation needs from the Nestos River. The rest areas meet irrigation needs by pumping, where considering the type and the extent of the crops as also as well operation data, the annual water consumption is estimated at 27×10^6 m^3. Taking into account the amounts of the two basic parameters of the groundwater hydrologic balance mentioned above (infiltration - water consumption), a lack of about 16×10^6 m^3 water is evaluated (Pliakas, et al., 2001, Sakkas, et al., 1998). It is estimated that a small part of this lack is replaced by the Nestos riverbed percolation, at rates depending on the run of the buried old streambeds and the distance from the river (Gkiougkis, 2009; Mwila, 2009).

There are two hydrogeological systems that are formed within the alluvial deposits of the wider study area (Pliakas, et al., 2001, Sakkas, et al., 1998): (a) The shallow system, consisting of phreatic and mostly of semi-confined aquifers extended down to a depth of about 30 m. Natural recharge to this system comes mostly from the infiltration of rainfall and less from stream bed percolation of the north hilly area. During the 90s, a great amount of small diameter (3″) shallow wells (up to 20 m depth) were pumping water out of the system. Nowadays, only few of them are operated, whilst many of the other shallow wells have been replaced by deeper wells (up to 50 m depth), like in Dekarchon area. (b) The deeper system, consisting of confined aquifers extended to a depth of at least 190 m. Natural recharge to this system comes to a great extent from river Nestos percolation through buried old stream beds, and from the lateral groundwater inflows coming from the adjoining Vistonis lagoon hydrogeological basin. There are about functional 50 deep wells (up to 320 m depth), located in the main study area.
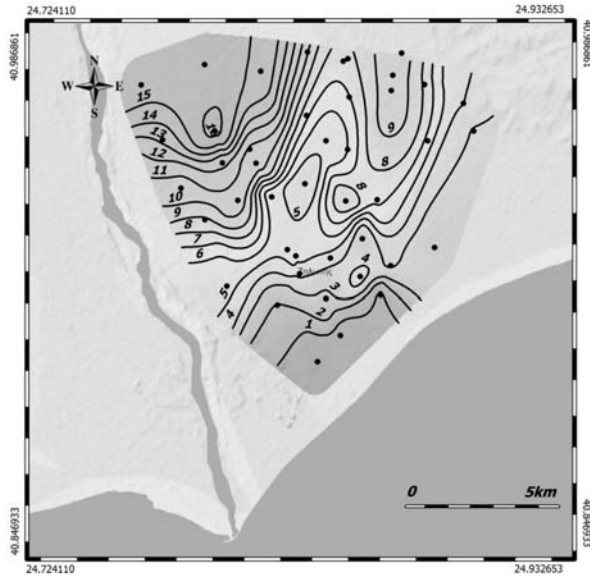
Fig. 2a: Piezometric map, October 2008 (Gkiougkis, 2009; Mwila, 2009).
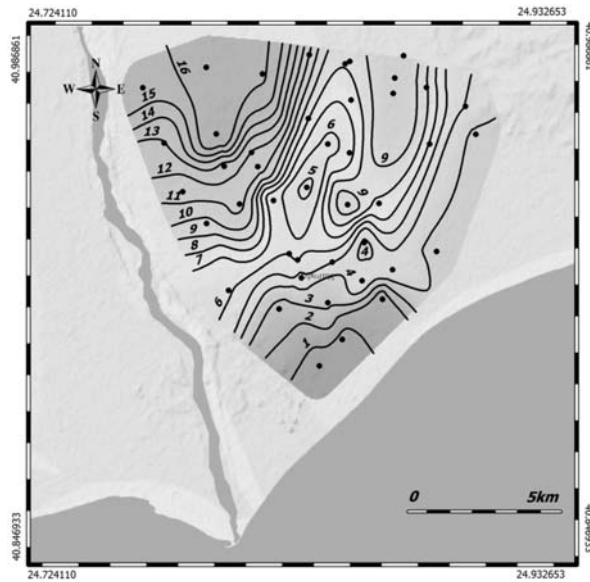
Fig. 2b: Piezometric map, April 2009 (Gkiougkis, 2009; Mwila, 2009).

Evaluation of the groundwater hydraulic parameters of the study area aquifers after working out the results from the pumping tests of 11 selected wells in the wider study area resulted in values for (Pliakas, et al., 2001, Sakkas, et al., 1998): (1) transmissivity (T), ranging from 4.0×10^{-4} to 1.1×10^{-2} m^2/sec, (2) storage coefficient (S), ranging from very low values to 10^{-3}, characterizing the aquifers of the study area as confined mainly westward, and in some sites as semiconfined.

Figure 2a shows the piezometric map of the study area as of October 2008 just after the irrigation period, while Fig. 2b shows the piezometric map for the same area in April 2009 before the irrigation period. Comparing the two maps it is worth noting that the major groundwater flow direction is from the northwest towards the south with minor flow from the N.E. and central parts of the study area towards the south.

3. Groundwater quality

The Laboratory of Engineering Geology of the Department of Civil Engineering, D.U.Th., Greece, in collaboration with the Hydrogeology Group of the Technical University of Darmstadt, Institute of Applied Geosciences, Germany, conducted a groundwater quality research at the study area during the summer of 2009. Groundwater samples were collected 30 selected wells for a period of two days, on 1/7/2009 and 2/7/2009. Sampling also included in situ measurements of the physicochemical parameters of the groundwater of the study area (pH, SEC-Specific Electrical Conductivity, Temperature). There are a few wells within the study area with SEC values above 1500 µS/cm. This could be attributed to seawater intrusion as these wells are in close proximity to the sea (Fig. 3). The wells with SEC values lower than 1500 µS/cm are mainly under constant fresh water recharge from Nestos River (Gkiougkis, 2009; Mwila, 2009).

Evaluation and assessment of the qualitative characteristics of the samples of the study area aquifer from the selected wells occurred between 3/7/2009 and 8/7/2009. Chemical analyses took place at the Laboratory of Engineering Geology of Civil Engineering Department of Democritus University of Thrace. The chemical analyses were for the determination of certain chemical parameters such as Ca^{2+}, Mg^{2+}, Na^+, K^+, HCO_3^-, Cl^-, SO_4^{2-}, NO_3^-, NO_2, NH_4, PO_4^{3-}, SiO_2, Fe^{2+}, Mn^{2+}, alkalinity M and total hardness.

The chemical analysis results show that most of the wells contain low chloride (Cl^-) with the exception of only 30% of the total wells studied which contain chloride with concentrations close to or above average. The average chloride concentration 216.64 mg/L in the wells from the study area is well below the limit of 250 mg/L (Cl^- concentration range: 15.60-1320.18 mg/L). Similarly, the nitrate (NO_3^-) concentrations in these wells show values below the maximum allowable standard for drinking water which is 44 mg/L, with the exception of a few that show values which are close to the standard or way above the standard (NO_3^- concentration range: 0.00-60.00 mg/L). Plotting and contouring of these results show the spatial distribution of the high and low values and gives insight on the possible sources of contaminations. Figure 4 shows high chloride ions concentrations in the coastal region to the east of the study area. Comparing the map for SEC (Fig. 3) to the map of chloride ion distribution (Fig. 4) it is observed that in both maps high values are observed in wells located in the coastal region to the east of the study area. The high SEC and chloride ion concentration in this region could be attributed to seawater intrusion whereas the low values to the west of the study area are as a result of continuous fresh water recharge from Nestos River. There is little or no evidence of any anthropogenic influence in the concentration levels and their distribution. Nitrate on the other hand show an even distribution across the whole study area with high values found to the northwest, south and southeastern parts of the area. This distribution pattern could be attributed to the fact that the area is under heavy agricultural activities where use of fertilizer is common, and hence the high values observed (Gkiougkis, 2009; Mwila, 2009).

The results of the calculated SAR (Sodium Absorption Ratio) values show that over 90% of the wells under investigation contain suitable water for irrigation as the SAR values are well below the critical value 10 (Fig. 5). The increase in the Na^+ ion concentration is an indicator of fresh water mix-
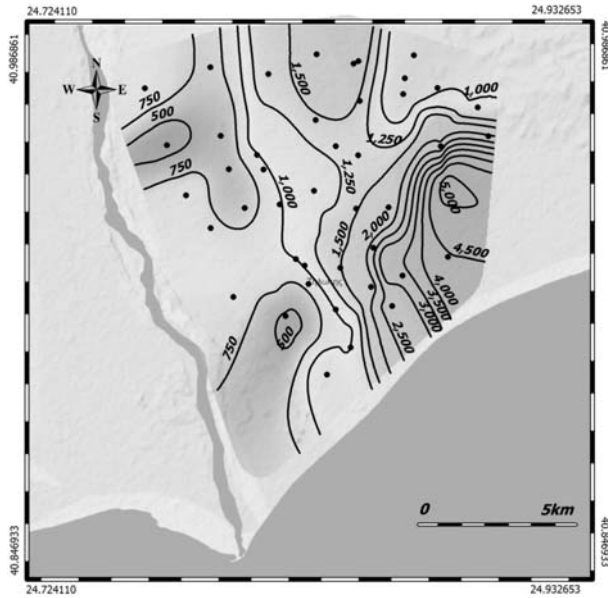
Fig. 3: Distribution of SEC values (μS/cm) (Gkiougkis, 2009; Mwila, 2009).
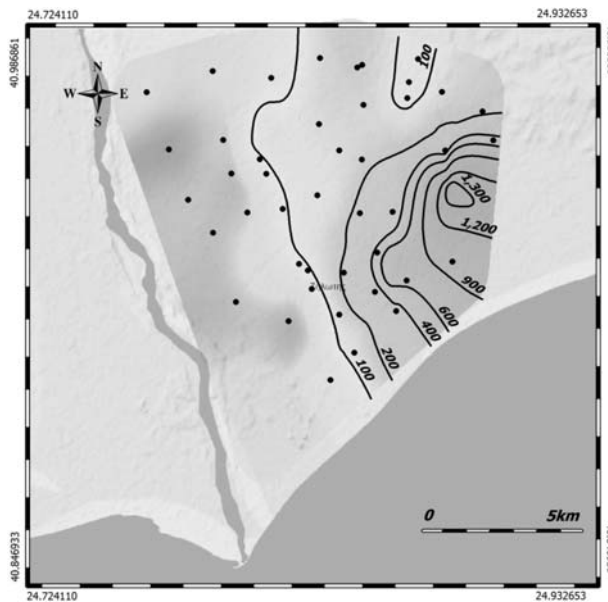
Fig. 4: Distribution of chloride ions (mg/L) of the groundwater samples of the study area (Gkiougkis, 2009; Mwila, 2009).

ing with saline water from the sea intruding the groundwater aquifer due to over pumping of groundwater for irrigation. However, this may also be as a result of evapotranspiration and/or calcite precipitation due to the presence of bicarbonates which effectively increase the Na^+ ions and tend to reduce the Ca^{2+} ion concentration in the groundwater thereby increasing the value of SAR and other
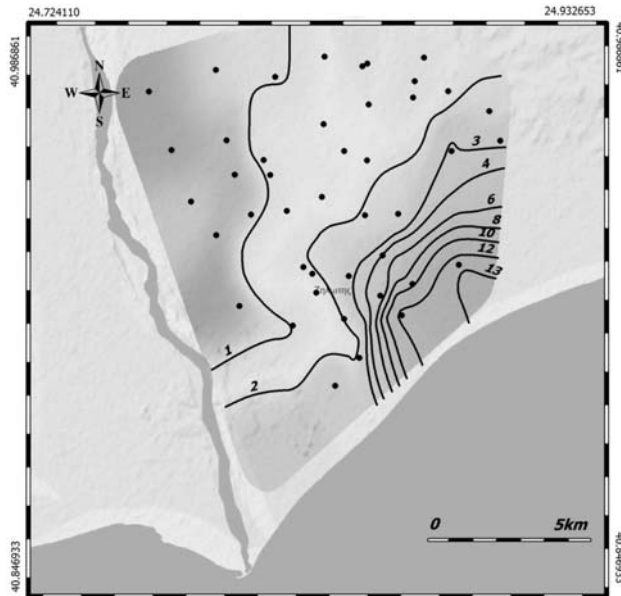
Fig. 5: Distribution of SAR values (Gkiougkis, 2009; Mwila, 2009).

toxic elements, particularly boron and chloride. The wells with higher to relatively high values of SAR are located to the east of the study area. Wells from the same location also contain relatively high amounts of chloride ion concentrations; have high values of specific electrical conductivity and pH values. All values of these parameters mentioned here affirm the argument of possible sea-water intrusion into the groundwater aquifer in the eastern delta of Nestos River (Gkiougkis, 2009; Mwila, 2009).

The research showed generally relatively low percentages for the %Na (Exchangeable Sodium Percentage - E.sp or Na%) in the groundwater samples. According to the qualitative classification of irrigation water after Wilkox 1955, it can be noted that most of the wells contain low levels of %Na and can be classified having groundwater of either excellent to good quality with a few wells having acceptable groundwater quality for irrigation. There is only about 10% of the total number of wells under investigation with questionable groundwater quality (high %Na values observed: 59.89-77.92). Most wells with good groundwater quality for irrigation are located near the River Nestos and hence are under constant freshwater recharge. Further east to the coastal region of the study area the groundwater quality is compromised as a result of saline water from the sea mixing with freshwater in the aquifer due to seawater intrusion (Gkiougkis, 2009; Mwila, 2009).

Results of calculated Revelle Coefficient values for the groundwater samples revealed that most of the wells contain relatively low chloride ion concentrations as indicated by the low Revelle coefficient values. Few wells nonetheless show Revelle Coefficient values greater than 1.0 (Fig. 6). Making reference to the groundwater contamination limits from those suggested by Kallergis (2000), it suffices to state that all of the few wells which show values that indicate groundwater contamination could be classified as belonging to the categories ranging between groundwater with low level of contamination to groundwater with medium level of contamination. The wells with Revelle coefficient results greater than 1.0 (Revelle values: 1.48-9.45) are located to the east of the study area.
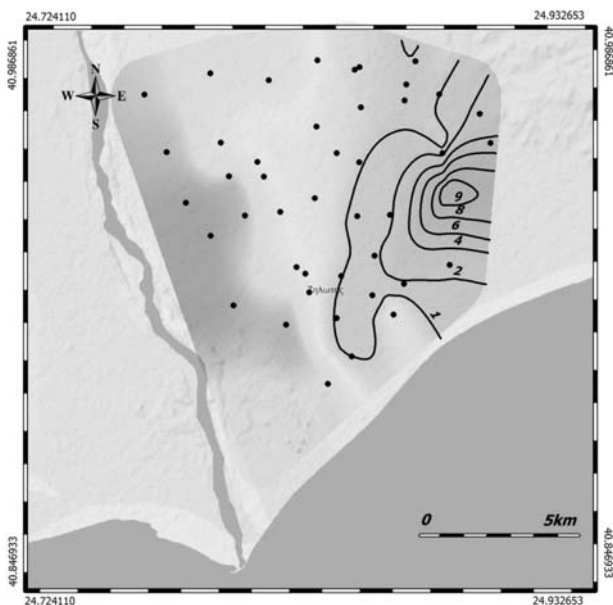
Fig. 6: Distribution of Revelle Coefficient values for the groundwater samples (Gkiougkis, 2009; Mwila, 2009).

This part of the study area has high chloride ion concentration and high values of electrical conductivity. The wells are close to the coast and as a result are susceptible to seawater ingress due to over abstraction of groundwater from the phreatic aquifer for irrigation purposes (Gkiougkis, 2009; Mwila, 2009).

4. Conclusions – managerial proposals

The problem of the groundwater salinisation at the study area appears to become serious, showing rapid deterioration in recent years. This finding makes the preparation of detailed studies on the region necessary, immediate and urgent to find efficient and certain solutions, for the region. Apart from proper groundwater artificial recharge applications at the study area, proposed by previous studies (Pliakas et al., 2001; Sakkas et al., 1998), the next step of enriching substantially the detailed elaboration of the seawater problem in the study area should focus on aspects related to (Pliakas, et al., 2007):

— conceptual model details (local geological details, hydrogeological boundaries),
— the hydraulic relationship between surface waters and groundwaters,
— the role of the Nestos River in the aquifer salinization process,
— hydrochemical modeling combined with proper additional field tests and hydrochemical types mapping,
— groundwater flow modeling of the studied aquifer system.

It is recommended that the environmental problem of seawater intrusion regime of the area should be assessed by the local authorities (relevant municipalities or prefecture) in the form of managerial reports which could include the following (Pliakas, et al., 2007):

- study of providing freshwater sources and design of proper groundwater artificial recharge facilities with continuous evaluation of their effectiveness,

- development of appropriate pumping scheme based on scientific evidence for the preservation of the entire piezometric surface of the area of investigation above sea level and organization of a series of educational seminars to the farmers of the area, in order to obtain appropriate knowledge for the pumping schemes which they should apply,

- construction of canals which will provide the migration of saline water towards preferred and certain parts of the study area,

- provision of specific measures for the problem of abandoned groundwater wells which may provide pathways for migration of saline water through different aquifer layers,

- thorough examination of the environmental impact assessment of each groundwater well which is about to be installed and inspection of the well drillers of the area and examination or evaluation of their scientific skills,

- development of a water authority, as demanded by Directive 2000/60/EC, to ensure the protection of the quality status of the groundwaters of the area.

The problem of seawater intrusion in Greece is a matter not only of insufficient or lack of groundwater resources management but also of poor legislation enforcement (Kallioras et al. 2004). The area of investigation is a typical example of lack of scientific groundwater resources management of coastal aquifers, which has resulted in the aggressive intrusion of seawater wedge at the mainland freshwater aquifer. The continuous over-pumping conditions and the overexploitation of the aquifer resources enhance the qualitative degradation of the aquifer and pose threats for a variety of factors of the area such as environmental, social, economic and agricultural development.

5. Acknowledgments

6. References

Daskalopoulos, D., 2007. Hydrogeological study of an aquifer system at the eastern delta of Nestos River. *Master Thesis, Postgraduate Course: Hydraulic Engineering, Department of Civil Engineering, Democritus University of Thrace, Xanthi*, (in Greek).

Gaaloul, N., Pliakas, F., Kallioras, A., and Marinos, P., 2008. Seawater intrusion in Mediterranean porous coastal aquifers. Cases from Tunisia and Greece. *Proceedings of the 8th International Hydrogeological Congress of Greece and the 3rd Middle and East Mediterranean Workshop on Fissured Rocks Hydrology, 8-10/10/2008, Athens*, pp. 281-290.

Gkiougkis, I., 2009. Investigation of seawater intrusion into coastal aquifers in deltaic environment. The case of Nestos River Delta. *PhD Thesis, Department of Civil Engineering, Democritus University of Thrace, Xanthi*, (in progress), (in Greek).

Kallergis, G., 2000. *Applied – Environmental Hydrogeology*. Volume B, published TCG, Athens, 345 p (in Greek).

Kallioras, A., Pliakas, F., and Diamantis, I., 2006. Conceptual model of a coastal aquifer system in northern Greece and assessment of saline vulnerability due to seawater intrusion conditions. *Environmen-*

tal Geology, Springer, Vol. 51, n. 3, pp. 349-361.

Kallioras, A., Pliakas, F., Diamantis, I., 2004. The harmonization of national law with the Directive 2000/60 EC for the protection and management of waters. *Environment and Law, Nomiki, Bibliothiki* 4:480–488 (in Greek).

Mwila G., (2009). Groundwater quality degradation due to seawater intrusion conditions in a coastal unconfined aquifer in Northern Greece. Master Thesis, Technical University of Darmstadt, Institute of Applied Geosciences, Tropical Hydrogeology, Engineering Geology and Environmental Management (MSc-Trophee), Darmstadt, Germany, 60 p.

Pliakas, F., Diamantis, I., and Petalas, C., 2001. Saline water intrusion and groundwater artificial recharge in east delta of Nestos River. *Proceedings of the 7th International Conference on Environmental Science and Technology, University of the Aegean, Dept. of Environmental Studies, and Global Nest, Ermoupolis, Syros, Greece,* 3-6/9/2001, Vol. 2, pp. 719-726.

Pliakas, F., Mouzaliotis, A., Kallioras, A., and Diamantis, I., 2007. Hydrogeological assessment of the salinization problem of Xilagani – Imeros aquifer system in SW plain area of Rhodope Prefecture, Greece. *Proceedings of the 11th International Conference of the Geological Society of Greece, Athens, Greece,* 24-26/5/2007, Vol. 2, pp. 536-547.

Sakkas, I., I. Diamantis and F. Pliakas, et al., 1998. Groundwater artificial recharge study of Xanthi – Rhodopi aquifers (in Thrace, Greece). Greek Ministry of Agriculture Research Project, Final Report. Sections of Geotechnical Engineering and Hydraulics of the Civil Engineering Department of Democritus University of Thrace, Xanthi, Greece, (in Greek).

Wilcox, L.V., 1955. Classification and use of irrigation waters, U.S. Dept. Agric. Circ. 969.

OPERATIONAL MECHANISM OF KARST SPRING "LOGARAS", NEAR THE VILLAGE "SKORTSINOU", ARCADIA, (PELOPONNESUS)

Karalemas N. and Lekkas S.

National and Kapodistrian University of Athens Faculty of Geology and Geoenvironment Department of Dynamic, Tectonic & Applied Geology,Panepistimioupolis, Zografou 15784 ATHENS, Greece, nkaralem@geol.uoa.gr, slekkas@geol.uoa.gr

Abstract

This paper presents information on the behavior of the Logaras karst spring, which is located 2.5 km north of Skortsinou village of the Municipality of Falaesia. This spring discharges the water table hosted in the carbonate rocks located in the area among Skortsinou, Petrina, Soulario and Voutsaras Villages. This area consists of thin-platy limestones of Pindos Unit that overlay the "First Flysch" formation, which is the stratigraphic bedrock of the aforementioned limestones. Aiming at the accurate determination of the boundaries of the spring's hydrological basin, the geological map of I.G.M.E., sheet "Megalopolis" (Papadopoulos 1997 και Luettig & Vingen 1964) was re-examined. The geological and tectonic observations that derived from this process contributed to the analysis of the spring's mechanical operation. This led to the conclusion Logaras Spring is a contact spring. Furthermore, discharge measurements of the spring took place for the period from 24/6/2006 to 26/10/2007 and the relevant hydrograph was drawn, from which the recession coefficient was calculated. More particularly, the spring's recession coefficient for the hydrological years 2005 – 2006 and 2006 – 2007 is $1,9 \cdot 10^{-3}$ and $4,3 \cdot 10^{-3}$ respectively, while the dynamic volume reach $5,4 \bullet 10^6$ m^3 and $1,7 \bullet 10^6$ m^3 respectively.

Key words: *Karst springs, operational mechanism, recession curve, Arcadia, Peloponnesus.*

1. Introduction

In this paper, the karst system located in the area among Skortsinou, Petrina, Soulario and Voutsaras Villages, southern Prefecture of Arcadia, is studied. This karst system is developed in thin-platy limestones of Pindos Unit, the majority of which are drained by Logaras Spring, located 2.5 km southern of Skortsinou Village (Fig. 1a).

In terms of this project, on-site research was conducted, through which the geological map of I.G.M.E., sheet "Megalopolis" (Papadopoulos 1997 και Luettig & Vingen 1964) was re-examined. The stratigraphic and tectonic observations that derived from this process contributed to the determination of the spring's mechanical operation. Furthermore, discharge measurements of the spring took place for a period longer than a hydrological year. The subsequent data processing and analysis led to the calculation of the spring's recession coefficient and dynamic volume; and provided information regarding the water flow within the karst aquifer and the behaviour of the spring.

This work was carried out in terms of the PhD thesis of the author, Nikolaos Karalemas, a thesis that is supported by the Research Project titled "Decision Support System for the Protection and Man-
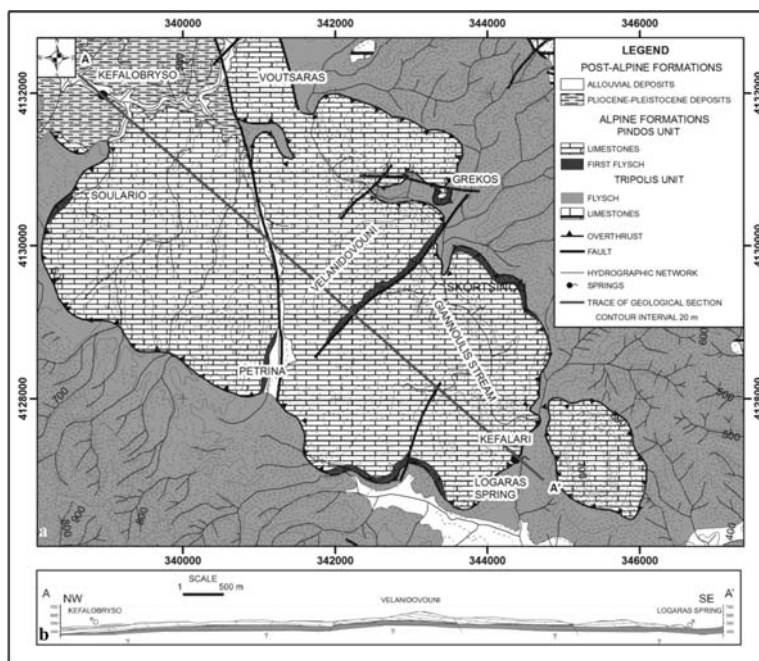
Fig. 1: (a): Geological map of the area of study (Papadopoulos 1997 και Luettig & Vingen 1964). (b): Geological cross-section showing the operational mechanism of the springs discharging the carbonate nappe in study.

2. Geological Conditions

The area of study consists mainly of alpine formations of Tripoli and Pindos Units, as shown in the map (Fig. 1a). The stratigraphic column of Tripoli Unit consists of three parts (Karotsieris and Lekkas 1988), (Georgoulis, 1989): The lowest part comprises slightly metamorphic formations, known as Tyros Beds, which underlie a sequence of carbonate rocks of neritic facies from the Upper Triassic to the Upper Eocene. This sequence of bitumenous thick-bedded to unbedded limestones and dolomites are known as Tripolitza kalk (Philippson, 1892). The upper part is the flysch of the unit, the sedimentation of which started in the Upper Eocene. The formations of Tripoli Unit found in the region of interest are mainly flysch, and in a small extent limestones, the latter shown at the northeastern part of the map. It must be noted that these limestones are hydrologically irrelevant to Logaras Spring. Tripoli Unit tectonically underlies Pindos Unit.

Moreover, only the upper section of Pindos Unit, known as "Arcadian Nappe", is found in the study area and more particularly the following formations: the lowest stragraphic layer is a clastic sequence of sandstones, pelites, and radiolarites in alterations with brecciated limestones of cenomanian age, known as "First Flysch" (Aubouin, 1959). The overlaying formation consists of platy

limestones with Globotruncanidae. This section of the unit is the most widely found in the central and southern part of Peloponnesus (Dercourt, 1964), (Fleury, 1980). Over the limestones, lie flysch transitional beds and finally, the flysch of the unit. Only the "First Flysch" and the upper cetaceous limestones appear in the area of interest.

The limestones of Pindos Unit contain high amounts of siliceous elements that obstruct the flow of the karst water. Also, the nature of these formations renders them particularly plastic; as a result, they are found intensely folded, and in some cases, the stratigraphic column appears inverted.

The post-alpine formations occupy a limited surface in the northwestern part of the area of study. These formations consist of Pliocene and Pleistocene deposits of the southeastern part of Megalopoli tectonic trough, and more particularly, of marls, clays, sands and slightly cohesive conglomerates in alterations (Luettig & Vingen 1964). At some locations, thin holocenic allouvian formations, mainly along streams, appear overlaying the aforementioned.

The area of study constitutes a tectonic nappe of Pindos Unit limestones of an area of 21.7 km^2, overlaying the "First Flysch", which is practically the impermeable ground of the hydrogeological basin in study. At several locations, where the "First Flysch" does not exist, the tectonically underlying flysch of Tripoli Unit is the impermeable ground.

Tectonically, the limestone nappe appears strongly deformed, due to folds. Furthermore, the area of study has been subjected to intense neotectonic tension, since it is located between the neotectonic horst of Taygetos and the neotectonic trough of Megalopoli, resulting in faults influencing the carbonate formations. These faults are considered to play a minor hydrogeological role.

3. Hydrogeological Conditions

The data above show that within the area of study, formations of two types of hydrogeological behaviour can be found in general. The formations of the "First Flysch" and the flysch of Tripoli Unit can be characterized as one type of hydrogeological behaviour and the limestones of Pindos Unit as the second one. The formations of the first type are characterized as low permeable at various locations, but they are practically considered as impermeable rocks, since they are much less permeable than limestones.

On the other hand, the limestones of Pindos Unit are karst formations of high permeability. However, these limestones are not karstified as intensely as other limestones (e.g. the limestones of Tripoli Unit). This phenomenon is owed to the following parameters: the nature, the deposition phase, the layers and the high content in clay minerals of these formations. Therefore, the limestones of Pindos Unit are less permeable than other limestones; nevertheless, they still are karst aquifers. Since the limestones of Pindos Unit overlay impermeable formations, a karst aquifer is generated within the limestones.

The limestones that constitute the nappe under study are relatively isolated hydrogeologically, because the impermeable bedrock extends perimetrically around the nappe. The high amounts of water discharged by Logaras Spring, as well as the fact that the flysch of Tripoli Unit in the wider area is of great thickness, prove that a hydraulic contact between the limestones of Pindos Unit and other underlying limestones does not exist.

Conversely, in the northwest section of the area of study, the limestones are in contact with postalpine formations of Megalopolis basin that are semipermeable. In this case, the limestones communicate hydraulically with post-alpine formations.

The aquifer hosted in the carbonate nappe, is mainly discharged by two springs. The largest quantity is discharged by Logaras Spring, which is located at an altitude of 430 m at the site called "Kefalari", on the southeastern border of the nappe. The second spring is located on the northwestern border of the nappe, at an altitude of 455 m, at the site called "Kefalovriso". The positioning of these springs demonstrates a synclinal structure of the impermeable ground of NW – SE direction, along which an underground drainage line is created. The quantities of water discharged by the springs show that the nappe is mainly discharged from Logaras Spring; only a small part of the nappe is discharged by the spring at "Kefalovriso". The difference in altitude of the two springs combined with the difference of their mechanical operation (Fig. 1b) indicates why the biggest part of the karst aquifer is discharged by Logaras Spring: Logaras Spring is a typical contact spring as the water that moves along the geological contact between permeable and impermeable rocks is discharged at its lower point. On the contrary, the second spring is an overflowing spring, since the post-alpine formations overlay the karst formations at the site "Kefalovriso". As a result, the ground water accumulates in a basin that is created in the limestones, between the impermeable bedrock and the post-alpine formations. The post-alpine formations present lower permeability in comparison to the karst formations. Consequently, a small amount of water drains to the water tables developed within the post-alpine formations and the remaining amount of water is discharged by the spring.

The existence of an underground watershed between the hydrogeological basins of the two springs can not be proved by the existent geological data, since the contact between permeable – impermeable, in the middle of nappe, has a very low slope, as shown at the geological cross-section (Fig. 1b). This makes the identification of the direction of its slope impossible. Nevertheless, these springs can operate even without the presence of an underground watershed. In this case, the aquifer is discharged by Logaras Spring at all times, and the operation of the spring at "Kefalovriso" starts only when the level of the water table rises over the altitude of the overflowing spring.

4. Discharge measurements – data processing

The discharge measurement conditions of Logaras Spring are ideal, partly due to the constructions made at the area of the spring. More particularly, a lake deep enough is observed on-site, on the southern boundary of which an open channel of 2.2 m width and 17 m length is found. The discharge measurements took place in the middle of this channel. At some point, this channel is divided in two branches that may lead the water either to sites where it can be used for irrigation or to the nearby stream feeding Evrotas River. Despite the fact that the channel has a concrete floor, the latter was covered with pebbles, gravel and more detailed material, which were removed with hand tools in order to render the measurements more accurate. These works were repeated before each measurement. The great water supply of the spring, combined with the fact of a constructed channel, led to the selection of the following discharge measurement equipment: Valeport Limited "Braystoke" BFM001 Current Flow Meters that were provided by the Laboratory of Tectonic and Geological Mapping of Department of Dynamic, Tectonic & Applied Geology of University of Athens.

The discharge measurements of the spring began on 26/4/2006, took place approximately every fifteen days and were continued until 26/10/2007. In the summer of 2007 the region northern of the spring was burned by fires that destroyed a great part of Peloponnesus. This fact combined with the heavy storms that occurred in subsequent November caused flooding phenomena of great intense. Large amounts of water that carried large amounts of solid materials were conveyed through the hydrographical network upstream of the spring, causing disasters (Fig. 2a) and leading to flood of the area of the spring. As a result, large amounts of mud were transferred in the lake (Fig. 2b) and

Fig. 2: (a): Disasters caused to Giannoulis Stream, upstream Logaras Spring by the storms of November 2007. (b): The lake formed at Logaras Spring, with muddy water after storms and the subsequent floods of November 2007.

the channel in which the flow measurements were taking place. As it was observed, the water flowing within the channel was muddy for a period greater than a month. Moreover, residues of the aforementioned solid materials remain both in the lake and the bottom of the channel until today. Therefore, the discharge measurements were stopped in October 2007 (548 days from the initiation of the discharge measurements).

The spring's hydrograph (Fig. 3) shows that the greatest discharge rate (1748 m³/h) was recorded at the first measurement, on 26/4/2006, which is indicative of the water shortage that prevailed during the following year. During the period that follows, the discharge rate decreases steadily until 19/10/2006, excluding the period from 8/7/2006 to 16/8/2006, during which the reduction rate of the flow declines. The recession of the spring seems to start on 19/10/2006. The commencement of the spring's recession appeared in a period later than expected, which is owed not only to large volume of precipitation that the region accepted during the hydrological year 2005 – 2006, but also to the increased rainfall occurrences during that summer. Subsequently, the recession curve continues a steady incline until 25/1/2007. After that, a very low value (310.5 m³/h) of the discharge rate (under the extension of the recession curve) was measured, because of the prolonged period of drought that occurred. It is possible that this value is not actual and that it is so low, because the flow was measured after the pumping of the water of the lake, that usually takes place in the summer time. The rainfall of February 2007 is responsible for the initiation of the increase of the curve of the hydrograph for the next hydrological year. Apparently, this rising of the curve was moderate, since it continued (with a maximum value of 585 m³/h) until 1/3/2007. After this date, the curve descended continuously until 23/6/2009, when it is estimated that the recession curve starts. From 1/3/2007 to 23/6/2007, the curve descends unevenly with numerous rate variations. This phenomenon is due to the scattered heavy rainfalls that occurred in the region during this dry year.

Since August 2007, the hydrograph has an irregular appearance, due to fires that occurred in the region. By extinguishing these fires, large quantities of water were drawn from both the lake located at the area of the spring and the drillings that are fed from the water table discharged by the spring. This resulted in the unexpected reduction of the spring's discharge rate in September 2007. Naturally, the aforementioned acts disturbed the balance of the hydrogeological system in the area of study.

The decline of the rate of reduction of the water supply during the first falling curve is particularly remarkable. This phenomenon is interpreted as an interruption of the groundwater supply in the
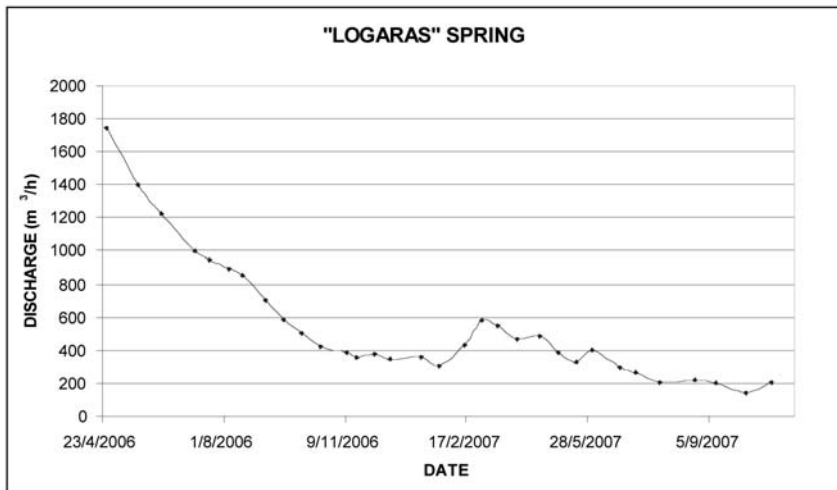
Fig. 3: The hydrograph of Logaras Spring.

karst system by another water body (Soulios, 1985). Practically, it is estimated that the specific form of this part of the hydrograph results from the intense pumping of drillings fed by the water table discharged by the spring. However, this form does not appear at the second falling curve of the hydrograph , due to the irregularities that take place.

Since recession curve of 2007 stopped abruptly, only the recession curve of 2006 (Fig. 4a) can lead to conclusions and to the calculation of the recession coefficient. Nevertheless, an attempt to process the recession curve of 2007 (Fig. 4b) was made, by excluding values estimated to have been influenced by the fires that took place in the wider area of the spring. Analysis of the recession curves and the use of the following expression:

(Maillet, 1905)

(where: Q_t is the discharge rate of the spring, Q_0 is the discharge rate of the spring at the beginning of the recession curves, α is the recession coefficient and t is the time when the discharge rate Q_t was measured) leads to the following equations:

και   for the years 2006 and 2007 respectively.

Consequently, the recession coefficients for the years 2006 and 2007 are $\alpha_{2006} = 0,0019$ and $\alpha_{2007} = 0,0043$ correspondingly. These values fall in the category of 10^{-3}, meaning that the water in the aquifer moves through joints and embedded gaps (Soulios, 1985), which is expected to happen within limestones of Pindos Unit. In any case, the determination of the recession coefficient for more hydrological years is necessary in order to draw accurate conclusions.

Furthermore, an attempt was made to estimate the amount of water stored in the karst system at the beginning of recession. Processing and integration of the equation above results in the following expression:

(Milanovic, 1981)
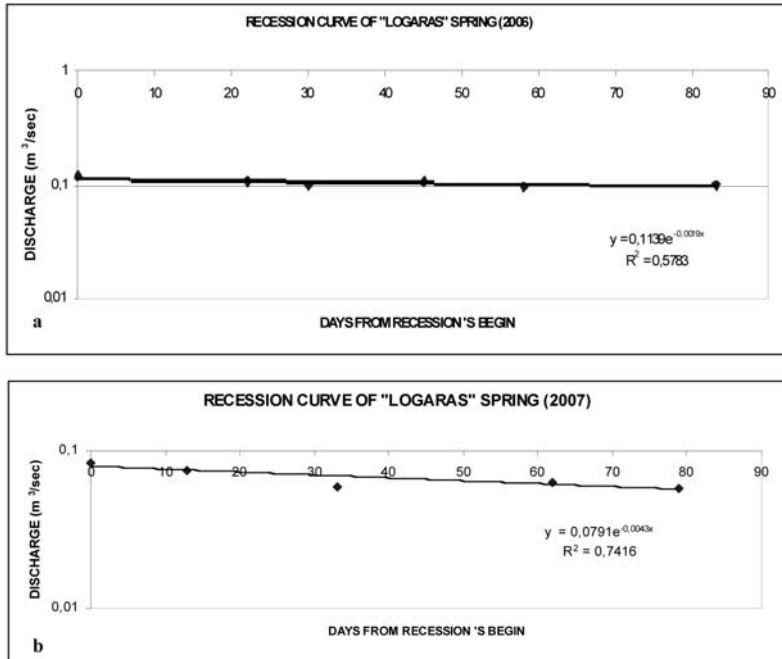
Fig. 4: (a): The recession curve of Logaras Spring (dry season 2006). (b): The recession curve of Logaras Spring (dry season 2007).

(where: V_t is the dynamic volume, Q_t is the discharge rate of the spring on time t and α is the recession coefficient)

By replacing the known values in the formula above:

(Kallergis, 2001)

(where: V_0 is the dynamic volume in m^3, Q_0 is the discharge rate of the spring in m^3/sec on time t_0, α is the recession coefficient).

According to all the above, the dynamic volume at the beginning of the recession of 2006 was estimated at about $5.4 \cdot 10^6$ m^3, while that at the beginning of the recession of 2007 was estimated to be $1.7 \cdot 10^6$ m^3. These values are particularly high for the water tables of the area and indicate that the capacity of the water table discharged by the spring is high. However, the significant difference in the values of the storage capacity of the years 2006 and 2007 is indicative of the severe drought that prevailed during the hydrological year 2006 – 2007.

Even though this case seems ideal to be used as a natural lysimeter for the calculation of the infiltration coefficient of the limestones of Pindos Unit, practically it is not feasible due to human activities that take place within the hydrogeological basin of the spring, such as the numerous drillings that uncontrollably pump the karst water table of Pindos Unit, removing large quantities of water from the water body; and the wastewaters fed to the water table from the four villages located on the limestones of the spring's hydrogeology basin that have no sewer.

The fact that fertilizers are used at the cultivations located on the spring's hydrogeological basin combined, with the wastewater of the four villages are responsible for the impaired water quality of the spring compared to other karst waters in the area. On the other hand, because of the large capacity of the aquifer, pollutants are subject to high dilution, resulting in the water quality not to be prohibitive for some uses (the electrical conductivity is maintained at about 600 μS/cm). In general, it has been observed in the wider region that karst water tables developed in limestones of Pindos Unit are worse in quality than water tables developed in limestones of Tripoli Unit or marbles of Mani Unit (Karalemas, 2006). The lithological variations of these formations, would justify the opposite phenomenon, as the limestones of Pindos Unit are platy limestones, characterized by the strong presence of clay minerals that generally impede the circulation of water and, thereby, reduce its speed and allow its subjection to infiltration. Probably, the difference in quality is owed to the pollution from human activities (settlements, cultivates) that are facilitated on the limestones of Pindos Unit (in opposition to the carbonate rocks of the other units), because of their milder relief, since they erode more easily, and their high concentration in clay minerals.

As mentioned above, the water of Logaras Spring follows the nearby stream and feed the Evrotas River. Specifically, Logaras Spring is one of the main springs of Evrotas River, the other being Vivari Spring located near Sellasia Village of the Municipality of Inounta. This proves the essential role of Logaras Spring to ecosystems in the wider region.

5. Conclusions

Summarizing all the above, the following conclusions are drawn:

Logaras Spring is a contact spring that discharges part of the Pindos Unit limestones located in the area among Skortsinou, Petrina, Soulario and Voutsaras Villages, at the southern part of the Prefecture of Arcadia. The spring shows high capacity compared with other springs in the area, which is proved by the fact that the discharge rate for the period from 26/4/2006 to 26/10/2007 ranges from 151 m^3/h to 1748 m^3/h, especially considering that the correspondent hydrological year was particularly dry.

The hydrograph of the spring determined that the recession coefficient corresponding to the recession curve of 2006 is $\alpha_{2006} = 0,0019$, while the recession coefficient of 2007 is $\alpha_{2007} = 0,0043$. These values fall in the category of 10^{-3}, meaning that the water in the aquifer moves through joints and embedded gaps (Soulios, 1985). Also, it was estimated that the dynamic volume at the beginning of the recession of 2006 was approximately $5.4 \cdot 10^6$ m^3, while that at the beginning of the recession of 2007 reached $1.7 \cdot 10^6$ m^3. These values indicate the high capacity of the aquifer discharged by the spring.

6. References

Aubouin, J., 1959. Contribution a l' etude geologique de la Grece septentionale, les confins de l' Epire et de la Thessalie. *Ann. Geol. Pays Hell*. 10, 526.

Dercourt, J., 1964. Contribution a l'etude geologique d'un secteur du Peloponnese septentrional. *Ann. Geol. Pays Hell*. 15, 418.

Fleury, J., 1980. Les zones de Gavrovo-Tripolitza et du Pinde-Olonos (Grece continentale et Peloponnese du Nord). Evolution d'une plateforme et d'un bassin dans leur cadre alpin. In: *Memoire de la Soc. Geol. Nord*, 651.

Georgoulis, J., 1984. Geological and Hydrogeological studies in the Province of Mantinea (Central Peloponnesus). IGME, Hydrological and Hydrogeological Studies 52 (in Greek, the name of author and

the title were translated in English).

Kallergis, G., 2001. Applied – Environmental Hydrogeology, 2nd Edition. Technical Chamber of Greece, Athens (in Greek, the name of author and the title were translated in English).

Karalemas, N., 2006. Operational Mechanism of Springs of Eastern Taygetos. *Master thesis*, National and Kapodistrian University of Athens, Greece (in Greek, the name of author and the title were translated in English).

Karotsieris, Z. & Lekkas, S. 1988. The geological structure surrounding the plateau of Tripoli. *Bull. Geol. Soc. Greece*. XX(1), 53-66 (in Greek, the name of author and the title were translated in English).

Luettig, G., and Vingen, R., 1964. Bundesanstalt für Bodenforschung, Hannover.

Maillet, E., 1905. Essais d hydraulique souterraine et fluviale. – Herman, Paris, h.t.

Milanovic, P., 1981. Karst hydrogeology. *Water Resources Publicatons*, Colorado.

Papadopoulos, P., 1997. Geological Map "MEGALOPOLIS" Sheet (scale 1: 50000) I.G.M.E.

Philippson, A., 1892. Der Peloponnes. In: «Versuch einer Landeskunde auf geographischer Grundlage, Berlin, 647.

Soulios, G., 1985. Contribution to the hydrogeological study of the karst aquifer systems of Greece. Aristotle University of Thessaloniki (in Greek, the name of author and the title were translated in English).

GROUNDWATER FLOW MODELLING OF THE ALLUVIAL AQUIFER IN THE MOURIA AREA, SW GREECE

Karapanos E.[1], Burgess W.[2] and Lambrakis N.[1]

[1] *University of Patras, Department of Geology, Laboratory of Hydrogeology, 26500, Patras, Greece, hekarapanos@upatras.gr, nlambrakis@upatras.gr*

[2] *Department of Earth Sciences, University College London, Gower Street, WC1E 6BT, London, United Kingdom, william.burgess@ucl.ac.uk*

Abstract

The objective of this paper is to study the impact of a reflooding of the former Mouria Lake on the hydraulic state of the Pyrgos area. The hydrogeological data acquired through field work were combined with the volumetric budget and the hydrological data from the entire Alfios River catchment in order to build the conceptual and numerical model of the groundwater flow system, which confirmed the hydraulic state before the drainage of the Mouria Lake. The model was also used to predict the future hydraulic state in case stresses change. For this purpose, Flowpath II, a numerical groundwater flow model, was used to evaluate the impacts of groundwater exploitation in the alluvium unconfined aquifer that is developing in the Holocene deposits. Due to the connection of the aquifer with the surface drainage canals near the coastal zone, the conceptual model was built upon irrigation data, rainfall data, and pumping rate data from the pumping stations that drain the area of the former Mouria Lake. These data were inserted in the model which was calibrated using a 24-month set of piezometric measurements. The simulation results show that the groundwater level before the drainage of the lake was 2m higher than the present situation and the same scenario will happen in case of reflooding the drained lake. Today, the pumping stations keep the groundwater level near the sea level throughout the hydrological year.

Key words: *groundwater modelling, unconfined aquifer, conceptual model, piezometric measurements.*

1. Introduction

The Mouria Lake, located in Western Peloponnese, was drained for cultivation during the late 60's. Today the c. 600-ha large former Lake and the surrounding area is used for cultivation and grazing. The sediments filling the drained Mouria Lake are Holocene alluvial deposits while gravel and sand dominate in the surrounding area (Fig. 1a). The eastern, western and northern margins of the study area consist of lagoonal sediments, while a sand barrier system and marine deposits constitute the southern margins (Streif, 1980).

The irrigation needs for cultivation are covered by the use of water from Alfios River, which is distributed through water canals in the area of 48 km². Deep wells (20-50m) have been abandoned in the last decade because of the deterioration of the water quality, while majority of the wells that appear in the unconfined aquifer (approx.10m) are of little use.
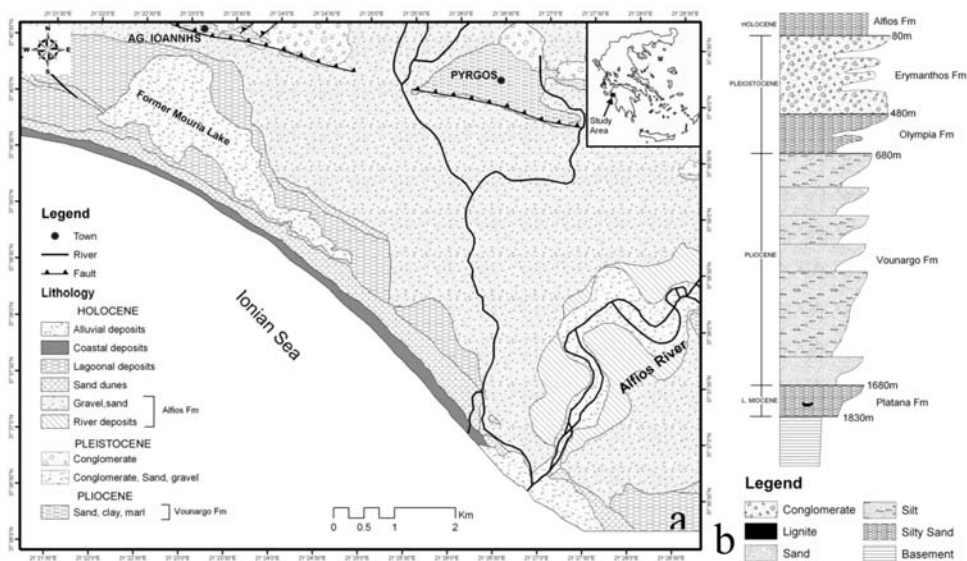
Fig. 1: (a) Geological map and (b) stratigraphy of the study area (Streif, 1980).

The aim of this study is to build a conceptual model that will represent the present conditions based on hydrological, lithological and hydrogeological data and to set up the numerical model of the unconfined aquifer that simulates the groundwater flow in the area of Pyrgos. The basic objective of the model is to confirm the hydraulic state and estimate the volumetric budget of the study area that represents the input and output volumes of water in the unconfined aquifer, in order to predict future heads in case stresses differ in the future (e.g. drought periods) and to investigate the potentiality of re-flooding the entire former lake, based on the results of the present study.

2. Geological – hydrogeological setting

The study area is part of the Pyrgos basin (Hageman, 1976, Koukouvelas et al., 1996) and consists of two sedimentary systems. The lower part consists of the marine-lacustrine Platana and Vounargo formations (Fm) (Fig. 1b). An overall coarsening-up trend characterizes both formations. The Platana Fm was deposited during the Late Miocene. Higher up, the lacustrine and marine sediments of the Platana Fm are interdigitated basinwards with the overlying Vounargo Fm, which is the major lithological unit in the Pyrgos basin (Kamberis, 1987). The upper sedimentary system consists of three formations. At the bottom, the 200m thick Pliocene Olympia Fm is a coarsening-up fluvio-lacustrine succession overlain by the 400m thick Erymanthos conglomerates, with sediment supply from the north. On top of this system the 80m thick Middle Pleistocene-Holocene Alfios Fm is exposed in the low-land area of the Pyrgos basin.

The lower coastal zone of the Pyrgos area is covered by Holocene alluvial deposits (Alfios Fm) in which an unconfined aquifer is developed. The aquifer is mainly recharged by the direct infiltration from precipitation in the rainy period and irrigation in the dry period, as well as lateral leakage along the Alfios riverbed. Piezometric measurements conducted in the Mouria area suggest that the underground water moves from the north-east area to the coastal zone while the hydraulic gradient varies from 0.1‰ to 8‰, with the mean value at 2.8‰ (Fig. 2). The lower values are near Alfios
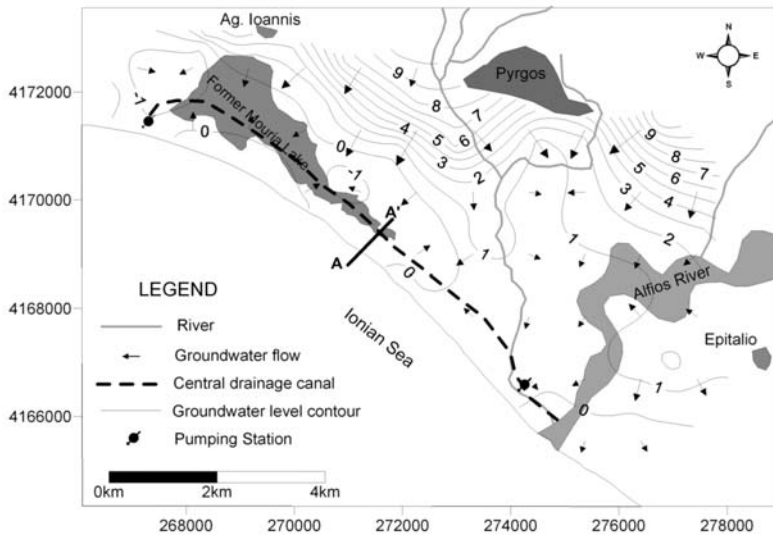
Fig. 2: Piezometric map of the unconfined aquifer at the Mouria area (June 2006).
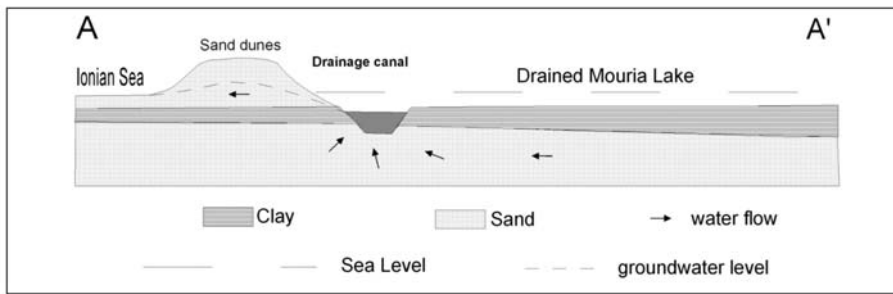
Fig. 3: Hydrogeological cross section of the line A-A' shown in figure 2.

River which indicates that sediments with higher hydraulic conductivity dominate in that area and there is increased recharge from the river to the aquifer. Near the coastal zone there is negative hydraulic gradient and seawater intrusion caused by the pumping stations that lead surface water and part of the underground water to the sea. The two pumping stations are located at the west and east edge of the drained Mouria lake and are used to drain the former lake area through drainage canals (Fig. 2&4). Due to the depth of the canals (approx. 4-5m), there is connection with the aquifer resulting in the drawdown caused by the use of pumping stations (Fig. 3).

3. Numerical Simulation

3.1 Conceptual model

The development of the model that simulates the groundwater flow in the area of Pyrgos was produced following the steps according to Anderson and Woessner (1992). The conceptual model was conducted using geological, hydrological and hydrogeological data that were collected during field work and is based on three coverages.

The first coverage describes the hydraulic conductivity of the unconfined aquifer and its spatial distribution. The study area was divided into two areas with different hydraulic conductivities. The second coverage includes the quantity and the distribution of the recharge data based on both rainfall and irrigation data. According to the hydrological balance in the Alfios River catchment, the volume of water that infiltrates and recharges the alluvial unconfined aquifer is 20% of irrigation and rainfall data (Karapanos, 2009). The third coverage includes streams and rivers that recharge the aquifer by lateral leakage (e.g. Alfios River) or cause a drawdown due to the use of pumping stations (e.g. drainage canals).

3.2 Description of the model – Creating the Grid

The well known Flowpath II software (Evsikov et al., 1998) was selected for the simulation of the unconfined aquifer in Pyrgos area, which resolves the three-dimensional groundwater flow equation (Rushton and Redshaw, 1979) using the finite differences arithmetical method (Anderson and Woessner, 1992). This method demands that the study area should be divided in cells with dimensions x, y and z. The grid that was produced divides the aquifer in cells 200x200m and consists of rows, columns and single layer in z axis.

The 45 km^2 study area is divided into 1209 cells. The NNE boundary of the aquifer consists of the Plio-Pleistocene deposits of Vounargo formation and Pyrgos fault zone (Fig. 4). Alfios River is the SE boundary of the simulation area, where the heads vary linearly. The NW boundary is parallel to a flow line and is simulated as no-flow boundary, while the SW boundary is the sea shore, which is a constant head equal to zero throughout the year. The base of the aquifer is a clay layer that is found in all lithological sections and is impermeable, with a mean elevation of -15 m. Since the aquifer is unconfined, it is not necessary to insert the elevation of the top of the aquifer. As regards the streams and the drainage canals, these were inserted in the model and proved to be significantly important toward the volumetric budget. The hydraulic conductivity was calculated through pumping tests to be 600 m/day in the simulation area while there is a zone of 300 m/day in the area of the former lake due to the existence of less permeable sediments (clay). Recharge rates were calculated to be 20% of the water from rainfall plus irrigation for each month, expressed as m/day as shown in table 1.

3.3 Initial – boundary conditions

According to the ASTM (D5609-94) standards there are 3 conditions: specified head condition, specified flow condition and variable head condition. The boundary conditions in the unconfined aquifer of Pyrgos were determined according to the geological and hydrogeological setting of the area.

According to the piezometric maps and the field work, the NE section of the aquifer extends parallel to Pyrgos fault zone and is simulated as a variable head boundary (Fig. 4). Across this boundary there is limited flow as the Pyrgos fault zone and the neogene deposits of Vounargo formation seem to be a hydraulic boundary. However, in order to simulate the amount of water coming in the aquifer from this zone, a recharge area has been used in which the input of water has been calculated using the hydraulic gradient, expressed as recharge rate, equal to 0.02 m/day (Fig. 4). At the west part of the town of Pyrgos along the fault zone, there is an influx zone that was simulated with a recharge rate of 0.61 m/day. Similarly, in the east part of Pyrgos town, the influx was simulated as recharge rate of 0.055 m/day. The NW boundary of the aquifer is simulated as a no-flow boundary as it is parallel to the flow lines, with no input or output of groundwater across this boundary. A no-flow boundary is also found at the south part of Pyrgos town because of the impermeable sediments of Vounargo formation.
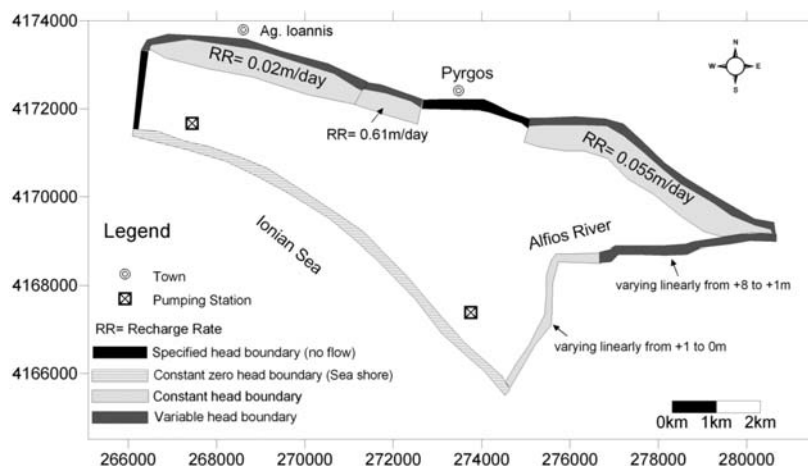
Fig.4 : Simulation grid at the Mouria area.

The SE boundary of the aquifer is Alfios River, simulated as variable head boundary, as the water level varies throughout the year especially towards the inner land. The head varies linearly from +8 m to +1 m, as it is found that the hydraulic head in that area (Epitalio Bridge) is constantly +1 m throughout the year (Karapanos, 2009). This happened throughout the period 2006-2007 that piezometric measurements took place and is attributed to the extensive use of pumping stations near Alfios River and the coastline that keep groundwater level to a certain level (Fig. 4). Thus, from that point until the Ionian Sea, the lower part of the river was simulated as constant head boundary varying linearly from +1 m to 0. The west boundary of the aquifer is the Ionian Sea simulated as constant head equal to zero.

The volume of water that is pumped from the drainage canals to the sea was simulated as negative hydraulic head at the central drainage canal that develops along the coastline. Because of the constant use of the pumping stations in order to maintain a certain water level to the canals, the hydraulic head is constantly below zero throughout the year. The volume of water pumped by the wells in the unconfined aquifer is minor and therefore not considered in the model, compared to the excessive volume of water pumped by the pumping stations. This volume is simulated by the model as constant negative hydraulic heads in the central drainage canal.

3.4 Calibration of the model

In the present study the trial and error method was used in order to calibrate the model and find the parameters that simulate better the aquifer. The evaluation of calibration is performed by the use of the Mean Error (ME), the Mean Absolute Error (MAE) and the Root Mean Square (RMS) (Anderson and Woessner, 1992).

Initially, the model was calibrated based on the piezometric measurements of June 2006 which is assumed to be the mean annual groundwater level and is representative for the two year simulation period. The aim of this calibration is to estimate the values of hydraulic conductivity as the other parameters remain the same and are known. The data used for the separate recharge zones were calculated according to the rainfall and irrigation data to be 0.00007 m/day for the whole area. The simulation was done in transient state conditions and the storativity value equals 0.2 (S=0.2) according to pumping tests.
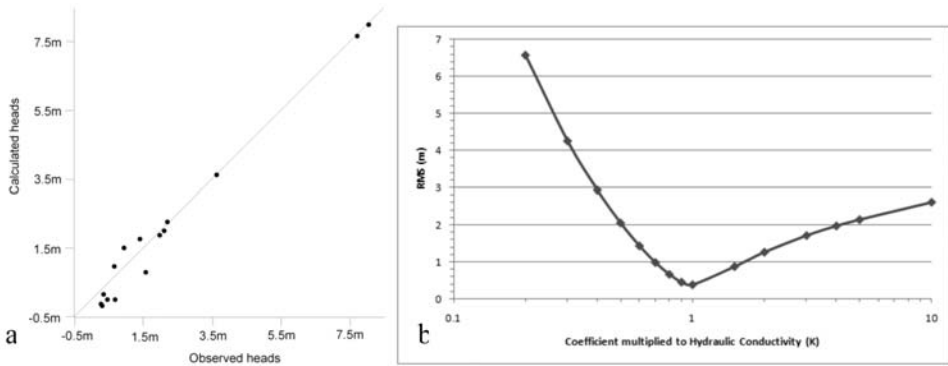
Fig. 5: (a) Correlation of the computed and the observed values, (b) Sensitivity analysis.

Table 1. Recharge rates based on rainfall and irrigation data.

Month	Irrigation (m)	Rainfall (m)	Summary (m)	Infiltration (20%) (m)	Recharge Rate m/day)
June 06	0.01246	0	0.01246	0.00249	0.00008
Sept 06	0.00807	0.0805	0.08857	0.01771	0.00059
Dec 06	0	0.0771	0.07710	0.01542	0.00051
Mar 07	0	0.0612	0.06120	0.01224	0.00041
Jul 07	0.01470	0	0.01470	0.00294	0.00010
Oct 07	0.00173	0.2351	0.23683	0.04737	0.00158
Dec 07	0	0.1033	0.10330	0.02066	0.00069

The RMS and MAE values are considered to be reasonable as they are MAE = 0.3 m and RMS = 0.38 m (Fig. 5a).

3.5 Sensitivity analysis

The sensitivity analysis is aimed to prove that the chosen parameter values play a very important role and are not randomly chosen. Thus, several values were used for the two zones of hydraulic conductivity and their impact was checked by the use of RMS (Fig. 5b). The model completed several simulations for 15 different pairs of conductivity values and results show that the lower RMS value is achieved only by the use of the conductivity values for which the model was calibrated.

3.6 Validation of the model

The uniqueness of the results of the model is achieved by the validation of the model. The results of the simulation are checked when new stresses are used toward a new set of observed heads. The validation of the model was done in transient conditions where S=0.2 and different recharge rates were used according to rainfall and irrigation data as shown in table 1.

Throughout the different simulations, the RMS error varies from 0.38 to 0.73 and the MAE from 0.30 to 0.63. Hence the model can simulate the groundwater system with good fit to the observed data and can be used to extract safe results about the volumetric budget and to predict future heads in different stresses.

Table 2. Volumetric budget for the case of September 2006.

Input	Infiltration	Alfios leakage	Summary
Percentage (%)	84.17	15.83	100
Output	Underground runoff	Drainage canals	Summary
Percentage (%)	14.32	85.68	100
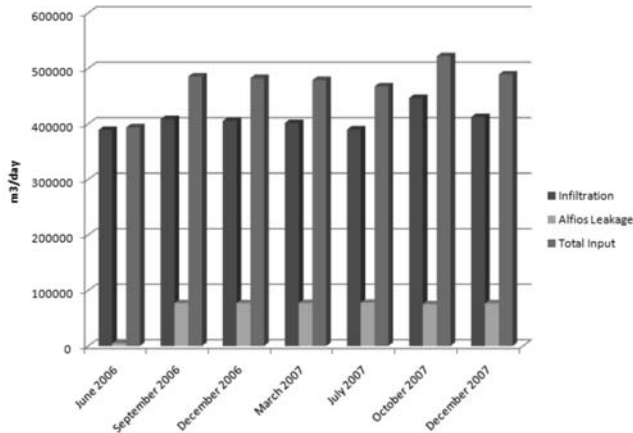
Fig. 6: Variation of the input in the unconfined aquifer.
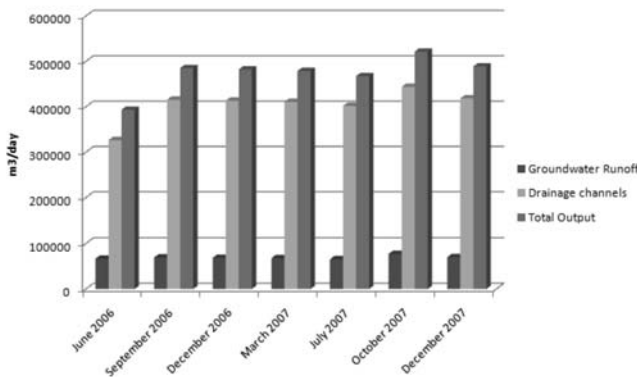
Fig. 7: Variation of the output in the unconfined aquifer.

3.7 Volumetric budget

One of the main objectives of the model is to estimate a reliable volumetric budget and estimate the volumes of water entering and departing from the aquifer. In the study area the volumetric budget is reflected by the following equation:

Direct Infiltration (20% of the Irrigation data + Rainfall data) + Alfios river Input = Groundwater output + Drains (from the drainage canals).

The direct infiltration was calculated as 20% of the volume of water coming from the rainfall and irrigation. The lateral leakage along the riverbed is calculated from the model by the use of the heads

Table 3. Volumetric budget in December 1990.

Input	Infiltration	Alfios leakage	Summary
Percentage (%)	81.96	18.04	100
Output	**Underground runoff**	**Drainage canals**	**Summary**
Percentage (%)	12.93	87.07	100

Table 4. Volumetric budget for recharge rate equal to 0.00008 m/day.

Input	Infiltration	Alfios leakage	Summary
Percentage (%)	90.34	9.66	100
Output	**Underground runoff**	**Drainage canals**	**Summary**
Percentage (%)	93.03	6.97	100

Table 5. Volumetric budget for recharge rate equal to 0.002319 m/day.

Input	Infiltration	Alfios leakage	Summary
Percentage (%)	94.13	5.87	100
Output	**Underground runoff**	**Drainage canals**	**Summary**
Percentage (%)	88.38	11.62	100

in nearby wells and the piezometric maps. The results for the simulation period of September 2006 are shown in table 2 as an example while the overall results are in figures 6 & 7.

As shown in table 2 for the case of September 2006, 15% of the underground water comes from Alfios River through lateral leakage while the rest 85% comes from direct infiltration of the rainwater during the winter period and the irrigation water during the summer period.

Drainage canals play a very important role in the area as they lead 85% of groundwater to the sea while the rest 15% is underground runoff towards the sea. The same results appeared when different recharge rates were inserted in the model showing that the drainage system at the former Mouria Lake keeps groundwater level at a certain level near the sea level throughout the hydrological year.

According to the results presented through the histograms in figures 6&7 for different recharge rates throughout the years 2006-2007, the largest amount of input and output groundwater was recorded during October 2007, because of the high level of precipitation (235.1 mm) in that month.

3.8 Prediction of the model

One of the advantages of the model after its calibration and validation is the simulation of the aquifer in different stress periods. In the study area, the aquifer is constantly recharged throughout the year even in the summer period because of the infiltration of water used for irrigation. So the scenario that was checked was that of heavy rainfall. The highest value of precipitation recorded for the Pyrgos area in the last 30 years was 347.8 mm in December 1990. This value equals to a recharge rate of 0.002319 m/day. The results in case the same scenario happens again in the future, are presented in table 3.
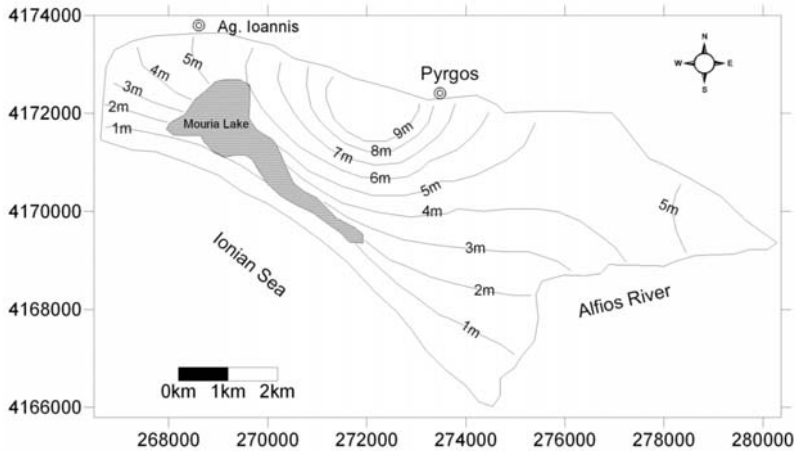
Fig. 8: Piezometric map of the study area before the drain of the Mouria Lake during the low water period.
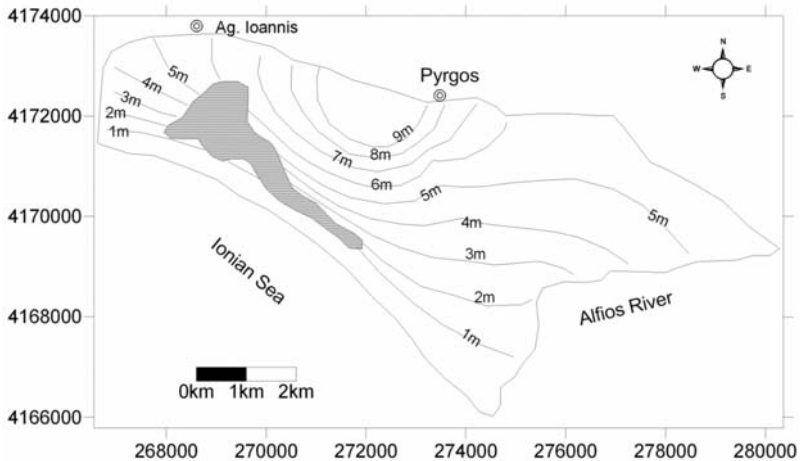
Fig. 9: Piezometric map of the study area before the drain of the Mouria Lake during the high water period.

Another hypothesis made, was that of simulating the aquifer before the drainage of the Mouria Lake that took place in 1960's, as the plans for future reflooding demand it. The lake surface was simulated as constant zero head surface without the drainage canals. The initial recharge rate inserted was 0.00008 m/day which is the lowest value recorded and secondly 0.002319 m/day, that is the maximum value. The results of the simulation for these two hypotheses are shown in tables 4&5 and figures 8&9 respectively.

Results indicate that the role of drainage canals is significant for the study area, as in the past decades before the drainage of the Mouria Lake the groundwater level was 2 meters higher and the lateral leakage from Alfios River was 10% less than the present situation.

4. Conclusions – Results

The numerical simulation of the alluvial aquifer in Pyrgos area was conducted using Flowpath II soft-

ware. The results were very satisfying regarding both the simulation of the piezometric surface and the reliable volumetric budget. According to this, 15% of the aquifer water derives from lateral leakage from Alfios River, while 85% derives from infiltration of the rainwater during the winter period and irrigation water during the summer period. The drainage canals play a very important role in the area as they lead 85% of the groundwater to the sea and the rest 15% is underground runoff towards the sea. Additionally, the prediction of the aquifer's piezometric surface and balance in case stresses change, was checked by the use of the model.

In the study area the aquifer is constantly recharged throughout the year even during the summer due to the water use for irrigation. According to heavy rainfall scenario, 18% of the aquifer water will derive from Alfios lateral leakage, while 82% from infiltration of the rainwater during the winter period and irrigation water during the summer period. Another hypothesis made was that of simulating the aquifer before the drainage of the Mouria Lake that took place in 1960 's. Results show that the role of drainage canals is significant for the study area as in the past decades the groundwater level was 2 meters higher, scenario that will happen again in case of reflooding the lake. According to the volumetric budget, the lateral leakage from the Alfios River was decreased 10% in relation to the present situation.

5. Acknowledgments

6. References

Anderson, M.P. and Woessner, W.W., 1992. Applied Groundwater Modelling: Simulation of Flow and Advective Transport. Academic Press, London.

ASTM, D 5609-94. Standard Guide for Defining Boundary Conditions in Ground – Water Flow Modeling. 4 pp.

Evsikov, I.I., Sychov, P.P., Sapozhnicov, A.P., Nova, K. 1998. Flowpath II for Windows, version 1.3.2. 2-D groundwater flow, remediation, and wellhead protection model. Waterloo Hydrogeologic Inc., Ontario, Canada.

Hageman, J., 1976. Stratigraphy and sedimentary history of the Upper Cenozoic of the Pyrgos area (Western Peloponnesus), Greece. Ann.Geol. Pays. Helleniques, 28, 299-333.

Kamberis, E., 1987. Geological and oil study of NW Peloponnese. PhD thesis. Polytechnic School. Section of Geological Sciences. Athens (in Greek).

Karapanos, E., 2009. Hydrogeological – hydrochemical parameters of the drained Mouria Lake (Prefecture of Ileia), controlling the rehabilitation and the sustainable management of the wetlands. PhD thesis. Department of Geology, University of Patras. 310 pp. (in Greek).

Koukouvelas, I., Mpresiakas, A., Sokos, E. & Doutsos, T., 1996. The tectonic setting and earthquake ground hazards of the 1993 Pyrgos earthquake, Peloponnese, Greece. Journal of the Geological Society, London, Vol. 153, pp 39-49.

Rushton, K.R., Redshaw, S.C. 1979. Seepage and Groundwater Flow. Numerical Analysis by Analog and Digital Analysis. John Wiley & Sons, ISBN 0471997544, 327 pp.

Streif, H., 1980. Geological map of Greece, Pyrgos sheet, 1:50000. Institute of Geological and Mining Research. Athens (in Greek).

RADON CHANGES ALONG MAIN FAULTS IN THE BROADER AIGION REGION, NW PELOPONNESE

Katsanou K.[1], Stratikopoulos K.[1], Zagana E.[1] and Lambrakis N.[1]

[1] *University of Patras, Department of Geology, Laboratory of Hydrogeology, 26500 Patras, katsanou@upatras.gr*

Abstract

In the present study the relationship between Rn and hydrochemical parameters in groundwater samples with the intense tectonics that prevail in the broader region of Aigion were investigated. Radon concentrations were measured in water samples collected from the unconfined aquifer, hosted in Plio-Pleistocene deposits, along the major faults of the research area. The spatial distribution of radon concentrations revealed the existence of three distinct zones along Aigion, Pyrgaki and Helike faults, respectively. The first two zones are characterized by high radon concentrations, whereas the third by low radon concentrations. It is also shown that ^{222}Rn and CO_2 concentrations display similar spatial distribution suggesting a common origin for these two gases, with CO_2 being the major carrier gas for radon in deep fluids. The deformation and fragmentation of rocks along the fault zones enables the circulation of those fluids resulting in elevated radon concentrations in groundwater. However, other factors, such as the mineralogical composition of the sediments along the fault planes may restrict this process. The distribution of radon along the fault zones suggests that radon measurements can be used as a tool for the detailed mapping of active faults and if combined with seismic data even as a tool for study earthquake prediction.

Key words: Radon 222, groundwater, fault tracing, Aigion.

1. Introduction

Radon (^{222}Rn) is a daughter nuclide of radium (^{226}Ra), which in turn derives from the long-living antecedent, uranium (^{238}U). The short half-life of ^{222}Rn (3.85 days) produced at great depth, limits its migration distance in the subsoil, unless it is lifted upward by a relatively fast-flowing carrier gas, such as CO_2, CH_4, or N_2, (Moussa et al., 2003 and references therein).

The amount of radon emitted from the Earth's crust into the atmosphere is usually small. However, unusual quantities of radon could be emitted above geological faults, geothermal sources, uranium deposits and volcanoes (Nishimura & Katsura, 1990).

Durrani & Ilic (1997) discussed the relation between geology and radon levels in groundwater, soil gas, and indoor air. Radium, the immediate precursor of radon gas, occurs virtually in all types of rocks and soils; its concentration varies from site to site depending on geological factors (Al-Tamimi & Abumurad, 2001).

Water and geo-gas discharges are strongly promoted in hydrothermal systems and seismically active zones. The distribution of radon in soil gas has therefore been applied in the exploration of ge-

othermal energy fields, the monitoring of volcanic activity, the prediction of earthquakes and the mapping of fault zones (Ioannides et al., 2003 and references therein).

The high permability, compared to the surrounding country rocks, that is often exhibited along fault zones often can turn fault zones into preferential pathways for adjective gas-carrying fluid transport. During their way to the surface, pressure decrease allows the gases (CH_4, CO_2, He, Hg, Rn, etc.) to escape from the fluids into soil gas and eventually into the atmosphere (King, 1986).

Anomalously high radon concentration in ground water has long been associated with faults. In addition to hydrological studies, numerous radon concentration determinations in ground waters and in soil gas have been performed in many seismically active areas in several countries, in order to elaborate a methodology to predict earthquakes. As known radon monitoring in soil gas and waters has been shown to be a promising method for predicting earthquakes. Radon levels are correlated with meteorological and hydrological data as well as with seismic activity, and often, abrupt changes in radon levels appear as precursors of earthquakes (King, 1986).

The radon variations are also caused by changes in meteorological parameters such as temperature, atmospheric pressure, wind velocity, humidity, rainfall, etc. The correlation of radon emission with meteorological factors is extremely useful for discriminating the genuine from spurious signals and has repeatedly been discussed (Singh et al., 1999).

It is found that the amplitude and shape of radon anomalies depend on the extent of fracturing, the dip angle, the type of rocks involved, the width of rupture zone, the permeability of fault-zone materials, the thickness and composition of the top-soil layer, the geomorphology, and the surface vegetation. Gas surveys are an effective method for locating unmapped faults provided that active faults are enriched in terrestrial gases due to the fact that they constitute significant "leaks" for the Earth's outgassing process (King, 1990, 1993).

Fractures and faults provide permeable pathways for fluids at a variety of scales, from great depths in the crust, to flow through fractured aquifers, geothermal fields and hydrocarbon reservoirs. Fracture-enhanced permeability depends on fracture density, orientation, and, mostly on the hydraulic conductivity of the different fractures and fault planes (Barton et al., 1995).

We aimed at gaining new insights on relationships between major tectonic features, including active and seismogenic structures, and fluid geochemistry on a regional scale in Aigion area (N. Peloponnese). Our main target was to identify geochemically anomalous areas characterized by the deepening of the hydrological circuits due to the presence of enhanced faulting and fracturing shown by spatial radon anomalies.

2. Aigion Region

2.1 Geological and hydrogeological setting

Geologically, the area belongs to the Olonos- Pindos isopic zone (Fig. 1a). The zone overthrusts towards the west the Gavrovo-Tripoli isopic zone and is composed of deep-sea sedimentary rocks deposited from the Triassic until the Palaeocene, when syn-orogenic turbiditic sedimentation commenced lasting until the Upper Eocene.

The pre-orogenic sequence of the zone is thought to represent a passive continental margin of the Apulian micro- continent (Degnan & Robertson, 1998). The bottom of the sequence is composed of Triassic clastic and carbonate rocks, which were deposited during the early stages of the Pindos
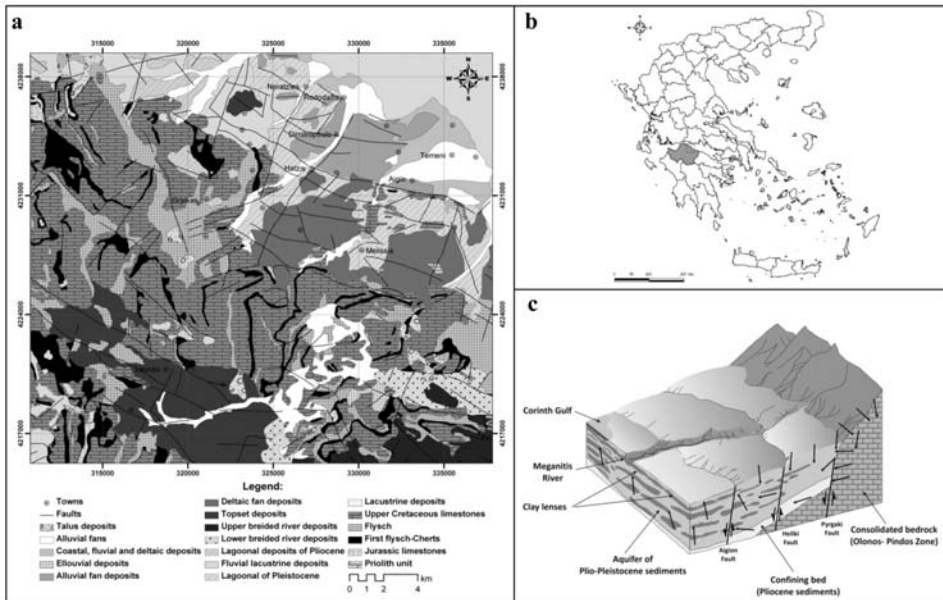
Fig. 1: a: Geological map of the region (Nikas, 2004), (b): geographical setting of Aigion region, (c): Schematic block diagram of the region.

ocean formation (Pe- Piper & Piper, 1991). A comfortable unit of pelagic limestones with red shale and siltstone intercalations deposited form the Late Karnian until the Liassic overlie the Triassic unit. During the Early Doggerian-Tithonian the red chert (radiolarite) unit was deposited. It represents a phase of rifting and is composed of red and green cherts accompanied by thin-bedded micritic limestones (Fleury, 1980). At the end of the Tithonian, a clastic unit composed of turbidite sediments, which derived from elevated parts of the Internal Hellenides to the East, was deposited and is usually referred as the "First Flysch" (Skourlis & Doutsos, 2003). The Mesozoic sequence ends with the deposition of platy pelagic limestones of Senonian age (Upper Cretaceous).

The pre-orogenic formations are overlain by a Flysch sequence deposited during Palaeocene and Eocene times, through a transitional sequence of Maastrichtian age. The Olonos- Pindos zone is heavily deformed by folds with NNW-SSE trending axes and thrust faults dipping to the NE and trending NW-SE (Skourlis & Doutsos, 2003).

The Upper Cretaceous limestones are the most permeable formation of the Olonos Pindos zone. They form a heterogeneous, slightly karstified aquifer that consists of carbonate beds of small thickness with chert intercalations. This aquifer, which is one of the major aquifers in the region lies in depth of 100 m and is extended to the Corinth Gulf where, it is discharged through sub marine springs.

Considering its hydraulic conductivity (k), it displays values that range between 7.1×10^{-5} and 6.7×10^{-3} m/s (Nikas, 2004). The joint network and the extension of the joints due to dissolution are factors that affect the movement and storage of water. Chert and flysch interferences form autonomous hydrogeological units which result in the presence of many low discharge springs (14-55 m^3/h).

A sequence of Plio-Pleistocene sediments as well as Holocene fluvial deposits was deposited uncomfortably above the Pindos zone formations. The sediments within the drainage basins are distinguished into three different facies, lacustrine- lagoonal marls, and marine sandstone, forming
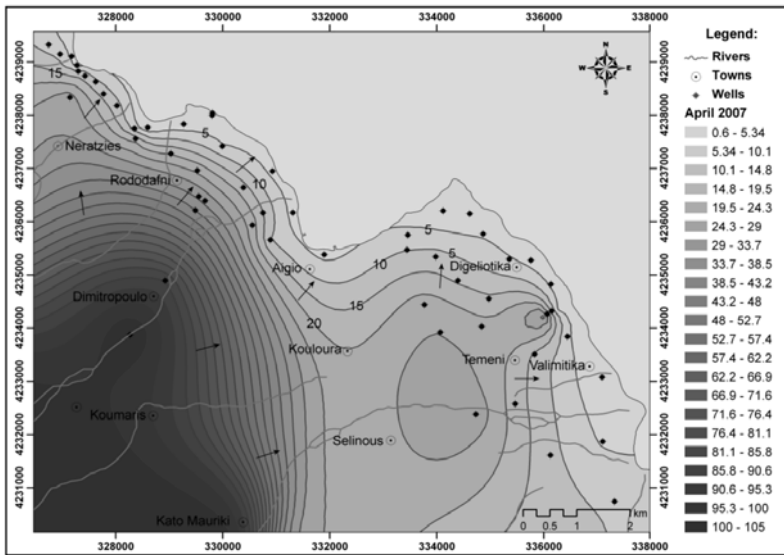
Fig. 2: Map showing of potentiometric surface (April 2007).

elevated terraces, and coarse-grained braided river or fan delta deposits (Poulimenos et al., 1989). Lacustrine-lagoonal marls are composed of coarsening upwards cycles with mudstone and silty sandstone beds (Zelilidis, 2000). Near bounding faults coarse-grained massive, matrix-supported, high dipping conglomerates accumulated. Moreover, in transfer zones thick interbedded mudstone-sandstone and conglomerate beds were deposited. Marine sandstone terraces are common in the northeastern part of the basin. Fan delta deposits include subaerial and sub-aqueous facies consisting of thick conglomeratic deposits (Poulimenos, 1993; Poulimenos et al., 1993). Their particle size differs with depth but also horizontally. The Plio-Pleistocene sediments are dipping towards the East and their thickness is increasing. The thickness of lacustrine-lagoonal deposits of Lower Pleistocene and alluvial deposits is increasing northwards and eastwards respectively.

The Plio–Pleistocene sediments form a uniform, unconfined aquifer with diverse permeability which is the second major aquifer of the area. Its hydraulic conductivity varies between 1.81×10^{-4} and 7.00×10^{-3} m/s (Nikas, 2004). From the potentiometric map (Fig. 2) it is shown that the Upper Pleistocene-Holocene alluvial fan in the plain area form a common water table due to contact of the aquifers that are hosted in the Plio-Pleistocene deposits. Moreover, along Selinous and Meganeitis river beds there is a zone of high fresh water income. Groundwater follows two main directions, one SE-NW and a second of SW-NE. The hydraulic gradient ranges between 4‰ -6‰ for the entire area, however along Selianitika village the hydraulic gradient reaches values that range between 15-20‰. The seasonal water table variations vary from 0.40 to 0.60 m.

The impermeable layer of the lacustrine-lagoonal sediments is the base of this aquifer, but also acts as the confining layer of the karstic aquifer. The aquifer of Plio-Pleistocene sediments is in many sites in direct contact with the karstic aquifer.

The aquifers are recharged mainly from direct infiltration of precipitation and river bed indirect infiltration. Direct infiltration also takes place in karstic aquifer along the outcrops of carbonate aquifer in the lowlands of the study area.

2.2 Tectonics

The eastern termination of the Corinth Gulf is a tectonically important area over the whole Greek Peninsula because of its high earthquake activity (Koukouvelas & Doutsos, 1996). A detailed mapping of the faults and formations has been carried out from many researchers (Poulimenos et al., 1989, Poulimenos, 1993; Doutsos et al., 1993; Koukouvelas et al., 1996, 1998, 2001; Zelilidis 2000; Pavlides et al., 2004), whereas uplifted shorelines, reversal of drainage patterns, earthquake induced landslides, both on land and offshore, faulted colluvial layers and historical and recent seismic activity provide evidence for the active deformation in the Gulf (Koukouvelas et al., 2001; Pavlides et al., 2004).

Furthermore, several geodetical surveys conducted in the area have shown that the Gulf of Corinth is at the present one of the most rapidly extending regions worldwide with an average extension rate between 4 and 14 mm/year (Clarke et al., 1998, Briole et al., 2000, Avalone et al., 2004).

Five active normal faults in the southern part of Aigion region namely, from south to north, the Pyrgaki, Melissia, Kerinia, Eliki and Aigion faults, control the accumulation of sediments at the western end of the Gulf of Corinth. These major faults, which control the environments of sedimentation of the Plio-Pleistocene deposits, also influence the configuration of hydrogeological units and the hydrology of the region.

3. Materials and methods

3.1 Sampling of groundwater and analytical procedures

In order to define the hydrochemical composition of the aquifer of the Plio-Pleistocene formation a total number of 18 samples were collected during May 2007 from springs and boreholes along the major faults of the region according to US EPA (1976) procedures. This choice arose from geological and structural considerations but also taking into consideration all the previous studies that have been carried out in the region. The sampling sites included 4 shallow wells, 11 cold springs as well as one spring with relatively elevated Tw (19□C) and a borehole with artesian flow, evident for deep flow circuits.

Two polyethylene bottles of 1 and 0.1 L volume, respectively were collected at each sampling site; the former containing bulk water sample for anion concentration analyses and the latter filtered (0.45 μm) and acidified with 0.5 mL ultrapure HNO_3.

The unstable physicochemical parameters (T_w, pH, Ec, O_2 and Eh) were measured *in situ*, using Consort® portable equipment. Additionally, alkalinity, CO_2 and H_2S concentrations were measured at the site using Hach® Digital Titrator and Hach® DR 2400 portable spectrophotometer, respectively. Anion (NO_3^-, NO_2^-, PO_4^{3-}, SO_4^{2-}, and F^-), SiO_2 and NH_4^+ concentrations were measured in a Hach® DR 4000 spectrophotometer except from Cl^-, which was measured using titration. Major cation (Ca^{2+}, K^+, Mg^{2+}, Na^+) concentrations were determined in a GBC® Avanta flame atomic absorption spectrophotometer. Trace element concentrations were measured using inductively coupled plasma-mass spectrometry (ICP-MS) in an ELAN 6100 Perkin-Elmer.

3.2 Measurement of Dissolved Radon and Thoron

Radon concentration in groundwater was measured using a portable radonmeter (SARAD RTM 2050). Radon levels in groundwater along the five different well-known traceable fault planes were measured. Every sample was measured directly after the sampling on a 2 h cycle. The error did not exceed 10% for the total number of samples. All measurements were reported in Bqm^{-3}.

Table 1. Descriptive statistics for water samples (n=17).

	units	mean	min	max	St dev
pH		7.30	6.91	8.23	0.35
Eh	mV	53.23	-219.00	153.00	116.50
Tw	°C	16.95	12.10	20.70	2.77
E.C.	μS/cm	786.54	204.00	1280.00	365.43
Th	Bqm^{-3}	378.50	223.00	433.00	103.71
Rn	$kBqm^{-3}$	3.07	1.10	6.70	1.94
H_2S	mg/l	0.02	0.00	0.30	0.08
CO_2	mg/l	128.23	57.00	267.00	53.39
Na^+	mg/l	37.42	2.10	282.00	67.44
K^+	mg/l	2.87	0.37	11.79	3.88
Mg^{2+}	mg/l	10.70	1.46	48.68	12.05
Ca^{2+}	mg/l	105.32	7.45	190.00	49.51
NH_4^+	mg/l	0.30	0.00	3.28	0.85
F^-	mg/l	0.64	0.00	8.20	1.90
HCO_3^-	mg/l	310.23	145.30	601.50	120.00
Cl^-	mg/l	16.43	0.00	73.10	20.14
SO_4^{2-}	mg/l	124.19	1.60	654.00	173.01
NO_3^-	mg/l	10.50	0.00	109.00	25.35
NO_2^-	mg/l	0.02	0.00	0.06	0.01
SiO_2	mg/l	10.27	0.70	25.10	5.59
Li	μg/l	15.63	0.61	36.32	14.26
U	μg/l	0.44	0.04	2.30	0.76
B	μg/l	340.30	31.95	846.00	441.45
Sr	μg/l	995.83	98.40	2480.17	980.05

The ^{222}Rn gas concentration is measured by the short living daughter products, generated by the radon decay inside a measurement chamber. Directly after the decay, the remaining ^{218}Po nuclei become charged positively for a short period, because some shell electrons are scattered away by the emitted alpha particle. Those ions are collected by the electrical field forces on the surface of a semiconductor detector. The collection of the short living daughter products on the surface of a semiconductor detector allows the separation of the single nuclides, with respect to their emission energy. The equilibrium between radon decay rate and ^{218}Po detector activity is given after about 5 half-life times (15 min). This time span defines the minimum achievable response time to a radon concentration step. The decay chain is continued by both beta emitters ^{214}Pb and ^{214}Bi followed by another alpha emitter, the ^{214}Po. The emission energies of ^{218}Po and ^{214}Po are different and therefore, it is possible to distinguish between the two nuclides by means of alpha spectroscopy. In case of ^{220}Rn, the direct daughter product ^{216}Po, which also underlies the ionisation process, is used to calculate ^{220}Rn activity concentration. The half-life of ^{216}Po is less than 1 s and therefore the equilibrium state between gas concentration and collected activity on the detector is present immediately. The single nuclides of ^{220}Rn decay chain will also be distinguished by alpha spectroscopy.
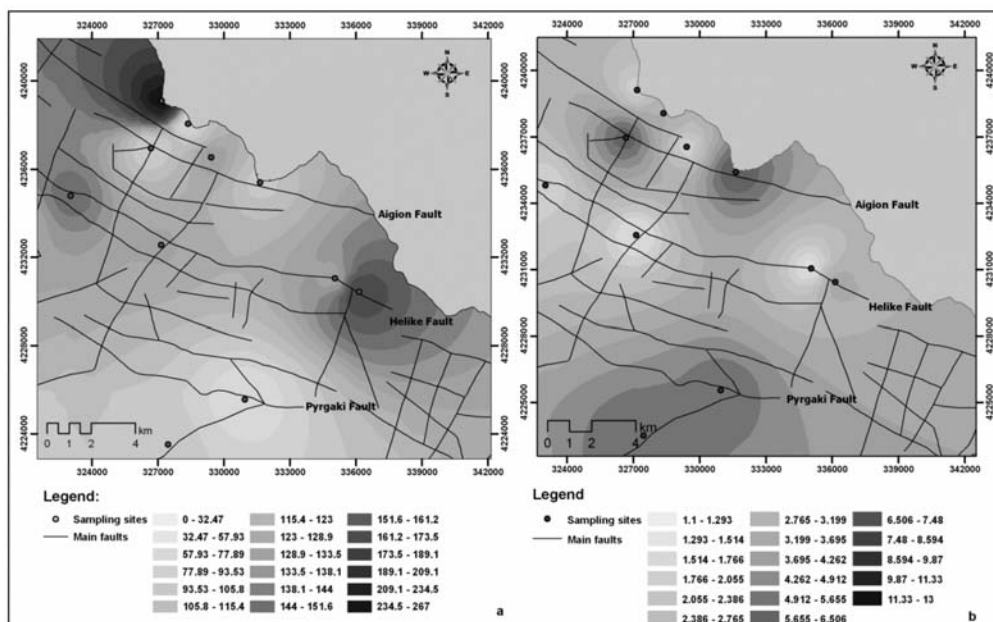
Fig. 3: Spatial distribution of measured values of (a) CO2 (b) Radon for the study area.

4. Results and discussion

Groundwaters of the study area can be grouped in three main hydrochemical types (Ca-HCO$_3$, Ca-HCO$_3$-SO$_4$ and Na-HCO$_3$). The CaHCO$_3$ water type prevails in the central part, though the other two types are found in the eastern and western margins of the area and are accompanied with a shift in NH$_4^+$, SO$_4^{2-}$, Na$^+$, K$^+$, F$^-$ and HCO$_3^-$ concentrations, as well as, enrichment in certain trace elements, such as B, Li, U. The descriptive statistics of the collected samples are shown in Table 1.

The measured radon concentrations vary between 1 and 8.2 kBqm^{-3}. The measured values for Aigion fault are consistent with those measured in soils from Richon et al, 2007 in the same region. As it is pointed out from the spatial distribution of ^{222}Rn (Fig. 3), along the Aigion, Pyrgaki and Helike faults three zones of elevated values are formed. Groundwater in the first two appears to have elevated values of Rn that reach 4 kBqm^{-3} on average, for Aigion fault and 6.5 kBqm^{-3} on average, for Pyrgaki fault. These anomalies can be related to the expected changes of rock properties along these fault zones, such as a large increase in the porosity and permeability of the deformed rocks. Through this porous and permeable medium, radon migrates upwards more easily (King, 1980; Kresl et al., 1993; Gudmundsson et al., 2001), whereas grain size reduction also affects uranium-bearing minerals found in the rock body resulting in an increase in radon emanation (Gundersen and Linda, 1991). This comes to an agreement with the existence of zeolites in the fault cores, evident of upward moving fluids from depth, during successive earthquakes (Koukouvelas and Papoulis, 2009).

The third zone is located along both eastern and western part of the Helike fault (Fig. 3) and appears to have unexpectedly low values (1.5 kBqm^{-3}, on average). In contrast to the other two fault zones the Helike fault appears to be sealed with clay minerals (Koukouvelas & Papoulis, 2009) suggesting a profound decrease in the permeability of the fractured zone resulting in restricted fluid circulation. Additionally, the same authors report, that the comparison of the mineralogical composition

of sediments along the planes of Pyrgaki and Aigion Faults and the presence of significant quantities of chlorite along their cores suggest deeper fluid circulation than the Helike Fault.

Radon has been used both to locate buried faults and to monitor faults for predicting earthquake activity. Anomalous high radon concentrations has been measured along many active faults worldwide (King 1986, 1990, 1993; Nishimura & Katsura, 1990; Kresl et al., 1993; Barton et al., 1995; Singh et al., 1999; Mancini et al. 2000; Gudmundsson et al., 2001; Ioannides et al., 2003; Moussa et al., 2003; Pizzino et al., 2004a, b; Richon et al., 2007). The Helike and Aigion faults are hosting strong and moderate earthquakes, respectively characterized by high slip rate (Koukouvelas & Doutsos, 1996, Tselentis et al. 1996). According to Koukouvelas & Papoulis (2009) although the Pyrgaki fault appears to have rather limited seismicity and generate moderate earthquakes, it is reasonable to suggest that it was much more seismically active in the past, taking into consideration that all faults control fan-deltas.

Furthermore oxidation of iron during faulting, deformation and subsequent weathering, results in distinctive iron-staining nature of many fault zones. Iron oxides and other metal oxides scavenge uranium and radium available through the weathering processes. These processes increase the radon emanation from rocks and soils, and make radon readily available to local groundwater (Al-Tamimi & Abumurad, 2001). Another source of high radon (^{222}Rn) values in the region could be connected with the carbonate rocks which appear to be enriched in U (Pizzino et. al., 2004a).

Two secondary zones with high ^{222}Rn concentrations were traced perpendicularly to the three major zones in the NW and NE margins of the region (Fig. 3). These anomalies coincide with hydrochemical differentiation noticed in these areas (Katsanou, 2007). The higher Ec and CO_2, Na, SiO_2, F^-, SO_4, HCO_3, Li, U contents together with their relatively high temperatures (up to 21$^\square$C) testify both, deep hydrological circuits and longer lasting water-rock interaction processes compared to the other shallow aquifers discharging throughout the entire area. However, the existence of deep fluid circulation in the central part as well, cannot be excluded. The absence of deep fluid signatures at this part can be attributed to the fact that they might be masked by the mixing of huge amounts of runoff water, which strongly recharges this area.

The worldwide distribution of springs in which HCO_3 concentration exceeds 1000 mg/l generally coincided with major seismic belts (King et al., 1993). In the margins of the region ^{222}Rn and HCO_3 exhibit a positive correlation, where both reach the highest values (8.2 kBqm^{-3} and 600 mg/l respectively). These relatively high values could be attributed to the presence of CO_2 uprising from deep, interacting with clay strata through active vertical faults of the region. The enhanced presence of CO_2 as typical gas phase along an active fault acts as catalyst for water-rock interaction processes. These necessarily involve the existence of a belt of fluid geochemistry anomalies that persist until the CO_2 reactions are present (Pizzino et. al, 2004a). The latter display a rough positive correlation between the variables indicating that increasing ^{222}Rn activities are prevailingly due to increasing water- rock interaction, which releases both major ion and ^{222}Rn and its parents to the groundwaters (D'Alessandro & Vita, 2003).

5. Conclusions

The present study has shown evidence of possible deep circulation of fluids in the investigated area due to the fact that is crossed by very active and seismogenetic fault segments (Helike and Aigion ones), associated to upraise of deep fluids.

The radon spatial distribution was distinguished into three major zones formed along Aigion, He-

like and Pyrgaki faults. Apart from these, two more, located in the NW and NE margins of the region were noticed. Water samples located in this region are significantly different compared to the rest. Noticeably high values of EC, T_w, CO_2, Na^+, SiO_2, F^-, SO_4^{2-}, Li, and slightly elevated U, H_2S, NH_4^+ and B concentrations together with low Eh values denote water-rock interaction processes and possible convection of fluids from great depth.

Radon stands out as a reliable tracer of recent fractured and faulted areas but also a geochemical pathfinder of deep fluid pathways in Aigion region. Thus, radon measurement may be a successful method for mapping even unknown faults or their specific features.

Since radon has been used both to locate buried faults and to monitor faults in hope of predicting earthquake activity, it is possible that the monitoring of radon emissions could be used as a tool towards this direction.

6. References

Al-Tamimi, M.H., Abumurad, K.M., 2001. Radon anomalies along faults in North of Jordan. *Radiat. Meas* 34: 397-400.

Avallone, P., Briole, A.M., Agatza-Balodimou, H., Billiris, O., Charade, C., Mitsakaki, A., Nercessian, K., Papazissi, D., Paradissis, and Veis, G., 2004. Analysis of eleven years of deformation measured by GPS in the Corinth Rift Laboratory area. *C. R. Geosci*. 336: 301-312.

Barton, C.A., Zoback, M.D. and Moos, D., 1995. Fluid flow along potentially active faults in crystalline rocks. *Geology* 23 (8): 683- 686.

Briole, P., Rigo, A., Lyon-Caen, H., Ruegg, J.C., Papazissi, K., Mitsakaki, C., Balodimou, A., Veis, G., Hatzfeld, D. and Deschamps, A. 2000. Active deformation of the Corinth rift, Greece: results from repeated Global Positioning System surveys between 1990 and 1995. *J. Geophys. Res*. 105: 25,605-25,625.

Clarke, P.J., Davies, R.R., England, P.C., Parsons, B.E., Billiris, H., Paradissis, D., Veis, G., Cross, P.A., Denys, P.H., Ashkenazi V. and Bingley, R., 1997. Geodetic estimation of seismic hazard in the Gulf of Corinth. *Geophys. Res. Lett*. 24: 1303-1306.

D'Alessandro, W., & Vita, F., 2003. Groundwater radon measurements in the Mt.Etna area. *Journal of Environmental Radioactivity* 65: 187-201.

Degan, P.J., Robertson, A.H.F., 1998. Mesozoic- early Tertiary passive margin evolution of the Pindos ocean (NW Peloponnese, Greece). *Sedimentary Geology* 117:33-70.

Durrani, S.A., Ilic, R. (Eds.), 1997. Radon Measurements by Etched Track Detectors: Application to Radiation Protection, Earth Sciences and the Environment. World Scientific, Singapore.

Fleury, J.J., 1980. Evolution d'une platforme et d'un bassin dans leur cadre alpin: les zones de Gavrovo-Tripolitze et du Pinde-Olonos. *Soc. Goel. Nord, Spec. Publ*. 4.

Gundersen, L.C.S., Linda, C.S., 1991. Radon in sheared igneous and metamorphic rocks. In: Gundersen, L.C.S., Wanty, R.B. (Eds.), 1991. Field Studies of Radon in Rocks, Soil and Water, *US Geol. Survey Bull*. 39-50.

Gudmundsson, A., Berg, S.S., Lyslo, K.B. & Skurtveit, E., 2001. Fracture networks and fluid transport in active fault zones, *J. Struct. Geol*. 23, 343-353.

Ioannides, K., Papachristodoulou, C., Stamoulis, K., Karamanis, D., Pavlides, S., Chatzipetros, A. and Karakala, E., 2003. Soil gas radon: a tool for exploring active fault zones, *App. Radiat. Isots*. 59: 205-213.

Katsanou, K., 2007. Environmental and hydrogeological study of the hydrological basins in the broader

area of Aigion region by the use of hydrochemical methods. Master thesis. University of Patras, in Greek.

King, C.Y., 1986. Gas Geochemistry Applied to Earthquake Prediction: An Overview. *J. Geophys. Res.* 91, 12, 269-12,281.

King, C.Y., 1990. Gas-geochemistry approaches to earthquake prediction. In Proc. International Workshop on Radon Monitoring in Radioprotection, Environmental Radioactivity and Earth Sciences, ITCP, Triest, Italy, April 13-14, 1989 (eds. L. Tommasino, G. Furlan, H. A. Khan, and M. Monin) (World Press, Singapore 1990) 244-274.

King, C.Y., Zhang, W. and King, B.S., 1993. Radon anomalies on three kinds of faults in California. *Pure Appl. Geophys.* 141: 111-124.

Koukouvelas, I. K. & Papoulis, D., 2009. Fluid involvement in the active Helike normal Fault, Gulf of Corinth, Greece. *J. Struct. Geol.* 31: 237-250.

Koukouvelas, I.K., Stamatopoulos, L., Katsanopoulou, D., Pavlides, S., 2001. A palaeoseismological and geoarchaeological investigation of the Eliki fault, Gulf of Corinth, Greece. *J. Struct. Geol.* 23: 531-543.

Koukouvelas, I.K., 1998. The Egion fault, earthquake-related and long term deformation, Gulf of Corinth, Greece. *Journal of Geodynamics* 26: 501-513.

Koukouvelas, I.K., Doutsos, T.T., 1996. Implications of structural segmentation during earthquakes: the 1995 Egion earthquake, Gulf of Corinth, Greece. *J. Struct. Geol.* 18(12): 1381-1388.

Kresl, M., Vakova, V., Klecka, M., 1993. Radon in soils overlaying several tectonic zones of the south Bohemian Moldanubicum. Jb. Geol. B. A. 136: 799-808.

Mancini, C., Quattrocchi, F., Guadoni, C., Pizzino, L., Porfidia, B., 2000. ^{222}Rn study throughout different seismotectonical areas: comparison between different techniques for discrete monitoring, *Ann. Geofis.* 43 (1): 31-60.

Moussa, M.M., Gabar, A., Arabi, M.E., 2003. Soil radon survey for tracing active fault: a case study along Qena- Safaga road, Eastern Desert, Egypt. *Radiat. Meas* 37: 211-216.

Nikas K., 2004. Hydrogeological conditions of NW Achaia. PhD Study. University of Patras.

Nishimura, S., Katsura, I., 1990. Radon in soil gas: application in exploration and earthquake prediction *In: Durrance, E.M. (Ed.). Geochemistry of Gaseous Elements and Compounds. The Ophrastus Publication, S.A. Athens*, 497-533.

Pavlides S.B., Koukouvelas I.K., Kokkalas S., Stamatopoulos L., Keramydas D., Tsodoulos I., 2004. *Quaternary International* 115-116: 139-154.

Pe-Piper, G., Piper, D.W.J., 1984. Tectonic setting of the Mesozoic Pindos basin of the Peloponnese, Greece. *Geol. Soc. Lond. Spec. Publ.* 17: 563-568.

Pizzino, L., Burrato, P., Quattrocchi, F. & Valensise G., 2004a. Geochemical signatures of large active faults: The example of the 5 February 1783, Calabrian earthquake (southern Italy). *Journal of Seismology* 8: 363-380.

Pizzino, L., Quattrocchi, F., Cinti, D., Galli, G., 2004b. Fluid geochemistry along the Eliki and Aigion seismogenic segments (Gulf of Corinth, Greece). *Comptes Rendus Geosciences* 336: 367-374.

Poulimenos, G., Albers, G. and Doutsos, T., 1989. Neotectonic evolution of the central section of the Corinth graben. *Z. dt. geol. Ges* 140: 173-182.

Poulimenos, G., 1993. Tectonics and sedimentation in the western Corinth graben. *Neues Jahrbuch fuer Geologie und Palaontologie Monatshefte* 10: 607-630.

Poulimenos, G., Zeilidis, A., Kontopoulos, N. and Doutsos, T., 1993. Geometry of the trapezoidal fan deltas and their relationship to extensional faulting along the south-western margins of the Corinth rift,

Greece. *Basin Research* 5: 179-192.

Quattrocchi, F., 1999. In Search of Evidence of Deep Fluids Discharges and Pore Pressure Evolution in the Crust to Explain the Seismicity Style of the Umbria-Marche 1997 –1998 seismic sequence (Central Italy). *Annali di Geophysica* 42 (4): 609-636.

Richon, P., Bernard, P., Labed, V., Sabroux, J.C., Beneïto, A., Lucius, D., Abbad, S. and Robe M.C., 2007. Results of monitoring ^{222}Rn in soil gas of the Gulf of Corinth region, Greece *Radiat. Meas* 42(1): 87-93.

Robertson, A.H.F., Clift, P.D., Degnan, P.J., Jones, G., 1991. Palaeogeographic and palaeotectonic evolution of the Eastern Mediterranean Neotethys. *Palaeogeogr. Palaeocl. Palaeoecol.* 87: 289-343.

Singh, M., Kumar, M., Jain, R.K. and Chatrath, R.P., 1999. Radon in ground water related to seismic events. *Radiat. Meas.* 30: 465-469.

Skourlis, K., Doutsos, T., 2003. The Pindos Fold-and-thrust belt (Greece): inversion kinematics of a passive continental margin. *Int. J. Earth Sci.* 92: 891-903.

Tselentis G.A., Melis N.S., Sokos E. and Papatsimpa K., 1996. The Egion June 15, 1995 (6.2 ML) earthquake, Western Greece. *Pure Appl. Geophys.*, 147, 83–98.

U.S. Environmental Protection Agency 1976. Quality criteria for water. Washington, DC, 501 pp.

Zelilidis, A., 2000: Drainage evolution in a rifted basin, Corinth graben, Greece. *Geomorphology*, 35: 69-85.

QUALITY CHARACTERISTICS OF SURFACE WATERS AT ASPROLAKKAS RIVER BASIN, N.E. CHALKIDIKI, GREECE

Kelepertzis E.[1], Argyraki A.[1], Daftsis E.[2] and Ballas D.[2]

[1] *Department of Economic Geology and Geochemistry, University of Athens, 157 84 Athens – Greece, kelepert@geol.uoa.gr, argyraki@geol.uoa.gr*

[2] *Hellas Gold S.A., edaftsis@hellas-gold.com, dballas@hellas-gold.com*

Abstract

The present study reports on a four sampling period (April 2008-July 2008-November 2008-February 2009) study of water quality in streams of NE Chalkidiki. A total of 80 surface water samples were collected and analysed for the major ions Ca^{2+}, Mg^{2+}, K^+, Na^+, Cl^-, HCO_3^-, SO_4^{2-}, NO_3^- and the trace elements Pb, Fe, Cd, Cu, Cr, Ni, Zn, Mn and As. Also pH, Electrical Conductivity (EC), Total Dissolved Solids (TDS), Temperature, as well as the stream water discharge at each sampling point, were determined in the field. The treatment and the subsequent evaluation of the data showed that the water samples are divided into three separate groups, reflecting the chemistry of water in the three sub-basins of the area i.e., Kokkinolakkas, Kerasia and Piavitsa. The water of the first one is possibly affected by the past mining activities of the area, whereas samples from the other two reflect the influence of sulphide mineralization on the hydrogeochemistry of the corresponding streams. No effect of the seasonal differentiation of stream water discharge was observed.

Key words: *Asprolakkas Basin, NE Chalkidiki, water quality, mining activities.*

1. Intoduction

The Asprolakkas stream drains materials from the geological formations of the North East Chalkidiki peninsula, Northern Greece. The deposits of the area have a long exploitation history that started at 600BC and continues today. During the last century, several mining companies exploited the sulphide and the associated manganese oxide ore deposits. In April 2004, the whole Kassandra mines property was transferred by the Greek State to "Hellas Gold S.A.", including the mineral rights in an area of 265 stremmas, the Stratoni Operation (Pb/Zn/Ag) and two projects for development, the Olympias carbonate-hosted (Pb/Zn/Au/Ag) and the Skouries porphyry (Cu/Au). The whole area has already been included in the ProMine Project, financed by the European Union. This project mainly aims at developing the first European GIS-based database containing the known and predicted metalliferous resources and calculating the volumes of potentially strategic metals (e.g. cobalt, niobium, vanadium, antimony, platinum group elements and REE) and minerals that are currently not extracted in Europe. Currently, in the Stratoni Operation, only the Mavres Petres deposit is mined, by overhand drift and fill method using cemented tailings for backfill.

Acid mine water, deriving from both Mavres Petres and Madem Lakkos mines, is directed to the water treatment plant, located next to the Stratoni flotation plant. The treatment is carried out in agitated reactors with hydrated lime $(Ca(OH)_2)$ for neutralization. Additional measures that have been

undertaken to prevent and effectively control acid mine drainage even under extreme conditions, include the construction of a new water treatment plant by the entrance of the mine and the closure of the exhausted Madem Lakkos mine by backfilling the old mining voids.

The main objectives of the present study are: a) to determine the physical and chemical characteristics of surface water from the streams running within the Asprolakkas river basin, throughout a hydrologic year, and b) to assess the possible impact of mineralization and mining activity on the hydrogeochemistry of the drainage system.

2. Site Description

2.1 Geology and Mineralization

Geologically the wider area belongs to the southernmost extension of the Serbo-Macedonian Belt, a series of metamorphic rocks that extends northward into Bulgaria and eastern Yugoslavia (Nebel et al. 1991). The Serbo-Macedonian Massif is divided into two formations: the Vertiskos formation (uppermost member) and the Kerdylia formation (lowermost member) (Kockel et al., 1977). The Kerdylia formation, which is of higher metamorphic grade, mainly consists of migmatitic biotite gneiss interlayered with several marble horizons, amphibolites and hornblende gneiss whereas the Vertiskos sequence, outcropping in the studied area, largely includes biotite-muscovite gneiss and amphibolites with hornblende amphibolite intercalation (Kockel et al., 1977). A fault zone (Stratoni – Varnava fault) separates the two formations, a major structural feature that dominates the area.

The area is also characterised by calc-alkaline postorogenic granitoids of Tertiary age (Nicolaou and Kokonis. 1980, Kalogeropoulos et al., 1989; Kroll et al., 2002): the Stratoni granodiorite (29Ma), the quartz-diorite porphyry of Fisoka and the Skouries shoshonitit porphyry being the host of a porphyry Cu-Au deposit (Figure 1). The intrusion age of Skouries deposit was determined at 19±1 Ma (Frei. 1995).

These intrusive bodies are strongly related to various ore deposits in the area. The mineralised zone is often referred to as the Stratoni-Piavitsa belt and the mineralization is classified as Pb-Zn-Ag carbonate replacement type mineralization (Madem Lakkos and Mavres Petres mines), both massive and disseminated in form (Nebel et al., 1991). In addition, the porphyry Cu-Au deposits in Skouries and Fisoka, south of Stratoni village, represent another ore type (Kockel et al., 1975) while Mn ores occur along the Stratoni-Varvara fault, especially at the west part of the studied area.

2.2 Physiography and hydrology

The area is characterised by mountainous relief with 92% of the surface covered by mainly deciduous forest. Streams within the Asprolakkas water basin originate from the Stratonikon Mountain and follow a general N-S direction. The three main streams that are studied are flowing through a mountainous landscape within the sub-basins of Piavitsa, Kerasia and Kokkinolakkas. They all discharge their water in Asprolakkas which has an E-W direction flowing towards the Golf of Ierissos. The climate is typical Mediterranean, with rainy winters and dry, warm summers. Flow rates of the streams are rapidly affected by rainfall and present strong variations, according to the pluviometric regime, resulting in the completely dry up of some streams during the summer months.

3. Methods

3.1 Sampling

Field work was performed in 4 sampling periods: April 2008, July 2008, November 2008 and Feb-
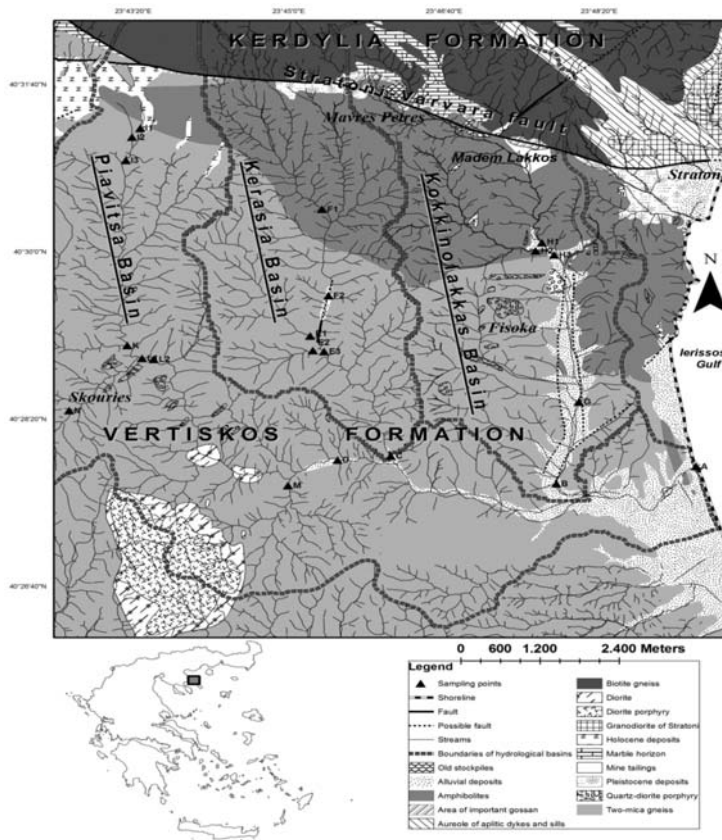
Fig. 1: Map of the study area showing geology, hydrological basins, old ore stockpile disposal areas and sampling points (after Kockel et al. 1977).

ruary 2009, covering all the seasons of a hydrologic year. Twenty one surface water samples were collected during each sampling period, corresponding to a final total number of 80 samples. The sampling points (Fig. 1) are located in three basins, named from east to west as Kokkinolakkas (samples: B, G, H1, H2, and H3), Kerasia (samples: E1, E2, E3, F1 and F2) and Piavitsa (samples: I1, I2, I3, K, L1, L2, M, N). The selection of the water samples was carried out in order to cover the three sub-basins that discharge their waters in Aspolakkas, contributing to its hydrogeochemistry. Samples B and G were only sampled at April 2008 and February 2009 because of lack of water during the dry period. Sample N represents water discharged by the old exploration adit of Skouries deposit.

Samples were taken using 1l polyethylene bottles, cooled during transport and then stored in the refrigerator at 4°C until analysis. The polyethylene bottles were previously rinsed with deionised water. Moreover, samples for metal analysis were filtered immediately in the field through 0.45μm Millipore filters, using 60 ml-syringes, stored in 50 ml polyethylene bottles under cooling conditions and acidified down to pH<2 with HNO_3 at the Hellas-Gold Quality Control Laboratory.

3.2 Field measurements

Field measurements such as pH, Electrical Conductivity (EC), Total Dissolved Solids (TDS), Tem-

perature (T) and Redox Potential (Eh) were measured in-situ using a Multi 350i instrument of WTW. The pH electrode was calibrated every 10 measurements, using standard solutions of pH 7 and 8. Stream water discharge was calculated in all cases using a 0012B (Display Unit) Model of Valeport, in previously defined stream sections. Data for the stream water discharges for the sampling period of April 2008 were obtained by the staff of Hellas Gold S.A., since it was not possible to measure the flow rates at the time of our visit to Stratoni village.

At the end of each sampling day, alkalinity (mg/l as $CaCO_3$) and nitrate (NO_3^-) concentrations were measured by using the digital titration method reported by the Hach Instruments (bromocresol green-methyl red indicator using H_2SO_4) for total alkalinity and the Hach DR850 portable colorimeter for the determination of nitrate.

3.3 Chemical analyses

Chemical analyses were performed at the Department of Geology and Geoenvironment of National and Kapodistrian University of Athens, the ACME Analytical Laboratories Ltd of Canada, and at the Laboratory of Quality Control of "Hellas Gold S.A." at Stratoni. In particular, K^+, Na^+, Ca^{++}, Mg^{++} and SO_4^{2-} concentrations were measured at the Laboratory of Quality Control at Stratoni while Cl^-, Pb, Zn, Mn, Cu, Ni, Cr, and Cd, at the Laboratory of Economic Geology and Geochemistry, University of Athens. Arsenic (As) concentration was only measured for November and February sampling periods at ACME Analytical Laboratories. Fe concentration was measured at the Laboratory of University of Athens (sampling periods April and July) and at ACME Analytical Laboratories (sampling periods November and February).

Sulphate was gravimetrically measured as $BaSO_4$, while chloride was measured photometrically using a Hach DR/4000 apparatus (detection limits being 1 mg/l and 0.24 mg/l respectively). Heavy metal (Fe for sampling periods April and July, Pb, Cu, Ni, Cr and Cd) concentrations were determined by graphite furnace, Atomic Absorption Spectroscopy (Perkin Elmer 1100B) whereas Zn and Mn were analysed by graphite furnace and by flame, Atomic Absorption Spectroscopy (Perkin Elmer 1100B), when necessary. Detection limits were calculated by standard deviations from 5 measurements of blank. Detection limits of graphite furnace (AAS) were: 5 μg/l for Fe, 1 μg/l for Pb, 5 μg/l for Zn, 1 μg/l for Mn, 0.5 μg/l for Cu, 1 μg/l for Ni, 0.5 μg/l for Cr and 0.5 μg/l for Cd whereas the detection limit of flame (AAS) was 0.01 mg/l for Zn and Mn. Potassium, Na, Ca and Mg concentrations were determined by Inductively Coupled Plasma Emission Spectroscopy (ICP/AES) with detection limits being 1 μg/l, 1 μg/l, 5 μg/l and 1 μg/l respectively. Arsenic and Fe (November and February sampling periods) were measured by Inductively Coupled Plasma Mass Spectroscopy (ICP/MS) with detection limits being 0.5 and 10 μg/l respectively.

Certified international reference materials for trace element content (low and high level) were also analysed in order to check the accuracy of the analytical data and close agreement with certified values was achieved for all metals. The accuracy of chemical analyses was also checked by the anion-cation balance, being lower than 5% for 80% of the total number of water samples.

4. Results and Discussion

4.1 Basic statistics of physico-chemical parameters

All the streams are characterised by alkaline pH values (mean 8.1) and present wide range of concentrations for most of the analysed parameters like EC and SO_4^{2-}, HCO_3^-, Ca^{2+}, Mg^{2+}, Mn and Zn, having a range of 328-1669 μS/cm, 28-857 mg/l, 79-265 mg/l, 40-231 mg/l, 11-94 mg/l, 3-7899 μg/l

Box and whisker plots for selective parameters

1=Piavitsa, 2=Kerasia, 3=Kokkinolakkas
Values in µS/cm for EC, mg/l for Ca, Mg, SO4, HCO3 and µg/l for Fe, Pb, Zn, Mn, Ni and As
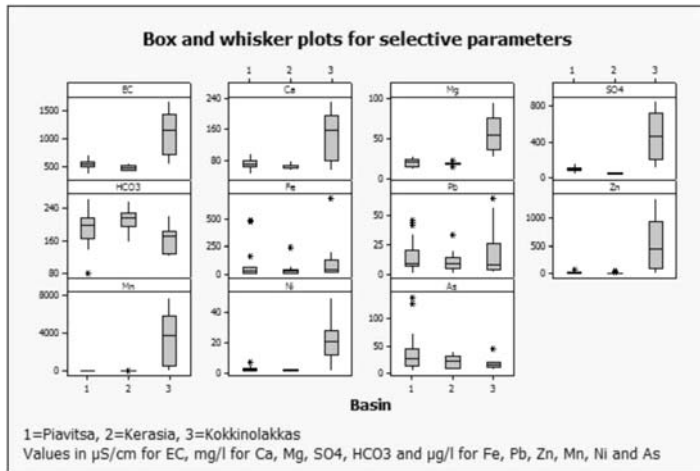
Fig. 2: Box and whisker plots for selected parameters of the three studied basins.

	Parameter	Unit	Mean	Median	Min	Max	Standard Deviation
Piavitsa	EC	µS/cm	514	520	328	685	79.71
	Ca	mg/l	68.5	65.7	40	96	12.26
	Mg	mg/l	18.5	18.5	11	27	4.84
	HCO$_3$	mg/l	193.6	200	79	265	37.54
	SO$_4$	mg/l	92.4	93.7	28	151	29.90
	Fe	µg/l	66.4	30.5	9	489	116.80
	Pb	µg/l	14.8	9.6	2	45	11.49
	Zn	µg/l	22.1	14.3	5	70	15.77
	Mn	µg/l	37.8	23.5	5	106	33.28
	Ni	µg/l	2.6	2	1	7	1.56
	Cd	µg/l	1	1	1	1	0
	As	µg/l	39.4	27.6	4	141	39.65
Kerasia	EC	µS/cm	455.4	458	376	536	47.47
	Ca	mg/l	59.9	58.4	51	75	5.96
	Mg	mg/l	17	16.9	13	21	1.64
	HCO$_3$	mg/l	212.0	215.5	155	260	24.55
	SO$_4$	mg/l	44.2	43	31	61	8.12
	Fe	µg/l	42.4	32	12	242	51.97
	Pb	µg/l	10.9	10	1	33	7.15
	Zn	µg/l	12.7	11	3	50	9.04
	Mn	µg/l	9.7	8.8	3	26	5.19
	Ni	µg/l	1.7	1.5	1	3	0.84
	Cd	µg/l	1	1	1	1	0
	As	µg/l	21.6	21.8	7	42	13.06
Kokkinolakkas	EC	µS/cm	1117.4	1135	510	1669	390.64
	Ca	mg/l	148.1	157	52	231	63
	Mg	mg/l	56.8	53	26	94	22.61
	HCO$_3$	mg/l	162.7	170.5	122	222	31.14
	SO$_4$	mg/l	482.9	461.6	107	857	260.64
	Fe	µg/l	119.9	43.5	9	681	186.85
	Pb	µg/l	17.8	8.5	2	64	20.61
	Zn	µg/l	546	440	10	1350	436.78
	Mn	µg/l	3547.3	3887.5	91	7899	2611.59
	Ni	µg/l	21.4	20.8	1	50	15.52
	Cd	µg/l	4.1	3.5	2	8	1.89
	As	µg/l	18.8	16.2	8	45	11.43

Table 1: Basic statistics of selected analysed parameters for the three basins. Data from the 4 sampling periods.

and 3-1350 µg/l respectively. In contrast, K, Na, NO$_3$, and Cl concentrations are very low presenting a range of 1-13 mg/l, 7-23 mg/l, 2-8 mg/l and 5-20 mg/l respectively whereas Fe, As, Pb, Ni, Cu and Cd mean values are 69.1 µg/l, 29.44 µg/l, 14.14 µg/l, 8.27 µg/l, 4.5 µg/l and 3.08 µg/l respectively.

Because of the great variability of some of the above mentioned analysed parameters, it was considered necessary to study the three basins individually. Table 1 shows a summary of the basic sta-

tistics of selected analysed parameters for each of the studied basins (Piavitsa, Kerasia and Kokkinolakkas), for all the sampling periods. Sample A was not included in order to obtain the basic statistics and was excluded for the further treatment since its chemistry is slightly affected by the sea (mean concentrations of Cl$^-$ and Na$^+$ being 255mg/l and 128mg/l respectively). The concentrations of major parameters such as K, Na, NO$_3$ and Cl and trace elements such as Cu and Cr are either very low or close to the detection limit of the analytical technique and they have been omitted in Table 1. The concentrations of these elements were always below the drinking water standards (200 mg/l for Na, 50 mg/l for NO$_3$, 250 mg/l for Cl, 2000 µg/l for Cu and 50 µg/l for Cr, according to the EU Council Directive 98/83/EEC on the quality of water intended for human consumption).

4.2 Comparison between the three basins

Most of the studied parameters present distinct differences between the three sub-basins of the area. Figure 2 visually displays the range of concentrations of the major constituents and the main differences between the three sub-basins as box-and-whisker plots, including values from all the sampling periods. The length of box indicates the interquartile range while the heavy horizontal line inside the box indicates the median. Whiskers are lines that extend from the box to the highest and lowest values excluding outliers (*). Outliers are defined as cases in which the values are between 1.5 and 3 times larger than the length of the box from its upper or lower border.

In general, it is observed that elemental concentrations in water samples from Kokkinolakkas are higher and of a wider range when compared to concentrations from Kerasia and Piavitsa samples. In particular, EC, Ca^{2+}, Mg^{2+}, SO$_4^{2-}$, Zn, Mn, Ni and Cd (Table 1) present considerable higher concentrations in the water samples from Kokkinolakkas basin indicating different natural and/or anthropogenic factors that control its water chemistry. On the contrary, concentrations of As in Piavitsa, where there is no mining activity, are approximately twice as much as the concentration in Kokkinolakkas whereas Fe and Pb concentrations do not show a clear trend presenting outliers and a subsequent wide range of values in the three basins. Same differences in water quality from the three basins were also reported in the study by Lazaridou-Dimitriadou et al. 2004.

Regarding the EU Council Directive 98/83/EEC, Pb, Mn and As concentrations in Piavitsa basin usually exceed the parametric values of 10 µg/l, 50 µg/l and 10 µg/l respectively, while Fe concentrations of sample N (old exploration adit of Skouries) exceed the guideline value of 200 µg/l. Concentrations of all the other elements are lower than the regulatory limits. Kerasia basin shows a similar pattern for all the studied elements, except for the fact that Mn levels are always below the drinking quality standards. Only sample F2 for February sampling period exceeds the corresponding limit of 200 µg/l, in regard to Fe concentration. Finally, water samples from Kokkinolakkas present SO$_4$, Mn, Ni, Cd, As and Pb concentrations that are usually considerable higher than the parametric values. The only exception is sample H2, which presents its own water chemistry.

Regarding the permissible environmental limits for surface waters intended to be used for irrigation, set for Chalkidiki Prefecture (Dec. No 96400/85, G.G. 573/B/85), all the studied water samples for all the analysed parameters present concentrations that do not exceed the corresponding values, except for Mn concentrations at Kokkinolakkas basin (the permissible limit for Mn is 2000 µg/l).

In respect with water types, according to the Piper diagrams presented in Figure 3 for April sampling period, two groups of waters can be differentiated. The first group is characterised by high Ca-HCO$_3$ and includes all samples from Kerasia and Piavitsa (except for sample M), as well as sample H2 from Kokkinolakkas stream, indicating the influence on water chemistry of the Ca-rich geological for-
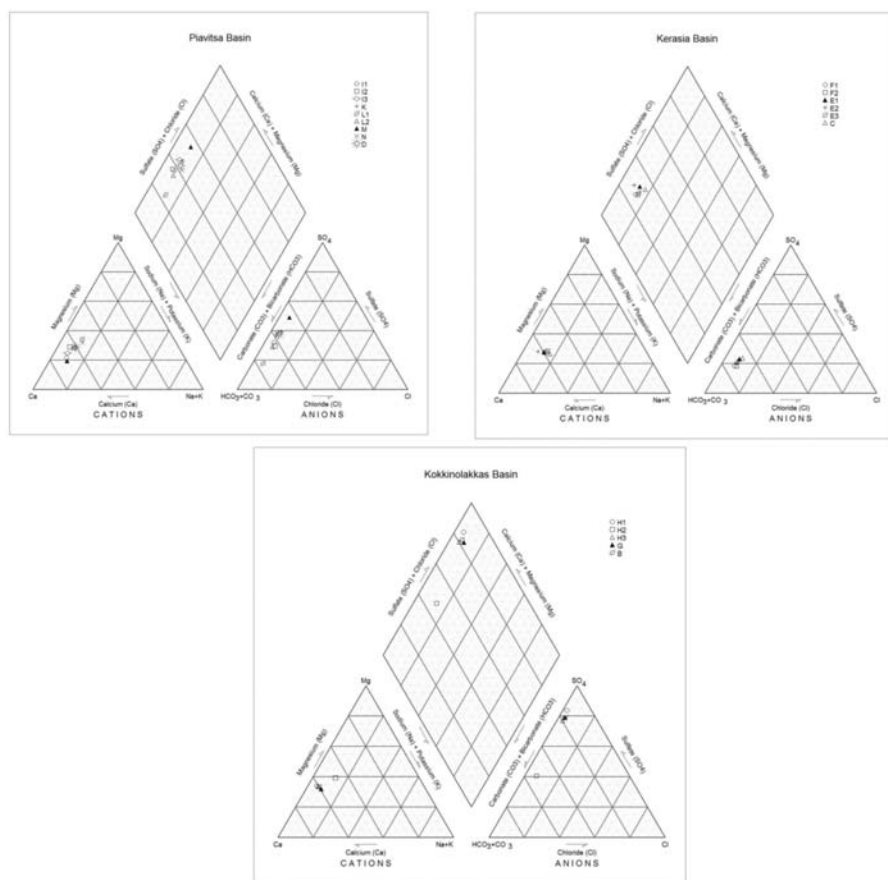
Fig. 3: Piper diagrams for the water samples for April sampling period.

mations outcropping at the North part of the studied area (marbles of Kerdylia formation). The second group is characterised by high Ca-SO$_4$, and consists of samples from Kokkinolakkas and sample M from Piavitsa, reflecting the influence of the polymetallic sulphide ore deposits.

The chemistry of sample H2, located within Kokkinolakkas, presents considerable differences in comparison with the other water samples of this basin, presenting the following mean concentrations: 118 mg/l for SO$_4^{2-}$, 56 mg/l for Ca^{2+}, 29 mg/l for Mg^{2+}, 4.5 μg/l for Pb, 13 μg/l for As, 17 μg/l for Zn, and 149 μg/l for Mn, while concentrations of Ni and Cd are below the detection limits. As a consequence, it may be suggested that it derives from a different area and drains different materials, being obviously unaffected by the presence of the extended sulphide mineralisation. Apart from the apparent influence of the sulphide mineralization on the water chemistry, the existence of various old stockpiles of mineral wastes that had been deposited in the past along Kokkinolakkas (Papakonstantinou et al. 1996), particularly at the North part of the stream (Figure 1), may have contributed to the elevated concentrations of sulphate and metals for the rest of the samples of this basin.

Figure 4 presents the Ficklin diagram for the water samples of Kokkinolakkas basin (except for sample H2), including all the sampling periods. The Ficklin diagram is used to describe the charac-
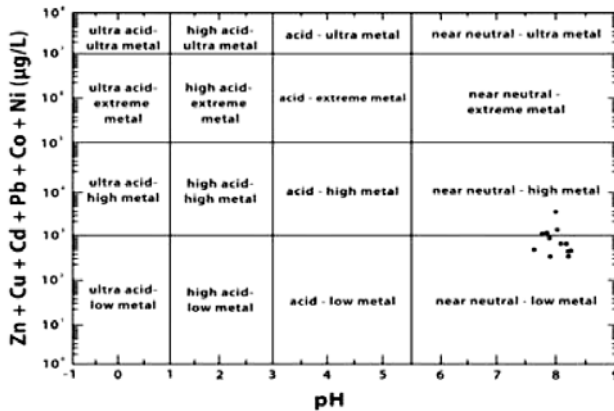
Fig. 4: Ficklin diagram showing the sum of dissolved base metal concentrations as a function of pH.

teristic drainage signature of different types of ore deposits (Ficklin et al. 1992). Differences in the sum of base metals (Zn, Cu, Cd, Pb, Co and Ni) allow to differentiate between different geological controls on water composition. The plotted waters are characterised by near neutral values of pH and low (sum of base metals<10^3) to high (sum of base metals>10^3) metal dissolved concentrations. The cluster of points falls within the field typically associated with pyrite-sphalerite-galena-chalcopyrite ores with hydrothermal carbonates or carbonate-rich host rocks (Seal et al., 2002).

4.3 Seasonal variation

Figure 5 displays the seasonal variation of SO_4^{2-} upstream to downstream for each of the studied basin. November is included in the dry period since no rainfall was recorded until then whereas April is included in the wet period. Major ions content, such as SO_4^{2-}, decrease in the wet period (April and February) because of dilution caused by the heavy rainfall during those months. This is true for all the samples from the three basins. Calcium, K^+, Na^+, Mg^{2+} and HCO_3^- are not represented in the figure but they exhibit a similar pattern.

In contrast, Zn concentration in Kokkinolakkas water samples (Figure 5), reaches maximum values during the wet period (April and February). The same behaviour is also noticed for Pb, Cd, As and Ni (not displayed in the figure). A possible explanation for this could be the fact that during the wet period, large quantities of water dissolve solid phases that hold these metals and are associated either with minerals of the primer sulphide mineralisation or with materials of the old mineral waste stockpiles. As a result stream water becomes enriched in those metals. Manganese reaches maximum values in winter but is also present in high concentrations during the rest of the sampling periods. For the waters of the other two basins, the seasonal pattern is unclear, and no safe conclusions can be conducted.

4.4 Comparison with previous data

There are extended historical monitoring data for the entire area of the three studied basins. As it has been already mentioned, concentrations of Mn for Kokkinolakkas basin (samples H1 and H3) exceed the permissible limits set by Chalkidiki Prefecture for irrigation water. The existence of the old stockpiles, upstream of the sampling area, can be considered as a major source for these high concentrations. A comparison of data produced by this study with earlier measurements seems to be necessary in order to evaluate the management of these deposits. Figure 6 shows that there is a significant gradual decrease in the concentration of Mn approaching or exceeding 60% of the concentration
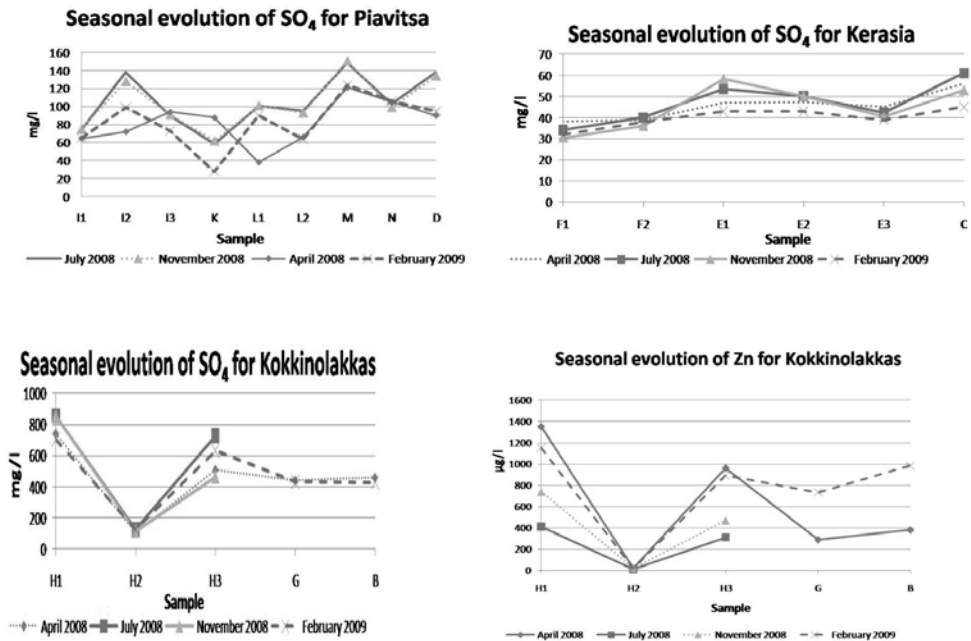
Fig. 5: Seasonal evolution of selected analysed variables.
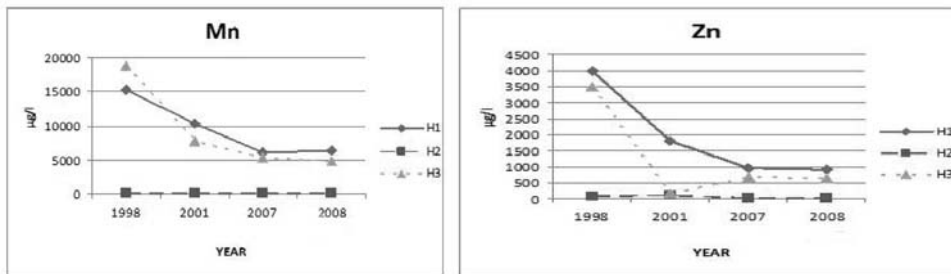
Fig. 6: Evolution of Mn and Zn concentrations in Kokkinolakkas stream water during the last decade.

measured in 1998. Similar behaviour is noticed for a variety of other metals i.e., Fe, Zn, Ni, Cd and As, for which concentrations are now consistent with the permissible limits for surface waters of Chalkidiki Prefecture. For the water of the other two studied basins, the comparison with previous data showed that there is not any significant change in the concentrations of the analysed parameters.

5. Conclusions

The studied area of Asprolakkas basin, located at North East Ckalkidiki, has a history of intense mining of sulphide deposits, which is evitable in the chemistry of water samples from Kokkinilolakkas stream except for the chemistry of sample H_2. The stream water of Kerasia and Piavitsa basins has a different chemical composition, influenced to a lesser extent by oxidation and metal release from outcrops of the sulphide mineralization occurring in the wider area. Only slight differences

were observed with respect to seasonal variation of the chemistry of stream water. During spring and winter sampling periods (wet period), the lowest SO_4^{2-}, Ca^{2+}, Na^+, K^+, Mg^{2+}, HCO_3^- concentrations were recorded, caused by the dilution of superficial runoff water, while Zn, Pb, As, Cd, and Ni concentrations for Kokkinolakkas stream water reach maximum values during the wet period. The comparison of chemical analyses with historical data, showed a gradual decrease regarding the concentrations of several metals in the water of Kokkinolakkas stream.

6. Acknowledgments

7. References

European Union Council: 1998, 'Council Directive on the quality of water intended for human consumption, 98/83/EC', *Official Journal of the European Communities*, Vol 330, 32-54.

Ficklin, W.H., Plumlee, G.S., Smith, K.S., McHugh, J.B., 1992. Geochemical classification of mine drainages and natural drainages in mineralised areas. In: (Kharaka, Y.K., Maest, A.S. Eds.), *Proceedings, 7th International Symposium. Water Rock interaction*, 381-384.

Frei, Robert., 1995. Evolution of Mineralising Fluid in the Porphyry Copper System of the Skouries Deposit, Northeast Chalkidiki (Greece): Evidence from Combined Pb-Sr and Stable Isotope Data. *Economic Geology*, 90, 746-762.

Greek Government Gazette 573/B/85, Prefectural Decision No 96400/85, on the disposal terms of liquid industrial wastes into natural receivers of Chalkidiki Prefecture.

Kalogeropoulos, S.I., Kilias, S.P., Bitzios, D.D., Nicolaou, M., and Both, R.A., 1989. Genesis of the Olympias Carbonate-Hosted Pb-Zn (Au, Ag) Sulfide Ore Deposit, Eastern Chalkidiki Peninsula, Northern Greece. *Ecomomic Geology,* 84, 1210-1234.

Kockel, F., Mollat, H., and Gundlach, H., 1975. Hydrothermally Altered and (Copper) Mineralized Porphyritic intrusions in the Serbo-Makedonian Massif (Greece). *Mineral Deposita* (Berl.), 10, 195-204.

Kockel, F., Mollat, H., and Walther, H.W., 1977. Erläuterungen zur geologischen Karte der Chalkidiki und angrenzender Gebiete 1:100000 (Nord-Griechenland). Hannover, Bundesanstalt Geowiss. Rohstoffe, 119 p.

Kroll, T., Müller, D., Seifert, T., Herzig, P.M., and Schneider, A., 2002. Petrology and geochemistry of the shoshonite-hosted Skouries porphyry Cu-Au deposit, Chalkidiki, Greece. *Mineralium Deposita*, 37, 137-144.

Lazaridou-Dimitriadou, M., Koukoumides, C., Lekka, E., and Gaidagis, G., 2004. Integrative evaluation of the ecological quality of metalliferous streams (Chalkidiki, Macedonia, Hellas). *Environmental Monitoring and Assessment*, 91, 59-86.

Nebel, Mark.L., Hutchinson, R.W., and Zartman, R.E., 1991. Metamorphism and Polygenesis of the Madem Lakkos Polymetallic Sulfide Deposit, Chalkidiki, Greece. *Economic Geology*, 86, 81-105.

Nicolaou, M., & Kokonis, D., 1980. Geology and development of Olympias mine, eastern Chalkidiki, Macedonia, Greece. In: (J.M. Jones, ed.), *Complex Sulfide Ores*. Inst. Mining Metallurgy, London.

Papakonstantinou, A., Veranis, N., & Polyzonis, E., 1996. Hydrochemical-Hydrogeological Study of Olympias-Stratonion, Chalkidiki (in Greek). Technical Report. IGME, Thessaloniki.

Seal II, R.R., Foley, N.K., Wanty, R.B., 2002. Introduction to geoenvironmental models of mineral deposits. In: Seal II, R.R., Foley, N.K. (Eds.), Progress on Geoenvironmetal Models for Selected Mineral Deposit Types, *US Geol. Surv. Open file* Rep.02-195.

APPLICATION OF FEFLOW FOR THE SIMULATION OF GROUNDWATER FLOW AT THE TIRNAVOS (CENTRAL GREECE) ALLUVIAL BASIN AQUIFER SYSTEM

Koukidou I.[1], Panagopoulos A.[2]

[1] *Aristotle University of Thessaloniki, Inter-departmental of Biology, Geology and Civil Engineering, "Ecological water quality and management at a river basin level", 54124 Thessaloniki, Greece, cookie@bio.auth.gr*

[2] *National Agricultural Research Foundation, Land Reclamation Institute, 57400 Sindos, Thessaloniki, Greece, panagopoulosa@gmail.com*

Abstract

FEFLOW is a relatively new simulation code that was applied and tested systematically for the first time in Greece at Tirnavos alluvial basin, which is part of the eastern Thessaly plain. The aim of this exercise is to apply and test the applicability and versatility of FEFLOW in the simulation of groundwater flow of the Tirnavos basin aquifer system, which is located in eastern Thessaly-central Greece. From the compilation and calibration of the mathematical model, it can be concluded that FEFLOW is a very powerful tool with many practical applications and capabilities. Application of FEFLOW at Tirnavos basin was successful. As deduced by field data analysis, groundwater resources of the study area are overexploited, a fact which bears negative effects not only for the study area, but also for the surrounding area, which is much greater in extent. This fact was well reproduced in the simulation. It is therefore of utmost importance to rationally manage regional groundwater resources aiming at aquifer restoration (quantity and chemical quality) and the environmental protection of both the aquifer system and the depended and interrelated ecosystems, in accordance to the water related EC Directives.

Key words: FEFLOW, numerical modelling, groundwater flow, simulation, hydrogeology, Thessaly.

1. Introduction

Mathematical models were presented for the first time at the end of 19th century (Anderson and Woessner, 1992), however, nowadays they have been developed greatly and their use has expanded considerably, because of their capability to manage large volumes of data, make infinite combinations and repeat the process as many times as needed. Hence, they offer high degrees of reproducibility in results and in parallel allow for exhaustive analysis and examination of alternative hydrogeological setup configurations and water resources management plans. In this development also contributed the establishment of national laws and European Directives that create a comprehensive frame of sustainable management for the long-term protection of all waters (surface, transient, underground and coastal) and ecosystems.

In their efforts to comply with the 2000/60/E.C. Water Framework Directive (WFD), and the 2006/118/E.C. Groundwater Daughter Directive (GWDD), member states of the European Com-
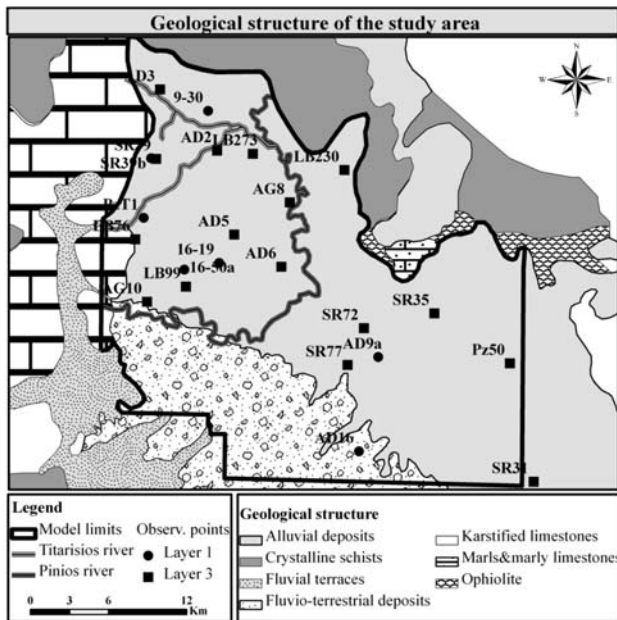
Fig. 1: Geological setup of the Tirnavos alluvial basin.

munity used numerical models in order to produce sound, trustworthy and easy to review and implement water resources management plans.

One of the available numerical models for the simulation of groundwater flow is the relatively new, finite element code, FEFLOW. Its systematic application has been attempted for the first time in Greece, at Tirnavos basin, an area where water has particular importance for its economic growth and social welfare, and which faces quality and quantity problems with its water resources.

Groundwater resources of the study area cover the largest part of water demands of eastern Thessaly plain. The main productive activity is agriculture, and 14% of the domestic agricultural products originate from this region. Consequently, for the development of this area water resources have to be managed in such a way, so as to avoid overexploitation and to ensure that the essential quantities of water for irrigation and domestic consumption are not exceeded.

2. Geological-hydrological characteristics

The alluvial basin of Tirnavos forms the north-eastern part of the eastern Thessaly plains of central Greece and administratively belongs to Larissa Prefecture. Hydrologically, it belongs to Pinios river basin and River Pinios and Titarisios flow through the study area. It is an active tectonic basin that is filled with Neogene and Quaternary deposits and is bounded by formations of the Pelagonian tectonic zone (Mountrakis, 1985), as illustrated in figure 1.

Carboniferous-Middle Triassic gneiss and schists of the Pelagonian zone crop out along the northern edge of Tirnavos plain and from the bedrock of the basin. To the west the basin is delineated by the karstified Tirnavos-Damasi-Koutsohero crystalline limestones (Sogreah, 1974). Two major springs emerge at the contact of the karstified system with the alluvial deposits. The Mati spring is used for irrigation, while the Agia Anna spring provides most of the domestic water demands of the adjacent town of Tirnavos (Constandinidis, 1978).

Neogene marls and marly limestones crop out along the south-western and north-eastern margins of the alluvial basin. The presence of these formations, especially so the former known as mid-thes-salian hills, is important because they separate hydrogeologically the eastern from the western Thessaly plain (Electrowatt, 1967).

Alluvial deposits that fill the basin are of fluvio-lacustrine to fluvio-torrential origin. Typically, the alluvial sediments are characterized by considerable lithological variations, and consist of intercalations of sand, gravel and clays (Compagnie Generale de Geophysique, 1972). The aquifer system of Tirnavos has been formed within the alluvium. It consists of a lower thick, predominantly confined aquifer, and a superimposed unconfined aquifer (Electrowatt, 1967).

Agriculture is the dominant economic activity and cultivated farms expand to some 86% of the spatial extend of the basin. Out of this percentage, only 32% are non-irrigated fields, thus account for xeric cultivations. It may easily be deduced that irrigation is the dominant water user in the region and accounts for some 90-95% of total water demands, whilst domestic water supplies take up only 3% of the annually abstracted volumes of water. Groundwater essentially covers all water demands through abstractions from numerous shallow wells and deep boreholes and surface water contributes only a minor percentage (Panagopoulos et al., 2006; Karyotis et al., 2008).

3. Methods

3.1 Conceptual model

Existing data and analyses from previous studies were considered for the compilation of the conceptual and mathematical models (Panagopoulos 1996, Hatzidiamantis et al., 2009; Syllaios et al., 2009). For the compilation of the conceptual model, hydrochemical, piezometric and water budget data were used. Based on these data, the aquifer system of Tirnavos consists of a lower thick (400m) predominantly confined aquifer, and a thin (40-70m) superimposed unconfined aquifer. The two aquifers in the centre of the basin are separated by a confining clay layer. The thick clay layer is present in the central area, but thins out and disappears towards the edges, where the upper and lower aquifers unify (Panagopoulos et al., 1995; Panagopoulos, 1996).

Lateral crossflow from the karst is the most important source of recharge to the aquifer system and also crossflow from the river Titarisios gorge via its highly permeable fluvio-torrential cone (Panagopoulos et al., 1995). Lateral crossflows from the river Pinios gorge do exist but are of minor importance compared to the previously discussed sources.

Minor crossflows from the crystalline bedrock along the north-eastern margin of the basin and also crossflows from the tertiary deposits of the Mid-Thessalian hills in the south-southwest of the study area recharge the aquifer system. Infiltration of precipitation also occurs and accounts for a small fraction (5-15%) of the system's recharge (Panagopoulos et al., 1995). During summer time irrigation returns also occur and contribute to the system's recharge (Panagopoulos et al., 2008).

The aquifer system of Tirnavos extends to the east-southeast towards which a significant lateral crossflow exists. Discharge is also indicated at the northern margin of the study area, where the river Pinios flows out of the Tirnavos basin (Panagopoulos et al., 1995). Apart from the natural discharge areas, artificial discharge also exists in the form of abstractions mainly for irrigation but also for domestic needs and for the small industrial units in the study area, through numerous shallow wells and deep boreholes (Katsilouli et al., 2004). It has to be stated that the study area is the main recharge zone of the southeastern extension of the aquifer system, hence groundwater abstractions from the

Tirnavos aquifer system strongly influence water budget of the southeastern extension of the system.

In previous studies (Panagopoulos, 1996), a general water balance of the alluvial system was calculated for year 1973 (a period of time during which the aquifer system would be in dynamic steady state conditions). Water balance calculations resulted that total inflow to the system is 188,100m^3/d and total outflow from the system is 183,000m^3/d. The calculated water balance served as a reference and guideline to the initial calibration of the designed groundwater flow model of the study area and as such it proved to be essential.

3.2 Numerical model

FEFLOW is a fully integrated 3D finite element model, which excels in cases that involve complex geological structures, unsaturated flow, density-dependent flow (saltwater intrusion) or thermal convection (FEFLOW, 2009). It is used not only for fluid, mass and heat transport, but also for saltwater infiltration simulation, for both porous and discontinuity (under conditions) media (FEFLOW, 2009).

The available element types include the quadrilateral and the triangular elements, where groundwater level is calculated in each node (Diersch, 1998). FEFLOW's finite element approach allows the user to perform local mesh refinements only in the areas of interest thus avoiding creation of excessive number of elements.

Amongst the advantages of the finite element method is the ability to represent key features of the modelling domain (geological contacts, boundary conditions, main stress zones, etc) with high precision (Raptanova et al., 2007). Out of all capabilities offered by FEFLOW, this paper focuses on the groundwater flow in porous media.

3.3 Model compilation and calibration

The system comprises of three layers or 4 slices, according to FEFLOW terminology. The modelling domain has an aerial extent of about 741.1km^2 and comprises of a 6-nodal triangular prismatic mesh that contains 501,726 mesh elements and 335,948 mesh nodes.

In order to better simulate the main evolution mechanisms that control groundwater flow, the resulting mesh has been refined in the areas of interest, i.e. the margins of the study area, rivers and wells, so that boundary conditions can be set more precisely.

3.3.1 Boundary conditions

It is suggested that under ideal conditions boundaries of the modelling domain coincide with natural hydrogeological boundaries of the region (Anderson and Woesner, 1992; Panagopoulos, 1996). Thus, the northern margin comprises the crystalline bedrock, where a small groundwater crossflow occurs. Tirnavos karst system was set as the western margin, from where the alluvial system is recharged primarily. The southern margin was set to the Mid-Thessalic hills, along which the system receives a small fraction of recharge as earlier discussed. No natural hydrogeological boundary may be identified along the eastern part of Tirnavos alluvial basin. To overcome this oddity the boundary was assumed along a line striking at almost N-S direction that coincides to the documented uplift of the bedrock. This uplift results in seasonal hydraulic cut off of the Tirnavos basin from its southeastern extension (Panagopoulos, 1996).

Boundary conditions of third type (Cauchy), using the "transfer function" of FEFLOW (FEFLOW, 2009), were assigned to all boundaries. This type of condition was selected because it provides the
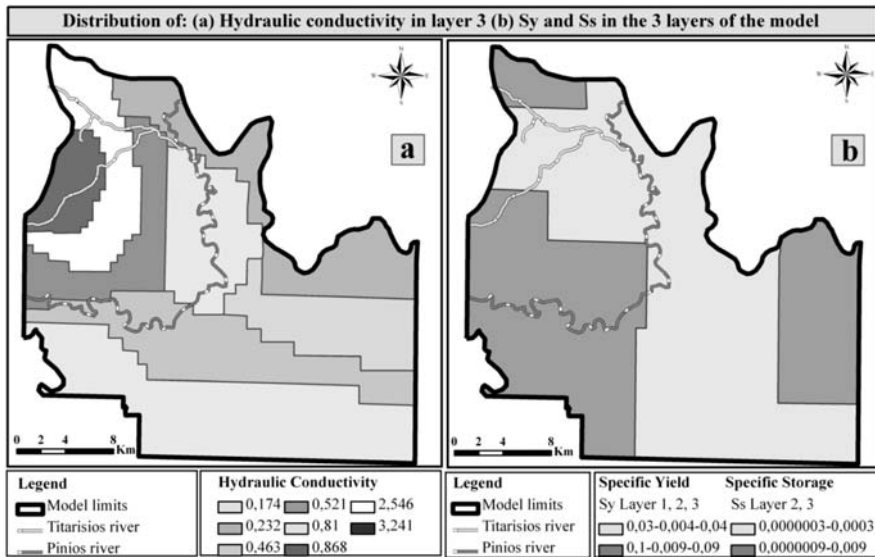
Fig. 2: a) Distribution of hydraulic conductivity in the third layer of the model (10^{-4} m/sec) and b) distribution of specific yield (Sy) and specific storage (Ss) (1/m) in the three layers of the model.

maximum degree of freedom to the flow domain within the modelling area, thus allowing for unbiased simulations. River Pinios and Titarisios were also simulated using Cauchy boundary conditions.

3.3.2 Stresses

Production wells that operate mainly in the central part of the modelled area were set as discharge points. For assigning the abstractions, the mean yields for year 1973-1974 for the steady state conditions was used, while for the transient state conditions, data from the period between 1973 and 1994 were considered. The "wells function" of FEFLOW was used to set the abstractions, which corresponds to Neumann boundary conditions.

Direct recharge from precipitation, was based on the characteristics of the soil cover and the lithological characteristics of the upper aquifer. Five discrete zones were separated on the basis of afore mentioned criteria. The infiltration rate "i", was expressed as the percentage depth rate of rainfall "R" and was assigned in each zone. Data from the meteorological stations of Larissa and Tirnavos that are located within the core of the modelling domain were used.

3.3.3 Distribution of hydraulic parameters

For the compilation of the mathematical model, the definition of hydraulic conductivity, specific storage and specific yield are required. The hydraulic parameter values that were used as input data in the designed model have been obtained from an older study (Panagopoulos, 1996), which was based on the pumping test analyses and on the geological and lithological characteristics of the system. The spatial distribution and the actual values initially assigned were reviewed during the calibration process.

Hydraulic conductivity values range from 0.0003 to $3.241 10^{-4}$ m/sec as indicatively illustrated in figure 2a for layer 3. Specific yield values range from 0.004 to 0.1 and specific storage values range from $3 10^{-6}$ to $9 10^{-4}$ 1/m (Fig. 2b).

Table 1. Range of values used for the hydraulic parameters K, Sy and Ss.

	Layer 1		Layer 2		Layer 3	
	Min	**Max**	**Min**	**Max**	**Min**	**Max**
Hydraulic conductivity (10^{-4} m/sec)	0.116	1.505	0.000029	0.002083	0.174	3.241
Specific yield	0.03	0.1	0.004	0.009	0.04	0.09
Specific storage (m^{-1})			0.0000003	0.0000009	0.0003	0.0009

In general, hydraulic parameters' values are lower to the central and eastern parts of the modelling domain and considerably lower in the confining clay layer compared the two aquifer units (Tab. 1). FEFLOW's convention regarding parameters' units has been followed in this presentation.

3.3.4 Calibration-verification of the model

The compiled model was initially calibrated under dynamic steady state (DSS) conditions and subsequently under transient state (TS) conditions. The following parameters were considered during the calibration process: water balance, divergence between measured-computed piezometric levels at selected observations points, shape of computed piezometric curves compared to the piezometric maps produced on the basis of field data and selected statistical parameters. For DSS calibration the hydrological year of 1973-1974 was selected, because it is characterized by average rainfall and no extreme stresses imposed on the system. A total of 26 observation points (Fig. 1) were employed (7 for the unconfined and 19 for the confined aquifer). A maximum of 3m deviation between modelled and monitored heads was assumed acceptable at this stage of calibration.

For the calibration in TS conditions the selected period was 1973-1994, because during this period a satisfactory volume of integrated data could be reclaimed. Hydrographs of 17 observation points (Fig. 1) were used (7 for the unconfined and 10 for the confined aquifer) for this calibration. A maximum of 5m deviation between modelled and monitored heads was assumed acceptable at this stage of calibration. Due to lack of data and the fact that the system is not highly stressed, a single stress period was assumed up to year 1984, following which 2 stress periods (winter-summer) are set per year.

Verification of the model was also performed using existing field data for the period 1994-2000 (Hatzidiamantis et al., 2009; Syllaios et al., 2009).

4. Results and conclusions

4.1 Results

The calibrated piezometry for both layers (unconfined and confined aquifers) matches well with the compiled piezometric maps for the examined period of time, especially in the core of the modelled domain, for both calibration stages (DSS, TS), as illustrated in the indicative figures 3a and 3b.

The water balance produced by the model in DSS conditions agrees well with the reference water balance estimated using available field data (Panagopoulos, 1996; Hatzidiamantis et al., 2009).

For DSS calibration the graph of measured versus computed piezometric data resulted in an insignificant deviation from target set of only three observation points (Fig. 4).
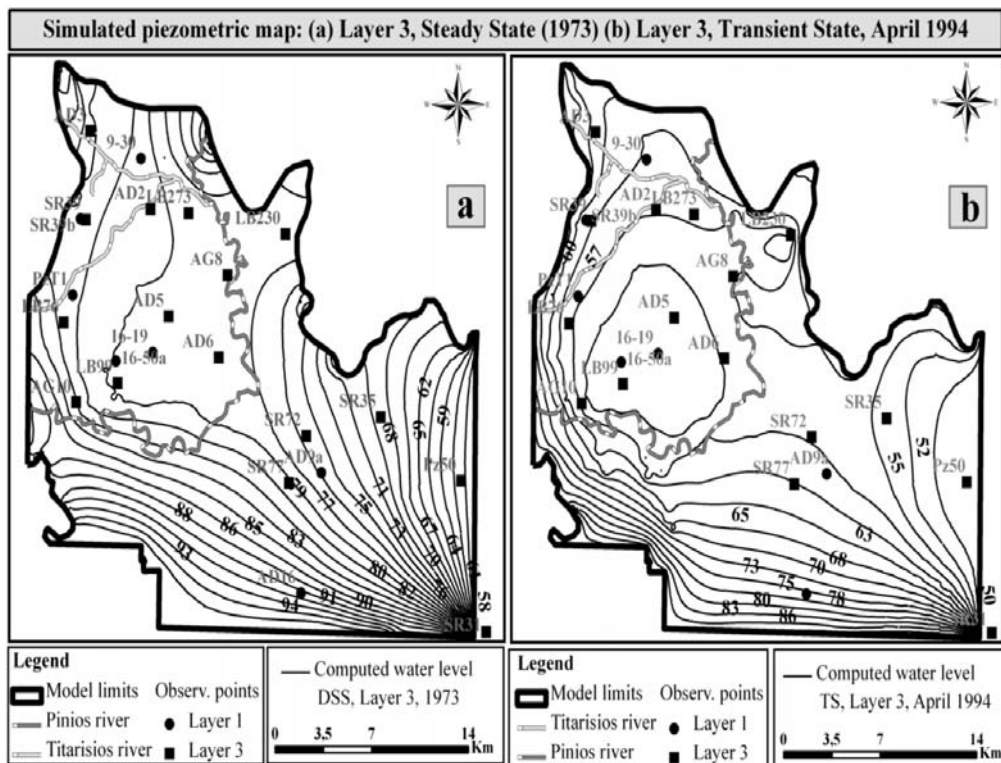
Fig. 3: a) Produced piezometric map for DSS conditions, layer 3, in meters a.o.d. b) Produced piezometric map for TS conditions, layer 3 in meters a.o.d.
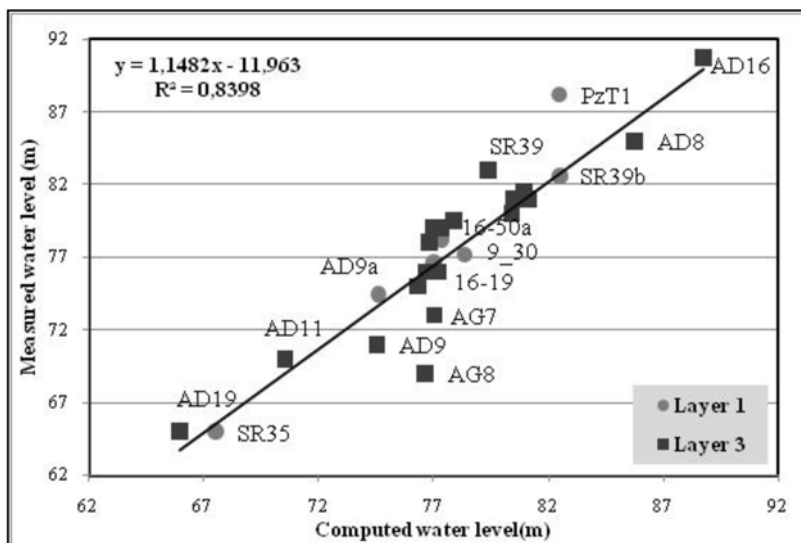
Fig. 4: Graph of measured-computed groundwater level at the observation points of the first and the third layer, DSS calibration.
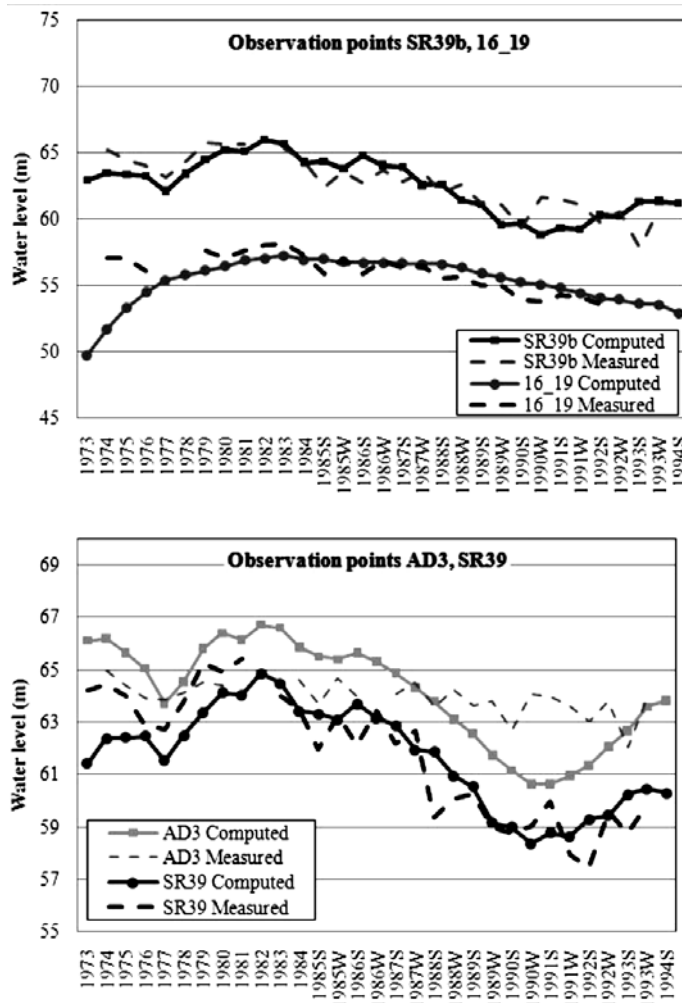
Fig. 5: Comparative hydrographs at selected observation points during the TS calibration period.

Table 2. Selected statistical parameters of calibrated model.

	Mean Error	*Mean Absolute Error*	*Root Mean Square*	*St. Deviation*
Dynamic Steady St.				
Layer 1 (unconfined aq.)	0,71	1,19	2,23	N/A
Layer 3 (confined aq.)	-1,04	3,68	3,56	N/A
Transient St.				
Layer 1 (unconfined aq.)	-0,22	1,67	2,09	1,56
Layer 3 (confined aq.)	0,31	3,02	4,52	3,72
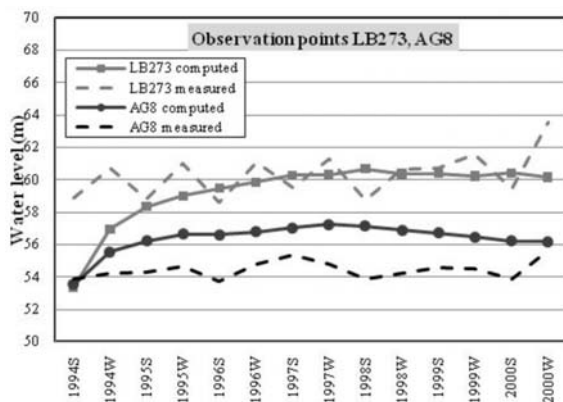
Fig. 6: Comparative hydrographs at selected observations points over the verification process.

Study of hydrographs at the selected monitoring points suggests that the results obtained from the calibrated model in TS conditions matches well with field data as illustrated in selected comparative hydrographs of figure 5.

The calculated statistical parameters for both steady and transient state calibration are acceptable as presented in Table 2.

Following calibration, the model was verified using field data for a period of 6 years as explained in a previous section of this paper (1994-2000). Results of this exercise suggest that the model can reproduce the main evolution mechanisms reasonably well. This is illustrated in figure 6 which presents indicatives comparative hydrographs at selected observation points.

4.2 Conclusions and discussion

Application of FEFLOW in the alluvial groundwater system of Tirnavos basin showed that it is a seamless, functional and reliable numerical model that enables accurate representation of boundary conditions and the system's geometry. Results of the calibrated and verified groundwater flow model allow for a deep insight in the groundwater flow mechanisms of the basin. The compiled model clearly demonstrated the need for immediate actions to be taken in the direction of restoration and protection of the aquifer system. Based on the calibrated model, a set of alternative water resources management scenarios may be designed and reliably tested in order to select the optimal water resources management scheme that will balance environmental protection and socio-economic welfare of the region, in accordance to the EC Directives.

Previous attempts to model the study area were also successful, using MODFLOW, which is a simpler finite difference code (Panagopoulos, 1996). However, FEFLOW provides a much more accurate representation of the aquifer's geometry, hence allows for better simulation of boundary conditions and focusing on specific parts of the modelling domain. As a result, the finite element approach presented in this paper provides a higher quality result, compared to that obtained from finite difference models.

It has to be stressed however, that due to the structure of the modelling code, FEFLOW is a much more demanding package compared to MODFLOW n terms of both required input data and also computational power. It is therefore suggested that perspective users should balance out the extra data and time required setting up and calibrating a FEFLOW model against the potential improved sim-

ulation accuracy obtained given the appropriate data, prior making a definitive decision on the modelling code to be selected. Last but no least, the initial investment required to obtain FEFLOW might be a limiting factor, as this is considerably higher than a finite difference code.

5. Acknowledgments

6. References

Anderson, M., Woessner, W., 1992. *Applied groundwater modeling. Simulation of flow and advective transport*. Academic Press, London 381pp.

Compagnie Generale de Geophysique, 1972. *Reconnaissance par prospection electrique dans la Plaine de Thessalie* (Grece). Grenoble: CGG.

Constandinidis, D., 1978. *Hydrodynamique d' un systeme aquifere heterogene. Hydrogeologie de la Thessalie Orientale*. Ph.D. thesis, Universite Scientifique et Medicale de Grenoble, 288pp.

Diersch, H.G., 1998. FEFLOW *interactive, graphics-based finite-element simulation system for modeling groundwater flow, contaminant mass and heat transport processes*. WASY Institute for Water Resources Planning and System Research Ltd., Berlin, Germany, 401-425.

Electrowatt Engineering Services, 1967. *Development of the plains of Thessaly. Preliminary study and feasibility report*. Ministry of Public Works, Athens, (in Greek).

FEFLOW 5.4, 2009. *Finite element subsurface flow and transport simulation system. User's manual*. WASY Institute for Water Resource Planning and Systems Research Ltd., Berlin, Germany, 202pp.

Hatzidiamantis, A., Zalidis, G., Alexandridis, Th., Gakis, K., Galanis, G., Partozis, A., Panagopoulos, A., Panoras, A., Arampatzis, G., Hatzigiannakis, E., Vrouchakis, J., Alexiou, G., Kalfountzos, D., Kotsopoulos, S., 2009. Study for irrigation water pricing at Pinios River Basin (Tirnavos sub-basin). Phase C.

Karyotis, Th., Charoulis, A., Panagopoulos, A., Tziouvalekas, M., Georgiou, Th., Karyoti, K., Mitsimponas, Th., 2008. Groundwater quality and threshold values for irrigation in the river Basin of Pinios, Greece. Session: Soil and Water – Practical Applications. *Abstracts, Int. Conference "EUROSOIL 2008"*, Vienna, 333pp.

Katsilouli, Ir., Karyotis, Th., Georgiou, Th., Mitsimponas, Th., Panagopoulos, A., Panoras, A., Pateras, D., Haroulis, G., Argyropoulos, G., Toulios, M., 2004. Nitrates in soils and water originated from agricultural sources: a case study in Thessaly, central Greece. *Proceedings 12th Nitrogen Workshop "Controlling nitrogen flows and losses"*, Wageningen Academic Publishers, 447-448.

Mountrakis, D., 1985. *Geology of Greece*. University Studio Press, Thessaloniki, 207pp (in Greek).

Panagopoulos, A., 1996. *A methodology for groundwater resources management of a typical alluvial aquifer system in Greece*. Ph.D. thesis, University of Birmingham, Birmingham, 251pp.

Panagopoulos, A., Karyotis, A., Georgiou, Th., Tsitouras, Al., 2006. Groundwater natural background levels and threshold definition in the Eastern Thessaly groundwater body (Pinios River Basin, Central Greece). *Greek Case Study Report, BRIDGE Project*, 23 pp.

Panagopoulos, A., Lloyd, J., Fitzsimons, V., 1995. Groundwater evolution of the Tirnavos alluvial basin, central Greece, as indicated by hydrochemistry. *3rd Hydrogeological Conference of the Hellenic Chap-*

ter of IAH, Heraklion, Crete, 232-244.

Panagopoulos, A., Pechlivanidou, S., Vrouhakis, Y., Karyotis, Th., Arampatzis ,G., Hatzigiannakis, E., Panoras, A., 2008. Determining reference conditions for groundwater bodies using simple historical data; the case of eastern Thessaly, Greece. *E-Proc. 36th Int. Congress of the International Association of Hydrogeologists*, Toyama, 1-7.

Rapantova, N., Grmela, A., Vojek, D., Haril, J., Michlek, B., 2007. *Groundwater flow modelling applications in mining hydrogeology*, 532pp.

Sogreah. "Final report". *Groundwater development project of the plains of Thessaly*, (in Greek). Athens: Land Reclamation Services of Greece, 1974.

Syllaios, N., Zalidis, G., Alexandridis, Th., Galanis, G., Christoforou, M., Strati, S., Cherif, I., Partozis, A., Panagopoulos, A., Vrouchakis, J., Pechlivanidou, S., Alexiou, G., Kalfountzos, D., Kotsopoulos, S., 2009. Study for irrigation water pricing at Pinios River Basin (Tirnavos sub-basin). Phase B.

INFILTRATION, EFFECTIVE POROSITY, TRANSMISSIBILITY AND CRITICAL YIELD OF WATER WELLS IN THE CARBONATE FISSURED AQUIFERS OF ATTICA – A CONTRIBUTION TO THE REGIONAL AND MANAGERIAL HYDROGEOLOGY

G. D. Kounis[1] and K. G. Kounis[2]

[1] *Hydrogeologist, Former Director of Hydrogeology,and Advisor at IGME, gdkounis@gmail.com*

[2] *Consultant in Civil and Underground Works Engineering , kkouniscve@yahoo.com*

Abstract

In the hydrogeological practice and the groundwater resources management the accurate knowledge on the infiltration, effective porosity, transmissibility, and on the sustainable yield of water wells is of fundamental value. It is so, because these parameters are the information primarily required in prediction and decisions relevant to the ground water abstractions and the hydrogeological evaluation of specific sites.

In this paper, we present these quantities from the carbonate fissured formations of Attica, non metamorphic (limestones, dolomitic limestones, dolomites) and metamorphic (marbles), which all are of great areal extent and thus of great interest for groundwater exploitation. In addition, they show good geomorphological, structural and lithologic resemblance with analogous formations elsewhere in this country, so that figures calculated can be reliably transferred for use.

In our work we used methods of increased reliability, and having known precipitation (P) we estimated

— *The Infiltration Index (I_c) from the yield of springs of well defined hydrogeological catchments (natural lysimeters) and results found fall in the range of values*
  $0.38P < I_c < 0.42P$
— *The Effective Porosity (p_e), obviously secondary because of the nature of the carbonate aquifers (fissure flow aquifers). We calculated it from groundwater level hydrograph and values found are in between*
  $1.31\% < p_e < 6.91\%$
with the most common in between
  $1.58\% < p_e < 4.8\%$
— *The Transmissibility (T), we calculated from pumping tests, with Jacob method, using semilogarithmic plots of drawdowns (s) versus time (t) from start of pumping. Values found are mostly (70%)in the range*
  $10m^3/h.m < T < 75m^3/h.m$
— *The Critical Yield (Qc) of water wells we calculated from the "characteristic well curve" Q vs. s (with Q and s standing for yield and drawdown respectively). Values are mostly in between*
  $15m^3/h < Qc < 75\ m^3/h$.

Cretaceous limestones showed the best of the parameters, followed by the marbles free of schist in-

tercalations and distant from schist boundary . Karstic processes on the fracture network, structures vulnerable to tectonic extension, like anticlines and tension faulting zones are the underlying reasons for better hydrologic performance and thus for higher values of the parameters studied. Dolomites outside the previous zones show very low values .

Key words : Attica, carbonate fissured, karstic aquifers, infiltration, natural lysimeters, effective porosity, critical yield, transmissibility.

1. Introduction

The experience, the senior of the authors has from the hydrogeology of the area of the wider Attica, after his work as a project manager and consultant (with IGME etc), raised the interest to go through the discussed hydrogeological issues and search them for more accurate approach, to the benefit of the hydrogeological practice. To this aim we examine basic quantities relative to the ground water study and exploitation and we introduce new and simple methods for the estimation of the critical yield of abstraction wells and of the specific yield (effective porosity) of aquifers .Further, we discuss the infiltration into the fissure flow carbonate aquifers and the transmissibility of same aquifers. We calculated infiltration index using natural lysimeters, it was found very representative and thus useful for further applications.

In addition, we present the generalized geological and hydrogeological structure and performance of the broader area to show the conditions under which the specified aquifers and sites of study perform.

2. Hydrogeology

2.1 General

The hydrogeological conditions of Attica almost fully conform to the geological and morphological structure. (Kounis et al., 2010).

Basic characteristics of almost all aquifers are their hydraulic continuity with sea, the low quality state at a distance of 4km from the coastline, the low infiltration rate, and the limited purely confined conditions.

Though the two aquifer systems, of the intergranular flow and of the fissure flow, predominate in Attica, due to the complicated geologic structure and the geomorphology, different aquifers can be distinguished by their particular conditions and problems, the hydraulic continuity between units being absent or of minor hydrogeological importance.

In the fissure flow system (carbonate system), which is of primary importance in this presentation, two main factors govern the existing hydrogeological conditions, namely the fissure network which shows a varying degree of widening of its elements, subsequent to the karstification process, and the impermeable substratum. Although a diffused circulation of ground water through the carbonate masses can well be accepted as the rule in Attica, some localized, convergent flow along major faults and relevant fracture zones, especially in West Attica, is equally taking place . Internal solution of all kind of fracturing for karstification reasons is varying in space, more pronounced being in West Attica and in the cretaceous limestone. Schist layers and similar lithologic elements in the marbles of East Attica have resulted in a comparatively decreased karstification of the mass. Pure dolomites hardly transmit water, except along heavily fractured zones, while dolomitic limestones show very locally high transmissibility.

In West Attica the principal ground water divide coincides with the major anticlinal axis of Par-
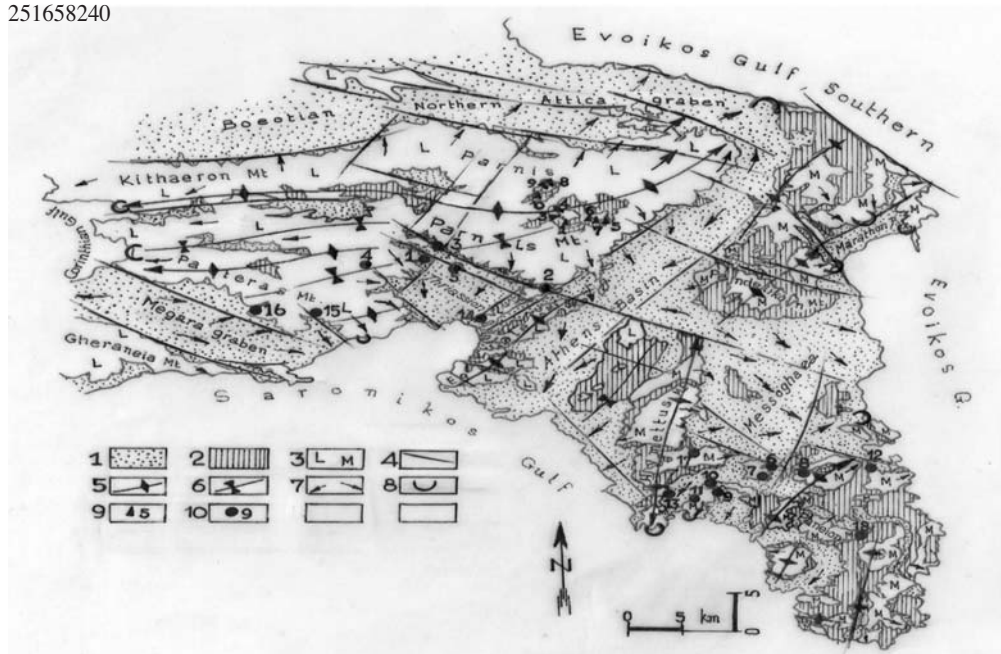
Fig. 1: Generalized hydrogeological map of Attica.
1.Dominantly clastics/low to moderately, very locally highly, yielding aquifers/aquitards and aquicludes (quaternary and neogen). 2. Dominantly aquicludes and aquitards / flysch, shales, sandstones and schists/ metamorphic in east Attica /except of the flysch, underlain of carbonates in west Attica, overlain or interchanged with marbles in east Attica (mesozoic, paleozoic). 3. Fissure, karstic flow aquifers, moderately to locally highly yielding / dominantly limestones, dolomites (L) and marbles (M) (mesozoic). 4. Fault, chiefly in the preneogene structure . 5. Aticline . 6. Synline. 7.Predominant GW flow. 8. GW discharge sites. 9. Springs with ref.no. 10. Borehole with ref. no.

nis-Kitheron Mt., along which the impermeable palaeozoic substratum crops out frequently. Approximately two thirds of the mass of the north limb of the anticline is drained to the Euboean Gulf, preferably by corverging flows to fractured zones and sites. Partial hydraulic interchange between the fissure and overlying porous system is evidenced. Ground water from the rest of the same anticlinal limb outflows to the Korinthian Gulf, again great faults being of prime importance in this drainage performance. The south anticlinal limb shows a rather diffused underground drainage pattern towards an extended front along Saronikos and Korinthian gulfs. A hydraulic relationship with the overlying porous system in low altitudes should he considered as a common situation. Due to a generally high slope gradient of the impermeable substratum in West Attica, circulation of water towards the saturation zone, formed approximately at sea level, is comparatively rapid and the mixing process with seawater therefore accentuated both in magnitude and areal extent.Water table in the saturation zone during dry season is formed at an average maximum of 10m above sea level, and depths to it are commonly between 200m and 300m, allowance being made for topography ,sea contamination and other technical and economic constraints.

In East Attica the main fissure aquifer is represented by the lower marble although other marble members in the lithological sequence are equally important, if not intruded by sea .Water table in lower marble is formed at an average maximum elevation of 5m above sea level in dry season,

higher elevations attained locally for tectonic mainly reasons. Common depths to the saturation zone are between 100m and 230m, allowances made for the various constraints and the mean annual fluctuation is of 5m. The upper marble horizon of the lithologic sequence and other marble units show a saturation zone at higher elevations too, depended on the position of their impermeable schist substratum. In that case maximum depths are commonly under 150m. Final receptor of flows in marble aquifers is the sea, either directly or through some porous medium hydraulically placed in between. (Fig. 1, Kounis, 1998, 1986).

2.2 Infiltration

We studied two jurassic – triassic and one cretaceous fissured and moderately karstic, carbonate masses, with very well defined geologic boundaries on the Parnis Mt. All three have an aquiclude/aquitard substratum, the palaeozoic stratigraphically the first two, the flysch and tectonically the third. Also all are discharging their annual replenishment through contact springs (natural lysimeters). These masses belong to the " Subpelagonic geotectonic zone " of Greece (or " Eastern Greece geotectonic zone" and crop out at elevations in between 680m and 1163m above msl.

Data on springs discharge used are of six years (1976 – 1982) and are highly accurate. Of the same period are the data on precipitation taken from raingauge measurements, at the altitude of 1020m.asl. The raingauge site is in the near vicinity and on very close elevation to those of the masses studied, while it is also representative of the overall climatic conditions of the area of interest (Mariolopoulos et al. 1955). The rest of the minor, influencing factors are the same (orientation, relief and inclination,vegetation etc), with the weathering mantle being moderate or thick and sporadic. Additionally, no other input and output except of that of precipitation and springs discharge respectively exists.

In table 1 the necessary data are given. From that, the very close results, as a calculated infiltration index (Ic), are revealed. A slight decrease of the index in the case of Platy Vouno and Borsi, in relation to that from Aghia Triada mass, is recognized, and as other geological factors are practically the same, we attribute the fact to the increased faulting that has brought about an increased fracturing, and preparation of surface karstification (erosional depression and doline forms), to produce and sustain soil and vegetation cover.

The resulted average infiltration index is 0.397, ie the infiltration of the water in the studied masses is the 39.7% of the precipitation on those masses .We calculate the infiltration index (Ic) as the ratio of the annual discharge (Qy) of the springs of a specified rock mass over the respective annual precipitation volume fallen on the area of the same mass.

The figure found we accept as a very accurate for further use in hydrogeological and natural water balance calculations .In addition, we suggest this as very representative for fissure flow carbonate aquifers, with moderately pronounced the surface karstic attack and forms, and more specifically for those of the "Eastern Greece geotectonic zone ". And this is mostly the case of the cretaceous and jurasic ,limestones, to a less extent of the triassic carbonates as well. Dolomitic component, especially if in abundance in the composition , as it is the case with the jurassic and particularly the triassic, reduces the infiltration index , sometimes considerably, in favour of the runoff for the decreased dissolubility and widening of the receiving the infiltration fissure network . Unless, and rarely, favourable but linear depleted depression forms have resulted from a strong faulting, without worthwhile soil and vegetation cover .

Finally, we think that values of the Ic appearing in various studies greater enough of those shown in the Table 1, either come out by the use of indirect methods of estimation, not fully applicable under

Table 1.

Feeding mass			Springs				Precipitation		Qy/Vp % Ic
Name	Elevat.n masl max min	Area km²	Ref. no	Name	Discharge		Height P,m	Volume Vp,m³ /year	
					Q, m³/h	Qy, m³/y			
Platy	1163		1	Roumani	19.38				
Vouno	820		2	Roumani	4.68				
			3	Kynigon	4.01				
			4	Goura	53.53				
areal figure		2.45			81.60	714816	0.7628	1868 860	38.25
Aghia Triada			5	Ag.Triada	13.01				
	1150		6	Dhassikon	5				
	990		7	Palaeochoriou	26.75				
areal figure									
		1.25			44.76	392098	0.7628	953500	41.12
Borsi			8	Ano Borsi	13.40				
	902		9	Balkeva	1.42				
	680		10	Mavromytou	4.23				
		0.55			19.05	166878	0.7628	419540	39.77

the specified conditions of study or by an underestimated evapotranspiration in the natural water balance approach (Kounis et al., 2005).

2.3. Effective porosity

It is known as the ratio (pe) of the volume of the gravitational water contained, at saturation state, in a rock mass over the total volume of that mass (rock and water). It is the specific yield of the unconfined aquifers (Todd, 1959).

We made use of the groundwater hydrograph, from boreholes sunk in carbonate aquifer (limestones, dolomitic limestones and dolomites) of the " Eastern Greece geotectonic zone ", in Attica .From such graphs we measured the annual ground water fluctuation (ΔH) and from the recession curve the annual recession (Re), so that all height of infiltrating water in the aquifer is taken into account, as in the condition supposed that no groundwater outflow from the aquifer takes place. This total height, resulting from the annual difference between maximum and minimum GW level fluctuation plus the annual component of the height lost by the ground water flow, is the real quantity, the most reasonable and corresponding to the infiltration, and the method approaches very well the value for the effective porosity or the specific yield of the aquifer.

Table 2.

BH1		BH2		BH3		BH4		BH5	
H (m)	Re (m/day)	H (m)	Re (m/day)	H (m)	Re (m/day)	H (m)	Re (m/day)	H (m)	Re (m/day)
7.27	(7.27-6.99)/49	8.31	(8.31-7.69)/15	9.46	(9.46-8.67)/45	7.58	(7.58-7.23)/48	7.52	(7.52-6.86)/9
	0.00571		0.0413		0.0175		0.00729		0.0733
6.99	(6.99-5.99)/65	7.69	(7.69-7.06)/53	8.67	(8.67-8.53)/19	7.23	(7.23-6.53)/16	6.86	(6.86-6.11)/69
	0.014		0.0118		0.00736		0.04375		0.0108
6.24	(6.24-5.67)/45	7.06	(7.06-6.9)/54	8.53	(8.53-7.51)/49	6.53	(6.53-5.85)/49	6.11	(6.11-5.29)/45
	0.0126		0.00296		0.0208		0.01382		0.0182
				7.51	(7.51-7.2)/54	5.85	(5.85-5.57)/50		
					0.00574		0.0056		
						5.57	(5.57-5.41)/48		
							0.00333		
ΣRe	0.0333		0.056		0.05148		0.0738		0.102
	0.0111		0.0186		0.01285		0.01476		0.034
Re_y (m)	4.05		6.789		4.69		5.387		12.41
ΔH (m)	1.6		1.41		2.26		2.17		2.00
Re_y+ ΔH	5.65		8.199		6.95		7.557		14.41
I (m)	0.2382		0.2382		0.2382		0.2382		0.2382
p_e (%)	4.21		2.9		3.42		3.15		1.65

The calculation of the height (GW column) lost by recession was carried out in a few segments of the recession curve, as indicatively in the Table 2 is shown.

The recession curve, which is of the, widely used, general form of

$$ht = h_o\, e^{-\lambda t}, \tag{1}$$

where h_t, h_0, t, λ, e stand for GW level at time t, at time 0, recession coefficient and the neperian base of logarithms respectively of the GW hydrograph, is segmented, for linear/graphical solution, in few parts and is calculated at specified h_t the slope $\Delta h/\Delta t$. Slopes found for the corresponding Δts are summed up and mean value is taken. Time is given in days and recession loss of GW level is determined for the specified year .The found annual recession loss of GW level (Re, in m) is added to the respective fluctuation width. Finally, the effective porosity is estimated by the ratio

$$pe = I/(\Delta H + Re), \tag{2}$$

where for the infiltration, in meters, we made use of the infiltration index we calculated for the same fissured carbonate aquifers of the area (2.2 above) and of the average precipitation, which is 600mm at the average elevation of 500m.asl for the area studied. Data on the GW level are of 1982 which is a hydrological year of the time period considered in the calculation of infiltration of the paragraph 2.2.

In the Table 2 are BH3 the borehole, H the GW level elevation, from points on the recession curve of the GW hydrograph, Re = $\Delta h/\Delta t$ the recession of GW level, ΣRe the sum of daily recession, the mean daily recession, Re_y the annual recession, ΔH the annual GW fluctuation (hmax – hmin), I the annual infiltration, p_e the effective porosity(specific yield).

2.4 Transmisibility

Transmissibility values (T) come out of the Jacob approach in unsteady state conditions of pumping tests and are by 93% less than 55m³/h.m, while by 43% are less than 11m³/h.m. Dolomites show the lowest values, even along fault routes , since no worthwhile improvement of the hydraulic performance of the indissoluble fissure network has been brought about .In this case values are of few m³/h.m or less (e.g sites 1,2,3,4,15,16, Fig.1) (Kounis et al 1983, Kounis 2008).

The higher values are associated with the dissoluble limestones and calcareous marbles, while hydraulic improvement of their fissure network and an increased karstification along extension preferably faults is the fact (Fig.1, sites 6,7,9,11,13) .In this case transmissibility values are mostly in between 10 m³/h.m and 50 m³/h.m.

In sites where schist intercalations are frequently present, or some schist boundary is nearby, sufficient reasons for a bad hydraulic performance of the fissure network and even for a hydraulic blockade, the transmissibility is very low to practically extremely low (e.g sites 12,17,18, Fig.1) .Where carbonates show a densely present fissuring and we attribute the case mostly in a brecciated mass the performance is highly improved, the rest of the favourable factors being present. In this case transmissibility is even greater of 100m³/h.m.

2.5 Critical yield

In the hydrogeological decision making the critical yield (or critical discharge, Qc) of an abstraction well is a useful quantity. Under steady state conditions of flow, it refers to the discharge of the well that divides the set of the pairs of values of the discharge (Q) and the respective drawdown (s) into two domains; the one below the critical yield where drawdown is practically small and increases quite proportionally (linearly) with the increase of discharge, the other , greater of the critical value, where drawdown is large and goes disproportionally (non – linearly) with the increase of discharge. On an arithmetic graph of Q vs.s the Qc value corresponds to the point of maximum curvature of the curve, and is approximately determined. To precisely find that point, we introduced the transformation logQ vs. logs ,i.e a plot on log – log paper .The above defined domains are shown in this transformation by straight lines of which the intersection point corresponds to the critical yield. (Kruseman et al. 1976).

The transformation comes out from the Dupuit formulae, for a steady state radial flow in a full penetrating well,

$$Q = 2\pi kb(H\text{-}h) / ln(R/r) \quad \text{(confined aquifers) and} \tag{3}$$

$$Q = \pi k(H\text{-}h)(H\text{+}h)/ln(R/r) \quad \text{(unconfined aquifers),} \tag{4}$$
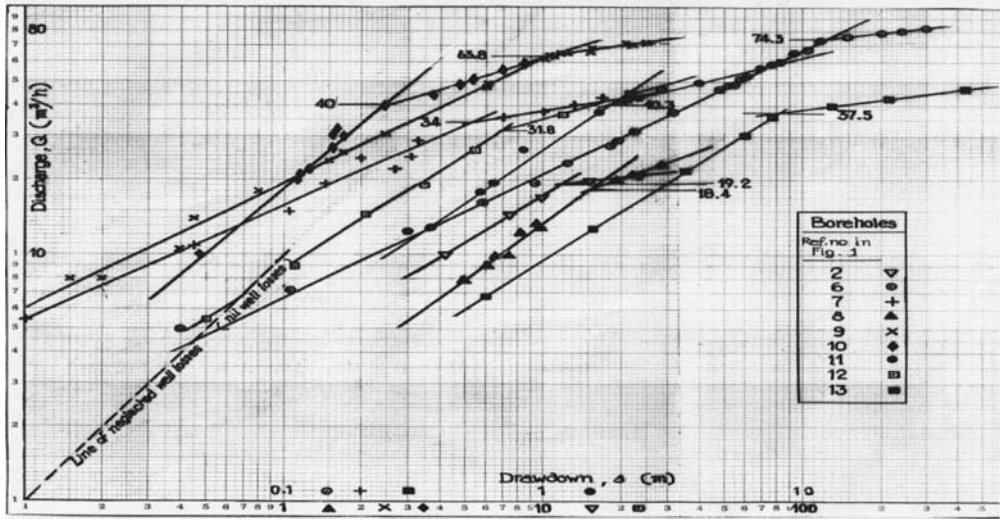
Fig. 2: Indicative curves Q vs. s in log – log transformation to precisely appear the critical yield, as the inter-section of the straight segments.

where Q, k, b, H, h, R, r stand for well discharge, permeability of the aquifer, thickness of confined aquifer, GW height at distance R from pumped well, GW height in the well, radius of influence of pumped well, well radius respectively, and π= 3.14, H-h =s the drawdown of the piezometric surface or of the GW level (Bogomolov 1965, Denisov 1957).

The logQ vs. logs transformation to exploit a graphical description and solution is apparent. In Fig. 2 are indicatively given some "characteristic curves" of boreholes to show the precise critical yield .Shown also is the line of practically nil well losses, and only of aquifers losses, totally expressed by s, that is the line for

$$Q=cs \qquad (5)$$

with c a constant, incorporating all constant quantities of the previous formulae. Yields with no well losses and hence with no energy consumption for them, are very low, as the log- curves of Fig.2 suggest. However, in groundwater exploitation and management the critical yield, as previously defined, is with no doubt preferred, if economic, quality and other constraints allow it. The higher values are offered by carbonate aquifers free of dolomite component, schists intercalations and alike boundaries. If brecciated the aquifer, critical yield is improved.

3. Conclusions

- For the natural water balance assessment and studies of fissure/karstic flow carbonate aquifers of the "Eastern Greece geotectonic zone " and of alike formations, an infiltration of approximately 0.4 of the respective precipitation is likely to be the proper figure.

- In same hydrolithology the pertinent specific yield (effective porosity) is in between 0.015 and 0.043.

- The transmissibility values that are mostly expected are in between 10m³/h.m and 75m³/h.m.

- While critical yield of boreholes is most likely to exist in the range of values from 15 m³/h to 75 m³/h

- Whatever the aquifer is the log Q vs. log s transformation offers the precise critical yield of an abstraction well and should be preferred in decisions, while also the annual recession loss from a well hydrograph has to be added in the annual GW level fluctuation to precisely determine specific yield in water balance studies.
- Consequently the hydrogeologist who will be on duty to preliminarily decide on the capabilities of specified hydrogeological sections, abstraction sites or catchments will be safely supported by the above quantities .These will also constructively serve comparative and detailed hydrogeological studies.

4. References

Bogomolov, G. 1965. Hydrogeolologie et notions de geologie d' ingenieur .Editions de la Paix, Moscou.

Denisov, N.Ya. 1957.Engineering geology and hydrogeology. State Publishing House for Architecture and Building Literature, Moscow.

Dounas, A., Kallergis, G., Morphis, A., Pagounis, M. 1980. 1976. Hydrogeological investigation of karstic brackish springs of Ag. Apostoli area (Kalamos –Attica). Hydrological and Hydrogeological Investigations. 31. IGME, Athens. (In greek) .

Kounis, G.D.,Vitoriou, A.C., Gioni, G.C., Dimitropoulos, D.C, 1983. Evaluation of groundwater resources in Greece. Institute of Geology and Mineral Exploration, Athens.

Kounis, G.D. 1986. Evaluation of vulnerability and quality of groundwater resourses in Greece. Institute of Geology and Mineral Exploration, Athens.

Kounis, G.D., Siemos, N. 1991. A site hydrogeological investigation of the aquifers of the Thriassion Pedhion for the water supply of the Hellenic Refineries. Institute of Geology and Mineral Exploration, Athens. (In greek) .

Kounis, G.D. 1998. A study for the hydrogeology of Attica. Institute of Geology and Mineral Exploration, Athens. (In greek) .

Kounis, G.D., Vitoriou, A. 2005.On the special groundwater quality alluvium aquifer of Loutraki ,in Korinth .Hydrogeological conditions, inflows, outflows and storage. *7th International Hydrogeological Conference*. *Proceedings* V.1, Athens .

Kounis, G. D. 2008. Hydrogeological quantities and findings of particular importance from the hydrogeological structure and performance of Attica, *8th International Hydrogeological Congress of Greece, Proceedings V.2*, Athens .

Kruseman, G.P. and De Ridder , N.A. 1976. Analysis and evaluation of pumping test data. International Institute for land Reclamation and Improvement Wageningen, The Netherlands.

Mariolopoulos, I.G., Karapiperis, L.N. 1955. The rainfalls in Greece. National Printing Office – Athens.

Shaw, E.M. 1994. Hydrology in practice. Chapman and Hall,London.

Soulios, G. A contribution to the hydrogeological study of the karstic systems of the greek territory. Scientific Annals of the Faculty of Sciences, Aristotle University ,Vol 3, No27. Thessaloniki. (in greek).

Todd, D.K. 1959. Groundwater hydrology. John Wiley and Sons, NewYork.

Wilson, E.W. 1993. Engineering Hydrology. McMillan, London.

RELATIONSHIP BETWEEN THE TRANSMISSIBILITY OF THE "ATHENS SCHISTS" AND THE PERCENTAGE OF THEIR COMPETENT ROCK COMPONENT

G. D. Kounis[1] and K. G. Kounis[2]

[1] *Hydrogeologist, Former Director of Hydrogeology,and Advisor at IGME, gdkounis@gmail.com*

[2] *Consultant in Civil and Underground Works Engineering , kkouniscve@yahoo.com*

Abstract

Aquitard formations consisted principally of "soft", ductile schists, crystalline or not, including,as a minor component, thin intercalations of "hard" rocks, like carbonates, quartzites, sandstones, quartz veinlets and the alike, though of low transmissibility, and thus very low yielding, are of great importance in some places where groundwater is demanded, especially in drought periods for irrigation of parks, and other uses.

To these formations belong the "Athens Schists" (from a long ago term, after R.Lepsius).

Formations like these, during the orogenic processes and their structural finishing, responded, under the compressive stresses, with a resultant normal extension strain contemporary or late, by folding affecting mostly the "plastic", ductile "soft", low rigidity components, by fracturing their competent, more rigid, "hard" components ; a fracturing hydraulically well performing, particularly that in carbonates which are better dissoluble into the circulating water.

Further, a very good measure of the yield of the unit saturation front under unit hydraulic head is the transmissibility of the formation, which in turn becomes a good decision making parameter in the exploitation of groundwater.

Therefore, the search for the correlation between the transmissibility (T) of the "Athens Schist" and the percentage (Hr) of the brittle, "hard", hydraulically well performing component arised as a hydrogeologically sound idea.

A very good and positive relationship T vs. Hr has been revealed, with an increase of transmissibility (ΔT) of "Athens Schists" per unit increase (ΔHr) of the percentage found in the range of values.

$$0.38X\ 10^{-2}\ lit/sec.m.Hr < \Delta T < 0.72\ X10^{-2}\ lit/sec.m.Hr$$

Values of T are very low, as expected for a formation of the hydrolithology of the "Athens Schist", and mostly in between

$$0.4X\ 10^{-2}\ lit/sec.m < T < 8.5\ X10^{-2}\ lit/sec.m$$

The percentage (Hr) of the hard member is commonly in the range of values

$$2.8\% < Hr < 17.5\%$$

Transmissibility is calculated under unsteady state conditions of pumping tests in boreholes, using the Jacob approach. Drawdown (s) with time (t) from start of pumping offers, with a very good accuracy, the appropriate linear segment on semi-logarithmic plot.

Values of T from pumping test data representing longer pumping time and a more expanded cone of depression to wider rock mass showed recharge condition with delayed yield. However, dependence of T on Hr is again positive and very good.

The percentage (Hr) of the "hard" rock component of the "Athens Schist" was measured on drilling cuttings and in outcrops of the formation (excavations for buildings foundations etc) in the closer vicinity of boreholes, and results found were well comparable to each other.

Key words : *Schists of Athens, transmissibility, hard rock, fracturing, lognormal distribution, correlation.*

1. Introduction

Serving for many years, the first of the authors, the theory and field praxis in general geology and hydrogeology with a particular interest in applying new methods and views, the hydrogeological performance of the schists of Athens raised the idea to search for the reason of their groundwater to occur and flow, weakly but in acceptable yield for irrigation of parks and for other very local needs. Observations on different occasions on the schists of Athens and during the hydrogeological study he carried out in the context of Athens METRO project, as well as during a period of serious drought when he proposed and were drilled boreholes in the schists to exploit whatever ground water they could supply for irrigation of small plots were among the data to check-up the idea. (Kounis 1980). Other professional priorities kept aside the analysis and presentation of the subject, until this paper to appear.

In this paper we present the hydrogeological performance of the schists of Athens, and more specifically the response of the saturation zone to pumping in relation to the lithologic composition. We found a very good correlation between the transmissibility and the "hard", competent to fracturing, component of the formation. Sustainable yields are very low, as such are transmissibility values, and the case is that of an aquitard and of similar formations.

We present the generalized geological conditions i.e lithology, and structural geology of the wider environment of the schists to show and justify the state and the consequent hydrogeological performance. Going through the transmissibilities calculated from pumping tests and the percentage of "hard" rock, found out at specified sites of boreholes, we proceed to the formulation of the relationship between transmissibility and that percentage.

2. General Geology

Hereafter, the synoptic lithologic composition and the tectonic structure of the wider Athens basin, in which the "Athens Schists" (after A. Lepsius nomenclature) exist, are presented. Thus , the necessary information is given to show the relation between the state of the schists and their hydrogeological performance.

2.1 Lithology

In the area of the Athens basin exist *Quaternary* deposits in which are recognised eluvium,scree and alluvial fans. Eluvium, incoherent and mainly finegrained is present on the limestones of the Filopappou as well as on the Athens schists, and is less than 0.5 m thick. Scree on the Athens
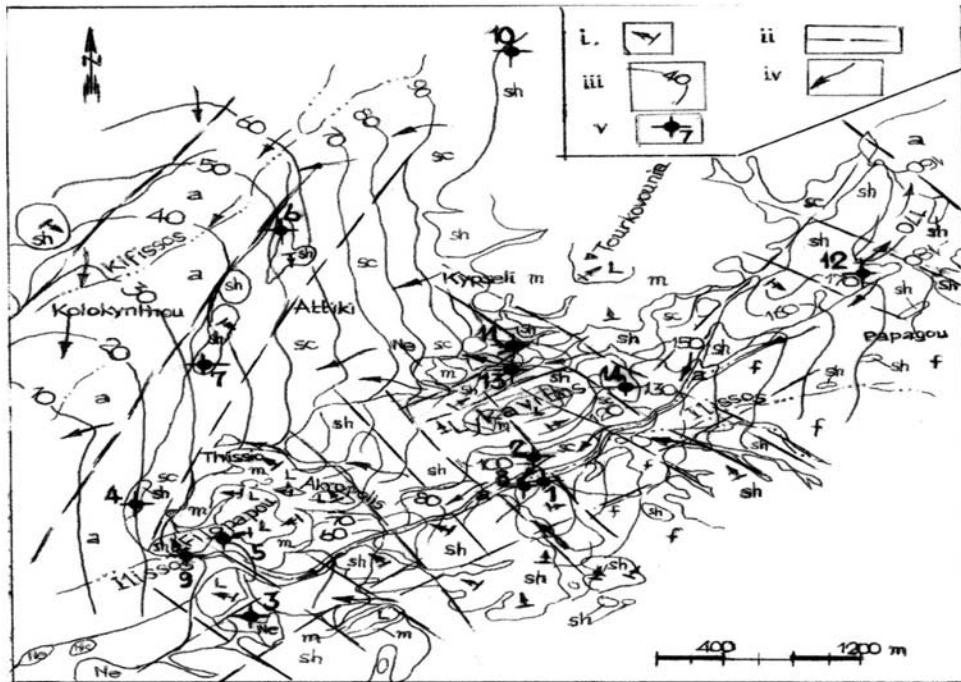
Fig. 1: Generalized hydrogeological map of the central Athens basin (sc: scree, young fans. a: alluvium along streams and plain morphology. f: alluvial fans. Ne: neogene. L: limestone, on the Athenian hills. m: marly limestones, marls, sandstones, conglomerates. sh: Schists of Athens. i: strike and dip of beds. ii: pre-quaternary fault. iii: GW level contour, masl. iv: predominant GW flow. v: borehole site, with ref. no).

hillslopes, is mainly medium to coarsegrained and less than 1m thick (olocene). Alluvial fans from the mountainous environment are developed to valleys (Ilissos) and plain (Kifissos) deposits. Those from Hemyttos mountain are characteristically made of mixed clastics (marble, schists etc) principally coarse grained with an increased roundness and a slight sorting of their elements, a comparatively increased permeability, and locally compact. Erosion cuts them quite deeply in the older sectors to show terrace sections (Pleistocene). Calcareous are mostly the fans from Aegaleo Mt,with comparatively weak their rest of characteristics (Kounis, 1980).

Maximum thickness of quaternary in 98% of the sites measured was found less than 10m, particularly where it overlies the preneogene substratum, the latter being in the wider Athens area the Schists of Athens.

The *Neogene (Pliocene)* is represented by light coloured mostly limestones, commonly medium bedded, and by clastics of different coherence, of a wide granulometry, rather sorted, ranging from clays to basal conglomerate chiefly calcareous. It crops out at the boundary of the Kifissos graben and locally on hilly sites of the Athens area. (Strefi, Ghyzi etc), while expected is under the quaternary of the downstream Kifissos zone. Observed thickness is less than 100m.

The *preneogene substratum* in descending stratigraphy is made of : The *limestones* of the Athens hills, light coloured, crystalline locally, brecciated or conglomerate towards their base (with fragments of rudistae and globotruncanae) (Katsikatsos, 2002).They overlie a characteristic clastic member from mixed, medium – finegrained sandstones, sandy marls and conglomerates,

which seems to go transitionally to hardened marls and marly limestones (Katsikatsos et al., 1976).This clastic and marly member attains a thickness in between 20m and 80m, while it resembles almost convincingly a transgression base of the sequence (Kounis, 1980).

Underlain are the *Schists of Athens* which are shaly , with usually thin sandstone layers, rarely clastic limestones, and sporadic small spilite and diabase bodies. They are equally chloritic ,sericitic schists with quartzites, graywackes and less frequently crystalline limestones, with the presence of all these metamorphics increasing with stratigraphic depth in the Schists. Maximum attained thickness is greater than 100m. In the metamorphic member crystalline limestone are locally a few meters thick ,while quartzite layers rarery are 0.2m thick,wedged out within 3m (Fig. 1) (Dounas et. al, 1976, Kounis, 1980, Gaitanakis, 1982).

2.2 Tectonics

The preneogene structural geology is expressed by a NWern principally, to W-SW compression,which has resulted in successive folds of NE axis mainly, most evident and intensive in the "plastic" schists mass of the structure, less pronounced in the calcareous, more elastic part. This geomechanic process is also well impressed in the underlain older structure, which is lifted particularly in the Pendelikon and Hymettus Mts,as well as in the rest of the metamorphosed Attica. The folding result on the Schists and the metamorphic geologic mass of the Athens basin as equally on the rest of metamorphic eastern Attica is very characteristic, dense and intensive, with very frequent the events of vertically erected or lain down folds. A very revealing evidence we recognise in the Pentelikon, with a dense sequence of synclines – anticlines of low wave length, even in the thick bedded " Lower Marble" (of A.Lepsius).Through a section of 3.5 km long only, 4 of the above binary forms can be mapped. In addition to that , where erosion and the marble quarries help to a good field observation the intense folded structure may lead to the false interpretation of stratigraphic repetition of marble and crystalline schists or metamorphosed intrusive. A similar strong folding of high elastic beds can be easily recognised in sites farther in east Attica i.e with horizontal folds of marbles in crystalline environment (Varkiza Barako hill, SE of Dionyssovouni etc).

On the contrary to the elastic, strongly folded central Attica (where the Athens Schists) and the entirely metamorphosed eastern Attica, in western Attica, from the eastern hillfoot of Aegaleo and Parnis westwards, folding is in general obtuse, of a long wavelength, with uncommon or lacking the extreme forms of vertical or horizontal folds, although stress pattern, as it is revealed by stratimetry and faulting, is generally the same applied in eastern Attica. That is, a NW to W strong compression, weaker towards NE, with a major tension result from NE to the E.According to the all above analysis, during the orogenic process the regional tectonic result seems to best conform to a kind of clash of the more plastic/less rigid structure of eastern Attica onto the more unyielding/elastic structure of western Attica, producing conditions for a mechanic/tectonic convenience, to benefit overriding westwards.

Folding is accompanied by shearing, with major elements the NW strike slip and NE reverse faults of restricted movement, as well as by a tension of the structure greater to the NE and to a less extent NWards.

Tension acted contemporarily to folding and later on to finish orogenic structure. To the latter process belong the NW and NE faults of the graben boundaries, that have been accommodated by prepared, mechanically weak routes of the preneogene structural process. As such faults are
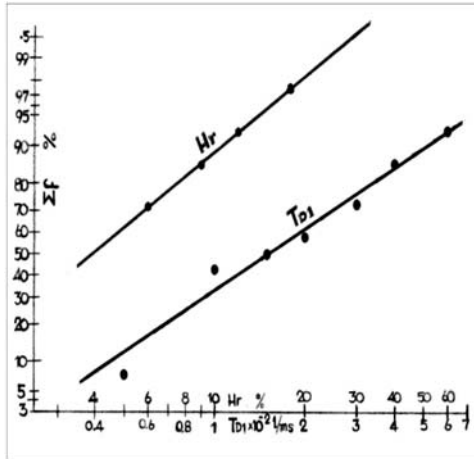
Fig. 2: Cumulative frequency (Σf) of the values of the hard rock component percentage (Hr) and of the transmissibility T.
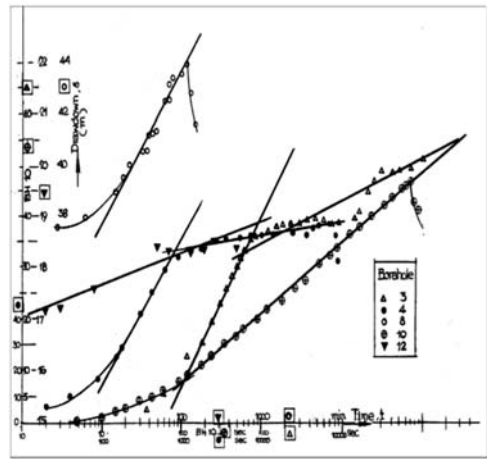
Fig. 3: Indicative diagrams of s vs. t.

understood indicatively, the major fault of the northern boundary of Thriassion Pedhion (west of Athens) to the east through Zefyri – Kalogreza –Pallini, as well as the minor of Fili through Acharnae to Anthoussa,the NE striking of the boundaries of Aegaleo and Parnes (Fig.1) (Kounis, 1998).

3. Hydrolithological structure and hydrological performance of the Schists of Athens

3.1 General

The hydrogeological conditions in the Schists of Athens are quite significantly differentiated in the zones of thick limestone intercalations or effusives (Ilissos, Thission, Metaxourghion, Ag. Panteleimon – Kypseli), but also everywhere the percentage of calcareous, quartzite and sandstone contribution to the schists mass is increased, indifferently if in thin layers or disseminated. Differentiation is also recognized along the faulting zones where incoherence and brecciation are produced, commonly present and best performing hydrogeologically if tension originated. The fault case is particularly important for improving with depth hydraulic continuity.

Additionaly, where aquiferous quaternary overlies a weathering mantle of the schists, considerably thick, an improvement of the hydrogeological performance is observed. In this case is also calcareous and quartzitic component responsible for improved conditions.

Groundwater level morphology is compatible to the topographic surface and a noticeable flow takes place through the compined weathering mantle of the microfractured schists and the quaternary cover, if the latter is thick enough. Otherwise, and this is the case discussed, flow though weak, is undertaken by the "hard" zones of the Schists (Fig.1).

Beside the major collective zone along the Kifissos, in the Athens basin few minor but remarkable groundwater flow axes are formed and more specifically running through Ilissos, Leof. Alexandras, Iridanos, Lykabettus-Omonia, Erithros Stavros towards SW. Depth to ground-

water level varies mostly in between 1m and 20m, with the lower values measured in central Athens where Schists are shallow, the higher in the Kifissos flow convergence.

Schists of Athens are aquitards allowing weak flow, and the case refers to the upper hydraulically best performing layers. They become locally insufficient to provide water (aquicludes), particularly where shaly component and structure persist and prevail extensively, producing hydrogeological blockade of the "hard", fractured members and of their hydraulic continuity.

3.2 The Transmissibility

Transmissibility (T) of the Athens Schists is found low to very low, with the 96% of values calculated being less than $8.4X10^{-2}$ l/sm and the 50% of them less than $1.5X10^{-2}$ l/sm. The range of values is $0.4X10^{-2}$ l/sm$<T<8.5X10^{-2}$ l/sm (Fig. 2), as it comes from pumping tests in boreholes under unsteady state conditions of flow. The Jacob approach is used and more specifically the first ,after the segment due to well storage, linear part of the diagram of drawdown (s) with time (t) from start of pumping on semilogarithmic paper (Fig.3) (Todd 1959; Kruseman et De Ridder, 1976).

Values from this first linear part inform about the performance of the borehole site and the immediate vicinity. Values of T from the next linear part of the diagram svs.logt have also been taken, where condition appeared. This segment mostly showed an additional delayed flow from rather leaky wheathering mantle of the Schists in the site neighbourhood, or flow from some improved fracturing of "hard" schist reached by depression cone, as its radius of influence expanded farther. A few svs.logt diagrams are indicatively given (Fig.3),while borehole sites are shown on the map (Fig. 1). Statistical distribution of values show a positive skewness and this conforms,as expected, to the permeability distribution (Krumbein and Graybill, 1965). As practically no accuracy is lost in the domain of values found, lognormal distribution is preferred and log-probability paper is used (Fig. 2).

3.3 The competent to fracturing component

Taking into account the lithological and structural conditions previously presented, it is the "hard" component of the Schists of Athens, layerd or disseminated, that shows a hydrogeological active fracturing in which groundwater is stored and flows.

Suffering tectonic stresses, especially in dynamic metamorphism conditions that hold extensively in the case studied, grain, brittle minerals are traversed by tension cracks strongly marked. (Harker 1962; Ramsay, 1967). In the case of selective, sorted deposition of these minerals in the form of layers of sandstone, limestone, quartzite or lenses and veinlets fracturing is particularly pronounced. In carbonate layers, internal erosion acted to the benefit of widening of fractures and of its performance. The more is spatially the abundance of the "hard" component of Schists with the associated fracturing, the better is hydrologically the athenian schists performance.

Entirely adverse effect has the "soft" component of schists of which ductile minerals and above all their depositional and metamorphic concentrations undergo significant shearing and folding, with the hydrologically active jointing playing practically a very second role in water flow. Fortunately, this disadvantage is to some extent counterbalanced by tensional detachments, which offer or improve hydraulic continuity in the mass. Jointing passes through the binary lithologic system and mostly diffracted at the boundaries. In the ductile, inelastic minerals and their depositional and metamorphic layers are understood the clay minerals (e.g caolin group) and those with primary micaceous, foliated and lamellar structure, or the dynamically similar.
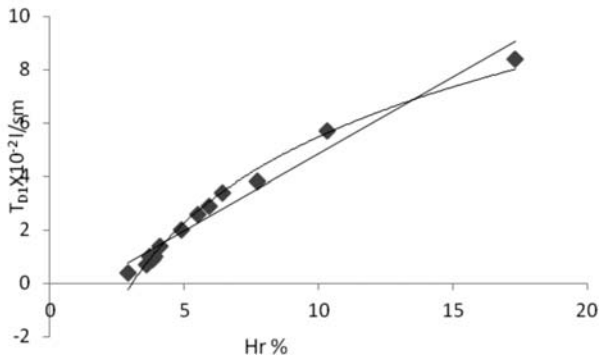
Fig. 4: Transmissibility (T_{D1}) vs. "Hard" rock component (Hr) (T_{D1}, from the first linear segment of drawdown vs. log time).

Measurements of the hard percentage over the whole sample have been taken from cuttings of boreholes (shown on the map). Diagnostically, on a given randomly taken sample, from a larger number of them from each borehole, white coloured greysh and hard cuttings represented calcitic, quartz and alike elements and were counted. Counted also were the friable cuttings, darkish coloured. A good magnification was accurately achieved. In certain samples microscopical observation and measurement was applied, as well.

Deviations among the samples in the specified borehole were efficiently distributed around a mean value kept for the further use. Where natural sections and particularly excavations for foundations existed, observations and measurements were taken. The counting was accomplished on a sufficient number of lines of adequate length each, and where possible perpendicular to the main structural feature (bedding etc). Results were well comparable to those of borehole cuttings and in most cases the latter were put in between.

When values were available from both approach methods, the mean value was finally accepted for correlation. Values (Hr) of "hard", competent to fracturing component of the Athens Schists show a positively skewed distribution, so that a log-propability fitting was preferred and shown on the diagram of Fig.2. Less than 50% of the values are in the range Hr ≤ 0.04, while Hr < 0.36 at a level of 99.75%. In the distribution diagram included are also measurements from excavations distant of boreholes vicinity. Scattering of points from the various places is very good to fit this distribution.

3.4 The relationship of transmissibility with the "hard"/competent to fracturing component.

The hydrogeological qualification of the Schists of Athens is offered from the presence of the competent to fracturing rock phase in their composition, for the tectonic reasons and conditions previously presented. This qualification is reflected to the transmissibility (T) values of the saturation zone. The regression of transmissibility values upon the percentage (Hr) of "hard" component shows a positive very good linear correlation. Using T values from the first linear segment (T_{D1}) of the drawdown (s) with time (t) i.e svs. logt , according to the Jacob approach, we found out

$T_{D1} = 0.5779$ Hr $- 0.927$, with a very high correlation coefficient, r = 0.987 (Fig.4)

The fitting of a logarithmic model made r higher and more specifically, we found that

$$T_{D1} = 4.6191 \text{ lnHr} - 5.1558, \text{ with r= } 0.9928 \text{ (Fig.4)}$$

Table 1.

Ref. No	$T_{D1}x10^{-2}$ (l/sm)	$T_{D2}x10^{-2}$ (l/sm)	$T_{(D1+D2)/2}$ $x10^{-2}$ (l/sm)	Hr (%)	BH Depth (m)	Site
1	5.7			10.3	86	Hilton
2	2.9			5.9	56	Evangelismos
3	0.7	2.4	1.55	3.6	69	Ag. Sostis
4	0.7	8	4.35	3.2	118	Serafeion
5	0.9	3.6	2.25	3.8	85	Filopappou
6	0.4	0.7	0.55	2.9	57	Park Atlantos
7	1	0.5	0.75	3.7	56	Akad Platonos
8	3.8			7.7	60	Idryma Erevnon
9	1.38			4.1	58	Lofos Koilis
10	2.6	6.6	4.6	5.5	92	Plateia Antheon
11	3.4	10	6.7	6.4	108	Evelpidon
12	8.4			17.3	74	Plat. Irinis
13	2	15	8.5	4.9	73	Plat. Argentinis
14	1	4	2.5	3.9	52	Elenas
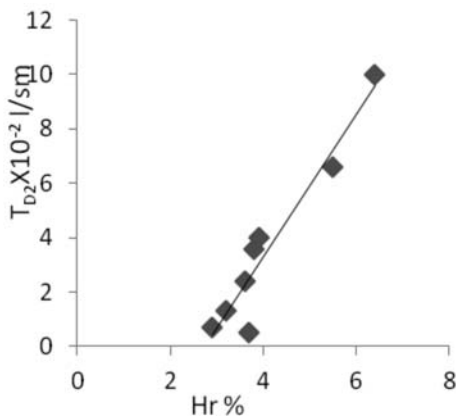
Fig. 5: Transmissibility (T_{D2}) vs. "Hard" rock component (Hr) (T_{D2}, from the second linear segment of drawdown vs. log time).
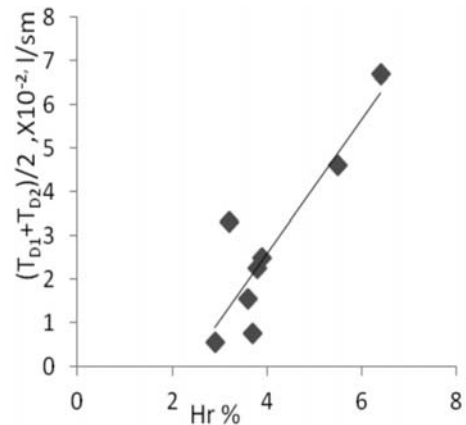
Fig. 6: Average Transmissibility (T) vs. "Hard" rock component (Hr) ($T_{D1, D2}$, as in Fig. 4,5).

To validate the idea of "hard" component being the vital factor for the hydrogeological performance use we made of transmissibility values from the second linear (T_{D2}) segment of the s vs logt approach.

The reasons this segment to appear is convincingly explained in a previous paragraph.

The relationship found is

$$T_{D2} = 2.6131Hr - 7.1416, \text{ with } r = 0.9567 \text{ (Fig.5)}$$

Taking mean values for the pairs T_{D1} and T_{D2}, which is an approach not uncommon for the estimation of the transmissibility of aquifers with drawdown responding to time in this way, we found

$$T_{(D1 + D2)/2} = 1.5334Hr - 3.5464, \text{ with } r = 0.8876 \text{ (Fig. 6)}$$

In Table 1 the sites of wells, transmissibility values, the percentage of "hard" component and other data are given.

4. Conclusions

Very low to low is the transmissibility of the schists of Athens with values usually not exceeding 300lit/hour.m.

With a hydraulic gradient of 0.02 to 0.05, through a flow front that reasonably corresponds to an abstraction well the groundwater yield is about $2.2m^3$/hour.

The participation of the hard component and more specifically of the carbonates, sandstones, quartzites and the alike in the form of layers, lenses, veinlets usually does not exceed 30% of the whole composition.

A linear correlation of transmissibility (T) with "hard" rock percentage (Hr) seems to hold for the Schists of Athens, at least in the domains of values $0.2X10^{-2}$l/sm < T < $8.5X10^{-2}$l/sm and 3% < Hr < 18%.

We think worthwhile, the relationship of T vs. Hr whatever it will be, to be searched in similar to schists of Athens formations.

An approximate prediction/estimation of the groundwater yield of a similar formation could be made on the basis of measurements of "hard" component percentage in natural or artificial field sections.

5. References

Dounas, A., Kallergis, G., Morphis, A. 1976. Hydrogeological investigation within the framework of the study for the Athens metropolitan underground railway(METRO). Hydrological and Hydrogeological Investigation, 19 IGME, Athens.

Dounas, A., Kallergis, G., Morphis, A. 1980. Contribution on the knowledge of the tectonic relation between the Parnes system and the metamorphic sequence of Grammaticon.Publications Office of the Academy of Athens vol. 54 (in greek).

Harker, A. 1962. Petrology for students. Cambridge University Press.

Gaitanakis, P., 1982. Geological map of Greece. Athinae- Piraieus sheet. 1 to 50000. IGME, Athens.

Katsikatsos, G., Kounis, G., Antoniades, P., Mettos, A., Papadopoulos, P., Gakis, A., 1976. Geological map of Metro area, 1 to 7500. IGME, Athens.

Katsikatsos, G., Mettos, A., Vidakis, M., Dounas, A., 1986 Geological map of Greece. Athinae - Elefsis sheet, 1 to 50000. IGME, Athens.

Katsikatsos, G. 2002. Geological map of Greece. Kifissia sheet 1 to 50000. IGME, Athens.

Koumantakis, J. 1998. Subsidences due to overpumping of ground waters. Necessary interventions. Nat. Tech. University of Athens.

Kounis, G. D. 1980 On the hydrogeological conditions of the area of the solar village no.3,

Lykovrissi Attica. Hydrological and Hydrogeological Investigations, 33. IGME, Athens.

Kounis, G. D. 1980. Athens Metro hydrogeological research. I Measurements and II Analysis of the hydrogeological Conditions. Hydrological and Hydrogeological Investigations, 34. IGME, Athens.

Kounis, G.D 1998. A study for the hydrogeology of Attica.. IGME, Athens.

Krumbein, W.C, Graybill, F.A, 1965. An Introduction to statistical models in geology Mc Graw-Hill Book Co.

Kruseman, G.P. and De Ridder N.A.1976. Analysis and evaluation of pumping test data. International Institute for land reclamation and improvement.1976. Wageningen, The Netherlands.

Marinos, P.G. 1991. Chapters of Engineering Geology. Nat. Tech. University of Athens.

Ramsay, J.G 1967. Folding and fracturing of rocks. Mc Graw-Hill Book Co.

Todd, D.K. 1959. Groundwater hydrology. John Wiley and Sons, New York.

BRACKISH KARST SPRINGS SIMULATION WITH "MODKARST" MODEL UNDER NOT ENOUGH DATA CONDITIONS (THE CASE OF THE "POTAMI" SPRING AT HIMARA ALBANIA)

Maramathas A.[1], Gialamas J.[2], Pambuku A.[3], Beshku H.[4], Vako E.[5]

[1] *National Technical University of Athens, School of Chemical Engineering, GR 15780 Athens, Greece, thamar@chemeng.ntua.gr*

[2] *National Center for Marine Research, Agios Kosmas Helliniko, GR-16604, Athens, Greece, jgiala@hcmr.gr*

[3] *Albanian Geological Survey Rr. Kavajes, Nr.153, Tirana-Albania, urtesi2001@yahoo.com*

[4] *Albanian Geological Survey Rr. Vasil Shanto, Laboratori i Ujrave, Tirana-Albania*

[5] *Tirana Polytechnic University, Energy, Water and Environmental Institute Rr. Durresit, Nr. 219, Tirana-Albania*

Abstract

A simulation is presented of the operation of a brackish karst spring with the MODKARST deterministic mathematical model under not enough data conditions. MODKARST is a deterministic mathematical model for karst springs, able to accommodate brackish water. It incorporates mass and energy balances in a system of reservoirs properly connected that approximates the karst system and the sea. A complete fitting for this model needs field measurements about spring discharge and spring water chloride concentration at least for a hydrological year. The particular case analysed is the "Potami" brackish karst spring at Himara in Albania. MODKARST simulated the hydrograph along with the variation with time of the chloride concentration. The fitting of the model was based only on chloride concentrations measurements of the spring water that have taken place from 1/5/2007 till 27/12/2007, since there were not spring discharge measurements except for a single one, which simply gave the order of magnitude of this parameter. From the simulation of the model, information was drawn about the recharge area, the effective infiltration coefficient and the dominant seawater intrusion mechanism of the spring. Taking the above information into account, a set of proposals for the sustainable development of the spring was sketched.

Key words: *brackish karst spring simulation, Modkarst model, Potami spring, Himara, South Albania.*

1. Introduction

The ground water salinization is an extremely important phenomenon in the countries around the Mediterranean Sea like Greece and Albania. This problem, which decreases the exploitable quantities of ground water in these regions, will get worse in the future due to intensive exploitation and climate changing (planet warming, rainfall diminishing, sea-level upraising). Thus, it is of great importance the development of a methodology in order to predict quantitatively, the salinization phenomenon and support the decision about the method of a sustainable exploitation. Such a methodology does not exist till now and every exploitation effort is based mostly on the empirical trial and error method.

The objective of this paper is the presentation of a methodology for the quantitative prediction of the salinization phenomenon for the karst ground water that outflows from coastal or submarine springs. The above-mentioned objective was the main goal of an E.C. funded project in the framework of the Greek-Albanian cooperation. As it is known, karst water is the ground water that flows in conduits formed by the erosion, in the carbonate rocks. Karst water is a very important portion of the whole ground water wealth in Greece and also in Albania. The above-mentioned methodology is based on the simulation of the spring using the MODKARST deterministic mathematical model.

For the above-mentioned purpose the "Potami" karst spring at Himara in Albania has been studied. The Albanian team bound itself to take a time series of measurements for the model fitting, that is, spring discharge, spring water chloride measurements and rainfall of the feed area of the spring. The Greek team undertook to simulate the spring using the mathematical model 'MODKARST' (Maramathas et al, 2003) and to suggest the most suitable method for its exploitation.

The main goal was achieved. The spring was satisfactorily simulated and some conclusions arouse about the seawater intrusion mechanism and the proper method for the sustainable development of the spring. The only problem was that the Albanian team did not take quite reliable discharge measurements of the spring since it did not possess the suitable instrumentation for it. Nevertheless, even if there were not such measurements the spring was simulated and in that way it has been proved that MODKARST model could be used even if there are not enough field data. This knowledge was one of the most important conclusions of the project. The above-mentioned innovative methodology of study for the specific spring is recommended for all the brackish karst springs.

In the next paragraphs the research work will be described and the conclusions and suggestions for the continuation of the research will be presented. The continuation of the research will be useful for both of the countries.

2. The Potami spring

The Potami spring is located at Himara town (Fig. 1), at southwestern Albania. It is a karst spring that appears along a front by 40m. Its elevation is 5 m above the mean sea level and the distance from the seaside of Ionian Sea is about 60m. The order of magnitude of the spring discharge is $1m^3$/sec while the chloride concentration of its water presents a small fluctuation during the year getting rates between 350 and 600 ppm (mg/l). In the sea in front of the spring and at a few hundred meters from the coastline there is fresh water outflow from the bottom that indicates the existence possibly another discharge point of the karst aquifer beyond the spring Potami. Due to limited financing, this point was not studied and was not taken into account for the simulation. However, in the future the relation with the spring must be examined since there is the possibility during the year this point sometimes to operate as submarine spring and sometimes as sinkhole contributing to the salinization of the spring water.

2.1 Geological structure of the Potami feed area

Carbonate and terrigenous formations of tectonic zones of Sazani (Pre-Apulian) and Ionian take place in the geological structure of the potami spring feed area (Meço et al., 2005) (Fig. 1).

Sazani zone, where the Potami spring is located (Fig. 2), exists at the most eastern part of the region. In this zone a variety of carbonate depositions were found. They are separated into tectonic blocks because of the strong tectonic activity caused to overthrust of eastern structures. Carbonates lithologically are represented by dolomites of lower Cretaceous (Cr_1) and dolomitic limestone of upper Cretaceous (Cr_2). Their thickness varies from 250m to 450m (Meço et al., 2005) (Fig. 2).

Fig. Scematic hydrogeological map of Himara, 1) Carbonate rocks, 2) Clays, sand and sandstones, 3) Sand and gravels, 4) Flysch, 5) Limit of hydrogeological units, 6) Tectonic line, 7) Natural Spring, 8) Submarine Spring
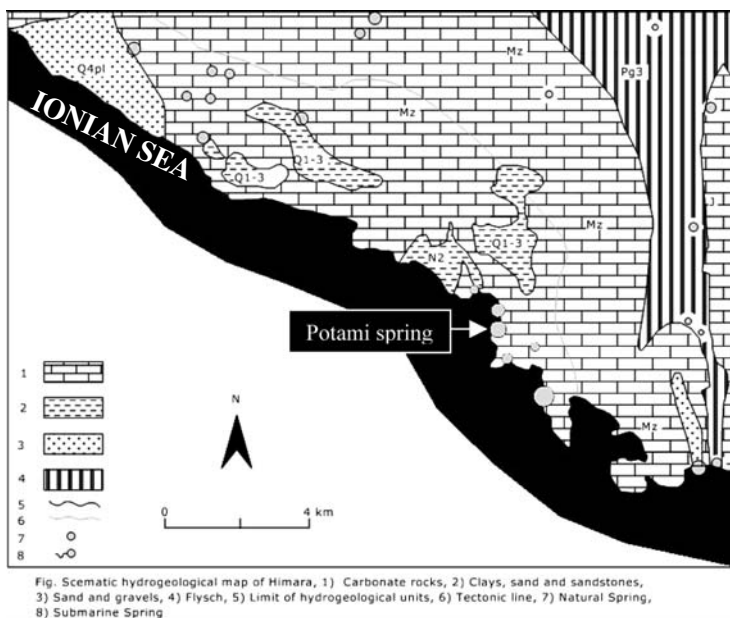
Fig. 1: Schematic hydrogeological map of Himara.

The Ionian zone is represented in the region by the Çika anticline and the Kudhesi Syncline. In Çika anticline there are carbonate depositions of Mesozoic, Paleocene and Eocene which are overthrusted about 10 km toward the eastern direction. These depositions, lithologically, are represented by diagenetic massive crystalline dolomite and limestone of upper Triassic, dolomite and limestone with flints of upper Jurassic (J_1), the phase of "Amonitico rosso", thin to medium layers of grey limestone (J_{1-2}), micritic, porcelain and argillaceous limestone (Cr_1) and bio-clastic turbid limestone (Cr_2, Pg_1, Pg_2). In this region the thickness of carbonate depositions varies from 1100 m to 1300 m. In the Kudhesi Syncline there are flysch depositions (Pg_3), siltstones, clays and sandstones (Meço et al, 2005).

Terrigenous depositions of Neogene (N) have limited spread and are represented by clays and sands with weak cementation (Meço et al., 2005) (Fig. 1).

Quaternary depositions represented by silty clays exist at the centre of the region (Meço et al., 2005).

2.2 Hydrogeological Conditions

Ground water is related with the complex of carbonate rocks, which have wide spreading in the area. Karst processes had favourable development conditions particularly in upper Cretaceous and Palaeogene-Eocene carbonates. Carbonate rocks complex has also been affected by the high tectonic and neotectonic activity, which have led to the development of a network of fractures. The above mentioned together with geological-structural favourable composition, have created the conditions for the development of remarkable aquifers (Eftimi et al, 1985; Beshku, 2009).

The rainfall and the snow, which are abundant, particularly in high altitudes, feed these aquifers, while they are discharged by surface and submarine springs. Surface springs (Fig. 1) are numerous, with discharge from 0.05l/s to 600l/s and spread in the entire area up to the elevation of 1525m above the mean sea level. The major springs are situated at the lower sites of the area or closed to seaside. The factors that influence the ground water drainage and the distribution of the springs in the area are
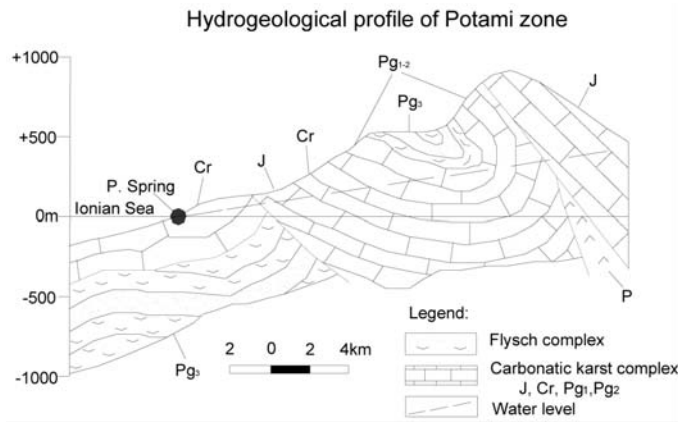
Fig. 2: Hydrogeological profile of Potami spring feed area.

flinty packs, bituminous schist, marls and the tectonics, which controls the presence of the previously mentioned impermeable formations, making impermeable screens. The morphology, characterized by rapid breaks of terrain, is another factor of drainage (Eftimi et al, 1985; Beshku, 2009).

Ground water discharge through submarine springs is favoured from the presence of the karst formations directly under the sea as they are identified at Himara, Porto Palermo and Qeparo (Eftimi et al, 1985; Beshku, 2009).

The potami spring feed area is structured by the formations of the Kudhesi Syncline (carbonate rocks and flysch) separated from the Sazani zone (Pre-Apulian) formations by a fault zone (Eftimi et al, 1985; Beshku, 2009). This fault zone makes an impermeable bar that prevents partially the sea intrusion to the reservoir of the spring (Fig. 2).

2.3 Chemical composition of ground water

The chemical composition of ground water is strongly related to lithological-mineralogical composition of carbonate rocks through which circulates and to the seawater intrusion.

The hydrochemical types of ground water that is spread in region are:

Hydrochemical type HCO$_3$-Ca: This type includes groundwater that circulates and appears in springs at high elevation, mainly from flinty limestone of Jurassic age. The water has salinity 0.17 to 0.35 gr/l, total hardness about 12°dH and temperature 7° - 12°C (Gjivogli et al 2004).

Hydrochemical type HCO$_3$-Ca-Mg: Includes groundwater from dolomitic limestone and dolomite. This water has salinity 0.25 to 0.4 gr/l, total hardness about 7-14°dH and temperature 12-15°C (Beshku 2009).

Hydrochemical type Cl-HCO$_3$-Ca-Mg: Includes the brackish springs, which flow at the seaside from limestone and dolomite as instance Potami and Spile (Himara) springs, some springs in Qeparo, Porto Palermo zone, etc. They are brackish as a result of the mixture of its water with seawater. The water has salinity 1-1.6 gr/l and total hardness about 14-19°dH (Beshku, 2009).

Hydrochemical type Cl-Na: This type includes the groundwater, which is directly under the seawater influence. The springs which discharge their water almost to sea level belongs to this type (e.g. saline springs of Qeparo) This water has salinity that vary from 6.5 to 7.5 gr/l and total hardness from 70 to 82°dH (Beshku, 2009).

3. The MODKARST model

Fig. 3: Hydrodynamic analogue of a karst spring. The reservoirs "karst 1" and "karst 2" represent the karst subsystems while the other one represents the sea.

MODKARST is a deterministic mathematical model which simulates the hydrograph (discharge versus time) of a karst spring and in case it is brackish the chloride concentration of the spring water versus time. MODKARST model is based on a hydrodynamic analogue of a karst spring that consists of a number of reservoirs properly connected with tubes. One of them emulates the seawater while the others the karst system. Each of these reservoirs is discharged to the tube that abuts to the spring (Fig. 3). Consequently, the spring discharge is given by the sum of these discharges. The chloride concentration of the spring water is determined by the solution of the problem of the mixture between fresh water of the karst reservoirs and salty water of the sea. Rainfall data constitutes the input information to the model, while hydrograph and the chloride concentration of the spring water versus time comprises the output information. The macroscopic mass balance equation and the macroscopic mechanical energy balance equation in a control volume and in the respective control surface have been used in each reservoir to calculate the corresponding discharge. On Table 1 the equations, the variables and the parameters of the model are presented. All the calibration parameters are effective and have a precise physical or geometrical meaning.

For the model fitting the least squares method is used. According to this method, an optimisation program was tasked with estimating the parameter values so that the following mathematical expression

would reach its smallest possible value: where are

the model-calculated values for the discharge and chloride concentration, the field measurements respectively and D the time period for the optimisation (number of days). A detailed description of the model can be found in the article of Maramathas et al, 2003.

MODKARST model has been used for the simulation of some important Greek brackish karst springs (e.g. Almiros at Heraklion, Crete, Greece) with great success. It can define the seawater intrusion mechanism of a karst spring and it can evaluate the alternative exploitation methods proposing the most suitable for each spring.

Table 1. Equations – Variables – Parameters of the model.

Equations

$$sS_1 \frac{dH}{dt} + Q_1 - \gamma \dot{P} S_1 = 0$$

$$sS_1 H \frac{dH}{dt} + \frac{Q_1^3}{2gS_2^2} - H\gamma \dot{P} S_1 + L\left[\frac{Q_1}{sS_1}\right]^2 Q_1 = 0$$

$$\frac{Q_2^2}{2gS_3^2} + \frac{p_3}{\rho_\theta g} - H_\theta = 0$$

$$p_3 - \rho_w g(H_\theta + h + \frac{s}{\pi}H) + L_\alpha Q_1^2 = 0$$

Model input information

Rainfall rate $\dot{P}$

Model output information

Spring discharge: $Q = Q_1 + Q_2$

$$\text{ppm Cl}^- = \frac{\rho_\theta C_\theta Q_2 + \rho_w C_w Q_1}{\rho_\theta Q_2 + \rho_w Q_1}$$

Variables

Q_1 Karst system discharge (L^3/T)
Q_2 Seawater discharge (L^3/T)
H Water level over discharge point (L)
P_3 Pressure at the intersection between the seawater tube and the freshwater one (M/LT^2)

Calibration Parameters

s Coefficient of storage
S_1 Recharge area (L^2)
γ Infiltration coefficient
S_2 Outflow-tube cross section of the karst-system reservoir (L^2)
L Energy loss coefficient ($L^{-1}T^{-2}$)
S_3 Outflow-tube cross section of the seawater reservoir (L^2)
H_θ Depth of the intersection between the sea water tube and the freshwater one (L)
π Specific yield
L_α Pressure loss coefficient of the sea-tube outlet region (ML^{-7})

Measured Parameters

g Gravity (L/T^2)
ρ_θ Seawater density (M/L^3)
ρ_w Freshwater density (M/L^3)
h Spring elevation (L)
C_w Fresh-water chloride concentration (ppm)
C_θ Sea-water chloride concentration (ppm)

4. The Potami spring simulation - Results and Discussion

The Albanian team has taken systematically chloride concentration measurements and rainfall measurements during the second half of 2007. The spring discharge has been measured occasionally by the Albanian team due to lack of proper instrumentation while it has been measured for one time by the Greek team with its own instrument during its visit in the area. Because of this, only the order of magnitude of this parameter (discharge) was available for the model fitting.

Contrary to the lack of discharge measurements, model fitting was successful. The simulation period was from 1/5/2007 until 31/12/2007. The results are shown in figures 4 and 5 where the chloride curve (spring water chloride concentration versus time) and the hydrograph (discharge versus time) respectively, are presented. In fig. 4 there are two curves that is the model-calculated curve (in blue) versus the experimental curve from the field measurements (in red). In Fig. 5 there is not experimental curve due to the lack of field measurements (spring discharge). In both of figures the corresponding rainfall measurements of the spring feed area are presented (column type). From the comparison between the model-calculated values (in blue) and the experimental one (in red) in fig. 4, is concluded that spring simulation is quite satisfactory. The daily fluctuation of the measured curve that one can observe in this figure does not have any relation with the sea intrusion mechanism. It is a local secondary phenomenon in the vicinity of the spring-water outflow, probably dew
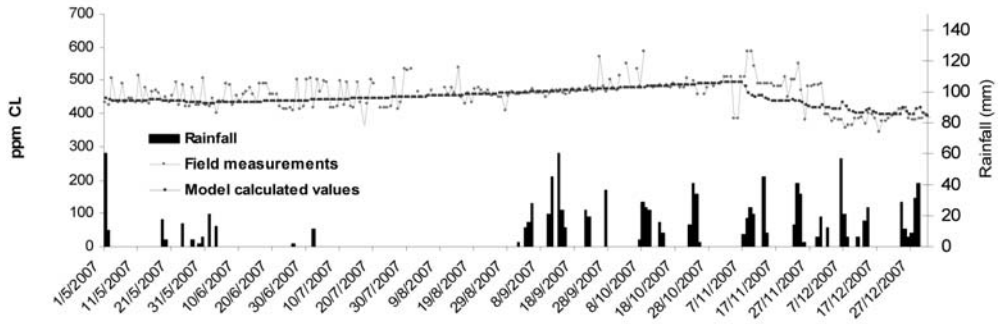
Fig. 4: The chloride concentration curve of the spring.
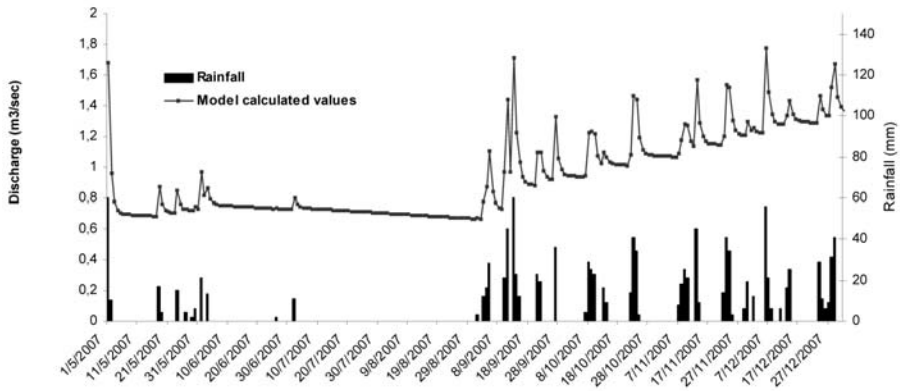
Fig. 5: The Hydrograph of the Potami spring (Discharge versus time).
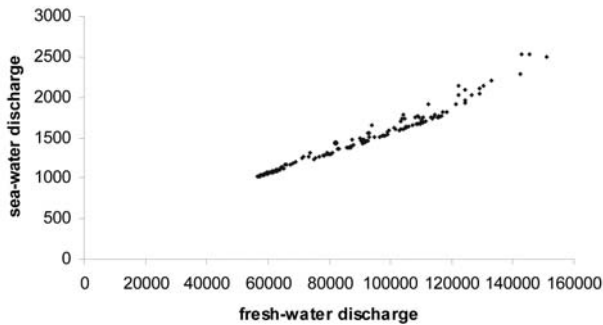
Fig. 6: The seawater discharge increases when the freshwater discharge increases too.

to the tidal fluctuation of the sea level. The chloride concentration simulation is more reliable than the discharge simulation, due to existence of abundant field measurements for the model fitting.

From the spring simulation has been concluded that the dominant seawater intrusion mechanism is the Venturi effect. This conclusion arises since the seawater discharge increases when the freshwater discharge increases too (Fig. 6) (Maramathas et al., 2006). The curve in fig. 6 (seawater dis-

charge versus freshwater discharge) has been calculated from the model after spring simulation.

Due to the above-mentioned seawater intrusion mechanism some exploitation works are rejected while some others seem to be effective (Maramathas et al, 2006). More specifically, works at the point of spring water outflow that prevent seawater intrusion through the artificial upraising of the karst aquifer piezometric level (e.g. dam construction in front of the spring), do not seem to be effective. On the other hand exploitation works (e.g. drills, tunnels) that could find the freshwater before the point of the seawater intrusion seem to be more efficient. In any case, the relation between the submarine freshwater outflow that mentioned before and the Potami spring must be researched through field study and simulation. If it is proved that the conduits concerned with this submarine freshwater outflow, works reversely some period of the year sending seawater to the aquifer, suitable works could be programmed in order to prevent this operation.

Finally, estimates for some useful parameters of the karst system have been arisen from the simulation. More specifically, the feed area of the spring estimated: $125km^2$ while the effective infiltration coefficient estimated: 0.4 (40%).

5. Conclusions

1. Model MODKARST can successfully simulates brackish karst springs even if there are not quite enough field measurements for a complete fitting.

2. The dominant sea-water intrusion mechanism for the Potami spring of Himara is the Venturi effect.

3. The feed area of the Potami spring is about $125km^2$, while the effective infiltration is 40%.

4. In a first approximation, the suitable method for the development of the spring is a drilling project upstream the salinization point.

7. References

Beshku H., 2009, Hydrogeology of Vlora - Saranda Region (in Albanian), *PhD Thesis*, Archive of National Library, Tirana-Albania.

Eftimi, R., Tafili, I., 1985, Hydrogeological map of Albania at 1:200000, Central Archive of Albanian Geological Survey.

Gjivogli G., Pambuku A., Oruci A., 2004, Water bearing study of coastal line of Vlore-Sarande (in Albanian), Archive of National Library, Tirana-Albania.

Maramathas, A., Pergialiotis, P., Gialamas, I., 2006, Estimation of sea intrusion mechanism of brackish karst springs by their simulation with the "MODKARST" deterministic model. *Hydrogeology Journal* 14, pp 657-662.

Maramathas, A., Maroulis, Z., Marinos-Kouris, D., 2003, A Brackish Karst Springs Model. Application on Almiros Crete Greece. *Ground Water*, 41, pp. 608-620.

Meço, S., Onuzi, K., Xhomo, A., 2003, Geological map of Albania at 1:200000, Central Archive of Albanian Geological Survey.

REMARKS ON THE KARSTIFICATION IN THE WIDER AREA OF THE UPPER MESSINIA CLOSED HYDROGEOLOGICAL BASIN (SW PELOPONNESUS, GREECE)

I. Mariolakos and E. Spyridonos

National and Kapodistrian University of Athens, Faculty of Geology and Geoenvironmetn, Department of Dynamic Tectonic & Applied Geology, GR-15784 Panepstimioupolis Zografou, Athens - Greece, mariolakos@geol.uoa.gr, vangelis@zedat.fu-berlin.de

Abstract

The Upper Messinia Basin is part of the Kalamata - Kyparissia graben structure, defined by two fault zones, one of E-W direction to the north and one of N-S direction to the east. The Tripolis and the Pindos alpidic units build up the basement of the region, and are covered by post-alpidic Pleistocene and quaternary deposits. The Basin is a closed hydrogeological system. In the upper cretaceous Pindos limestones, we observe two different karst types, according to drilling results. In the western part of the basin, where the limestones appear on the surface, the merokarst type is observed and water flow is limited in separated karstic conduits. On the contrary, in the central part of the basin, where the limestones underlie the clastic post-alpidic formations, the holokarst type is observed and a rich karstic aquifer is developed. This is explained by the closed hydraulic conditions. In the western part of the basin the karstic aquifer is unconfined, while in the central part it is confined, due to the overlying impermeable post-alpidic sediments and the overall closure of underground flow to the south. It appears that the confined conditions led to the development from merokarst to holokarst in this region.

Key words: closed hydrogeological system, aquifers under pressure, karst types, merokarst, holokarst, Upper Messinia Basin, Peloponnesus, Southern Greece.

1. Introduction

The Upper Messinia basin is located in the SW part of Peloponnesus, 20 km NNW of the city of Kalamata (Fig. 1). It covers an area of ~295 km². The basin forms a closed hydrogeological system, as described by Mariolakos, 1988. The aim of this work is to describe the karstification types of the carbonate rocks that build the basement of the basin and investigate the interaction of neotectonics, hydrogeological conditions and karstification type.

2. Geological setting

The Messinia region, on SW Peloponnesus, is one of the most active areas in the Hellenic Arc, as it lies about 60 km from the Ionian trench, where the collision between the African and Eurasian plate occurs. By the end of the thrust movements (Middle Miocene), the largest part of the area is land and the morphogenic procedures begin. During Early-Pleistocene, when the sea transgression reaches its biggest extent, from the geotectonic point of view, the mountains of Kyparissia and Pylos belong to
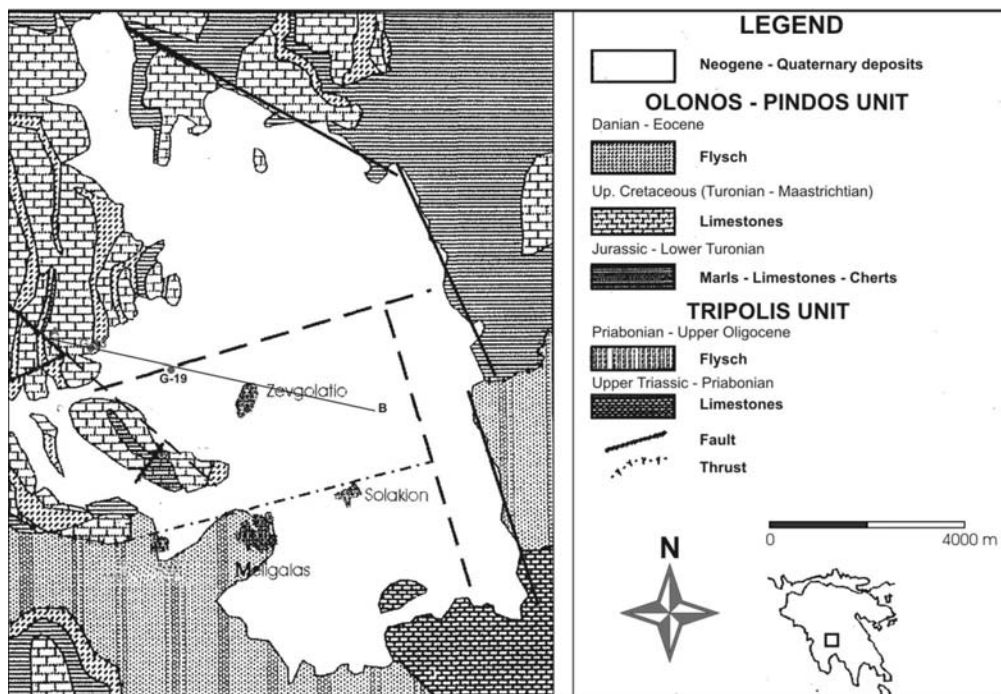
Fig. 1: Study Area position and simplified geological map (modified after Mariolakos, 1988).

the island arc (Marcopoulou - Diacantoni et al., 1989, 1991). By the end of Early-Pleistocene the area starts uplifting again. The Upper Messinian Basin remains land during this evolution, building a palaeo-isthmus between the Basins of Lower Messinia to the south and Kyparissia to the west. The post alpine deposits outcropping in the wider area can be distinguished into marine and terrestrial formations. The marine deposits occur only in the Kyparissia - Kalo Nero graben and consist of marls, sandstones and conglomerates of Late Pliocene – Lower Pliocene and Early Pleistocene age (Fountoulis, 1994). The terrestrial deposits mainly represent red-colored siliceous sands and conglomerates alternating with clay occurring in all basins.

The Neotectonic structure of the greater area of SW Peloponnesus is characterised by the presence of tectonic grabens and tectonic horsts (1st order structures) striking NNW-SSE and E-W (Mariolakos et ál. 1987). The Kalamata - Kyparissia graben is such a 1st order neotectonic macro-structure. At the margins or inside the 1st order neotectonic macrostructures, neotectonic structures of minor order (2nd, 3rd, ...) exist, the strike of which is perpendicular or parallel to the trends of the 1st order ones (Mariolakos et al., 1989).

The 2nd order neotectonic macro-structures inside the major Kalamata - Kyparissia graben are the Lower Messinia graben, the Meligalas horst, the Upper Messinia basin, the Dorion basin and the Kyparissia - Kalo Nero graben (Fig. 2).

The kinematic evolution of these neotectonic units is complicated since block rotation differentiates the uplift and subsidence rates throughout the margins of the neotectonic blocks. The neotectonic
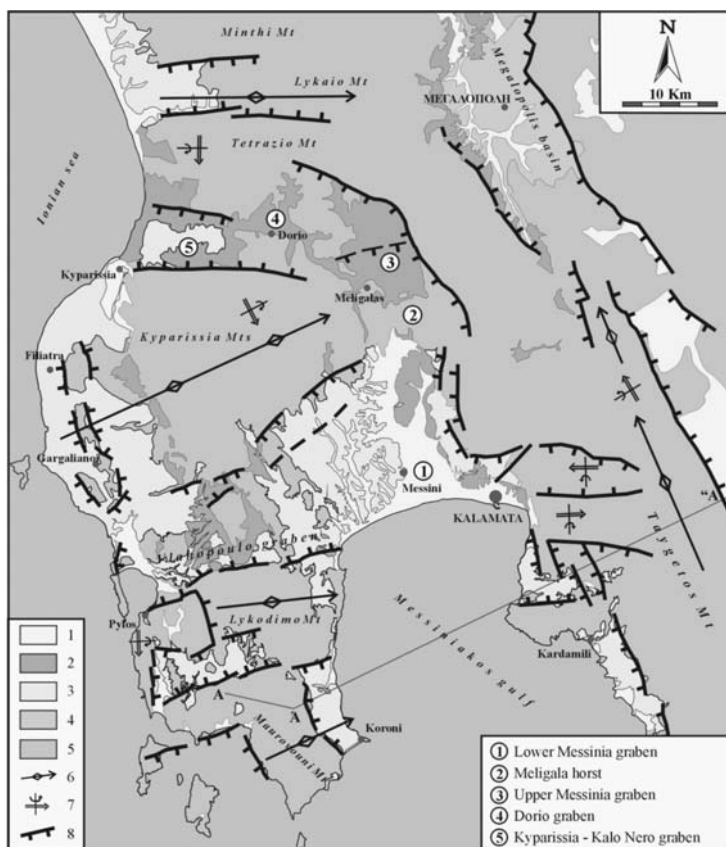
Fig. 2: Tectonic sketch map showing the neotectonic macrostructures of SW Peloponnesus. 1:Holocene deposits, 2:Terrestrial deposits, 3:Marine deposits, 4:Lacustrine deposits (Megalopolis basin), 5:Pre-Neogene basement, 6:macrofold axis, 7:Rotational axis, 8:Fault zones. (from Mariolakos et al., 2001).

structures of minor order are dynamically related, as they have resulted from the same stress field but they have a different kinematic evolution. This differentiation has initiated either during the first stages of their creation, or later, during their evolution (Mariolakos et al., 1995).

The Upper Messinia basin basement consists of two alpidic geotectonic units, the Tripolis unit and the Olonos – Pindos unit (Lalechos, 1974, Katsikatsos, 1980 and Mariolakos, 1988). The central part of the basin is covered by post alpidic sediments of pleiocene to quaternary age, positioned discordant on the alpidic basement. The thickness of these sediments is large related to the basin extend and in the central part it exceeds 280 m (Fig. 3) (Mariolakos, 1988).

On the western boundary of the basin the sediments are deposited unconformably on the Pindos unit rocks, mainly on radiolarites, Upper Cretaceous limestones and flysch. On the northern and the eastern part, the sediments are in tecnical contact to the alpidic formations, as a result of the action of the boundary fault zone of the Kalamata – Kyparissia Graben.

To the south, the post alpidic sediments cover the Tripolis unit flysch and to the southeast the Tripolis limestones. To the southwest the basin is connected by a narrow plain zone, covered by post-alpidic sediments of small thickness, to the Dorion - Kopanaki basin.
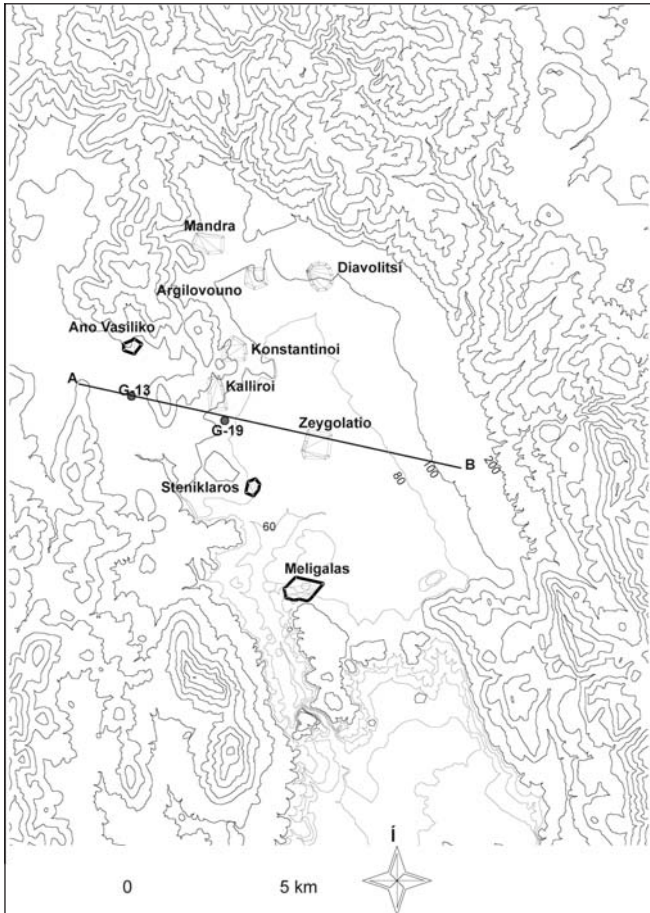
Fig. 3: Topographical map of the Upper Messinian Basin.

While the highest elevation to the East and North of the basin, on the water divide reaches1080 & 1040 m, the central part of the basin, covered by post alpidic formations, has an average elevation of 80 m. The post-alpidic sediments extend over 81 km^2 and can be divided in two geomorphologic regions. To the northern and eastern boundary of the basin alluvial cones prevail with higher topographical slope and consisting of coarse grained material. The central part of the basin is flat and covered by fine grained sand and clay material of small thickness. The deeper sediment horizons consist of more coarse grained material. At a depth of 25 – to 40 m, a clay horizon exists with thickness of about 5 to 20 m.

3. Hydrogeological conditions

3.1 Surface aquifers

Two aquifers are present in the post alpidic sediments, a phreatic aquifer in the upper sediments and a second one, under pressure, below the clay horizon at the depth of 25 to 40 m. The clay horizon serves both as the base of the phreatic aquifer and the overlying confining unit of the deeper aquifer. The main inflow to these aquifers comes from the large karstic aquifers in th Tripolis limestones on the eastern boundary of the basin (Mariolakos, 1988, Spyridonos, 1994).
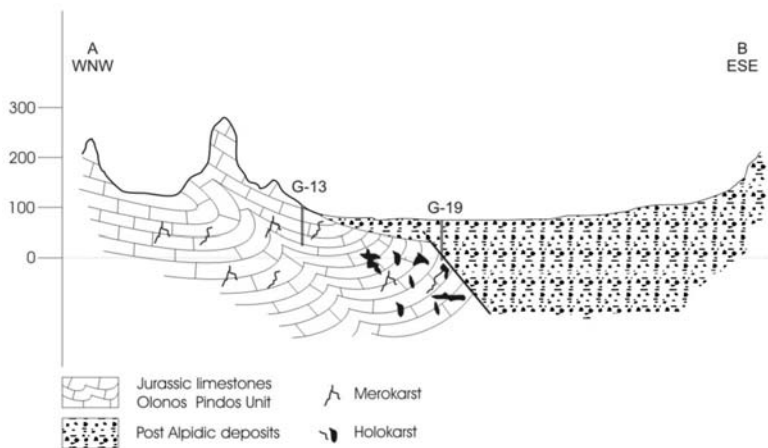
Fig. 4: Geological sketch A-B (Distance A-B 12km, elevation scale 10X exaggerated).

3.2 Deeper aquifers

The main aquifers in the area are located in the karstified carbonate formations of the Tripolis unit. The upper Cretaceous limestones at the southeastern part of the basin are part of the limestone mass that reaches northern of the city of Kalamata. In the deeper part of these limestones a large karstic aquifer is developed, which feeds the karstic springs at Pidima and Ag. Floros, on the eastern boundary of the Lower Messinia basin, southern to the study area.

The upper cretaceous limestones of the Pindos unit appear on the surface on the western part of the basin. Small temporary springs are located on the western boundary of the basin. Drilling results indicate that groundwater flow in these limestones appears in separated karstic conduits. On the contrary, under the plain part of the basin (between Mandra-Argilovouno-Zeygolatio-Kalliroi and Konstntinoi), where these limestones underlie the alpidic sediments, a large karstic aquifer is present.

3.3 Morphotectonic characteristics of the basin affecting groundwater flow

The geometrical characteristics of the basin, as a result of the neotectonic activity, are an important factor affecting groundwater flow. The northern and eastern boundaries of the basin are the fault zones that formed the Kalamata – Kyparissia Graben. To the south the basin is bounded by the Meligalas horst (Tripolis flysch). To the west the basin is bounded by the Olonos – Pindos flysch and the limestones (fig. 2).

Groundwater flows from the east through the fault zones into the sediments filling the basin, but out flow to the south is hindered by the flysch and the Pindos zone formations. So the ground water is trapped in the sediments and the only way for outflow is surficial flow, a fact that often leads to flooding of the plain region around Meligalas in the spring (Mariolakos, 1988, Spyridonos, 1994).

4. Karst description

Karstification in the Tripolis unit limestones shows all the characteristics of the holocarst type (after Cvijič, 1926): that is development of all karstic forms, in the surface as well as in depth. This explains the large water potential of the aquifers in these formations.

The limestones of the Olonos – Pindos unit appear on the northern and the western part of the basin. The karst developed in these limestones is of the merokarst type (Cvijič, 1926): that is not fully developed karst, due to preferential groundwater flow, resulting in fewer and isolated karstic conduits. This karst type develops usually in limestones with marly content or with impermeable intercalations. This kind of karstification explains the small temporary springs on the western boundary of the basin. Wells drilled in these region yielded little amounts of water, even if drilled near to springs, a fact that supports the existence of isolated conduits.

The same limestones show a different grade of karst development in the region under the post-alpidic sediments. There the karst characteristics are of the holokarst type, and the yield of wells in this region was between 120 and 200 m³/h.

This situation is clearly demonstrated in the geological section of Fig. 4: Drillhole G-13 is located less than 1 km behind the Ano Vasiliko spring and it drilled the napped Upper Cretaceous limestones of the Pindos Unit. It yielded a small amount of water, indicating that no large water reservoir is developed in the limestones and the spring is fed by linear flow through separated karstic conduits. On the contrary, drillhole G-19 drilled the same limestones under the post alpidic sediments, and met a rich aquifer developed in this formation. Pumping of this drillhole influences the Steniklaros spring, which is more than 2 km away, confirming the existence of a karstic aquifer of the holokarst type.

5. Conclusions - Results

The main aquifers of the region are located in the karstified limestones of the Tripolis and the Olonos - Pindos units.

The karstification of the Tripolis limestones is of the holokarst type, resulting in an aquifer system of large dimensions and potential, extending in the Taygetos mountain mass to the east of the study area. This aquifer system feeds the large springs of Ag. Floros and Pidima and also feeds the aquifers in the post-alpidic sediments filling the Upper Messinia basin.

The Olonos – Pindos limestones show two types of karstification. In the regions where they appear on the surface, the karstification is of the merokarst type, resulting in smaller isolated aquifers and temporary springs. On the contrary, the limestones of the same unit underlying the post-alpidic sediments are fully karstified and hosting an aquifer of large potential.

This differentiation can be explained by the hydrogeological conditions of the basin. The post alpidic sediments, especially the clay horizon, serve as a confining layer for the underlying aquifer, causing artesian conditions. This aquifer is also fed by the Tripolis limestones to the east. This results in lower flow velocities in the limestones under the sediments compared to the limestones exposed at the surface. Also, water under pressure can dissolve more CO_2 and therefore hold more $CaCO_3$ in solution, a fact that also helps karst evolution.

6. References

Cvijič J. (1926). Das Karstphänomen, *Pencks geograph., Wien, Abh. 5,3*, 279p.

Fountoulis, I., (1994). Neotectonic evolution of Central-West Peloponnesus. Phd Theses, National and Kapodistrian University of Athens, Faculty of Geology and Geoenvironment, GAIA 7, 386 p.p. (in Greek with English abstract).

Katsikatsos, G. (1980). Geological Study of the Vasiliko – Ithomi region, Messinia. I.G.M.E., *Geologi-*

cal and Geophysical Studies, v. XXI, Nr. 1, 176 p, 12 plates, Athens (in Greek).

Lalechos, N. (1974). Geological Structure of Central-Western Peloponnesus. I.G.M.E., *Geological recognisions, Nr. 53*, 94 p., 17 plates, Athens (in Greek).

Marcopoulou-Diacantoni, A., Mirkou, M.-A., Mariolakos, I., Fountoulis, I. (1991). Stratigraphic and paleogeograph.ic observations at the post-alpine sediments of the Filiatra area (SW Peloponnesus, Greece), and their neotectonic interpretation. - *Bull. Gr. Geol. Soc., v. XXV/2*, p. 593-608, Thessaloniki, (in Greek).

Marcopoulou-Diacantoni, A., Mirkou, M-R., Mariolakos, I., Logos, E., Lozios, S., Fountoulis, I. (1989). Stratigraphic observations at the post-alpine of the Thouria-Ano Amphia (SW Peloponnesus, Greece), and their neotectonic interpretation. - *Bυll. Geol. Soc. Greece*, ν. XXIII/3, ϱ. 275-295, Athens, (in Greek).

Mariolakos, I. (1988). The application of the Darcy's Law in closed geomorphological and hydrogeological systems, Example: the basin of Ano Messinia (SW Peloponnisos). In: *Proceedings of the 3ʳᵈ Congress of the Geol. Soc. of Greece, Bull. Gr. Geol. Soc.,v. XX/3*, 77-96, Athens (in Greek).

Mariolakos, I., Sabot, V., Alexopoulos, A., Danamos, G., Lekkas, E., Logos, E., Lozios, S., Mertzanis, A., Fountoulis, I. (1987). Microzonic study of Kalamata (SW Peloponnesus, Greece), (Geomorphology, Geology, Neotectonics). - Earth Planning Protection Organization, Report, 110ϱ., Athens, (in Greek).

Mariolakos, I., Fountoulis, I., Logos, E., Lozios, S. (1989). Surface faulting caused by the Kalamata (Greece) earthquakes (13-9-1986). - *Tectonophysics, 163,* p. 197-203.

Mariolakos, I., Fountoulis, I., Marcopoulou-Diacantoni, A., Mirkou, M.-R. (1994). Some remarks oη the cinematic evolution of Messinia province (SW Peloponnesus, Greece) during the Pleistocene, based oη neotectonic, stratigraphic and paleoecological observations. *Munster. Forsch. Geol. Palaont.* 76, ϱ. 371-380, Münster.

Mariolakos I., Lozios S. And Logos E. (1995). The neotectonic macrostructure of southern Peloponnesus. The earthquakes of September 13, 1986. Seminar on active faults, XV Congress of the Carpatho-Balcan Geological Association, 51-60, Athens.

Mariolakos, I., Fountoulis, I. & Ladas, I. (2001). The paleogeographic evolution of SW Peloponnese during Quaternary period. In: *Proceedings of the 9th Congress Geol. Soc. Greece, Bull. Geol. Soc. Greece, v. XXXIV/1* pp. 37-45, (In Greek with English abstract).

Spyridonos, E., (1994). Simulation of the phreatic aquifer of the Ano Messini basin (SW Peloponnesus) using mathematical modeling. In: *Proceedings of the 7th Congress of the Geol. Soc. of Greece, Bull. Gr. Geol. Soc., XXX/4*, pp. 275-283, Thessaloniki (in Greek).

USE OF STABLE ISOTOPES IN THE DETERMINATION OF THE MEAN ALTITUDE OF RECHARGE AND THE INVESTIGATION OF FUNCTION MECHANISM OF SPRING WATERS IN ARGOLIS PENINSULA (GREECE)

Matiatos I.[1], Alexopoulos A.[1], and Zouridakis N.[2]

[1] *University of Athens, Faculty of Geology and Geoenvironment, 15784 Athens, Greece,*
imatiatos@geol.uoa.gr, aalexopoulos@geol.uoa.gr

[2] *NCSR Demokritos, Isotope Hydrology Laboratory, Aghia Paraskevi, 15310 Athens, Greece,*
nizouri@chem.demokritos.gr

Abstract

In the present study, the isotopic composition ($\delta^{18}O$) of several spring waters in Argolis peninsula is examined. The use of the specific isotope aimed at the determination of the altitude of recharge areas, while the credibility of the extracted results was verified by in situ geological observations. The applied methodology included the construction of a linear diagram which correlates the stable isotopic values ($\delta^{18}O$) in meteoric waters and the altitude. Isotopic data, concerning meteoric waters, came from: a) rain gauge stations of GNIP network (IAEA/WMO), b) rain tanks and selected wells located in Mt. Arachnaio, c) improvised rain collectors which were put in several sites in the peninsula. A decrease of 0.45‰ $\delta^{18}O$ per 100m altitude was determined. The average isotopic composition of the examined springs, as far as $\delta^{18}O$ is concerned, resulted from 14 sampling periods between October 2005 and March 2008. This ^{18}O-content of spring waters was used to derive the recharge area and consequently to evaluate the mechanism of water renewal.

Key Words: *hydrogeology, stable isotopes, Argolis peninsula, mean altitude of recharge.*

1. Introduction

Isotopes which are naturally produced and incorporated into the hydrological cycle are often referred to as "Environmental Isotopes". The methodologies that were based on naturally occurring isotopes (stable and radioactive) were used for various hydrogeolecal problems encountered in water resources assessment which led to the establishment of a scientific field known as "Isotope Hydrology".

In particular, stable isotopes, such as Oxygen-18 can have several applications in hydrogeology (Schiavo et al., 2009; Bono et al., 2007; Trabelsi et al., 2007; Boronina et al., 2005; Majumdar et al., 2005; D' Alessandro et al., 2004; Yurtsever & Araguas, 1993) such as:

— The determination of groundwater system boundaries.

— The identification of hydraulic connections between an aquifer and surface waters or between different aquifer units.

— The study of origin (genesis) of water and the delineation of processes involved (process tracing)

during flow and circulation of water.

— The determination of the source(s), the processes and the rate of replenishment in groundwater systems.
— The evaluation of the dynamics of geothermal systems.
— The identification of the source(s) and the mechanisms of salinization in coastal aquifers.

The contribution of stable isotopes in the investigation of groundwater movement is based on the isotopic content of atmospheric waters, because the major changes in the isotopic composition of natural waters occur in the atmospheric part of the water cycle (Yurtsever & Gat, 1981). Therefore, the subsurface waters "inherit" the isotopic characteristics of the meteoric water inputs and further change a little, except as a result of mixing with waters of a different origin and composition. From this point of view, stable isotopes can work as ideal tracers. Among the factors that affect the isotopic composition of atmospheric waters and subsequently groundwater is the altitude (Sharp, 2007; Clark & Fritz, 1997). This parameter, known as "altitude effect", is significantly useful in hydrogeology because it gives us the opportunity, on one hand, to distinguish the groundwater coming from small or high altitudes and on the other hand to determine the mean altitude of recharge (Tazioli, 2007).

2. Geological setting

The geological status in Argolis peninsula differs notably in comparison to the rest of the Peloponnese, because it consists of a wide variety of geological formations which, as far as the facies is concerned, are similar to those of several stratigraphic units. Moreover, the sudden change of lithology is attributed either to tectonics or a rough transition of statigraphy. In addition, the substantial lithological heterogeneity in horizontal and vertical direction leads to the appearance of many individual springs mostly of small capacity.

According to Bortolloti et al. (2002a, 2003), the geological setting of the study area comprises of (Fig.1):

— Neritic limestones of Trapezona, which become pelagic with cherts in places, while in the upper parts they are covered by coarse-grained carbonate and ophiolitic breccias (Baumgartner, 1985). In the lower parts, volcanic formations were identified at many sites (Renz, 1906b, Gaitanakis & Photiades, 1991).
— An ophiolitic mélange consisting of pillow lavas and dolerites and locally of cherts, siltstones, serpentinised mafic and ultramafic rocks.
— A tectonic mélange characterized mainly by the presence of silts, sandtones and marls which occupies the largest part of Adheres mountain ridge. In this matrix, big turbiditic rocks of different lithology such as volcanic rocks, radiolarites, limestones, granodiorites (Photiades & Keay, 2000), pyroclastic rocks, andesites, dolomites (Aranitis, 1963), quartz sandstones, serpentinites and basalts (Clift & Robertson, 1989) are present.
— A "post-Ypresian" flysch which represents alterations of calcareous schists, marls, sandy marls, sandstones, conglomerates and limestones and covers mainly the Nafplio-Lygourio basin (Baumgartner, 1985; Kantas, 1991).
— Neritic limestones which successively become pelagic in the upper parts followed by marls and flysch ("Akros formation", according to Decrouez, 1975). At the bottom of the formation, a tectonic mélange (Iliokastron area) of "sheared" serpentinites and clastic slices of several rocks such as dunits, basalts, cherts and limestones (Gaitanakis & Photiades, 1993, Photiades & Economou,
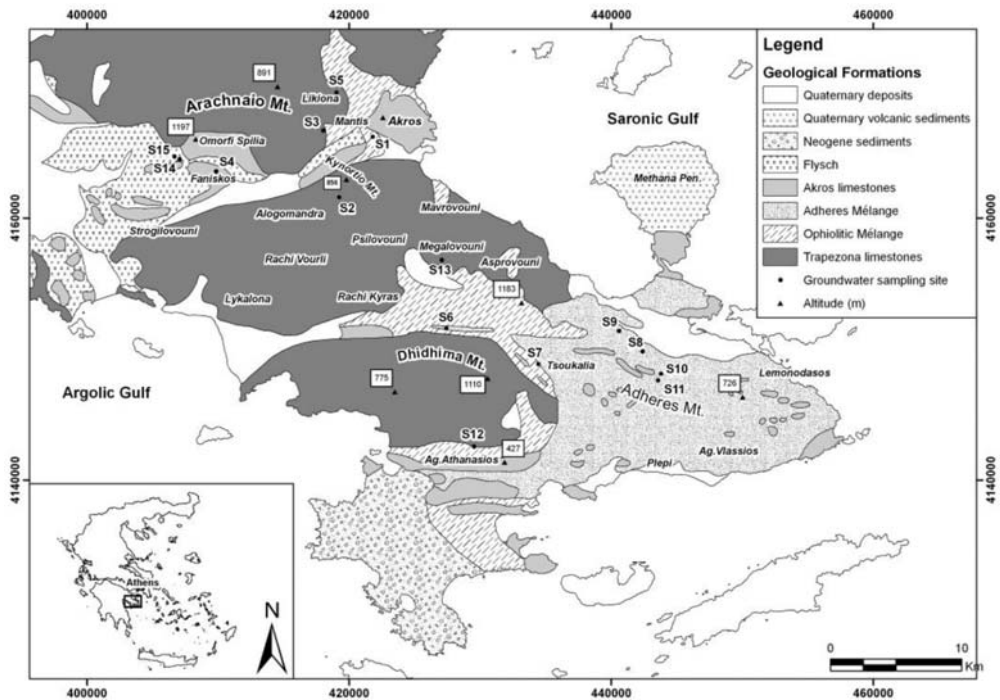
Fig. 1: A simplified geological map of the study area (modified after Clift & Dixon, 1998) and the location of the groundwater sampling sites.

1991) is present.

— Neogene deposits of Miocene – Pliocene age occupying the Porto Cheli-Kranidi geological trough, in the southwestern part of the peninsula (Gaitanakis & Photiades, 2007). The sequence includes calcareous marls, marly limestones and conglomerates with sandstones intercalations. The pebbles of the conglomerates which origin from the weathering of sandstones, limestones and parts of the ophiolitic mélange are lying inside a calcareous sandstone matrix.

— A quaternary volcanic formation consisting of loose volcanic sediments with tuff blocks and dacide and andesite domes (Fytikas, 1980), covering almost the entire Methana peninsula.

— Recent deposits comprising of alluvial fans, debris cones and loose sediments of silts, sands and pebbles.

3. Methods

3.1 General

The orography represents a substantial factor in the rise and the adiabatic freezing of water vapors, which induces the occurrence of precipitation events. At higher altitudes, where the temperature is decreasing, the rain is expected to be more depleted in heavy isotopes and therefore the values of $\delta^{18}O$ will be more negative (Clark & Fritz, 1997). In the area under study, the altitude effect of the precipitation on isotopic composition has been obtained by using data coming from: a) four rain gauge stations (Thission, Patras, Pendeli and Hellinikon) from the Global Network of Isotopes in Precipitation (G.N.I.P.) constructed by the International Atomic Energy Agency (I.A.E.A.) in coopera-
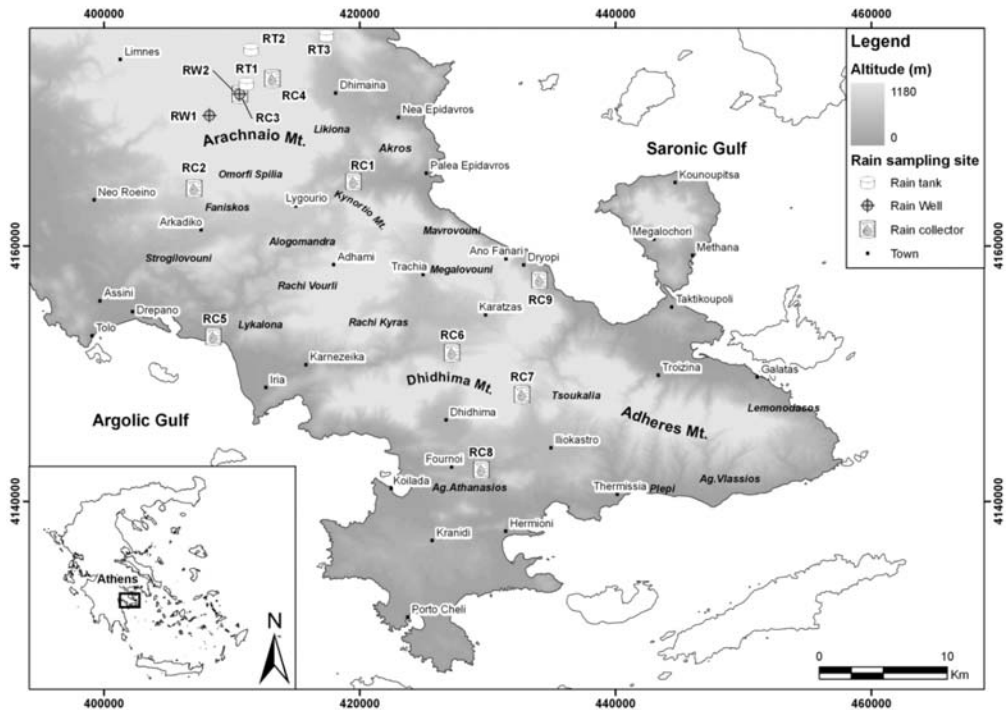
Fig. 2: Topographic map of the study area and the location of rain sampling sites.

tion with World Meteorological Organization (W.M.O.), b) three rain tanks (sites: RT1, RT2 and RT3, and selected wells (sites: RW1 and RW2) in Mt. Arachnaio, c) nine improvised rain collectors (sites: RC1-RC9) (Fig.2). In order to evaluate their mean altitude of recharge, fifteen groundwater sites (springs) in the peninsula were repeatedly sampled during the period between October 2005 and March 2008 (Fig.1).

The sampling from the rain tanks, the wells and the springs was carried out on a monthly basis, and the samples were collected in 20ml polyethylene containers which were firstly rinsed in clear water several times and then filled to the top to minimize air entrapment. At the same time, these specific bottles contained a special membrane which halters the occurrence of evaporation phenomena. After the samples were tightly sealed, they were stored in a portable fridge until they were transported to the laboratory for the isotopic analyses.

In order to obtain supplemental information concerning the isotopic signature of meteoric waters in the region, we constructed nine rain collectors according to the instructions given by the I.A.E.A. In particular, we used 5-litre polyethylene vessels with a funnel adapted to each sample container, so as to increase the gathering area of the rain water. Moreover, we put medical paraffin oil in every vessel, in order to avoid evaporation until the samples were collected. The medical paraffin oil layer floating over the water had a thickness of about 0.5cm. The sampling of the rain collectors was performed on a monthly basis and the rain water was transferred in similar to the aforementioned 20ml polyethylene bottles, which were then transported to the laboratory.

The stable isotope ratios ($^{18}O/^{16}O$) were measured at the Isotope Hydrology Laboratory of N.C.S.R. "Demokritos", Athens, Greece. The $^{18}O/^{16}O$ ratios were defined with the help of an Isotope Ratio

Table 1. Mean isotopic composition of rain water according to the gauge stations from the GNIP network (IAEA/WMO).

Station	X	Y	$\delta^{18}O$ (‰)	Altitude (m)
Hellinikon	476113.6	4194466.6	-5.80	27
Patras	306546.9	4238905.0	-5.21	100
Thission	475257.7	4202235.8	-6.13	107
Pendeli	488152.7	4211083.5	-7.72	498

Table 2. Mean isotopic data of rain water obtained by the rain tanks (RT) and the wells (RW) located in the highlands of Mt. Arachnaio. The sampling period is between October 2005 and March 2008.

Site	X	Y	$\delta^{18}O$ (‰)	Altitude (m)
RT1	411147.0	4172668.0	-7.22	798
RT2	411499.0	4175356.0	-6.33	687
RT3	417381.0	4176467.0	-5.23	370
RW1	408243.0	4170203.0	-6.66	641
RW2	410616.0	4171869.0	-6.94	712

Mass Spectrometer (SIRA Series II) (CO_2 equilibrated) and then were expressed in δ ‰, i.e. per mille deviation vs. the reference V-SMOW. The measurements standard uncertainties are 0.1 ‰ for $\delta^{18}O$. The validity of the results was obtained by the repetition of the measurements and their comparison with respective isotopic analyses carried out in foreign laboratories (i.e. Environmental Isotope Laboratory-University of Arizona-USA) to which several samples were sent.

3.2 Data analysis

The applied methodology aimed, initially, at the construction of a line which represents the relation between the isotopic content ($\delta^{18}O$) of precipitation and the altitude at the collection site, for each of the three sampling groups (GNIP network, rain tanks and wells, rain collectors). All the imported data concerned long-term mean values of $\delta^{18}O$, while at the second stage of the processing, we were able to derive from the three lines an average rate of isotopic depletion with altitude.

The selection of the specific stations (Hellinikon, Patras, Thission, Pendeli) from GNIP network (Table 1) was based on the fact that they showed the longest and most complete time series from all the available stations, while at the same time they are located closer to the study area. The long term mean $\delta^{18}O$ values of Hellinikon, Patras and Thission stations resulted from monthly measurements, while those of Pendeli station from rainfall event measurements. Moreover, for the mean isotopic concentration of Pendeli station we included the $\delta^{18}O$ values given by Argiriou & Lykoudis (2006), for the same station and for the period 2000-2003.

The data obtained from the rain tanks have the advantage that they represent long-term mean values, because the rain water is gathered in them during the whole year. The two wells, that were included in this sampling group, are located in the same area with the rain tanks (Table 2). The selection of the two wells was based on the fact that the collected water comes from the immediate storage of the meteoric water. The in situ hydrogeological observations along with the measured electrical con-

Table 3. Mean isotopic composition of rain water based on rain collectors (RC) located throughout the Argolis peninsula. The sampling period is between October 2006 and April 2007.

Rain Collector	X	Y	$\delta^{18}O$ (‰)	Altitude (m)
RC1	419512.0	4165023.2	-4.88	132
RC2	407049.7	4164484.1	-6.13	413
RC3	410622.8	4171866.4	-6.87	716
RC4	413167.8	4173089.5	-6.86	820
RC5	408549.0	4152884.7	-4.03	18
RC6	427198.6	4151617.2	-6.32	300
RC7	432677.1	4148344.2	-6.10	490
RC8	429510.7	4142465.8	-4.43	127
RC9	434053.7	4157307.5	-5.14	175

ductivity of the water verified that the groundwater in the aquifer originates as local recharge. In particular, the wells are constructed in a terra rossa plain with no lithological alterations which resulted by the weathering of the carbonate formations covering Mt. Arachnaio. In addition, their depth is small, and the electrical conductivity of the gathered water does not exceed 100μS/cm, just like the water in the rain tanks. Similar electrical conductivity values are mentioned by Nastos et al. (2007) in rain water samples collected at several locations across Greece.

As far as the nine rain collectors are concerned, the mean values of $\delta^{18}O$ came from data recorded on a monthly basis during the period between October 2006 and April 2007 (Table 3). The installation of the rain collectors was based on several criteria such as the different elevations, the best spatial allocation and the collection of rain water which falls on recharge areas of some of the groundwater sampling sites.

The average $\delta^{18}O$ content in precipitation is plotted against the altitude for each data group in Fig.3. The three dashed lines were determined by the method of least squares and gave a similar rate of $\delta^{18}O$ depletion with altitude. From these lines we extracted the regression line AB which defines the overall relation of the two parameters and whose slope led to the determination of an average rate of -0.45‰ $\delta^{18}O$ / 100m. This value places among the ranges of –0.15‰ and –0.50‰ (Clark & Fritz, 1997) and –0.10‰ ως –0.60‰ (Mook, 2005) per 100-m rise in altitude given for the most parts around the world.

It should be mentioned that the calculated ratio is approximately given, so the more data concerning meteoric waters, is added the more reliable the result will be. Scientific studies have proven that the rate of depletion of $\delta^{18}O$/100m can also vary on a seasonal basis, as the isotopic content is related to the origin of air masses that affect the area as well as to the sampling period (Bortolami et al. 1979, Payne & Yurtsever 1974).

In order to estimate the mean altitude of recharge of the springs, we plotted on a $\delta^{18}O$ versus altitude diagram the line AB which represents the average rate of depletion, together with the groundwater sampling points. The pair of values for the latter concerned their long-term mean isotopic content of $\delta^{18}O$ and the elevation at the site of the sampling (Fig.4).

From the relation developed and illustrated in Fig.4, we observe that the majority of the groundwa-
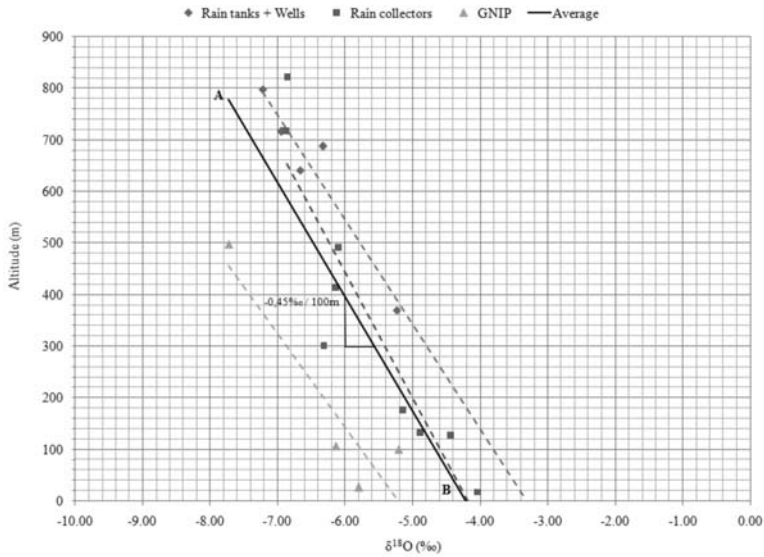
Fig. 3: Diagram of mean δ¹⁸O values in rain water versus elevation at the collection site derived from the three sampling groups.
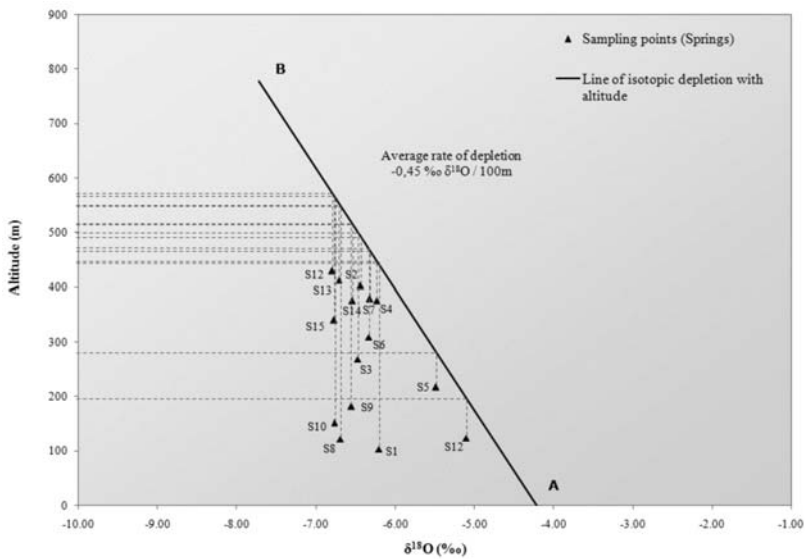
Fig. 4: Diagram of mean δ¹⁸O values in groundwater samples versus the altitude. A decrease of 0.45‰ δ¹⁸O per 100m altitude is typical for the study area.

ter samples are located beneath the line AB, which means that their mean altitude of recharge is most likely to be higher than the altitude at the sampling site. The points that are very close to the line show that the mean altitude of the intake area is almost the same with the elevation of sampling, which means that the replenishment of these springs probably takes place locally. On the contrary, the springs plotted very far from the line underline that they are mainly recharged from much higher altitudes than the one of the sampling site.

Table 4. Mean altitude of recharge (m) of the groundwater sampling sites (springs) as it derived from the linear diagram of Figure 4.

Sampling site	$\delta^{18}O$ (‰)	Mean altitude of recharge (m)	Sampling site	$\delta^{18}O$ (‰)	Mean altitude of recharge (m)
S1	-6.21	442	S9	-6.56	519
S2	-6.44	493	S10	-6.77	566
S3	-6.47	500	S11	-5.10	567
S4	-6.23	447	S12	-6.80	198
S5	-5.48	282	S13	-6.71	573
S6	-6.34	471	S14	-6.54	553
S7	-6.32	467	S15	-6.77	516
S8	-6.69	549			

As it is depicted in the diagram above, in order to calculate the mean altitude of recharge of the studied springs, we drew from each point a line parallel to the altitude axis until it intersects with the line AB. From the intersection point we drew a second line parallel to $\delta^{18}O$ axis until it touches the altitude axis. The derived value corresponds to the mean altitude of recharge of the sampling point. All the results of the aforementioned procedure are given in Table 4.

4. Conclusions-Results

The extracted mean altitude of the intake area of the springs under study, as it was defined with the help of oxygen isotope ratios, is in agreement with real topographic, geological and hydrogeological setting, according to in situ observations. In particular, spring S1 is mainly replenished by Mantis area (450m), part of the southwestern edges of Akros Mountain, while spring S2 is recharged by the southwestern part of Kynortio Mountain (500m) located very close to the ancient theatre of Epidaurus. Moreover, the water in spring S3 origins from the southeastern edges of Arachnaio Mountain (500m), in spring S4 from the eastern side of Faniskos mass (460m) and in spring S5 from the eastern verge of Arachnaio Mountain, from an area called Likiona (300m). Spring S6 recharges from the northern part of Dhidhima ridge (500m), spring S7 from the hilly area of Tsoukalia (480m), while springs S8, S9, S10 and S11 from independent aquifer units on Adheres mountain ridge (560m, 520m, 580m and 580m respectively). The water in spring S12 origins from the mountainous area of Ag. Athanasios (200m), in spring S13 from Megalovouni Mountain (580m) and in springs S14 and S15 from the southern part of Arachnaio Mountain and specifically from an area called Omorfi Spilia (560m and 520m respectively).

To sum up, the use of isotopic methods in hydrogeology contributes significantly to the solution of problems and the investigation of physical procedures that are difficult to confront with the conventional ways of study. In particular, the application depends primarily on the estimation of the isotopic content ($\delta^{18}O$) of meteoric waters of a certain geographic area and allows the determination of the mean altitude of recharge of groundwater reservoirs. However, the results should be verified by in situ geological observations. Therefore, even if the Argolis peninsula is a region which is not characterized by an intense relief, the application of stable isotopes methodology led to the identification of the areas that replenish a series of springs in the peninsula, which coincides absolutely with the geological explanation, as far as the function mechanism is concerned.

5. References

Aranitis, S., 1963. Die Entstehung der Eruptivgesteine yon Hermioni-Gebiet und die mit ihnen verbundenen Vererzung, *Ann. Geol. Pays Hell*. 14, 211-323.

Argiriou, A. A. & Lykoudis, S., 2006. Isotopic composition of precipitation in Greece, *Journal of Hydrology* 327, 486-495.

Baumgartner, P.O., 1985. Jurassic sedimentary evolution and nappe emplacement in the Argolis Peninsula (Peloponnesus, Greece), *Mém Soc. Helv. Sci. Nat*. 99,1-111.

Bono, P., Brun, C., Fiori, C., Gonfiantini, R. & Zucco, F., 2007. The use of oxygen and deuterium in the water dynamics assessment of two lakes in the volcanic structure of mount vulture, southern Italy, *Proceedings, Advances in Isotope Hydrology and its Role in Sustainable Water Resources Management (IHS—2007)*, Vienna, Austria, Vol. 2, pages: 165-173.

Boronina, A., Balderer, W., Renard, P., and Stichler, W., 2005. Study of stable isotopes in the Kouris catchment (Cyprus) for the description of the regional groundwater flow, *Journal of Hydrology* 308, 214-226.

Bortolami, G. C., Ricci, B., Susella, G. F. and Zuppi, G. M., 1979. Isotope hydrology of the Val Corsaglia, Maritime Alps, Piedmont, Italy, In *Isotope Hydrology 1978*, Vol. I., IAEA Symposium 228, June 1978, Neuherberg, Germany: 327-350.

Bortolotti, V., Carras, N., Chiari, M., Fazzuoli, M., Marcucci, M., Photiades, A. & Principi, G., 2002a. New geological observations and biostratigraphic data on the Argolis Peninsula: Palaeogeographic and geodynamic implications, *Ofioliti* 27 (1), 43-46.

Bortolotti, V., Carras, N., Chiari, M., Fazzuoli, M., Marcucci, M., Photiades, A. & Principi, G., 2003. The Argolis Peninsula in the palaeogeographic and geodynamic frame of the Hellenides, *Ofioliti* 28 (2), 79-94.

Clark, I. D. & Fritz, P., 1997. *Environmental Isotopes in Hydrogeology*, Lewis Publishers, New York, pp. 328.

Clift, P.D. & Robertson, H. F., 1989. Evidence of a late Mesozoic ocean basin and su bduction-accretion in the southern Greek Neo-Tethys, *Geology* 17, 559-563.

Clift, P.D. & Dixon, J. E., 1998. Jurassic ridge collapse, subduction initation and ophiolite obduction in the southern Greek Tethys, *Eclogae geol. Helv*. 91, 128-138.

D' Alessandro, W., Federico, C., Longo, M. & Parello, F., 2004. Oxygen isotope composition of natural waters in the Mt Etna area, *Journal of Hydrology* 296, 282-299.

Decrouez, D., 1975. Etude statigraphique et micropaleontologique du Cretace d' Argolide (Peloponnese, Grece), *These Univ. Geneve*, pp. 259.

Fytikas, M., Innocenti, F. & Mazzuoli, R., 1980. Methana sheet-Geological map in scale 1:500000, IGME, Greece.

Gaitanakis, P. & Photiades, A.D., 1991. Geological structure of SW Argolis (Peloponnesus, Greece), *Bull. Geol. Soc. Greece* 25 (1), 319-338.

Gaitanakis, P. & Photiades, A.D., 1993. New data on the geology of Southern Argolis (Peloponnesus, Greece), *Bull. Geol. Soc. Greece* 28 (1), 247-267.

Gaitanakis, P. & Photiades, A. D., 2007: Spetses sheet-Geological map in scale 1:50000, IGME, Greece.

Kantas, K., 1991. Hydrogeological explanation of salt-water intrusion in karstic aquifers in the NE Argolis limestones (Peloponnesus, Greece*), Bull. Geol. Soc. Greece* 25 (4), 183-201.

Majumdar, N., Majumdar, R.K., Mukherjee, A.L., Bhattacharya, S.K. & Jani, R.A., 2005. Seasonal variations in the isotopes of oxygen and hydrogen in geothermal waters from Bakreswar and Tantloi, Eastern India: implications for groundwater characterization, *Journal of Asian Earth Sciences* 25,

269-278.

Mook, W.G., 2005. *Introduction to Isotope Hydrology*, Taylor & Francis, 288p.

Nastos P.T., Alexakis, D., Kanellopoulou, H.A. & Kelepertsis, A.E., 2007. Chemical composition of wet deposition in a Mediterranean site Athens, Greece related to the origin of air masses, *J. Atm. Chem.* 58, 167-179.

Payne, B.R. & Yurtsever, Y., 1974. Environmental isotopes as a hydrogeological tool in Nicaragua. In *Isotope Techniques in Groundwater Hydrology 1974*, IAEA, Vienna, 1, 193-202.

Photiades, A.D. & Ecomomou, G. S., 1991. Alteration hydrothermale sous-marine des basaltes et des dolerites (facies zeolitique) de l' unite moyenne "volcanique" de l' Argolide septentrionale, (Peloponnese, Grece), *Bull. Geol. Soc. Greece* 25 (2), 301-319.

Photiades, A.D. & Keay S., 2000. Mid-Late Jurassic granodiorite basement in southern Argolis Peninsula (Greece): tectonostratigraphic implications. In Panayides, I., Xenophontos, C. and Malpas, J. (eds), 2000, *Proceedings of the Third International Conference on the Geology of the Eastern Mediterranean*, Geol. Surv. Dpt. Cyprus, 233-239.

Renz, C. 1906b. Trias und Jura in der Argolis, *Zeitschrifi der Deutschen Geologirchen Gesellenschaft* 58, 379-395.

Schiavo, M.A., Hauser, S., & Povine, P.P., 2009. Stable isotopes of water as a tool to study groundwater–seawater interactions in coastal south-eastern Sicily, *Journal of Hydrology* 364, 440-449.

Sharp, Z., 2007. *Stable Isotope Geochemistry*, Pearson Education, USA, pp. 344.

Tazioli, A., Mosca, M. & Tazioli, G. S., 2007. Location of recharge area of Gorgovivo spring, central Italy, *Proceedings, Advances in Isotope Hydrology and its Role in Sustainable Water Resources Management (IHS—2007)*, Vienna, Austria, Vol. 2, pages: 27-35.

Trabelsi, R., Charfi, S., Chkir, N., Abidi, B. & Zouari, K., 2007. Contribution of isotopic indicators to the assessment of groundwater mixture between Continental Intercalaire and Djeffara aquifers (Southeastern Tunisia), *Proceedings, Advances in Isotope Hydrology and its Role in Sustainable Water Resources Management (IHS—2007)*, Vienna, Austria, Vol. 2, pages: 9-17.

Yurtsever, Y. & Gat, J.R., 1981. Atmospheric waters. In Gat JR, Gonfiantini R. (eds) Stable Isotope Hydrology: Deuterium and oxygen-18 in the water cycle, *IAEA Tech Rep Ser* 210, 103–142.

Yurstever, Y. & Araguas Araguas, L., 1993. Environmental isotope applications in hydrology: an overview of the IAEA's activities, experiences, and prospects, *Tracers in Hydrology* (Proceedings of the Yokohama Symposium, July, 1993), IAHS Publ. no. 215.

IAEA: http://nds121.iaea.org/wiser.

IMAGING SEAWATER INTRUSION IN COASTAL ZONE OF KAVALA (N. GREECE) WITH ELECTRICAL RESISTIVITY TOMOGRAPHY

Mertzanides Y.[1], Economou N.[2], Hamdan H.[2], Vafidis A.[2]

[1] *Prefecture of Kavala,65110, Kavala - Greece, mertzan@gmail.com*

[2] *Lab. of Applied Geophysics, Tech. Univ. of Crete, 73100, Chania – Greece, vafidis@mred.tuc.gr*

Abstract

The needs for water supply in the western coastal zone of Kavala (N. Greece) have been rapidly increased during the last decades because of the high tourist and agricultural development. This resulted to a number of wells that drilled along the coastline. During summer period, when human and irrigation consumptions are maximized, phenomena of groundwater salinization are observed. Although restrictions to new drillings have been taken, salinization in some aquatic systems of the area tends to become a major environmental and economical issue. The only available information till now was a timeseries of groundwater electrical conductivity measurements, in some of the wells of the area. This information is useful but not adequate for the study of the salt intrusion mechanism. Geophysical investigation was carried out and electrical resistivity tomography (ERT) was chosen as the most appropriate technique for the case. The geophysical survey was set in a site between the coastline and an existing borehole. The 2D ERT profiles gave a clear image of geoelectrical heterogeneities, associated with seawater intrusion in the coastal aquifers, contributing to future measures towards a rational management of ground water resources in the area.

Key words: seawater intrusion, coastal aquifers, electrical resistivity tomography, underground water conductivity, Prefecture of Kavala – N. Greece.

1. Introduction

Salinization of coastal aquifers is a major environmental problem for arid and semiarid regions of the planet. Its cause mechanism is related to the disturbance of the equilibrium between fresh and seawater in coastal water aquifers. Under normal conditions, the flow of underground freshwater toward the sea, maintains the boundary "fresh-saline water" zone near the cost and far below land surface. Overexploitation of ground water resources, due to overpumping wells or decrease of precipitation, displaces the boundary zone towards the land (Fig. 1a and 1b). This causes degradation to underground water quality and may result to ground subsidence with subsequent damages to buildings and infrastructure works, salinization of fertile soils and extinguish of aquatic ecosystems. Its quick and acute reaction to short and long-term climatic changes, may finally lead to desertification. Concerning the increasingly concentration of global population in coastal areas, it is obvious that this environmental problem has also ecological, social, cultural, economical and political aspects (Lambrakis and Kalergis, 2001; Kallergis, 2002).
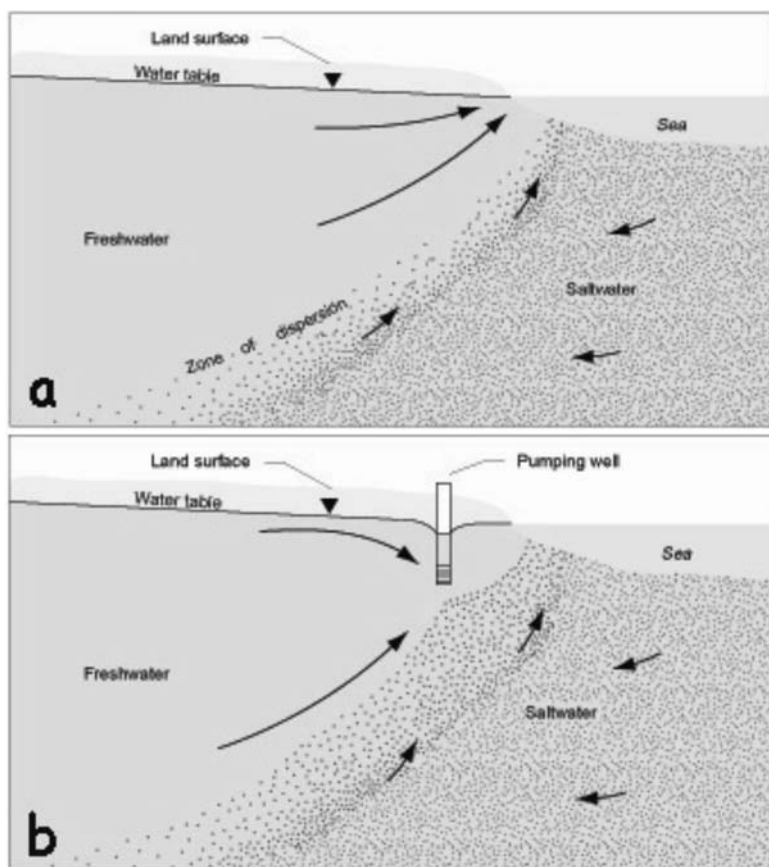
Fig. 1: Mechanism of salinization of coastal aquifers. a) The boundary fresh-saline water zone and b) Disturbance of this zone due to overpumping wells (From Barlow, P.M.; 2000; USGS Fact Sheet 085–00).

More or less common practices to reverse the seawater intrusion are (Bear et al., 1999; Ahlfeld and Mulligan, 2000; James et al., 2001; Ziegenbalg et al., 2002):

— Reduction of fresh water recovery.

— Relocation of coastal wells.

— Artificial surface recharge.

— Extraction of seawater before it reaches wells.

— Construction of impermeable subsurface barriers.

— Combination of the above.

A clear image of the extent and shape of saline water intrusion is the first step before planning any actions. At this step, geophysics appears to be an enlightening and reliable tool (Telford et al., 1990; Parasnis, 1997). Although geophysical survey is not new in ground water investigation, the advances in geophysical instrumentation and the development of sophisticated inverse algorithms, in the last two decades, made possible the fast acquisition and processing of large data sets (Kirsch, 2009). The result was quick information over large areas at a relatively in-

expensive cost, compared to other methods e.g. borehole drilling and trenching. The use of geophysical measurements was established for mapping subsurface features, estimating properties and monitoring processes important to hydrologic studies, such as those associated with water resources and gave birth to "Hydrogeophysics" as a unique subdiscipline (Rubin and Hubbard, 2005; Hubbard and Rubbin, 2006; Vereecken et al., 2006; Miller, 2009).

In seawater intrusion imaging, resistivity methods are the most preferable, because electrical resistivity is highly sensitive to subsurface water saturation and pore water salinity (Archie, 1942; Barker, 1990; Mualem and Friedman, 1991; Ewing and Hunt, 2006). Among them, the Electrical Resistivity Tomography (ERT) is considered as one the most efficient techniques in imaging such properties and processes associated to subsurface geoelectrical structure (Daily et al., 1992; Park, 1998; Muller et al., 2003; Singha and Gorelick, 2005; Mohnke et al., 2006; Nguyen et al., 2009). In order to eliminate limitations of resolution decrease with increasing depth of investigation, ERT techniques based on variations of borehole, surface-to-borehole and cross-hole measurements, have been proposed (Asch and Morrison, 1989; Daily and Owen, 1991; Slater et al., 2000; Zhou and Greenhalgh, 2000; Friedel et al., 2004; Marescot et al., 2002; Tsourlos et al., 2004, 2005; Wilkinson et al., 2008). Along with spatial, ways for time resolution extent with time-lapse techniques, have been reported to literature (Tsourlos et al., 2003, 2005; Oldenborger et al., 2007).

This paper presents a study on imaging seawater intrusion in western coastal zone of Kavala (N. Greece). The ERT measurements were carried out by Laboratory of Applied Geophysics / Technical University of Crete and Georesources S.A., as part of the project: "Integrated system for water quality management and olive trees optimization, using Geographical Information Systems in Prefecture of Kavala", supervised by Directorate of Land Reclamation and Directorate of Planning and Programming/Prefecture of Kavala and carried out from November 2007 to November 2008, with consortium of contractors: DRAXIS S.A.-I.M.C. S.A. The project was 80% co-founded by the European Regional Development Fund, under the Framework of the Operational Program: Information Society (IS), Priority Axe: Action Line 2 - Citizens and Quality of Life, Measure 2.4 - Regional Geographical Information Systems and Innovative Actions.

2. Selection of test site

2.1 General description

The present study concerns the north Aegean coasts and particularly the western coasts of prefecture of Kavala. Prefecture of Kavala is located in the northeast of Greece and is the easternmost prefecture of geographic region of Macedonia. Nestos river from east, Strymonas river from west and Paggaeo and Lekani mountains, from north, are its physical borders. The area of the prefecture, including the island of Thassos, is 2.113 km^2 and the population is 145.000. Most of the major economical activities, tourism and agriculture are concentrated along the 200 kilometres of coastline, plus 115 kilometres more, on Thassos island. The western coasts, have been rapidly developed the last two decades mainly due to increasing touristic interest and secondly due to extended cultivation of vineyards and olive trees. The absence of significant surface water resources led to overexploitation of underground water resources and phenomena of salinization on coastal aquifers have been shown up. The test site is located 48 kilometres SW from Kavala, in Karyani coastal zone (Fig. 2).

Previous studies in nearby coastal zones of Macedonia and Thrace, based mostly on hydroge-
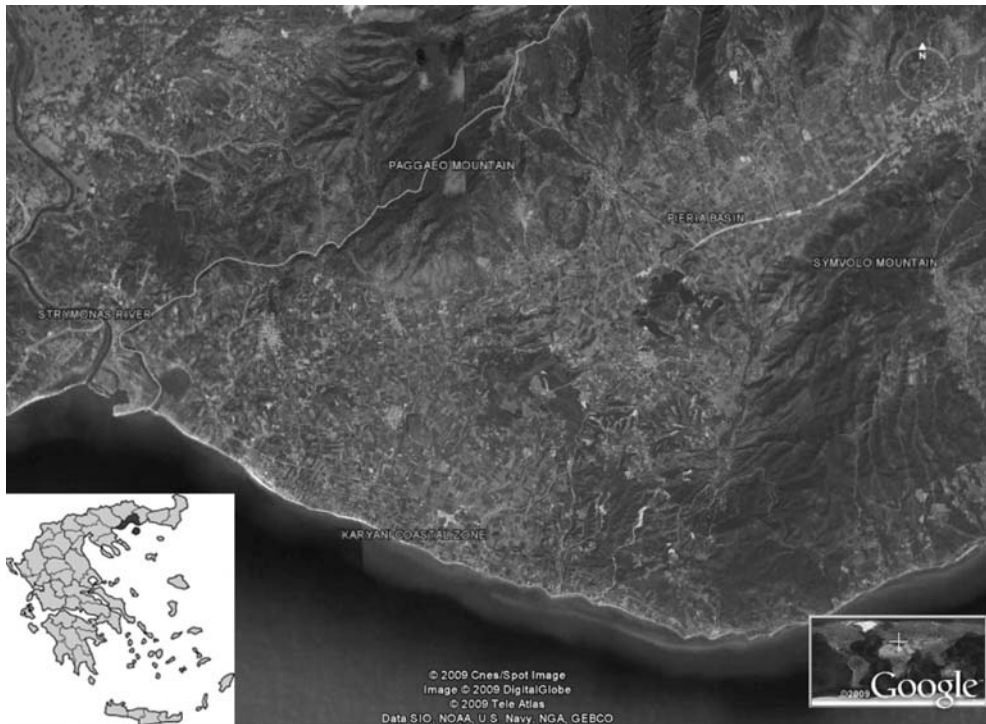
Fig. 2: Test site is located to western coasts of Kavala (N. Greece), to Karyani coastal zone.

ological and geochemical data, have pointed out the problem of seawater intrusion (Diamantis and Petalas, 1989; Petalas and Diamantis 1999; Pliakas et al., 2001; Ziegenbalg et al., 2002; Kallioras et al., 2006a and 20006b; Petalas et al., 2009).

2.2 Geological-hydrological setting

The test site is a strand plain, surrounded by a hilly landscape and is bounded by Symvolo mountain ridge to the east, Strymonas river to the west, Paggaeo mountain to the north and Aegean Sea to the south.

Geotectonically, the area at large of Karyani, is on the west border of Rhodope zone. It is composed by metamorphic (marbles. gneisses, schists), igneous (granodiorites) and sedimentary (mainly quaternary) rocks. The quaternary sediments are pleistocene and holocene deposits. The former, consists mainly of sand, pebbles, sandy clays and marls with frequent intercalations of calc-tufa lenses and loose conglomerates and has a thickness of 30 m. The latter, which covers the area of interest, consists of fluviatile-torrential sediments, sand, pebbles, cobbles, fans and recent coastal deposits and has a thickness of 10-15 m.

The mean annual rainfall at Karyani as recorded by rain gauge station 1.2 km W from test site, is 408.5 mm, while the maximum and minimum annual rainfall is 241.7 mm and 689.0 mm, respectively (Petalas et al., 2004). The most dry period is May to September (29.7% of annual rainfall) whereon the needs for water are highly increased. These facts show that Karyani has one of the most arid climates in the region of eastern Macedonia and Thrace and explain why

Fig. 3: The survey line started 80 m from sea shore and ended to "Zygoures" borehole.

during the period May to September there is an overexploitation of underground water resources. Groundwater recharge occurs by direct infiltration of atmospheric precipitations.

3. Measurements and interpretation

The objective of this study was to image the seawater intrusion in coastal aquifers. The ERT technique was considered to be the most appropriate mean for the achievement of this objective, since it provides information about the vertical and lateral changes of the electrical resistivity and is highly sensitive to saturated pore spaces. Moreover, the point information of high values of electrical conductivity in nearby wells, could be enhanced.

The survey line was in the SW-NE direction perpendicular to the seashore. It was selected by plan, to start 80 m from the coastline and end to an existed borehole, named "Zygoures" (Fig. 3).
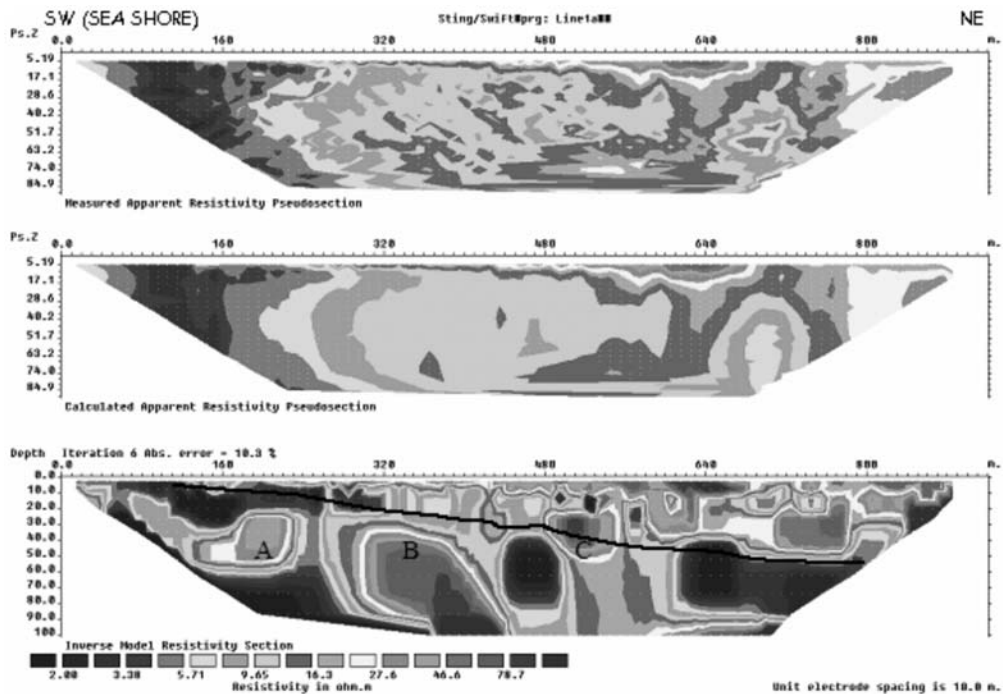
Fig. 4: Geoelectrical tomography line produced by robust inversion. Pseudosection of the measured (top) and calculated (middle) apparent resistivity. On the geoelectrical section (bottom) the black line indicates the subsaline water front. Three resistivity zones (A, B, C) are shown.

The borehole, has being pumped during the period May to September, to irrigate local fields. Measurements of electrical conductivity of pumping underground water, carried out by Directorate of Land Reclamation / Prefecture of Kavala, exhibited values that varied from 1200 to 4300 µS/cm, with pick values measured at the end of irrigation period.

The instrument used for ERT data acquisition was the AGI Sting R1 and measurements were carried out in the test site of Karyani, on August 2008. The Wenner-Schlumberger electrode array and the roll-along technique were applied. The electrode separation was 10 m and the survey line 930 m. The roll-along technique employed four consecutive equal length spreads consisting of 49 electrodes. The recorded contact resistances at the electrodes were less than 1 kOhm. Two geoelectric sections were obtained, by combining data from all the spreads and using the 2D inversion algorithms (the robust and the L2 norm) of RES2DINV software (Claerbout and Muir, 1973; Loke, 1998, 2002).

Fig. 4, displays the pseudosections of the measured and calculated apparent resistivity as well as the geoelectric section produced by robust inversion. The final inversion RMS error was 10.3%, after rejecting 11% of the total sum of 1373 data collected. The geoelectrical section exhibits heterogeneity (the resistivity values range from 2 to 100 Ohm·m) and the depth of investigation approximately 100 m. Very low resistivity zones present on this section could be attributed to formations of increased porosity and water salinity. The high values of electric conductivity (up to 4300 µS/cm), measured on water samples of the nearby borehole, advocate
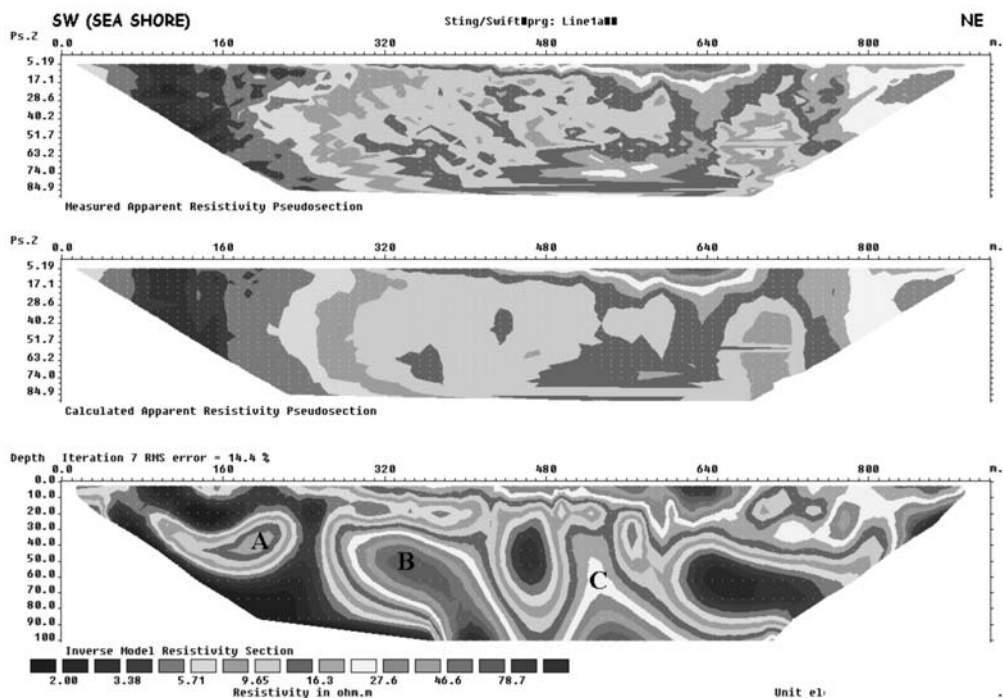
Fig. 5: Geoelectrical tomography line produced by L2 norm inversion. Pseudosection of the measured (top) and calculated (middle) apparent resistivity. The geoelectrical section (bottom) is smoother, compared to that on Fig. 4. The subsaline water front and the intermediate resistivity zones (A, B, C) are again clearly distinguished.

this interpretation. These zones are present at shallower depths (less than 10 m) to the SW (close to the seashore). Their upper limit could define the subsaline water front. The high resistivity zones A, B and C (> 20 Ohm·m) are attributed to non-permeable formations such as marls, marly limestones and gypsum.

Fig. 5, displays the measured and calculated apparent resistivity pseudosections and the geoelectric section produced by the L2 norm inversion. The final inversion RMS error was 14.4%, after rejecting 16% of the total sum of 1373 data collected. This geoelectrical section is smoother compared to that produced by robust inversion. The possible subsaline water front and the three resistivity zones (A, B, C) are again clearly shown.

4. Discussion and conclusions

The seawater intrusion at western coasts of Kavala (N. Greece) was studied. The area was preferred because of its increasing touristic and agricultural development which followed by overexploitation of underground water resources. The test site was selected to start from sea shore and end to a borehole where the electric conductivity of pumping water had been measured, up to 4300 μS/cm. Along this 1000 m line, measurements of apparent resistivity were carried out. Data were inverted and the 2D ERT profiles gave a clear image of underground inhomogeneities up to 100 m depth.

The very low resistivities (2-4 Ohm·m) in geoelectric section could be attributed to the sea water intrusion. The subsaline water front seems to displace fresh water up to 400 m to inland. There, it starts to incline into the underground aquifers, with 15^0 angle, all along the ERT line. This could explain the high values of electrical conductivity measurements of ground water at the end of the survey line. ERT offered the first general image of ground water salinization in the area. It could guide to specific constraint measures for future wells (like distance from sea shore and maximum depth) and be an effective tool for rational management of ground water resources.

To better understand saltwater intrusion mechanism and subsurface heterogeneity in the area, deep, time-lapse ERT monitoring following the pumping schedule of the nearby borehole and chemical analysis of synchronous water samples could provide the complementary information.

5. Acknowledgements

6. References

Ahlfeld, D.P., and A.E., Mulligan, 2000. Optimal management of flow in groundwater systems. Academic Press, London.

Archie, G. E., 1942. The electrical resistivity log as an aid in determining some reservoir characteristics. *Transaction of American Institute of Mining, Metallurgical and Petroleum Engineers,* 146, pp.54–62.

Asch, T.H., and H.F., Morrison, 1989. Mapping and monitoring electrical resistivity with surface and subsurface electrode arrays. *Geophysics*, 54, pp. 235-244.

Barker, R.D., 1990. Investigation of groundwater salinity by resistivity methods, *Geotechnical and Environmental Geophysics,* v. II, n. 5, Soc. Explor. Geophysicists, *Inv. in Geophysics*, (ed.) S. Ward, 201-212.

Bear, J., Cheng, A.H.-D., Sorek, S., Ouazar, D., and I., Herrera (eds.), 1999. Seawater intrusion in coastal aquifers-Concepts, Methods and Practices, Kluwer Academic Puplishers, 625 p.

Cheng, A.H.D.; Halhal, D., Naji, A., and D., Ouazar 2000. Pumping optimization in saltwater intruded coastal aquifers. *Water Resources Research*, 36, no.8, 2155-2166.

Claerbout, J.F., and F., Muir, 1973. Robust modeling with erratic data. *Geophysics, 38,* pp. 826-844.

Daily, W., and E. Owen, 1991. Cross-borehole resistivity tomography. *Geophysics*, 56, pp.1228–1235.

Daily, W., Ramirez, A., LaBrecque, D. and J., Nitao, 1992. Electrical resistivity tomography of vadose water movement. *Water Resour. Res*., 28, pp.1429-1442.

Diamantis, J., and C. Petalas, 1989. Sea water intrusion into coastal aquifers of Thrace and its impact on the environment. *Toxicological and Environmental Chemistry*, Vols. 20-21, pp. 291-305.

Directorate of Land Reclamation/Prefecture of Kavala, 2008. Record Room, Kavala.

Ewing, R. P., and A. G. Hunt, 2006. Dependence of the electrical conductivity on saturation in real porous media. *Vadose Zone Journal*, 5, pp.731–741.

Friedel S., Hansruedi Maurer H., Herfort M., and N., Van Meir, 2004. Application of single-hole geoelectrical tomography to characterize a coastal aquifer. *SEG Technical Program Expanded Abstracts- 2004*, pp.620-623.

Hubbard, S.S., and Y. Rubin, 2006. Hydrogeological characterization using geophysical methods, in J. Delleur, ed., *Handbook of groundwater engineering*, CDCPress, section 14–1.

James, G.A., Hiebert, R., Warwood, B.K. and A., Cunningham, 2001. Subsurface biofilm barriers for controlling saltwater intrusion. *Proceedings of 1st International conference on saltwater intrusion and coastal aquifers-Monitoring, modeling and management*. Essaouira, Morocco, April 23-25, 2001.

Kallergis, G., 2002. The salinization of aquifers from environmental point of view. *Proceedings of 6th Greek Hydrogeology Congress*, Xanthi, Greece, 8-10th November 2002, pp.V-XII.

Kallioras, A., Pliakas, F., and I., Diamantis, 2006a. Conceptual model of a coastal aquifer system in northern Greece and assessment of salinevulnerability due to seawater intrusion conditions. *Journal of Enveronmental Geology*, (in press, DOI: 10.1007/s00254-006-0331-0).

Kallioras, A., Pliakas, F., Diamantis, I., and G., Kallergis, 2006b. Seawater intrusion and management of coastal aquifers in Greece: The case study of Rhodope weastern coastal aquifer. *International Water Association, IWA, Proceedings of 10th International Conference on Diffuse Pollution*, Istanbul, Turkey, 18-22 September 2006.

Kirsch, R., 2009. Groundwater Geophysics: A tool for Hydrogeology, 2nd ed. XX, Springer, 548 p.

Lambrakis, N., and G., Kallergis, 2001. Reaction of subsurface coastal aquifers to climate and land use changes in Greece. Modelling of groundwater refreshening patterns under natural recharge conditions. *Journal of Hydrology*, v.245, pp.19-31.

Loke, M. H., 1998. Rapid 2D resistivity IP inversion using the least-squares method. Program manula, Pengan, Malaysia.

Loke, M. H., 2002. 2D and 3D electrical imaging surveys, tutorial.

Marescot, L., Palma Lopes S., Lagabrielle R., and D., Chapellier, 2002. Designing surface-toborehole electrical resistivity tomography surveys using the Frechet derivative. *Proceedings of the 8th Meeting of the Environmental and Engineering Geophysical Society – European Section*, pp.289-292.

Miller, R., 2009. Editorial. *The Leading Edge,* S.E.G., Oct. 2009, v.28, no 10, p.1210.

Mohnke, O., Prokoph, K., and U., Yaramanci, 2006. Electrical resistivity tomography (ERT) as a tool for monitoring moisture dynamics in soil filled containers. *Proceedings of 12th European Meeting of Environmental and Engineering Geophysics*, B026.

Mualem, Y., and S.P., Friedman, 1991. Theoretical prediction of electrical conductivity in saturated and unsaturated soil. *Water Resources Research*, 27, pp.2771–2777.

Müller, M., Mohnke, O., Schmalholz, J., and U. Yaramanci, 2003. Moisture assessment with small-scale geophysics-The Interurban Project. *Near Surface Geophysics*, 1, pp.171–182.

National Statistical Service of Greece 2009. Latest statistical data: Population census 2001. *Press Release NSSG*, Athens.

Nguyen, F., Kemna, A., Antonsson, A., Engesgaard, P., Kuras, A., Ogilvy, R., Gisbert, J., Jorreto, S., and A., Pulido-Bosch, 2009. Characterization of seawater intrusions using 2D electrical Tomography. *Near Surface Geophysics, Vol 7*, pp.377-390. Special issue on Hydrogeophysics.

Oldenborger, G. A., Knoll, M., Routh, P., and D. LaBrecque, 2007. Timelapse ERT monitoring of an injection/withdrawal experiment in a shallow unconfined aquifer: *Geophysics*, 72, no. 4, pp.177–187.

Parasnis, D.S., 1997. Principles of Applied Geophysics. 5th ed.: Chapman & Hall.

Park, S., 1998. Fluid migration in the vadose zone from 3-D inversion of resistivity monitoring data. *Geophysics*, 63, no. 1, pp.41-51.

Petalas, C., and I., Diamantis, 1999. Origin and distribution of saline groundwaters in the Miocene aquifer system in coastal Rhodope area, Thrace-NE Greece. *Hydrogeology Journal*, 7/3, pp.305-316.

Petalas, C., Pliakas, F., Diamantis, I., and A., Kallioras,2004. Study of the distribution of precipitation in district of eastern Macedonia and Thrace for the period 1964-1998. *Bulletin of the Geological Society of Greece vol. XXXVI, Proceedings of the 10th International Congress, April 2004, Thessaloniki, Greece*, pp. 1054-1064.

Petalas, C., Pisinaras, V., Gemitzi, A., Tsihrintzis, V.A., and K., Ouzounis, 2009. Current conditions of saltwater intrusion in the coastal Rhodope aquifer system, northeastern Greece. *Desalination*, 237, pp. 22-41.

Pliakas, F., Diamantis, I., and C., Petalas, 2001. Saline water intrusion and ground water artificial recharge in east delta of Nestos river. *Proceedings of 7th International Conference on Environmental Science and Technology*, University of Aegean, Dept. of Environmental Studies, and Global Nest, Ermoupolis, Syros, Greece, 3-6th September 2001, vol.2, pp.719-726.

Rubin, Y. and S.S. Hubbard, 2005. Hydrogeophysics, X, Springer, 523 p.

Singha, K., and S. M., Gorelick, 2005. Saline tracer visualized with three-dimensional electrical resistivity tomography: Field-scale spatial moment analysis. *Water Resources Research*, 41, W05023, doi: 10.1029/2004WR003460.

Slater, L., Binley, A.M., Daily, W., and R., Johnson, 2000. Cross-hole electrical imaging of a controlled saline tracer injection. *Journal of Applied Geophysics*, 44, pp.85-102.

Telford, W.M., Geldart, L.P., and R.E. Sheriff, 1990. Applied Geophysics, 2nd ed.: Cambridge University Press.

Tsourlos, P., Ogilvy R.D., Meldrum P.I., and Williams G.M., 2003. Time-lapse monitoring in single boreholes using electrical resistivity tomography. *Journal of Environmental and Engineering Geophysics*, 8, pp.1-14.

Tsourlos, P., Ogilvy R.D., and C., Papazachos, 2004. Borehole-to-surface ERT inversion. *Proceedings 10th European Meeting of Environmental and Engineering Geophysics*, 6-9th September 2004, Utrecht, The Netherlands.

Tsourlos, P., Ogilvy R.D., and P., Meldrum, 2005. Time-lapse Monitoring using Borehole-to-Surface Electrical Resistivity Tomography. *Proceedings 11th European Meeting of Environmental and Engineering Geophysics*, 6-9th September 2005, Palermo, Italy.

Vengosh, A., and E. Rosenthal, 1994. Saline groundwater in Israel: its bearing on the water crisis in the country. *Journal of Hydrology, 156*, pp. 389-430.

Vereecken, H., Binley, A., Cassiani, G., Revil, A., and K. Titov, 2006. Applied Hydrogeophysics, *Proceedings of the NATO Advanced Research Workshop on Soils and Groundwater Contamination: Improved Risk Assessment, St. Petersburg, Russia, 25-29 July 2004*. Series: NATO Science Series: IV: Earth and Environmental Sciences , Vol. 71, XII, 383 p.

Wilkinson, P B, Chambers, J E, Lelliott, M., Wealthall P., and R.D., Ogilvy 2008. Extreme sensitivity of crosshole electrical resistivity tomography measurements to geometric errors. *Geophysical Journal International,* Vol. 173, 49-62.

Zhou, B., and S.A., Greenhalgh, 2000. Cross-hole resistivity tomography using different electrode Configurations. *Geophysical Prospecting*, 48, pp.887-912.

Ziegenbalg, G., Dimitriadis, K., and E., Sarrikostis, 2002. CRYSTECHSALIN-A European project to manage and reduce saline water intrusion in coastal aquifers. *Proceedings of 6th Greek Hydrogeology Congress*, Xanthi, Greece, 8-10th November 2002, pp.13-21.

TELEMETRY NETWORK FOR MONITORING QUALITY OF IRRIGATION WATER IN KAVALA (N.GREECE)

Mertzanides Y.[1], Ziannos V.[1], Tsobanoglou C.[1], Kosmidis E.[2]

[1] *Prefecture of Kavala,65110, Kavala - Greece, mertzan@gmail.com*

[2] *Draxis Environmental S.A. ,54623, Thessaloniki - Greece, kosmidis@draxis.gr*

Abstract

In places where primary and secondary economic sectors are significant proportion of local economy, the quantity and quality of irrigation water has not only environmental but also economical and social affects in local society. A rational management of water resources demands reliable and quick information of the quality of irrigation water especially during summer. The monthly scheduled samplings that are usually followed by the state services in some cases are not adequate. A telemetry network of four stations for real-time monitoring the quality of irrigation water was designed by Directorate of Land Reclamation/Prefecture of Kavala. It covers the most important agricultural areas of prefecture, including the island of Thassos. Stations are equipped with modern and robust instrumentation (multiparameter sensors, data loggers, modems, ups, sophisticated software, etc) to measure physicochemical characteristics of surface and ground water. The records are 24 hours a day and they are transmitted via GPRS. It consists an innovative initiative for local authorities to have the ability of real-time information about the quality of irrigation water and hereupon plan their actions. The system is expected to provide useful scientific data and an effective tool towards a policy of rational management of local water resources.

Key words: irrigation water quality, telemetry network, real-time monitoring, design criteria, Prefecture of Kavala – N. Greece.

1. Introduction

Kavala is located in the northeast of Greece and is the easternmost prefecture of geographic region of Macedonia. Nestos river from east, Strymonas river from west and Paggaeo mountain, from north, are its natural borders. Kavala is not the typical agricultural region, but there are 500.000 stremmas of cultivated land and about a quarter, out of the total population of 145.000 people are farmers. This is the reason why the supply of good quality irrigation water is a priority issue for local authorities.

The national programme of irrigation water quality monitoring, supervised by Directorate of Geology-Hydrology/Directorate General of Land Reclamation/Ministry of Rural Development and Food (MiRDeF) and supported by Directorate of Land Reclamation/Prefecture of Kavala, have been providing water quality information, the only available till now. According to this, within the territory of Kavala prefecture, monthly scheduled samplings from surface irrigation water bodies are made. Samples are sent to Laboratory of Soil-hydrology and Geology/MiRDeF, where they are analysed for physical (electrical conductivity, pH), chemical (Cl$^-$, Ca^{+2}, Mg^{+2}, Na$^+$, alkalinity), irrigational (vestigial Na$_2$CO$_3$, dissolved Na and Mg, S.A.R., CaCO$_3$) and environmental (dissolved O$_2$, NO$_3^-$, dissolved Cd) parameters. The monitoring programme has been providing a long time series of data that

contributed to the understanding of major pollution mechanisms of surface and underground irrigation water systems. On the other hand, it is obvious that a monthly sampling step, acts like a "low-pass filter" to hydrology systems condition. Additional high frequency information could conceal other potential threats, while real-time information could also drive to immediate actions.

The Water Framework Directive (WFD) 2000/60/EC (Council of the European Union, 2000), represents the European Union policy for all kind of inland water and the actions that all Member States should take are mentioned. Among others, guidelines for systematic water quality monitoring are described. Greek legislation was harmonized to WFD, with Law 3199/2003 (Hellenic Republic, 2003) and water quality monitoring, for public administration, was put on a new footing.

This paper presents the work of design and operation of a telemetry network for real-time monitoring of irrigation water in Kavala. It was part of the project: "Integrated system for water quality management and olive trees optimization, using Geographical Information Systems in Prefecture of Kavala", supervised by Directorate of Land Reclamation and Directorate of Planning and Programming/Prefecture of Kavala and carried out from November 2007 to November 2008, with consortium of contractors: DRAXIS S.A.-I.M.C. S.A. The project was 80% co-founded by the European Regional Development Fund, under the Framework of the Operational Program: Information Society (IS), Priority Axe: Action Line 2 - Citizens and Quality of Life, Measure 2.4 - Regional Geographical Information Systems and Innovative Actions. The aim of this Measure was to formulate a strategy and an action plan for the IS in all regions, to encourage innovative pilot activities related to the development of IS applications at regional and local levels and to establish and support geographical and environmental mapping and administrative systems at a central, regional and local level.

2. Objectives of monitoring

It is important to define the objectives of monitoring, before proceeding to network design. The legislative framework is given by WFD, while guidelines and issues concerning water quality monitoring are listed in literature (EEA, 1996; 1997; Chilton, & Milne, 1994; Zacharioudakis et al., 2001; Wagner et al., 2001). The local-prefectorial and real-time character of the system focusing on specific agricultural needs of each area, and the parallel existence of the monthly step sampling programme, were incorporated. These specifications formed the particular frame within which the objectives of the whole attempt had to:

— Be oriented to irrigation needs.
— Incorporate innovative technology.
— Combine system reliability to operational autonomy.
— Provide high frequency data.
— Contribute to the understanding of the influence of agricultural activities to surface and underground water systems.
— Create a database with minimum human intervention and easy access to interested parties.
— Give immediate warnings in case of water quality alteration.
— Help to optimise local irrigation schedules.
— Lead to a rational management of water resources.
— Reduce bureaucracy in public administration.
— Follow the guidance of the relative legislation.

— Operate complementary to national irrigation water quality programme (MiRDeF) and to forthcoming national water quality monitoring programme (Supervised by Directorate of Water/Eastern Macedonia and Thrace Region Authorities).

3. Network design

Design criteria had to satisfy the objectives mentioned above and intend to incorporate economic, technical and social aspects, ensuring a cost effective operation. Scientific criteria, applied according to design theory for water quality monitoring (EEA, 1996; 1997; Wagner et al., 2001). Area catchments were scanned and appropriate monitoring points were searched out. The aim was the hydrological and hydrogeological characteristics of each water system, to be examined. These would reflect the flow mechanisms, the interaction of ground water to precipitation and surface water, the residence time of physicochemical contaminants, the geochemical characteristics of aquifers and the consequences of agricultural activities. Economic and social aspects concerned the "specific weight" of each water body according to its contribution to prefectorial agricultural product and gross income. Emphasis was given to land, highly contributed to local rural economy but also sensitive to potential danger of pollution. Technical aspects had to do with system sustainability and vulnerability to nature and human factors. Points, protected from extreme weather phenomena, floating objects, flood, passing animals, human "curiosity" and, if possible, with easy access to power supply, were searched out. According to these criteria, three areas of interest were defined: Area A, eastwards, comprised by Nestos river basin, Area B, westwards, comprised by Pieria basin and Area C, at the north part of the island of Thassos.

Area A belongs to catchment area of Nestos river. More than 35% of the total cultivated land of Kavala is there and it is covered by an extensive surface irrigation network. Surface water comes from Nestos to more than 160.000 stremmas of cultivated land, consisting mainly of bread crop and secondly green fallow, asparagus, rice and kiwi trees. More than 150.000.000 m^3 of river water is diverted every year to West Adducent Canal (WAC), with a flow up to 22 m^3/h. WAC is branched off to five smaller canals that irrigate the valley through canalets. Gravity and subterranean drainage is accomplished by four drainage ditches (T1-T4), that discharge into the sea. Part of water in T 's is pumped back to refill canals. Nestos valley is the most productive agricultural area in Kavala, with the most extensive irrigated land.

Area B lies between Paggaeo mountain at the north and Symvolo mountain southward and is known as Pieria basin. There are more than 30.000 stremmas of cultivated land, mainly bread crops and intensive cultivations. About 20.000 stremmas are irrigated by a pipeline network, supplied by 70 main public boreholes, 120-200 m deep and some tens of swallow, private ones. Precipitates and Paggaeo mountain water bodies are the main sources of Area's B underground aquifers. Although there is also considerable arable land along the west coasts of Kavala, local economy has been gradually turning to tourist activities and this was the reason that this area was exempted from monitoring.

North part of island of Thassos was selected as Area C. There are about 80.000 stremmas of cultivated land, all over the island, covered by olive trees are irrigated by pipeline local networks supplied by public boreholes, 80-150 m deep. Southern part has been more rapidly developed due to increasing tourist interest, while northern part's economy, leans up more on agricultural production.

In the defined Areas A, B and C, according to MiRDeF monitoring programme, monthly samplings have been carried out in two sites, in both, rivers Nestos and Marmaras. Also, during summer period, three more samplings (at the beginning, middle and end of summer) are added to the schedule,
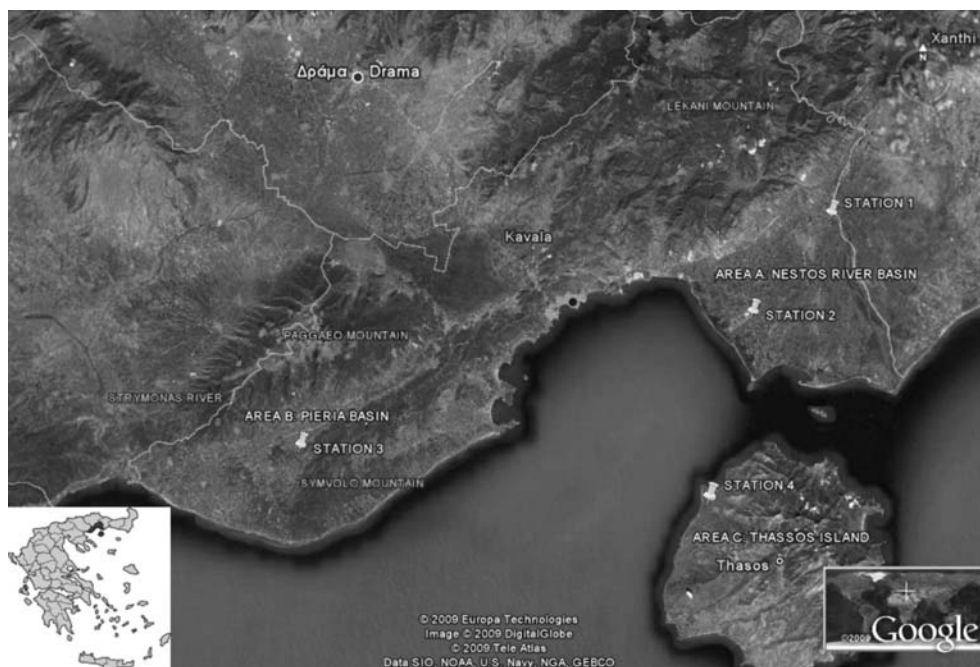
Fig. 1: The telemetry network for monitoring quality of irrigation water in prefecture of Kavala consists of four stations: STATIONS 1 and 2 in Area A (Nestos river basin), STATION 3 in Area B (Pieria basin) and STATION 4 in Area C (NW of Thassos island).

in six more sites for surface and five sites for underground irrigation water: In surface water of drainage ditches T1-T4 (six points), and in underground water of Thassos island (five wells in N-NW coasts). The results from analysed samples, have been showed that in the system of Area A, the quality of "output" water that discharge from T's ditches into the sea, is downgraded compared to the "input" water that enters WAC,. In Area C, the overpumping boreholes, during summer, have been causing phenomena of water salinization along the N-NW coastal aquifers of the island. In Area B, there is lack of data about quality of underground water. This general view acted as background knowledge for the forthcoming additional data and as a guide for the final selection of monitoring points.

4. Network set out

In order design criteria and cost efficiency to be achieved, four stations were decided to set: Two stations in Area A, one station in Area B and one in Area C (Fig. 1).

One station at the beginning and one at the end of the surface irrigation network, in Area A, could bring valuable information: Examining the input and output "signal" of the system, its characteristics could be identified. The existing irrigation network infrastructure offered two points that seemed to be ideal: A lodge, acting as "control room" for the water watchman that controls the floodgates and the flow of water from WAC to the valley, according to everyday water needs. It is the check point for input "signal" and STATION 1 was set there (Fig. 2). The second point had to be somewhere at the end of drainage ditches, in order system "response" to be checked. STATION 2 was put

Fig. 2: STATION 1 was put at the beginning of irrigation network of Nestos river basin, in a floodgate room in WAC. A plastic case was plunged into WAC and the sensors were put inside the case to be protected.

Fig. 3: STATION 2 was put at the end of irrigation network of Nestos river basin, in T2 drainage ditch. A plastic case to protect the sensors was used.

in T2 ditch, nearby a lodge with pumping equipment for refilling canals with the water of T2, which is partly reused before discharges into the sea, 2.5 km further down (Fig. 3).

STATION 3, in Area B, was tried to be set inside an existing pumped borehole of Pieria basin. Since this was impossible, because inside all boreholes pumping equipment was placed and moreover the adjacent piezometers were not wide enough, the idea of a "by pass" branch was adopted. The pumped borehole would drive part of underground water into a branch pipe, specially manufactured for the case. Sensors were put inside this "flow cell", and circuitous water was driven back to underground aquifer, through the piezometer (Fig. 4).

The same procedure followed in Area C, except that "by pass" system was not necessary. The adjacent piezometer of an existing borehole located on the N-NW coasts of Thassos island, was wide enough for sensors to be plunged and STATION 4 was placed there (Fig. 5).

Maximum protection for all the four stations was achieved, using the existing infrastructure (lodges for data and communication units, canal "nest" for surface and piezometers for underground sensors)
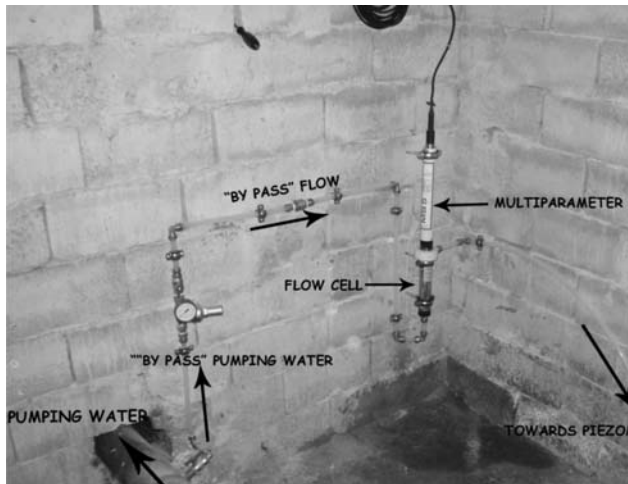
Fig. 4: In Area B (Pieria basin) STATION 3 was put in a borehole lodge. A "by pass" system was designed to drive the pumping water into a flow cell where the sensors were put and circuit back the water underground, through the adjacent piezometer.
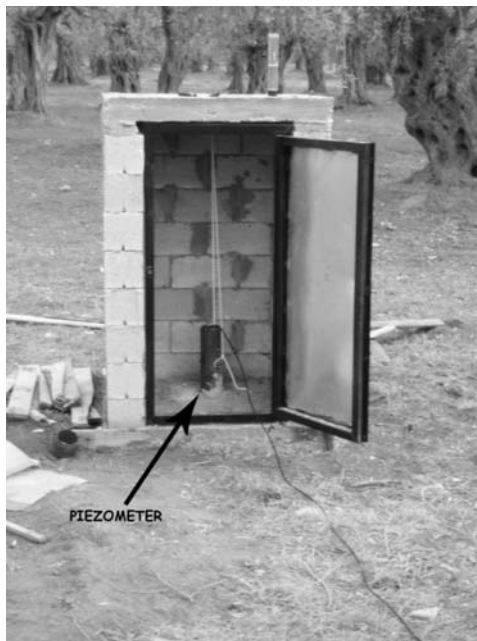
Fig. 5: In Area C (Thassos island), STATION 4 was plunged in the piezometer of an existing borehole and a small lodge to protect the sensors was constructed.

and manufacturing extra more when this was not enough (plastic cases for surface water sensors, underground pipes for power supply and communication cables etc.).

5. Operation

5.1 Measurement issues

Guided from the background information described in section 3 and budget limitations, the monitoring of physicochemical parameters of temperature, pH, electrical conductivity, dissolved oxygen, turbidity and water level was considered, at first phase, as adequate.

Fig. 6: The equipment of "OTT Messtechnik GmbH & Co. KG" was used in each station.

The choice of the appropriate measurement cycle, demanded a clear picture of the hydrological-hydrogeological conditions and mechanisms of potential pollution in each monitoring site and definition of monitoring objectives. The latter, as mentioned in section 2, was oriented to high frequency-real-time monitoring, while the former was still under investigation: Generally, surface water (like this in Area A) is specified by fast flows and underground water (like this in Areas B and C) by slower flows. This dictated more frequent measurements for STATION 1 and 2, than that for STATIONS 3 and 4. On the other hand, the examination of influence of continuous borehole pumping, in underground aquifers, requires high frequency monitoring. It was considered that setting a beginning rate of one measurement per hour, could be adequate.

5.2 Equipment

A success operation of a water quality telemetry network is finally ruled by the management of data acquisition, maintenance, transmission, processing and reporting. The accuracy, protection, continuity, and easiness of these procedures had to be ensured by the use of robust hardware and sophisticated software. The equipment of "OTT Messtechnik GmbH & Co. KG" was considered to meet the requirements. Specifically, each station was equipped with the following devices: (Fig. 6)

- OTT Hydrolab Minisonde 5. A multiparameter probe carrying temperature, pH, conductivity, dissolved oxygen (luminescence-LDO), turbidity (self cleaning) and depth sensors.
- OTT Duosens standard. A data logger with display and operating button ("jog-shuttle") for entering observer values and for offset settings.
- OTT additional equipment: Wavecom M1306B, GSM/GPRS 900/1800 MHz modem, charger and battery as buffer, overload protection system.

Data are transmitted via GPRS and stored to a web server on Prefecture of Kavala's data room. Software packages OTT Hydras 3 and Hydras RX, are used, for communication management in the measuring network, equipment configuration, data reading, data management from measuring sites to measuring network, data processing and storage and data evaluation.

Data accessibility and report policy for the interested parties have been considering. SMS and e-mail alarms for each measured parameter in each station have been planning to warn when a measured parameter excesses the specified limit value. By this way, critical information will be instantly received and immediate actions will be enabled.
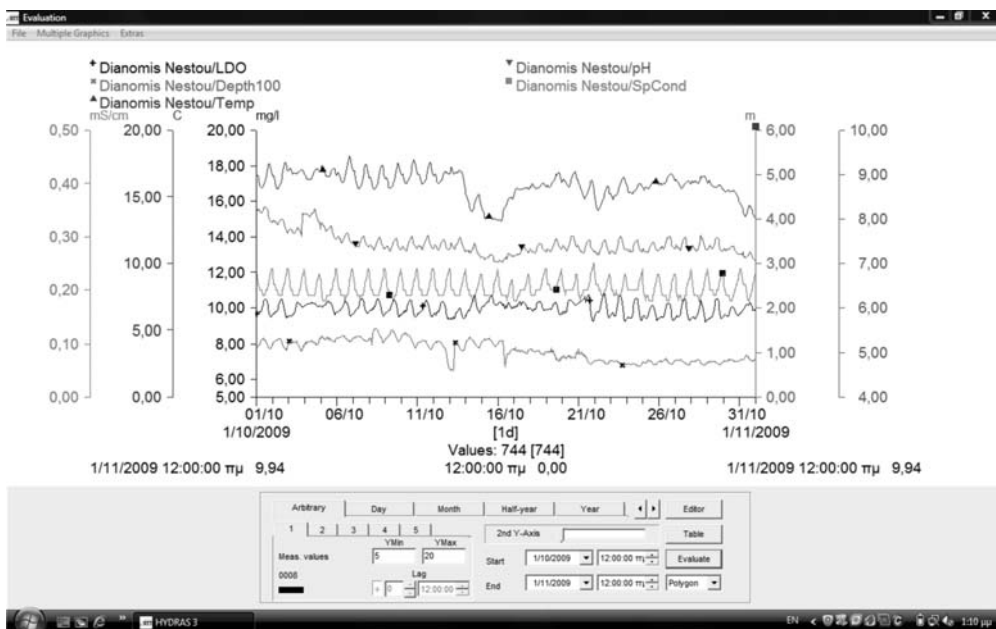
Fig. 7: Data (dissolved oxygen, water level, temperature, pH, electric conductivity) recorded on STATION 1, on October 2009 and plotted with OTT "Hydras 3" software package.

In Fig. 7, a timeseries of data, hourly measured on STATION 1 (Dianomis Nestou-WAC) on October 2009 is illustrated. The raw data set consists of temperature, pH, electrical conductivity, dissolved oxygen (LDO) and water level measurements and is plotted with OTT "Hydras 3" software package. The good physicochemical quality of the river water is obvious from the range of the parameters values. The presumable dependence of these parameters upon the daily variation of temperature is clearly indicated. The main disturbance which is observed between the 13th and 16th of October, is attributed to a rainfall. The water level data are not directly correlated to the above, since the water flow in WAC is controlled.

6. Conclusions

The rational management of water resources has been dictated from the increasing need for good quality water and the new legislation in force. A telemetry network for real-time water quality monitoring was set, supervised by Directorate of Land Reclamation/Prefecture of Kavala. It is comprised of four stations, placed on selected sites in irrigation canals and boreholes within prefecture of Kavala. Objectives, design criteria and operation issues are presented. The attempt is an innovative action for local authorities' administration. It aims to supplement water quality databases, with the missing high frequency information. The operation of such a network can eliminate time between a pollution event and actions to take and become a reliable tool for local bureaus and scientists.

7. Acknowledgements

8. References

Chilton, P.J. and Milne, C.J. 1994. Groundwwater Quality Assessment: A National Strategy for the NRA, Technical Report WD/94/40C. *Hydrogeology Series*, British Geological Survey, Keyworth, Nottingham, UK.

Council of the European Union 2000. Directive 2000/60/EC of the European Parliament and of the Council of 23 October 2000 establishing a framework for Community action in the field of Water Policy. Available online at: http://ec.europa.eu/environment/water/water-framework/

Directorate of Land Reclamation/Prefecture of Kavala, 2008. Record Room, Kavala.

EEA, 1996. Requirements for Water Monitoring. Topic Report No 1/1996.

EEA, 1997. European Freshwater Monitoring Network Design. Topic Report No 10/1996.

Hellenic Republic/Ελληνική Δημοκρατία, 2003. Νόμος υπ' αριθ. 3199: Προστασία και διαχείριση των υδάτων-Εναρμόνιση με την Οδηγία 2000/60/ΕΚ του Ευρωπαϊκού Κοινοβουλίου και του Συμβουλίου της 23ης Οκτωβρίου 2000. *Εφημερίς της Κυβερνήσεως της Ελληνικής Δημοκρατίας*, τεύχος 1ο, Αρ. Φύλλου 280, 9 Δεκεμβρίου 2003, 4821-4828.

National Statistical Service of Greece 2009. Arable land and areas of Greece: 2000-2007 (provisional data). Press Release NSSG, Athens.

Wagner, R.J., Mattraw, H.C., Ritz, G.F., and Smith, B.A., 2001. Guidelines and Standard Procedures for Continuous Water-Quality Monitors—Site Selection, Field Operation, Calibration, Record Computation, and Reporting. *U.S. Geological Survey Water-Resources Investigations Report 00-4252*, 53 p.

Zacharioudakis, G., Streetly, M. and Fermor., M., 2001. Design, implementation and operation of a large scale groundwater quality monitoring network. *Bull. Geol. Soc. Greece* vol. XXXIV/1, *Proceedings of the 9th International Congress*, Athens, 1999-2005.

INTERNATIONAL HYDROGEOLOGICAL MAP OF EUROPE: SHEET D6 "ATHINA"

Nikas K.[1], Antonakos A.[2], Kallergis G.[3] and Kounis G.[1]

[1] Institute of Geological and Mineral Exploration (IGME), Spirou Loui 1, Olympic Village Thrakomake-dones, Greece, k_nikas2006@yahoo.gr

[2] General Secretariat for Civil Protection, Evagelistrias 2, 105 63 Athens, aantonako@yahoo.gr

[3] Emeritus Professor, University of Patras, georgios.kallergis.1@ontelecoms.gr

Abstract

Hydrogeological maps adopting international standards and covering the whole Greek territory are lacking today in Greece. Sheet D6 - Athina of the International Hydrogeological Map of Europe, scale 1:1,5 million can serve, among many other uses, for such a map. Although relatively limited amount of hydrogeological information is conveyed in the map, because of its small scale, it can serve very well as a guide for information, teaching purposes, planning and scientific work. Besides, because it has fully adopted the standards set from a number of relevant organisations (IAH, IAHS, COHYM, CGMW, UNESCO etc) for the compilation of such kind maps, it can serve equally well as a model for the generation of larger scale Hydrogeological maps.

Key words: *Europe, Hydrogeological Map, IAH, hydrolithological categories.*

1. Introduction

A picture says more than a thousand words, but a map says more than a thousand pictures. Maps were already being used by medieval scientists even though such maps today may appear very naïve. A more scientific approach was only possible with the advent of land surveying and spheric trigonometry.

Geologists were among the first to develop techniques for mapping. Thanks to international scientific organisations, a high degree of standardisation with regard to presentation, inherent philosophy and legends with recommended symbols, ornaments and colours, had already been arrived at more than a century ago. On the basis of local, (large-scale) regional maps, national maps were developed and, with the appearance of atlases, the need for continental maps arose. Geological maps included in atlases are generally at an extremely small scale, often 1: 5,000,000 or even 1: 10,000,000. It is evident that such a small scale map can only depict very general features such as the general location and disposition of aquifers and non-aquifers, together with a broad picture of the surface drainage. For more detailed information it is obvious that a map needs a larger scale, e.g., 1: 1,000,000.

2. The International Hydrogeological Map of Europe

In 1960, the International Association of Hydrogeologists (IAH- International Association of Hydrogeologists) initiated a project for the preparation of an International Hydrogeological Map of Europe (IHME), having realized that although a large number of hydrogeological maps at various scales existed in almost all European countries, none of them were the same in their scientific ap-

proach, content, presentation, or use of cartographic symbols, making comparison practically impossible and even leading to erroneous conclusions. The fact that no obvious effort was being made to prepare maps in a uniform way lead to the suggestion that a small-scale map covering the whole of Europe should be prepared. However, even for a relatively small continent like Europe, such a map exceeds normal paper size. To remedy this situation, therefore, it was decided to divide the surface area into a composite of several maps.

The general purpose of the map was to provide a simplified representation of ground water in Europe as related to the geological situation. The main objective was to show the location, geographic extent, movement and constitution of the major groundwater bodies, classified according to the main types of aquifers.

Whereas large-scale maps are used for practical purposes and therefore need to contain as many details as possible, maps on a medium or small scale only give a general picture and are used primarily for information, teaching purposes, planning and scientific work.

In order to prepare an international map, agreement must be reached by the participating countries and international organisations regarding scale, an easily applicable legend and a meaningful scientific approach. Since the suggested map was the first international venture in the field of hydrogeological mapping, it was essential, from the very beginning, to secure the collaboration of a large number of scientists and to make full use of the experience of countries with a long tradition in mapping activities and hydrogeology. It is, therefore, not surprising that it took ten years to gather and evaluate such information and to establish suitable models for discussion by the scientists involved. Although the model which was finally adopted had been discussed in great detail, serious problems emerged during the preparation of the actual map, and these had to be solved at international level. The compilation of the sheets comprising the map is far from being a routine job and shows that hydrological mapping needs to be developed further. At the start of the actual work, it was understood that both the legend applied and the scientific approach had to be flexible so that, on the one hand, individual or unique events could be shown and, on the other, the necessary uniformity and clearness of the map could be maintained. The history of this map, therefore, reflects an attempt at perfection and an aim for uniformity, as well as the peculiarities of an international undertaking. These peculiarities stem from the different ways of identifying problems in different countries, from varying hydrogeological interpretations to different national regulations concerning the compilation and publication of data and information. These rather limiting factors and the varying amount of information available in each country would have led to an unjustified simplification of the map if the permitted or actual minimum of information available in certain countries had been taken as a standard. This difficulty was overcome by the flexible nature of the map which contains all information necessary for the understanding of the hydrogeological situation.

Historically, as it has already been said the Project was established in the sixties of the last century. Since then the project has passed the following stages of preparation:

1960 XXI International Geological Congress in Copenhagen: IAH Commission on Hydrogeological Maps (COHYM) was appointed to prepare a small-scale European Hydrogeological Map project (to serve as a model for small-scale hydrogeological maps in other parts of the world)

1962 Preprint (black & white) of an International Legend for Hydrogeological Maps

1970 Coloured print of an International Legend for Hydrogeological Map Basis for

1974 General Legend for the International Hydrogeological Map of Europe

1970 Print of the first sheet C5-Bern

1985 Print of 15 sheets, usually with explanatory notes

1986-1998 Project stagnated (due to changes in East and Southeast Europe).Only 4 sheets were prepared by BGR

1998 UNESCO and BGR started a new work program for the completion of the map project on the Iberian Peninsular and in SE - Europe

1999 XXIX IAH Congress in Bratislava: Regional Editorial Meeting for the implementation of Sheet D5-Budapest (12 countries involved)

4/2000 Editorial Meeting in Madrid for the implementation of the Sheets A5-La Coruña and C6-Lisboa)

9/2000 Regional Editorial Meeting in Bucharest for the implementation of Sheet E5-BucureSti (5 countries Involved)

11/2002 Regional Editorial Meeting in Athens for the implementation of Sheet D6-Athens (9 countries Involved)

More specifically, the compilation of sheet D6 –Athina initiated in the early eighties. The Greek Institute of Geological and Mineral Exploration (IGME) provided the first two National editors (G. Kallergis and G. Kounis). As it has already been said, political and economic problems in South-East Europe but also organisational and financial difficulties in the supporting agencies Unesco and BGR, resulted in stagnation in working on the map for more than 20 years. In 2002 due to a new initiative of Unesco and the BGR the program reactivated. A regional meeting was held at that year in IGME Athens with all participating countries and decisions were taken towards the finalisation of the map. IGME provided also the Scientific Sheet Editor/Coordinator (K. Nikas) taking into account that the old editors had already been retired. K Nikas was assisted in his national editorial work by Mr. A. Antonakos who worked at that time for IGME.

2.1 Choice of Scale for the International Hydrogeological Map of Europe

When choosing a scale there must always be a compromise between the size of the paper, the number of sheets forming the composite, and the amount of information to be included. The European geologists agreed to a scale of 1 : 1,500,000 which allows sufficient detail but which is still viable economically and is also easy to use. The individual map sheets are organized in a pattern with horizontal (numbers) and vertical (letters) rows. Each sheet has a key (say B5) and is named after an important city (e.g. Paris). Since a map on flat paper never fully concurs with reality (curved earth surface) a projection has been chosen which, for the European degrees of latitude, minimises the deviations from reality. This projection as well as the geographic base map were provided by the Commission for the Geological Map of the World (CGMW), affiliated to the International Council of Scientific Unions (ICSU) and the International Union of Geological Sciences (IUGS).

In view of the success of the International Geological Map of Europe the same scale and division of sheets has been applied for the metallurgenic map and the Quarterny map of Europe.

It was logical to issue a hydrogeological map at the same scale, with the same projection and topographic base. The advantages are obvious: low cost, easy comparability, similar scientific approach, similar systematic.
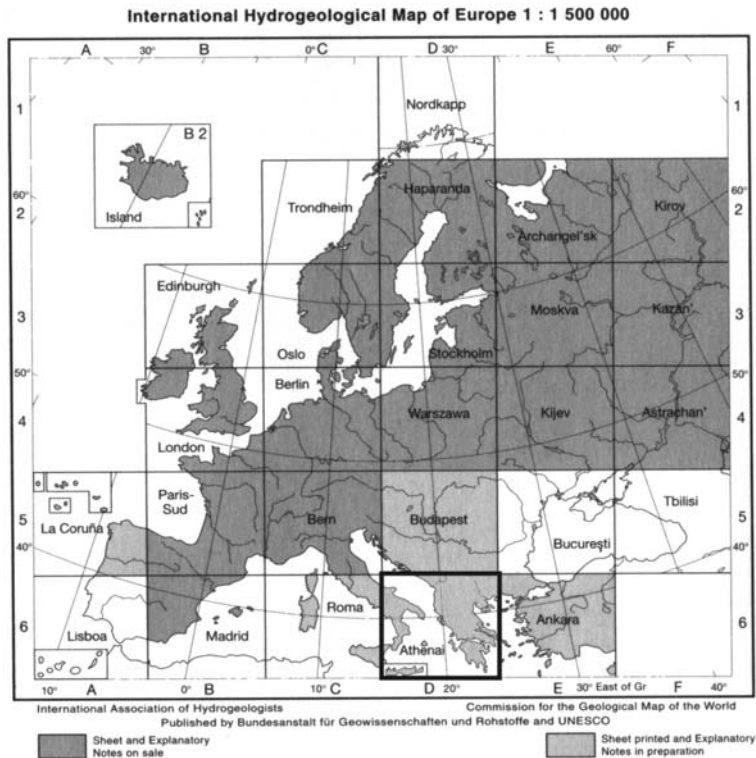
Fig. 1: State of preparation of IHME sheets.

2.2 General characteristics

The map has been drawn up along the same lines as the International Geological Map of Europe. While the latter consists of 49 sheets, the International Hydrogeological Map of Europe will no doubt be composed of less than 35 sheets, as certain regions outside Europe, in particular North Africa, will not be included. However, available space on the map will be used to portray Iceland, parts of Ireland and the island of Crete. Each sheet measures approximately 92 x 69 cm and contains not only a section of the map but also the legend in English, German and another language, either French, Russian or Spanish, depending on the country depicted. Cross sections, details of ground-water yield and quantity, together with a bibliography are also shown.

In order to make the map comparable with other international maps as well as to save costs, it seemed advisable to compile the map according to the scale used in other related maps. As the International Geological Map of Europe was prepared at a scale of 1: 1,500,000, the same scale was chosen for the Hydrogeological Map of Europe in view of the close connection between the geological structure and the hydrogeological features.

By using six colors (blue, green, red, brown, violet and orange - sometimes in different tones) as well as black and grey for point symbols, superimposures and lines, very detailed information concerning the aquifers, ground water, springs, surface water, artificial works and geological features has been included on the map. The following is a brief summary of the actual contents:

a) Sky blue has been used for ground water in porous rocks; the depth of the blue indicates whether the aquifer is extensive and highly productive or whether it is local or incoherent. Superimposures refer to the type of rock and are applied in accordance with the stratigraphical symbols in the legend of the International Geological Map of Europe.

b) Green refers to ground water in jointed massive rocks; the depth of the colour indicates either extensive and highly productive aquifers, often found only at great depth, or local or incoherent aquifers into which streams flow.

c) Brown indicates regions generally without or only with local ground water; the depth of the colour indicates either that the aquifers are shallow or very deep but unproductive.

For a), b) and c) superimposures refer to the property and/or composition of the rock.

d) Violet lines may indicate, in special cases, the contour lines of the groundwater table, groundwater divides or boundaries of certain types of ground water.

e) Orange symbols refer to the quality of the ground water, and its temperature.

f) Royal blue symbols indicate springs giving the amount of discharge and the continuity of production.

g) Prussian blue indicates surface water.

h) Red symbols illustrate artificial works, such as wells, water-works, dams, canals and pipelines.

i) Black or green lines represent geological features, such as faults, overthrusts and border of certain formations.

k) The base map consists of grey lines.

A particular problem related to coloured maps should be raised here. Although the same printer was used for each map sheet, there are, nonetheless, slight differences in the colours between the different sheets as each series of map sheets was printed at varying intervals of time. When looking at one single sheet, the map and legend are homogenous. However, if two sheets, of a different series, are placed side by side slight differences become visible. Hence, at present, the composition of all the map sheets on a wall is not fully satisfactory. Modern technology can surely overcome this problem when and if all the map sheets are re-printed at some time in the future.

2.3 Legend for the International Hydrogeological Map of Europe

The IAHS (International Association of Hydrological Sciences) began studying the idea of a universally-applicable legend in 1954 and established a Standing Committee on Hydrogeological Maps in 1960 to study methods of presenting hydrological data on both small-scale and large-scale maps, and to make recommendations on the standardisation of symbols. The IAH also undertook the preparation of a legend from 1959 onwards and formed, for this purpose, a Working Group on Hydrogeological Maps. The legend was issued by IAHS and by UNESCO in 1963 with a view to having it tested by map-makers and hydrogeologists in different countries, under different hydrogeological conditions and at different scales. The experience gained from issuing this draft served for the establishment of a legend which was published by UNESCO and IAHS in 1970 in four of the working languages of UNESCO (Struckmeier & Margat 1995).

Although not directly linked to the Hydrogeological Map of Europe but rather as a result of other

Ornament:	a pattern of marks, lines or other symbol denoting the occurrence of a particular factor over an area of ground as represented upon the map; e.g. a stipple to represent sandy strata.
Symbol:	a single graphical representation to denote the presence of a particular factor at a point location on the map; e.g. a small circle to show the location of a spring.
Line:	a solid or broken line may be used either to delimit an area such as an aquifer outcrop, or to join points of equal altitude (contour), equal thickness (isopachyte), or similar parameters.
Sign:	a sign may consist of a line, a symbol, or an ornament, or a combination or any or all of these. Colour: a colour refers to an even "wash" of constant tone. It may be used for lines, symbols or ornaments as well as for emphasising areas of importance.
Tone:	screens may be used in order to reduce the density of a colour. The value of the tone is usually expressed as a percentage of the original or full (100%) colour.

B   Groundwater and rocks
1. Intergranular aquifers

| blue | | 1.1 Extensive and highly productive aquifers |

| screened blue | | 1.2 Local or discontinuous productive aquifers or extensive but only moderately productive aquifers |

2. Fissured aquifers, including karst aquifers

| green | | 2.1 Extensive and highly productive aquifers |

| screened green | | 2.2 Local or discontinuous productive aquifers, or extensive but only moderately productive aquifers |

3. Strata (intergranular or fissured rocks) with local and limited groundwater resources or strata with essentially no groundwater resources

| screened brown | | 3.1 Strata with local and limited groundwater resources |

| brown | | 3.2 Strata with essentially no groundwater resources |

| brown stripes | | 3.3 Where there is an extensive aquifer immediately underlying a thin cover the option be used of continuing the appropriate aquifer colour crossed by brown stripes (one mm wide and three mm separation) |

Fig. 2: Aquifer type proposed ornament by the standard legend of Hydrogeological Maps.

regional mapping projects, the 1970 issue of the standard legend was refined scientifically and regional supplements were also issued.

Certain terms are used rather loosely in both hydrogeology and cartogaphy, and it is easy for misunderstandings to arise. A short list of definitions is included here which refer to the usage for hydrogeological maps.

Some of the basic ornaments used in the standard legend for aquifer types, Lithology and groundwater features are shown in figures 3 to 4.

Recommended ornaments:

1. Lithology of sedimentary rocks

1 clay, clayey loam, mud, silt, marl
2 clayey-loamy alteration products
3 loess
4 sands (units can be distinguished by variation of thickness of points)
5 gravels (distinction by variation of the arrangement of circles)
6 moraines
7 peat
8 lignite
9 pyroclastics
10 made ground
20 claystone, siltstone, shale
21 sandstone (distinction by variation of size)
22 conglomerate
23 limestones (distinction by variation of rectangle size)
24 dolomites (distinction by variation of parallelogram size)
25 travertine
26 marlstone
27 flysch
28 complex alternation of different lithology
29 radiolarite, lydite, siliceous shale
30 rock salt
31 gypsum

2. Lithologies of igneous and metamorphic rocks

40 acid to intermediate extrusives (distinction by variation of triangle size)
41 basic extrusives (distinction by variation of triangle size)
42 ultrabasite, serpentinite
43 acid to intermediate intrusives (distinction by variation of arrangement of crosses)
44 basic intrusives
45 slate, phyllite, mica schist, etc.
46 gneiss
47 gneiss and granite, undifferentiated
48 marble
49 quartzite
50 metamorphic rocks, undifferentiated

3. Examples of combined types

1+4
2+4+5
1+30
4+9
4+7
26+31
21+40
20+21
20+23
21+23
21+26
21+45
23+26
23+45

Fig. 3: Lithology proposed ornament by the standard legend of Hydrogeological Maps.

3. Description of sheet D6 "Athina"

Sheet D6 "Athina" includes the whole of Albania and FYROM and the largest part of Greece (Part of Thrace and eastern Greek islands of the Aegean Sea are included in the adjacent sheet of E6 – Ankara). As a total, nine countries of the SE part of Europe contribute to the D6 sheet. The geographical distribution of these countries is shown in Figure 5 whereas in table 2 and Figure 6 the area and percentage of each country is shown.

As it can be seen from the table Greece occupies the larger part of the sheet namely 47% while Italy occupies 20%, Albania, F.Y.R.O.M and Bulgaria almost 10% each and the rest 4.6% is occupied by other countries.

4. The Greek part of sheet D6 "Athina"

The preparation of the Greek part of sheet D6 was done by the use of Geographical Information Systems and incorporates the digitization of 75 aquifer types grouped in six categories. Polygon

Groundwater and springs

Colour: violet (ITC No. 062,)

	1.1	Contours of the potentiometric surface (solid or broken lines with height relative to reference level)
←	1.2	Direction of groundwater flow
a) b)	1.3	Connection between karstic loss and resurgence a) proven, b) inferred
a) b)	1.4	Groundwater divide a) stationary, b) periodically changing
	1.5	Limit of area with confined groundwater
	1.6	Limit of area of artesian flow
	1.7	Lens of fresh water surrounded by salt water
	1.8	Limit of area with insignificant natural replenishment to the groundwater (50% screen colour)

average discharge of a) less than 100 1/s
b) 100 - 1000 1/s,
c) more than 1000 1/s

a) b) c)

	1.10	Spring
	1.11	Perennial karst spring	Fresh water
	1.12	Submarine spring
	1.13	Spring
	1.14	Perennial karst spring	Brackish water
	1.15	Submarine spring
	1.16	Group of springs (relevant symbols are enclosed of circles)
	1.17	Temporary karst spring (large: 0 - less than 1 m^3/s, small: 0 - more than 1 m^3/s)

Surface water and karst hydrography

Colour: blue (ITC No. 006)

	3.1	Stream with perennial runoff
	3.2	Stream with intermittent runoff
	3.3	Dry valley, possibly with episodical runoff (ephemeral stream)
	3.4	Sander
	3.5	Stream ending in inland depression
cf. 2.9		Stream with mineralized water (blue stream with orange band)
	3.7	Karstic loss in river valley
	a)	a) perennial flow downstream
	b)	b) seasonal flow downstream
	c)	c) no flow downstream
	3.8	Aven
	3.10	Dry doline
	3.11	Limit of karst area
	3.12	Main surface water divide
	3.13	Secondary water divide
	3.14	Flow gauging station mean annual runoff [m^3/s] catchment area [. 1000 km^2]
	3.15	Glacier
	3.16	Glacier burst from ice dammed lake
	3.17	Waterfall
	3.18	Fresh water lake
cf. 2.10		Lagoon or lake with mineralized water (blue shore line with orange band inside)
cf. 2.11		Periodical salt-water lake (broken blue shore line with orange band inside)
cf. 2.12		Shotts (playas) with episodical water (dotted blue shore line with orange band inside)
	3.19	Periodical fresh water lake
	3.20	Dry lake with only episodical water
	3.21	River marsh
	3.22	Bog

Fig. 4: Groundwater and surface water features proposed ornament by the standard legend of Hydrogeological Maps.

Table 2. Area distribution of countries participating in IHME sheet D6 "Athina".

COUNTRY	Area	Area (%)
GREECE	117,576.1	47.01
ITALY	45,700.7	18.27
ALBANIA	28,624.4	11.44
F.Y.R.O.M	25,348.2	10.13
BULGARIA	21,305.0	8.52
SERBIA	6,496.1	2.60
MONTENEGRO	4,636.1	1.85
CROATIA	277.0	0.11
BOSNIA HERCEGOVINA	154.9	0.06
SUM	250,118.4	100.00

boundaries were adopted by the 1:1,500,000 geological map of Europe sheet D6, while the hydrogeological classification was done according to existing hydrogeological data and the judgment of the editors.

A huge number of hydrological and hydrogeological features were also digitized counting 572 karstic springs grouped in eight categories (Scagias 1978, 1986, Kourmoulis 1979, 1984, Kallergis and
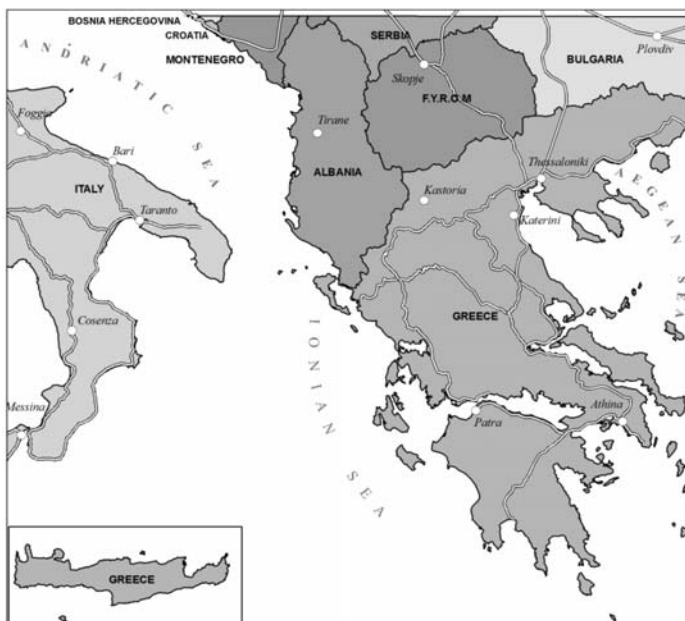
Fig. 5: Geographical distribution of countries participating in IHME sheet D6 "Athina".
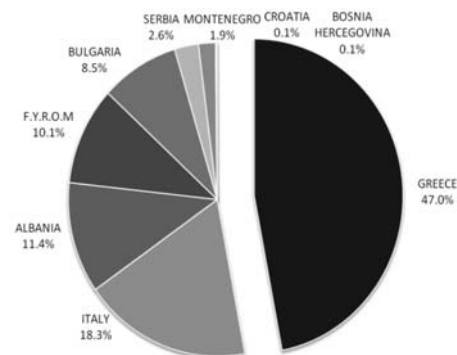
Fig. 6: Pie diagram of area distribution of countries participating in IHME sheet D6 "Athina".

Scagias, 1980, Knithakis, 1983, Kakavas, 1984, Stamos and Manakos, 1986, Vergis, 1987) 298 mineral springs grouped in three categories (Orfanos et.al. 1995), 23 dams and 5 water tanks and their capacities (Hellenic Ministry of Rural Development and Food 2006), 22 major and 49 minor river basin boundaries, 4,339 Km^2 of sea water intrusion zones and 3,030 Km^2 of artesian flow zones. Because this map has fully adopted the standards set from a number of relevant organisations (IAH, IAHS, COHYM, CGMW, UNESCO etc.) for the compilation of such kind of maps, can serve very well as a hydrogeological map of Greece, scale 1:1,5 million (Greek part of the map) as well as a model for the generation of larger scale Hydrogeological maps.

As it is understood the map due to its small scale includes many details presented by the use of colors and patterns that cannot be represented satisfactory here. Therefore the authors of this paper concluded that is better for the understanding of the readers the actual map to be shown as a poster

during the time of the Congress. The actual map can be obtained from the IGME – Athens library (in due time also purchased from the UNESCO, http://publishing.unesco.org/maps.aspx) and in digital format (without legend) from the BGR web site at: http://www.bgr.de/app/fishy/ihme1500/

5. Acknowledgments

6. References

ANON. (1970): International Legend for Hydrogeological Maps - UNESCO/IAHS/IAH/Institute of Geological Sciences, 101 pp.; London.

Hellenic Ministry of Rural Development and Food, 2006. Dams and water tanks of the Ministry of Rural Development and Food. 104 pp. Athens (In Greek).

Kakavas, N., 1984. Inventory of karstic springs of Greece. VI. East Central Greece (Fthiotis Province). Abstract in English. IGME Athens.

Kallergis, G., Scagias, S. 1980. Inventory of karstic springs of Greece. III. Thessaly. Abstract in English. IGME Athens.

Knithakis, M., 1983. Inventory of karstic springs of Greece. IV. Hydrological basin of Strimonas R. IGME Athens.

Kourmoulis, N., 1987. Inventory of karstic springs of Greece. Eastern Central Greece (Prefectures of Phocida and Phtiotida). IGME Athens.

Kourmoulis, N., 1979. Inventory of karstic springs of Greece. II. Crete. Abstract in English. IGME Athens.

Kourmoulis, N., 1984. Inventory of karsic springs of Greece. V. Western Central Greece Abstract in English. IGME Athens.

Liakouris, D., 1995. Geology and dams of Public Power Corporation. Public Power Corporation S.A., 349 pp. Athens (In Greek).

Orfanos G., Sfetsos K., and Gioni G., 1995. Thermal-Mineral Springs Map of Greece scale 1:500.000. IGME Athens.

Scagias, S. 1978. Inventory of karstic springs of Greece. Inventory of karstic springs of Greece. I. Peloponnesus-Zakynthos-Kefallinia. IGME Athens.

Scagias, S. 1986. Inventory of karstic springs of Greece. VIII. Water District of Eastern Central Greece. (Euboea Province). IGME Athens.

Stamos, A., Manakos, A. 1986. Inventory of karstic springs of Greece. IX Water District of Western Macedonia. Abstract in English. IGME Athens.

Struckmeier, W., Margat, J. (Ed.) 1995: Hydrogeological Maps: a Guide and a Standard Legend. Int. Contibution to Hydrogeol., Vol. 17; Hannover.

Vergis, S., 1987. Inventory of karstic springs of Greece. Water District of Thrace. IGME Athens.

MEASUREMENT OF PREFERENTIAL FLOW DURING INFILTRATION AND EVAPORATION IN POROUS MEDIA

Papafotiou A.[1], Schütz C.[1], Lehmann P.[2], Vontobel P.[3], Or D.[2], and Neuweiler I.[1]

[1] *Leibniz Universität Hannover, Institute of Fluid Mechanics and Environmental Physics in Civil Engineering, 30167 Hannover, Germany, papafotiou@hydromech.uni-hannover.de, schuetz@hydromech.uni-hannover.de, neuweiler@hydromech.uni-hannover.de*

[2] *Soil and Terrestrial Environmental Physics, ETH Zürich, 8092 Zürich, Switzerland, peter.lehmann@env.ethz.ch, dani.or@env.ethz.ch*

[3] *Paul Scherrer Institute, 5232 Villigen, Switzerland, peter.vontobel@psi.ch*

Abstract

Infiltration and evaporation are governing processes for water exchange between soil and atmosphere. In addition to atmospheric supply or demand, infiltration and evaporation rates are controlled by the material properties of the subsurface and the interplay between capillary, viscous and gravitational forces. This is commonly modeled with semi-empirical approaches using continuum models, such as the Richards equation for unsaturated flow. However, preferential flow phenomena often occur, limiting or even entirely suspending the applicability of continuum-based models. During infiltration, unstable fingers may form in homogeneous or heterogeneous porous media. On the other hand, the evaporation process may be driven by the hydraulic coupling of materials with different hydraulic functions found in heterogeneous systems.

To analyze such preferential flow processes, water distribution was monitored in infiltration and evaporation lab experiments using neutron transmission techniques. Measurements were performed in 2D and 3D, using homogeneous and heterogeneous setups. The experimental findings demonstrate the fingering effect in infiltration and how it is influenced by the presence of fine inclusions in coarse background material. During evaporation processes, the hydraulic coupling effect is found to control the evaporation rate, limiting the modeling of water balances between soil and surface based on surface information alone.

Key words: *preferential, infiltration, evaporation, unsaturated, drying, unstable, fronts, neutron, imaging, radiography, tomography.*

1. Introduction

A significant part of water exchange between the subsurface and the atmosphere occurs through infiltration and evaporation in the unsaturated zone. Infiltration and evaporation are governed concurrently by relevant flow and transport processes both in the atmosphere and the subsurface, posing thus an inherent complexity when it comes to the description and prediction of such systems. For a given atmospheric supply or demand, infiltration and evaporation processes in the subsurface are controlled by the soil properties and the interplay between capillary, viscous and gravitational forces.

In order to achieve predictions for such problems, these effects are commonly described by assigning effective medium properties to the soil (ie. permeability), combined with continuum-based models for flow, such as the Richards equation for the unsaturated zone. Nevertheless, continuum-based approaches have certain limitations, as the substitution of real materials with effective media dictates that some processes vanish during the averaging procedure. Such limitations are revealed when preferential flow phenomena arise and need to be accounted for, as a basic feature of such models is the stability of the solution.

A typical example of preferential flow is the formation of unstable wetting fronts during infiltration in initially dry porous media. Instability in wetting fronts is triggered by pore-scale heterogeneity, stemming from different pore sizes and shapes, that determines the local forces and therefore the overall front propagation features in the air-filled pore space. Such effects have therefore been studied on the pore-scale consideration with pore-network models (DiCarlo 2006) and invasion-percolation models (Glass and Yarrington, 1996). On the effective medium scale, preferential flow has been widely investigated with 2D experiments of infiltration in homogeneous porous media using Hele-Shaw cells (Glass et al., 1989; DiCarlo, 2004). Similar 2D experiments have also been conducted using inclusions of fine material in coarse background, showing that heterogeneity tends to locally eliminate the instability in the inclusions (Hill and Parlange, 1972; Sililo and Tellam, 2000; Rezanezhad et al., 2006). Nevertheless, due to the typically fast propagation of infiltration fronts, monitoring preferential flow in 3D has been limited to delineating unstable wetting fronts and finger diameters (Glass et al., 1990; Tullis and Wright, 2007). Saturation measurements have thus been restricted to 2D setups that carry a degree of uncertainty related to the influence of the boundaries on the flow process. In the first part of the work presented here we extend saturation measurements to 3D, discussing whether our 2D knowledge on preferential flow is indeed relevant for the 3D space and focussing on the effect of material interfaces. For that purpose, we measure water saturation distribution in a 3D column during unstable wetting for a homogeneous case as well as for a case with fine material inclusions in a coarse background.

Similar limitations of classical continuum models are encountered when preferential flow is induced by evaporation. On the pore scale, evaporation from porous media causes water movement from the larger pores near the drying front to smaller pores near the surface, driven by the capillary pressure difference. This effect, termed as capillary pumping (Yiotis et al., 2001), has extensively been investigated from a pore-scale consideration (Prat, 1993; Prat, 2002; Yiotis et al., 2004). Experimental work is also found on the medium scale, using initially wet or party wet homogeneous porous media subject to evaporation (Shokri et al., 2008). Similarly to the pore-scale pumping effect, the effect of hydraulic coupling has been demonstrated on the medium scale using coupled vertical columns of different materials (Lehmann and Or, 2009). In this case, preferential water flow is induced from the coarse-textured to the fine-textured column through the coupling of the materials, sustaining high evaporation rates through the fine-textured surface for longer periods. These observations indicate that, in order to predict evaporation rates from soils, one needs to account for the subsurface structural features and the emerging preferential flow paths additionally to the classical drying front dynamics considerations. In the second part of this work, we investigate the effect of hydraulic coupling by monitoring water saturation distribution during evaporation from a heterogeneous structure that consists of a tortuous fine-textured inclusion embedded in a coarse background.

2. Description of experiments

2.1 Infiltration experimental setup

The infiltration experiment was carried out in 3D using an aluminium cylindrical column with 150
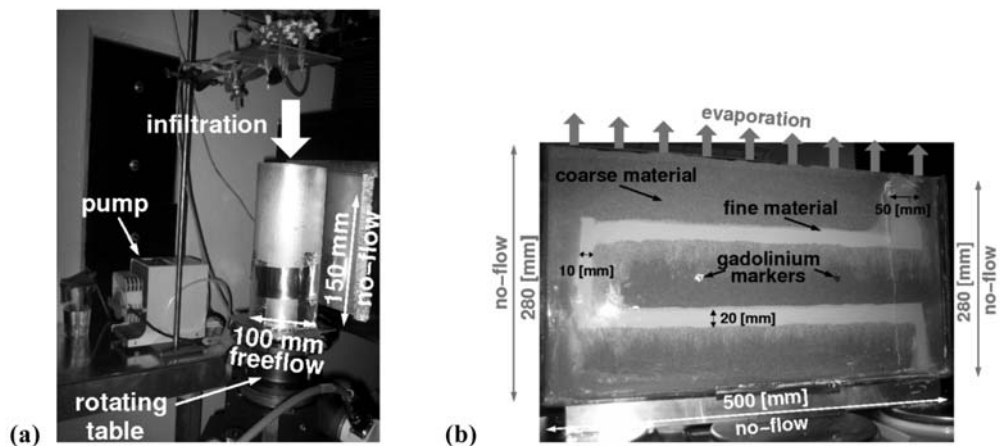
Fig. 1: Experimental setups: infiltration experiments (a), evaporation experiment (b).

mm height and 100 mm inner diameter (Fig. 1a). The experiment was first performed with a homogeneous packing of a coarse material. Then it was repeated with fine-textured inclusions embedded in the coarse background. The inclusions were lunate-shaped in the horizontal plane and were introduced symmetrically with respect to the centre of the column at z=15 and 30 mm, each having a height of 10 mm. This inclusion configuration left a wide opening of the coarse material towards the bottom. The coarse material chosen was quartz sand with grain sizes ranging from 0.7 to 1.2 mm. Quartz sand with grain sizes from 0.1 to 0.3 mm was used as a fine material. The sands were packed by simply pouring the particles into the column entirely dry, which also corresponds to the initial condition for the infiltration experiments. The base of the column was perforated to avoid the ponding of water at the bottom and to prevent any air pressure build-up inside the porous medium. A fine metal grid sealed the outlets to keep the sand particles from flowing out with water.

The top of the column was open to the atmosphere and subjected to a constant infiltration rate of 10 ml/min (Fig. 1a). The infiltration water mass was delivered equally to the sand surface by distributing the inflow into tubes ending at several injection points. Additionally, the top of the structure was covered with a 20 mm thick layer of the fine material, to ensure an initial homogeneous spreading of the water mass in this layer through capillarity and prevent the formation of artificial preferential flow paths near the injection points. The bottom boundary was of free-flow type and any water reaching the bottom was collected in an external container positioned under the column.

2.2 Evaporation experimental setup

The evaporation experiment was carried out in 2D using a Hele-Shaw cell with 280 mm height, 500 mm width and a thickness of 20 mm. The heterogeneous structure consisted of a tortuous fine-textured inclusion connecting bottom and top of the cell in a coarse-textured background (Fig. 1b). As coarse background material, quartz sand with grain sizes ranging from 0.7 to 0.9 mm was used. The fine material was quartz powder with grain sizes in the range of 0 to 0.06 mm with a mean value of 0.012 mm diameter. This resulted in a contrast of the saturated hydraulic conductivity of several orders of magnitude. In order to achieve a fully saturated initial condition, the entire structure was packed under water. The sand was first flushed an immersed in separate glass beakers. Artificial

variations of porosity during the wet packing were prevented by depositing the wet sand particles from a constant falling distance into the water-filled Hele-Shaw cell and mixing the packed particles each 10-20 mm (Lehmann et al. 2008). Shaping the tortuous inclusion was achieved by placing metal sheets that were slowly shifted after the fine particles had settled. Despite the painstaking procedure, some mixing of the two materials near the boundaries of the inclusion was inevitable due to the large grain size contrast.

The top of the Hele-Shaw cell was open to the atmosphere and acted as the evaporative surface (Fig. 1b). A hair-dryer, blowing with a constant fan speed from a fixed distance towards the evaporative surface, was used to manipulate the evaporation rate. This offers the advantage of a faster evaporation process without having any influence on the water distribution inside the porous medium (Shokri et al., 2008).

2.3 Measurement techniques

Water movement inside the porous media was monitored using thermal neutron transmission technology in the NEUTRA station of the Spallation Neutron Source (SINQ) of the Paul Scherrer Institute, Switzerland. The following measurements were performed:

- Infiltration experiments (fast process): 2D width-averaged dynamic water distribution by means of fast radiography in time increments of 4 s during the front propagation. Additionally, 3D reconstruction of infiltration patterns by means of tomography obtained by rotational scanning in steps of 2°.

- Evaporation experiment (slow process): 2D water distribution by means of slow radiography in time increments of 30 mins for a period of 6.5 d.

Measuring water distribution in porous media with neutron imaging is based on relating water saturation to neutron intensity detected on a scintillator behind the scanned medium. The neutron intensity I passing through quartz sand, water and cell or column walls (ie. glass or aluminium) is

$$I = Io \exp(-\alpha q dq – \alpha w dw – \alpha c dc) \tag{1}$$

with the source neutron beam intensity Io, the neutron attenuation coefficients αq, αw, αc and effective thicknesses dq, dw, dc for quartz, water and cell or column wall, respectively. The recorded intensity I was filtered to correct source beam intensity variations and neutron scattering effects. Consequently, the water effective thickness dw can be deduced by comparing each image (intensity I) to a reference entirely wet or dry image (Iref) that thus has a known water thickness dref equal to dwet or zero.

$$dw = dref – (1/\alpha w) \ln(I/Iref) \tag{2}$$

In a similar fashion, the coefficient αw can be determined with Eq. (1) using the mean values *mwet* and mdry of intensities at entirely wet and dry conditions

$$\alpha w = -\ln(mwet/mdry)/dwet \tag{3}$$

Combination of Eqs. (2) and (3) yields the water saturation

$$Sw = dw/dwet = dref/dwet + \ln(I/Iref) / \ln(mwet/mdry) \tag{4}$$

The term dref/dwet obviously reduces to one or zero, depending on the reference image used.

In the infiltration experiment, the water mass in the system was defined by the water inflow prescribed with the balance. For the evaporation experiment, however, the evaporative mass was, naturally, not
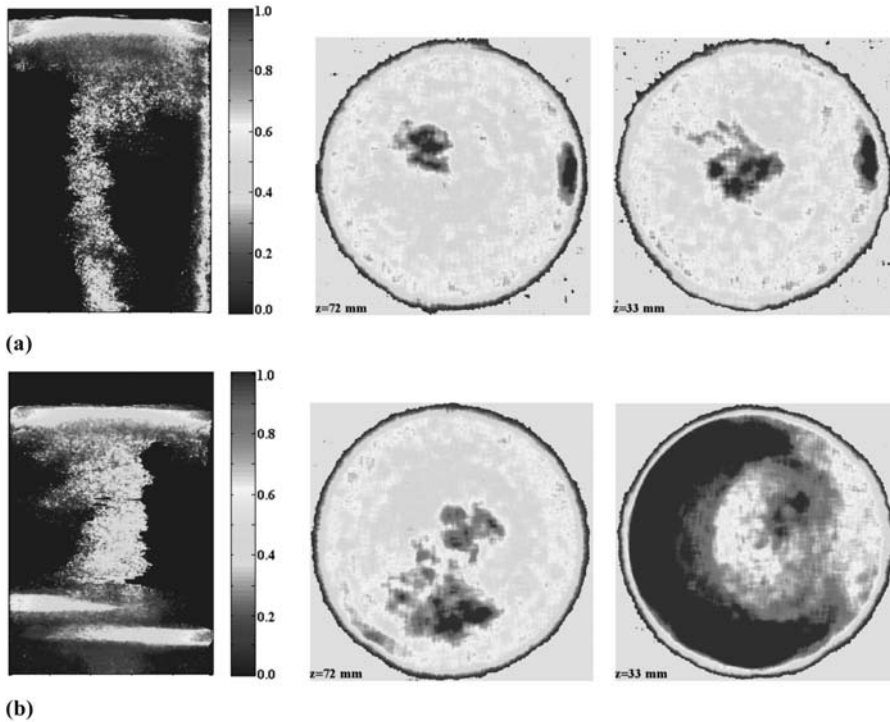
Fig. 2: Finger formation during wetting: (a) in the homogeneously packed coarse material and (b) with lunate-shaped inclusions of fine material. The left image illustrates depth-averaged saturation obtained with neutron radiography. Middle and right image qualitatively depict neutron intensities in cross-sections (100 mm diameter) of the column at heights z=72 and z=33 mm, respectively.

predefined and therefore the total water mass in the Hele-Shaw cell was recorded continuously with digital balances. This was done for the entire measurement period of 6.5 d and was also continued after the end of the saturation measurements until t=13 d. More details are given in Sect. 3.2.

3. Results

3.1 Infiltration experiments

With the application of the infiltration rate, water first distributed in the fine material at the top and saturated it. Consequently, preferential flow in the infiltration experiments occured in terms of unstable finger formation in the coarse material (Fig. 2). The fingers formed at the interface between the fine and the coarse material and then vastly propagated through the coarse material towards the bottom of the column, driven by gravity. It must be stated that fingering here was triggered purely by pore-scale effects and was not initiated with any kind of artificial structures or variations in the infiltration rate.

The homogeneous packing (Fig. 2a) resulted in the formation of two fingers. The vertical propagation is illustrated here with a radiography image (left), while cross-sectional neutron intensities delineate the finger area in the column at z=72 and 33 mm (middle and right image). The first finger came in contact with the wall of the column soon after its formation at the fine-coarse interface and then reached the bottom within 22 s, remaining attached to the wall. Nevertheless, the second fin-
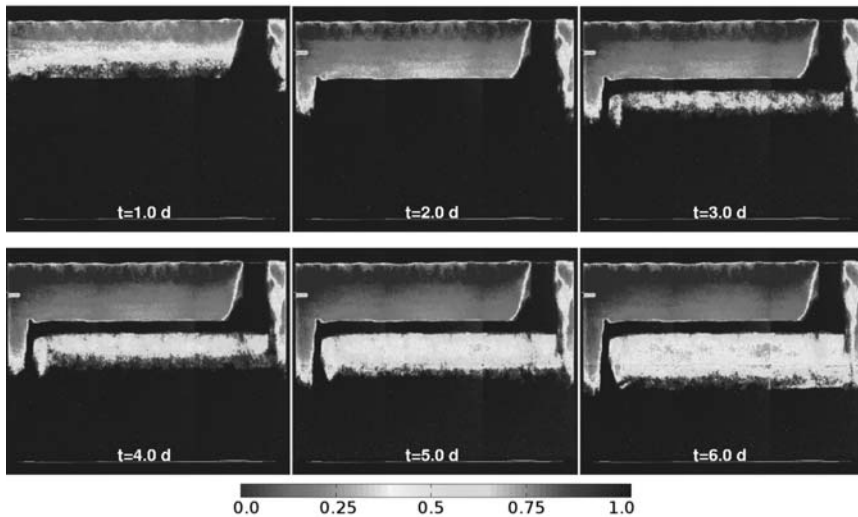
Fig. 3: Water saturation distribution determined with neutron radiography during the evaporation experiment at t=1, 2, 3, 4, 5 and 6 days.

ger formed in the middle of the column, reaching the bottom within 36 s. These observations indicate that boundaries can, indeed, introduce preferential pathways for water and possibly create or accelerate preferential flow phenomena at the walls. However, fingering also occurs away from the column walls, demonstrating that unstable wetting is also relevant for 3D applications.

The heterogeneous case (Fig. 2b) demonstrates the formation of a finger and its behaviour in the presence of the two symmetric, lunate-shaped fine material inclusions. Also in this case, the vertical propagation is illustrated with a radiography image (left) while cross-sections are shown at z=72 and 33 mm (middle and right image). Once more, the finger was formed near the centre of the column (left and middle image), however in this case it was eliminated at the lower region of the column near the fine inclusions (left and right image). This happened despite the fact that the central cross-sectional area was not occupied by fine material due to the symmetric lunate shapes of the inclusions; a configuration that would, in general, allow finger propagation through the centre. However, any hydraulic connection of the finger to the fine material drives water into the inclusion due to the capillary pressure difference, interrupting the finger propagation and forming a smeared-out infiltration front. Through this pronounced pore-scale capillary effect, material interfaces dominate the system and determine the stability of the wetting front. This is visible in the radiography image (left) as well as in cross-sectional image near the inclusions (right). In the cross-section at z=33 mm, the finger is still discernible near the centre of the column, as well as its hydraulic connection to the (at this stage wet) upper inclusion. Despite the fact that the infiltration rate from the top was continued, fingering effects underneath the inclusions were not observed even after the inclusions were saturated. However, this presumably also relates to the limited height of the column.

3.2 Evaporation experiment

The saturation distribution obtained with neutron radiography during the evaporation experiment is given in Fig. 3 for the times t=1, 2, 3, 4, 5 and 6 d. The saturation images also allow a straight-forward derivation of the change of total water mass in the porous medium during the evaporation
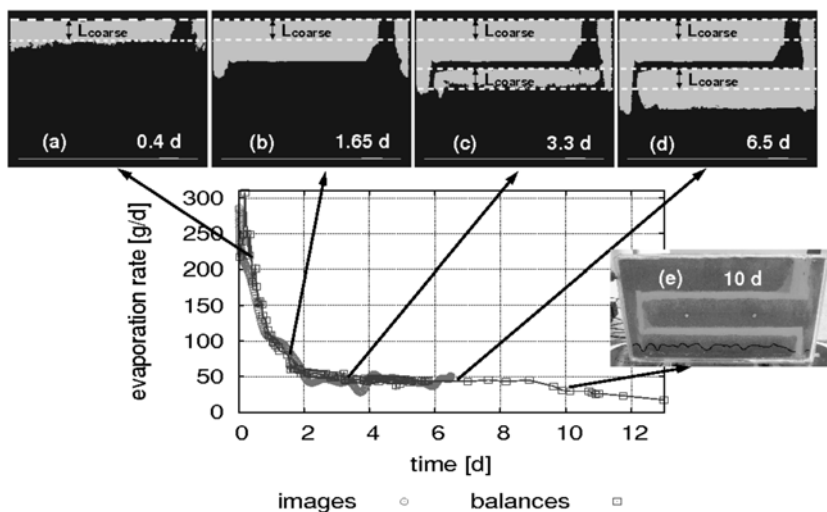
Fig. 4: Evaporation rate determined from the saturation images and the digital balance measurements. Front positions at different phases of the evaporation process (t=0.4, 1.65, 3.3, 6.5 days and qualitatively at t=10 days) are also illustrated.

process. It is thus possible to derive the evaporation rate based on information from the neutron radiography alone. This evaporation rate is compared to the one measured with the digital balances during the experiment in Fig. 4. This procedure is commonly followed as a calibration method for neutron imaging as an additional correction of intensity variation and scattering errors. However, in this case agreement between the radiography-based mass balance and the balance measurements was obtained without any calibration.

The evaporation rate is characterized by three periods: (1) and initial period from t=0 to t=0.4 d with rate values fluctuating between 200 and 250 g/d, (2) a falling rate period from t=0.4 to t=1.65 d with a vast decrease of rate from 250 to 60 g/d and (3) a constant rate period from t=1.65 to t=6.5 with slow rate decrease from 60 to 44 g/d. Additionally, the balance measurements indicate that the rate of 44 g/d was maintained until t=9 d. Although the evolution of the evaporation rate resembles the classical consideration of a first (high rates) and a second (low rates) stage of evaporation, the origins of this pattern have to be closely examined, accounting for the fact that this rate stems from a coupled system of two materials. The saturation images show that the top of the fine material remained saturated until the end of the experiment, it is thus safe to conclude that the fine material sustained first stage evaporation. This is, however, not the case for the coarse material. An estimation of the drying front depth that initiates the transition from first to second stage evaporation can be given by the characteristic evaporation length Lcoarse of the coarse material (Lehmann et al. 2008). Derivation of the material characteristic lengths and comparison of this information to the deduced drying front images (Fig. 4) reveals that the drying front reaches depth Lcoarse at t=0.4 d, indicating that this time corresponds to the end of first stage evaporation of the coarse material.

Nevertheless, the structure continued to supply high evaporation rates within the range of 44 to 60 g/d until t=9 d. This evaporative mass can be attributed to (i) mass that originated from the drying front and reached the surface as vapour diffusion through the coarse material, (ii) first-stage evaporation of the fine material, which, since the fine material remained saturated throughout the entire meas-

urement, translates to a hydraulic coupling effect of the two materials. The evaporative mass supplied through the vapour diffusion mechanism (i) can be estimated based on Penman's model (Penman 1940), using the medium porosity, the diffusion of vapour in free air, the saturated vapour density at the front, the vapour density at the surface, the water content above the front and the drying front depth. Based on this approach, the maximum diffusive flux (ie. for the front position shown in Fig. 4b) obtained during the second stage evaporation from the coarse material in this setup was found in the order of 0.01 g/d. This value corresponds to 1 g/d per m², a finding that agrees with previous observations on diffusive fluxes during second stage evaporation from porous media (Shokri et al. 2008).

This diffusive flux is negligible compared to the 44 g/d evaporation rate measured until t=9 d, denoting that the measured rate was mainly sustained through first stage evaporation from the fine material. This strong contrast of contribution of evaporative mass originating on the one hand from the diffusion-driven process and on the other hand from the material coupling, highlights the significance of hydraulic coupling effects during evaporation from heterogeneous porous media. Water is drawn from the coarse material background into the fine material and flows through the tortuous path towards the fine-textured evaporative surface, supplying the evaporative demand. Practically, this effect sustains higher evaporation rates for longer periods than one would predict by neglecting the coupled behaviour of the system. This preferential water flow through the inclusion is driven by the atmospheric demand but is strongly controlled by the contrast of hydraulic properties of the materials as well as the properties of the inclusion geometry, especially with respect to connectivity.

4. Conclusions

The first part of the presented work deals with monitoring preferential flow during infiltration in porous media. We present the 3D measurement of water saturation distribution during unstable wetting in initially dry porous media. Two different cases are examined: a homogeneous case using a coarse material and a heterogeneous case with fine material inclusions embedded in the coarse background. The experiments showed that preferential flow phenomena can be significant for 3D problems of infiltration, however, one has to be aware of artificial boundary effects, ie. when investigating such processes in 2D. The existence of fine inclusions eliminated, at least locally, the fingering effect, even though the inclusion configuration used here could, theoretically, allow the finger propagation towards the bottom. This behaviour stems from capillary pressure difference in the materials and reveals that material interfaces play a dominant role in the 3D infiltration process: any hydraulic connection between the finger and the inclusion (even through few pores) can stabilize the wetting front.

The second part presents 2D measurements of water saturation distribution during preferential flow induced by hydraulic coupling of materials during evaporation from heterogeneous porous media. The structure under examination consisted of a tortuous fine-textured inclusion, connecting the bottom to the evaporative surface at the top, embedded in a coarse background. The experiment revealed the significance of the coupling effect: even though the end of first stage evaporation for the background material was reached soon, the structure continued to supply high evaporation rates through the fine-textured surface until the entire background material was practically dried out. The observations made here reveal that evaporation rates can be strongly underestimated when neglecting the coupling behaviour of materials in the subsurface. Therefore, in order to achieve predictive modelling of evaporation from soils, it is necessary to account for subsurface structural features of heterogeneity.

5. Acknowledgments

6. References

DiCarlo, D.A., 2004. Experimental measurements of saturation overshoot on infiltration. *Water Resources Research* 40(4), W04215.

DiCarlo, D.A., 2006. Quantitative network model predictions of saturation behind infiltration fronts and comparison with experiments. *Water Resources Research* 42(7), W07408.

Glass, R.J., Steenhuis, T.S. and Parlange, J.Y., 1989. Mechanism for finger persistence in homogeneous unsaturated porous media: theory and verification. *Soil Science* 148, pp. 60-70.

Glass, R.J., Cann, S., King, J., Baily, N., Parlange, J.Y. and Steenhuis, T.S., 1990. Wetting front instability in unsaturated porous media: a three-dimensional study in initially dry sand. *Transport in Porous Media* 5, pp. 247-268.

Glass, R.J. and Yarrington, L., 1996. Simulation of gravity fingering in porous media using a modified invasion-percolation model. *Geoderma* 70, pp. 231-252.

Hill, D.E. and Parlange, J.Y., 1972. Wetting front instability in layered soils. *Soil Sci. Soc. Am. Proc.* 36, pp. 697-702.

Lehmann, P., Assouline, S., and Or, D., 2008. Characteristic lengths affecting evaporative drying of porous media. *Physical Review E* 77(5), 056309.

Lehmann, P. and Or, D., 2009. Evaporation and capillary coupling across vertical textural contrasts in porous media. *Physical Review E* 80, 046318.

Penman, H.L., 1940. Gas and vapor movements in the soil: I. The diffusion of vapors through porous media. *Journal of Agricultural Science* 30, pp. 437-462.

Prat, M., 1993. Percolation model of drying under isothermal conditions in porous media. *International Journal of Multiphase Flow* 19(4), pp. 691-704.

Prat, M., 2002. Recent advances in pore-scale models for drying of porous media. *Chemical Engineering Journal* 86, pp. 153-164.

Rezanezhad, F., Vogel, H.-J., and Roth, K., 2006. Experimental study of fingered flow through initially dry sand. *Hydrol. Earth Syst. Sci. Discuss.* 3, pp. 2595-2620.

Shokri, N., Lehmann, P., Vontobel, P., and Or, D., 2008. Drying front and water content dynamics during evaporation from sand delineated by neutron radiography. *Water Resources Research* 44, W06418.

Sililo, O.T.N. and Tellam, J.H., 2000. Fingering in unsaturated zone flow: a qualitative review with laboratory experiments on heterogeneous systems. *Ground Water* 38(6), pp. 864-871.

Tullis, B.P. and Wright, S.J., 2007. Wetting front instabilities: a three-dimensional experimental investigation. *Transport in Porous Media* 70, pp. 335-353.

Yiotis, A.G., Stubos, K., Boudouvis, A.G. and Yortsos Y.C., 2001. A 2-D pore-network model for the drying of single-component liquids in porous media. *Advances in Water Resources* 24, pp. 439-460.

Yiotis, A.G., Boudouvis, A.G., Stubos, K., Tsimpanoyiannis, I.N. and Yortsos Y.C., 2004. The effect of liquid films on the drying of porous media. *AIChE Journal* 50, pp. 2721-2737.

GEOCHEMICAL INVESTIGATION OF AQUIFER POLLUTION FROM WASTE MANAGEMENT.
THE CASE OF KOMOTINI LANDFILL (GREECE)

Raco B.[1], Dotsika E.[2], Psomiadis D.[2], Doveri M.[1], Lelli M.[1], Zisi N.[2], Papakonstantinou K.[3] and Lazaridis A.[4]

[1] *Institute of Geosciences and Earth Resources, Via G. Moruzzi 1, 56124 Pisa, Italy, b.raco@igg.cnr.it, doveri@igg.cnr.it, m.lelli@igg.cnr.it*

[2] *Stable Isotope Unit, Institute of Materials Science, NCSR Demokritos, Agia Paraskevi Attiki, Greece, edotsika@ims.demokritos.gr, dapsom@ims.demokritos.gr, nzissi@ims.demokritos.gr*

[3] *Georesources Technology S.A., Perigiali, Kavala, Greece, cmp@georesources.gr*

[4] *Greek Ministry of National Education and Religious Affairs, Andrea Papandreou 37, Marousi 15180 Greece*

Abstract

According to European legislation, environmental control and monitoring of landfills has become of crucial importance. This study includes a thorough geochemical approach aiming to evaluate the environmental impact of the landfill of Komotini, N. Greece. Samples of waters were taken from inside the working landfill as well as from the area of the neighbouring old landfill. The waters were analyzed chemically (major elements and heavy metals) and isotopically (D and ^{18}O). Also, biogas flow was measured and the ratio CH_4/CO_2. Based on the geomorphological, hydrogeological and land use data of the area, we proceeded to analyses of waters both from the area of the landfill and from the wider region (drainage basin). The obtained results were used to construct digital maps (GIS) in order to determine the special dispersion of the polluted aquifers. The biogas flow in the old and new garbage burial sites was measured by accumulation chamber device for methane and carbon dioxide ratio determination. The obtained results show an important agent of pollution in the water samples downstream from the landfill and in a distance more than 2km, along the dispersion of the leachate. The land use of the area was taken into account to evaluate the importance and the criticality of the situation.

Key words: aquifer pollution, waste, landfill, Komotini, Greece.

1. Introduction

Integrated management of urban waste has become one of the top priorities of the national and especially of the European environmental policy, which has adapted the basic principles of sustainable development: reduction, reuse, recycle and safe disposal. Therefore, there has been commenced an intense effort of closing and restoring old landfills and installing new ones, which will correspond to modern advanced specifications.

Landfill monitoring is a vital chapter for detecting and precluding possible environmental impacts during both operation and restoral. In Greece, the subject of monitoring and supervising of landfills remains still a side issue in planning and installing of such a project, rendering the present frame-

work in total inconsistence with the relative European directives.

Isotopic composition of elements is a powerful and refined instrument to obtain information about origin and history of the examined chemical species. Light elements isotopic composition in particular, being affected by great relative mass differences among the isotopes of a same element, offers many possible applications in monitoring, also because of the sensible fractioning occurring at environmental temperatures (Clark and Fritz, 1997). This kind of analysis has become an integrating essential part in the study of environmental impact of landfills, being able to provide information and evaluation instruments not obtainable with other methods (see Hackley et al., 1996; Doveri et al., 2007).

2. Area of study

The study site is the landfills of Komotini (Thrace, N. Greece), including the old restored one (OL) and the new operating landfill (NL) (Fig. 1, map). NL began its operation in 1994, substituting OL in the vicinity. OL was set out of operation due to several negative effects in the region and also after reaching its operational maximum. NL is located NW of Stylario village, approximately 7km NE of the city of Komotini, at 150m above sea level. The total surface of NL reaches up to 113000m^2. OL is approximately 6,5km eastward of Komotini, near village Kalhas, at 100m above sea level. Its surface is 57000m^2 and its subbasin exits to SSW, covered by bushy vegetation. The study area belongs to the graben of Xanthi – Komotini. NL is at a medium (old) level of morphological relief (the relief is characterized by hills and alluvial sediments at the lower altitudes). The slopes are relatively small and vary between 2,6 – 16%. The eastern part of the region of the landfills is marked by small hills and wide shallow basins. There are some eroding phenomena by the local streams, with a quite low activity though. The area belongs to the drainage basin of river Fyliris, which is considered to be the most important in the region of the Xanthi – Komotini plain. To the north, it is parted from the older metamorphic bedrock by a fault (NE dir), to the SW it is parted from the Tertiary basin of Nestos-Prinos by the tectonic horn of Avdira and to the NE it borders the Tertiary basin of Alexandroupolis. Mean annual outflow of the Fyliris river basin is 305·10^6 m^3 or 9,67m^3/s, which equals to rainfall of 204,7 mm. Mean annual underground flow of Fyliris is 2,73 m^3/s and equals to rainfall of 57,7mm. Evaporation of the basin of Fyliris river during 1980-81 was 479,7mm. The active percolation during the same year was 63mm. Fyliris river, after exiting the chrystalline schist, covers a distance of 25-35km on the Holocene sediments. The landfill region is on the Pleio-Pleistocene sediments. Inside the rough materials, local aquifers appear. Deep and rich aquifers are not excluded. In the vicinity of the landfill a poor shallow aquifer is formed. Its development takes place in the layers of sand and gravels, which covers the first 6-8 meters depth at the north. At the south, the aquifer is developed again in the layers of sand and gravels up to 11 meters depth, where it stops on the clay strata. Possibly, there is a deeper and richer aquifer, but the contact of the two is considered very unlikely because of the clay-strata.

3. Methods

The integrated approach included a) chemical and isotopic analysis of leachate in the landfill body, with the aim of indicating eventual differences between OL and NL and to characterize the leachate from external waters, b) chemical and isotopic analysis of piezometers and some external wells to point out an eventual contamination or a lack of leachate containment, c) a measurements-survey of diffused biogas, aimed at evaluating the global amount of biogas released from soil and estimating the efficiency of the covering and d) chemical analysis of biogas.

Water samples were analyzed as follows: cations and heavy metals by optical ICP-OES, anions by liquid chromatography, ammonia by a specific electrode and COD through spectrometry. Oxygen
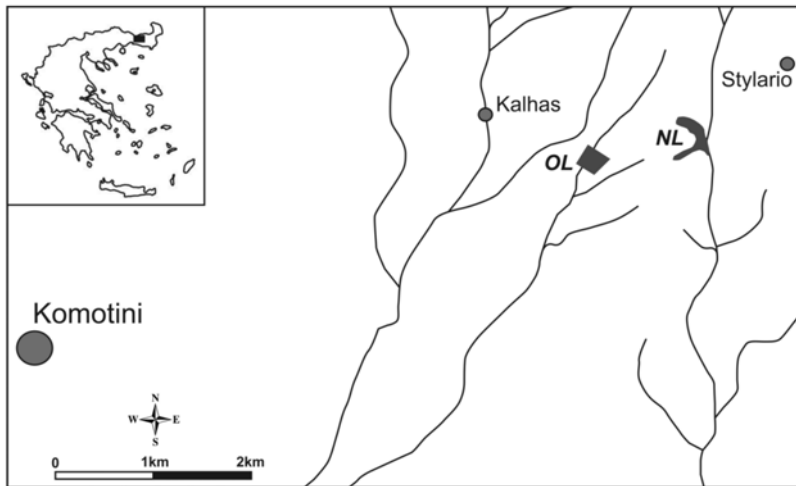
Fig. 1: Simplified map of the study area showing the main urban sites. NL: New landfill; OL: Old landfill. The region south of the two landfills is entirely used for agricultural activities.

and Hydrogen isotopic compositions were analyzed through mass spectrometry respectively of CO_2, obtained by equilibration with the water itself, and of H_2, obtained by reaction to metallic zinc at 400°C. Isotopic analyses have been carried out according to the usual preparation and measurement techniques with mass spectrometry for δ^2H, $\delta^{13}C$ and $\delta^{18}O$ and with liquid scintillation for ^3H. All results have been reported with the usual $\delta‰$ unit (difference in parts per 0.1 per cent between the measured isotopic correlation, for example $^{18}O/^{16}O$, in the sample and the same rate in a international agreed standard) vs. the SMOW standard (average isotopic composition of oceanic waters) for hydrogen and oxygen stable isotopes in waters, vs. PDB (composition of a sea biogenic carbonate as reference) for carbon.

The biogas flux measurements were carried out with the stationary method of accumulation chamber (Witkamp, 1969; Kucera and Kirkham, 1971; Kanemasu et al., 1974; Parkinson, 1981, Tonani and Miele, 1991; Chiodini et al., 1996; Chiodini et al., 1998) considering the lower weather dependence conditions indicated by Trégourès et al. (1999). This method allows to measure the increase of concentration of a given gas specie inside a sealed chamber, open only on the bottom, in touch with the ground; a non stationary version has been used to measure the diffused gas emissions in landfills (Cossu et al., 1997).

A detailed description of this instrumentation has been reported by Chiodini et al. (1996, 1998) and in Raco et al. (2005). In Raco et al. (2005), also the influence of weather parameters, especially of atmospheric pressure, was considered. For what chemical analysis of gas are concerned, widely standardized methodologies have been used; in particular gas chromatography for CO_2, CH_4, O_2+ Ar, N_2 concentrations.

Samples collected by sucking with syringe by pass, in pyrex containers: 1) in OL, in three different spots, by a metallic tube with holes, which was dipped 20cm in the permeable covering inside the collectors (chimneys) of degassing, 2) in NL, using again the metallic tube, dipped 50cm in the temporary covering of the garbage at the active part of the landfill.

108 CO_2 and CH_4 soil flux measurements were made, covering the whole area of NL, with the ex-

Table 1. Physicochemical characteristics of samples.

Sample	North	East	Type	Depth (m)	Date	T (°C)	pH	Cond µS/cm (20°C)	meq/l HCO₃⁻
GR1	41,1391	25,4886	borehole	25,0	19/09/2007	21	6,85	1786	8
perc	41,1372	25,4922	leachate		19/09/2007	28	7,53	67100	
GR2	41,0938	25,4932	borehole	85,0	19/09/2007	21,1	7,04	1880	8,5
GR3	41,1439	25,4907	well	4,4	19/09/2007	21,6	7,27	1926	10,6
GR4	41,1279	25,4924	spring		19/09/2007	20	6,57	1197	7
GR5	41,1279	25,4926	open trench surface	3,0	19/09/2007	19,5	7,16	1098	6,5
GR6	41,1240	25,4936	well	5,6	19/09/2007	20	6,86	1630	8,7
GR7	41,1413	25,4921	well	4,7	20/09/2007	19,5	7,29	1418	7
GR8	41,1384	25,4809	well	8,9	20/09/2007	18	7,37	2130	6,4
GR9	41,1302	25,4733	well	5,9	20/09/2007	19,5	6,7	4090	12,2
GR10	41,1282	25,4922	open trench surface		20/09/2007	19,9	7,7	9000	

ception of the cultivated area. The covered surface was calculated to be around 10200 m², the dimension of sampling network was of 10m x 10m and the location of sampling spots is shown in figure 2. Several measurements took place in OL, which were located on a matrix with cell 20m x 20m. We also measured at the inclined perimeter of the landfill. The rest part was covered sparsely. There were no fluxes in the region, except from the degassing tubes (chimneys).

4. Data analysis

4.1 Chemistry of waters

The water samples are shown in table 1, which includes also a general description of the sampling sites and of the parameters measured during the campaign. Measurements took place four times during the year for the general chemical parameters (T, pH, Cond) and two times for the basic chemical elements. Based on the fact that the measured values where similar between the periods of measurement, GIS maps and data process were structured on one period data set (19/09/2007). Also, values of heavy metal composition of the water samples were measured (Cr, Ni, B, Hg, As were measured at the laboratory). A first glance at table 1 and in particular at the measured data set shows a range of conductivity included between 1000 and 2000 µS, typical of surface water wells in cultivated area, with the only exception of well GR9 down the old landfill and of GR10, which appeared to be contaminated by leachate also at the sight. Leachate shows a value of 67100 µS/cm, this value is extremely high if compared to that of other similar measurements shown by literature and suggests that we are in presence of real leachate, even if this one was sampled under the form of overflowing, immediately down the area of waste disposal and not far from subsuperficial water flows.

The first step for the interpretation of these analyses is made by a hydrochemical classification of waters here obtained with the well known Langelier-Ludwig (LL) diagrams.
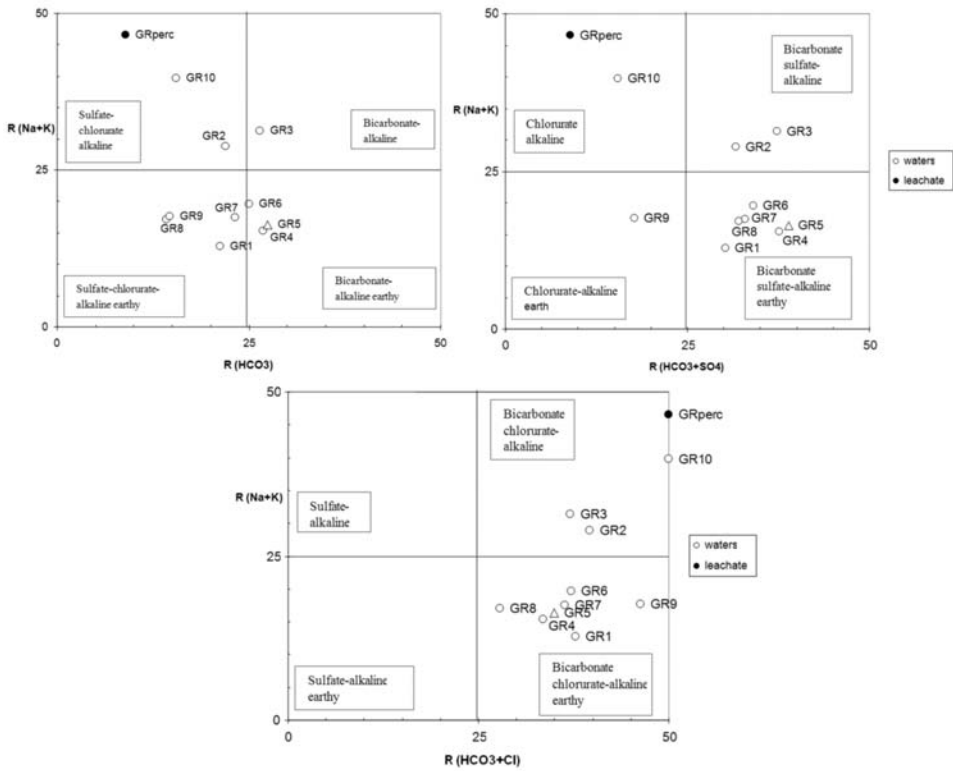
Fig. 2: $LL_{(HCO3)}$ diagrams.

The chemical composition of a water sample is shown in LL diagram, using Ri reaction values, which have been calculated from the concentration of their major constituents (cations and anions) expressed in eq/l (or meq/l). By keeping the cations groups constant, three LL diagrams could be made, LL_{HCO3}, LL_{Cl} and LL_{SO4}, which have bicarbonate, chlorurate and sulfate as respective isolated ions. LL_{HCO3} diagram allows distinguishing waters with bicarbonate as main ion from the sulfate-chlorurated ones. LL_{Cl} and LL_{SO4} diagrams will allow identifying within the group of sulfate-chlorurated waters those with a dominant component of sulfate or chloride. From LL diagrams in figure 2 it can be observed that eight samples have a sulfate chlorurated alkaline-earthy composition, GR2 and GR3 samples have an alkaline dominant and GR9 and GR10 are respectively chlorurated alkaline-earthy and chlorurated-alkaline. The leachate sample shows an evident chlorurated-alkaline composition.

The always present correlation between the above parameters, in case of samples with visible (GR10) or possible (GR9) contamination from leachate and leachate itself is very clear and shows the tracing reliability of such parameters in this particular geological context, where the content of Cl and bicarbonate is not particularly high. It is important to notice that this observation is not trivial as it may appear. In fact, geological formations rich in chloride and/or bicarbonate are obviously quite common and especially their content in chloride can easily reach very high peaks in slow circulation systems or in those affected by sea intrusion or geothermal contribution.

4.2 Isotopic composition of waters
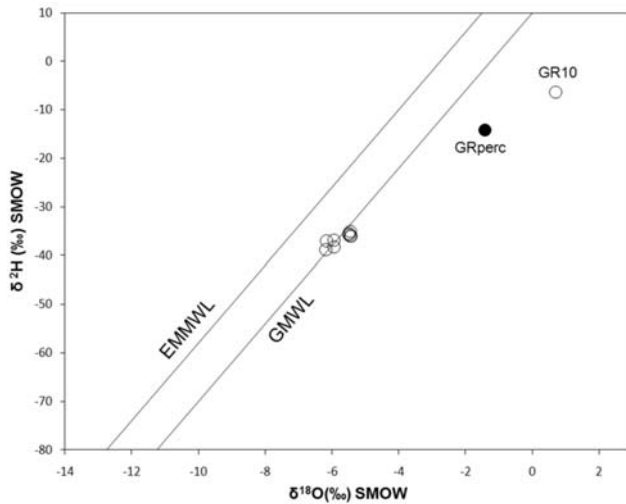
Fig. 3: δD versus δ^{18}O diagram.

Data referring to isotopic composition of waters have been interpreted with the classical δ^{2}H‰ versus δ^{18}O‰ diagram, shown in figure 3. In the same diagram are shown, as usual, the lines corresponding to the points where average isotopic compositions of waters with direct meteoric origin can be localised (in details, the "world meteoric line" and that originating from data on central Mediterranean rain (Gonfiantini, 1983; IAEA, 2007).

The results concerning sampled waters appears to be in agreement with those of the world meteoric line and with the results of some measurements on regional waters carried out during a previous study (Grassi et al., 1996). This area, compared to others at higher altitude or affected by mountainous barriers, produces isotopic compositions more aligned along the world meteoric line rather than on the Mediterranean one. The deepest sample (GR2, -90m) shows slightly lower isotopic values but similar results can be observed also in GR1 (-30m) and in the more superficial well GR9 (-6,3m).

The samples GRperc (leachate) and GR10 (small open-cut sinking in the torrent which morphologically drains the waste disposal plant with evident presence of leachate), show an isotopic composition typical of local meteoric waters subject to a broad process of evaporation (IAEA, 1981). In the leachate sample (GRperc) there is no trace of δ^{2}H‰ shift towards values of higher isotopic composition and located, in the above quoted diagram, over the meteoric waters line, a shift which often characterize landfill leachate samples after the isotopic exchange with methane inside biogas.

Isotopic composition of dissolved inorganic carbon in water of GR1, 2, 3, 4, 5, 6, 7, 8 samples shows δ^{13}C(DIC)‰ values typical of superficial water streams in cultivated areas, resulting from the mixing of carbon from organic material oxidation, up to -30‰, with carbon from atmospheric CO_2 or carbonatic mineral dissolution; they both originate a δ^{13}C(DIC) close to 0‰ (Clark and Fritz, 1997) (Fig. 4). A minor superficial component is in agreement with the slightly higher value of the deep well GR2. GRperc sample is strongly enriched in ^{13}C due to the methanegenesis generating methane with low δ^{13}C values and consequent carbon isotopic enrichment in the coexisting CO_2 and therefore in the originating DIC; the same can be observed in GR10 which shows a large component of leachate. A separate consideration must be made for GR9 sample. In this superficial well down the old remediate landfill, the measured value (+3.3‰) is hardly justified in the case of a superficial well
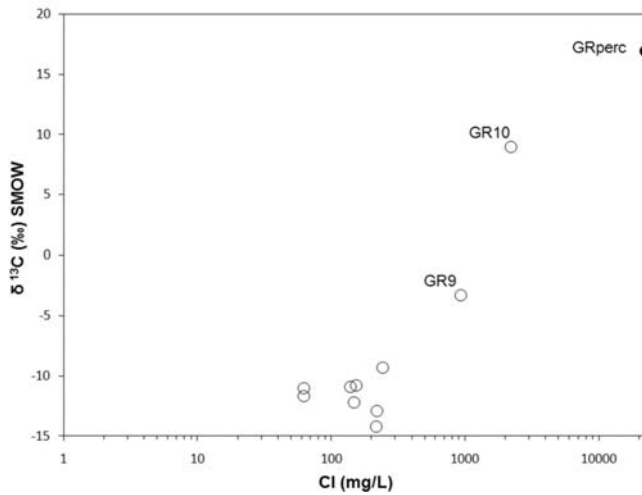
Fig. 4: $\delta^{13}C$ versus Cl diagram. The Cl content is reported in logarithmic scale.
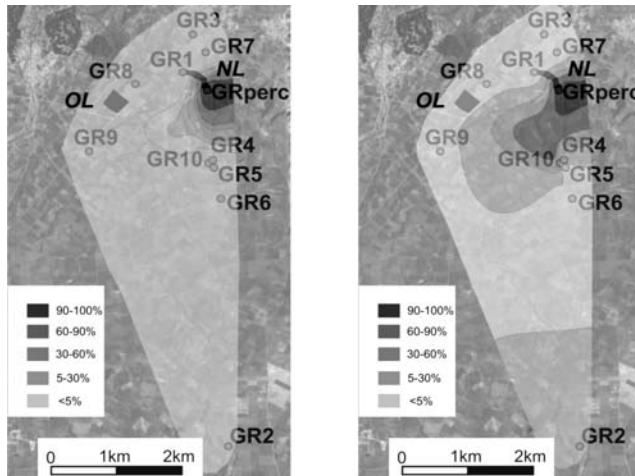
Fig. 5: Percentage of leachate contamination in waters of the region, based on Cl- (left) and B-(right) composition.

from a cultivated area, even according to what was measured in the other investigated wells. An acceptable hypothesis interprets this value as a trace of leachate coming from the old landfill.

4.3 Contamination

Based on GIS analysis, maps of the water contamination percentage regarding the Cl and B composition from leachate have been created (Fig. 5).

The study of these maps shows the percentage of participation of the polluted liquid (leachate) in the waters of the region. The contamination level of groundwaters is relatively low (<5% leachate intrusion) in distances over 1km. In the region around the leachate sampling site (circle of 300m radius) the contamination percentage increases rapidly, reaching dangerous values. Sample GR2 shows an increased level of contamination regarding some of B. The chemical measurements of the water samples render them either in the suggested limits for drinking water (EU standards, Bouwer, 1978),
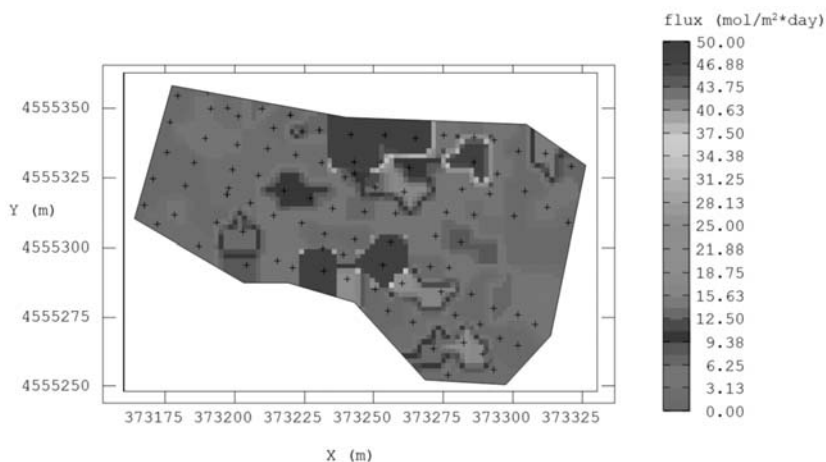
Fig. 6: Isoflux map.

(GR1, GR3, GR4, GR5, GR6, GR7, GR8) or quite above the acceptable limits (GR2, GR9, GR10, GRperc). Sample GR9 has relatively high concentrations of the selected elements, a fact that can be explained by a possible leachate contamination from the old landfill rather than by water use in the area (i.e. agriculture).

4.4 Biogas

In order to calculate the total flux of soil biogas, Sinclair's (1974; 1991) methodology and Sichel's (1966) calculations were used. Isoflux maps were produced by processing all biogas flux rate data with ISATIS, a program developed by Fontembleu School, which uses the Kriging method to extrapolate values (Clark, 1979 and relative references). Being the distribution of log-normal type the log-normal kriging was used, to build the map shown in figure 6.

5. Conclusions-Results

The procedure here described, the obtained results and their interpretation must be considered as an applicative test, already able to reveal some useful information about the environmental state of the site and also aiming to acknowledge and develop the proposed integrated approach. The chemical and isotopic composition of the leachate is in agreement with literature, except two notable differences. The first, chemical one, is that the dominant anion is the chloride, while typically the leachate is dominated by bicarbonate of ammonium; the second, isotopic one, is that the content in tritium was estimated low, showing possible dilutions of the sample. Both these observations are well explained by the young age of the landfill. An extremely important observation from the environmental point of view is the fact that the waters of the well GR9, located downstream of the old site, show a contamination from the leachate, based on the chemical parameters than isotopic. The contamination of the torrent that drains the new landfill (GR10) is obvious at any part of it. However the characterization of the leachate shows the need of a future monitoring by means of appropriate methods.

The emission of biogas in NL of Komotini, estimated as the sum of CO_2 and CH_4, resulted to 109 (168÷85 Nm3/h) with a specific flow of about 11 Nl/m2, a value rather high, but typical of landfill sites with no proper installations for the capture of the biogas. OL, closed and covered, has a low

emission, measurable only in the north slope while an important flow is present, as expected, in the chimneys of degassing.

6. Acknowledgments

7. References

Chiodini, G., Frondini, F., Raco, B., 1996. Diffuse emission of CO2 from the Fossa crater, Vulacno Island (Italy). *Bull. Volcanol.*, 58, 41-50.

Chiodini, G., Cioni, R., Guidi, M., Marini, L., Raco, B., 1998. Soil CO2 flux measurements in volcanic and geothermal areas. *Applied Geochemistry*, 13, 543-552.

Clark, I., 1979. *Practical Geostatistics*, Department of Mineral Resources Engineering, Royal School of Mines, Imperial College of Science and Technology, London, 129pp.

Clark, I., Fritz, P., 1997. *Environmental Isotopes In Hydrogeology*. Lewis Publishers, CRC Press, Boca Raton - New York, 328pp.

Cossu, R., Muntoni, A., Chiarantini, L., Massacci, G., Serra, P., Scolletta, A., Sterzi, G., 1997. Biogas emissions measurements using static and dynamic flux chambers and infrared method, Proceedings Sardinia 97, *sixth International Landfill Symposium*, S. Margherita di Pula, Cagliari 13-17 October, CISA.

Doveri, M., Leone, G., Mussi, M., Raco, B., Tifirò, S., 2007. The value of isotopic analyses in monitoring MSW landfills impact on groundwaters. *Geoitalia 2007, Sesto Forum Italiano di Scienze della Terra*, Rimini 12-14 sett. 2007, Federazione Italiana delle Scienze della Terra: Epitome vol. 2, 2007: 380-381.

Gonfiantini, R., 1983. La composizione isotopica delle precipitazioni. *Rend. Soc. It. Min. Petrol.*, 38: 1175-1187.

Grassi, S., Kolios, N., Mussi, M., Saradeas, A., 1996. Groundwater circulation in the Nea Kessani low-temperature geothermal field (NE Greece). *Geothermics*, V. 25 n° 2:231-247.

Hackley, K. C., Liu, C. L., Coleman, D. D., 1996. Environmental isotope characteristics of landfill leachates and gases. *Ground water*, 34, 5: 827-836.

IAEA, 1981. *Stable Isotope Hydrology*, Deuterium and Oxygen-18 in the Water Cycle. Interntional Atomic Energy Agency, Vienna, pp. 337.

IAEA, 2007. http://www.iaea.org/programmes/ripc/ih/index.htm

Kanemasu, E.T., Power, W.L., Sij, J.W., 1974. Field chamber measurements of CO2 flux from soil surface. *Soil Science*, 118,4, 233-237.

Kucera, C., Kirkham, D. R., 1971. Soil respiration studies in tall grass Prairie in Missouri, *Ecology*, 52, 912 – 915.

Parkinson, K.J., 1981. An improved method for measuring soil respiration inthe field, *J. Appl. Ecology*, 18, 221-228.

Raco, B., Cioni, R., Guidi, M., Scozzari, A., Lelli, M., Lippo, G., 2005. Monitoraggio del biogas diffuso dal suolo da discariche RSU: il caso di Legoli, Peccioli, Pisa. *Rifiuti Solidi* 2005.

Sichel, H.S., 1966. The estimation of means and associated confidence limits for small samples for log-normal population, Proc. 1966 *Symp. South African Institute of Mining and Metallurgy*.

Sinclair, A.J., 1974. Selection of threshold values in geochemical data using probability graphs. *Journal*

of Geochemical Exploration, 3, 129 – 149.

Sinclair, A.J., 1991. A fundamental approach to threshold estimation in exploration geochemistry: probability plots revisited, *Journal of Geochemical Exploration*, 41, 1 – 22.

Tonani, F., Miele, G., 1991. Methods for measuring flow of carbon dioxide through soils in volcanic settimg, Napoli '91. *International Conference on Active Volcanoes and Risk Mitigation*. Napoli, 27 August-1 September. (abstract).

Trégourès, A., Beneito, A., Berne, P., Gonze, M.A., Sabroux, J.C., Savanne, D., Pokryszka, Z., Tauziède, C., Cellier, P., Laville, P., Milward, R., Arnaud, A., Levy, F., Burkhalter, R., 1999. Comparison of seven methods for measuring methane flux at a municipal solid waste landfill site. *Waste Management Research*, 17, 453 – 458.

Witkamp, M., 1969. Cycles of temperature and carbon dioxide evolution from litter and soil, *Ecology*, 50, 922 – 924.

LAND SUBSIDENCE DUE TO EXCESSIVE GROUND WATER WITHDRAWAL. A CASE STUDY FROM STAVROS - FARSALA SITE, WEST THESSALY GREECE

Rozos D.[1], Sideri D.[1], Loupasakis C.[1] and Apostolidis E.[2]

[1] *National Technical University of Athens, School of Mining and Metallurgical Engineering, Laboratory of Engineering Geology and Hydrogeology, 9, Heroon Polytechniou Str 157 80, Zografou (Athens) Greece, rozos@metal.ntua.gr, dsideri@metal.ntua.gr, cloupasakis@metal.ntua.gr*

[2] *Institute of Geology and Mineral Exploration, Engineering Geology Department, Sp Louis Str. 1, Olympic Village, 136 77 Acharnae, Athens, Greece, emmapost@ath.forthnet.gr*

Abstract

Land subsidence manifestation due to ground-water overexploitation in the Stavros – Farsala site (eastern part of Western Thessaly Basin) has been noticed since 1990. Because of this overexploitation, an excessive drawdown of the ground water level (20 to 40m) was noticed in the various successive aquifers the last decades. The subsidence phenomena resulted to the formation of tensile surface ruptures, which occurred since 2002, affecting roads and buildings.

The geological environment of the study area consists of terrestrial Pleistocene deposits containing sands and gravels interbedded with clayey silt to silty clay horizons. These alternations of aquifers (permeable coarse-grained deposits) with aquitards (impermeable to low permeability strata) create a number of successive semi-confined to confined aquifer, initially artesian. This study examines the geological and the hydrogeological conditions of the wider study area, aiming to clarify their relationship with subsidence phenomena and to provide solutions for their suspension. Note that those phenomena are expected to be more incensed during the next few years.

Key words: *aquifers overexploitation, land subsidence, excessive groundwater drawdown, Thessaly Greece.*

1. Introduction

During the years, numerous studies have been conducted globally, in areas subjected to land subsidence due to the overexploitation of aquifers (Kallergis, 1971; Andronopoulos et al., 1991; Liu et al., 2004; Xue et al., 2005; Li et al., 2006; Serva & Brunamonte, 2007; Shi et al., 2007; Loupasakis & Rozos, 2009). Land subsidence, triggered by excessive groundwater drawdown and resulted from the compaction of the drained loose sedimentary formations, manifests with an increasing rate during the years. The rising needs for water leads to the over pumping of ground reservoirs causing non reversible damages to the aquifers. Thessaly plain, Kalochori village near Thessaloniki, Megalopolis in Peloponnesus, Anargiri region on the southwest of Florina and Messara valley in Crete are some of the regions affected by these phenomena.

The Stavros – Farsala study area is a part of West Thessaly basin. Thessaly basin is lowland in Central Greece, with an extent of 4,520 km², mainly drained by Pinios River. Thessaly basin is subdivided,
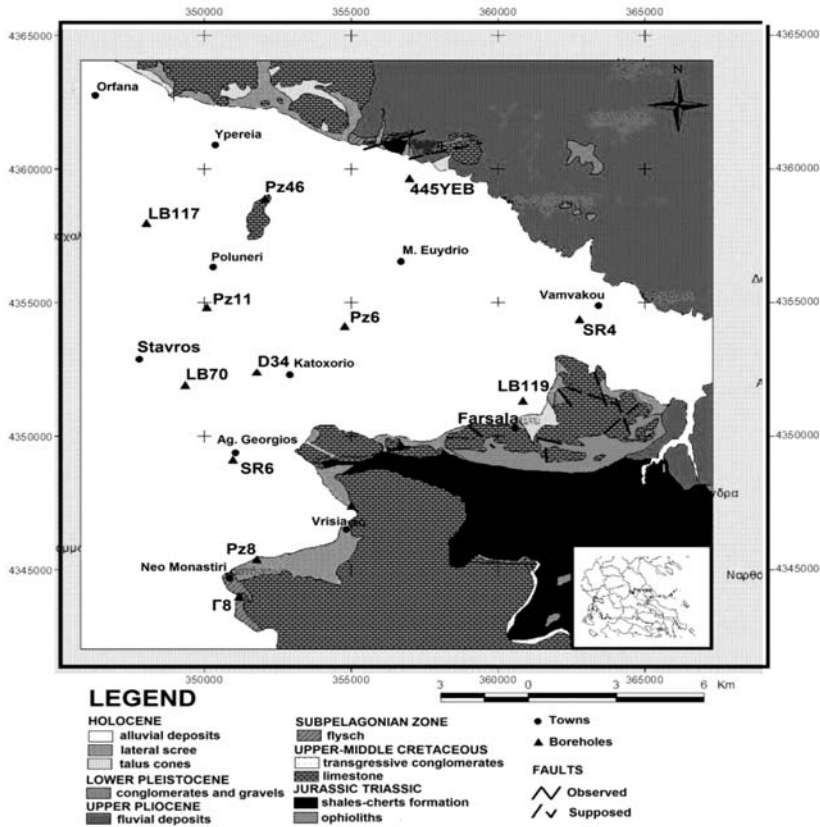
Fig. 1: Simplified geological map of Stavros – Farsala wider area. The locations of the water wells used for piezometric measurements are also presented.

by a group of hills, in two subbasins, the westerner and the Eastern. Stavros-Farsala study site is located in the eastern part of the western subbasin. These subbasins are two main individual hydrogeological units, developing high potential aquifers. The overexploitation of these aquifers led to the manifestation of extended damages due to land subsidence phenomena. This paper aims to presents the intenseness of those phenomena and to correlate them with the ground water withdrawal.

2. Geological setting

According to the geological map of Greece (IGME, 1969) and the field mapping conducted during the study, Mesozoic Alpine formations outcrop in the margins of the study area, while, post alpine deposits are presented in the lowland of the basin (Fig. 1). The Mesozoic Alpine formations belong to the Pelagonian (Subpelagonian) geotectonic zone and they constitute the bedrock of Quaternary deposits of Stavros – Farsala area. These formations consist of Schist–chert formation, Ophiolites, Limestones and Flysch sediments (Mariolakos et al., 2001; Rozos & Tzitziras, 2002).

The post-alpine deposits, some of which are related with the subsidence phenomena, include:

- Neogene deposits: Fluvial and lacustrine formations, consisting of red clayey silts and cohesiveless clayey sands with scattered gravels and pebbles of various origin and semi coherent
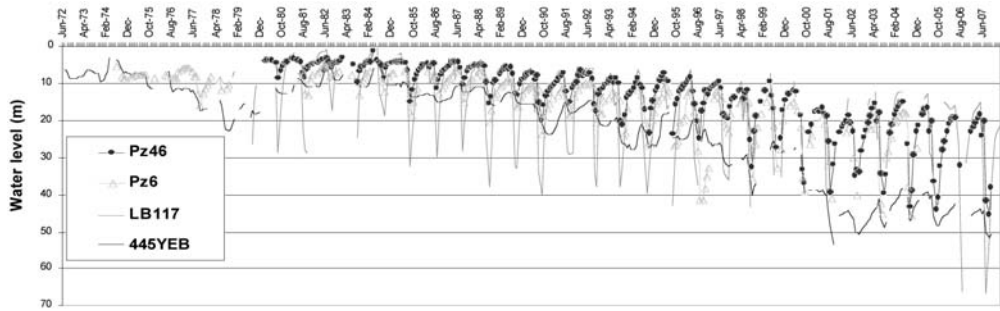
Fig. 2: Ground water table fluctuations in relation to the time in Pz46, Pz6, LB117, and 445YEB water wells.

conglomerates. The lacustrine deposits include friable gray to light gray marls in layers with a thickness of 5-20 cm, along with intercalations at places of sandstones and conglomerates (Mariolakos et al., 2001).

• Pleistocene deposits: Terrestrial formations of clayey silts, sandy silts, sandy clays and sands, with grits and gravels. These deposits appear extensive surface development at Farsala - Karditsa – Trikala basin, and gain considerable thicknesses even near the margins of that basin. Because of their lithology, they develop high potential aquifers that undergo intensive exploitation. (Rozos & Tzitziras, 2002).

• Holocene deposits: Alluvial deposits consisting of clays to sandy clays fluvial deposits of variant thickness, depending on their origin, the paleo relief, but also on the paleo climatic conditions.

3. Hydrogeological conditions

The quaternary deposits contain the main aquifers of the wider study area. The aquifers constitute a system of unconfined shallow aquifers, extending in the upper layers, and successive confined - artesian aquifers developing in the dipper permeable layers (Marinos et al, 1995; Marinos et al, 1997). This system besides the percolated surface water is also supplied by water through the lateral infiltration from the karstic aquifers of the alpine carbonate formations, outcropping in the margins of the basin. In general, the richest aquifers are developed in the western subbasin of Thessaly plain, due to their rich supply both from the big infiltrating part of the surface runoff and the lateral infiltration. The exploitable water potential of the above described system is about $400\times10^6\,\mathrm{m}^3$.

In order to study the ground water fluctuation in Stavros – Farsala region, thirteen (13) water wells were monitored from 1972 to 2007. The piezometric level monitoring data proved that during the years a sufficient drawdown of the ground water level takes place, reaching up to values of 67m (Fig. 2). It appears that even if a small recharge of aquifers takes place every year during the rainfall period, the final tendency is a stable drawdown. The mean piezometric level drawdown exceeds the 40 m and the mean annual drawdown rate was estimated to be 60 cm/year. It is noticeable that the changes of the ground water level were not caused by a corresponding reduction of the mean annual rainfalls. According to the meteorological data form three local stations, namely Farsala, Domokos and Myra, the mean annual rainfalls were nearly stable during the last thirty years, with a small exception during the period 1977 to 1984 (Fig. 3).
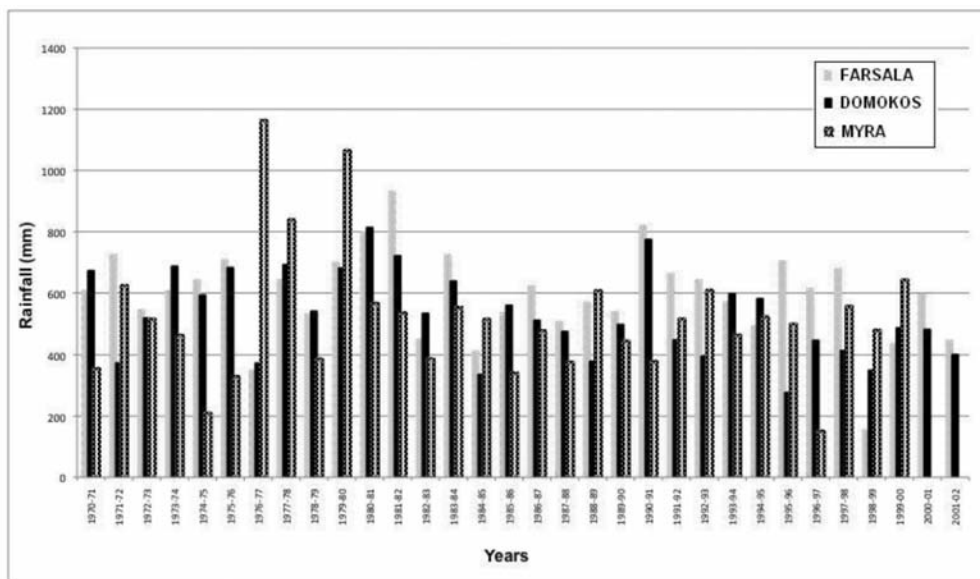
Fig. 3: Mean annual rainfall fluctuation (data from Farsala and Domokos stations of the National Meteorological Service, and Myra station of the Ministry of Agriculture).

4. Surface subsidence ruptures in Stavros – Farsala site

In the eastern part of Thessaly basin the land subsidences phenomena occurred for the first time in 1996 (Soulios, 1997; Soulios, 1980). With a time delay, in Farsala site, west Thessaly, these phenomena, with the form of surface ruptures, were firstly manifested in 2002. The overexploitation of the ground water resulted to the activation of the subsidence mechanism in the discharged aquifers and subsequently led to the manifestation of the accompanying phenomena on the surface, apart from the land depression.

Therefore, along the margins of the basin were the bedrock outcrops and generally in areas were the thickness of the deposits is small, fractures of the ground occur, as a result of the tensile forces action. On the contrary, in the parts of the basin with thick deposits the compaction of the formations can become noticeable by the extraction of the water well pipes from the ground.

Farsala city is built partly on the bedrock Alpine formations and partly on the Pleistocene deposits. The variations on the geotechnical behaviour of the foundation formations lead to the manifestation of numerous tensile fractures, in several sections of the town. Precisely, in the centre of the town, an area extending 50 m x 360 m (Fig. 4) was intensively damaged. The road pavements present multiple fractures, redisplayed afterwards any repair works. Also, several buildings, intersected by the ruptures, were intensively damaged requiring expensive reconstruction works. Small ground ruptures have been also presented in the northern part of the town in an area covering 180 m × 200 m. Also, beyond the south western limits of the town and at the west of the railway line, two more extensive ruptures were observed with total length 1,000 m and 2,500 m respectively. The northern one has a mean azimuth of about 100° and shows a vertical displacement at a rate of 20 to 50 cm. Respectively, the southern rapture, with a mean azimuth of about 110°, presents a vertical displacement of 15 to

Fig. 4: Satellite pictures (from Google Earth) pointing the location of the surface raptures along Farsala town. Pictures FA2, FA3 and FA9 show roads and buildings damaged by the surface raptures.
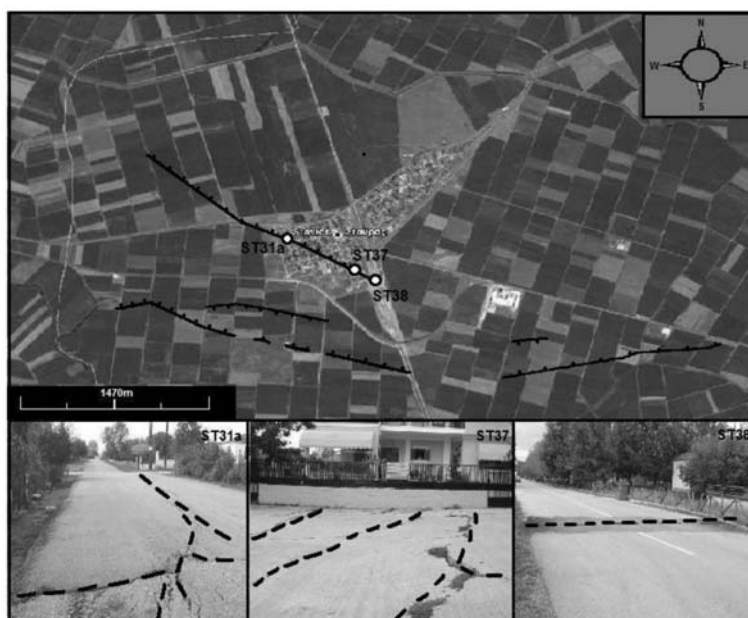
Fig. 5: Satellite pictures (from Google Earth) pointing the location of the surface raptures along Stavros town. Pictures ST31a, ST37 and ST38 present roads damaged by the surface raptures.
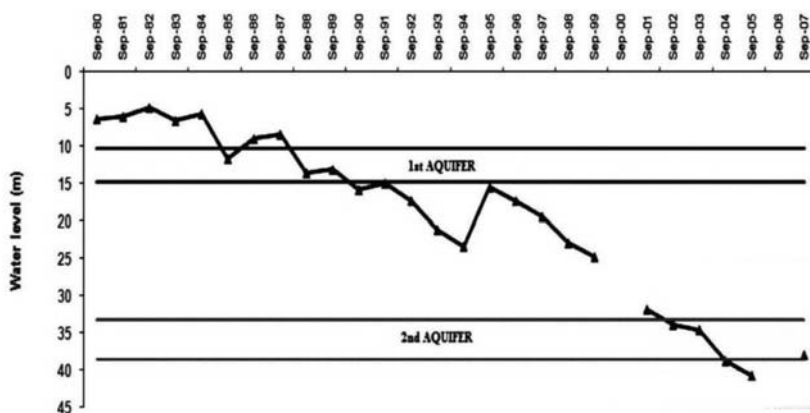
Fig. 6: Ground water table fluctuations with time in Farsala site (Pz46 borehole). The exhaustion of the first two aquifers is obvious.

150 cm (Apostolidis and Georgiou, 2007).

In Stavros small town, the main ground rupture was found westwards the railway line. This tensile rupture has a total length of about 2,100 m, an azimuth of 105° and a vertical displacement at a rate of 60 cm (Fig. 5). The trace of the rapture affects road pavements and numerous buildings (Apostolidis and Georgiou, 2007). The buildings founded along the trace of the ruptures present several damages, such as cracks in the stonework, distortions in doors, windows, stockyards and pavements. Also, several ground ruptures are located at the south of the town, intersecting cultivated areas.

5. Correlation of land subsidences with overexploitation of ground water

In order to correlate the land subsidences phenomena in the wider study area of Stavros - Farsala with the overexploitation of the aquifers, the loggings of water wells were evaluated. According to loggings from Farsala region (water well PZ6), the first aquifer is located at a depth of 10.3 m to 14.8 m, and consists of sand and gravel. The second aquifer consists of conglomerates and is located at depth 33.3 m, with a mean thickness 5.2 m. Respectively in Stavros site, the logging of water well D34 revealed that the first unconfined aquifer starts from the surface up to a depth of 2.6 m. The second confined aquifer is located at a depth from 5.6 m to 8.7 m, while a third aquifer, consisting of quaternary deposits, appears from 13.3 m to 15.8 m.

The diagram of Figure 6 correlates the water tables fluctuations in respect to time in Farsala site. It reveals that from 1984 until 2005 the ground water level was dramatically decreased. The first aquifer was completely drained, at September 1991, as the ground water level reached the depth of 15.82 m, and the second one at September 2005, as the water level reached the 38.5 m in depth. Respectively, in the case of Stavros site, the first and second aquifers were drained in September 1976 (Fig. 6). The drawdown of the ground water level kept on going until September 1978 (depth of ground water level 15.45m). Finally, at September 2001, with only a few recharges the ground water level reached the depth of 22.15m and all three aquifers were drained. The thorough examination of the data referring to ground water level and rainfall reveals that the mean annual drawdown is roughly constant for all water wells in the study area with a value of 60 cm/year.

From the above discussion it is obvious that the biggest part of the aquifers in Thessaly plain is
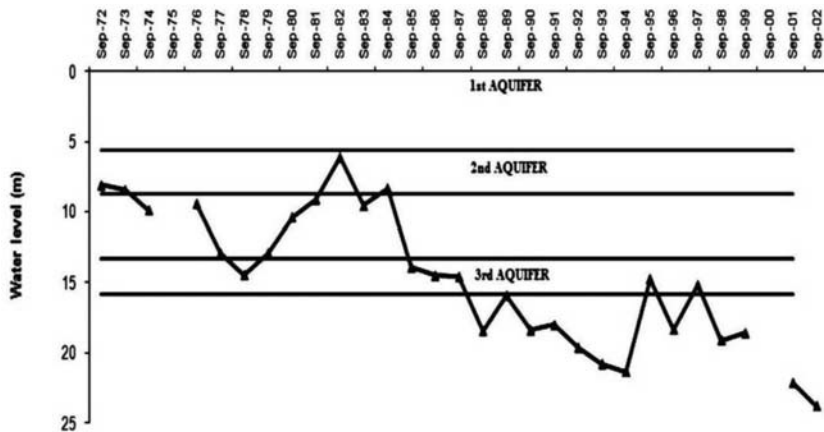
Fig. 7: Ground water table fluctuations with time in Stavros site (D34 borehole). The exhaustion of the first three aquifers is obvious.

under a status of over exploitation, following by a continuous lowering of the ground water level year by year. What differs locally is the intension of overexploitation and the time of the beginning of the ground water table lowering.

6. Conclusions-Results

The majority of the aquifers in Thessaly plain are under a regime of overexploitation, resulting in a systematic drawdown of the ground water level. In Farsala – Stavros subplain the consistent over-exploitation led to the complete draining of the overlay shallow unconfined aquifer and the progressive drawdown of the successive confined - artesian aquifers. This phenomenon resulted to the compaction of the compressible intercalated clayey horizons, and the manifestation of intensive land subsidence since 2002.

Land subsidence phenomena become visible on the margins of the basin, with the form of surface ruptures that cause failures in residences and other buildings but also in the street pavements. The geotechnical and hydrogeological parameters of deformed formations contribute to the mechanism of subsidences manifestation. The subsidence deformations, usually take place in an area with alternations of impermeable to semi-permeable compressed formations, such as silty clays to clayey silts, with permeable ones, like sandy to silty sandy horizons.

Because of the increasing need for water, especially for irrigation purposes during the summer period, the reactivation of existing ground ruptures and also the manifestation of new ones are considered to be very possible. The rational exploitation of aquifers in combination with their artificial enrichment will cause progressive increase of ground water level and suspension of the subsidence phenomenon.

7. References

Andronopoulos V., Rozos D. Hatzinakos I. I., 1991. Subsidence Phenomena in the Industrial Area of Thessaloniki-Greece. *4th International Symposium on Land Subsidence, IAHS, UNESCO, May* 12-17, 1991, Houston, Texas, USA.

Apostolidis E., Georgiou H., 2007. Engineering Geological of the surface ground ruptures in Thessalia

basin sites. Recording and, documentation. *Institute of Geology and Mineral Exploration (IGME), unpublished report (in Greek)*.

I.G.M.E., 1969. *Geological map of Greece, Farsala Sheet* (scale 1:50.000), Athens, I.G.M.E. Publications.

Kallergis G., 1971. Ground subsidences during the drawdown of artesian aquifers due to their limited elasticity (in Greek). Technika Chronika magazine, *pp*. 599-602. Athens.

Kallergis G., 1973. Hydrogeological study in sub-basin of Kalampaka (Western Thessaly). *Institute of Geology and Mineral Exploration (IGME), unpublished report (in Greek)*, vol. XIV, No 1, Athens.

Li C., Tang X., Ma T., 2006. Land subsidence caused by groundwater exploitation in the Hangzhou-Jiaxing-Huzhou Plain, China, *Hydrogeology Journal 14:1652-1665*.

Liu C., Pan Y., Liao J., Huang C., Ouyang S., 2004. Characterization of Land Subsidence in the Choshui River alluvial fan, Taiwan, *Environmental Geology 45:1154-1166*.

Loupasakis C., Rozos D., 2009. Land Subsidence Induced by Water Pumping in Kalochori Village (North Greece) - Simulation of the Phenomenon by Means of the Finite Element Method. *Quarterly Journal of Engineering Geology and Hydrogeology, Geological Society of London*, 42, pp. 369-382.

Marinos P., Thanos M., Perleros V., Kavadas M., 1995. Water dynamic of Thessaly basin and the consequences from its overexploitation. *Proceedings of the 3rd Hydrogeological Congress (in Greek), Heraklion Crete*.

Marinos P., Perleros V., Kavadas M., 1997. Deposited and karsic aquifers of Thessaly plain. New data for the status of their overexploitation. *Proceedings of the 4th Hydrogeological Congress (in Greek). Athens*.

Mariolakos H., Lekkas S., Papadopoulos T., Alexopoulos A., Spyridonos E., Mandekas I., Andreadakis E., 2001. Underground tectonic structure in Farsala plain (Thessaly) as a determinative factor of the formation of the hydrogeological conditions of the area. *Proceedings of the* 9th *Congress of Greek Geological Society (in Greek)*.

Rozos D., Tzitziras A., 2002. Report of the Engineering geological examination of ground water in Farsala area. *Institute of Geology and Mineral Exploration (IGME).Unpublished report (in Greek)*.

Rozos D., 2007. Landslides, Subsidences and Settlement in textbook of Engineering Geology I. 352pp (in Greek). *Lab. of Eng. Geology and Hydrology, School of Mining and Metallurgical Engineering, NTUA, Athens*.

Serva L., Brunamonte F., 2006. Subsidence in the Potina Plain, Italy, *Bull Eng Geol Env 66:125-134*.

Shi X., Xue Y., Wu Z., Ye S., Zhang Y., Wei Z., Yu Z., 2007. Characterization of regional land subsidence in Yangtze Delta, China: the example of Su-Xi-Chang area in the city of Shanghai, *Hydrogeology Journal 16:593-607*.

Soulios G., 1997. Subsidence de terrains alluviaux dans le sud-est de la plaine de Thessalie, Grèce. *Proceedings International Symposium on Engineering Geology and the Environment. Balkema, Rotterdam*.

Soulios G., 1980. Subsidences of recent deposits due to pumping of underneath aquifers An example from Greek territory. *Technika Chronika magazine, Athens*.

Xue Y., Zhang Y., Ye S., Wu Z., Li Q., 2005. Land subsidence in China. *Environmental. Geology 48:713-720*.

GROUNDWATER QUALITY OF THE HYDROLOGICAL BASIN OF AMYROS RIVER, AGIA AREA THESSALY, GREECE

Skordas K.[1], Tziritis E.[2], and Kelepertsis A.[2]

[1] School of Agricultural Sciences, Department of Ichthyology and Aquatic Environment, University of Thessaly, Fitokou Str., N. Ionia, Volos, 38446 Greece. kskord@uth.gr

[2] Faculty of Geology, Section of Economic Geology and Geochemistry, University of Athens, Panepistimioupolis, Ano Ilisia, 15784, Greece. evtziritis@geol.uoa.gr, kelepertsis@geol.uoa.gr

Abstract

The area of Agia (Thessaly, Central Greece) is a highly cultivated region, whose hydrogeochemical status is influenced both by natural and manmade factors. Chemical analyses of 40 groundwater samples from the examined area, revealed that geology has a significant impact to aquifers chemistry, mainly expressed through the presence of carbonate rocks and evaporitic minerals of the Neogene formations of the area., as well as the ultrabasic rocks of the substrate. The manmade influence is assessed through the elevated values of nitrates (values up to 168,7 mg/L). Furthermore, the analytical results of the groundwaters revealed that NO_3^-, Fe and Se, in several samples, exceeded the EC and SMCL (USEPA) limits. More specifically, the 20% of NO_3^- samples exceeded the EC limits as well as the 2,5% of Se in samples. The 2,5% of Fe in samples exceeded both the EC and SMCL (USEPA) limits.

Key words: hydrogeochemistry, environment, risk assessment, Agia area, Thessaly.

1. Introduction

The hydrogeochemistry of natural waters is mainly influenced by the chemical composition of the predominant geological formations of a hydrological basin. The specific hydrogeochemical characteristics depend on the chemistry of rock-forming minerals including metal sulfide minerals such as pyrite FeS_2. The physical process of erosion creates favourable conditions for mineral dissolution, that leads to enrichment of ions, metals or metalloids, which often tend to reach hazardous concentrations in terms of toxicity for the natural or mankind environment (Alexakis and Kelepertsis 1998; Vardaki and Kelepertsis 1999; Kelepertsis et al. 2001; Robinson and Ayotte, 2006; Negrel 2006; Lang et al., 2006, Tziritis et al., 2008). According to Kelepertsis et al. (2006b), elevated concentrations of As and Sb were detected in natural waters of Eastern Thessaly, a fact which has been mainly attributed to the occurring sulfide mineralization of the area (arsenopyrite, orpiment realgar, etc.).

Moreover, physicochemical (temperature, pH, Eh) and biological parameters (microbial catalysis), as well as other geochemical processes (adsorption, ion-exchange, complexation etc) have a great impact to ground and surface waters, affecting either direct or indirect their quality status (Kelepertsis, 2000; Siegel, 2002). Other factors, such as rainwater or climatic conditions seem to affect water chemistry, but only in specific cases, were favorable conditions occurring. Apart from natural factors of enrichment, mankind effect seems to be dominant in many regions, especially in sites of agri-

cultural, industrial and mining activities (Shivkumar et al. 1997; Kabata – Pendias and Pendias, 1999; Kabata – Pendias, 2001; Djabri et al., 2003, Tziritis, 2009).

The study area (Amyros river Basin) is situated in the Prefecture of Larissa, Eastern Thessaly, Central Greece, about 400 km northern of Athens. The basin extends in an E-W direction between latitudes 39° 041'00'' – 39° 045'00'' and longitudes 22° 041'00'' -22° 047'00''. Relief is smooth with low hills and cultivated areas of apple and cherry trees, surrounded by the mountains of Kissavos and Maurovouni.

The scope of the present research aims to:

1) Research and define the spatial distribution of heavy metals and metalloids in natural waters of Agia region, Thessally.

2) Define the relation between geology and groundwaters.

3) Assess the level of potential pollution in terms of potability regarding the EC Directive and determine the pollution sources.

2. Geological setting

The alpine substrate of the basin (Fig.1) (Greek Pelagonian zone) is consisted from bottom to top of (Katsikatos,; Migiros 1983; IGME 1981 and 1984):

• Paleozoic (Pre-Carboniferous) crystalline basement of the Pelagonianzone. It includes gneiss-schists, amphibolite schists and amphibolites.

• Neopaleozoic – Lower Mesotriassic formations. They include a variety of metamorphic rocks of sedimentary origin and coarse-grained marble and cipolines .

• Middle Upper Cretaceous – Upper Jurassic marbles.

• Pre-Upper Cretaceous tectonic cover. It is wholly metamorphosed with a thickness of 1000m. It includes a variety of formations and an ophiolitic complex.

• Marbles of Agia (Upper Cretaceous).

• Neogene sediments: composed of marly limestones, marls and conglomerates.

• Quaternary sediments: consisting of unconsolidated material with sand and rounded and angular pebbles in the torrent beds and alluvial sediments.

In the southeastern part of the studied area there are many small occurrences of iron oxides-hydroxides with copper and antimony arsenic mineralization Kelepertsis et al. (2006b). Copper occurs as malachite $[Cu_2(CO_3)(OH)_2]$, antimony as stibnite (SbS_3) and arsenic as arsenopyrite $(FeAsS)$. There are also outcrops of manganese oxides. All the above ore occurrences are found within the metamorphic rocks of the basement and the ophiolitic bodies (Migiros 1993). No mining activity has been reported in the whole mineralised area, although some of the ore deposits may show an economic interest.

In general, in the wider area of Agia the predominant geology is dominated by the existence of the Pelagonian zone, as it has been already mentioned, especially in the southern, northern and northeastern parts of mountain Ossa, where there are developed the Upper-Cretaceous formations of the tectonic nappe (mainly serpentinites, metamorphic basic and ultrabasic rocks and secondary marbles). The aforementioned tectonic nappe is characterized by intense tectonism which created sec-
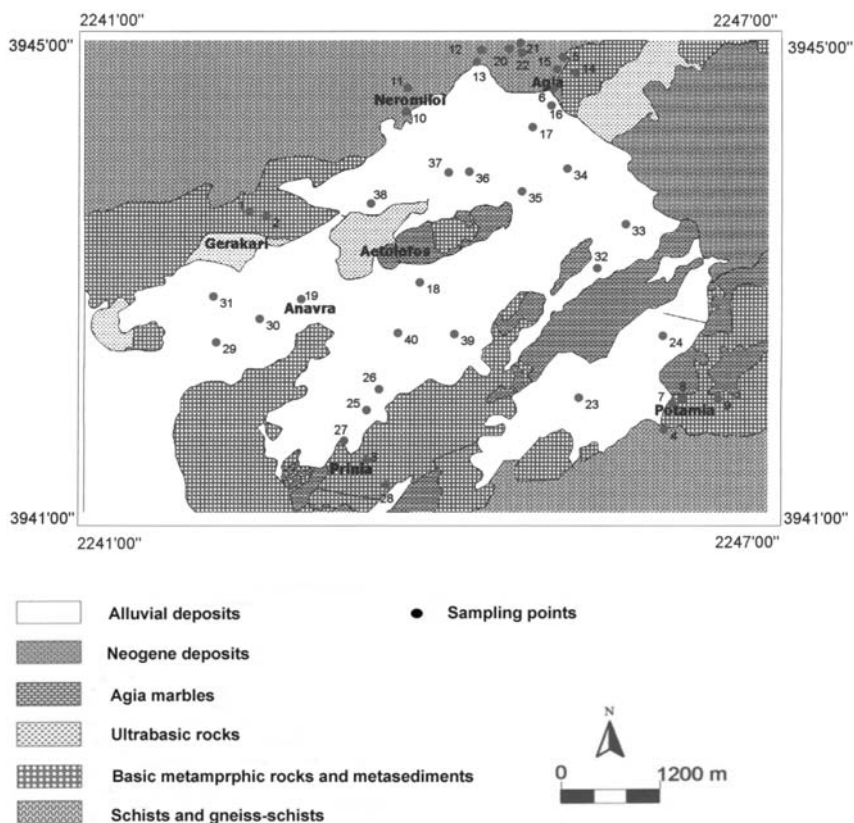
Fig. 1: Sites of groundwater samples and geological map of the area.

ondary tectonic fractions and a vast number of mylonitized zones. The above fact poses favorable conditions for water flow, and the permeability of these formations seems to be elevated. In this hydrogeological system it can be also added the aquifer of the karstified marbles. These aquifers impose the deeper hydrogeological system of the tectonic nappe. Apart form this deeper system, in the area Agia basin there are developed clastic fluvial formations, whose permeability vary, both vertical and horizontal. These clastic formations compile the upper hydrogeological system, which is quite inhomogeneous and frequently develop local aquifers with different hydrogeological properties.

3. Materials and methods

3.1 Sampling and analysis

Totally forty groundwater samples were collected during field work (Januray-March 2006) from all the available boreholes and springs, covering an area of 65km^2 (Fig. 1). During sampling, all necessary precautions were taken in order to avoid any possible contamination. Totally 27 parameters were determined (Table 1), including major ions (Ca^{2+}, Mg^{2+}, K^+, Na^+, Cl^-, NO_3^-, SO_4^{2-} and HCO_3^-) and trace elements (B, Ba, Br, Cr, Cu, Fe, Li, Mn, Ni, P, Pb, Se, Si, Sr, U and Zn). Samples were vacuum filtered through a 0,45 μm pore size membrane, acidified to a final concentration of about 1% nitric acid and then stored in a polyethylene container in order to be analyzed. Major anions were

Table 1. Results of chemical analyses for the analyzed parameters of the 40 groundwater samples and risk-based parametric values.

	Mean	Minimum	Maximum	Parametric value (EC[a])	MCL (USEPA[b])	SMCL (USEPA[b])
$Ca^{++}(\mu g\,l^{-1})$	83.596	32.570	180.800	None	None	None
$Mg^{++}(\mu g\,l^{-1})$	24.230	7.660	58.480	None	None	None
$K^+ (\mu g\,l^{-1})$	1.875	910	3.540	12.000	None	None
$Na^+ (\mu g\,l^{-1})$	11.522	3.380	24.980	200.000	None	None
$HCO_3^-(\mu g\,l^{-1})$	308.777	145.070	483.900	None	None	None
$NO_3^- (\mu g\,l^{-1})$	32.450	1290	168.700	50.000	None	None
$SO_4^-(\mu g\,l^{-1})$	33.603	8.810	148.700	250.000	None	250.000
$Cl^-(\mu g\,l^{-1})$	14.275	4990	33.240	250.000	None	250.000
$B (\mu g\,l^{-1})$	25	7	76	1.000	None	None
$Ba (\mu g\,l^{-1})$	13	3	34	None	2.000	None
$Br (\mu g\,l^{-1})$	420	17	4.561	None	None	None
$Cr (\mu g\,l^{-1})$	5	0	26	50	100	None
$Cu(\mu g\,l^{-1})$	3	0	27	2.000	None	1.000
$Fe (\mu g\,l^{-1})$	65	0	1.143	200	None	300
$Li (\mu g\,l^{-1})$	3	0	6	None	None	None
$Mn (\mu g\,l^{-1})$	6	0	123	50	None	50
$Ni (\mu g\,l^{-1})$	1	0	9	20	None	None
$P (\mu g\,l^{-1})$	50	20	146	None	None	None
$Pb(\mu g\,l^{-1})$	1	0	1	10	15	None
$Se (\mu g\,l^{-1})$	2	0	19	10	50	None
$Si (\mu g\,l^{-1})$	9.210	4.881	16.205	None	None	None
$Sr (\mu g\,l^{-1})$	196	48	575	None	None	None
$U (\mu g\,l^{-1})$	1	0	9	None	None	None
$Zn (\mu g\,l^{-1})$	18	3	147	None	None	5.000

NA: not applicable

measured photometrically using attach DR/4000 apparatus (except HCO_3^- which were measured with titration), while the rest of the parameters (major cations and trace elements) were analyzed by Inductively Coupled Plasma Mass Spectroscopy (ICP/MS). Data quality was assured by introduction of internal reference samples and by analyzing duplicates of 10 samples. The precision was calculated and found between the international standards.

3.2 Statistical analysis

The data obtained from chemical analyses was statistically processed, in order to extract potential correlations between the examined parameters and the relevant natural or manmade processes. For this purpose, correlation and R-mode factor analysis were performed. In correlation analysis, the possible linkage between two single variables was assessed with the estimation of correlation coefficient (Pearson Correlation Coefficient - r). Values close to 1 state absolute (high) correlation while the sign denotes if it is proportional or not (Drever 1997). Results are shown on Table 2.

On the other hand, R-Mode Factor Analysis is a technique of management, simplification, and assessment of data bases, in order to extract and grade correlations between parameters and to specify their contribution into a common polyparametric process. The basic aim is to specify individual factors, few in number, which will explain the variation of a large number of variables and data (Kelepertzis et al. 2006; Panda 2006). Initial data has been standardized in order to eliminate the influence from different units. Principal Components Analysis (Davis 1984) was performed as an extraction technique, because it explains properly the extracted results, even in cases of non-normal distribution of initial data input (Brown, 1998). Finally, factor loadings were optimized with Varimax rotation method. Results are shown on Table 3.

4. Geochemical results and discussion

The results of chemical analyses were compared with the upper acceptable limits of the 98/83/EU Directive (EC 1998) and the maximum contaminant levels as well as the secondary maximum contaminant levels of EPA (EPA 2001) for drinking water. The mean values of all the analyzed parameters do not exceed as much the EC limits (1998) as the EPA limits (2001). There is an exception concerning the maximum fluctuation values for NO_3^- (1290-168700 µg l^{-1}), Fe (0-1143 µg l^{-1}), Mn (0-123 µg l^{-1}) and Se (0-19 µg l^{-1}). According to the chemical analyses there is an excess of the critical levels in 11 groundwater samples in Agia, Thessaly area. Contamination of NO_3^- (sampling sites A2, A23, A25, A26, A27, A30, A31, A38), Fe (sampling sites A8), Mn (sampling sites A32), Se (sampling sites A13) over the risk-based drinking water criteria given by the EC (1998) and EPA (2001) of the Agia Thessaly groundwaters was observed. The percentages (%) of the total groundwater samples, which exceed the critical levels of EC (1998), are as follows: 20% of the samples for NO_3^-, 2,5% for Fe, 2,5% for Mn and 2,5% for Se, while, regarding the critical levels of EPA (SMCL), is 2,5% for Fe and 2,5% for Mn.

The areas with high values of NO_3^-, that exceed as much the critical levels of EC (1998) as well as the levels of EPA (2001), are those where the boreholes are found in direct geological relation with the basic metamorphic rocks and metasediments of the Pre-Upper Cretaceous tectonic nappe and are presented in the studied area as follows: (Gerakari, Prinia west part sampling sites A2, A25, A26, A27, A30, A31, A38 and Potamia southeast part sampling sites A23). Regarding the Fe, Mn, Se, only in one sample of each element (sampling A8, A32, A13 respectively) the values exceed the critical levels of EPA (SMCL).

Table 2 shows that the parameters Ca^{2+}, Mg^{2+}, K^+, Na^+, HCO_3^-, NO_3^-, SO_4^{2-}, Cl^-, B and Sr are inter-correlated and associated with the carbonate-Neogene rocks of the area such as the Cretaceous limestones and marls, and also with the evaporitic minerals of the Neogene formations. Another important fact is the strong correlation between Br and Se (r = + 0,95) and this should be attributed to manmade origin due to pesticide sprayings in the broader cultivated area.

Principal component factor analysis with a varimax rotation was applied to the data in order to cre-

Table 2. Correlation coefficient matrix from Agia for the parameters of the analyzed groundwater samples.

	Ca^{2+}	Mg^{2+}	K$^+$	Na$^+$	HCO$_3^-$	NO$_3^-$	SO$_4^{2-}$	Cl$^-$	B	Ba	Br	Cr	Cu	Fe	Li	Mn	Ni	P	Pb	Se	Si	Sr	U	Zn
Ca^{2+}	1																							
Mg^{2+}	0,68	1																						
K$^+$	0,38	0,44	1																					
Na$^+$	0,55	**0,78**	0,40	1																				
HCO$_3^-$	**0,75**	**0,77**	0,31	**0,73**	1																			
NO$_3^-$	**0,75**	**0,71**	0,33	0,44	0,39	1																		
SO$_4^{2-}$	**0,77**	0,67	0,52	0,55	0,41	**0,78**	1																	
Cl$^-$	**0,77**	**0,88**	0,50	**0,79**	**0,70**	**0,80**	**0,73**	1																
B	0,61	**0,80**	0,43	0,59	0,49	**0,72**	**0,75**	**0,79**	1															
Ba	0,15	0,28	0,49	0,27	0,10	0,11	0,37	0,20	0,31	1														
Br	-0,27	-0,23	-0,20	-0,15	-0,21	-0,24	-0,19	-0,30	-0,31	-0,23	1													
Cr	0,43	0,55	0,34	0,15	0,30	0,55	0,46	0,38	0,62	0,29	-0,21	1												
Cu	0,04	0,39	-0,03	0,68	0,44	0,01	-0,04	0,32	0,23	-0,08	0,02	-0,14	1											
Fe	-0,16	-0,13	-0,05	0,08	-0,06	-0,19	-0,16	-0,14	-0,19	0,06	0,17	-0,15	0,20	1										
Li	0,35	0,65	0,21	0,65	0,61	0,23	0,35	0,56	0,59	0,31	-0,18	0,11	0,44	-0,06	1									
Mn	0,16	0,12	0,39	0,27	0,12	-0,12	0,41	0,18	0,16	0,42	-0,05	-0,13	-0,06	-0,03	0,19	1								
Ni	0,07	0,25	0,44	0,05	0,24	-0,08	0,10	0,10	0,19	0,38	-0,13	0,52	-0,08	-0,01	0,07	0,37	1							
P	0,34	0,39	0,55	0,16	0,16	0,40	0,43	0,38	0,52	0,27	-0,37	0,52	-0,16	-0,13	0,06	0,08	0,12	1						
Pb	-0,35	-0,21	-0,06	-0,03	-0,31	-0,25	-0,10	-0,20	-0,03	0,17	0,03	-0,15	0,17	0,32	-0,12	0,17	0,05	-0,01	1					
Se	-0,25	-0,20	-0,17	-0,10	-0,20	-0,24	-0,11	-0,26	-0,26	-0,21	**0,95**	-0,25	0,02	0,16	-0,14	0,06	-0,10	-0,37	0,07	1				
Si	0,44	**0,73**	0,37	0,42	0,58	0,49	0,32	0,59	0,60	0,22	-0,34	0,65	0,12	-0,18	0,44	-0,12	0,30	0,52	-0,29	-0,38	1			
Sr	**0,79**	**0,85**	0,49	0,68	0,61	**0,81**	**0,88**	**0,82**	**0,83**	0,37	-0,19	0,51	0,11	-0,16	0,51	0,20	0,07	0,47	-0,18	-0,14	0,56	1		
U	0,25	0,19	0,15	0,25	0,27	-0,01	0,28	0,15	0,20	0,39	-0,14	-0,06	-0,20	-0,03	0,58	0,41	0,06	-0,04	-0,06	-0,09	-0,03	0,32	1	
Zn	0,08	0,11	0,11	0,20	0,08	0,10	0,07	0,09	0,06	0,18	0,03	-0,02	0,20	**0,90**	0,04	-0,01	-0,02	0,11	0,28	0,02	0,04	0,14	0,10	1

Table 3. Varimax rotated factor loadings and percentage of variance for the 5 extracted factors of the analyzed groundwater samples.

Variable	Factor 1	Factor 2	Factor 3	Factor 4	Factor 5
Ca^{2+}	0,85				
Mg^{2+}	0,79	0,50			
K^+	0,52				
Na^+	0,64	0,65			
HCO_3^-	0,56	0,61			
NO_3^-	0,88				
SO_4^{2-}	0,94				
Cl^-	0,66				
B	0,78				
Ba					0,59
Br				-0,78	
Cr				0,52	
Cu		0,84			
Fe			0,57		
Li		0,61			0,49
Mn					0,67
Ni				0,39	
P				0,57	
Pb			0,58		
Se				-0,81	
Si				0,62	
Sr	0,93				
U					0,80
Zn			0,68		
% Variance	**29.5**	**12,1**	**10,8**	**8.1**	**6,5**

ate factors each representing a cluster of interrelated variables within data set. The proportion of the variance explained by five factors the rotated factor loadings and the communality are presented in Table 3. In the present study, the element distribution in the groundwater samples of the Agia area is explained through five factors, which interpret the 67% of the total variance of the data set. The first factor explains the 29,5% of the total variance, with high positive factor loadings the parameters of Ca^{2+}, Mg^{2+}, K^+, Na^+, HCO_3^-, NO_3^-, SO_4^{2-}, Cl^-, B, Sr. This factor interprets the impact of the carbonate rocks and the evaporitic minerals of the Neogene formations in the area. The second factor explains the 12,1% of the total variance and as the parameters of Na^+, HCO_3^-, Cu and Li with high positive factor loadings (0,61 to 0,84). This factor possibly reflects the anthropogenic impact which is associated with phosphate fertilizers. The third factor explains the 10,8% of the total variance and includes as the parameters of Fe, Pb and Zn with medium factor loadings and explains the co-pre-

cipitation of Pb and Zn with Fe oxides. The fourth factor explains 8,1% of the total variance and shows positive loadings for Cr, Ni, P, Si and negative for Br and Se. Table 3 shows highly negative factor loadings for the parameters Br and Se and interprets the various sprayings with pesticides that take place in the cultivated fields of the studied area. We can also assess that the parameters of Cr, Ni, U, Li present positive factor loadings that emanate from the ultrabasic rocks of the area. Finally, the fifth factor explains the 6,5% of the total variance, and consists the parameters of Ba, Mn, U, Li which are associated with the weathering process of schists and micaschists of the metamorphic substrate.

5. Conclusions

The area of Agia (Thessaly, Central Greece) is a highly cultivated region, whose hydrogeochemical status is influenced both by natural and manmade factors. Chemical analyses of 40 groundwater samples from the examined area, revealed that geology has a significant impact to aquifers chemistry, mainly expressed through the presence of carbonate rocks and evaporitic minerals of the Neogene formations of the area., as well as the ultrabasic rocks of the substrate. The manmade influence is assessed through the elevated values of nitrates (values up to 168,7 mg/L. As far as the risk assessment for the manmade environment is concerned, the analytical results revealed that NO_3^-, Fe and Se, in several samples, exceeded the EC and SMCL (USEPA) limits. More specifically, the 20% of NO_3^- samples exceeded the EC limits, posing a direct threat to manmade environment. Furthermore the 2,5% of Se in samples, also exceeded the highest parametric levels. The 2,5% of Fe in samples exceeded both the EC and SMCL (USEPA) limits. Factor analysis grouped the elements in five factors. These factors interpret the main processes that affect the hydrogeochemical variance of aquifers. The five factors explained the 67% of the total variance. The first factor reflects the presence of carbonate rocks and evaporitic minerals of the Neogene formations of the area, and is related to the elements Ca^{2+}, Mg^{2+}, K^+, Na^+, HCO_3^-, NO_3^-, SO_4^{2-}, Cl^-, B, Sr,. The second factor with positive loadings for the parameters of Na^+, HCO_3^-, Cu and Li explains their anthropogenic origin, which owed to the fertilization that take place in the cultures of the studied area. The third factor includes the elements Fe, Pb and Zn and reflects the co-precipitation of Pb and Zn with Fe oxides, while the fourth interprets the presence of ultrabasic rocks in the studied area. Finally, the fifth factor includes the elements Ba, Mn, U, Li, which are associated with the weathering products of schists and micaschists. Conclusively, the hydrogeochemical status of Agia aquifers is majorly influenced by both anthropogenic and natural factors. The above factors in general se good quality conditions for the uses of groundwater, except few samples, where the concentration of nitrates exceeds the upper limits of potability, as they are set by EU.

6. References

Alexakis, D. and Kelepertsis, A.,(1998); The relationship between the chemical composition-quality of groundwaters and the geological environment in the East Attiki area, Greece. *Mineral Wealth*, Vol.109, pp. 9-20.

Angino, E. E., 1983: Geochemistry and water quality. In "Applied Environmental Geochemistry". London Academy Press, Thorton I. (Ed).p.171-199.

Brown C.E. (1998) Applied multivariate statistics in geohydrology and related sciences. Springer-Verlag, Berlin.

Davis J. (1984) Statistics and data Analysis in Geology. 2nd ed. Wiley, New York, pp.646.

Djabri, L., Hani, A., Laouar, R., Mania, J., Mudry, J., Louhi, A., 2003: Potential pollution of groundwa-

ter in the valley of the Seybouse River, North- Eastern Algeria. Environ.Geol. 44: 738-744.

Drever J. (1997) The geochemistry of natural waters: Surface and groundwater environments. Prentice-Hall, 3rd ed., p.436.

E.E.C. 1998. Council Directive (98/83/EC) of 3 November 1998 on the quality of water intended for human consumption. Offic J Eur Commun, L 330.

E.P.A. (Environmental Protection Agency), 2001. National Primary and Secondary Drinking Water Standards. Rules and Regulations Federal Register, Vol. 66, No. 14.

Harmon, H. 1976: Modern factor analysis, 3rd edn. University of Chicago Press, Chicago.

IGME. AYIA-PANAYIA AYIAS SHEET. 1984: Geological Map 1:50000, Department of Geological Maps of IGME, Athens, Greece.

IGME. PLATYCAMPOS SHEET. 1981: Geological Map 1:50000, Department of Geological Maps of IGME, Athens, Greece.

Kabata – Pendias A. 2001: Trace Elements in Soils and Plants, Thrird Edition, CRC Press, Boca Raton London New York Washington, D.C. pp. 413.

Kabata – Pendias A. and Pendias, H. 1999; Biogeochemistry of Trace Elements, 2nd ed., Wyd. Nauk PWN, Warsaw, 1999, 400 (PO).

Katsikatos, G., Migiros, G. and Vidakis, M. 1980: Remarks on the geology of the area between Mavrovouni and Olympus (Greece). *26e Congres-Geologique Internationale*, Paris, III, 1391 (Abstract).

Katsikatos, G., Migiros, G. and Vidakis, M. 1982: La structure geologique de la region de la Thessalie oriental (Grece). *Ann. Soc. Geol. Nord*, *CI*, 177-188.

Kelepertsis, A. 2000: Applied Geochemistry, Macedonian Publications, Greece.

Kelepertsis, A., Alexakis, D., Kita, I. (2001); Environmental geochemistry of oils and waters of Susaki area, Korinthos, Greece. *Environ Geochem and Health* 23: 117-135.

Kelepertsis, A., Alexakis, D., Skordas, K.,(2006b); Arsenic, antimony and other toxic elements in the drinking water of Eastern Thessaly in Greece and its possible effects on human health. *Environ Geol.,* 50, pp.76-84.

Lang, Y.C., Liu,C.Q., Zhao, Z.Q., Li, S.L. and Han, G.L. 2006:Geochemistry of surface and ground water in Guiyang, China: Water/rocks interaction and pollution in a Karst hydrological system. *Applied Geochem* 21: 887-903.

Martin,H., 1968: Pesticide manual, British Crop Protection Council, Martin, H., Ed., 1968, 464.

Migiros, G. 1983: Γεωλογική μελέτη περιοχής Κάτω Ολύμπου Θεσσαλίας. Διδακτορική διατριβή, Πανεπιστήμιο Πατρών.

Migiros, G. 1993: Mineral deposits of the Agia area. Institute of Geology and Mineral Exploration, Athens, Greece. Internal Report.

Negrel, P. 2006; Water-granite interaction: Clues from strontium, neodymium and rare earth elements in soil and water. *Applied Geochem* 21:1432-1454.

Panda U.C., Sundaray S.K., Rath P., Nayak B.B., Bhatta D. (2006) Application of factor and cluster analysis for characterization of river and estuarine water systems – A case study: Mahanadi River (India). Journal of Hydrology, vol.331, p.434-445Alexakis, D. and Kelepertsis, A.,(1998); The relationship between the chemical composition-quality of groundwaters and the geological environment in the East Attiki area, Greece. *Mineral Wealth*, 109, pp. 9-20.

Robinson Jr,G.R. and Ayotte, J.D. 2006: The influence of geology and land use on arsenic in stream sediments and ground waters in New England,U.S.A. *Applied geochem* 21:1482-1497.

Sensi, N. and Polemio, M., 1981: Trace element addition to soil by Application of NPK fertilizers,

Fert.Res., 2, 289.

Shivkumar, K., Paude, A.K., Biksham, G. 1997: Toxic trace element pollution in ground waters around Patancheru and Bolaraun industrial areas, Andhra Pradesh, India: a graphical approach. *Environmental Monitoring and Assessment*, 45; 57-80.

Siegel, F.R.,1990: Exploration for Mississippi-Valley type stratabound Zn Ores with stream suspensates and stream sediments, Virginia, U.S.A. J. Geochem. Explor., 38: 265-283.

Siegel, F.R.,2002: Environmental Geochemistry of Potentially Toxic Metals. Springer-Verlag Berlin Heidelberg New York.

Smith, I.C. and Carson, B. L., 1981: Trace Metals in the Environment, Vol. 6, Ann Arbor Scientific Puplications, Ann Arbor, MI, 1981, 1202.

Tziritis E., 2009. Groundwater and soil geochemistry of Eastern Kopaida region, (Beotia, central Greece). *Central European Journal of Geosciences* 1(2)2009, Versita, p.219-226.

Tziritis E., Vassilopoulos A., Evelpidou N., 2008. Soil environmental study of Eastern Kopaida plain and risk assessment of potential hazards. Risk assessment and pollution hazards in environmentally sensitive European regions,GRINMED, ISBN:978-96098765-0-6, p. 70-95.

Vardaki, C. and Kelepertsis, A., 1999: Environmental impact of heavy Metals (Fe, Ni, Cr, Co) in soils, water and plants of Triada in Euboea from ultrabasic rocks and nickeliferous mineralization. *Envir. Geochem. & Health*, 21: 211-226.

GROUNDWATER QUALITY OF THE AG. PARASKEVI/TEMPI VALLEY KARSTIC SPRINGS - APPLICATION OF A TRACING TEST FOR RESEARCH OF THE MICROBIAL POLLUTIO (KATO OLYMPOS/NE THESSALY)

Stamatis G.

Agricultural University of Athens, Institute of Mineralogy-Geology, Iera Odos 75, GR-118 55 Athens, stamatis@aua.gr .

Abstract

The study of the Kato Olympos karst system, based on the implementation of tracer tests and hydro-chemical analyses, is aimed at the investigation of surface-groundwater interaction, the delineation of the catchment area and the detection of the surface microbial source contamination of the Tempi karst springs. The study area is formed by intensively karstified carbonate rocks, metamorphic formations, Neogene sediments and Quaternary deposits. The significant karst aquifer discharges through karst springs in Tempi valley and in Pinios riverbed. The karst springs present important seasonal fluctuations in discharge rate, moderate mineralization with TDS between 562 to 630 mg/l and they belong to Ca-HCO$_3$ water type. The inorganic pollution indicators, such as Na$^+$, K$^+$, Cl$^-$, NO$_3^-$, NH$_4^+$, PO$_4^3$, show low concentrations and do not reveal any surface influences. On the other hand, the presence of microbial parameters in karst springs proclaims the high rate of microbial contamination of karst aquifer. Tracer tests reveal hydraulic connection between the surface waters of Xirorema – Rapsani basin and the karst aquifer. The high values of groundwater flow velocity upwards of 200 m/h, show the good karstification rate of the carbonate formations and the cavy structure dominated in the study area, as well as the low self purification capability of the karst aquifer.

Key words: *Hydrochemistry, microbiological analyses, tracer test, karst aquifer, Kato Olympos, NE-Thessaly-Greece.*

1. Introduction

In many regions the karst systems are parts of the bare karst and are characterized by the absence of soil cover, which contributes to the filtration of the infiltrated surface waters. Karst aquifers are also characterized by great fluctuations in water levels, high flow velocities, short residence times and fast hydraulic reactions to hydrologic events. Thus, karst aquifers are particularly vulnerable to chemical and microbial contamination. Therefore, karst groundwater needs special protection. The major part of the study area is formed by intensively fractured and karstified carbonate formations, in that a significant aquifer is developed. The karst aquifer discharges through riparian karst springs in Tempi valley as well as in Pinios riverbed. The most important spring is Agia Paraskevi spring with high discharge rate (>1000 l/s). All karst springs present good water quality regarding the inorganic chemical load. On the contrary the intense presence of microbial parameters proclaims the microbial contamination of the karst aquifer. This significant karst aquifer of the study area remains up today

unexploited and the karst waters flow into Pinios River. In future this large amount of karst water could contribute positively in the increasing demand for drinking water, after suitable treatment, or for irrigation use or for artificial recharge in the aquifers situated in delta plain of Pinios River. This study deals with the Kato Olympos karst system using hydrochemical and tracer methods. The main goal of the study is the investigation of the groundwater quality and the hydraulic connection between surface- and karst water, the delineation of the catchment area as well as the detection of the surface microbial source contamination of the karst springs. The cost of this study is reimbursed from the Laboratory of Mineralogy and Geology of the Agriculture University of Athens.

2. Geological setting

The study area covers the south part of Kato Olympos Mountain at East Thessaly (Fig. 1), with the valley of Tempi spreading out at its southeastern edge. The direction of the valley is SW-NE and it is crossed by Pinios River, which drains Thessaly plain and falls into Aegean Sea. The major part of the valley is composed by carbonate formations of the Olympos – Ossa Unit, which also explains the general geomorphological situation of the broad area. Due to the tectonic structure of the area, the carbonate rocks outcrop at the central part, while the metamorphic formations, which belong to the overthrusted units, occur at the fridge of the study area. The carbonate and metamorphic formations define the bare and covered karst system of Kato Olympos respectively. Limestones are fractured and extremely karstified. Profound karstic landforms like dolines, swallow holes, dry valleys and canyons, can be remarked on the limestones surface, which reveal the development of the exo- and endokarstic processes in the area.

The mountain of Kato Olympos is formed by pre-alpine and alpine formations, which belong to a) Olympos-Ossa-, b) Ampelakia- and c) Pelagonian-Units. At the northeastern part of the basin the pre-apline and apline formations are overlaid by post-alpine lacustrine and continental deposits of Neogene-Quaternary age (Fig. 1). Olympos – Ossa Unit is considered to be autochthonous to parautochthonous at least and it is regarded as a tectonic window, being older than the metamorphic formations of Ampelakia- and Pelagonian-Units. Kato Olympos Massif forms an anticlinorium with NNE main direction axis. Primary cross structures of NNE and secondary ones of E-W direction are also presented (Katsikatsos et al., 1980, Jacobshagen, 1986). This geotectonic Unit consists of a series of crystalline limestones and dolomites up to 1000 m visible thickness, overlaid normally by meta-flysch rocks such as phyllites, schists and schist-sandstones with intercalations of thin (20-50m) sandy crystalline limestone. The formations of Ampelakia Unit (Blueschist Unit) are widely distributed in the south-western part of the area and their thickness exceeds locally 500m (Katsikatsos et al., 1980). These formations consist of sedimentary rocks (meta-pelites and meta-greywackes) with intercalations of meta-basites and marbles. In general, these rocks are intensively fractured, folded and altered.

The Pelagonian-Unit includes metamorphic formations such as a) gneiss and gneiss-schists of Palaeozoic age up to 600 m thick, b) schists, gneiss schists and amphibolites with marble and sipolines alternations of neo-Palaeozoic to middle-Triassic age up to 600m thick and c) metamorphic basic ophiolitic rocks, amphibolites, prasinites and serpentinites of the Pre-upper Cretaceous tectonic cover with a total thickness reaching 500 m as well as of upper Cretaceous marbles up to 200 m thick. These rocks occupy a significant part of Kato Olympos and are formed in the north-eastern as well as south-western part of the study area. The Neogene formations consist of conglomerates, marls and silts, outcropped mainly in the eastern part of the study area, where are widely exposed and their thickness exceeds 300m. The Pleistocene sediments are represented by old debris cone and collu-
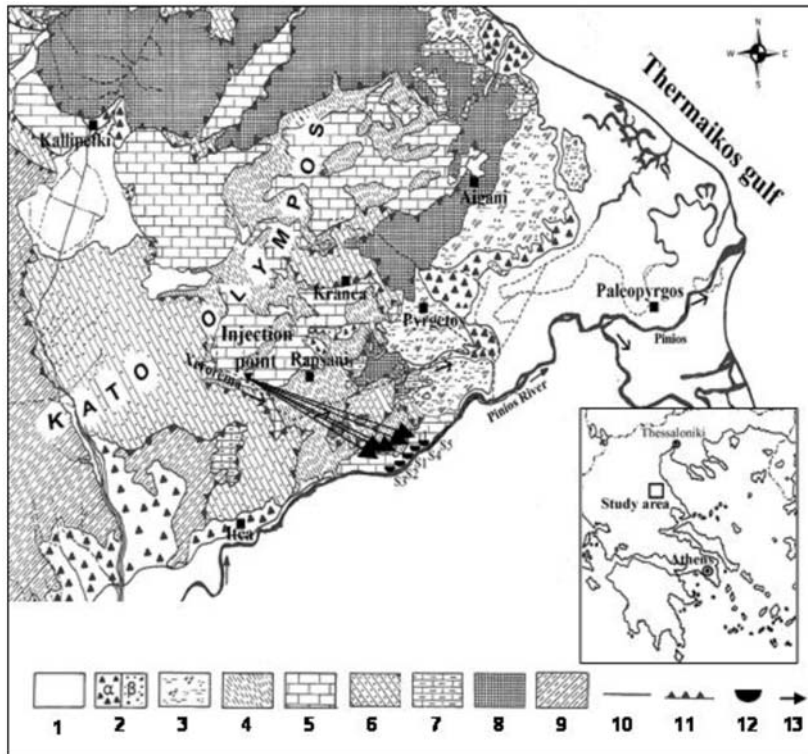
Fig. 1: A simplified geological map of the study area (Katsikatsos et al. 1987) (1: Alluvial deposits (Holocene); 2: Old talus cones (α) and Fluvio-lacustrine deposits (β) (Pleistocene); 3: Terrestrial and lacustrine deposits (Neogene); 4: Flysch epizonally metamorphic (M. Eocene); 5: Crystalline limestones (Jurassic-M. Eocene); 6: Blue schists, gneiss-schists, gneisses and prasinites; 7: Marbles (M.-U. Jurassic-U. Cretaceus); 8: Metamorphic basic ophiolitic rocks (Preuppercretaceus tectonic nappe); 9: Gneisses, gneiss-schists and amphibolites (Precarboniferous-M. Triassic); 10: Geological boundary; 11: Overthrust; 12: Monitoring carstic springs S1-S5; 13: Presence of the tracer).

vial deposits, as well as by terrace and basin deposits. The Holocene deposits are developed in Pinios delta area. They consist of loose materials such as silts, red-clays and sands with low participation of coarse clusters (Godfriaux, 1968, Katsikatsos, 1992).

3. Hydrogeology

The hydrogeological conditions of the study area depend directly on the presence of carbonate rocks and the predominant tectonic structures. An important karst aquifer is formed into the crystalline limestones and dolomites of Olympos – Ossa Unit. It is considered that significant quantities of the karst water flow towards E and fall into Pinios delta plain as well as into Thermaikos Gulf through fractured zones. Part of this water seeps through shear zones of metamorphic rocks to the eastern and western slopes. Significant quantities of the karst water seeking outlets at the lower topographic positions in Tempi valley form characteristic karst springs with high discharge rates near or into the riverbed of Pinios.

Depending on their discharge the most important springs are S1 (Agia Paraskevi) with discharge rate from 400 upwards to 1000 l/s, S2 from 2 to 150 l/s, S3 with discharge rate between 1 and 60 l/s, S4 from 5 to 200 l/s and S5 from 10 to 250 l/s (Fig. 1). The discharge rates of these springs are significantly high especially during the wet period, when they exceed 100 l/s. Table 1 shows the discharge rates and the chemical parameters of the springs during the investigation period of this study. An aquifer of limited importance is formed in metamorphic rocks such as phyllites, schists, gneisses, amphibolites and meta-flysch. Locally, where the effective porosity due to lithology and fractured tectonic increases significantly, low discharge springs are occurred. The springs with discharge rates lower than 1 l/s, are caused by the presence of metasand and crystallized carbonate horizons in the meta-flysch formations. In the middle and upper part of the Blueschist formations of Ampelakia-Unit, a limited number of springs with lower than 0,5 l/s discharge rate are developed. In these formations, the increase of secondary porosity due to lithology and tectonic structure can be observed.

The major part of the northeastern area is formed by ultrabasic massifs (ophiolites, serpentinites). In the synclinal structures of these formations an aquifer of local importance is formed and feeds some springs with low discharge rates, ranging between 0,1 and 2,5 l/s. According to their geomorphological position and the flow direction, the spring water infiltrates underground and recharges the underlying carbonate massif.

4. Material and Methods

Hydrochemical analyses: Sampling of karst springs S1, S2, S3, S4, S5 and of surface water in Xirorema basin took place on 3.1.2007 aiming at the investigation of the hydrochemical character of the springs. The criterion for the sampling was the discharge rate of every spring. For the rest of the karst springs all physicochemical parameters were measured in situ. Portable devises were used in order to measure the physicochemical parameters, such as T ºC and electrical conductivity EC (WTW/LF-330), pH value (WTW/330i), dissolved oxygen DO (WTW/OXI-96) and the discharge Q l/s (Flow Probe FP101/Global Water). In the laboratory of Mineralogy-Geology Section of the Agriculture University of Athens with the use of titration methods, spectral photometer (HACK, DR/3000), flame photometer (INTECH/420) and atom absorption spectrometer (GBC/908/AA) the parameters, Hardness, Ca^{2+}, Mg^{2+}, Na^+, K^+, HCO_3^-, Cl^-, SO_4^{2-}, NO_3^-, NO_2^-, NH_4^+, PO_4^{3-}, SiO_2, $KMnO_4$, Fetot, Mn^{2+}, Cu^{2+}, Ni^{2+}, Zn^{2+} were detected. The microbiological analyses were conducted in the Laboratory of Chemical Analyses, DEYA-Larisa.

Tracer Tests: On 3.1.2007 tracer tests took place in the basin of Xirorema, western from Rapsani town, at the Milos - Stalagmatia location, where a shallow hole is occurred and total infiltration of surface water can be observed. The quantity of 3 kg Uranine dye was used. The dye was dissolved in approximately 50 lt plastic bottles of water. At 11:00 the solution was injected into the shallow-hole. Samples were taken every one - two hours from three karst springs with high discharge rates in Tempi valley (S1:2400 l/s, S2:120 l/s and S5:235 l/s) in order to check the appearance of the dye. In the rest of the karst springs qualitative controls took place using charcoal bags. In every outflow point 10gr. charcoal bags were installed. In the Laboratory the dye was flushed from the charcoal bags with the use of ethyl alcohol. The Uranine dye was detected in the flushing solution. The sampling began on 3.1.2007, at 18:00 and finished on 7.1.07 at 22:00. The goal of this experiment was to determine the interaction between the surface waters of Xirorema basin and the karst groundwater as well as to detect the surface microbial source contamination of the karst springs. In all 245 water samples were taken. The water samples were collected into 50 ml polythene plastic vials, and maintained in darkness until their analysis. The detection of the Uranine dye took place in the laboratory of Hydrogeology Section of IGME – Athens with the use of the PERKIN/ELMER LS3 Spectrofluorometer.

Table 1.

Sampling points	S1 (Ag. Paraskevi)	S2 (Xenonas)	S3 (Platanos)	S4 (Restorant)	S5 (Phylakio OSE)	Xyrorema
Discharge l/s	2430	120	15	25	235	42
Temperature ºC	14.5	14.2	14,5	14.2	14.6	4,5
El. Cond. µS/cm	671	685	640	695	581	98
pH	6.8	7.1	6.9	7.1	6.9	7.1
O_2 mg/l	8.9	9.4	9,6	9.8	9.6	10.2
$KMnO_4$ mg/l	2.6	4.6	4.6	4.5	4.6	9.8
TDS mg/l	630	608	593	620	562	112
Hardness						
Total ºdH	21.8	21.0	19,8	25.8	18.8	3.3
Temporal "	21.0	20.1	19,6	23.8	18.4	3.0
Permanent "	0.8	0.9	0,2	2.0	0.4	0.3
Main Elements						
Ca^{2+} mg/l	113.6	114.6	108,8	115.2	102.1	18.2
Mg^{2+} "	25.6	21.8	20,4	23.8	20.2	3.5
Na^+ "	8.5	5.6	6,9	6.6	5.1	3.5
K^+ "	0.9	1.2	0,9	0.8	0.8	0.4
NH_4^+ "	0.028	0.032	0,024	0.032	0.026	0.036
HCO_3^- "	457.5	439.2	427,1	451.4	402.6	67.1
Cl^- "	14.2	10.6	14.2	10.6	14.2	4.6
SO_4^{2-} "	0.5	6.2	7,1	2.8	8.1	6.4
NO_3^- "	3.2	1.8	1,2	2.0	1.2	4.5
PO_4^{3-} "	0.15	0.22	0,12	0.26	0.12	0.28
SiO_2 "	5.8	6.2	6.4	6.0	7.4	2.5
Tracer Elements						
Fe_{tot} ppm	0.001	0.003	0,002	0.003	0.004	<0.001
Mn^{2+} "	0.022	0.018	0,028	0.024	0.025	<0.001
Cu^{2+} "	0.006	0.008	0,008	0.004	0.002	<0.001
Ni^{2+} "	0.001	0.001	0,001	0.001	0.001	<0.001
Zn^{2+} "	0.001	0.001	0,001	0.001	0.001	<0.001

5. Results of chemical analyses

Table 1 shows the results of chemical analyses. Agia Paraskevi spring (S1) presents the highest discharge rate (2430 l/s) among all other water manifestations (15-235 l/s) in this part of Pinios River basin. All karst springs show almost identical chemical character with negligible differences.

This hydrochemical similarity indicates that the karst springs discharge from the same groundwater body. The temperature ranges between 14,2 ^{0}C and 14,6 ^{0}C, the pH value between 6,8 and 7,1 and the electrical conductivity from 581 to 695 μS/cm. All spring waters are almost saturated in O_2 (8,9-9,8 mg/l). The TDS value ranges from 562 to 630 mg/l. Regarding their chemical character the karst groundwaters and the surface water of Xirorema belong to the hydrochemical type of Ca-HCO_3. The total hardness ranges from 18,8 and 25,8 ^{0}dH, thus the waters are hard waters (18-30 ^{0}dH) (Matthess 1973). Ca^{2+} (102,1-115,2 mg/l) and Mg^{2+} (20,2-25,6 mg/l) are the dominant cations, while Na^+ and K^+ show low concentrations. HCO_3^- (402,6-457,5 mg/l) is the dominant anion, while all the other anions present low concentrations (Cl^-:10,6-14,2 mg/l, SO_4^{2-}:0,5-8,1 mg/l, NO_3^-:1,2-3,2 mg/l, NH_4^+:0,024-0,032 mg/l, PO_4^{3-}: 0,12-0,26 mg/l). In all spring waters the absence of inorganic pollution is noticeable (low concentrations of NO_3^-, NH_4^+ and PO_4^{3-}). The $KMnO_4$ values are also low (2,6-4,6 mg/l), revealing that the presence of organic compounds are insignificant. The trace elements concentrations Fe_{tot}, Cu^{2+}, Ni^{2+} και Zn^{2+} are at the limit of detection, with exception of Mn^{2+}:0,018-0,028 ppm. Generally the karst waters of Tempi valley show good water quality regarding their chemical parameters, which are in low levels and under the upper permissible limits according to the European Directive 99/83 EU for drinking water quality.

6. Microbial contamination of karst aquifer

The microbiological analyses, which took place (6.11.2006) in water sample from Agia Paraskevi (S1) spring have shown the microbial contamination of the karst aquifer. In table 2 the results of the microbiological analyses are presented. As it is shown, many of the microbiological parameters are found in high levels, which means that the karst water is unsuitable for drinking water supply without further treatment. Surface waters which are contaminated by human activity, sink underground and endanger the groundwater quality. This microbial contamination could be caused, because there are many sheepcotes in the area especially very close to Xirorema stream. The sewages from septic tanks of Rapsani settlement could also contribute to this microbial contamination of the karst spring, although Rapsani is built on meta-flysch formations (Fig. 1).

The microbial and the inorganic chemical load is transported via Xirorema stream in the shallow-hole and after few hours has already reached the karst aquifer. The limited self – purification capability of the karst aquifer and the high flow velocities allow the appearance of the microbial parameters in the karst springs. These conditions are encouraged particularly at the wet period, where obviously the animal wastes will increase considerably.

Table 2.

Microbial Parameters	Spring S1	98/83EE
Total Coliforms	10-240	0/100 ml
Fecal Coliforms	0-50	0/100 ml
Escherichia Coli	0-50	0/250 ml
Enterokokkes	0-41	0/250 ml
Bacteria colony/ml water at 37°C / 48h	0-3	20/1 ml
Bacteria colony/ ml water at 22°C / 72h	0-4	100/1 ml
Pseudomonas	0	0/250 ml

7. Tracer Test in karst springs

Within the frame of this study, tracer tests took place in order to investigate the hydraulic connection between the surface waters of Xirorema basin and the karst groundwaters and to evaluate the impact of the microbial hazard on Tempi karst springs. The injection point was a shallow hole located in the above mentioned basin (Fig. 1). During the investigation period a total infiltration of surface water was observed. The day, when tracer tests took place, the surface runoff of Xirorema stream was measured in 42 l/s. The Uranine dye was detected in all karst springs. In S1, S2 and S5 springs the dye was detected after sampling and chemical analysis, while in the rest of the springs after flush of the charcoal bags with ethyl alcohol.

Figure 2 demonstrates the breakthrough curve for Uranine in S1 spring with the representative times after injection (t1: time of first appearance of Uranine, t2: passage time of maximum concentration, t3: passage time of 50% of the recovered Uranine amount in the sampling point and t4: Last appearance of the dye). The curve of recovered Uranine is also depicted in figure 2. The breakthrough curve for Uranine has, except the peak of the maximum concentration, other three characteristic peaks with high dye concentrations. Their appearance has to do with the snow melting and the increase in surface runoff, which has probably flushed the dye from the karstic conduits in the karst system.

This type of curve (steep and narrow) is characteristic for intensively karstified systems (Mull et al. 1988; Käss 1992; Wernli 2003). The cavy conditions, which dominate in the middle part between the injection point and the Agia Paraskevi spring of Tempi, were confirmed after the discovery of a cave from a speleologist team at the I.M Agion Theodoron location, south from Rapsani (Fig. 1). Two characteristically photos from this cave are shown in figure 3. The photos depict the karstification rate of the carbonate formations.

In table 3 the results of the second tracer test are presented. The maximal flow velocity (V_{max}), which is taken as the velocity that corresponds to the first appearance of the tracer, ranges from 258 m/h

Table 3.

Monitoring springs		**S1**	**S3**	**S5**	Mean value
Elevation	(m)	10	11	10	10,3
Total distance from Injection point	(m)	6.030	5.929	6.180	6.046
Initial arrival of Uranine dye	t1 (h)	23	23	23	23
	V_{max} (m/h)	262	258	269	263
Maximal concentration	t$_2$ (h)	27	27	27	27
	V_{Cmax} (m/h)	223	220	229	224
Discharge of 50% conc. Uranine dye	t$_3$ (h)	30	28	33	30
	V_a (m/h)	201	212	188	200
Last appearance	t$_4$ (h)	101	93	105	100
	V_{min} (m/h)	60	64	59	61
Discharge duration of Uranine dye	t$_1$ - t$_4$ (h)	78	70	82	77
Residence time	t$_0$ - t$_4$ (h)	101	93	105	100
Total recovery Uranine	Conc. (gr)	7,93	1,14	0,87	-
		Σ=9,94 gr = 0,33%			
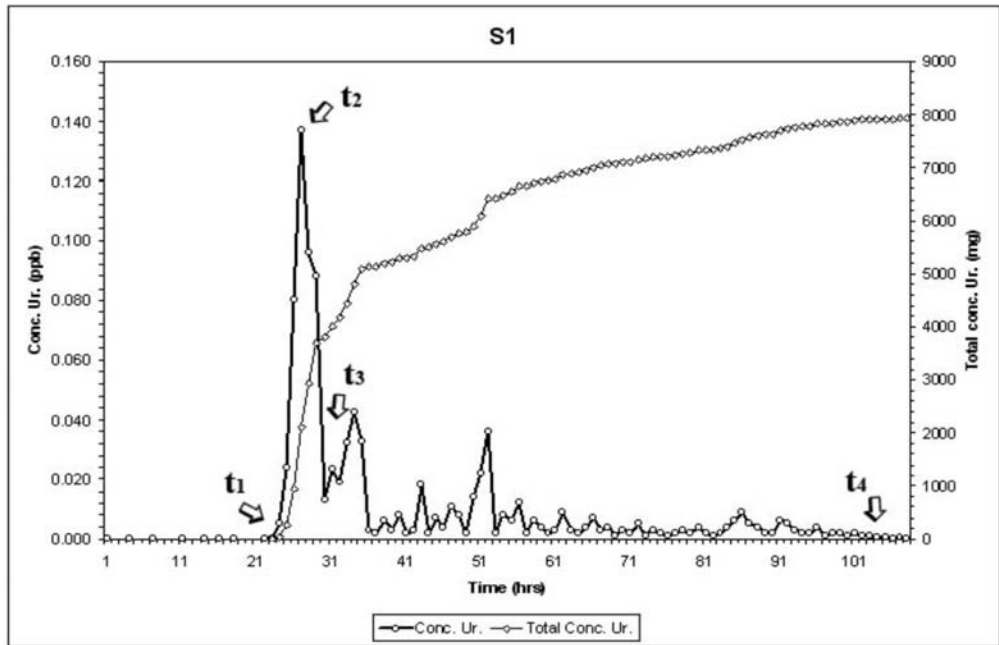
Fig. 2: Breakthrough curve for Uranine, S1 spring (Ag. Paraskevi) and the respective cast line (t1: time of first appearance of Uranine, t2: passage time of maximum concentration, t3: passage time of 50% of the Uranine in the sampling point and t4: Last appearance of the dye).
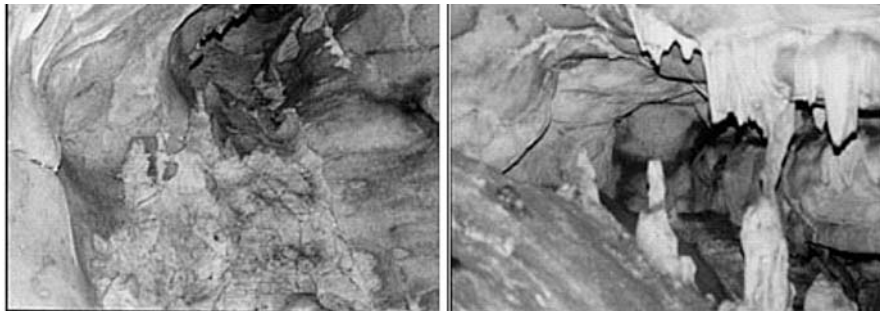
Fig. 3: Characteristic photos from the Routsi/Rapsani cave near I. M. Ag. Theodoron location (Fotos Ath. Argyroulis) (www.rapsani.com).

to 269 m/h. The dominant velocity (V_{Cmax}), which is defined as the time that corresponds to the passage time of the maximal concentration, ranges from 220 m/h to 229 m/h. Furthermore, the mean flow velocity V_a, which corresponds to the time in the breakthrough curve, at which 50% of the recovered tracer amount has passed the sampling point, varies between 188 m/h and 212 m/h. The mean value of the flow velocities is 229 m/h.

The recovered Uranine amount at the sampling springs was 9,94gr, that represents 0,33% of the total injected amount of Uranine, which was 3 Kg. This low amount of the recovered dye, could be probably explained, because of the existence of other karst springs into the riverbed or at not ac-

cessible locations at the north-eastern part of the Pinios River basin. Another explanation could be that an amount of the dye was trapped in the fissures of the karst system. Generally the flow velocities of the karst aquifer is very high due to the intensively karstification. Tracer tests in karst system of Ossa Mountain has shown similar flow velocities (Stamatis and Zagana 2004). The values of the flow velocities of the Kato Olympos karst system and of the Olympos karst System are comparable with the values of the flow velocities derived from tracer tests in karst systems of east Peloponnesus (Morfis and Zojer 1986).

8. Conclusions

The hydrogeological study took place in the karst system of Kato Olympos based on the implementation of tracer tests and hydrochemical methods, gave follow results:

- The karst aquifer discharges in karst springs, which emerge in Tempi valley. Another significant amount of the karst water discharges within the riverbed of Pinios River and another one in river's deltaic plain as well as into Thermaikos Golf. The groundwater flow direction trend S-SE and is defined from the tectonic structure as well as from the fractured zones, which characterize the study area.

- The karst water flow velocities present high values (V_a:188-212 m/h), revealing the intensively karstification rate of the carbonate formations and probably the cavy conditions dominate in the area.

- The Tempi karst springs, which are fed from the carbonate massif of Kato Olympos show moderate TDS (562-630 mg/l), slightly acid to slightly basic character, relatively high total hardness and belong to Ca-HCO_3 hydrochemical type.

- The inorganic pollution indicators, such as Na^+, K^+, Cl^-, NO_3^-, NH_4^+, PO_4^{3-} present low concentrations and do not reveal any surface influences. On the other hand, the presence of microbial parameters in karst springs proclaims the high rate of microbial contamination of karst aquifer, which has to do with the existence of sheepcotes and the settlement of Rapsani in the catchment area of the springs. This shows also the low self – purification capability of the karst system. The karst water could be suitable for drinking water supply after further treatment.

9. Acknowledgments

10. References

Jacobshagen V. 1986. Geologie von Griechenland. Borntraeger, Berlin-Stuttgart, 363 pp.

Godfriaux I., 1968. Etude geologique de la region de l' Olympe (Grece). –Ann. Geol. Pays Hellen., 19, 1-283.

Katsikatsos G., Migiros G. and Papazeti E. 1980. Geological map of Greece, 1:50.000, Rapsani sheet. – IGME, Athens.

Käss W. 1972. Zweite Internationale Fachtagung zur Untersuchung unterirdischer Wasserwege mittels künstlicher und natürlicher Markierungsmittel, Freiburg i. Br. 1970. – Geol. Jb., C2:382 S., Hannover.

Käss W. 1992. Geohydrologische Markierungstechnik. Band 9 Lehrbuch der Hydrogeologie, Herausgeber G. Matthess, Borntraeger, Berlin-Stuttgart.

Matthess G. 1973. Die Beschaffenheit des Grundwassers. Borntraeger, Berlin-Stuttgart, 324 pp.

Morfis A. and Zojer, H. 1986. Karst Hydrogeology of the Central and Eastern Peloponnesus (Greece). 5th International Symposium on Underground Water Tracing, Athens, 1986. – Steir. Beitr. Hydrogeologie, B.37/38: 301 S., Graz.

Mull D. S., Liedermann T.D., Smoot J.L., Woosley L.H. 1988. Application of day-tracing techniques for determining solute-transport characteristics of ground water in karst terranes. U.S. Environmental Protection Agency, pp 117.

Stamatis G. and Zagana E. 2004. Application of tracer and hydrochemical methods on the karst system of N. Ossa mountain (NE Thessaly, Greece).- 10th Int. conf. of Geol. Soc. Greece, Bull. Geol. Soc. of Greece, XXXVI/4, 2067-2076.

Wernli H. R. 2003. Einfuerung in die Tracerhydrologie. Geograph. Inst. Uni Bern, pp 120.

ENVIRONMENTAL – HYDROGEOLOGICAL INVESTIGATIONS ON THE CLAY DEPOSITS IN THE BROAD AREA OF MESOLOGGI – AITOLIKO LAGOONS

Zagana E.[1], Lemesios I.[1], Charalambopoulos S.[1], Katsanou K.[1], Stamatis G.[2], and Lambrakis N.[1]

[1] *University of Patras, Department of Geology, Laboratory of Hydrogeology, 26500 Patras, Greece, zagana@upatras.gr*

[2] *Agricultural University of Athens, Institute of Mineralogy-Geology, Iera Odos 75, 118 55 Athens*

Abstract

A hydrogeological study took place in the broader area of Mesologgi – Aitoliko lagoons (West Greece) aiming at the investigation of a) the hydrogeological conditions of the area as well as the surface and groundwater influences on the quality of the clay deposits found in the lagoons and b) the properties of the clay in order to be identified as "therapeutic peloids". Due to their location, the clay deposits could be influenced and possibly polluted from the surface waters. The aquifer of the unconsolidated formations presents low hydraulic conductivity, while the carbonate aquifer is bounded from the foregoing aquifer and therefore the possibility of clay pollution from the groundwater is very limited. pH of the sediments showing neutral and alkaline values, limits the mobility of some pollutants. Seawater affects some of the clay samples, which present high electrical conductivity. Iron and manganese show also high concentrations, while some of trace elements such as Cd, Hg, Hf, Be, Ag present concentrations under the detection limit. Most of the organic material of the clay consists of humus and therefore they could be suitable for fangotherapy.

***Key words:** clay sediments, trace elements, fangotherapy, Mesologgi – Aitoliko lagoons, West Greece.*

1. Introduction

The properties that a natural resource (water, gas, clay) should present in order to be identified as "natural therapeutic resource" were not clearly described in Greek legislation. Especially for the clays, the references are quite limited. The first legislation 2188/1920 which concerns "About Therapeutic Springs" in Greece has determined the "therapeutic springs" as well as the process of their recognition and the ownership condition. According to the last law 3498/2006, which concerns "The Development of Therapeutic Tourism" in Greece, "the therapeutic natural resources comprise a commodity, as part of our natural inheritance and therefore belong to the Greek state which manages and protects them. The therapeutic natural resources are the natural cold, thermal, mineral, thermal mineral waters and gases as well as the peloids (clay, mud, peat), of specific geographical location, which present curative properties according to both the experience of the past and modern scientific validation". In the same law, it is referred that for the recognition of the therapeutic natural sources, their certification is needed. More specifically, their hydrochemical character is defined in relation to the contained dissolved salts and gases, the trace elements and the total radioactivity. Other cat-

egories are distinguished according to their minerality, their temperature and osmotic pressure. According to the same law, the conduction of hydrogeological, radiological and medical studies is required for the certification of a therapeutic natural resource. Studies for the current situation and the existing facilities, as well as microbiological, physical and chemical analyses that are carried out in laboratories that function according to the applying arrangements are also necessary. Since this study took place before 2006, it is based on the legislation plan of 8th November 2005.

Generally, the rudiments of Balneology appeared as early as the 5th century BC when Herodotus called attention to the methods of prescription and application of mineral waters (Albu et al, 1997). Therapeutic Tourism was developed even in the ancient time in the area of Mesologgi – Aitoliko, since the clay deposits found in the broader area have been always considered as therapeutic. During summer, many people visit the area and especially the sites of interest of the current study (Agia Triada, Panagia and Rebakia). However, Therapeutic Tourism needs to be further organized in the area for, a) the safety of the bathers, b) the development of the area, c) the protection and sustainability of the environment, d) the improvement of services provided to the visitors by public and private sector. The hydrogeochemical study conducted by the Hydrogeological Laboratory, Department of Geology of the University of Patras, is conformed with the effort of the local Authorities, to further organize Therapeutic Tourism in the broad area of Mesologgi – Aitoliko. The study was dictated by the District of West Greece and was conducted on the sites of therapeutic clays suggested by the local authorities of Mesologgi-Aitoliko. This paper presents the methodology of the hydrogeological - hydrogeochemical study as well as the first results.

2. Study area

The lagoons of Mesologgi – Aitoliko are located in Western Greece, in the south-western part of prefecture of Aitoloakarnania. The lagoon system of Mesologgi – Aitoliko is the biggest in Greece and one from the biggest and more important, ecologically and economically, in Europe. The importance of lagoons has been recognized internationally and has been included in the beneficial and protective provisions of convention RAMSAR (Mpali et al, 1986).

The relief of the broad area of Mesologgi – Aitoliko lagoon is very gentle and is formed from Koutsiliaris Mt. (434m) in the West and Arakynthos Mt. (410m) in the East (fig. 1). The lagoon area is limited between Acheloos River in the West and Evinos River in the East and has been formed by tectonic activities and sedimentation processes. The tectonic activities of Upper Miocene constructed the tectonic trench of Patras Gulf, part of which is the study area. During Holocene, Acheloos River has transported and deposited enormous quantities of sediments resulting to the extension of the land (Marinos, 1993; Psilovikos, 1975). The current shape of the lagoon is due to engineering works of the last 70 years. According to Blachos (2005), the first intervention that changed the lagoon's shape, took place in 1930, with the construction of the Mesologgi port canal and the separation of the eastern part of the lagoon (Kleisova) from the main lagoon, and the construction with dredges of the Tourlida islet. From 1960 onwards, extended irrigation works in the broad area, large-scale exsiccations, as well as interventions for the construction of salt works in particular places of the lagoon, took place.

The geology of the broad area is structured from a) Ionian Zone sediments, which are the conglomerates located in the Aitoliko area, limestones and the flysch of Arakynthos Mt., b) Olocene deltaic, lacustrine-marine deposits and c) recent fluvial deposits (Marinos, 1993).
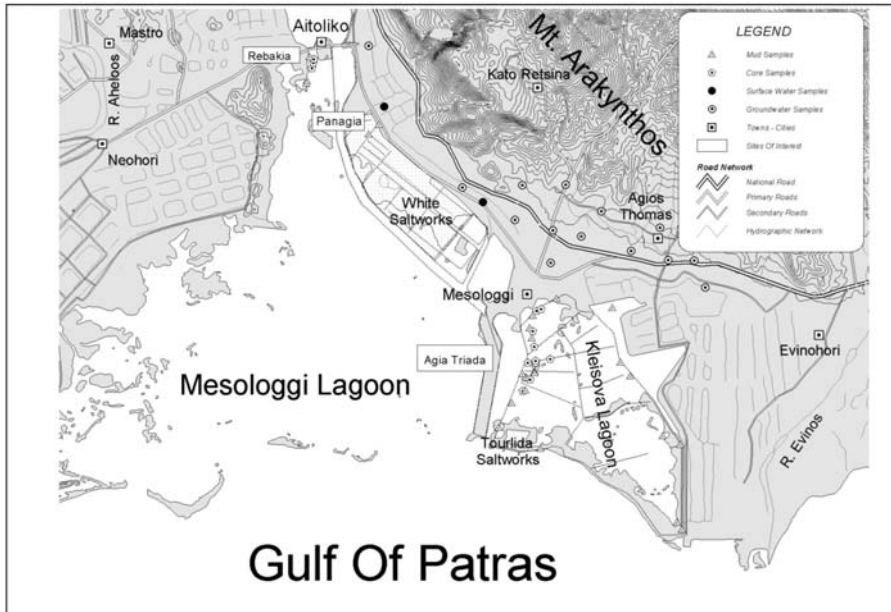
Fig. 1: Study area and sampling sites.

3. Methods

3.1 General

The investigation of the hydrogeologial conditions of the broad area of Mesologgi and the quality of the surface and groundwater as well as the clays was based on the German reference «DEUTSCHER TOURISMUSVERBAND E.V & DEUTSCHER HEILBAEDERVERBAND E.V» (Deutscher Tourismusverband E.V, 2005) as well as the proposed law of 8th November 2004 for the therapeutic natural resources.

The framework of the research project was planned to include all the tasks needed for the better examination of the hydrogeological status and the quality of water and sediment of the study area, so that this project could act as a key report for the development and utilization of therapeutic resources on both administrative and organization level.

Specifically, for the hydrogeological study that was anticipated in the proposed law of 8th November 2004, record of water occurrences in the area, study of the aquifers, measurements of the water level and collection of water samples were included among the field activities. Clay samples were also collected in order to measure the physicochemical parameters of the clays.

Thirteen (13) surface and groundwater samples were collected and analyzed in total. Fifteen (15) sediment samples from both the bath locations and the lagoon bed were also collected. Field tasks for the clay sampling took place with a local boat. For the sampling of the bed sediment cores, a van veen type core-sampler of 6 cm diameter was used. All sample sites are shown in figure 1.

3.2 Water samples analyses

The physicochemical parameters were measured in situ during sampling. A portable CONSORT®

conductivity-temperature device was used for the determination of temperature, electrical conductivity and pH, whereas the chromato-metric method of MERCK was used for the measurement of dissolved oxygen. Dissolved CO_2 and alkalinity were determined with titration method. The rest of elements were determined in the Hydrogeology laboratory of the Department of Geology, University of Patras, immediately after the collection. Cl^- ions were calculated with titration, while for SO_4^{2-}, NO_3^-, NO_2^-, NH_4^+, PO_4^{3-} a HACH® DR/4000 spectrophotometer was used. Ca^{2+}, Mg^{2+}, Na^+ and K^+ were estimated by atomic absorption spectroscopy (GBC Avanta). Finally, for the trace-metals Ag, As, B, Ba, Be, Cd, Cr, Co, Cu, Ga, Li, Fe, Mn, Mo, Ni, Hg, Pb, Sr, Zn, U, V the ICP-MS (inductively coupled plasma mass spectrometer) technique was used in a PERKIN-ELMER® ELAN 6100 device.

3.3 Clay samples analyses

The physicochemical parameters like grain–size, electrical conductivity, total moisture, organic material content, total organic carbon and humus content were determined in the Department of Geology, University of Patras. Trace elements were also determined with the use of both total resolution method and BCR-SEP (sequential extraction method) method. The use of sequential extraction schemes gives the opportunity to study metal distribution in different sediment phases and helps to predict metal mobility and their possible transfer from sediment to aquatic media (Larner et al., 2006; Thomas et al, 1994). The total resolution method was carried out for the surface sediment of every sediment core.

4. Results

4.1 Hydrogeology

In the broad area aquifers are hosted in carbonate rocks and fluvial deposits. The carbonate rocks aquifer located north from Mesologgi city presents remarkable yield capacity and it possibly feeds lateral the aquifer developed in fluvial deposits. The last one is very extended and feeds a large number of shallow wells and boreholes. The aquifer is developed in coarse – grained material mixed with clay and silt. Therefore it presents low hydraulic conductivity. The well discharge ranges between 5 and 15 m^3/h. The potentiometric-surface map, which has been constructed from water level measurements, shows a north to southwest groundwater flow direction. That means, some quantities of groundwater flows into lagoons. According to estimated water balance of the area, 40% of the precipitation reaches as surface water the lagoons (Lemesios, 2008). Surface waters from the draining channel – system of Acheloos River reach also the lagoons. As it is shown in figure 1, Kleisova lagoon is protected from surface runoff, therefore the clay deposits at the bath locations in this lagoon could only be influenced from the seawater and the physicochemical conditions of the lagoon.

4.2 Water Quality

Groundwater from fluvial deposits presents elevated electrical conductivity, due to the dissolution of the salts contained in the sediments. Ca^{2+}, Na^+, Mg^{2+} and HCO^{3-} dominate. Nitrate concentrations show low levels. All samples of surface water present very high electrical conductivity (up to 94,3 mS/cm). This is due to seawater influences. The extreme values of electrical conductivity could be attributed to evaporation. Nitrate concentrations show low levels. Table 1 presents the results of the chemical analyses of surface and groundwaters. The concentration of the most trace elements show low levels in ground waters, while in surface waters they present elevated concentrations. This is also

Table 1. Chemical analyses (mg/l) of groundwater (W4-W14) and surface water (REM1-L2).

Sampling sites	W4	W5	W8	W12	W13	W14	REM1	REM2	PAN1	SK2	SK4	L2	MIN	MAX	MEAN
T° C	17.4	18.6	16.8	17	18.1	16.4	21.2	20.3	21.3	18.7	17.2	21.5	16.4	21.5	18.7
EC	1365 µS/cm	980 µS/cm	2.53 mS/cm	2.51 mS/cm	1752 µS/cm	829 µS/cm	1535 µS/cm	1007 µS/cm	73.5 mS/cm	12.8 mS/cm	53.8 mS/cm	94.3 mS/cm	829 µS/cm	94.3 mS/cm	
pH	7.6	7.7	7.2	6.9	7.2	7.6	7.9	8.3	8.1	8.2	8.0	8.2	6.9	8.3	7.7
Redox (mV)	130.0	151.0	134.0	21.0	147.0	123.0	135.0	133.0	158.0	209.0	241.0	115.0	21	241	141
DO	259.0	160.0	325.0	349.0	265.0	122.0	211.0	104.0	257.0	127.0	268.0	216.0	104	349	222
Ca^{2+}	98.0	77.0	139.0	185.0	116.0	482.0	142.0	59.0	1256.0	115.0	265.0	405.0	59	1256	278
Mg^{2+}	10.4	4.8	42.3	15.0	11.3	10.6	14.7	18.0	165.0	165.0	689.5	797.0	5	797	162
Na^{+}	43.0	25.1	62.6	68.6	29.2	123.8	34.5	39.9	7700.0	1104.0	5200.0	10320.0	25	10320	2063
K^{+}	1.4	7.0	1.9	1.0	2.2	4.7	1.4	2.8	407.0	65.6	302.0	554.0	1	554	113
NO_3^{-}	1.0	14.0	1.0	9.0	0.0	0.0	0.0	14.0	1.0	14.0	24.0	3.0	0	24	7
NH_4^{+}	0.0	0.0	0.1	0.1	0.1	0.2	0.0	0.2	0.5	0.1	0.1	0.0	0	0	0
NO_2^{-}	0.0	0.0	0.0	0.0	0.0	0.0	0.0	0.0	0.0	0.0	0.0	0.0	0	0	0
HCO_3^{-}	322.1	290.4	480.7	403.8	363.6	250.1	395.3	163.5	135.4	278.2	219.6	174.5	135	481	290
SO_4^{2-}	31.5	43.5	198.5	91.3	63.8	22.7	68.3	42.0	5475.0	262.5	2562.0	4100.0	23	5475	1080
Cl^{-}	58	26	119	220	38	205	300	400	12520	2620	18500	19500	26	19500	4542

due to seawater influences. Strontium shows in both ground and surface waters higher levels. This is due to the dilution of the limestones of the broader area as well to the seawater influences. In table 2 the trace elements of ground and surface waters are shown. Surface runoff from streets due to dissolution of solid, liquid and gas pollutants however, will presumably be particularly invidious.

4.3 Clay Quality

The concentrations of all pollutants and specifically of trace elements in sediments are related with the physical properties of the sediments, such as their grain-size, mineral composition, pH, temperature, redox potential and the biological activity (Salomons and Forstner, 1984). Grain size distribution of sediments used the method of burette showed that sediments belong to clay and silt-clay classes. An increase in sand material along with a depth increase was also observed (Lemesios, 2008). In general pH of sediments is a parameter, which presents the general chemical character of the sediment. pH values of most sediment samples present neutral to alkaline character (Table 3). Therefore it could constrain the movement of some trace elements. The highest pH value measured in some samples reaches 9.4. Electrical conductivity is very high in samples that have been influenced from seawater. The organic material content is very important and reaches up to 10%. The concentration of TOC in sediments is low compared to the organic material. This, in combination with

Table 2. Trace elements (μg/l) of groundwater (W4-W14) and surface water (REM1-L2).

	W4	W5	W8	W12	W13	W14	REM1	REM2	PAN1	SK2	SK4	L2	MIN	MAX	MEAN
Ag	<3	<3	<3	<3	<3	<3	<3	<3	<3	<3	<3	<3			
As	<3	<3	<3	<3	<3	<3	<3	<3	60	10	39	75	10	75	46
B	40	81	133	56	54	75	101	117	4083	647	2186	4678	40	4678	1021
Ba	22	31	64	59	37	18	32	26	97	43	52	17	17	97	41
Be	<5	<5	<5	<5	<5	<5	<5	<5	<5	<5	<5	<5			
Cd	<3	<3	<3	<3	<3	<3	<3	<3	<3	<3	<3	<3			
Co	<3	<3	<3	<3	<3	<3	<3	<3	<3	<3	<3	<3			
Cr	13	8	9	9	9	6	18	127	354	45	170	390	6	390	97
Cu	3	7	<3	<3	<3	6	<3	5	116	16	77	152	3	152	48
Ga	<3	<3	<3	<3	<3	<3	<3	<3	4	2	2	1	1	4	2
Li	9	6	13	17	11	3	10	14	213	43	165	319	3	319	69
Fe	<10	<10	<10	17	<10	<10	35	227	289	40	50	288	17	289	135
Mn	3	9	15	4	<4	129	4	72	29	9	60	27	3	129	33
Mo	<3	<3	<3	<3	<3	<3	<3	<3	10	6	7	13	6	13	9
Ni	5	5	<5	<5	<5	<5	8	15	48	38	<5	23	5	48	20
Pb	<3	<3	<3	<3	<3	<3	<3	<3	<5	<3	<3	<5			
Sr	235	226	1743	466	432	310	839	325	25321	1284	4593	8471	226	25321	3687
U	<3	<3	<3	<3	<3	<3	<3	<3	<3	<3	<3	4	4	4	4
V	4	4	3	3	2	2	6	40	105	17	50	116	2	116	29
Zn	9	11	28	116	20	46	28	30	112	46	94	103	9	116	54
Hg	<5	<5	<5	<5	<5	<5	<5	<5	<5	<5	<5	<5			
Hf	<2	<2	<2	<2	<2	<2	<2	<2	<2	<2	<2	<2			

the relatively low concentrations of organic nitrogen suggests the dominance of compounds rich in hydrogen. Humus comprises the bigger part of the organic material in sediments as it is derived from the determination of their concentration. This fact encourages the use of clays for curative purposes (Komatina, M. 2004). In the international literature does not exist trace elements concentrations standards for therapeutic peloids. Table 4 shows the concentrations of trace elements determined with the total resolution method of the clay samples of the study area. Generally the concentrations of trace elements have been considered as low, with exception the iron and manganese concentrations, which are relatively high. Papatheodorou et al. , 2002 have also shown that Fe chemistry is an important factor in Klisova lagoons sediment.

5. Conclusions

For the identification of natural resources (clays, waters and gases) as therapeutic, hydrogeological – hydrogeochemical studies have to be conducted. The following observations were derived from

Table 3. Physicochemical parameters of the clay samples.

Sampling sites	pH	EC (µS/cm)	Moisture Content (%)	Organic Content (%)	TOC (%)	TON (%)	Humus Content (%)
T1	9.4	3470	70.2	6.6			
T2	7.9	1975	26.2	3.4			3.2
T3	7.9	2850	55.3	8.3	2	0.2	7.9
T4	7.6	5870	35.1	6.5		0.2	6.9
T5	8.2	2250	62.1	9.8	2.4	0.1	9.6
T6	9.4	3480	57	9	2.3	0.3	8.2
T5A	9	4350	56.9	8	2.2	0.1	7.8
T10	7.7	2460	51.7	8.5	2	0.1	8.2
T11	7.7	3000	37.7	7.2		0.1	6.8
T12	8	2370	38.9	5.4		0.1	5.1
T13	7.7	3750	68.4	13.1	3.3	0.3	11.2
T14	9.1	4050	53.4	8.2	2.1	0.1	7.6
T15	8	2560	33.5	5.3		0.1	5

Table 4: Trace elements (mg/l) in clay samples.

	T1	T2	T3	T4	T6	T5A	T10	T11	T13	T14	MIN	MAX	MEAN
As	8.1	3.5	8.5	10.6	9.6	9.7	11.7	12.6	8.8	7.0	3.5	12.6	9.0
Ag	0.6	0.4	0.7	0.2	0.7	0.3	0.6	0.7	0.5	0.3	0.2	0.7	0.5
Ba	166.9	290.0	177.6	76.5	208.3	155.1	202.0	197.2	170.7	155.8	76.5	290.0	180.0
Cd	0.2	0.0	0.2	0.1	0.1	0.2	0.2	0.1	0.2	0.2	0.0	0.2	0.2
Co	17.3	12.8	17.2	6.5	16.1	17.2	18.0	16.7	23.3	16.7	6.5	23.3	16.2
Cr	116.9	191.2	154.9	88.1	163.9	143.6	168.2	156.8	143.7	137.8	88.1	191.2	146.5
Cu	38.6	20.8	41.8	12.9	29.4	36.8	36.1	33.4	42.8	43.3	12.9	43.3	33.6
Ga	17.6	18.9	19.5	8.0	20.5	17.7	20.5	19.2	18.4	18.1	8.0	20.5	17.9
Li	80.8	52.5	84.2	28.9	71.8	77.5	74.2	73.2	80.2	80.1	28.9	84.2	70.3
Fe	43217	29346	45693	12687	39470	44172	42755	38165	42645	45578	12687	45693	38373
Mn	723	399	965	353	718	825	626	795	917	641	353	965	696
Mo	9.9	0.2	3.4	1.3	4.0	5.7	13.1	3.9	11.4	7.4	0.2	13.1	6.0
Pb	22.5	14.1	23.7	8.8	15.5	20.3	17.0	30.3	27.1	22.9	8.8	30.3	20.2
Sr	237	93	176	372	208	206	211	581	175	140	93	581	240
U	3.9	1.4	2.4	1.4	2.4	2.9	4.5	2.9	3.7	2.9	1.4	4.5	2.8
V	82	56	98	35	89	96	101	95	103	100	35	103	85
Zn	36	8	41	18	24	38	33	19	25	42	8	42	28
Hg	0.3	0.0	0.1	0.1	0.1	0.1	0.0	0.1	0.1	0.1	0.0	0.3	0.1
Hf	2.2	2.2	2.7	0.2	3.0	1.3	2.8	3.0	2.0	1.2	0.2	3.0	2.1

the hydrogeological - hydrogeochemical study in the broader Mesologgi – Aitoliko area: Aquifers are hosted in carbonated rocks and alluvial deposits. The carbonate rocks aquifer presents remarkable yield capacity; the aquifer hosted in fluvial deposits show low hydraulic conductivity. Surface water, which comprises at least 40% of the rainfall, flows into lagoons. Pollution from trace elements in both ground and surface waters is insignificant and therefore the chemical composition of lagoon clays is not risk to be degraded by ground and surface waters of the broader area, which flow into lagoon. Sediments pH presents neutral to alkaline values and it constrains the movement of some trace-metals. The impact of seawater is quite obvious in most of the samples, which present relatively high values of electrical conductivity. The concentration of TOC in sediments is low compared to the organic material. Most of the organic material of the clay consists of humus and therefore they could be suitable for fangotherapy. The concentrations of trace elements calculated with the total resolution method present low values.

6. References

Blachos, N., 2005. Estimation of the environmental situation in Mesologi lagoon with the determination of heavy metals and the natural radioactive nuclides. Master Thesis (in greek)-Department of Biology, University of Patras.

Deutscher Tourismusverband E.V. and Deutscher Heilbaederverband E.V., 2005. Begriffsbestimmungen - Qualitaetsstandards fuer die Praedikatisierung von Kurorten, Erholungsorten und Heilbrunnen. *12. Auflage*, Floettmann Verlag GmbH, Guetersloh, Bonn 2005.

Komatina, M. 2004. Medical Geology, Effects of Geological Environments on human health. Elsevier, 488.p.

Larner, B. L., Seen, A. J. and TOWNSEDND, A.T., 2006. Comparative study of optimised BCR sequential extraction scheme and acid leaching of elements in the certified reference material NIST 2711. *Analytica Chimica Acta* 556, 444-449.

Lemesios, I, 2008. Environmental – Hydrogeological study of the aquifers of the broad area of Mesologgi in relation to the natural therapeutic sources of the area. *Master Thesis*, University of Patras, 203 pages.

Marinos, P., 1993. Hydrogeological conditions in Delta area of Acheloos River; Specifically the river – groundwater interactions (In Greek). Ministry of Environment, Athens, 92 p.

Mpali, F., Korovetsi, A., Dionisopoulou, L., Pergantis, F., Daniilidis, D., Makris, K. and Mpaliotas, S., 1986 . Project of delimitation of water lands of convention RAMSAR, Water land Mesologgi, 98. pages (in greek).

Papatheodorou, G., Hotos, G., Geraga., M., Avramidou, D. And Vorinakis, T., 2002. Heavy metal concebatrtions in sediments of Klisova Lagoo (Southeaster Mesolonghi – Aetolikon Lagoon comlex), W, Greece, Fresenius Environmental Bulletin,No11, pp. 951-956.

Psilovikos, A., 1995. Water management estimations in the low land baisn of Acheloos River. For the development of the lagoons area and the broad area of Mesologgi – Etoliko. (In greek) Issue G1. Ministry of Environment, Athens, 498 p.

Salomons and Forstner, 1984. Metals in the Hydrocycle, Springer-Verlag, Berlin, Heidelberg, 349p.

Thomas, R.P., Ure, A..M., Davidson, C.M. and Littlejohn, D., 1994. Three-stage sequential extraction procedure for the determination of metals in river sediments. *Analytica Chimica Acta* 286, 423-429.

12ο ΔΙΕΘΝΕΣ ΣΥΝΕΔΡΙΟ ΤΗΣ ΕΛΛΗΝΙΚΗΣ ΓΕΩΛΟΓΙΚΗΣ ΕΤΑΙΡΙΑΣ
ΠΛΑΝΗΤΗΣ ΓΗ: Γεωλογικές Διεργασίες και Βιώσιμη Ανάπτυξη

12th INTERNATIONAL CONGRESS OF THE GEOLOGICAL SOCIETY OF GREECE
PLANET EARTH: Geological Processes and Sustainable Development

◈

ΓΕΩΦΥΣΙΚΗ
GEOPHYSICS

ARCHAEOMAGNETIC STUDIES IN KILNS FROM N. GREECE

Aidona E. [1], Kondopoulou D.[1], Alexandrou M.[1], and Ioannidis N.[1]

[1] *Department of Geophysics, School of Geology, Aristotle University of Thessaloniki, 54124 Thessaloniki - Greece, aidona@geo.auth.gr, despi@geo.auth.gr*

Abstract

Archaeomagnetism combines the magnetic properties of baked materials with Archaeology. The archaeomagnetic method can be applied to any kind of permanent - in situ or displaced- burnt structures, such as kilns, ovens, hearths, burnt floors, tiles, bricks and pottery fragments, the latter for intensity measurements only.

In this study we present the latest archaeomagnetic results from archaeological sites which are distributed in N. Greece (Polymylos, Sani, Thesssaloniki). The Natural Remanent Magnetization (NRM) and the magnetic susceptibility of the samples have been initially measured. The samples have been subjected to magnetic cleaning (AF and Thermal demagnetizations) and this procedure revealed the characteristic component of the ancient magnetic field. Rock magnetic experiments such as acquisition of the Isothermal Remanent Magnetization (IRM) and thermomagnetic analysis have been performed in pilot samples in order to identify the main magnetic carriers. Finally the secular variation curves for Greece and the SCHA.DIF.3K model were used in order to date these archaeological structures. This dating improved or modified the estimated archaeological ages.

Key words: archaeomagnetism, kilns, Northern Greece, dating.

1. Introduction

Archaeomagnetism is the discipline of palaeomagnetism which studies archaeological materials such as kilns, ovens, bricks and tiles and in general any kind of burnt clays, since they usually carry a stable magnetization that is almost entirely a thermoremanence. This stable magnetization has 'fossilized' the direction and the intensity of the field at the time and the place of the last firing. The main purpose of archaeomagnetism is first the establishment of accurate secular variation curves (SVC) from well dated –with other independent methods- structures and second the potential dating of relevant material for places and periods where such curves are available.

During the last decades several authors have studied the variations in intensity and direction of the geomagnetic field for the last 7000 and 5000 years respectively in Greece. Intensity data reported since 1980 (Liritzis and Thomas 1980) are by far more numerous (for a thorough review see De-Marco et.al., 2008) whereas directional data appeared in 1984 (Downey and Tarling, 1984). Recently new archaeomagnetic data have been obtained following severe selection criteria (Evans & Kondopoulou, 1998, Kovacheva et al., 2000, Spatharas et al., 2000, Kondopoulou & Spatharas, 2002, Tarling et al., 2004, Evans 2006) which leaded to the construction of new intensity (Spatharas, 2005, DeMarco et al., 2008) and directional SVC for Greece (DeMarco, 2007).

In this paper we present new archaeomagnetic data obtained from three archaeological sites in N. Greece and we attempt to date them using the secular variation curves available for Greece and the regional model SCHA.DIF.3K (Pavon-Carrasco et al., 2009).

2. Description of sampling sites

Samples were collected from 3 different archaeological sites situated in N. Greece as shown in Fig.1. Short description of the sites is given below, respecting a chronological order.

Polymilos (ML and SO)
The recent excavations, due to the construction of the New Egnatia Road, close to the ancient settlement of Polymilos, brought to light a part of an ancient city inhabited from the prehistoric times until the Late Antiquity. The main activity of the city was during the 3rd century B.C. The two ceramic kilns sampled were in an excellent condition and destinated to preservation (Fig.1). Therefore sampling was delicate and restrained only to the kilns floor. A total of fifteen samples were obtained from both kilns (7 samples from ML and 8 samples from SO).

Sani (Megali Kipsa - SAN8)
Few years ago, the excavation of a palaeochristian farm in Megali Kipsa of Kassandra has started. This complex consists of several buildings but the most impressive feature of the site is the ceramic kilns complex. The archaeological excavation brought to light nine, well preserved, kilns while the remains of other three were detected. From the archaeological investigation it appeared that this complex operated as a small ceramic industry not only for the construction of the settlement but also for providing bricks to other adjacent areas. On the basis of coins found in the site it is believed that these kilns started to be in action at the beginning of the 4th Century AD. From this site one kiln was sampled (Fig.1) and in total 10 samples were collected.

Thessaloniki (RS1)
The archaeological excavations in the centre of Thessaloniki due to the construction of the subway revealed a laboratory area with several ceramic kilns in front of the actual main Railway Station. The archaeological information indicates that this workshop area was in use for several centuries (Roman and Byzantine times) as it is shown from the coins and the potteries found in the site. One kiln was sampled and in total eighteen independently oriented samples were obtained.

3. Sampling and measurements

All the collected samples were independently oriented with regard to the geographic north and the local horizontal plane by means of a small plexiglas plate glued on the top of the material. The dip was measured with a bubble inclinometer and the azimuth by using magnetic and sun-compasses.

A total of 43 hand samples were collected from the four kilns and from them 149 specimens (standard cylinders or 2x2cm cubes) were prepared in the laboratory.

The remanent magnetization was measured using a Minispin magnetometer (Molspin, Newcastle, UK). Alternating Field (AF) demagnetization was performed at the field strength of 5-60mT with 5 mT interval and 60 – 100 mT with 10mT interval by using an Molspin-MSA2 AF- tumbler demagnetizer (Molspin, Newcastle, UK). The magnetic susceptibility was measured using a KLY-2 susceptibility bridge (Agico, Brno, Czech Rep.). The anisotropy of magnetic susceptibility was measured using a Kappa bridge KLY 2 and a MF K1. Anisotropy parameters i.e lineation (L), foliation (F), degree of anisotropy (P'), shape factor (T) reflecting the alignment of particles and shape of magnetic susceptibility ellipsoid, have also been calculated using the program ANS 21 (Jelinek, 1977).
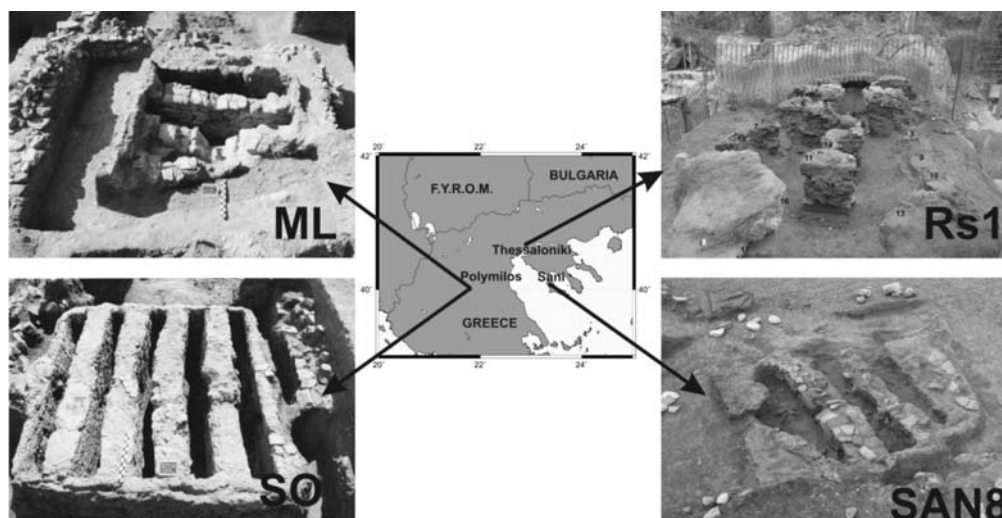
Fig. 1: Simplified map showing the geographical distribution of the sampled archaeological sites and the corresponding photos of the kilns: on the left side the two kilns (ML and SO) from Polymilos are shown, while on the right side the kiln (RS1) from Thessaloniki and the kiln SAN8 from the archaeological site of Megali Kipsa are presented.

High-temperature behavior of magnetic susceptibility (thermomagnetic analysis) for determination of the Curie point of magnetic minerals present in the material was performed on a Bartington susceptibility meter with a furnace attached, and a Kappa bridge KLY 2. Magnetic susceptibility changes were recorded continuously from room temperature up to 700°C and back.

In pilot samples from each site an isothermal remanent magnetization (IRM) was imparted with a pulse magnet and a maximum field of 2.5 T and a stepwise acquisition curves of IRM were obtained for selected samples.

Thermal stepwise demagnetisation of composite IRM (Lowrie, 1990) was performed in selected samples in order to obtain unblocking temperatures of soft-, medium- and hard magnetic components. The following strengths of the magnetic field to induce the three components were used: soft – 0.1T, medium – 0.5T, hard – 2T.

4. Results

4.1 Rock magnetism

The identification of the magnetic carriers is critical in order to evaluate the suitability of material for obtaining reliable archaeomagnetic results. IRM curves revealed the dominance of magnetite (or titanomagnetite) in most of the cases (Fig.2a). Only in the case of Thessaloniki (RS1) two distinct groups are observed. One, with a low coercivity component which saturates at about 100 mT and a second one with two magnetic mineral phases, with low coercivity and high coercivity respectively which is not able to saturate at 1200mT. The thermal demagnetization of the 3- axes composite IRM results are shown in Fig.2b.The demagnetization along the x axis (soft component) revealed unblocking temperatures from 580° to 650°C indicating magnetite with different Ti contents and small portions of hematite. In the case of the RS1 the highest magnetization is recorded along the z axis (hard component) with a sharp decrease at about 200°C, indicative for the presence of goethite. The variation of the low-field susceptibility with temperature exhibits a stable behav-

Table 1. Mean anisotropy parameters for the magnetic susceptibility anisotropy ellipsoids for the studied sites. N = number of samples, L = lineation, F = Foliation, P = anisotropy degree, T = shape parameter of Jelinek (1981).

Site	*N*	*L*	*F*	*P*	*T*
Thessaloniki	23	1.019	1.055	1.075	0.452
Polymilos	35	1.032	1.040	1.058	0.598
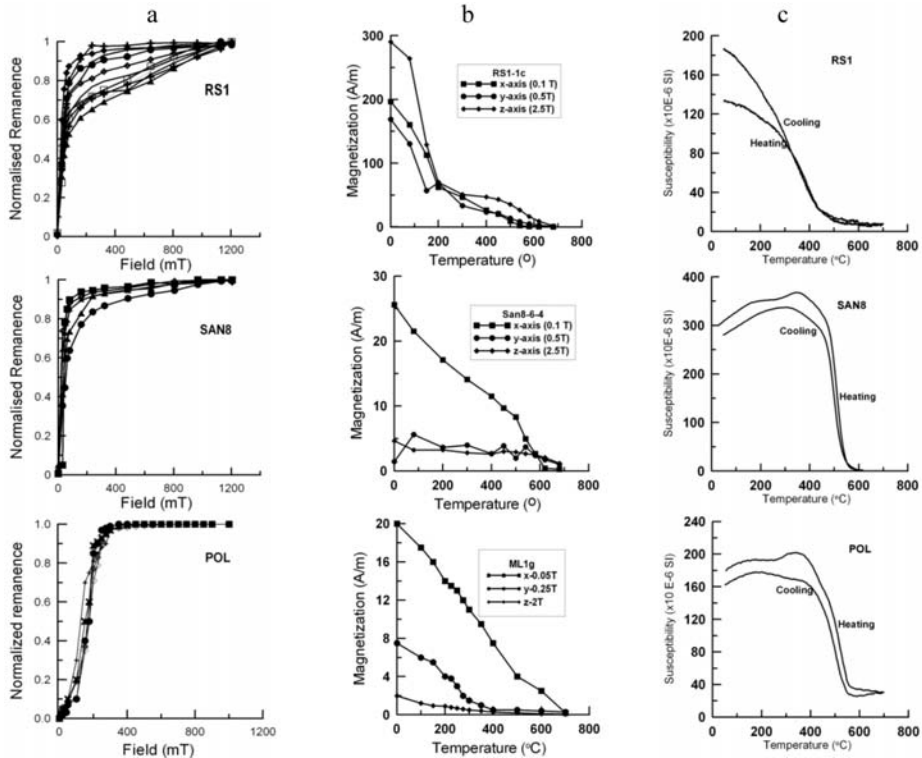
Fig. 2: Rock magnetic experiments. a) IRM curves from the three archaeological sites. b) Demagnetization of the 3-axes composite IRM of pilot samples, and c) thermomagnetic curves. (For details see text).

ior, even if the shape of the thermomagnetic curves differs from sample to sample. Heating and cooling curves are almost reversible, indicating minor mineralogical changes. The Curie temperatures vary from 500° to 580°C, characteristic for the presence of magnetite or titanomagnetite.

The anisotropy of magnetic susceptibility was measured in selected samples from the archaeological sites of Thessaloniki and Polymilos. Since the effect of the shape anisotropy can be substantial for bricks and tiles and minor for baked clays, we performed indicative anisotropy measurements to the samples of Sani. The anisotropy degree ranges from 2% to 4% which is insignificant. The mean anisotropy parameters for the other two studied sites are reported in Table 1. The shape of the AMS ellipsoid is oblate (T>0) in both cases. Generally, the samples were not particularly anisotropic, with the degree of anisotropy (P) varying between 2 and 14% for Polymilos and a mean value of 1.058 (Spatharas, 2005), while in Thessaloniki, samples seem to be more anisotropic with P values varying from 4% to 15% and a mean value of 1.075.
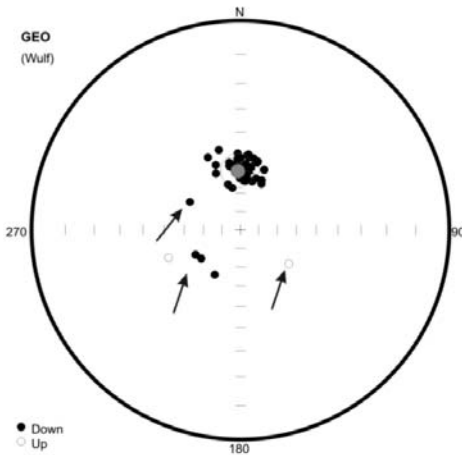
Fig. 3: Stereographic projection of the NRM distribution of samples from Thessaloniki. Dots represent specimens measurements (full dots correspond to positive inclinations while open dots indicate negative inclinations). Black arrows point to the rejected data.

4.2 Archaeomagnetic results

The NRM of all 149 specimens from the three archaeological sites has been measured using a Molspin spinner magnetometer. At least one specimen from each sample was demagnetised, in order to define the characteristic magnetic component. The NRM directions seem to group satisfactorily. Nevertheless, in some cases directions of specific samples were rejected since they show values totally different from the expected ones as it is seen in the stereographic projection of the distribution of NRM (Fig. 3).

The magnetic cleaning reveals the presence of one stable component of magnetization with a weak viscous component (Fig.4a). The majority of the samples were demagnetised successfully up to 100mT, but there were cases where the demagnetization was not complete up to 100mT (Fig.4b).

The demagnetization of the rejected samples (due to their deviating NRM directions) did not modify their directions. With a more careful observation of these samples position into the kilns, we noticed that they gathered either in the entrance or in the outer part of the kiln and most probably they have not been sufficiently burnt and therefore in their original magnetization was not totally cancelled (Jordanova et al, 2004, Aidona et al., 2008). Consequently, these results were not included to the computation of the mean characteristic remanence direction of the sites.

The characteristic remanent magnetization (ChRM) directions were calculated using the principal component analysis (Kirschvink, 1980). In the final calculations we did not take into consideration samples with variations in declinations bigger than 20° with respect to the mean value and a_{95} bigger than 10°. The mean calculated directions and their statistics are presented in Table 2 and their stereographic projection in Fig. 5.

In order to obtain a full archaeomagnetic record for the archaeological site of Sani, paleointensity measurements were performed. A total of 11 specimens with a volume of about 0.75 cm^3 have been analyzed using the continuous high temperature magnetization measurement method, shortly defined as the "Triaxe" technique (Le Goff and Gallet, 2004; Gallet et al., 2006). The technique involves several continuous zero field heating and cooling cycles up to a maximal temperature of 650° C with a rate of 25°C/min and one in-field cooling cycle. During the latter cycle, a field of 40 or 50 μT was applied parallel to the NRM. Magnetization was monitored through all cycles with a three-
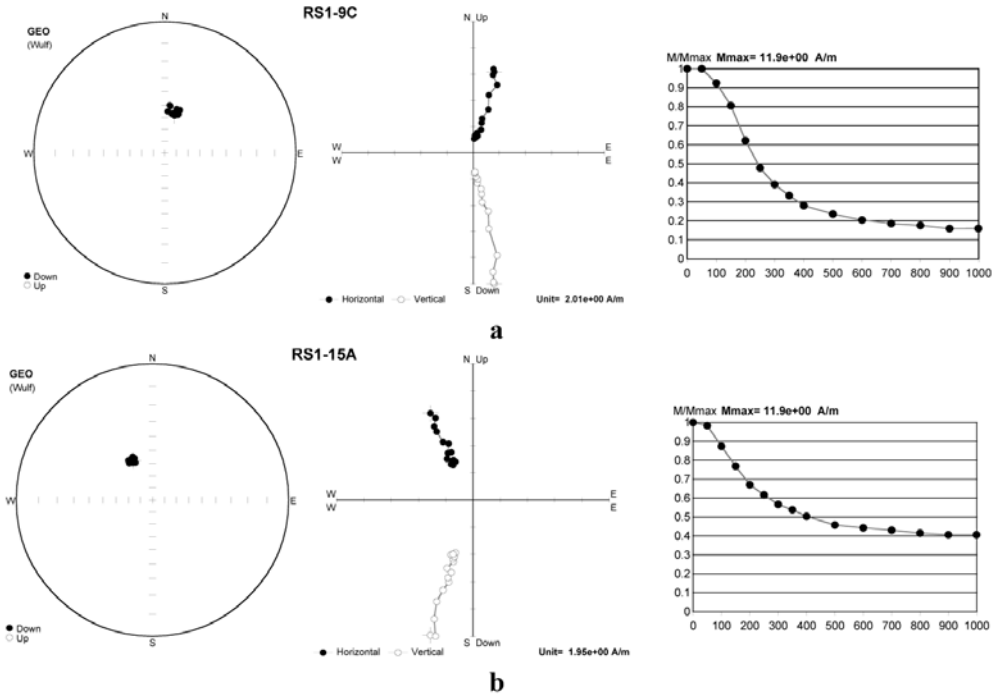
Fig. 4: Stereographic projection, Zijderveld diagram and demagnetization curve of a) specimen where the demagnetization is successful up to 100mT, b) specimen where the demagnetization is not complete up to 100mT

Table 2. Mean ChRM directions for each archaeological site. n: number of samples; D: declination; I: inclination; F: intensity; k: precision parameter; a₉₅:semi-angle of cone of confidence

Site	Lat/Long	n	D°	I°	k	a₉₅	F(μT)	Archaeological age	Archaeomagnetic dating
Polymilos	40°/21.9°	14	348.1	52.6	57.18	5.3	66.0	300-200 B.C	393-170 BC
Sani	40.07°/23.3°	6	357.2	49.1	159.8	5.3	61.9	3rd-4th A.D	350-475 AD
Thessaloniki	40.7°/23.1°	14	358.5	56.9	81.73	4.4	-	4th -13th A.D	700-1054 AD
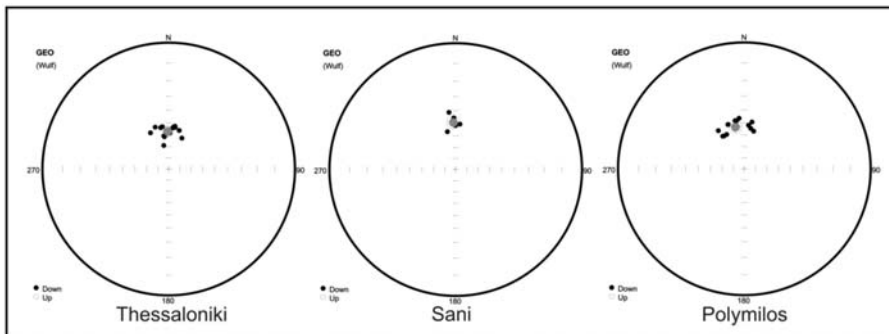
Fig. 5: Stereographic projection (lower hemisphere) of the samples (black dots) used for the calculation of mean directions (red dot) for the three sites respectively.
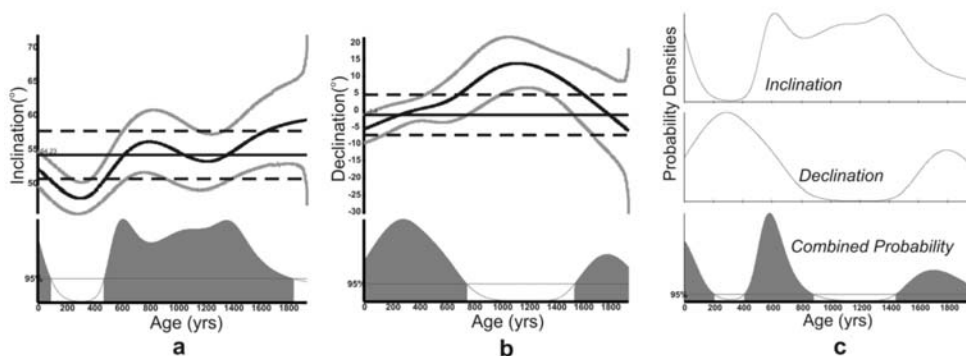
Fig. 6: Archaeomagnetic dating of Thessaloniki site. a,b) In the upper part of the graphs, the reference curves for inclination and declination (black line) with its error bands (grey lines) respectively. The mean site direction (relocated to Athens) is depicted with its error (dashed lines). In the lower part the probability densities for I and D, respectively at 95% of probability level. c) final dating after combining the probabilities of (a) and (b).
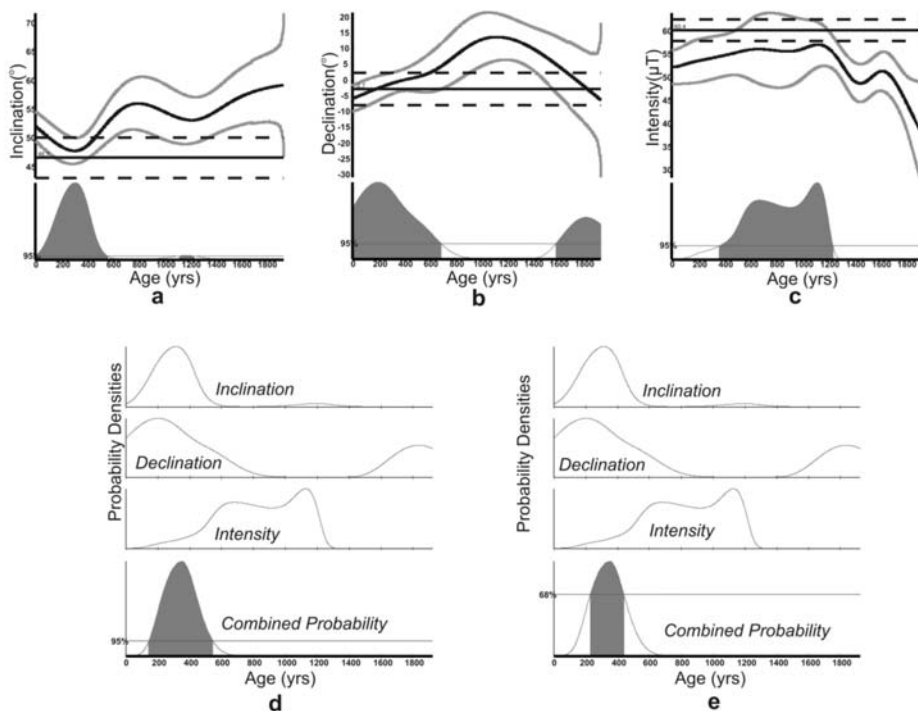
Fig. 7: Archaeomagnetic dating of Sani site. a,b,c) Dating of inclination, declination and intensity respectively. Symbols as Fig.6. d,e) final dating after combining the probabilities of (a), (b) and (c) for 95% and 68% probability respectively.

axis vibrating sample magnetometer within a Helmholtz coil system covered by a mu-metal shield.

The mean intensity value calculated from the samples which met all required criteria (details in Gallet et al., 2006) is 61.9 ± 2.2μT.
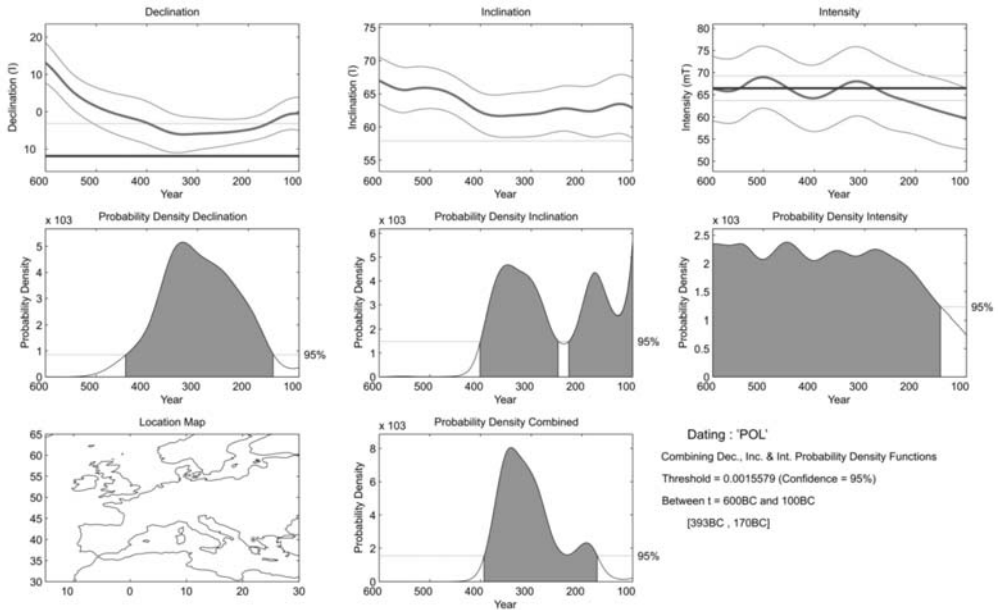
Fig. 8: Archaeomagnetic dating of Pol at 95% of probability level, using the declination, inclination and intensity curves as proposed by Pavon-Carrasco et al., 2009.

5. Archaeomagnetic dating

In the last decade archaeomagnetic dating became an attainable and common practice due to the development in statistical treatment of archaeomagnetic data based on bivariate statistics or Bayesian hierarchical technique (Le Goff et al., 2002; Lanos et al., 2005).

The archaeomagnetic dating is possible only in regions where a well established secular variation curve is available. The first directional SVC for Greece have been constructed by DeMarco (2007), while for the intensity the first attempt was made by Spatharas (2005). A new, improved version was published by DeMarco et al., 2008.

In order to date archaeomagnetically our results, the obtained data for the studied areas (Table 2) have been recalculated to the geographical coordinates of Athens, where the Greek SVC also referred to as a reference site. The relocation was made by using the virtual geomagnetic pole (VGP) method proposed by Noel and Batt (1990). The dating was performed by using the Bayesian hierarchical approach (Lanos et al., 2005). This method allows the calculation of the probability densities separately for each geomagnetic field element after comparison with the reference SV curves. The final dating interval is obtained by combining the separate probability densities in order to find the best solution.

In Figs. 6,7 the final dating for Thessaloniki and Sani sites is presented. For Thessaloniki site, the comparison of the directional data gives three time intervals: 0-205AD, 410-880AD and 1445-1950AD at 95% confidence level. According to the archaeological findings the most probable interval is the second one (410-880AD). This time interval represents the last firing of the kiln. Even if the reference SVC for this time span is not very well constrained, the estimation obtained from the dating is more precise and narrower than the archaeological one (400-1300AD).

For Sani, the full archaeomagnetic field vector was used for the dating. The combination of the three geomagnetic elements (D, I, F) yields a time interval from 144-545AD at 95% confidence level. According to the archaeological findings the kiln is dated in the end of the 3rd century or beginning of the 4th AD. If instead of 95% of probability the 68% is calculated then, the obtained time interval is 229-440AD, which is much smaller and closer to the archaeological estimations (Fig.7).

For the archaeological site of Polymilos, the archaeointensity value had been already estimated by Spatharas, (2005). Since this value is used by DeMarco et al., (2008) for the elaboration of the new intensity SV for Greece we did not use the Greek curves for dating this site in order to avoid any circular reasoning. Instead, the regional archaeomagnetic model for Europe for the last 3000yrs, SCHA.DIF.3K proposed by Pavon-Carrasco et al., (2009) was used. The obtained time period, when taking into account the archaeological constraints is 393-170 BC. (Fig.8).

6. Conclusions

The material studied here has proved to be reliable for an accurate recording of the ancient geomagnetic field. This is confirmed by absence of alteration and strong anisotropy, and the presence of multiple magnetic carriers. The grouping of the obtained directions is estimated satisfactory with a_{95} parameter lying at the limit of worldwide accepted as trustworthy values. A further control of the obtained D,I values by comparing them to the existing dataset for Greece (DeMarco, 2007) shows a very satisfactory convergence in all but one cases: the I value of Polymilos is by~10° lower than the other data. The D values are slightly diminishing versus age. Though the existing error bars do not allow a firm conclusion, this could be related to the westward drift observed for mid-latitude azimuthal motions over the last 3000yrs, for the time period 800BC-900AD (Dumberry and Finlay, 2007).

A continuing study in the above archaeological sites will possible clarify this observation.

7. Acknowledgments

8. References

Aidona E., Scholger, R., Mauritch, H., Perraki, M., 2008. Remanence acquisition in a Roman-style gold furnace. Physics and Chemistry of the Earth, 33, 438-448.

DeMarco, E., 2007. Complete magnetic and archaeomagnetic measurements in archaeological sites: contribution to the SVC for Greece. PhD Thesis, Aristotle University of Thessaloniki, Thessaloniki, 293pp.

DeMarco, E., Spatharas, V., Gomez-Paccard, M., Chauvin, A., Kondopoulou, D., 2008. New archaeointensity results from archaeological sites and variation of the geomagnetic field intensity for the last 7 millennia in Greece. Phys. and Chem. of the Earth 33, 578–595.

Downey, W.S., Tarling, D.H., 1984. Archaeomagnetic dating of Santorini volcanic eruptions and fired destruction levels of Late Minoan civilization. Nature 309, 519-523.

Dumberry M., Finlay C., 2007. Eastward and westward drift of the Earth's magnetic field for the last

three millennia. Earth Planet. Sci. Let., 254, 146-157.

Evans, M.E. and Kondopoulou, D., 1998. Archaeomagnetism in Macedonia, Greece: A progress Report. Phys. Chem. Earth, 23, (9-10), 1027-1028.

Evans, M.E., 2006. Archaeomagnetic investigations in Greece and their bearing on geomagnetic secular variation. Phys. Earth Planet. Int., 159, 90-95. doi:10.1016/j.pepi.2006.06.005.

Gallet, Y., A. Genevey, M. Le Goff, F. Fluteau, and S. A. Eshraghi 2006. Possible impact of the Earth's magnetic field on the history of ancient civilizations, Earth and Planetary Science Letters, 246, 17-26.

Jelinek, V., 1977. The statistical theory of measuring anisotropy of magnetic susceptibility of rocks and its applications. Geofizika, Brno.

Jelinek, V., 1981. Characterization of the magnetic fabric of rocks. Tectonophysics, 79, 63-67.

Jordanova, N., Kovacheva, M., Kostadinova, M., 2004. Archaeomagnetic investigation and dating of Neolithic archaeological site from Boulgaria. Phys. Earth Planet. Int., 147, 89-102.

Kirschvink, J.L., 1980. The least-squares line and plane and the analysis of palaeomagnetic data. Geophysical Journal of the Royal Astrological Society, 62: 699-718.

Kondopoulou, D., and Spatharas, V., 2002. Magnetomineralogy of archaeomagnetic materials from N. Greece. Proc. 5th European Meeting on Ancient Ceramics, Athens 1999. In: Kilikoglou, V., Hein, A., Maniatis Y. (Eds.), Modern trends in scientific studies on ancient ceramics. BAR International Series, 1011, 389-402.

Kovacheva, M., Spatharas, Y., Liritzis, Y., 2000. New archaeointensity results from Greek materials. Archaeometry, 42 (2), 415-429.

Lanos, Ph., Le Goff, M., Kovacheva, M., Schepp, E., 2005. Hierarchical modelling of archaeomagnetic data and curve estimation by moving average technique. Geophys. J. Int., 160, 440-476.

Le Goff, M., Gallet, Y., Genevey, A., Warme, N., 2002. On archaeomagnetic secular variations curves and archaeomagnetic dating. Phys. Earth Planet. Int., 134, 203-211.

Le Goff, M. and Y. Gallet, 2004. A new three-axis vibrating sample magnetometer for continuous high-temperature magnetization measurements: applications to paleo- and archeo-intensity determinations, Earth and Planetary Science Letters, 229, 31-43.

Liritzis, Y. and Thomas, 1980. Palaeointensity and thermoluminiscence measurements on Cretan kilns from 1300 to 2000 BC. Nature, vol.283, 54-55.

Lowrie, W., 1990. Identification of ferromagnetic minerals in a rock by coercivity and unblocking temperature properties. Geophys. Res. Let., 17 (2), 159-162.

Noel, M., Batt, C., 1990. A method for correcting geographically separated remanence directions for the purpose of archaeomagnetic dating. Geophys. J. Int., 102, 753-756.

Pavón-Carrasco, F. J., Osete, M.L., Torta J.M., Gaya-Piqué L.R., 2009. A regional archaeomagnetic model for Europe for the last 3000 years, SCHA.DIF.3K: Applications to archaeomagnetic dating. Geochemistry, Geophysics, Geosystems, 10, Q03013, doi: 10.1029/2008GC002244.

Spatharas, V., 2005. Archaeomagnetic and magnetic measurements in archaeological materials in Macedonia and Thrace (N. Greece). PhD Thesis, Aristotle University of Thessaloniki, Thessaloniki, 179pp (in Greek).

Spatharas, V., Kondopoulou, D., Liritzis Y., and G. Tsokas., 2000. Archaeointensity results from two ceramic kilns from N. Greece. J. Balkan Geophys. Soc., 4, 67-72.

Tarling, D.H., Kondopoulou, D. and Spatharas, V., 2004. An archaeomagnetic study of the LM IB Kilns. In: Soles, J.S., Davaras, C. (Eds.), *Mochlos IC – Period III. Neopalatial Settlement on the Coast: The Artisans' Quarter and the Farmhouse at Chalinomouri. The small Finds*. Prehistory Monographs **9**, INSTAP Academic Press, Philadelphia, Pennsylvania, 2004.

GEOPHYSICAL RESEARCH FOR GEOLOGICAL STRUCTURE DETERMINATION IN THE REGION OF SOUTH MESOGHEIA (ATTICA)

Alexopoulos J.D.[1] and Dilalos S.[1]

[1] *National and Kapodistrian University of Athens, Faculty of Geology and Geoenvironment, Department of Geophysics - Geothermics, 157-84, Panepistimiopolis, Athens, Greece, jalexopoulos@geol.uoa.gr, sdilalos@geol.uoa.gr*

Abstract

During the last years the broader area of Koropi (Mesogheia-Greece), has faced rapidly increasing problems concerning irrigation and watering of the town, due to the brackish water in the water supply boreholes. Our main target is to determinate the subsurface geological structure of the study area, located NE of the Koropi city, where alterations of schists and carbonates, from three different post-alpine units, mainly appear and relate it with the groundwater flow paths. The dominant geological outcrops of the area are the Athenian Schist (Laurion-Attica Unit), the dolomitic marbles (Vari-Kirou Pira Unit) and the Lower Marble (Hymittos Unit). A geophysical research was carried out in the area mainly based on the geoelectrical methodology, including by executing fifteen Vertical Electrical Soundings and one Electrical Resistivity Tomography. The interpretation results of the geophysical data have been evaluated and combined with "in-situ" resistivity measurements and calibrated with cores coming from drilled boreholes revealing the area. Through this combining process important elements of the local geological subsurface structure have been determined, as the formation of the dolomitic marbles (massive or karstified) was found tilting southwards beneath the Athenian Schist. From a hydrogeological point of view, this alone adds a significant parameter to the subsurface geological structure which is highly related to the groundwater flow that is responsible for many problems and could be used for solving many others.

Key words: *Electrical soundings, Resistivity tomography, Koropi.*

1. Introduction

During the last few years, in the study area the economic development is quite increased, with many industries and agriculture, with the second covering a major part of the Mesogheia area. The industrial zone is located north-westwards of the Koropi town. The geological structure of the area is quite complicated, consisting of 3 different lithological units. Due to some existing hydrogeological problems of the area, including the appearance of brackish water in almost every borehole in the area, a geophysical investigation has been carried out, in order to determine in detail the geological structure of the area. The study area is located SSE of Koropi city, around the road leading to Markopoulo and east of the road to Vari.

The geological formations outcropping in the area, are schists from three different units generally,

impermeable and conductive formations, but also two types of marbles, either massive or locally karstified, comprising a complicated hydrogeological regime. Additional data come from several boreholes that are mainly used for irrigation and watering. For many of these boreholes, core data were kindly provided by Dr. Spyridon Lekkas, Professor of Hydrogeology, to the authors.

2. Geological setting

A typical succession from the shallowest to the deepest formations at the region of Mesogheia contains the following (Fig. 1): The Quaternary deposits, the Neogene formations, the allochthonous unit members of Cretacious limestones and the underlying Athenian Schist, the autochthonous unit members of superior marble and the underlying Kaissariani Schist, the Lower Marble, the Pirnaris dolomites and finally the Vari Schist.

A rough description of the post-alpine deposits follows:

- The Pleistocene deposits cover the major part of the study area. They mostly consist of non-homogeneous inarticulate conglomerates and red clays. Their thickness varies from some meters to hundreds of metres, eastwards and north-westwards. They are characterized by the presence of a calcareous crust, caused by the climatic influence.

- The Neogene deposits are comprised by marls, sandstones, calcareous marls and conglomerates, with pebbles coming from marbles, schisteous marbles, ultrabasic and pyrites.

The alpine formations can be categorized in the following three tectono-stratigraphic units.

- The Laurion-Attica Unit: Consisted of the Athenian Schist, whose thickness reaches up to 120 meters thick, according to drilling data. This schist consists mostly of phyllites, argillaceous schists, green schists with low content of metamorphic sandstones and quartz with high content of basic and ultrabasic formations.

- The Hymittos Unit: is represented by the Kaissariani Schist and the Lower Marble (Jurassic). This schist contains muscovites, calcareous schists with chlorites, limestones, serpentinites and marbles intercalations. The Lower Marble outcrops mainly at the southern parts of the study area, having a significant thickness and a variety of colours, as white, bluish or reddish.

- The Unit of Vari-Kirou Pira: It is the basement unit of Attica, including three different formations in the study area, which are the dolomites of Pirnaris, the dolomitic marbles (sipolines and impure marbles) and the Vari Schist. The dolomites of Pirnaris, are located eastwards of the study area with maximum thickness equal to 250 meters. They are crustal thin-bedded with various colours, from white to reddish, covering the Vari Schist where they interpose. The dolomitic marbles appear southwards of the area and are composed of a continuous alternation of crystalline marbles and dolomitic marbles, including levels of schists with muscovites, chlorites and limestones (Lekkas and Lozios, 2000).

3. Resistivity Survey

The resistivity survey was applied in the area, due to the existing geological formations and their different impact on resistivity. The geoelectrical data include six (6) "in-situ" resistivity measurements next to boreholes and surface outcrops of the geological formations, fifteen (15) ver-
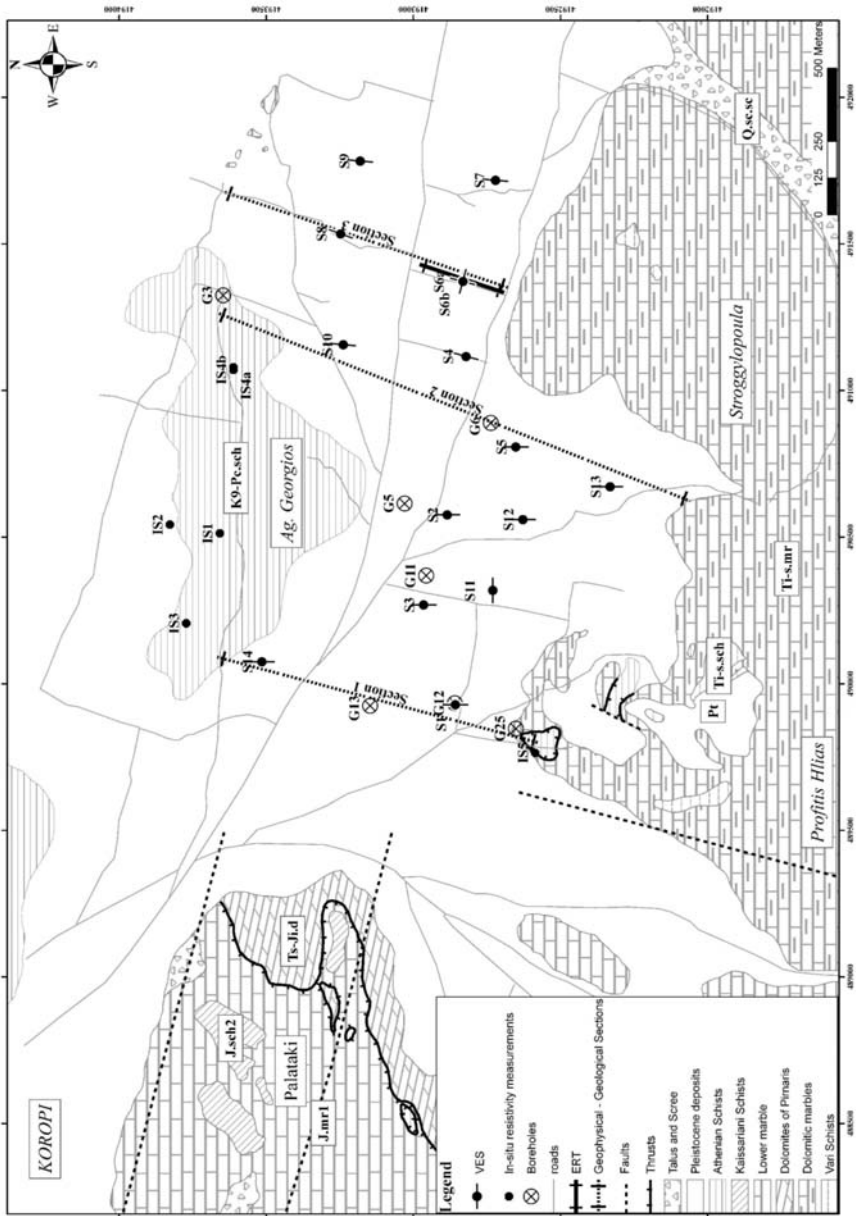
Fig. 1: Simplified and modified geological map (Ihyane and Lekkas, 2008) of the study area, along with the boreholes located in the area and all the geophysical measurements. Q.cs.sc: Tales and Scree, Pt: Pleistocene deposits, K9-Pc.sch: Athenian Schist, J.sch2: Kaissariani Schist, J.mr1: Lower marble, Ts-Ji.d: Dolomites of Pirnaris, Ti-s.mr: Dolomitic marbles, Ti-s.sch: Vari Schist.

Table 1.

Geological Formation	Resistivity (Ohm.m)
Pleistocene deposits	17 - 25
Athenian Schist	43 - 200
Dolomitic marbles	350 - 900
Vari Schist	150 - 200
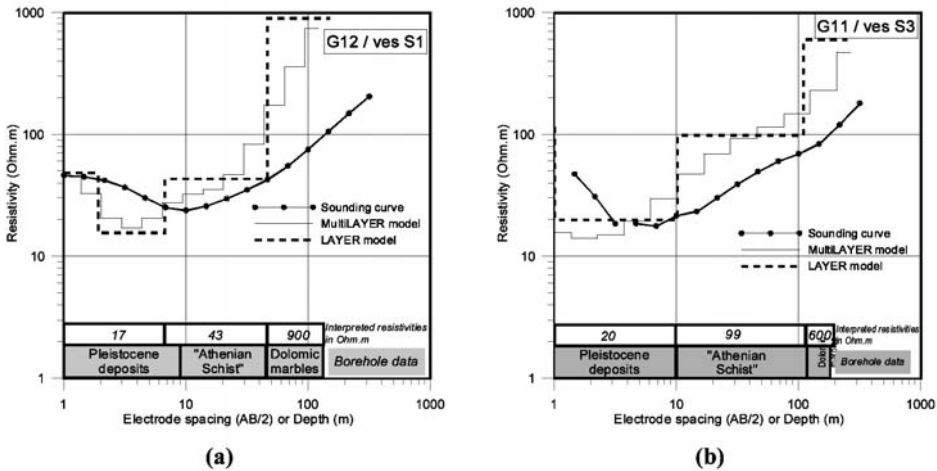
Fig. 2: Interpretation results of VES S1 (a) and S3 (b) integrated with the corresponding drilling data of G12 and G11.

tical electrical soundings (VES) for the investigation of the geological structure and a 200-m electrical resistivity tomography (ERT), for a more detailed evaluation. All these data were collected in the flat area between the Ag.Georgios and Stroggylopoula hills.

3.1 "In-situ" resistivity measurements - Calibration

In order to calibrate and better evaluate the geoelectrical results, four (4) "in-situ" resistivity measurements were carried out, above outcrops of the existing geological formations and mostly above Athenian schist's outcrops, applying the *Schlumberger* array, with maximum AB length equal to 215 meters. Furthermore, some soundings (S1, S3) were carried out next to existing boreholes (waterless during the resistivity measurements period), for which the drilling data were provided by Prof. Lekkas Sp. This ensured the best possible calibration and interpretation of processing results (Fig. 2) and contributed to an accurate definition of the corresponding resistivity limits of each geological formation (Table 1).

Specifically, the interpretation results of the S1 sounding, carried out next to borehole G12 (Fig. 2a), revealed for the Pleistocene deposits, resistivity values of approximately 17 Ohm.m, for the Athenian Schist values of 43 Ohm.m and for the massive dolomitic marbles 900 Ohm.m. Furthermore, the interpretation of S3, calibrated with the G11 borehole data (Fig. 2b), revealed 20 Ohm.m resistivity for the Pleistocene deposits, 99 Ohm.m for the Athenian Schist and approximately 600 Ohm.m indicating the dolomitic marbles.
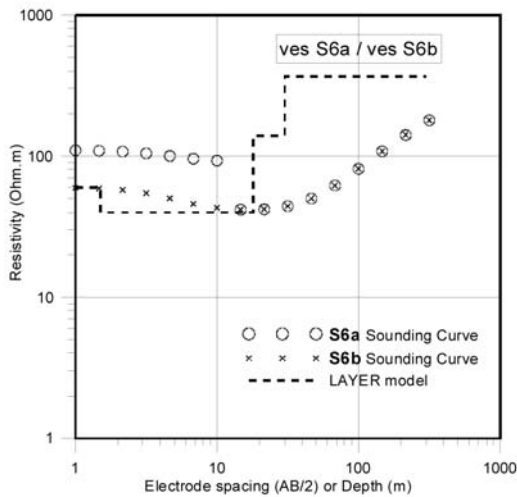
Fig. 3: Field data of VES S6a and S6b ("cross-direction") and processing results, based on VES S6b.

3.2 Vertical Electrical Soundings

Fifteen (15) resistivity soundings (VES) were conducted, using the *Schlumberger* array. Maximum current electrode spacing (AB) reached up to 928 meters with a quite good distribution around the study area, considering the district construction (traffic streets, residences, fences, etc) and vegetation. An *ABEM Terrameter SAS300C* and *Booster 2000* were used for the field measurements. The geophysical data were processed by applying the automatic method of Zohdy and Bisdorf (Zohdy, 1989), composing a "multilayer" model. Beyond this, the commercial software package IX1D (v3) of Interpex, was used in order to come up with the "layered" model.

At the location of S6 (Fig. 1), two separate sounding were carried out, first the S6a (N15° electrodes expansion) and then the S6b (N105° electrodes expansion), with fixed centre, but with perpendicular direction. These "cross-direction" soundings carried out due to an unexpected parallel shift of S6a curve's part (Fig. 3). Based on Zohdy et al. (1974), this shift usually derives from a subsurface vertical and thin geological formation or fault crossing perpendicular the electrode spacing expansion. One way to qualitatively check the existence of this possible geological anomaly, was the sounding S6b (Fig. 3), with the perpendicular electrodes expansion. Normally, at the curve of S6b there will not be any parallel shift, considering that its direction would now be parallel to any possible existing geological anomaly that caused the curve shift of S6a.

3.3 Electrical Resistivity Tomography

Due to the problem derived from the S6a curve's shift, combined with the curve of the perpendicular S6b sounding, the necessity of a more detailed geophysical technique was essential. The best solution for this unusual problem was the implementation of the Electrical Resistivity Tomography method, by which we obtain detailed data for the lateral and vertical resistivity distribution.

Consequently, a 200-m electrical resistivity tomography profile was carried out, using the *ABEM Terrameter SAS300C* along with the *ABEM* electrode selector *ES-464*. The system had 60 electrodes, providing the automatic measurements of apparent resistivity, using the Wenner array with an electrode spacing of 2.5m. The centre of the ERT profile, at 100m, is identical with
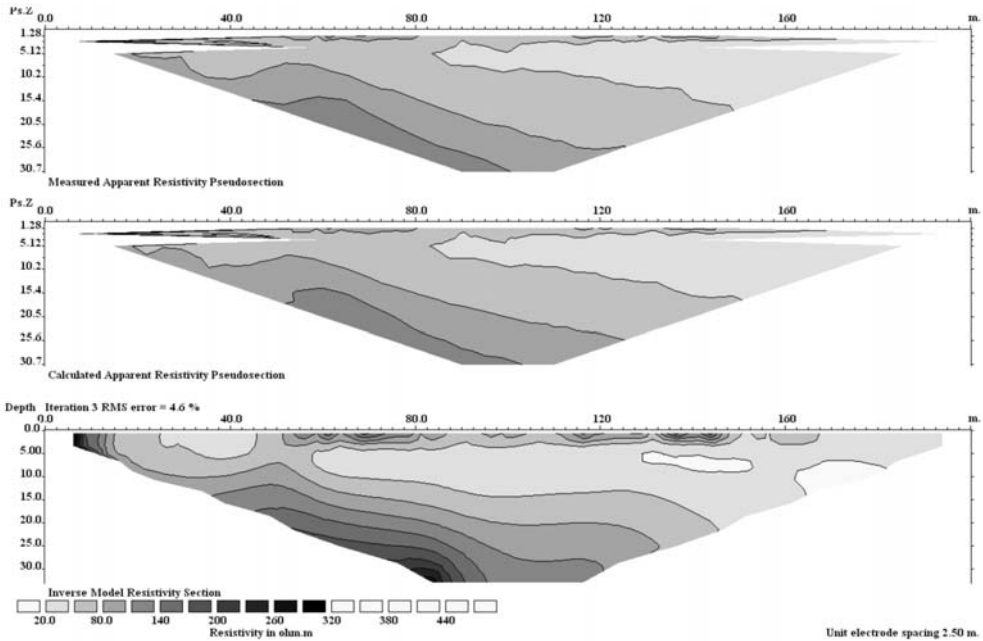
Fig. 4: Processing results of the ERT method. Top: Measured apparent resistivity pseudosection, Middle: Calculated apparent resistivity pseudosection, Bottom: Inverse model resistivity section.
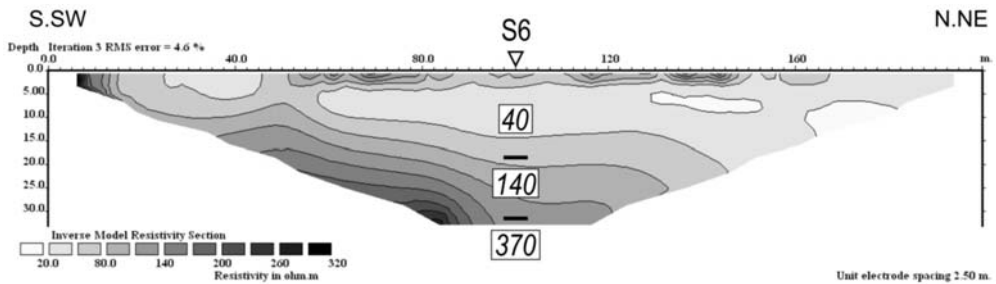
Fig. 5: Combined 2D resistivity tomography inversion model and 1D results of VES S6b.

the centre of the "cross-direction" soundings S6a and S6b (Fig. 5), in order to have the best evaluation of the processing results. The direction of the ERT profile is the same with the one of S6a (N105º).

The electrical resistivity tomography measurements (totally 190 points), were processed with the *RES2DINV* software of *GeoTomo* (Fig. 4).

The inverse model resistivity section, derived from this processing, indicated a tilted geoelectrical structure, which by no means can be connected with a vertical geological formation that was supposed to cause the curve shift of S6a. As it seems, this tilt was sufficient enough to shift the curve of S6a.
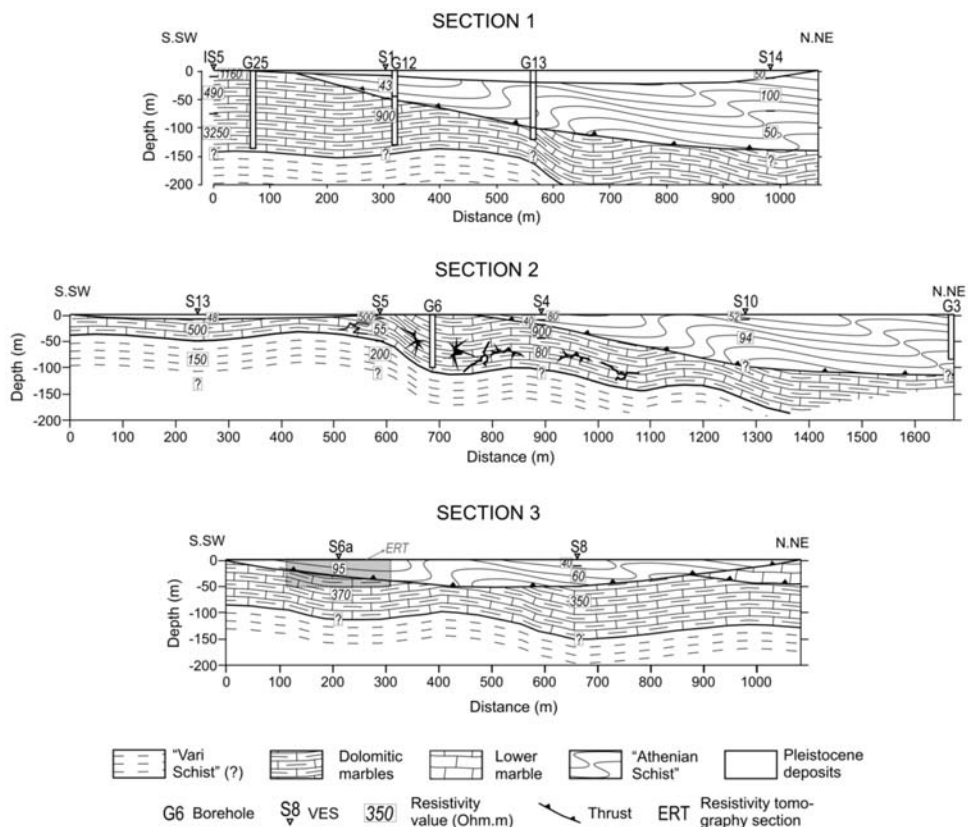
Fig. 6: Integrated geological and geophysical sections (the locations of these sections are illustrated in the geological map of Fig. 1).

At Fig. 5, the 2D inversion model of the resistivity tomography is illustrated along with the 1D layer results of the sounding S6b, revealing a first layer of 40 Ohm.m resistivity and approximately 18m thickness. Underlying this, a more resistive formation seems to be present, with resistivity around 140 Ohm.m and 14m thickness, tilting to NNE. The deepest investigated geoelectrical layer is even more resistant, up to 370 Ohm.m.

3.4 Integrating geophysical and geological results

Based on the interpretations of all the geophysical data of the study area, including all the soundings and the resistivity tomography, combined with the surface geological data and drilling stratigraphy columns, three (3) geoelectrical-geological sections were constructed (Fig. 6), in a NNE-SSW direction, beginning from Stroggylopoula hill and ending at Ag. Georgios hill (Fig. 1), in an effort to illustrate the subsurface geological structure of the small valley.

In these sections, five (5) different geological formations have been investigated, one of which is the geoelectrical basement of the Vari Schist, an impermeable formation contributing significantly at the hydrogeological conditions of the area. The presence of the Pleictocene deposits, covering almost all the area, is obvious. This layer seems to cover the thrust of the folded Athen-
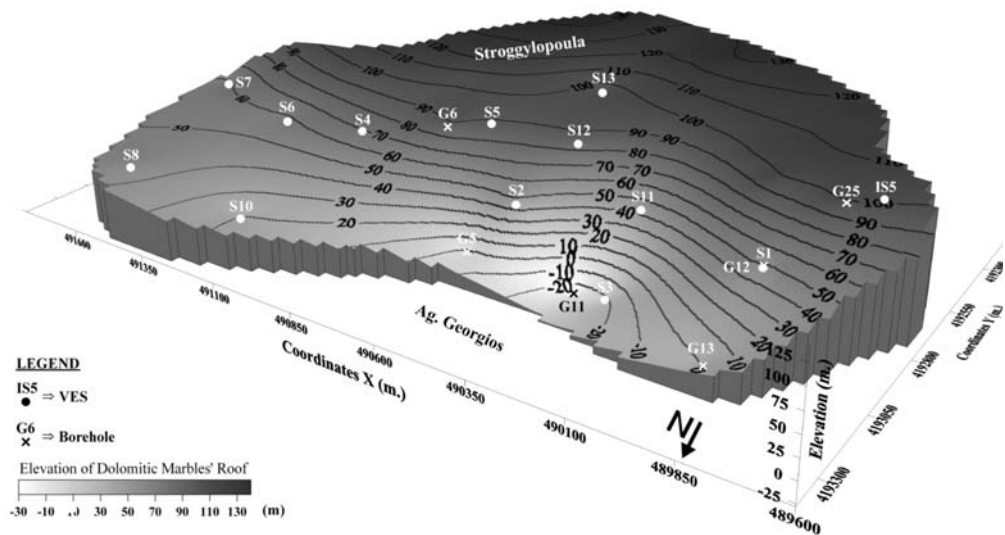
Fig. 7: 3-D representation of the dolomitic marbles' roof elevation.

ian Schist over the locally karstified dolomitic marbles, appearing on the surface of Stroggy-lopoula hill. In this karstified formation the brackish aquifer (Section 2, S4-S5 area, 55-80 Ohm.m) of the area is probably located, from which the boreholes pump the water out.

In Sections 1 and 2, the Athenian Schist appears with a tilt to NNE, exceeding until a depth of almost 150 meters near the soundings S14 and S10. On the contrary, in section 3, located at the boundaries of the valley, between the two hills, the Athenian Schist is illustrated with a maximum depth of approximately 50 meters and overlying the Lower marble at the NNE edge of the section.

In Section 3 (Fig. 6), the grey box corresponds to the Resistivity Tomography (Fig. 5). The two techniques seems to fit quite well, both illustrating the tilt of the first geoelectrical-geological to NNE.

4. Conclusions-Results

After the evaluation of the geophysical measurements combined with the geological and borehole data, the formation of the dolomitic marbles seems to have been investigated at all the soundings. Based on this, a 3-D representation has been produced (Fig. 7), illustrating the elevation of the roof of the dolomitic marbles formation (massive or karstified). The tilt of the dolomitic marbles to the North is definite, with the Athenian Schist overlying with an increasing thickness to the North. The maximum depth for the roof of the dolomitic marbles is approximately 110 meters (absolute elevation is -27m., when surface elevation is +137m.), located northwards of the area (Fig. 7) and based on combined geophysical and drilling data. The thickness of the overlying Athenian Schist at this point is approximately 100 meters.

The impermeable formation of Vari Schist has been investigated as the geoelectrical basement (150-200 Ohm.m) only in few soundings, such as S2, S3, S4, S11, S12 and S13, all located in the central part of our study area. The AB extent of the other soundings wasn't possibly enough

to investigate the formation of Vari Schist, located in greater depths, likely due to the tilt of the overlying dolomitic marbles to the North.

Regarding specifically the geophysical processing results, the model evaluation of the sounding S06a fits with the inverse model of the electrical resistivity tomography (Fig. 4), raising no doubts for the processing results. Moreover, the evaluation of the geophysical data with the valuable drilling data, leads to a better determination of the subsurface geological structure of the area, where no faults have been investigated, as the formations are quite folded.

5. Acknowledgments

6. References

Ihyane, B., 2007. Hydrogeological study of the grainy and karstic aquifers of the region between Koropi-Markopoulo and airport. *Master thesis, National Kapodistrian University of Athens,* Athens, 148p.

Ihyane, B., Lekkas, S., 2008. Degradation anthropogene de la nappe karstique de la region de Mesogheia (Attique, Grece). *Proceedings of 8th International hydrogeological congress of Greece,* Athens, Vol.2, 829-838.

Lekkas, S. and Lozios, S., 2000. Tectonic structure of Mt. Hmyittos. *Ann. Geol. Pays Hellen.*, Vol.38, 47-62.

Loke, M.H., 1999. *Electrical imaging surveys for environmental and engineering studies – A practical guide to 2D and 3D surveys*, Malaysia, 57p.

Zohdy, A.A.R., 1989. A new method for the automatic interpretation of Schlumberger and Wenner sounding curves, *Geophysics,* Vol. 54-2, 245-253.

Zohdy, A.A.R, Eaton, G.P. and Mabey, D.R., 1974. Application of surface geophysics to groundwater investigations. *Techniques of water-resources investigations*, U.S. Geological Survey, Book 2, Chapter D1, 116 p.

CONTRIBUTION OF GEOPHYSICAL METHODS TO THE INVESTIGATION OF GEOTHERMAL CONDITIONS IN THE SOUTHWESTERN PART OF THE STRYMON BASIN (MACEDONIA, NORTHERN GREECE)

Arvanitis A.A.[1], Stampolidis A.D.[2], and Tsokas G.N.[2]

[1] Institute of Geology and Mineral Exploration, Division of Geothermal Energy and Thermal Mineral Waters, Entrance C, Olympic Village, 13677, Acharnae, Attica, Greece, arvanitis@igme.gr

[2] Department of Geophysics, School of Geology, Aristotle University of Thessaloniki, 54124, Thessaloniki, Greece, astamp@geo.auth.gr, gtsokas@geo.auth.gr

Abstract

The Strymon basin is one of the most important sedimentary basins in Northern Greece where significant geothermal fields are located. The SW part of the Strymon basin manifests geothermal interest. Available geophysical data (seismic, gravity, magnetic and electrical data) contributed to the identification of major faults that control the fluid-flow paths of the geothermal field and the estimation of depth to the metamorphic basement. The former is of great importance because the geothermal aquifer is expected to be at the contact of the basal conglomerate with the metamorphic basement. The highest thermal gradient values (10-15°C/100 m) were observed in the western part of the study area near the known geothermal field of Therma – Nigrita. Other important geothermal anomalies (>6°C/100 m) occur in the Patriki area, north of the village of Ivira and in the area between the villages of Patriki and Achinos. Geothermal interest manifests itself in the following areas: north of Mavrothalassa (>4°C/100 m), southwest of Ivira and east of Agios Dimitrios. It appears furthermore that the main thermal anomaly is associated with two NW-SE fault systems that affect the basement in the areas of Patriki and north of Achinos - Ivira correspondingly. These faults have been detected by the use of geophysical surveys. The presence of NE-SW faults extends the anomaly southwestwards.

Key words: Strymon basin, geothermal fields, Ivira, Achinos, geophysical methods, Serres.

1. Introduction

The Strymon basin is a typical post-orogenic graben. It has been formed between the Serbomacedonian Massif (SMM) to the Rhodope massif to the east. The eastern margins of the basin belong to the Pangeon Unit of the Rhodope massif composed of marbles, gneisses and mica schists. The Vrondou granitic complex intrudes the metamorphic rocks of the Pangeon Unit. The Serbomacedonian massif is divided into two crystalline 'series': (a) the Kerdylia Series (at the SW margins of the basin) composed of migmatic gneisses, amphibolies and marbles and (b) the Vertiskos Series made up of intercalations of schists, leucocratic and augen gneisses and amphibolites. Late Paleozoic, Cretaceous and Paleogene granitoid bodies intruded into the Serbomacedonian massif. The

total thickness of Neogene and Quaternary sediments at the center of the basin is approximately 4000 m. The principal faults are oriented in NW-SE, NNE-SSW to NE-SW and WNW-WSE to W-E directions. The Strymon basin is of primary geothermal interest. Some important low enthalpy geothermal fields exist. The Therma - Nigrita, Sidirokastro, Lithotopos - Iraklia and Agistro fields have already been characterized officially as 'proven' and/or 'probable low temperature geothermal fields' with water temperatures between 40 and 74°C. The geothermal aquifers are located at relatively shallow depths (30-500 m). The geothermal anomaly occurs mainly due to deep fault systems being normal and strike-slip structures. In the central part of the Strymon basin of the Strymon basin three deep exploration oil boreholes (STR-1, STR-2, STR-3 at depths of 3651, 2678 and 3144 m respectively) were drilled. In borehole STR-1 the average geothermal gradient is 31°C/km and the temperatures of 57, 66, 106 and 135°C were measured at depths of 1209, 1475, 2884 and 3651 m correspondingly. The geothermal gradient for the Strymon basin has been estimated to fluctuate from 25 to 36°C/km at depths of more than 2000 m (P.P.C., 1988). The geothermal conditions in the Strymon basin are favourable as a result of the active extension tectonics and the increased heat flow. Tertiary granitoids of Vrondou and Pangeon increased the regional heat flow. Additionally, the large deep and open faults of the basin are favourable for the uprising of the geothermal fluids at relatively shallow and exploitable depths or at surface. The general geological settings favour the formation of a geothermal field including: (a) the existence of conglomerates and breccias on the top of the basement and as interbedded strata, (b) the presence of an impermeable cap consisting of Neogene clayey and marly sediments and (c) the water circulation into the permeable sediments and the fractured crystalline rocks supplying continually the reservoir (Arvanitis, 2003).

A new very interesting geothermal area has been recently explored in the southwestern part of the Strymom basin. This area extends from the villages of Choumniko and Patriki in the west to the villages of Efkarpia and Tragilos in the east (Fig. 1) covering an area of about 25 km². It was explored by the Aristotle University of Thessaloniki (School of Geology) and I.G.M.E. during 1993-2002. The preliminary geothermal investigation was performed mainly by the Aristotle University (Arvanitis, 2003) and included geological and tectonic study of the area, interpretation of available geophysical data (seismic, gravity, magnetic and geoelectrical data), a detailed thermometric survey with water temperature measurements of existing water supply and irrigation wells, water sampling and chemical analyses, hydrochemical study etc. This paper presents the results of the interpretation of available geophysical data that contributed to the identification of major faults controlling the fluid-flow paths of the geothermal field and the estimation of depth to the metamorphic basement.

2. Geological and tectonic setting

Geologically the southwestern part of the Strymon basin belongs to the Serbomacedonian massif. The crystalline basement is composed of mica schists, biotite gneisses, amphibolitic gneisses, marbles, plagioclase gneisses, pegmatites, quartzites, etc. Neogene and Quaternary sediments have been deposited over the basement rocks (Fig. 1). These sediments consist of the basal conglomerates, limestones, sandy limestones, sandstones, sands, marls, sandy marls, marly limestones, silts, clays, sandy clays with interbedded strata of gravels and cobbles. The main characteristic of these deposits is their clayey-marly composition and therefore they can form an impervious cap for the geothermal fluids. In these sediments there are shallow aquifers containing waters at temperatures of 25-35°C and deeper aquifers bearing higher temperature waters (50-60°C). The total thickness of the Neogene and Quaternary sediments ranges from a few meters (close to the basement) to 1000 m (north of the villages of Achinos and Ivira) or more reaching up to 4 km in the central part of the Strymon basin (Arvanitis, 2003).
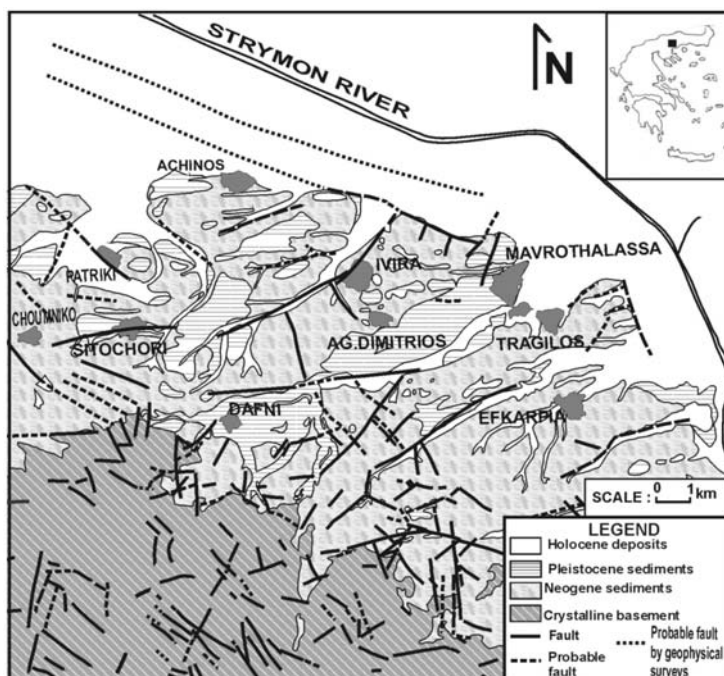
Fig. 1: Simplified geological map of the southwestern part of the Strymon basin (Arvanitis, 2003).

The tectonic setting in the area is very complicated. The faults are oriented in NE-SW, NW-SE and E-W directions affecting the crystalline basement and the overlying sediments. The gradual tectonic subsidence of the basement from south to north is characteristic. Fig. 1 is a simplified geological map showing the faults in the southwestern part of the Strymon basin. The interpretation of available geophysical (seismic, geoelectrical, gravimetric) surveys has revealed the presence of large faults covered by sediments.

3. Geophysical Methods

3.1 Seismic methods

In the Strymon basin, seismic surveys conducted by Public Petroleum Corporation (P.P.C.) during 1977-1979. A total of 11 seismic reflection lines (12-18 km long) were measured by P.P.C. and processed by BEICIP-FRANCE in 1980 (P.P.C. Strymon Report, personal communication). Interpretation results from 4 seismic reflection lines namely LINE-7, LINE-99 and LINE-13 of the P.P.C. surveys were used in this study to define the geological and tectonic setting of the geothermal area in the SW part of the Strymon basin. The numbers along the seismic profiles constitute the C.D.P. (Common Depth Point) positions. In multichannel reflection profiling, C.D.P. is the unique point on an individual reflector from which seismic reflection information is recorded in traces at different offsets. The traces are sorted by computer into gathers with the same C.D.P. The C.D.P. method is a seismic data acquisition and processing technique which transforms field recordings from seismic surveys into pseudo-cross-sectional images of the earth's geologic layering beneath the survey line. Velocity analysis, gathering, stacking and migration are routinely applied to the 'raw' data. The C.D.P. method helps the migration and stacking processes. Deep exploration oil borehole STR-1 is
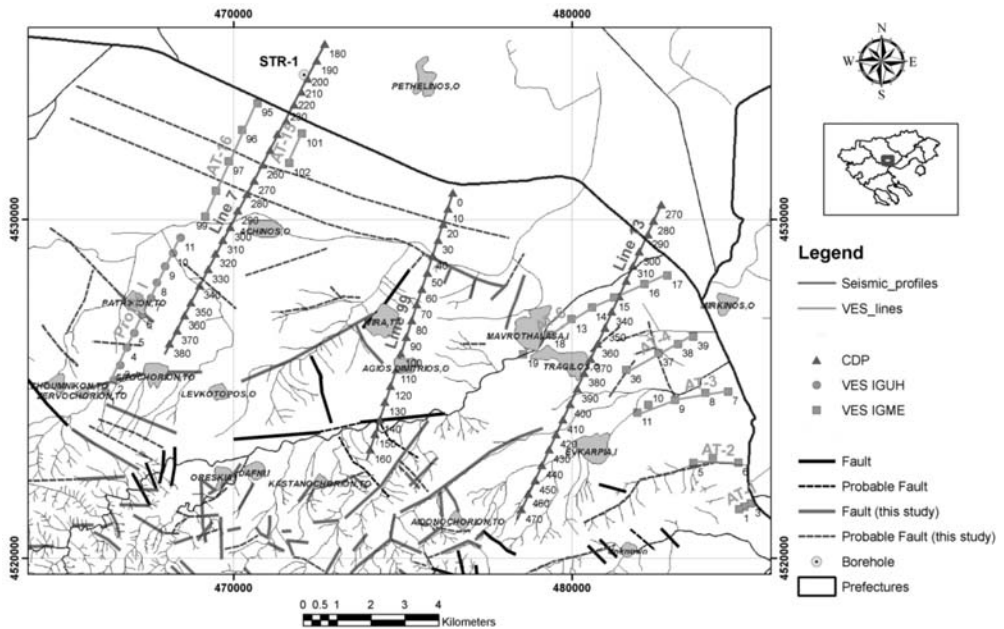
Fig. 2: Location map of the southwestern part of the Strymon basin illustrating the positions of the seismic lines LINE 7, LINE 99 and LINE 13 and the VES profiles from University of Hamburg (IGUM) and IGME.

located next to C.D.P. 200 on the seismic Line 7 (Fig. 2). The lithology column of this well consists of Pleistocene deposits (0-870 m depth), Pliocene sediments (870-1711 m) and Miocene formations (1711-3651 m). The basement was penetrated at a depth of 3651 m. Correlation between seismic records and borehole geological data was performed. Pleistocene deposits Vp velocity values range between 1.9 and 2.2 km/sec, Pliocene sediments between 2.9 and 4.0 km/sec, while Miocene sediments shown slightly higher velocities from the overlain ranging between 3.0 and 4.18 km/sec. The Vp velocity of the basement was calculated about 5.0 km/sec. The suggestions for the Vp velocity values and the results of the seismic profile 'Line-7' were confirmed by some wells. For example, near CDP 380, a well, 210 m deep, has penetrated gravels and pebbles probably belonging to basal conglomerate at the bottom. This means that the basement is expected to be a few meters deeper than 210 m. Based on the data from seismic profile 'Line-7' the basement depth is estimated to be about 239 m indicating a very good correlation between the seismic data and the well data.

The seismic surveys can considerably aid the structural investigation in the SW part of the Strymon basin. All the above-mentioned seismic profiles show a general northward dip of the basement towards the basin centre. The total thickness of sediments exceeds 3.5 km in the basin centre. Miocene sediments show a significant increase in thickness (650-1600 m) in the central part of the basin. The thickness of Pliocene sediments ranges from 180 m at the margins to 1000 m in the area of the Strymon River. There is similarly a gradual increase in thickness of Pleistocene deposits ranging from 200 m at the margins to 550-850 m in the centre of the basin. Seismic reflection data have been used to provide information on the tectonic setting of the study area. Normal faults have been identified resulting in the deepening of the basement. The location of a major normal NW-SE trending fault along the southwestern margin of the basin has been traced north of the villages of Achinos, Ivira and Mavrothalassa and south of the Strymon River. This fault (or probably fault zone) is responsi-
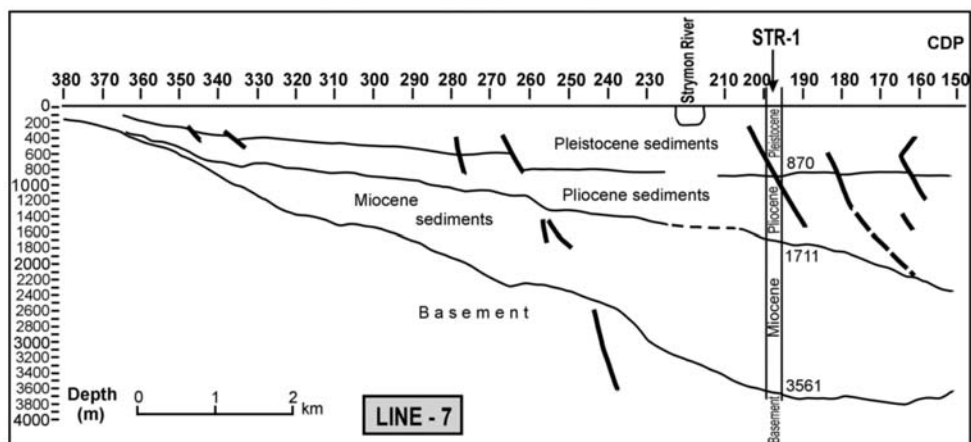
Fig. 3: Interpreted profile of seismic Line-7.

ble for the large-scale and abrupt deepening of the basement. The presence of a tectonic terrace system in the area confirms the results of the seismic reflection surveys. The interpretation of these seismic reflection data allowed the correlation between other terraces and faults or fault systems of a minor geothermal interest in the study area.

Seismic profile Line-7 indicates the existence of faults between CDP 270 and 250 (Fig. 3). These faults have influenced Pleistocene deposits, Pliocene sediments and Miocene formations as well as the basement of the basin. All these faults can be considered as a fault zone affecting the basement and the overlying sedimentary sequence and the basin deepens northwards. This fault zone is located at a small distance (about 1 km) north of the probable structural terrace extended between the area of the village of Achinos and north of Mavrothalassa (Fig. 1, 2). Another fault is noted on profile Line-7 at CDP 280 affecting Pleistocene and Pliocene sediments. This fault may be related to the above-mentioned fault zone. The location of this fault coincides with the pre-mentioned terrace. Other two small faults are recognized between CDP 350 and 330 located southwest of the village of Achinos. The total thickness of Neogene and Quaternary sediments increases from the margins towards the central part of the basin and the basement deepens from 161 m at CDP 380 to 3100 m below sea level (bsl) in the area of the Strymon River. In the area of the village of Achinos the basement depth is estimated to be about 1550 m bsl.

The first interpretation of seismic profile Line-99 (Fig. 4) shows a large normal fault between CDP 50 and 40. This fault affects the basement and the basement abruptly deepens northwards from 1305 m to 1830 m bsl. The thickness of Miocene sediments increases from 430 m to 950 m. This fault is located at about 2 km north of Ivira and coincides with the above-mentioned terrace of Achinos - Mavrothalassa. The small faults observed between CDP 50 and 20 affecting Pleistocene and Pliocene sediments may be associated with the large-scale basement fault. Two normal faults are recognized between CDP 120 and 100 on this seismic profile. The second fault detected between CDP 110 and 100 displays antithetic dip. These faults are located in the area of the village of Agios Dimitrios. Pleistocene deposits increase in thickness from 210 m SW of the village of Ag. Dimitrios to 550 m at CDP 0. The thickness of Pliocene sediments increases gradually from 420 m SW of Ag. Dimitrios to about 960 m at CDP 20. An abrupt increase in thickness of these sediments is observed between CDP 20 and the Strymon River bed. Miocene sediments have a significant thickness (about 950 m)
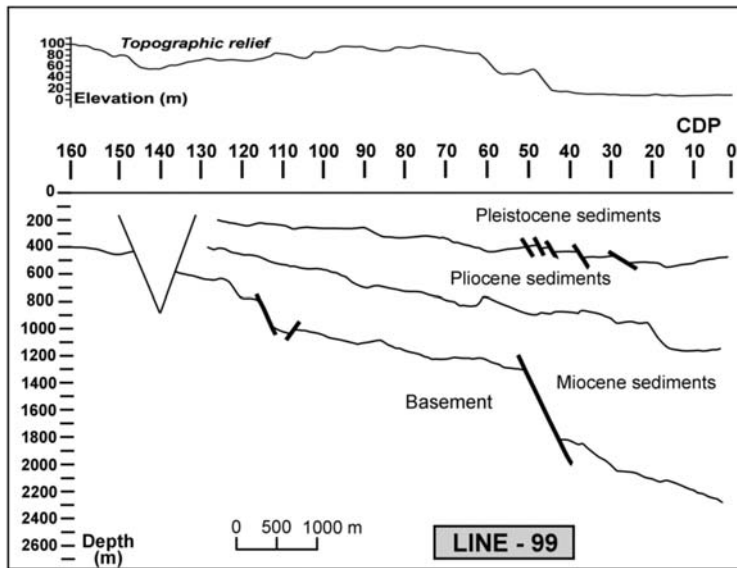
Fig. 4: Interpreted profile of seismic Line-99 (first interpretation).

at CDP 40 reaching 1140 m. In the area of the villages of Ivira and Agios Dimitrios and southwest of CDP 40, Miocene sediments have a thickness of 400-460 m, decreasing to 220-320 m southwest of the village of Ag. Dimitrios.

The second interpretation of seismic profile Line-99 (Fig. 5) shows a probable normal fault between CDP 60 and 50 affecting Pleistocene and Pliocene sediments. The downward extension of this fault indicates a northward dip of the basement due to the action of a large normal basement fault. The main characteristic of this profile is the basement uplift between CDP 80 and 50. This uplift is located north and northeast of the village of Ivira and coincides with a relatively small increase in topographic relief of this area (Fig. 4). Two faults have been identified between CDP 40 and 20 affecting Pleistocene and Pliocene deposits. Another normal fault has been detected at CDP 100 close to the village of Agios Dimitrios. This fault with throw of about 108 m seems to deepen the basement and the thickness of Miocene sediments increases. Miocene sediments show a considerable thinning southwest of CDP 100 and they are wedged at CDP 130. Their thickness ranges from 600 to 800 m between the villages of Agios Dimitrios and Ivira. A decrease in their thickness is observed in the area between the village of Ivira and the Lochagos Height where basement uplift is also observed and then the thickness increases up to 834 m in the Strymon River bed. Pliocene sediments increase in thickness from 520 m at CDP 130 to 1030 m at CDP 0 with a value of 840 m at CDP 80. The thickness of Pleistocene deposits remains almost constant (230-299 m) between CDP 130 and 70 and then it increases significantly towards the Strymon River bed, reaching 580 m.

Seismic profile Line-13 shows a group of 7 normal faults between CDP 370 and 300 located northeast and north of the village of Tragilos (Fig. 6). These successive faults have affected Pleistocene and Pliocene sediments. The continuous deepening of the basement between CDP 370 and 300 indicates that these faults are probably extended to greater depths affecting the basement. In this area, Miocene formations increase in thickness significantly. Therefore, the group of 7 faults is likely associated with a large-scale fault zone. The basement deepens gradually from 760 to 1200 m between the villages of Efkarpia and Tragilos along this line. There, the thicknesses of Neogene and Qua-
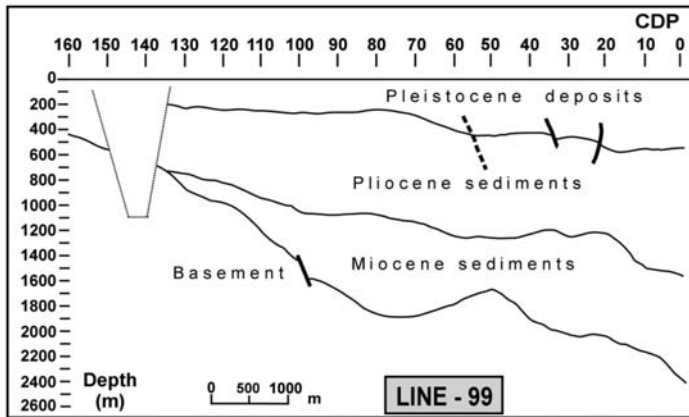
Fig. 5: Interpreted profile of seismic Line-99 (second interpretation).
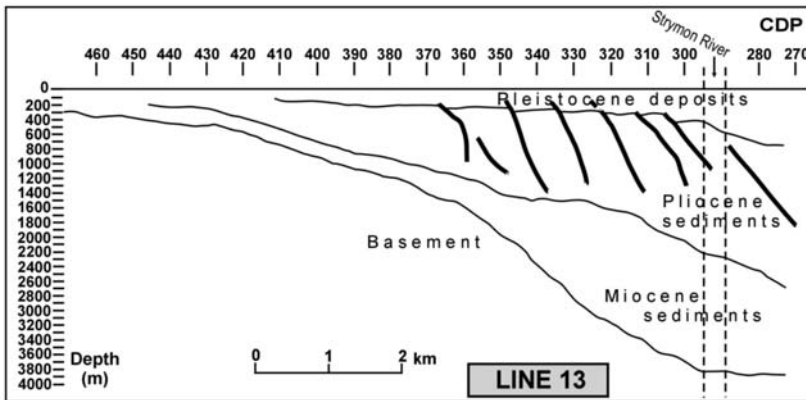
Fig. 6: Interpreted profile of seismic Line-13.

ternary sediments vary from 150 to 230 m for Pleistocene deposits, from 380 to 700 m for Pliocene sediments and from 230 to 265 m for Miocene formations. A significant increase in thickness of Miocene sediments is observed northeast of CDP 370 towards the Strymon River bed reaching 1648 m there. Miocene sediments have a thickness of the order of 200 m west of the village of Efkarpia.

3.2 Geoelectrical methods

Geoelectrical surveys were carried out mainly by the Institute of Geophysics of the University of Hamburg (P.P.C., 1981) and the Institute of Geology and Mineral Exploration (I.G.M.E.) in order to investigate the local geological and tectonic conditions studying the spatial distribution of the resistivity values in the subsurface and detecting faults that affect the sediments and probably penetrate the underlying basement. The locations of these geoelectrical surveys are shown in Fig.2.

Deep geoelectrical surveys (exploration depth >500 m) were carried out at various places in the Strymon basin by the Institute of Geophysics of the University of Hamburg (Prof. J. Makris) in the frame of a project called 'Geothermal Energy Project - Serres basin area - Geoelectrical survey' and financed by Public Power Corporation (P.P.C.) of Greece (P.P.C., 1981). Vertical electrical sound-
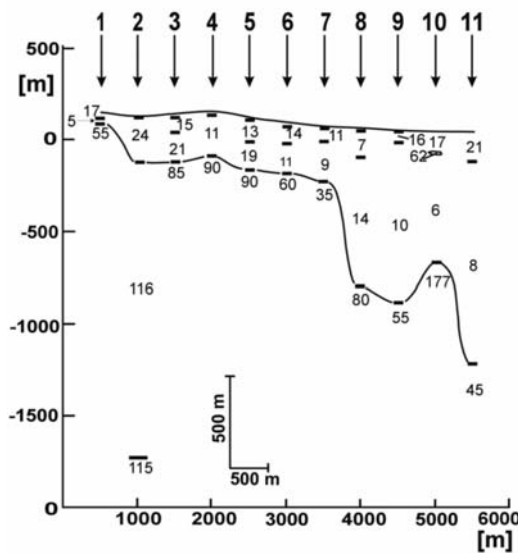
Fig. 7: Geoelectric section 'Profile I' (P.P.C., 1981).

ings (V.E.S.) were performed using the Schlumberger array with current electrode spacing AB/2=3,000 m.

One of these geoelectric sections runs across the study area in a SW-NW direction. This resistivity section is characterized as 'Profile I' and its location is shown in Fig. 2. Fig. 7 illustrates the geoelectric section interpreted by Prof. J. Makris (P.P.C., 1981). Two geoelectric layers are distinguished in this cross-section. The upper layer is variable in thickness and has low resistivities ranging from 5 to 24 Ωm. This layer corresponds to Neogene and Quaternary sediments of the area. The low resistivity values can be explained by reduced porosity and permeability due to the clayey composition of these sediments. It is confirmed by the comparison of the resistivity structure with data from irrigation and water supply wells close to some vertical electrical soundings. The lower geoelectric layer has relatively high resistivities ranging from 35 to 177 Ωm and corresponds to the basement. A large normal fault has been found between VES 7 and 8, in the village of Patriki. This fault has a throw of about 570 m and the basement deepens abruptly from 300 to 870 m. Another large normal fault has been detected between VES 10 and 11 having a throw of about 560 m and the basement deepens northeastwards from 670 to 1230 m below sea level (bsl). A probable tectonic uplift of approximately 220 m occurs between VES 9 and 10, north of the village of Patriki. Finally, an important normal fault has been recognized between VES 1 and 2, in the area between the villages of Zervochori and Sitochori, having a throw of 210 m. The deepening of the basement by 76 m between VES 4 and 5 can be explained by the probable presence of a normal fault there.

Geoelectrical surveys at shallow depths (<500 m deep) were carried out by I.G.M.E. (Nikolaidis and Theodoridis, 1986). These surveys comprised 30 Vertical Electrical Soundings (V.E.S.) arranged along 7 profiles (AT-1, AT-2, AT-3, AT-4, AT-6, AT-15 and AT-16). The locations of these profiles are shown in Fig. 2. All the vertical electrical soundings were made with the Schlumberger array. The main characteristic is the low resistivity values of the Quaternary and Pliocene sediments related to their clayey composition. Some probable and proven normal faults were identified on these profiles. Especially, a proven normal fault has been identified between VES 97 and VES 96 in profile AT-16. The position of this fault coincides with the location of the fault zone between CPD 270 and
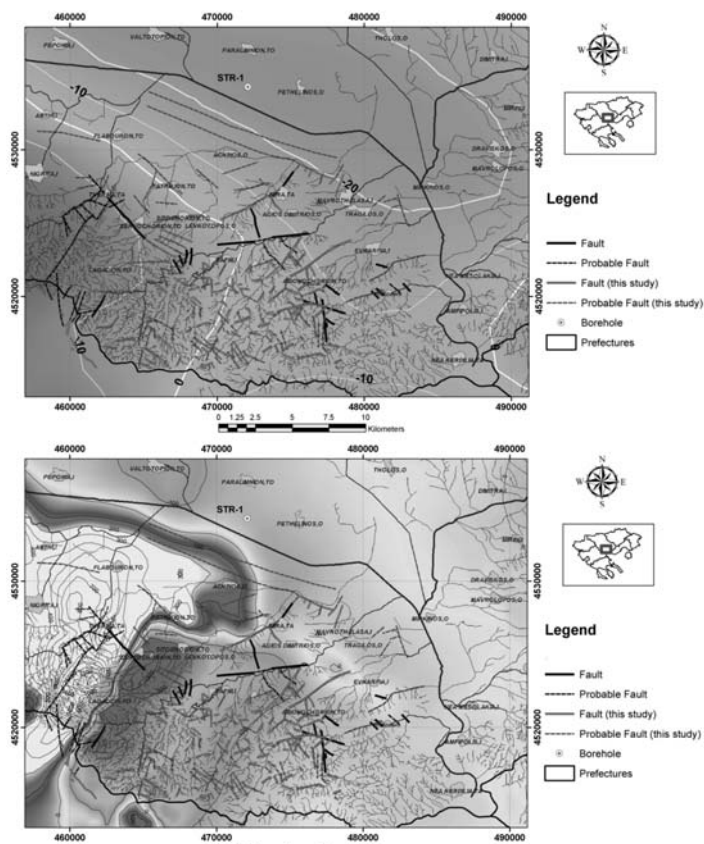
Fig. 8: Bouguer (top) and magnetic (bottom) anomaly maps in the SW part of the Strymon basin.

250 on seismic profile 'Line-7'. Probable normal faults have been detected at the following locations: (a) between VES 4 and 5 in profile AT-2, (b) close to VES 9 in profile AT-3, (c) between VES 36 and 37 in section AT-4 and (d) between VES 14 and 15 in profile AT-6. The probable faults detected in sections AT-3 and AT-4 coincide with the fault zone between CDP 350 and 320 of seismic profile 'Line-13'. In addition, the probable fault noted close to VES 37 in section AT-4 has been detected in the area of a terrace located at a distance of about 2 km east of the village of Tragilos.

3.3 Gravimetric and magnetic methods

The SW part of the Strymon basin was studied by means of regional scale gravity and magnetics. The Bouguer anomaly data used in this study were extracted from the public domain Greek gravity data bank (Lagios et al., 1988). The cell size of this data set was 4 km. Positive gravity anomalies are observed over the metamorphic rocks of Serbomacedonian Massif, while negative anomalies are associated with the Strymon basin (Fig. 8). Aeromagnetic data from 1966 survey of Macedonia and Thrace were recompiled, processed (Stampolidis, 1999) and used in the present study to delineate the edges of the magnetized bodies in the area. Metamafic bodies are cropping out in the Serbomacedonian massif. The Therma proto-ophiolitic mafic rock assemblage is extended further under the basin sediments, as revealed from the magnetic data (Fig. 8).
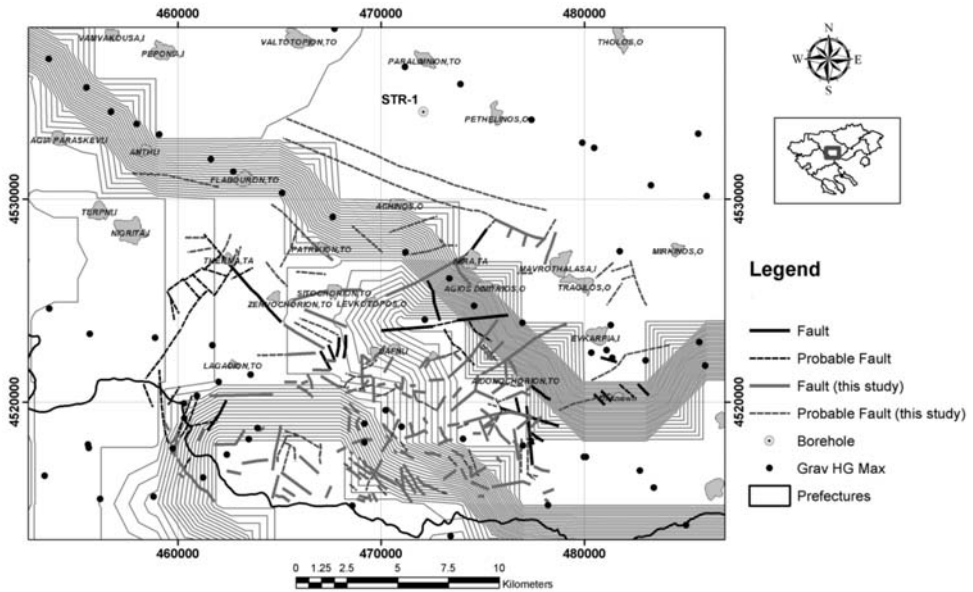
Fig. 9: Terracing of the Bouguer anomaly in a large part of the Strymon basin. The main faults of the basement in the SW part of the basin are noted.
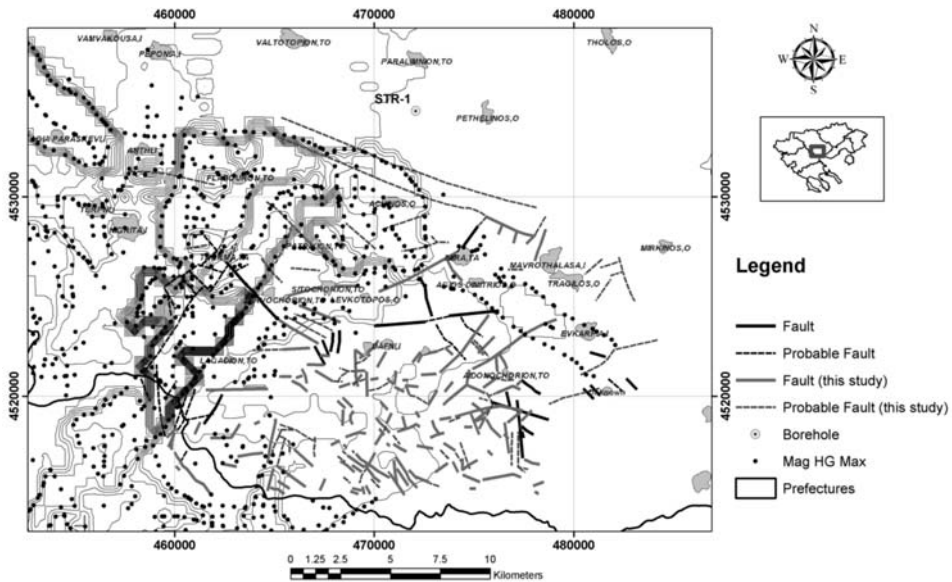
Fig. 10: Terracing of the magnetic anomaly in a large part of the Strymon basin. The main faults of the basement in the SW part of the basin are noted.

Horizontal gradient maxima were used to reveal the horizontal boundaries of the gravity and magnetic sources. According to Blakely and Simpson (1986) and Grauch and Cordell (1987) the maximum values of horizontal gradient will be located near vertical sides. Cordell and McCafferty (1989)
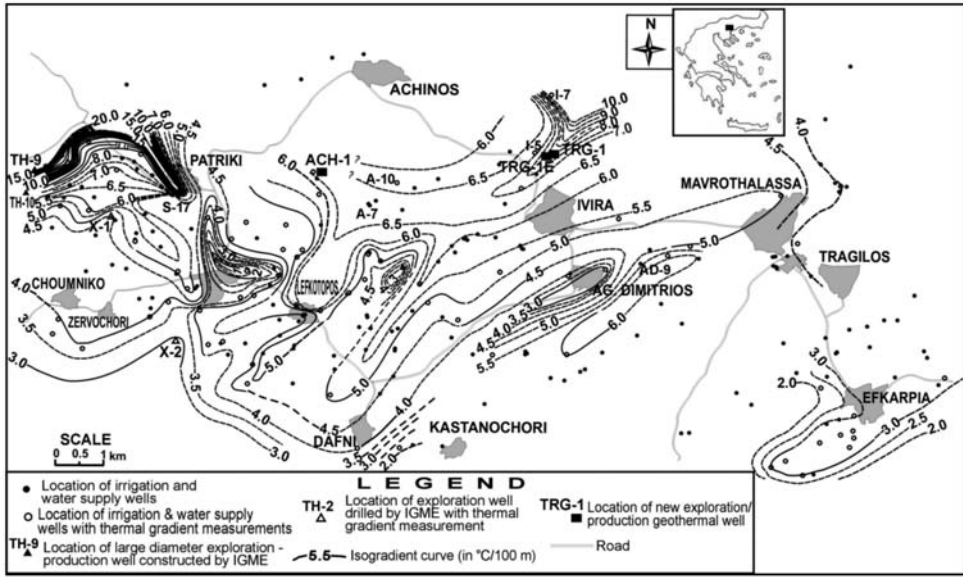
Fig. 11: Isogradient map (in oC/100 m) in the southwestern part of the Strymon basin based on the temperature measurements into existing irrigation and water supply wells (Arvanitis, 2003).

have presented an iterative method that they called "terracing" to transform the potential field data into uniform domains separated by abrupt domain boundaries. Terracing method used in conjunction with horizontal gradient maxima to delineate the body boundaries. The terracing of the Bouguer depicts the boundary between the metamorphic basement and the sediments of the basin (Fig. 9). This boundary is running parallel with the probable faults NE from Achinos that were recognized from the interpretation of the seismic profiles. The low resolution of the data set is the main reason for the insufficient details of the gravity boundaries. On the contrary the horizontal gradient maxima and terracing of the magnetic field (Fig. 10) evince more details for the magnetic bodies' boundaries. The exact position and the direction of the faults that were detected in this study near the Therma geothermal field coincide with the detected magnetic boundaries. A probable fault that was detected close to Patriki runs parallel to a terracing boundary. Southeast of Zervochori the HG Maxima align with a detected fault. The tectonic lines northeast of Achinos coincide with the northeast boundary of the concealed magnetic body and it is interpreted as a dispersed metamafic body similar to that outcropping in Therma.

4. Geothermal situation in the area - Relationship with tectonic setting

During preliminary geothermal investigation in the southwestern part of the Strymon basin a detailed thermometrical survey took place. All existing wells (about 230) for water supply and irrigation purposes were measured. In 80 boreholes up to depth of 300 m geothermal gradient measurements were possible. In most boreholes temperatures measured were constantly higher than the normal ones. For example, the temperatures of 37.7, 34.6, 28.6, 34.2 and 30.5 oC were recorded at depths of 270, 280, 122, 300 and 235 m respectively in boreholes in the areas of Patriki, north of Ivira, south and southwest of Achinos. An isogradient map was drawn based on the measurements in irrigation and water supply wells (Fig. 11). The study area is characterized by an increased geot-

hermal gradient, 2-3 times higher than the normal one. The isogradient curve corresponding to 3°C/100 m delineates the area at the margins of the basin close to the crystalline basement. The geothermal gradient is higher with values as high as 10-15°C/100 m in the western part of the study area near the known Therma - Nigrita low enthalpy geothermal field. Other significant thermal anomalies (geothermal gradient >6°C/100 m) occur in the Patriki area, north of the village of Ivira and in the area between the villages of Patriki and Achinos. Geothermal interest manifests itself in the areas north of Mavrothalassa (gradient >4°C/100 m), southwest of Ivira (Ivira - Dafni - Lefkotopos) and east of Agios Dimitrios. The isogradient map illustrates the correspondence between the geothermal data and the tectonic structure of the field. Furthermore, it appears that the main geothermal anomaly is associated with two NW-SE fault systems that affect the basement in the areas of Patriki and Achinos - Ivira respectively. The presence of NE-SW faults extends the anomaly southwestwards (Arvanitis, 2003). Faults intimately associated with geothermal anomalies in the study area have been detected by geophysical methods using mainly data from previous seismic and geoelectric surveys and their locations have been correlated positively with geomorphological features, the drainage pattern and lithology data from wells.

5. References

Arvanitis, A., 2003. Geothermal study in the SW part of the Strymon basin. *PhD Thesis*. Aristotle Univ. of Thessaloniki, Thessaloniki.

Blakely, R.J., and Simpson, R.W., 1986. Approximating edges of source bodies from magnetic or gravity anomalies. *Geophysics*, 51, 1494-1498.

Cordell, L., and McCafferty, A.E., 1989. A Terracing Operator for Physical Property Mapping with Potential Field Data. *Geophysics*, 54, 621-634.

Geosoft, 1997. OASIS Montaj Data Processing and Analysis (DPA) System for Earth Science Applications. Version 4.1 user Guide. Geosoft Inc., 290 pp.

Grauch, V.J.S., and Cordell, L., 1987. Limitations of determining density or magnetic boundaries from the horizontal gradient of gravity or pseudogravity data. *Geophysics*, 52, 118-121.

Lagios, E., Hipkin, R. G., Angelopoulos, A., and Nikolaou, S., 1988. The Gravity Anomaly Map of Greece - A Recompilation. I.G.M.E.

Nikolaidis, M. and Theodoridis, T., 1985. Geoelectrical investigation in the Strymon basin. Institute of Geology and Mineral Exploration (I.G.M.E.), 9 pp. + 12 figures and maps.

P.P.C. (Public Petroleum Corporation), 1988. Evaluation of deep holes, Athens, 42-53.

P.P.C. (Public Power Corporation), 1981. Geothermal Energy Project. Serres basin area. Geoelectrical survey. IfG (Prof. Dr J. Makris), Hambourg.

Stampolidis, A., 1999. The magnetic field of Macedonia and Thrace and its relation to the geological and geophysical structure of the area. *PhD thesis*, Aristotle Univ. of Thessaloniki.

COMPILATION OF A UNIFIED AND HOMOGENEOUS AEROMAGNETIC MAP OF THE GREEK MAINLAND

Chailas, S.[1], Tzanis, A.[1], Kranis, H.[2] and Karmis, P.[3]

[1] *Department of Geophysics – Geothermy, National and Kapodistrian University of Athens, Panepistimiopoli, 15784 Zografou, Greece; schailas@geol.uoa.gr; atzanis@geol.uoa.gr*

[2] *Department of Dynamic, Applied and Tectonic Geology, National and Kapodistrian University of Athens, Panepistimiopoli, 15784 Zografou, Greece; hkranis@geol.uoa.gr*

[3] *Institute of Geology and Mineral Exploration, Geophysics Department, Sp. Loui 1, Olympic Village, 13677 Acharnae – Athens, Greece, karmis@igme.gr*

Abstract

We present a unified and homogeneous digital aeromagnetic map of the Hellenic mainland, based on the 1:50,000 map series of IGME. These maps cover the areas A1, A2, B, C1, C2, C3, D1 compiled by Hunting Geology and Geophysics Ltd. and measured at nominal ground clearances (flight altitudes) 150m AGL, 150m AGL, 300m AGL, and 2300m AMSL respectively (part of C2 with 3000m AMSL). We also include the entire area of Northern Greece, measured by ABEM AB with nominal ground clearance 275±75m AGL. The original map sheets were digitally imaged, georeferenced, digitized along contour lines and interpolated onto regular 250´250m grids. The unified aeromagnetic map was constructed by collating the mosaic of the resulting gridded data. Using upward/downward continuation techniques various homogeneous versions of the map, were compiled by referencing of the observed mosaic total magnetic field to a unique constant ground clearance or to a unique constant elevation above mean sea level. This is the first time there is a complete and unified image of the magnetic signature of the isopic zones and rock formations comprising the Hellenic mainland, with particular reference to the ophiolite suites, which provides additional insight into the Alpine and post-alpine tectonics of the area.

Key words: Greece, aeromagnetic map.

1. Introduction

The scope of the work reported herein is very clear: To compile a unified and common-referenced aeromagnetic map of Greece, out of the fragmentary information existing in a multitude of 1:50000 scale maps produced by different contractors for the Institute of Geological and Mining Research (IGME).

The original aeromagnetic data set was acquired in two stages: In 1966, ABEM AB conducted a field campaign over Central/ Eastern Macedonia and West Thrace (the hatched area in Fig. 1). In 1977, Hunting Geology and Geophysics Ltd conducted a second campaign extending over West Macedonia, Thessaly, eastern Central Greece, and eastern Peloponnesus (Areas A, B, C and D in Fig. 1). Both contractors delivered the raw data in analogue or digital magnetic tape and the end product in 1:50000 scale contour maps compiled so, as to comply with the corresponding topographic

maps of the Hellenic Army Geographical Survey (HAGS) and the 1:50000 geological maps of IGME.

The "original" 1:50000 scale maps did not comprise a uniform set. Each contractor used different reduction and processing schemes, which resulted in significant inconsistencies at the boundaries between their respective survey areas. Moreover, ground clearance was different between sub-areas surveyed by the same contractor, so that their respective 1:50000 maps were not directly comparable (for details see below). In *several* occasions, when the boundary between two sub-areas surveyed with different ground clearances would straddle a single HAGS/IGME sheet, the *same* 1:50000 aeromagnetic map would be produced with *different* data and contouring schemes (for an example see Fig. 2); this would certainly hinder interpretation and often beget confusion to the novice or unfamiliar with the analysis of potential fields.

National or regional scale maps of commonly reduced and referenced aeromagnetic data for the entire Hellenic territory at different absolute elevations have not been systematically produced. In consequence, regional or spatially extended aeromagnetic anomalies could not be recognized and evaluated. Even local anomalies straddling the boundaries between two maps were discontinued and had to be reconstructed by the interested investigator. Finally, until recently, no information whatsoever existed in some digital form. The only hitherto known attempt to unify a significant subset of the aeromagnetic data and investigate aeromagnetic anomalies at large scales was that of Stampolidis (1999) who *reprocessed* the original flight line data collected by ABEM in Northern Greece.

Inasmuch aeromagnetic surveys aim at the detection of extended – regional scale anomalies and are best suited for strategic scale investigations, the aforementioned limitations and difficulties have hindered their utilization, to the point of leaving a valuable resource mostly unexploited and largely ignored. Herein, we attempt to remedy this situation by producing a unified aeromagnetic map of Greece for the first time and thus bring up an important piece of infrastructure and asset of pure and applied Earth-scientific research.

2. Data Sources

As mentioned above, the compilation of the unified and homogeneous aeromagnetic map of Greece is based on the 1:50,000 map series of IGME, produced by ABEM AB and Hunting Geology and Geophysics Ltd.

The ABEM maps (ABEM, 1967), were produced with measurements at a nominal constant ground clearance (GC) of 275±75m above ground level (AGL) i.e. in constant ground clearance mode. The direction of the flight lines (tracks) was NE-SW and the mean distance between them was about 1km. Connection (tie) lines for crossover adjustment of the data were also flown at NE-SW direction, with a mean distance of 10km.

Hunting Geology and Geophysics Ltd. has generally used a magnetic field measurement spacing of 200–250m and has flown on a NE-SW direction, but at different GC's and track densities depending on the topography. The data collection schemes are as follows (also see Fig. 1):

- Area A1 (Thessaloniki basin): Nominal GC 150m AGL at a nominal distance of 400m between tracks.
- Area B (Thermaikos Gulf): Nominal GC l 150m above mean sea level (AMSL) at a nominal distance of 400m.
- Area C1 (Paikon Mountain): Nominal GC 300m AGL at a nominal distance of 800m.
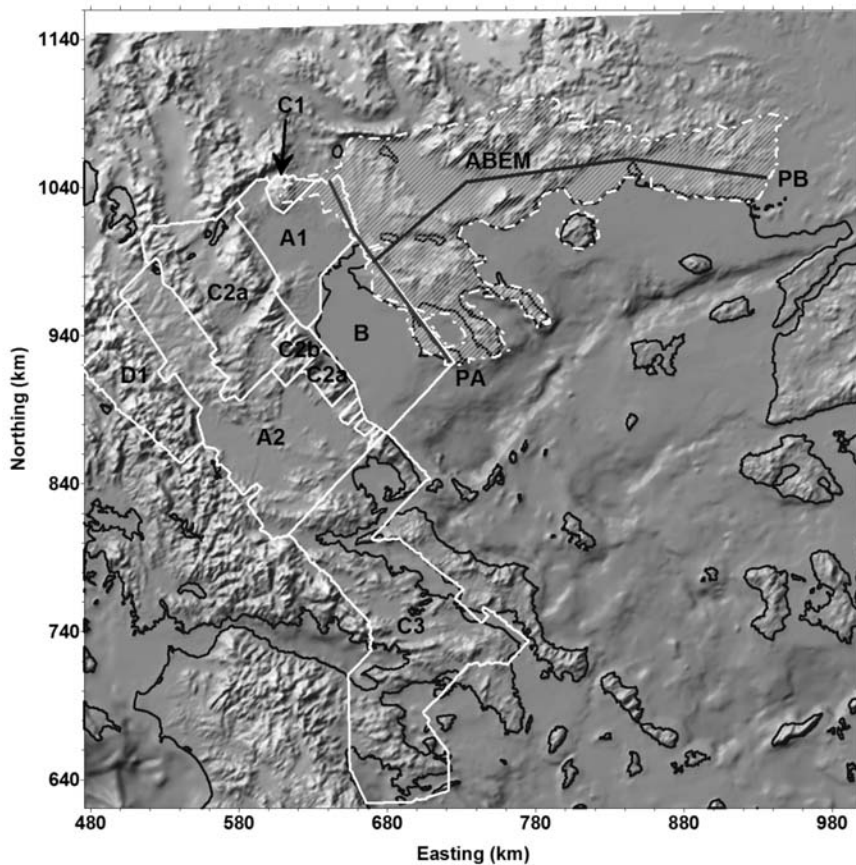
Fig. 1: Map showing the area coverage of the aeromagnetic data.

- Area C2a (the highlands between Thessaloniki and Thermaikos basins to the east and the Pindus Mt. chain to the west, including the Florina and Ptolemais basins): Nominal GC 300m AGL at a nominal distance 800m between tracks.

  – Exception is the area of Mt. Olympus, (area C2b) where the flight level was 3000m AMSL with the same nominal distance between lines.

- Area A2 (the Mesohellenic trough and the Karditsa and Larissa basins): Nominal GC was 150m AGL at a nominal distance of 400m.

- Area C3 (Eastern Central Greece): Nominal GC 300m AGL at a nominal distance of 800m.

- Area D1 (the Pindus Mt. chain): Nominal flight level was 2300m AMSL at a distance of 1000m between tracks.

In all cases, connection lines were flown at a NE-SW direction and a spacing of 10km. The IGRF correction was based on the IGRF model for the epoch 1977.3. A constant value of 150nT was added to the magnetic anomaly values prior to plotting the contour maps. It is probably worth noting that the original raw data set delivered by Hunting Ltd in magnetic tapes, has been irreversibly damaged and all that was left from this important survey are the 1:50000 contour maps.
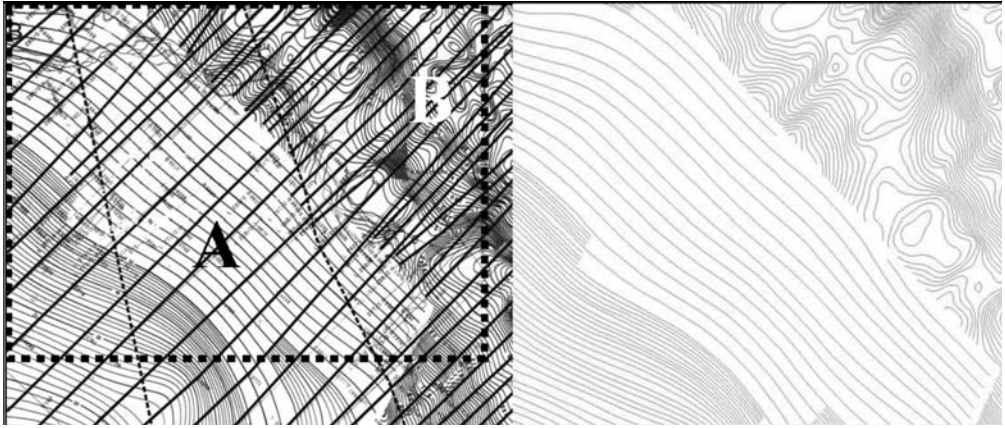
Fig. 2: Left: Part of the aeromagnetic map of sheet 'Kalampaka', scale 1:50.000.The continuous NE-SW lines indicate the primary flight lines and the dashed NW-SE lines the connecting (tie) lines. Area A was measured at a constant ground clearance of 2300m and flight line spacing of approx. 1000m Area B was measured at a cgc of 150m, with flight line spacing 400m. The change in the detail and the appearance of local anomalies is evident. Right: The digitized contour lines for the inset rectangle faithfully reproduce the original map.

3. Digitization and Gridding Procedure

The original 1:50000 map sheets were initially converted to a high resolution raster image format (typically TIFF). The contour lines were then digitized to vector form (image coordinates) with sufficiently high sampling densities, so as to faithfully reproduce the original image. Fig. 2 shows a part of an original map in raster format (left) and the resulting plot of the digitized contours. The boundaries between neighbouring areas with different flight parameters were also digitized. Using the corners of the map sheets as control points, the map were georeferenced and the image coordinates were transformed to Cartesian coordinates in the UTM projection. The digitized contour lines were subsequently stored in area-files according to the data collection schemes (flight line characteristics) detailed of Section 2. The area files were then interpolated to a regular grid, using a grid spacing of 250m.

The selection of the grid spacing was an exercise in optimal compromise and deserves some attention. First, let it be noted that the magnetic measurements along flight lines were taken at intervals of the order of 200m and certainly £250m. In consequence:

1. This interval is directly comparable to the flight line spacing of 300m for areas measured at 150m AGL. When projected to a direction perpendicular to a flight track, the distance is approx. 353m, longer than the nominal distance between lines. This ensures the faithful reproduction of the local aeromagnetic anomalies.

2. For lines flown 800 and 1000m apart (areas measured at 300m and 275m AGL respectively), the projection at a direction perpendicular to the line is respectively 44% and 35% the distance between flight tracks. This is just sufficient to ensure reproduction of aeromagnetic anomalies with minimal noise (interpolation artifacts) at short wavenumbers.

3. For track lines spaced 1000m and 800m apart and flight levels 2300m and 3000m respectively, the measured field is already smooth enough, to ensure that short wavenumber artifacts will not be introduced during interpolation.

On collating the mosaic of the resulting gridded areas to build a first draft of the aeromagnetic map,
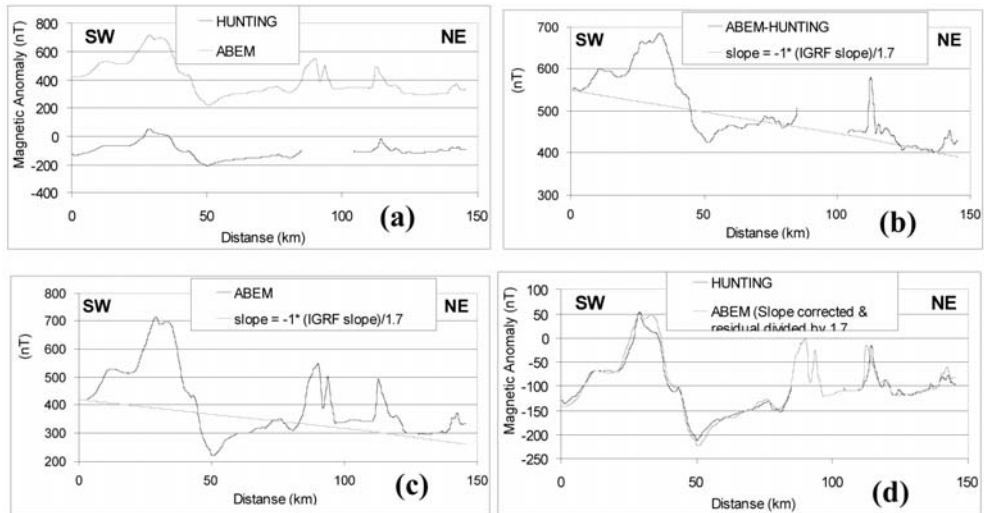
Fig. 3: (a) The total magnetic field along the profile PA in the overlapping region of the ABEM and Hunting survey areas (see Fig. 1). (b) Plot of the difference between the profiles of Fig. 3a. The trend line was calculated as a scaled function of the IGRF slope along the profile. (c) Plot of the ABEM profile with similarly calculated trend line. (d) The profiles of Fig. 3a after reduction of the ABEM data for the trend and scaling for the 1:1.7 distortion factor (see text for details).

we observed an offset of ~450nT (mean datum value) between the Hunting and ABEM data sets in the region where areas A and C1 C2 overlap (Fig. 1 and Fig. 3b), which could not be attributed to the ~125m difference in the flight level: although ABEM was flying higher than Hunting, their contoured magnetic field values were already higher than those of Hunting! In order to investigate the reasons behind the difference of the two data sets, a SW-NE profile was sliced from both data sets across the overlapping region (profile PA in Fig. 1). As can be seen in Fig. 3a, the same local magnetic features are present in both profiles, but the ABEM data is not only upwards offset, but also appears to be vertically exaggerated! Subtraction of Hunting's values from ABEM's profile revealed the existence of a regional trend in the differences (Fig. 3b). Comparing these differences with the slope of the IGRF model for the epoch 1966.5, we found that the trend line is actually a scaled version of the IGRF with a ratio equal to 1:1.7. We have also found that this trend can be *exclusively* attributed to the ABEM data (Fig. 3c). After subtracting the trend from the ABEM profile and scaling the residual curve, the Hunting and ABEM profiles have practically coincided (Fig 3d). The discrepancy between the Hunting and ABEM maps can therefore be attributed to a distorted (erroneous) IGRF correction of the ABEM data.

The first draft of the "unified" Greek aeromagnetic map was constructed by collating the mosaic of the gridded areas, after correcting the ABEM data for the offset of 450nT and the Hunting data for the constant of 150nT added prior to plotting. The result is shown in Fig. 4. It is immediately apparent that the boundaries between different areas are discontinuous and the texture of the map inhomogeneous and different between different survey areas, as a result of the differences in the data acquisition procedures.

An additional observation is that the ABEM data exhibit a persistent eastward downward slope. The comparison of the map of Fig. 4 with the aeromagnetic map of Turkey (Akin, 2007; comparison is not presented herein) has also shown differences of the order of 200nT at the boundaries. Given the analysis presented above for the differences between the Hunting and ABEM data, it would appear
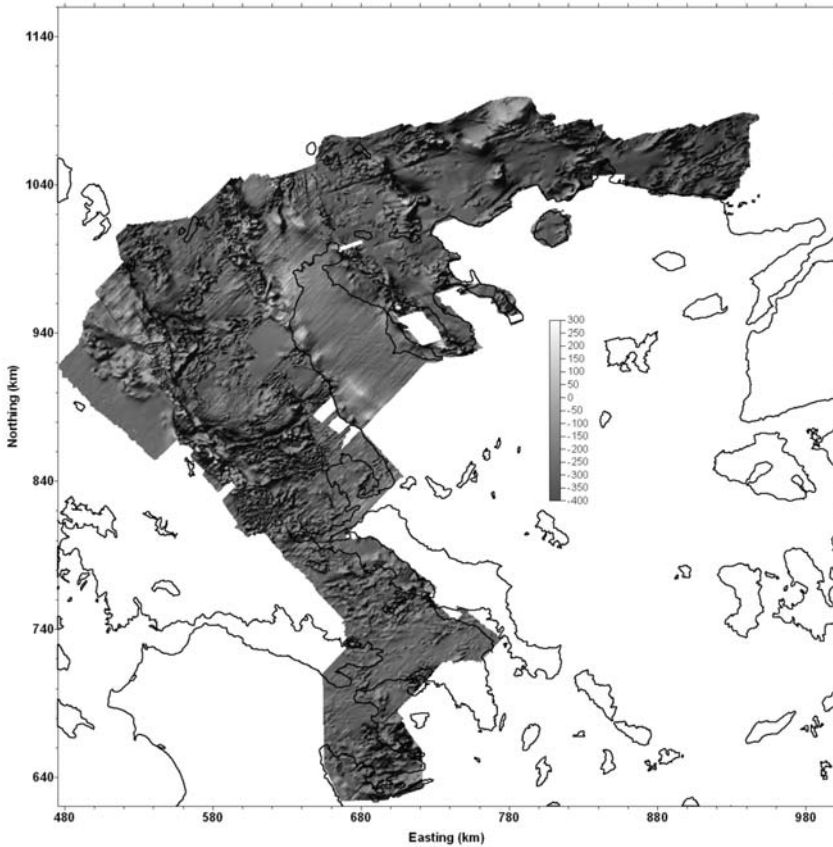
Fig. 4: The mosaic aeromagnetic map produced by digitizing the 1:50.000 scale aeromagnetic maps by Hunting Ltd and ABEM AB. A constant value of 450nT has been subtracted from the ABEM data and a constant value of 150nT from the Hunting data; the latter has been arbitrarily added prior to plotting. The obvious discontinuities across area boundaries are due to the different data collection schemes (see Section 2). The eastward downward slope observed in the ABEM data is due to a distorted IGRF correction (see text for details).

that the same distorted IGRF correction is to blame for the downward slope, as well as for the discrepancy between the Greek and Turkish data. In order to confirm the effect, we have constructed a W-E profile along the ABEM area, as shown in Fig. 1 (profile PB). The profile is plotted in Fig. 5a, together with the trend line calculated as a scaled version of the IGRF model for the epoch 1966.5, in the same manner as per Fig. 3c. Fig. 4d shows the same profile before (continuous black line) and after de-trending and re-scaling (continuous grey line). It is apparent that the original and corrected profiles exhibit a difference of approx. 200 nT at the east end of the profile, approximately the same as the difference observed between the Greek and Turkish data. It is therefore confirmed that the aeromagnetic contour maps delivered by ABEM are distorted. The actual reason for this distortion is still not known, but the previous analysis indicates, either incorrect reduction of the data, or a recorder calibration error. What is important however is that the effect has been recognized and may be reversed using the procedure described above.

The map of Fig. 4 is certainly unified, inasmuch as this is the first time that the mosaic of the different aeromagnetic surveys over mainland Greece has been put and presented together. At the same
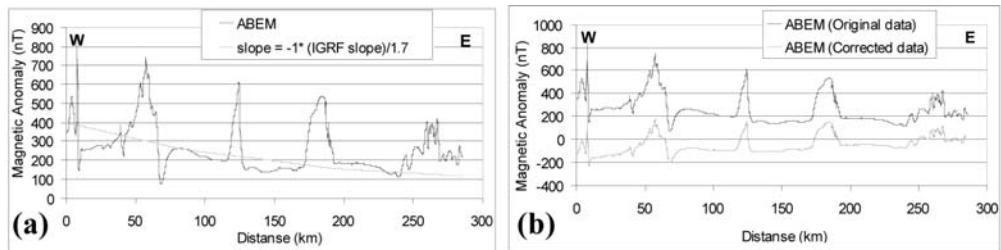
Fig. 5: (a) An E-W profile sliced from the ABEM data (Profile PB in Fig. 1). The trend line has been determined as per Fig. 3c. (b) The same profile before and after de-trending and re-scaling as per Fig. 3d.

time, it is very inhomogeneous and unusable for strategic planning and extended/ regional scale studies! In this form, it is only useful for the analysis of local or extended aeromagnetic anomalies limited to within areas of uniform data collection schemes (see Fig.1 and Section 2). Moreover, the ABEM data require additional processing (de-trending and re-scaling) in order to represent the true amplitudes of local aeromagnetic anomalies. The homogenization of the mosaic map of Fig. 4 leading to the construction of the first complete aeromagnetic map of mainland Greece is presented in the following Section 4.

4. Homogenization

As mentioned previously, by "homogenization" of the mosaic map of Fig. 4, we imply the reference of the entire map to a common and *unique* constant ground clearance, or to a *unique* elevation AMSL. This is an exercise in upward/ downward continuation with the added difficulty that the observation surface (flight altitude) is not flat – the aircraft flew at a constant clearance (height) above the ground surface, following the contours of the terrain. Thus, direct methods of up- or downward continuation assuming flat observation surfaces (e.g. Fourier-based) cannot be applied because the magnetic field intensity obeys an inverse square attenuation law. We need to apply continuation of the field between arbitrary surfaces and in such cases the method of choice is the method of equivalent sources.

We have chosen to use the highly accurate and computationally efficient approach described by Xia et al (1993). This is a two-stage procedure: The first step requires the computation of an equivalent source layer at a horizontal surface below the lowest elevation of the observation and continuation surfaces. The layer is in fact a grid of sources which is iteratively assigned with a distribution of magnetizations through forward calculation of the anomaly on the observation surface, so as to faithfully reproduce the observed total magnetic field. In a second step, the field is up- or downward continued to any arbitrary surface by forward computation on the basis of the equivalent source layer.

In our case, the exact observation surface (flight contour) is not known, but may be approximated to arbitrary precision on the basis of a digital elevation model (DEM). Herein, we have used a 100´100 m DEM based on the 1:50.000 scale maps of the HAGS. The DEM grid was re-interpolated to the nodes of the aeromagnetic grid and the appropriate adjustments were applied at each node, in order to reproduce the ground clearance parameters of the area at which the grid point belongs.

On the basis of the thusly approximated observation surface, the procedure of Xia et al (1993) was applied separately for each area described in Section 2 and the final "unified and homogeneous" aeromagnetic map was constructed by collating the mosaic of up- or downward continued grids, commonly referenced to a *unique* constant ground clearance, or to a *unique* elevation AMSL. Prior to upward continuation, the ABEM data was de-trended and re-scaled according to the procedure of
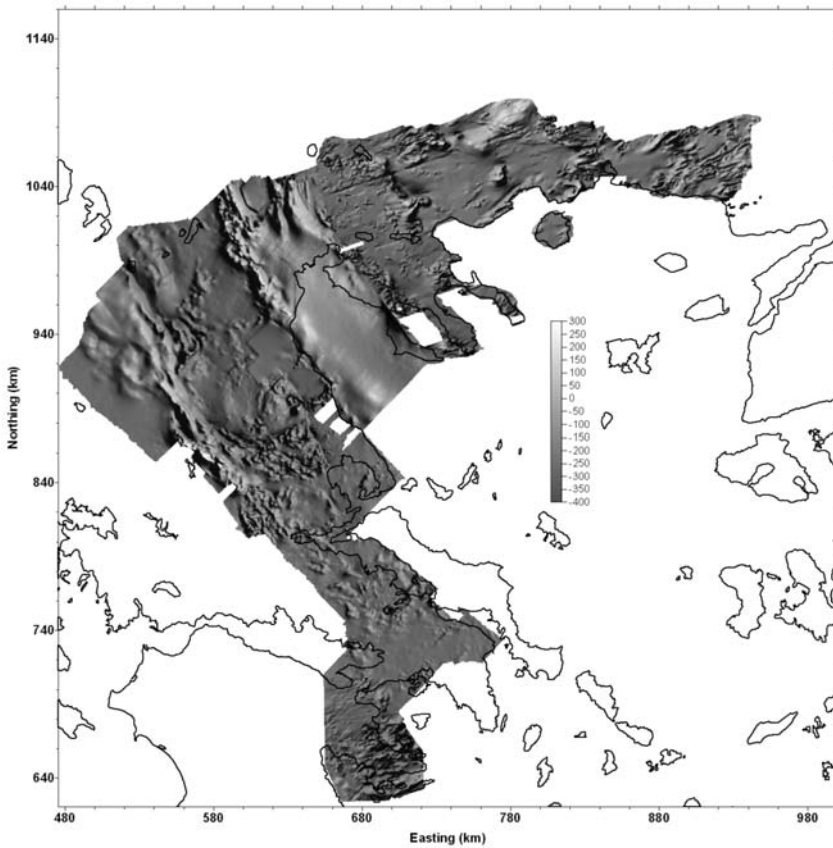
Fig. 6: The aeromagnetic map of the Hellenic mainland homogenized at 300 m AGL In this final product the ABEM data have been de-trended and re-scaled according to the discussion of Section 3. The map is presented in shaded relief form, lit from the NW.

Section 3, in order to correct for the distorted IGRF correction and the resulting grid was adopted only after demonstrating compliance with the Hunting and Turkish data.

Herein we present two versions of the unified and homogeneous map. Fig. 6 illustrates the map at a *constant ground clearance* of 300m AGL and Fig. 7 is the same, upward continued to a *constant altitude* of 3000m AMSL. Both maps are presented in the form of a shaded relief lit from the NW, in order to accentuate their respective characteristics and facilitate the brief discussion to be presented in Section 5.

5. Brief Discussion and Conclusions

The unified and homogeneous maps presented herein show for the first time, a complete and unified image of the crustal magnetic field at regional – national scale. In these images, the signatures of many isopic zones and rock formations comprising the Hellenic mainland are clearly seen, with particular reference to the ophiolite suites. Thus, a different and very interesting glimpse at the Alpine and post-alpine tectonics of the Hellenic territories is possible.

To begin with, the aeromagnetic data roughly delineate the boundaries of isopic zones, or groups of isopic zones. Thus, from east to west, the following groups of zones can (more or less) clearly be
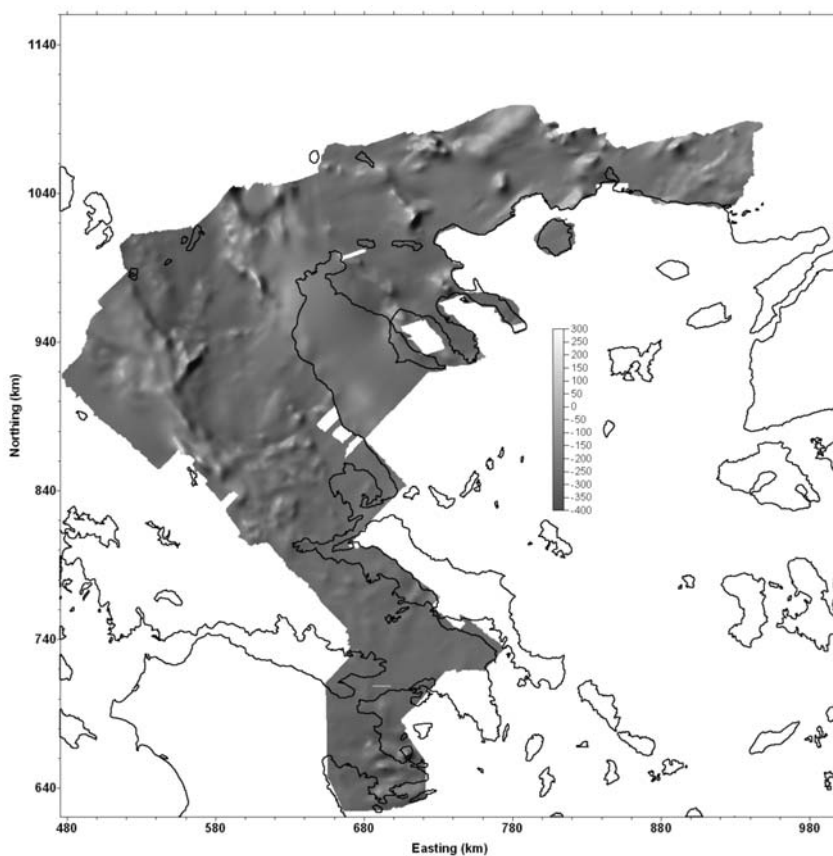
Fig. 7: The aeromagnetic map of the Hellenic mainland homogenized at 3000 m AMSL In this final product the ABEM data have been de-trended and re-scaled according to the discussion of Section 3. The map is presented in shaded relief form, lit from the NW.

defined: (a) The Rhodope massif; this can be distinguished from the Circum-Rhodope belt at the SE of Evros due to the remarkable roughness of the magnetic terrain observed there, presumably due to tectonism. (b) The Serbomacedonian massif; (c) the Circum-Rhodope and Peania zones; (d) the Paikon and Vardar zones; (e) the Pelagonian and Sub-Pelagonian zones.

These groups of zones are mainly differentiated (bounded) by the emplacement of intrusive rocks, especially at northern Greece and, mainly, the emplacement of ophiolite suites. Conversely, the Pindos and Gavrovo zones at the W-NW end of the map and glimpses of the Parnassus zone stand out because of the low to very low magnetizations of their associated stratigraphic sequences.

The magnetic signatures of the ophiolite sequences of the Pelagonian and Sub-pelagonian zones deserve some attention and will be briefly commented starting at the north. The magnetic signature of the Pindos ophiolites appears stronger than those of Vourinos, which according to Papanikolaou (2009) belong to the H4 Axios-Vardar terrane. This may suggest that the Vourinos and Pindos ophiolites do not link beneath the sediments of the Mesohellenic Trough, as proposed by Rassios et al. (1983) and Jones & Robertson (2001). A conspicuous, NE-SW anomaly is observed north of Kalambaka, marking, more or less, the northern boundary of Mt Antihasia. Quite interestingly, it lays on the SW-prolongation of the Aliakmon – Servia Fault Zone and also marks the southernmost bound-

ary of the Vourinos ophiolites.

An arcuate "trough" can be seen, passing east of Karditsa, marking the northern limit of Mt Phyllion and reaching close to the SW flanks of Mt Ossa. It separates the southern part of the Thesally basin from the northern one. Within the former, the Tertiary and Quaternary sedimentary cover appears to be considerably thinner, while the underlying alpine occurrences appear intensely dismembered and dissected by NW-SE, NE-SW and probably E-W tectonic contacts (faults). Actually this area appears to be also bounded on the east by a NNW-SSE discontinuity, the nature of which is at present enigmatic. A little further to the south, a practically straight, ENE-WSW discontinuity marks the southern margin of the Thessaly plain. It can be traced from the Nea Anchialos on the NW part of Pagasitikos Gulf to Domokos and it coincides with the Nea Anchialos Fault, which marks the northern boundary of the Almyros Basin (Caputo & Pavlides, 1993), locus of several earthquakes in the previous century (Papadimitriou & Karakostas, 2003). It is also noteworthy that this ENE-WSW discontinuity seems to change polarity, as at its eastern part (Almyros basin) it appears to be a steep, south-dipping fault, while in the west, the downthrown block is the northern one, corresponding to the Karditsa plain.

The area of eastern Central Greece (Sterea Hellas) is weaved with an intricate pattern of intermediate amplitude anomalies due to an ophiolite sequence dismembered and dissected mainly by NW-SE, NE-SW faulting. The nature of these features has recently been discussed by Tzanis et al (2010). Finally, the magnetic signatures of (Sub-pelagonian) rocks at the Argolis peninsula in central-eastern Peloponnesus is also quite rough, with prevailing E-W and NW-SE discontinuities, the nature of which is yet to be determined.

Returning to northern Greece, the signature of the Axios-Vardar ophiolites, as well as the boundaries of this ophiolite suture are clearly discernible, both inland and offshore, in the Thermaikos Gulf. The strong, indented anomaly on the western margin of the Strymon half-graben does not seem to correspond to the inferred fault that bounds the basin on the west, which develops on the hanging-wall of the Strymon Valley Detachment (Dinter, 1998). Instead it appears to be related to the boundary between the Vertiskos and Kerdyllia Units, (Papanikolaou, 1993). Another interesting observation is that the high-angle, NW-SE normal faults that bound the Strymon and Drama basins are not directly identifiable in the aeromagnetic map. Some tertiary intrusive bodies appear to have stronger magnetic signature than others. For example, the Vrondou pluton, north of Serrai, stands out very clearly, while the Symvolon granite, west of Kavala is less prominent. However, even in this latter case, its boundaries, which are related to the major Kavala-Xanthi-Komotini Fault (KXK), are seen as extended linear "troughs" oriented NE-SW and most probably correspond to the Symvolon Shear Zone, according to Dinter (1998). A structure of similar orientation (NE-SW) is also observed at the delta of Nestos River, parallel to the present-day coastline. This zone may also correspond to a sheared block, related to the KXK or a structure parallel to it. As a matter of fact, further to the east, in the Alexandroupolis- Evros area, several NE-SW to ENE-WSW lineations, most probably related to faults with predominant strike-slip character, can be observed. A high-intensity 'islet' is located at the south-eastern part of the Drama supradetachment half-graben. This feature may be related to a buried intrusive body, related to the Symvolon granite, which has been cut off and displaced by the combined activity of the KXK and the Drama Faults (see Stampolidis and Tsokas, 2004 for additional information). Between Xanthi and Porto Lago, the observed high magnetic values may equally be related to buried intrusive bodies; this, in turn, can be associated with the Nea Kessani geothermal field (Kolios et al., 2005). It is also worth noting that while many linear features can be directly associated with faulting as discussed above, others may not be as easily explainable. A prime example is the long NE-SW lineament parallel to the Greek-Bulgaria border along the line Mavrovouni – Falakron – West Rhodope Mts., whose nature is at present a mystery!

To conclude our brief presentation, we note that herein we have presented the first regional – national scale digital maps of homogeneous aeromagnetic data at different reference surfaces. As shown in the brief discussion above, these maps offer the opportunity to conduct studies of regional or spatially extended aeromagnetic anomalies, as well as local, kilometric scale anomalies; this was hitherto not feasible with the existing inhomogeneous, printed 1:50000 scale map series. Inasmuch as the aeromagnetic maps are principally used for the analysis of extended – regional scale features and strategic planning, the new set of maps contribute an important piece of geo-scientific infrastructure and the opportunity to utilize a valuable resource for pure and applied geophysical and geological research.

6. Acknowledgements

7. References

ABEM, 1967, Final Report on an Airborne Geophysical Survey carried out for the Greek Institute for Geology and Subsurface Research during the year 1966 by ABEM-AB Elektrisk Malmletning, Stockholm

Akin, U., 2007. Aeromagnetic Map (Total Intensity) of Turkey, General Directorate of Mineral Research and Exploration, Ankara, Turkey

Caputo, R. & Pavlides, S., 1993. Late Cainozoic geodynamic evolution of Thessaly and surroundings (central-northern Greece). *Tectonophysics*, 223, 339-362.

Dinter, D., 1998. Late Cainozoic extension of the Alpine collisional orogen, north-eastern Greece: Origin of the north Aegean basin. *Bull. Geol. Soc. America*, 110, 1208-1230.

Jones, G., Robertson, A.H.F., 1991. Tectono-stratigraphy and evolution of the Mesozoic Pindos Ophiolite and related units, Northwestern Greece., *J. Geol. Soc. London* 148, 267– 288.

Kolios, N., Koutsinos, S., Arvanitis, A., Karydakis, G., 2005. Geothermal Situation in North-eastern Greece, Proc. World Geothermal Congress Antalya, Turkey, 24-29 April 2005, 1-14.

Papadimitriou, E. & Karakostas, V, 2003. Episodic occurrence of strong (M_wv6.2) earthquakes in Thessalia area (central Greece). *Earth Plan. Sci. Let*., 215, 395-409.

Papanikolaou, D., 1993. Geotectonic evolution of the Aegean. Proc. 6th Congress of the Geological Society of Greece, *Bull. Geol. Soc. Greece*, 28/1, 33–48.

Papanikolaou, D., 2009. Timing of tectonic emplacement of the ophiolites and terrane paleogeography in the Hellenides. *Lithos*, 108, 262-280.

Rassios, A., Beccaluva, L., Bortolotti, V., Moores, E.M., 1983. The Vourinos ophiolite complex. *Ofioliti* 8, 275– 292.

Stampolidis, A., 1999. The Geomagnetic field in Macedonia and Thrace and its relationship with the geophysical and geological structure of the area, Doctoral Dissertation, Aristotelian University of Thessaloniki, 258pp (in Greek).

Stampolidis, A. and Tsokas G., 2004. Location of magnetic contacts and depth estimates for the magnetic sources from the aeromagnetic data of Macedonia and Thrace, Proceedings of the 10th Int. Congress, Thessaloniki, April 2004, in *Bull. Geol. Soc. Greece*, vol. XXXVI, 1252 – 1261 (in Greek).

Tzanis, A., Kranis, H. and Chailas, S., 2010. An investigation of the active tectonics in central-eastern mainland Greece, with imaging and decomposition of topographic and aeromagnetic data. *J. Geodyn*., 49, 55 – 67 (doi:10.1016/j.jog.2009.09.042).

Xia, J., Sprowl, D.R. and Adkins-Heljeson, D., 1993. Correction of topographic distortions in potential-field data: A fast and accurate approach; *Geophysics*, 58(4), 515-523

IMPLEMENTATION OF A NON-SPLITTING FORMULATION OF PERFECTLY MATCHED LAYER IN A 3D – 4TH ORDER STAGGERED-GRID VELOCITY-STRESS FINITE-DIFFERENCE SCHEME

Skarlatoudis A.A[1], Papazachos C.B.[2]

[1] *Geophysical Laboratory, Department of Geology, University of Thessaloniki, Thessaloniki-Greece, askarlat@geo.auth.gr*

[2] *Geophysical Laboratory, Department of Geology, University of Thessaloniki, Thessaloniki-Greece, kpapaza@geo.auth.gr*

Abstract

One of the major problems in numerical simulations of wave propagation in elastodynamics using grid-point methods is the truncation of the computational space by artificial boundaries. These boundaries produce spurious reflections, polluting the results with artificial noise, therefore several efforts have been realized in order to achieve transparent or non-reflecting boundaries for truncating the computational space. Perfectly Matched Layer (PML) has been one of the most efficient methods for implementing artificial boundaries at the edges of the computational models. However the application of PML requires the "tuning" of several variables, for which very limited work has been presented. In the present study we employ the Non-Splitting formulation of PML (NPML) technique presented by Wang & Tang (2003), based on the introduction of small perturbations in the wavefield. The NPML formulation shows the same accuracy with the originally introduced PML but is easier to be implemented because it does not require the field splitting. The main scope of this paper is to perform a full analysis of the efficiency of NMPL based on numerical tests using a 3D–4th order staggered-grid velocity-stress finite-difference scheme. The analysis consists of direct, quantified comparisons with reference solution waveforms from a semi-analytical method (Discrete Wavenumber Method) with synthetic waveforms produced using the most popular Absorbing Boundary Conditions (ABCs) and PML, in various canonical models (homogeneous and layer over half-space).

Key words: Finite-Difference, Perfectly Matched Layer, Non-Splitting Formulation.

1. Introduction

Numerical methods which are employed for wave propagation problems are necessarily applied in bounded media, using artificial boundaries (e.g. grid planes without neighbor grid planes from one side). On these artificial boundaries the energy of the computation area needs to be absorbed. Two solutions have been proposed for this problem, namely the absorbing boundary conditions (ABCs) and the absorbing layers. Berenger (1994) introduced an absorbing layer in 2-D and later (Berenger, 1996) in 3-D time domain electromagnetic numerical simulations, which he named (PML), since it had the property of being perfectly "matched" with the computation area medium. This means that at the bulk medium - absorbing layer interface, no spurious reflections were produced, while the

transmitted waves inside the layer were perfectly absorbed. PMLs have been eventually implemented in other scientific domains, such as computational acoustics and elastodynamics.

In elastodynamics, PMLs were first formulated for the P-SV case by Hastings et al. (1996) using compressional and shear potentials in the PML region. Since then, Chew and Liu (1996), Collino and Tsogka (2001), Festa and Nielsen (2003), Marcinkovich and Olsen (2003) amongst other researchers studied various aspects of PML properties. More Recently Komatitsch and Martin (2007) and Martin et al. (2008) presented an unsplit convolutional PML with improved performance at grazing incidence for purely elastic and poroelastic media.

Historically, the PML was formulated based on field splitting to avoid convolutional operations in the time domain. The Non-Splitting formulation of PML (NPML) uses perturbed equations to reduce automatically to the original wave equations in the inner layer, being equally efficient with PML and at the same time easier to implement. In the present work we use the NPML technique presented by Wang & Tang (2003), in order to perform a full analysis of the efficiency of NMPL using numerical tests with a 3D–4th order staggered-grid velocity-stress finite-difference scheme (Moczo et al., 2002, Kristek et al., 2002 and Kristek and Moczo, 2003). The analysis consists of direct comparisons of finite-difference synthetic waveforms with waveforms from discrete wavenumber method (DWN), which is used as a reference solution, for various canonical models (homogeneous and layer over half-space). Finally quantitative comparisons of synthetic waveforms produced using the most popular ABCs and PMLs for the same canonical models are also presented, in an attempt to exhibit the superiority of the latter as an artificial boundary in numerical computations, especially when the PML parameters are properly optimized.

2. The Non-Splitting (NPML) Formulation

The Non-Splitting formulation is essentially based on a coordinate stretching technique. Assume $p \in \{x, y, z\}$, the following coordinate transformation is defined:

$$(1)$$

where $p \in \{x, y, z\}$ are the transformed (stretched) coordinates, i is the imaginary unit and ω the angular frequency. Functions Ω_p are the attenuating functions in the PML zone, which depend on the layer thickness, the material velocity, the theoretical reflection coefficient and some additional constants. The properties of these functions and typical values of the theoretical reflection coefficient and constants used will be examined later in this work.

After coordinate stretching, the modified nabla operator is given by equation:

$$(2)$$

and the corresponding equation of motion becomes:

$$(3)$$

where ϱ is density, $\vec{V}$ is the velocity vector t is time and ⟶ the stress vector. After applying the Fourier

Transformation, equation (3) yields

(4)

which after some algebra leads to equation:

(5)

Applying the inverse Fourier Transformation to equation (1) we obtain

(6)

If we define the following convolutional operator:

(7)

the inverse Fourier Transformation of equation (5) yields

(8)

Time derivative of Hooke's law for elastic media is given by equation

(9)

where $\quad \{x, y, z, t\}$ is the stress tensor $\quad \{x, y, z, t\}$, is the strain tensor and **c** is the elastic coefficients tensor. In the frequency domain equation (9) becomes

(10)

The relation between strain and the particle velocity field, $\vec{v}\,(x, y, z, t)$ is given by equation:

(11)

By applying again the coordinate stretching technique according to equation (1) and after taking into account equation (11), equation (10) becomes

$$(12)$$

where $u, v,$ and w are the three velocity components.

After applying the inverse Fourier Transformation to previous equation (12) leads (after rearranging), to:

$$(13)$$

Since equation (13) involves time derivatives, can be expressed also as:

$$(14)$$

which is the most often used NPML formulation (Wang and Tang, 2003).

3. Implementation on NPML in a 3D-4th Order Staggered-grid Velocity-Stress Finite-Difference Scheme

The NPML formulation has been incorporated in the 3D–4th order staggered-grid velocity-stress finite-difference scheme proposed by Moczo et al. (2002). More information on this scheme can be found in Kristek et al. (2002) and Kristek and Moczo (2003). In this study we employed the time marching scheme by Wang and Tang (2003), using the trapezoidal rule (e.g. Davis and Rabinowitz, 1975), of 2nd order accuracy, for example:

$$(15)$$

where m is the time index, $P \in \{u, v, w\}$ and $p \in \{x, y, z\}$. In equation (15) functions Ω_p are the attenuating functions inside the PML layer. In the medium they are equal to zero, so the system of equa-

tions for velocity- stress NPML scheme is reduced to the original system of wave equations. Functions Ω_p are non-zero inside the PML layer, so that only waves propagating perpendicular to the PML plane are attenuated and consequently only the corresponding Ω_p functions have to be considered non-zero. For example, if a wave is propagating in the xz plane normal to x or z direction only Ω_x or Ω_z has to be computed, respectively. At the edges of the computational model (e.g of the xz plane) both and have to be computed. Different types of functions have been proposed by several authors for the attenuation, Ω_p, functions. In this work a slightly modified form of the function proposed by Collino and Tsogka (2001) were used, namely:

$$ \tag{16} $$

where δ is the thickness of the PML layer in grid points, p is the index of the current PML plane, V is the P-wave PML medium velocity, τ is a tuning variable and R the theoretical reflection coefficient. This theoretical reflection coefficient describes the desirable minimum reflection at the PML interface and is a function of the layer thickness (Collino and Monk, 1998a). This formulation shows the same accuracy with the originally introduced SPML but is easier to be implemented because it does not require the field splitting. In terms of computational efficiency the NPLM scheme used in this paper is equal to SPML, but in memory storage it is slightly less efficient than SPML since more variables have to be kept in core memory.

4. Numerical Testing Of The Non-Splitting PML Formulation

In order to numerically test the accuracy of NPML formulation, FD synthetics were compared using the Discrete Wavenumber method (DWN) (Bouchon, 1981; computer code Axitra Coutant, 1989). The comparisons were made for two different models, a homogeneous space and a surface layer over a homogeneous half-space. For the homogeneous model, calculations of synthetics were performed for two different values of V_p/V_s ratio, 4 and 1.78 (model A and B respectively), for examining the stability of the scheme in models with high velocity contrasts. For all types of models, a FD calculation was performed also for an enlarged version of each computational model, with the same source - receiver geometry but located far from the borders, in order to avoid any spurious reflections (reflection - free FD solution). A double-couple point source was used for all the FD computations. The source was simulated using a body-force term by a method suggested by Frankel (1993) and adapted for a staggered-grid by Graves (1996). A Gabor signal,   was used as a source time function. Here, f_p is the predominant frequency, γ controls the width of the signal, θ is a phase shift and t_s=1. For testing both types of incident waves, two different values for the strike of the source were used (45° and 0°), in order to have "pure" P or S waves impinging on the PML boundary, according to the radiation pattern of a double-couple point source.

4.1 Homogeneous Model

The efficiency of PML for different incidence angles of the wavefield was tested in this model for both types of incident body waves. Models A and B have the same S wave velocity β=562(m/s), density ϱ=2000 (Kg/m^3) and quality factors Q_p=Q_s=1000 and different P wave velocity α_A=2248(m/s) and α_B=1000(m/s). The size of the grid spacing h was determined using the rule that the minimum wavelength λ_{min} propagates in the grid with sufficient accuracy, must be six times larger than the grid
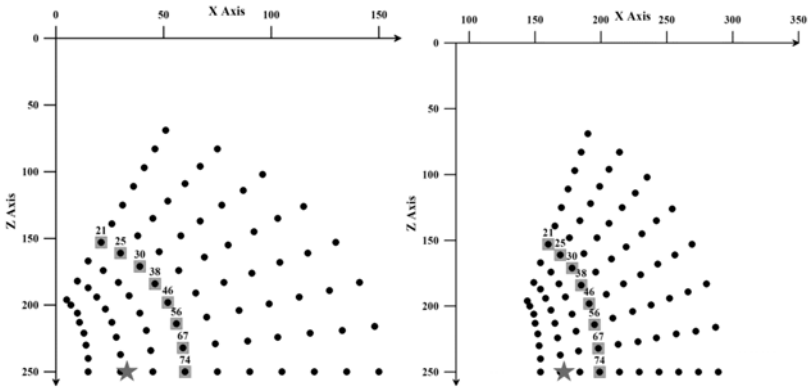
Fig. 1: Left: Source-receiver geometry for the incidence angle test. Black circles denote the position of receivers and stars show the source. With the light gray squares the receivers recordings plotted in Fig 2 are shown. Right: Source-receiver geometry for the enlarged model. The PML-inner medium interface is positioned at x=0 in both cases.
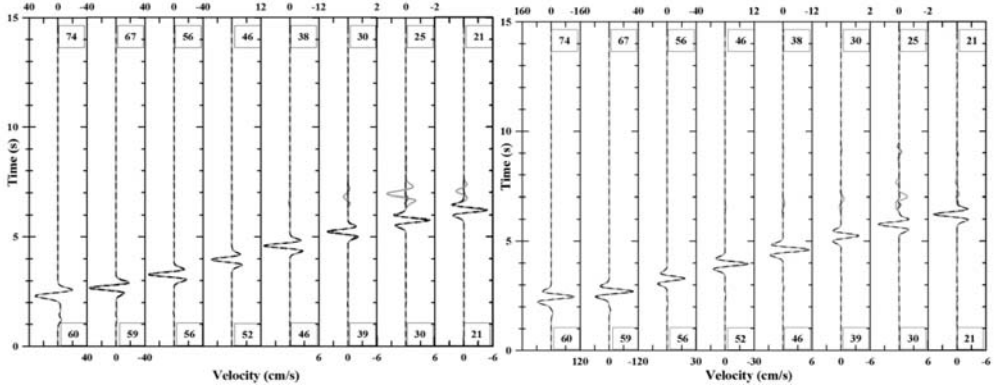
Fig. 2: Left: Longitudinal components of FD and DWN synthetics for model A and direct P waves incidence (left) and model B for direct S waves incidence (right). DWN synthetics are depicted with a black continuous line, FD synthetics with 30 grid-spacings PML thickness with a dark gray line, FD synthetics with 10 grid-spacings PML thickness with a light gray line and FD synthetics with 30 grid-spacings PML thickness for the enlarged model with a black dashed line. The numbers on top correspond to the number of the receiver plotted (Fig. 1), while numbers at the bottom correspond to the distance from the PML boundary in grid steps.

spacing ($h=\lambda_{min}/6$), which has been shown appropriate by stability and grid dispersion analysis in a homogeneous medium (Moczo et al., 2000). The number of grid cells of the computational models were MX=300, MY=300, MZ =500, the spatial grid spacing was h=30 m and the time steps for model A and B were dt_A=0.006 s and dt_B=0.013 s, respectively. For the enlarged models the number of grid cells for the incidence angle and surface tests were MX=350, MY=300, MZ=500 and MX=350, MY=350, MZ=400 respectively. The spatial grid spacing and the time steps for enlarged models (model A and model B) were the same.

4.2 Incidence angle test

The test was implemented using eight profiles of ten receivers each, which corresponded to eight in-
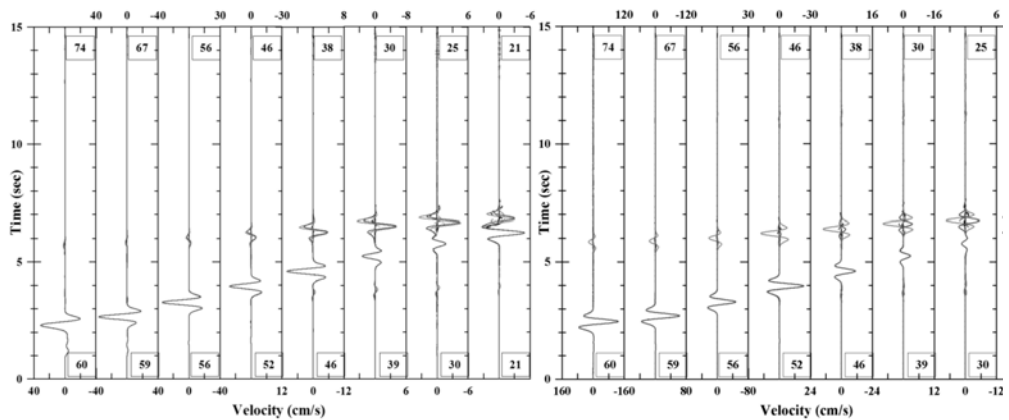
Fig. 3: Longitudinal components of FD and NRB synthetics for model A and direct P waves incidence (left) and for model B and direct S waves incidence (right). Coloring and numbering is described in the 3rd paragraph of current page.

cidence angles (0^0 to 70^0) with a step of 10^0 degrees. In Fig. 1 the configuration of source and receivers positions for the normal (left) and the enlarged (right) models are shown, respectively. The longitudinal components of the fourth receiver from the PML boundary of each profile (shown in Fig. 1) computed for direct incidence of P waves for model A and S waves for model B, are plotted in Figs. 2 together with the DWN synthetics. For receivers 74 and 78 no DWN synthetics were available because of intrinsic limitation of the method which does not allow computing solutions for receivers with equal depth or epicentre as the source.

In Fig. 2 DWN synthetics are depicted with a black continuous line, FD synthetics with a PML thickness of 30 grid spacings with a dark gray line, FD synthetics with a PML thickness of 10 grid spacings with a light gray line and FD synthetics for the enlarged model with a black dashed line.

4.3 Comparison with non-reflecting boundaries

The efficiency of PML comparing to other, commonly used, non-reflecting boundaries (NRB) was also tested for the previously described models. Five non-reflecting boundaries were used in these comparisons, namely Clayton and Engquist (1977), Higdon (1991), Peng & Toksöz (1994, 1995) and a combination of the first-order operator of Higdon (1991) with the A1 condition of Clayton and Engquist (1977) as implemented by P.-C. Liu and R. J. Archuleta (Moczo et al., 2002).

The computations were performed with the same source-receiver geometry and source parameters described for models A and B. The FD calculations were performed again for ten and thirty grid steps PML thicknesses. The synthetic waveforms were compared with the DWN solutions and for the quantification of these comparisons the single value envelope and phase misfits were calculated (Kristekova et al., 2006). In Fig. 3 the longitudinal components of the waveforms produced for all the non-reflecting boundaries, together with the 10 and 30 PML FD solutions for model A and direct P waves (left) and for model B and direct S waves (right) incidence are shown.

The 30 and 10 PML FD solutions are depicted with the sparse and dense black dashed lines, respectively, while the FD solutions for the enlarged model are shown with the black solid line. The solutions computed with the use of A1 condition of Clayton and Engquist (1977) and the Higdon (1991) operator are denoted with dark and light gray solid lines, respectively. The Peng & Toksöz
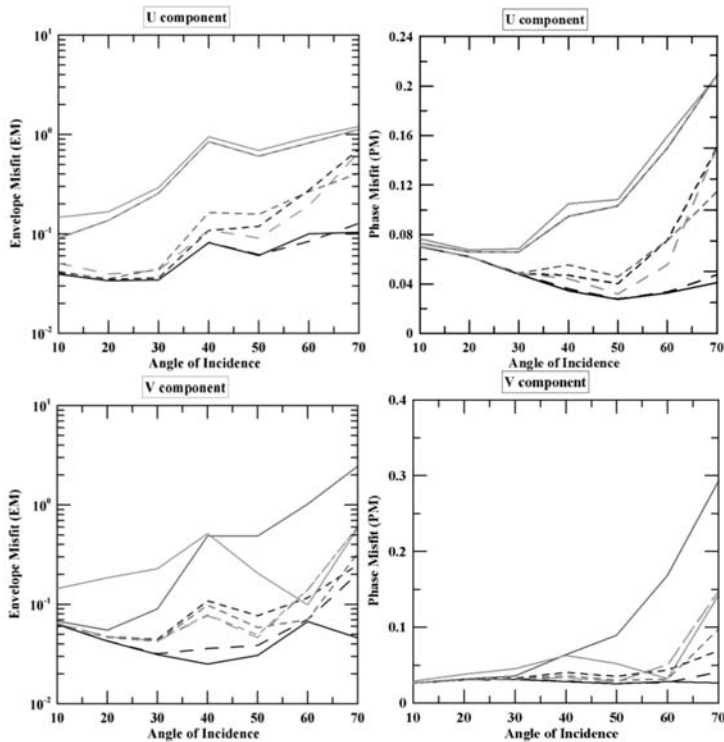
Fig. 4: Envelope and phase misfits for the horizontal component of FD and NRB synthetics for model A and direct P waves incidence (top) and for model B and direct S waves incidence (bottom). DWN synthetics are depicted with a black continuous line, FD synthetics with 30 grid-spacings PML thickness with a dark gray line, FD synthetics with 10 grid-spacings PML thickness with a light gray line and FD synthetics with 30 grid-spacings PML thickness for the enlarged model with a black dashed line.

(1994, 1995) solutions, for maximum attenuation set for the perpendicular displacement component of the P and S waves, are shown with the sparse and dense dashed light gray lines, respectively. Finally, the solution computed with the P.C. Liu and R. J. Archuleta non-reflecting boundary is denoted with the dense dark gray dashed line. Results from all comparisons performed, are quantified in Fig. 4, where the single value envelope and phase misfits are plotted against the incidence angle for the longitudinal components of both (A and B) models. The envelope misfit verifies the visual inspection of the calculated waveforms, with a noticeable diminished efficiency of the PML boundaries in the vicinity of the critical incidence angle and generally for grazing incidence angles.

Furthermore, envelope misfits are higher for model A than model B for the horizontal component, which might be an indication that PML can perform better than other non-reflecting boundaries in models with high Poisson ratios. Finally, it can be noticed that the 10-grid PML performs slightly worse for direct S wave incidence in comparison to direct P wave incidence for both models A and B, which suggests the need of thicker PML zones in cases that S waves are arriving at the computational model boundaries.

Phase misfits have much smaller values than the envelope misfits. This is strong indication that the errors introduced in the FD solutions from PML and other non-reflecting boundaries in general, are mostly due to changes in the amplitude and not in the phase of the waveforms. Phase misfits do not
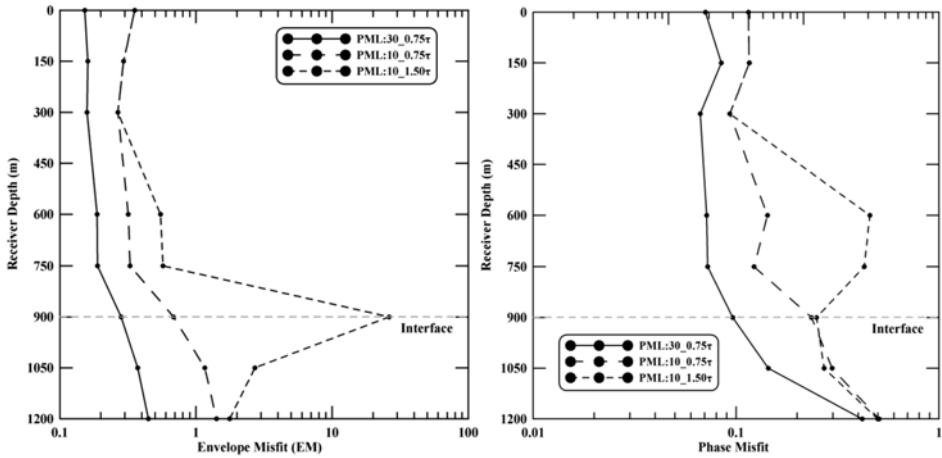
Fig. 5: Average envelope and phase misfits of the three components of each receiver plotted against receiver's depth for the LHS model.

exhibit the same trend as the envelope misfits becoming smaller with increasing incidence angles for the longitudinal component. Furthermore, on the contrary to amplitude misfits, phase misfits seem to be independent of the velocity contrasts or the type of the impinging wave.

4.4 Layer over half-space model

The second model used to test the efficiency and the overall behavior of NPML is a surface layer over a half-space (LHS) model. The size of the grid spacing h is the same determined and used for the homogeneous models (h=30 m). The number of grid cells in the x, y, and z directions are MX=400, MY=400, and MZ=300 and the time step dt=0.002 s. A double-couple point source with the same Gabor signal as a source time function was used for the FD computations in LHS model.

The test was implemented by using nine equidistant receivers positioned parallel to the Z axis, normal to the free surface. The first receiver was located at the free surface, while the deepest receiver at the depth of 1200 m. Moreover the seventh receiver was placed exactly on the layer – half-space interface in order to examine the behavior of the NPML in the vicinity of this internal boundary. The source was placed at a point with Cartesian coordinates (300, 4500, 450) m.

FD calculations were performed for ten and thirty grid steps PML thicknesses and two different values of the tuning variable τ [0.75, 1.5]. For the 3rd receiver no DWN synthetics were available due to the intrinsic limitation of the DWN method previously mentioned.

The single value envelope and phase misfits were calculated for the horizontal and vertical components of all receivers, using as a reference solution the DWN synthetics when possible. In Fig. 5 the averaged envelope and phase misfits for the three components of each receiver are plotted against the receiver's depth for all three combinations of PML thicknesses and τ values.

From these figures, the trend of thicker PML zones to produce better results can be observed, while the 10 grid-spacings PML zone performs better for lower values of the tuning variable τ (=0.75). Moreover the decreased efficiency of PML in the vicinity of the layer – half-space interface should be pointed out for all combinations of zone thicknesses and tuning variable values. Small phase misfits for all computations are also consistent with the results drawn from the homogeneous models, showing that NPML affect mostly the amplitude of the waves.

5. Conclusions-Results

The performance of a NPML technique was tested for the Cartesian coordinate system, as implemented for a 3D-4th order staggered-grid velocity-stress Finite-Difference scheme. Numerical tests were performed for investigating its overall performance in a layer over half-space and homogeneous half space models with high and low Poisson ratios. The results were compared with the semi-analytical solution provided by the Discrete Wavenumber Method (DWN) and quantified using a single value envelope and phase misfit, in order to study the influence of the NPML not only on the amplitude, but also on the phase of the impinging waveforms.

In all tests the Non-Splitting formulation did not exhibit instability problems in any of the models used (high and low Poisson ratios, LHS). NPML performance appeared to be better at almost vertical incidence angles and is reduced at grazing angles. Moreover their efficiency for the critical angle of incidence depends on the PML thickness. The trivial conclusion that thicker PML zones result in weaker artificial reflections was deducted from all the tests performed. For computations with high accuracy demands, a thicker PML zone is suggested (30 grid-spacings), providing that the memory cost from the thickest PML zone is affordable.

The comparison of the NPML with other, commonly used, Non-Reflecting boundaries is clearly in favor of PML. The envelope and phase misfits calculated, for any PML thickness and for all incidence angles exhibited systematically lower values. The higher efficiency of PML is shown for both horizontal components. Envelope misfits are higher for model A than model B, suggesting that PML perform better than non-reflecting boundaries in high Poisson ratios models. The poorer performance of 10-grid PML zones in direct S wave incidence comparing to direct P wave incidence for both models A and B might be related with the choice of the wave velocity used in Eq. (16). After several tests performed the P wave instead of S wave velocity was preferred, resulting in better and more stable results.

Phase misfits exhibit much smaller values than the envelope misfits. This is a strong indication that the errors introduced in the FD solutions from PML and other non-reflecting boundaries are mostly due to changes in the amplitude and not in the phase of the waveforms.

The artificial reflections in thinner PML zones are probably due to the boundary used for the termination of the PML zone. On the contrary, for thicker PML zones artificial reflections are probably caused by the finite contrast in properties between successive grid nodes, suggesting that the discrete PML zones behave almost as solid bodies. Stronger attenuation will enhance the contrast in properties of successive nodes for thicker zones while for thinner zones will produce stronger reflections from the PML interface. Thus the optimum solution should be based on a compromise between the thickness of the zone and the applied attenuation between successive nodes.

6. Acknowledgments

7. References

Berenger, J., (1994). A perfectly matched layer for the absorption of electromagnetic waves: *J. Comput. Phys.*, 114, 185–200.

Berenger, J. P. (1996). Three-dimensional perfectly matched layer for the absorption of electromagnetic waves, *J. Comp. Phys.*, 127, 363–379.

Bouchon, M. (1981). A simple method to calculate Green's functions for elastic layered media, *Bull. Seism. Soc. Am.*, 71, 959–971.

Chew, W., and Q. H. Liu, (1996). Perfectly matched layers for elastodynamics: a new absorbing boundary condition, J. Comp. Acoust., 4, 341–359.

Clayton, R., and B. Engquist, (1977). Absorbing boundary conditions for acoustic and elastic wave equations, *Bull. Seismol. Soc. Am.*, 67, 1529 – 1540.

Collino, F., and P., Monk, (1998a). Optimizing the perfectly matched layer, *Comput. Methods Appl. Mech. Eng.*, 164, 157–171.

Collino, F., and C. Tsogka, (2001). Application of the PML absorbing layer model to the linear elastodynamic problem in anisotropic heterogeneous media, Geophysics, 66, 294–307.

Coutant, O. (1989). Program of numerical simulation AXITRA. Res. Rep. LGIT (in French), Universite Joseph Fourier, Grenoble.

Engquist, B., and Majda, A., (1997). Absorbing boundary conditions for the numerical simulation of Waves: *Math. Comp.*, 31, 629–651.

Festa, G. and S. Nielsen, (2003). PML Absorbing Boundaries, *Bull. Seismol. Soc. Am.*, 93, 891–903.

Frankel, A. (1993). Three-dimensional simulations of ground motions in the San Bernardino Valley, California, for hypothetical earthquakes on the San Andreas fault, *Bull. Seism. Soc. Am.*, 83, 1020–1041.

Graves, R. W. (1996). Simulating seismic wave propagation in 3D elastic media using staggered-grid finite differences, *Bull. Seism. Soc. Am.*, 86, 1091–1106.

Hastings, F., Schneider, J. B., and Broschat, S. L., (1996). Application of the perfectly matched layer (PML) absorbing boundary condition to elastic wave propagation, *J. Acoust. Soc. Am.*, 100, 3061– 3069.

Higdon, R. L., (1991). Absorbing boundary conditions for elastic waves, Geophysics, 56, 231-241.

Komatitsch D. and R. Martin (2007). An unsplit convolutional perfectly matched layer improved at grazing incidence for the seismic wave equation, *Geophysics*, 72, 155–167.

Kristek, J., P. Moczo, and R. J. Archuleta, (2002). Efficient methods to simulate planar free surface in the 3D 4th-order staggered-grid finite-difference schemes, *Studia Geophys. Geodet.*, 46, 355–381.

Kristek, J., and P. Moczo, (2003). Seismic wave propagation in viscoelastic media with material discontinuities—A 3D 4th-order staggered-grid finite-difference modeling, *Bull. Seismol. Soc. Am.*, 93, 2273–2280.

Kristekova, M., J. Kristek, P. Moczo and S.M. Day, (2006). Misfit criteria for quantitative comparison of seismograms, *Bull. Seismol. Soc. Am.*, 96, 1836-1850.

Marcinkovich C. and K. Olsen, (2003). On the implementation of perfectly matched layers in a three-dimensional fourth-order velocity-stress finite difference scheme, *J. Geophys. Res.*, 108, 2276 – 2292.

Martin R., D. Komatitsch, and A. Ezziani, (2008). An unsplit convolutional perfectly matched layer improved at grazing incidence for seismic wave propagation in poroelastic media, *Geophysics*, 73, 51–61.

Moczo, P., J. Kristek, and L. Halada (2000). 3D fourth-order staggered grid finite-difference schemes: stability and grid dispersion, *Bull. Seism. Soc. Am.*, 90, 587–603.

Moczo, P., J. Kristek, V. Vavrycuk, R. J. Archuleta, and L. Halada, (2002). 3D heterogeneous staggered-grid finite-difference modeling of seismic motion with volume harmonic and arithmetic averaging of elastic moduli and densities, *Bull. Seism. Soc. Am.*, 92, 3042–3066.

Peng, C. and M. N. Toksöz, (1994). An optimal absorbing boundary condition for finite difference modeling of acoustic and elastic wave propagation, *J. Acoust. Soc. Am.*, 95, 733-745.

Peng, C., and Toksoz, M., (1995). An optimal absorbing boundary condition for elastic wave modeling, *Geophysics*, 60, 296–301.

Wang, T., and X. Tang, (2003). Finite-difference modeling of elastic wave propagation: A nonsplitting perfectly matched layer approach, *Geophysics*, 68, 1749–1755.

A MATLAB PROGRAM FOR THE ANALYSIS AND INTERPRETATION OF TRANSIENT ELECTROMAGNETIC SOUNDING DATA

Andreas Tzanis

University of Athens, Department of Geophysics and Geothermy, Zografou 15784, Greece,
atzanis@geol.uoa.gr

Abstract

Herein we present a software system, written in MATLAB, to interpret TEM sounding data. The program, dubbed maTEM, is designed to process, model and invert multiple soundings, either individually, or simultaneously along profiles. The latter capability allows for laterally constrained inversion, so as to generate pseudo-2D or 2D resistivity sections based on the program EM1DINV v2.13 by the Hydro-Geophysics Group of the University of Aarhus, Denmark. Using maTEM, the analyst may import and display data multiple data sets, denoise and smooth the data, perform approximate inversions, design 1-D model(s) graphically, perform forward modelling and inversion and generate/ update data base in which to store the results. Finally, the analyst may use the data base to create 2-D and 3-D displays of the geoelectric structure with built-in graphical functions. maTEM is highly modular so that additional functions can be added at any time, at minimal programming cost. Although the software presented herein is focused on the analysis of TEM data, the maTEM concept has been designed ready to incorporate additional electrical and EM geophysical sounding methods and to mutually constrained analysis of different geophysical data sets.

Key words: *Electromagnetic sounding, TEM, MATLAB, geophysical interpretation.*

1. Introduction

The Transient Electromagnetic (TEM) exploration method is becoming increasingly popular for its effectiveness and robustness in hydrogeological, environmental, engineering geological applications, as well as general geological and geophysical mapping. In fact, due to its sensitivity in resolving small contrasts in generally highly conducting structures, it has become the EM method of choice for such applications, as the detection and mapping of subterranean water concentrations and flow paths, detection and monitoring of salination processes in coastal aquifer systems, detection and monitoring of aquifer pollution and pollutant migration, detection and mapping of buried faults, deep lifelines, leakage, UXO etc.

A pre-requisite for TEM applications in hydrogeological and environmental studies is the quality of the data and interpretation scheme, with particular emphasis on the latter. This is because in most modern applications, it is not sufficient to map the conductive targets only, but also to measure their volume, delineate and characterize the hosting structures and cover materials, measure the volumetric water content, the differences in water conductivity due to pollution etc.

Due to the rather involved physics of the TEM method, the existing analysis and interpretation software is relatively limited, both in numbers and availability. In general one can find: (1) High cost

commercial software from a handful of manufacturers. (2) Extreme scarcity of open source software. In fact, the author only knows of the MATLAB forward code by Ingeman-Nielsen and Baumgartner (2006) and the old inversion codes of Walter Anderson; the latter are written in plain FORTRAN and are available from the USGS (Anderson, 1982a-c), but cannot be put to work by a person unfamiliar with old and contemporary editions of FORTRAN, let alone the complete absence of a visual presentation of the results. (3) Limited availability of inversion software, which is usually offered as an executable, without (or with limited) data management and display facilities; this is usually provided by academic institutions, e.g. the University of Oulu, Finland and the University of Aarhus, Denmark.

With the above two exceptions aside, the academic free software community has hitherto not produced remedies. The software presented herein, *maTEM (MAtlab Transient ElectroMagnetics),* marks the beginning of an effort to create an advanced TEM analysis and interpretation package, which may also be expandable and customizable to the needs of a particular user, with little programming effort. Although easy to say, this would be a truly demanding and ambitious undertaking, had it not been for the existence of powerful, general purpose computing engines. On this basis, the realization of such a project is feasible because a computing engine will generally provide a complete high level programming environment, inclusive of graphics, which facilitates the development of advanced software because all the complexities pertaining to low level interfacing, programming and functionality are taken care by the engines themselves. This is much easier and faster than building programs from scratch in some conventional high level language such as C, C++ or FORTRAN.

2. Specifications and programming environment

A modern program, like maTEM aspires to be, should be able to offer a complete solution to the problem of analysis, interpretation and visualization of TEM survey data, allowing the user to:

1. Import and handle *multiple* TEM sounding data, i.e. from more than one sounding locations and more than one type of instruments.

2. Visualize and inspect the data.

3. Process the data with utilities enabling noise suppression, smoothing etc.

4. Perform fast approximate inversions (inverse mappings). These may assist in the interpretation effort, but their primary function would be to provide insight and guidelines for the design of 1-D interpretative models.

5. Design 1-D interpretative models.

6. Perform interactive, 1-D forward modelling and/or inversion for each sounding separately.

7. Perform simultaneous inversion of multiple soundings, either 2-D, or 1-D with application of lateral constraints (in quasi-layered earth structures this amounts to proxy-2D inversion).

8. Display the interpretation in the form of resistivity cross-sections with publication quality graphics; moreover, generate composite displays by overlaying more than one cross-sections.

9. Have the data and results organized in a data base in an automated and transparent manner, so that he/she may be able to concentrate on the analysis only.

10. Be able to repeat any one of the steps 1-9 above at *any* time, in order to improve/ correct the interpretation and seamlessly introduce the results into the data base.

The realization of these specifications requires an appropriate programming and computational environment and careful selection of the interpretation (modelling and inversion) approach.

General purpose scientific computing engines are not many: The most commonly available are the proprietary IDL™ and MATLAB™ and the freeware OCTAVE and SCILAB. Of course, there is an abundance of other (proprietary or non-proprietary) scientific data analysis software, which is generally not suitable, as it is usually specialized (e.g. statistical analysis, curve fitting, data modelling, graphics etc.) and does not provide a sufficiently general and versatile enough programming environment for the development of integrated and advanced software. Of all those, MATLAB™ is the most widespread, diverse and versatile to such an extent, that it has become the *de facto* standard in scientific and technical computing.

MATLAB was not available until the later part of the 1980's, and prior to that, FORTRAN was the language of choice for serious numerical computation. C was making its first steps towards establishing a foothold in the world of scientific computation, but it didn't offer built-in facilities for doing complex arithmetic and this was a serious drawback. Conversely, FORTRAN lacked some of C's advantages such as structures, pointers, and dynamic memory allocation.

The appearance of MATLAB and its imitators made a big impact in the scientific community. MATLAB was originally written to provide easy access to matrix software developed by the LINPACK and EISPACK projects, familiar to FORTRAN programmers for being robust collections of tools for linear algebra. To do this, MATLAB also introduced a new vector-oriented programming language, an interactive environment, and built-in graphics. These features offered many advantages and boosted productivity in comparison to more traditional application development environments. Since, MATLAB has evolved to embed a large collection of state-of-the-art numerical tools, high quality graphics, object-oriented extensions, a built-in interactive debugger, web services and a host of other facilities. Of course, C and FORTRAN have also evolved, with some advanced editions also offering high-level (visual) application development environments. However, neither offers as many treats as MATLAB, graphics for instance being a major issue.

The requirement for a suitable and accurate modelling and inversion method is quite more difficult due to the scarcity of the publicly available software. Anderson's (1982a-c) pioneering FORTRAN codes are robust but insufficient because they deal only with the single/ coincident loop and central loop configurations. Karmis (2003) has developed FORTRAN programs to perform inversion of single- and multiple sounding data, which he has dubbed "*pointem*" and "*linetem*" respectively. While maTEM was being developed, these programs were not publicly available.

The remaining options were either to develop new modeling and inversion code, or, until this is done, to use the program "em1dinv" developed by the Hydro-Geophysics Group of the University of Aarhus, Denmark. This program is well known and tested by the EM geophysical community and is delivered by its author(s) in stand-alone executable form, upon application. It may perform inversion of single or multiple soundings simultaneously; in the latter case, by introducing lateral constraints between soundings, i.e. restraining the variation between homologous layers with respect to each other, it may also perform quasi-2D inversion in layered earth structures (Auken and Christiansen, 2004; Christiansen and Auken, 2004; Auken et al, 2005). An additional important advantage is the possibility to adjust the transmitter waveform to the specifications of different instrument manufacturers. On the downside, the program cannot, at present, handle earth models with complex and frequency-dependent resistivity. Thus, in some cases it may fail to interpret data affected by induced polarization effects. Moreover, because it assumes paramagnetic earth materials, it cannot handle super-paramagnetic phenomena appearing in magnetized or iron-rich soils.
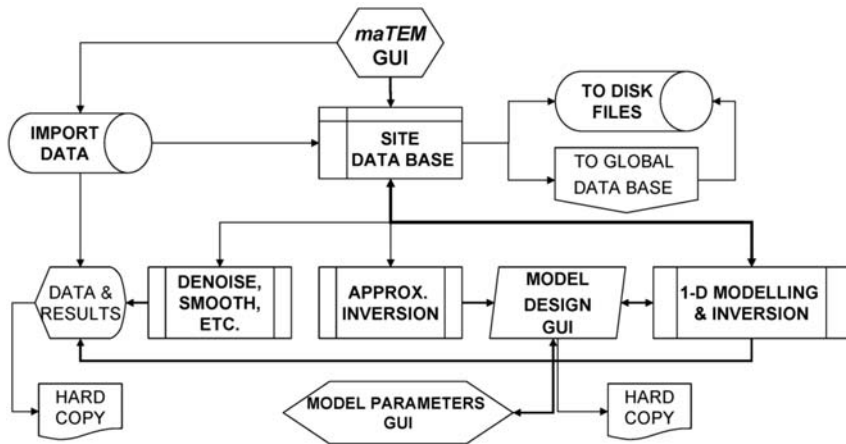
Fig. 1: Flowchart of a data analysis child process.

3. Program architecture

It should be apparent, even to the novice, that the specifications set at the beginning of Section 2, may only be realized by enabling the execution of multiple parallel processes. maTEM is designed so that each one of these processes will comprise the analysis of an individual TEM sounding at a given site (a *data analysis process*). The data and the results are assembled in a site-specific data base (DB). The individual site-DBs, in turn, contribute to the formation of a global-DB which can be independently handled, exported and re-imported. The global-DB also feeds with data and initial earth models the process of for multiple simultaneous inversions and assimilates the results for permanent storage and display. A GUI driven *parent* process, the *maTEM GUI*, controls the *data analysis child processes*. This design philosophy is illustrated and explained in the flowcharts of Figures 1-3.

Fig. 1 shows the (more or less self-explanatory) flow of work and information in a data analysis child process. Data processing (de-noising, smoothing etc.) are controlled by the maTEM GUI; the results are fed back to the site-DB and are hence available for the approximate and 1-D layered modelling and inversion operations. The site-specific Earth Model is designed and handled interactively (graphically) in an independent *Model Design* GUI which, in fact, is *child* of the maTEM GUI. This is supplied with the results of approximate inversion, which can be displayed at the user's discretion. The model design GUI generates a child process, the *Model Parameters GUI*, in which the user may manually introduce layer resistivities, thicknesses and most importantly, vertical and lateral constraints for the inversion. The site-DB can be exported in the form of a sounding data file (tem-file) and a sounding model file (mod-file).

Fig. 2 shows that the site-DBs of the parallel analysis child processes are collated to form the global-DB, in a manner that will be explained later. At present, the global-DB can be stored as a MATLAB binary file (mat-file). The information necessary for multiple simultaneous inversions (data and initial earth models) is extracted from the global-DB and the results are re-introduced for permanent storage. In addition, the results of the inversions can be extracted from the global-DB and stored independently as an ASCII file, the inv-file, to be available for visual inspection/ editing and display in the form of cross sections. An existing inv-file is not destroyed by subsequent write operations – any new results are merely appended to it, therefore caution should be exercised in order to keep the file free of unwanted repetitions.
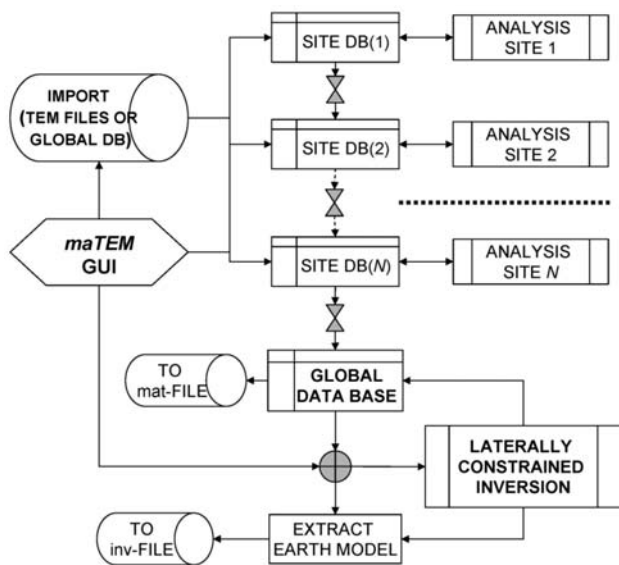
Fig. 2: Outline of the simultaneous analysis of multiple TEM soundings. Each "ANALYSIS" box corresponds to a data analysis child process.
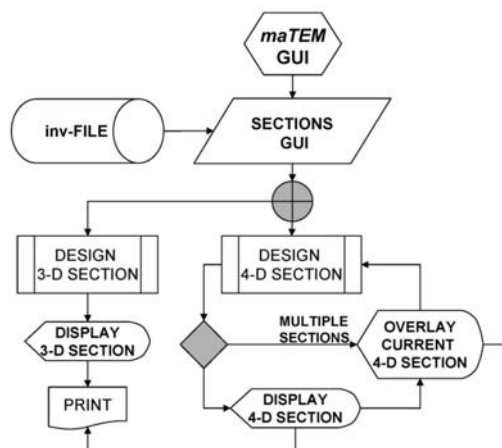
Fig. 3: Flowchart for the construction and display of interpretative cross-sections.

Fig. 3 shows how maTEM constructs and displays interpretative cross sections. The maTEM GUI launches yet another child process, the *Sections GUI*, through which the interpretation is imported from the inv-file, or extracted from the global-DB. The soundings available in the inv-file are displayed in map form and the user congigures the cross-section by pointing and clicking. Cross-sections can be displayed in either 3-D (planar) or 4-D (volume) mode. In the latter case, multiple cross-sections can be overlaid in a single graph, thus enabling visualization of lateral correlations and changes in the geoelectric structure of the entire study area.

As is already clear, maTEM has been designed to be GUI-driven at all levels. This requires object-oriented programming and defines the frame and course of realizing the design specifications. In addition, one has to consider that all child processes must be executed in parallel and that the site- and global-DBs must be updated automatically every time there's some action by the user. Given that in the GUI-driven, object-oriented environment of MATLAB, the information pertaining to modifica-

tions of graphical objects (in our case the graphical representations of data and earth models) is directly accessible through their respective handle structures, the following method for passing information between processes and data bases was adopted:

Let the data comprise $n = 1,\ldots, N$ soundings, with each sounding comprising $m_n = 1,\ldots, M_n$ channels (gates). Then, the handles of the graphical objects can be organized in data constructs comprising *homologous* 1´N *data structure arrays of data structures*, in such a manner, that the n-th element of a data structure array will comprise a $1 \times M_n$ data structure array whose fields are the handles of the M_n *homologous* graphical objects of the n-th sounding. Given that the m_n-*th* handle is actually a data structure conveying the properties of the graphical object, a strict hierarchy of data structures is thus created, organizing the available information in a manner directly accessible by reference. Any modification of the m_n–th graphical object is registered in the respective m_n–th handle and the hierarchical data construct is instantaneously updated with the new information.

The homologous structure arrays of graphical objects used in maTEM are associated with:

a. Data manipulation and management: This construct contains the graphical objects representing the data of the n-th sounding. It allows the user to hide/show entire soundings for convenience, and, more importantly, to earmark any m_n–th data channel for *de-activation/re-activation*. The term *de-activation* implies the *exclusion* of the m_n–th data channel from further consideration and is applied to measurements heavily distorted by early time effects or by noise, to the point of being irrecoverable.

b. Error bar manipulation and management: This construct contains the graphical objects representing the *observational error* associated with the m_n–th data channel in the n-th sounding.. It allows the user to hide/show the error bars associated with the data of each sounding separately, thus facilitating the visual inspection and evaluation of individual soundings.

c. Earth Model manipulation and management: This construct contains the handles of the graphical objects representing the 1-D geoelectric structural model used for the interpretation of the n-th sounding and is displayed in the "Model Design GUI".

d. Inversion parameters management: This contains the vertical and horizontal constraints applied to the inversion of the n-th model during the interpretation of the n-th sounding.

The site-DB is a data structure whose fields are alphanumeric and numeric constants and arrays containing all the useful information pertaining to an individual sounding. This includes survey-and-site-related information from the header(s) of the sounding data file, site coordinates, Tx/Rx size(s) and configuration, ramp duration, the channel central times, the sounding data in the form of impulse response, late-time apparent resistivity and true resistivity with associated uncertainties, the earmarks of the deactivated data channels, the approximate inverses, the interpretative 1-D Earth model and the associated theoretical response curves. It should be expected that the global-DB would be a $1 \times N$ data structure array of the site-DB data structures, symbolically named $\mathbf{D}(n)$. When some graphical object pertaining to the n-th sounding data or model parameters is interactively modified during the course of the analysis, the corresponding field of the $\mathbf{D}(n)$ is automatically updated via the pertinent handle. Likewise, if, after such a modification an approximate inversion or layered 1-D modeling or inversion is executed, the pertinent fields of $\mathbf{D}(n)$ are automatically updated by direct substitution of the results. The global-DB can be exported as a MATLAB mat-file, together with the ":inversion parameters" construct. This amounts to saving the analysis session. Re-importing the global-DB amounts to re-instating the session at the point at where it has been saved. This is an effective way to ensure the seamless continuity of work.
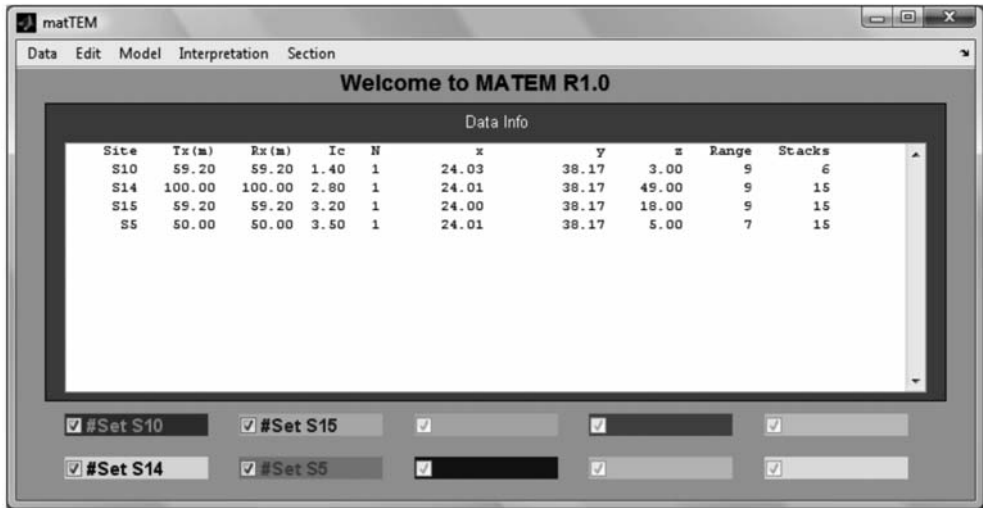
Fig. 4: The maTEM GUI after importation of data from four soundings collected with the TEM-FAST 48 system. The GUI displays key information about the soundings.

Every other graphical object not included in the above description is assigned with a unique *identification tag"*, using the 'tag' property of the object. The retrieval and registering of information in these objects is based upon acknowledgement of their ID tag. Finally, it should be noted that maTEM also features a collection of constants (keywords) and variables by which the user can choose between different modes of data and model displays, and tune the execution of em1dinv. The assignment of these parameters is also GUI driven and they can change during the course of analysis (runtime variables). They are organized in yet another global data structure whence they are passed to the appropriate calling routine. The specification and explanation of these variables is beyond the scope of this work.

4. Implementation

The maTEM GUI can be seen in Fig. 4, after a data set has been imported for analysis. The "Data" menu facilitates importation/ exportation of data and results, as well as general functions pertaining to the mode of data display (impulse response or apparent resistivity) and the type of the coordinates adopted for the survey. At present maTEM may accept the following types of data:

— Multiple *single-site* TEM data files in the TEM-FAST 48, AMIRA and em1dinv formats (each file contains one sounding).

— Multi-site TEM data files in the TEM-FAST 48 and AMIRA formats (each file contains more than one soundings)

— maTEM mat-files (i.e. the global-DB) in MATLAB binary format.

Upon importation the maTEM GUI displays important information as per Fig. 4. The (coloured) boxes indicate the colour associated with the data and models of each sounding and the checkboxes can be used to hide/ show the respective soundings for convenience.

The data is displayed in the "DATA" window as per Fig. 5a; this also comprises a GUI with menus
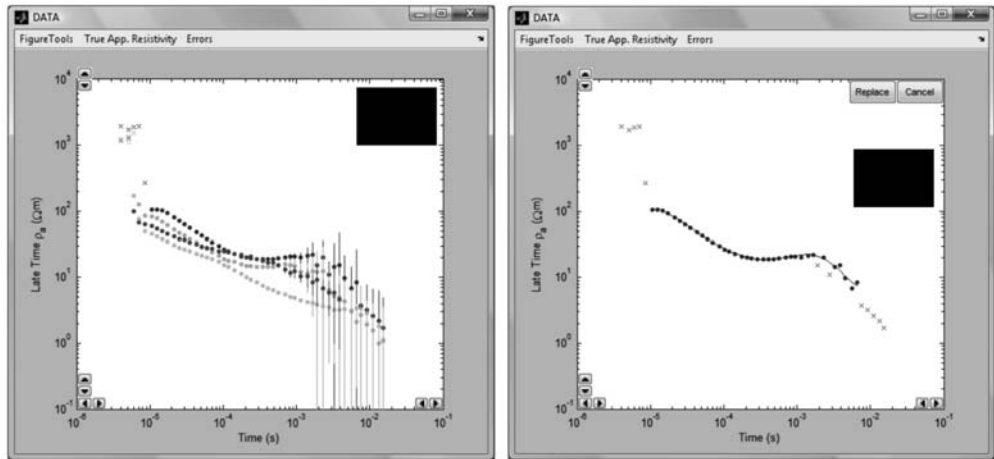
Fig. 5: (a) The four soundings shown in Fig.4, displayed as late time apparent resistivities. (b) Sounding with concealed errors, deactivated channels (x-markers) and a smooth model (continuous line) computed with a 9th order exponential spectrum and pending acceptance.

facilitating concealment/ projection of true apparent resistivity curves and error bars. The "Edit" menu offers de-noising and smoothing utilities. At this point de-noising comprises the de-activation of distorted data channels. This is done by pointing and clicking on the graphical representation of a data channel (solid circle). A deactivated channel is marked with x and may be re-activated in the very same way. Smoothing is possible with least squares smoothing splines (e.g. Wahba, 1990) or by fitting the decaying impulse response data with a function of the form

and recalculating the late time and true apparent resistivities (exponential spectrum method). An example is shown in Fig. 5b.

The "Model" menu initializes the Model Design GUI, in which layered Earth models can be created and manipulated via the dedicated "Handle" menu (Fig. 6). The models are introduced graphically, by pointing and clicking; for convenience and precision, the cursor coordinates (depth and resistivity) are indicated at the bottom of the Model Design GUI. The results of approximate inversion may also be overlaid to assist in the design. A model can be updated with insertion or deletion of layers and can be modified by capturing and shifting the breakpoints of the model (solid squares in Fig. 6 and 7a) with the mouse. There can be one layered model per sounding.

Upon completion of the graphical construction of an Earth model, the respective "Model Parameters GUI" is displayed. This, offers additional means of controlling the interpretation by allowing the manual fine-tuning of the model resistivities and thicknesses, as well as the definition of "prior information weights" (to fix or restrain the variation of a parameter depending on the existence of independent information), vertical constraints (restrain the variation between consecutive layers), and horizontal constraints (restrain the variation of homologous layers in neighbouring soundings during laterally-constrained inversion of multiple soundings along profiles).

The menu "Interpretation" is used to compute approximate inverses with the methods of Barsukov
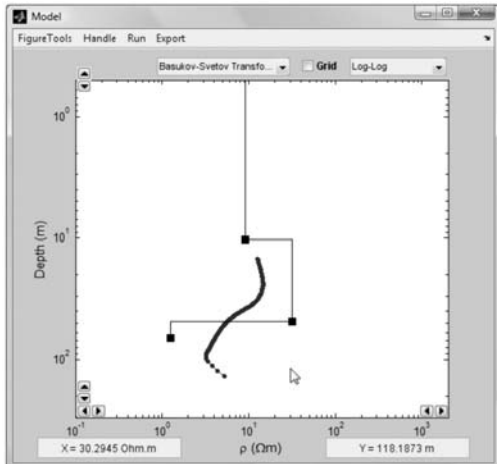
Fig. 6: The Model Design GUI during the graphical construction of a layered earth model
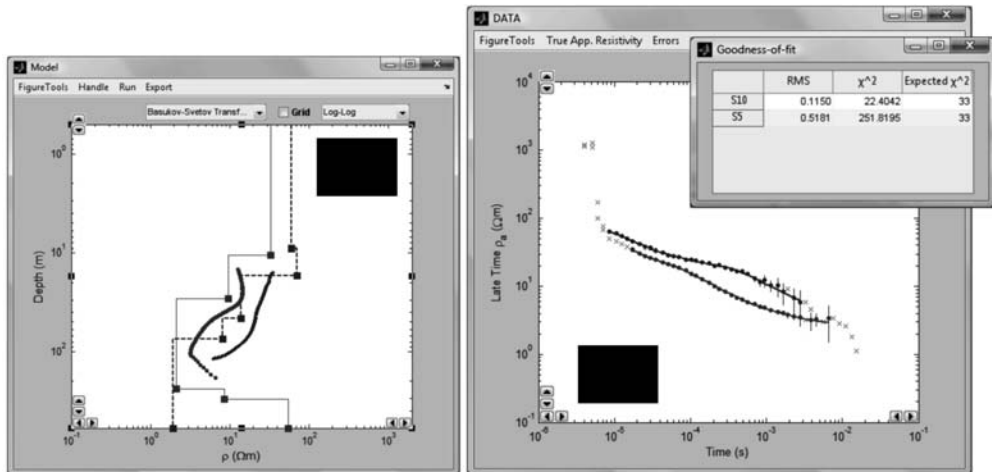
Fig. 7: Simultaneous inversion of two soundings. (a) The final models are displayed in the Model Design GUI; approximate inverses are overlaid for comparison. (b) The model theoretical responses (continuous lines) are laid over the measured data. The "Goodness-of-fit" window displays the corresponding RMS and χ^2 metrics.

and Svetov (Barsukov et al, 2007) or S-inversion (Tartaras et al, 2000), to perform interactive forward modelling and inversion and to adjust the source waveform and the control parameters necessary for the execution of em1dinv. The latter (modelling and inversion) is also possible – and more versatile – via the "Run" menu of the Model Design GUI (Fig. 6 and 7a). Interactive forward modelling can be done either by capturing and shifting the breakpoints of the model (solid squares in Fig. 6 and 7a) with the mouse, or by typing the updated model parameters in the appropriate boxes of the Model Parameters GUI. The progress of the modelling exercise and the quality of the interpretation is monitored both visually and numerically by means of the RMS and c^2 metrics projected on a separate, "Goodness-of-fit" window (Fig. 7b). Only one sounding can be modelled at a time in this manner. Conversely, more than one sounding can be inverted simultaneously, with or without vertical and lateral constraints. Fig. 7 displays the result of such an exercise for two de-noised soundings (S5 and S10 in Fig. 4). The results of the interpretation may be exported in the various available
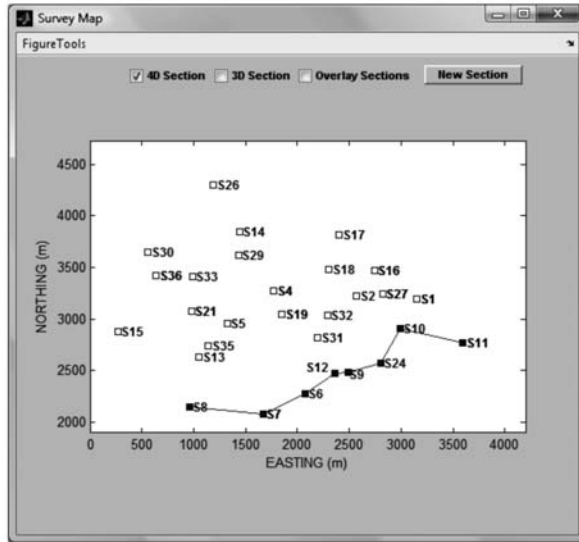
Fig: 8. The "Survey Map" GUI, used for designing a cross section.
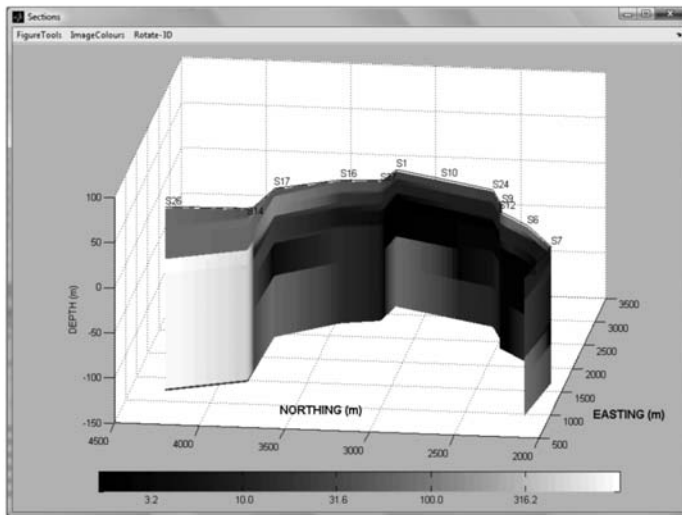
Fig. 9: A 4-D (volume) representation of two sections joined at S1, as viewed from the NE.

formats, via the "Export" menu of the Model Design GUI, or the appropriate menu entry under the "Data" menu of the maTEM GUI.

Finally, the menu "Section" allows the user to import the results of the interpretation from an inv-file and to build interpretative cross-sections. The locations of the interpreted soundings are displayed in the "Survey Map" GUI (open squares in Fig. 8), where the user may design the section by selecting the mode of presentation (3D or 4D) and pointing and clicking on the desired sounding locations. When in three-dimensional (4D) display mode, sections can be overlaid (multiple sections can be displayed on the same graph) as per Fig 9; they can also be freely rotated (menu "Rotate-3D") in Fig. 9, and redrawn with a variety of different colour schemes (menu "ImageColors" in Fig. 9).

5. Epilogue

At the present stage of development maTEM provides a relatively broad and functional range of tools for the analysis of any type of TEM data (single loop, coincident loop and offset configurations). Overall, it offers a decent and in several aspects advanced and versatile means of treating TEM data, and may even stand competitively against commercial analysis programs.

Nevertheless, one can think many additional tools that can be included in future releases. One can think of several improvements in the code, addition of more advanced processing techniques and graphical utilities etc. One important development may be the incorporation of a means to model data with induced polarizaton effects. This would certainly increase the range of applications for the benefit of the user.

Another very important point, as well as one for which very few remedies exist, is the joint (mutually constrained) interpretation of different geophysical prospecting methods. It is common knowledge that every individual electrical or electromagnetic prospecting method is subject to physical limitations that restrain its scope of application. It is also common knowledge that two or more methods jointly applied and interpreted, are much more effective because they may compensate for each other's limitations. However, the geophysical software community is reacting slowly to the dearth of software solutions, at least in the public domain.

Em1dinv is one shiny exception: it is a pioneering application and very handy in this respect, because in addition to any kind of TEM loop configuration, it may handle dc resistivity data (Schlumberger and Wenner arrays), controlled-source frequency domain EM (FEM) and natural field EM (AMT/MT) sounding data in any combination. maTEM has an architecture readily expandable to incorporate any number of additional data analysis processes (different prospection methods) and thus can be expanded to meet the challenge of mutually constrained geophysical data analysis with relatively minor programming effort.

Finally, maTEM may be available from the author upon request, subject to the applicant having secured a license to use em1dinv from its own authors. For an application to use em1dinv see http://www.geofysiksamarbejdet.au.dk/page559.aspx.

6. Acknowledgments

7. References

Anderson, W.L., 1982a. Calculation of transient soundings for a coincident loop system (Program TCOLOOP). *USGS* Open-File Report 82-378.

Anderson, W.L., 1982b. Nonlinear least-squares inversion of transient soundings for a coincident loop system (Program NLSTCO), *USGS* Open-File Report 82-1064

Anderson, W.L., 1982c. Nonlinear least-squares inversion of transient soundings for a central induction loop system (Program NLSTCI), *USGS* Open-File Report 82-1129

Auken E. and Christiansen A.V. 2004. Layered and laterally constrained 2D inversion of resistivity data. *Geophysics* 69, 752–761.

Auken, E., Christiansen, A.V., Jacobsen, B.H., Foged, N. and Sørensen, K.I., 2005. Piecewise 1D laterally constrained inversion of resistivity data, *Geophysical Prospecting*, 53, 497–506.

Barsukov, P.O., Fainberg, E.B. and Khabensky, E.O., 2007. Shallow investigations by TEM-FAST technique: Methodology and examples, in V.V. Spichak (editor), *Methods in Geochemistry and Geophysics, Volume 40,* 56-77.

Christiansen, A. V. and Auken, E., 2004: Optimizing a layered and laterally constrained 2D inversion of resistivity data using Broyden's update and 1D derivatives. *Journal of Applied Geophysics*, 56, 247-261.

Ingeman-Nielsen, T. and Baumgartner, F. 2006. CR1Dmod: A Matlab program to model 1D complex resistivity effects in electrical and electromagnetic surveys. *Computers & Geosciences,* 32, 1411–1419

Karmis, P., 2003. Automated interpretation of transient electromagnetic soundings. Doctoral Dissertation, N.K University of Athens (in Greek).

Tartaras, E., Zhdanov, M.S. Wada, K. Saito, A. and Hara, T., 2000. Fast Imaging of TDEM data based on S-inversion. *Journal of Applied Geophysics,* 43, 15–32.

Wahba, G., 1990. Spline models for observational data. In: *CBMS-NSF Regional Conference Series in Applied Mathematics* 59, Soc. Industrial and Applied Mathematics, Philadelphia, Pennsylvania (1990), p. 169.

LARGE SCALE VERTICAL ELECTRICAL SOUNDINGS SURVEY IN ANTHEMOUNTAS RIVER BASIN FOR EVALUATING HYDRAULIC COMMUNICATION BETWEEN SUB BASIN AQUIFERS

Vargemezis G.[1] and Fikos I.[1]

[1] *Aristotle University of Thessaloniki, Department of Geology, Laboratory of Applied Geophysics, 54124 Thessaloniki, Greece, varge@geo.auth.gr, ifikos@geo.auth.gr*

Abstract

In Anthemountas river basin a number of studies have taken place mainly because of the significant drop of underground water level observed in the beginning of the last decade. Data from existing hydrowells show the existence of a complex aquifer with the two main underground water bodies situated east and west of the region of Vasilika and Galarinos villages respectively. A large scale geophysical survey took place consisting of Vertical Electrical Soundings (VES) and Electrical Resistivity Tomography (ERT). The main area of interest is in the central region of the basin between Vasilika and Galarinos villages where eighty five (85) VES (Schlumberger array), located on a regular grid revealed a three dimensional model for the sedimentary formations while mapping the bedrock down to a depth of more than 600m has been achieved. In the same area, ERT measurements and geological information derived from borehole data are used to obtain a more detailed geological model for the area of interest. From surface to bedrock depth, the hydraulic communication between these two water bodies is examined. Furthermore significant geological features are observed and discussed.

Key words: Vertical Electrical Soundings, complex aquifer, Anthemountas river basin.

1. Introduction

In previous decades the increasing urban development along with intense agricultural activity in Anthemountas river basin resulted in significant drop of underground water level. With the support of local authorities, many scientists focused their interest on the broader area and studied the geological and the hydrogeological setting (IGME 1996, Nagoulis 1998, Theodossiou et al 2005). Geophysical methods were also used in large scale (Savvaidis et al 2000) providing information regarding bedrock depth on the western part Anthemountas river basin based on gravity and magnetic measurements. Thanasoulas (1983) with electrical soundings and Fikos et al (2000) with repeated ERT measurements focused on small scale surveys near the coastline and the city of Thermi.

In recent years the watershed management approach forced by 2000/60/EC, better known as water framework directive, pointed out the significance of a good understanding of hydrogeology in watershed management. In the case of Anthemountas river basin the available data revealed a very complex system of aquifers with significant extent in both lateral and vertical sense. Understanding the interaction among these underground water bodies will allow better planning and management of water resources. A large scale geophysical investigation focusing on the area west of Vasilika vil-
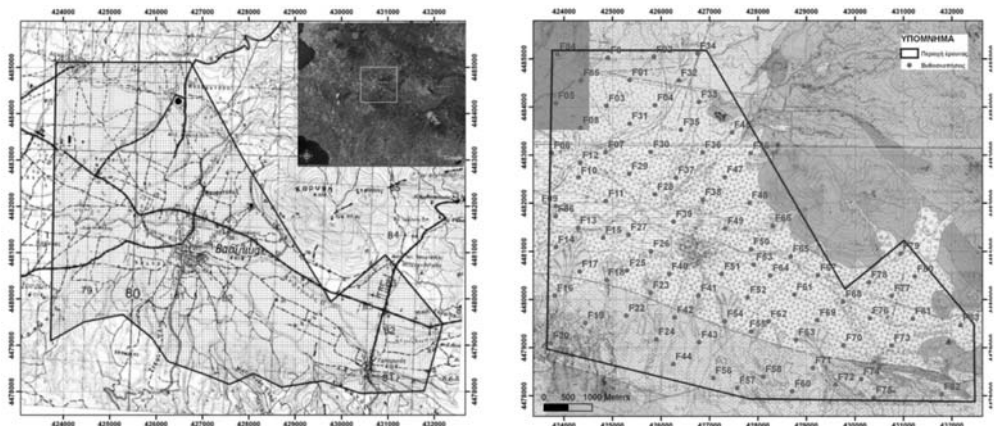
Fig. 1: (left): Survey area shown on topography map and survey area with exact location of the VES is also shown on geological map provided by IGME (right).

lage up to the eastern limits of Galarino village was conducted as part of LIFE04ENV/GR/000099 WATER AGENTA project. Eighty five (85) vertical electrical soundings (VES) were executed in a nearly regular grid with a distance of 750 meters between adjacent VES, surveying an area of 36 km^2 (Fig.1), aiming to map the bedrock as well as sediments in smaller depths and examine their hydrogeological features.

2. Geological – Hydrogeological setting

According to the geology map provided by IGME (1:50000) the study area is covered with sediments deposits consisting of: i) Valley deposits: sandy clay, ii) Lower terrace system: gravels and sand under a clayey cover, iii) Upper terrace system: grits and pebbles with loam or sandy clay, iv) Fans of different age, v) Red clay series: red to brick red, silty clays with mica and calcareous concretionary bodies, while the area to the north and south are covered by vi) Limestones recrystallised, vii) Granodiorite, viii) Gabbro and ix) Dunites and peridotites. The location of the cross section shown on figure 2 can be seen on geology map of figure 1 and it becomes obvious that the area of interest is covered by sediments while the bedrock seen near point A2 dips due to tectonic faulting to the center of the basin to unknown depth. Similar behaviour can be observed near the north end of the cross section (towards point A3) where the bedrock (peridotites) is dipping to southeast direction. These fault systems also affect the red clay series creating a new valley that is filled with sand and gravel of the lower terrace system.

The hydrogeology varies significantly for the area of interest due to the anisotropy of the sediments of the basin. Their behaviour is driven mainly by their primary porosity and the secondary porosity caused from the faulting tectonics making it easier for water flow in certain areas. Data from more than 90 boreholes located in Anthemountas river basin were used to get a better understanding of the hydrogeological setting down to a depth of 200 meters although many of them stop in smaller depths. According to these data the sediments mainly consist of: sands, silts, clay, gravels and pebbles with large variations in their thickness and their granulometry. In these types of sediments the primary porosity varies between 20% and 35% and their permeability K from $10^{-8} – 10^{-2}$ m/s (Kallergis 1999) depended on the percentage of clay present. According to Theodossiou et al(2005), analysis of pumping tests in the eastern part of Anthemountas river basin, transmissivity (T) ranges between 1,3x10$^-$
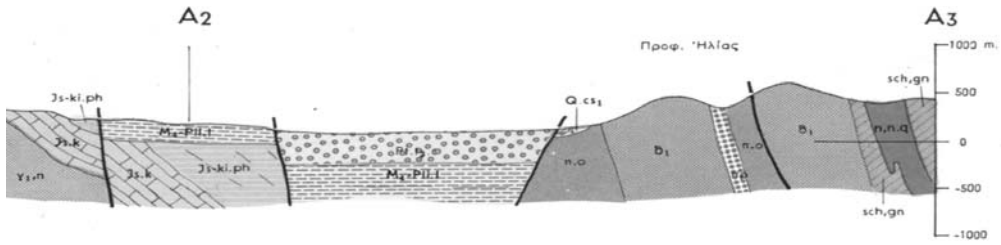
Fig. 2: Cross section A2 - A3 shown on geological map of figure 1, provided by IGME
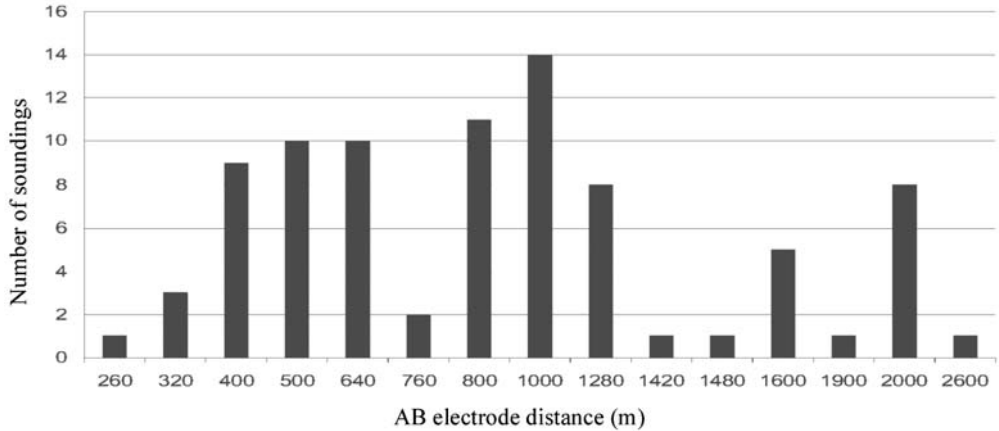
Fig. 3: Number of VES for different values of current electrode distance

[4] m²/s and 1,3x10⁻³ m²/s and can be characterized as medium to high, hydraulic conductivity (K) ranges between 3,4x10⁻⁶ m/s and 2,9x10⁻⁵ m/s reflecting permeable formations of medium conductivity and storativity (S) ranges between 4,3x10⁻⁴ and 6,2x10⁻².

In the above mentioned formations, there is a complex system of aquifers that develop in the permeable sediments and which is characterised by significant anisotropy. In the area of interest two different aquifers can be identified based on the existing information: a) an unconfined aquifer in the depths of 10 to 30 – 40 meters and b) a confined aquifer located deeper (> 50 meters) that is known to continue down to a depth of more than 200 meters but the majority of the existing hydro wells do not provide information deeper than 150 meters.

3. Geophysical investigation

3.1 VES Field Data and interpretation

A grid of 85 VES was planned and the exact location of each VES can be seen on Fig. 1. Each set of measurements was complete only after the bedrock could be identified in the sounding and that is why the current electrode distance AB varied between 260 meters and 2600 meters (Fig. 3). Measurements were taken with Syscal (V11.4) IRIS instrument and the IPI2WIN software (distributed by Geoscan-M Ltd) has been used for the inversion of field data. The initial model for the inversion was extracted by the use of theoretical curves for Sclhuberger soundings and the final RMS values varied between 0,5% and 7%.

Sounding F04

N	ρ	h	d	Alt
1	103	25.7	25.7	-25.67
2	37.8	58.7	84.3	-84.34
3	5.55	90.1	174	-174.4
4	1450			

Sounding F03

N	ρ	h	d	Alt
1	46.7	32.92	32.92	-32.924
2	18.42	27.82	60.74	-60.739
3	23.93	114	174.7	-174.72
4	10.21	65.17	239.9	-239.9
5	22.65	126.8	366.7	-366.71
6	23.14	236.3	603	-602.97
7	1900			

Sounding F07

N	ρ	h	d	Alt
1	141	13.1	13.1	48.9
2	31.2	18.2	31.3	30.7
3	129	18	49.3	12.7
4	40.3	104	153	-91.23
5	19.8	125	278	-216
6	18	443	721	-658.7
7	2241			

Sounding F15

N	ρ	h	d	Alt
1	13.35	34.64	34.64	-34.64
2	18.11	35.48	70.12	-70.12
3	15.12	102.6	172.7	-172.72
4	24.97	94.07	266.8	-266.79
5	11.91	553.7	820.5	-820.49
6	502.3			

Sounding F32

Fig. 4: Example of interpretation for 4 representative VES measured in the survey.

Some typical examples of the results are presented in Fig. 4 where the reader can see the original measurements along with the resulting curve and the corresponding table of resistivity (ϱ), thickness (h), relative (to the surface) depth (d) and absolute elevation of the floor (Alt)of each identified layer. As it can be seen for example on sounding F15, the depth of investigation is more than 820 meters and the deeper identified layer appears with high resistivity (ϱ=502 Ohm-m) and can be interpreted as the bedrock beneath the basin's sediments.

3.2 Analysis and evaluation

The resistivity values range from very few to few thousands ohm-m. This range corresponds to the large range of range of sediments and rock present in the area. Based on literature and on previous

Table 1.

Resistivity (Ohm-m)	Assumed formation	Colour Scale
0-10	Clay	A
10-20	Sandy clay with possible gravel	B
20-30	Sand with clay and gravel layers	C
30-50	Pebbles and gravel with water	D
50-80	Marl or weak conglomerate	E
80-150	Weathered bedrock	F
>150	Bedrock	G
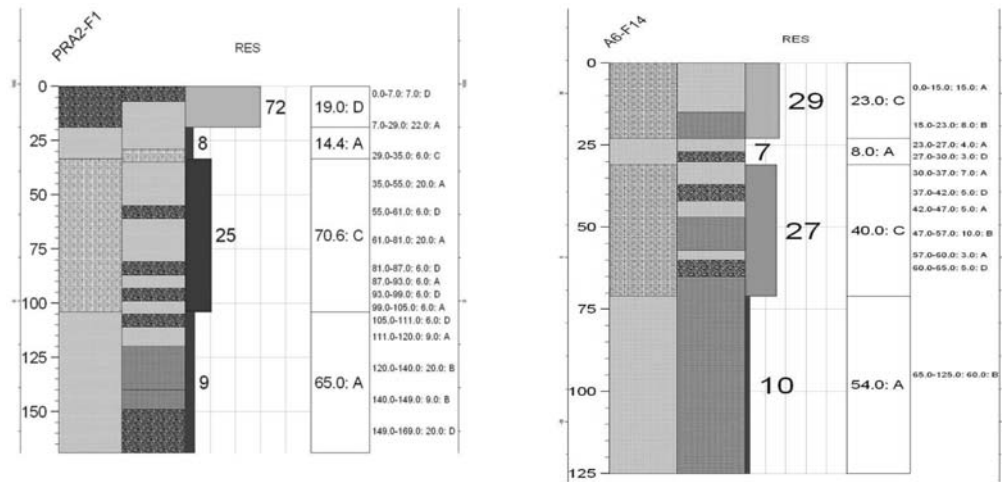
Fig. 5: Examples of calibration of table 1 based on borehole data near VES location.

experience, we created seven different groups corresponding to seven different formations, in order to evaluate the resistivity values.

To evaluate and further calibrate this table we compared soundings results with borehole data in 11 cases where the distance between borehole and VES location was small. Examples of these comparisons are shown in Fig. 5 where for each case we can see (in columns from left to right) formations based on colour scale from table 1, lithostratigraphy, formation resistivity value, layer thickness and on the most right column the ceiling and bottom of each formation based on the borehole data and the corresponding formation from Table 1.

Following this analysis we evaluated the results by creating pseudo-2D slices from adjacent VES, describing the variation of resistivity in 4 different orientation groups, more specifically we created 15 N-S oriented slices, 13 NE-SW oriented slices, 6 NW-SE oriented slices and 4 E-W oriented slices. Chosen examples of some of them are shown in the following figures where the horizontal axis shows distance along the line and vertical axis shows absolute altitude. In each figure, on the left part we see the location of the shown line on the geology map and on the right part the 2D pseudosection of apparent resistivity (top) and the true resistivity (bottom). Table's 1 relation between resistivity value and
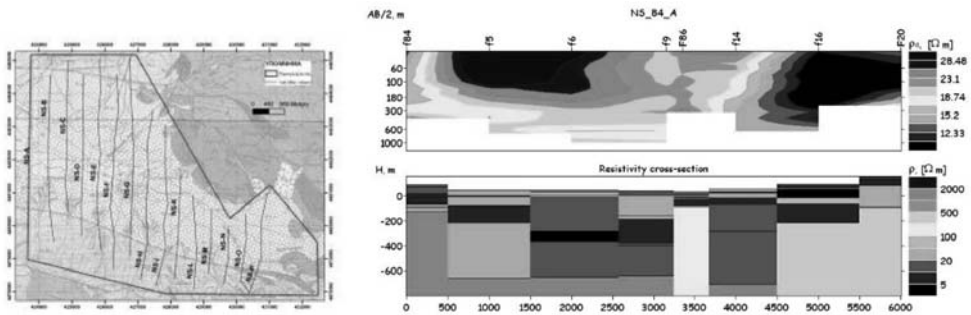
Fig. 6: N-S oriented vertical pseudosection A
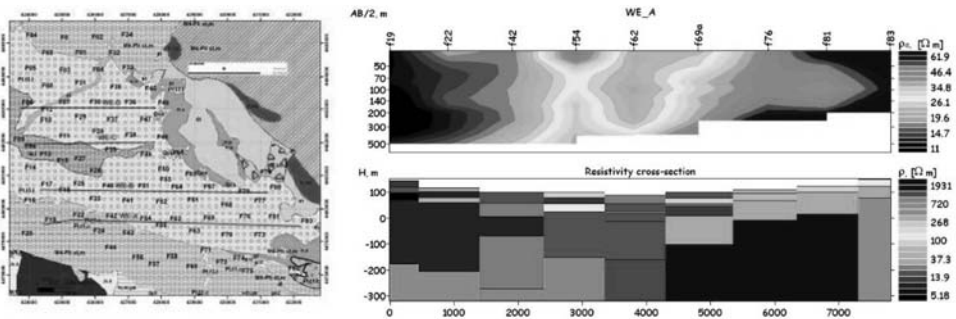
Fig. 7: W-E oriented vertical pseudosection A

different geological formation can be used here for better understanding of these images. In general the bedrock shows high resistivity (~500 Ohm-m) and appears with colours range from orange to red. Sediment formations have different colours with special hydrogeological interest in those with values from 20 to 50 Ohm-m (blue and light blue colours). Black represents clay formations with no hydrogeological interest while green may represent marl formations that may have some interest in those cases where faults have created cracks capable to host underground water.

In the northern part of pseudosection A we can see the sudden change of the depth of bedrock from 160 meters (F84) to more than 600 (F5). This can only be explained by the existence of a fault which is in agreement with the tectonic mapping of the area (Tranos et al, 2004). Same is observed also in the southern part of the pseudosection between F20 and F16 where the bedrock again appears to drop in depths greater than 600 meters due to another fault, also identified by Tranos et al (2004). Another important feature in the same picture is that the bedrock on the southern part appears relatively much lower values than the bedrock on the northern part. This is due to the fact that to the north, the bedrock consists of granite or peridotites while to the south the bedrock probably consists of calcareous rocks and/or schist.

In same way in Fig. 7 we see a typical W-E vertical pseudosection that reveals the way the bedrock dips to the west, also changing due to tectonic contact to calcareous rocks or schist in the western part. In smaller depths (higher altitudes) the stratigraphy appears to have a clear lateral transition.

Similarly, horizontal slices at various altitudes (depths) have been created in order to have a better way to observe the lateral variations of the stratigraphy in the area of interest and identify specific areas of better hydrogeological characteristics. In this attempt, we created two maps (Fig. 8.) show-
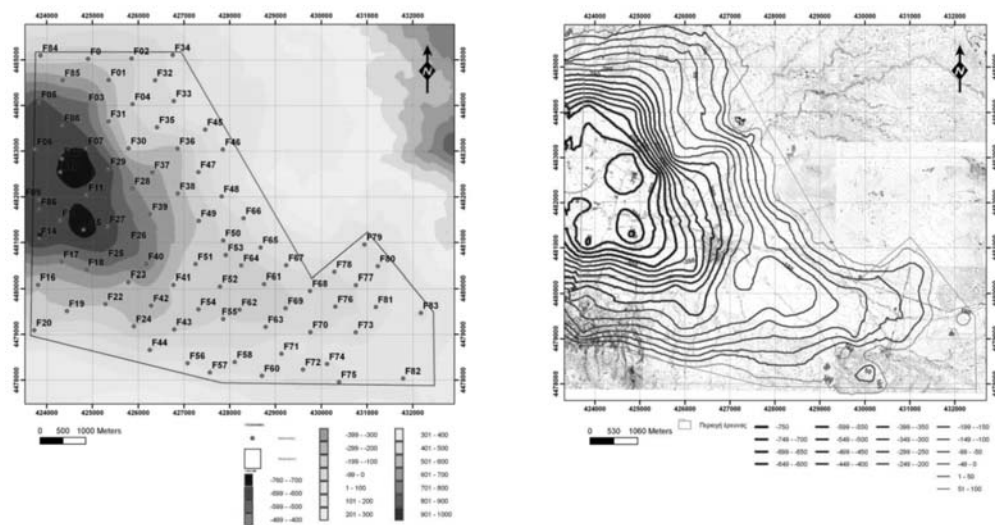
Fig. 8: Map of the expected altitude of the bedrock ceiling (left image) and the isodepth lines (right image) in the studied area.
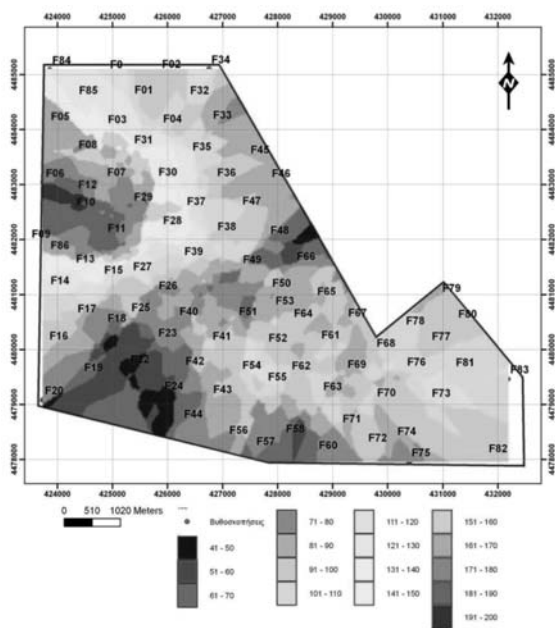
Fig. 9: Map of the expected thickness of formations C, D and E down to depth of 300 meters in the studied area.

ing the altitude and depth of the bedrock ceiling in the sense that all sediments above the bedrock can potentially be exploited for water resources. However, since realistically most hydrowells don't drill deeper than 300 meters we examined the first 300 meters depth in the investigated area. To do this, we examined once again the formations of Table 1 and chose formations C (Sand with clay with gravel layers) and D (Pebbles and gravel with water) as the most promising possible water resources. Formation E (Marl or weak conglomerate) was also accounted for due to the fact that tectonic reasons may increase its effective porosity.

Table 2.

Formation	Expected Permeability
C & E	Medium to High
D	High
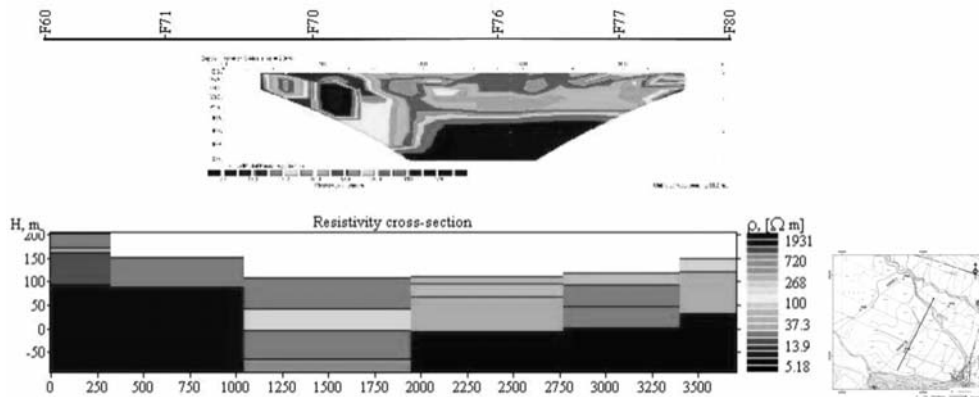
Fig. 10: Results of the ERT measured in the area shown on the top right image. The image on the left shows the pseudosection created from the adjacent VES along with the ERT inversion.

Based on typical permeability values for sediments (Kallergis 1999) we characterized the three formations (C, D and E) in terms of expected permeability (Table 2) and created maps (Fig. 9) showing the expected total thickness of these formations down to 300 meters depth.

3.3 Electrical Resistivity Tomography data and interpretation

The above mentioned analysis in two dimensional was based on adjacent 1D VES. In order to validate the vertical pseudosections we applied an electrical resistivity tomography (ERT) almost parallel to one vertical pseudosection. The location (Fig. 10) was selected based on the expected (from VES and borehole data) small depth of the bedrock since we know that the maximum depth of investigation with the ERT measurements couldn't be greater than approximately 250 meters.

The ERT result shows that the common part of the two sections is similar. The depth of the bedrock is around 150 meters in both cases. Furthermore the change of depth of the bedrock observed somewhere between F76 and F70 is clearly seen in the ERT approximately at the 450 meter of the ERT line.

4. Conclusions-Results

The results shown in this work show that when studying river basins with concern to water management and decision making VES can be a very useful tool. In the case of Anthemountas river basin:

    i) The depth of bedrock surface, in the examined area, has been mapped even at depths greater than 800 meters west of Vassilika village (Fig. 11).

    ii) The slope of bedrock depth reveals the location of possible fault lines and therefore providing useful geological information.

Moreover the analysis of sediments resistivity values reveals the following:

    iii) There is significant anisotropy of the sediments due to change of the sediments sorting.

    iv) Primary hydraulic continuity is often interrupted however near fault lines the operative porosity increases.
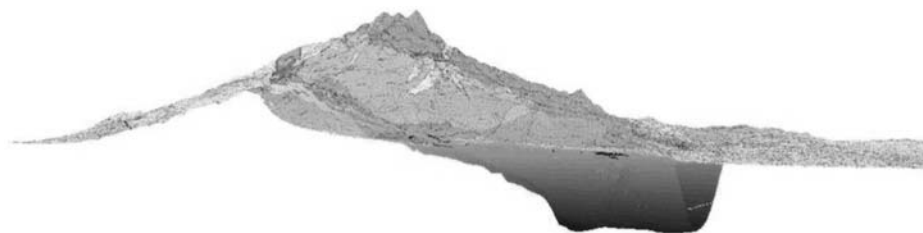
Fig. 11: Three dimensional image showing the bedrock surface dipping west (view from NW).

    v) In the sediments examined, the percolation of water cannot be vertical revealing the significant role of inflow from margins of the basin.

    vi) The area between the two water bodies developed west and east of the Vassilika and Galarinos villages is occupied by sediments with average to very good permeability thus allowing hydraulic communication.

    vii) Moving from east to west near Vassilika significant clay layers are identified explaining the existence of confined and unconfined aquifers as we move further west.

The above conclusions offer important information for a large area of the basin, allowing a better understanding of the hydrogeological model and thus allowing scientists to plan water resources management.

5. Acknowledgments

6. References

Alexei A. Bobachev, Igor. N. Modin, Vladimir A. Shevnin 1990-2001. Geoscan-M Ltd., Moscow, Russia. Available online at: http://www.geol.msu.ru/deps/geophys/ipi2win.htm

Fikos I, Vargemezis G., Tsokas G.N., Hatzidimitriu P. and Dimopoulos G., Diachronic study of free aquifers using the method of electric tomography: a case study in northern Greece, *European Journal of Environmental and Engineering Geophysics* 7 (2002), pp. 185–193

Savvaidis A.S., Tsokas G.N., Papazachos C.B., Kontopoulou D. 2000. A geophysical study of the ophiolite complex and the sedimentary basins in the northwest part of the Chalkidiki peninsula (N. Greece). *Surveys in Geophysics*, 21, 567-595

Theodossiou N., Latinopoulos P. 2005. Evaluation and optimization of groundwater observation networks using the Kriging methodology, July 2005. Available online at: www.sciencedirect.com

Tranos M.D., Meladiotis I.D. and Tsolakopoulos E.P. 2004. Geometrical characteristics, scaling properties and seismic behavior of the faulting of the Chortiatis region and Anthemountas basin (Northern Greece), 5th International Symposium on Eastern Mediterranean Geology, Thessaloniki, Greece, 14-20 April 2004

Thanassoulas C. 1983. Geophysical study of Anthemountas basin (V.E.S.), IGME (in Greek).

IGME 1996. Qualitative examination of surface and underground water of prefecture of Thessaloniki, IGME Dept. of Thessaloniki (in Greek).

Kallergis G.A. 1999. Applied-Environmental Hydrogeology, Technical Champer of Greece, pp330 (in Greek)

Nagoulis Ath. 1998. Hydrological study of Anthemountas basin, ANATOLIKI S.A. (in Greek)

CONTRIBUTION OF DEEP ELECTRICAL RESISTIVITY TOMOGRAPHY TECHNIQUE TO HYDROGEOLOGICAL STUDIES: CASES FROM AREAS IN KAVALA (NORTH GREECE)

Vargemezis G.[1], Tsourlos P.[1] and Mertzanides I.[2]

[1] *Department of Geophysics, Aristotle University of Thessaloniki, 54124 Thessaloniki - Greece, varge@geo.auth.gr ,tsourlos@geo.auth.gr*

[2] *Prefecture of Kavala, mertzan@gmail.com*

Abstract

The most common geophysical method widely used in hydrogeological surveys concerning deep investigations (150-300m of depth) is the resistivity method and particularly the Vertical Electric Sounding (VES) using the Schlumberger array. VES interpretations assume 1D geoelectrical structure yet it is obvious that such an interpretation assumption is not valid in many cases where 2D and 3D geological features exist. In such cases the application of geoelectrical techniques which can provide both vertical and lateral information concerning the resistivity variations is required. Techniques such as the electrical resistivity tomography, mostly used for the 2D and 3D geoelectrical mapping of near surface applications can be adapted to be used for larger investigation depths provided that modified equipment (viz. cables) is used.

In the present paper, the application of deep electrical resistivity tomography (ERT) techniques is applied. ERT array of 21 electrodes, at a distance of 50 meters between them (total length 1000 meters) has been used in several studied areas located in the prefecture of Kavala (North Greece). In several cases near surface structure has been compared with VLF data.

The aim of the survey was to study in detail the geological-hydrogeological structure the area of interest in order to suggest the best location for the construction of hydrowells with the most promising results.

The 2D images of the geological structure down to the depth of at least 200 meters allowed the better understanding of the behaviour of layered geological formations, since in several cases resistivity values have been calibrated with data from pre-existing boreholes.

Key words: *Electrical tomography, hydrogeology, hydrowells.*

1. Introduction

Kavala is located in the northeast of Greece and is the easternmost prefecture of geographic region of Central Macedonia (Fig. 1). Its physical borders are the mountains of Paggaeo and Lekani from the north, and rivers Nestos and Strymonas, eastwards and westwards correspondingly. Agricultural production holds a significant role on local economy with almost a quarter out of the total active population being farmers cultivating approximately 50.000 acres of land. The increasing need for water resources mainly for irrigation, but also for tourist or industrial use, rendered water management a major priority issue for local authorities. Significant role in water management strategy is the suc-

Fig. 1: Kavala is located at northeast of Greece and is the easternmost prefecture of geographic region of Macedonia.

cessful location of adequate water resources. Past experience in the exploration for underground water resources in the Prefecture of Kavala suggested that there were many cases where unsuccessful water drillings had a significant cost. In an attempt to reduce this cost the aid of geophysical methods was asked as a preliminary tool for suggesting the best location for the construction of hydrowells with the most promising results. This paper presents the results of geophysical investigation carried on by *Laboratory of Applied Geophysics/School of Geology/Aristotle University of Thessaloniki (A.U.Th.)*, within the framework of a borehole drilling project, directed by *Directorate of Land Reclamation/Prefecture of Kavala*.

2. General information

Geomorphology of Kavala is dominated by the mountainous bodies of Paggaeo, Lekani and Symvolo. Among them, there are extended plain lands, eastwards (delta of river Nestos), in the middle (Philippi marsh) and westwards (Pieria basin). These are the main arable areas, with secondary ones lying between local semi-mountainous regions (Fig. 2).

Geology of Kavala is generally characterised by the presence of crystalline rocks, marbles and sedimentary rocks. Crystalline rocks (granites, granodiorites, gneisses) are fragmented and locally containing water reservoirs. Marbles are extensively karstified and constitute the main underground fresh water reservoir of the area. Sediments are paleogenic, neogenic, and recent alluvial deposits, with interesting hydrogeology regime within the neogenic sandstones-conglomerates and pleo-pleistocenic deposits (Pliakas et al. 2002).

3. Project objectives

The water borehole drilling project of Kavala prefecture for 2006-2009, comprised of ten drillings and for six of them the contribution of prior geophysical exploration was requested. Three drillings were planned to provide irrigation water for the area between Paggaeo and Symvolo mountains (Pieria basin) and three in the semi-mountainous area at the surroundings of the city of Kavala. There water boreholes were planned mainly for irrigation use, but also for supporting domestic water supply, especially during the summer period.
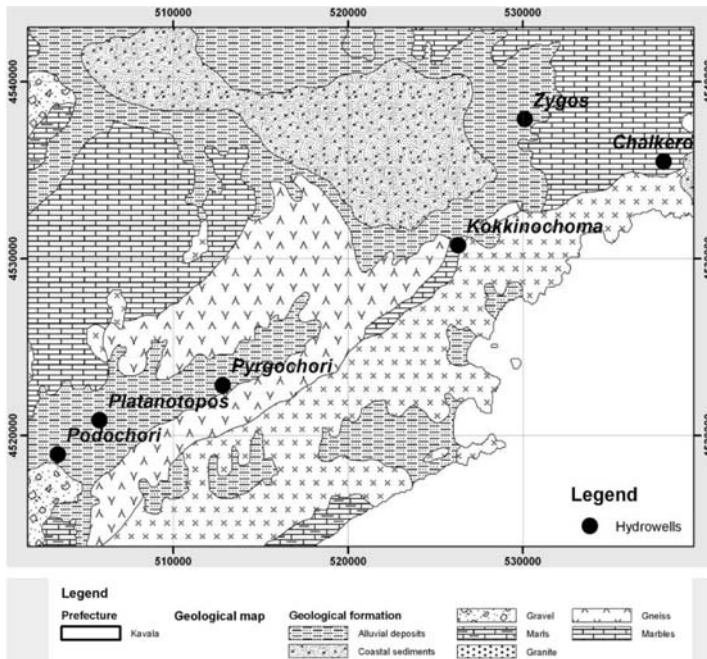
Fig. 2: General geomorphology and geology of prefecture of Kavala. The six suggested borehole drilling points are also shown.

The particular areas of interest were in the municipal departments of Pyrgochori, Podochori, Platanotopos in Pieria basin and Kokinochoma, Zygos and Chalkero. On Pyrgochori, Platanotopos and Zygos, irrigation water was transferred from many kilometres away, raising the cost of local agricultural production. On Podochori, Kokinochoma, Zygos and Chalkero the irrigation water supply was not adequate, resulting into reduced agricultural production. In Podochori, Pyrgochori and Chalkero, several unsuccessful drilling attempts were recorded in the past. A possible reason could be the absence of any particular hydrogeological or geophysical examination of the area.

The objective of the project was the search of the most promising and appropriate drilling location by adopting following step-by-step procedure. An initial examination of the local geological and hydrogeological conditions together with any relevant prior information is required in order to locate wider regions which can be favourable for positioning the well. A second step is to examine various other additional criteria which have to be taken into account such as: the land ownership regime of the area, accessibility of the potential areas, proximity to existing hydrowells, proximity to electric power supply, cost for water transfer etc. This required a very close multi-parametric examination of the areas of interest which resulted in limiting the selected candidate sites. So only after defining major and alternative sites of interest the geophysical investigation was carried out aiming to provide subsurface geological and hydrogeological information which will position with an increased detail the well in the most promising location.

4. Geophysical survey

In most of the areas where the authorities of the prefecture of Kavala were interested for additional water supply, underground water was expected in neogenic sediments as well as marble and metamorphic rocks. In several cases the thickness of sediments was estimated from surrounding wells but in other cases there was no prior information about the geological, hydrogeological status of the area.
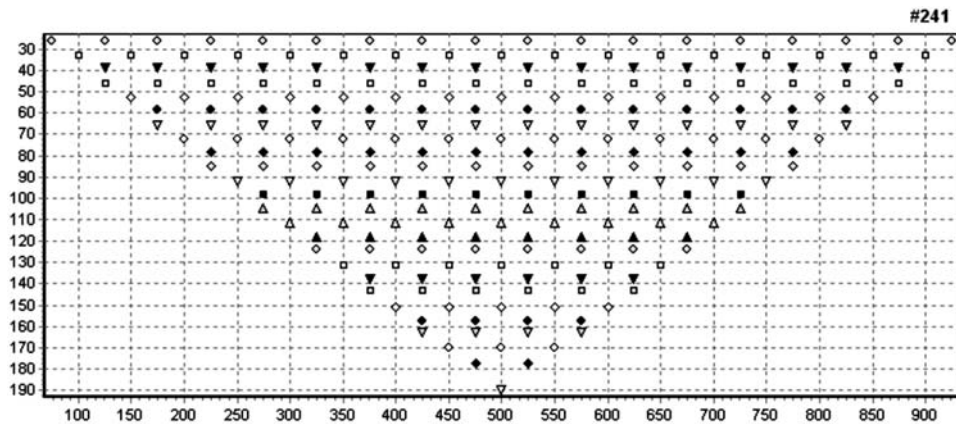
Fig. 3: Predicted distribution of location of apparent resistivity measurements, using the Dipole Dipole array with the proposed equipment.

Considering the factors of (a) hydrogeological structure, (b) cost of construction and (c) cost of exploitation of water boreholes, it stands that the average depth of interest is about 200-250 meters, especially in the prefecture of Kavala. In such a case the most widely used, low cost, geophysical method for such investigation depths is the Schlumberger vertical electrical sounding (VES), (Koefoed, 1979). To reach the depth of 250 meters, an experienced team needs more than one hour of field work, and the result is the 1D geoelectrical model below the fixed centre of the measuring array. Commonly, more than one VES soundings are carried out in an investigation site to cross-validate the findings. The main disadvantage of the VES procedure is that interpretation is carried out by considering earth layers as being horizontal (1-D model). Therefore more complicated (2-D, 3-D) geological structures not only cannot be predicted by the 1-D modelling procedure but actually can become a significant source of noise which can result in erroneous interpretation of the VES data.

In nature, the most common case of stratigraphy formed in sedimentary basins is the 2 or 3D one since strata are usually inclined or laterally ended. Because of this reason, in this paper, the application of 2D electrical resistivity tomography (ERT) (Dahlin, 2001) instead of 1D VES is suggested. Although this is perfectly feasible from a theoretical point of view the application of ERT is not common for such large investigation depths due to increased cable logistics required and for investigation depths of 200-250m, practically no commercially easy to use cables exist. The main difficulties for such cables arise from the fact that from one hand we need an appropriate resolution in order to describe adequately the subsurface but from the other hand we need to get the maximum investigation depth. A reasonable compromise between these two is to use a cable of 21 electrodes with the separation of 50 meters. A special multi-core cable like this with a total length of 1000 meters was constructed by the Geophysical Lab of AUTH. It consists of two special cable drums with 500 meters of multicore cable each, weighting aprox. 35 Kgrs each. The cable can be readily carried in the field and a crew of 4 persons can measure up to 3 sections in one day's work.

Since electrode line is settled on the field, different arrays can be measured using an automated ERT instrument with multiplexer. Geoelectrical data were obtained using a 10-chanel resistivity meter (IRIS INSTRUMENTS) with a 48 cable multiplexing ability. The arrays measured in this survey are the Dipole-Dipole and Wenner-Schlumberger arrays as arrays having electrodes at "infinity" are not practical to measure at such scales.

The distance of current and potential electrodes for various separations was $1n*a, 2n*a$ and $3n*a$ where a is 50 meters and maximum n was 8. A typical map of the measurements locations by the use of the parameters described above in the so-called pseudosection of apparent resistivity measurements is depicted in Figure 3. As it can be seen in Figure 3, although the electrode separation is 50 meters the design of the measurements selecting various combinations of current and potential electrodes can achieve more detailed investigation of the underground, resulting in the best resolution.

Interpretations were obtained by inverting data with an iterative smoothness constrain scheme (Kim, 2009) based on a finite element forward solver (Tsourlos, 1995). Elevation information was incorporated in the interpretation in order to correct data from topography effect.

The deep resistivity tomography has been applied in several places at the prefecture of Kavala in the frame of the project mentioned above. In every case the best location for the construction of the hydrowell was proposed according to the results of the ERT where the final interpretation was taking into account the general geological structure of the regional area and lithostromatography information from the surrounding area where it was available.

5. ERT results-Drilling Data

In the following paragraphs, the drilling information for every hydrowell is described as well as the result of the correspondent ERT profile in order to explain the decision that was made.

• *Pyrgochori borehole*

In Pyrgochori the two 1km long ERT profiles perpendicular to each other were measured. These ERT profiles aimed to investigate the depth and the behaviour of the marble as the bedrock of the area, as well as the sedimentary deposits (Fig. 4). The profile of NE-SW direction showed a dipping of the bedrock most likely associated to a local basin (at 300-500 meters of the ERT section), and therefore the construction of the well has been proposed at that location.

Drilling operations were carried out on July of 2006 and stratigraphy was described by alterations of red clays, pebbles, sands, and conglomerates. Drilling stopped at 177 metres depth, because of a thick layer of green marl that was continuous for the last 24 metres. Production string and pumping test which followed resulted to water supply of more than 100 cubic metres per hour. Hydrostatic and pumping ground water levels were at 1.5 metres and 21 metres correspondingly (Fig. 4).

• *Podochori borehole*

In Podochori area, two (2) ERT almost parallel lines of an average direction of 305° have been measured in order to investigate any lateral changes in the sedimentary formations as well as the depth to the bedrock (Fig. 5). Test drilling has been suggested to the second ERT line where a possible fault of the bedrock has been detected.

Drilling operations were carried out on October 2007. Lithology showed mainly alterations of clays (green, yellow, black, red), pebbles, marly conglomerates/sandstones/limestone and sandstones (Fig. 5). Drilling stopped at 220 metres, after a continuous layer of black clay that was found at 210 metres. Poor aquifers found on few thin layers of pebbles. Production string and pumping test followed resulted to a water supply of 20 cubic metres per hour. Hydrostatic and pumping ground water levels were at 58.5 metres and 165 metres correspondingly. It is noted that, in the same area there had been two unsuccessful drilling attempts in the past and the water supply of the existing boreholes never exceeded 30 m³/h.
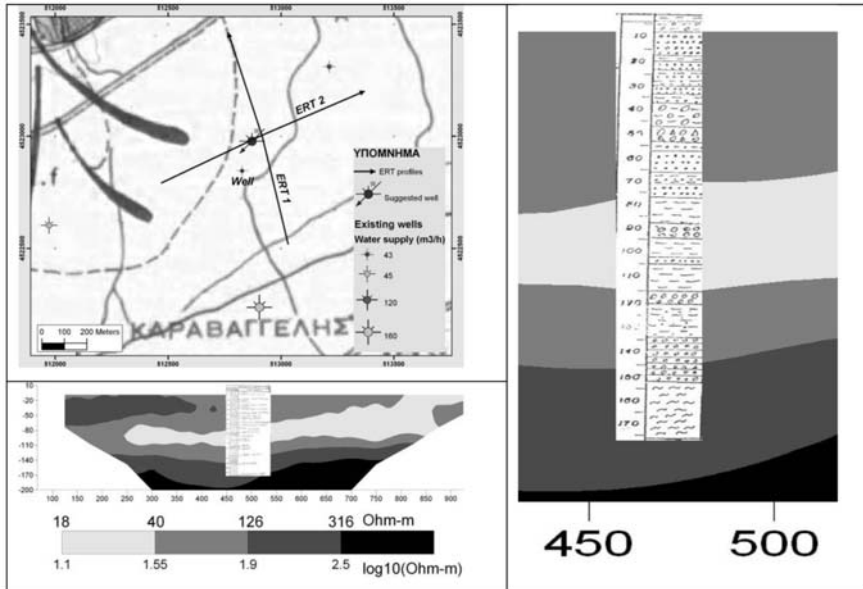
Fig. 4: Lithology log for Pyrgochori borehole. Inversion image refers to line ERT 2.
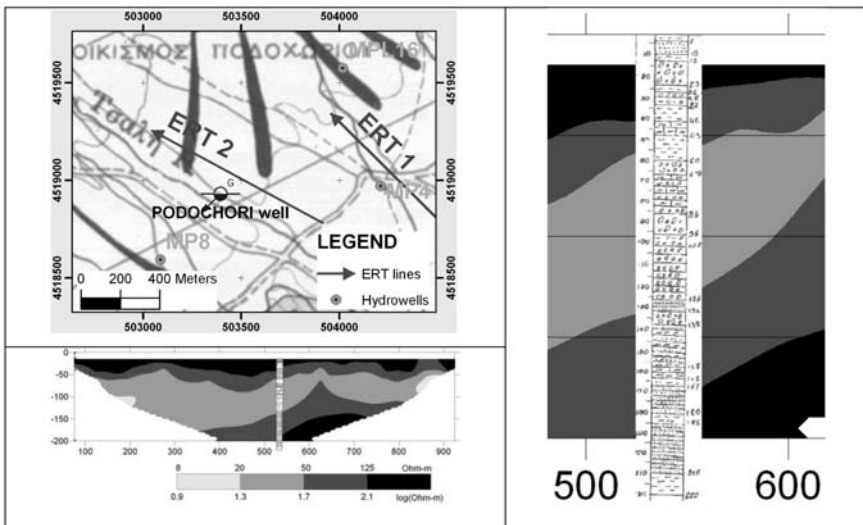
Fig. 5: Lithology log for Podochori borehole. Inversion image refers to ERT 2.

• *Platanotopos borehole*

The ERT line in Platanotopos area has been measured in a direction perpendicular to the contact of the marble formation with sediments in order to check the dipping of the marble (Fig. 6).

Water borehole have been suggested to the southern part of the profile since a very sharp dipping of the bedrock towards the south has been detected at the horizontal distance of 400 meters showing the existence of a fault.
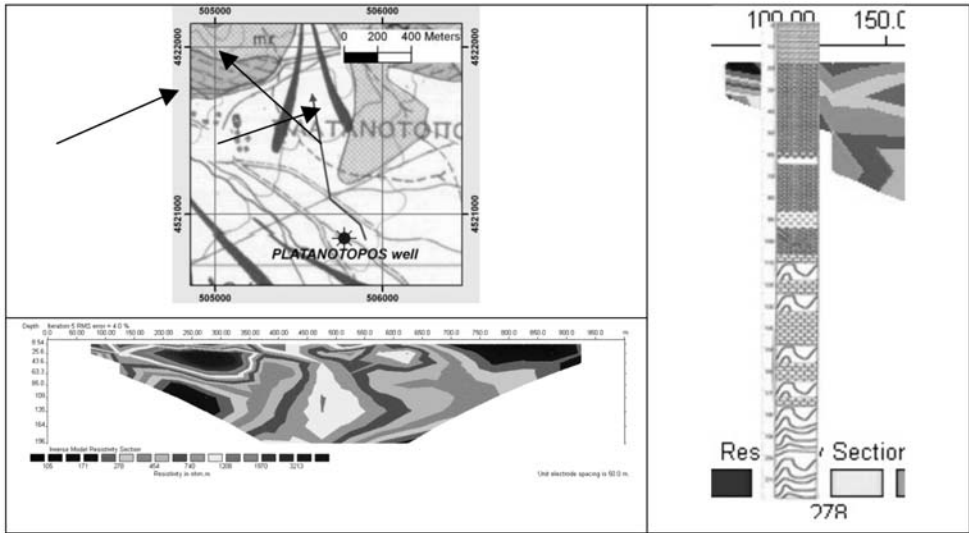
Fig. 6: Lithology log and tubing for Platanotopos borehole.

Drilling jobs carried out during August and September of 2008. For the first 100 metres, the known stratigraphy of the area was met, consisting of altered layers of pebbles, conglomerates and clays. But at 106 metres deep, where alterations of marbles and gneiss have been met, drilling paused because of a gap found. Good news was that this gap was a rich aquifer filled of big amounts of water, probable due to a fault bell. Casing of 10.5 inches diameter has been applied to the depth of 105 metres. Drilling continued with narrower cut inside (8.5 inches) until 220 metres depth, with alterations of marbles and gneisses. The pumping test was the second pleasant surprise: Continuous pumping by 150 cubic metres per hour, reduced the hydrostatic ground water level only for a meter: From 66.2 to 67.2 metres deep (Fig. 6).

• *Zygos borehole*

The target of the geophysical survey in the case of Zygos was the investigation of the nature of the sedimentary formations focused on the distribution of clay sediments. This, two ERT lines have been measured which were crossing each in order to extract information about the dipping of strata. Interpretation of geoelectrical data showed that the bedrock formation was deeper than 200 meters. Until 160 metres depth aquifers constituted by pebbles and gravel horizontally stratified were expected.

Drilling operations were carried out on November 2008. During the first 170 metres of drilling, alterations of clays (red, yellow, green), pebbles and conglomerates were found. Deeper, between 170-200 metres, fragmented layers of gneiss and conglomerates were met. Layers of conglomerates were rich water reservoirs as shown later by pumping test: More than 100 cubic metres per hour water supply and water level reduced from 35 metres (hydrostatic) to 43 metres deep (24 hours pumping) (Fig. 7).

• *Kokkinochoma borehole*

One ERT line has been measured in this area, aiming to investigate the lateral contact between the formations of gneisses and marble.

Drilling jobs carried out on November and December of 2008. The lithology was the expected: Gneisses and gneiss-schists, partly fragmented. Drilling stopped at 224 metres depth. Pumping test
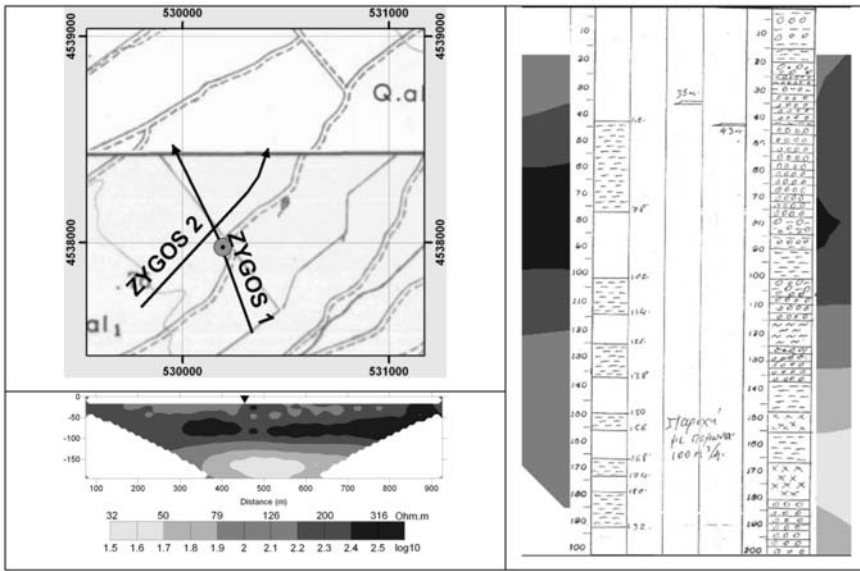
Fig. 7: Lithology log and tubing for Zygos borehole. Hydrowell's location is pointed with a black triangle on the ERT inversion image.
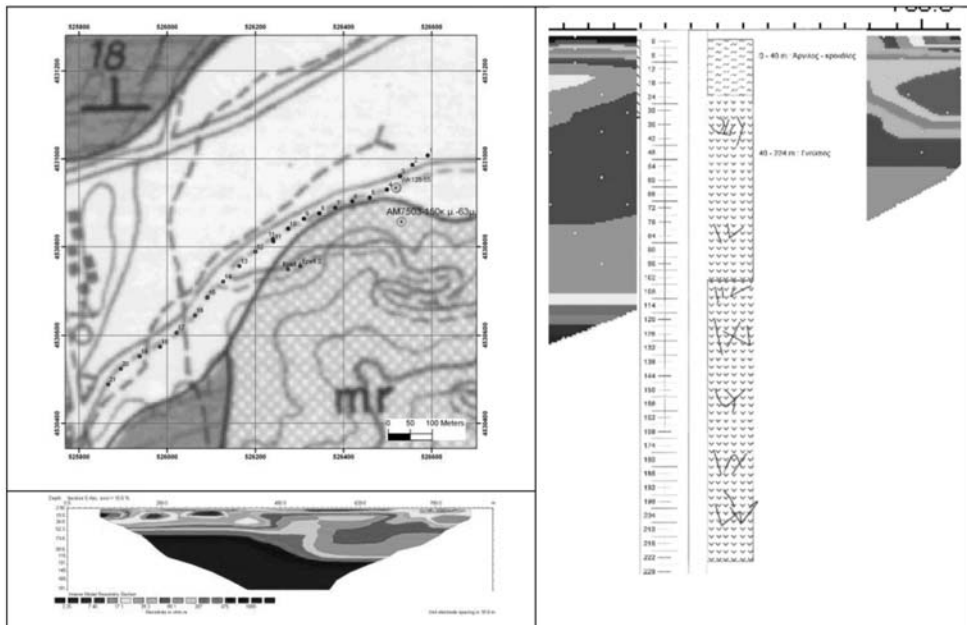
Fig. 8: Lithology log for Kokkinochoma borehole.

that followed, resulted to water supply of 50 cubic metres per hour. Hydrostatic and pumping ground water levels were at 15 metres and 88 metres correspondingly (Fig. 8).
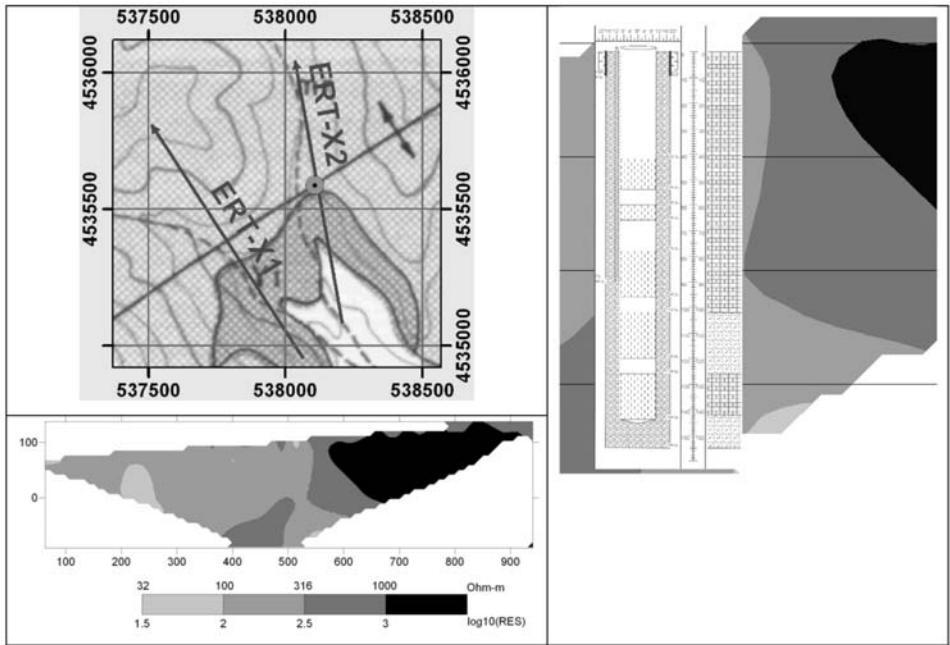
Fig. 9: Lithology log and tubing for Chalkero borehole. ERT inversion scheme refers to ERT-X2 line.
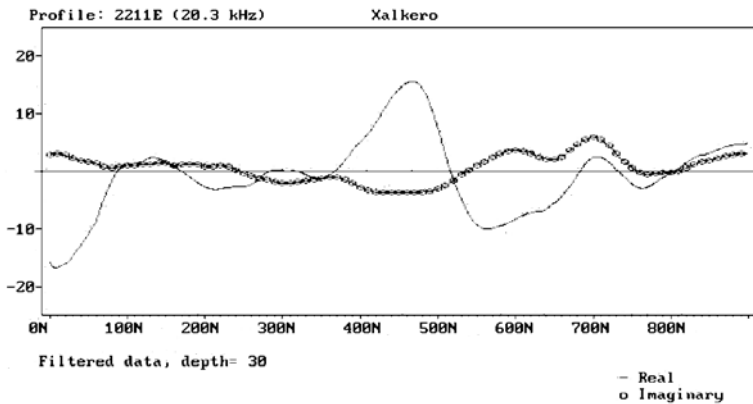
Fig. 10: VLF profile along with the ERT profile.

• *Chalkero borehole*

The target of the geophysical survey in this area, was (a) prospecting for possible detection of secondary porosity in the formation of marbles, (b) study of the contact between granite and marble and (c) study of the broad-crested anticline as it is characterized in the geological map of the area by IGME. Two ERT lines have been measured perpendicularly to the contact line. In addition, a VLF line has been measured at the same line where ERT-X2 has been realized, in order to provide more detailed information about lateral change noticed at the resistivity distribution as the inversion of the ERT data showed (Fig. 9).

Drilling operations have been carried out on August and September of 2009. After 9 metres of mixed clays and conglomerates, fresh marble was found. The fragmentation was detected after the depth of 31 metres and continued with alterations of fresh and fractured rocks. At the depth of 100 metres, fragmented granodiorite was found and fragmented zones of marbles and granodiorites were continued until the depth of 152 metres. This zone is considered to be the one suggested by the resistivity and VLF survey as a conductive one and as it was proved it was an extremely rich water aquifer. Pumping test that followed resulted to water supply of more than 180 cubic metres per hour. Hydrostatic level was at depth 16.80 metres and pumping ground water level at 63.7 metres (Fig. 9).

It can be seen that VLF anomaly showing a faulting zone dipping to the beginning of the profile is totally in agreement with the ERT inversion.

5. Discussion

A discussion on the results of the present study, should not only contain "pure" scientific issues, concerning the ERT techniques applied, but also refer to the objectives defined on section 3. Following these objectives, it should be mentioned that:

- In all six cases, drilling points suggested, resulted to productive boreholes.
- In all six cases, there was relative to total lack of hydrogeological information, adequate to drive to documented choice of drilling points.
- In two cases (Platanotopos and Chalkero) the amount of underground water supply, was far beyond expectations.

According to these, the borehole drilling project of *Directorate of Land Reclamation/Prefecture of Kavala*, was strongly supported by the geophysical research, it became more efficient and contributed to the welfare of local societies.

On the other hand, drilling data crosschecked to ERT profiles, offered a valuable "feedback" to interpretation given, contributing to better understanding the potentials and limitations of the applied techniques.

6. Acknowledgements

7. References

Dahlin T., 2001. The development of DC resistivity imaging techniques. *Computers & Geoscience*, 27, (9), 1019-1029.

Directorate of Land Reclamation/Prefecture of Kavala, 2008. Record Room, Kavala. National Statistical Service of Greece 2009. Arable land and areas of Greece: 2000-2007 (provisional data). Press Release NSSG, Athens.

Koefoed, O. (1979). Geosounding principles, 1, Resistivity Sounding Measurements. Elsevier, Amsterdam.

Kim, Y.H., 2009. DC2Dpro – User's Manual, KIGAM, Daejon, Korea.

Pliakas, F., Diamantis, I. and Petalas., C., 2002. Hydrogeological research for sufficiency and quality of drinking water in municipalities of Kavala – Some management suggestions. *Proceedings of the 6th National Hydrogeological Congress*, Xanthi, 413-426.

Tsourlos P., 1995. Modeling interpretation and inversion of multielectrode resistivity survey data. *Ph.D. Thesis,* University of York.

THE APPLICATION OF ENVIRONMENTAL MAGNETISM TECHNIQUES FOR POLLUTION ASSESSMENT IN URBAN AND SUBURBAN AREAS IN GREECE: STATE OF THE ART AND CASE STUDIES

Zananiri I.[1], Kondopoulou D.[2] and Spassov S.[3]

[1] *Institute of Geology and Mineral Exploration (I.G.M.E.), Spirou Loui 1, Olympic Village, 3rd Entrance, 136 77 Acharnae, Greece, izanan@igme.gr*

[2] *Department of Geophysics, School of Geology, Aristotle University of Thessaloniki, 541 24 Thessaloniki, Greece, despi@geo.auth.gr*

[3] *Centre de Physique du Globe de l' Institut Royal Météorologique de Belgique, Dourbes B-5670, Belgium, simo.spassov@oma.be*

Abstract

Environmental magnetism is a comparatively new discipline, applied in Greece only during the last decade for the study of anthropogenic pollution. The rationale of the method is based on the property of iron oxides and sulphides to attract and absorb heavy metals, organic contaminants and even radioactive pollutants. Thus, the measurement of the magnetic susceptibility, both in situ and in the laboratory, along with several other magnetic parameters constitutes a rapid and cost effective technique for characterization and mapping spatial pollution distribution. In order to quantify the correlation between magnetic susceptibility and a specific pollutant for a studied area geochemical analyses are carried out for key samples. Towards the scope of pollution assessment environmental magnetism studies have been recently carried out in the Kozani-Ptolemaida basin and the tanneries of Thessaloniki. The preliminary results of these two cases, characterized by different contaminant sources, i.e. flying ash pollution in the former and heavy metal in the latter, are presented here. In general, the application of magnetic methods proved a useful tool in the assessment of the main sources of pollution and the location of spatial distribution of major contaminants.

Key words: magnetic methods, geochemical methods, nanoparticles, environment, anthropogenic pollution.

1. Introduction

The major environmental problems in Greece range from air pollution, water pollution and solid waste disposal to land degradation, forest fires, threat of the natural reservations, and noise problems. However, some of these problems are of local importance and of low intensity, only. Greece has no specific clean-up legislation, unlike the United Kingdom and other European countries. Contaminated sites are treated in the general environmental protection legislation, and in the waste legislation. Up to now, there are no registers about contaminated sites, neither on a national basis nor at a regional level. Site investigations are usually isolated cases. According to an international report on waste disposal sites (Ferguson, 1999), 3500 out of 5000 facilities in Greece have been revealed to operate without any environmental protection control.

In order to keep the living quality in urban agglomerations as high as possible, political decisions are needed which require trustable and economic scientific methods. Chemical investigations are often long-winded and expensive, thus their application is limited when the pollution degree of large areas has to be estimated. In contrast, magnetic methods offer the great advantage that low concentrations (in the order of ppm) of ferromagnetic phases can be detected, identified and quantified without costly sample preparation and within short measurement time.

2. Philosophy of environmental magnetism for pollution assessment

Environmental magnetism involves the application of rock and mineral magnetic techniques to situations in which the transport, deposition or transformation of magnetic grains is influenced by environmental processes in the atmosphere, hydrosphere and lithosphere (Verosub & Roberts, 1995). An important aspect of environmental magnetism is that its techniques are relatively rapid, simple, non-destructive, inexpensive, and can be applied to a wide range of materials, including rocks, sediments, soils, atmospheric particulates and biological materials. The studies encompassed by this discipline can be divided in three major categories:

  a) *Regional and global climate*, concerning short- and long-term estimation, through the study of lake sediments and ice cores, for the former case, and loess and deep sea sediments for the latter.
  b) *Anthropogenic pollution*, by studying sediments (aeolian, marine, lake, rivers) and soils.
  c) *Biomagnetism,* which concerns magnetic bacteria and human/animal tissue.

A thorough review of environmental magnetism principles and applications can be found in Evans and Heller (2003) and Walden et al. (1999).

2.1 Heavy-metal pollution

Motivations for controlling heavy metal concentrations are diverse (Zevenhoven & Kilpinen, 2001), as some of them are dangerous to health or to the environment (e.g. Hg, Cd, As, Pb, Cr), some may cause corrosion (e.g. Zn, Pb) and some are harmful in other ways (e.g. Arsenic may pollute catalysts). Within the European community the 13 elements of highest concern are As, Cd, Co, Cr, Cu, Hg, Mn, Ni, Pb, Sn, and Tl, the emissions of which are regulated in waste incinerators. Some of these elements are actually necessary for humans in minute amounts (Co, Cu, Cr, Ni) while others are carcinogenic or toxic, affecting, among others, the central nervous system (Hg, Pb, As), the kidneys or liver (Hg, Pb, Cd, Cu) or skin, bones and teeth (Ni, Cd, Cu, Cr).

Heavy metal pollution can arise from many sources but most commonly is due to the purification of metals, e.g., the smelting of copper and the preparation of fuels. Electroplating is the primary source of chromium and cadmium. Through precipitation of their compounds or by ion exchange into soils and muds, heavy metal pollutants can localize and lay dormant. Unlike organic pollutants, heavy metals do not decay and thus pose a different kind of challenge for remediation. Currently, plants or microorganisms are tentatively used to remove some heavy metals such as mercury. Plants which exhibit hyper accumulation can be used to remove heavy metals from soils by concentrating them in their bio matter. Some treatment of mining tailings has occurred where the vegetation is then incinerated to recover the heavy metals.

2.2 Basic principles

Iron is one of the most common elements in the Earth's crust. In combination with oxygen and sul-

phur it forms magnetic minerals, which occur to a greater or lesser extent universally. Nanometre sized particles are of particular interest because they occur in great quantities, implying a large surface area. Due to these properties, nanoparticles can provoke biological reactions itself (Shukla, et al., 2000; Smith et al., 2000; Diabaté et al., 2002) or act as a vehicle for other toxic components. Iron oxides and sulfides have excellent adsorbent properties and attract not only heavy metals (Cornell and Schwertmann, 1996; Watson et al. 1995) but also organic contaminants (Apblett et al., 2001) and even radioactive pollutants (Watson et al., 2001). For obvious reasons magnetic methods can be used for the characterisation of pollution and have become commonplace by many international laboratories (e.g. Dearing et al., 1996; Petrovsky et al., 1998; Evans & Heller, 2003; Hanesch et al., 2003).

2.3 Magnetic minerals and pollutants

Iron minerals in the environment result from various biogeochemical processes, such as weathering, soil formation, diagenesis of sediments and bacterial metabolism, but also human activities like fossil fuel combustion, waste incineration, metal smelting and working produce considerable amounts of iron minerals as contained in fly ashes and particulate matter (PM). Particle fractions smaller than 10 µm (PM10) are of particular interest because they can be inhaled deeply into the lung and induce there cytotoxic and inflammatory effects, when iron and other heavy metals become bioavailable. Studies on fly ash highlighted that transition metals like Fe, Cu, Ni or V seem to play an important role (van Maanen et al. 1999). Diabaté et al. (2002) suggested that pro-inflammatory responses of cells could be induced by metals attached to the particle surface or by the large number of fine and ultrafine particles with a large surface/volume ratio. There are different source groups of PM. For instance, from the 26'402 tons of PM10 emitted in Switzerland in 2001, 33 % were allotted to industry, 25 % to agriculture and forestry, 23 % to road traffic and 11 % to rail traffic. Household, aviation and energy production related PM10 emissions contributed only with 5, 3 and 0.4%, respectively (Heldstab 2002). This itemisation may be different in other countries, in particular concerning energy production in emerging markets. The largest emitters in Europe in 2000/2001 were Spain with 29'300 t, Hungary with 17'200 t and Greece and England with 14'000 t each (von Blottnitz 2006). In view of the small particles size, air suspended PM represents an enormous risk exposure for human health.

In general, particulates originating from combustion processes contain between 2 and 20 wt % of magnetic iron-oxides, with the highest values being observed in fly-ash resulting from coal combustion. Magnetite (Fe_3O_4) and related spinels as well as haematite ($\alpha\text{-}Fe_2O_3$) are the main magnetic minerals often found in industrial fly-ashes. They form during the burning process and are often observed in the form of spherules. Their magnetic grain size ranges from sub-micron single-domain and probably also superparamagnetic particles to large multidomain particles, probably between 2 and 50 µm. Fly-ashes emitted from fossil fuel burning power plants, smelting and cement factories are very rich in heavy and transition metals such as As, Be, Co, Hg, Ni, Se.

2.4 Measurements

A generalized sequence of the stages followed in an environmental magnetic analysis of rock, sediment or soil samples is presented in Fig. 1.

In situ measurements of the low-field magnetic susceptibility is the primary step in every enviromagnetic study for pollution assessment (Fig. 2a). A grid is set up in dimensions depending on the nature of the survey, i.e. to study a large area measurements are taken every 500 – 1000 m, while for detailed analysis of specific targets a grid of 0.5 or 1.0 m spacing may be required. Simultaneously, top soil samples for laboratory magnetic measurements are collected at regular intervals, using
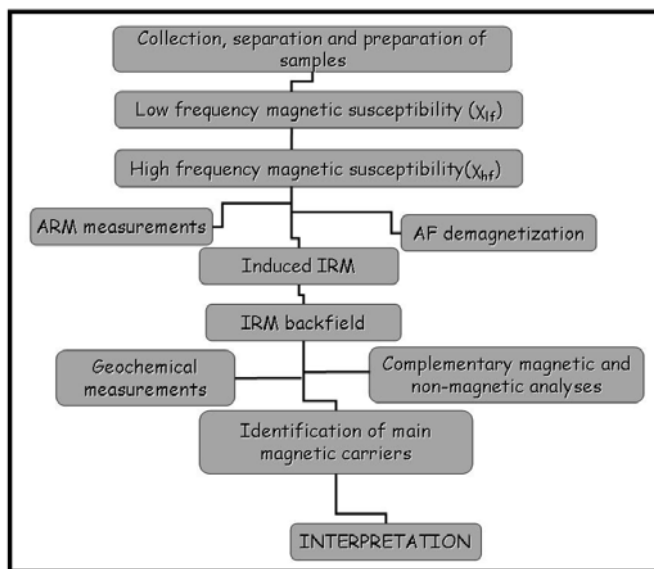
Fig. 1: Generalized sequence of stages in an environmental magnetic analysis of rock, sediment or soil samples (after Maher & Thompson 1999).

plastic tools and bags/containers to avoid magnetic contamination. In order to reduce the biasing effect of air, water and pebbles the samples are then dried at room temperature, disaggregated and sieved, retaining the fraction smaller than 500 μm.

An innovative sampling technique towards the elaboration of magnetic measurements for pollution assessment involves the collection of appropriate tree-leaves, i.e. of large surface area and suitable surface properties (e.g. *Acer Plantanoides*). This method is based on the fact that tree-leaves, particularly those species with sticky leaves, in urban environments have a good potential to remove the atmospheric PM and, thus, can be ideal pollution monitoring markers, and has been successfully applied to many crowded cities [e.g. Beijing (Zhang et al., 2006); Zurich (Hannam & Heller, 2001)].

In the laboratory, the low-field mass specific (χ) magnetic susceptibility is measured and percentage frequency-dependent magnetic susceptibility: , being the susceptibility measured at high frequency, usually one order of magnitude higher than χ_{LF}, is calculated. Moreover, the temperature dependence of low-field magnetic susceptibility is monitored from room temperature up to 700°C and vice versa (Fig. 2b).

Beyond the threshold of susceptibility measurements, studies utilizing mineral magnetic properties are concerned with the measurement of magnetic characteristics affected by the concentration, grain size and shape of magnetic minerals (Table 1). These characteristics are determined by applying ar-

Table 1. Commonly measured magnetic parameters

Magnetic Parameter	*Symbol*	*S.I. Unit*
Mass specific susceptibility	χ	m^3/kg
Frequency dependent susceptibility	χ_{fd}	%
Isothermal remanent magnetization	IRM	Am^2/kg
Anhysteretic remanent magnetization	ARM	Am^2/kg
Susceptibility of ARM	χ_{ARM}	m^3/kg

Fig. 2: (a) In situ measurement of the magnetic susceptibility, (b) Laboratory equipment (Bartington Instruments Ltd., Witney, UK) for magnetic susceptibility measurements, (c) Sample used for laboratory experiments, (d) Hysteresis loops measurement (University of Lancaster).

tificial magnetic fields and measuring either the in-field or remanent response:

- Isothermal remanent magnetisation (IRM) is induced with an impulse magnetiser, with fields reaching up to 2.7 T, and subsequent backfield experiments are performed by subjecting the sample to the inverse magnetic field.

- Stepwise alternating field demagnetisation of both natural and isothermal remanent magnetisation.

- Hysteresis loops are measured (Fig. 2d) and the following parameters are determined: coercive force (H_c), coercivity of remanence (H_{cr}), saturation magnetization (J_s) and saturation remanent magnetization (J_{rs}).

- Anhysteretic remanent magnetization (ARM) is acquired by subjecting the sample to a DC bias field in the presence of an alternating field with decreasing peak amplitude. The ARM is expressed as a mass-specific susceptibility of ARM (χ_{ARM}) by normalizing with the DC field. The ARMs are then demagnetized at successive steps (e.g. 10, 25, 50, 75, 100, 125, 150, 200, 250 and 300 mT).

From the results of these experiments several diagnostic magnetic parameters are calculated, the most commonly used being: mass-normalised saturation IRM (SIRM), χ_{ARM}/SIRM, and the percentages of high-field IRM (HIRM, i.e. the remanence acquired between 300 and 1000 mT). The SIRM reflects the concentration of magnetic minerals, the χ_{ARM}/SIRM ratio the contribution of ul-

trafine magnetite grains (~ 20-30 nm), and HIRM the presence of haematite (if the HIRM resists subsequent demagnetisation). Finally, having obtained multi-parameter magnetic data sets, two multivariate statistical methods can be applied to robustly characterize and/or differentiate the sediments; cluster analysis (using fuzzy c-means) and non-linear mapping, using one of the available programs (e.g. Vriend et al., 1988). Both techniques have been applied successfully to a number of environmental data sets (Maher et al., 2008).

3. History of environmental magnetism in Greece

Environmental sciences in general are quite well developed in Greece, focussing mainly on other research fields like chemistry, biology and meteorology. However, up to now, magnetic methods have not been thoroughly applied to pollution studies. Investigations performed by universities and national research institutes have identified and characterised a multiplicity of contaminated industrial sites. The relevant projects involve collection of historical data relating to a site, geological and hydrogeological data, chemical and physical measurements of soils or liquids (surface or groundwater, leachates etc). Contaminated sites are rather related to improper dumping of household and industrial wastes, than to mining areas and tailing ponds, to lignite-operating power plants and to petroleum refining and storage sites.

The first appearance of combined magnetic and geochemical data was through a PhD Thesis (Zeri, 1995) which, nevertheless, referred to polluted sites in the northwestern Mediterranean, followed by a pilot study at the Vouliagmeni Lake (Zeri et al., 1997) and an MSc Thesis (Tema, 2003). Finally, in the framework of a Joint Research and Technology Programme (2004-2006) between Greece and the United Kingdom, funded by the General Secretariat for Research and Technology of Greece and the British Council, the first integrated magnetic study towards pollution assessment was carried out. The project was entitled "Application of environmental magnetic techniques in detecting nanoparticle contamination". The research team comprised 3 groups: the first from the Aristotle University of Thessaloniki (Prof. D. Kondopoulou, Dr. A. Atzemoglou, Dr. I. Zananiri and Dr. S. Spassov, a visiting specialist from Belgium), the second from the University of Manchester (Prof. D. Polya, Dr. A. Gault) and last from the University of Lancaster (Prof. B. Maher, Dr. V. Karloukovski). The Greek research team had a strong background in rock magnetism and all the necessary experience to perform the required magnetic measurements, while the British research team had a long experience on environmental issues and especially heavy metal pollution. Moreover, they had all the necessary equipment and knowledge to perform geochemical measurements and additional and specialised magnetic experiments.

The target of this innovative, for Greece, project, that took into account the sparcity of similar works in the geographic region of Greece, was two-fold: (a) to investigate the interrelationship between susceptibility enhancement and elevated heavy metal concentrations and, thus, estimate the spatial distribution of several pollutants (b) to allow Greek scientists benefit from the long tradition of UK laboratories, pioneers in environmental magnetism, and acquire the know-how for the use of magnetic techniques towards pollution assessment; thus, dissemination of the results and the state-of-the-art was a key issue that would constitute this discipline, nowadays increasingly applied by the Hellenic scientific community (e.g. Sarris et al., 2008), essential in environmental research.

Towards these scopes, three urban and suburban sites, with different pollution sources, were studied: the broader Kozani region, the old tanneries of Thessaloniki and a school yard, remediated former solid waste disposal site, at Potters Hill (UK). An overview of the results from the first two cases is presented, while the third case is still in progress.
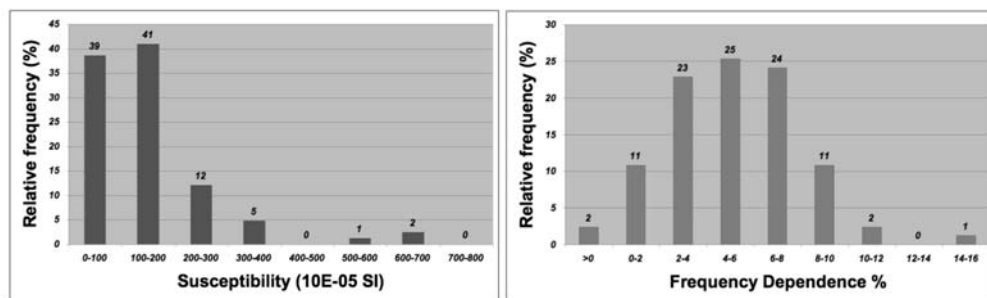
Fig. 3: Laboratory low-field magnetic susceptibility (left) and susceptibility frequency dependence (right) histograms.
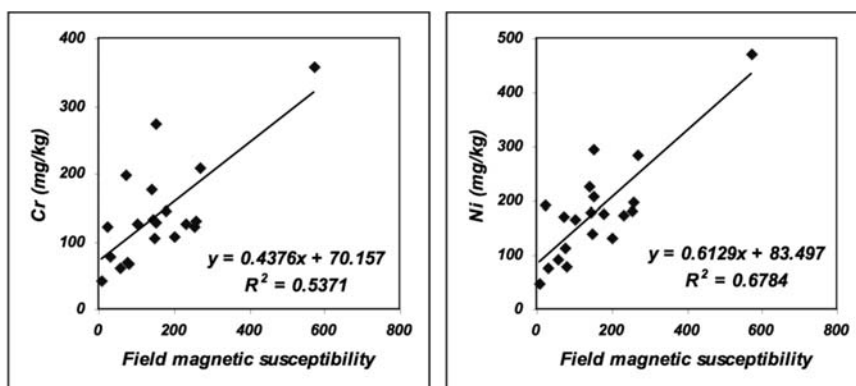
Fig. 4: Correlation of Cr and Ni in soils with corresponding field magnetic susceptibility values.

3.1 The case of Kozani – flying ash pollution

In the basin extending between Kozani and Ptolemaida four power plants are operating, on lignitic resources from that same basin. The target of the project carried out by Zananiri et al. (2006) was two-fold: (a) to challenge the correlation between ferrimagnetic mineral content and geochemical properties of samples from polluted areas, (b) to estimate the spatial distribution of several pollutants within the study area. The main pollution source is flying ash from the emissions of the four power plants.

The magnetic susceptibility was mapped with a resolution of 1×1 km and soil samples were collected from each grid point. The in situ susceptibility values exhibit significant variation, ranging from very low background values (7×10^{-5} SI) to high values (730×10^{-5} SI), with a mean of 140×10^{-5} SI. The same variation arises from laboratory low and high frequency magnetic susceptibility, with a mean frequency dependence of 5% (Fig. 3). Additional laboratory experiments were performed to determine the type and size of main magnetic carriers: isothermal remanence acquisition, stepwise alternating field demagnetisation of anhysteretic remanence magnetisation and hysteresis loops. The magnetic analyses were complemented by geochemical measurements and correlations between the various magnetic parameters and the concentration of specific pollutants were established (Fig. 4). A fair linear correlation was found between magnetic susceptibility, both field and laboratory measured, and the concentrations of soil Cr, Ni, and Mn, whereas the correlation between magnetic susceptibility and concentration of Zn and Cu in soil was poor, suggesting that the pollutants are physically not related to the magnetic minerals.
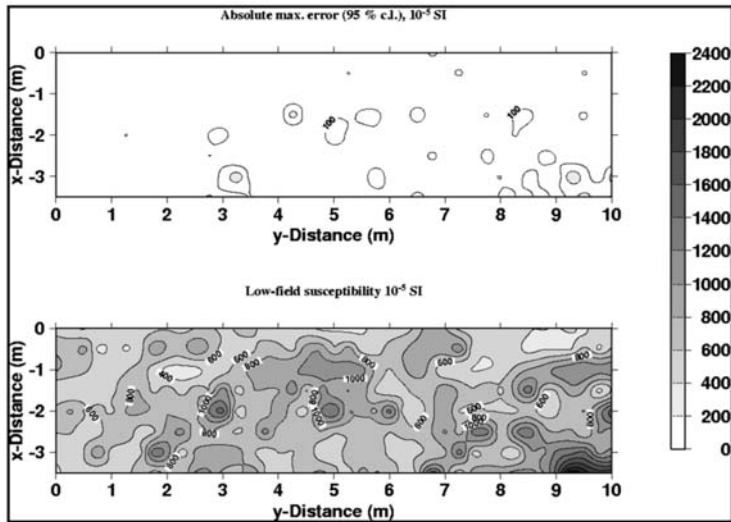
Fig. 5: Spatial distribution of susceptibility values *(bottom)*, along with the corresponding absolute measurement errors *(top)*.

3.2 The case of the tanneries of Thessaloniki – heavy metal pollution

The correlation between magnetic susceptibility and concentrations of key toxic components was tested (Spassov et al., 2004) at the highly polluted, nowadays closed, industrial area in Thessaloniki (Northern Greece), on which tanneries are situated inter alia. The tanneries of Thessaloniki constituted, from 1970, the place of first industrial activity, but later on they were developed arbitrarily. Malodorous surface channels with polluted liquids, storage of dangerous chemical substances without precautions etc. resulted in the pollution of subsoil and underground waters and the progressive demission of the environment. The geological conditions in the region, as they were recorded by shallow drillings (Atzemoglou & Skianis, 2003 and references therein) are unconsolidated sediments up to 5 m depth, consisting of sands, fluvial and torrential deposits and red clays with limestone conglomerates.

Relying on existing information, a grid was set up and high-resolution (0.5 × 0.25 m) screening of magnetic susceptibility was performed. Soil samples were collected for rock magnetic and geochemical laboratory measurements at certain grid points (resolution of 0.5 × 1.0 m). For an assessment of the background signal sampling of unpolluted sites from the same soil type was also performed.

The susceptibility values may be divided in three categories: a) "background" values between 400 and 700 × 10^{-5} SI spread over the whole area, b) local anomalies with values between 800 and 1000 × 10^{-5} SI (Fig. 5, e.g. at x = -1 m, y = 5 m) and c) peak values > 1000 × 10^{-5} SI measured at single points (Fig. 5, e.g. at x = -2 m, y = 3 m). In order to normalize the field measurements we compared them with laboratory measurements performed on soil samples. We found that field values of ~800 × 10^{-5} SI correspond approximately to 400-450 × 10^{-8} m^3/kg.

Preliminary magnetic measurements on dried and sieved (<0.032 mm) samples with intermediate susceptibility values indicate that 95% of the saturation isothermal remanent magnetization (SIRM) is acquired between 0 and 300 mT. The non-reversible temperature dependence of the low-field susceptibility exhibits a Hopkinson peak and is characterised by a considerable decrease near 580°C. Above 580°C the susceptibility is nearly zero. These results indicate that the magnetic signal is car-

ried by low-coercivity ferrimagnetic minerals, mainly magnetite with possible traces of iron sulfates. We did not find evidence for a high concentration of maghemite, which characterises fly ashes. Preliminary geochemical measurements indicated concentrations of 40-4000 mg(Cr^{3+})/kg, 41-155 mg(Zn)/kg, 15-35 mg(As)/kg and 0-65 (Dichloronethane)/kg in soils.

4. Conclusions

The application of enviromagnetic techniques is based on the fact that human activities, like fossil fuel combustion, waste incineration, metal smelting and working, produce considerable amounts of iron minerals, easily detected by field and laboratory measurements of magnetic properties. Thus, they constitute an innovative, non-evasive, rapid and cost-effective method for tracing and quantifying nanoparticle pollution. However, it is important to point out that magnetic techniques do not substitute geochemical measurements, since a general numeric *magnetic susceptibility – pollutant concentration* relationship has not yet been established, but they can contribute significantly to an optimum geochemical survey planning by defining areas of increased interest and thus cut down excavation cost and time.

The discipline of environmental magnetism for the assessment of pollution distribution and its sources is highly prominent worldwide and during the past few years is being developed in Greece as well. The Aristotle University of Thessaloniki, in the framework of a bilateral cooperation between Greece and the UK, implemented magnetic environmental research in several areas with different pollution sources. From the realization of this project, important conclusions for the specific areas were drawn and the method know-how was acquired by Greek researchers. In particular:

- The topsoil studied in the vicinity of the lignite-bearing power plants in the Kozani-Ptolemaida basin was characterized by significant variation, reaching high values, and the increased magnetic susceptibility is due to the presence of anthropogenic magnetic particles contained in industrial dust and fly ashes.

- Magnetic susceptibility values, remarkably above background, were detected in the tanneries of Thessaloniki, indicating high concentrations of heavy metals. This conclusion was verified by complementary geochemical measurements and attributed to influx of liquid and waste pollutants that resulted from leather manufacturing.

5. Acknowledgements

6. References

Apblett, A.W., Al-Fadul, S.M., Chehbouni, M. & Trad, T., 2001. Removal of Petrochemicals from Water Using Magnetic Filtration. *Proceedings of the 8th International Environmental Petroleum Consortium*.

Atzemoglou, A. & Skianis, G., 2003. Geophysical investigation in Thessaloniki tanneries in the framework of NORISC project, *Internal report of the Institute of Geology and Mineral Exploration*, pp. 20.

Cornell, R.M. & Schwertmann, U., 1996. *The Iron Oxides,* VCH, Weinheim, Germany, pp. 703.

Dearing, J.A., Hay, K.L., Baban, S.M.J., Huddleston, A.S., Wellington, E.M.H. & Loveland P.J. 1996. Magnetic susceptibility of soil: an evaluation of conflicting theories using national data set, *Geophysical Journal International,* 127, 728-734.

Diabaté, S., Mülhopt, S., Paur, H.R., Wottrich, R. & Krug, H.F., 2002. In vitro effects in incinerator fly ash on pulmonary macorphages and epithelial cells, *International Journal of Hygiene and Environmental Health,* 204, 323-326.

Evans, M.E. & Heller, F., 2003. Environmental Magnetism – Principles and Applications of Enviromagnetics. *Academic Press*, pp. 299.

Ferguson, C.C., 1999. Assessing Risks from Contaminated Sites: Policy and Practice in 16 European Countries, *Land Contamination & Reclamation,* 7 (2), 33.

Hanesch, M., Scholger, R. & Rey, D., 2003. Mapping distribution around an industrial site by measuring magnetic parameters of tree leaves, *Atmospheric Environment,* 37, 5125-5133.

Hannam, J. & Heller, F., 2001. Magnetic investigation of roadside leaves in Zürich, Switzerland, *Environmental Magnetism Network MAGazine*, 04.

Heldstab, J. 2002, PM10-Emissionen des Verkehrs, Statusbericht Teil Schienenverkehr, Umwelt-Materialien, №144, Luft, Bundesamt für Umwelt, Wald und Landschaft (ed.), Bern, pp. 48 [in German with English abridgement].

Maher, B.A. & Thompson, R., 1999. Quaternary Climates, Environments and Magnetism. *Cambridge University Press*, pp. 390.

Maher, B.A., Watkins, S.J., Brunskill, G., Alexander, J. & Fielding, C.R., 2008. Sediment provenance in a tropical fluvial and marine context by magnetic 'fingerprinting' of transportable sand fractions, *Sedimentology,* DOI 10.1111/j.1365-3091.2008.00999.x.

Petrovsky, E., Kapička, A., Zapletal, K., Šebestová, E., Spanilá, T., Dekkers, M.J. & Rochette, P., 1998. Correlation between magnetic parameters and chemical composition of lake sediments from Northern Bohemia – Preliminary study, *Phys. Chem. Earth,* 23 (9-10), 1123-1126.

Sarris, A., Kokinou, E., Aidona, E., Kallithrakas-Kontos, N., Koulouridakis, P., Kakoulaki, G., Droulia, K. & Damianovits, O., 2008. Environmental study for pollution in the area of Megalopolis power plant (Peloponnesos, Greece), *Environ. Earth Sc.,* DOI 10.1007/s00254-008-1676-3.

Shukla, A., Timblin, C., BeruBe, K., Gordon, T., McKinney, W., Driscoll, K., Vacek, P. & Mossman, B.T., 2000. Inhaled particulate matter causes expression of nuclear factor (NF)-□B-related genes and oxidant dependent NF-ϰB activation in vitro. *American Journal of Respiratory Cell and Molecular Biology, 23*, 182-187.

Smith, K.R., Veranth, J.M., Hu, A.A., Lighty, J.S. & Aust, A.E., 2000. Interleukin-8 levels in human lung epithelial cells are increased in response to coal fly ash and vary with the bioavailability of iron as a function of particle size and source of coal. *Chemical Research in Toxicology, 13*, 118-125.

Spassov, S., Zananiri, I., Kondopoulou, D., Atzemoglou, A., Polya, D., Maher, B., Egli, R. & Heller, F., 2004. Application of environmental techniques in detecting nanoparticle contamination, *Contribution to Geophysics and Geodesy*, Vol. 34, Special Issue, 141-143.

Tema, E., 2003. Application of magnetic methods on the investigation of the environmental conditions on lake sediments. A case study: Koumoundourou Lake and Kerkini Lake. *Master Thesis,* Aristotle University of Thessaloniki, pp. 113.

von Blottnitz, H. 2006. A comparison of air emissions of thermal power plants in South Africa and 15 European countries, *Journal of Energy in Southern Africa,* 17, 72-81.

van Maanen, J.M.S., Borm, P.J.A., Knaapen, A., van Herwijnen, M., Schildermann, P.A.E.L., Smith, K.R., Aust, A.E. & Tomatis, M. 1999. In vitro effects of coal fly ashes: Hydoxyl radical generation, iron release, and DNA damage and toxicity in rat lung epithelial cells, *Inhalation Toxicology,* 11, 1123- 1141.

Vriend, S.P., van Gaans, P.F.M., Middelburg, J. & de Nijs, A., 1988. The application of fuzzy c-means

analysis and non-linear mapping to geochemical datasets: examples from Portugal, *Appl. Geochem.*, 3, 213-224.

Verosub, K.L. & Roberts, A.P., 1995. Environmental magnetism: Past, present and future. *Journal of Geophysical Research,* 100 (B2), 2175-2192.

Walden, J., Oldfield, F. & Smith, J., 1999. Environmental Magnetism: A practical Guide. *Quaternary Research Association*, pp. 243.

Watson, J.H.P., Ellwood, D.C., Deng, Q.X., Mikalovsky, S., Hayter, C.E. & Evans, J., 1995. Heavy metal adsorption on bacterially produced FeS. *Minerals Engineering, 8*, 1097-1108.

Watson, J.H.P., Croudace, I.W., Warwick, P.E., James, P.A.B., Charnock, J.M. & Ellwood, D.C., 2001. Adsorption radioactive metals by strongly magnetic iron sulfide nanoparticles produced by sulfate-reducing bacteria. *Separation Science and Technology, 36*, 2571-2607.

Zananiri, I., Kondopoulou, D., Gault, A., Atzemoglou, A., Polya, D., Maher, B. & Spassov, S., 2006, Application of magnetic properties of nanoparticles in detecting pollution: Theory and a case study from Kozani region, NW Greece, *Travaux Géophysiques,* XXVII, 10th Castle Meeting on New Trends in Geomagnetism Abstracts, 128.

Zeri, Ch., 1995. Application of the magnetic methodology in open marine systems. The case of NW Mediterranean, *PhD Thesis,* University Athens, pp. 142.

Zeri, Ch., Chroneou, A. & Scoullos, M., 1997. Geochemical observations and magnetic characteristics of the Vouliagmeni Lake, *Proceedings of the 5th Hellenic Symposium of Oceanography and Fishery,* Vol. II, 333-336.

Zevenhoven, R. & Kilpinen, P., 2001. *Control of Pollutants in Flue Gases and Fuel Gases*. TKK, Espoo 2001.

Zhang, C.X., Huang, B.C., Li, Z.Y. & Liu, H., 2006. Magnetic properties of highroad-side pine tree leaves in Beijing and their environmental significance, *Chin. Sci. Bull.,* 51 (24), 3041–3052.

12ο ΔΙΕΘΝΕΣ ΣΥΝΕΔΡΙΟ ΤΗΣ ΕΛΛΗΝΙΚΗΣ ΓΕΩΛΟΓΙΚΗΣ ΕΤΑΙΡΙΑΣ
ΠΛΑΝΗΤΗΣ ΓΗ: Γεωλογικές Διεργασίες και Βιώσιμη Ανάπτυξη

12th INTERNATIONAL CONGRESS OF THE GEOLOGICAL SOCIETY OF GREECE
PLANET EARTH: Geological Processes and Sustainable Development

◈

ΣΕΙΣΜΟΛΟΓΙΑ
SEISMOLOGY

EVIDENCE FOR INDUCED SEISMICITY FOLLOWING
THE 2001 SKYROS MAINSHOCK

A.K. Adamaki,[1] G. M. Tsaklidis,[1] E. E. Papadimitriou,[1]
and V. G Karakostas.[1]

[1] *Department of Geophysics, School of Geology, Aristotle University of Thessaloniki, GR54124 Thessaloniki - Greece, aadama@geo.auth.gr, ritsa@geo.auth.gr, vkarak@geo.auth.gr*

[2] *Mathematics Department, Aristotle University of Thessaloniki, GR54124 Thessaloniki – Greece, tsaklidi@math.auth.gr*

Abstract

Estimation of the seismicity rate changes caused by a major earthquake is based upon the assumption that the earthquake occurrence can be described by stochastic processes. Three stochastic models are applied to the data, i.e. the homogeneous Poisson model, the non-homogeneous Poisson model with two different rate functions, and the Autoregressive model AR(2). The two latter models seem to be adequate to properly simulate the earthquake production in a given area. The identification of the model which best fits the data, enables the estimations of the seismicity rate changes and the numbers of the earthquakes following a specific main shock.

Key words: Seismicity rates, induced seismicity, Skyros aftershock sequence

1. Introduction

Many researchers have focused on applying statistics and the probability theory to earthquake sequences, in order to study the temporal and spatial distribution of triggered activity following large earthquakes. A useful tool in statistics for modeling and analyzing spatial data is a point process, which can be used as a model for random events in time. Many point process models, where each point represents the time and location of an event, have been proposed (Vere–Jones, 1992; Ogata, 1999; among others) and several attempts have been made to estimating the changes in earthquake production that have been caused by a specific event. The special case of seismicity rate decreases (i.e. seismicity shadows) was also examined in previous studies (Marsan, 2003; Marsan and Nalbant, 2005).

The simplest approach to this goal is to consider a stationary process taking into account only the background seismicity (Toda et al., 1998, 2002), which however leads to underestimation of the rate change (Marsan, 2003; Felzer et al., 2003). Then, stationarity cannot be generally assumed and the declustering of the catalog is a common way to remove nonstationarity from the data (Matthews and Reasenberg, 1988; Kilb et al., 2000; Gomberg et al., 2001; Wyss and Wiemer, 2000). On the other hand, aftershocks comprise a major portion of an earthquake catalog including important information about the rate changes. Therefore other researchers have tried to model the aftershocks rather than remove them, e.g. Marsan (2003) tested several models such as the autoregressive model, a sum of N power-laws, proposed by Utsu (1970) as a generalization of the model presented in Ogata and Shimazaki (1984) and Woessner et al. (2004) and the ETAS model (Ogata, 1988).

The purpose of the present work is to study the temporal structure of triggered sequences at short time scales after a large earthquake. Therefore certain statistical models are applied on data from the 2001 Skyros sequence, i.e. the homogeneous Poisson model, the non–homegeneous Poisson model and the autoregressive model AR(2).

2. Methods

In order to analyze the data, firstly the homogeneous and non–homogeneous Poisson model is considered:

Homogeneous and Non – homogeneous Poisson model: A Poisson process with constant rate λ, i.e. a time-independent rate, is known as a homogeneous Poisson process. In this case, the waiting times of the point process are exponentially distributed with a mean **$\mu = 1/\lambda$**. The expected number of earthquakes in any interval of length **t** equals to **λt**, and the probability that there are exactly **n** occurrences in this interval is given by

$$(1)$$

By replacing the constant **λ** with a function **λ(t)**, which gives the rate of earthquakes at time **t**, the process becomes a non–homogeneous Poisson process. In this case, the number of earthquakes in any interval is also time dependent, and the mean rate in an interval $[t, t+\Delta t]$ is given by

$$(2)$$

The probability that there are exactly **n** occurrences within the specific interval is then given by:

$$(3)$$

Two functions expressing **λ(t)** are tested in the present study, namely

$$(4)$$

and

$$(5)$$

both selected because of their property of allowing the rate decaying as time passes; they differ in that. $\lambda(t)$ given by equation (4) decays rapidly to zero while $\lambda(t)$ given by (5) may decay smoothly to 0 (by a suitable choice of the parameters).

In each case a specific region must be selected, with dimensions a few times larger than the main rupture length. Determining the study area, the threshold magnitude must be defined to ensure the completeness of the data set. The next step is to define the duration of the earthquake catalog, which depends on the purpose of the specific study. This means that, naming T_0 the time of occurrence of the main shock, the catalog expands within the interval $[T_0, T]$ where T is located several days after T_0.

Continuing with the data processing, the time intervals between consecutive events occurring at times t_i (t_i are measured from the beginning of the observation period, i.e. T_0) are computed and tested using the chi–square test; the null hypothesis is that the inter–arrival times are exponentially

distributed with a mean **μ**. If the null hypothesis is true, then the number of occurrences follows a Poisson distribution with a rate **λ**, which is constant during the tested interval (homogeneous Poisson process).

Next, since the rate of the aftershock sequence over the first few days after the main shock is characterized by strong changes, (different) constant rates are assumed over sub–intervals of the time period examined. To deal with that, the time interval $[T_0, T]$ is separated into short intervals $[T_i, T_{i+1}]$, each one tested for its homogeneity as a Poisson process with a rate parameter λ_i. Each λ_i is computed taking into consideration the number of events in the respective time interval, which is not necessarily equal in all sub–intervals. The entire set $\{\lambda_i\}$ is then used as the input data to fit the selected equation that best describes their evolution within $[T_0, T]$. In the present study the equation for the function **λ(t)** which is fitted to the data is of the form $\lambda(t)=$, and the parameters a and b are estimated by the least squares' method.

Finally, the non–homogeneous Poisson process is assumed to have a rate function of the form $\lambda(t)=$, the parameters **a** and **b** being estimated by the maximum likelihood method. This intensity function can be an increasing or decreasing function, according to whether b>1 or b<1 respectively. Based on the form of λ(t), the aforementioned process is named a process with a Weibull rate function or simply a Weibull process. The special case of b=1 is the exponential case, which has a constant hazard rate and is characterized by the memoryless property. The maximum likelihood estimators for a and b are given by

$$(6)$$

Autoregressive Model: Another way to model the sequence of the earthquakes is to consider a random variable Z(t), t≥0, representing the number of earthquakes at any time t. The set {Z(t)}, t≥0, constitutes a time series, i.e. a family of stochastic processes. The model which is fitted to the data is the autoregressive model of order p, p∈N⁺, abbreviated as AR(p). In statistics, signal processing e.t.c., AR(p) is often used to model and predict various types of natural phenomena. The AR(p) model assumes that

$$(7)$$

where ϕ_i are the unknown parameters and α_t is a white noise function with a zero mean and variance σ^2. The time series is considered to be stationary. Then the parameters ϕ_i can be estimated using several methods, e.g. the Yule–Walker equations which constitute a set of linear equations relating the unknown parameters with the autocorrelations. Then:

$$(8)$$

where the coefficients ϱ_i , *i=1,2,…,p-1* stand for the autocorrelations which give the correlations of the values of the process against time-shifted versions of themselves.

3. Models application to the 2001 Skyros sequence

An investigation is now performed to the 2001 Skyros sequence, with the main shock of M_w=6.4 to have occurred on July 26, 2001 Skyros. Based on the data and results for this sequence from Karakostas et al. (2003), a region is selected as mentioned before, i.e. a few times larger than the rup-

Table 1. The values of the means μ of the exponential distributions of the inter–arrival times, and the λ–rates of the respective Poisson distributions.

time period	No of data	statistical X^2	μ	λ
$(-600, \mathbf{T_0})$	19	3.9660	31.5454	0.0317
$(\mathbf{T_0}, 4)$	116	2.1857	0.0340	29

ture length. The catalog used was found to be complete for events with $M_c \geq 3.5$. The events are separated into two sets, for the time intervals; $[T_0 - t_B, T_0]$ and $[T_0, T_0 + t_A]$, where T_0 is the time of occurrence of the main shock and t_B and t_A denote selected time periods before and after the main shock, respectively.

3.1 Homogeneous Poisson process

The homogeneous Poisson process assumes constant rates, λ_B and λ_A, before and after T_0, respectively. It is selected that $t_B = 600$ days and $t_A = 4$ days and the homogeneous Poisson model is fitted to the recorded data in order to estimate the number of events in each time interval. The goodness of fit is tested by means of the chi-square test. Within $[T_0 - t_B, T_0]$ 19 events occurred preceding T_0 whereas 116 events followed T_0, occurring into the interval $[T_0, T_0 + t_A]$. The inter-arrival times of the earthquakes are then tested for being exponentially distributed. The values of the statistical X^2, the parameter μ of the exponential distribution of times between subsequent events, and the estimated mean λ (per day) of the two homogeneous Poisson processes, before and after the main shock, are summarized in Table 1.

600 days before the main shock there are 19 data, giving a rate of 0.0317 events per day, with a mean inter-arrival time of length 31.5454 days. On the other hand, 4 days after the earthquake there are 116 data, which lead to a rate of 29 events per day and a mean inter-arrival time of length 0.034 days. As it is shown in Table 1, those time intervals were tested by means of the chi-square test, and the statisticals X^2 are smaller than the critical value which is equal to 5.02 at the a=0.05 significance level (for two degrees of freedom).

The following step is to compute the probability of having specific numbers of events in the two different time intervals, using equation (1), where λ takes the values λ_B and λ_A. The duration t of the time period (0, t) appearing in equation (1) can either be smaller or larger than t_B and t_A. If it is assumed that the process does not change for times outside the intervals $[T_0 - t_B, T_0]$ and $[T_0, T_0 + t_A]$, then t can be larger than t_B and t_A (extrapolation). Then the probability derived via (1) refers to a homogeneous Poisson process with the same parameter λ as the one estimated within the corresponding interval. The results of this procedure can also be presented using the survival function which is derived through the Poisson cumulative distribution function given by

$$(9)$$

and representing the probability of having up to N earthquakes during the procedure with rate λ. In

Figure 1 the survival functions   estimated for the time periods before and after

the main shock are shown; the plots are derived in Matlab by connecting the points   , x=0, 1, … . Then, the probabilities of having more (or less) than any number of events can be derived by
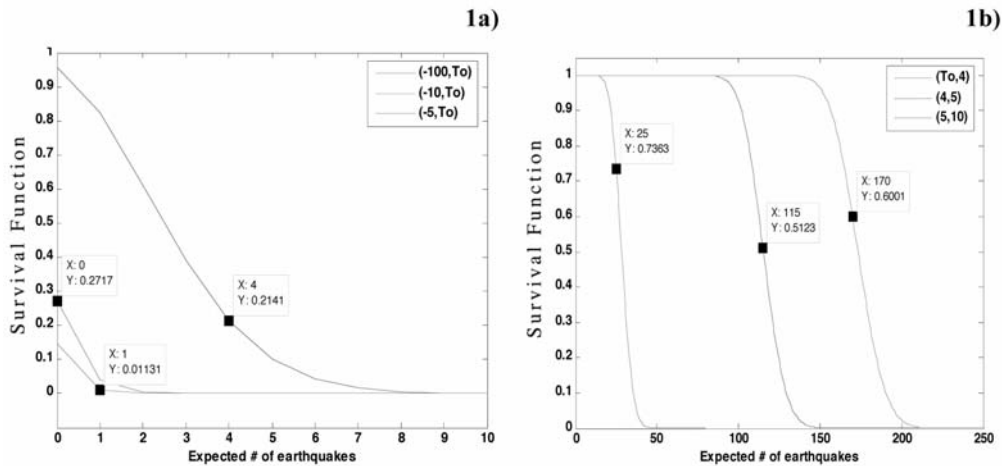
Fig. 1: Estimated survival curves of the number of events in the time periods (a) before and (b) after the main shock, using the homogeneous Poisson model.

means of the survival functions, e.g. in Figure 1b the probability of having more than 17 earthquakes in the interval [1, 2) is 0.989 (18 events are observed), the probability of having more than 25 earthquakes during the fifth day is 0.736 (18 events are observed) and the probability of having more than 170 earthquakes in the time interval (5, 10) is 0.600 (36 events are observed). It is obvious that the homogeneous Poisson model does not fit well the data, especially for large values of t. This observation leads to a need of replacing the constant rate λ with $\lambda(t)$.

3.2 Non–homogeneous Poisson process

Dividing the aftershock sequence into subsets corresponding to short time intervals, each one is tested for its homogeneity as a Poisson process (using the chi–square test). The length of the intervals is not necessarily the same, whereas there are different values, λ_i, for the rates of each interval. The values of means μ_i (of the exponentially distributed inter–arrival times) and mean λ_i are shown in Table 2. In Figure 2 the values of λ_i are plotted versus time t (in days) after T_0 (main shock occurrence time), which is mentioned as 0–time. Because of the fact that λ is decaying with time t, formula (4) can be adopted. In order to estimate the values of the parameters a and b in (4), the least–squares method is applied and the results are given in Table 3. Now, for the first three days after T_0, the time interval is divided into four subintervals and the respective four–different–values of λ_i are found. Fitting the curve $\lambda(t)=$ to the data is shown in Figure 3.

If the estimated $\lambda(t)$ can be accepted also for larger intervals than the first three days since the main shock, then it comes out that the number of earthquakes during those intervals will not change significantly, as the function $\lambda(t)$ decays to zero rapidly as t increases. It should be mentioned that assuming that the process does not change out of the time borders which were set for the parameter estimation, is a rather arbitrary admission. In Figure 4b the theoretical cumulative number of events along with the observed data is presented.

In Figure 4a the estimated probabilities of having a number of events in different time intervals are presented, using the survival function. Equation (3) can be used in this case to estimate the Poisson probability, where the expected number of events in any interval (t; t+Δt) is λ(t; t+Δt), given by (2);

Table 2. The values of the parameters μ of the exponential inter-arrival times, and the rates λ of the Poisson distributions in subsequent time intervals.

Time period (in days)	μ	Λ
$(T\alpha_0, 0.12)$	0,0046	208,3333
(0.12, 0.36)	0,0096	104,1667
(0.36, 1)	0,0217	43,75
(1, 3)	0,0695	14,5
(3, 5)	0,0643	13,5
(5, 9)	0,1390	7,5
(9, 16)	0,2167	4,5714
(16, 36)	0,5936	1,65
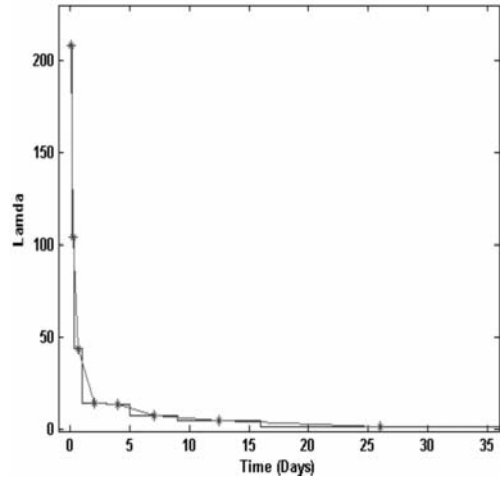
Fig. 2: Rates λ_i plotted versus time (in days).

Table 3. Estimated rate function $\lambda(t)=\exp(\alpha+b*t)$, using the least squares method.

	Value	Standard Error
α	5,49772	0,10446
b	-3,06949	0,66913
Adj. R²= 0,96145		
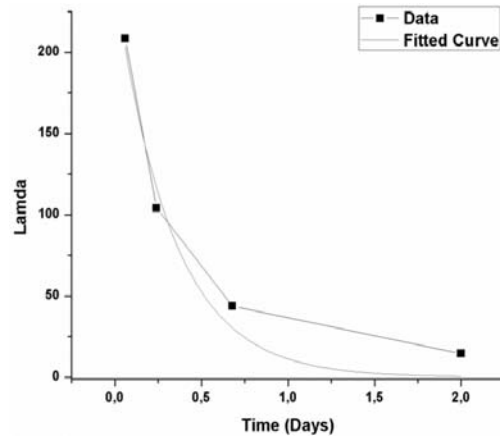
Fig. 3: Observed data λ_i and fitted function $\lambda(t)= e^{a+bt}$.

e.g. the probability of having more than 50 earthquakes within the interval $[T_0, 1]$ is 0.9993 (78 events are observed), and the probability of having more than 90 earthquakes in the interval $[T_0, 5]$ is 0.111 (134 events are observed). Obviously, the model underestimates the number of events as time increases, as it is shown in Figure 4b.

3.3 Non–homogeneous Poisson process with a Weibull rate function

In this case equation (5) is used to compute the expected number of events in any time interval as given in (2) and (3). In Table 4 that follows, the estimated values of parameters a and b for the Weibull rate functions are shown. These parameters are derived from equations (6) using the maximum likelihood method. The values presented in Table 4 come up from different sets of data each one being a subset of the one that follows. For example, if the data come up from observing only

4a)   **4b)**
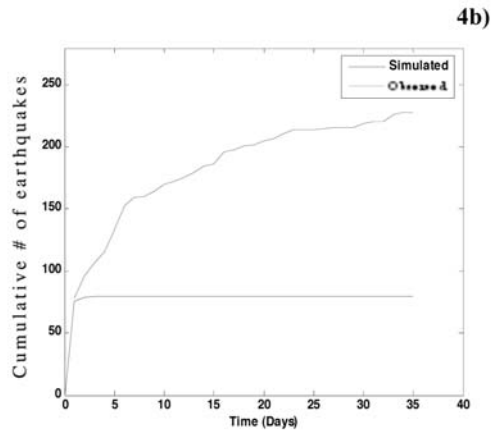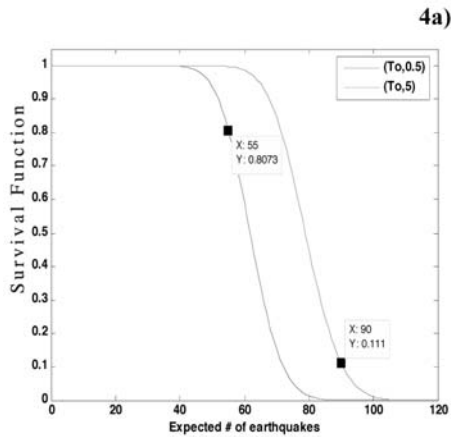
Fig. 4: a) Survival functions of the number of events in time periods after the main shock, using the non-homogeneous Poisson model with $\lambda(t) = e^{a+bt}$. b) Cumulative density function of the theoretical number of the aftershocks (via the non-homogeneous Poisson model), and the cumulative number of observed data.
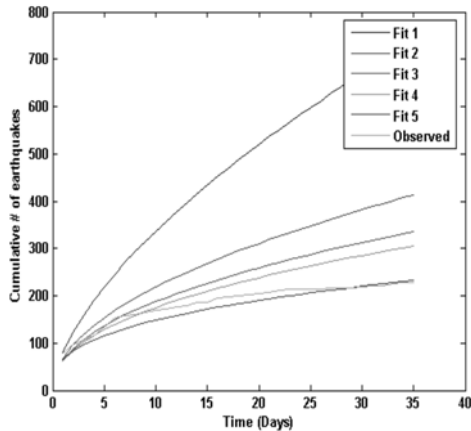
Fig. 5: Cumulative number of earthquakes for the Weibull-rates case for different data set.

Table 4. Estimated parameters of the Weibull distributions

Time period (in days)	estimated a	estimated b
(1^{rs}t day	$9.1338*10^{-4}$	0.6257
1^{rs}-2nd day	$2.5054*10^{-4}$	0.5085
1^{rs}-3rd day	$1.2807*10^{-4}$	0.4647
1^{rs}-4th day	$8.7278*10^{-5}$	0.4435
1^{rs}-30th day	$8.7228*10^{-6}$	0.3584

the first day after T_0, then the expected number of events for the following days is overestimated, as shown in Figure 5. Taking more and more data into account (from the first 2, 3, 4 days etc) the estimation of the oncoming process comes closer and closer to the observation and the model fits the data well.

Assuming that the underlying process is the Weibull process which is known up to the third day after T_0, equations (2) and (3) are used to compute the possibility of having specific numbers of events into several time intervals, and then the survival function is estimated. The results are summarized in Figure 6, and the probabilities of having more (or less) than any number of events can be derived by means of the survival functions. For example, the probability of having more than 10 earthquakes during the fourth day is 0.8971 (9 events are recorded), and the probability of having
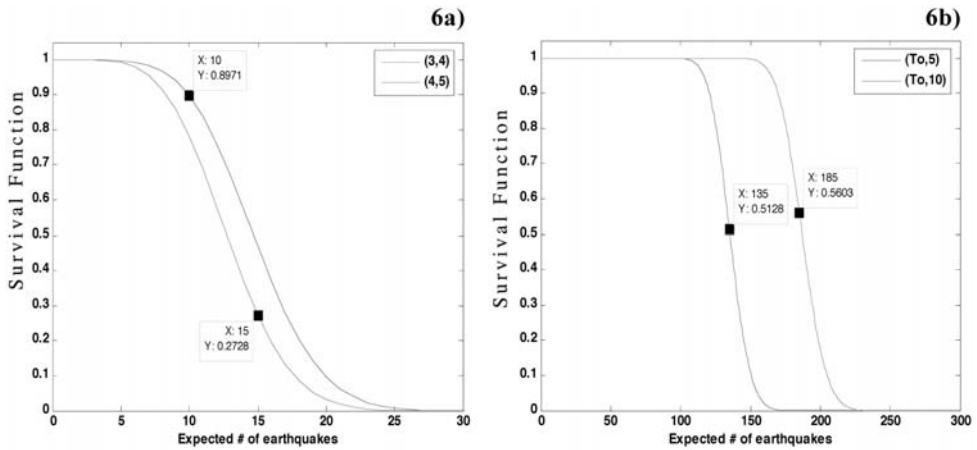
Fig. 6: Survival functions of the number of events in various time periods after the main shock, using the non-homogeneous Poisson model with $\lambda(t)=\alpha^{-b}bt^{b-1}$.
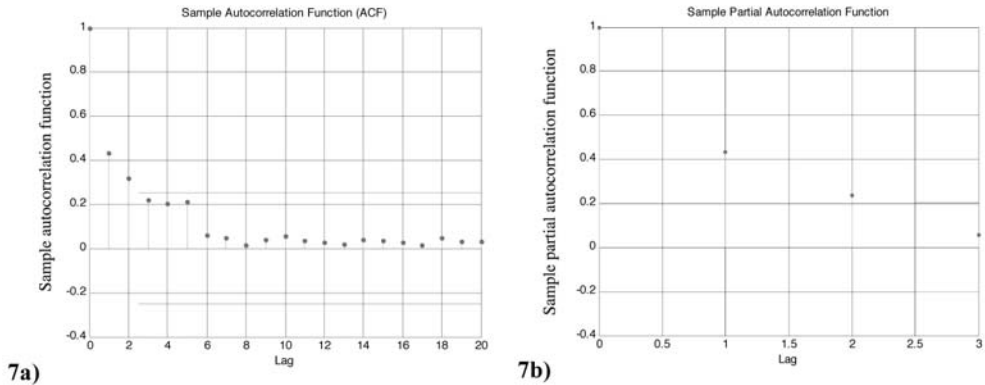
Fig. 7: a) Sample autocorrelation function (ACF) and b) sample partial autocorrelation function (PACF) for the number of events of the time period $[T_0, 20]$.

more than 135 earthquakes within $[T_0, 5]$ is 0.5128 (134 events are recorded). It turns out that the model is adequate for describing the earthquake sequence, especially for 1<t<10.

3.4 Autoregressive model AR(p)

The number of earthquakes can be considered as a time series and among the several models dealing with that, the Autoregressive model AR(p) can be chosen and applied to the data, following Marsan (2003). AR(p) models explain a series of observations where the value of an observation depends on the (values of the) p past observations. Here the random variable Z_t of the AR(p) model represents the number of earthquakes at time t. Finding the order p of the model and using the Yule-Walker equations to estimate the unknown parameters, the numbers of earthquakes, Z_t, in different future time intervals can be estimated.

The first step is to estimate the partial autocorrelation coefficients in order to determine the order p

Table 5 and 6. Autocorrelation Function (ACF) and Partial Autocorrelation Function (PACF) and the bounds (a=0.05).

ACF	Bounds
0.4267	0.2884
0.3126	-0.2884
0.2079	
0.1995	
0.2041	

PACF	Bounds
0.4288	0.2884
0.2374	-0.2884
0.0465	

of the model. If p=k, k∈N⁺, is selected and the kth autocorrelation comes out to be statistically insignificant, then the last variable may be omitted and the real order of the model is less than k. In Figure 7 and Table 6 the partial autocorrelation function is shown. In this case the initial assumption is p=3. The values z_t taken into account are the number of earthquakes in subsequent time intervals with duration 2.4 hours each. It turns out that the assumption of the order to be 3 must be rejected (a=0.05), and the order ends up to be p=2. In the correlogram shown in Figure 7, the autocorrelation coefficients are found to be close to zero for k≥3. The next step is to estimate the parameters of the AR(2) model, using the Yule-Walker equations given in (8). It is found that ϕ_1= 0,4772 and, ϕ_2= 0,1831, thus

The values of the parameters indicate that the AR(2) is stationary since $\phi_1+\phi_2<1, \phi_2-\phi_1<1, -1<\phi_2<1$.

4. Discussion–Conclusions

In the present study certain statistical models are applied to the 2001 Skyros aftershock sequence, aiming to figure out whether there is a specific statistical approach of the phenomenon which can lead to a simulation of its evolution. The earthquakes' sequence is assumed to be a stochastic process, following the homogeneous or the non-homogeneous Poisson model. The homogeneous Poisson model with constant rate λ doesn't fit well the data, especially in the case of long time periods which were tested, before and after the main shock. This fact leads to the need of applying a non–homogeneous Poisson process with a time dependent rate, λ(t), which is considered to obey two certain forms (equations (4) and (5)). In the first case the rate λ(t) is rapidly decaying to zero as time t passes, implying that no events are expected after a few days following the main shock. This was not in accordance with the observation, as the aftershock sequence does not actually decay to zero in such a short time interval. In the second case the Weibull-type rate λ(t) is considered (equation 5), and the associate parameters are estimated using the maximum likelihood method. It turns out that the non–homogeneous Poisson model fits quite well the data and the results, presented in the previous section, show that this model provides a good approach to the aftershock sequence, compared with the previous model.

Finally, the earthquake sequence is tested via time series analysis, using the Autoregressive model of order 2; that is the number of earthquakes at some time interval was supposed to depend linearly on the number of the earthquakes of the two preceding time intervals. The data analysis shows that the AR(2) model fits adequately the data.

5. Acknowledgments

References

Felzer, K.R., Abercombie, R.E., and Brodsky, E.E. (2003), Testing the stress shadow hypothesis, EOS Trans. AGU 84(46), Fall Meet. Suppl., Abstract S31A–04.

Gomberg, J., Reasenberg, P.A., Bodin, P., and Harris, R.A. (2001), Earthquake Triggering by Seismic Waves Following the Landers and Hector Mine Earthquakes, *Nature* 411, 462–466.

Karakostas, V.G., Papadimitriou, E.E., Karakaisis, G.F., Papazachos, C.B., Scordilis, E.M., Vargemezis, G., and Aidona, E. (2003), The 2001 Skyros, Northern Aegean, Greece, earthquake se quence: off-fault aftershocks, tectonic implications, and seismicity triggering, *Geophys*. Res. 30, doi:10.1029/2002GL015814.

Kilb, D., Gomberg, J., and Bodin, P. (2000), Triggering of Earthquake Aftershocks by Dynamic Stresses, *Nature* 408, 570–574.

Marsan, D. (2003), Triggering of Seismicity at Short Timescales Following Californian Earthquakes, *J. Geophys*. *Res*. 108, doi:10.1029/2002JB001946.

Marsan, D., and Nalbant, S. S. (2005), Methods for measuring seismicity rate changes: Areview and a study of how the Mw 7.3 Landers earthquake affected the aftershock sequence of the Mw 6.1 Joshua Tree earthquake, *Pure Appl*. *Geophys*., 162, 1151–1185.

Matthews, M.V. and Reasenberg, P.A. (1998), Statistical Methods for Investigating Quiscence and other Temporal Seismicity Patterns, *Pure Appl*. *Geophys*. 126, 357–372.

Ogata, Y. (1988), Statistical Models for Earthquake Occurrences and Residual Analysis for Point Processes, *J. Am. Stat. Ass*. 83, 9–27.

Ogata, Y. (1999), Seismicity Analysis through Point-process Modeling: A Review, *Pure Appl*. *Geophys*. 155, 471–507.

Ogata, Y. and Shimazaki, K. (1984), Transition from Aftershock to Normal Activity: The 1965 Rat Islands Earthquake Aftershock Sequence, *Bull*. *Seismol*. *Soc*. *Am*. 74, 1757–1765.

Toda, S., Stein, R.S., and Takeshi, S. (2002), Evidence from the AD 2000 Izu Islands Earthquake Swarm that Stressing Rate Governs Seismicity, *Nature* 419, 58–61.

Toda, S., Stein, R.S., Reasenberg, P.A., Dieterich, J.H., and Yoshida, A. (1998), Stress Transferred by the 1995 Mw=6.9 Kobe, Japan, Shock: Effect on Aftershocks and Future Earthquake Probabilities, *J. Geophys*. *Res*. 103, 24543–24565.

Utsu, T. (1970), Aftershocks and Earthquake Statistics (II)-Further Investigation of Aftershicks and other Earthquake Sequences Based on a New Classification of Earthquake Sequences, J. Fac. Sei., Hokkaido University, Ser. VII, 3, 197–266.

Vere–Jones, D., Statistical Methods for the Description and Display of Earthquake Catalogs. In Statistics in the Environmental and Earth Sciences (eds. Walden A.T. and Guthorp P.) (Edward Arnold Publisher 1992), pp. 220–246.

Woessner, J., Hauksson, E., Wiemer, S., and Neukomm, S. (2004), The 1997 Kagoshima (Japan) Earthquake Doublet: A Quantitative Analysis of Aftershock Rate Changes, *Geophys*. *Res*. *Lett*. 31, doi:10.1029/2003 GL018858.

Wyss, M. and Wiemer, S. (2000), Change in the Probaqbility for Earthquakes in Southern California due to the Landers Magnitude 7.3 *Earthquake, Science* 290, 1334–1338.

SEISMICITY CHANGES DETECTION DURING THE SEISMIC SEQUENCES EVOLUTION AS EVIDENCE OF STRESS CHANGES

Astiopoulos A. C.[1], Papadimitriou E.[1], Karakostas V[1], Gospodinov D. [2], and Drakatos G.[3]

[1] *Geophysics Department, School of Geology, Aristotle University of Thessaloniki, GR54124 Thessaloniki, tasosast@geo.auth.gr, ritsa@geo.auth.gr, vkarak@geo.auth.gr*

[2] *Geophysical Institute, Bulgarian Academy of Sciences, Sofia, Bulgaria, drago_pld@yahoo.com*

[3] *Institute of Geodynamics, National Observatory of Athens, GR11810, g.drakat@gein.noa.gr*

Abstract

The statistical properties of the aftershock occurrence are among the main issues in investigating the earthquake generation process. Seismicity rate changes during a seismic sequence, which are detected by the application of statistical models, are proved to be precursors of strong events occurring during the seismic excitation. Application of these models provides a tool in assessing the imminent seismic hazard, oftentimes by the estimation of the expected occurrence rate and comparison of the predicted rate with the observed one. The aim of this study is to examine the temporal distribution and especially the occurrence rate variations of aftershocks for two seismic sequences that took place, the first one near Skyros island in 2001 and the second one near Lefkada island in 2003, in order to detect and determine rate changes in connection with the evolution of the seismic activity. Analysis is performed through space–time stochastic models which are developed, based upon both aftershocks clustering studies and specific assumptions. The models applied are the Modified Omori Formula (MOF), the Epidemic Type Aftershock Sequence (ETAS) and the Restricted Epidemic Type Aftershock Sequence (RETAS). The modelling of seismicity rate changes, during the evolution of the particular seismic sequences, is then attempted in association with and as evidence of static stress changes.

Key words: aftershock sequence, stochastic models, seismic quiescence, MOF, ETAS, RETAS, Coulomb stress changes.

1. Introduction

Seismicity anomalies during the seismic sequences evolution and especially the seismic quiescence phenomenon have attracted much attention as one of the precursors to a large earthquake (Utsu, 1968; Ohtake et al., 1997; Wyss and Burford, 1987; Kislinger, 1988; Ogata, 1992, 1999). Its recognition in complex aftershock sequences, where the activity is high, is difficult. Nowadays, the application of statistical models has prevailed, in order to point out such a phenomenon. Interpreting the model application results in association with the corresponding results of other processes such as the Coulomb stress changes due to the coseismic slip of strong main shocks, can provide a tool in assessing the imminent seismic hazard.

Aiming to reveal the evolution pattern of two seismic sequences that took place in the Greek territory, the first one in the vicinity of Skyros Island, in 2001, and the second one along the west coast of Lefkada Island, in 2003, the aftershocks' temporal behaviour is examined based upon the application of Gospodinov and Rotondi (2006) software. This includes the selection of the appropriate statistical model, among MOF (Utsu, 1969), ETAS (Ogata, 1988) and RETAS (Gospodinov and Rotondi, 2006) and the data elaboration based upon the selected model. The spatial distribution of the static stress changes that resulted from the main shocks, are associated either with relative quiescence or excitation of the aftershock activity, which is observed when examining the aftershocks temporal distribution.

2. Method

2.1 Statistical models

The first statistical approach for the temporal distribution of aftershocks was introduced by Omori (1894), the well known Omori Law, which relates the aftershock occurrence rate, $\lambda(t)$, gradual decay in a time interval, t, after the main shock occurrence, with the relation:

$$(1)$$

where c and K are parameters. Relation (1) was transformed by Utsu (1969), in the Modified Omori Formula (MOF):

$$(2)$$

where p is a parameter indicative for a seismic sequence, expressing regional properties.

Ogata (1988) proposed the idea of self – similarity by extending the capacity of generating secondary events to every aftershock of the sequence through the formulation of the Epidemic Type Aftershock Sequence (ETAS) whose conditional intensity function is:

$$(3)$$

where every i corresponds to every event at time t_i.

Gospodinov and Rotondi (2006) offer the Restricted Epidemic Type Aftershock Sequence (RETAS) model, which is based on the assumption that not all events in a sample but only aftershocks with magnitudes larger than or equal to a threshold M_{th} can induce secondary seismicity. Then the conditional intensity function for the model is formulated as:

$$(4)$$

Varying M_{th} between the cut–off magnitude M_o and the main shock magnitude M_i, different versions of RETAS are examined, between ETAS and MOF models, considering these two models as limit cases.

2.2 Parameters estimation

For the models parameters Ogata (1983) proposed the maximum likelihood estimates (MLE) which maximize the log–likelihood function. A single form for this function is (Gospodinov and Rotondi, 2006):

$$(5)$$

where N is the number of earthquakes of magnitude larger than or equal to M_o which occur at times t_i, i = 1,...,N, in the interval under study [0, T].

2.3 Akaike criterion

A large number of statistical models can be applied at every seismic sequence. Thus, the Akaike Information Criterion (AIC, Akaike, 1974) is used as a measure for selecting the best among competing models for a fixed data set. It is defined by:

$$(6)$$

where θ stands for the model parameters, L is the maximum likelihood for a particular model, and k is the number of parameters of the model. The model with the smaller AIC shows the better fit to the data.

2.4 Residual process analysis

Having obtained the best among the proposed models (Akaike criterion), there is still the possibility of the existence of a better one. It can be seen precisely how well or poorly the estimated model is fitted to an aftershock sequence by inspecting the cumulative number of aftershocks with respect to the transformed time (Ogata, 1988). The integration of the nonnegative conditional intensity function produces a transformation of time from t to τ so that the occurrence time t_j are transformed 1:1 into τ_j and the earthquakes follow the standard stationary Poisson process on the new axis if the intensity function is the true one for the data:

$$(7)$$

The process is called a **residual process** and its mean and standard deviation are used to study possible deviations of the data from the model (Ogata, 1992).

2.5 Coulomb stress changes calculations

This process includes the static stress changes calculations and the examination of their spatial distribution in connection with the spatial distribution of the aftershock activity. It has been observed in several cases that in addition to the main rupture, neighboring fault segments or minor active structures are activated soon after the main occurrence, which are the sources of aftershock clustering both in space and time. Oftentimes, relative quiescence takes place before this secondary activation. These occurrence patterns in the aftershock activity are then interpreted in terms of the stress field static changes.
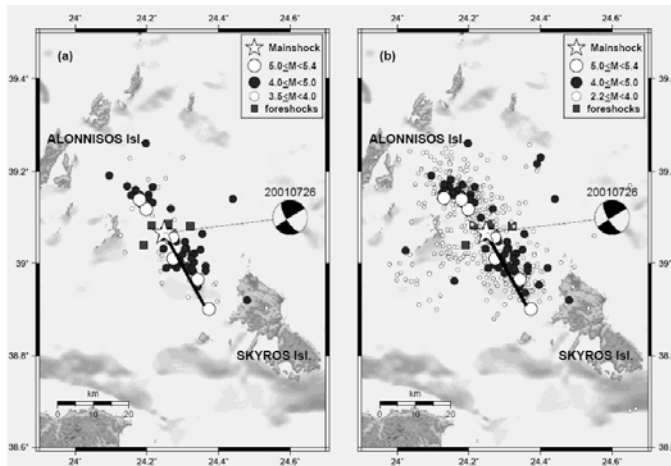
Fig. 1: a) The spatial distribution of the aftershocks ($M_w \geq 3.5$) which occurred in the first day after the main shock. Two separate clusters are shown, the one associated with the main rupture (black continuous line) and the second with an along strike adjacent fault segment. b) Spatial distribution of the aftershocks ($M_w \geq 2.2$) which occurred in the first month after the main shock. In addition to the activated segments shown in (a), a third cluster appears which striking NE–SW.

2.6 Data

The data used for the current analysis are taken from the monthly bulletins of the Central Seismological Station of Geophysics Department of the Aristotle University of Thessaloniki and the Institute of Geodynamics of the National Observatory of Athens. A unified catalog was compiled which covers the time interval from the beginning of each seismic sequence up to February of 2009. The data samples were checked for completeness and a threshold magnitude was assigned for each seismic sequence.

3. Seismic sequences analysis

3.1 Skyros seismic sequence

On 26 July 2001 an earthquake of $M_w = 6.4$ occurred at the submarine area between the islands of Allonisos and Skyros (39.05°N, 24.248°E), at the western part of central Aegean Sea. The rupture took place on a left–lateral NW–SE trending strike slip fault with a length of about 24 km (Karakostas et al., 2003). North Aegean region is dominated by right–lateral strike slip faults, trending NE-SW, as well as smaller normal faults (Papazachos et al., 1998). The fault which is connected with the main shock is conjugate to the right–lateral ones and appears to mark the boundary between them and the E–W trending normal faults of the Greek mainland (Karakostas et al., 2003). The sequence was attracted the interest of several scientists resulted in source models and stress field analysis (Zahradnik, 2002; Roumelioti et al., 2004; Ganas et al., 2005).

Aftershock activity was particularly intense, with seven aftershocks of $M_w \geq 5.0$ in the first day after the main shock occurrence. The epicentral distribution of the aftershocks of $M_w \geq 3.5$ which occurred in the first day delineate the main rupture, along with an along strike activated neighboring fault segment (Karakostas et al., 2003; Figure 1a). Smaller magnitude ($M_w \geq 2.2$) aftershock activity continued for a month onto the aforementioned segments, along with onto a seismic band to the WSW from the main shock epicenter, striking NE–SW (Figure 1b).

The RETAS model was applied on two data sets. Firstly, a catalogue of aftershocks was considered that covers the period from 26 July 2001 up to 26 February 2009, in a zone defined by the vertices 38.6°N–23.9°E; 39.3°N–24.8°E. The magnitude of completeness, calculated by the ZMAP software package (Wiemer and Zuniga, 2001) was found equal to $M_0 = 3.5$, which resulted to 449 events re-

Table 1. Model parameters estimated for two data sets, for Skyros sequence, 2001.

Data sets	Model	M_{th}	AIC	μ	k	α	c	p
26/07/2001–26/02/2009	ETAS	3.5	437.553	0	0.032	1.803	0.029	1.046
26/07/2001–30/07/2001	RETAS	4.0	-679.516	0	0.123	0.971	0.003	0.896
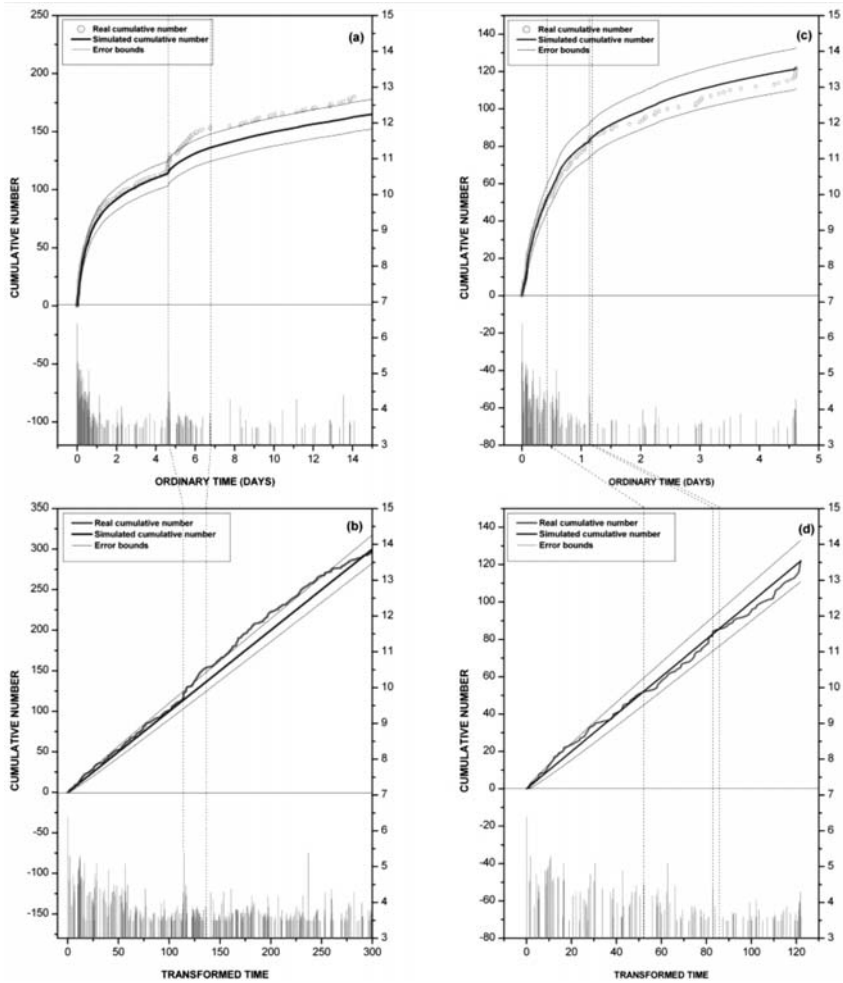
Fig. 2: Cumulative number of earthquakes (yellow circles and red solid lines) against ordinary (a, c) and transformed (b, d) lapse time respectively, in addition to the theoretically expected cumulative function (blue solid lines) due to the best fitting statistical model. Thin, solid blue lines stand for error bounds. Dashed lines appoint specific time periods and moments during the sequence evolution.

maining in the complete catalogue. The smallest AIC value as it is calculated by the Akaike criterion corresponds to the magnitude $M_{th}=3.5$ which is the smallest of the particular data set. Subsequently, ETAS is the best model to fit the data, meaning that all events with $M_o \geq 3.5$ are capable to produce secondary aftershocks. The estimated model parameters, for two data sets, μ, for the back-

ground seismicity, k which is related to the of the main shock and the cut-off magnitude M_o, α which measures the magnitude efficiency of a shock in generating its aftershock activity, c which is a regularizing time scale that ensures that the seismicity rate remains finite close to the main shock and p that is a coefficient of attenuation are shown in Table1. The table also contains the best fitting model, the smallest AIC value and the corresponding magnitude, M_{th}.

The model fitness to the data is verified graphically through the cumulative number curves. Real and expected number of aftershocks are plotted versus the normal and transformed time (Fig. 2). Yellow circles and solid red line indicate the real cumulative number of aftershocks and solid blue line represents the expected cumulative number curve. Figures 2a and 2c show the process in real time whereas Figures 2b and 2d depict the process in transformed time. Thin solid blue lines stand for error bounds determined after the standard deviation of the model process. Figures 2a and 2b show the curves for a 15–days period after the main shock occurrence. Generally, a quite good fit of the expected to real data for the whole period is revealed, except for a two days interval (between the dashed lines) immediately after the main shock, when an M_w=5.4 aftershock occurred on 30 July 2001. Obviously, the seismic activity increased after this event (first dashed line). Unlikely, relative seismic quiescence precursor to this large aftershock was not appeared. Particularly, in Figure 2b it is recognized that the activation period is separated in two sub-periods (red curve's slope). The first sub-period lasts two hours and the occurrence rate is highly increased, while the second one lasts about 44 hours and the occurrence rate seems to be decreased.

The above process was based on a 7.5 years data set and revealed seismicity behaviour, taking into account the whole data set. In order to identify possible deviations in real time before the M5.4 aftershock occurrence, the RETAS model is applied on a second data set which contains events that belong to the same zone, as defined previously, but they occurred in the time interval from the main shock up just before this aftershock (up to 30/07/2001). The magnitude threshold was found equal to M_o=3.5, above which the data were assessed to be complete, with the final number of events for processing to be equal to 123. The smallest AIC was calculated for M_{th}=4.0, which identifies that the best fit model is RETAS with the corresponding triggering magnitude. Model's parameters are shown in table 1.

In Figures 2c and 2d a period of relative quiescence is revealed before the large aftershock occurrence, which was not evidenced previously in Figures 2a and 2b, when the larger data set was considered. This means that the aftershocks which occurred after this particular aftershock affected and changed the temporal distribution of the events that occurred before. Relative quiescence begins about 10 hours after the main shock (first dashed line), it is interrupted for a time interval of about 20 minutes (between second and third dashed line), because of a cluster of aftershocks that occurred 17 hours after the beginning of the quiescence period, and reaches the large aftershock about 3 days later, with a total duration of about 4 days.

In order to investigate the possible triggering of this secondary sequence, in other words the "sequence in a sequence", the spatial distribution of its members are superimposed on the spatial distribution of the static stress changes due to the main shock co seismic slip. For this reason the stress field changes are calculated for an observational plane parallel to the aftershock zone which trends NW of the main shock (140°/70°/-110°), at a depth of 12 km and an apparent coefficient of friction μ́=0.6. Figure 3a shows the spatial distribution of Coulomb stress changes along with the epicenters of aftershocks that occurred during the first sub-period that corresponds to the particularly increased seismicity. It is observed that the aftershocks of the first sub-period and the largest aftershock epicenters are located into the northern lobe of the positive stress changes. The spatial distribution
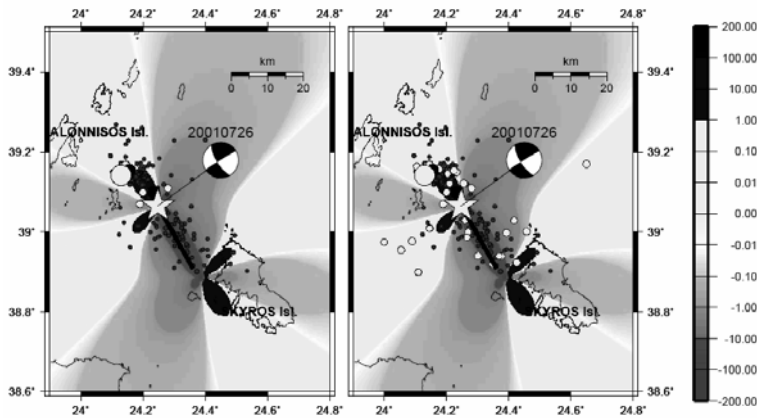
Fig. 3: Coulomb stress changes (in bars), due to Skyros main shock, calculated at a depth of 12 km, with μ′=0.6, for an observational plane parallel to the aftershock zone which trends NW of the main shock epicenter (140°/70°/-110°). The distribution of aftershock epicenters are shown for (a) the first sub-period and (b) for the whole period. Main shock is depicted by a yellow star, the M5.4 aftershock with a green circle, aftershocks of magnitudes 4.0≤M_w≤5.0 with red circles, aftershocks of magnitudes 3.5≤M_w<4.0 with yellow circles and the aftershocks prior to the M5.4 with blue circles.

of all aftershocks are plotted onto the stress field static changes in Figure 3b, where in addition to the clustered activity inside the northern lobe, a cluster is observed inside the southwestern lobe of positive stress changes. The precursory relative quiescence in association with the location of the lobes of positive static stress changes, explain satisfactorily the time and location of the largest aftershock occurrence.

3.2 Lefkada seismic sequence

On 14 August 2003 an earthquake of magnitude M_w=6.2 occurred near the NW coast of Lefkada Island (38.744°N–20.539°E). It is associated with a dextral strike slip fault, trending NNE–SSW with a length of about 15 km (Karakostas et al., 2004). This fault is a part of Lefkada segment of the Cephalonia Transform Fault Zone (CTFZ, Scordilis et al., 1985). Lefkada and Cephalonia constitute the most active regions, in terms of shallow seismicity, in the broader Aegean region. The CTFZ is considered to be the boundary between the continental collision of the Outer Hellenides and the Adriatic micro plate to the north and the oceanic subduction of the Eastern Mediterranean lithosphere under the Aegean Sea to the south (Papazachos and Comninakis, 1971).

Intense aftershock activity followed the occurrence of the main shock. The main cluster of aftershocks is located to the NW of the island, defining a NNE–SSW seismic band, in agreement with the strike of one of the main shock nodal planes (18°/60°/–175°), which is considered the fault plane (Karakostas et al., 2004). Main shock epicenter is located at the southern part of this cluster, implying a unilateral rupture, whereas two more clusters, well separated, appeared to the north and south of the main cluster, respectively (Karakostas, 2008). Aftershock activity also extended from the SW edge of Lefkada Island up to the NW coasts of Cephalonia Island, probably triggered by the main shock since it was located inside a lobe of positive static stress changes (Karakostas et al., 2004).

The RETAS model applied onto three data sets. The events of the first data set occurred during the

Table 2. Model parameters estimated for three data sets, for Lefkada sequence, 2001

Data sets	Model	M_{th}	AIC	μ	k	α	c	p
14/08/2003-01/02/2009	ETAS	3.8	623.943	0	0.025	2.68	0.094	1.059
14/08/2003-16/11/2003	MOF	6.2	-365.929	0	17.741	1.106	2.585	1.691
14/08/2003-25/03/2007	ETAS	3.7	283.41	0	0.026	2.767	0.228	1.092

period 14 August 2003–1 February 2009 in a region defined by the vertices 38.2°–20.1°, 39.1°–20.8°. A completeness magnitude of M_o=3.8 was estimated by the ZMAP software and thus a complete catalogue of 464 aftershocks was derived. The smallest AIC value was calculated for M_{th}=3.8 which implies that the best–fit model is ETAS and thus, each aftershock of M≥3.8 can trigger secondary aftershocks. Model's parameters are shown in Table 2.

Two periods of intense activation which followed the occurrence of the main shock and of a M5.7 event, respectively, are shown in Figure 4a. The later, occurred on 25 March 2007 near the NW Coast of Cephalonia Island (second dashed line), which is comprised into the study area. A smaller activation was triggered by an aftershock of magnitude M_w=4.8 which occurred on 16 November 2003 (first dash line). Model's fitting at the intense activation which follows the main shock (Fig. 4b) is insufficient. Periods of relative seismic quiescence which are connected with the large aftershocks are also revealed (Fig. 4b). The above process was based on the first data set which includes the aftershocks that occurred during the whole time interval from 2001 up to 2009. In order to seek for possible quiescence periods precursor to the aforementioned M4.8 and M5.7 events, in real time, the RETAS model is applied on two different data sets with events that occurred at the same region, as defined previously, but in more confined time intervals, that is from the main shock up just before the occurrence times of these two shocks, respectively.

Thus, in the case of the M4.8 event, a catalogue of 175 events was considered, with a magnitude cut-off of M_w=3.8, determined with the ZMAP software (Wiemer and Zuniga, 2001). The smallest AIC value is for a triggering magnitude of M_{th}=6.2, which is equal to the magnitude of the main shock and this result recognizes the MOF model to fit best the aftershock temporal evolution of this particular data set. This means that only the main shock can trigger secondary aftershocks. Model parameters are shown in table 2. Figures 4c and 4d evidence that the model fits very well the data, while a period of relative seismic quiescence prior to the M4.8 event is not observed.

In the case of the M5.7 event, a catalogue of 397 aftershocks was prepared, with magnitudes above the cut–off M_o=3.7 determined by the ZMAP software. The smallest AIC was calculated for M_{th}=3.7 which identifies the best fit model to be ETAS. Model's parameters are shown in table 2. Figures 4e and 4f show that this particular model cannot fit sufficiently well the temporal evolution pattern of the real data, because periods are revealed in which the curve of the expected, by the model, data exceeds the error bounds.

In order to investigate the possible triggering of the sequences which followed with main shocks of M4.8 (16/11/2003) (secondary sequence) and M5.7 (25/03/2007), the aftershock spatial distributions are plotted onto maps depicting the spatial distribution of the static stress changes due to the 2003 main shock. The static stress changes are calculated, at a depth of 8 km and an apparent coefficient of friction μ=0.6, firstly, for a dextral strike slip fault in agreement with the fault plane solution of the May 1983 event (28°/82°/172°) which is the stronger event located in the vicinity of M4.8's (16/11/2003) epicenter. Figure 5a evidences that the members of this secondary sequence,
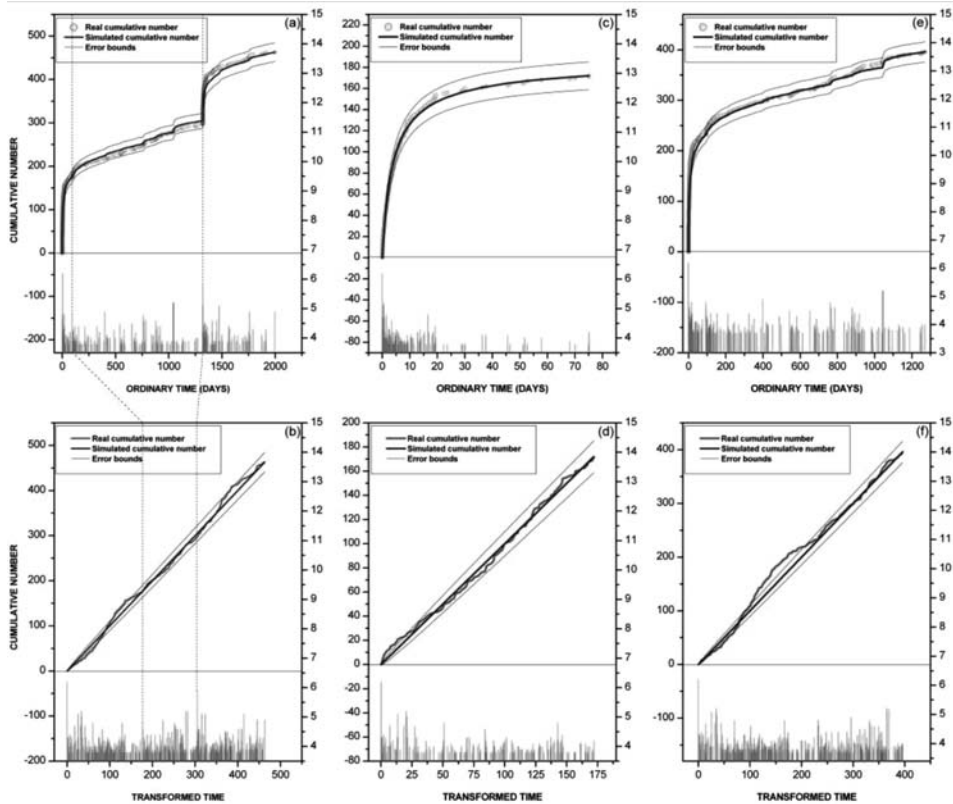
Fig. 4: Cumulative number of earthquakes (yellow circles and red solid lines) against ordinary (a, c, e) and transformed (b, d, f) lapse time respectively, in addition to the theoretically expected cumulative function (blue solid lines) due to the best fitting statistical model. Thin, solid blue lines stand for error bounds. Dashed lines appoint specific time periods and moments during the sequence evolution. (a, b), (c, d), (e, f) correspond to the first, second and third data sets, respectively.

which increased the rate of real seismicity (Fig. 4a) are located inside the southern lobe of positive Coulomb stress changes. The stress field is then calculated according to the fault plane solution of the M5.7 event (216°/75°/–175°). It is observed that this main event and its aftershocks, which comprise the intense seismicity period, are located mainly into the southern lobe of positive stress changes (Fig. 5b).

4. Conclusions

From the temporal distribution of Skyros aftershock sequence, a precursory relative quiescence was observed before the stronger aftershock of M5.4, which occurred in the first day after the main shock. This fact in association with the location of this particular aftershock epicentre into the positive stress changes lobe, guides to the conclusion that assessment of a seismic excitation inside a seismic sequence, in real time, is quite possible. It is remarkable that this period was revealed when the appropriate model was applied at the second data set only, which covered the time interval between the main shock and just before the M5.4 event, but not in the model application to the whole data set.
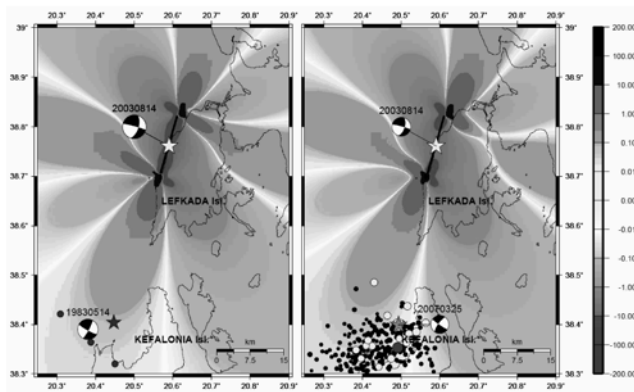
Fig. 5: Static Coulomb stress changes (in bars), due to Lefkada main shock (yellow star) at a depth of 8 km with μ=0.6 (a) for a representative dextral strike slip fault (28°/82°/172°) of an event occurred on May 1983 near to the M4.8 aftershock (blue star). Blue circles show the epicenters of a cluster of aftershocks that followed the M4.8, all located into the southern lobe of positive stress changes. (b) Static stress changes calculated for the M5.7 event (orange star) faulting type (216°/75°/-175°). Aftershocks of magnitudes $2.5 \leq M_w \leq 4.0$ are shown with red circles, $4.0 \leq M_w < 5.0$ with green circles and the ones of $5.0 \leq M_w < 5.7$ with blue circles. M5.7 and its aftershocks are located, mainly, into the southern lobe of positive stress changes.

The analysis of Lefkada seismic sequence evidences abrupt changes in the occurrence rate of aftershocks and later seismicity, after the occurrence of two strong events. The spatial distribution of the members of these two secondary sequences is associated with positive static stress changes, revealing their possible triggering form the 2003 main shock.

Finally, analysis of different sets in both sequences evidenced that the most appropriate statistical model that fits the data can be different, when the analysis concerns different data sets even inside the same aftershock sequence.

5. Acknowledgments

6. References

Akaike, H., 1974. A new look at the statistical model identification, IEEE Trans. Automat. Control., AC–19, 716–723.

Erikson, L., 1986. User's manual for DIS3D: A three-dimensional dislocation program with applications to faulting in the Earth. Masters Thesis, Stanford Univ., Stanford, Calif., 167pp.

Ganas, A., Drakatos, G., Pavlides, S. B, Stavrakakis, G. N, Ziazia, M., Sokos, E., and Karastathis, V. K., 2005. The 2001 M_w=6.4 Skyros earthquake, conjugate strike–slip faulting and spatial variation in stress within the central Aegean Sea. J. Geodynamics, 39, 61–77.

Gospodinov, D. and Rotondi, R., 2006. Statistical analysis of triggered seismicity in Kresna region of SW Bulgaria, (1904) and the Umbria–Marche Region of Central Italy (1997). Pure Appl. Geophys, 163, 1597–1615.

Karakostas, V. G., Papadimitriou, E. E. and Papazachos, C. B., 2004. Properties of the 2003 Lefkada, Ionian Islands, Greece, earthquake seismic sequence and seismicity triggering, Bull. Seism. Soc. Am., 87, 463–473.

Karakostas, V. G., 2008. Relocation of aftershocks of the 2003 Lefkada sequence: Seismotectonic implications /Proc. 3rd Hellenic Conf. Earthquake Engineering & Engineering Seismology, Athens 5–7 Nov. 2008/, CD ROM, pp.16.

Kisslinger, C., 1988. An experiment in earthquake prediction and the 7th May 1986 Andreanof Islands earthquake, Bull. Earthquake Res. Inst. Univ. Tokyo, 61, 1–65.

Ogata, Y., 1988. Statistical models for earthquake occurrences and residual analysis for point processes. J. Am. Stat. Assoc. 83, 9–27.

Ogata, Y., 1992. Detection of precursory relative quiescence before great earthquakes through a statistical model, J. Geophys. Res., 97, 19, 845-19,871.

Ogata, Y., 1999. Seismicity analyses through point process modeling: A review, Pure Appl. Geophys., 155, 471–507.

Ohtake, M., T. Matumoto, and G. V. Latham, 1997. Seismicity gap near Oaxaca, southern Mexico as a probable precursor to a large earthquake, Pure Appl. Geophys., 115, 375–385.

Omori, F., 1894. On the aftershocks of earthquakes. J.Coll. Sci., Imp. Univ. Tokyo 7, 111-200.

Papazachos, B. C., E. E. Papadimitriou, A. A. Kiratzi, C. B. Papazachos, and E. K. Louvari, 1998. Fault plane solutions in the Aegean and the surrounding area and their tectonic implications, Bull. Geof. Teor. Appl., 39, 199–218.

Papazachos, B. C. and P. E. Comninakis, 1971. Geophysical and tectonic features of the Aegean Arc, J. Geophys. Res. 76, 8517–8533.

Roumelioti, Z., Kiratzi, A. and Dreger, D., 2004. The source process of the 2001 July 26 Skyros Island (Greece) earthquake, Geophys. J. Intern., 156, 541–548.

Scordilis, E. M., Karakaisis, G. F., Karakostas, B. G., Panagiotopoulos, D. G., Comninakis, P. E. and Papazachos, B. C., 1985. Evidence for transform faulting in the Ionian Sea: The Cephalonia Island earthquake sequence, Pure Appl. Geophys., 123, 288–397.

Utsu, T., 1968. Seismic activity in Hokkaido and its vicinity (in Japanese), Geophys. Bull. Hokkaido Univ., 13, 99–103.

Utsu, T., 1969. Aftershocks and earthquake statistics (I): some parameters which characterize an aftershock sequence and their interaction. J. Fac. Sci., Hokkaido Univ., Ser. VII 3, 129–195.

Wessel, P. and Smith, W. H. F., 1998. New, improved version of the Generic Mapping tools Released, EOS Trans. AGU, 79, 579.

Wiemer, S. and Zuniga, R. F., 2001. ZMAP: A software package to analyze seismicity, EOS, Trans, 44, 456.

Wyss, M., and R. O. Burford, 1987. A predicted earthquake on the San Andreas fault, California, Nature, 329, 323–325.

Zahradnik, J., 2002. The weak–motion modelling of the Skyros island, Aegean Sea M_w=6.5 earthquake of July 26. Studia Geophys. Geodaet., 46, 753–771.

SOURCE PARAMETERS OF MODERATE AND STRONG EARTHQUAKES IN THE BROADER AREA OF ZAKYNTHOS ISLAND (W. GREECE) FROM REGIONAL AND TELESEISMIC DIGITAL RECORDINGS

Chousianitis K.[1], Agalos A.[1], Papadimitriou P.[1], Lagios E.[1] and Makropoulos K.[1]

[1] Department of Geophysics-Geothermics, National & Kapodistrian University of Athens, 15784 Panepistimiopolis – Greece, chousia@geol.uoa.gr, aagalos@geolo.uoa.gr, ppapadim@geol.uoa.gr, lagios@geol.uoa.gr, kmacrop@geol.uoa.gr

Abstract

The source parameters of all the moderate and strong events that occurred in the broader area of Zakynthos Island for the period 1997–2009 are determined using two different techniques depending on epicentral distance. For the strong events we employed teleseismic body-wave modeling between 30° and 90°, while for moderate events a regional moment tensor inversion approach was used. In both cases we used broadband waveform data with a good signal-to-noise ratio. The calculated focal mechanisms are representative of the displacement and strain fields of the broader area. Those associated with the Cephalonia transform fault are consistent with dextral strike-slip motion. The area between the island of Zakynthos and the Western coast of Peloponnese is also characterized by strike–slip faulting, while reverse faulting is mainly observed south of Zakynthos Island. Using both techniques, we also retrieved the source parameters of the biggest events of the seismic sequence of April 2006 near the southern coast of Zakynthos Island. The depths of the located events of the sequence vary mainly between 10 and 25 km. The fault plane solutions revealed thrust type faulting in all cases, something which can be related with upward motions in the southern part of the Island observed by DGPS measurements.

Key words: source parameters, teleseismic modeling, moment tensor inversion, Zakynthos Island.

1. Introduction

Body-wave modeling has proven quite effective in determining the earthquake source parameters (eg. Kikuchi & Kanamori, 1991; Kikuchi et al., 1993; Papadimitriou P., 1983; Papadimitriou et al., 2006; Chousianitis, 2009). It can be divided into teleseismic and regional depending on the epicentral distance of the recorded phases. The magnitude threshold for source parameters determination using teleseismic body-wave modeling is approximately $M_w=5.7$, as teleseismic phases become too weak for smaller events and thus regional data must be used, which are generally much more complicated by strong interaction with the heterogeneous crust and upper mantle structures (Papadimitriou P., 1988). However at regional distances the above mentioned threshold is lowered to approximately $M_w=3.8$, and frequency-magnitude relations have lead to the obvious conclusion that regional-distance modeling has allowed researchers to increase the number of studied events, especially in areas with regional broadband instrumentation (Saikia et al., 2001; Agalos et al., 2008).

Two kinds of regional waveform data are typically used for source estimation, surface waves (Thio & Kanamori 1995) and body waves (Fan et al., 1994; Dreger & Helmberger, 1993). In the present study body waves are used, which are generally less affected by shallow heterogeneities and are more stable than surface waves, although they have a lower signal-to-noise ratio due to their smaller energy. In general, the teleseismic body waves contain the information on the overall moment release rate and the depth range of the rupture area, while regional waveforms contain most of the information on the detailed slip process in the source area. Therefore, it is important to use both the teleseismic body wave and regional data to estimate the detailed and stable source process.

The most reliable solutions of 100 events, taking into account the station coverage and the correlation error related to the fitting of the synthetics to the data, that occurred during the time interval from 1997 until 2009 in the broader area of Zakynthos Island are presented in this study. The objective of this paper is to present a dense database of regional focal mechanisms for intermediate and strong events which fully cover the broader area of Zakynthos Island, a very active region of particular scientific interest. Synthetic seismograms were generated for P, SH and SV broadband waveform data in order to determine the strike, dip and rake of the fault plane, the centroid depth, the seismic moment and the source time function of each modeled earthquake. For the implementation of teleseismic modeling the data used comes from the IRIS (Incorporated Research Institutions for Seismology) Global Digital Seismographic Network (GDSN), while the observed waveforms for regional modeling were taken from stations belonging mainly to the Hellenic Unified Seismological network, as well as stations from Mednet and Geofon networks. At the same time, we were able to study the strongest events of the seismic sequence that occurred near the southern coast of Zakynthos Island during April and May 2006 and correlate them with DGPS results. These measurements carried out on Zakynthos Island for the time period August 2005 – July 2006 revealed intense uplift in the southern part of the Island, bounding the area of Laganas Bay (Lagios et al., 2007; Chousianitis, 2009).

2. Geological-Tectonic Setting

The study area is located in Western Greece, near the boundary between the African and the Eurasian lithospheric plates, at the northwestern end of the Hellenic Arc – Trench System. This boundary comprises a zone of volcanic activity and intense seismicity that results in numerous earthquakes and extends along South Ionian Sea and Western Peloponnesus, continues along the islands of Kythera and Antikythera to south of Crete and terminates to Rhodes Island. The plate movements along the Hellenic Arc – Trench System and the associated seismicity have also formed a series of sea basins extending from Cephalonia to Rhodes. This zone has been formed along the boundary of the two lithospheric plates as the northern segment of the African plate south of the Adriatic Sea, which comprises the Eastern Mediterranean oceanic lithosphere, is subducted beneath the higher density continental lithosphere of Eurasia - part of which is the Aegean microplate (Le Pichon & Angelier, 1979). This subduction zone terminates against the Cephalonia transform fault, a major dextral strike-slip fault, which follows the submarine Cephalonia valley west of the island chain from Lefkas to Cephalonia and links this subduction with the continental collision between the Apulia microplate and the Hellenic Foreland, which is observed north of Lefkada (Finetti & Morreli, 1973; Scordilis et al., 1985; Anderson & Jackson, 1987; Papadimitriou P., 1988) (Fig. 1).

The broader area of Zakynthos Island is presently one of the most seismo-tectonically active areas not only in Greece, but also in the entire Mediterranean region (Jackson & McKenzie, 1988). This is reflected on the existed comprehensive catalogues of seismic events for Greece, where the occurrence of more than 4500 intermediate-size earthquakes during the last 50 years, with several large and de-
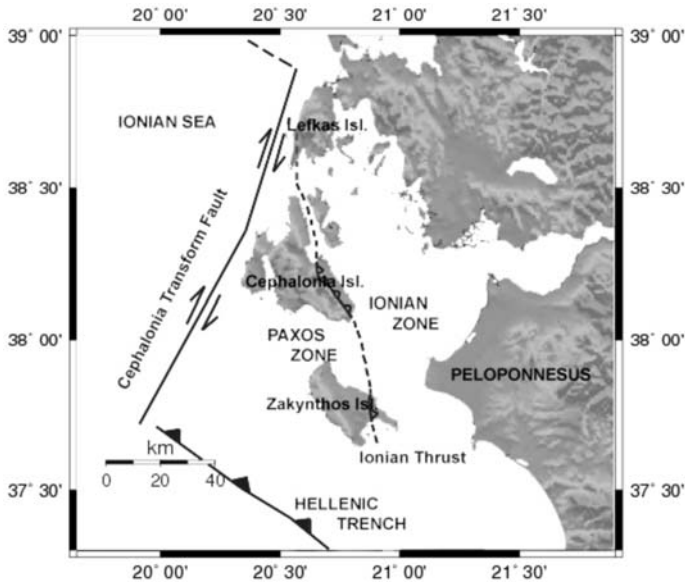
Fig. 1: Main tectonic features of Central Ionian Islands. The subduction zone (line with teeth), the Cephalonia transform fault (arrows) and the continental collision boundary (dashed line) are shown.

structive events among them, can be confirmed (Makropoulos & Burton, 1981). The area is characterized by horizontal compression almost perpendicular to the Hellenic Arc, which is thought to have been initiated during the Miocene (Hatzfeld et al., 1990). Consequently, most of the earthquakes in this particular region of the Hellenic Arc involve reverse motion. Palaeomagnetic studies of Cenozoic rocks in the Aegean region (Kissel & Laj, 1988) demonstrate that parts of Western Greece have undergone substantial clockwise rotation during the Neogene simultaneously with compression.

The geology of the study area is characterized by complex structural and stratigraphic features. Two geotectonic zones from west to east are defined, the Pre-Apulian or Paxos and the Ionian, with their boundary being the Ionian thrust, which is considered to represent the most external Hellenide structure. These geotectonic zones are defined on the basis of different sedimentary facies of exposed Mesozoic and Cenozoic rocks and different tectonic styles. Compressive tectonism related to Alpine deformation and major recurrent movement of evaporite successions during both Mesozoic and Cenozoic time has produced complicated folding and different type of faulting. The Pre-Apulian Zone experienced significant late Neogene and Quaternary shortening (Underhill, 1989). The corresponding stratigraphy of Paxos zone contains a thick series of Mesozoic to Palaeogene carbonates that are overlain by a series of folded Oligocene to earliest Tortonian deepmarine marls and interbedded turbiditic calcareous sandstones (Underhill, 1989). Respectively, the known stratigraphic succession consists of 6000-7000 m of chiefly carbonate and evaporite strata of Triassic to Eocene age overlain by 1000-4000 m of Oligocene and Lower Miocene flysch deposits.

3. Teleseismic Body-Wave Modeling

A teleseismic body-wave modeling was employed in order to determine the source parameters of the largest events that occurred in the broader area of Zakynthos Island for the past decade. At these dis-

tances, the shape of the seismic waves depend upon both the depth of the source and the orientation of the nodal planes and they have paths that lie almost entirely within the lower mantle and are not affected by the local structure of the upper mantle. In the present analysis, the source parameters have been constrained by a visual comparison between observed and synthetic waveforms on a trial and error basis. The waveform data used consisted of digital recordings obtained from the Incorporated Research Institution for Seismology (IRIS) and Global Digital Seismographic Network (GDSN) broadband components.

The calculation of a synthetic seismogram $W(t)$ is based on the convolution of four linear operators:

where $U(t)$ is the far-field displacement, $S(t)$ is the source time function, $Q(t)$ is the attenuation and $I(t)$ is the instrument response. The far-field wave displacement recorded at azimuth ϕ and epicentral distance Δ, is calculated using the formula (Kanamori & Stewart, 1976; Aki & Richards, 1980):

where $U(t)$ is the vertical, radial or transverse displacement in case of P-, SH- or SV-waves, respectively, $g(\Delta)$ is the geometric spreading, α is the Earth radius, R denotes the radiation pattern in case of P-, SH- or SV-waves, c denotes the Vp or Vs velocity, ϱ is the density, i_h and i_0 is the angle of incidence at the source and the receiver respectively, C is the free surface effect and M_0 is the seismic moment.

Only seismograms recorded at epicentral distances between 30° and 90° with a good signal-to-noise ratio were used, a constraint that ensures the avoidance of complexities due to the upper mantle response and to core phase effects. Body waves at these distances do not experience triplication or diffraction near the core-mantle boundary that severely complicate the observed waveforms. Instrument responses were deconvolved from the original recordings to obtain true ground displacement records. The waveforms were band-pass filtered generally at corner frequencies f1=0.02 Hz and f2=0.2 Hz using a Butterworth filter in order to remove the high frequency noise and to attain a good signal-to-noise ratio. In addition, for the estimation of the attenuation factor Q(t), we used Futterman's operator with t* equal to 1 second for P waves and 4 seconds for SH and SV waves (Futterman, 1962). Overall we computed the source parameters of six earthquakes close to Zakynthos Island with moment magnitudes M_w>5.4. Information on the focal parameters of the events studied is given in Table 1.

Table 1. Source parameters determined by teleseismic waveform modeling.

Date	Origin Time	M_w	M_0 (dyn·cm)	Depth (km)	Source Duration (sec)	Strike (º)	Dip (º)	Rake (º)
18/11/1997	13:07	6.5	$0.8 \cdot 10^{26}$	40	10	116	86	70
31/01/2005	01:05	5.6	$3.5 \cdot 10^{24}$	10	4	342	12	115
18/10/2005	15:25	5.7	$5.5 \cdot 10^{24}$	15	4,5	12	15	130
11/04/2006	00:02	5.4	$1.8 \cdot 10^{24}$	18	4	142	59	70
11/04/2006	17:29	5.5	$2.5 \cdot 10^{24}$	13	4	140	70	85
12/04/2006	16:52	5.6	$3.5 \cdot 10^{24}$	13	4	25	25	135

4. Regional Moment Tensor Inversion

The seismic moment inversion method is widely employed in determining focal mechanisms from local and regional broadband seismograms via the production of reliable synthetic waves at distances less than 1000 km. The advantage of this approach is that the magnitude threshold of events that can be analyzed has been lowered to less than 4 comparing to teleseismic waveform modeling. The method of P arrivals, for a long time, was the only method that could be used with regional and local waveforms in order to reveal the focal mechanism. Recently it was succeeded, to produce reliable regional synthetic waves (Fukuyama & Dreger, 2000; Ichinose et al., 2003). From that moment it was quite easy to use the regional waveforms and the produced synthetic ones to calculate source parameters through a linear inversion procedure. One of the inversion methods is the frequency-wavenumber (F-K) integration method (Saikia, 1994; Zeng & Anderson, 1995; Bouchon, 2003). This method which is applied in the present study mainly for moderate earthquakes, calculates synthetic waves directly compared with the observed ones for a given velocity structure. Synthetics were generated using the reflectivity and frequency-wavenumber summation technique proposed by Zeng and Anderson, (1995). This code based on the generalized reflection and transmission coefficient method computes 10 fundamental Green functions as it is described by Herrmann and Wang, (1985). These 10 Green functions are then combined together with the moment tensor elements in order to produce the 3 components of motion for a known focal mechanism known as the tangential, radial and vertical component as proposed by Jost and Herrmann, (1989). In more detail the methodology computes differential seismograms directly in a layered elastic half-space. First the medium velocity differential field is computed with respect to the velocity change in the layer and then multiplies it by the original elastic wave field. The obtained differential waves are propagated directly to the receiver using the generalized R/T matrix method. The synthetics are calculated using the discrete wavenumber summation and imaginary frequency technique (Bouchon, 1979). The applied moment tensor inversion used the codes of Ichinose et al. (2003), for different source depths.

A very significant parameter which is strongly connected with the quality of the obtained focal mechanism solution is the azimuthal coverage. In order to minimize the bad effects of the possible poor azimuthal coverage we used only stations with good signal to noise ratio. The observed waveforms for the selected earthquakes were taken from stations belonging to the Unified Hellenic network and to the Mednet and Geofon networks with a good signal to noise ratio. In most cases we used at least three or four stations. The strong ones were modeled using data from more than eight stations. In all cases for the presented solutions the fit between observed data and synthetics was quite good. Instrument responses were deconvolved to receive pure displacement. The regional broad-band data were also band-pass filtered in frequencies between 0.01-0.05 Hz for events larger than $M_w > 5.0$ and between 0.02-0.05 Hz for events with $M_w < 5.0$. Finally the horizontal components were rotated to the radial and tangential components. Over 100 earthquakes which occurred in the broader area of Zakynthos Island have been modeled using this method for the time period 1997-2008 (Fig. 2a).

5. Strongest Events of April 2006 Seismic Sequence

Using both regional and teleseismic modeling, we also obtained a significant number of focal mechanism solutions belonging to the seismic sequence of April 2006 near the southern coast of Zakynthos Island (Fig. 2b). In the following section we discuss the modeling results at regional and teleseismic distances for two of the strongest events of the sequence, which occurred on 4 and 12 April respectively.
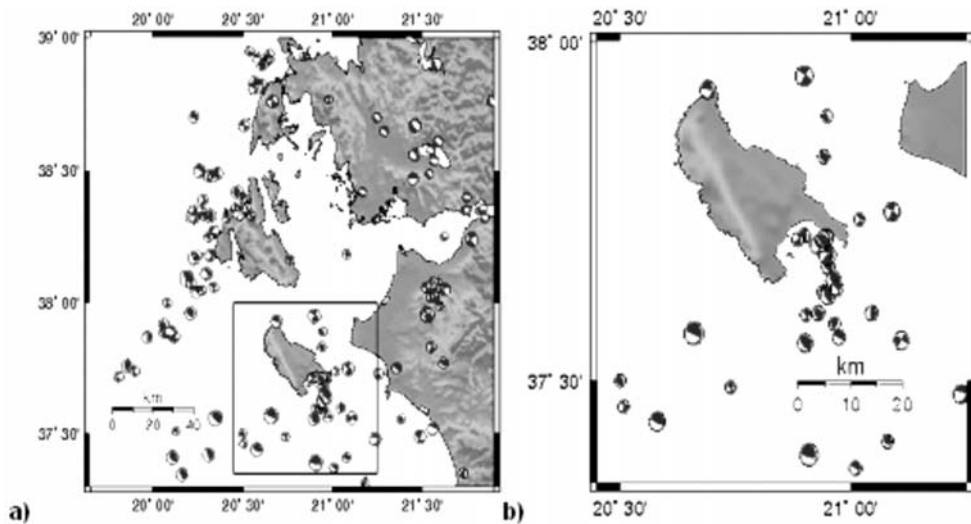
Fig. 2: a) Focal mechanism solutions of moderate and strong earthquakes for the period between 1997 and 2008. Black quadrants denote compression and white dilatation. b) Focal mechanism solutions belonging to the seismic sequence of April 2006.
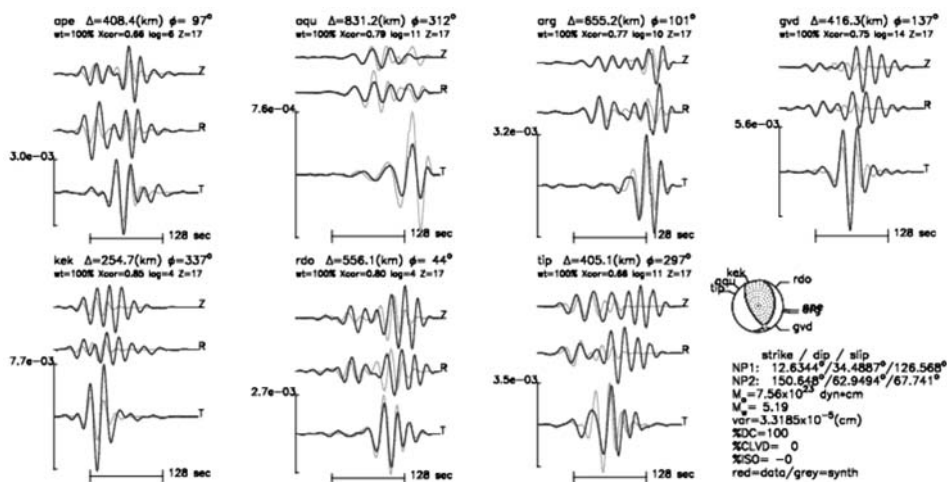
Fig. 3: Best fit focal mechanism obtained from comparison between synthetic and observed regional broad-band records for the April 4, 2006 (22:05), M_w=5.2 earthquake.

Event of April 4, 2006 (22:05)

On April 4, 2006 (22:05 GMT) the first earthquake of magnitude M_w=5.2 of a series of four events, belonging to the seismic sequence of April 2006, with magnitudes M_w>5.0 occurred. The epicenter of this event (20.951°E, 37.626°N) was located near the southern coast of Zakynthos Island and was felt in the broader area. The lack of available data at teleseismic distances led us to employ the seismic moment tensor inversion method for regional broadband seismograms at distances less than
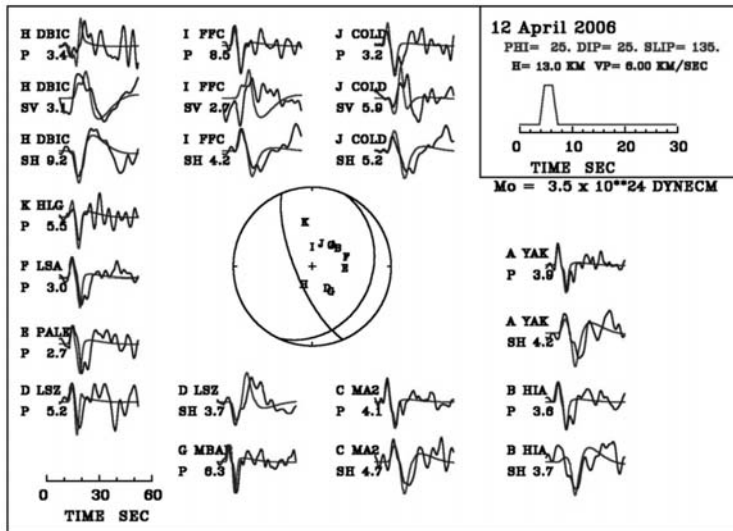
Fig. 4: Best fit focal mechanism and source time function (inset) obtained from comparison between synthetic and observed broad-band records for the April 12, 2006 (16:52) earthquake.

1000 km. The production of reliable synthetic waveforms revealed thrust faulting with strike=13°, dip=34° and rake=127°, while the focal depth is 17 km and the seismic moment of the order of 7.56·10²³ dyn·cm (Fig. 3). The focal mechanism reported by Harvard (strike=359°, dip=25°, rake=117°, depth=19.5 km) is not far from the solution shown in figure 3.

Event of April 12, 2006 (16:52)

On April 12, 2006 (16:52 GMT) the strongest event (M$_w$=5.6) of the seismic sequence of 2006 occurred. The epicenter (20.963˚E, 37.648˚N) is located at the same area with the one of the April 4th earthquake and a few kilometres south of the epicenters of the events that took place the previous day. The available data allowed us to employ teleseismic body-wave modeling. Synthetic waveforms were generated using a simple trapezoidal source time function of 4 sec duration. Here, 11 teleseismic stations with good azimuthal coverage for the generation of P waves, 7 for SH waves and 3 for SV waves were used. The selected stations provide a satisfactory azimuthal coverage of the focal sphere, which helped us to accurately define the nodal planes of the focal mechanism. Finally, the obtained focal parameters revealed fault plane solution with strike=25°, dip=25°, rake=135°, which indicates thrust faulting. The seismic moment is equal to 3.5·10²⁴ dyn·cm, and the focal depth was found to be 13 km. The result obtained by the method shows quite satisfactory fitting between the observed and the synthetic waveforms for both P, SH and SV waves (Fig. 4). The focal mechanism reported by Harvard for this event (strike=2°, dip=23°, rake=121°) is in a good agreement with the calculated one, while the estimated depth (20.5 km) is slightly different. However, fixing the depth equal to that of the Harvard solution, the synthetics displayed a mismatch shape with the observed.

All the calculated fault plane solutions of the April 2006 seismic sequence are distributed on a NW-SE direction, and revealed a compressional regime, with a small differentiation in the direction (Fig. 2). The focal depths of the most hypocenters are confined between 10 and 25 km, which might reflect the absence of shallow rupture in this area.
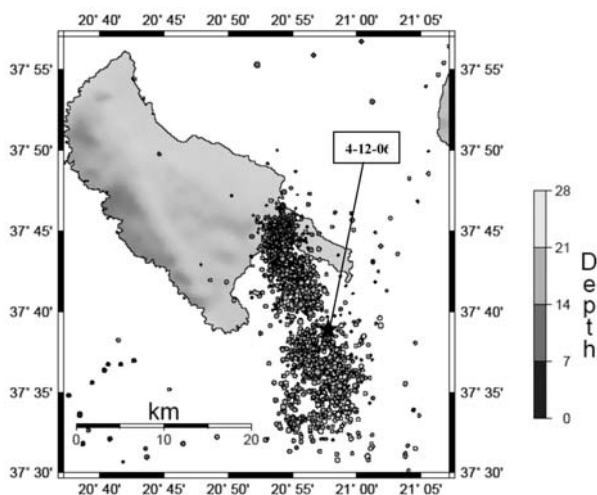
Fig. 5: Epicenter distribution map of the April 2006 seismic sequence. Approximately 1600 events are plotted with RMS < 0.1sec, ERH < 3km and ERZ < 2km.

6. Epicenter Distribution of April 2006 Seismic Sequence

The intense seismic activity during April-May 2006 led the Earthquake Planning and Protection Organization (E.P.P.O.) to the installation of a temporary seismological network constituted of five digital seismographs on Zakynthos Island. The collection of seismic data for this experiment began in April 14, 2006 and lasted up to July 9, 2006. The location of all the earthquakes that were recorded during the operation of the E.P.P.O. seismological network was determined by the help of HYPO71 (Lee and Lahr, 1975) and Hypoinverse with almost similar results. On the whole, nearly 3500 hypocenters with magnitude > 1.7 were located and 1600 of them (with RMS < 0.1sec, ERH < 3km and ERZ < 2km) are presented in figure 5. Examining the epicenter distribution map, it can be observed that the seismicity is grouped in two main clusters in a general NNW-SSE direction. The first cluster is located inside the Gulf of Zakynthos Island, while the other one continues southwards. The two clusters are separated by a narrow region in which absence of the intense seismicity is observed (Chousianitis, 2009). The largest event of the sequence that was occurred on April 12 (denoted with a star in figure 5) and discussed earlier belongs to the southern cluster, very near to the intermediate area.

7. Conclusions

The most reliable source mechanisms and seismic moments of a significant number of events that occurred during the time interval from 1997 until 2009 in the broader area of Zakynthos Island are presented. Seismograms recorded by digital broadband stations at local and regional epicentral distances and at teleseismic distances between 30° and 90° were used. We employed two different techniques, which both allow good accuracy in the determination of the fault plane solution and ensure reliable estimation of the scalar seismic moment. For regional distances we used a moment-tensor inversion method, while for teleseismic distances we employed body-wave modeling.

The calculated focal mechanisms in the westernmost part of the studied area around Cephalonia Island clearly show dextral strike-slip motion associated with the transform zone along the Central Ionian Islands and emphasize the importance of the component of right-lateral shear within that region. This motion is consistent with tectonic studies (e.g. Underhill, 1989) GPS geodetic observations (Lagios et al., 2007; Chousianitis, 2009), and also with the focal mechanisms computed in this area (Scordilis et al., 1985; Papadimitriou P., 1988; Hatzfeld et al., 1990). Reverse faulting appears west and south of Zakynthos Island,

along the external part of the Hellenic Arc, which is associated with crustal shortening and active subduction. Over this zone, the depths revealed by the calculated fault plane solutions varied between 10 and 40 km. Normal faulting is observed around the Trihonis Lake, where neotectonic studies suggest N-S extension (Mercier et al., 1987). Of special interest is the area between the island of Zakynthos and the Western coast of Peloponnese where shallow and deeper events of strike–slip faulting occur.

Finally, using both methodologies we were able to study the strongest events of the seismic sequence that occurred near the southern coast of Zakynthos Island on April 2006, which is grouped in two main clusters separated by a narrow aseismic region (Chousianitis, 2009). Overall, more than 15 earthquakes of magnitude $M_w > 4$ occurred for a period of two months from April until May, 2006. In all cases, the obtained focal mechanisms revealed thrust motions in a general NNW-SSE direction that may be explained by the compressive tectonics that dominate south of Zakynthos Island and can be correlated with upward motions observed for the same time period, as deduced by DGPS measurements in the southern part of the Island (Lagios et al., 2007; Chousianitis, 2009).

8. Acknowledgments

9. References

Agalos A., Papadimitriou P. and Makropoulos K., 2008. Rupture Histories of Strong Earthquakes. 31st General Assembly of the European Seismological Commission, held at the Creta Maris Conference Center, Hersonissos, Crete Greece, Book of Short papers, p 9-16.

Aki, K. and Richards, P.G., 2002. Quantitative Seismology. University Science Book, 2nd edition, Sausalito, California.

Anderson, H. and Jackson J., 1987. Active tectonics of the Adriatic region. Geophys. *J. R. Astr. Soc.*, 91, 937-983.

Bouchon M., 1979. Discrete wave number representation of elastic wave fields in three-space dimensions. *Journal of Geophysical Research,* 84, 3609–3614.

Bouchon, M., 2003. A review of the discrete wavenumber method. *Pure Appl. Geophys.* 160, 445–465.

Chousianitis K., 2009. Seismic source properties and ground deformation study of the broader area of Cephalonia and Zakynthos Islands using Geophysical and Space techniques. Doctorate Thesis, Department of Geophysics-Geothermics, University of Athens, p.280 (in Greek).

Dreger, D.S. and Helmberger, D.V., 1993. Determination of source parameters at regional distances with three component sparse network data, *J. Geophys. Res.,* 98 , 8107–8125.

Fan, G., Ni, J.F. and Wallace, T.C., 1994. Active tectonics of the Pamirs and Karakorum, *J. Geophys. Res.,* 99 , 7131–7160.

Finetti, I. and Morreli C., 1973. Geophysical Exploration of the Mediterranean Sea. *Boll. Geof. Teor. ed Appl.,* 15, 263-341.

Fukuyama, E. and Dreger, D.S., 2000. Performance test of an automated moment tensor determination system for the future "Tokai" earthquake. *Earth Planets Space,* 52, 383-392.

Futterman, W.I., 1962. Dispersive body waves. *Journal of Geophysical Research,* 67, 5279-5291.

Hatzfeld, D., Pedotti, G., Hatzidimitrioiu, P. and Makropoulos, K., 1990. The strain pattern in the western Hellenic arc deduced from a microearthquakes survey. *Geophys. J. Int.* 101, 181-202.

Herrmann, T. and Wang, G.Y., 1985. A comparison of synthetic seismograms. *Bull. Seism. Soc. Am.*, 75, 41-56.

Ichinose, G.A., Anderson, J.G., Smith, K.D. and Zeng, Y., 2003. Source parameters of eastern California and western Nevada earthquakes from regional moment tensor inversion, *Bull. Seism. Soc. Am.*, 93, 61-84.

Jackson, J. and McKenzie, D., 1988. The relationship between plate motions and seismic moment tensors, and the rates of active deformation in the Mediterranean and Middle East. *Geophysical Journal of the Royal Astronomical Society*, 93, no.1, 45-73.

Jost, M.L. and Herrmann, R., 1989. A student's guide to and review of moment tensors. *Seism. Res. Lett.*, 60, 37-57.

Kanamori, H. and Stewart, G.S., 1976. The mechanism of the Guatemala earthquake of February 4, 1976, revealed by teleseismic surface-wave and body-wave analysis. Eos, Transactions, American Geophysical Union, 57, 950.

Kikuchi, M. and Kanamori, H., 1991. Inversion of complex body waves; III, *Bull. Seismol. Soc. Am.*, 81, 2335-2350.

Kikuchi, M., Kanamori, H. and Satake, K., 1993. Source complexity of the 1988 Armenian earthquake; evidence for a slow after-slip event, *Journal of Geophysical Research*, 98, 15,797-15,808.

Kissel, C. and Laj, C., 1988. The Tertiary geodynamical evolution of the Aegean arc: a paleomagnetic reconstruction. *Tectonophysics* 146, 183-201.

Lagios E., Sakkas V., Papadimitriou P., Damiata B.N., Parcharidis I., Chousianitis K. and Vassilopoulou S., 2006. Crustal deformation in the Central Ionian Islands (Greece): Results from DGPS and DInSAR analyses (1995-2006). *Tectonophysics*, 444, 119-145.

Le Pichon, X. and Angelier, J., 1979. The Hellenic arc and trench system: a key to the noetectonic evolution of the Eastern Mediterranean area. *Tectonophysics* 60, 1-42.

Makropoulos, K. and Burton, P., 1981. A catalogue of Seismicity in Greece and the Adjacent Areas. *Geophys. J. R. Astr. Soc.*, 65, 741-762, and Microfiche GJ65/1.

Mercier, J.-L., Sorel, D. and Simeakis, K., 1987. Changes in the state of stress in the overriding plate of a subduction zone, the Aegean arc from the Pliocene to the Present, Ann. *Tectonicae*, 1, 20-39.

Papadimitriou, P., 1983. Etude de repliques de seismes de Corinthe (1981), Rapport de stage du DEA, IPG Paris.

Papadimitriou, P., 1988. Etude de la structure du manteau superieur de l'Europe et modelisation des ondes de volume engendrees par des seismes egeens, Doctorat de l' Universite Paris VII, Paris, France.

Papadimitriou, P., Kaviris, G. and Makropoulos, K., 2006. The Mw=6.3 2003 Lefkada earthquake (Greece) and induced stress transfer changes, *Tectonophysics*, 423, 7–30.

Saikia, C.K., 1994. Modified frequency-wavenumber algorithm for regional seismograms using Filon's quadrature: modelling of Lg waves in eastern North America. Geophys. J. Int., 118, 142-158.

Saikia, C.K., Woods, B.B. and Thio, H.K., 2001. Calibration of the regional crustal waveguide and the retrieval of source parameters using waveform modeling. *Pure Appl. Geophys.*, 158, 1301–1338.

Scordilis, E.M., Karakaisis, G.F., Karacostas, B.G., Panagiotopoulos, D.G., Comninakis, P.E. and Papazachos, B.C., 1985. Evidence for transform Faulting in the Ionian Sea: The Cephalonia Island earthquake Sequence of 1983. *PAGEOPH,* 123, 388–397.

Thio, H.K. and Kanamori, H., 1995. Moment-tensor inversions for local earthquakes using surface waves recorded at TERRAscope, Bull. Seismol. Soc. Am., 85 , 1021–1038.

Underhill, J.R., 1989. Late Cenozoic deformation of the Hellenide foreland, western Greece. *Geol. Soc. Am. Bull.* 101, 613-634.

Wessel, P. and Smith, W.H.F., 1998. New improved version of the generic mapping tools released. Eos Trans. AGU 79, 579.

Zeng, Y. and Anderson, J.G., 1995. A method for direct computation of the differential seismogram with respect to the velocity change in a layered elastic solid. *Bull. Seismol. Soc. Am.*, 85 , 300–307.

A CROSS-CORRELATION TECHNIQUE FOR RELOCATION OF SEISMICITY IN THE WESTERN CORINTH RIFT

Kapetanidis V.[1], Papadimitriou P.[1] and Makropoulos K.[1]

[1] *National and Kapodistrian University of Athens, Faculty of Geology and Geoenvironment, Department of Geophysics-Geothermics, 15784 Athens, Greece, vkapetan@geol.uoa.gr, ppapadim@geol.uoa.gr, kmacrop@geol.uoa.gr*

Abstract

Local seismological networks provide data that allow the location of microearthquakes which otherwise would be dismissed due to low magnitudes and low signal-to-noise ratios of their seismic signals. The Corinth Rift Laboratory (CRL) network, installed in the western Corinth rift, has been providing digital waveform data since 2000. In this work, a semi-automatic picking technique has been applied which exploits the similarity between waveforms of events that have occurred in approximately the same area of an active fault. Similarity is measured by the cross-correlation maxi-mum of full signals. Events with similar waveforms are grouped in multiplet clusters using the nearest-neighbour linkage algorithm. Manually located events act as masters, while automatically located events of each multiplet cluster act as slaves. By cross-correlating the P-wave or S-wave segments of a master event with the corresponding segments of each of its slave events, after appropriately aligning their offsets, the measured time-lag at the cross-correlation maximum can be subtracted from the arrival-time of the slave event. After the correction of the arrival-times, a double-difference technique is applied to the modified catalogue to further improve the locations of clusters and distinguish the active seismogenic structures in the tectonically complex Western Corinth rift.

Key words: cross-correlation, multiplets, clustering, master events, double-difference, relocation, Corinth Rift, Greece.

1. Introduction

The Western Corinth rift is one of the most tectonically active regions in Greece. Its continuous microseismicity is closely monitored by permanent seismological stations of the Universities of Athens and Patras as well as by the Corinth Rift Laboratory (CRL) local network (Bernard et al., 2006). The growing quantity of waveform and catalogue data makes imperative the need for automatic location algorithms with improved accuracy. Some groups of events are strongly clustered in space. When their magnitudes and focal mechanisms are similar, then their recorded waveforms on each recording station are also similar. These events are called multiplets (Poupinet et al., 1984) and can be useful for relocation procedures, which is the subject of this paper.

The primary mathematical tool for the detection of multiplets and for the extraction of information from their similar waveforms is the cross-correlation function (Schaff & Waldhauser, 2005; Hansen et al., 2006). The characteristics of the cross-correlation function will be discussed below,
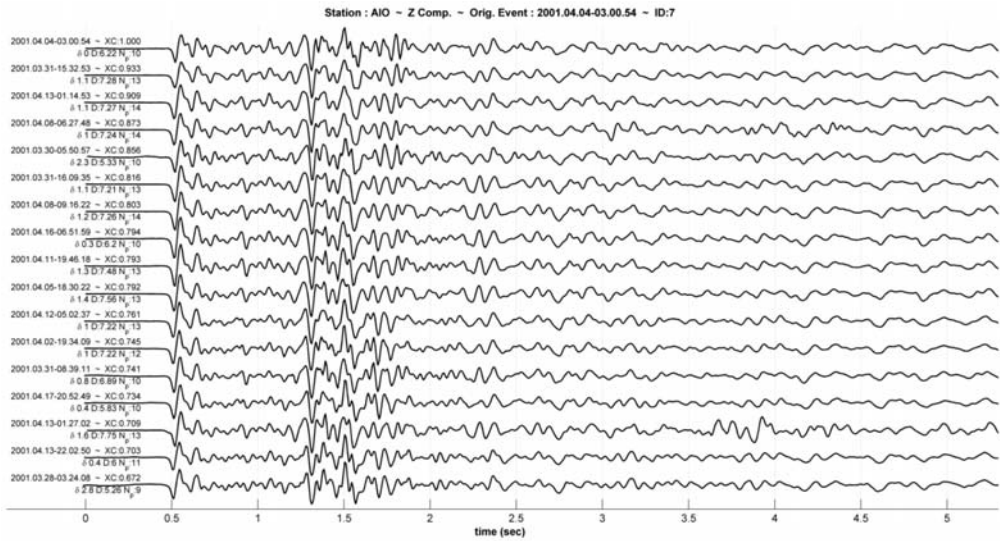
Fig. 1: vertical component waveforms of multiplets recorded at the AIO station during March-April 2001.

as well as its advantages in comparison to its spectral counterpart, the coherence function (Rubin et al., 1999; Waldhauser et al., 1999). An automated procedure will be run on several groups of earthquakes to produce cross-correlation matrices that will reveal the existence of multiplets, which will then be grouped in clusters by applying a nearest-neighbour linkage on the matrix.

A semi-automatic procedure to improve the locations of events will also be demonstrated. This will be done by using a small amount of manually picked events from multiplet clusters as "Master Events" in order to correct or add more P or S-wave arrival-times to the other multiplets ("Slave Events") of the same cluster, thus 1) improving the database without having to manually pick the arrival-times for all these events, 2) being able to add arrival-times correctly even if the signal-to-noise ratio is low.

Finally, the multiplets will be relocated with a double-difference algorithm (Waldhauser & Ellsworth, 2000) using both catalogue and waveform cross-correlation differential travel-time data to improve the location of the multiplets' hypocenters. This has been applied to a selected group of events during 2000-2001 and 2005-2006, for the purposes of the present work, before applying it to the whole time period.

2. Waveform Similarity

It is expected by the theory of elastic wave propagation through layered media (Aki & Richards, 1980) that earthquakes with similar focal parameters should produce similar waveforms. By reversing the argument, when two events have similar waveforms it is expected that they also have similar focal parameters. This is true when the properties of the medium are also similar, so that the ray-paths don't change significantly.

A pair of such events is called doublet. A cluster of more than 2 similar events is called multiplet (Fig. 1 and 6c). In the present paper the similarity between the focal parameters of two events is estimated by the degree of similarity between their full waveforms, containing P-
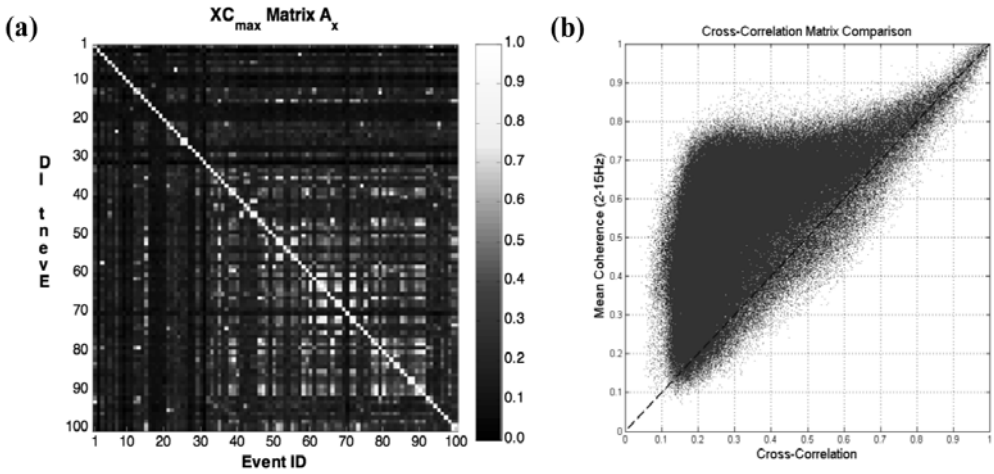
Fig. 2: (a) Cross-correlation matrix for the first 100 events of Group A_s; (b) element-by-element comparison between cross-correlation (XC_{max}, *horizontal axis*) and mean coherence (m_{coh}, *vertical axis*) matrices for Group A_s.

waves, S-waves and coda-waves. In the case of local microearthquakes it has been observed that recordings of a single vertical component from a single station is usually enough to distinguish different groups of multiplets with strong similarity between events of a single cluster and apparent dissimilarity between events of different, although neighbouring clusters, allowing for a detailed distinction of groups of events with different properties within a larger cluster.

The quantification of similarity between a pair of waveforms x,y has been done in two ways: a) by cross-correlation in the time-domain, and b) by spectral coherence in the frequency-domain. The cross-correlation function between two waveforms has a positive maximum value, XC_{max}, on a certain time-lag τ_m. When this offset is applied to the first time-series, x(t), its waveform fits best to the other time-series, y(t), provided that the XC_{max} is relatively high. If there is no correlation between the two time-series both maximum and minimum values of the cross-correlation function will be close to zero. A strong negative (close to -1) indicates that the two time-series are negatively correlated.

When dealing with absolute times, the difference between the times of the first sample of each time-series has to be taken into account. This is crucial because it allows for a calculation of the time-lag of XC_{max} for a custom initial temporal alignment of the two time-series. More specifically, the two time-series could be aligned at the arrival-time of the P-waves or S-waves. Then, if these waveforms are similar, the time-lag provides a measure of the difference that arises between the corresponding picked arrival-times, which have been used for the temporal alignment, when the similar waveforms are shifted in time to fit together.

The spectral coherence measures the similarity between the spectra of the two time-series. It is the equivalent of the cross-correlation in the frequency domain and has been preferred by several authors (Got et al., 1994; Kilb & Rubin, 2002) or used as an additional weight (Schaff et al., 2004). In the case of local microearthquakes, the mean spectral coherence, m_{coh}, between 2-15Hz could be used as a measure of similarity between pairs of waveforms (similar mean values of coherence have been used by Got et al., 1994;Schaff et al., 2004). This spectral region

avoids long period as well as high frequency noise while it contains most of the information content that is generated by a local event. Concerning the time-domain, before applying the cross-correlation function, a band-pass filter is needed as well, mainly for the removal of long-period trends which can greatly affect the results of the cross-correlation. The equivalent value of the time-lag, τ_m, in the spectral domain, which can be used as an offset for the best temporal fit of the two waveforms, can be estimated by the slope of the phase of the cross-spectrum, which is the Fourier Transform of the cross-correlation (Poupinet et al., 1984).

A comparison between the results of the two methods has been done on a sample of 1134 events (Group A_s) which took place between March 26th 2001 and April 18th 2001 in the Western Corinth rift. In April 8th 2001 a $M_L=4.7$ event occurred 5km south of the city of Aigion, very close to AIO station of the CRL network (Lyon-Caen et al., 2004; Janský et al., 2004; Zahradnik et al., 2004). There was some foreshock activity in the region, as well as a spatially dense series of aftershocks. AIO station provided waveform data during that period of time.

A comparison of full-waveform recordings (in a window containing P, S, and coda-waves) of the vertical component of station AIO has been done between all possible combinations of pairs of events of that group. The XC_{max} and m_{coh} values were calculated. This led to the construction of the corresponding 1134x1134 square matrices. An element-by-element comparison has been done between the values of the XC_{max} and m_{coh} matrices (Fig. 2b). Although there's good correlation between XC_{max} and m_{coh} values above 0.85, it is apparent that the m_{coh} values are prone to faster saturation than the corresponding XC_{max} values: the threshold can be lowered much more in the XC_{max} axis than in the m_{coh} axis until it meets the noise background. This means that there are many cases with relatively high m_{coh} for a pair of events with very low XC_{max}. This observation is in agreement with a similar point made by Schaff et al. (2004), who used the sum of XC_{max} with m_{coh} instead of either function alone, with 1.70 threshold.

On the other hand, the value for the time-lag that corresponds to the global maximum of the cross-correlation can be directly calculated in the time-domain with an accuracy that is limited by the sampling rate (0.008sec for a sampling rate of 125samples/sec, as in the case of AIO station). The error of measurement of the equivalent time-lag in the spectral domain by the slope of the cross-spectral phase derives from a weighted least-squares linear fit and is usually much lower than the sampling interval. The weights for each spectral sample are given by the corresponding coherence (Poupinet et al., 1984). In this work the temporal cross-correlation function has been used for the calculation of time-lags in order to avoid some possible instability issues which appear in the frequency-domain.

The limitation in the accuracy of the calculation of time-lag τ_m from the cross-correlation function can be surpassed by re-sampling the cross-correlation function using non-linear spline interpolation in a region that includes the global maximum, XC_{max}. Afterwards, the time-lag of the interpolation can be calculated with accuracy limited by the re-sampling rate. 1000 samples per second are usually more than enough for a good estimation of the time-lag. Similar approach has been taken by Deichmann & Garcia-Fernandez (1992) who used a 2nd degree polynomial interpolation (parabola) around the global maximum of the cross-correlation.

3. Data Preparation, Clustering

The available catalogue data for the years 2000-2001 are spatially separated in 2 groups. Group A consists of 1954 events of a swarm that took place during the time period between February-
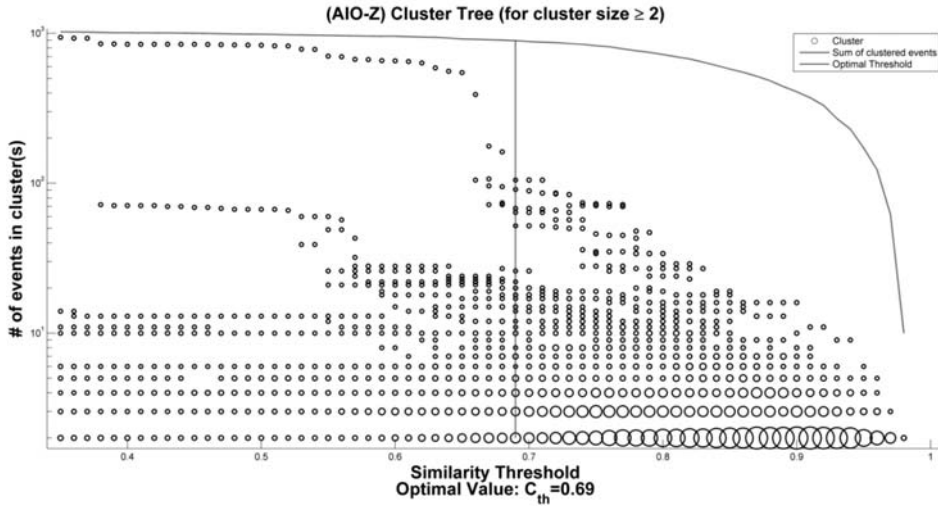
Fig. 3: Tree-diagram of multiplet clusters for Group A_s. Circles denote clusters formed on each similarity threshold (horizontal axis), circle size corresponds to the number of clusters containing the same number of events. The envelope curve is sum of clustered events on each similarity threshold. The vertical dashed line marks the optimal threshold C_{th}=0.69.

July 2001, with epicenters close to the station AIO of the CRL network. Group B consists of 1827 events with epicenters mainly within the gulf, covering the time-period between May 2000 – December 2001. Some extra criteria that have been applied on the choice of these groups are Azimuthal Gap<=320, N_{ph}>=8, RMS error <0.2sec, Location Error <=1.5km for Group A, and Gap<=270, N_{ph}>=5, RMS error<0.3sec, Location Error<5km for Group B, where N_{ph} is the number of arrival-times. The azimuthal gap limit for Group A is lower due to the fact that the epicenters of this group are at the margins of the network. For the year 2005, 1232 events were selected (Group C) with the following criteria: N_{ph}>=9, Location Error<3km. The seismicity during that year is dispersed and there are only a few small clusters spread around the whole area. On the other hand, the seismic activity during year 2006 was increased and the spatial distribution was separated in 3 groups using a ward linkage method: groups D, E and F contain 1108, 888 and 1652 events respectively.

A cross-correlation matrix is constructed for each group of earthquakes using full-waveform data on a single station and component of choice (usually the one which is closer to the group, like station AIO for Group A). The cross-correlation matrices contain information of similarity between all combinations of event-pairs within the group in a temporal sequence. The visualization of the cross-correlation matrix can provide a quick preview of the existence of temporally separated multiplet groups.

The clustering is achieved by the use of simple or nearest-neighbour linkage algorithm. For a certain threshold value C_{th}, which can be modified, all rows of the matrix are scanned and the events are grouped according to the logic "if a pair (A,B) has XC_{max}>=C_{th} and the same is true for a pair (B,C), then all three events (A,B,C) belong to the same cluster", or in simpler words "if A is similar to B and B is similar to C, then A should be similar to C, possibly with a different degree of similarity". A direct comparison of A with C may not result in a XC_{max}>=C_{th}, but these events

are connected together through B. This could be the case for events with different depths, with A and C being at the top and bottom respectively while B being in the middle. Pairs like A-B or B-C are called "close-relatives" while pairs like A~C are called "distant-relatives".

This type of linkage can lead to wide clusters which consist of events with i.e. a) slightly different source duration but similar location of hypocenter and similar focal mechanism, or b) similar source and mechanism but slightly different hypocenter etc. Two whole sub-clusters A and C could be connected through a single event B so it is important that the threshold is chosen carefully. The number of clusters and their sizes (the number of events they contain) is also controlled by the chosen threshold value. While its choice is generally subjective, a special criterion has been used in order for one to find the "optimal threshold" value C_{th}. In Fig. 3 the circles represent clusters of Group A_s which are formed for the various choices of threshold value (horizontal axis) while the vertical, log-scale axis shows the size of each cluster. The envelope curve, above the circles, shows the sum of all events which are contained in clusters with size equal or larger than 2 for each threshold value. Circle size corresponds to the number of clusters of a certain cluster-size (containing the same number of events). A large number of doublets (clusters containing 2 events) is formed for high threshold values (big circles at the bottom of Fig. 3). As the threshold is lowered, more events are being clustered (the envelope curve is always increasing with the threshold decreasing). At very low thresholds, most events are grouped on what could be called the "main branch", the largest cluster that tends to accumulate all the smaller ones. In some cases there can be two or more large branches which will eventually connect once the threshold becomes low enough.

For a certain threshold value the difference between the sum of clustered events (envelope curve) and the size of the largest cluster is maximized. This is proposed as the optimal threshold value, C_{th}, which is denoted by the dashed vertical line in Fig. 3. Note that the maximization of that difference is not obvious graphically as the vertical axis is in log-scale, whose purpose is to make the branching of the smaller clusters clearer.

4. Master Events - Relocation

For the time-span 2005-2006 the available arrival-times data have been generated by an automatic picking algorithm. Although it is able to pick both P and S-wave arrival-times, like all automated processes, it has its downfalls. Some arrivals are not picked at all, while some others are erroneously picked. The resulting distribution of epicenters is dispersed with a few well-located events and many others with relatively large location errors. While the best solution to this problem is to manually pick the arrivals for all those small events, it is also time-consuming given that in 2006 alone there have been over 10000 events recorded in the Western Corinth rift by the local network. It is interesting to find out what can be achieved by applying a semi-automatic procedure that will replicate manual picks of arrival-times in sub-groups of events that have been identified as multiplets.

After applying the cross-correlation and clustering procedures, as described in the previous paragraph, a fraction of events have been grouped in multiplet clusters. One event from each cluster must be selected according to the following criteria: 1) the one with the largest number of picked arrival-times, 2) if more than one event were derived from step (1), then select the event with the smallest RMS error. These events, which will be called "Master Events", should possibly have acceptable signal-to-noise ratio in most stations and should be easily manually picked. By exploiting their similarity to the other multiplets (slaves) of the cluster to which they belong, the manually picked arrival-times will be instantiated to all the slave events, be-
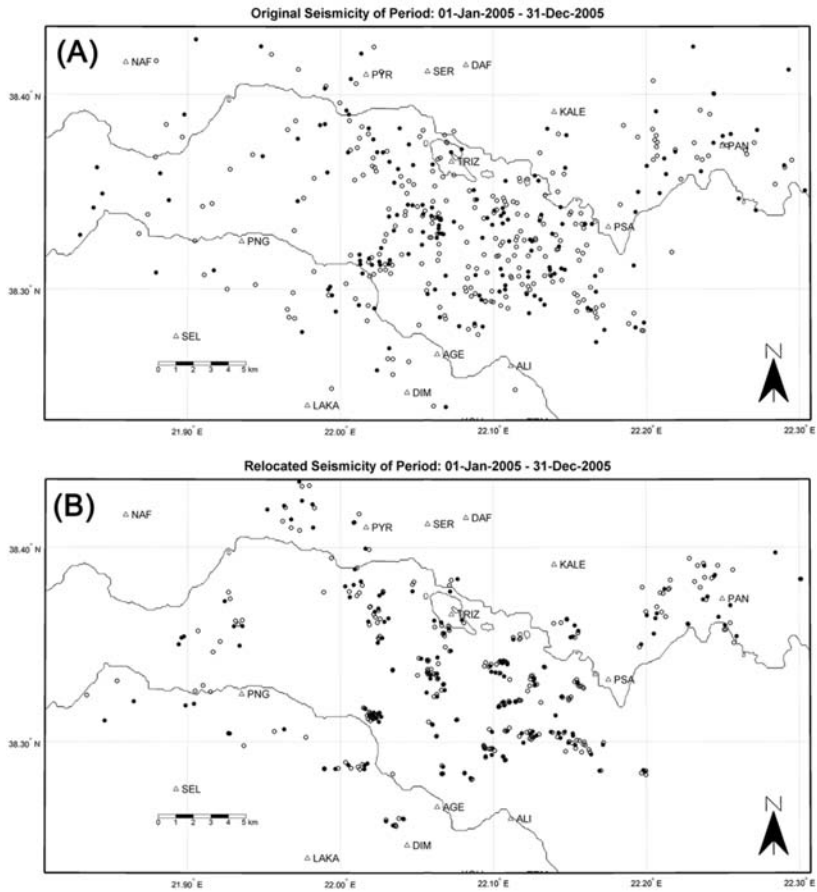
Fig. 4: (A): automatically located epicenters of multiplet clusters belonging to group C (year 2005); (B): the same events relocated using the Master Events method and HypoDD. Master Events are represented by filled circles while slave events are represented by hollow ones.

ginning with the close-relatives. Theoretical arrival-times of P and S-waves at all stations need also be calculated for all slave events, in order to properly crop the corresponding waveform windows as will be described next.

For every master event the cross-correlation matrix (which has been created by using the Z-component of the closest station to the group of epicenters) can supply a group of close-relatives for a given XC_{max} threshold. Although the optimal threshold C_{th} is advised, lower thresholds can also be used but with caution. Higher values will only result in less automatically corrected events. The P-wave part of a master event's waveform on each station/component is cropped before the S-wave arrival. The S-waves are cropped separately as well. Then for each slave waveform, on the same station/component, the master P-wave window slides along the time axis until the two waveforms match.

This is easily done by calculating the correlation coefficient between the amplitudes of the master/slave waveforms for each window until it reaches a maximum value that is above an ac-
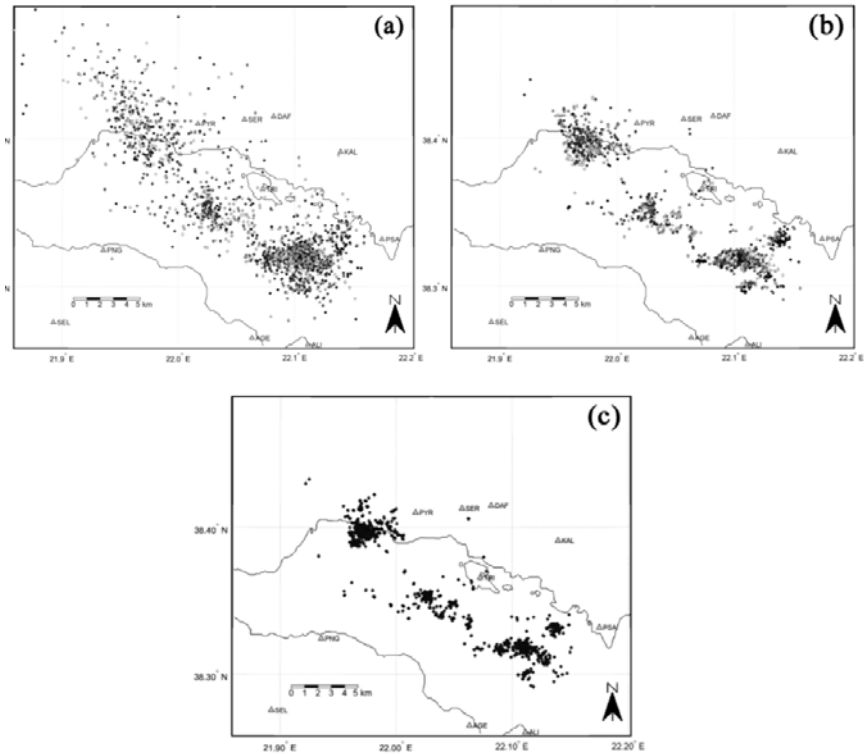
Fig. 5: (a): automatically located epicenters of multiplet clusters belonging to groups D, E and F (year 2006); (b): the same events relocated using the Master Events method; (c): final relocation with a double-difference technique (HypoDD).

ceptable threshold (e.g. 0.7). Both waveforms have to be band-passed prior to this procedure, in order to remove long period and high frequency noise thus allowing the strongly cohered part of their spectrum to be compared. The length of the time-series for a slave-event must extend to some seconds before the automatic (or theoretical) P-wave arrival-time and up to about 1 minute after the S-wave arrival (when one deals with small, local events). This is important in cases of arrival-times that have been largely miscalculated by the automatic picking algorithm.

Suppose a certain master event, M, recorded at station PSA and the time-series $M(t)$ of its cropped P-wave on the vertical component. The manually picked P-wave arrival-time for this event on this station is on $t=t_P$ with $t=0$ at the first sample of the series. The corresponding waveform of a slave event, S, is divided into a family of time-series called $S_i(t)$, where the index i refers to a certain sliding-window with equal length to the $M(t)$ series and which shifts by one sample each time. In $S_i(t)$, the relative time is $t=0$ at the first sample of each window. The correlation coefficient is calculated between M and S_i for every i until it maximizes above a threshold when $i=m$. When it does, $S_{i=m}$ and M should be highly similar. Then, the absolute time of the sample at $S_{i=m}(t=t_P)$ should correspond to the correct arrival-time of the P-wave of the slave event on station PSA. The same process is repeated for all stations and available components and for every slave event, for both P and S-wave windows.

Some post-processing is needed in order to evaluate the results before exporting the output files with the final arrival-times information for each slave event. A criterion for good-quality of the result is the small temporal difference of all corrections made for the arrival of a certain phase on a certain station in all available components: if they are not in good agreement this is an indication of a possible source of error. Another criterion for the quality assessment is the availability, both in the master and slave event, of the vertical-component for the P-waves and of at least one horizontal component for the S-waves. The daily status of each of the 3 components of all stations has been checked and time-periods of non-availability of certain components have been marked in a detailed table to be used whenever waveforms are used in cross-correlations.

The maximum value of the correlation coefficient, C_{max}, which corresponds to the best fit between the master and slave waveform windows, should also have a strong impact on the value of the weight to be applied on the arrival-time. If its value is too low (i.e. $C_{max}<0.5$) then the correction must be discarded, while for intermediate values (i.e. $0.5<C_{max}<0.75$) the weight should be lowered and the use of that correction should depend on whether the other criteria are fulfilled as well.

When the first pass of corrections on arrival-times of all slave events has been completed, these corrected events can be used as master events themselves and the whole procedure is repeated. Old master events (those with the manually picked arrival-times) should not be affected by this second-level pass. By repeating the process, the corrections are applied to distant-relatives of the original master events, hence the whole cluster is corrected by using close-relatives in a master/slave hierarchy on each step, until there are no more relatives to be found. That's the main reason why the optimal XC_{max} threshold, C_{th}, should be used on the cross-correlation matrix as the nearest-neighbour linkage is working here as well.

Although the matrix has been created by using a single station - single component and full-waveforms, the Master Events method is using all stations and components as well as P-waves and S-waves separately. Events with partially similar waveforms can have different t_S-t_P durations, while having similar both P and S-waves. Full-waveform comparison is mostly affected by the S-wave and coda, but dissimilarities in the P-waves and difference in t_s-t_p duration can slightly decrease the XC_{max} as well. This dissimilarity usually increases in distant-relatives within the same multiplet cluster, while it should not be noticeable in close-relatives. So, the Master Events method may replicate the manually-picked arrival-times of the master events to the slave events, but it does not strictly replicate t_S-t_P time differences. That's the main reason why the hypocenters of multiplets in the final results are usually close together but not all at the exact same spot.

5. Conclusions-Results

The method of "Master Events" was used in several earthquake groups. In group C (year 2005) 180 master events were used to correct 328 slave events (Fig. 4). In groups D, E and F (year 2006) a total of 361 master events were used to correct 1261 slave events (Fig. 5). Followed by relocation with a double-difference method, the results are quite impressive. It is possible to expand this method to improve/add more arrival-times for events outside the previous groups. Depending on the threshold value used in such a procedure it is possible to correct 221 out of 4330 (5.1%) events from year 2005 and 321 out of 4428 (7.2%) events of 2006 by using a combination of 2130 master events (508 from year 2005 and 1622 from year 2006). If that value is lowered to C_{th}=0.35 the corrected events arise to 330 (7.6%) and 539 (12.2%) for years 2005 and 2006 respectively. The hypocentral depths are also improved as a result of the relocation procedure. This has been shown in a series of cross-sections of the study area elsewhere (Καπετανίδης, 2007).
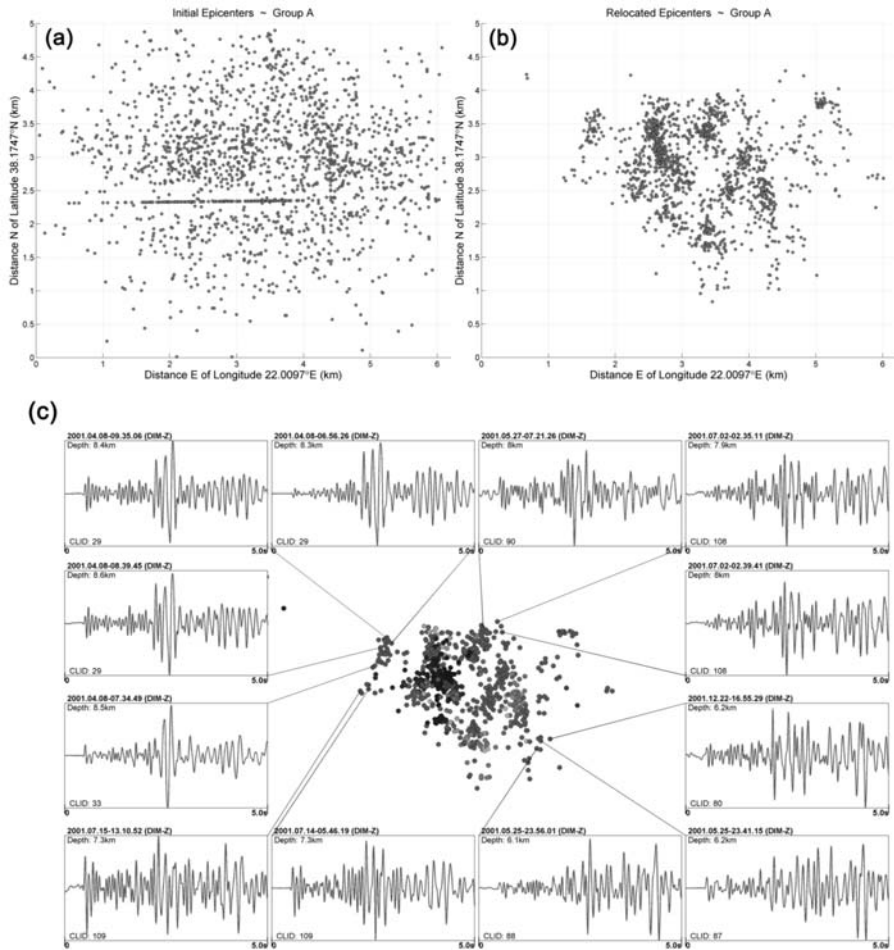
Fig. 6: (a): initial locations of earthquakes in Group A; (b): relocated epicenters using the double-difference method; (c): seismic recordings of the vertical component of station DIM for certain events of Group A. CLID number is the Cluster-ID to which each event belongs. Waveform recordings of events with the same Cluster-ID are similar.

This method could also be expanded to correct other parts of the catalogue by increasing the number of master events, or even be applied for the improvement/addition of arrival-times in events of previous years, since temporal separation poses no limitation to multiplets. The improved catalogue, alongside with cross-correlation differential travel-times were used as input data to a double-difference procedure implemented in the HypoDD software (Waldhauser, 2001). A total of about 5700 events from years 2000-2001 were relocated, 1357 from group A (Fig. 6) and 1449 from group B. From the grouped events of years 2005-2006 a total of 1170 events from year 2005 were relocated (group C) as well as 3508 events from groups D, E and F of year 2006.

6. References

Aki, K. & Richards, P. G. 1980. *Quantitative Seismology*, Freeman, San Francisco, 2nd edition, 1980.

Bernard, P., Lyon-Caen, H., Briole, P., Deschamps, A., Boudin, F., Makropoulos, K., Papadimitriou, P., Lemeille, F., Patau, G., Billiris, H., Paradissis, D., Papazissi, K., Castarède, H., Charade, O., Nercessian, A., Avallone, A., Pacchiani, F., Zahradnik, J., Sacks, S. & Linde, A. 2006. Seismicity, deformation and seismic hazard in the western rift of Corinth: New insights from the Corinth Rift Laboratory (CRL), *Tectonophysics* 426, 7–30, 2006.

Deichmann, N., & Garcia-Fernandez, M. 1992. Rupture geometry from high-precision relative hypocenter locations of microearthquake clusters, *Geophys. J. Int.* 110, 501–517.

Got, J.-L., Frechet, J. & Klein, F.W. 1994. Deep fault plane geometry inferred from multiplet relative location beneath the south flank of Kilauea. *J. Geophys. Res.* 99, 15375-15386.

Hansen, S.E., Schwartz, S.Y., DeShon, H.R. & Gonzalez, V., 2006. Earthquake Relocation and Focal Mechanism Determination Using Waveform Cross Correlation, Nicoya Peninsula, Costa Rica. *Bulletin of the Seismological Society of America*, Vol. 96, No. 3, pp. 1003–1011.

Janský J., Zahradník J., Sokos E., Serpetsidaki A. & Tselentis G.A. 2004. Relocation of the 2001 Earthquake Sequence in Aegion, Greece, *Studia Geophysica et Geodaetica*, Volume 48, Number 2, April 2004, pp. 331-344(14).

Kilb, D. & Rubin, A.M. 2002. Implications of diverse fault orientations imaged in relocated aftershocks of the Mount Lewis, ML 5.7, California, earthquake. *J. Geophys. Res.* Vol. 107, No. B11, 2294, doi:10.1029/2001JB000149, 2002.

Lyon-Caen, H., Papadimitriou, P., Deschamps, A., Bernard, P., Makropoulos, K., Pacchiani, F. & Patau, G. 2004. First results of the CRLN seismic network in the western Corinth Rift: evidence for old-fault reactivation. *C. R. Geoscience* 336 (2004) 343–351, Tectonics.

Poupinet, G., Ellsworth, V. L. & Frechet, J. 1984. Monitoring velocity variations in the crust using earthquake doublets: An application to the Calaveras fault, California, *Journal of Geophysical Research*, Volume 89, Issue B7, p. 5719-5732.

Rubin, A.M., Gillard, D., Got, J.-L. 1999. Streaks of microearthquakes along creeping faults, *Nature* 400,635 -641.

Schaff, D.P., Bokelmann, G.H.R, Ellsworth, W.L., Zanzerkia, E., Waldhauser, F. & Beroza, G.C. 2004. Optimizing Correlation Techniques for Improved Earthquake Location, *Bulletin of the Seismological Society of America*, Vol. 94, No. 2, pp. 705-721, April 2004.

Schaff, D.P. & Waldhauser, F. 2005. Waveform Cross-Correlation-Based Differential Travel-Time Measurements at the Northern California Seismic Network. *Bulletin of the Seismological Society of America*, Vol. 95, No. 6, pp. 2446–2461.

Waldhauser, F., Ellsworth, W.L. & Cole, A. 1999. Slip-Parallel Seismic Lineations on the Northern Hayward Fault, California. Geoph. Res. Let. 26, pp. 3525-3528.

Waldhauser, F. & Ellsworth, W.L. 2000. A double-difference earthquake location algorithm: Method and application to the northern Hayward fault, *Bull. Seismol. Soc. Am.*, 90, 1353-1368, 2000.

Waldhauser, F. 2001. HypoDD: A computer program to compute double-difference earthquake locations, *U.S. Geol. Surv. open-file report*, 01-113, Menlo Park, California, 2001.

Zahradnik, J., Jansky, J., Sokos, E., Serpetsidaki, A., Lyon-Caen, H. & Papadimitriou, P. 2004. *Modeling the ML4.7 mainshock of the February-July 2001 earthquake sequence in Aegion*, Greece. Journal of Seismology 8: 247–257, 2004.

Καπετανίδης, Β. 2007. *Μελέτη Σμηνοσεισμών Δυτικού Κορινθιακού κόλπου με χρήση μεθόδων Ετεροσυσχέτισης και Συνοχής: επαναπροσδιορισμός σεισμικών παραμέτρων,* Μεταπτυχιακή Διατριβή Ειδίκευσης, Εθνικό και Καποδιστριακό Πανεπιστήμιο Αθηνών, 312 σελ.

SEISMIC SOURCES AND MAIN SEISMIC FAULTS IN THE AEGEAN AND SURROUNDING AREA

G.F. Karakaisis, C.B. Papazachos, and E.M. Scordilis

Department of Geophysics, School of Geology, Faculty of Science, Aristotle University, GR54124, Thessaloniki, GREECE, karakais@geo.auth.gr, kpapaza@geo.auth.gr, manolis@geo.auth.gr

Abstract

A seismic source is defined, in the present work, as the part of the seismogenic layer of the earth's crust with a circular horizontal dimension (E, R), where E is the epicenter of the largest earthquake (mainshock) ever occurred in this seismic source and radius equal to the half fault length of this largest earthquake (R=L/2). In addition to foreshocks and aftershocks other smaller mainshocks occur in other smaller faults of this source or in parts of the main fault.

All available historical and instrumental data concerning strong (M$\geq$6.0) shallow (h$\leq$60 km) and intermediate depth (60km<h$\leq$100km) shocks which occurred in the Aegean area between 464 B.C. and 2008 are used in the present work in an attempt to identify the seismic sources in this area, as well as to determine the basic parameters of the largest fault in each source. A particular procedure is followed to identify 155 seismic sources in this area and determine the basic parameters of the largest fault in each source. Declustering has been also performed to define mainshocks in the Aegean area and the completeness of this mainshock catalogue has been determined. Results are summarized in table (1).

1. Introduction

It is well known that the generation of strong earthquakes is a result of seismic slip on large seismic faults and that the seismic energy (and seismic moment) released by an earthquake is proportional to the dimensions of the ruptured fault and to the slip on this fault (Aki, 1966). It is also known that fault rupture is due to the relative movement of huge crustal blocks (Reid, 1911).

The largest earthquake in a region (characteristic earthquake) is due to the break of the largest (main) fault of this region and this break is repeated at relatively long time intervals (Schwartz and Coppersmith, 1984). Smaller earthquakes occur more frequently by rupture of parts (segments) of the main fault or of smaller faults in the nearby region (vicinity of the main fault). The region which includes the main (largest) fault as well as the nearby smaller faults and has a (linear) dimension equal to the length of the main fault is called *focal region* in the present work.

Much work has been done to locate and study seismic faults in the Aegean area by using seismological and geological data. Thus, Papazachos and his colleagues (2001) combined seismological and geological data to determine properties of 159 seismic faults where 567 strong shallow earthquakes occurred in the Aegean area since antiquity.

The purpose of the present paper is to use seismological data (location of earthquakes, fault plane so-

lutions) to define focal regions and the corresponding main faults where all known strong (M³6.0) earthquakes with depth h≤100km occurred since 464 BC in the Aegean area (34ºN-43ºN, 18ºE-30ºE).

2. The Data

The data used in the present study are instrumental, which concern earthquakes that occurred in the Aegean area since 1911 when the first seismograph was installed in Athens (a two-horizontal component Mainka type mechanical seismograph), and historical, which concern strong earthquakes (M³6.0) that occurred in the same region since 464 BC. The parameters (origin time, epicenter coordinates and magnitude) for the instrumental period (1911-2008) are based mainly on seismographic records and partly on macroseismic information (Papazachos et al., 2009) while these parameters for historical earthquakes are entirely based on macroseismic information (Papazachos and Papazachou, 2003).

The data required for the present study must be *accurate* to a reasonable degree and *homogeneous* in respect to the magnitude of earthquakes. These data must also be *complete*, that is, the data sample used must include all earthquakes which occurred in a certain region during a certain time interval and have magnitudes larger than a certain value. Accuracy concerns location of earthquake focus and earthquake magnitude. The present study deals with shallow (h≤60km) and intermediate-depth (60km<h≤100km) earthquakes. The error in the epicenter coordinates is about 20 km. The error in the magnitude is 0.3 or less. All magnitudes are in the moment magnitude scale. Completeness of the instrumental data is as follows:

$$M \geq 5.2, \ 1911\text{-}2008 \tag{1}$$

That is, the data samples include all earthquakes which have moment magnitude equal to or larger than 5.2 and occurred in the Aegean area between 1.1.1911 and 31.12.2008. The completeness for the historical data (464BC-1910) is examined in section (7). The earthquake catalogues used in the present study can be found at the site http://geophysics.geo. auth.gr/ss/station_index_en.html/.

3. Determination of Focal Regions in the Aegean

The focal region of a shallow mainshock is defined, in the present work, as the part of the seismogenic layer which cuts the earth's surface in a circle with center, E, the epicenter of the mainshock and radius equal to the half of the length of the fault ruptured during the generation of the mainshock (the focal region, actually, is a cylindrical part of the crust with height equal to the thickness of the seismogenic layer). In a first approximation the length, L (in km), of the faults in the Aegean area is given by the relation:

$$\log L = 0.51 \cdot M - 1.85 \tag{2}$$

where M is the moment magnitude of the earthquake (Papazachos and Papazachou, 2003). Relation (2) is used to calculate the fault length, L_{max}, of the largest earthquake ever occurred in the focal region and the radius of this focal region is $R=L_{max}/2$. Smaller mainshocks also occur in the focal region by rupturing of other smaller faults or parts of the main fault. Thus, to determine E and R for each focal region of the Aegean area the following procedure has been applied by using the earthquake catalogue (M≥6.0 since 464BC, M≥5.2 since 1911) described in section (2).

First, the epicenter of the largest earthquake of the catalogue is considered as the center, E, of the largest focal region in the Aegean and its magnitude is used to calculate L by relation (2) and the radius R (=L/2) of this region. All earthquakes with epicenters within this region are excluded from

the original catalogue and the same procedure is applied in the remaining part of the catalogue to determine the second largest focal region in the Aegean area. This procedure is repeated for the third, fourth, etc. largest focal region of the Aegean till all earthquakes with M≥6.0 are excluded from the catalogue. In cases when more than one earthquakes of equal magnitude are the largest in the remaining catalogue, they are sorted by decreasing origin time and the corresponding focal regions are defined in this order, i.e. the most recent largest earthquake is firstly considered, then the second most recent largest earthquake, etc. For the mainshocks of the catalogue with M<6.5 the radius of the focal region based on relation (2) is within the error range of the epicenter location. For this reason, in such cases this radius is taken equal to 15 km. It must be also noted that the well documented earthquakes in the Aegean area have moment magnitudes M≤7.6. For this region the maximum radius of the focal regions in the Aegean area was considered equal to 53 km. There are, however, two earthquakes in the catalogue (365 A.D., 1303) for which larger magnitudes have been estimated, but such big earthquakes have a very large return period (~1000 yrs) and only parts of their faults usually break. Magnitudes equal to 7.7 have been assigned for both these earthquakes for the purpose of the present paper.

After the application of the procedure described above 218 shallow circular focal regions have been identified in the Aegean and its surrounding area. A mapping of these regions revealed that in many cases there is overlap of adjoining focal regions.

In addition to the shallow (h≤60km) focal regions defined in the present work, there have been also defined in the southern part of the Aegean area four (4) focal regions of intermediate focal depth (60km<h≤100km) where very strong destructive earthquakes have occurred (D_1, D_2, D_3, D_4 in fig. 6.6 of Papazachos and Papazachou, 2003). Available information for these four focal regions is given in table (1) with code numbers 152, 153, 154 and 155 whereas data completeness is given by relations (1) and (13).

4. Orientations of the Largest Faults and Their Slip Vectors

The orientation of a seismic fault is defined by its strike, ξ (the angle between the intersection of the fault and horizontal plane with the north direction), and by its dip, δ (the angle between the intersection of the fault plane and the normal to the fault strike vertical plane and the horizontal projection of this intersection). The slip vector, which shows the slip direction of the hanging wall of the fault, is determined by the rake, λ (the angle between the slip vector and the strike direction of the fault) and defines the kind of faulting (normal, thrust, strike-slip dextral or strike-slip sinistral).

To define the strike, ξ, the dip, δ, and the rake, λ, for the main fault of a focal region, i.e. the fault where the largest earthquake in this region has occurred, all reliable fault plane solutions which are available for earthquakes located in the corresponding focal region have been used to determine a typical solution by a method proposed by Papazachos and Kiratzi (1992). This typical fault plane solution is adopted as the fault plane solution for the corresponding main fault.

In many cases we encountered the following situation: the typical fault plane solution for a certain focal region, (B), was of the same type with the solution determined earlier for an adjoining focal region, (A), where the magnitude of the largest earthquake was larger than the magnitude of the largest earthquake in region (B). Taking this fact into account we incorporated all data (earthquakes and fault plane solutions) of the region (B) in the region (A) in the cases of significant overlap of both regions. This resulted in 151 typical fault plane solutions. We then compared the values of strike, dip and rake of these solutions with the corresponding values determined for the major faults

in the Aegean and surrounding area (Papazachos et al., 2001). We found that the values of the attributes (strike, dip, rake) of the majority of these 151 typical fault plane solutions were close to those of Papazachos et al. (2001) which were based on a large amount of well documented seismological and geological data. For this reason, the information on the strike, ξ, dip, δ, and rake, λ, listed in table (1) for almost all typical fault plane solutions comes from the work of Papazachos et al. (2001). In the same table corresponding symbols are used to denote thrust faults in the subduction area (TS), thrust faults in the continental area (TC), normal faults (N), strike-slip dextral faults (SD) and strike-slip sinistral faults (SS). Figure (1) shows on a map of the Aegean area these 151 main faults denoted with the corresponding symbols. The length of the symbols used to denote these faults is proportional to the length calculated according to the relations presented in the next section whereas the center of each fault coincides with the center of the respective focal region.

5. Length, Width and Slip of Main Faults

Several empirical relations between the basic fault parameters (fault length, width, fault slip) and the magnitude of the corresponding earthquake have been proposed (Kanamori and Anderson 1975, Bonilla et al. 1984, Wesnousky 1986, Wells and Coppersmith 1994, Smith and Stock 2004, Papazachos and Papazachou 2003, among others). There are, however, differences among these relations which stem from uncertainties of the data used. Papazachos et al. (2004) used a considerable number of published reliable global data which are homogeneous (fault parameters estimated by the same method, earthquake magnitudes in the same scale), fairly accurate (accurate fault parameters, magnitudes) to relate the fault length, L (in km) and the fault width, w (in km) of the fault as well as the mean slip (displacement) of a fault, u (in cm) with the moment magnitude, M for three kinds of faults (strike-slip faults, dip-slip continental faults and dip-slip faults in subduction regions). These relations are as follows:

(a) Strike-slip faults (F_1)

$$\log L = 0.59M - 2.30,$$
$$\log w = 0.23M - 0.49, \qquad (3)$$
$$\log u = 0.68M - 2.59,$$

which hold for 6.0≤M≤8.0,

(b) Dip-slip continental faults (F_2)

$$\log L = 0.50M - 1.86,$$
$$\log w = 0.28M - 0.70, \qquad (4)$$
$$\log u = 0.72M - 2.82,$$

which hold for 6.0≤M≤7.5 and for both normal and thrust faults in continental regions,

(c) Dip-slip faults in subduction regions (F_3)

$$\log L = 0.55M - 2.19,$$
$$\log w = 0.31M - 0.63, \qquad (5)$$
$$\log u = 0.64M - 2.56,$$

which hold for 6.7≤M≤9.2. These relations have been used to calculate the three parameters for each
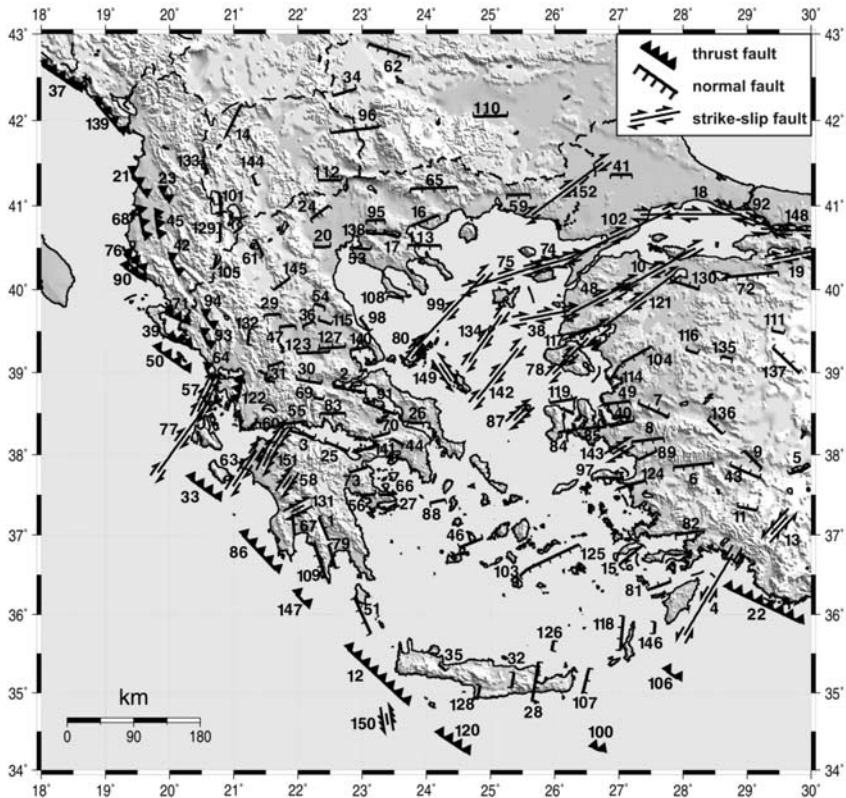
Fig. 1: The main seismic faults of shallow (h≤60km) mainshocks in the Aegean area. The center of each fault coincides with the center of the respective focal region whereas its length has been determined by a set of relationships appropriate for the kind of each fault. The numbers correspond to the code numbers listed in table (1).

of the shallow main faults defined in the present work for the Aegean area. In table (1) the corresponding symbols (F1, F2, F3) are shown to denote the kind of each of the shallow main faults of the Aegean area determined in the present work. Thus, by applying the proper set of relations (3, 4, 5) the corresponding values of L, w, u, have been calculated by using the corresponding magnitude, M, and these values are listed in table (1).

6. Declustering of Data

Declustering of data means the use of the original catalogue described in section (2) to create a catalogue that includes mainshocks only. Earthquakes of the original catalogue included in a focal region are spatially and temporally clustered and a procedure must be applied to make a temporal declustering of these earthquakes by excluding associated shocks. Such shocks are the ones preceding (preshocks) or following (postshocks) each mainshock in the focal region. Such declustering is performed in the present work by assuming that the preshock period is equal to the postshock period and independent of the mainshock magnitude. As a measure of clustering the ratio, $C_v = \sigma/T$, is used where T is the mean repeat time of the earthquakes of the cluster and σ is its standard deviation (Kagan and Jackson, 1991). C_v takes a value: equal to 1 for Poissonian distribution, larger than 1 for clustered shocks, equal to zero for periodic generation of shocks and an intermediate value (e.g. C_v=0.5) for
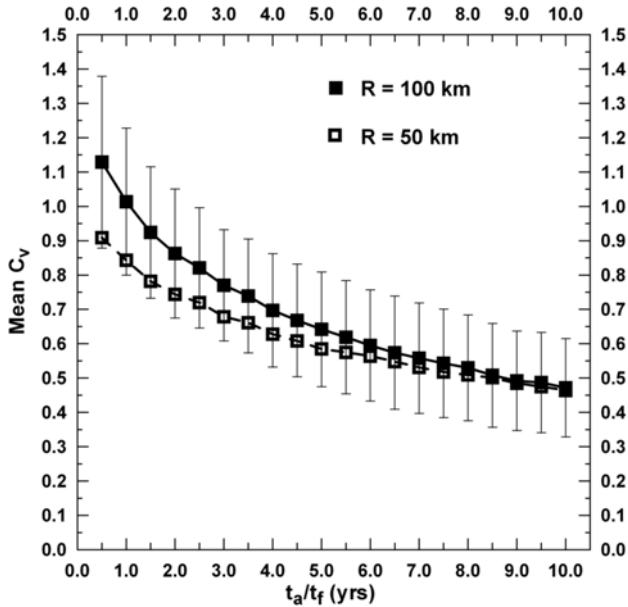
Fig. 2: Variation of the average value of the ratio C_v (=σ/T) with the duration of the time windows (in years) before (t_f) and after (t_a) a mainshock. All earthquakes that occurred in these time windows are considered as associated shocks (preshocks and postshocks, see text for explanation).

quasi-periodic behavior as are the earthquakes which follow the time predictable model. Thus, the optimum time duration of associated shocks (preshocks, postshocks) for which a proper declustering is obtained is that one for which C_v takes its smallest value. To define this optimum time duration the following procedure was followed:

By using a circle with center coinciding with the center, E, of each focal region and a constant radius, R (e.g. R=50 km), the sample of all earthquakes which occurred during the instrumental period (M≥5.2, 1911-2008) and have epicenters within the circle is defined. Considering the largest earthquake of the sample as the largest mainshock we excluded from the initial sample all shocks which occurred within a time window ±0.5 yrs from the origin time of the largest mainshock. This procedure is repeated on the remaining sample and so on till all mainshocks of the region are defined. If the number of these mainshocks is larger than three (n≥3), the mean return period, T, its standard deviation, σ, and their ratio, C_v, for Δt=±0.5 yrs are defined. This is repeated for several time windows (0.5, 1.0, ..., 9.5, 10.0 yrs) and the corresponding pairs of time windows and C_v are formed. This procedure is followed for the mainshocks occurred in the instrumental period in each one of the regions with centers, E, and the same radius (e.g. R=50 km) and the average $C_{v,ave}$ value is calculated for each of the defined time windows. Figure (2) is a plot of $C_{v,ave}$ as a function of Δt for R=50 km and another such plot for R=100 km. It is obvious that in both plots the value of $C_{v,ave}$ decreases with time up to Δt=8.5 yrs where $C_{v,ave}$=0.50 and that for larger time windows $C_{v,ave}$ is practically constant. It is, therefore, concluded that declustering must be made in each originally defined focal region by excluding preshocks and postshocks which occurred in a time window ±8.5 yrs from each mainshock of the focal region. It is also concluded that σ=0.50 · T, which is an important result used in the next section to define completeness of the historical data.
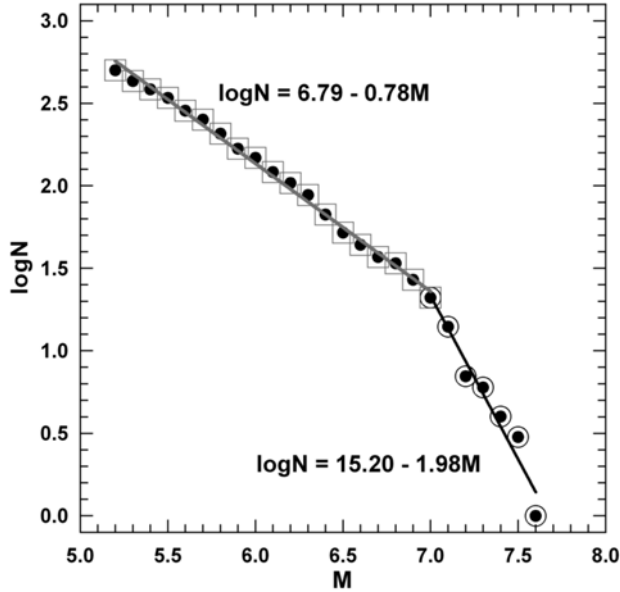
Fig. 3: The cumulative frequency-magnitude distribution of the shallow mainshocks with M≥5.2 which occurred in the Aegean area during 1911-2008.

To decluster the initial sample of earthquakes included in each focal region and define the mainshocks of this region, the following procedure is applied: The largest earthquake of the focal region is considered as mainshock and all shocks of the region which occurred within a time window ± 8.5 yrs from the origin time of the largest mainshock are excluded. The same procedure is applied on the remaining sample to determine the second largest mainshock, etc. till all mainshocks of the focal region are defined. Thus, the mainshocks of all focal regions form the catalogue of mainshocks of the whole Aegean area.

Figure (3) shows the cumulative frequency-magnitude distribution of all mainshocks of the Aegean area which occurred during the instrumental period (1.1.1911-31.12.2008). The data are fitted in the least squares' sense by the following relations:

$$\log N = a_1 - b_1 M, \text{ for } 5.2 \leq M < 7.0 \tag{6}$$

$$\log N = a_2 - b_2 M, \text{ for } M \geq 7.0 \tag{7}$$

with
$$b_1 = 0.78, a_1 = 6.79, a_{1r} = 4.80 \tag{8}$$

$$b_2 = 1.98, a_2 = 15.20, a_{2r} = 13.21 \tag{9}$$

Parameters a_{1r} and a_{2r} are the reduced values of a_1 and a_2 to one year. The parameter a_2 can be also calculated by the relation:

$$a_2 = a_1 + 7.0(b_2 - b_1) \tag{10}$$

Then, the mean return periods for the mainshocks are given by the relations:

$$T = 10^{b_1 M - a_{1r}} \text{ for } M < 7.0 \tag{11}$$

$$T = 10^{b_2 M - a_{2r}} \text{ for } M \geq 7.0 \tag{12}$$

The values of the scaling parameters (b_1=0.78, b_2=1.98) can be considered constant and holding for all focal regions. For this reason, if instrumental data for mainshocks with M≤7.0 are available for a particular focal region, relation (6) can be used to calculate a_1 and relation (10) to calculate a_2 for this region. Then, relation (11) or relation (12) can be used to calculate the mean return period.

7. Completeness of Historical Mainshocks

Another basic requirement of any historical earthquake catalogue, in addition to the homogeneity in the magnitude determination, is the assessment of its completeness, i.e. the assessment of the minimum magnitude above which the catalogue is considered to be fully reported. Traditional methods of estimating completeness of an earthquake catalogue are the frequency-magnitude and the time-magnitude distributions. Both these procedures led to the conclusion that earthquakes in the whole Aegean area investigated in the present work (34ºN-43ºN, 18ºE-30ºE) are complete for the period and magnitude range defined by relation (1) and by the relation:

$$M≥6.5, 1845-2008 \tag{13}$$

Furthermore, completeness is defined for historical mainshocks with $M^36.5$ in each circular region (E, R=100km) where E are the centers of the 151 shallow focal regions. For this purpose we used the information for the mainshocks that occurred during the instrumental period (1911-2008) and are located within the circle (E, R=100km) to determine the value a_1 by the relation (6) assuming b_1=0.78. Then, we used these two values and b_2=1.98 to calculate a_2 by the relation (10). After reducing a_1 and a_2 to one year (a_{1r}, a_{2r}) we can use the relations (11, 12) to calculate mean return periods for any historical earthquake. For example, we considered all mainshocks which are located within the circle (E, R=100km) and for each of them we calculated its mean return period, T, by applying relation (11) or (12) according to its magnitude. Then, the time period T^*=T+2·σ (with σ=C_v · T=0.50 · T) is calculated and subtracted from the origin time, t_e, of the earliest strong (M≥6.0) mainshock of the instrumental period to define a time t=t_e-T^*. If the mainshock occurred after this time, t, it is included in the complete data, otherwise it is not. In this way each circular region (E, R=100km) includes epicenters of mainshocks which occurred during the instrumental and historical times and form complete samples of mainshocks. Information on the completeness of mainshocks in each focal region is given in table (1).

8. Conclusions

The present work aimed at facilitating seismic hazard studies by proposing a methodology of identification of focal regions. Such a region includes the main fault where the largest mainshock occurs, and smaller faults where smaller mainshocks also occur. These focal regions can be considered as spatial clusters of earthquakes. Clustering is usually attributed to foreshocks and mainly to aftershocks but even if these shocks are omitted from the data clustering still prevails, because spatial clustering occurs not only in the rupture zone of a mainshock but also in a broader area where other mainshocks occur.

The proposed methodology is applied in the Aegean area where 155 focal regions and their respective main faults were identified. This number of focal regions can be compared to that of Papazachos et al. (2001) who, using a large amount of seismological (distribution of epicentres, macroseismic information, focal mechanisms) and geological data (surface fault traces, stratigraphic and geomorphological data), determined the properties of 160 faults where the known major (M≥6.0) shallow earthquakes have occurred in the Aegean area. Fault dimensions and maximum slip were determined by appropri-

Table 1. Information on the focal regions and their main faults. After the code number, N, and the name of the focal region, the year of occurrence and the moment magnitude, M, of the largest mainshock ever occurred in this region are given. The next two columns show the geographic coordinates (north latitude, east longitude) of the center, E, of the main fault of this region whereas its length, L (in km), width, w (in km) and maximum slip, u (in m) are listed in the following three columns. The strike, ξ, the dip, δ, and the rake, λ, of the main fault are shown next. The next two columns show the type, T, of the main fault (N=normal, TC=thrust in continental regions, TS=thrust in subduction regions, SS=strike-slip sinistral, SD=strike-slip dextral) and the formulae, F, used to calculate L, w, and u (relations 2, 3, 4). The last column gives information on the data completeness in the focal region, in addition to the completeness of the whole catalogue (1911, M≥5.2, 1845, M≥6.5). The symbol, C, denotes that only the whole catalogue completeness applies in this case.

N	Name	Year	M	Lat	Lon	L (km)	w (km)	u (m)	ξ	δ	λ	T	F	Completeness
1	Sparti	-464	6.8	37.08	22.40	35	16	1.19	340	47	-98	N	F2	1842-6.6, 1750-7.1
2	Skarfia	-426	7.0	38.79	22.80	44	18	1.66	282	47	-90	N	F2	1817-6.6
3	Heliki	-373	6.8	38.25	22.07	35	16	1.19	290	30	-79	N	F2	1817-6.6
4	Rhodes	-227	7.5	36.25	28.40	133	17	3.24	30	80	-41	SS	F1	1741-6.7, 1513-7.1, 1481-7.2, 1303-7.3, 227 BC-7.5
5	Acigol	-90	6.6	37.80	29.80	28	14	0.86	248	35	-105	N	F2	C
6	Aydin	-27	7.2	37.87	28.16	55	21	2.31	83	42	-99	N	F2	1653-7.1
7	Turgutlu	17	7.0	38.54	27.53	44	18	1.66	294	45	-115	N	F2	C
8	Torbali-a	47	7.0	38.18	27.45	44	18	1.66	83	45	-115	N	F2	C
9	Laodicaea	60	6.8	37.94	29.09	35	16	1.19	133	42	-99	N	F2	C
10	Sarikoy	160	7.4	40.24	27.60	116	16	2.77	240	70	-155	SD	F1	1766-6.6, 1659-7.0, 1556-7.1, 1343-7.2, 740-7.4
11	Aphrodisias	241	6.6	37.33	29.00	28	14	0.86	280	42	-99	N	F2	C
12	Elaphonnesus	365	7.7	35.22	23.23	111	57	2.33	315	17	99	TS	F3	C
13	Cibyra	417	6.5	37.12	29.50	34	10	0.68	221	85	19	SS	F1	C
14	Tetovo	518	7.0	42.01	21.00	44	18	1.66	30	49	-87	N	F2	C

N	Name	Year	M	Lat	Lon	L (km)	w (km)	u (m)	ξ	δ	λ	T	F	Completeness
15	Cos island	556	7.0	36.75	27.19	44	18	1.66	50	48	-78	N	F2	C
16	Paggaeon Mt	620	6.8	40.83	24.00	35	16	1.19	70	53	-93	N	F2	1797-6.6
17	Volvi	677	6.4	40.65	23.46	22	12	0.61	286	37	-84	N	F2	1829-6.7
18	N. Marmara	740	7.5	40.90	28.13	133	17	3.24	89	90	177	SD	F1	1766-6.8, 1556-7.1, 1509-7.2, 740-7.4
19	Iznik	1065	7.1	40.43	29.84	77	14	1.73	77	90	177	SD	F1	1766-6.6, 1719-6.7
20	Veroea	1211	6.4	40.51	22.38	22	12	0.61	271	45	-94	N	F2	C
21	Dyrrachio	1273	6.8	41.28	19.50	35	16	1.19	334	27	93	TC	F2	C
22	Kastelorizo	1303	7.7	36.12	29.26	111	57	2.33	294	27	99	TS	F3	1741-6.8, 1609-7.2, 1481-7.3, 1303-7.4
23	Elbasan	1380	6.0	41.13	19.91	14	10	0.32	331	27	93	TC	F2	1833-6.6
24	Edessa	1395	6.7	40.92	22.34	31	15	1.01	56	45	-84	N	F2	C
25	Xylokastro	1402	6.8	38.10	22.60	35	16	1.19	295	30	-79	N	F2	C
26	Eretria	1417	6.4	38.39	23.83	22	12	0.61	93	40	-90	N	F2	C
27	Hydra	1457	6.3	37.35	23.45	19	12	0.52	243	48	-78	N	F2	C
28	Hierapetra	1508	7.2	35.15	25.70	55	21	2.31	10	47	-98	N	F2	C
29	Meteora	1544	6.4	39.70	21.60	22	12	0.61	90	30	-90	N	F2	C
30	Lamia	1545	6.8	38.89	22.17	35	16	1.19	283	47	-88	N	F2	1794-6.6
31	Agrafa	1566	6.4	39.10	21.65	22	12	0.61	76	50	-82	N	F2	1817-6.6
32	Kasteli	1595	6.4	35.16	25.35	22	12	0.61	190	47	-98	N	F2	C
33	Zante	1633	7.0	37.58	20.53	46	35	0.83	310	18	118	TS	F3	1767-6.6, 1752-6.7, 1636-7.1, 1469-7.2
34	Kyustendil	1641	6.7	42.33	22.73	31	15	1.01	256	53	-93	N	F2	C

N	Name	Year	M	Lat	Lon	L (km)	w (km)	u (m)	ξ	δ	λ	T	F	Completeness
35	Chania	1646	6.0	35.32	24.25	14	10	0.32	313	47	-98	N	F2	C
36	Pinias	1661	6.2	39.59	22.16	17	11	0.44	69	43	-90	N	F2	C
37	Dubrovnic	1667	7.2	42.50	18.30	55	21	2.31	310	29	85	TC	F2	C
38	Tenedos	1672	7.0	39.69	25.84	68	13	1.48	260	90	177	SD	F1	1809-6.6, 1756-6.7, 1737-6.8, 1672-7.0
39	Corfu	1674	6.5	39.37	20.15	25	13	0.72	294	43	90	TC	F2	1820-6.6, 1786-6.7, 1769-6.8
40	Izmir	1688	6.8	38.38	27.05	35	16	1.19	256	45	-115	N	F2	C
41	Arkadople	1689	6.6	41.37	27.04	28	14	0.86	90	53	-93	N	F2	C
42	Tepeleni	1701	6.4	40.30	20.06	22	12	0.61	339	27	93	TC	F2	C
43	Denizli	1702	7.0	37.79	28.96	44	18	1.66	292	42	-99	N	F2	C
44	Parnitha	1705	6.3	38.16	23.55	19	12	0.52	119	57	-80	N	F2	C
45	Berat	1713	6.6	40.79	19.80	28	14	0.86	357	27	93	TC	F2	C
46	Melos	1733	6.8	36.90	24.70	35	16	1.19	250	45	-90	N	F2	C
47	Trikala	1735	6.4	39.56	21.84	22	12	0.61	89	43	-90	N	F2	C
48	Etili	1737	7.2	39.90	26.72	89	15	2.02	243	90	177	SD	F1	1809-6.6, 1766-6.9, 1737-7.0, 1659-7.2, 1354-7.4
49	Foca	1739	6.8	38.63	26.98	35	16	1.19	84	45	-115	N	F2	C
50	Paxoi	1743	7.1	39.16	20.03	49	19	1.96	310	43	90	TC	F2	1809-6.6, 1786-6.7, 1769-6.8, 1743-7.0
51	Cythera	1750	7.2	35.98	23.01	55	21	2.31	158	50	-80	N	F2	C
52	Didymotecho	1752	7.4	41.20	26.20	116	16	2.77	54	90	177	SD	F1	1798-6.8, 1750-7.1, 1494-7.5
53	Anthemous	1759	6.5	40.49	22.99	25	13	0.72	278	53	-93	N	F2	C
54	Elassona	1766	6.1	39.81	22.34	15	10	0.37	109	47	-87	N	F2	C

N	Name	Year	M	Lat	Lon	L (km)	w (km)	u (m)	ξ	δ	λ	T	F	Completeness
55	Nafpaktos	1769	6.8	38.39	21.94	35	16	1.19	85	40	-125	N	F2	1817-6.6
56	Argos	1769	6.4	37.50	23.09	22	12	0.61	266	48	-78	N	F2	C
57	Lefkada	1769	6.7	38.70	20.55	45	11	0.92	30	77	178	SD	F1	1786-6.6, 1767-6.7, 1723-6.9, 1636-7.1, 1469-7.2
58	Ladonas	1783	6.1	37.66	21.83	20	8	0.36	37	89	176	SD	F1	1791-6.6, 1769-6.8, 1752-7.0
59	Komotini	1784	6.7	41.13	25.44	31	15	1.01	90	53	-93	N	F2	1752-6.6, 1719-6.8
60	Patra	1804	6.4	38.20	21.70	30	10	0.58	37	89	176	SD	F1	1820-6.6
61	Kastoria	1812	6.5	40.50	21.40	25	13	0.72	160	49	-87	N	F2	C
62	Sofia	1818	7.2	42.81	23.42	55	21	2.31	110	53	-93	N	F2	C
63	Kyllini	1820	6.9	37.83	21.17	59	13	1.26	37	89	176	SD	F1	1767-6.6, 1752-6.7, 1723-6.9, 1658-7.0, 1636-7.1, 1469-7.2
64	Preveza	1826	6.2	39.00	20.60	17	11	0.44	340	43	113	TC	F2	1786-6.6, 1767-6.7, 1743-6.9, 1469-7.2
65	Drama	1829	7.3	41.21	24.12	62	22	2.73	90	53	-93	N	F2	C
66	Epidavros	1837	6.3	37.50	23.37	19	12	0.52	275	43	-100	N	F2	C
67	Messini	1846	6.6	37.13	21.93	28	14	0.86	358	47	-98	N	F2	C
68	Fier	1851	6.8	40.80	19.56	35	16	1.19	353	27	93	TC	F2	C
69	Gravia	1852	6.0	38.68	22.32	14	10	0.32	281	47	-88	N	F2	1817-6.6, 1794-6.7
70	Thebe	1853	6.5	38.24	23.30	25	13	0.72	256	40	-90	N	F2	C
71	Egoumenitsa	1854	6.5	39.65	20.12	25	13	0.72	300	43	90	TC	F2	1786-6.8
72	Bursa	1855	7.4	40.18	29.08	69	24	3.22	83	45	-90	N	F2	1766-6.7, 1719-6.9, 1509-7.2
73	Corinth	1858	6.5	37.81	22.94	25	13	0.72	255	43	-100	N	F2	1817-6.6
74	Saros	1859	6.9	40.32	25.97	59	13	1.26	75	55	-145	SD	F1	1672-6.6, 1471-7.0, 1354-7.1

N	Name	Year	M	Lat	Lon	L (km)	w (km)	u (m)	ξ	δ	λ	T	F	Completeness
75	Lemnos	1864	7.3	40.16	25.24	102	15	2.37	253	88	-170	SD	F1	1776-6.6, 1765-6.7
76	Vlora	1866	6.6	40.34	19.45	28	14	0.86	320	27	93	TC	F2	C
77	Cephalonia	1867	7.4	38.20	20.20	116	16	2.77	40	57	172	SD	F1	1786-6.6, 1767-6.7, 1752-6.8, 1723-7.1, 1469-7.2
78	Lesvos	1867	7.0	39.20	26.25	68	13	1.48	45	89	-172	SD	F1	1809-6.6, 1739-6.8
79	Gythio	1867	6.8	36.73	22.53	35	16	1.19	346	47	-98	N	F2	1798-6.9
80	Alonessos	1868	6.3	39.26	23.86	26	9	0.49	40	77	175	SD	F1	C
81	Symi	1869	6.8	36.36	27.63	35	16	1.19	250	48	-78	N	F2	C
82	Marmaris	1869	6.8	37.03	28.11	35	16	1.19	80	42	-99	N	F2	1653-7.1, 1513-7.2
83	Delfoi	1870	6.8	38.50	22.54	35	16	1.19	91	40	-90	N	F2	1817-6.6
84	N. Chios	1881	6.5	38.29	26.20	25	13	0.72	82	45	-115	N	F2	C
85	Urla	1883	6.8	38.33	26.61	35	16	1.19	266	45	-115	N	F2	C
86	Filiatra	1886	7.3	36.78	21.40	67	43	1.29	320	32	106	TS	F3	1811-6.8
87	Psara	1890	6.2	38.49	25.46	23	9	0.42	229	84	-153	SD	F1	C
88	Kythnos	1891	6.4	37.42	24.18	22	12	0.61	80	48	-78	N	F2	C
89	Efessos	1893	6.6	37.99	27.45	28	14	0.86	244	45	-115	N	F2	C
90	Chimara	1893	6.6	40.20	19.43	28	14	0.86	309	27	93	TC	F2	C
91	Atalanti	1894	7.0	38.57	23.25	44	18	1.66	294	50	-70	N	F2	C
92	Cimanzic	1894	7.2	40.84	29.05	89	15	2.02	110	70	-155	SD	F1	1766-6.6, 1719-6.7, 1509-7.1, 1343-7.2, 740-7.4
93	Paramythia	1895	6.3	39.41	20.56	19	12	0.52	337	43	113	TC	F2	1825-6.6
94	Jannina	1898	6.3	39.64	20.59	19	12	0.52	332	43	113	TC	F2	1820-6.7

N	Name	Year	M	Lat	Lon	L (km)	w (km)	u (m)	ξ	δ	λ	T	F	Completeness
95	Sohos	1902	6.5	40.83	23.21	25	13	0.72	90	53	-93	N	F2	C
96	Kresna	1904	7.3	41.89	22.88	62	22	2.73	266	53	-93	N	F2	1818-6.7
97	Samos	1904	6.8	37.71	26.87	35	16	1.19	91	45	-115	N	F2	C
98	Keramidi	1905	6.4	39.58	23.04	22	12	0.61	327	50	-82	N	F2	C
99	Athos	1905	7.5	39.75	24.38	133	17	3.24	225	89	-172	SD	F1	C
100	Stravo Trough	1910	6.0	34.27	26.67	13	17	0.19	291	47	99	TS	F3	C
101	Ochrid	1911	6.7	41.02	20.79	31	15	1.01	179	49	-87	N	F2	C
102	Ganos	1912	7.6	40.65	26.98	153	18	3.78	245	80	165	SD	F1	1826-6.6, 1766-6.7, 1752-6.8, 1737-6.9, 1659-7.1, 1354-7.4
103	Santorini	1919	6.1	36.53	25.52	15	10	0.37	50	40	-90	N	F2	C
104	Bergama-a	1919	7.0	39.22	27.29	44	18	1.66	61	45	-115	N	F2	1809-6.8
105	Erseke	1919	6.3	40.33	20.71	19	12	0.52	196	49	-87	N	F2	1812-6.7
106	Stravo sea Mt.	1922	6.3	35.23	27.83	19	21	0.30	303	25	90	TS	F3	1513-7.2
107	Zakros	1922	6.8	35.16	26.49	35	16	1.19	14	47	-98	N	F2	C
108	Valta	1923	6.4	39.91	23.52	22	12	0.61	102	53	-93	N	F2	1776-6.8
109	Mani	1927	7.1	36.68	22.34	49	19	1.96	164	44	-79	N	F2	1750-7.1
110	Plovdiv	1928	7.0	42.05	25.00	44	18	1.66	270	37	-84	N	F2	C
111	Emet	1928	6.2	39.49	29.48	17	11	0.44	281	43	-94	N	F2	C
112	Valadovo	1931	6.7	41.30	22.50	31	15	1.01	273	53	-93	N	F2	C
113	Ierissos	1932	7.0	40.53	23.97	44	18	1.66	93	53	-93	N	F2	C
114	Bergama-b	1939	6.6	38.98	26.93	28	14	0.86	31	45	-115	N	F2	1772-6.6, 1739-6.8

N	Name	Year	M	Lat	Lon	L (km)	w (km)	u (m)	ξ	δ	λ	T	F	Completeness
115	Larissa	1941	6.3	39.61	22.42	19	12	0.52	291	47	-88	N	F2	C
116	Bigadik	1942	6.2	39.25	28.14	17	11	0.44	287	45	-115	N	F2	C
117	Edremit	1944	6.9	39.49	26.46	39	17	1.41	74	46	-114	N	F2	1809-6.6, 1737-6.7, 1672-6.9
118	Karpathos	1948	7.1	35.76	27.05	49	19	1.96	185	47	-98	N	F2	C
119	N. Chios	1949	6.7	38.65	26.10	31	15	1.01	261	45	-115	N	F2	C
120	Ptolemy Mt	1952	7.0	34.35	24.41	46	35	0.83	305	29	105	TS	F3	C
121	Yenise	1953	7.4	39.86	27.30	116	16	2.77	233	70	-160	SD	F1	1809-6.6, 1766-6.7, 1737-7.1, 1659-7.2, 1354-7.4
122	Katouna	1953	6.3	38.80	21.10	19	12	0.52	195	60	135	TC	F2	1743-6.6, 1723-6.7, 1658-6.9, 1636-7.0, 1469-7.1
123	Sofades	1954	7.0	39.24	22.24	44	18	1.66	271	47	-88	N	F2	C
124	W. Buyuk	1955	6.9	37.63	27.21	39	17	1.41	73	45	-115	N	F2	C
125	Amorgos	1956	7.5	36.73	25.99	78	25	3.80	65	40	-90	N	F2	C
126	Dionysades	1956	6.0	35.60	25.97	14	10	0.32	10	47	-98	N	F2	C
127	Farsala	1957	6.8	39.30	22.54	35	16	1.19	269	47	-88	N	F2	C
128	Pitsidia	1959	6.3	35.01	24.82	19	12	0.52	193	44	-79	N	F2	C
129	Koritsa	1960	6.5	40.68	20.79	25	13	0.72	185	49	-87	N	F2	C
130	Manyas	1964	6.9	40.06	28.02	39	17	1.41	287	46	-95	N	F2	1659-7.0, 1556-7.1, 1509-7.2, 740-7.4
131	Megalopole	1965	6.1	37.33	22.00	20	8	0.36	245	57	159	SD	F1	1820-6.6
132	Arta	1967	6.4	39.43	21.23	22	12	0.61	11	49	-87	N	F2	1820-6.6
133	Peshkope	1967	6.3	41.46	20.56	19	12	0.52	161	49	-87	N	F2	C
134	Ag. Efstratios	1968	7.1	39.41	24.92	77	14	1.73	216	86	145	SD	F1	C

N	Name	Year	M	Lat	Lon	L (km)	w (km)	u (m)	ξ	δ	λ	T	F	Completeness
135	Demirci	1969	6.1	39.18	28.69	15	10	0.37	104	34	-90	N	F2	C
136	Alasehir	1969	6.6	38.34	28.50	28	14	0.86	313	34	-90	N	F2	C
137	Gediz	1970	7.1	39.15	29.60	49	19	1.96	312	35	-90	N	F2	C
138	Stivos	1978	6.5	40.67	23.21	25	13	0.72	275	46	-70	N	F2	1829-6.7
139	Shkodra	1979	7.1	42.04	19.05	49	19	1.96	325	29	85	TC	F2	1667-7.2
140	N. Aghialos	1980	6.5	39.29	22.96	25	13	0.72	82	43	-90	N	F2	C
141	Peraxora	1981	6.7	38.07	23.06	31	15	1.01	253	44	-84	N	F2	C
142	East of Skyros	1981	7.2	38.98	25.11	89	15	2.02	40	67	-166	SD	F1	C
143	Torbali-b	1992	6.2	38.06	27.01	23	9	0.42	238	85	-167	SD	F1	C
144	Bitola	1994	6.1	41.30	21.32	15	10	0.37	343	49	-87	N	F2	C
145	Kozani	1995	6.6	40.07	21.75	28	14	0.86	237	45	-101	N	F2	C
146	Katavia	1996	6.2	35.83	27.56	17	11	0.44	184	47	-98	N	F2	C
147	Tainaro	1997	6.4	36.19	22.05	21	23	0.34	320	32	106	TS	F3	1798-6.8, 1750-7.1
148	Izmit	1999	7.5	40.70	30.00	133	17	3.24	91	76	179	SD	F1	1766-6.6, 1719-6.8
149	N. Skyros	2001	6.4	39.00	24.30	30	10	0.58	238	85	-161	SD	F1	C
150	SW of Crete	2004	6.0	34.66	23.39	17	8	0.31	172	87	10	SS	F1	C
151	Andravida	2008	6.3	37.96	21.52	26	9	0.49	29	89	-178	SD	F1	1820-6.6, 1811-6.7, 1766-7.1
152	NE Peloponnes	1898	7.0	38.10	22.40	-	-	-	128	62	118	-	-	C
153	Cythera	1903	7.2	35.90	22.60	-	-	-	61	70	144	-	-	C
154	Crete	1856	7.7	35.00	24.70	-	-	-	37	47	146	-	-	C
155	Rhodes	1926	7.6	36.40	28.00	-	-	-	80	65	77	-	-	C

ate global relations for each kind of faulting. We found that the lengths of thrust and normal faults are smaller than the lengths proposed by Papazachos et al. (2001) for the same faults whereas strike-slip faults are larger. The earthquakes within each focal region were declustered in time, in order to identify the mainshocks of the region. It is found that the mainshocks exhibit quasi-periodic behaviour when the preshock and postshock time periods are both equal to 8.5 years. Regarding the completeness of the historical part of the earthquake catalogue used we found that this catalogue is complete since 1845 for mainshocks with M≥6.5 in the whole Aegean area. In many focal regions, however, completeness for earthquakes with magnitudes larger than 6.5 are extended further back in time.

9. Acknowledgements

10. References

Aki, K., 1966. Generation and propagation of G waves from the Niigata earthquake of June 16, 1964. *Bull. Earthq. Res. Inst. Tokyo Univ.*, 44, 23-88.

Bonilla, M.G., Mark R.K. and Lienkaemper, J.J., 1984. Statistical relations among earthquake magnitude, surface rupture length and surface fault displacement. *Bull. Seismol. Soc. Am.*, 74, 2379–2411.

Kanamori H. and Anderson, D.C., 1975. Theoretical basis of some empirical relations in seismology. *Bull. Seism. Soc. Am.*, 65, 1073-1096.

Kagan, Y.Y. and Jackson, D.D., 1991. Long-term earthquake clustering. *Geophys. J. Int.*, 104, 117-133.

Papazachos, B.C., Mountrakis, D.M., Papazachos, C.B., Tranos, M.D., Karakaisis, G.F. and Savvaidis, A.S., 2001. The faults which have caused the known major earthquakes in Greece and surrounding region between the 5th century BC and today. *2nd Greek Conference on Earthquake Engineering and Engineering Seismology*, Thessaloniki, 28-30 September 2001, 1, 17-26.

Papazachos, B.C., Scordilis, E.M., Panagiotopoulos, D.G., Papazachos, C.B. and Karakaisis, G.F. 2004. Global relations between seismic fault parameters and moment magnitude of earthquakes. *Bull. Geol. Soc. Greece*, 36, 1482-1489.

Papazachos, B.C. and Papazachou, C.B., 2003. The earthquakes of Greece, *"Ziti Publications, Thessaloniki"*, 273pp.

Papazachos, B.C., Comninakis, P.E., Scordilis, E.M., Karakaisis, G.F. and Papazachos, C.B., 2009. A catalogue of earthquakes in Mediterranean and surrounding area for the period 1901-2008, *Publ. Geoph. Laboratory, University of Thessaloniki*.

Papazachos, C.B. and Kiratzi, A.A. 1992. A formulation for reliable estimation of active crustal deformation and an application to central Greece. *Geophys. J. Int.*, 111, 424-432.

Reid, H.F., 1911. The elastic-rebound theory of earthquakes. *Bull. Dep. Geol. Univ. Calif.*, 6, 412-444.

Schwartz, D.P. and Coppersmith K.J., 1984. Fault behavior and characteristic earthquake: Examples from the Wasatch and San Andreas fault zones. *J. Geophys. Res.*, 89, 5681-5698.

Smith G.C. and Stock Ch., 2000. Evidence for different scaling of earthquake source parameters for large earthquakes depending on faulting mechanism. *Geophys. J. Int.*, 143, 157-169.

Wells D.L. and Coppersmith K.J., 1994. New empirical relationships among magnitude, rupture length, rupture width, rupture area and surface displacement. *Bull. Seism. Soc. Am.*, 84, 974-1002.

Wesnousky S.G., 1986. Earthquake, quaternary faults and seismic hazard in California. *J. Geophys. Res.*, 91, 12587-12631.

EARTHQUAKE RELOCATION IN GREECE USING A UNIFIED AND HOMOGENIZED SEISMOLOGICAL CATALOGUE

Karakonstantis A.[1] and Papadimitriou P.[1]

[1] *National and Kapodistrian University of Athens, Department of Geology-Geoenvironment, Laboratory of Seismology, Ilisia, Zografou, 157 84 - Greece, akarakon@geol.uoa.gr, ppapadim@geol.uoa.gr*

Abstract

In this study phase data from the Cornet seismological network installed by the Geophysics-Geothermics Department (University of Athens) and the permanent networks of the Geodynamic Institute of the National Observatory of Athens and of the Geophysics Department of Thessaloniki (Aristotle University), for the decade 1996-2006, were merged. The data were jointly used to relocate the earthquakes that occurred in the broader area of Greece. Initially, single-event algorithms were applied by minimizing spatiotemporal residuals. Following, the hypocenters were relocated using a double-difference algorithm where rms, as well as the horizontal and vertical location errors (erh, erz) were minimized and a consequence of that better locations were achieved. After that process the spatial distribution of the epicenters outlined major local tectonic features in Greece. Moreover, the same methodology was applied to the aftershock sequences of large earthquakes and the results were successfully compared with those obtained by available local networks that were deployed.

Key words: *earthquake relocation, homogenized seismological catalogues, seismotectonics, Greece.*

1. Introduction

The determination of seismotectonic characteristics was a difficult procedure before the commencement of the Hellenic Unified Seismological Network (HUSN) in 2007, and that's because of not sufficient initial phase data that each Institute used. The geometry and the density of each network allowed researchers to locate earthquakes better in some regions than in others. A result of that procedure was the determination of different catalogues, in terms of hypocenter location and quality of the final solution. That could not facilitate us in order to make certain conclusions for seismotectonics in areas where an earthquake sequence occurred or the frequency of background seismicity was high. In this case merging phase data from three institutes (University of Athens, Geodynamic Institute of National Observatory of Athens and Aristotle University of Thessaloniki) was considered necessary in order to achieve azimuthal coverage with seismological stations and better hypocenter locations with single-event algorithms. Besides the previous factors that were mentioned, also the lack of a reliable 1-D layered velocity model per area is a common factor that produces important residuals in body wave arrivals. In this case of study, a double difference algorithm (hypoDD) has been applied to the phase data, targeting the hypocenter relocation of the merged catalogue for the decade 1996-2006 in Greece. Residuals between observed and theoretical travel-time differences (or double-differences) are minimized for pairs of earthquakes at each station while linking together all observed event-station pairs (Waldhauser and Ellsworth, 2000).
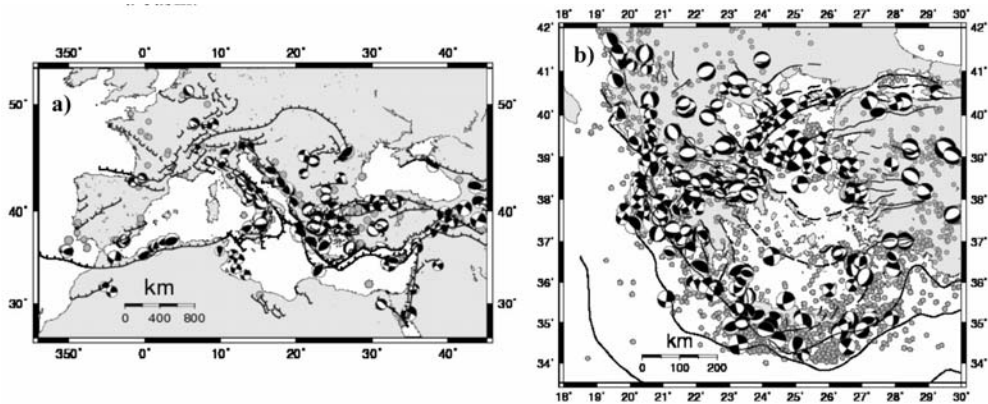
Fig. 1: a) Main faults in the broader area of Europe and significant earthquakes (CMT solutions) b) Main rupture zones in the area of Greece with focal mechanism solutions of significant earthquakes between 1996 and 2006 determined by S-L of UoA, NOA-G.I, A.U.TH, I.N.G.V.

From the whole data set that was processed, three areas will be presented in this case of study that include aftershock sequences of Athens 1999, Skyros 2001 and the background seismicity of Mygdonia basin.

Greece is located to the eastern end of Europe where a variety of geological procedures take place such as the Alpine orogenesis. The creation of the Alpine mountain chain, which is one of the most important geological features, is caused by the collision between Europe and Africa (Fig.1a). Furthermore, an intense deformation observed in Greece and surrounding areas produces important seismicity concentrated in certain seismic zones, such as the Hellenic Arc, characterized by subduction, the North Aegean, dominated by dextral strike-slip faulting, and the back arc area dominated by normal faults (Fig.1b).

Two main fault systems, the Hellenic Trench and the North Aegean Trough, dominate the Eastern Mediterranean, while the majority of the seismicity is located along these tectonic zones. In Fig.1a epicenters as well as focal mechanisms of large (M≥5.8) earthquakes throughout Europe are presented. Earthquakes and focal mechanisms with magnitude M≥4.0 in the Hellenic peninsula and surrounding areas are shown in Fig.1b. Earthquakes with magnitude greater than 6 for the time period 1900-2008 are shown with triangles. Similar focal mechanism solutions are observed in some regions as the Ionian Sea, the North Aegean and the Corinth Gulf. On the contrary, in other areas, as south of Crete, different fault plane solutions appear. Three main types of focal mechanisms can be distinguished: a.) dextral strike-slip motion in the vicinity of the Cephallonia-Lefkas, NW Peloponnesus and North Aegean areas, b.) reverse faulting southern of the Ionian islands and along the Hellenic arc and c.) Normal faulting in the back-arc region.

2. Data and analysis

2.1 Data sources

Data from three different seismological networks were used to form a joint catalogue that would supply better source parameters. The used earthquake catalogues were the ones of the Department of Geophysics of the National and Kapodistrian University of Athens (Cornet network), the Institute of Geodynamics of the National Observatory of Athens and the Department of Geophysics of the Aris-

Table 1. Number of earthquakes per network per year.

Year/Catalogue	Merged Catalogue	CORNET	G.I-N.O.A	A.U.TH
1996	3843	799	2560	2783
1997	5407	2087	3228	3219
1998	4380	788	2866	2086
1999	3942	710	1646	1438
2000	4115	742	3200	1488
2001	4136	751	3040	1873
2002	3239	472	2550	1121
2003	4035	382	6392	1709
2004	4987	399	3333	2662
2005	6481	178	5465	2139
2006	6383	463	5037	2797
total	50.948	7771	39317	23315
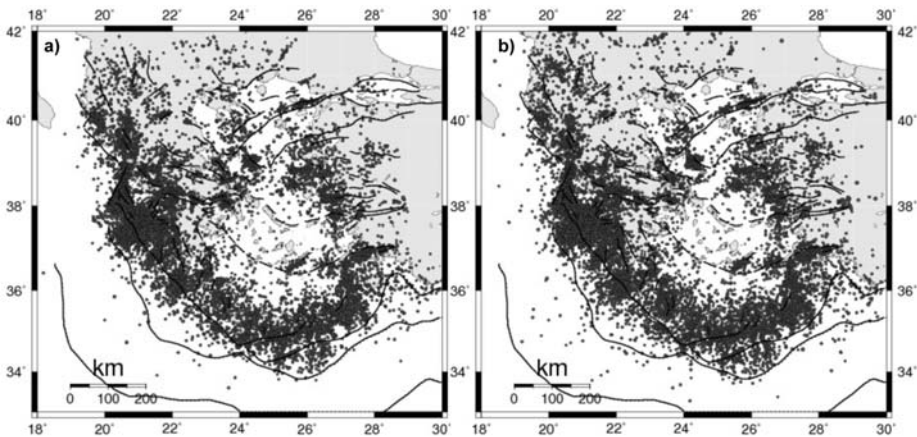
Fig. 2: Located seismicity (M≥3.2) from a) G.I-N.O.A b) Unified-Homogenized Catalogue.

totle University of Thessaloniki. The joint catalogue includes data from 1996, where the CorNet seismological network started its operation until 2006. By 2004 the first stations of the AtheNet seismological network started to operate, while the Hellenic Unified Seismological Network (HUSN) became operational in 2007. Figure 2 (a and b) shows the located seismicity of the GI-NOA and the merged catalogue respectively, while in Table 1 the statistics of the joint and the sub-catalogues are presented.

Each seismological network has its benefits depending on the quantity, geometry and location of the stations. Networks such as Cornet provided better locations for earthquakes that occurred in or near the Eastern Corinth Gulf while the respective network of AUTH enriched the catalogue with well-located events that occurred in Northern Greece. On the other hand the geometry of NOA's seismological network provides a more representative earthquake distribution. Using data from ATHU,

NOA and AUTH networks better results are achieved for earthquakes that occurred in the study area, because of the larger number and better distribution of stations. Merging the data from these different sources, a better location of epicenters can be achieved, by reducing the spatial and temporal (rms) errors. Specifically, the joint catalogue contains 50.948 events of magnitude greater than 1.8 (M_D), in the area between 34°-42° N and 19°-29° E, with mean rms equal to 0.67 seconds and respective mean spatial errors 5.9, 5.7 and 13.3 km (erx, ery, erz).

2.2 Merging and homogenizing the phases of different catalogues

After the collection of phase-arrival data from the three institutes, a process took place, in three main steps:

- Merging phase data, of these three different catalogues, identifying the earthquakes that were recorded by stations of more than one network and completing the joint catalogue by adding the "single-network" events. This process was done manually by comparing the arrival times of the different network stations that were mentioned previously. The catalog magnitudes were calculated using the signal duration (M_D).

- The result was an input file of phase arrivals for a single-event program such as HYPO71 or HYPOINVERSE. By re-weighting the P and the S phases and applying a 1-D layered velocity structure, we achieved an improvement of temporal and spatial residuals. The velocity model concludes 7 layers in 0, 4.2, 7, 11.5, 16.5, 35 and 80 km depth with respective velocities of 4.8, 5.7, 6.1, 6.3, 6.5, 7.8 and 8.1 km/sec (Kaviris, 2003). In HYPO71 the phase arrival was weighted as "4" (not taken into account) beyond 400 km, while in HYPOINVERSE there has been a progressive reduction of phase weight from 1 to 0 (100%-0%) from 50 to 400 km. The results are shown in Fig.2 for the decade 1996-2006.

- The final catalogue obtained by this procedure was processed by the HYPODD double-difference algorithm (Waldhauser and Ellsworth, 2000), where, as it will be mentioned in a next paragraph, the residuals were minimized. As a result hypocenter locations were ameliorated and alignment of epicenters with main rupture zones of the studied areas was achieved.

The merged input data file was divided in sub-areas, where the algorithm could give better results. These sub-areas were selected using certain criteria such as:

- The distribution of surface mapped rupture zones.

- The Map of seismic sources of surface earthquakes designed by Papaioannou and Papazachos (2000).

- The epicenter distribution through this time period.

Generally the mean spatial errors for the "common" earthquake events of the joint catalogue varied from 1.2 to 4.5 km (erx and ery) and 4.5 to 8 km (erz).

2.3 Double-Difference algorithm (HypoDD)

HYPODD (Waldhauser and Ellsworth, 2000) is an algorithm that minimizes residuals between observed and calculated travel time differences (or double-differences) for pairs of neighboring earthquakes at each station that recorded both events, as it can be seen from eq. 1. In this way errors caused by unmodeled velocity structure are minimized without the use of station corrections. A minimum 1-D layered velocity model is used to predict the travel time differences and partial derivatives (eq. 2).
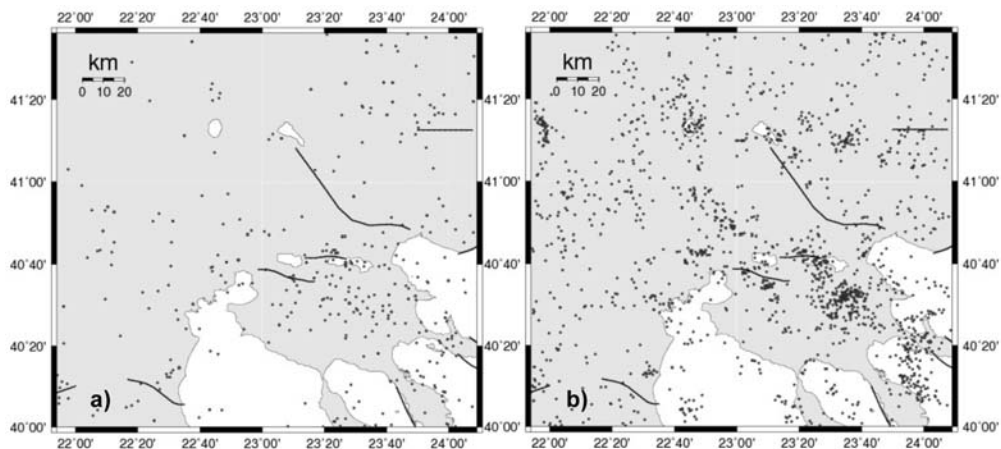
Fig. 3: a) Initial catalogue data of G.I-N.O.A b) Final Catalogue of unified homogenized data for Central Macedonia region (M≥2.0).

(eq. 1)

Where m=(x, y, z) **(eq. 2)**

Inter-event distance and misfit weighting is applied after each iteration to catalogue data, to optimize their quality dynamically during relocation. Horizontal and vertical relative spatial errors can be minimized by approximately one order of magnitude under certain conditions.

In this case of study more than 28.000 events of $M_D{\geq}2.0$, throughout Greece, were relocated with hypoDD. The data set will be uploaded to the site of the Seismological Laboratory of the University of Athens after the final processing and verification. Throughout the areas where the relocation procedure has taken place, a different approach of defying "strong links" was adopted. The main factors that had been taken into account were the size of the dominant clusters, the network coverage of the area, and the occurrence of an aftershock sequence that could reduce the maximum separation distance in ph2dt input parameter file.

3. Results

The procedure of merging phases and homogenization through single-event algorithms contributed to the enrichment of the initial catalogue data especially in regions with apparent low rates of seismicity. An ideal example is in the region of Central Macedonia, in Mygdonian basin. From a few tens of earthquakes that were recorded from G.I-N.O.A (Fig. 3a) the final catalogue reached 760 seismic events with M≥2.0, because of the addition of data from stations of AUTH's seismological stations in the region (Fig.3b). The case of Attica should be considered similar where a great part of the 1999 aftershock sequence was recorded by Cornet seismological network (Fig. 7b) and the joint catalogue's recorded events rose up to 30%. Partially, this conclusion seems to fit in the aftershock sequence of July 2001 as well (Skyros earthquake) where the northern cluster appears to be enriched with more earthquakes (Fig.5b) than the respective from the initial catalogue (Fig. 5a).

Fig. 4: a) Located earthquakes with HYPO71 b) Relocated data with HYPODD c) Located events with HYPOINVERSE d) Relocated events with HYPODD using a HYPOINVERSE processed primary catalogue (M≥2.0).

Besides the necessity of using merged data from all institutes in this kind of cases that reveals the importance of the National Seismological Network, what should also be emphasized, according to the relocation results, is the need of good initial data quality. As shown in figures 4, 6 and 8 the unified and homogenized catalogue data which were processed with HYPOINVERSE produce much better results during the relocation stage than the respective that were processed by HYPO71. This means that the choice of a single-event algorithm should be done carefully by taking into account all the possible aspects (advantages/disadvantages). Specifically, a single-event algorithm such as HYPOINVERSE shows its advantages during the processing of events that are located within the seismic network array while HYPO71 shows more reliable results for epicentres that lie outside of it.

In the area of Mygdonian Basin, 701 out of 760, located with HYPO71, events of the background seismicity (M≥2.0) were relocated with HYPODD, giving a first result that could be rated as satisfactory. The mean temporal errors (rms) were reduced from 0.50 sec to 0.14 sec while the spatial errors (erx, ery, erz) were increased from 2.5, 2.5 and 5.3 km to 3.7, 3.6 and 6.3 km respectively. These data were also processed by HYPOINVERSE, where 697 events were relocated with HYPODD in an even better location. The mean temporal residual (rms) that was determined by HYPOINVERSE was 0.29 seconds while the respective one obtained by the relocation process was 0.11 seconds. During the step of hypocenter location with HYPOINVERSE the spatial errors reached 1.7, 1.8 and 7.9 km (erx, ery, erz). The respective spatial errors obtained by the relocation with the double-difference algorithm (HYPODD) were 1.7, 1.8 and 2.7 km (erx, ery, erz). This way it can be clearly seen
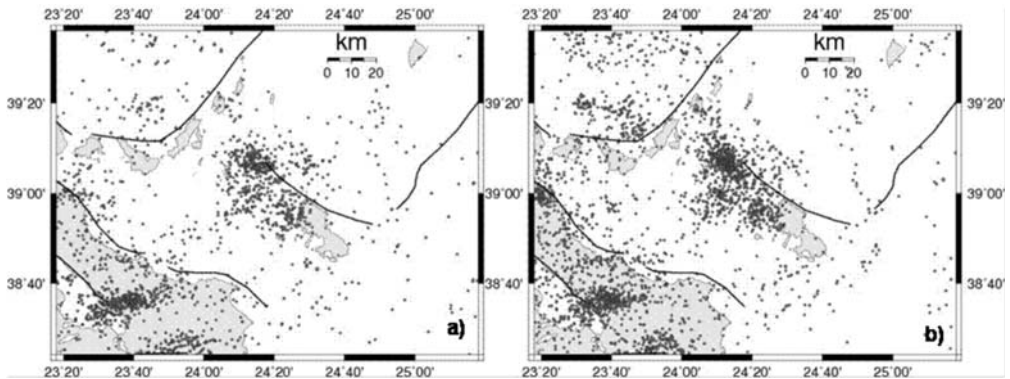
Fig. 5: a) Initial catalogue data of G.I-N.O.A b) Final Catalogue of unified homogenized data for Skyros region (M≥2.0).

that epicentres are concentrated in fault zones of NW-SE direction with a great cluster in Chalchidiki, in the normal faults that are located between Zervochoria and Arnaia, and a smaller cluster in the northern part of Thessaloniki-Gerakarou fault zone. The distribution of relocated events is in accordance with the seismotectonic regime of the area (Tranos et al., 2002) and the focal mechanisms that were determined by the University of Athens (S.L-U.o.A) and the Geodynamic Institute of the National Observatory of Athens (G.I-N.O.A).

Analyzing the aftershock sequence of Skyros earthquake (2001), the contribution of a relocated catalogue is clear (Fig. 6d). As in the example of Mygdonian basin, even here HYPOINVERSE contributes to a better located event catalogue. For the decade 1996-2006, 910 events of M≥2.0 were located to the area north, north-west of Skyros Island. The mean rms obtained by HYPO71 in this case, was 0.6 seconds while the respective spatial errors by the x, y and z axis were 2, 5.3 and 3 km. During the first relocation of hypocenters determined by HYPO71, the image gets clearer as it can be seen in Fig. 6b, (rms=0.19 sec, erx=4 km, ery=4km, erz=5.7 km) while in the second step that relocation of HYPOINVERSE locations takes place (Fig. 6c), the differentiation of the clusters (Fig. 6d) and their connection to local faults is easier (rms=0.13 sec, erx=2.5 km, ery=2.6 km, erz=3.5 km). According to Fig. 6d, what appears more likely to have happened in this case, is the activation of two major clusters of NW-SE direction and about 25 and 10 km length respectively, with possibly another, western of these two, 5 km long (Karakonstantis, 2009). These results are directly comparable with the respective ones of Benetatos et al. (2002) and Roumelioti et al. (2003) for the same region. All the solutions that came up with the relocation through HYPODD are in accordance with the focal mechanisms of the S.L-U.o.A and G.I-N.O.A for this time period.

The epicenter of the Athens Earthquake was located in Thriassion basin at a depth of 9.4 km, obtained by the double-difference algorithm procedure. Out of 966 earthquakes of the aftershock sequence, with mean rms and spatial errors (erx, ery, erz) equal to 0.81 sec, 3.4, 4.1 and 12.1 km, 823 were relocated in a new location with the respective errors reduced to 0.12 sec and 1.9, 2.1 and 2.6 km (erx, ery, erz). As it can be seen from Fig. 8c, using HYPOINVERSE a better concentration of events is achieved around main rupture zones than the respective of HYPO71 (Fig. 8a). After this process, the mean temporal residuals (rms) reached 0.36 seconds while the respective spatial ones were determined as 4.6, 5.1 and 18.2 km (erx, ery, erz). After the relocation (Fig. 8d), the mean temporal (rms) and spatial errors (erx, ery, erz) were reduced significantly. The mean rms value was equal to 0.06 seconds and mean erx, ery, erz reached 1.15, 1.21, 1.59 km respectively. The optimization of the final
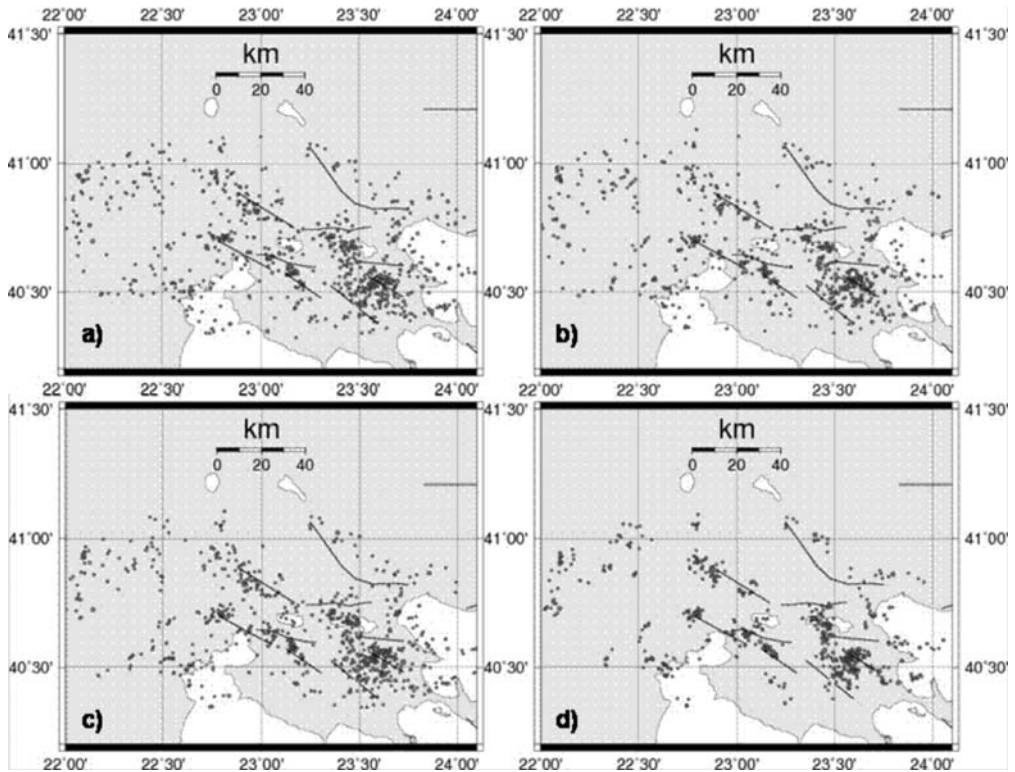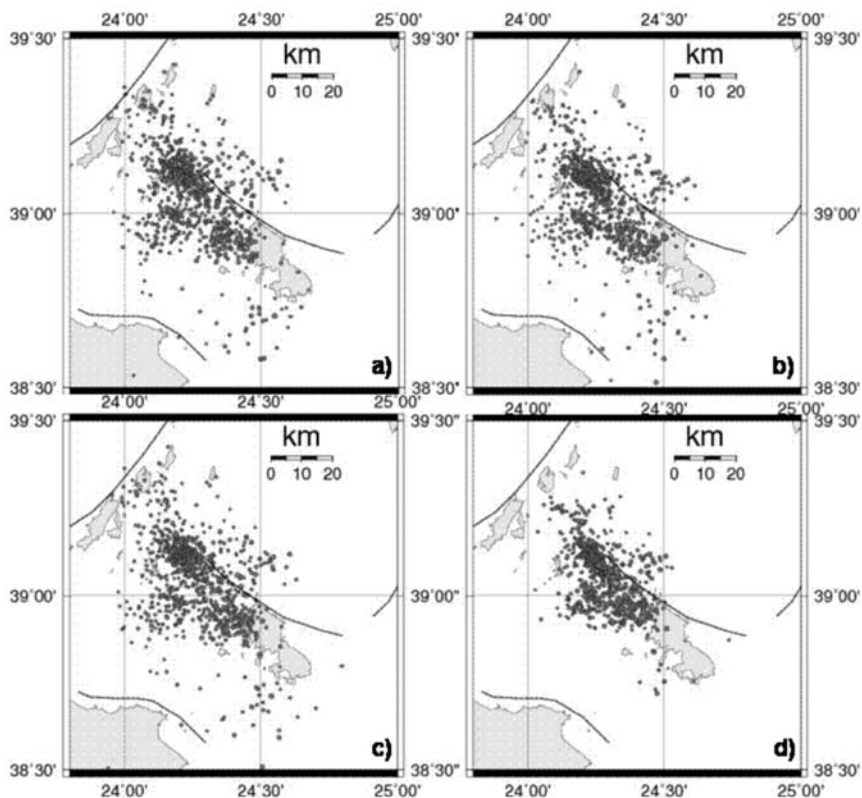
Fig. 6: a) Located earthquakes with HYPO71 b) Relocated data with HYPODD c) Located events with HYPOINVERSE d) Relocated events with HYPODD using a HYPOINVERSE processed primary catalogue (M≥2.0).

results leads to clustering of the earthquake sequence in two main parts. The first one is located WNW of the main shock epicenter while the second one is found eastern of it.

The distribution of epicenters in Fig. 8 b, d shows the activation of the Parnitha's fault escarpment. It is clear that the majority of aftershocks is located on a rectangular area around it (Karakonstantis, 2009) that extents along Thriassion basin with main direction WNW-ESE. It should be noted that the initially located events showed an important activity outside the fault area due to the large spatiotemporal errors. In addition a smaller cluster located NE of the epicentral area could be related to the Phyli's fault.

The earthquakes that occurred within 13 minutes before the main shock were located along the Parnitha fault, in the western cluster of the focal area, mainly at depths 11-14 km, a clue that characterizes them as foreshocks.

The results of the aftershock distribution of the Athens earthquake were successfully compared with those obtained by Papadimitriou et al. (2002), where a local network had been set up to record the aftershock sequence (3.500 events). The existence of two main clusters is shown in the rose diagrams of azimuth and dip orientation distribution by Voulgaris et al. (2001) and in the focal mechanisms that were determined by Papadimitriou et al. (2000) in the area.
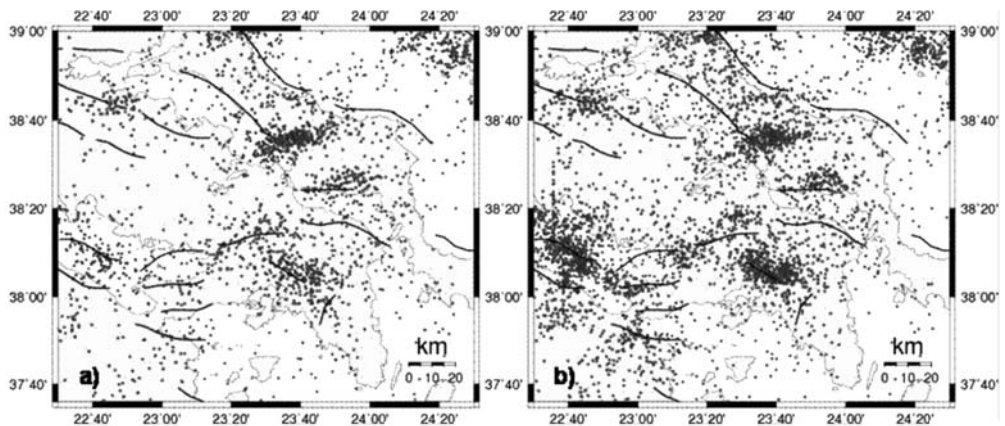
Fig. 7: a) Initial catalogue data of G.I-N.O.A b) Final Catalogue of unified homogenized data for Attica region (M≥2.0).
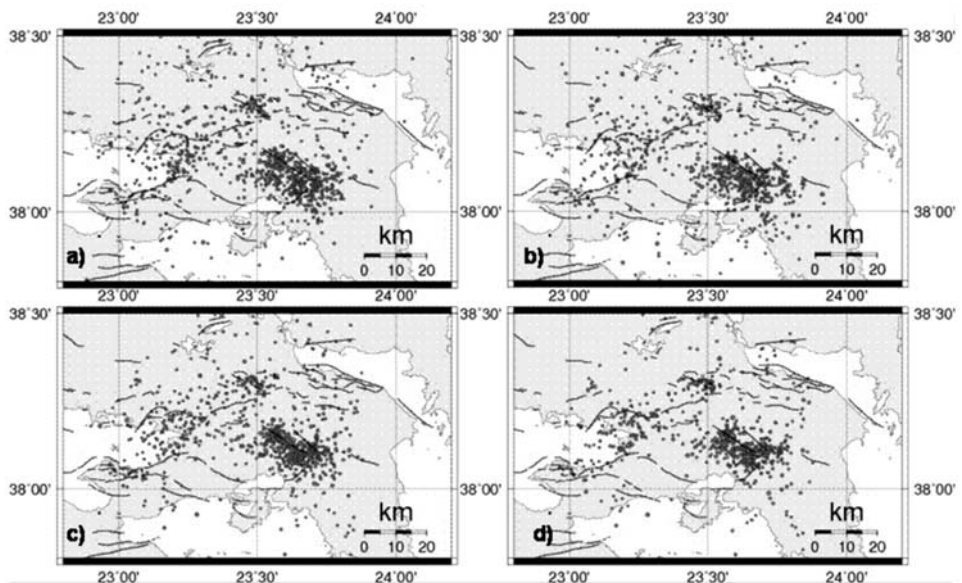
Fig. 8: a) Located earthquakes with HYPO71 b) Relocated data with HYPODD c) Located events with HYPOINVERSE d) Relocated events with HYPODD using a HYPOINVERSE processed primary catalogue (M≥2.0).

4. Conclusions

In this study the importance of using data from more than one permanent seismological network, as well as the need of using different algorithms in data processing to obtain better results was revealed.

During this study, data from three different catalogues were manually merged and processed by two different single-event location algorithms in order to achieve better locations and compare temporal and spatial residuals obtained by these two programs. In fact, some cases show that small spa-

tial residuals don't necessarily mean a good location. That can be clearly seen by the qualitative comparison in certain cases, where HYPO71 spatial errors are smaller while the respective epicenters seem to be worse located than those of HYPOINVERSE. This process contributed to our effort to reveal more reliable spatial errors during the location step.

Phase data of the joint catalogue were used as an input file to HYPODD and by intervening in the parameters of the program we could achieve the optimization of the final result. In order to obtain better results it is necessary to have good primary epicenter locations and a more dense coverage of stations in the epicentral area. This task was achieved by merging and homogenizing the available data. Moreover, some relocated aftershock sequences, as the Athens and Skyros earthquakes, clearly reveal the dimension of the activated fault area. The mean spatial and temporal errors that were obtained through this procedure were minimized by up to one order of magnitude in areas with a dense coverage of stations by these three networks.

The results obtained by the double difference algorithm, in most cases, indicated a concentration of seismicity that in special cases was located along main rupture zones. Consequently they can be successfully compared to those obtained by available local networks that were deployed in the study area.

5. References

Benetatos, C., Roumelioti, Z., Kiratzi, A., Melis, N., 2002. Source parameters of the M 6.5 Skyros island (North Aegean Sea) earthquake of July 26, 2001. *Ann. Geophys.* 45, 513–526.

Karakonstantis, A., 2009. Unification-Homogenization of seismological catalogues and re-assessment of focal parameters of earthquakes during 1996-2006 period. Application to Seismotectonics of the Hellenic peninsula, *Master thesis*, National and Kapodistrian University of Athens, 262 pp.

Kaviris, I.G., 2003. Study of properties of the Eastern Corinth Gulf Seismic sources, *PhD thesis*, Athens 2003, pp.56-61, 74-84,238-241.

Papadimitriou, P., Kaviris, G,. Voulgaris, N., Kassaras, I., Delibasis N., and Makropoulos, K., 2000. Source Parameters Determination of the September 7, 1999 Athens Earthquake. *Book of Abstracts*, p. 33, XXVII ESC General Assembly, Lisbon, Portugal.

Papadimitriou, P., Voulgaris, N., Kassaras, I., Kaviris, G., Delibasis, N., Makropoulos, K., 2002. The M_w=6.0, 7 September 1999 Athens Earthquake, *Natural Hazards* 27: p.15-33.

Roumelioti, Z., Kiratzi, A., Melis, N., 2003. Relocation of 26 July 2001 Skyros Island (Greece) earthquake sequence using the double-difference technique*, Physics of the Earth and Planetary Interiors* 138, pp.231-239.

Tranos, M. D.; Papadimitriou, E. E.; Kilias, A. A., 2002. Thessaloniki-Gerakarou Fault Zone (TGFZ): the western extension of the 1978 Thessaloniki earthquake fault (Northern Greece) and seismic hazard assessment, *Journal of Structural Geology*, v. 25, iss. 12, p. 2109-2123.

Voulgaris, N., Pirli, M., Papadimitriou, P., Kassaras, I. and Makropoulos, K., 2001. Seismotectonic Characteristics of the Area of Western Attica derived from the study of the September 7, 1999 Athens Earthquake Aftershock Sequence. *Bull. Geol. Soc. of Greece*, vol. XXXIV, no 4, p. 1645-1654.

Waldhauser, F., Ellsworth, W., 2000. A Double-Difference Earthquake Location Algorithm: Method and Application to the northern Hayward Fault, California*, Bulletin of the Seismological Society of America* 90,6, pp.1353-1368.

MICROSEISMICITY AND SEISMOTECTONIC PROPERTIES OF THE LEFKADA – KEFALONIA SEISMIC ZONE

Karakostas, V. G.[1], Papadimitriou, E. E.[1], Karamanos Ch. K.[1] and Kementzetzidou, D. A.[1]

[1] *Aristotle University of Thessaloniki, School of Geology, Department of Geophysics, 54124 Thessaloniki, Greece, vkarak@geo.auth.gr, ritsa@geo.auth.gr, chrikar@geo.auth.gr, dkementz@auth.gr*

Abstract

Microseismicity, focal–mechanisms, and previously–published focal parameter data are used to determine the current tectonic activity of the prominent zone of seismicity in Lefkada and Kefalonia Islands. Recordings from a local network installed and operated on the two Islands, as well as from permanent stations there, were used to obtain accurate microseismicity locations, which in turn is exploited to reveal properties of smaller localized active structures and the large–scale crustal faulting. The microseismicity substantially agrees with the historic seismicity and delineates a relatively narrow, major zone of activity that extends along the western coasts of both Islands. Cross sections were used in order to provide a detailed characterization of the microseismicity and a high–resolution picture of the seismically defined structures. For the investigation of the past seismic activity relocation of the hypocenters of older events was performed, using a reliable velocity model and time delays for the regional stations, calculated on the basis of the accurately determined focal parameters using the local recordings. The yielding location improvement contributes to the geometry identification of the active structures, which were previously obscured by location errors, and which constitute a critical input for the study area seismic hazard assessment.

Key words: microseismicity, relocation, active structures, Ionian Islands.

1. Introduction

Local scale earthquake location studies of small magnitude earthquakes lend insight into seismogenic zone processes and are well suited to define the geometry and volume of the seismogenic zones and to constrain their thickness along strike and downdip. Detailed investigation of the local seismicity in the area of the central Ionian Islands, the most active in Greece and its surroundings, is then demanded, which is expected to add information to the location of active faulting and their characteristics. The 2003 Lefkada sequence provided for first time the proper data for a detailed look at the properties of the dominant rupture system (Karakostas et al., 2004), as well as on the activation of secondary structures capable to produce additional and severe damage, thus posing significant seismic hazard (Karakostas, 2008; Karakostas and Papadimitriou, 2010). These findings demonstrated the need for a detailed analysis of earthquake occurrence and faulting, which in turn requires the accurate knowledge of the precise spatial location of earthquake hypocenters, especially in the case of offshore or smaller secondary faults.
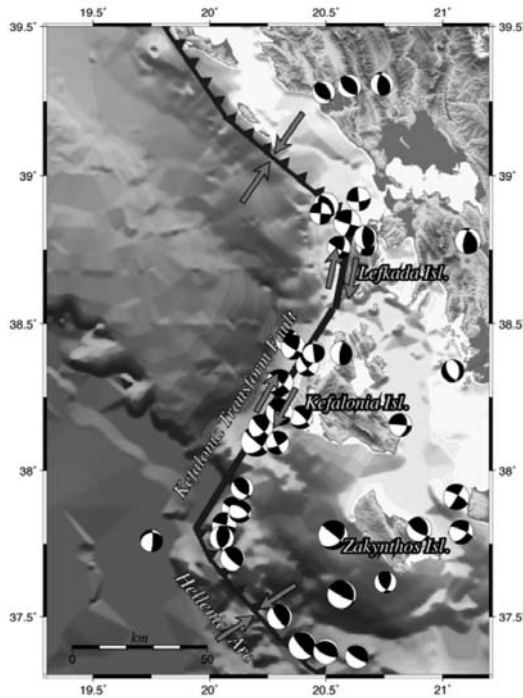
Fig. 1: Main active boundaries along with the fault plane solutions of strong events that occurred in the study area during the last four decades. Arrows show relative plate motion.

For the purpose of our study, which is firstly the determination of the properties of active structures in the area of Lefkada and Kefalonia Islands, we use data from the recently established network of three–component seismograph stations in these Islands to obtain the first reliable earthquake source parameter estimates for the region's microseismicity. We use the spatial distribution of seismicity and fault plane solutions to specify the properties of the major faults and further identify secondary active ones and to constrain their geometry and kinematics. In addition, for the whole area of central Ionian Islands, because of documented bias in routine analysis, we relocate larger earthquakes using the recordings of regional permanent networks. Recent seismicity over the last 45 years (1964–2008) defines bands of activity, increasing confidence in the geometry of the associated faults.

2. Seismotectonic setting

The area of central Ionian Islands, namely Lefkada and Kefalonia, constitutes the most active zone of shallow seismicity in the Aegean and its surroundings. This area is amongst the most active deforming ones in the Alpine – Himalayan belt, with its prominent feature the subduction of the eastern Mediterranean oceanic lithosphere under the Aegean (Comninakis & Papazachos, 1971) along the Hellenic Arc. The seismic activity is very high throughout the arc, where thrust faulting dominates with the axis of maximum compression oriented NE–SW (Fig. 1). North of Lefkada Island a thrust faulting zone terminates, which runs along the south western coast of former Yugoslavia and continuous along the coastlines of Albania and north western Greek mainland, where the axis of maximum compression is almost perpendicular to the direction of the Adriatic–Ionian geologic zone. This zone resulted from the continental collision between the external Hellenides and the Adriatic microplate.

Between continental collision to the north and oceanic subduction to the south, the Kefalonia – Lefkada dextral strike–slip fault system is developed, in accordance with the known relative motion between Aegean and eastern Mediterranean. The dextral strike–slip nature of this fault system was first recognized by Scordilis et al. (1985) who determined the fault plane solutions of the 1983 (M7.0) Kefalonia main shock and its largest aftershock (M6.3). This kind of faulting was further confirmed by waveform modelling for the 1983 main shock by Kiratzi & Langston (1991) and for the 1972 Kefalonia earthquake (M6.3) by Papadimitriou (1993).

The area is of exceptional scientific interest from the seismotectonic point of view for several investigators. For the frequent strong events taking place there during the last five decades, waveform modelling has been accomplished (Papadimitriou, 1988; Kiratzi & Langston, 1991; Papadimitriou, 1993; Baker et al., 1997) providing reliable fault plane solutions, which are depicted in Figure 1. In the same figure the main active boundaries are also shown along with arrows indicating relative plate motion. Papazachos et al. (1998) grouped the most reliable focal mechanisms and found a representative mechanism for Kefalonia with strike=33°, dip=56° and rake=163°, whereas for Lefkada the corresponding values are: strike=11°, dip=60° and rake=165°.

Historical information and instrumental data reveal that the occurrence frequency for the stronger (M≥6.5) events in the study area is almost constant during the last four centuries with one such shock per decade (Papadimitriou & Papazachos, 1985). The maximum observed earthquake magnitude in Kefalonia equals to 7.4 and in Lefkada to 6.7 (Papazachos & Papazachou, 2003). Moderate magnitude events are also very frequent, oftentimes located onshore, constituting an additional threat from the seismic hazard view point. It is then of importance to exploit the proper data that are available to us, aiming to define the geometric and kinematic properties of the active structures that have been activated and are possible candidates to host future moderate to strong events.

3. Catalogue compilation of local earthquakes

3.1 Local network operation

A portable seismic network was deployed in the study area consisting of seven 3–component digital stations equipped with broad–band (30s) and short period (1Hz) sensors, all equipped with GPS antenna for timing. These stations operated in continuous mode since the middle of 2007 with a sampling frequency of 125 samples/sec. The spacing between stations varied between 5 to 10 km, allowing accurate earthquake locations (red squares in Fig. 2). In addition to the recordings of the local network, data from the stations of the national regional seismological network, installed on the two islands (blue diamonds in Fig. 2), are also available for our study.

3.2 Focal parameters determination

For the earthquakes hypocentral determination the HYPOINVERSE (Klein, 2002) computer program was used, for which in addition to the arrival times of the seismic waves at the seismological stations, an accurate velocity model is needed. We adopted the 1–D velocity model and a velocity ratio of V_p/V_s=1.80 proposed by Haslinger et al. (1999) for a broader area that the one of the present study.

The accuracy in the hypocentral determination was checked by the distribution of the errors in the determination of the occurrence time (rms), the epicentral coordinates (erh) and the focal depth (erh). As it can be seen from Figure 3a, all rms values are smaller than 0.5 sec, with the
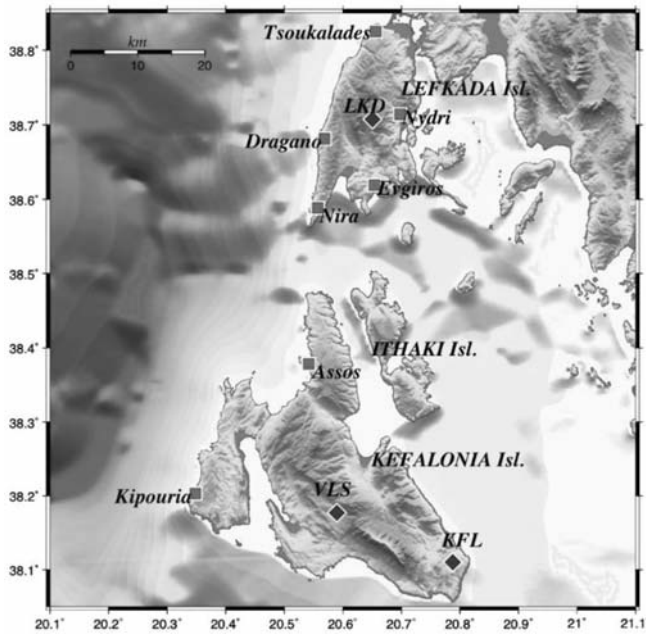
Fig. 2: The locations of the stations of the local seismological network (red rectangles), along with the permanent ones (blue diamonds) of the national seismological network.
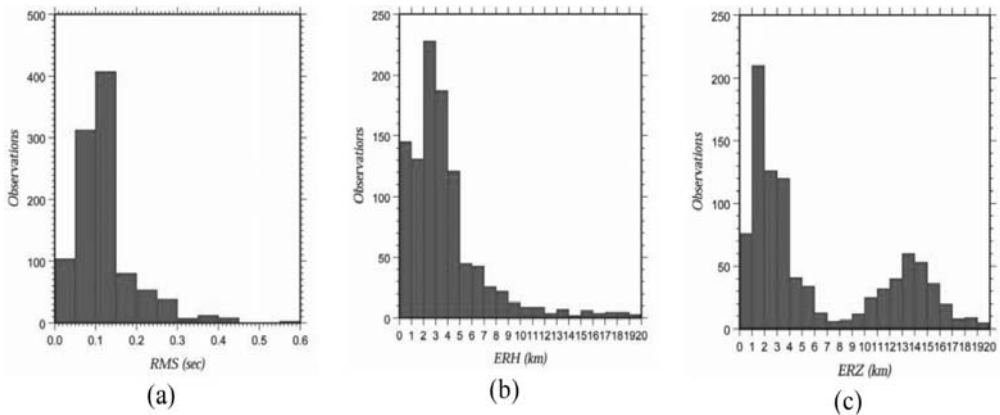
Fig. 3: Histograms of the (a) root mean square in the occurrence time (rms), (b) epicentral determination error (erh) and (c) depth determination error (erz), of local events locations.

vast majority being less than 0.2 sec. The errors in the epicentral determination are mostly less than 10 km, with the 80% of them being less than 5 km (Fig. 3b). The maximum in this distribution appears at 3–4 km, with 25% of the events assigned an erh<3 km. The errors in focal depth determination are less of 20 km, with most of these values being less than 7 km and the maximum at the range 0–4 km (fig. 3c). This distribution exhibits two clusters, in the range of 0–7 km and 8–20 km, respectively. This second cluster can be attributed to the limited number of observations of the lower magnitude events as well as to the fact that a significant portion of the activity occurred outside the local network.
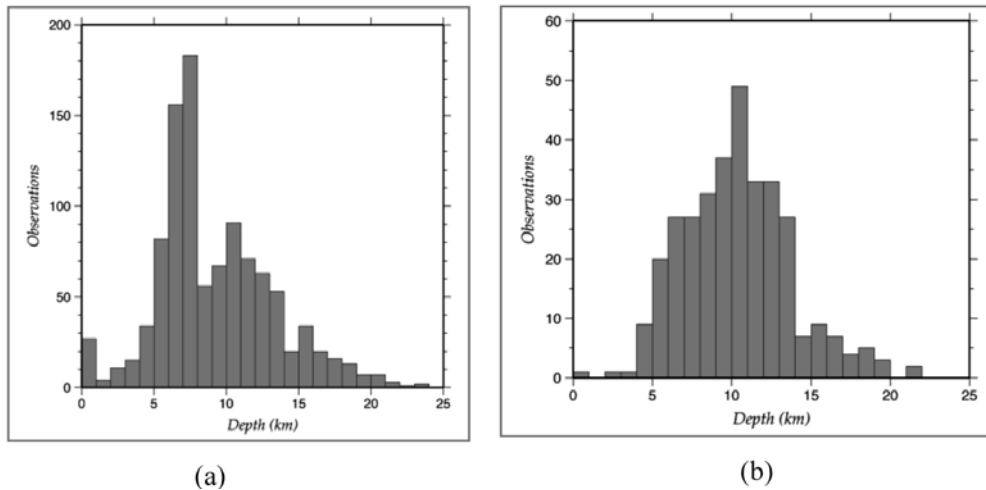
Fig. 4: Focal depths distribution of (a) all the events that occurred in the study area during the period covered by our data, and (b) the best located events.

Earthquake magnitudes were estimated from the maximum amplitude of the recordings at each seismological station. For this purpose simulation filters were used, which transformed the recordings of a sensor (preferentially broad band) to Wood Anderson recording, provided that the transfer function permits this transformation. Magnitudes were estimated from the maximum amplitudes at the two horizontal components of each station of the local network, after transformation, and the mean value was adopted as the assigned magnitude of each event.

3.3 Distribution of focal depths

The knowledge of the depth distribution provides valuable information on the geometry of the active structures. In tectonically complex areas, like the area of central Ionians, this information is unambiguously necessary. The focal depths of all the events recorded by the local network are between 0 and 24 km, with the vast majority of them between 4 and 16 km (Fig. 4a). It must be noted here that in this data sample events that were recorded by a small number of stations or located far from the local network, are also included. The depth distribution of the best located events (rms≤0.2 sec, erh≤2.0 km, erz≤2.0 km) is depicted in Figure 4b, which reveals that the seismogenic layer extends between 4 and 15 km, with a maximum of activity at 10–11 km depth.

3.4 Fault plane solutions determination

The onsets of at least six first arrivals of the P waves at the seismological stations and the FPFIT (Reasenberg & Oppenheimer, 1985) computer program were used for the focal mechanisms determination. Since the quality of the solutions depends on factors such as the azimuthal coverage as well as the distribution of the arrivals on the projection plane, reliable fault plane solutions were feasible for a limited number of events. These reliable solutions are exploited for the definition of the properties of the active structures and are presented in a later section.
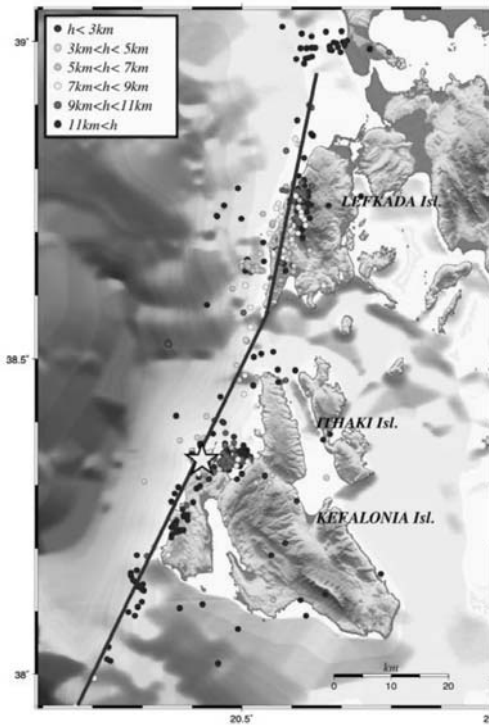
Fig. 5: Spatial distribution of the best located local events, along with the trace of the Kefalonia – Lefkada fault system trace.

4. Properties of the active structures

4.1 Spatial distribution of the seismic activity

Figure 5 depicts the epicentral distribution of the best located events (rms≤0.2 sec, erh≤2km, erz≤2 km), along with the trace of the dextral strike–slip active boundary of the Kefalonia – Lefkada fault system. It must be noted here that this activity is not representative for the whole area, but only for the part with adequate network coverage. It is observed that most activity is narrowed along the western coastlines of Lefkada and the north western coastline of Kefalonia. The activated area in Lefkada coincides with the aftershock area of the 2003 strong (M6.2) main shock (Karakostas et al., 2004). It then provides strong evidence that this structure is appreciably active.

In the area of Kefalonia where increased activity appeared, an M5.9 event occurred on March 27, 2007. The epicentre of this main shock is shown with an asterisk in Figure 5 and is located with data from the national regional network, because the local network installed a couple of weeks later. Since this occurrence the activity continued with a high rate as far as moderate and smaller magnitude events concerns, many of them felt in the nearby villages. Continuous activity is also present along the western peninsula, which extends along the south western offshore area.

Figure 6 exhibits a cross section parallel to the strike of the fault system, as this is traced in Figure 5. This figure evidences two main clusters, the one at the area of the 2007 seismic excitation and the second one at the central part of Lefkada Island. It is also prominent that the focal depths are concentrated between 4 and 15 km, while larger depth concentrations concern earthquakes occurred outside the local network with probably larger uncertainty in the depth determination.
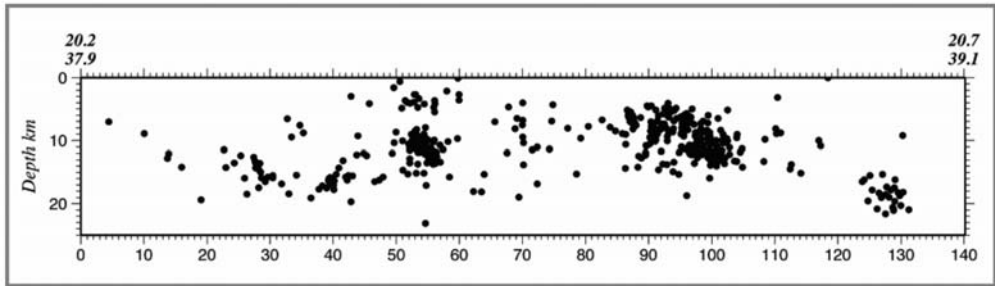
Fig. 6: Cross section parallel to the line defined by 37.9°–20.2° and 39.1°–20.7°, almost parallel to the strike of the Kefalonia – Lefkada fault system.

4.2 Microseismicity in Lefkada Island

Figure 7a depicts the best located earthquakes along with the high quality determined fault plane solutions as lower hemisphere equal area projections. The reason we use the chosen data is because the definition of the geometry and kinematics of the active structures demands the most accurate data sample. In addition to the seismic zone striking NNE–SSW, along the main tectonic structure, two more distinctive clusters are apparent, which in turn prefigure two secondary active structures. The first is located offshore the south western coastline, strikes at WNW–ESE, in full accordance with the fault plane solutions of five events of this cluster. This strike, implying left–lateral strike–slip motion, supports the characterization of this structure as a conjugate one of the dominant NNE–SSW dextral strike slip motion. Although the occurrence of a strong or moderate earthquake there is not known there, its length is capable to accommodate an event of M5.5.

The second active structure revealed by the local data is located in the central western onshore part of the Island. It strikes at NNW–SSE, in agreement with four fault plane solutions of events encompassed in this cluster. With a length of 7 km, it can be associated with an event of M5.5. It was the most active structure during the operation of the local network, partially due to the fact that this location was well azimuthally covered by local stations. It is worth to note that this structure was also activated during the 2003 seismic sequence, and severe damage to the natural and built environment was reported. Although such macroseimic effects were expected along the west coastline where the main rupture took place (Karakostas, 2008), the severity of damage at this particular place evidenced the activation of secondary faults.

4.3 Microseismicity in Kefalonia Island

The best located events that occurred in the area of Kefalonia are shown in Figure 7b, and mainly form two clusters, the first one in Palliki peninsula (west part of the Island) and the second at the Gulf of Myrtos (north western part of Island). The spatial epicentral concentration of the first cluster is not adequate to reveal the properties of the structure that host this data set. An adequate number of fault plane solutions, however, and the consistency among these solutions, support a NNE–SSW striking thrust faulting. Even though this kind of faulting is first suggested here, its kinematics is consistent with the local stress field (almost E–W orientation of the maximum compression axis, in agreement with the strong events fault plane solutions depicted in Figure 1).
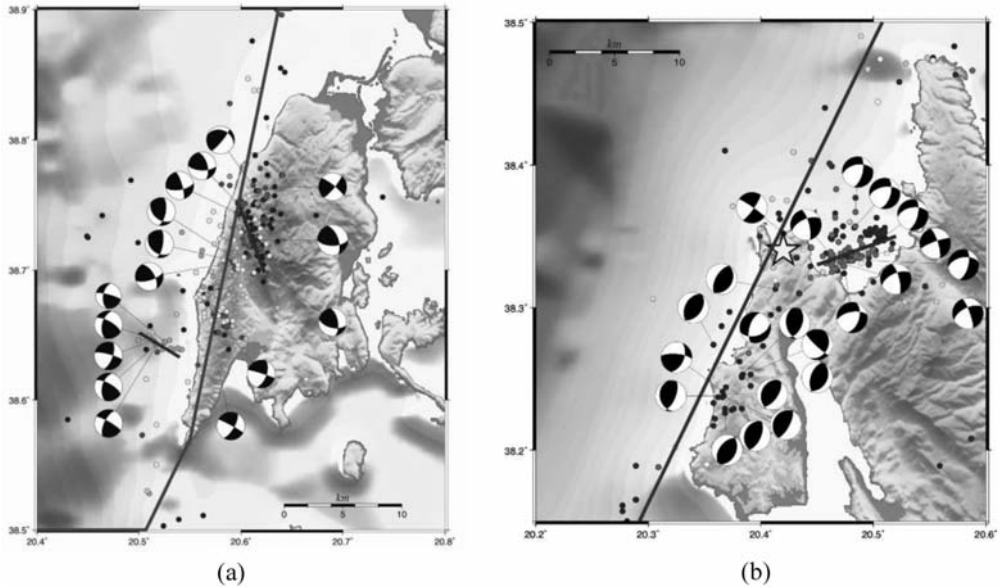
Fig. 7: (a) Spatial distribution of best located local microseismicity in Lefkada area along with fault plane solutions determined for some of these events, shown as lower hemisphere equal area projections. (b) Spatial distribution of best located local microseismicity in Kefalonia area along with fault plane solutions determined for some of these events, shown as lower hemisphere equal area projections.

A very energetic seismic sequence followed the 2007 main shock in the Gulf of Myrtos, to the north western offshore area of Kefalonia, where both the epicentral distribution and fault plane solutions of an adequate number of events, reveal a structure of 5–6 km in length, striking at ENE–WSW, and exhibiting oblique faulting.

5. Relocation of the regional catalogue

5.1 Regional data collection

The relocation of the events that occurred in an area broader than the one covered by the local network, which accommodates the highest activity of Greece and its surroundings, during 1964–April 2008 was attempted. In order to achieve high relocation accuracy, an adequate number of body waves (both P and S) recordings, at the seismological stations of the broader area, for each earthquake were seeking. For the interval 1964–May 2006 data were taken mainly from the International Seismological Center (ISC, http://www.isc. ac.uk). For the interval June 2006–April 2008 the phases collected at the Seismological Station of Geophysics Department, of the Aristotle University of Thessaloniki. Data were gathered from 745 seismological stations in total.

5.2 Focal parameters determination

For the hypocentral relocation an attempt was made to define a regional velocity model for the study area, based on the recordings of the permanent seismological network. The derived model agreed satisfactorily with the one proposed by Haslinger et al. (1999) for the area of Ionian Islands and north western Greek mainland. Therefore, this latter model was finally used after
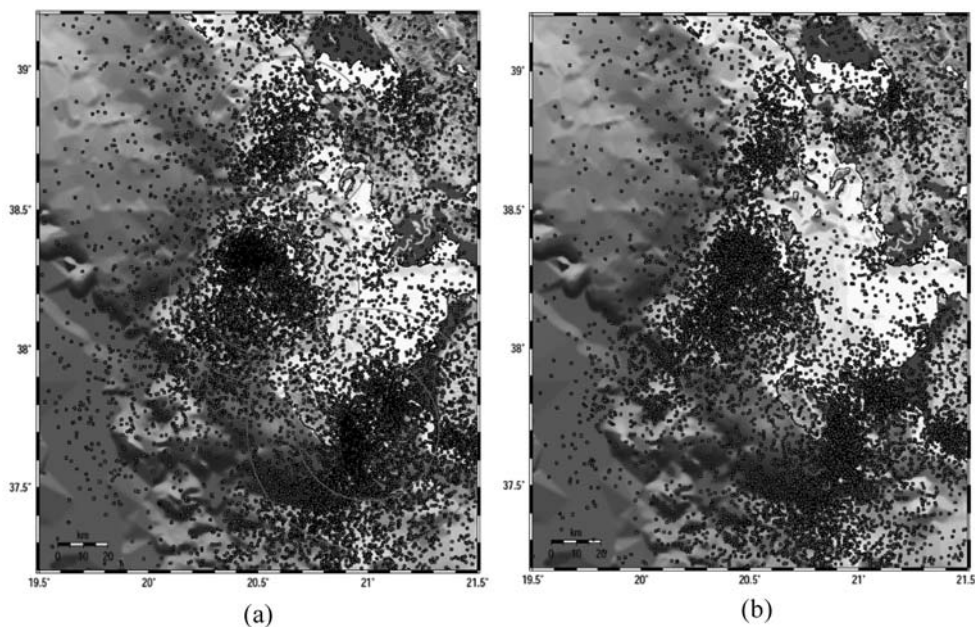
Fig. 8: (a) Spatial distribution of regional seismicity upon which the three regions were defined for the application of HYPOINVERSE computer program. (b) Spatial distribution of the relocated earthquakes that occurred in the area of Lefkada, Kefalonia and Zakynthos Islands during 1964 – 08/04/2008.

confirming its appropriateness for the certain area. Since this model was one dimensional, and in order to take into account lateral crustal inhomogeneities, time delays were estimated for each seismological station. The HYPOINVERSE (Klein, 2002) computer program was applied and the initial relocation resulted to 13041 preliminary determined hypocenters.

5.3 Estimations of stations residuals

For the estimation of time delays, that is the difference between the theoretical and the observed travel time from the earthquake focus to the seismological station, the area of interest was separated into three subareas on the basis of epicentral concentration (Fig. 8a). For the station residuals estimation in each subarea, the earthquakes with an adequate number of recordings were taken into account. For Lefkada and Kefalonia areas in particular, the focal parameters of the local events were also considered, whereas for Zakynthos the best available data based on the recordings of the permanent network. The station delays were estimated separately for each subarea and each seismological station, because the ray paths are different. Thus, in each subarea individual sets of station delays were estimated and used for the relocation.

5.4 Determination of focal parameters

After detailed elaboration of the available data and station delays, the hypocentral relocation was accomplished. From the errors distribution in the determination of the occurrence time (rms), epicentral coordinates (erh) and focal depth (erz), it is observed that more than the 60% of the relocated events exhibit rms errors less than 0.8 sec, whereas more than 50% exhibit erh

and erz less than 5 km and 8 km, respectively. The epicentral distribution of the relocated events is depicted in Figure 8b.

A significant reduction in the scatter of epicentral distribution is observed, which in combination with independent fault information furnishes important contribution to the configuration of the regional active structures. A particular case is the aftershock area of the 1983 strong main shock (M7.0), which occurred in the southwest offshore area of Kefalonia Island. The delineation of aftershock epicentres is evident in Figure 8b, It is worth to mention here that whereas the formal errors in the relocated seismicity are satisfactorily accurate, errors resulted from faults misassociation can be larger.

6. Conclusions

The microseismicity recorded by the local network installed and operated in the area of central Ionian Islands, provided the means of identifying secondary active structures and their geometric and kinematic properties. The particular structures although of smaller lengths than the ones associated with the stronger events (M≥6.0) in this region, are capable to accommodate moderate events (5.0≤M≤5.9). For this reason they must be taken into consideration in the future seismic hazard assessment studies, in particular because they are located onshore and near to the built environment. It must be mentioned here that the 1994 M5.4 Lefkada earthquake, produced considerable damage in the villages of the north western part of the Island. The exploitation then of the microseismicity for the identification of active structures and definition of their properties, is necessitated for a seismotectonically complex area, like the area of central Ionian Islands.

7. Acknowledgments

8. References

Baker, C., Hatzfeld, D., Lyon–Caen, H., Papadimitriou, E. and Rigo, A., 1997. Earthquake mechanisms of the Adriatic Sea and western Greece: implications for the oceanic sudbuction – continental collision transition. *Geophysical Journal International*, 131, 559–594.

Haslinger, F., Kissling, E., Ansorge, J., Hatzfeld, D., Papadimitriou, E., Karakostas, V., Makropoulos, K., Kahle, H.–G. and Peter, Y. (1999). 3D crustal structure from local earthquake tomography around the gulf of Arta (Ionian region, NW Greece). *Tectonophysics,* 304, 201–218.

International Seismological Center, 2001. On–line Bulletin, http://www.isc.ac.uk/ Bull, *International Seismological Center, Thatcham, United Kingdom*.

Karakostas,V., 2008. Relocation of aftershocks of the 2003 Lefkada sequence: Seismotectonic implications *Proc. 3rd Hellenic Conf. Earthquake Engineering & Engineering Seismology, Athens 5–7 Nov. 2008*, CD ROM, pp.16.

Karakostas, V. G. and Papadimitriou, E. E., 2010. Fault complexity associated with the 14 August 2003 M_w6.2 Lefkada, Greece, aftershock sequence. *Acta Geophysica*, 58, doi: 10.2478/s11600–010–0009–6.

Karakostas, V. G., Papadimitriou, E. E. and Papazachos, C. B., 2004. Properties of the 2003 Lefkada,

Ionian Islands, Greece, earthquake seismic sequence and seismicity triggering, *Bulletin Seismological Society America*, 94, 1976–1981.

Kiratzi, A. A. and Langston, C., 1991. Moment tensor inversion of the January 17, 1983 Kefallinia event of Ionian Islands. *Geophysical Journal International*, 105, 529–535.

Klein, F. W., 2002. User's Guide to HYPOINVERSE–2000, a Fortran program to solve earthquake locations and magnitudes. *U. S. Geol. Surv. Open File Report 02–171 Version 1.0*.

McClusky, S., Balassanian, S., Barka, A., Demir, C., Georgiev, I., Hamburger, M., Hurst, K., Kahle, H., Kastens, K., Kekelidze, G., King, R., Kotzev, V., Lenk, O., Mahmoud, S., Mishin, A., Nadariya, M., Ouzounis, A., Paradisis, D., Peter, Y., Prilepi, M., Reilinger, R., Sanli, I., Seeger, H., Tealeb, A., Toksoz, M. N. and Veis, G., 2000. GPS constraints on crustal movements and deformations in the Eastern Mediterranean (1988–1997): Implications for plate dynamics. *Journal Geophysical Research*, 105, 5695–5719.

Papadimitriou, E. E., 1993. Focal mechanism along the convex side of the Hellenic Arc and its tectonic significance. *Bolletino Geofisica Teorica Applicata*, 35, 401–426.

Papadimitriou, E. E. and Papazachos, B. C., 1985. Evidence for precursory seismicity patterns in the Ionian Islands (Greece). *Earthquake Prediction Research*, 3, 95–103.

Papadimitriou, P., 1988. Etude de la structure du manteau superieur de l' Europe et Modelisation des ondes de volume engendrees par des seismes Egeens. *These de Doctorat, Univ. Paris VII, France*, 1988.

Papazachos, B. C. and Comninakis, P. E., 1971. Geophysical and tectonic features of the Aegean arc. *Journal Geophysical Research,* 76, 8517–8533.

Papazachos, B. and Papazachou, K., 2003. The earthquake of Greece, *Ziti Publications*, pp. 317.

Papazachos, B. C., Papadimitriou, E. E., Kiratzi, A. A., Papazachos, C. B. and Louvari, E. K., 1998. Fault plane solutions in the Aegean Sea and the surrounding area and their tectonic implications. *Bolletino Geofisica Teorica Applicata*, 39, 199–218.

Papazachos, C. B., 1999. Seismological and GPS evidence for the Aegean–Anatolia interaction. *Geophysical Research Letters*, 26, 2653–2656.

Scordilis, E. M., Karakaisis, G. F., Karakostas, B. G., Panagiotopoulos, D. G., Comninakis, P. E. and Papazachos, B. C., 1985. Evidence for transform faulting in the Ionian Sea: The Cephalonia Island earthquake sequence. *Pure Applied Geophysics,* 123, 388–397.

Reasenberg, P. and Oppenheimer, D., 1985. FPFIT, FPPLOT and FPPAGE: Fortran programs for calculating and displaying earthquake fault plane solutions. *U. S. G. S., Open–File Report*, 95–515, 24pp.

Wessel, P. and Smith, W. H. F., 1998. New, improved version of the Generic Mapping Tools Released. *EOS Trans. AGU*, 79, 579.

ACTIVE SEISMOTECTONIC STRUCTURES IN THE AREA OF CHIOS ISLAND, NORTH AEGEAN SEA, REVEALED FROM MICROSEISMICITY AND FAULT PLANE SOLUTIONS

Karakostas, V. G.[1], Papadimitriou, E. E.[1], Tranos, M. D.[2] and Papazachos, C. B.[1]

[1] Geophysics Department, School of Geology, Aristotle University of Thessaloniki, GR54124, Thessaloniki, Greece, vkarak@geo.auth.gr, ritsa@geo.auth.gr, kpapaza@geo.auth.gr

[2] Geology Department, School of Geology, Aristotle University of Thessaloniki, GR54124, Thessaloniki, Greece, tranos@geo.auth.gr

Abstract

Data from a digital seismological network operating during April–July 2002 were used for the microseismicity study of the area around Chios Island (East Aegean Sea, Greece). Numerous microearthquakes were detected and more than 950 well–located hypocenters were obtained along with 96 reliably determined focal mechanisms. The epicentral distribution and focal mechanisms of several earthquakes revealed that the NE–SW striking dextral strike–slip faults dominate in the study area as is the dominant pattern in North Aegean Sea. An earthquake swarm near Psara Island and a cluster offshore the west coast of Chios Island are associated with NW–SE trending left–lateral strike–slip faults, orthogonal to the dextral ones. Near the west coast of the Island the microseismicity evidences that oblique faulting dominates, whereas onshore and offshore the North Chios Island, clusters of events manifest the activation of either E–W or N–S striking normal faults. This complex deformation pattern is the manifestation of the dextral strike–slip faulting termination against conjugate sinistral ones, the transition from strike–slip to normal through the oblique faulting, as well as the activation of biaxial normal faulting in places.

Key words: *conjugate strike–slip and normal faults, transition zone, Chios Island, North Aegean.*

1. Introduction

The study area occupies the eastern central part of the Aegean microplate (Fig. 1) a highly deformed extensional back–arc area. The subduction of the eastern Mediterranean oceanic plate under the Aegean microplate (Papazachos and Comninakis, 1970, 1971) and the westwards motion of the Anatolian microplate along the North Anatolian fault (McKenzie, 1970, 1972, 1978) condition the deformation pattern in this area. The motion of the Anatolian microplate is transferred in the Aegean area as a simple translation, taking place along the central and southern part of the coasts of Turkey and the neighbouring Greek islands. The Aegean moves almost uniformly in a SSW direction (~200–220º) with an average velocity of ~30mm/yr, which increases from 25mm/yr in the central and southern part of the western coast of Turkey to 30–35mm/yr near the south western part of the Hellenic arc (Papazachos, 1999), with the significant increase being due to the strong N–S extension in the Aegean and western Turkey (McClusky et al., 2000). As a result of these motions, the northern
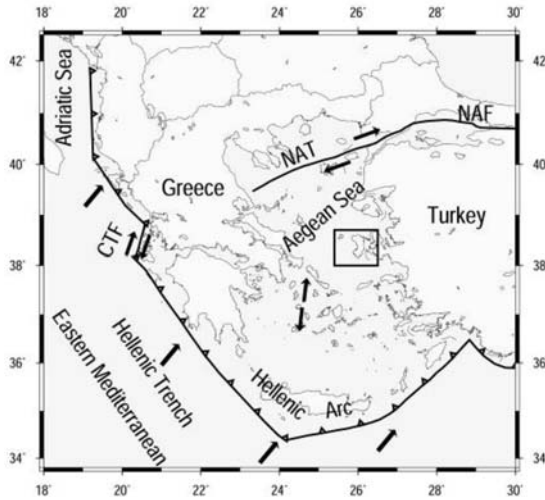
Fig. 1: Main seismotectonic properties of the Aegean and surrounding regions. The study area is denoted by a rectangle.

Aegean is dominated by dextral strike–slip faulting of northeasterly strike, co–existing with normal faulting. Both faulting types are consistent with several fault–plane solutions of recent strong earthquakes (Papazachos et al., 1998) as well as neotectonic observations (Tranos, 2009).

The structure of the area east of Chios Island was investigated by seismic reflection exploration evidencing that the active deformation of both onshore and offshore western Turkey is dominated by crustal extension, whereas strike–slip was evidenced too. The latter is considered to be of greater importance than previously thought (Ocakoğlu et al., 2004). Approximately E–W trending grabens and their basin–bounding active normal faults are the most prominent neotectonic features of this part of western Turkey that is currently experiencing an approximately N–S continental extension at a rate of 30–40 mm·year^{-1} (Bozkurt, 2001), and is no faster than ~0.5 mm·year^{-1} across any individual active normal fault (Westaway, 1994). This extension is related to the spreading and thinning of the crust immediately after the cessation of the Palaeogene shortening (Seyitoğlu and Scott, 1996).

The intense seismic activity in the study area is substantiated by numerous historical earthquakes, with the 1881 (6.5) being the most murderous earthquake in the Greek territory (Papazachos and Papazachou, 2003). During the instrumental period, Chios Island has been struck twice and close in time, in 1941 (M6.0) and 1949 (M6.7). The 1881 and 1949 earthquakes, the stronger more recent events in the study area, ruptured the South Chios and North Chios normal faults, respectively (Papazachos et al., 2001), and caused tsunamis that affected the coasts of Chios Island and Cesme (Altinok et al., 2005).

Microearthquake activity and its relation with the faulting pattern in the study area were not studied up to now. Accurate earthquake location was difficult to be achieved when using teleseismic records, since uncertainties in the structure of the crust and upper mantle can result in errors in earthquake locations of a few tens of kilometres if local or close regional seismological stations are absent. Such errors prevent precise correlations of seismicity with active faults. The purpose of the present study is the exploitation of data collected by a temporary network of nine digital seismological stations that were installed and operated for three months on Chios and neighbouring islands. Their hypocenters, located as much accurately as possible, and fault plane solutions determination, contribute to investigate the local seismic activity and fault kinematics. Even though microseismicity is not completely representative of the properties of the major faults associated with strong earthquake occurrence, it may provide valuable information for defining the seismotectonic
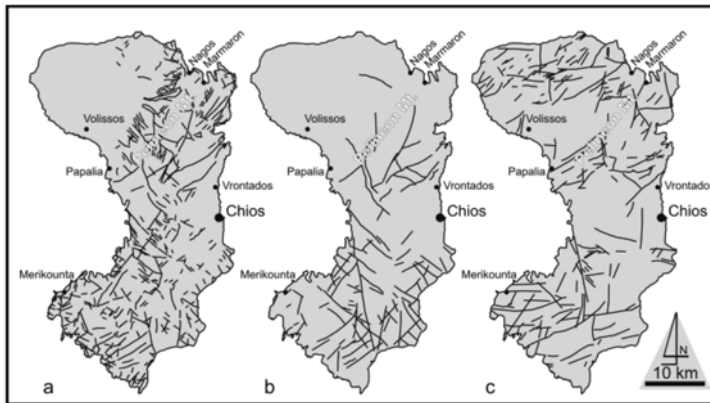
Fig. 2: Simplified structural map of Chios Island showing the fault pattern according to (a) the geological map at scale 1:50.000 (Bescenecker et al., 1971), (b) the geological map presented by Zanchi et al. (2003), and (c) our interpretation of the satellite imagery.

properties of an investigated area.

2. Geology of Chios Island

The Island of Chios represents the most proximal to the Anatolian microplate part of the Aegean microplate. It has the shape of upright bin with the central northern parts to form a mountain terrain (Pelineon Mt.) striking NNE–SSW (Fig. 2). The island consists of pre–alpine and alpine rocks that grouped into two units (Zanchi et al., 2003): The Lower Unit (autochthonous of Besenecker et al., 1968) includes siliclastic turbidites and embedded olistoliths of Silurian to Carboniferous rocks and a Mesozoic carbonate succession, and the Upper Unit (allocthonous, Besenecker et al., 1968), which occurs in isolated klippen, displaced by faults related to the Neogene Aegean extension. It includes Upper Carboniferous turbidites, Lower Permian sandy to marly carbonates and Middle Permian shallow–water limestones, overlain by red siltstones and Jurassic platform carbonates.

Late Tertiary metamorphic collapse of Cordilleran type processes dominated the Cycladic archipelago and caused a major shallow–dipping ductile shear zone at the deeper levels and low–angle normal faults in its upper levels elongate domes over which a pervasive N–NNE–stretching lineation is warped (Lister et al., 1984). The succeeding neotectonic evolution of the Aegean Sea concerns WNW–ESE steeply dipping normal faults and NE–SW strike–slip faults that form elongate submarine basins (Kilias et al., 1998). To the east of the study area, i.e. the Minor Asia region is dominated by E–W large active faults that bound similarly oriented elongated valleys along which an intense seismic activity is well established (Ocakoglu et al., 2004). This deformation is related to an approximately N–S continental extension at a rate of 30–40 mm·year^{-1} (Bozkurt, 2001).

The geological mapping of the island of Chios (Besenecker et al., 1971) figures out a fault pattern that is mainly dominated by NNE–SSW faults and WNW–ESE to NW–SE along which several geologic formations have been horizontally separated, thus implying the significance of the strike–slip component of displacement. On the other hand, our fault mapping through the Landsat satellite imagery, which was mainly based on the well used morphotectonic criteria associated with faults, suggests that the recently formed fault pattern is mainly dominated by NE–SW and E–W striking faults. More precisely, the mapped NE–SW faults seem to be the major faults of the island that have
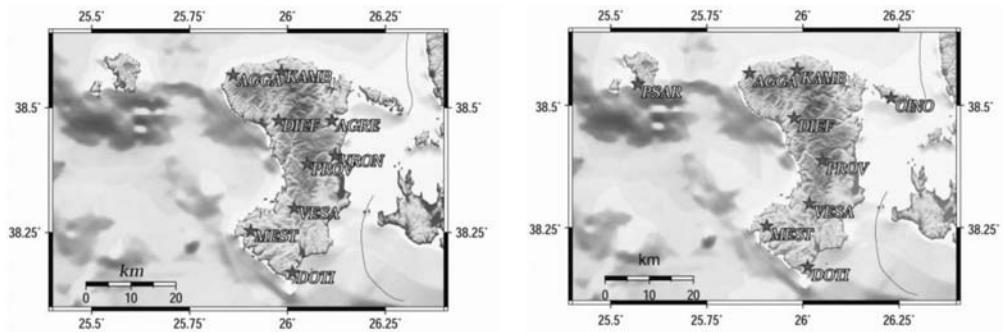
Fig. 3: Locations of the portable seismological stations during the first phase (left part) and the second phase (right part) of the experiment. Stations with code names PSAR and OINO, are positioned on Psara and Oinouses Islands, respectively.

been embraced at parts the previous NNE–SSW fault segments, whereas the E–W faults are of smaller length and are limited by the presence of the NE–SW striking faults (Fig. 2).

One of the most important NE–SW faults hence named the Chios fault is the one running along the SE mountain front of the Pelineon Mt. This fault with a length of at least 7 km runs close to the Northern suburbs of the Chios city (Vrontados area) and is characterised by recent activity, since it has affected such young deposits as Quaternary. Besides, strike–slip slickenlines have been observed to be overprinted by dip–slip slickenlines along fault surfaces, entailing a normal activation.

3. Data and procedures

We analysed the P and S wave arrival times and P wave first motions from a local network that was installed and operated in the area during April–July 2002. The seismic network consisted of nine 3–component stations equipped with broad–band sensors, all connected to GPS antenna for timing. The first choice was to place the network on Chios Island (April–June) in order to locate the microseismicity on the Island as much accurately as possible, with station spacing about 10 km (Fig. 3, left). During the second phase of the experiment, two stations were moved to the nearby Oinouses and Psara Islands, the latter being an area with very high seismic activity (Fig. 3, right). The stations operated in continuous mode with a sampling frequency of 125 Hz, allowing the detection and location of 868 events both on land and offshore.

Arrival time data from the detected events were considered, and by the use of a regional velocity model (Panagiotopoulos, 1984), the best located events were selected in a procedure to define a local velocity model. The criteria applied for dataset selection were the minimum phase number to be no less than 10, the distance to the closer station smaller than 20 km and the "gap" less than 200°. Accurate solutions considered the ones having a root–mean–square residual (rms) less than 0.4 s, a horizontal location and a depth error both less than 5.0 km. In addition to these criteria, the most important one was the solution stability, i.e., the solution being immutable independently of the input crustal model or the initial focal depth. Thus, 43 events were selected and used to construct travel time curves, and after repetitive iterations a local velocity model was obtained (v_1=5.6 km·sec^{-1}, d_1=1.3 km, v_2=5.94 km·sec^{-1}, d_2=5.3 km, v_3=6.34 km·sec^{-1}, d_3=∞) and a best v_p/v_s ratio equal to 1.756. For improved hypocenters a set of station delays was used in addition with the one–dimensional velocity model as input to HYPO71 (revised, Lee and Lahr, 1975). In the location procedure, the P– and S– arrivals er-
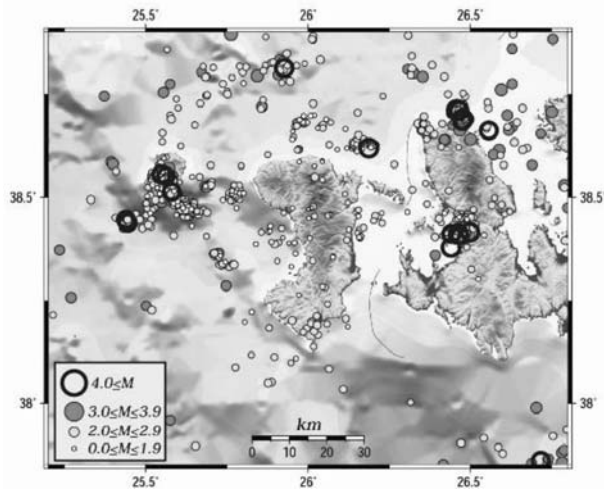
Fig. 4: Spatial distribution of the seismicity recorded by the local network.

rors were taken less than 0.3 s and 0.7 s, respectively. The final locations had an average root–mean–square residual (rms) of 0.10 s, a mean horizontal error of 1 km, and a mean error in the depth determination equal to 4 km. Depths range between 2–20 km with a remarkable pick on 6–8 km.

Magnitude determination for all the located events was performed from maximum amplitudes (a) and hypocentral distances (R), according to a relation of the form:

$$ \tag{1} $$

where c_1 was taken equal to 1.0, c_2, which depends on the attenuation, was considered equal to 1.199, that is a standard value for the territory of Greece and epicentral distances less than 100 km according to Scordilis (1985). The local magnitudes of 30 events commonly recorded by both the permanent and local seismological networks were used for the calculation of c_3 in each seismological station of the temporary network. The local magnitudes of the microearthquakes were then transformed into equivalent moment magnitudes based on a relation suggested by Papazachos et al. (1997).

The configuration of the network allowed determining reliable individual microearthquake focal mechanisms. All the single–event, lower–hemisphere focal mechanisms were determined, when more than 5 arrivals were available, using the FPFIT computer program (Reasenberg and Oppenheimer, 1985). In order to avoid misleading determination and to ensure the nodal plane constraints, the station azimuthal coverage as well as the distribution of the compressions and dilatations, were taken into account. The above criteria deterred the focal mechanisms determination of all the recorded events, but the ones located inside the network. A total of 96 mechanisms were computed with a gap smaller than 180º sampling a minimum of three quadrants. Most of the reliable solutions in the study area exhibit either strike–slip or normal faulting.

4. Results

4.1 Spatial distribution of the seismicity

The epicentral distribution of the located events is shown in Figure 4, where four different symbols were used to denote four different magnitude ranges. A complex spatial distribution appears with spa-
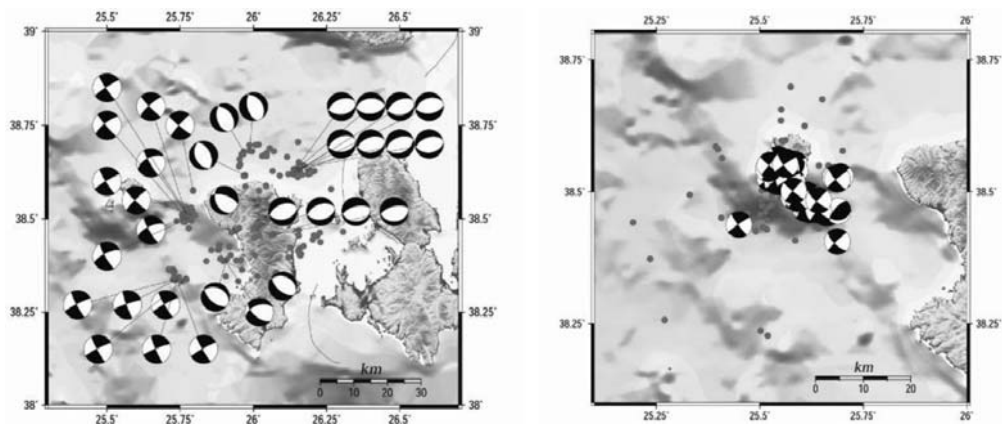
Fig. 5: Fault plane solutions of the 96 events around Chios (left) and close to Psara (right) Islands.

tially distinct clusters, evidencing the existence of a diverse faulting pattern. The most dense cluster is located near Psara Island, where two groups were observed, the larger one striking NNW–SSE and the smaller one striking NNE–SSW. Minor clusters of smaller magnitude events are also observed in the sea area between Psara and Chios Islands, which in some cases define small active structures. The onshore seismicity is weak (M≤3.0), whereas in the northern sea area an offshore cluster is observed with an event of M=4.3. The seismic activity is more intense in the Erithraea peninsula, along the western coast of Asia Minor, with several events of M≥4.0. A tight cluster of less than 10 km radius was formed near the city of Tçesme, and one more adjacent to the east coastline of Erithraea Peninsula that continues to the east up to the Smyrne gulf.

It is worth to note here the lack of seismicity in the offshore area to the south of Erithraea peninsula up to Chios Island. The elongated dimension of this area is almost 30 km and coincides with the meizoseismal area of the destructive 1881 earthquake with M=6.5 (Papazachos and Papazachou, 2003). This presents evidence for seismic quiescence prevailing on the associated south Chios fault even in microearthquake activity.

4.2 Focal mechanisms of the earthquakes

The most reliable fault plane solutions determined from first–motion polarities for 96 events are shown in Fig. 5. Nearly all the focal mechanisms close to Psara Island and the sea area between Psara and Chios Islands show strike–slip faulting, whereas the focal mechanisms offshore and onshore Chios show transtensional or normal faulting. Nearby located events exhibit similarities in their fault plane solutions, and in particular, the events that seem to be associated with the same active structure. To detect possible spatial changes in the style of faulting we show focal mechanisms grouped by style of faulting and belonging to the same spatial cluster. These mean focal mechanisms are summarized in Table 1 and shown in Fig. 6, along with the orientation of the axis of maximum extension (T–axis), which is prevalent in the study area. Although since the completion of the WWSSN in 1964, no strong events have been recorded in the study area and therefore focal mechanisms are not available, information on predetermined focal mechanisms of two strong earthquakes that occurred in nearby areas is used for comparison with the fault plane solutions determined in this study.

Table 1. Mean fault plane solutions for the seven clusters.

Area	Lat.	Long.	Plane 1			Plane 2			P axis		T axis	
			ϕ^o	δ^o	λ^o	ϕ^o	δ^o	λ^o	ϕ^o	δ^o	ϕ^o	δ^o
Area 1	38.520	25.769	234	76	-171	142	82	-13	52	8	144	14
Area 2	38.632	25.986	162	46	-70	315	47	-108	225	43	72	44
Area 3	38.631	26.148	85	45	-77	249	47	-101	159	43	355	45
Area 4	38.342	25.744	153	84	-5	244	84	-173	154	6	63	6
Area 5	38.399	25.895	277	35	-116	129	59	-71	39	31	187	55
Area 6	38.466	26.039	84	36	-80	254	55	-95	164	35	354	54
Psara	38.514	25.584	141	80	-6	232	83	-169	142	7	51	10
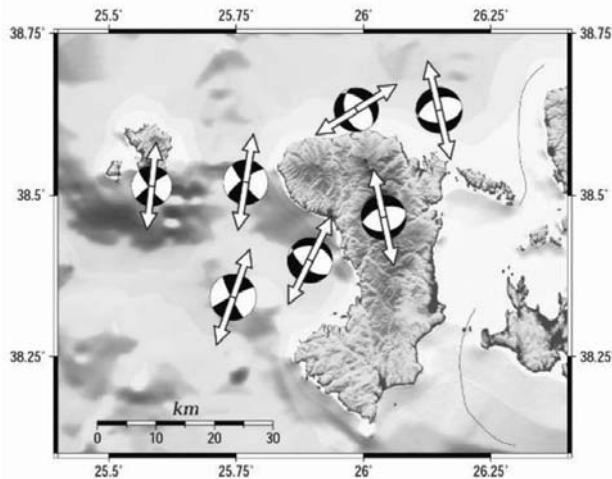
Fig. 6: Composite focal mechanisms corresponding to the seven clusters of microseismicity.

Mechanisms related to small–magnitude earthquakes are not usually associated with the finite slip on major faults and their slip vectors could be associated with the motion of randomly distributed preexisting faults, but P or T axes should be oriented as the main stress directions. Therefore, the direction of axis of maximum extension in the present case is a very useful parameter and is shown together with the mean focal mechanisms in Fig. 6.

A cluster of 62 events was located adjacent to the southwestern coast of Psara Island, forming en elongated structure trending NW–SE (Fig. 5, right and mean mechanism in Fig. 6), evidencing that the nodal planes with this strike might be considered as the fault planes and that the sinistral strike–slip motion prevails in this area. Another cluster of 6 events off the southwestern coast of Chios Island seems to be the continuation of the former active structure (Fig. 5, left and mean mechanism in Fig. 6). The strike–slip faulting events forming a cluster off the northwestern coast of Chios Island are distributed in a rather NE–SW lineament suggesting their association with the dextral strike–slip faults prevailing in the North Aegean Sea (Fig. 5, left and mean mechanism in Fig. 6) and in accordance with the 2001, M5.6 event (strike=244º, dip=79º, rake=–164º). The coexistence of left–
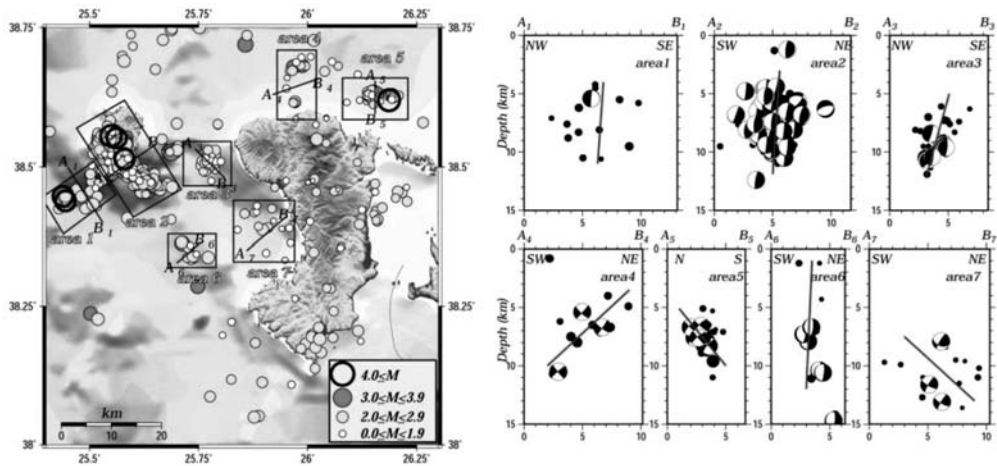
Fig. 7: The seven clusters of the microseismicity circumscribed by rectangles (left part) and the corresponding cross sections (right part).

lateral and right–lateral strike–slip faulting or possibly conjugate faulting has also been observed in the western part of the Aegean Sea, where such activation was observed during the 2001 Skyros Island sequence (Karakostas et al., 2003).

West of Chios Island, the results suggest that oblique extension prevails (Fig. 5, left and mean mechanism in Fig. 6), while the cluster offshore the northern coast exhibits rather E–W extension (Fig. 5, left and mean mechanism in Fig. 6). The orientation of the mean T–axis determined from this cluster is positioned rather perpendicular to the ones determined from the rest clusters, implying biaxial extension. A tectonic association is possible between the normal faulting events located at the northern inland part of Chios (Fig. 5, left and mean mechanism in Fig. 6) with the Vrontados–Karies fault as already found by the geological field observations. In the sea area north of the northeastern coast of Chios the determined 8 fault plane solutions clearly exhibit similar with the previous group normal faulting in almost ENE–WSW trending fault planes (Fig. 5, left and mean mechanism in Fig. 6). This mean fault plane solution is in agreement with the mechanism of the 1969, M5.9 event (strike=100º, dip=60º, rake=–90º) that occurred eastwards on Erithraea Peninsula.

In summary, the complex faulting pattern exhibits several distinctive seismotectonic features. First, the evidence of the left–lateral NW–SE trending strike–slip faults that seated orthogonal to the prevalent NE–SW dextral strike–slip faults in North Aegean Sea. Second, the transtensional faulting between strike–slip and normal faulting from west to east. Third, the active two almost parallel normal faulting structures, onshore and offshore Chios Island, in agreement with the stress pattern that holds in western Asia Minor. Fourth, the E–W extension offshore the northern coast of Chios Island that evinces the biaxial extension. Thus, from the above spatial distribution it is reasonable to conclude that west of the Chios Island strike–slip faulting prevails, and going to the east through a transition zone of oblique normal faulting, biaxial extension on almost E–W or N–S normal faults is emerging.

4.3 Geometry of the active structures

In order to investigate further the geometry of the active structures we divided the region into seven rectangles comprising the seismicity clusters, shown in Fig. 7 (left) along with seismicity and the lo-
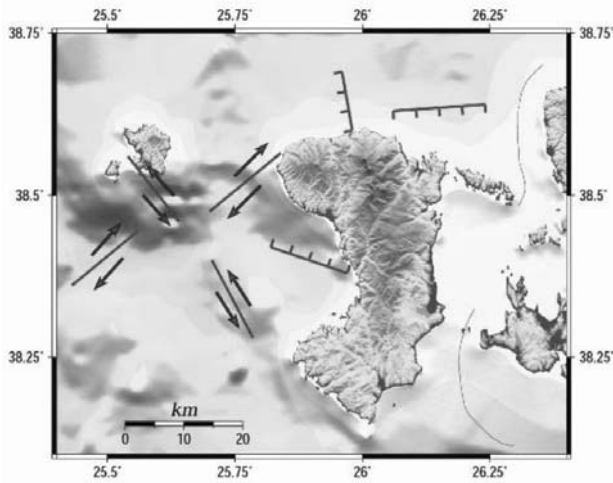
Fig. 8: The identified active structures associated with the analysed microseismicity.

cations of cross sections. The sections, which are perpendicular to the mean trend of the seismicity and are deliberately chosen to be narrow to reveal details, were performed with front projections of the focal mechanisms that were determined in each rectangle (Fig. 7, right). The thickness of the seismogenic layer comes to 15 km, with the vast majority of the hypocenters being between 5 and 10 km in all sections. The dips of the nodal planes are in good agreement with the mean dips of the clusters defined by the hypocenters alone. A summary of the above analysis is illustrated on the map of Fig. 8.

5. Discussion and conclusions

The purpose of this study is to characterize the active deformation onshore and offshore Chios Island. Numerous geological studies have been carried out in the broader Aegean region as well as in western Turkey, but poor detailed structural analysis has been done for the study area. On the other hand, seismological station coverage form the permanent seismological network was not adequate to permit a detailed seismological investigation. Our results show that a dense seismological network is essential to detect and accurately locate microseismicity and then to image active structures in areas which either were not activated during the instrumental period or the historical record is incomplete. The microseismicity within the study area was lower than the average seismic activity of the broader Aegean region during the local network operation. The largest local events occurred in Psara Island and offshore the northeastern coasts of Chios Island. Microseismicity was completely absent on the south Chios fault where the 1881 event occurred, and hence this area still requires further investigation to reveal this fault configuration.

In addition to the prevailing stress pattern in a certain area, faulting may occur on preexisting zones of weakness and therefore, the data set should contain focal mechanisms of diverse dislocation types. The fault plane solutions determined in the present study exhibit a complex fault pattern including dextral and sinistral strike–slip motion, transtensional as well as biaxial extension. Biaxial extension not only in almost N–S but also in the orthogonal east–west direction has been suggested for western Turkey by Westaway (1994) and Cihan et al. (2003) who thus explained the complex faulting there. In accordance with the findings of the present work are the results derived from the analysis of the seismic activity taking place within the Gulf of Sigarcik, 50 km southwest of Izmir (Aktar et

al., 2007), in that the aftershock activity was clustered in two distinct zones, roughly perpendicular to each other. Fault plane solutions of the three major (M≥5.4) events of the sequence are consistent with the orientation of both zones, striking NNW–SSE and NE–SW, respectively, which form a conjugate strike slip system. This difference in the orientation of the extension for different sub areas suggests that the study area is affected by internal deformation, which controls the activation of the active structures and their faulting type.

6. Acknowledgments

7. References

Aktar, M., Karabulut, H., Özalaybey, S. and Childs, D., 2007. A conjugate strike –slip fault system within the extensional tectonics of Western Turkey. Geophys. J. Int., 171, 1363–1375.

Altinok, Y., Alpar, B., Özer, N. And Gazioglu, C., 2005. 1881 and 1949 earthquakes at the Chios–Cesme Strait (Aegean Sea) and their relation to tsunamis. Nat. Haz. & Earth Syst. Sci., 5, 717–725.

Besenecker, H. Durr, S., Herget, G., Jacobshagen, V., Kauffmann, G., Ludtke, G., Roth, W. and Tietze, K., 1968. Geologie von Chios (Agais). Geol. Paleontol., 2, 121–150.

Besenecker, H. Durr, S., Herget, G., Kauffmann, G., Ludtke, G., Roth, W. and Tietze, K., 1971: Chios (2 sheets), Geological map of Greece at scale 1:50000, I. G. S. R., Athens.

Bozkurt, E., 2001. Neotectonics of Turkey – a synthesis. Geodan. Acta, 14, 3–30.

Cihan, M., Saraç, G. and Gökçe, O., 2003. Insights into biaxial extensional tectonics: an example from the Sandikli graben, West Anatolia, Turkey. Geological J., 38, 47–66.

Karakostas, V. G., Papadimitriou, E. E., Karakaisis, G. F., Papazachos, C. B., Scordilis, E. M., Vargemezis, G. and Aidona, E., 2003. The 2001 Skyros, Northern Aegean, Greece, earthquake sequence: off–fault aftershocks, tectonic implications, and seismicity triggering, Geophys. Res. Lett., 10.1029/2002GL015814.

Kilias, A. A., Mountrakis, D. M., Tranos, M. D. and Pavlides, S. B., 1998. The pre-volcanic metamorphic rocks of Santorini Island: Structural evolution and kinematics during the Tertiary (South Aegean, Greece). In: European Laboratory Volcanoes, Proc. 2nd workshop on Europ. Lab. Volcanoes, eds: R. Casale, M. Fytikas, G. Sigvaldasson and G. Vougioukalakis, Europ. Comm., Sci. Res. Develop., 23–36.

Lee, W. H. K. and Lahr, J. C., 1975. HYPO71 (revised): A computer program for determining hypocenter, magnitude and first motion pattern of local earthquakes, U. S. G. S. Open File Rep., 75–311.

Lister, G. S., Banga, G. & Feenstra, A., 1984. Metamorphic core complexes of Cordilleran type in the Cyclades, Aegean Sea, Greece. Geology, 12, 221–5.

McClusky, S., Balassanian, S., Barka, A., Demir, C., Georgiev, I., Hamburger, M., Hurst, K., Kahle, H., Kastens, K., Kekelidze, G., King, R., Kotzev, V., Lenk, O., Mahmoud, S., Mishin, A., Nadariya, M., Ouzounis, A., Paradisis, D., Peter, Y., Prilepi, M., Reilinger, R., Sanli, I., Seeger, H., Tealeb, A., Toksoz, M. N. and Veis, G., 2000. GPS constraints on crustal movements and deformations in the Eastern Mediterranean (1988–1997): Implications for plate dynamics *J. Geophys. Res.*, 105, 5695–5719.

McKenzie, D. P., 1970. The plate tectonics of the Mediterranean region. Nature, 226, 239–243.

McKenzie, D. P., 1972. Active tectonics of the Mediterranean region. Geophys. J. R. astron. Soc., 30, 109–185.

McKenzie, D. P., 1978. Active tectonics of the Alpine–Himalayan belt: the Aegean Sea and surrounding regions. Geophys. J. R. astron. Soc., 55, 217–254.

Ocakoğlu, N., Demirbağ, E. and Kuşçu, I., 2004. Neotectonic structures in the area offshore of Alaçati, Doğanbey and Kuşadasi (western Turkey): evidence of strike–slip faulting in the Aegean extensional province. Tectonophysics, 391, 67–83.

Panagiotopoulos, D. G., 1984. Travel time curves and crustal structure in the southern Balkan region. Ph. D. Thesis, Univ. of Thessaloniki, pp. 173 (in Greek).

Papazachos, B. C. and Comninakis, P. E., 1970. Geophysical features of the Greek island arc and eastern Mediterranean ridge. Com. Ren. Des Sceances de la Conference Reunie a Madrid, 1969, 16, 74–75.

Papazachos, B. C. and Comninakis, P. E., 1971. Geophysical and tectonic features of the Aegean arc. J. Geophys. Res., 76, 8517–8533.

Papazachos, B. C. and Papazachou, C., 2003. The earthquakes of Greece. Ziti Publ., Thessaloniki, Greece, 317 pp.

Papazachos, B. C., Kiratzi, A. A. and Karakostas, V. G., 1997. Toward a homogeneous moment magnitude determination in Greece and surrounding area. Bull. Seism. Soc. Am., 87, 474–483.

Papazachos, B. C., Papadimitriou, E. E., Kiratzi, A. A., Papazachos, C. B. and Louvari, E. K., 1998. Fault plane solutions in the Aegean Sea and the surrounding area and their tectonic implications. *Boll. Geof. Teor. Appl.*, 39, 199–218.

Papazachos, B. C., Mountrakis, D. M., Papazachos, C. B., Tranos, M. D., Karakaisis, G. F., and Savvaidis, A. S., 2001. The faults that caused the known strong earthquakes in Greece and surrounding areas during 5th century B. C. up to present, 2nd Conf. Earthq. Engin. and Engin. Seism., 2–30 September 2001, Thessaloniki, 1, 17–26.

Papazachos, C. B., 1999. Seismological and GPS evidence for the Aegean–Anatolia interaction. Geophys. Res. Lett., 26, 2653–2656.

Reasenberg, P. and Oppenheimer, D., 1985. FPFIT, FPPLOT and FPPAGE: Fortran programs for calculating and displaying earthquake fault plane solutions. U. S. G. S., Open–File Rep., 95–515, 24pp.

Scordilis, E. M., 1985. Microseismicity study of the Servomacedonian zone and the surrounding area. Ph. D. Thesis, Thessaloniki Univ., Greece, pp. 250 (in Greek with English abstract).

Seyitoğlu, G. and Scott, B. C., 1996. The cause of N–S extensional tectonics in western Turkey: tectonic escape vs back–arc spreading vs orogenic collapse. J. Geodynamics, 22, 145–153, 1996.

Tranos, M. D., 2009. Faulting of Lemnos Island: a mirror of faulting of the North Aegean Trough (Northern Greece). Tectonophysics, 467, 72–88.

Wessel, P. and Smith, W. H. F., 1998. New improved version of the Generic Mapping Tools released. EOS, Trans. Am. Geophys. U., 79, 579.

Westaway, R., 1994. Evidence for dynamic coupling of surface processes with isostatic compensation in the lower crust during active extension of western Turkey. J. Geophys. Res., 99, 20,203–20,233.

Zanchi, A., Garzanti, E., Larghi, C., Angiolini, L. and Gaetani, M., 2003. The Variscan orogeny in Chios (Greece): Carboniferous accretion along a Palaeotethyan active margin. Terra Nova, 15, 213–223.

RECENT SEISMIC ACTIVITY IN CENTRAL GREECE REVEALING LOCAL SEISMOTECTONIC PROPERTIES

Karamanos, Ch. K.[1], Karakostas, V. G.[1], Seeber, L.[2], Papadimitriou, E. E.[1] and Kilias, A.A.[3]

[1] *Aristotle University of Thessaloniki, School of Geology, Department of Geophysics, GR54124 Thessaloniki, Greece, chrikar@geo.auth.gr vkarak@geo.auth.gr, ritsa@geo.auth.gr*

[2] *Lamont–Doherty Geological Observatory of Columbia University, Palisades, New York 10964, USA, nano@ldeo.colubia.edu*

[3] *Aristotle University of Thessaloniki, School of Geology, Department of Geology, GR54124 Thessaloniki, Greece, kilias@geo.auth.gr*

Abstract

The December 2008, M=5.2 earthquake occurred in the Voiotikos–Kifissos basin near the town of Amfikleia in Central Greece and was followed by an intense sequence with hundreds of earthquakes. Mainshock source characteristics derived from the recordings of the Greek National Seismological Network are consistent with previous known earthquakes as well as with the current nearly N–S extensional regime. The adequate azimuthal coverage and the calculated time residuals at each seismological station ensure high location accuracy, whereas the stations operated close to the seismic excitations constrained 80% of the focal depths between 8 and 12km. Distances from the mainshock epicenter to the 10 closest seismological stations vary from 15 to 75 km. Hypoinverse and HypoDD were used for locations, and FPFIT was used for fault plane solutions of events with an adequate number of clear first arrivals. The hypocenters and focal mechanisms illuminate a ≈10km–long fault zone striking nearly E–W with oblique normal faulting and a small left lateral component. The Voiotikos–Kifissos basin is bordered in the south by two left–stepping en echelon segments known as the Pavliani fault zone and the Parnassos detachment, which strike NW and dip NE. In our preferred interpretation, the Amfikleia mainshock ruptured a previously recognized south–dipping fault antithetic to the basin border faults. This fault may be associated with the left step on the border fault, which would be releasing if that fault had a sinistral component.

Key words: Central Greece, microseismicity, relocation, active structures.

1. Introduction

Small and moderate magnitude earthquakes offer an opportunity to explore the active tectonic regime without causing damage. Earthquakes can 'illuminate' active faults, not only by specifying their location, but also their geometry and kinematics, or the way they move. A powerful way to map active faults is to combine earthquake data with good resolution and structural data from surface investigations. Central Greece is considered an area of high seismicity and has experienced large and damaging earthquakes, both within and before the instrumental era (Table 1 and Figure 1). Central Greece is characterized by extensional normal faulting, which connects strike slip faulting in the North Aegean trough along the continuation of the NAF into the Aegean Sea and in the Ionian Is-

Table 1. Historical data of large events in the broader area of our interest (Papazachos and Papazachou, 2003).

Date	Latitude (ϕ^o_N)	Longitude (λ^o_E)	Magnitude
–426	38.85	22.78	7.0
–226	38.60	22.70	6.4
551	38.80	22.80	6.8
04/10/1740	38.90	22.60	6.6
27/04/1894	38.56	23.24	7.0

lands region. Earthquake data are essential in testing hypotheses in such complex tectonic systems.

The purpose of this study is to examine the 2008 aftershock sequence in the Voiotikos–Kifissos basin and illuminate the active structure in the area. We use the recordings from the 10 closest seismological stations in order to determine the focal parameters with maximum possible accuracy. The spatial distribution of aftershock hypocenters along with the fault plane solutions of the main shock and of the largest aftershocks is combined in order to constrain the geometry and the kinematics in the region.

2. Seismotectonic setting

Central Greece is in the back–arc area of the Hellenic Arc and has experienced extension since the Early Miocene (Le Pichon and Angelier, 1978; Mercier et. al., 1989). This extensional deformation has resulted in many fault–bounded grabens, the most important striking WNW–ESE, such as the Sperchios River graben, the Maliakos Gulf, the Corinthiakos Gulf and the South Evoikos Gulf. These first order morphotectonic features, are emblematic of many other fault controlled basins, including the North Gulf of Evia and the Voiotikos–Kifissos basin in our study area. The WNW–ESE striking Arkitsa–Kammena and Kallidromon fault zone are the main border faults of these basins, respectively, on their SW side (Fig. 1). These fault zones belong to the Sperchios Fault system, which represents an extensional zone between the Cephalonia Transform Fault and the North Anatolian fault (Kilias et al., 2008). Cross–cutting relationships and other geologic data suggest a chronology of fault activity leading to the currently active (late Quaternary) faults. Examples of the latter include the Arkitsa–Kammena and the Hyampholis faults, intersecting and yet active, the later being a WSW–ENE striking fault, which is considered that acted as a barrier in the propagation of the 1894 earthquake rupture of the Atalanti f.z. (Ganas et al., 1998). The Kallidromon fault zone (Fig. 1), however, may be inactive (Palyvos et al., 2006).

The Amfikleia sequence

On the 13th of December 2008 (08:27.19 GMT time) an earthquake of M=5.2 occurred in the Voiotikos–Kifissos Basin near the town of Amfikleia in Central Greece (black triangle in Fig. 2). The Voiotikos–Kifissos is a composite half graben bordered on the SW side by the NE–dipping Pavliani–Parnassos fault (Kranis & Papanikolaou, 2001). This fault comprises three en echelon segments stepping to the left. The longest SE segment has been characterised as a detachment, but its trace is remarkably linear, suggesting a steep dip (Fig. 1). The footwall of this fault rises to the Parnassos Mountains range. On the NE side, the basin is bordered by the Kallidromon Mountains, which are on the footwall side of a set of NE–dipping faults bordering the submerged Evia Basin. The dominant faulting in the study area is clearly NW–SE trending and dipping to the north with normal dis-
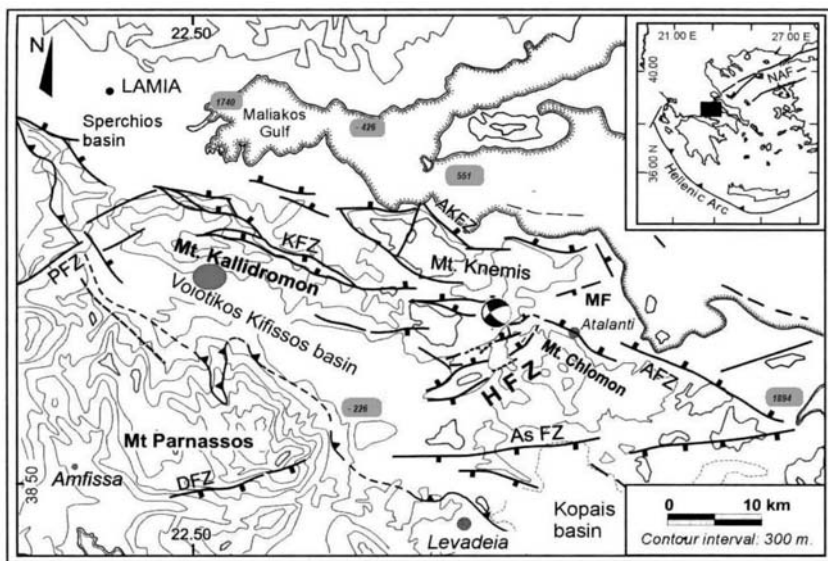
Fig. 1: Regional tectonic setting of Central Greece (modified from Kranis et al., 2001). The area of the seismic sequence occurrence is shown with the red ellipse. Large earthquakes that occurred in the past are shown with the orange rectangles. Thick hachured lines: Normal faults and/or fault zones; thick lines with triangles: alpine thrusts. HFZ: Hyampholis, AFZ: Atalanti, AKFZ: Arkitsa–Kammena Vourla, KFZ: Kallidromon, AsFZ: Aspledon, PFZ: Pavliani, DFZ: Delphi, MF: Megaplatanos fault. Focal mechanism solution from Hatzfeld et al. (1999).
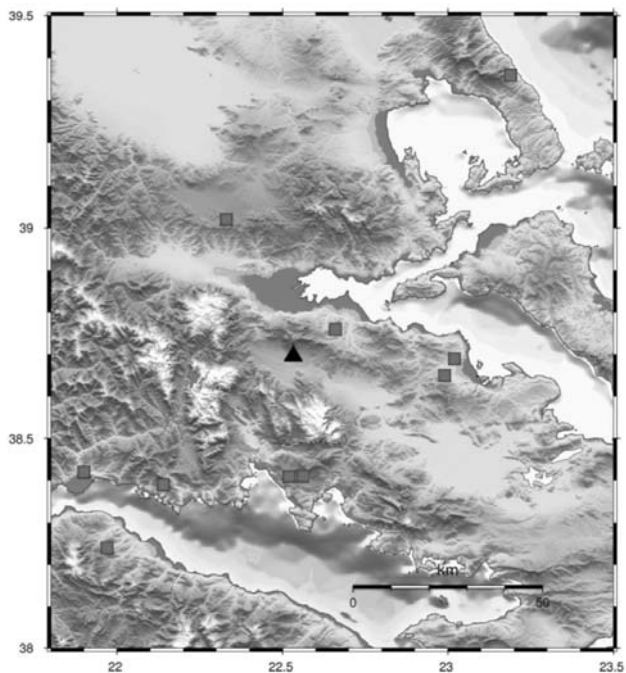
Fig. 2: Mainshock (black triangle) and location of the 10 closest seismological stations (red squares).
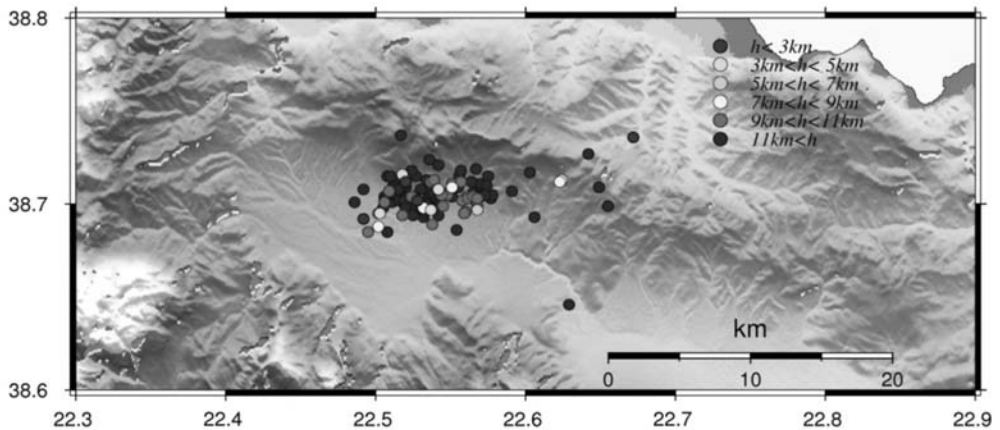
Fig. 3a: Spatial distribution of the epicenters according to their focal depths using Hypoinverse.

placement. Secondary features particularly important to this study include a systematic left–lateral component on many of these faults (REF) and secondary south–dipping faults at the northern end of the Voiotikos–Kifissos Basin.

2.1 Focal parameters determination

The 2008 Amfikleia mainshock was followed by an intense aftershock sequence. This study analyzes all the aftershocks of the first two days (13th and 14th of December) as recorded by the 10 closest seismological stations of the Greek National Seismological Network (red squares in Fig. 2). The 1d velocity model used was derived from an earlier study in the same area using the travel–times curves from a temporary seismological network that was operating for a six months period in 2005 (Karakostas et al., 2006). A $V_p/V_s = 1.76$ was calculated with the Wadati method, as well as time delays (station corrections) for each of the ten seismic stations the recordings of which were used in the analysis. With the term 'time delay' we mean the difference between the theoretical and observed travel time from the hypocenter of the earthquakes until the seismological station. A total of 116 earthquakes were processed by the Hypoinverse (Klein,2002) computer program, resulting in the epicentral distribution in Fig. 3a, and then they have been relocated with HypoDD (Waldhauser, 2001) (Fig. 3b).

The improvement in resolution can be appreciated by comparing statistical parameters of the hypocenters obtained by these procedures. Histograms in Figure 4 compare the root mean square error between observed and predicted arrival time (RMS), the calculated error in epicentral coordinates (ERH) and the error in focal depth (ERZ). After the location process with Hypoinverse, all RMS values are smaller than 0.36 sec, while 75% of them are smaller than 0.2 sec. When the same dataset was relocated with HypoDD, the RMS values are concentrating in the 0.1–0.26 sec range. The epicentral errors that derived from Hypoinverse have values smaller than 0.8 km. More than 70% of these values are even smaller than 0.4 km. After the relocation process with HypoDD these errors have values smaller than 0.7 km, with 90% of the events having values under 0.4 km. The maximum in this distribution is appearing between the values 0.2–0.4 (Hypoinverse) and 0.1–0.2 (HypoDD). As for the errors in focal depths, all the earthquakes have errors less than 5.5 km, with 80% of them having values even less than 2km with HYPOINVERSE. After the relocation with HypoDD, 90% of the events have erz smaller than 1km.
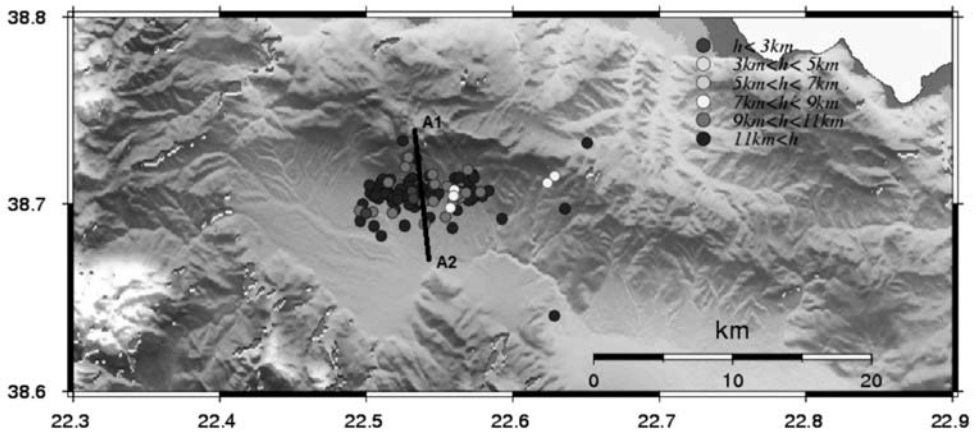
Fig. 3b: Spatial distribution of the epicenters according to their focal depths using HypoDD.
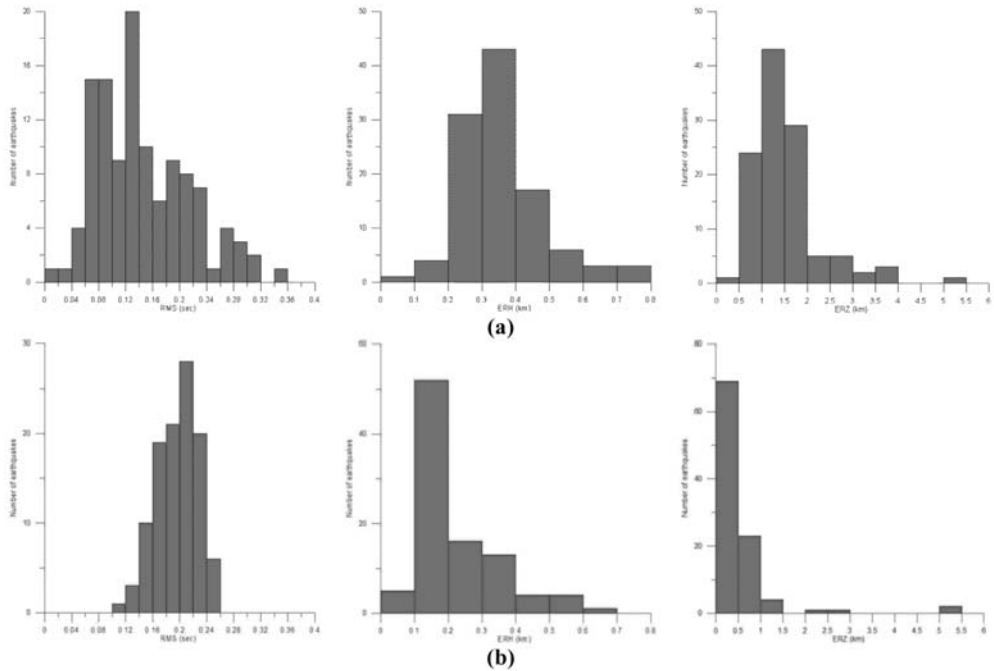
Fig. 4: Histograms of the root mean square error in the occurrence time (rms), epicentral determination error (erh) and depth determination error (erz), of hypocenters in this study. (a) Hypoinverse results, (b) HypoDD results.

2.2 Focal depths

The distribution of the hypocenters relocated by HypoDD is more concentrated than the distribution of hypocenter from HYPOINVERSE which is symptomatic of greater relative location accuracy. The epicentral distribution is tighter in Fig. 3b than Fig. 3a. and clearly shows a WSW–ENE striking source zone, in agreement with the focal mechanisms. The focal depths calculated using Hypoinverse
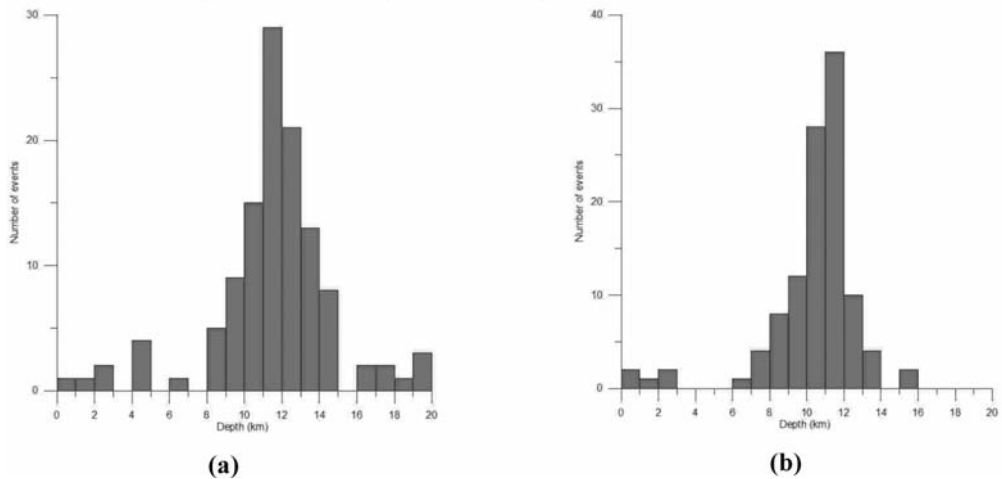
Fig. 5: Focal depths distribution of (a) Relocated events using Hypoinverse, and (b) Relocated events using HypoDD algorithm.

were found between 0 and 24 km, with most of them between 8 and 15 km (Fig. 5a). The same data processed with HypoDD yielded a seismogenic layer significantly thinner, with the majority of the events occurring between 9 and 12 km (Fig. 5b).

The magnitudes of the earthquakes in this study were calculated from the maximum amplitudes in the two horizontal components of each station of the regional network. Waveforms from these stations were converted to Wood–Anderson recordings using simulation filters. The maximum amplitudes in these simulated recordings weighted for distance yielded local magnitudes for each recording. The mean value of these magnitudes was adopted as the magnitude for each event.

2.3 Fault plane solutions determination

Fault plane solutions were determined with the FPFIT algorithm (Reasenberg & Oppenheimer, 1985). This program requires at least six first arrivals of the P waves, and the mainshock and 5 aftershocks fit this criterion (Table 2 and Figure 7). The steeper nodal planes in these solutions are very similar, striking nearly E–W and dipping to the south steeply, also including a small sinistral component. We consider this result quite robust. Collectively, our results indicate normal faulting with a small sinistral strike–slip component. The focal mechanism we obtain for of the mainshock is in good agreement with the focal mechanisms for the same event proposed by AUTH (94/77/-76), by NOA (92/69/-64) and Global CMT Solution (94/67/-85).

2.4 Spatial distribution

Figure 7 (a–c) exhibit cross sections perpendicular (A1–A2) to the almost E–W striking spatial distribution of the sequence (as shown in Fig 3b). The distribution of hypocenters is narrow in both depth and N–S direction. This distribution is consistent with the focal mechanism, but cannot readily discriminate whether the source fault is represented by the north or south dipping nodal planes. We propose the mainshock rupture to be on the steep south–dipping plane for a number of reasons listed below, which are based primarily on the relationship of the earthquake parameters and the pattern of faulting around the Voiotikos–Kifissos Basin.

Table 2. Strike, dip and rake of the steeper nodal planes for the mainshock and 5 aftershocks obtained with FPFIT. The first four rows show the parameters for the mainshock from all available sources (As mentioned in the text).

Date/Time	Magnitude	Strike	Dip	Rake
13/12/2008 08:27:19 (FPFIT)	5.2	92	70	-70
13/12/2008 08:27:19 (AUTH)	5.2	94	77	-76
13/12/2008 08:27:19 (NOA)	5.2	92	69	-64
13/12/2008 08:27:19 (Global CMT)	5.2	94	67	-85
13/12/2008 10:36:46	2.8	97	68	-75
13/12/2008 11:40:33	3.0	92	67	-81
13/12/2008 11:52:52	4.0	94	60	-82
13/12/2008 14:01:20	3.0	94	57	-63
13/12/2008 16:24:32	2.6	91	54	-80
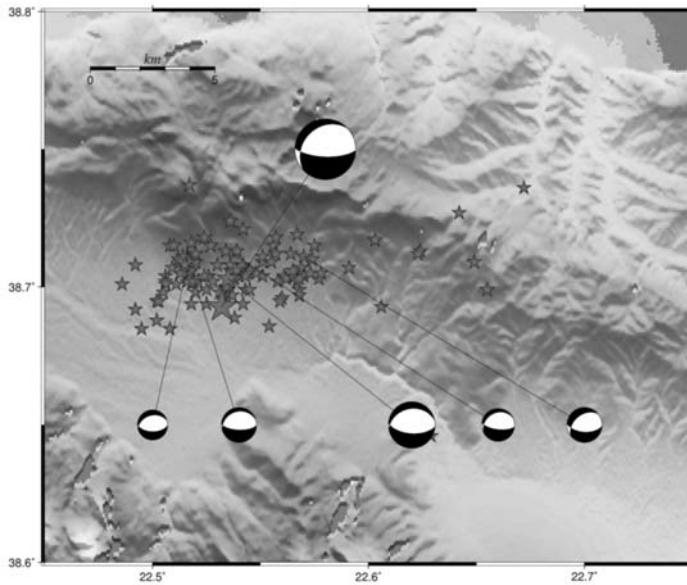
Fig. 6: Focal mechanisms of the main event and the 5 largest aftershocks as they were derived from the use of FPFIT.

A fault striking E–W and dipping south is mapped on the NW end of the Kallidromon Range (as described by Kranis, 2002). This fault would intersect the hypocenters if the dip was ≈60°, which is within the uncertainty of the focal mechanism for the mainshock.

The main border fault of the basin could also intersect the hypocenters, but the strike of the fault is clearly inconsistent with both the hypocenter distribution and with the north–dipping nodal planes of the focal mechanisms (Fig. 6).
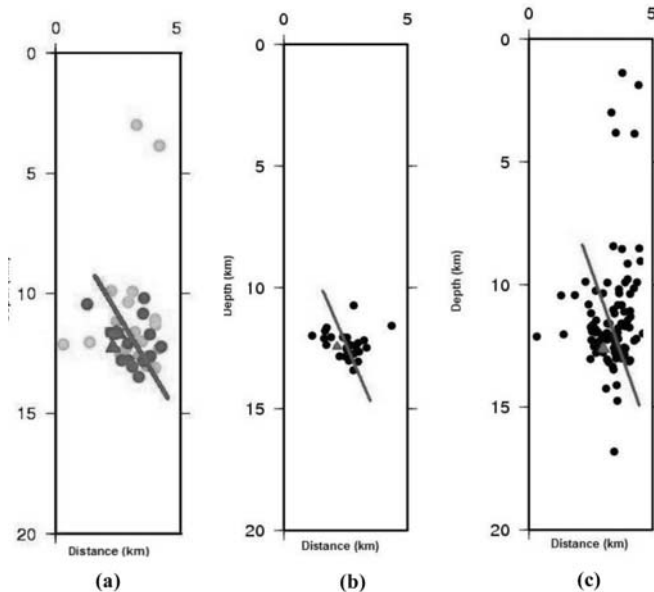
Fig. 7: Cross sections perpendicular to the strike of the spatial distribution of the earthquakes. (a) green hypocenters are earthquakes that occurred in the first two hours of the excitation while red ones indicate the hypocenters in the next six hours, (b) hypocenters of the largest events (min magnitude M=2.0) and (c) hypocenters of all the events. The red triangle in all three cross sections shows the hypocenter of the mainshock.

3. Conclusions

The distribution of faults around the Voiotikos–Kifissos basin, the southwestward dip of syntectonic strata in the basin, and the morphology of the uplifted blocks suggest that the Parnassos fault on the SW side of the basin is the main border fault. This implies that the south–dipping fault at the north end of the basin is a secondary antithetic fault cut by the border fault. The earthquake sequence could therefore have occurred near the intersection between these faults. While the mainshock was probably on the south–dipping antithetic fault, as we propose, some of the aftershocks may have originated on the main NE–dipping border fault. This may account for a hypocenter distribution that does not clearly outline a single fault plane. The antithetic fault proposed to be the source of the mainshock faces a major left step on the main border fault of the basin. This left step could be associated with localized extension additional to the regional pattern of extension, if the border fault includes a sinistral component. This is likely, based on sinistral components on other faults in the region, and on the general pattern of N–S extensional tectonics in central Greece applied to the NW strike of this fault.

4. Acknowledgments

5. References

Ganas, A., Roberts, G.P., Memou, T., 1998. Segment boundaries, the 1984 ruptures and strain patterns along the Atalanti Fault, central Greece. Journal of Geodynamics 26 (2–4), 461–486.

Hatzfeld., D., Ziazia, M., Kementzetzidou, D., Hatzidimitriou, P., Panagiotopoulos, D., Makropoulos, K., Papadimitriou, P., Deschamps, 1999. Microseismicity and focal mechanisms at the western termination of the North Anatolian Fault and their implications for continental tectonics. Geoph. J. Int., 137, 891-908.

Karakostas, V., Karamanos, C., Papadimitriou, E., Kassaras, I. & Makropoulos, K., 2006: Microseismicity and faulting geometry in central Greece – 1st European Conference on Earthquake Engineering and Seismology: 1-10, Geneva.

Klein, F. W., 2002. User's Guide to HYPOINVERSE–2000, a Fortran program to solve earthquake locations and magnitudes. *U. S. Geol. Surv. Open File Report 02–171 Version 1.0*.

Kilias, A., Tranos,M., Papadimitriou, E.& Karakostas, V., 2008: The recent crustal deformation of the Hellenic orogen in Central Greece; the Kremasta and Sperchios Fault Systems and their relationship with the adjacent large structural features – Z.dt. Ges. Geowiss., 159/3, p.533-547.

Kranis, H.D., Palyvos, G., Livaditis, G. & Maroukian, H., 2001. The Hyampholis Zone: geomorphological and tectonic evidence of a transverse structure in Lokris (Central Greece). Bull. Geol. Soc. Greece, XXXIV/1, 251-257.

Kranis, H.D. & D.I. Papanikolaou, 2001. Evidence for detachment faulting on the NE Parnassos mountain front (Central Greece). Bull. Geol. Soc. Greece, XXXIV/1, 281-287.

Kranis, H.D. Kinematics of active faults in Lokris, Central Greece-Block rotation within a crustal-scale shear zone? Proceedings of XVII. Congress of Carpathian-Balkan Association, Bratislava, September 1st – 4th , 2002.

LePichon, X., Angelier, J., 1978. The Hellenic Arc and Trench system: a key to the neotectonic evolution of the eastern Mediterranean area. Tectonophysics 60, 1-42.

Mercier, J.L., Sorel, D., Vergely, P., Simeakis, K., 1989. Extensional tectonic regimes in the Aegean basins during the Cenozoic. Beasin research 2, 49-71.

Palyvos, N., Bantekas, I., Kranis, H.D. 2006. Transverse fault zones of subtle geomorphic signature in northern Evia island (central Greece extensional province): An introduction to the Quaternary Nileas graben. Geomorphology 76 (2006), 363-374.

Papazachos, B. and Papazachou, K., 2003. The earthquake of Greece, *Ziti Publications*.

Reasenberg, P. and Oppenheimer, D., 1985. FPFIT, FPPLOT and FPPAGE: Fortran programs for calculating and displaying earthquake fault plane solutions. *U. S. G. S., Open–File Report*, 95–515, 24pp.

Waldhauser, F. (2001). HYPODD—A program to compute double-difference hypocenter locations, U.S. Geologic Survey Open-File Report.

Wessel, P. and Smith, W. H. F., 1998. New, improved version of the Generic Mapping Tools Released. *EOS Trans. AGU*, 79, 579.

ANISOTROPY STUDY OF THE FEBRUARY 4TH 2008 SWARM IN NW PELOPONNESUS (GREECE)

Kaviris G.[1], Papadimitriou P.[1], and Makropoulos K.[1]

[1] *Department of Geophysics, University of Athens, 157 84 Athens, Greece,*
gkaviris@geol.uoa.gr ,ppapadim@geol.uoa.gr,kmacrop@geol.uoa.gr

Abstract

The Gulf of Corinth, located in central Greece, is characterized by normal faulting and by high seismicity since the antiquity. On 4 February 2008 a seismic swarm burst in NW Peloponnesus characterized by the occurrence of two moderate-size earthquakes of moment magnitudes 4.7 and 4.5, respectively. Analysis of the data revealed the existence of shear-wave splitting. The events that were chosen for the anisotropy study fit the selection criteria, having clear and impulsive S wave arrival phases on the horizontal components. In addition, the amplitude of the S wave phase on the vertical component was smaller than on the horizontal ones. The representations that were used to determine the polarization direction of the fast split shear wave, the time delay between the two split shear waves and the polarization direction of the source were the polarigram and the hodogram. The uniform fast shear wave polarizations, irrespective of the azimuth of each event, are consistent with the general NNE-SSW direction of extension in the Gulf and, therefore, in agreement with the extensive dilatancy anisotropy (EDA) model. Finally, a decrease of the time delay values was observed after the occurrence of the first moderate earthquake, implying changes of the medium's properties.

Key words: *Anisotropy, shear wave splitting, temporal variation, stress field, EDA model, Gulf of Corinth, NW Peloponnesus.*

1. Introduction

The Gulf of Corinth, located in Central Greece, is one of the faster expanding and most seismically active continental rifts around the world and is characterized by normal faulting in an approximate E-W direction. Several strong historical earthquakes have destroyed cities in the Gulf, such as Heliki in 373 BC. Since 1911, the instrumental seismicity in the Gulf of Corinth is also intense (Makropoulos and Burton, 1981; Ambraseys & Jackson 1990) and includes several large events with M>6 from 1928 (Corinth, Ms 6.3) until 1995 (Aigion, Ms 6.2). In NW Peloponnesus, in the area between the Corinth Rift and Zakynthos island, there is a transition zone characerised by dextral strike-slip faulting.

Four months before the occurrence of the Mw=6.4 Andravida earthquake (Ganas et al., 2009), on 4 February 2008, which could influence the physical properties of the medium in the broader area, a seismic swarm, characterized by two moderate-size earthquakes ~M4.6, burst about 40km NE of the epicenter of this event. A known normal fault in the vicinity of the epicentral area is the Chalandritsa fault (Ch. F. in Fig. 1), with an approximate E-W strike. It is interest-
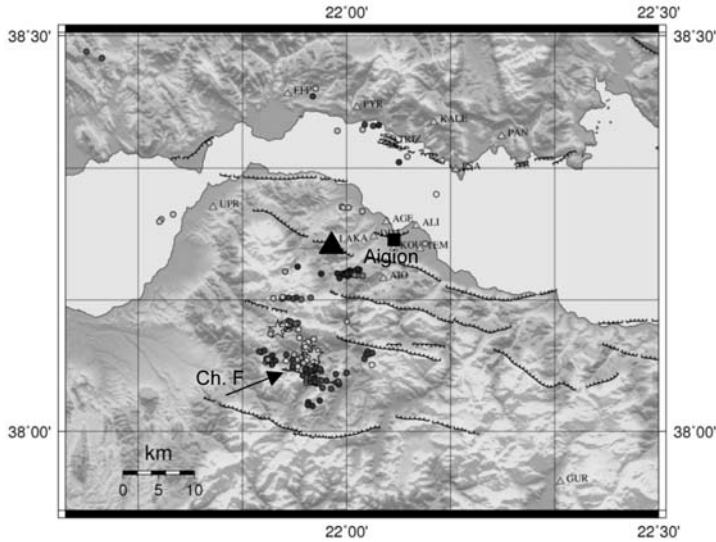
Fig. 1: Location of events of the February 4th 2008 swarm in NW Peloponnesus. The major shocks are depicted as stars. The location of LAKA station is also indicated with a triangle. Ch. F. is the Chalandritsa Fault.

ing that the calculated focal mechanisms of the two main events of this swarm reveal dominant strike-slip (Kapetanidis et al., 2008). This is not in agreement with the well-known normal faults of the area which have a dominant E-W strike, thus it is an interesting case of transition between normal and strike-slip faults.

Several anisotropy studies have been performed in Greece. The shear-wave splitting phenomenon was observed in Milos island (Booth et al., 1989), Kalamata (Bouin, 1994), Almyros (Karnassopoulou, 1996), Gulf of Corinth (Bouin et al., 1996; Papadimitriou et al., 1999; Kaviris et al., 2008) and Attica (Papadimitriou et al., 2000), leading to conclusions for the local stress-field.

2. LAKA Station – Method Used

LAKA station (Fig. 1) is located on the south coast of the Gulf of Corinth, west of the city of Aigion. This station belongs to the ATHENET network, which is the permanent network of the Seismological Laboratory of the University of Athens and part of the Hellenic Unified Seismological Network. The relatively small epicentral distance of this station from the February 4th 2008 seismic swarm permits the detection of many microearthquakes (Fig. 1).

The analysis of earthquakes of the 4 February 2008 sequence in NW Peloponnesus that were recorded by the LAKA station revealed the existence of shear-wave splitting, which is related to the existence of anisotropic medium. It is worth noticing that the observation of stress aligned seismic shear-wave splitting in almost all in situ rocks, in various sedimentary and crystalline geological regimes, below some critical depth, usually between about 500 m and 1 km is nearly universal (Kaneshima, 1990; Crampin and Lovell, 1991; Coutant, 1996; Gamar and Bernard, 1997; Papadimitriou et al., 1999; Crampin and Chastin, 2001; Hao et al., 2008). Shear-waves split into two approximately orthogonal fixed-polarizations with different velocities, which is characteristic of propagation in media with some form of elastic anisotropy. Shear wave splitting can easily be recognized into the polarigram or the three-component particle motion of shear-wave
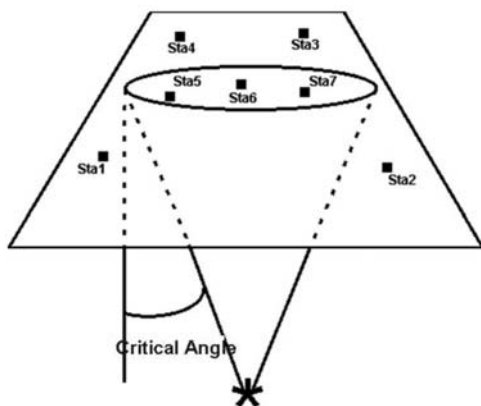
Fig. 2: All events selected for the anisotropy study are located within the shear-wave window, represented by the circle. The critical angle is equal to 45°.

arrivals and is the key diagnostic phenomenon for analyzing seismic anisotropy (Crampin, 2003).

All the events that were selected for the anisotropy study are located close to the LAKA station, within the shear-wave window (Fig. 2), having incident angles smaller than the critical. In addition, they have clear and impulsive S wave arrival phases on the horizontal components, while the amplitude of the S wave phase on the vertical component is smaller than on the horizontal ones. When the above conditions are true, scattered and converted phases (e.g. SP) are rejected (Booth and Crampin, 1985). A visual inspection and a plot of the particle motion in the three planes of projection were used to select the events that match the criteria mentioned above. The representations used in the present study in order to determine the splitting parameters, which are the polarization direction of the S_{fast} wave, the time delay between the two split shear waves and the source polarization direction, are the polarigram (Bernard and Zollo, 1989) and the hodogram.

An example of an event that is located close to the LAKA station and fulfils the selection criteria is presented in Figure 3A. A band-pass filter in the frequency range 0.5-25 Hz was used. The event occurred on 3/2/2008 01:02 GMT, with an azimuth equal to 206° and an angle of incidence equal to 38°, within the shear-wave window. Both the polarigram and the hodogram of the N-E plane are presented, where shear-wave splitting is evident. The angle between the north and the fast axis (S1) is the polarization direction, which is equal to N103°.

Then, the seismograms are rotated in the fast (S1) and slow (S2) direction and the obtained polarigram and hodogram are presented in Figure 3B. In this figure, the obtained polarization vector is oriented almost parallel to the fast component. The measured time delay is equal to 0.070s, represents the magnitude of the anisotropy and is removed in order to obtain the polarization direction of the source.

To measure the polarization direction of the source, the fast component is temporally moved towards the slow one for an interval of time equal to the time delay (0.070 sec) and the obtained waveforms (recorded and filtered) are presented in Figure 3C. The obtained polarization angle is 57° from the fast axis (F57°). The polarization direction of the source is the sum of this angle and of the polarization direction (N103°) and is equal to N160°. Following, in Figure 3D, the horizontal components are rerotated to their initial directions (E-W, N-S, angle of rotation -103°). The obtained waveforms are theoretically those that would be recorded in the case that the medium between the hypocenter and the station (LAKA) was not anisotropic. The polarization direction of the source is directly measured and is found equal to N160°.
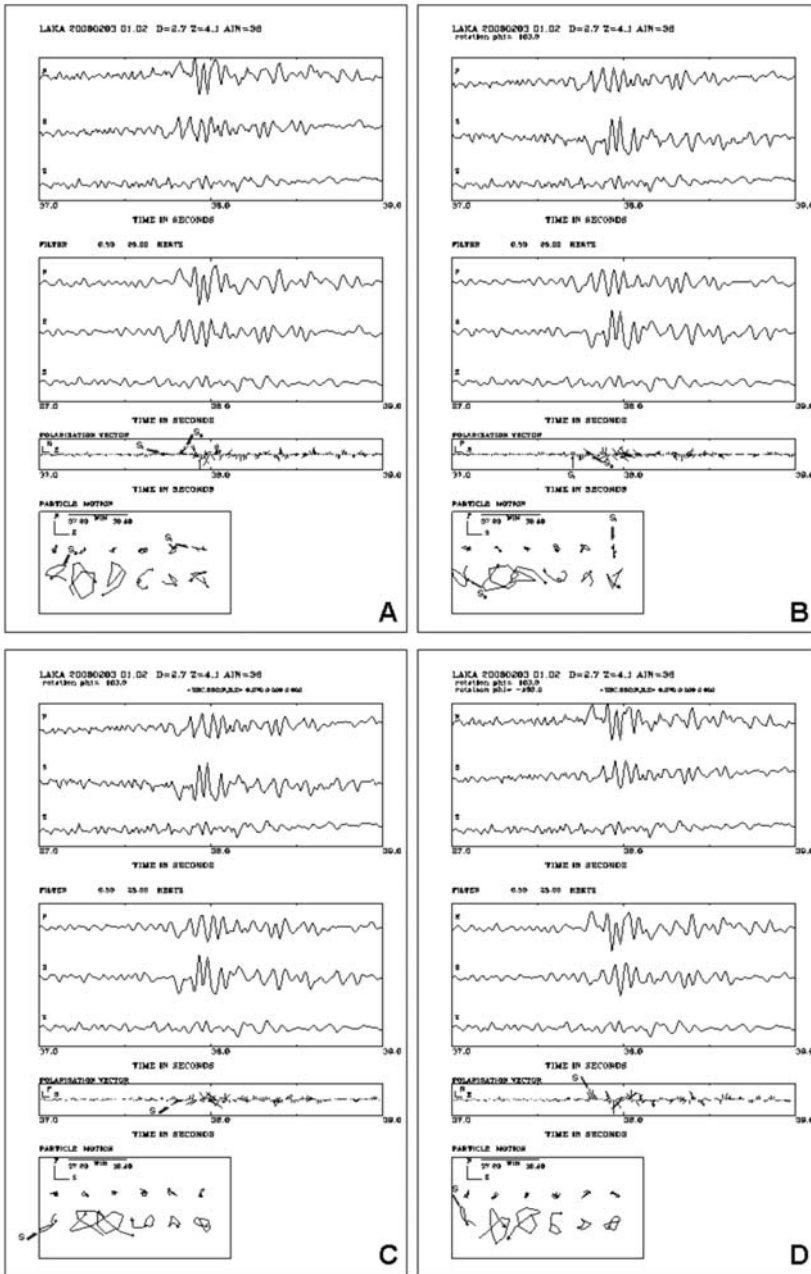
Fig. 3: (A) Original traces of an earthquake recorded at LAKA station, filtered traces, polarigram and hodogram in the N-E plane. (B) Traces rotated parallel and orthogonal to the polarization direction of the fast shear wave, filtered waveforms of the rotated traces, polarization vector and hodogram in the fast-slow plane where the time delay is measured. (C) Traces rotated parallel and orthogonal to the polarization direction of the fast shear wave after the correction of the time delay, filtered waveforms, polarigram and hodogram. (D) Traces re-rotated to the N-S and E-W directions, filtered waveforms, polarigram and hodogram from which the polarization of the source is estimated.
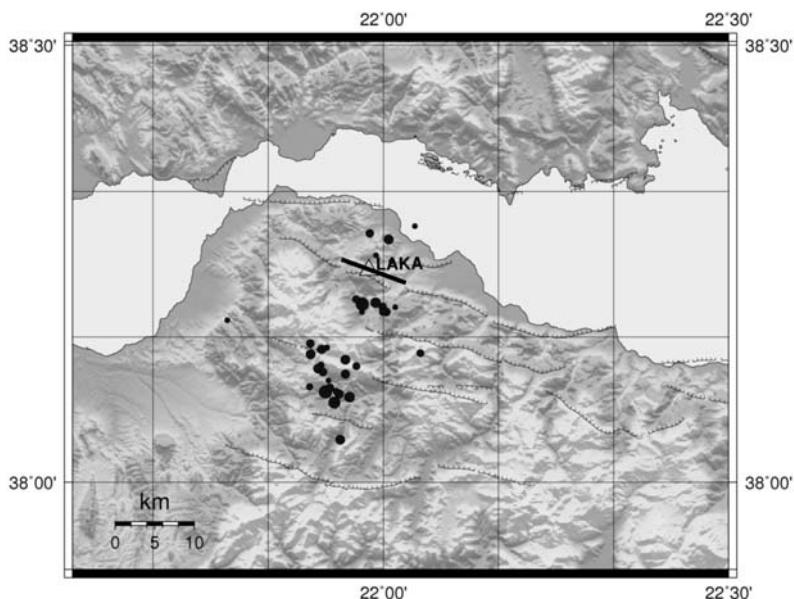
Fig. 4: Selected events for the anisotropy study at LAKA station and mean polarization direction.
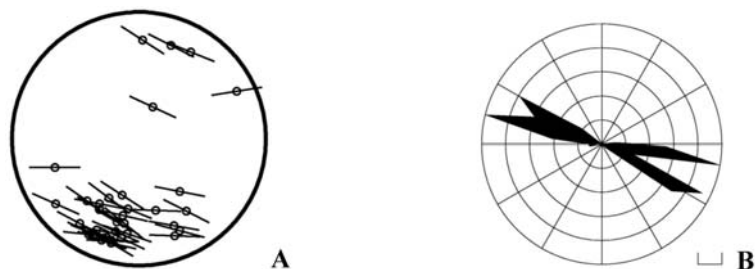
Fig. 5: Present Study: (A) Polar equal-area projections on the upper hemisphere of the fast shear wave polarizations at LAKA station. The circle represents an angle of incidence equal to 45°. (B) Rose diagram of the fast shear wave polarization directions at LAKA station.

3. Results of the Anisotropy Study

During the analysis of the events of the 4 February 2008 sequence in NW Peloponnesus that were recorded by the LAKA station, 36 were selected for the anisotropy study (Fig. 4). The angles of incidence of the selected events vary between 14° and 44°. The back azimuth range of the selected epicenters is quite satisfactory, varying between 2° and 318° with two gaps, the first between 64° and 142° and the second between 251° and 318°. Furthermore, the back-azimuths of the 83% of the selected events vary between 142° and 232°.

The polarization directions of the fast shear wave are presented on equal-area projections of the upper hemisphere (Fig. 5A). The outer circle defines the shear wave window and represents an angle of incidence equal to 45°. The length of the bars is proportional to the time delay between the fast and slow shear waves. The values of the time delays at LAKA station vary be-
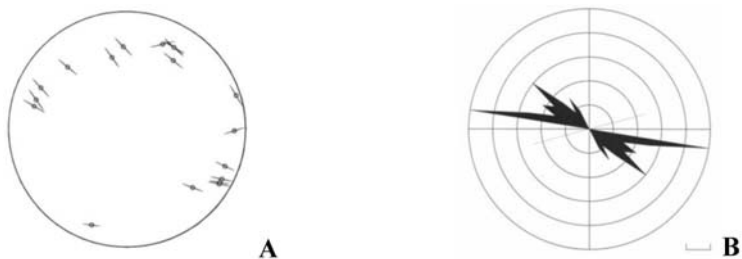
Fig. 6: (A) Polar equal-area projections on the upper hemisphere of the fast shear wave polarizations at LAKA station from Kaviris et al., 2008. (B) Rose diagram of the fast shear wave polarization directions at LAKA station from Kaviris et al., 2008.

tween 0.020s and 0.090s, while the S_{fast} polarization directions of the fast shear wave vary between N81° and N129°. The coherence of the fast shear wave polarizations at LAKA station, irrespective of the azimuth of each event, is consistent with shear-wave splitting due to the seismic wave propagation through an anisotropic medium.

The rose diagram of the S_{fast} polarization directions for all the selected events at LAKA station is presented in Fig. 5B. Two main S_{fast} polarization directions of about N100° and N120° are observed, with a mean value equal to N110°±2°, as presented in Fig. 4.

It is worth noticing that a previous anisotropy study was also performed for the LAKA station using 19 events recorded during the year 2000 (Kaviris et al., 2008). The values of the time delays for these events varied between 0.024sec and 0.104sec, while the polarization directions of the fast shear wave between N72° and N150° (Fig. 6A). The main S_{fast} polarization direction was N123°, while a secondary one equal to N100° was also observed (Fig. 6B). It is obvious that in both cases similar main polarization directions are obtained, with higher variation in the previous study.

4. Temporal Variation of time delay

One of the splitting parameters measured in the present study is the time delay between the two split shear waves. Time delays are sensitive to small changes in microcrack geometry, since changes in shear wave splitting monitor the small-scale stress-induced deformation of microcracks throughout the rock mass before a level of microcracking known as fracture criticality is reached when rocks are expected to fracture (Crampin and Chastin, 2003). Temporal variations in shear-wave time-delays have been observed before several earthquakes with magnitudes M 1.7 to M 7.7 (Crampin and Peacock, 2008). These observations have been performed in different regions, worldwide, such as Iceland (Crampin et al., 1999), China (Gao et al., 1998), U.S.A. (Liu et al., 1997) and Taiwan (Crampin and Gao, 2005). Whenever there is adequate data, these characteristic patterns of temporal variation are seen before all larger earthquakes and earthquakes can be stress-forecasted (Crampin, 1999). A necessary condition for fracturing is that cracks are so closely-spaced that shear-strength is lost and rocks fracture whenever there is any disturbance (Gao and Crampin, 2008).

As it is already mentioned in the previous section, the obtained values of the time delays at LAKA station vary between 0.020sec and 0.090sec. The first major event of February 4th 2008
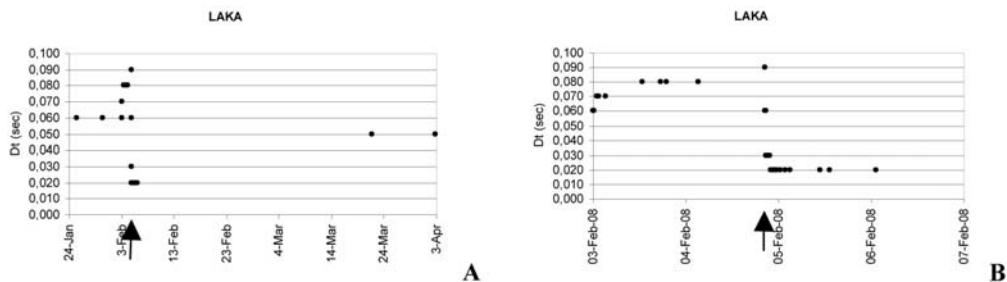
Fig. 7: Shear-wave splitting time-delays at LAKA station for the period: (A) 25 January to 2 April 2008 and (B) 3 to 6 February 2008. The arrows indicate the time of the first major event.

occurred at 20:25GMT. It is important to notice that the time delays before the occurrence of this shock vary between 0.060 and 0.090 sec, while afterwards between 0.020 and 0.060 sec (Fig. 7A, B). This decrease clearly indicates a change of the medium's properties after the occurrence of the first major event. Various anisotropy studies are performed in Greece, but this is the first time that temporal variation of the time delay is observed before the occurrence of an earthquake.

5. Conclusions

On 4 February 2008, two moderate earthquakes ~M4.6 triggered a seismic swarm in NW Peloponnesus. Analysis of the data revealed the existence of an anisotropic upper crust around LAKA station and an anisotropy study was performed. Using the appropriate selection criteria, a dataset comprising of 36 events was obtained. Scattered and converted phases that could lead to false identification of the split shear waves were identified and rejected.

Almost linear polarization was observed, with a mean direction equal to N110°. The uniformity of the fast shear wave polarizations, irrespective of the azimuth of each event, is consistent with what is expected for shear-wave splitting due to propagation through an anisotropic medium. These observations are consistent with the general NNE-SSW direction of extension in the Gulf of Corinth and, therefore, in agreement with the extensive dilatancy anisotropy (EDA) model. Finally, it is worth mentioning that an important reduction of time delay values was observed immediately after the occurrence of the first major event, implying changes of the medium's properties.

6. References

Ambraseys, N. N. and Jackson, J. A., 1990. Seismicity and associated strain in central Greece between 1890 and 1988. *Geophys. Jour. Inter.*, 101, 663-708.

Bernard, P. and Zollo, A., 1989. Inversion of near-source S polarization for parameters of double-couple point like sources. *Bull. Seism. Soc. Am.*, 79, 1779-1809.

Booth, D. C. and Crampin, S., 1985. Shear wave polarizations on a curved wavefront at an isotropic free surface. *Geophys. J. R. Astron. Soc.*, 83, 31-45.

Booth, D. C., Scjleper, S., Crampin, S., Ochmann, N. and Wohlenberg, J., 1989. Shear-wave splitting observations on Milos, Greece. *Geothermics*, 18, 597-610.

Bouin, M.-P., 1994. Analyse de la polarisation des ondes S en source proche: Rupture et Structure. *Phd Thesis*, Universite Paris 7, Paris.

Bouin, M.P., Tellez, J. and Bernard, P., 1996. Seismic anisotropy around the Gulf of Corinth, Greece, deduced from three-component seismograms of local earthquakes and its relationship with crustal strain. *J. Geophys. Res.*, 101, 5797–5811.

Coutant, O., 1996. Observation of shallow anisotropy on local earthquake records at the Garner Valley, Southern California, downhole array. *Bull. Seism. Soc. Am.*, 86, 477-488.

Crampin, S., 2003. The New Geophysics: shear-wave splitting provides a window into the crack-critical rock mass. *The Leading Edge*, 22, 536-549.

Crampin, S. and Lovell, H. L., 1991. A decade of shear-wave splitting in the Earth's crust: What does it mean? What can we make of it? and What should we do next? *Geophys. J. Int.*, 107, 387-407.

Crampin, S. and Chastin, S., 2001. Shear-wave splitting in a critical crust: II - compliant, calculable, controllable fluid-rock interactions, in Anisotropy 2000: Fractures, converted waves, and case studies, *Proc. 9th Int. Workshop on Seismic Anisotropy*, Camp Allen, 2000, eds. Ikelle, L. T. & Gangi, T., SEG Open File Publication No. 6, 21-48.

Crampin, S. and Chastin, S., 2003. A review of shear-wave splitting in the crack-critical crust. *Geophys. J. Int.*, 155, 221–240.

Crampin, S. and Gao, Y., 2005. Comment on ''Systematic analysis of shear-wave splitting in the aftershock zone of the 1999 Chi–Chi, Taiwan, earthquake: shallow crustal anisotropy and lack of precursory changes, by Liu, Teng, Ben-Zion, *Bull. Seismol. Soc. Am.*, 95, 354–360.

Crampin, S. and Peacock, S., 2008. A review of the current understanding of shear-wave splitting in the crust and common fallacies in interpretation. *Wave Motion*, 45, 675-722.

Crampin, S., Volti, T. and Stefansson, R., 1999. A successfully stress-forecast earthquake, *Geophys. J. Int.*, 138, F1–F5.

Gamar, F. and Bernard, P., 1997. Shear wave anisotropy in the Erzincan basin and its relationship with crustal strain. *J. Geophys. Res.*, 102, 20373-20393.

Ganas, A, Serpelloni, E., Drakatos, G., Kolligri, M., Adamis, I., Tsimi, Ch. and Batsi, E., 2009. The Mw 6.4 SW-Achaia (western Greece) earthquake of 8 June 2008: Seismological, field, GPS observations and stress modeling. *J. Earthq. Eng.*, in press, 2009.

Gao, Y., Wang, P.-D., Zheng, S.-H., Wang, M., Chen, Y.-T. and Zhou, H.-L., 1998. Temporal changes in shear-wave splitting at an isolated swarm of small earthquakes in 1992 near Dongfang, Hainan Island, southern China. *Geophys. J. Int.*, 135, 102–112.

Gao, Y. and Crampin, S., 2008. Shear-wave splitting and earthquake forecasting, *Terra Nova*, 20, 440-448.

Hao, P., Gao, Y. and Crampin, S., 2008. An Expert System for measuring shear-wave splitting above small earthquakes. *Comp. Geosci.*, 34, 226-234.

Kaneshima, S., 1990. Origin of crustal anisotropy: Shear wave splitting studies in Japan. *J. Geophys. Res.*, 95, 11121-11133.

Kapetanidis, V., Agalos, A., Moshou, A., Kaviris, G., Karakonstantis, A., Papadimitriou, P. and Makropoulos, K., 2008. Preliminary Results from the Study of a Seismic Swarm Occurred in February 2008 in NW Peloponnesus, Greece. *Book of Abstracts* (Poster), 31st Gen. Ass. ESC, p. 110, Crete, Greece.

Karnassopoulou, A., 1996. Joint investigation of source parameters and seismic anisotropy using microearthquakes in Greece, Arkansas and Northeast Brazil. *PhD thesis*, University of Edinburgh.

Kaviris, G., Papadimitriou, P. and Makropoulos, K., 2008. An Overview of Anisotropy Studies in Central Greece using recordings around the Gulf of Corinth (Greece) and aftershocks of the 1999 Athens Earthquake. *Short Papers, 31st ESC General Assembly*, Hersonissos, Crete, Greece, 215-223.

Liu, Y., Crampin, S. and Main, I., 1997. Shear-wave anisotropy: spatial and temporal variations in time delays at Parkfield, Central California. Geophys. J. Int., 130, 771–785.

Makropoulos, K. C. and Burton, P. W., 1981. A catalogue of seismicity in Greece and adjacent areas. *Geophys. J. R. Astron. Soc.*, 65, 741-762.

Papadimitriou, P., Kaviris G. and Makropoulos, K., 1999. Evidence of shear-wave splitting in the Eastern Corinthian Gulf (Greece). *PEPI*, 114, 3-13.

Papadimitriou, P., Kaviris G., Voulgaris, N. and Kassaras, I., 2000. Shear-wave splitting analysis using aftershocks of the 7th September 1999 Earthquake: Preliminary Results. *Ann. Geol. Pays Hellen.*, 1e Serie, T. XXXVII, FASC. B, p. 89-103.

SEISMICITY RATE CHANGES IN ASSOCIATION WITH TIME DEPENDENT STRESS TRANSFER IN THE REGION OF NORTHERN AEGEAN SEA, GREECE

Leptokaropoulos K. M.[1], Papadimitriou E. E.[1], Orlecka–Sikora B.[2] and Karakostas V. G.[1]

[1] *Geophysics Department, School of Geology, Aristotle University of Thessaloniki, GR54124 Thessaloniki, kleptoka@geo.auth.gr, ritsa@geo.auth.gr, vkarak@geo.auth.gr*

[2] *Seismology and Physics of the Earth's Interior, Institute of Geophysics, Polish Academy of Sciences, Warsaw, Poland, orlecka@igf.edu.pl*

Abstract

The region of northern Aegean has suffered several strong earthquakes since the beginning of the 20th century, causing extensive damage and loss of lives. For the seismic hazard assessment in the area, several studies have been accomplished, among them being the ones dealing with the Coulomb stress changes due to the seismic slip caused by major earthquakes, in addition with the constant tectonic loading on the major regional faults. The aim of the present study is to evaluate if seismicity rate changes from 1964 to 2008 are associated with changes in the stress field. For this purpose the stronger events ($M_w \geq 5.8$) that occurred in this period were considered and their contribution to the stress field evolution was investigated by calculations performed just before and after their occurrence. This influence was then examined in connection with the occurrence rate of small events ($M_w \geq 3.8$) for the respective time intervals. After defining the probability density function (PDF) of the small events distribution, a rate/state model was used to correlate static stress changes with seismicity rate and to compare the observed with the expected seismicity rate for each time period.

Key words: *Coulomb stress, rate/state model, seismicity rates, North Aegean (Greece).*

1. Introduction

The propagation of the North Anatolian fault to the west, sustains the existence of strike slip faults, most of them dextral, along the North Aegean Trough and the surrounding area. The back-arc extension of the Aegean due to the subduction of the Eastern Mediterranean oceanic plate under the Eurasian, is the second but most prominent dominant effect in the region. Superposition of these two deformation fields, yields an extension increase in the back arc region, leaving almost no significant contraction and reverse faulting in the Aegean. The region exhibits the highest deformation rates and seismicity, moving rapidly towards the SW, due to the combined effect of Anatolia westward motion and subduction rollback (Armijo et al., 2003; Flerit et al., 2004; Papazachos et al., 2006).

Frequent strong earthquakes in the study area are known from both instrumental and historical data. Since 1964, 11 strong earthquakes (M≥5.8) occurred in the study area with eight of them being associated with dextral strike slip faulting, two with oblique normal faulting and one with sinistral strike slip fault. As it is shown in Fig. 1, most of these earthquakes are associated with the regional
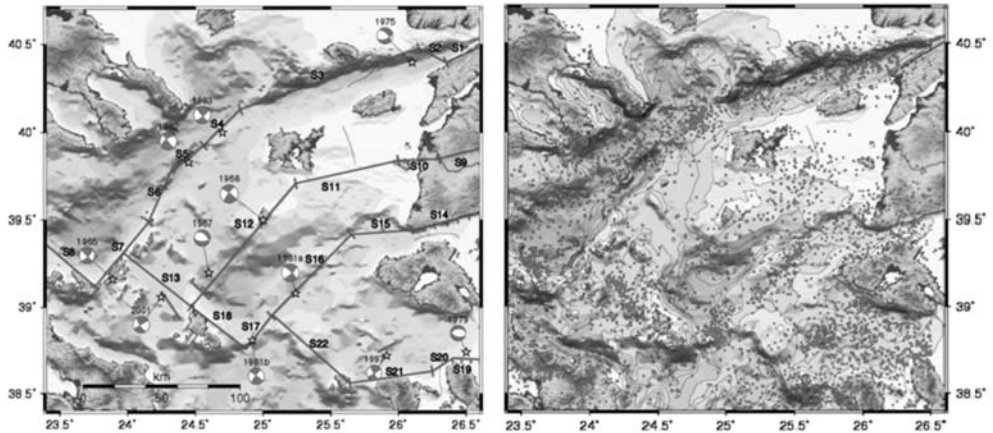
Fig. 1: Morphological map of the region: Gray lines represent the major faults with their code names while red lines show the fault segments that have been ruptured since 1964, giving M≥5.8 earthquakes. Stars denote the epicenters of these events. The fault plane solutions and the year they occurred are also noted (left). M≥3.8 seismicity for the period 1964 – 2008 is marked with red dots (right).

major faults. Similar is the distribution of seismicity with M≥3.8, which is mostly concentrated along the North Aegean Trough (NAT) and in its sub-parallel branches whereas in the south-eastern part the seismicity is more diffused.

The objective of this work is the qualitative and quantitative study of the correlation between the observed seismicity rate at the interevent periods and the expected one, as it is predicted by a model which associates seismicity rate changes with changes in the stress field. Results also depend strongly on the previous (background) seismicity rate, and on the choice of the selected model parameters, such as the apparent friction coefficient, constitutive fault parameter, aftershock duration and distribution of secular tectonic stressing rate. Regions with high seismicity rates are marked, and it is illustrated why some areas appear to be almost aseismic. Finally, estimation is attempted of the regions where seismicity rate is supposed to be high, meaning that they may accommodate a major earthquake in the future. As a conclusion, the seismic hazard assessment seems to be time–depended, and therefore a more accurate determination is necessary in order to avoid or diminish the destructive consequences of an imminent earthquake.

2. Data

Most of the fault segments are submarine, and therefore definition of their geometrical and kinematic properties, directly from geological observations is extremely difficult. In this case data is extracted by indirect means. The boundaries and the lengths, L, of the fault segments were determined on the basis of the submarine and continental morphology, seismicity distribution of the last 45 years, aftershock distribution of the stronger events and the reliable available fault plane solutions (Figure 1). Fault plane solutions also provide information on the mean dip and rake of each fault segment. The along strike and downdip components of the slip vector were computed in terms of the geometry of each segment. Fault width, w, was set to:

(1)

Table 1. Source parameters of the 11 earthquakes with M≥5.8 modeled for coseismic Coulomb static stress changes calculations.

Year	Date	Mw	M_0 (dyn·cm)	φ	δ	λ	Reference
1965	9 Mar	6.1	$1.47 \cdot 10^{25}$	44	75	175	Taymaz et al., (1991)
1967	4 Mar	6.3	$2.43 \cdot 10^{25}$	313	43	-56	Taymaz et al., (1991)
1968	19 Feb	7.0	$34.5 \cdot 10^{25}$	216	81	173	Kiratzi et al., (1991)
1975	27 Mar	6.2	$2.0 \cdot 10^{25}$	68	55	-145	Taymaz et al., (1991)
1979	14 June	5.9	$0.67 \cdot 10^{25}$	262	55	-108	Taymaz et al., (1991)
1981	19 Dec	6.8	$22.4 \cdot 10^{25}$	47	77	-167	Kiratzi et al., (1991)
1981	27 Dec	6.3	$3.82 \cdot 10^{25}$	216	79	175	Taymaz et al., (1991)
1982	18 Jan	6.6	$7.32 \cdot 10^{25}$	233	62	-177	Taymaz et al., (1991)
1983	6 Aug	6.6	$12.1 \cdot 10^{25}$	50	76	177	Kiratzi et al., (1991)
1997	14 Nov	5.8	$0.404 \cdot 10^{25}$	58	83	175	Louvari, (2000)
2001	26 Jul	6.4	$5.61 \cdot 10^{25}$	148	76	-1	GCMT

where h, the width of the seismogenic layer. In this case, seismogenic layer lies between 3 – 15 km, as it comes from the determination of focal depths of the larger events (Papazachos et al. 2008), and from studies of aftershock sequences with accurate depth determinations. Information on the source parameters of the 11 main shocks included in the model and for which fault plane solutions obtained from body waveform inversion is given on Table 1.

Smaller magnitude seismicity data were taken from the re-located catalog (Papazachos et al., 2008), which provides more reliable information regarding focal parameters. The catalog contains more than 15,000 events occurred in the region of interest for the time interval from 1964 to May 2008.

3. Method

The evaluation of seismicity rate changes in terms of Coulomb static stress changes, is performed on the basis of a rate/state model, modified from Dieterich (1994). Seismicity rate, R, is assumed to be a function of secular stressing rate,   . Given a background reference seismicity rate, **r**, the expected seismicity rate, R, is expressed as:

$$ \qquad (2) $$

where, -A is a fault constitutive parameter, σ is the total normal stress, t_a, is the characteristic relaxation time for the perturbation of earthquake rate (aftershock duration), t, is a given time step for seismicity rate calculation and ΔCFF is the coseismic Coulomb stress changes, given by:

$$ \qquad (3) $$

where Δτ, is shear stress change, $\Delta\sigma_n$, is the normal stress change and μ′, the apparent coefficient of friction, including pore pressure effects.

Background and observed seismicity rate at any interevent time interval is translated into earthquake probability with the use of a probability density function (PDF). This function determines the background seismicity rate at the center of each cell of a normal grid superimposed on the study area and these values are considered constant in time as the same is considered for the secular tectonic stressing rate. Probability is calculated with the application of a PDF proposed by Silverman (1986) and has the form:

$$(4)$$

$$(5)$$

where X_i, Y_i, are the epicentral coordinates of earthquakes (longitude, λ and latitude, ϕ, respectively), x, y, are the coordinates of the centers of the bins, on which the value of PDF is going to be estimated, n, is the number of the events and h, is the smoothing parameter (or window width), having the same units with X_i, Y_i, x, y. Finally from the fundamental equation of the probability theory => n=P·N, the seismicity rate is estimated for the given time period, Δt as follows:

$$R=n/\Delta t \qquad (6)$$

This rate, corresponds to the real seismicity rate of the given time period and is compared with the value of expected seismicity rate for the respective time period. Note that the region has been divided into a grid of 60x60 =3600 rectangular cells of 5km side. Values of model parameters are estimated in the center of each cell.

4. Estimation of Model Parameters

The parameters that are needed to be calculated for the seismicity rate determination are the Coulomb Stress changes (ΔCFF), due to the coseismic slip of the major (M≥5.8) events, the background seismicity rate, r, the values of stressing rate   , and its distribution along the major faults of the region as well as the aftershocks duration, t_a.

4.1 Coulomb stress changes calculations

Static stress changes are considered to be associated with the coseismic slips of the 11 stronger (M≥5.8) events that occurred in the study area. Calculations were performed for the whole area, although coseismic slip alters the stress state in a limited area, depending upon the magnitude of the modeled event. ΔCFF is calculated from (5) with μ' set to 0.4 (Stein et al., 1997; Nalbant et al., 1998). Shear modulus G, is assumed to be 33GPa and Poisson ratio 0.25 (Papadimitriou & Sykes, 2001). The width of seismogenic layer, **h** in the region consider to extend down to 15km and calculations were done at the depth of 8km. Fault plane solutions (Table 1) provide fault parameters and ΔCFF are calculated in respect to the fault plane that caused the stress perturbation. Components of slip, u, in strike, SS, and dip, DS, directions were estimated using the value of seismic moment, M_o, considering the rake angle:

$$M_o=GuLw \qquad (7)$$

where G, is the shear modulus, L, is the fault length estimated from aftershock distribution along the

fault segments and scaling laws (Wells & Coppersmith, 1994; Papazachos et al., 2004) and fault width, w, is estimated using (1).

4.2 Estimating the Stressing Rate

The determination of the stressing rate on the major faults of the study area is necessary for the expected seismicity rate estimation. It is assumed that the stressing rate is time independent and its spatial distribution is non uniform, but it is concentrated in specific zones of weakness, which define the major regional faults (Scholz, 1990). The values of stressing rate are used to determine the state variable γ, applied in the rate/state model, for each time step. In the present study, the slip rates on the major faults as they were defined from geodetic data (Flerit et al., 2004; Reilinger et al., 2006) were used in order to determine the stressing rates onto them. Geometrical characteristic and slip rates of these fault were estimated as described in section 2. In calculations, only 60% of the slip rate value was considered for accounting the seismic part of the secular tectonic motion. Different values for seismic coupling along the NAF and its surroundings have been proposed and they vary between 20-75% (Ward, 1998; Ayhan et al., 2001; Bird & Kagan, 2004), but most of them conclude to a value close to 60%.

The estimated values of the stressing rate at the center of each fault segment vary from 0.0025 to 0.086 bar/yr and they are assigned for narrow stripes of 5km width on either side at the fault trace of each segment. A percentage of stressing rate value is considered for each cell at these zones. For the rest of the cells, a very low value of stressing rate was set in order to avoid singularity computations. Thus every cell has two components of Coulomb stress change, one due to coseismic slip and one because of tectonic loading. These values will be used in the rate/state model in order to calculate the seismicity rate changes. A mean value of 0.0275 bar/year yielding from Gaussian fitting of data was later used as simplification to test results come from different approaches. This value appears to be in agreement with the ones given by Parsons et al. (2004) for the Sea of Marmara. Considering also that the slip rates are higher at the eastern part of NAF, this value is also consistent with the ones proposed by Straub et al. (1997) and Stein et al. (1997) for the NAF segments.

4.3 Estimating the background seismicity rate

Seismicity rate changes in a region are determined with regard to a reference seismicity rate. This reference rate must be free of dependent events that are aftershocks, triggered by a main shock. Habermann & Wyss (1984) defined the background seismicity rate as the rate of occurrence of events which one considers normal for some region. This happens when the only influence in the region is the tectonic loading and there is no stress perturbation because of other earthquakes. Therefore the recognition and removal of such dependent events is very important for the procedure in order to estimate and interpret properly the changes of the seismicity rate.

The catalog used for this procedure must be complete over a minimum magnitude, M_c, and also not to include dependent events (aftershocks). Determination of M_c is very important when seismicity rate is studied because only the events with $M \geq M_c$ must be included to determine accurately real and modeled seismicity rates. M_c was calculated for the entire time period as well as for the interval 1981-2008. In both cases it was found roughly equal to 3.8. That leaves less than 5,000 events at the complete and homogenous catalog considering the 44 years period.

The next step is the identification and removal of the aftershocks. In seismicity studies two main clusters of earthquakes are recognized. Those whose rate decays with time such as aftershocks and swarms
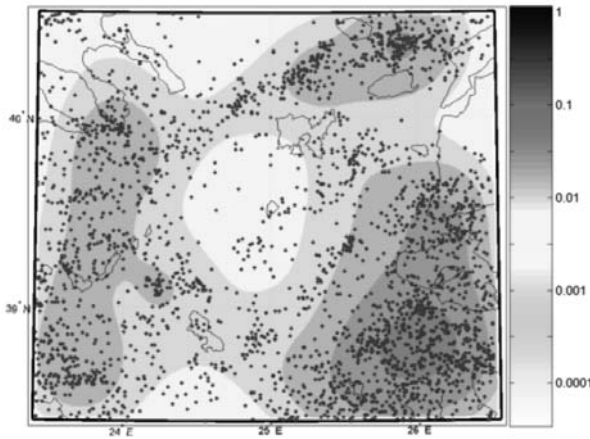
Fig. 2: Background seismicity rate estimated from PDF (equation 4). Smoothing parameter was found by equation 8, equal to 0.22. Red colors indicate higher rates. Blue dots represent epicenters of the earthquakes (M≥3.8) occurred during the period 1964–2008, with aftershocks being excluded.

and those whose rate and spatial distribution is time independent at a specific area. The declustering procedure in this study was based on Reasenberg's (1985) algorithm. Aftershock populations are identified by modeling an interaction zone about each earthquake in the catalog. These zones are constructed with one spatial and one temporal parameter. Spatial limits of the zone are defined by the estimate of stress redistribution in the vicinity of each earthquake (magnitude-dependent), whereas temporal extend of the zone is determined with an Omori's law based probabilistic model. Every event that occurs within this interaction zone of a prior event is considered statistically dependent on it (aftershock). After declustering, the final data set contains 2800 events which represent the background seismicity of the region, which is translated in terms of probabilities with use of PDF.

4.4 Choice of window width

It is clear from (9), that the value of probability is a function of the smoothing parameter, h. It represents the expanse of the area which is being influenced by each value of P1. Many methods have been proposed for a proper h value estimate (Silverman, 1978; Hall et al., 1991; Sain et al., 1994). In general, high values of the window width represent better systematic variation, while smaller values make random fluctuation clearer. In the present study the Silverman's (1986) formulation was applied:

$$\tag{8}$$

where $\sigma^2=0.5(s_{xx} + s_{yy})$ and s_{xx} and s_{yy} are sample variances of X_i and Y_i respectively and K the number of events included in the period of interest. The background seismicity rate for the study period (1964-2008) is shown in Fig. 2. Rate/state formulation as it was discussed, gives the values of expected seismicity rate after a main shock. These values are compared with the real seismicity rate for this period as it yields from PDF equations. Qualitative fitting can be estimated by comparison of the patterns of observed and expected seismicity and the locations of the events that occurred during the respective periods. Quantitative comparison can be done by calculation of the correlation coefficient between the observed and expected values of seismicity rate. Time windows for calculations correspond to interevent periods except from December 1981 to January 1982 (3 main shocks), where time intervals are too short and catalogue is too poor to provide reliable results.

Table 2. Correlation coefficients between expected and observed seismicity rate at 7 time windows according to 13 different approaches discussed in the text. Last column shows the mean value of each model, while last line shows the mean value of all models for each time interval. Bold values stand for the highest value for each time period. Total average is 0.5581±0.037. Model 'c' results were not included in this average estimate. Correlation Coefficient was computed by application of the formula:

where x, y, the values of the observed and expected seismicity rate respectively and n, the number of cells.

	67-68	68-75	75-79	79-81	83-97	97-01	01-08	average
a1	**0.5811**	0.4778	0.2566	0.5479	0.7153	0.7197	0.7519	0.5786
a2	0.4788	0.5142	0.2993	0.5221	0.7284	0.7287	0.7608	0.5760
a3	0.3601	**0.5684**	0.2944	0.5019	0.7065	0.7023	0.7842	0.5597
a4	0.5371	0.4693	0.2976	0.5355	0.7022	0.7041	0.7327	0.5684
b1	0.5688	0.4441	0.2401	0.5361	0.6868	0.7088	0.7254	0.5586
b2	0.4665	0.472	0.2848	0.51	0.6921	0.7084	0.7281	0.5517
b3	0.3561	0.5298	0.2768	0.4881	0.6767	0.6885	0.7640	0.5400
b4	0.5189	0.4314	0.2798	0.5246	0.6629	0.6833	0.6955	0.5423
c*	0.1919	0.1	0.002	0.255	0.35	0.4316	0.22	0.2215
d	0.3537	0.517	**0.3238**	0.471	0.6833	0.5571	0.5987	0.5007
e1	0.4469	0.4097	0.2623	0.4357	0.6516	0.6321	0.6277	0.4951
e2	0.4882	0.5467	0.3162	0.5435	0.7655	0.7747	0.8175	0.6075
e3	0.4910	0.5553	0.3223	**0.5630**	**0.7763**	**0.7869**	**0.8342**	0.6184
average	0.4706	0.4946	0.2878	0.5149	0.7040	0.6996	0.7351	

5. Results

Calculations of the expected seismicity rate and their correlation with real seismicity rates were done considering 13 different assumptions, shown in Table 2, in order to test the influence of the variance of model parameters on the results. Parameters examined are the window width, h, the aftershock duration, t_a and the value and distribution of the secular tectonic stressing rate, $\dot{\tau}$. Cluster 'a' models, assume spatially uniform stressing rate, $\dot{\tau}$=0.0275bar/yr and aftershock duration t_a=25yr, yielding a constant value of Aσ=0.6875bar. The window width at each period was selected according to equation (8) for 'a1' and was set to 0.22, 0.12 and 0.3 in a2, a3 and a4, respectively. Cluster 'b' models, have the same approach with cluster 'a' except for the aftershock duration, which was set to 15yr. Results are better considering h=0.22, and t_a=25yr and therefore these values were used in the other models. Model 'c', assumes spatially varying stressing rate as it was discussed in 4.2, resulting to an Aσ value varying from 0.01 to 3.65 bars. Model 'd', also assumes spatially varying stressing rate, but Aσ was set to be uniform and equal to 0.4 bars. Cluster 'e' models, assume spatially uniform stressing rate value equal to 0.01, 0.05 and 0.064 bar/yr, respectively.
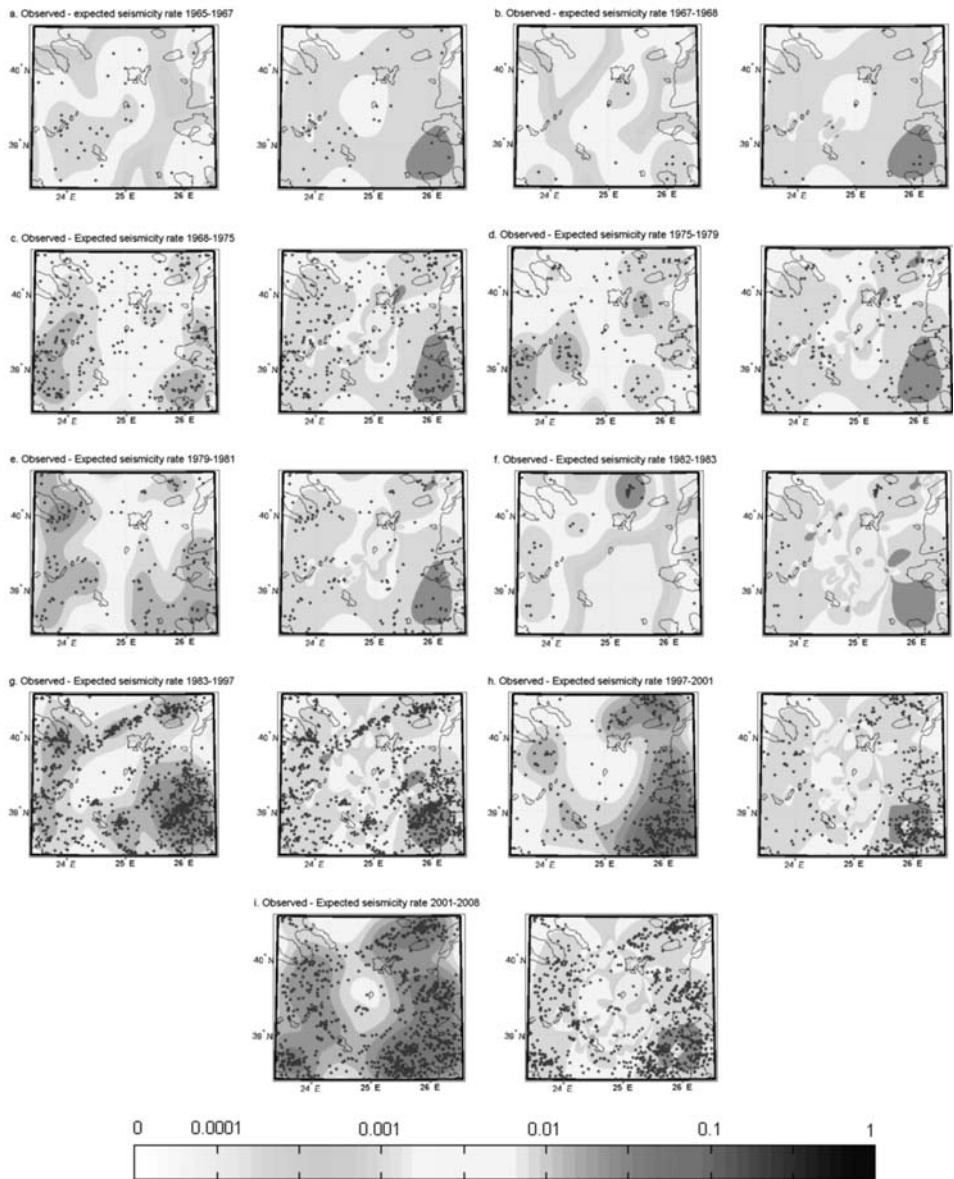
Fig. 3: Comparison of observed and expected seismicity rates in the study area with t_a=25yrs, =0.0275bar/yr and h=0.22. Warm colors represent high seismicity rate, cold colors stand for low rates. Blue dots, represent the epicentral location of earthquakes occurred in the interevent time of each case. Qualitative and quantitative correlation is better in the three last figures (3g, 3h, 3i) corresponding to seismicity rates after 1983.

Patterns of observed – expected seismicity, extracted from model 'a1' are shown in Fig. 3. As it is shown in Table 2 and Fig. 3, time periods after 1983 produce better correlation between observed and expected values of seismicity rate. This happens because of the better quality of the catalog after 1983, the longer interevent times, which provide larger sample and possible stress perturbation

in the region by earthquakes occurred before 1964 and therefore they are not included in modeling. Another evidence supporting this aspect is that the time periods 1965-1967 and 1982-1983, provide almost zero correlation irrespective to the model (they are not included in Table 2). Very high values of expected seismicity rate, yielding from modeling, were set to the highest value of background seismicity rate.

6. Discussion and Conclusions

Seismicity rate changes in the region of North Aegean, Greece, from 1964 to 2008 were studied, in association with Coulomb stress changes due to seismic slip caused by the 11 stronger events ($M_w \geq 5.8$) that occurred in this time interval. This influence was then examined in connection with the occurrence rate of small events ($M_w \geq 3.8$) for the respective time intervals. Seismicity was translated into earthquake probability for events with $M_w \geq 3.8$ and a rate/state model was used to associate static stress changes with seismicity rate and to compare and correlate the observed with the expected seismicity rate for each time period.

The mean correlation coefficient come from application of all models, except 'c', is 0.5581±0.037. It means the model can explain over half of seismicity distribution independently on the approach. Mean value is also very high during the 3 latest time intervals, approaching 72%. Better results arise considering aftershock duration to be 25 rather than 15 or 5 years. In the last case the mean correlation coefficient equals to 0.48, much lower than the average computed by the other models. Choice of a window width equal to 0.22, not only provides good correlation coefficient, but also better patterns for qualitative comparison. Very high values of h (>0.3), as applied in early periods on models 'a1' and 'b1', result to an oversmoothed pattern that does not reflect real seismicity distribution. However the choice of h and t_a, slightly affects the results.

Assuming non-uniform stressing rate and Aσ (model 'c'), the correlation is very low. This happens because of the lack of knowledge regarding the uncertainties concerning the spatial influence of the stressing rate assigned in limited areas, in combination with epicentral location uncertainties and difficulties in accurate estimate of the Aσ parameter value. Considering a uniform value of Aσ (model 'd'), the correlation is also lower, but comparable with the ones obtained from the other models. Variation of uniform stressing rate value   , also affects the results. The higher the value of stressing rate applied, the better the yielding correlation. Especially in 'e3' model (=0.064 bar/yr), the higher the correlation coefficient exceeds 83% (for 2001–2008 interval) with an average near 62%. This fact shows that influence of tectonic loading is very important, and therefore stressing rate has to be more accurately estimated for future applications.

The results obtained in this study demonstrate that the methodology applied is efficient for seismic hazard assessment. The number of events with magnitude larger than or equal to 3.8 can be estimated for any time period, given a magnitude-frequency relation. For the stronger events, which are rare, the occurrence probability can be estimated instead. For a stationary Poisson process the value of this probability, P, is P=1–exp(N), where, N, is the number of expected events in a time interval and area of interest (Toda & Stein, 2003).

As shown in Fig. 3, the area with the highest expected value of seismicity rate is the south-eastern part of the region. A distinct shadow zone appears to occupy the central part of the study region, yielding from high negative ΔCFF values by the stronger earthquakes occurred there. Characteristic pattern of the 1968 M7.0 event is present, although 40 years have already passed. Earthquake absence is obvious in this region, especially after 1990. A mean correlation coefficient of 73.5% for

the time interval 2001-2008, confirms that the model becomes more accurate when data are more sufficient and influence of former events, not included in the stress calculations has disappeared. Nevertheless, modeling and parameter values estimation can be improved for future applications, for a more reliable time-dependent seismic hazard assessment to be achieved.

7. Acknowledgments

8. References

Armijo, R., Flerit, F., King, G. and Meyer, B., 2003. Linear elastic fracture mechanics explains the past and present evolution of the Aegean, *Earth Planet. Sci. Lett.* 217, 85–95.

Ayhan, M. E., Bűrgmann, R., McCluskey, S., Lenk, O., Aktug, B., Herece, E. and Reilinger, R. E., 2001. Kinematics of the M_w=7.2, 12 November 1999, Dűzce, Turkey earthquake, *Geophys. Res. Lett.,* 28, 367–370.

Benetatos, C., Z. Roumelioti, A. Kiratzi, and N. Melis (2002), Source parameters of the M 6.5 Skyros Island (North Aegean Sea) earthquake of July 26, 2001, *Ann. Geophys.,* 45, 513–526.

Bird, P. and Kagan, Y., 2004. Plate–tectonic analysis of shallow seismicity: apparent boundary width, beta, corner magnitude, coupled lithosphere thickness and coupling in seven tectonic settings, *Bull. Seismol. Soc. Am.,* 94, 2380–2399.

Dieterich, J. H., 1994. A constitutive law for rate of earthquake production and its application to earthquake clustering, *J. Geophys. Res.*, 99, 2601–2618.

Dieterich, J. H., and Kilgore, B., 1996. Implications of fault constitutive properties for earthquake prediction, *Proc. Natl. Acad. Sci.*, 93, 3787–3794.

Erikson, L., 1986. *User's manual for DIS3D: A three–dimensional dislocation program with applications to faulting in the Earth*. Masters Thesis, Stanford Univ., Stanford, Calif., 167 pp.

Flerit F., Armijo, R., King, G. and Bertrand, M., 2004. The mechanical interaction between the propagating North Anatolian Fault and the back-arc extension in the Aegean, *Earth Planet. Sci. Lett.*, 224, 347–362.

Habermann, R. E. and Wyss, M., 1984. Background seismicity rates and precursory seismic quiescence: Imperial Valley, California, *Bull. Seismol. Soc. Am.,* 74, 1743–1755.

Hall, P., Sheather, S. J., Jones, M. C., and Marron, J. S., 1991. On optimal data-based bandwidth selection in kernel density D. estimation, *Biometrika,* 78, 263–269.

Kiratzi, A. A., Wagner, G. S., and Langston, C. A., 1991. Source parameters of some large earthquakes in Northern Aegean determined by body waveform inversion, *Pure Appl. Geophys.,* 135, 515–527.

Louvari, E., 2000. *A detailed seismotectonic study in the Aegean Sea and the surrounding area with emphasis on the information obtained from microearthquakes*. PhD Thesis, Aristotle Univ., Thessaloniki, Greece, pp. 373.

Nalbant, S. S., Hubert, A. and King, G. C. P., 1998. Stress coupling between earthquakes in northwest Turkey and the north Aegean Sea, *J. Geophys. Res.*, 103, 24,469–24.486.

Papadimitriou, E. E. and Sykes, L.R., 2001. Evolution of the stress field in the northern Aegean Sea

(Greece), *Geophys. J. Int.*, 146, 747–759.

Papadopoulos, A., A. Ganas, and A. Plessa (2002), The Skyros earthquake (M_w6.5) of 26 July 2001 and precursory seismicity patterns in the North Aegean Sea, *Bull. Seismol. Soc. Am.*, 92, 3, 1141–1145.

Papazachos, B. C., Scordilis, E. M., Panagiotopoulos, D. G., Papazachos, C. B. and Karakaisis, G. F., 2004. Global relations between seismic fault parameters and moment magnitude of earthquakes, *Bull. Geol. Soc. Greece,* 36, 1482–1489.

Papazachos, B. C., Karakaisis, C. B., Papazachos, C. B. and Scordilis, E. M., 2006. Perspectives for earthquake prediction in the Mediterranean and contribution of geological observations, *Geolog. Soc. London, Spec. Publ.,* 260, 689**–**707.

Papazachos, B. C., Comninakis, P. E., Karakaisis, G. F., Karakostas, B. G., Papaioannou, Ch. A., Papazachos, C. B. and Scordilis, E. M., 2008. A catalogue of earthquakes in Greece and surrounding area for the period 550BC–2008. Geophysics Dept., Thessaloniki University, 2008.

Parsons, T., 2004. Recalculated probability of M≥7 earthquakes beneath the Sea of Marmara, Turkey, *J. Geophys. Res.,* 109, B05304, doi:10.1029/2003JB002667.

Reasenberg, P., 1985. Second order moment of central California Seismicity, 1969–1982, *J. Geophys. Res,* 90, B7, 5479–5495.

Reilinger, R., et al., 2006. GPS constraints on continental deformation in the Africa-Arabia-Eurasia continental collision zone and implications for the dynamics of plate interactions, *J. Geophys. Res.*, 111, B05411, doi:10.1029/ 2005JB004051.

Sain, S. R., Baggerly, K. A., and Scott, D. W., 1994. Cross-validation of multivariable densities, *J. American Stat. Assoc.,* 89, 807–817.

Scholz, C. H., 1990. The Mechanics of Earthquakes and Faulting, *Cambridge University Press, Cambridge,* 439, 439pp.

Silverman, B. W., 1978. Choosing the window width when estimating a density, *Biometrika,* 65, 1-11.

Silverman, B. W., 1986. Density Estimation for Statistic and Data Analysis, *Chapman and Hall, London*, 9, 21pp.

Stein, R. S., Barka, A. A. and Dieterich, J. H., 1997. Progressive failure on the North Anatolian fault since 1939 by earthquake stress triggering, *Geophys. J. Int,* 128, 594–604.

Straub, C., Kahle, H.–G. and Schindler, C., 1997. GPS and geologic estimates of the tectonic activity in the Marmara sea region, NW Anatolia, *J. Geophys. Res.,* 102, 27,587–27,601.

Taymaz, T., Jackson, J. and McKenzie, D., 1991. Active tectonics of the north and central Aegean sea, *Geophys. J. Int.*, 106, 433–490.

Toda, S. and Stein, R. S., 2003. Toggling of seismicity by the 1997 Kagoshima earthquake couplet: A demonstration of time-dependent stress transfer, *J. Geophys. Res.*, 108, B12, 2567, doi:10.1029/2003JB002527.

Ward, S. N., 1998. On consistency of earthquake moment release and space geodetic strain rates: Europe, *Geophys. J. Int.*, 135, 1011–1018.

Wells, D. L. and Coppersmith, K. J., 1994. New empirical relationships among magnitude, rupture length, rupture width, rupture area and surface displacement, *Bull. Seismol. Soc. Am.* 84, 974–1002.

Wessel, P. and Smith, W. H. F., 1998. *New, improved version of the Generic Mapping Tools Released*, EOS Trans. AGU, *79*, 579.

MOMENT TENSOR DETERMINATION USING A NEW WAVEFORM INVERSION TECHNIQUE

Moshou A.[1], Papadimitriou P.[1] and Makropoulos K.[1]

[1] *National and Kapodistrian University of Athens, Faculty of Geology and Geoenvironment, Department of Geophysics - Geothermics, Panepistimioupolis Zografou 15784, Athens, Greece, amoshou@geol.uoa.gr, ppapadim@geol.uoa.gr, kmacrop@geol.uoa.gr*

Abstract

In this study a new waveform inversion methodology was developed to determine the source parameters of an earthquake. This technique is based on analyzing data recorded both at teleseismic and regional distances. To apply the inversion three different methods, which are the normal equations, the QR-decomposition and the singular value decomposition (SVD), were successfully tested, similar results were obtained and the SVD method was selected. The proposed inversion methodology was applied to large, as well as to earthquakes of moderate magnitude. Analysis of moderate events is crucial for seismogenic volumes, where an important number of such earthquakes occur which allow the calculation of their source parameters. Thus, the seismotectonic characteristics of the study area can be determined. The proposed methodology is successfully applied to events located in Greece and its surrounding regions in near real time.

Key words: focal mechanism, moment tensor inversion, body waves.

1. Introduction

Moment tensors represent the key information for seismotectonic studies. The moment tensor as a mathematical description of equivalent forces and moments is used to study the source processes. The propagation and the source effects characterize variations of the observed seismograms. Mathematically, each one of these effects can be calculated in order to generate synthetic seismograms that can be compared directly to the corresponding observed ones. The best solution is obtained by the minimization of the difference between the observed and the synthetic seismograms (Aki and Richards, 1980).

A seismic source is represented by a moment tensor M with six independent elements. However in most tectonic earthquakes, there is no change of volume at the source (Kikuchi and Kanamori, 1991) and thus we have five independent elements of the moment tensor. Then the synthetic seismogram can be calculated by the linear combination of the five terms which are elements of the matrix M and the corresponding Green's function. A powerful tool for the moment tensor calculation is the waveform inversion. In the past different methodologies were developed both in time (Das and Kostrov, 1990; Hartzell and Heaton, 1983; Kanamori, 1972; Kikuchi and Kanamori, 1982; Langston and Helmberger, 1975; Langston, 1976; Madariaga and Papadimitriou, 1985; Papadimitriou, 1988) and frequency domain (Brune, 1970; Cotton and Campillo, 1995). Langston and Barker (1981, 1982) developed a method using a generalized inversion technique to determine the source parameters of an earthquake.

In the present study we propose a new technique of waveform inversion to rapidly estimate both source time function and the seismic moment tensor of an earthquake. We assume a pure double – couple source mechanism to stabilize the solution when data from a small number of seismic stations are used. This method is based on the eigenvalues and eigenvectors analysis of the moment tensor in order to calculate its components, (Jost and Hermann, 1989). In the case where the sum of the eigenvalues vanishes the moment tensor has only deviatoric components. In general a seismic moment tensor can be decomposed into a dipole of forces, the best double couple (DC), which indicates the slip movement along the fault surface (Lay and Wallace, 1995) and in a compensated linear dipole (CLVD) which describes seismic sources with no volume changes.

An important number of moderate earthquakes were analysed in near real time and the results are published on the website of the Department of Geophysics of the University of Athens: www.geophysics.geol.uoa.gr. In the present study two earthquakes, one large recorded at teleseismic distances and one moderate at regional, are presented.

2. Methodology

2.1 Seismic source representation

Seismic sources can be represented by equivalent forces, producing displacements on the earth's surface, which are identical to those created by the physical process of the source. The displacement field $u_n(x, t)$ using the representation theorem for body – waves (Aki & Richards, 1980) can be calculated at a position x and time t in the following equation:

$$(1)$$

where $u_i(\xi, \tau)$ is the dislocation function, $G_{nk,1}$ is the partial derivative of Green's function and expresses the nth component of the displacement at position x and time t. Note that x is a vector that denotes the position of a station and ξ denotes the position vector of a point source on the rupture surface. Σ is the fault plane surface, η_j is the jth component of the n which is the vector normal to Σ. Furthermore, c_{ijkl} is the elastic constant tensor of Hooke law while $u(\xi, \tau) \cdot c_{ijkl}$ denotes the moment density tensor m_{kl} which can be define as:

$$(2)$$

The representation theorem for displacement at x due to general discontinuity $u(\xi,\tau)$ across Σ is

$$(3)$$

Thus, for an effective point source

$$(4)$$

where the moment tensor components are

$$(5)$$

The dimension of the symmetric matrix M is 3x3 and depends on the type of faulting. The three diagonal elements represent vector dipoles, while the six off-diagonal elements represent force couples. Considering no volume change, the trace of the matrix is equal to zero. Otherwise there an isotropic part exists, where positive values indicate explosion and negatives implosion. In the case where the determinant is equal to zero, the deviatoric moment tensor represents a pure double couple (DC). In general, the moment tensor can be decomposed in an isotropic part, in a pure double couple and a compensated linear vector dipole (CLVD).

The last equation indicates that the displacement in a position x and time t is defined as a convolution between the moment tensor and the partial derivative of Green's tensor. Furthermore, a synthetic seismogram, in teleseismic distances, can be calculated at a specific geographical position using the following equation:

$$\tag{6}$$

where $g(\Delta, h)$ is the geometric spreading, r_0 is the radius of the earth, ϱ is the density at the source, R denotes the radiation pattern, c denotes the v_P (P waves) or v_S (S waves) velocity and is the moment rate.

The discrete wavenumber method of Bouchon (1981, 2003) to compute the Green's function was used to calculate the source parameters for regional waveforms. In this study the method by Zahradnik et al. (2005) was modified and then adapted for the analysis using regional – local data.

The moment tensor is represented by a 3x3 symmetric matrix. Using a set of data which consists of synthetics and the corresponding observed recordings, it is possible to construct nx6 matrix and, by applying the Generalised Inverse Method, to calculate the source parameters of the earthquake.

2.2 Inverse Problem

Following, the data, denoted by a vector D, can be represented by a linear combination of a non square matrix G representing elementary Green's functions and a vector M representing the model parameters:

$$D = G \cdot M \tag{7}$$

The dimension of the matrix G is nxm where n is the number of observations and m the number of fundamental Green functions. The inverse problem consists of inverting the non symmetric matrix G in order to determine the parameters of the model. Several methods exist to calculate the inverse of the matrix G like the normal equations, QR-decomposition, and the singular value decomposition (SVD). All three methods are used and the obtained results were similar. In the present study the singular value decomposition method is chosen and can be used either in overdetermined or underdetermined systems. First, two symmetrical matrices the $U = GG^T$ and the $V = G^TG$ that have the same eigenvalues are defined. Following, the diagonal matrix Λ is defined by calculating the positive square root of the non zero eigenvalues, named singular values (Lanczos, 1950). Thus, the model parameter M can be calculated by the relation:

$$M = G^{-g} \cdot D \tag{8}$$

where   is the generalised inverse matrix. The matrix G is decomposed into:

$$G = U \cdot \Lambda \cdot V^T \qquad (9)$$

The obtained eigenvectors are parallel to the principal stress axes and the norm of the matrix is equal to the seismic moment which is symmetric and has 6 independent elements. In case of an earthquake both the trace and the determinant of the matrix must be equal to zero. Considering the two constraints the obtained moment tensor consists of 5 independent elements.

In summary, by creating five elementary Green functions it is possible to calculate a synthetic seismogram that can directly be compared to the observed one. The model parameters are estimated by minimizing the difference between observed and synthetics.

3. Source parameters determination

For large earthquakes synthetic seismograms are calculated at teleseismic distances between $30°<\Delta<90°$ while for regional – local events for distances less than $\Delta<6°$. Green's functions are generated and combined in order to produce the P, SV, SH movements. Broad band data are tested and each component of good quality is selected and used for the inversion. For large events waveforms at teleseismic distances (epicentral distances between $30°$ and $90°$) were selected from stations belonging to the Global Seismograph Network (GSN). For moderate events regional data from the Hellenic Unified Seismological Network (HUSN) were used. We applied deconvolution of instrument response from all the waveforms and integration of the data to produce displacement waveforms. For the teleseimsic events the synthetic seismograms were generated for a point source in a half space. The attenuation effect is taken into account using Futterman's (1962) operator with $t^*=1$ sec for P – waves and $t^*=4$ sec for S – waves. The regional – local data were generally band passed between 0.02 and 0.1 Hz and then converted into displacement with a sampling rate of 0.2 sec.

The proposed methodology was successfully applied to the largest earthquakes that happened recently in Greece as well as to a large number of moderate events. Following, two examples will be presented. The first application concerns the most recent large event which is the 2009 Crete earthquake. The second example is a moderate event that occurred in the area of the Corinth Gulf.

3.1 The M_w=6.2 2009 Crete earthquake

On 1 July 2009 (09:30 GMT) an earthquake of magnitude M_w=6.2 occurred south of Crete island. Using waveforms from HUSN the epicenter was manually located at $33.92°$N, $25.47°$E. Broadband teleseismic recordings from GSN network were collected and those at epicentral distances between $30°$ and $90°$ degrees were selected. For the inversion method, 11 teleseismic stations were used with satisfactory azimuthal coverage for the generation of P waves, 3 for SH and 2 for SV waves. The moment tensor components and the focal depth of the mainshock were determined using a single trapezoidal source time function with a duration of 5 sec. Reverse type faulting was revealed after applying body wave inversion. The obtained focal mechanism is $\phi=101°$, $\delta=62°$ and $\lambda=87°$. The seismic moment is equal to $3.2 \cdot 10^{25}$ dyn·cm, for a focal depth equal to 22 km. The inversion resulted a DC equal to 90%, while the compensated linear vector dipole was equal to 10%.

It is worth noticing that after several applications the percentage of these quantities depends on the quality of the data. For this reason a second methodology was developed and applied to better estimate the final solution, as well as the variance of the parameters, based on grid search.

The second methodology was developed mainly for moderate events recorded at regional distances in cases of low DC percentage, noisy waveforms etc. This technique is based on the use of an iter-
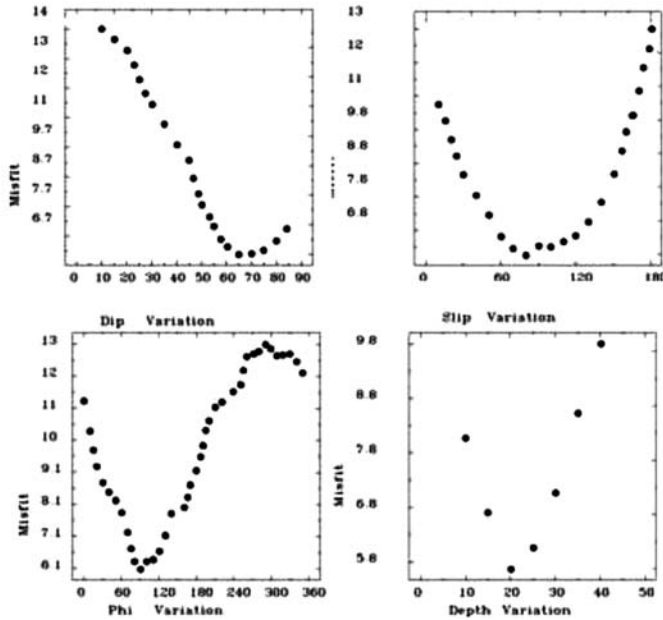
Fig. 1: Misfit of the source parameters of the 2009/07/01 Crete Earthquake.

ation procedure. As initial parameters the solution resulted by the inversion procedure is used. The source parameters determined using this technique is more accurate, while the range of each parameter can be individually estimated.

Figure 1 presents the results of this technique. In the first stage the dip, the rake and the depth were fixed and the azimuth varied, as described in the low left subfigure. Initially the azimuth varies between 0° and 359° with a step of 10°. A clear minimum was observed around 90°. Following, the same procedure is applied for the range 90°±20° with a step of 1° in order to determine a more accurate final minimum value which was found equal to 92°±5 °. Using the same procedure the dip was determined. Initially, in the upper left subfigure, the dip varies between 10° and 80° with a step equal to 5° and indicates a minimum around of 70°. Following, for the range 60° - 80° (step 1°) the dip was 67°±3°. In the upper right subfigure the variation of rake indicates a minimum around 80°, while after the second iteration 80°±5°. Finally, following the same procedure (low right subfigure) the depth was initially found around 20 km and finally 22±3 km.

Comparing the results of both methodologies, the obtained values for all parameters are similar. Nevertheless, the results obtained by the second method are preferred, since the misfit between the recorded waveforms and the synthetics is more satisfactory. Furthermore, a better estimation of the errors of the source parameters is achieved.

The results of the applied modeling are presented in Fig. 2. For this event the selected stations presented a good azimuthal coverage. The complexity presented in the observed waveforms is probably due to the seismic source. In this study a simple trapezoidal source time function is applied therefore no high frequencies are observed in the synthetics. However the obtained source parameters were precisely determined.

The main shock was followed by the occurrence of numerous aftershocks. The source parameters of the five largest moderate aftershocks (M>4) were computed. Their focal mechanisms revealed reverse type of faulting, as the main shock, while their depths vary between 15 and 25 km.
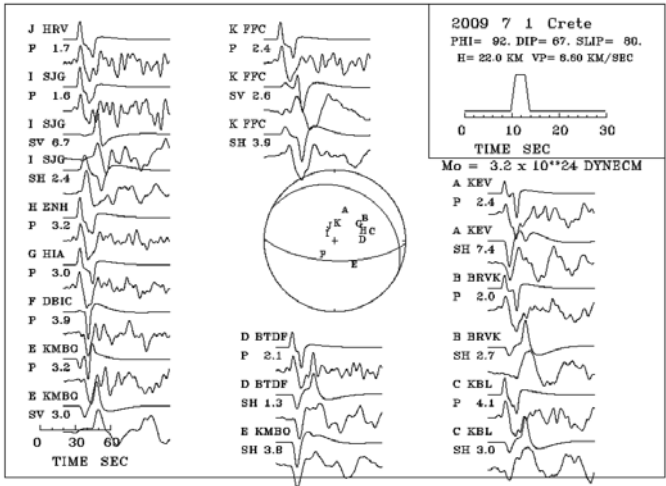
Fig. 2: Body wave modelling of the 2009/07/01 Crete earthquake.
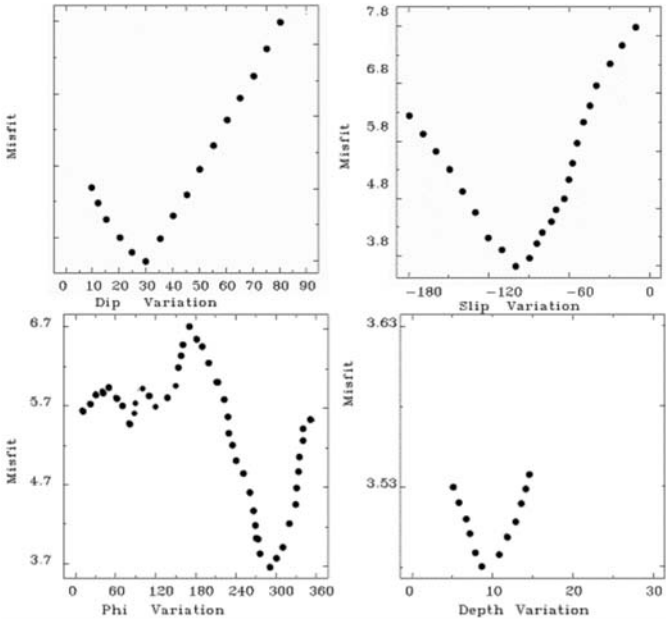
Fig. 3: Misfit of the source parameters of the 2009/06/07 Aigion earthquake.

3.2 The M_w=4.2 earthquake in the Corinth Gulf (07/06/2009)

On 7 June 2009 (08:57 GMT) an earthquake of magnitude M_w =4.2 occurred in the Corinth Gulf, near to Aigio town. The event was manually located at 38.14° N, 22.68° E, using recordings of the HUS Network. To determine the source parameters of this moderate event 7 station in local and regional distances were used.

The source parameters were first calculated applying the moment tensor inversion method. The best fit solution is: ϕ=265°, δ=25°, λ= -78° and seismic moment $1.1 \cdot 10^{22}$ dyn · cm for a depth of 7 km. Furthermore, normal faulting was indicated. The calculated double couple was found equal to 68%, while the compensated linear vector dipole (CLVD) to 32%.
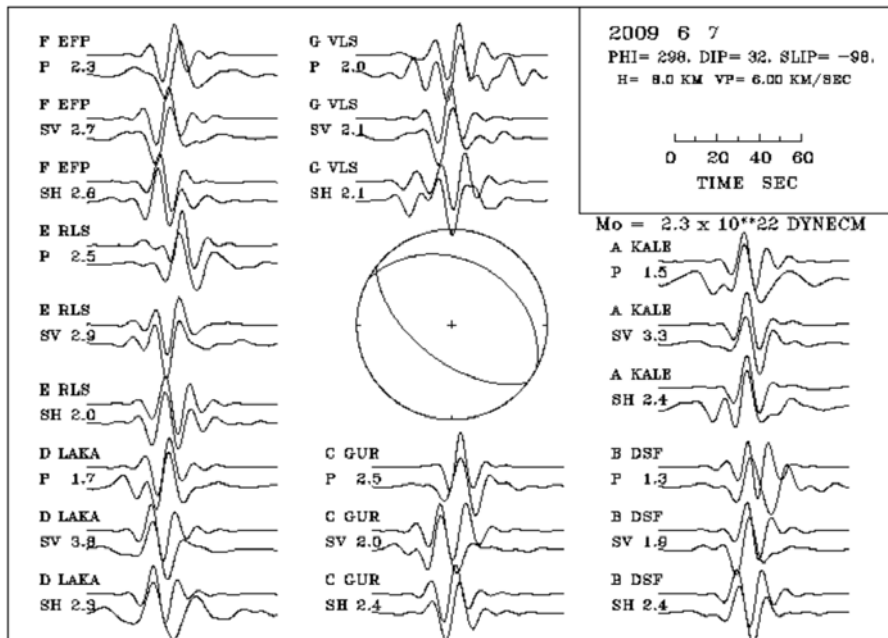
Fig. 4: Body wave modelling of the 2009/06/07 earthquake in the Corinth Gulf

The inversion procedure did not provide a high double couple component. For this reason, the second method is applied, using as starting solution the one obtained by the moment tensor inversion and the results are present in Fig. 3. In the first stage the dip, the rake and the depth were fixed and the azimuth was left to vary as described in the low left subfigure. The minimum was close to 300° while the obtained solution was 298°±10°. The upper left subfigure indicates the dip variation with a minimum close to 30°, while the obtained final solution was 32°±5°. Following the same procedure the rake (upper right subfigure) was estimated close to -100° while the final solution was 98±5°. In the down left subfigure the variation of azimuth is described. Finally, the depth (down right subfigure) was initially found around 8 km, which was also the final solution.

The results of the applied procedure are presented in Fig. 4. For this event 7 three components stations of HUS Network were used. Waveforms with a good signal to noise ratio were selected in regional distances. As we can see the fit between the synthetics and the corresponding observed is in good agreement and as a result the calculated source parameters are well determined.

4. Discussion

In this study, source parameters were calculated for the strongest events that occurred during the period 1995 – 2009 using teleseismic body wave modelling. The obtained source parameters of those earthquakes present in Table 1.

In most cases, the inversion procedure revealed simple source time function, as in the cases of the Aigio, Kozani and Athens earthquakes. In addition, cases with complicated source time functions were also considered, as the 2003 Lefkada earthquake. Between 14 February 2008 and 20 February 2008 three strong (M_w>6.0) earthquakes occurred in the sea, close to the town of Methoni. For two

Table 1. Earthquakes source parameters determinate in the present study.

Date	Time	Event	Lon (E)	Lat (N)	M$_w$	Depth km	Strike o	Dip o	Slip o
1995-05-13	08:47:13	Kozani	40.15	23.65	6.5	15	260	34	-90
1995-06-15	00:15:23	Aigio	38.40	22.48	6.2	12	277	28	-30
1999-09-07	11:56:34	Athens	38.10	23.56	6.0	8	105	56	-82
2001-07-26	00:21:46	Skyros	39.03	24.27	6.5	14	160	65	7
2002-01-22	04:35:00	Karpathos	35.56	26.73	6.2	90	95	89	50
2003-08-14	05:14:54	Lefkada	38.82	20.60	6.3	15	80	170	15
2006-01-08	13:34:54	Kythira	36.23	23.39	6.6	65	205	45	55
2008-01-06	05:14:18	Leonidio	37.09	22.65	6.0	85	114	75	120
2008-02-14	10:09:22	Methoni	36.30	21.69	6.7	35	290	16	69
2008-02-14	12:08:54	Methoni	36.34	21.92	6.1	38	337	11	123
2008-02-20	18:27:05	Methoni	36.21	21.71	6.0	16	249	67	-9
2008-06-08	12:25:28	Andravida	37.95	21.53	6.4	23	218	89	176
2008-07-15	03:26:32	Rodos	35.92	27.84	6.3	56	280	82	-40
2009-07-01	09:30:09	Crete	33.92	25.47	6.2	20	92	67	80
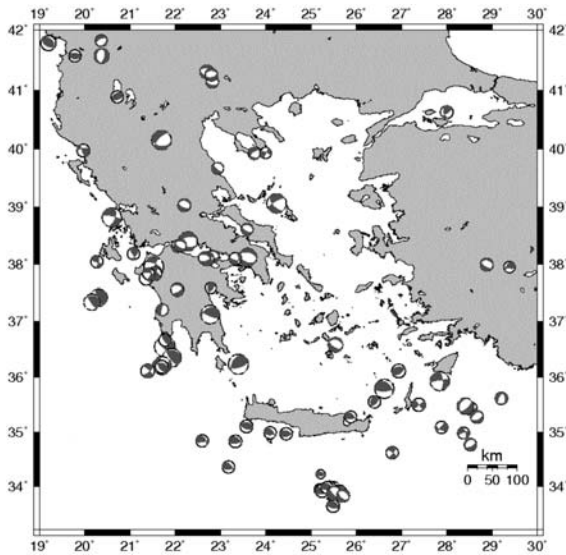
Fig. 5: Focal mechanisms solutions determined in this study between 1995 – 2009.

of these events complicated source time functions was also calculated. In total, source parameters for 14 large earthquakes were successfully determined in different seismotectonic settings.

The knowledge of the source parameters for moderate earthquakes is very important for seismically active regions, especially in the case where no large events occur. In general, it gives the opportunity for analytical studies, reveal the tectonics and the seismogenic characteristics of a specific re-

gion as in the case of the May 2009 seismic sequence that occurred at the lake Doirani (north of Thessaloniki). The area was activated for the first time during the last decades. The modelling of the strongest earthquakes, using regional data of this sequence were studied and revealed the tectonics of the region which is characterized by normal faulting. Thrust type faulting appears south of Zakynthos island, of the town of Methoni and close to the Kythira island, while in the eastern Aegean region different types of faulting appeared. Common events were compared with other studies (Agalos et al., 2007) and they were in very good agreement. The focal mechanisms solutions for the events determined in this study are appear in the Fig. 5.

5. Conclusions

In the present study, the results of a new developed method were presented. In the proposed methodology data both from teleseismic and from local-regional distances were used. This methodology is useful for regions were important moderate seismicity is observed. For the inversion P, SH and SV waves are used. Mathematically, the moment tensor inversion is an overdetermined problem and the general solution is separated in a DC and a CLVD part. In this case the components of the seismic moment tensor can be calculated using the generalized inverse technique by applying different methodologies. The most commonly used is the singular value decomposition method and this is the one also used in this study.

For teleseismic events this method gives, in general, satisfactory results. On the contrary, this is not always the case for moderate events due to poor quality of the large period component. For that reason a second methodology, based on a grid search was developed to overcome this difficulty. The proposed methodologies were successfully applied to a large number of moderate earthquakes that occurred in Greece the recent years. It is worth noticing that in some seismic crises like Doirani (north of Thessaloniki), Evia and Ionio islands, no large event recently occurred. The obtained results can contribute to the study of the seismotectonic characteristics of these regions.

6. References

Agalos A., Papadimitriou P., Voulgaris N. & Makropoulos K., 2007. Source Parameters Estimation from Broadband Regional Seismograms for Earthquakes in the Aegean Region and the Gorda Plate. *Proceedings of 11th International Congress, Athens, May 2007* Available online at: http://www.geophysics.geol.uoa.gr

Aki & Richards P.G 1980. *Quantitative Seismology*, W.H. Freeman, San Fransisco, 1, 55.

Brune, J., 1970. Tectonic stress and spectra of seismic shear waves *J. Geophys. Res.*, 75, 4997-5002.

Bouchon, M., 1981. A simple method to calculate Green's functions for elastic layered media, *Bulletin Seismological Society of America, Vol. 71, p.p. 959 – 971*

Cotton, F., Campillo, M., 1995. Inversion of strong ground motion in the frequency domain: Application to the 1992 Landers, California earthquake *J.Geophys. Res., 100, 3961-3975.*

Das, S., & Kostrov, B., 1990. Inversion seismic slip rate history and distribution with stabilizing constraints: Application to the 1986 Andrean of Islands earthquake, *J. Geophys. Res., 95, B5, 6899-6913.*

Futtermann, W., 1962. Dispersive body waves, *J. Geophys. Res. 67, 5279-5291.*

Hartzell, S., Heaton, T., 1983. Inversion of strong ground motion and teleseismic waveform data for the fault rupture history of the 1979 Imperial Valley, California earthquake, *Bull.Seism.Soc Am.* 76, 649-674.

Helmberger D. (1974). Generalized ray theory for shear dislocations, *Bull. Seis. Soc. Am.* 64, 45 – 64

Jost, M., Hermann, R., 1989. A student's Guide to and Review of Moment Tensors, *Seismological Re-*

search Letters, 60 (2), 37 – 57.

Kanamori, H., 1972. Determination of effective tectonic stress associated with earthquake faulting, the Tottori earthquake of 1943, *Phys. Earth. Planet. Interiors*, 5, 426-434.

Kikuchi, M., Kanamori, H., 1982. Inversion of complex body waves, *Bull. Seism. Soc. Am.*, 72, 491 – 506.

Kikuchi, M., Kanamori, H., 1991. Inversion of complex body waves – III, *Bull. Seism. Soc. Am.*, 81(6), 2335 – 2350.

Lanczos, C., 1950. An iteration method for the solution of the eigenvalues problem of linear differential operators, J. Res. N. B. S., 45, 255 – 282.

Langston, C., Helmberger, D., 1975. A procedure of modelling shallow dislocation sources, *Geophysics, J. R. Astr. Soc.*, 42, 117-130.

Langston, C., 1976., A body wave inversion of the Koyna, India, earthquake of December 10, 1967, and some implications for body wave focal mechanisms, *J. Geophys. Res.*, 81, 2517-2529.

Langston C. & Barker J. (1981). Inversion of teleseismic body waves for the moment tensor of the 1978 Thessaloniki, Greece, earthquake, *Bull. Seism. Am.*, 71, 1423 – 1444.

Langston, C., Barker, J., Pavlin, G., 1982. Point – source inversion techniques, *Physics of the Earth and Planetary Interiors*, 30, 228 – 241.

Lay, T., Wallace, T., 1995. *Modern Global Seismology*, Press, New York.

Madariaga, R., Papadimitriou, P., 1985. Gaussian beam modeling of upper mantle phases, *Annales Geophysicae* 3, 6, 799-812.

Meju, M., 1994. *Geophysical Data Analysis: Understanding Inverse Problem Theory and Practise*, Course Notes Series, Volume 6, S.N. Domenico.

Menke, W., 1984. *Geophysical Data Analysis, Discrete Inverse Theory*, Academic, San Diego, CA

Papadimitriou, P., 1988. *Etude de la structure du manteau superieur de l' Europe et modelisation des ondes de volume engendrees par des seismes egeens*, Doctorat de l' Universite Paris VII, Paris France.

Zahradnik, J., Serpetsidaki, A., Sokos, E., and Tselentis, G., 2005. Iterative deconvolution of regional waveforms and a double-event interpretation of the 2003 Lefkada earthquake, Greece, *Bull. Seismol. Soc. A.*, *Vol. 95, p.p. 159-172*

INFLUENCE OF STRESS TRANSFER IN PROBABILITY ESTIMATES OF M≥6.5 EARTHQUAKES IN GREECE AND SURROUNDING AREAS

Paradisopoulou P. M.[1], Papadimitriou E. E.[1], Karakostas V. G.[1], Lasocki S.[2], Mirek J.[3], Kilias A.[4]

[1] *Geophysical Laboratory, School of Geology, Aristotle University of Thessaloniki, PO Box 352-1, 54006, Thessaloniki, ppara@geo.auth.gr, ritsa@geo.auth.gr, vkarak@geo.auth.gr*

[2] *Institute of Geophysics, Polish Academy of Sciences, Warsaw, Poland, lasocki@igf.edu.pl*

[3] *Faculty of Geology, Geophysics and Environmental Protection, AGH University of Science and Technology, Krakow, Poland, jmirek@seismo.geol.agh.edu.pl*

[4] *Department of Geology, School of Geology, Aristotle University of Thessaloniki, GR-54124, Thessaloniki, Greece, kilias@geo.auth.gr*

Abstract

The coseismic stress changes due to strong earthquakes (M≥6.5) that occurred in Greece and its adjacent areas since the beginning of the 20th century (instrumental era) are calculated and the future seismic hazard expressed in terms of the probabilities of occurrence of M≥6.5 events is assessed. Calculations of the change in Coulomb failure stress reveal that 61 out of 67 ruptures were brought closer to failure by the preceding shocks. A new insight on the evaluation of future seismic hazards, in the study area, is given by translating the calculated coseismic stress changes into earthquake probability. We incorporated the effect of stress change into the time–depended probability estimates using an earthquake nucleation constitutive relation, which includes both permanent and transient effects of stress changes. Taking into account the current stress changes onto each major fault, the probability calculations were performed and given for the whole study area during the next 30 years.

Key words: *Greece, strong earthquakes, coseismic stress changes, stress transfer, earthquake probabilities, seismic hazard.*

1. Introduction

Many destructive earthquakes occurred in the territory of Greece and the adjacent areas, some of them being close both in time and space. For this reason the investigation of possible connection of these occurrences through stress transfer is of paramount importance for seismic hazard purposes. Thus, the first goal of the present study is to calculate the coseismic stress changes caused by the strong earthquakes of M≥6.5 that occurred during the instrumental era that is since the beginning of the 20th century in the study area. As a second step the static stress changes on specific faults that have accumulated until now will be incorporated into probabilistic models, in an attempt to assess the seismic hazard in the study area.

Earthquake triggering or delay due to changes in stress was recognized more than a decade ago (e.g.

Harris, 1998 and references therein) and is worked out in assessing earthquake occurrence and future seismic hazard in a certain area. Stein (1999), reviewing the role of stress transfer, emphasized the earthquake interaction as a fundamental feature of seismicity, that promises a deeper understanding of the earthquake occurrence and a better description of the seismic hazard, when stress transfer is incorporated into probability models (Stein et al., 1997; Toda et al., 1998). In association with physical fault models and fault properties, such models were more developed and statistically assessed (Parsons, 2004, 2005 among others). Another investigation, in the area of Western Turkey, was performed by Paradisopoulou et al. (2010) who calculate static stress changes of M≥6.5 events and estimated the probability of an earthquake occurrence in the next 30 years from 2008.

The present study differs from the previously mentioned ones in calculations of static stress changes and estimation of probabilities for the whole territory of Greece and its adjacent areas. We start with the stationary and conditional probability models estimating the probability of occurrence in the next 30 years from the studied date (2009) of an earthquake with M≥6.5 on known fault segments of the study area. Then the accumulated stress changes due to coseismic slips of the modeled events are incorporated into the estimation of earthquake probability. Change in the probability on a given fault is calculated from the change in seismicity rate, which is computed by taking into account both permanent and transient effects.

2. Stress change calculations

The Coulomb stress changes are calculated for earthquakes with M≥6.5 that occurred in the study area since 1900. An earthquake can be modelled as a slipping dislocation in an elastic half space (Okada, 1992) enabling estimation of stress transfer to other faults. Earthquakes occur when stress exceeds the strength of the fault. The closeness to the failure is quantified using the change in Coulomb failure function (ΔCFF). In its simplest form, the Coulomb failure stress change is (modified from Scholz, 1990) (eq. 1):

$$(1)$$

where $\Delta\tau$ is the change in shear stress on a fault (set positive in the direction of fault slip), $\Delta\sigma$ is the change in normal stress (set positive for extension) and μ' is the apparent coefficient of friction, which is assumed to incorporate changes in pore pressure (Harris and Simpson 1998) and material properties of the fault zone. $\Delta\sigma$ and $\Delta\tau$ are calculated for a fault plane at the observing (field) point. For increasing shear stress in the direction of relative slip on the observing fault $\Delta\tau$ is positive. $\Delta\sigma$ is positive for tensional normal stress. The shear modulus and Poisson's ratio are fixed at $3.3\cdot10^5$ bar and 0.25, respectively. Coulomb stress changes are calculated according to the geometry of the target fault, which is the fault of the subsequent strong earthquake in our sample, and at the appropriate depth. In our study area it is known that the majority of the foci of the crustal earthquakes are located in the depth range of 3 to 15 km, which defines the brittle part of the crust. Considering all the above information the seismogenic layer in our calculations is taken to be in this range for all the strong events (M≥6.5) modeled, and stress changes are calculated at the depth of 10km.

3. Probability Calculations

3.1 Methodology

An attempt is made in this section to estimate probabilities for the occurrence of future strong (M≥6.5) events on the fault segments associated with events of M≥6.5 that occurred either during the instrumental period or in the past centuries and for which available information exists. For a

probabilistic earthquake forecast in a region under the influence of past events it is considered that the stress transfer might fasten or delay the next earthquake. The methodology followed is that by Stein et al. (1997); Toda et al. (1998) and Parsons (2004, 2005) who considered both permanent and transient effect of the stress changes on earthquake probabilities.

Two models for estimation of earthquake probabilities are generally in use: the stationary Poisson model and the conditional probability model (Cornell et al., 1968; Hagiwara, 1974). Using both of the mentioned models we estimate the probability of an earthquake to occur in the next 30 years from 2009.

• Poisson model: This model is one that treats earthquakes as occurring at random in time (t) about an average interevent time (T_r). The probability of at least one event in the time interval (t, t+Δt) is given by:

$$(2)$$

• Conditional Probability model: In this model, probability can increase with time to represent increasing stress on a fault segment toward an uncertain stress threshold. A time–dependent probability (in any time interval (t, t+Δt)) is calculated by a probability density function f(t) as (Working Group of California Earthquake Probabilities, 1990):

$$(3)$$

where P is the probability that an earthquake will recur at some time T in the interval (t, t+Δt) and f(t) is the applied probability density function of recurrence time. The probability, conditional on the earthquake not occurring prior to t, is:

$$(4)$$

We assume a lognormal probability distribution of recurrence time (e.g. Nishenko and Buland, 1987):

$$(5)$$

where   is the average interevent time, s_t: the standard

deviation of interevent time.

• Permanent effect of stress change: Increasing (or decreasing) Coulomb stress on a fault segment permanently shortens (or lengthens) the time required for tectonic stressing to bring the segment to failure and thus causes a permanent change in conditional probability. The conditional probability model can be adapted to estimate the effect of stress changes by equating the stress change with the time required to accumulate stress through secular stressing. Therefore, for the calculation of the probability for the fault of interest an adjusted time by the clock change must be taken into account. The 'life clock change' of the fault of interest can be estimated by:

$$(6)$$

where ΔCFF: is the stress change due to nearby event and   : is the tectonic stressing rate in bar/yr. Thus, to calculate the conditional probability for the fault of interest taking into account an adjusted time by the clock change the following equation is used:

$$(7)$$

• Transient effect of stress change: The existence of foreshocks and aftershocks demonstrate that when an earthquake occurs there is a large transient increase in the probability of additional earthquakes in the surrounding area. A quantitative explanation of aftershock distributions and decay, and foreshock statistics, is given by a single model in which the rate of earthquake occurrence is perturbed by the local stress changes caused by a prior earthquake (Dieterich, 1994; Dieterich & Kilgore, 1996). We use this model to estimate the rate–state transient effect that describes an expected enhanced rate of earthquake nucleation resulting from a stress increase and can be expressed as a probability. For a stress decrease the rate of nucleation declines and eventually recovers. Because the transient effect of the stress change is expressed as a change in expected rate of segment events, it is convenient to formulate the probability analysis as a non–stationary Poisson process in which the probability of an earthquake occurring in the interval (t, t+Δt) is given by:

$$(8)$$

where, P is the net probability, which combines the transient and permanent effects of the stress change on earthquake probability and $R(t)$ is the expected earthquake rate following a stress step. Δt is measured from the time of the stress step (we use 30 years for these computations). To evaluate eq. (2), we obtain N, by integrating the solution for $R(t)$ following a stress step (Dieterich, 1994). For the interval 0 to Δt, this yields:

$$(9)$$

where r_p is the permanent background component of the earthquake rate following the stress step:

$$(10)$$

where P_c is the permanent probability from eq. 7, t_α is the characteristic duration of the transient effect, σ, is the normal stress, A, is a fault constitutive constant and ΔCFF is the calculated Coulomb stress change. Note that the transient effect disappears if ΔCFF=0, that is $N=r_p \cdot \Delta t$. We calculated Aσ of eq. (9) by knowing the parameters t_α and ΔCFF and using the equation (Dieterich, 1994):

$$(11)$$

3.2 Parameter calculations

• Mean interevent time (T_r): For this estimation it was necessary to collect historical information and paleoseismological investigations for earthquakes with M≥6.5 that associated with fault segments of the study area. Historical information are mainly taken from Papazachos and Papazachou (2003), Ambraseys and Jackson (2000) and Ambraseys (2002). Some of paleoseismic records are found on the North Anatolian Fault (NAF). This information is useful especially in the cases of large events that seem to have broken multiple segments or in cases of clustering, like the three large earthquakes in 1343, 1344 and 1354, which according to Rockwell et al. (2001), comprise a mini–sequence rupturing much of the NAF. At Duzce fault (S127) there are 3 events observed (Pantosti et al., 2008), 2 events are noted at nearby Izmit segment (S125) (Parsons, 2004; Pondard et al. 2007; Klinger et al. 2003) and 3 events are associated with the Cinarcik (S124) segment, with an observed mean frequency of 170 years and a modelled ~250 year interevent time (Parsons, 2004; Pondard et al. 2007). At Marmaras 1 and 2 (S123, S122 respectively) 3 and 4 events observed according to Parsons (2004) and Papazachos and Papazachou (2003). Observations on the Ganos fault (S121) support T_r~275 years (Rockwell et al., 2001). Parsons (2004) gives a calculated mean interevent time of 207 years. Paleoseismological data for Mudurnu segment and Yenice fault are taken from Palyvos et al. (2007) and Kurcer et al. (2008).

In the area of Corinth Gulf, in Eliki's (S43) and Xylokastro fault (S44), a mean interevent time of 242±60 years and 119±20 years was found respectively (Briole et al., 2000). The Eliki fault is associated with 373 B.C. and 1748, 1861 earthquakes result an average time 270-1200 years (Koukouvelas et al. 2001). Collier et al. (1998) give a calculated mean interevent time equal to 330 years. According to Pavlides et al. (2004) one paleoearthquake occurred before 1894 earthquake on Atalanti's fault supporting a mean interevent time of of 1000 years. Pantosti et al. (2004) are estimated, for the same fault, a mean interevent time of 660-1200 years.

Using all the above data the mean interevent time (T_r) is calculated for each segment of the study area. In cases where only one or two events were reported for a particular fault segment, the interevent times are set equal to 500 years. Table 1 gives the calculated values of T_r for some faults of the study area.

• Duration of transient effect (t_α): Dieterich (1994) based on the constitutive formulation for rate of earthquake activity, derived from laboratory observations of rate– and state–dependent fault properties. A consequence of clustering statistics and time–dependent nucleation is that earthquake rates at all magnitudes undergo a strong transient amplification at the time of a step increase of stress, followed by $1/t$ decay to their background rate. In the present study, t_a, was set equal to 10% of the minimum interevent time. Thus, for the area of North Anatolian fault t_α=25 yr, considering a minimum return period of 250 years. For the same area a regional aftershock decay time for M≥6.7 earthquakes was found to be ~35 years by Parsons et al. (2000). A value of t_α=50 yr was set for the rest part of our study area due to the longer observed interevent times (~ 500 years). For the southern part of Corinth Gulf the t_α was set equal to 30 years and for the Ionian Sea equal to 10 years because at these areas the mean interevent times are smaller.

• Tectonic stressing rate ( ): This parameter is important for the calculation of T′ (eq. 6) and consequently the permanent probability P_c (eq. 7). Stressing rates are calculated in each fault segment from the yearly slip rate. For parts of North Anatolian Fault,   is found equal to 0.04-0.25bar/yr with a mean value 0.10 bar/yr. These values are in agreement with the ones from Stein et al. (1997), who estimated a value of 0.15bar/yr along most of the NAF system and from Parsons et al. (2000) who
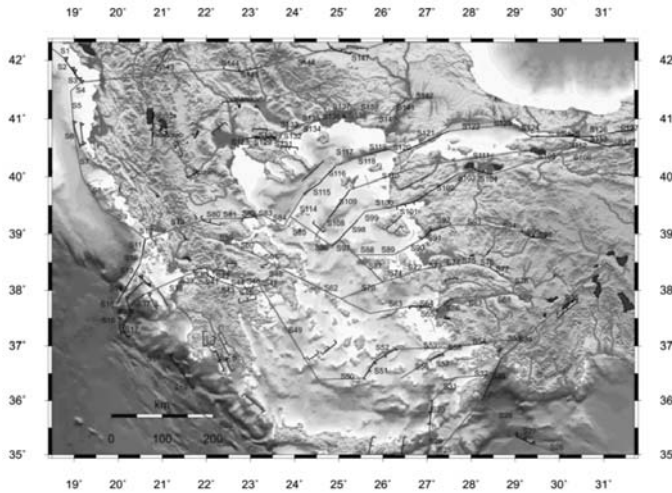
Fig. 1: Map of the main active structures of the study area (red color) along with the faults for which the coseismic changes were calculated (black colors). The faults that are associated with historical earthquakes of M≥6.5 are shown in blue. The code names of fault segments are shown next to each segment.

calculated =0.1bar/yr, and Parsons (2004) with values of in the range of 0.01-0.064bar/yr. For the remaining part of the study area the values of stressing rate are in the range of 0.003-0.25 bar/yr.

- Coulomb Stress Changes (ΔCFF): The ΔCFF value on each fault segment is achieved by extending the calculations of the accumulated static stress changes due to the coseismic slip of the modeled events up to 2009. Since uncertainties are involved in these estimations and because stress change is spatially variable, we consider three different values, i.e, the minimum, maximum and average calculated ΔCFF values, and consequently three different clock changes values as revealed from eq.6 and three values of permanent probability (eq. 7). The effect of the stress step in the probability estimates becomes more evident in the cases where the fault segment has recently failed (e.g Izmit, Duzce and Methoni faults) and where a fault segment is located along strike with a previously failed segment, resulting in the positive static stress changes on the first segments. In these cases the differences between the probability estimates before and after the stress step are significant and must be included in any assessment for the future seismic hazard.

- Probability calculations: We first calculate the probability using Poisson model (eq. 2) and Conditional probability model (eq. 4) using Δt=30years for all fault segments of the study area (S1-S148) and for some individual faults that are connected with historical strong (M≥6.5) events (fig. 1). The net probability (eq. 8) of events rupturing each fault segment combines both the permanent and transient effects of a stress step. Net probability is obtained first by computing the permanent effect of a stress change on the conditional probability using eq. (7). Then the equivalent background rate r_p for the permanent effect is obtained using eq. (10) to evaluate eq. (9) and eq. (8) for the net probability.

4. Results and Conclusions

The present study is an effort to interpret the occurrences of strong (M≥6.5) earthquakes in Greece and broader area and to evaluate the future seismic hazard incorporating Coulomb Stress changes (ΔCFF) to probability estimates. Generally different parameters, such as the duration of transient effect (t_α), the stressing rate and stress step (ΔCFF), were taken into account for probability calculations. The affect of the stress step becomes more evident in the cases in which the fault segment has

Table 1. Estimated 30 year probabilities larger than 0.10. The first column is the code name of each fault segment. The second column gives the recurrence time, T$_r$ and the third column gives the stressing rate of each segment in bars/yr. The fourth and fifth columns give the Poisson-ian and Conditional probabilities. The three next columns give the minimum, maxi-mum and average probability of occurrence for the next 30 years modified by the permanent effect of ΔCFF. The last three columns give the corresponding probabilities modified by both the permanent and transient effect of ΔCFF.

Segment Code Name	Tr (years)	$\dot{\tau}$ (bars/year)	Stressing Rate Poison	Cond. probability before the stress step Conditional	Cond. probability after the stress step (Permanent effect) Min P(30)	Max P(30)	Avg P(30)	Cond. probability after the stress step (Permanent + Transient effect) Min P(30)	Max P(30)	Avg P(30)
S11	82.5	0.0817	0.3049	0.4995	0.3074	0.4876	0.3745	0.2583	0.4843	0.3404
S13	85.7	0.1756	0.2954	0.6963	0.0031	0.9293	0.4172	0.0001	0.9505	0.3660
S20	124	0.0073	0.2149	0.4215	0.0000	1.0000	0.3953	0.0000	0.9997	0.3956
S22	500	0.0198	0.0582	0.1171	0.0001	0.7494	0.1329	0.0000	0.7789	0.1338
S43	113	0.0522	0.2332	0.4496	0.4410	0.5638	0.4773	0.4407	0.5663	0.4782
S44	145	0.0445	0.1869	0.2567	0.2499	0.2929	0.2617	0.2500	0.2922	0.2617
S67	246	0.0425	0.1148	0.1041	0.1000	0.2992	0.1123	0.0956	0.5282	0.1214
S69	500	0.0529	0.0582	0.0923	0.0931	0.0935	0.0934	0.0932	0.0938	0.0936
S100	137	0.0275	0.1967	0.3908	0.3878	0.9878	0.6311	0.3877	0.9778	0.6300
S103	1013	0.0197	0.0292	0.0218	0.1454	0.9472	0.3646	0.2530	0.9990	0.7162
S122	141	0.2583	0.1917	0.3815	0.3689	0.3733	0.3721	0.3691	0.3734	0.3722
S123	298	0.2041	0.0958	0.1979	0.0013	0.2989	0.1848	0.0009	0.3024	0.1844
S124	281	0.2147	0.1013	0.0756	0.0808	0.3347	0.1174	0.0850	0.6589	0.1597
Edessa	500	0.0075	0.0582	0.1236	0.1317	0.1414	0.1381	0.1319	0.1418	0.1385
Tetovo	500	0.0067	0.0582	0.1146	0.1279	0.1493	0.1384	0.1277	0.1487	0.1380
Eratini	399	0.0254	0.0724	0.0830	0.0254	0.0883	0.7489	0.2058	0.0909	0.9334
Messini	500	0.0076	0.0582	0.0217	0.0365	0.1394	0.0623	0.0631	0.5031	0.1625
Kalamata	500	0.0093	0.0582	0.0946	0.0093	0.1803	0.2570	0.2089	0.1989	0.2957

recently failed (e.g. Izmit segment, S125) and where a fault segment is located along strike with previously failed segment, resulting in the positive static stress changes on the first segments. In these cases different probability values were estimated before and after the stress step and these differences must be included in any assessment for the future seismic hazard. Moreover, the choice of tectonic stressing rate has a significant effect to the final probability results. The is related with the time, T′, and therefore it could be for example lead to smaller clock changes for a given stress change, and hence to smaller probability values. For this reason several values of have been used for each fault zone as already mentioned. The duration of the transient effect (t$_\alpha$) has been used to calculate both
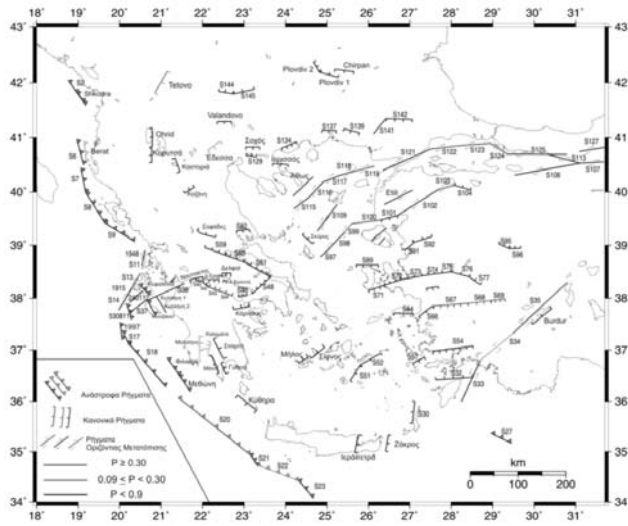
Fig. 2: Map of estimated time dependent probabilities for the occurrence of an earthquake with magnitude M≥6.5 for next 30 years (after 2009), in each fault segment of the study area. The values of probability and the corresponding color are depicted in the inset at the lower left corner of the map.

the Aσ factor and the net probability. For this calculation we were based on Dieterich (1994) and t_α was set ~ 10% of mean interevent time (T_r) for each fault segment. The detailed value of t_α for each area affect our results but this estimation cannot be analysed in the framework of this study.

In more detail, probability estimations are carried out for 148 fault segments (S1-S148) and for faults that are related with historical earthquakes of M≥6.5. Calculations are not performed for the fault segments where there is not information available for the occurrence of such events. Due to the large amounts of data the calculated parameters needed to estimate probabilities and the values of estimated time dependent probabilities are given in Table 1 only for some faults of the study area for which the value of the net, average, probability is considered greater than 0.10.

Fig. 2 shows the fault segments for which the time dependent probability is estimated for the occurrence of an earthquake with M≥6.5 for next 30 years after the studied date (2009). The color of each fault corresponds to the mean value of estimated probabilities after permanent and transient effect. For low probability values (P<0.09) the fault has blue color while green and red color indicate higher probability values (0.09 ≤ P < 0.30 and P≥0.30, respectively).

The first result in probability estimates is that for some of the segments the values that have been calculated from the renewal model based on the lognormal distribution are different from those values based on the Poisson model ranging between 5% and 35%. These results are in agreement with previous investigations, especially at Marmara and Izmit region (Stein et al., 1997; Parsons, 2004). The variation between the values occur due to the following reasons: For the conditional probabilities estimations, we use mean interevent time equal to 500 years for some fault segments, because reliable historical information was not available. In the cases where the Poissonian probabilities are larger than the conditional ones for some fault segments, the time elapsed since the last event of M≥6.5, is shorter than the estimated mean interevent time. In addition, for the same mean interevent time, the Poissonian probability model estimation, that treats earthquakes as occurring at random in time, is different from conditional probabilities model which takes into account the time passed from the last earthquake in a fault. Therefore, we consider that the results from time dependent probability estimation are more reliable than the Poissonian ones. Generally the uncertainties involved in

these estimates concern the mean interevent time and the corresponding standard deviation, the aftershock duration (t_α) and the value of $A\sigma$ (we calculate the $A\sigma$ value using eq. (11) considering that t_α is known from previous investigations).

The ΔCFF values, calculated according to the faulting type of each fault segment, are incorporated into the probability estimates, as the permanent stress effects and both the permanent and transient effects. For this purpose we consider minimum, maximum and average values of ΔCFF, as well as the minimum, maximum and average values of clock advance or delay (eq. 6). It is interesting to note that these values affect the estimated probabilities, by increasing them in comparison with Poissonian and increasing the conditional probability estimates when positive values of ΔCFF are found on the certain fault segment, or decreasing them in the cases of negative corresponding ΔCFF values. For example, in the Izmit fault segment, the ΔCFF effect decreases substantially the conditional probabilities (by a factor of 10^{-5}). The stress transfer between adjacent fault segments considerably influences the probability estimates. For certain fault segments the differences between Poissonian and conditional estimates before the stress step are significantly different than the ones incorporating the stress step, and worth to be mentioned for the future seismic hazard assessment. For example, for the fault segments along the north Marmara Sea (S122, S123 and S124) the Poissonian probabilities found equal to 0.19, 0.09 and 0.10, respectively, whereas the corresponding time dependent ones equal to 0.38, 0.18 and 0.16, respectively.

The opposite but also significant consequence of ΔCFF effect is observed for the Izmit (S125) and Duzce (S127) segments last ruptured in 1999, yielding a 30–year Poisson probability of 0.10 and 0.05, respectively, whereas the time–dependent probabilities on these segments are ~0%. The calculated probability value for the area of North Aegean Sea found equal to 0.63 for Edremit fault segment (S100) and 0.7 in north western Turkey (Yenise, S103). In the area of Ionian Sea the Lefkada (S11) and Kefalonia (S13) fault segments ruptured in 1940-1960 indicating low mean interevent times. The time dependent probability estimated 0.34 and 0.36 for S11 and S13 faults respectively. The ΔCFF effect resulted in high probability estimates for normal fault segments being along strike with previous ruptures, in the study area. Specifically for Aydin (S67) and Denizli (S69) fault segments in central western Turkey the mean probability value after permanent and transient effect is estimated 0.12 and 0.10 respectively whereas in the area of Corinth Gulf the calculated time dependent probabilities were 0.47 and 0.26 for the Eliki (S43) and Xylokstro (S44) fault segments, respectively. For fault segments with N-S direction such as Tetovo fault in the northern of the study area and in south Messini fault (Peloponnesus) the corresponding probabilities are equal to 0.13 and 0.16, respectively. For Edessa and Kalamata faults the probability estimated 0.23 and 0.14 respectively. These values are high for this area because two strong earthquakes occurred (1986, M=6.0, in Kalamata and 1990 M=6.0 in Edessa) but both of them are under 6.5 so we do not take them into account. The results from probability estimates for reverse faults indicate high values in Tenaro (S20) (0.40) and Elafonisos (S22) (0.13) fault segments respectively.

5. Acknowledgments

6. References

Ambraseys, N. N., 2002. The seismic activity of the Marmara Sea region over the last 2000 years. *Bulletin Seismological Society of America* 92, 1-18.

Ambraseys, N. N., and J. A. Jackson, 2000. Seismicity of Marmara (Turkey) since 1500. *Geophysical Journal International* 141, F1-F6.

Briole, P., Rigo, A. Lyon-Caen, H., Ruegg, J.C., Papazissi,K., Mitsakaki, C., Balodimou, A., Veis,G., Hatzfeld, D. and Deschamps, A., 2000. Active deformation of the Corinth rift, Greece: Results from repeated Global Positioning System surveys between 1990 and 1995. *Journal of Geophysical Research* 105, 605-625.

Chatzipetros, S., Kokkalas, S., Pavlides, S., and Koukouvelas, I., 2005. Palaeoseismic data and their implication for active deformation in Greece, Journal of Geodynamics, 40, 170-188A.

Collier, R. E., Pantosti, D., D'addezio, G., De Martini, P.M., Masana, E. and Sakellariou, D., 1998. Paleoseismicity of the 1981 Corinth earthquake fault: seismic contribution to extensional strain in central Greece and implications for seismic hazard. *Journal of Geophysical Research* 103, 30001-30019.

Cornell, C. A., Wu, S. C., Winterstein, S. R., Dieterich, J. H. and Simpson, R. W., 1968. Seismic hazard induced by mechanically interactive fault segments. *Bulletin Seismological Society of America* 83, 436–449.

Deng, J. and Sykes, L., 1997. Evolution of the stress field in Southern California and triggering of moderate size earthquakes: A 200–year perspective. *Journal of Geophysical Research* 102, 9859–9886.

Dieterich, J. H., 1994. A constitutive law for rate of earthquake production and its application to earthquake clustering. *Journal of Geophysical Research* 99, 2601–2618.

Dieterich, J. H. and Kilgore, B., 1996. Implications of fault constitutive properties for earthquake prediction. *Proceedings of the National Academy of Sciences U.S.A,* 93, 3787–3794.

Erikson, L., 1986. User's manual for DIS3D: A three–dimensional dislocation program with applications to faulting in the Earth. Master's Thesis, Stanford Univ., Stanford, Calif., pp. 167.

Hagiwara, Y., 1974. Probability of earthquake occurrence as obtained from a Weibull distribution analysis of crustal strain, *Tectonophysics*, 23, 313-318.

Harris, R. A., 1998. Introduction to special section: Stress triggers, stress shadows and implications for seismic hazard. *Journal of Geophysical Research* 103, 24,347-24,358.

Harris, R. and Simpson, R., 1998. Suppression of Large Earthquakes by Stress Shadows: A Comparison of Coulomb and Rate – and – State Failure. *Journal of Geophysical Research* 103, 24439–24451.

Hubert-Ferrari, A., Barka, A., Jacques, E., Nalbat, S.S., Meyer, B., Armijo, R., Tapponnier, P. and King, C. P. G., 2000. Seismic hazard in the Sea of Marmara following the 17 August 1999 earthquake. *Nature* 404, 269-272.

Klinger, Y., Sieh, K., Altunel, E., Akoglu, A., Barka, A., Dawson, T., Gonzalez, T., Meltzner, A. and Rockwell, T., 2003. Paleoseismic Evidence of Characteristic Slip on the Western Segment of the North Anatolian Fault, Turkey. *Bulletin of Seismological Society of America* 93, 2317–2332.

Koukouvelas, I.K., Stamatopoulos, L., Katsanopoulou, D. and Pavlides, S., 2001. A palaeoseismological and geoarchaeological investigation of the Eliki fault, Gulf of Corinth, Greece. *Journal of Structural Geology* 23, 531-543.

Kurcer, A., Chatzipetros, A., Tutkun, S. Z., Pavlides, S., Ates, O. and Valkaniotis, S., 2008. The Yenice–Gonen active fault (NW Turkey): Active tectonics and palaeoseismology. *Tectonophysics*, 453, 263–275.

Nishenko, S. P. and Buland R., 1987. A generic recurrence interval distribution for earthquake forecasting. *Bulletin Seismological Society of America* 77, 1382–1399.

Okada, Y., 1992. Internal deformation due to shear and tensile faults in a half space. *Bulletin of Seismo-*

logical Society of America 82, 1018-1040.

Palyvos, N., Pantosti, D., Zabci, C. and D' Addezio, G. 2007. Paleoseismological evidence of recent earthquakes on the 1967 Mudurnu valley earthquake segment of the North Anatolian Fault zone. *Bulletin Seismological Society of America* 97, 1646–1661.

Pantosti, D., De Martini, P.M., Papanastassiou, D., Lemeille, F., Palyvos, N. and Stavrakakis, G. 2004. Paleoseismological Trenching across the Atalanti Fault (Central Greece): Evidence for the Ancestors of the 1894. Earthquake during the Middle Age and Roman Times. *Bulletin Seismological Society of America* 94, 2, 531-549.

Pantosti, D., Pucci, S., Palyvos, N., De Martini, P. M., D' Addezio, G., Collins, P. E. F. and Zabci, C., 2008. Paleoearthquakes of the Düzce fault (North Anatolian Fault Zone): Insights for large surface faulting earthquake recurrence. *Journal of Geophysical Research* 113, doi:10.1029/2006JB004679.

Papazachos, B. C. and Papazachou, C., 2003. *The earthquakes of Greece*. Ziti publications, Thessaloniki, pp. 289.

Paradisopoulou, P. M., Papadimitriou, E. E., Karakostas, V. G., Taymaz, T., Kilas, A., and Yolsal, S., (2010). Seismic hazard evaluation in western Turkey as revealed by stress transfer and time-dependent probability calculations. *Pure and Applied Geophysics* doi: 10.1007/s00024-010-0085-1.

Parsons, T., 2004. Recalculated probability of M≥7 earthquakes beneath the Sea of Marmara, Turkey. *Journal of Geophysical Research* 109, doi:10.1029/2003JB002667.

Parsons, T., 2005. Significance of stress transfer in time–dependent earthquake probability calculations. *Journal of Geophysical Research* 110, doi: 10.1029/2004JB003190.

Parsons, T., Toda, S., Stein, R. S., Barka, A. and Dieterich, J. H. (2000). Heightened odds of large earthquakes near Istanbul: An interaction–based probability calculation, *Science*, 288, 661–665.

Pavlides S.B., Valkaniotis S., Ganas A., Keramydas D. and Sboras S., 2004. The Atalanti active fault: re-evaluation using new heological data. Bulletin of the Geological Society of Greece vol. XXXVI, *Proceedings of the 10th International Congress*, Thessaloniki, 1560-1567

Pondard, N., Armijo, R., King, G. C. P., Meyer, B. and Flerit, F., 2007. Fault interactions in the Sea of Marmara pull–apart (North Anatolian Fault): earthquake clustering and propagating earthquake sequences. *Geophysical Journal International* 171, 1185–1197.

Rockwell, T., Barka, A., Dawson, T., Akyuz, S. and Thorup, K., 2001. Paleoseismology of the Gazikoy–Saros segment of the North Anatolia fault, northwestern Turkey: Comparison of the historical and paleoseismic records, implications of regional seismic hazard and models of earthquake recurrence. *Journal of Seismology* 5, 433–448.

Scholz, C., 1990. *The mechanics of earthquakes and faulting*. Cambridge University Press, Cambridge, pp. 439.

Stein, R. S., 1999. The role of stress transfer in earthquake occurrence. *Nature* 402, 605-609.

Stein, R.S., Barka, A.A., and Dieterich, J.D., 1997. Progressive failure on the North Anatolian fault since 1939 by earthquake stress triggering. *Geophysical Journal International* 128, 594-604.

Toda, S., Stein, R. S., Reasenberg, P. A., and Yoshida, A., 1998. Stress transferred by the 1995 Mw=6.9 Kobe, Japan shock: Effect on aftershocks and future earthquake probabilities. *Journal of Geophysical Research* 124, 439-451.

Wessel, P., and Smith, W. H. F., 1998. New improved version of the Generic Mapping Tools Released. *EOS Trans. AGU* 79, 579.

Working Group on California Earthquake Probabilities (WGCEP), 1990. Probabilities of large earthquakes in the San Francisco Bay region. California, *U.S. Geol. Surv. Circ. 1053*, 51.

SPACE REGULARITY MANIFESTATION OF THE TEMPORAL VARIATION OF SEISMIC PARAMETERS: POSSIBILITY FOR THE STRONG SEISMIC ACTIVITY ASSESSMENT

Popandopoulos George[1] and Baskoutas I.[2]

[1] *Earthquake Planning and Protection Organization, Seismotect. Div., Xanthou32, 15451 Athens. gpapadopoulos@oasp.gr*

[2] *Geodynamic Institute, National Observatory of Athens, P.O. Box 20048 118 10 Athens, i.basko@.gein.noa.gr*

Abstract

In the present work the detailed analysis of the space-time variation, of the seismic energy released and b-value was performed, in order to study the space regularity manifestation of the temporal variation of seismic parameters, to test the reliability of the results and to compare the obtained temporal profiles in relation to the strong earthquake activity.

The study was carried out in the subduction zone along the western part of the Hellenic trench arc system. The earthquakes data, witch occurs in the five adjacent local areas in the period 1980 -2007 were used.

The reliability of the results is tested positively for "internal" dubiety, against independent seismic data sets from adjacent local areas, being in common the processing method, and the properties of seismic catalogue.

It was found that in the majority of the cases (23 of 32) the significant temporal variation changes, considered as anomalies, can be related to the preparation process of the strong earthquakes Ms>5.7, acting as intermediate term precursors. Based on these findings the quality index of the successful intermediate term earthquake predictions reach up to 71.9%.

It is observed that the temporal variation of the seismic energy released anomalies were time shifted in respect to the central areas, toward to N-NE and S-SE direction. Moreover it is found that the strong earthquakes occurrence also shows immigration, in respect to the central areas, along the concatenation of the adjacent local areas. These two observations may reveal the formation of a tectonic wave, in the broader area south of Zakynthos Island, Its velocity was estimated to be as 100 to 150 km/year.

Key words: seismicity parameters, temporal variation analysis, b-value, seismic energy, Greece.

1. Introduction

Seismicity parameters and their time and space analysis is a very common approach (Habermann and Wyss, 1984; Papadopoulos and Voidomatis, 1987; Bowman et al., 1998; Bowman and King, 2001; Bowman and Sammis, 2004; Papazachos, 2000; Wiemer, 2001; Papadopoulos et al., 2004), to investigate geodynamic regime in seismic active regions. Significant changes of the seismicity rate have been reported in several areas of the world (Wiemer and Wyss, 2002; Enescu and Ito, 2003;

Baskoutas et al., 2007). In many cases temporal changes of the seismicity parameters, can be correlated to strong earthquake occurrence and they may consider as indicators of fore-coming strong earthquakes (Wyss and Baer, 1981; Gao and Gao, 2002; Zavyalov, 2002, Enescu and Ito, 2003, Monterosso, 2003; Papadopoulos and Baskoutas, 2006).

In this work, the temporal variation of the seismic parameters was examined, in order to reveal their space regularity in the western part of the Hellenic trench Arc system. This region is characterized for its high seismic activity in the Greek territory and the frequent occurrence of large earthquakes also. Moreover the reliability of the methodology, using independent sets of seismic data is tested. The presence of the subduction front between African and Euro-Asiatic tectonic plates also stimulates further interest to interpret the obtained results. Finally, given that the temporal changes of the seismicity parameters can be correlated to strong earthquake occurrence, here it is also examined the possibility to assess the results for intermediate term earthquake predictions in the area.

2. Method and analysis

The quantity logE2/3 and the parameter b-value have been obtained by the means of the Fast Big Earthquakes Estimation (hereafter FastBEE) algorithm and the respective analysis tool, develop and proposed by Papadopoulos and Baskoutas, (2003, 2009). In the FastBEE algorithm b-value were obtained by the maximum likelihood estimation method (Gusev, 1976; Van Wormer et al., 1976) using relationship proposed by Zavyalov and Sobolev, 1980, as follow:

where N_Σ is the number of earthquakes in the examined time window; N is the number of earthquakes in the magnitude range $M_{min}+n\Delta M$; n=0,1,2,3,4 … is the weighting factor, ΔM is the unit of the magnitude increment equal to 0.20 and σ_b is the standard deviation of b-value determination.

Standard errors of b-value were calculated by the relationship:

The seismic energy released, in the form $logE^{2/3}$, is obtained by the means of the relationship:

where energy E is derived using the relationship, $E=10^{1.5Ms+4.7}$, proposed by Papazachos and Papazachos (2000a) for Greek territory. In these estimates standard error is calculated by relationship: $\sigma_{logE}=0,4343/\sigma_E$

The time series of the seismic parameters were calculated applying a smoothing time window of 13 months, with one-month step. The current average value of parameters was assigned to the end of the smoothing window. Then obtained time series were then filtered with a triangular form filter. Length of the applied time window is defined as 13 months. The applied filter allows passing the periods equal or greater of the half filter width (Jenkins and Watts, 1968). Definition of the filter length
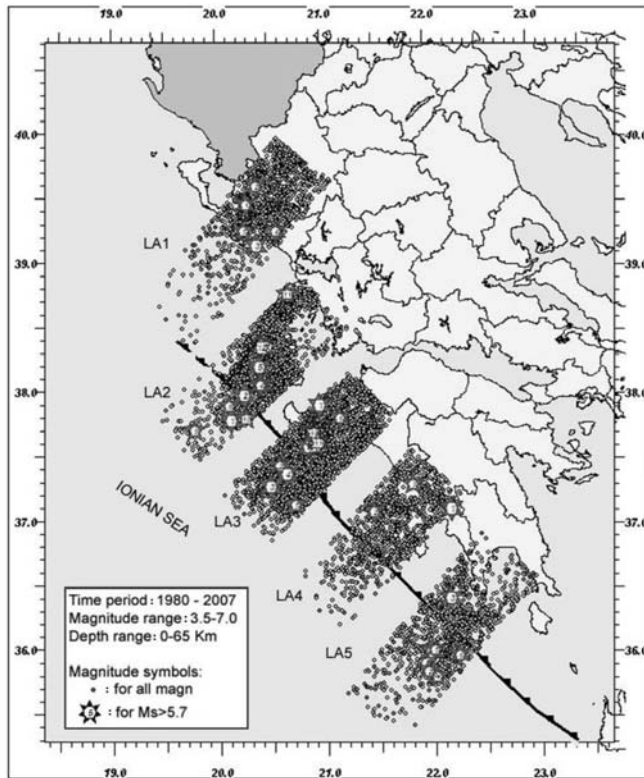
Fig. 1: Seismic epicentres map of the individual local areas. Size of the events is unique for the better spatial representation of the seismicity.

defined as long as 13 months makes the fluctuations with wave periods more than 6 months more evident. Filtered time series are displayed, as bold curves, superposed to the smoothed thinner one. Additionally chronologically numbered arrows have also marked the strong earthquakes origin time, within the examined time period, perpendicular to the time axis (see Figs 2 and 3).

3. Data

To reveal the spatial regularity of the seismic parameters temporal variation and to test the objectivity of the FastBEE analysis tool, six adjacent local areas (hereafter LA_1 ... LA_5) were defined. Their size is about 200x60 km each, with the major axis drafted perpendicular to the subduction front of the western part of the Hellenic Trench Arc system. Figure 1, shows the seismic epicenters maps of all 5 local zones. This region was chosen because for its high seismic activity, which provides enough data for the statistical assessment of the results and because of its geodynamic characteristics. The seismic data from each local area constitute "statistical independent samples", in order to test the reliability of the methodology.

The seismic data were taken from the catalog of the Geodynamic Institute of National Observatory of Athens in the period 1980 to 2007. In this period the catalogue is quasi uniform for magnitude of completeness 3.5 after 1990 and 4.0 in the period 1980 to 1990 at the local areas LA_1 in the northern part and LA_4 and LA_5, at the southern part. Table 1 shows the total number of earthquakes, for each local area, with Ms > 3.5, which were used in the present study. Table 2 shows the list of all strong earthquakes with M > 5.7 which occurred in each local area and displayed in the respective time series output plots.
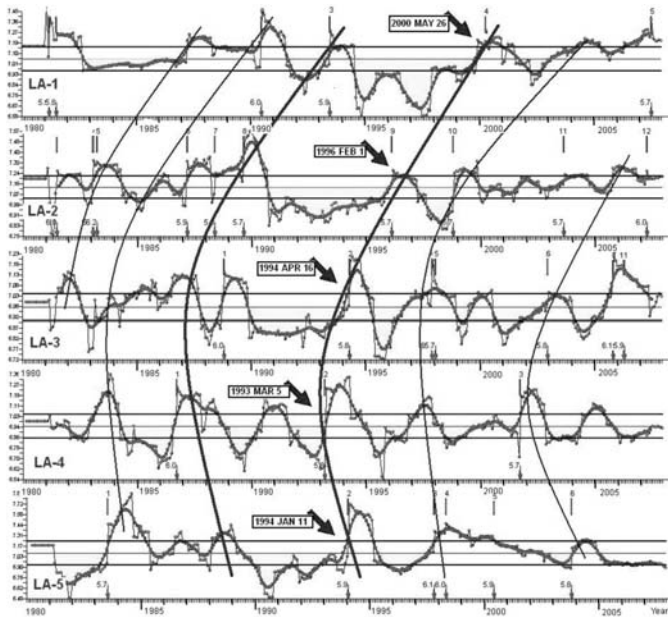
Fig. 2: Temporal variation plots of seismic energy released in adjacent seismogenic local areas in the Ionian Sea region. Solid and dashed lines connect the picks of the anomalies in the seismic energy time series (discussed in detailed in the text). Numbered arrows perpendicular to the time axis shows the origin time of strong earthquakes in each local area.
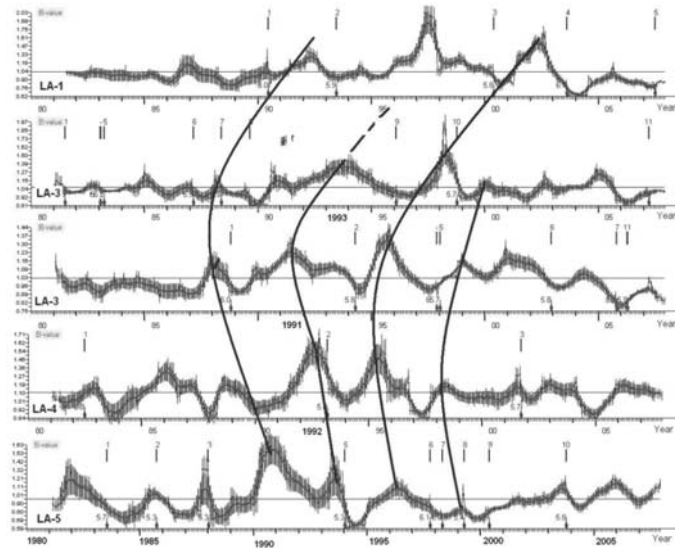
Fig. 3: Temporal variation plots of b-value obtained in adjacent seismogenic areas in the western part of the Hellenic arc. Thinner numbered arrows perpendicular to the time axis shows the origin time of strong earthquakes in each local area.

Table 1. Number of earthquakes used in this study for each local area.

Local Areas	Date Number of Earthquakes
LA_1	1627
LA_2	2731
LA_3	4707
LA_4	1195
LA_5	1954

Table 2. List of the strong earthquakes at each local area.

	Date	Or. Time	Lat	Lon	Depth	Magn
LA_1	1981 MAR 10	15 16 18.0	39.30	20.80	0	5.8
	1990 JUN 16	02 16 20.4	39.13	20.38	38	6.0
	1993 JUN 13	23 26 40.0	39.25	20.57	5	5.9
*	**2000 MAY 26**	**01 28 22.0**	**38.91**	**20.58**	**5**	**5.8**
	2007 JUN 29	18 09 11.2	39.25	20.26	19	5.7
LA_2	1981 JUN 24	18 41 26.0	37.80	20.00	0	5.7
	1981 JUN 28	17 20 21.0	37.90	20.10	0	6.0
	1983 JAN 17	12 41 30.9	37.97	20.25	9	6.7
	1983 JAN 19	00 02 15.5	38.05	20.41	6	6.0
	1983 JAN 31	15 27 .6	38.05	20.41	2	5.8
	1983 MAR 23	23 51 7.6	38.19	20.40	10	6.2
	1987 FEB 27	23 34 54.1	38.37	20.42	1	5.9
	1988 MAY 18	05 17 42.7	38.35	20.47	1	5.8
	1989 AUG 24	02 13 13.4	37.89	20.11	1	5.7
*	**1996 FEB 1**	**17 57 56.5**	**37.72**	**19.85**	**1**	**5.7**
	1998 OCT 8	03 50 17.1	37.79	20.27	5	5.7
	2007 MAR 25	13 57 58.2	38.34	20.42	15	6.0
LA_3	1988 OCT 16	12 34 5.4	37.90	20.96	4	6.0
*	**1994 APR 16**	**23 09 36.4**	**37.43**	**20.58**	**30**	**5.8**
	1997 NOV 18	13 07 36.9	37.26	20.49	5	6.6
	1997 NOV 18	13 13 48.3	37.36	20.65	5	6.1
	1998 JAN 10	19 21 54.3	37.12	20.73	5	5.7
	2002 DEC 2	04 58 56.4	37.80	21.15	17	5.8
	2005 OCT 18	15 25 59.5	37.58	20.86	22	6.1
	2006 APR 4	22 05 3.3	37.58	20.93	18	5.7
	2006 APR 11	00 02 41.5	37.64	20.92	18	5.7
	2006 APR 11	17 29 28.4	37.68	20.91	18	5.9
	2006 APR 12	16 52 1.2	37.61	20.95	19	5.9
LA_4	1986 SEP 13	17 24 33.8	37.10	22.19	1	6.0
	1993 MAR 5	**06 55 6.4**	**37.07**	**21.46**	**1**	**5.8**
	2001 SEP 16	02 00 48.5	37.29	21.83	5	5.7
LA_5	1983 JUL 14	02 54 21.6	35.80	22.03	18	5.7
*	**1994 JAN 11**	**07 22 53.3**	**35.84**	**21.95**	**40**	**5.9**
	1997 OCT 13	13 39 39.2	36.41	22.18	6	6.1
	1998 APR 29	03 30 37.1	35.99	21.98	5	6.0
	2000 MAY 24	05 40 37.5	36.00	22.01	5	5.9
	2003 OCT 17	12 57 8.7	35.96	22.25	37	5.8

*Bold typed lines shows the sequence of the events correlated with the main seismic energy anomalies reported as an example in the main text. In Fig. 2 they appear as solid arrows, which indicate their origin time.

4. Results

Figures 2 and 3, shows the time series of the temporal variation plots of seismic energy released and b-value plots respectively, in adjacent seismogenic local areas in the Ionian Sea region.

In both figures the origin time of the main strong earthquakes Ms>5.7 are shown with red arrows vertical to the time axis at each local areas. Solid curved dashed lines connect the picks of the sharp changes of the seismic energy and b-value time series respectively. In figure 2 the labelled (with the date of earthquake origin time) oblique arrows shows the spatio temporal shifting of sharp changes of the along the sequence of all local areas.

Table 3 shows the catalogue seismic parameters of all 32 strong earthquakes in the examined time period at each local areas. In both figures same phases of the temporal variation estimates fluctuations, can be considered as anomalies in respect to their relative mean values, (line parallel to time axis). Specifically, the parameter $\log(E^{2/3})$ of the seismic energy released passes a relative minimum (valley shape curve), before the strong earthquake occurrence and then increases as seismic activity develops further to the aftershock activity. In the opposite, b-value shows a clear decreasing phase prior to the occurrence of a strong earthquake, after having past a relative maximum. It is observed, that in the majority of the cases, there is a correlation between temporal variation anomalies with strong earthquakes of at each local area. In some other case instead of singular strong earthquake, this correlation is related to a cluster of strong earthquakes. An example of this case is the strong seismic activity occurred in the period 4 to 12 of April of 2006, at the local area 3 (LA_3 in Figure 2). Here is to note that the duration of anomalies observed before the strong earthquakes is about 1 to 4 years. Their observed size and duration seems to be not proportional the magnitude of the associated strong earthquake. Detail analysis of this relation is beyond to the scope of this work and is going to examine in future study.

To evaluate the correlation of the seismic energy released anomalies with the strong earthquakes, all the cases from all local areas were examined, by the means of the prediction quality index estimation proposed by Kasahara (1981):

$$p=m/n$$

Where p is the probability of occurrence of the strong earthquake related to an anomaly presence, m is the number of successful prediction and n is the total number of the strong earthquakes examined. Table 3 shows the number of the strong earthquakes, the respective successful correlation with seismic energy anomalies and the failed cases at each local area. There were six cases of anomalies, which are not accompanied by an earthquake and 8 cases of strong earthquakes, which were uncorrelated.

Table 3. Number of the successful and failed cases in each local area

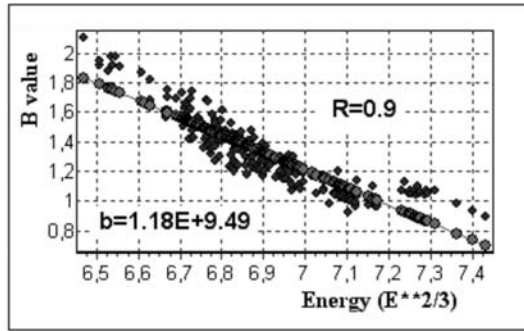| Local area	Number of EQs	Successful cases	EQ with no anomaly	Anomaly With no EQ
LA_1	5	4	1	1
LA_2	9	6	2	1
LA_3	8	5	2	1
LA_4	3	3	-	3
LA_5	7	5	3	0
Sum	32	23	8	6

Fig. 4: Seismic parameters b-value and log $E^{2/3}$ temporal variation correlation, for the local area 4.

It was found that in the majority of the cases, 23 of 32 the correlation is strong. Thus temporal variation anomalies of the seismic energy released can be considered as intermediate term earthquake precursors. The quality index of the successful cases is then calculated as:

$$P = 23*100/32 = 71.9\%$$

Comparison of the parameters log $E^{2/3}$ and b-value curves (Fig. 2 and 3) shows antiphase of their temporary variations fluctuations, namely the temporary decrease phases of parameter log $E^{2/3}$ correspond to an increase one of the b-value. The correlation analysis between time series of these parameters shows a correlation coefficient of 0,9. Fig. 4 shows, as an example, the correlation of parameters log $E^{2/3}$ and b-value, for the local area 4. The observed strong correlation factor between two independent parameters proves also the objectivity of the methodology to obtain seismic parameters temporal variation.

The careful visual inspection of Fig. 2 shows that the seismic energy released reveal anomalies (fulfilled with yellow colour) can be correlated, across the sequence of the individual graphs. The key point to follow these correlations come from the observation of the similar shape and size anomalies formed first at LA_2 and LA_3 in the period 1990 to 1995. Almost similar shape and size anomalies, except LA_4, can be distinguished to the rest areas, LA1 toward to north and LA4, LA5 to south. This sequence of correlated anomalies is denoted by the two thicker blue solid lines of Fig. 2.

Continuing the inspection of Fig. 2, next to the major sequence of the anomalies during 1990-1995, consecutive minor size anomalies at neighbour local areas can be identified. Albeit the smaller size of the anomalies and the weaker correlation, this last still can be evident. Moreover an immigration of the strong earthquakes can be observed, starting from the central areas to the adjacent local areas, toward NE and SE, which also can be and correlated. For instance, in figure 2, the case of the stronger correlation of the Ms = 5.8 strong earthquake of April 16, 1994 occurred in LA_3, can be associated with the anomaly, starting in 1990. Similar anomalies shifting and strong earthquakes immigration can be observed to the NE direction, associated to the 1993, March 5, in LA4 and 1994 January 11, in LA5, earthquakes respectively. Again similar anomalies associated to the Ms=5.7, 1996, February 1, in LA2 and to the Ms=5.8, 2000, May 26 in the LA1 earthquakes, are spreading toward SE direction.

On the basis of previously mentioned observations it is possible to talk about a propagation of the anomalies, which shows a clear time shifting and space migration in either side of the middle local areas, toward to north and south. This observation is clearer for the seismic energy plots than those of b-value. From this observation we may conclude that strong earthquakes occurrence can be ex-

pected with 1 or 2 years delay, in the neighbour adjacent local areas, next to LA_4 (being a reference point), toward north and south. Weak correlation on temporal variation of b-value anomalies (figure 3) may be related to the seismic catalogue incompleteness, which seems to influence the quality of the b-value results, at least at the northern and southern local area.

5. Discussion-Conclusions

In this work were examined the space regularity of the temporal variation of the seismicity focusing on seismic energy released and the b-value, under the assumption that its temporal changes are closely related to the seismic activity of the observed region. Moreover the reliability of the analysis method was tested, since "internal" estimates objectivity of any procedure is a source of dubiety, (Steyerberg et al., 2003)

In this work the reliability of the FastBEE tool analysis to compute seismicity parameters temporal variation was tested, taking seismic data sets from adjacent local areas, so that they can considered "statistical independent samples".Thus obtained temporal variation estimates, being in common the processing method and definition of all analysis parameters as well as the earthquake catalogue properties, was tested positively.

It is observed that in many cases, sharp fluctuation anomalies, which can be considered as anomalies, can be correlated with strong earthquakes seismic activity. Precisely their origin time lies within the increasing phase of seismic energy and the decreasing one of b-value, after have passed a relative minimum and maximum respectively. Thus temporal variation anomalies of the seismic energy released can be considered as intermediate term earthquake precursors. Nevertheless, the size and the duration of the anomalies observed seem to be not proportional to the magnitude of the associated strong earthquake. Some times despite of the anomaly presence there is no earthquake but the anomaly can be correlated to a cluster of smaller size earthquakes. In few other cases there are earthquakes without the presence of an anomaly. The quantitative assessment of the successful intermediate term earthquake predictions, within the limits of the examined local areas and time period was found to be approximately 72%.

It is found a clear temporal shifting of the temporal variation fluctuations toward to N-NE and S-SE directions. At the same time it is also observed a spatio-temporal immigration of the strong earthquakes toward to northern and southern regions. In both cases the shifting is considered in respect to the central local areas 3 and 4.

From the combination of these two observations and taking in to account the geodynamic regime in he region, we may assume the formation of a tectonic wave in the broader area south of Zakynthos Island, which propagates toward to E-NE and E-SE. Knowing the distances of the geometrical centres of consecutive local areas and the mean time sifting of the energy anomalies, then we can infer that the propagation velocity of the detected "tectonic wave" can be estimated to be as 100- 150 km/yr.

One possible hypothesis of the formation of the observed "tectonic" wave can be based on the geodynamic regime dominated the examined region. Entire region is characterized by the presence of the subduction zone as a result of the convergence between Eurasian and African tectonic plates. It is possible to assume that the presence of the constant regional tectonic stress acting along the western part of Greek arc system, cause the rock breaking and released first the energy in the central areas LA_3 and LA_4 and then propagates further to southern and to northern directions. One explanation, why this effect take place in these regions, may be the smaller interior rock friction in this

areas, in respect to the adjacent one. According to the findings of this work local areas LA_3 and LA_4 may be a key point of the collision between the two lithospheric plates, in the WS part of the Greek arc system. Certainly, such plausible hypothesis however it explains the observed shifting of anomalies of the seismic parameters temporary variations and need further investigation.

As a conclusion can state that the reliability of the analysis to obtained temporal variation of the seismicity was tested positively. The study of its space regularity, revealed the presence of a "tectonic" wave. The high probability of successful intermediate term earthquake prediction was also proved. We hope that the FastBEE algorithm will be useful for the study and continuous monitoring of the seismicity temporal variation. It is also believed that these results can add information and contribute in the seismic hazard assessment in highly seismogenic regions.

6. References

Baskoutas I. Papadopoulos G. A. Karakostas V. and Papadimitriou E. 2007. Recent 2005-2006 strong seismic activity in Greece under the aspect of seismicity parameters temporal variation. Bulletin of Geological Society of Greece. XXX/3, 1055-1062p.

Baskoutas I. Papadopoulos George and G. Panopoulou, 2004. Long temporal variation of seismic parameter for seismic pattern identification in Greece.10th International Congress of GSG. Thessaloniki, April 2004

Bowman, D. D., and G. C. P. King (2001), Accelerating seismicity and stress accumulation before large earthquakes, *Geophys. Res. Lett.*, 28, 4039-4042.

Bowman, D. D., Ouillon, G., Sammis, C. G., Sornette, A., and Sornette, D. (1998). "An observational test of the critical earthquake concept". J. Geophys. Res., 103, pp 24359-24372.

Bowman, D., and C. G. Sammis (2004), Intermittent critical and the Gutenmberg-Richter distribution, Pure Appl. Geophys., 161. 1945-1956.

Earthquake catalogue. Geodynamic Institute of National Observatiry of Athens. (www.gei.noa.gr)

Enescu B. and Ito K. 2003. Values of b and p: their Variations and Relation to Physical Processes for Earthquakes in Japan. Annuals of Disas. Prev. Res. Inst., Kyoto Univ., No.46 B.

Gao A. and Gao S. S. 2002. Temporal variation of seismic b-values beneath NE Japan island arc. Geoph. Res. Letters, 29, 9.

Gusev A. A. 1976. Indicator earthquakes and prediction. In Seismicity and Deep Structure of Siberia and Far East, Nauka, Novosibirsk, 1976 (in Russian), 241 247.

Habermann R. E. and Wyss M. 1984. Background Seismicity Rates and Precursory Seismic Quiescence: Imperial Valley, California, Bull. Seismol. Soc. Am. 74, 1743-1755p

Jenkins, G. M and Watts D. G. 1968. Spectral Analysis and its Applications (Holden–Day Publishing Co., New York.

Kasahara K. Earthquake mechanics. Canbridge earth sciences series . Univ. of Tokyo 1981

Monterroso Juarez, D. A. 2003. Statistical Seismology Studies in Central America, b-value, seismic hazard and seismic quiescence, Comprehensive Summaries of Uppsala Dissertations from the Faculty of Science and Technology, Acta Universitalis Upsaliensis, 897, 27 pp. Uppsala, ISBN 91-554-5761-4.

Papadopoulos George and Baskoutas I. 2006. Prognostic character of FastBEE analysis for seismic hazard assessment in Greece. 2nd International Workshop on Earthquake Prediction, Rion Patras June 26, 2006.

Papadopoulos George and Baskoutas I. 2009. New tool for the temporal variation analysis of seismic parameters. Nat. Hazards Earth Syst. Sci., 9, 859-864. (www.nat-hazards-earth-syst-sci.net/9/859/2009\

Papadopoulos George, I. Baskoutas and G. Stavrakakis, 2003. Tools for the Fast Estimation of Expected Big Earthquake in predefined seismic prone areas. 1th International Workshop on Earthquake Prediction. Athens, November 2003.

Papadopoulos Geras. and Voidomatis Ph. 1987. Evidence of periodic seismicity in the inner Aegean seismic area. Pageoph 125 4. 613-628p.

Papazachos C. B. and Papazachos B. C. 2000. Accelerated preshock deformation of broad regions in the Aegean area. Pure and Appl. Geophys. 157, 163-168p.

Steyerberg E. W, Bleeker S. E. Moll H. A. Grobbee D. E. and. Moons K. G. 2003. Internal and external validation of predictive models: a simulation study of bias and precision in small samples. J. Clin. Epid. 56(5) 441-448p.

Van Wormer J. D. Gedney L. D. Davies J. N. Condal N. 1976. Vp/Vs and b-values: a test of the dilatancy model for earthquakes precursors. Geophys. Res. Lett. 2, 11, pp.514-516.

Wiemer, S., 2001. A software package to analyze seismicity: ZMAP. Seismological Research Letters 72, 373-382.

Wiemer S. 7 Wyss M. 2002. Spatial and temporal variability of the b-value in seismogenic volumes: An overview, Advances in Geophysics, 45, 259-302.

Wyss M. and Baer M (1981). Seismic quiescence in the western Hellenic arc may foreshadow large earthquakes. Nature, 289: 785-787p.

Zavialov A. D. and Sobolev G. A. 1980. Some regularities of seismic regime and earthquake prediction. Proc. 17th Gen. Assembly of ESC. Budapest. 65-69.

Zavyalov A. D. 2002. Testing the MEE prediction algorithm in various seismically active regions in the 1985-2000 period: results and analysis. // Izvestiya. Physics of the solid Earth, 38, JVs 4 262-275p.

INCORPORATING DIFFERENT SOURCE RUPTURE CHARACTERISTICS INTO SIMULATIONS OF STRONG GROUND MOTION FROM THE 1867, M7.0 EARTHQUAKE ON THE ISLAND OF LESVOS (NE AEGEAN SEA, GREECE)

Roumelioti Z.[1] and Kiratzi A.[2]

[1] *Archaeologikou Mouseiou 46, 54641 Thessaloniki, Greece, zroum@auth.gr*

[2] *Department of Geophysics, Aristotle University of Thessaloniki, P.O. Box 352-1 Thessaloniki, Greece, Kiratzi@geo.auth.gr*

Abstract

We apply the stochastic method for finite-faults (Beresnev and Atkinson, 1997, 1998) to simulate strong ground motion acceleration from the 1867 earthquake that devastated the Island of Lesvos in NE Aegean Sea. Recent geological data are taken into account to construct realistic models of the earthquake source, while a first-order approximation of the site effect variation throughout the entire island of Lesvos is achieved following an empirical approach suggested by Wald and Allen (2007). We test several source models including different segments of the Agia Paraskevi fault, which is most probably the seismogenic fault of the 1867 earthquake. Stronger ground motion is predicted in the central part of the island, i.e. around the assumed seismogenic structure. A significant site effect is evident along the eastern coast of Lesvos, where the capital of Mytilene lies, strongly hit by the 1867 earthquake, and around the gulfs of Kalloni and Geras in the south and southeast parts of the island. Synthetic peak ground acceleration values are converted to macroseismic intensities through an empirical relation and discussed in comparison with available reports on the macroseismic effects of the 1867 earthquake.

Key words: strong ground motion, Lesvos, simulation.

1. Introduction

A recent approach to study historical earthquakes is based on modelling the available macro-seismic data by simulating the seismic wave field (e.g. Zollo et al., 1999; Emolo et al., 2004). To do so, one has to start from one or more source models available in the literature, compute synthetic time histories of strong ground motion, extract appropriate peak values, usually of engineering interest, convert them to intensities through empirical relations and discuss the results in terms of differences between synthetic data and observations. The ultimate goal is to better understand destructive historical earthquakes and thus to improve the ability to predict scenarios that will help planners and decision makers to prepare for the next event.

In the present work we adopt the aforementioned approach to study the most destructive event in the known earthquake history of the Island of Lesvos in North Aegean Sea, the M7.0 (Papazachos and Papazachou, 2003) earthquake of March 1867.

2. The 1867 earthquake

The event or rather a sequence of at least four strong events (most probably one foreshock, the main-shock and two strong aftershocks), spaced closely in time, occurred on the afternoon (6 p.m. local time) of March 7, 1867. It caused severe shaking of the entire Island of Lesvos and was felt as far away as in central Greece, Çanakalle and Izmir in western Turkey. Most scientists place the epi-center of the earthquake somewhere in the central part of Lesvos, where the maximum macroseis-mic intensity values were reported (IX-X in Kloumidados village which was later named as Napi – Fig. 1; Kampouris, 1978; Ambraseys and Finkel, 1995; Papazachos and Papazachou, 2003).

Although its dramatic impact established the 1867 earthquake as a turning point in the history of the Island of Lesvos accurate records on the fatalities and damage it caused are absent from official archives (Kampouris, 1978 and references therein). We do know that hundreds of people were killed in Mytilene, the capital of the island, in villages in the central part of the island and in villages around the Gulf of Geras, to the S-SW of Mytilene. The exact number of fatalities ranges from about 600 to more than 1000, while the corresponding numbers for injured people range from few hundreds to more than 2000. Most villages, especially at the central and eastern parts of Lesvos were either completely or partly destroyed.

Even back in the time of the 1867 earthquake scientists related the distribution of damage on Lesvos to the variability of the surface geology, hence the site effects. According to a geology expert who was sent to Lesvos as a delegate of the French government (Kampouris, 1978), the impact of the earthquake was dramatic in the central part of the island which is covered by volcanic rocks, lighter in the eastern part of the island where schist and marble dominate the surface geology and almost inexistent in the SE part of Lesvos which is covered by ophiolites (mountainous area between Polich-nito and Agiasos in Fig. 1). Great damage was also observed in villages around the gulfs of Geras and Kalloni, which were situated on recent loose deposits. Local scientists also note (Kampouris, 1978) that the dramatic consequences of the earthquake within the capital of the island, Mytilene, were due to the fact that the central market (where most severe damage was observed) was sited on the ruins of the ancient city of Evripos as well as to the very poor quality of the structures.

Most catastrophic historical earthquakes on the island of Lesvos, as well as the 1867 event, have been related to the Agia Paraskevi – Kalloni fault (Papazachos and Papazachou, 2003), a NNE-SSW trend-ing right-lateral strike-slip structure which cuts across the island. This structure consists nowadays the predominant tectonic feature on Lesvos. Its segments on the island's surface and its probable contin-uation within the Gulf of Kalloni are shown in Figure 1 (as suggested by Pavlides et al., 2008).

3. Simulation of Strong Ground Motion

3.1 Method

Strong ground motions were simulated using the FINSIM code of Beresnev and Atkinson (1998). This code implements the stochastic strong ground motion simulation technique for finite earth-quake sources (Beresnev and Atkinson, 1997, 1998), which is based on the pioneering work of Boore (1983). Detailed description of the method is given in the aforementioned references.

3.2 Model

The applied technique requires modeling of the three fundamental effects that shape strong ground motion: the source, the attenuation along the propagation path of the seismic waves and the local site
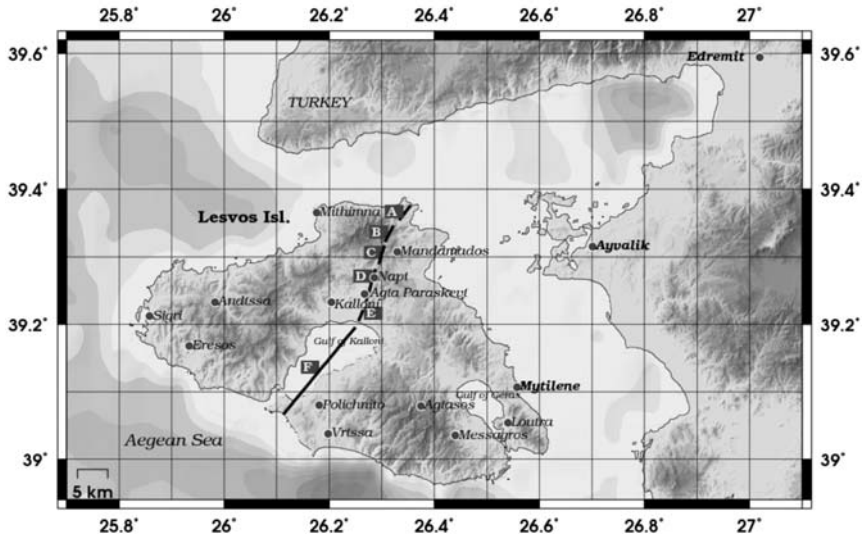
Fig. 1: Segments of the Agia Paraskevi – Kalloni fault as suggested by Pavlides et al. (2008).

conditions at the site of interest (observation/simulation points). Basic modeling parameters for each one of these effects are described in the following.

Propagation Path: Parameterization of the propagation path includes empirical description of the geometric attenuation and the anelastic attenuation of the seismic waves. For the geometric attenuation we applied a geometric spreading operator of $1/R$, where R is the distance from the seismic source, while the anelastic attenuation was described through a frequency-dependent quality factor, $Q(f)=100f^{0.8}$, applicable to the broader Aegean area (Hatzidimitriou, 1993, 1995).

Near-surface attenuation of the seismic waves was modeled using the kappa, $\varkappa$, operator of Anderson and Hough (1984) and diminishing the simulated spectra by $\exp(-\pi \varkappa f)$. Simulations at all sites of interest were performed assuming rock site conditions at the ground surface. The value for the kappa operator for rock adopted herein is the one proposed by Margaris and Boore (1998).

Site Effects: In the present work, which aims to produce a picture of the distribution of strong ground motion throughout the entire Island of Lesvos, we do not include detailed information on the site effect variation. To our knowledge, such information is not available. However, we attempt a first-order incorporation of the site effect in our final strong ground motion parameters distribution maps following an empirical approach suggested by Wald and Allen (2007). In the aforementioned study it is shown that there is correlation between the slope of the topography of a region and the V_{S30} (average shear-wave velocity at the top 30 meters of the soil column) values, which are often used to characterize the site effect. Wald and Allen (2007) proposed a global database of topographic-slope based V_{S30} which can be used to derive first-order site-condition maps when geotechnical site-specific data are insufficient or inexistent. Part of the original V_{S30} database, which covers the area of interest in the present study, was re-sampled using the spatial interval of the strong motion simulations grid (0.01°) and each grid point was assigned a V_{S30} value. Based on this value and the amplitude of the peak ground acceleration in the synthetic accelerogram at the corresponding grid point we selected an appropriate empirical amplification factor for the PGA following the suggestion of Borcherdt (1994).

<u>Source</u>: Modeling of the 1867 earthquake source was primarily based on the available neotectonic information and geological mapping of the Agia Paraskevi - Kalloni structure. The segments of the fault, as have been recently described in Pavlides et al. (2008) are shown in Figure 1. Within the frame of the present work we tested several rupture scenarios by combining different mapped segments and several locations of the rupture initiation point on each fault model surface. Due to space limitations we cannot show results from all tested cases. However, we summarize in the following section our basic conclusions from the comparative examination of resulting PGA distributions and present our preferred scenario. The last one involves surface rupture along segments E, D, C and B (Figure 1) i.e. a total length of approximately 16.5 km (the surface projection of the fault model is mapped in Figure 2). The documented length of the surface expression of the 1867 earthquake is 3-7 km although it is likely that it continues offshore (Pavlides et al., 2000). In any case, we believe that our scenario surface rupture length surpasses that of the 1867 event. Based on this length and appropriate empirical relations (Wells and Coppersmith, 1994; Pavlides and Caputo, 2004) the moment magnitude of the scenario event is M 6.5-6.6.

Although we do not know the rupture propagation characteristics of the studied event it is possible to place the rupture initiation point on the model surface following rules that are based on the international seismological experience. Regarding the depth of the hypocenter (assumed to coincide with the rupture initiation point in FINSIM) we know that most large magnitude strike-slip earthquakes nucleate close to either the fault base or the fault's half width (e.g. Somerville et al., 1999; Manighetti et al., 2005, Mai et al., 2005). Thus, in our fault model, which includes three sub-faults along dip, a realistic location of the hypocenter is on the deepest (third) sub-fault. Rupture propagation is more difficult to be realistically modeled. However, in the case of the 1867 event it is most probable that rupture propagated unilaterally toward NNE. This scenario is favored both by earthquake statistics (McGuire et al., 2002; Manighetti et al., 2005) and the reported damage of the 1867 event in western Turkey (e.g. in Ayvalik and Edremit).

3.3 Results

As mentioned above we tested numerous rupture scenarios regarding the source dimensions of the 1867 event and the location of the rupture initiation point (controlling basically the directivity of the rupture). Our basic conclusions from the comparative study of their resulting PGA distribution patterns are summarized in the following.

The total, sub-surface length of the fault model in our preferred scenario (Figure 2) does not exceed 30 km, while its surface expression length is 16.5 km as discussed in the previous section. Both lengths were determined by the employed empirical relations (see section 3.2). When larger source dimensions were introduced in simulations (and, thus, larger earthquake magnitude) synthetic PGA values in the west part of Lesvos were too high to explain the fact that most villages in that area remained intact by the examined historical event.

The addition of segment A (Figure 1) in the surface rupture of the 1867 fault model does not change the resulting PGA distribution pattern in any significant way and as there were no documented surface brakes along it we chose not to introduce it in our simulations.

The rupture of segment F increases the strong motion level in the northeastern part of Lesvos and most importantly toward the Turkish town of Ayvalik and Edremit, which suffered significant damage from the 1867 earthquake. However it cannot explain the low degree of damage within the valley of Troy in western Anatolia (>60 km to the north of Lesvos Isl.), which is located along the strike
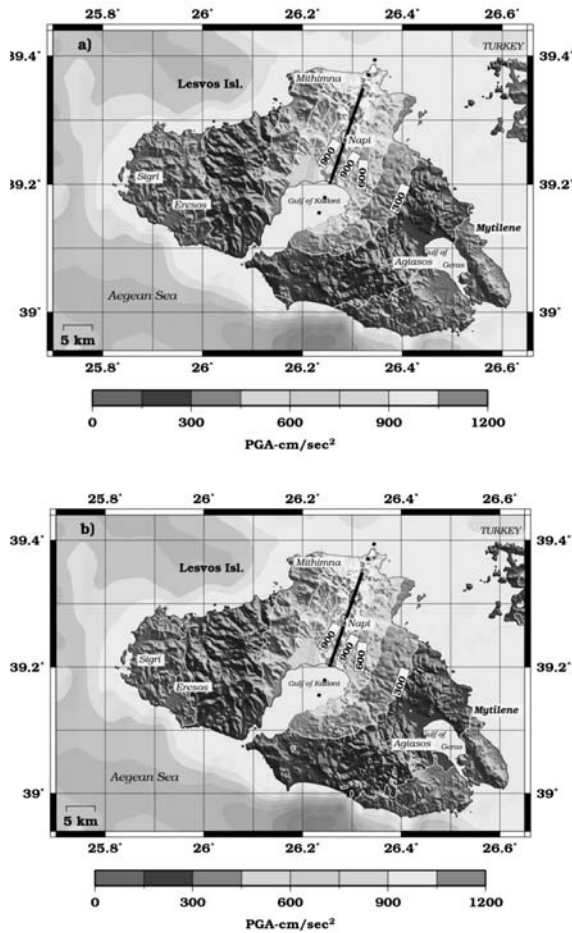
Fig. 2: Synthetic PGA distribution map (contoured in units of cm/sec²) for a scenario earthquake of M6.5 on the Agia Paraskevi zone. The surface projection of the adopted fault model is shown by a black line (continuous where surface rupture is allowed and dotted elsewhere) a) Plotted values correspond to surface geological conditions corresponding to rock b) synthetic values after the gross incorporation of the site effect (see text).

of the on-land segments of the Agia Paraskevi fault. Similar increase in PGAs toward NNE is achieved if the on-land segments are ruptured up to the surface and the hypocenter is located in the southern part of the fault model (i.e. introduce rupture directivity toward the north).

In Figure 2 we map the distribution of synthetic PGA values as derived from the application of the finite-fault stochastic strong ground motion simulation technique (spacing in simulation grid was 0.01°) in the case of our preferred model (described in the previous section). Our preferred source model places the surface rupture of the 1867 seismogenic fault in the central part of Lesvos, starting from the Gulf of Kalloni and extending along a NNE-SSW direction in accordance with historical information. It provides realistic synthetic PGA values on the Island of Lesvos and directivity effects toward western Turkey.

In Figure 2a we plot the synthetic values as were computed for surface site conditions corresponding to rock (site category B; Margaris and Boore, 1998; Klimis et al., 1999) and in Figure 2b we plot the corresponding values after the empirical corrections for the amplification of the local geology and non-linear response of soil (Borcherdt, 1994). In general, the effect of the empirical correction to introduce the site response is rather small; however an increase in synthetic PGA values
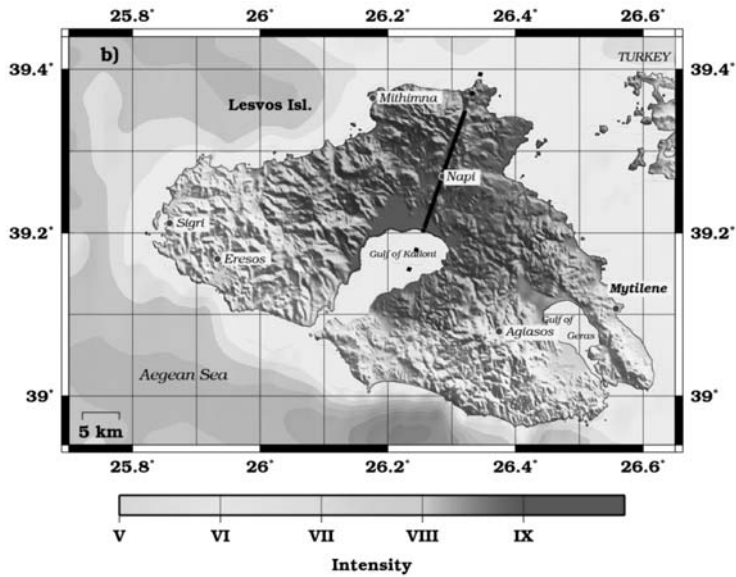
Fig. 3: Synthetic Modified Mercalli Intensity (MMI) map for the 1867 earthquake. The surface projection of the adopted fault model is shown as a black line (continues where surface rupture is allowed and dotted elsewhere).

is evident in the SE part of the island and more specifically around the Gulf of Geras and along the SE coast where the heavily damaged capital of Mytilene lies. Thus, even a rough incorporation of the site amplification manifests that local site conditions were among the important factors that shaped the strong ground motion distribution pattern.

Overall, the strongest ground motion is predicted along the adopted fault trace with PGA values that exceed 1g at several simulation points. Such large values are indicative of the strength of the shaking in the near-fault area. However, the distribution of strong ground motion at such close distances from the source greatly depends on the rupture characteristics of the earthquake and its slip distribution pattern, factors that cannot be realistically modelled for an historical earthquake. In any case, the simulated motions are extremely strong in accordance with the reported devastation of villages in this area and the location of the macroseismic epicentre by a number of researchers (Kampouris, 1978; Ambraseys and Finkel, 1995; Papazachos and Papazachou, 2003).

High PGA values around the Gulf of Kalloni, where many villages were destroyed by the 1867 event are due to the location and orientation of the fault model. In this area, the proximity to the seismogenic source appears to be the prevailing factor in the shaping of strong ground motion. The effect of soft soil formations along the coastline is masked by the strong source effect.

The placement of the hypocenter location in the SSW part of the fault model and thus the directivity of the rupture propagation to the NNE causes the asymmetry in the PGA distribution towards the coast of western Turkey.

To convert synthetic PGA values to Macroseismic Intensities (herein intensity values are in the Modified Mercalli scale, MMI) so as to be comparable to historical damage information we used the empirical relations of Atkinson and Sonley (2000). Although such relations based on data from Greek earthquakes are available in the literature (Theodulidis and Papazachos, 1992; Koliopoulos

et al., 1998; Tselentis and Danciu, 2008) they are all based on the epicentral distance which in the case of the 1867 is much less constrained compared to the closest-to-the-fault distance required in Atkinson and Sonley (2000). Results are mapped in Figure 3. Synthetic intensities are quite high throughout the entire surface of the island with values being larger than IX in its central part. The heavily damaged capital of Mytilene lies within the VIII-IX intensity zone, both because of its small distance from the seismogenic source and the site effect of the soft soils close to the coastline. Following the PGA distribution pattern of Figure 2b synthetic intensities are increased by approximately one unit around the Gulf of Geras. To the west of the island (Sigri, Eresos) intensities drop below VI and that explains the absence of significant damage as reported in historical documents.

The synthetic MMI of Figure 3 compare quite well to the map of isoseismals of Papazachos et al. (1997) although the area covered by the aforementioned map is much larger (37°N, 22°E - 42°N, 31°E). For the Island of Lesvos and the neighbouring western coast of Turkey Papazachos et al. (1997) suggest intensities of VIII-X and VII-VIII respectively, which are similar to those proposed in the present work.

4. Conclusions

The destructive 1867 earthquake on the Island of Lesvos was studied by examining several rupture scenarios, simulating the strong ground motion throughout the entire island and comparing synthetic values to available macroseismic information. Among the tested scenarios our preferred one includes surface rupture on four on-land mapped segments (B-E in Figure 1) of the Agia Paraskevi fault, rupture initiation on the southern part of the fault model and thus directivity toward NNE.

The simulated earthquake magnitude is M 6.5 i.e. significantly smaller compared to the value of 7.0 inferred by processing of historical macroseismic intensities (Papazachos et al., 1997; Papazachos and Papazachou, 2003). However, examination of larger magnitude earthquake scenarios result in very high PGA values in the west part of Lesvos, which contradict the documented absence of damage in this area. A smaller magnitude is also predicted by empirical relations (Wells and Coppersmith, 1994; Pavlides and Caputo, 2004) based on the surface rupture length inferred by historical data. Even if we consider the scientific finding of Pavlides and Caputo (2004) that co-seismic fault rupture lengths in the Aegean Sea and neighbouring lands have systematically lower values compared to similar parameters in the world-wide database (e.g. in those consisting the basis for the herein adopted empirical relations of Wells and Coppersmith, 1994) and use a much larger surface rupture length than the one documented (in our simulations we used 16.5 km compared to 3-7 km reported in historical archives) the magnitude of the simulated event is not larger than M 6.6. This discrepancy may be due to the fact that the magnitude evaluations based on historical macroseismic data inherently include the effect of lower vulnerability of the structures in the time of the event occurrence.

The contribution of site effects in the distribution of PGAs, although they are only grossly incorporated in our simulations, is evident in the synthetic maps; increased levels of shaking are predicted along the east coast of Lesvos and around the gulfs of Kalloni and Geras. However, the combinational effect of high vulnerability of the structures of that time is still required to explain the devastation of Mytilene.

5. Acknowledgments

were produced using the GMT software (Wessel and Smith, 1998). This work was funded by the General Secretariat of Research and Development of Greece (PEP-NAEGEAN).

6. References

Ambraseys, N. N., and Finkel, C. F., 1995. The seismicity of Turkey and adjacent areas, *Publ. Eren Ltd.*, Istanbul, pp. 240.

Anderson, J. G., and Hough S. E., 1984. A model for the shape of the Fourier amplitude spectrum of acceleration at high frequencies, *Bull. Seism. Soc. Am.* **74,** 1969-1993.

Atkinson, G. M., and Sonley E., 2000. Empirical Relationships between Modified Mercalli Intensity and Response Spectra, *Bull. Seism. Soc. Am.* 90(2), 537-544.

Beresnev, I. A., and Atkinson G. M., 1997. Modeling finite-fault radiation from the ω^n spectrum, *Bull. Seism. Soc. Am.* 87, 67 – 84.

Beresnev, I. A., and Atkinson G. M., 1998. FINSIM – a FORTRAN program for simulating stochastic acceleration time histories from finite faults, *Seism. Res. Lett.* 69, 27 – 32.

Borcherdt, R. D., 1994. Estimates of site-dependent response spectra for design (methodology and justification), *Earthquake Spectra* 10, 617- 653.

Boore, D. M., 1983. Stochastic simulation of high-frequency ground motions based on seismological models of the radiated spectra, *Bull. Seism. Soc. Am.* 73, 1865 – 1894.

Emolo A., Iannaccone G., Zollo A., Gorini A., 2004. Inferences on the source mechanisms of the Irpinia (Southern Italy) earthquake from simulations of the kinematic rupture process, *Annals of Geophysics* 47, 1743-1754.

Hatzidimitriou, P. M., 1993. Attenuation of coda waves in Northern Greece, *Pure and Appl. Geophys.* 140, 63 – 78.

Hatzidimitriou, P. M., 1995. S-wave attenuation in the crust in Northern Greece, *Bull. Seism. Soc. Am.* 85, 1381 – 1387.

Kampouris, Z. P., 1978. Calamities in Lesvos in the 19th century, *Publ. J. A. Paspate*, Mytilene pp. 77 (in Greek).

Klimis, N. S., Margaris, B. N. and Koliopoulos, P. K., 1999. Site dependent amplification functions and response spectra in Greece, *Journal of Earthquake Engineering* 3, 237 – 247.

Koliopoulos, P. K., Margaris, B. N., and Klimis, N. S., 1998. Duration and energy characteristics of Greek strong motion records, *J. Earthq. Eng.* 391-417.

Mai, P.M., Spudich, P., and Boatwright J., 2005. Hypocenter locations in finite-source rupture models, *Bull. Seism. Soc. Am.* 95(3), 965-980.

McGuire, J. J., Zhao, L., and Jordan, T. H., 2002. Predominance of unilateral rupture for a global catalog of large earthquakes, *Bull. Seism. Soc. Am.* 92, 3309 – 3317.

Manighetti, I., Campillo, M., Sammis, C., Mai, P.M., and King G., 2005. Evidence for self-similar, triangular slip distributions on earthquakes: Implications for earthquake and fault mechanics, *J. Geophys. Res.* 110.

Margaris, B. N., and Boore D. M., 1998. Determination of $\Delta\sigma$ and κ_0 from response spectra of large earthquakes in Greece, *Bull. Seism. Soc. Am.* 88, 170 – 182.

Papazachos, B. C., Papaioannou, Ch. A., Papazachos, C. B., and Savvaidis, A. A., 1997. Atlas of isoseismal maps for strong earthquakes in Greece and surrounding area, *Publ. Geoph. Lab. Univ. Thessaloniki,* 4, pp 200.

Papazachos, B. C., and Papazachou C., 2003. The earthquakes of Greece, *Ziti Publ. Co.,* Thessaloniki,

Greece, pp. 286 (in Greek).

Pavlides, S., and Caputo, R., 2004. Magnitude versus faults' surface parameters: quantitative relationships from the Aegean region, *Tectonophysics* 380, 159-188.

Pavlides, S., Caputo, R., and Chatzipetros, A., 2000. Empirical relationships among earthquake magnitude, surface ruptures and maximum displacement in the broader Aegean region, *Proc. of the 3rd International Conf. on the Geology of the Eastern Mediterranean*, eds. Panayides, I. and Xenophontos C.

Pavlides et al., 2008. Identification of active tectonic structures using geologic data, Report included in the final report of the project "*Contribution of advanced methods of Geosciences in seismic risk management with emphasis to the built environment of the North Aegean Sea Islands*" funded by General Secretariat of Research and Technology, [PEP –NAEGEAN], 2006 – 31.05.2008.

Somerville, P., Irikura, K., Graves, R., Sawada, S., Wald, D., Abrahamson, N., Iwasaki, Y., Kagawa, Smith, N., and Kowada A., 1999. Characterizing crustal earthquake slip models for the prediction of strong ground motion, *Seism. Res. Let.* 70, 59-80.

Theodulidis, N. P., and Papazachos, B. C., 1992. Dependence of strong ground motion on magnitude-distance, site geology and macroseismic intensity for shallow earthquakes in Greece: I, peak horizontal acceleration, velocity and displacement, *Soil Dyn. Earthq. Eng.* 11, 387-402.

Tselentis, G.-A., and Danciu L., 2008. Empirical relationships between Modified Mercalli Intensity and Engineering Ground-Motion Parameters in Greece, *Bull. Seism. Soc. Am.* 98(4), 1863-1875.

Zollo A., Emolo A., Herrero A., Improta L., 1999. High frequency strong motion modelling in the Catania area associated with Ibleo-Maltese fault system, *J. Seismology* 3, 279-288.

Wald, D. J., and Allen T. I., 2007. Topographic slope as a proxy for seismic site conditions and amplification. *Bull. Seism. Soc. Am.* 97(5), pp. 1379-1395, doi: 10.1785/ 0120060267.

Wells, D. L., and Coppersmith, K. J., 1994. New empirical relationships among magnitude, rupture length, rupture width, rupture area and surface displacement, *Bull. Seism. Soc. Am.* 84, 974-1002.

Wessel, P., and Smith, W.H.F., 1998. New improved version of the Generic Mapping Tools released. *EOS Trans.* AGU 79, 579.

MODERATE MAGNITUDE EARTHQUAKE SEQUENCES IN CENTRAL GREECE (FOR THE YEAR 2008)

Roumelioti Z.[1] and Kiratzi A.[2]

[1] Archaeologikou Mouseiou 46, 54641 Thessaloniki, Greece, zroum@auth.gr

[2] Department of Geophysics, Aristotle University of Thessaloniki, P.O. Box 352-1 Thessaloniki, Greece, Kiratzi@geo.auth.gr

Abstract

The small-to-moderate magnitude earthquake sequences offshore NE Evia island (Mantoudi, October 2008) and in central Greece, to the NW of the town of Amfiklia (December 2008) are studied in terms of their source parameters and strong shaking in nearby populated areas. Moment tensors of the strongest events of the sequences, their seismogenic faults and the distribution of slip on them are sought through the inversion of regional broadband waveforms. We then apply a forward modelling technique, which incorporates synthetic Green's functions calculated for a 1D velocity model, previously proposed for the broader studied area, to get a first-order evaluation of the distribution of strong ground shaking around the hypocenters. The Mantoudi earthquake sequence is found to be associated to an offshore NE-SW trending normal fault that dips to the NW, with a considerable dextral strike-slip component. The Amfiklia earthquake sequence is related to a pure normal, E-W trending fault which dips to the south. This conclusion is drawn by both the distribution of aftershocks and the inversion process for the computation of slip on the seismogenic fault of the strongest event of the sequence ($M_w5.1$). Forward modelling of strong ground shaking based on event-specific moment tensor and slip distribution indicates low levels of expected ground motion in accordance with the limited observed damage.

Key words: *moment tensor, slip distribution, shake map, seismicity, Greece.*

1. Introduction

Earthquake swarms and seismic sequences of moderate magnitude earthquakes are rarely responsible for significant damage in the natural and built environment of modern cities. However, they often have a phychological impact on the populations of the broader areas of their occurrence and are of scientific interest as their study can provide information on the seismotectonics and their data can be used to test and validate real and near-real time seismological applications. Herein, we study two earthquake swarms that occurred in central Greece, the first one offshore NE Evia Island and the second one close to the town of Amfiklia, during the year 2008. We present moment tensor solutions for the strongest events of the sequences and slip distributions for the two main events. Specific slip distributions are further incorporated into forward modelling of strong ground motion to provide shake maps for the broader epicentral areas.
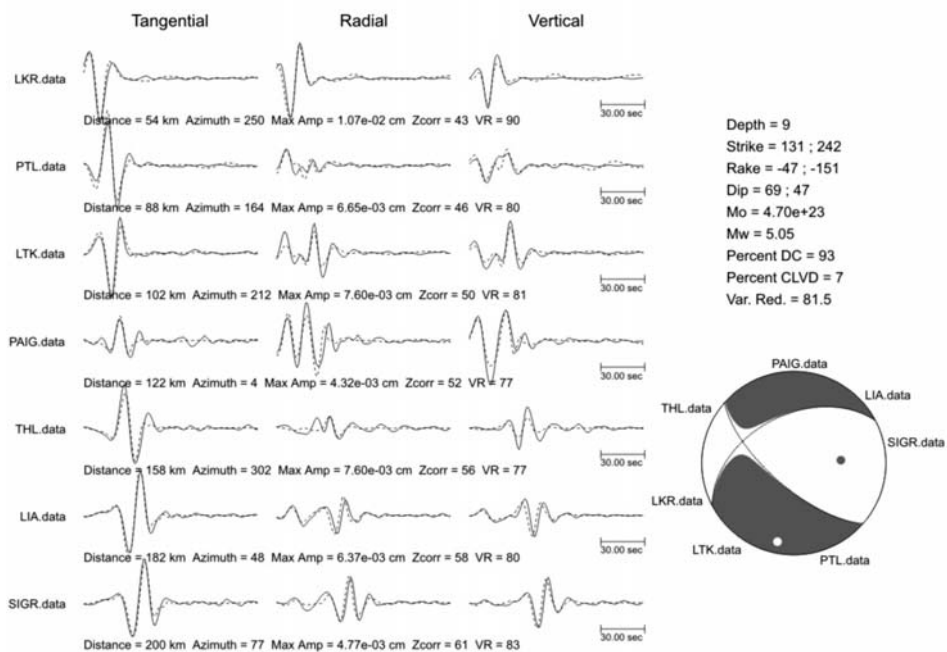
Fig. 1: Moment tensor solution for the 14 October 2008, GMT 02:06 earthquake (No 1 in Table 1). Used stations provide the best azimuthal coverage of the epicentre without over-weighting any azimuth. For each station waveform fit between observed (continuous lines) and synthetic (dashed lines) vertical, tangential and radial components are shown (left). Solution parameters are summarized in the right part of the figure.

2. The 14 October 2008 moderate magnitude sequence offshore NE Evia Island (Aegean Sea)

2.1 Seismotectonic regime

On October 14, 2008 a moderate magnitude (M_w5.1) sequence initiated offshore the NE coast of Evia Island which faces the Aegean Sea. Evia Island lies in the transition zone from strike-slip faulting to the east, due to the strands of the North Anatolian Fault (NAF) that enter to the Aegean Sea, to normal faulting to the west in central Greece. From this point of view, its pattern of deformation is always interesting, to seek for example the mode in which the shear motion from the east is crossing into mainland Greece.

2.2 Moment tensors of the October 2008 stronger earthquakes

Moment tensors of the stronger events of the sequence were computed by the Time-Domain Moment Tensor inversion method (TDMT_INV) developed at the Berkeley Seismological Laboratory (Dreger, 2002, 2003). In the specific method full broadband waveforms of the three recorded components of motion are low-pass filtered and inverted to derive the moment tensor. In the inversion procedure theoretical Green's functions are required to model the propagation of the seismic waves.

Data used in all herein applications were gathered through the Hellenic Unified Seismological Network (HUSN) of Greece. Prior to the inversion procedure, waveforms were band-pass filtered between 0.02–0.08 Hz, 0.05-0.08 Hz or 0.05-0.10 Hz depending on the magnitude of each analyzed
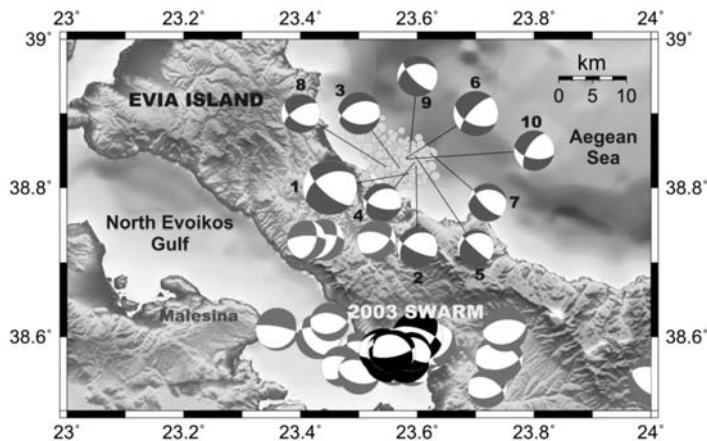
Fig. 2: The 14 October 2008 focal mechanisms (red beach-balls; numbering as in Table 1) and previous focal mechanisms determined by waveform modelling available for Evia Island (Hatzfeld et al., 1999; Benetatos et al., 2004; Roumelioti et al., 2010; National Observatory of Athens – http://bbnet.gein.noa.gr). Earthquake epicenter locations are from the on-line catalog of the Aristotle University of Thessaloniki (https://seismology.geo.auth.gr). The 2003 swarm focal mechanisms are depicted in black-and-white colours.

Table 1. Source parameters of the studied events offshore Evia Island (epicentre locations are from the on-line archive of the Department of Geophysics of the Aristotle University of Thessaloniki, http://seismology.geo.auth.gr).

No	Date	hh:mm:ss	Lat (°N)	Lon (°E)	h (km)	M_0 ×10²²	M_w	Str1	Dip1	Rake 1	Str2	Dip2	Rake 2	Inverted Stations	Clvd (%)	Vr (%)
1	081014	02:06:35.1	38.819	23.584	9	47.1	5.05	242	47	-151	131	69	-47	7	7	81.5
2	081014	02:16:58.6	38.829	23.598	9	3.75	4.32	234	32	-147	115	73	-62	6	17	80.3
3	081014	02:35:47.0	38.827	23.569	7	0.96	3.93	247	47	-113	99	48	-68	5	9	80.2
4	081014	03:13:32.6	38.833	23.594	8	0.30	3.59	236	36	-132	104	64	-64	4	0	83.5
5	081014	04:39:40.8	38.842	23.597	9	0.15	3.39	237	24	-164	132	84	-67	3	2	87.5
6	081015	19:29:24.4	38.840	23.581	6	2.32	4.18	223	70	-135	114	48	-27	6	2	82.4
7	081027	10:41:37.6	38.846	23.623	7	0.27	3.55	263	32	-137	135	69	-66	4	6	87.7
8	081129	06:43:18.3	38.829	23.545	8	0.31	3.60	238	64	-135	124	50	-35	2	6	75.5
9	090116	01:21:56.9	38.848	23.587	10	0.57	3.77	251	40	-148	136	70	-55	2	7	91.5
10	090331	02:20:01.8	38.839	23.583	7	0.53	3.75	211	62	-142	101	57	-33	2	6	80.6

event and thus the signal-to-noise ratio in its waveforms. Synthetic Green's functions for all herein applications were produced using the FKRPROG code of Saikia (1994) and the velocity model of Novotny et al. (2001), which has been successfully used in similar studies of earthquakes of the broader Aegean area (e.g. Benetatos et al., 2004; Roumelioti et al., 2008a, 2010).

We computed moment tensor solutions for ten events (Table 1 summarizes the source parameters of
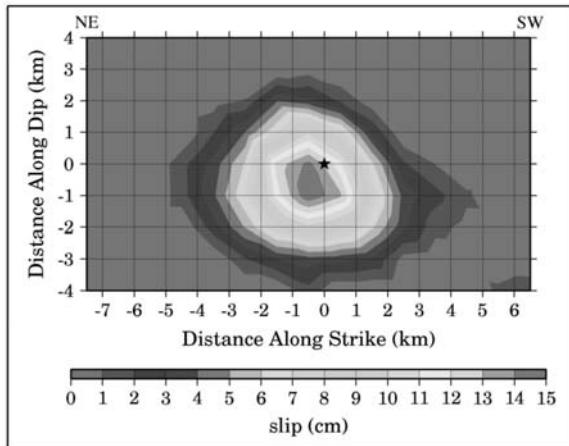
Fig. 3: Slip distribution (slip in cm) for the October 14, 2008; GMT 02:06 Mw5.1 event, onto the fault plane (i.e. the nodal plane that dips to the NW in Fig. 1). The slip area expands almost symmetrically around the adopted hypocenter location (asterisk). Note that the 0 in this figure corresponds to the depth of 9 km obtained from the MT solution.

the analyzed events). The last three columns summarize quantitative measures for the quality of each computed MT. For further description of the parameters the reader is referred to the original work of Dreger 2002, 2003) within the epicentral area of the 14 October 2008, two of which, however, occurred few months after the burst of the main activity. In Figure 1 we indicatively show the moment tensor solution for the strongest, Mw5.1, event of the sequence. In Figure 2 we show the computed focal mechanisms along with previous known mechanisms of earthquakes (all from waveform inversion) on and around the Evia Island. Clearly normal faulting is prevailing combined with strike-slip motions. For the 2008 events the fault plane for the Mw5.1 event is the one that dips to the NE (see section 2.3), implying dextral strike-slip motion and a slip vector trending N41^{O}E. The most recent intense seismic activity, prior to the one studied herein, was the 2003 swarm close to the town of Psahna (black coloured beach balls in Figure 1), a rock burst region in Evia, like the town of Mantoudi which was close to the 2008 events.

2.3 Slip model for the Oct 14, GMT 02:06 Mw 5.1 event

To obtain the slip distribution model for the GMT 02:06 Mw 5.1 event (Fig. 3) we used the methodology of Dreger and Kaverina (2000) and Kaverina et al. (2002), in which regional distance ground motions recorded on broadband instruments are inverted for slip through a least squares scheme. The applied method requires simplifying assumptions including constant rupture velocity and dislocation rise time and poses slip positivity, seismic moment minimization and smoothing constraints during the inversion procedure.

Both nodal planes were tested as candidate seismogenic (Roumelioti et al., 2008b) as the applied methodology is capable of uniquely determining the causative fault plane of the earthquake and realistically determining the gross characteristics of the slip distribution (both along strike and down dip). These characteristics are adequate to incorporate the major source effect on expected strong ground motions. For the M$_w$5.1 event the nodal plane that dips to the NW (that is the one with strike 242°) was statistically detected as the fault plane. This implies that the azimuth of the slip vector is N41^{o}E and its plunge 21°, in accordance with the direction of the shear motion transferred from the
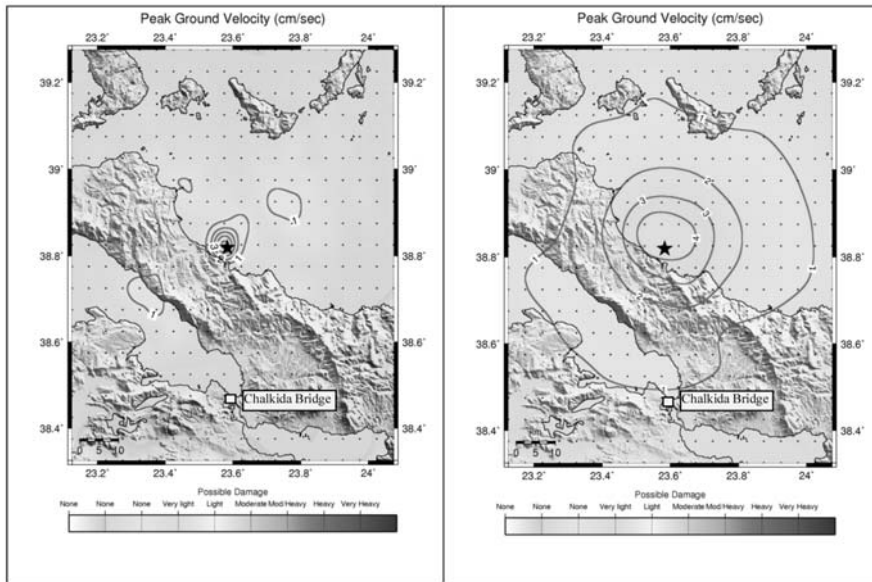
Fig. 4: Left : Distribution of synthetic PGV's for the 14 Oct. 2008 Mw5.1 event, based on the slip model of Fig. 3. Right: Distribution of PGV's obtained using the empirical relations of Skarlatoudis et al. (2003, 2007) for comparison.

east (Kiratzi, 2002). Slip appears in one symmetric patch expanding around the adopted hypocenter location. Average slip in the ruptured area is ~4cm and peak slip reaches 15 cm very close to the rupture initiation point.

2.4 Deterministic Computation of PGV maps (Shake Map) for the strongest Mw 5.1 event

We incorporated the regionally derived slip model (Fig. 3) in the forward calculation of strong ground motion within a grid 50×50 km centered at the epicentre location. As in the inversions described in the previous section, for the forward problem we used the code of Kaverina et al. (2002). We computed full velocity waveforms up to 5 Hz and retrieved their peak values to construct maps with the distribution of the specific strong ground motion measure (Fig. 4a). Details on this part of the applied methodology and relative references are also included in Roumelioti et al. (2008b). Site effects at the nodes of the grid were grossly described based on the topography gradient as suggested by Wald and Allen (2007). For reasons of comparison we additionally computed synthetic PGV values using the empirical relations of Skarlatoudis et al. (2003, 2007) (Fig. 4b). By comparing the two maps in Figure 4 it becomes obvious that peak PGVs in Fig. 4a are concentrated in a smaller region and decay much faster compared to corresponding values in Fig. 4b. The closest observed strong motion record of the specific earthquake was obtained by ITSAK at the Bridge of Chalkida (Figure 4) and PGV was of the order of 0.23 cm/sec (N. Theodulidis, personal communication), a value which lies between the two independent evaluations mapped in Figure 4.

3. The December 2008 Amfiklia Earthquake Sequence

3.1 Seismotectonic regime

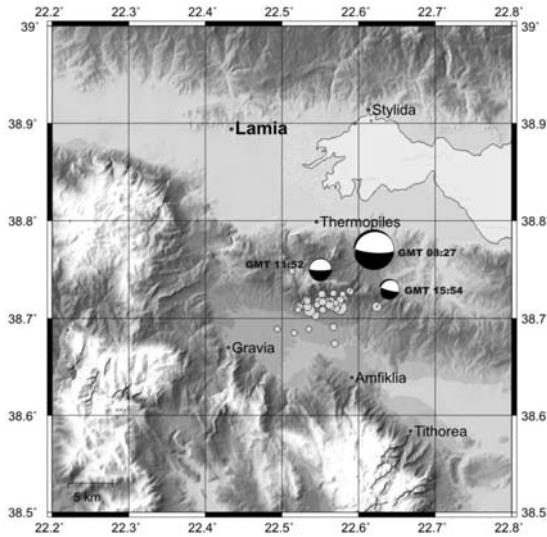On the 13th of December 2008, 08:27 GMT, an earthquake measuring M$_w$5.1 occurred at about 10

Fig. 5: Left: Distribution of epicentres (yellow circles, diameters are analogue to the earthquake magnitude) of the December 2008 Amfiklia sequence. Beach balls for the computed focal mechanisms (Table 2) are also plotted.
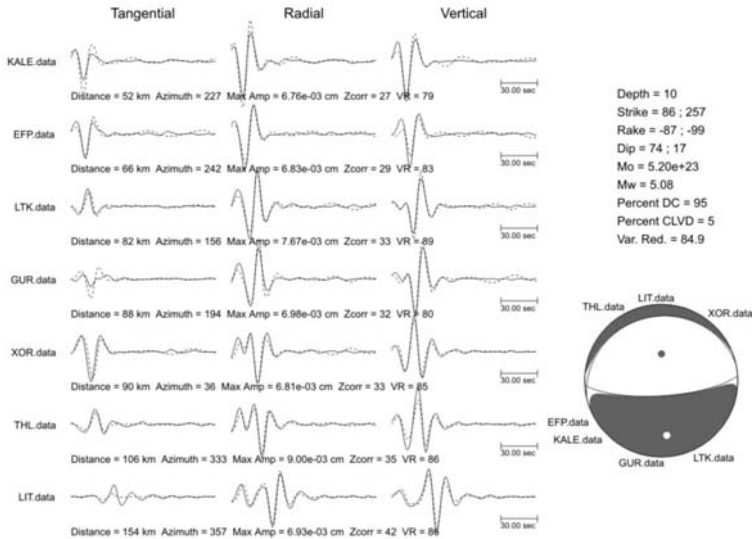

Fig. 6: Moment tensor solution for the 13 December 2008, GMT 08:27 earthquake (No 1 in Table 3). For each station waveform fit between observed (continuous lines) and synthetic (dashed lines) vertical, tangential and radial components are shown (left). Solution parameters are summarized in the right part of the figure.

km SE of the town of Lamia in central Greece, close to the small town of Amfiklia (herein the sequence is named after this town). Despite its moderate magnitude the earthquake caused minor damage (mostly cracks and plaster falls) to one church and to more than twenty residences, mostly of rock, in Amfiklia and nearby villages. Limited landslides were also observed and as a consequence traffic in one country road was interrupted for a few hours. Epicenters of this small sequence (Figure 5) are gathered on top of the south facing slope of the topographic high to the north of Amfiklia. For this area there are no reports for significant tectonic structures. Known large faults have been mapped to the north (e.g. Ganas and Papoulia, 2000; Roberts and Ganas, 2000) and dip to the

Table 2. Focal mechanism parameters of the December 2008 sequence to the NW of Amfiklia. Earthquake epicentre locations are those of the online archive of the Aristotle University of Thessaloniki (http://seismology.geo.auth.gr).

No	Date	hh:mm: ss	Lat (°N)	Lon (°E)	h (km)	M_0 ×10^{22}	M_w	Str1	Dip1	Rake 1	Str2	Dip2	Rake 2	Inverted Stations	Clvd (%)	Vr (%)
1	081213	08:27:19.9	38.711	22.576	10	52.0	5.1	86	74	-87	257	17	-99	7	5	84.9
2	081213	11:52:52.6	38.717	22.563	7	0.48	3.7	90	81	-88	257	9	-103	4	3	84.7
3	081213	15:54:40.5	38.712	22.624	7	0.31	3.6	112	80	-75	237	18	-144	4	2	74.8
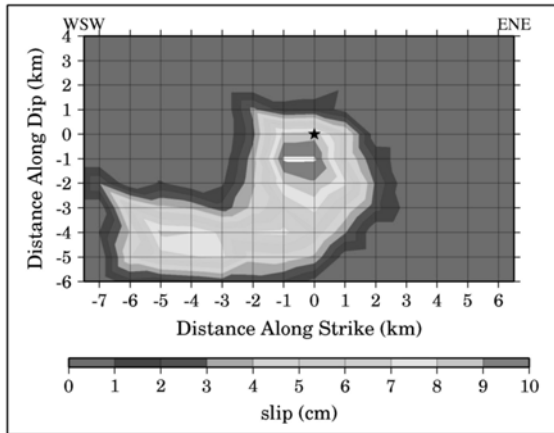
Fig. 7: Slip distribution (slip in cm) for the 13 December 2008, GMT 08:27 earthquake Mw5.1 event, onto the fault plane (i.e. the nodal plane that dips to the S in Fig. 5). The slip area expands around and to the west of the adopted hypocenter location (asterisk). Note that the 0 in this figure corresponds to the depth of 10 km obtained from the MT solution.

north. In this frame, the 2008 sequence appears to be related to a small, antithetic to the known large faults, structure that bounds the Gravia – Amfiklia depression to the north. The occurrence of the 2008 sequence was studied in the frame of the general seismicity of the area by Chouliaras (2009).

3.2 Moment tensors

Following the TDMT_INV approach we computed the moment tensors of the largest events of the sequence. Due to the small magnitudes of the events we were capable of obtaining stable inversions for only three events. For reasons of space economy we present the results for only the main event of the sequence (Figure 6); however all detailed solutions are available upon request. Basic parameters of the computed moment tensors are listed in Table 2 and corresponding beach-balls are plotted in Figure 5.

3.3 Slip distribution

The slip distribution of the 13 December 2008, GMT 08:27 event was computed by inverting the exact broadband waveforms (and corresponding frequency intervals) previously used to calculate its moment tensor (depicted in Figure 6) to ensure the sufficiency of the employed 1D velocity model. The extracted slip distribution model is shown in Figure 7. Most slip appears concentrated very close to the adopted hypocenter location and the rupture area extends to the WSW of it. Average slip within the ruptured area is ~3.5 cm while the peak value is 10 cm and appears at a distance of ~1 km to the west of the hypocenter.
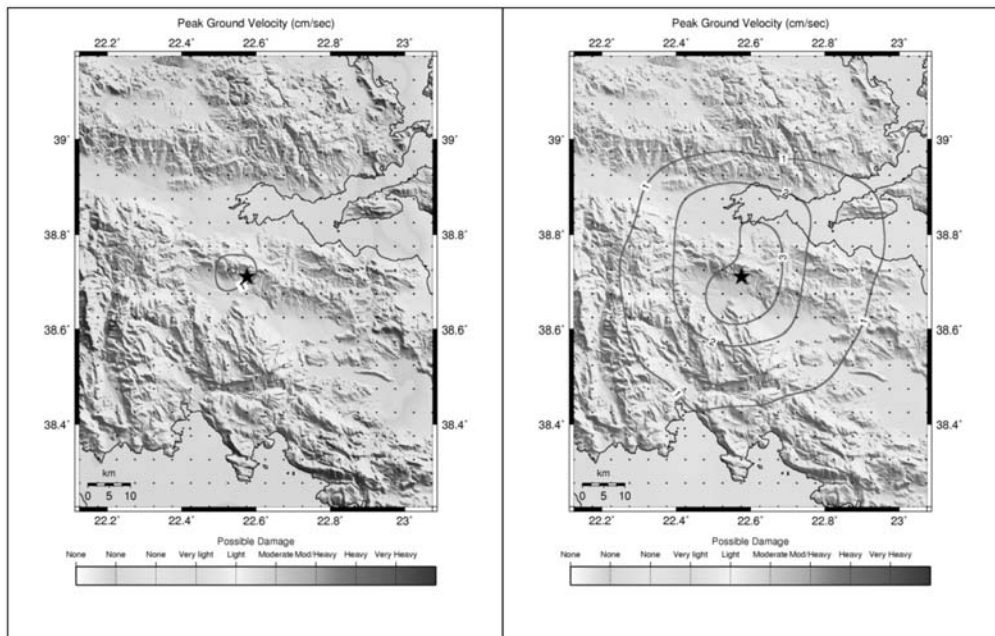
Fig. 8: Left : Distribution of synthetic PGV's for the 13 December 2008, GMT 08:27 event, based on the slip model of Fig. 7. Right: Distribution of PGV's obtained using the empirical relations of Skarlatoudis et al. (2003, 2007) for comparison.

3.4 Shake maps

The synthetic PGV map of the 13 December 2008, GMT 08:27 earthquake as derived through forward modelling based on the specific slip distribution of Figure 7 is presented in Figure 8a. In Figure 8b the corresponding map based on values computed through appropriate empirical relations (Skarlatoudis et al. 2003, 2007) is also shown for comparison.

4. Results - Discussion

No strong earthquake has occurred in Evia Island during instrumental times, and tectonic information from moderate size seismicity, like the one studied herein, is valuable. Previous work (Hatzfeld et al., 1999; Kiratzi, 2002) has shown that the deformation in northern Evia Island is taken up mainly by normal and strike-slip faulting. Depending on the orientation of the activated faults, in respect to the present state stress field, dextral or sinistral horizontal motion is observed. The recent earthquakes showed that an almost N-S extensional field prevails in NE Evia Island with a few strike-slip focal mechanisms, suggesting that this part is mostly affected by the normal faulting system of central Greece.

Regarding the small sequence to the NNW of Amfiklia in central mainland, it is related to an E-W trending normal fault, in accordance with the N-S direction of extension indicated by geodetic and geological data of the broader area (Clarke et al., 1998; Briole et al., 2000; Roberts and Ganas, 2000). However, the specific seismicity is observed on an antithetic to the prevailing faults of the broader area structure.

Synthetic PGV maps were constructed for both examined main events using a deterministic approach in comparison to empirical strong ground motion relations. Both approaches predict very light or no damage in both applications; however they lead to significantly different PGV distributions with the first one providing lower levels of strong ground motion. Such differences are, in fact, expected in the near fault region of an earthquake where the source effect is significant. This effect is incorporated in the deterministic approach whereas in the empirical relations it is smoothed out during the regression process. For earthquakes of magnitude around 5, such as the ones studied in this paper, the source effect is expected to be hardly observed at distances larger than 20-25 km from the epicentre. Thus, at larger distances (>25 km) the differences in the two PGV sets should be sought in the modelling of the attenuation and/or site effects. The only observed strong ground motion record, which was obtained during the 14 October 2008, M_w5.1 Mantoudi earthquake, shows PGV which lies between the two independently derived synthetic values. More observed records as well as stronger events are necessary for further validating and improving the herein applied methodology for incorporating the source effect in strong ground motion distributions in the near source region.

5. Acknowledgments

6. References

Benetatos C., Kiratzi A., Kementzetzidou K., Roumelioti Z., Karakaisis G., Scordilis E., Latoussakis I. and Drakatos G., 2004. The Psachna (Evia Island) earthquake swarm of June 2003. *Bulletin of the Geological Society of Greece*, XXXVI (3), 1379 - 1388.

Briole P., Rigo A., Lyon-Caen H., Ruegg J., Papazissi K., Mitsakaki C., Balodimou A., Veis G., Hatzfeld D. and Deschamps, A. (2000). Active deformation of the Corinth rift, Greece: Results from repeated Global Positioning System surveys between 1990 and 1995, *J. Geophys. Res.*, 105(B11), 25605–25625.

Clarke P. J., Davies R. R., England P. C., Parsons B., Billiris H., Paradissis D., Veis G., Cross P. A., Denys P. H., Ashkenazi V., Bingley R., Kahle H.- G., Muller M.-V. and Briole, P. (1998). Crustal strain in central Greece from repeated GPS measurements in the interval 1989–1997, *Geophys. J. Int.*, 135(1), 195–214, 1998.

Chouliaras G. (2009). Seismicity anomalies prior to the 13 December 2008, M_S=5.7 earthquake in central Greece, *Nat. Hazards Earth Syst. Sci.* 9, 501-506.

Dreger D. S., 2002. Time-Domain Moment Tensor INVerse Code (TDMT_INVC) Version 1.1. *Berkeley Seismological Laboratory,* pp. 18.

Dreger D. S., 2003. TDMT_INV: Time Domain Seismic Moment Tensor INVersion. *International Handbook of Earthquake and Engineering Seismology*, W. H. K. Lee, H. Kanamori, P. C. Jennings and C. Kisslinger (eds.), Vol. B, pp. 1627.

Dreger, D. S., and Kaverina A., 2000. Seismic remote sensing for the earthquake source process and near-source strong shaking: a case study of the October 16, 1999 Hector Mine earthquake, *Geophys. Res.*

Lett. 27, pp. 1941–1944.

Ganas, A., and Papoulia I., (2000). High-resolution, digital mapping of the seismic haxard within the Gulf of Evia rift, Central Greece using normal fault segments as line sources, *Natural Hazards* 22, 203-223.

Hatzfeld, D., Ziazia, M., Kemenzetzidou, D., Hatzidimitriou, P., Panagiotopoulos, D., Makropoulos, K., Papadimitriou, P. and Deschamps, A., 1999. Microseismicity and focal mechanisms at the western termination of the North Anatolian Fault and their implications for continental tectonics. *Geophys. J. Int.*, 137, 891-908.

Kaverina A., Dreger D., and Price E., 2002. The Combined Inversion of Seismic and Geodetic Data for the Source Process of the 16 October 1999 Mw 7.1 Hector Mine, California, Earthquake, *Bull. Seism. Soc. Am. 92,* pp. 1266-1280.

Kiratzi A., 2002. Stress tensor inversions along the westernmost North Anatolian Fault Zone and its continuation into the North Aegean Sea. *Geophys. J. Int.*, 151, 360-376.

Novotný O., Zahradník J., and Tselentis G.-A., 2001. North-Western Turkey earthquakes and the crustal structure inferred from surface waves observed in Western Greece. *Bull. Seismol. Soc. Am.,* 91, pp. 875-879.

Roberts G. P. and Ganas, A. (2000). Fault slip directions in central and southern Greece measured from striated and conjugated fault planes: Comparison with focal mechanism and geodetic data, *J. Geophys. Res.,* 105, 23443–23462.

Roumelioti, Z., Benetatos, C., Kiratzi, A. and Dreger D., 2008a. Near-real time moment tensors for earthquakes in Greece based on seismological data of the Hellenic Unified Seismological Network. *3rd National Conference of Earthquake Engineering and Engineering Seismology,* Athens, 5-7 November, 2008, paper ID:1789.

Roumelioti, Z., Kiratzi, A. and Dreger D., 2008b. Near-Real Time Shake Maps for Earthquakes in Greece: pilot application. *3rd National Conference of Earthquake Engineering and Engineering Seismology,* Athens, 5-7 November, 2008, paper ID: 2105.

Roumelioti, Z., Kiratzi A. and Benetatos Ch. (2010). Time domain moment tensors of earthquakes in Greece and its surroundings for the years 2006-2007: the database of the Aristotle University of Thessaloniki, *Journal of Geodynamics*, in press.

Saikia C. K., 1994. Modified frequency-wavenumber algorithm for regional seismograms using Filon's quadrature; modeling of Lg waves in eastern North America. *Geophys. Journ. Int., 118,* pp. 142-158.

Skarlatoudis, A. A., Papazachos C. B., Margaris B. N., Theodulidis N., Papaioannou Ch., Kalogeras I., Scordilis E. M., and Karakostas V., 2003. Empirical peak ground-motion predictive relations for shallow earthquakes in Greece. *Bull. Seism. Soc. Am.* 93, pp. 2591-2603.

Skarlatoudis, A. A., Papazachos C. B., Margaris B. N., Theodulidis N., Papaioannou Ch., Kalogeras I., Scordilis E. M., and Karakostas V., 2007. Erratum to "Empirical peak ground-motion predictive relations for shallow earthquakes in Greece. *Bull. Seism. Soc. Am.* 97(6), pp. 2219-2221, doi: 10.1785/0120070176.

Wald, D. J., and Allen T. I., 2007. Topographic slope as a proxy for seismic site conditions and amplification. *Bull. Seism. Soc. Am.* 97(5), pp. 1379-1395, doi: 10.1785/ 0120060267.

Wessel, P., and Smith, W.H.F., 1998. New improved version of the Generic Mapping Tools released. *EOS Trans.* AGU 79, 579.

CORRELATIONS OF THE MEAN TIME AND MEAN MAGNITUDE OF ACCELERATING PRESHOCKS WITH THE ORIGIN TIME AND MAGNITUDE OF MAINSHOCK

Scordilis E. M.

Department of Geophysics, School of Geology, Faculty of Science, Aristotle University, GR54124, Thessaloniki, GREECE, manolis@geo.auth.gr

Abstract

Forty-five preshock sequences preceding corresponding strong (M≥6.4) mainshocks which occurred recently (since 1980) in a variety of seismotectonic regimes (W. Mediterranean, Aegean, Anatolia, California, Japan, Central Asia, South America) have been examined to identify new predictive properties. It has been observed that the mean origin time,   , and the mean magnitude,   of the accelerating preshocks of each sequence are correlated with the origin time, t_c, and the magnitude, M, of the mainshock, respectively. The following relations have been derived:

where s_a (in Joule $^{1/2}$/yr.10^4 Km^2) is the Benioff strain rate in each preshock (critical) region and σ is the corresponding standard deviation. The possibility for using these relations as constraints in attempts for intermediate term earthquake prediction is discussed.

Keywords: *Accelerating strain, accelerating preshocks, critical earthquake, intermediate-term earthquake prediction.*

1. Introduction

Shocks which are considered as related genetically to an ensuing strong mainshock are foreshocks and preshocks. Foreshocks are generated in the mainshock fault region within a short time (days to weeks) before the mainshock. Foreshocks, however, are usually small and almost unidentifiable before the generation of the mainshock. Preshocks occur years before a strong (M>6.0) mainshock in a relatively broad region and their magnitudes are relatively large (M>4.0). Properties of preshocks are known before the generation of the mainshock and for this reason knowledge of their space, time and magnitude distribution is of significance for inter-mediate-term prediction of strong mainshocks.

Preshocks can be separated in two categories. The first category includes preshocks which release accelerating seismic strain energy (accelerating preshocks) and their foci are located in a relatively broad region (critical region). The second category includes smaller preshocks which release decelerating seismic strain energy (decelerating preshocks) and their foci are located in a narrower region (seismogenic region).

Accelerating preshocks have been observed by many seismologists (Tocher, 1959; Varnes, 1989; Sykes and Jaumé, 1990; Knopoff et al., 1996; Brehm and Braile, 1999; Tzanis et al., 2000; Ben-Zion and Lyakhovsky, 2002; Karakaisis et al., 2003; Scordilis et al., 2004; Papazachos et al., 2005) and interpreted in terms of the critical point dynamics (Sornette and Sammis, 1995; Rundle et al., 2003). Bufe and Varnes (1993) proposed the following relation for the time variation of accelerating preshocks:

(1)

where S(t) is the cumulative Benioff strain (square root of seismic energy) released by accelerating preshocks, t is the time to the mainshock, t_c is the origin time of the mainshock and A, B and m are constants with m<1. Bowman et al. (1998) proposed a curvature parameter, C, which is defined as the ratio of the root-mean-square error of the power-law fit (relation 1) to the corresponding linear fit error, to quantify the deviation of the time variation of the Benioff strain from linearity.

Decelerating preshocks have been also observed before many strong mainshocks and their time variation is also expressed by a relation of the form (1) with m>1 (Papazachos et al., 2005, 2006a). The decelerating seismic strain is attributed to static stress shadow (Papazachos et al., 2006a) that can be interpreted by the Stress Accumulation Model (Bowman and King, 2001; King and Bowman, 2003).

Papazachos et al. (2006a), based on published information on decelerating and accelerating precursory seismic strain and on relative global data, developed the Decelerating-Accelerating Seismic Strain (D-AS) model. This model is formed of a series of empirical relations, most of which have been physically interpreted and can be used to estimate (predict) the origin time, epicenter coordinates and the magnitude of strong mainshocks. The 2σ model uncertainties are δx≤150Km for the epicenter, ±2.5 years for the origin time and ±0.4 for the magnitude of the ensuing mainshock. This model has been already used for a successful, scientifically valid prediction in 2002 of a large earthquake which occurred in southwestern Aegean on 8 January 2006 (Papazachos et al., 2006b, 2007).

In the present work, global data are used to define new properties of accelerating preshock sequences. These properties are expressed by empirical relations that can be used as additional constraints in the effort for intermediate term earthquake prediction. In particular, correlations are observed between the mean origin time,   , and the mean magnitude,   , of accelerating preshocks with the mainshock origin time, t_c, and magnitude, M, respectively.

2. The Data

Data concerning preshock sequences of 45 strong (M≥6.4) mainshocks, which occurred in a variety of seismotectonic regimes, are used in the present study. Of these mainshocks: three (3) occurred in Western Mediterranean (with M≥6.8 since 1980), nine (9) in Aegean (M≥6.4 since 1980), five (5) in Anatolia (M≥6.4 since 1980), eight (8) in California (M≥6.4 since 1980), eight (8) in Japan (M≥7.0 since 1990), nine (9) in Central Asia (M≥7.0 since 1990) and three (3) in South America (M≥7.7 since 1995). The first four columns of table (1) list the region, origin time, t_c, epicenter coordinates, E(φ,λ), and magnitude, M, of all these forty five mainshocks.

Data concerning the accelerating preshocks of these forty five mainshocks needs to be accurate with respect to their epicenter location and magnitude, and homogeneous with respect to their

Table 1. Region, origin time, tc, epicenter coordinates, E(ϕ,λ) and magnitude, M, of each mainshock are given in the first four columns for all 45 mainshocks. Q is the center and R (in km) is the radius of the preshock (critical) region, t_{sa} is the start time of the accelerating preshock sequence, M_{min} is the minimum preshock magnitude, s_a (in Joule$^{1/2}$/yr. 10^4km^2) is the strain rate in the critical region,   is the mean origin time and   the mean magnitude of the accelerating preshocks which occurred between the origin time, t_c and the time, t_e, when the maximum (best) value of the quality index is observed.

Region	t_c	E(ϕ,λ)	M	Q(ϕ,λ)	R	t_{sa}	M_{min}	n	logs_a		
W. Mediterranean											
1	1980:10:10	36.2, 01.4	7.1	40.0, -03.4	796	1927	5.2	52	4.43	1949.2	5.4
2	1980:11:23	40.8, 16.3	6.9	45.2, 13.2	373	1939	5.1	72	5.21	1961.3	5.4
3	2003:05:21	36.9, 03.8	6.8	36.9, 06.2	432	1911	5.4	54	4.50	1962.9	5.5
Aegean											
1	1980:07:09	39.3, 22.9	6.5	37.1, 19.7	183	1964	4.9	27	5.97	1970.7	5.3
2	1981:02:24	38.1, 23.0	6.7	38.2, 26.1	140	1959	4.7	29	5.71	1971.7	5.0
3	1981:12:19	39.0, 25.3	7.2	36.8, 21.8	253	1967	5.0	62	5.95	1973.8	5.3
4	1983:01:17	38.1, 20.2	7.0	37.7, 18.6	242	1963	4.9	49	5.78	1971.4	5.2
5	1995:05:13	40.2, 21.7	6.6	41.7, 21.2	174	1970	5.0	27	5.65	1983.7	5.3
6	1997:10:13	36.4, 22.2	6.4	35.9, 20.5	163	1965	4.8	46	5.41	1983.7	5.0
7	1997:11:18	37.5, 20.7	6.6	38.4, 20.2	208	1984	4.8	100	6.07	1990.1	5.0
8	2001:07:26	39.1, 24.4	6.4	37.1, 26.2	295	1982	4.9	126	5.82	1991.9	5.1
9	2003:08:14	38.7, 20.5	6.4	37.3, 19.0	239	1984	4.9	64	5.79	1993.5	5.2
Anatolia											
1	1983:07:05	40.2, 27.3	6.4	41.7, 24.8	151	1946	4.6	33	5.31	1967.7	4.8
2	1992:03:13	39.7, 39.6	6.6	38.4, 37.9	223	1951	4.8	51	5.27	1972.2	5.0
3	1995:10:01	38.1, 30.2	6.4	36.4, 27.0	238	1978	4.8	112	5.89	1986.5	5.0
4	1996:10:09	34.5, 32.1	6.8	34.6, 28.4	224	1974	4.8	93	5.65	1985.3	5.0
5	1999:08:17	40.8, 30.0	7.5	39.6, 30.2	291	1981	5.3	29	5.84	1990.4	5.5
California											
1	1980:11:08	41.1, -124.6	7.3	41.1, -124.4	262	1956	5.0	70	5.61	1970.1	5.3
2	1983:05:02	36.2, -120.3	6.4	38.1, -122.1	140	1938	4.8	45	5.19	1967.2	5.1
3	1987:11:24	33.0, -115.9	6.6	35.5, -119.7	384	1953	5.0	125	5.39	1973.5	5.4
4	1989:10:18	37.1, -121.9	6.9	35.7, -120.4	430	1955	5.0	154	5.38	1976.0	5.4
5	1992:04:25	40.3, -124.2	7.1	38.4, -124.1	299	1955	5.1	55	5.32	1973.3	5.4
6	1992:06:28	34.2, -116.4	7.3	33.7, -119.6	428	1956	5.1	80	5.35	1976.5	5.5
7	1994:01:17	34.2, -118.5	6.6	35.2, -116.1	197	1953	4.7	52	5.29	1974.1	5.0
8	2003:12:22	35.7, -121.1	6.5	35.5, -117.6	135	1977	4.6	35	5.56	1991.4	4.9

Region	t_c	$E(\phi,\lambda)$	M	$Q(\phi,\lambda)$	R	t_{sa}	M_{min}	n	$\log s_a$		
Japan											
1	1993:07:12	42.9, 139.2	7.7	38.7, 136.3	572	1969	5.5	141	6.04	1980.5	5.8
2	1994:10:04	43.7, 147.4	8.3	41.5, 148.0	746	1982	5.6	135	6.08	1986.9	6.0
3	1995:01:16	34.6, 135.0	7.0	34.3, 137.3	198	1983	5.0	65	6.17	1988.6	5.2
4	2003:05:26	38.8, 141.6	7.0	38.5, 139.3	223	1985	5.1	54	5.86	1993.4	5.3
5	2003:09:25	41.8, 143.9	8.3	41.8, 143.4	2503	1964	6.0	310	5.26	1983.9	6.3
6	2003:10:11	37.8, 142.6	7.0	34.7, 143.0	165	1987	4.8	50	5.91	1994.5	5.1
7	2004:09:05	33.2, 137.1	7.4	31.7, 135.2	443	1972	5.4	87	5.84	1989.2	5.7
8	2005:08:16	38.3, 142.0	7.2	40.4, 141.2	172	1996	5.1	24	6.37	1999.4	5.4
Central Asia											
1	1990:06:20	37.0, 49.1	7.4	34.6, 51.4	798	1949	5.3	223	5.29	1972.5	5.6
2	1992:08:19	42.1, 73.6	7.2	42.2, 75.0	306	1963	5.3	39	5.48	1977.5	5.5
3	1997:02:27	30.0, 68.2	7.0	27.8, 70.0	510	1940	5.2	115	4.90	1976.1	5.5
4	1997:05:10	33.9, 59.8	7.3	30.5, 63.2	622	1942	5.5	66	5.00	1980.7	5.9
5	1997:11:08	35.1, 87.4	7.5	36.4, 87.7	690	1940	5.2	151	4.79	1983.0	5.5
6	2000:12:06	39.6, 54.8	7.0	39.4, 54.1	488	1958	5.2	92	5.20	1981.1	5.4
7	2001:01:26	23.4, 70.2	7.6	25.8, 68.2	701	1955	5.5	31	5.03	1981.6	5.8
8	2001:11:14	35.9, 90.5	7.8	37.9, 94.7	654	1948	5.4	65	4.91	1982.5	5.7
9	2005:10:08	34.5, 73.6	7.5	31.5, 73.7	586	1976	5.3	75	5.27	1988.6	5.6
South America											
1	1995:10:09	19.1, -104.2	7.9	22.1, -103.2	1565	1966	5.6	166	5.04	1979.0	5.9
2	2001:01:13	13.0, -88.7	7.7	10.0, -87.2	1020	1965	5.5	259	5.34	1983.3	5.8
3	2001:06:23	-16.3, -73.6	8.3	-18.8, -74.1	1062	1965	5.6	196	5.33	1981.4	5.9

magnitude scale. These data must also be complete, that is, to include all preshocks which occurred in certain region and certain time period and have magnitudes larger than a certain value. The epicenter locations have an error of less than 30km which is satisfactory for the present work which concerns circular regions (critical regions) with radii of hundreds of kilometers. The error in magnitudes is less than 0.3 which is also satisfactory for the purpose of the present work. All magnitudes are in the moment magnitude scale or converted to this scale form other scales (m_b, M_s, M_{JMA}) by appropriate formulae (Scordilis, 2005, 2006).

Complete data are needed for two purposes. The first purpose is to calculate the Benioff strain rate, s_a (in Joule$^{1/2}$/year.10^{4}Km^2), which is needed in the present work. Data of preshocks with M≥5.2 are used for this purpose. Such complete data (with M≥5.2) are available since 1911 for the whole Mediterranean (W. Mediterranean, Aegean, Anatolia), since 1930 for California, since 1926 for Japan, since 1940 for central Asia and since 1965 for South America. The second purpose for which complete data are needed is the calculation of the Benioff strain for the whole duration of each preshock sequence (from the start time, t_s, of each sequence to the origin time, t_c, of the mainshock) in order to reliably calculate the average time,   , and the average magnitude,   , of each sequence. We checked very carefully all 45 sequences and found
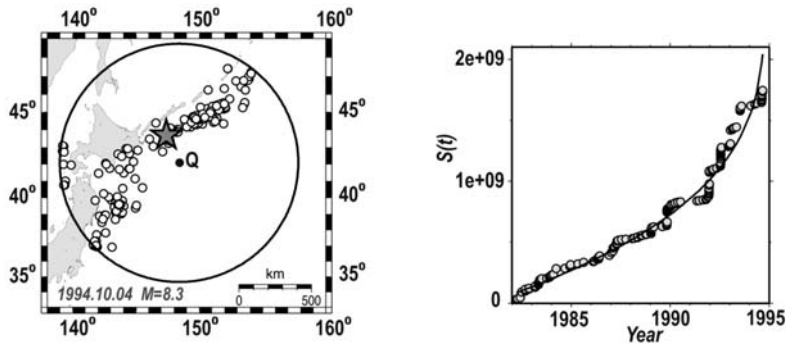
Fig. 1. The circular critical region where accelerating preshocks (open circles) occurred before the generation of the big (M=8.3) mainshock of October 4, 1994 in northern Japan (43.7ºN, 147.4ºE). The star denotes the mainshock epicenter while Q is the center of the circular region (solid circle). On the right of the map, the time variation of the cumulative Benioff strain, S(t), for the accelerating preshocks is given. The solid line represents fitting to the data of a power-law (relation 1).
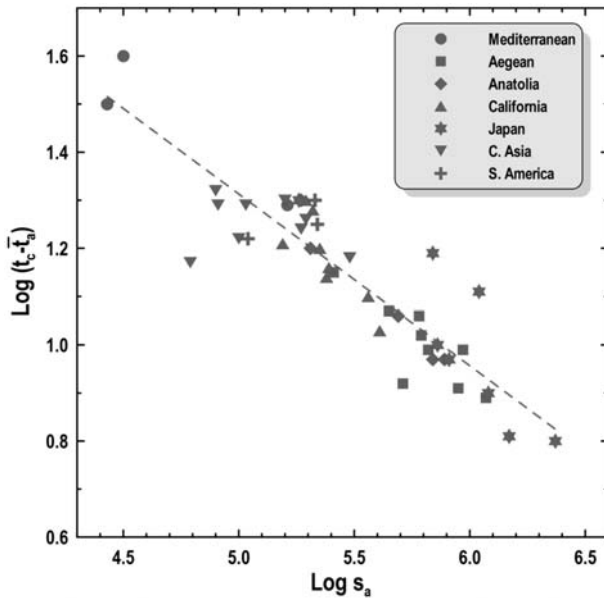

Fig. 2: Variation of the logarithm of the time difference between the origin time, t_c, of the mainshock and the mean origin time, , of accelerating preshocks with the logarithm of the Benioff strain rate, s_a, in the preshock (critical) region. The data are fitted by a straight line (dashed line) in the least-squares' sense.

that all sequences are complete for the corresponding periods between t_s and t_c. Such catalogues, for each of the regions considered, have been already compiled for the needs of other studies where details on the procedure followed are given (Karakaisis et al., 2006; Papaioannou et al., 2006; Papazachos et al., 2006c; Scordilis et al., 2006;).

3. Procedure Followed

The circular regions where accelerating preshocks occurred have been identified and the start time, t_s, of each accelerating preshock sequence has been calculated in previous work (Papazachos et al., 2005, 2006a). The fifth and sixth column of Table (1) list the geographic coor-
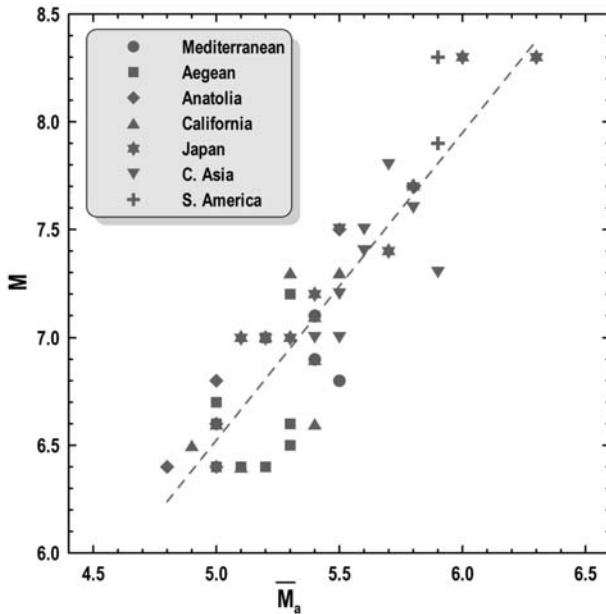
Fig. 3: Variation of the mainshock magnitude, M, with the mean magnitude, , of accelerating preshocks. The data are fitted by a straight line (dashed line) in the least-squares' sense.

dinates of the center, Q, and the radius, R (in km), of each circular region (critical region) where the epicenters of accelerating preshocks are located. In the same table the start time, t_{sa} (in years), the minimum preshock magnitude, M_{min}, and the number, n, of accelerating preshocks are also listed. These listed values have been defined by constraints put by the D-AS model which was developed on the basis of observations and theoretical considerations (Papazachos et al. 2005, 2006a).

It has been shown (Papazachos et al., 2006b) that the cumulative Benioff strain is increasing with the time to the mainshock, according to the power law relation (1), up to a certain time, t_e, (about 3 years before the generation of the mainshock) and then it declines. This decrease of the Benioff strain during the last phase of the accelerating sequence is due to increase of the frequency and mean magnitude of preshocks. The left part of figure (1) shows the circular critical region, its center, Q, the epicenters of accelerating preshocks and the epicenter of the big mainshock (M=8.3) which occurred on 4.10.1994 in northern Japan. The right part of this figure shows the time variation of the cumulative Benioff strain for these preshocks.

The time, t_e, when this decrease starts is accurately determined by a plot of a quality index, q_a, as a function of the time to the mainshock, while the time when this index gets its largest value is the time, t_a, when declination starts (Papazachos et al., 2006b).

For this reason, preshocks which occurred between the start time, t_s, of each sequence and the time, t_e, when the decrease of the Benioff strain starts, have been considered. The average of the origin time and the average of the magnitude of these shocks have been calculated for each preshock sequence. The calculations of the mean preshock time, , and of the mean preshock magnitude, , were repeated by taking in all 45 cases t_e equal to the origin time of the mainshock minus three years. It was found that the calculated values remained almost unchanged, which shows the robustness of estimations of and .

4. Results

Accelerating preshock seismic strain in the critical region starts decreasing at certain time, t_e, before the mainshock. For this region we considered in the present paper the mean time, ⎯, and the mean magnitude, ⎯, of the accelerating preshocks that occurred from the start time, t_s, up to the time t_e. The values of ⎯ and ⎯ are listed in Table (1).

Figure (2) shows a plot of the logarithm of the time difference, ⎯, between the origin time of the mainshock, t_c, and the mean origin time, ⎯, of the accelerating preshocks against the logarithm of the Benioff strain rate, $\log s_a$. The data are fitted, in the least squares' sense, by the relation:

$$ \tag{2} $$

Figure (3) shows a plot of the mainshock magnitude against the mean magnitude, ⎯, of accelerating preshocks. The data are fitted, in the least squares' sense, by the relation:

$$ \tag{3} $$

where σ, in both relations (2) and (3), is the standard deviation.

Relations (2) and (3) fit well a large sample of data and are of global validity because these data concern regions of a variety of seismotectonic regimes and of several levels of seismicity (with values of $\log s_a$ from 4.5 for west Mediterranean to 6.5 for Japan). These relations can be used as additional constraints for the estimation (prediction) of the origin time and magnitude of an ensuing mainshock by the D-AS or any other predicting model.

5. Discussion

In the D-AS model developed by Papazachos et al., (2006a) one of the constraints on which the estimation (prediction) of the origin time, t_c, of the ensuing mainshock is based, is a relation similar to relation (2). In that relation the start time, t_{sa}, of the accelerating preshock sequence is used instead of ⎯ which is used in the present work. The data in this relation are more scattered (σ=0.10) than the data used to derive relation (2) (σ=0.07), although both procedures were applied in the same preshock sequences. In the beginning of an accelerating sequence the frequency of preshocks is very small and almost indistinguishable from the background seismicity. This has an effect on the accuracy of definition of t_{sa} which then affects the accuracy of estimation (prediction) of the origin time, t_c, of the mainshock. On the contrary, ⎯ is based on the origin time of a large number of preshocks and for this reason is robust which results in more accurate estimation (prediction) of the origin time of the probably ensuing mainshock.

The mean magnitude, ⎯, of the three largest accelerating preshocks is also used by the D-AS model as a constraint for the estimation (prediction) of the mainshock magnitude (Papazachos et al., 2005, 2006a). Similarly, ⎯ is based on a much larger sample of observations and for this reason its estimation is more reliable. This justifies the use of relation (3) as an additional constraint for the estimation (prediction) of the mainshock magnitude.

The results of the present work are based on the origin times and magnitudes of preshocks occurred up to the time t_e (about three years before the occurrence of the mainshock). This puts

a limit to the estimation of the mainshock origin time and magnitude by this procedure, because relations (2) and (3) cannot be applied until the time when the maximum value of the quality index is observed. The identification of that time suggests a continuous monitoring of the seismic activity of the area where a D-AS pattern is observed. As a result of this monitoring the initial estimation (prediction) of the parameters can be improved by the use of newly coming additional data. The results of the present work can contribute to such an improvement in the estimation of the origin time and magnitude of an ensuing mainshock.

Relations similar to (2) and (3) probably hold for decelerating preshocks. The available data, however, do not allow, at present, the definition of such relations for decelerating preshocks because these are much smaller than accelerating ones and for this reason strict completeness of data samples comprising small magnitudes is difficult to be achieved.

6. Acknowledgements

7. References

Ben-Zion, Y. and Lyakhovsky, V., 2002. Accelerated seismic release and related aspects of seismicity patterns on earthquake faults, *Pure and Appl. Geoph.* 159, 2385-2412.

Bowman, D.D., Quillon, G., Sammis, C.G., Sornette, A. and Sornette D., 1998. An observational test of the critical earthquake concept, *J. Geophys. Res.* 103, 24359-24372.

Bowman, D.D. and King G.C., 2001. Accelerating seismicity and stress accumulation before large earthquakes, *Geophys. Res. Lett.* 28, 4039-4042.

Brehm, D.J. and Braile L.W., 1999. Intermediate-term earthquake prediction using the modified time-to-failure method in southern California, *Bull. Seism. Soc. Am.* 89, 275-293.

Bufe, C.G. and Varnes D.J., 1993. Predictive modeling of seismic cycle of the Great San Francisco Bay Region, *J. Geophys. Res.* 98, 9871-9883.

Karakaisis, G.F., Savvaidis, A.S, and Papazachos, C.B., 2003. Time variation of parameters related to the accelerating preshock crustal deformation in the Aegean area, *Pure Appl. Geophys.* 160, 1479-1491.

Karakaisis, G.F., Scordilis, E.M., Papazachos, C.B. and Papazachos, B.C., 2006. A catalogue of earthquakes in California for the period 1901-2006, *Publ. Geoph. Laboratory, University of Thessaloniki.*

King, G.C., and Bowman D.D., 2003. The evolution of regional seismicity between large earthquakes, *J. Geophys. Res.* 108(B2), 2096, doi:10.1029/2001JB000783.

Knopoff, L., Levshina, T., Keilis-Borok, V.J. and Mattoni C., 1996. Increase long-range intermediate-magnitude earthquake activity prior to strong earthquakes in California, *J. Geophys. Res.* 101, 5779-5796.

Papaioannou, Ch.A., Scordilis, E.M., Papazachos, C.B., Karakaisis, G.F. and Papazachos, B.C., 2006. A catalogue of earthquakes in central and south America for the period 1900-2006, *Publ. Geoph. Laboratory, University of Thessaloniki.*

Papazachos, B.C., Scordilis, E.M., Papazachos, C.B. and Karakaisis, G.F., 2006b. A forward test of the precursory decelerating and accelerating seismicity model in California, *J. Seismology* 10, 213-224.

Papazachos, B.C., Comninakis, P.E., Scordilis, E.M., Karakaisis, G.F. and Papazachos, C.B., 2006c. A catalogue of earthquakes in Mediterranean and surrounding area for the period 1901-2006, *Publ. Geoph. Laboratory, University of Thessaloniki.*

Papazachos, B.C., Karakaisis, G.F., Papazachos, C.B. and Scordilis, E.M., 2007. Evaluation of the Results for an Intermediate-Term Prediction of the 8 January 2006 M_w 6.9 Cythera Earthquake in the Southwestern Aegean, *Bull. Seism. Soc. Am.* 97, 347-352.

Papazachos, C.B., Karakaisis, G.F., Scordilis, E.M. and Papazachos B.C., 2005. Global observational properties of the critical earthquake model, *Bull. Seism. Soc. Am.* 95, 1841-1855.

Papazachos, C.B., Karakaisis, G.F., Scordilis, E.M. and Papazachos B.C., 2006a. New observational information on the precursory accelerating and decelerating strain energy release, *Tectonophysics* 423, 83-96.

Rundle, J.B., Turcotte, D.L., Shcherbakov, R., Klein, W. and Sammis, C., 2003. Statistical physics approach to understanding the multiscale dynamics of earthquake fault systems, *Rev. Geophys.* 41, 5/1-5/30.

Scordilis, E.M., 2005. Globally valid relations converting M_s, m_b and M_{JMA} to M_w, *Meeting on earthquake monitoring and seismic hazard mitigation in Balkan countries. NATO ARW, Borovetz , Bulgaria, 11-17 September 2005*, 158-161.

Scordilis, E.M., 2006. Empirical global relations converting M_s and m_b to moment magnitude, *J. Seismology* 10, 225-236.

Scordilis, E.M., Papazachos, C.B., Karakaisis, G.F. and Karakostas,V.G., 2004. Accelerating seismic crustal deformation before strong mainshocks in Adriatic and its importance for earthquake prediction, *J. Seismology* 8, 57-70.

Scordilis, E.M., Papazachos, C.B., Karakaisis, G.F. and Papazachos B.C., 2006. A catalogue of earthquakes in central Asia for the period 1901-2006, *Publ. Geoph. Laboratory, University of Thessaloniki.*

Sornette, D., and Sammis C.G., 1995. Complex critical exponents from renormalization group theory of earthquakes: implications for earthquake predictions, *J. Phys. I.* 5, 607-619.

Sykes, L.R. and Jaumé S., 1990. Seismic activity on neighboring faults as a long term precursor to large earthquakes in the San Francisco Bay area, *Nature* 348, 595-599.

Tocher, D., 1959. Seismic history of the San Francisco bay region, *Calif. Div. Mines Spec. Rep.* 57, 39-48.

Tzanis, A., Vallianatos, F. and Makropoulos K., 2000. Seismic and electrical precursors to the 17-1-1983, M=7 Kefallinia earthquake, Greece, signatures of a SOC system, *Phys. Chem. Earth (a)* 25, 281-287.

Varnes, D.J., 1989. Predicting earthquakes by analyzing accelerating precursory seismic activity, *Pure Appl. Geophys.* 130, 661-686.

Wessel, P. and Smith, W., 1995. New version of the Generic Mapping Tools, *EOS* 76-329.

ON THE SENSITIVITY OF GROUND MOTION PREDICTION EQUATIONS IN GREECE

Segou M., Voulgaris N., Makropoulos K.

Department of Geophysics-Geothermics, Faculty of Geology and Geoenvironment, Panepistimioupoli Zografou, Athens - Greece 15784, msegou@geol.uoa.gr, voulgaris@geol.uoa.gr, kmacrop@geol.uoa.gr

Abstract

Ground motion prediction equations, widely known as attenuation relations, are common input for probabilistic and deterministic seismic hazard studies. The construction of a ground motion model to describe such a complex phenomenon as the effects of seismic wave propagation is highly dependable on a number of parameters. The quality and the distribution of strong motion data, which is the original input for the calculation of any ground motion model, can be thought as one of the main parameters that heavily influence the form of ground motion prediction equations. The selected processing scheme, involving significant choices about a series of adjustments and filter specifications, implemented to remove low and high frequency noise, is related with the credibility of the calculated ground motion parameters such as the spectral ordinates. Once a set of response variables for a number of predictors is available, the researcher's interest is related with the mathematical definition of the ground motion model, in terms of selecting the appropriate parameters and the determination of their coefficients of the equation. Another significant part involves the selection of the optimum solver in order to achieve high confidence level coefficients and a computationally inexpensive solution. Each method should be evaluated through statistics but the researcher should bear in mind that residual analysis and statistical errors, although they can adequately represent the efficiency of the mathematical equations, do not always provide information about where our efforts should lie in terms of further improvement. The scope of this paper is to point out the multi-parametric nature of the construction of ground motion prediction equations and how each of the aforementioned development stages influences the credibility of the proposed attenuation relations.

Key words: processing scheme, corrected acceleration, spectral ordinates, attenuation, mathematical model, earthquake engineering.

1. Introduction

The estimation of ground motion is an important tool for engineering seismology especially in terms of seismic hazard studies. Since the Long Beach earthquake in 1933 the scientific interest lies in calculating ground motion displacement from the accelerogram. During the last decades many researchers (Converse and Brady, 1992; Boore, 2008, Boore and Bommer, 2005) suggested different processing schemes for deriving corrected time series and spectral ordinates. The credibility of spectral acceleration is directly linked with the construction of ground motion prediction relations. In the effort of deriving an elaborate but subtle processing scheme a number of tests have been conducted and their results helped determining the suggested processing procedure. In addition, a sensitivity

test has been performed partly through statistical analysis, exploring how spectral ordinates can be influenced by the processing scheme.

In this paper we evaluate the multi-parametric nature of ground motion prediction equations construction which involves the determination of the mathematical model and the selection of the appropriate algorithm for solving the strong ground motion equation.

2. Data resources

The database used in this study consists of 434 three-component strong motion records provided – in their uncorrected form- by the internet site of the European Strong Motion Database[1], the Geodynamic Institute of the National Observatory of Athens[2] and ITSAK[3]. Strong motion records had been reprocessed following a subtle processing scheme to ensure minimum influence on the derived spectral ordinates.

During the first steps of the database's development a larger number of strong motion records has been closely reviewed and a quality factor has been assigned by following a number of criteria listed in Douglas (2003) in order to exclude poor quality records from ground motion prediction equation development.

Metadata information plays an important role in compiling a database for engineering seismology studies. In terms of faulting type seismic events are characterized as having normal, strike slip and thrust or reverse rupture. However, site conditions is one of the most critical parameters. Soil site conditions are characterized by following the NEHRP site categorization using the value of the shear wave velocity on the upper 30 m (V_{s30}) as a criterion for assigning a site class. However, the problem lies in the availability of V_{s30} since only 42 percent corresponds to a measured geophysical parameter. A list of criteria has been issued by following the standards of NGA project (Darragh and Power, 2005) with some modifications to assign a V_{s30} value in sites with missing metadata information.

In the following table we present the distribution of strong motion data through site classes and faulting types, after assigning critical metadata information.

Table 1.

Site class	NEHRP	Normal	Reverse	Strike-Slip	Total
ROCK	A&B	42	24	20	86 (~19.81%)
STIFF SOIL	C	87	27	96	220(`50.69%)
SOFT SOIL	D&E	54	30	54	138(~31.79%)
		183 (~42,16%)	81 (~18,66)	170 (~39,17%)	

---

3. Processing Scheme

The final database contains strong motion data from Greece, Italy, Turkey and Iran which have been reprocessed by individual component. Although the majority of the data used comes from Greece, 271 records, in order to achieve a more complete magnitude-distance distribution of the data the final database included a number of events from the aforementioned countries of similar seismo-tectonic environment. For homogenising the magnitude scales we have used the re-determined epicenter coordinates and body wave magnitude available at the internet site of the International Seismological Center. It is noted that Scordilis (2006) empirical relation had been used for converting into moment magnitude. Strong motion record processing has been performed with Proschema software (Segou and Voulgaris, 2010). Instrument adjustment has been applied for analogue records whereas for digital records this was not necessary due to the flat instrument response over a wide period range. Filter design involved a fourth order bandpass Butterworth followed by phase preserving implementation with varying cut off frequencies in order to sufficiently remove the noise without damaging the frequency content of interest. In some cases before filtering a cosine taper was applied at the edges of the time series to reduce Gibb's effect. Two main points closely related to filtering should be pointed out; the first one is related to the selection of the integration operator since ground motion velocity and displacement should be eventually provided and the second one to the decision whether computations should take place in the time or frequency domain. Concerning the first point results favoured the use of the ideal integrator, with frequency response equal $1/i\omega$ whereas for the second question the authors believe that frequency domain implementation is more consistent. Of course Plancerel theorem supports either choice but since both the noise identification and evaluation of filter implementation afterwards, involve Fourier spectrum representation, frequency domain computation sufficiently deals with the problem in hand. Additionally, frequency domain computation is more time effective which is an important aspect when processing a great number of strong motion records.

Response spectra have been calculated through the analytical solution of Nigam and Jennings (1969) for damping values equal 0%, 2%, 5%, 10% and 20% of the critical damping. In order to avoid uncertainty, related at such an early stage with the orientation of the instrument's transducers, we have calculated response spectra for a damping value equal 5% of the critical damping for the ground motion measure, known as GMRotI50, introduced by Boore et al. (2006), which corresponds to the orientation independent geometrical mean of the two horizontal components. For each type of response spectra the Usable Data Bandwidth (UDB) is provided to ensure further use of credible spectral acceleration values within these limits.

Analytical documentation of the processing scheme followed during database development can be found in Segou et al. (2008).

3.1. The influence of the processing scheme on spectral ordinates

The remaining question is the influence of the decisions described in the last paragraph on the derived spectral ordinates, further used in implementing ground motion prediction equations. In order to demonstrate the differences caused by following another processing scheme we compared intermediate products and spectral ordinates of the suggested processing scheme and the one followed by the European Strong Motion Database. This comparison included almost 250 strong motion records and it has been extended to peak ground acceleration and velocity as well as pseudo-spectral acceleration and velocity for damping values equal 0% and 5% of the critical damping.
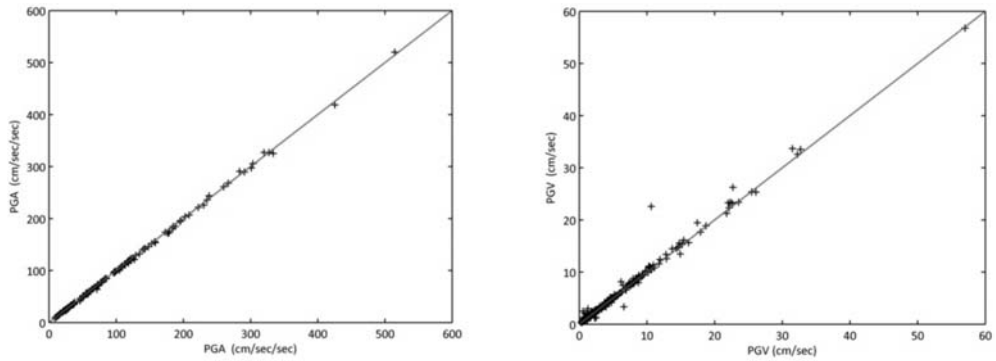
Fig. 1a-b: Influence of processing schemes on the estimation of spectral parameters. Diagram showing peak ground acceleration and velocity derived from the current processing scheme versus the ones from the European Strong Motion Database. It is also noted that the comparison is carried out for the maximum horizontal component.

Figure 1a and 1b correspond to peak ground parameter comparison showing that peak ground velocity is more influenced by the selected processing scheme. The above remark has been in fact anticipated since it is the peak ground velocity's characteristic to emphasize medium to long periods.

As far as spectral parameters (fig. 2-3) are concerned the influence observed is directly linked to the period estimator under consideration. To illustrate the differences we collate response spectra calculated from a digital strong motion record for pseudo-spectral acceleration and velocity. In figure 2a undamped spectral ordinates of ESMD appear having higher values at short periods (up to 1 sec) which can be related with the analytical solution of Chopra (1995) followed by the agency. Although, both analytical solutions, the one of Nigam and Jennings (1969) and Chopra (1995), derive credible response spectra the authors found that the latter solution is often linked with the presence of some irregular peaks in lower damping values. Once again the differences due to the vicinity of filter's cut off frequencies are evident at long periods, especially at the pseudo-spectral velocity response spectra. The diagrams in figure 3 of period estimators at 0.1 sec and 2 sec point out the benefits of using a subtle processing scheme. The strong non linear behaviour of frequency response of elliptical filters near the pass band is responsible for the distortion of the spectral ordinates near the cut off frequencies.

4. The mathematical model of the ground motion prediction equation

The scope of this paragraph is to point out the differences of the mathematical models used in the first stage of the development of a new set of ground motion prediction equations. However, it should be noted that the presentation of the derived equations with the necessary analytical description of the suggested method is beyond the scope of this paper.

The basic mathematical model of attenuation relations can be described by the following form given by Campbell (2003)

$$\ln Y = a + b\,M - c\,\ln D - d\,R + e\,F + f\,S + \varepsilon \tag{1}$$

In the equation above the logarithm of the ground motion is described as a function of magnitude M, R equals the source-to-site distance, D a diversified distance metric whereas F and S correspond to dummy variables for modelling fault type and soil site conditions. In other words in any mathe-
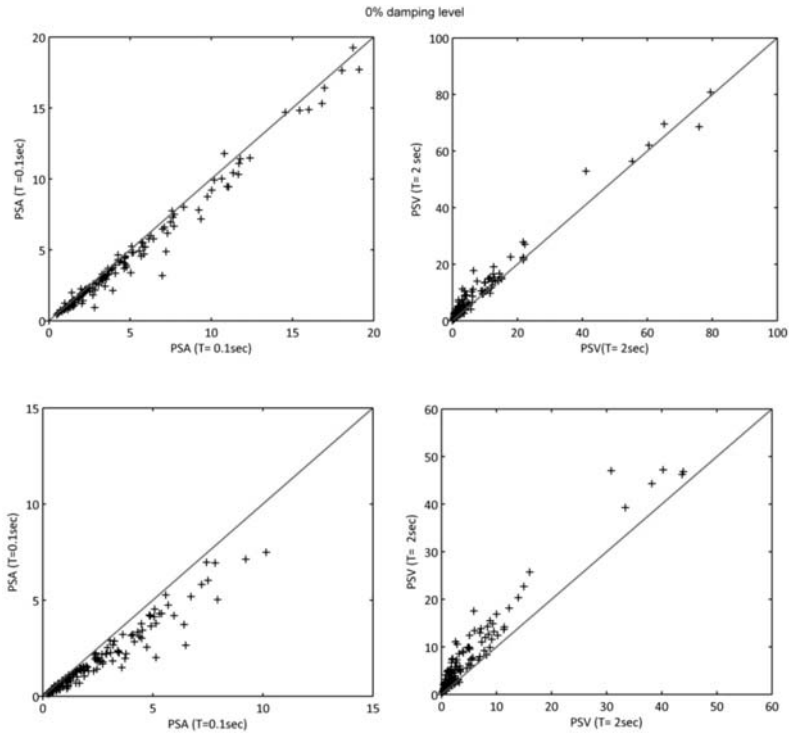
Fig. 2a-b: Influence of processing schemes on the spectral parameters. Comparison of pseudo-spectral acceleration and velocity for 0% and 5% damping, of the current processing scheme and the ESMD.

matical model we can distinguish independent variables, represented by the physical observations, predictors expressing the main modelling parameters, corresponding to magnitude and distance, and the remaining parameters implicitly represent random variables of the model.

However, depending on the available data and recent trends in engineering seismology the described model above can be significantly altered. In this paper we use two types of mathematical models in order to point out the influence of latter.

The first mathematical model (M1) is given by the equation (2)

logY = a + b M + c M2 - d log[R2 + (d - h)2] 1/2 + e1 N + e2 SS + e3 RS + f1 STS + f2 SFS + εσ1

The main difference with the basic equation (1) is the inclusion of a squared magnitude term and the representation of distance metric in terms of epicentral distance R and focal depth d. The consideration of epicentral distance and depth is important to adequately model the source-to-site distance since we cannot determine a common depth for seismic events due to different geotectonic environments in the broader Greek area. The square magnitude term prevents saturation of ground motion for close distances and large magnitudes. In terms of faulting type, represented with e1…3 dummy variables we found normal and strike slip ground motions very close whereas reverse faulting tends to exhibit stronger ground motions. As far as site conditions, stiff and soft soil sites correspond to amplified, by a constant factor, ground motion.
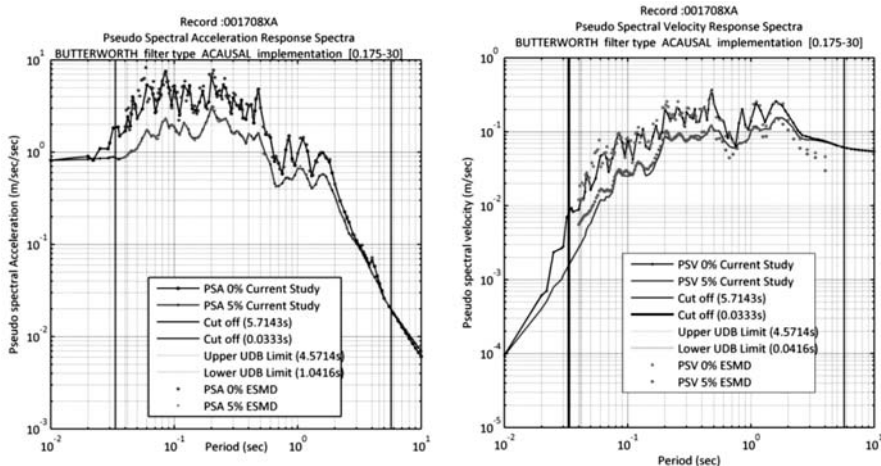
Fig. 3a-b: Influence of processing schemes on the estimation of spectral parameters. Diagrams showing spectral ground motion parameters of the current processing scheme versus the ones from European Strong Motion Database, the pseudo-spectral acceleration and velocity for 0% and 5% damping level and for 0.1 , 1 and 2s period of interest.

The second mathematical model (M2) is given by the equation (3)

$$logY = a + b\ M + c\ M2 - d\ log[\ R2 + (d - h)2]\ 1/2 + e1\ N + e2\ SS + e3\ RS + f\ (M,R,Vs30) + εσ2$$

The difference between the two mathematical models concerns the term introduced for site conditions. In equation (2) the terms f1 STS, f2 SFS representing a linear amplification model had been replaced by a function f (M,R,Vs30) predicting linear and non-linear amplification factors. To calculate linear and non-linear amplification terms we followed the methodology introduced by Boore and Atkinson (2008) as part of the Next Generation Attenuation project of Pacific Earthquake Engineering Research Institute. Spectral amplification coefficients proposed in Boore and Atkinson (2008) were considered to be an improvement of the ones suggested in Choi and Stewart (2005) and they have been further used in this research study.

It should be noted that there is a clear distinction between the last two equations in terms of modeling soil site conditions. In equation (2) soil conditions are represented through NEHRP site class categories and soil site amplification factors are provided for stiff and soft soil sites corresponding to site class C and D. It is noted that strong motion data of site class A and B were considered as corresponding to rock site condition. Equation (3) allows for continuous values of shear wave velocity measured at the upper 30 m (Vs30) but in any case we should point out the broad range of Vs30 values in each NEHRP site class category.

4.1. The influence of the mathematical model

To determine the influence of the mathematical model we conducted pure error analysis as originally suggested in Douglas and Smit (2003) in magnitude-distance bins separately for each soil site class and faulting type. The length of each bin has been determined equal with 0.2 units of magnitude and 5 km distance. In case the number of earthquakes exceeded three, the error has been determined as the average absolute residuals. No trends in the residuals have been revealed through this practice but this is due to the scarcity of strong motion data inside the bins.
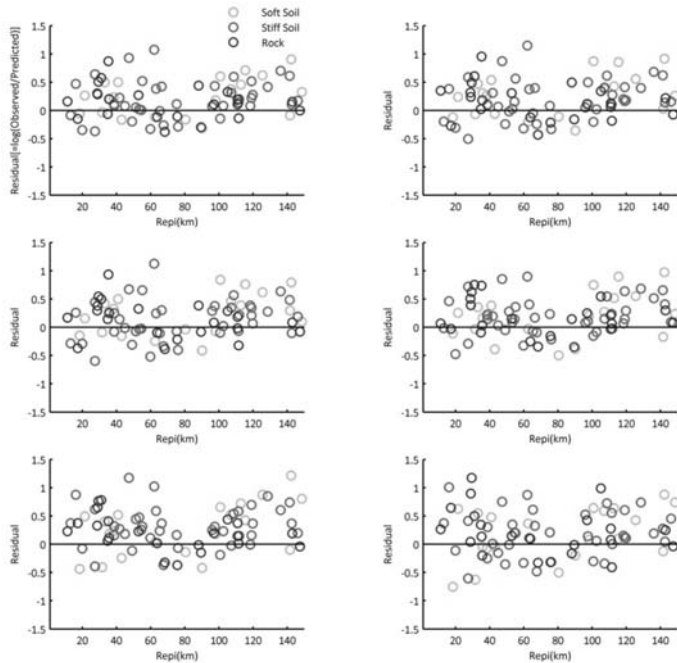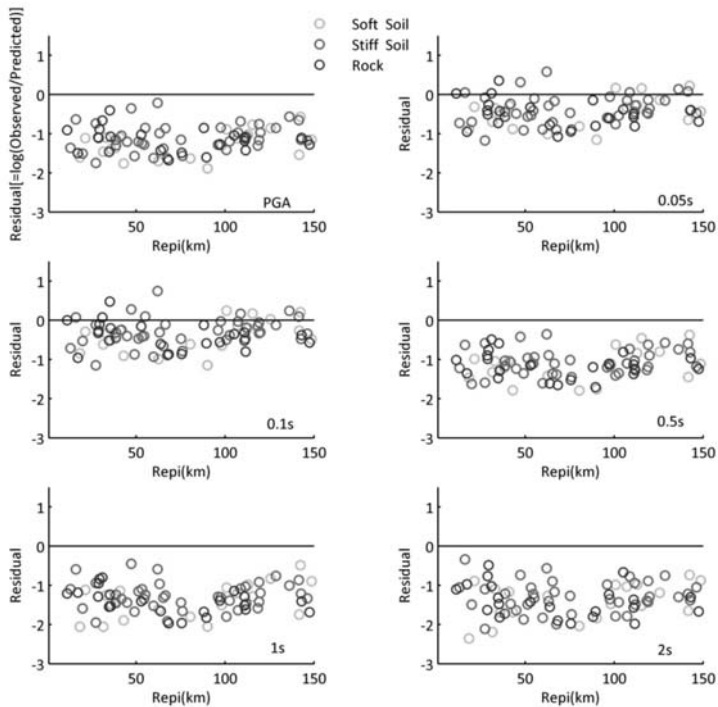
Fig. 4: Residual analysis of the approach considering linear terms for soil site conditions (eq.2). Diagram of residuals versus distance for different soil classes for discrete period estimators.

Additionally, typical residual analysis has been implemented for predicted ground motion estimated from the two mathematical models for spectral acceleration for various period estimators as well as peak ground acceleration. In figures 4 and 5 the residuals are calculated as the difference of the logarithm of the estimated from the logarithm of the predicted ground motion. From the comparison of figures 4 and 5 the suggested mathematical model corresponds to equation (2), since the residuals of the mathematical model proposing a linear term for soil behaviour yields better distributed residuals (fig. 4) than mathematical model of equation (3), incorporating a non linear term for modelling soil behaviour. The reasons behind the difference concerning the distribution of the residuals can be found in site classification and on the quality of the metadata information. Analytically, since there is no measurement in Greece for the Vs30 value of reference site conditions, we considered it to be equal with 760 m/s by following standards of NGA project (Darragh and Power, 2005); nevertheless this is acknowledged to be a possible source of error.

Of course in close relation with the aforementioned observation is the fact that there is a broad range of Vs30 values in each NEHRP site class category but in residual analysis we arbitrary decided that rock, stiff and soft soil conditions correspond to 760 m/s, 520 m/s and 250 m/s respectively.

5. Selecting the appropriate mathematical solver

Based on the maximum likelihood criterion statistical analysis provides a systematic procedure known as regression analysis for the empirical determination of the mathematical model between observed values and model predictors. However in the case under study the mathematical model is expressed through a non-linear equation imposing limitations concerning its solution. Since linearization of equation (2) through a set of linear equations would not adequately represent the

Fig. 5: Residual analysis of the approach considering non linear terms for soil site conditions (eq.3). Diagram of residuals versus distance for different soil classes for discrete period estimators.

problem in hand we had to consider steepest decent and Levenberg - Marquandt as possible solvers for determining the coefficients of equation (2) by regression analysis. The results of combining the aforementioned solvers are given in figure 6. The problem is nearly obvious, not very good magnitude scaling and there is no way to control the coefficients in order to be consistent with their physical meaning. Another disadvantage has been the necessity for providing initial conditions for the model's coefficients in order for regression analysis to begin. This actually implies that the final results are strongly driven by our initial guess.

Another possibility for solving the mathematical equation is related with optimization techniques. Whereas regression analysis provides a unique fit for the model, optimization leads to the determination of the best solution among other good solutions for the given problem. The "problem" corresponds to an objective function (model) describing the minimization of the residuals between predicted and observed ground motion. Following the minimization path there are many possibilities for selecting the appropriate mathematical solver; deterministic algorithms using least squares rule or stochastic ones, like Genetic Algorithms (GA), Simulated Annealing (SA) and Pattern Search (PS), known in programming as direct search methods.

In first place the theoretical aspects of these algorithms have been taken into consideration. Afterwards a crash-test for the efficiency of these algorithms has been designed in order to select the appropriate mathematical solver for equation (2). The aforementioned test involved comparison of the ground motion prediction equations, presented in figure 7, derived with constrained minimization through (1) non-linear least squares (LSQ), (2) non-linear least squares augmented by initial popu-
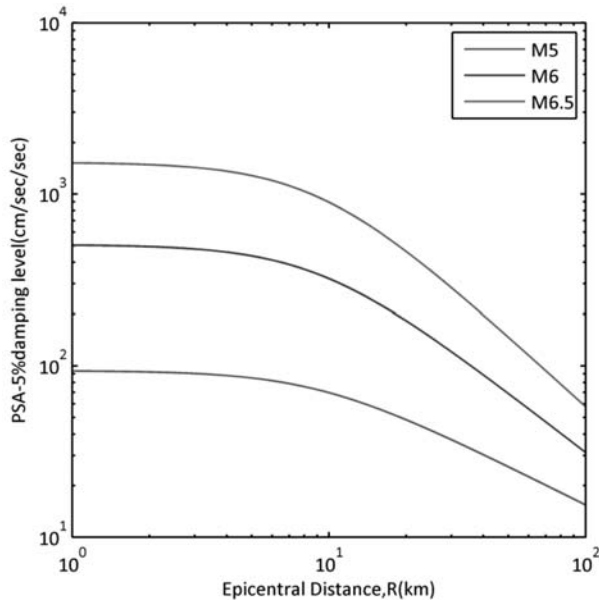
Fig. 6: Coefficient determination through regression analysis. Traditional regression analysis in least squares sense supports the implementation of mixed effects method to determine the coefficients of the mathematical model described by equation 2.

lation development (LSQP), (3) Genetic Algorithm (SGA), (4) Genetic Algorithm augmented by initial population development (GADP), (5) Hybrid Genetic Algorithm (HGA), corresponding to Genetic Algorithm solution refined with deterministic algorithm implementation for local search, (6) deterministic algorithm used in the solver previously suggested (CONMIN), (7) Pattern Search algorithm (PS) and (8) Simulated Annealing (SA).

5.1. The influence of the mathematical solver

In figure 7 the ground motion predictions equations are presented, following the mathematical model of eq. (2) for which the coefficients have been determined each time with a different mathematical solver. The algorithms converge to almost the same solution when a sufficient number of data is present, in other words different algorithms handle data scarcity in different ways. An advantage of using Genetic Algorithms supported by Diverse Population development (GADP) is that magnitude scaling is captured nicely, by taking into consideration even few observations corresponding to close distance range. The ability of optimization techniques to conform to the whole set of the observations and not only to carefully selected convenient observations is considered to be a major strong point.

Even though developed 50 years ago, it was only recently that Genetic Algorithms had been used in solving seismological problems. The stochastic nature expressing the ability to explore natural systems characterized for their complexity constituted their main advantage.

6. Conclusions-Results

In this paper we have focused on the multi-parametric nature of the construction of ground motion prediction equations. The scope had been to determine the possible sources introducing errors in
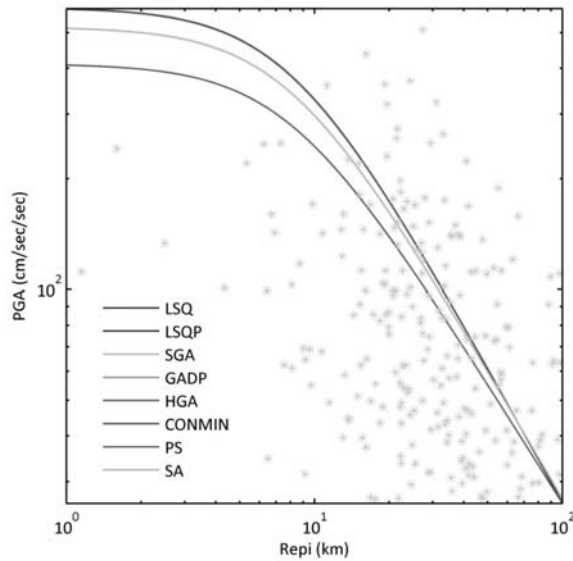
Fig. 7: Coefficient determination through optimization. Under LSQ and LSQP, non linear least square optimization without and with development of initial population, under SGA, GADP and HGA the simple genetic algorithm, the genetic algorithm with development of initial population with Latin Hypercube, and the hybrid genetic algorithm with combined use of deterministic elements for local search, CONMIN the aforementioned algorithm of deterministic nature whereas under PS and SA is noted the pattern search and simulated annealing algorithm. Points in the diagram represent data corresponding only the rock site conditions and normal style-of-faulting, used in the first stage of the determination of coefficients of the mathematical model in equation 2.

the procedure and suggest a course of action in order to derive spectral ground motion prediction equations.

The processing scheme has an important role in deriving credible spectral ordinates and its development should be based on protecting the actual frequency content while removing in the more subtle way the indentified noise.

The distribution of data in terms of magnitude and distance is the controlling factor of the construction of ground motion prediction equations. A dense distribution concerning the type of faulting and soil conditions can easily foreshadow the trends of strong ground motion whereas a poor one may reflect in some cases non typical behaviour especially for spectral acceleration of specific period estimator. The quality of the distribution is closely related with the following selection of the mathematical model.

The mathematical model includes predictors, independent and random variables. In this paper we examined the efficiency behind distance metrics and the modelling term of soil site conditions. Linear terms predicting constant site amplification for stiff and soft soil sites and a combination of linear and non-linear amplification factors has been introduced forming two different mathematical models. Quite explicitly linear modelling of soil conditions provides better ground motion prediction which is also observed when studying the residuals.

Depending on the mathematical model the last important selection is related with the mathematical solver responsible to determine the coefficients of the mathematical model. Regression analysis versus optimization techniques combined with a number of different algorithms such as Genetic Algo-

rithms have been compared. The results of the minimization problem derived from genetic algorithm with stochastic elements such as mutation, survival and crossover augmented by initial population development with Latin Hypercube design have proven to be the most credible.

The systematic analysis of the parameters that influence the construction of strong ground prediction equations pointed out usual pitfalls of the procedure.

7. Acknowledgements

8. References

Boore, D. M. 2008. TSPP—-A Collection of FORTRAN Programs for Processing and Manipulating Time Series. *U.S. Geological Survey* Open-File Report 2008-1111 (Revision 1.6).

Boore, D. M., and Atkinson, G. M. 2008. Ground-motion prediction equations for the average horizontal component of PGA, PGV, and 5%-damped PSA at spectral periods between 0.01 s and 10.0 s. *Earthquake Spectra*, 24, 99-138.

Boore, D. M., and Bommer, J. J. 2005. Processing of strong-motion accelerograms: needs,options and consequences. *Soil Dynamics and Earthquake Engineering*, 25, 93-115.

Chopra, A. K. 1995. Dynamics of Structures. Prentice Hall, Englewood Cliffs, NJ.

Converse, A. M., and Brady, A. G. 1992. BAP: Basic Strong-Motion Accelerogram Processing Software; Version 1.0. 92-296A, United States Department of the Interior, U.S. Geological Survey.

Darragh, R., and Power, M. 2005. NGA Documentation.

http:// peer.berkeley.edu/nga/NGA_Documentation.xls, [accessed 11 March 2010].

Douglas, J., and Smit, P. M. 2001. How Accurate Can Strong Ground Motion Attenuation Relations Be? *Bulletin of Seismological Society of America*, 91, 1917-1923.

Douglas J. 2003. What is a poor quality strong-motion record?, *Bull. Earthq. Eng.*, 1,141-156.

Nigam, N. C., and Jennings, P. C. 1969. Calculation of response spectra from strong-motion earthquake records. *Bulletin of Seismological Society of America*, 59, 909-922.

Segou, M., Voulgaris, N., Makropoulos, K. C., and Stavrakakis, G. N. 2008. A review of the Greek strong motion database: needs, improvements and future development. In Proceedings of the 31st general *Assembly of the European Seismological Commission ESC2008*, Hersonissos, Crete, Greece, 7-12 September 2008, 422-427.

Segou, M. and Voulgaris, N. 2010. PROSCHEMA: a Matlab application for processing strong motion records and estimating earthquake engineering parameters, accepted for publication, Computers & Geosciences.

STUDY OF THE 2ND DECEMBER 2002 VARTHOLOMIO EARTHQUAKE (WESTERN PELOPONNESE) M5.5 AFTERSHOCK SEQUENCE

Serpetsidaki A.[1], Sokos E.[1] and Tselentis G-A.[1]

[1] *University of Patras, Department of Geology, Seismological Laboratory, 26500 Patras, Greece, annaserp@upatras.g, esokos@upatras.gr, tselenti@upatras.gr*

Abstract

On the 2 December 2002 an earthquake (M_w=5.5) occurred near the city of Vartholomio (western Greece) causing damage in more than 1000 buildings. The University of Patras Seismological Laboratory permanent network stations recorded the mainshock and the aftershocks. Furthermore, twenty-six sites were instrumented to study the aftershock sequence. We identified more than 500 aftershocks with Md ranging from 2.0 to 4.3 during the first 30 days following the mainshock. The spatial and temporal evolution of the aftershock sequence is presented. We use the 370 earthquakes recorded at a minimum of 20 stations, with RMS less than 0.1 s and uncertainties less than 1 km, to infer the precise distribution of the seismicity in the fault region. The mainshock moment tensor inversion results are used in parallel to the aftershock sequence distribution in order to identify the causative fault. The results suggest a strike slip fault with dextral movement, which is trending NNE-SSW and fits the regional tectonics.

Key words: *moment tensor, centroid, waveform inversion, fault plane, Vartholomio.*

1. Introduction

An earthquake of Mw=5.5 occurred on 2 December 2002 at a distance of 10 km from the center of the city of Vartholomio (Fig. 1); The epicenter was located in south western Greece, in the coastal area of western Peloponnese. Although the earthquake magnitude was moderate, the damage reported was serious, since the intensity reached V$^+$. Seventeen people were wounded, eight buildings collapsed and tenths of buildings were seriously damaged, in the city of Vartholomio, while over a thousand were reported with damage in twenty nine nearby settlements (ITSAK, 2003).

The seismogenic area is situated in the external part of the Hellenic Arc, which is characterized by intense neotectonic deformation and high seismicity. More specifically, this area is part of the neotectonic depression (graben) of Pirgos, which is delimited by two faults of NW- SE and NNE-SSW direction and it is characterized by co-sedimentation tectonism (Le Pichon et al., 1995).

Throughout its history, Vartholomio has been severely affected by strong earthquakes. Damaging earthquakes occurred at the area in 1954 and 1988 with magnitudes M=5.8 and M=6.0, respectively. The 16th October 1988 earthquake caused serious damage in the city of Vartholomio reaching a seismic intensity of VII, a value which has been higher than would normally be expected for the particular magnitude and epicentral distance. The focal mechanisms calculated for

these events revealed pure strike slip faulting. Kiratzi and Louvari (2003) mention that the sense of motion of the strike-slip faults of the western Peloponnese could not be evidenced from the aftershock distribution of the major events (i.e. Vartholomio in 1988, Pirgos in 1993). The dextral sense of strike slip motion is favoured, parallel to the strike of the Cephalonia strike-slip fault, which would result in clockwise rotations of the NW margin of the Hellenic trench. The absolute peak ground acceleration (PGA) in Zakynthos island (R~20km) measured by ITSAK's strong motion records, was 90.7cm/sec^2. The estimated PGA for Vartholomio by synthetic strong motion calculations (ITSAK, 2003), was 113cm/sec^2. The aftershock activity was mainly concentrated around the coastal area southwest of Vartholomio city.

The PATNET network of Patras Seismological Laboratory (UPSL) operated in the area since 1991 and up to 2000, recorded the mainshock and the aftershock sequence. Stations operated by the National Observatory of Athens (NOA) also recorded the sequence. Furthermore, twenty-six sites in the area were instrumented by UPSL, to study the aftershock sequence. We identified more than 500 aftershocks with Md ranging from 2.0 to 4.3 during the first 30 days following the mainshock. In this paper results obtained by seismological data from PATNET network, NOA network and the temporary seismological network following the 2 December 2002 earthquake are analysed. The mainshock was located using the available records and the source parameters were determined by moment tensor inversion. Aftershock sequence data and source parameters were combined in order to clarify the geometry of the causative fault.

2. Location

The mainshock was located by HYPOINVERSE code (Klein, 2002), using manual P and S readings from short period records of PATNET stations and two broad band stations of NOA (RLS, ITM), in distances up to 140km (Fig. 1). The uncertainty was evaluated by repeating calculations with: a) various starting depths, varying from 10km up to 20km; the 17km depth was favoured by the residuals. b) two Vp/Vs ratios, 1.76 and 1.78; the latest provided the best results and c) three 1D crustal models: Haslinger et al., 1999, Tselentis et al., 1996, and Novotny et al., 2001. The model by Tselentis et al., 1996 provided the least RMS residuals.

The aftershocks occurred during the first week (2 – 10 December 2002), were recorded by the Patras Seismological Network (PATNET) stations; they were located using P and S manual readings and using the parameters that were favoured by the test concerning the mainshock (Fig. 2A). During the following days the aftershocks were recorded both by PATNET and a portable network of 26 stations, which was installed in the area (Fig.1) for a period of one month (9th December 2002 – 10th January 2003).

Each station was equipped with a three-component 4Hz SIG borehole sensor, a 24-bit Earth Data recorder and a GPS unit. The instruments have flat transfer function for velocity in the frequency range from 1Hz to 50Hz. The recording was continuous with a sampling frequency of 100Hz. During the operation of the network hundreds of earthquakes were recorded. The initial hypocentral locations were determined using the program HYPO71 (Lee and Lahr, 1975). The local magnitudes M_D of these events were within 0.5 and 4.5, while their depths varied between 5 and 20km. (Fig. 2B). The magnitudes were computed using the coda duration method (Lee and Lahr, 1972), with the same parameters used in the mainshock processing.

A dataset of 50 events, commonly recorded and located by the permanent network PATNET and the temporary microseismic network of Vartholomio, was created. This group of events is con-
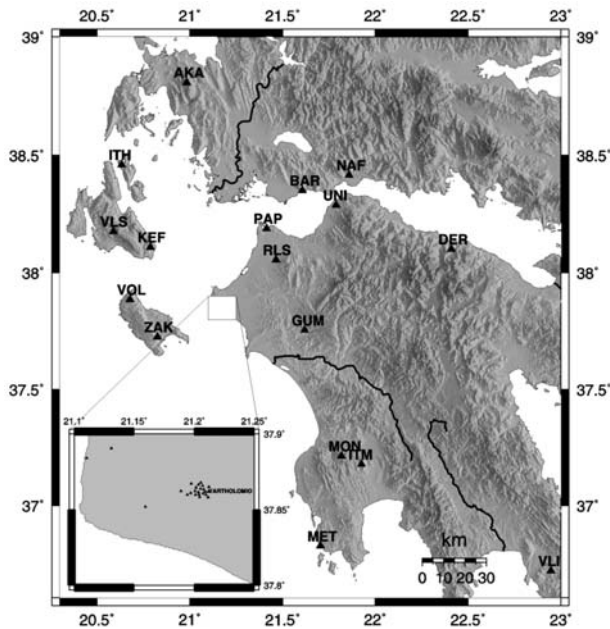
Fig. 1: Distribution of the seismological stations, which recorded the mainshock and the aftershock sequence. White rectangle shows the study area where the microseismic network (inset) was installed.
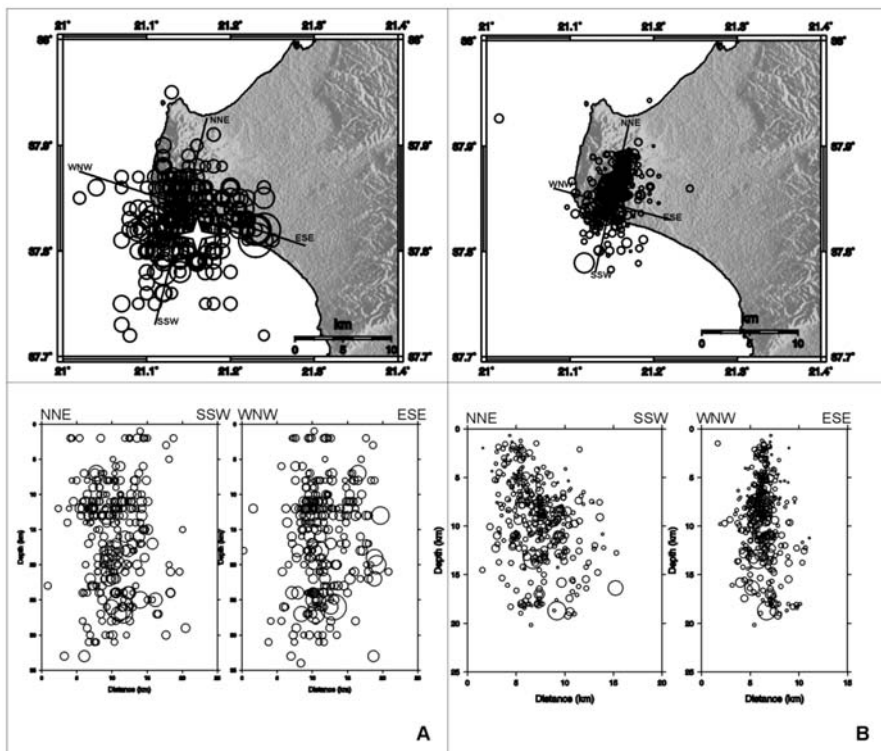
Fig. 2: Aftershock sequence distribution and cross-sections, located by the permanent network PATNET (A) and the temporary network (B).
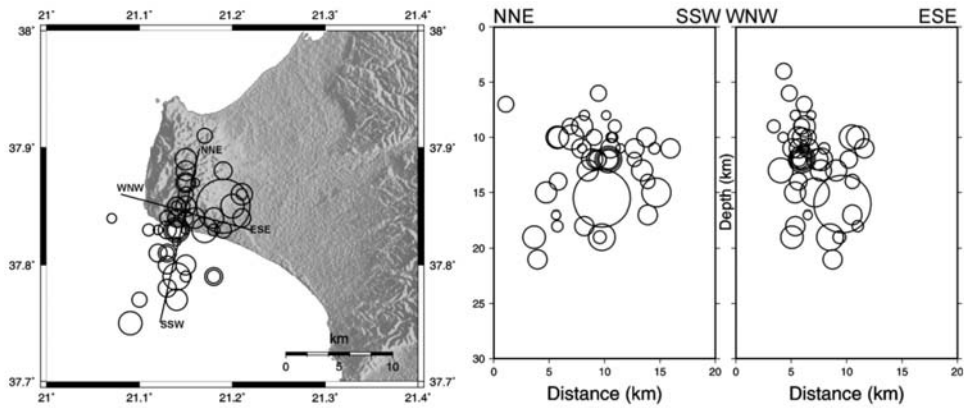
Fig. 3: Thirty-eight relocated hypocenters distributed in map and cross-sections.

sidered as the most accurately located, since the hypocenter locations were provided by local and regional station records. This indicates a complete azimuthal coverage but also a large number of P and S readings. The mainshock and the 50 most accurately located aftershocks were relocated by HYPODD (double difference) software Waldhauser (2001). Catalog P- and S-wave data were used in the procedure derived from stations within 140 km from the centre of the epicentral area. Fifty initial sources and 35 stations were combined in the procedure, and parameters were set, following Waldhauser (2001) suggestions for datasets containing a small number of events. The maximum number of neighbour events was set to the number of the initial sources. The double-difference residuals for the pairs of earthquakes at each station were minimized by weighted least squares using the method of singular value decomposition. The 1D-velocity model to calculate the theoretical travel-times was the Tselentis et al. (1996) model.

The HYPODD final results include 38 relocated events, which form a single cluster (Fig. 3). Most of the events are located in the sea area SSW of the Vartholomio city and the large percentage of the hypocenters is located in depths between 9 and 16km. The mainshock relocated hypocenter was at 20km.

The distribution of the epicentres, in all the cases, suggest a fault plane striking NNE-SSW and according to the cross-sections is almost vertical, slightly dipping to the east (Fig. 2 and Fig. 3).

3. Moment Tensor

The moment tensor inversion is performed by the so-called iterative deconvolution of Kikuchi and Kanamori (1991), modified for regional distances by Zahradnik et al., 2005. Complete waveforms are used, without separation of individual phases; full wave Green functions are calculated by the discrete wavenumber method in a 1D velocity model. Easy processing of many events is possible due to a user-friendly Fortran-Matlab program package called ISOLA (Sokos and Zahradnik, 2008). The present work focuses on the case of the single-source and deviatoric inversion (no volume change). The results are presented in terms of the double-couple component of the deviatoric solution, represented by the scalar moment, strike, dip and rake.

We used the mainshock records from four broadband stations of NOA; ITM, VLI, VLS and RLS. In some cases broadband records of moderate near earthquakes at stations of NOA network

Table 1. Moment tensor solution.

Origin (GMT)	Lat (N) (deg.)	Lon (E) (deg.)	Depth (km)	Scalar moment (Nm)	Mw
04:58:56	37,8557	21,1793	20	2.173e+17	5,5
Strike I	**Dip I**	**Rake I**	**Strike II**	**Dip II**	**Rake II**
209°	83°	178°	299°	88°	7°
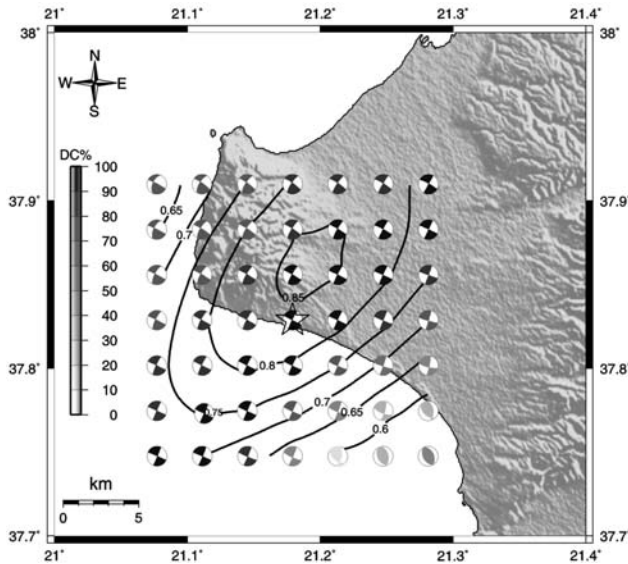
Fig. 4: Moment tensor inversion and source grid search. The star represents the initial epicenter position.

equipped with Lennartz Le-3D/20s (20-sec) sensors exhibit long period, pulse like signals; Numerical simulation of the pulses allows their removal, thus making the records fully utilizable for waveform inversion in seismic source studies (Zahradnik and Plesinger, 2005). The RLS station records were corrected for such disturbances according to Zahradnik and Plesinger, 2005.

The MT calculation was performed in crustal model provided by Tselentis et al., 1996 and at the 0.020 - 0.10 Hz frequency range. The centroid was determined by repeated calculations of the MT in a volume grid of trial source positions not far from the hypocenter, aiming at optimizing the fit between the observed and synthetic waveforms. Next, the so-called hierarchic grid search was applied (Zahradnik et al., 2008), using a progressively finer grid (1km) while approaching towards the likely centroid position.

The optimum source position (C) was identified at the location shown in Fig.4, a few kilometers northeast of the epicenter at depth of 20km. The moment tensor inversion revealed a strike – slip fault (Table 1); nodal plane I is trending NNE – SSW and nodal plane II is trending WNW – ESE while, both are steeply dipping. The variance reduction per component varied from 62% up to 97%, indicating an excellent fit between observed and synthetic waveforms, while the DC percentage was 90.5% (CLVD 9.5%). The activated fault produced an Mw5.5 earthquake. Ap-
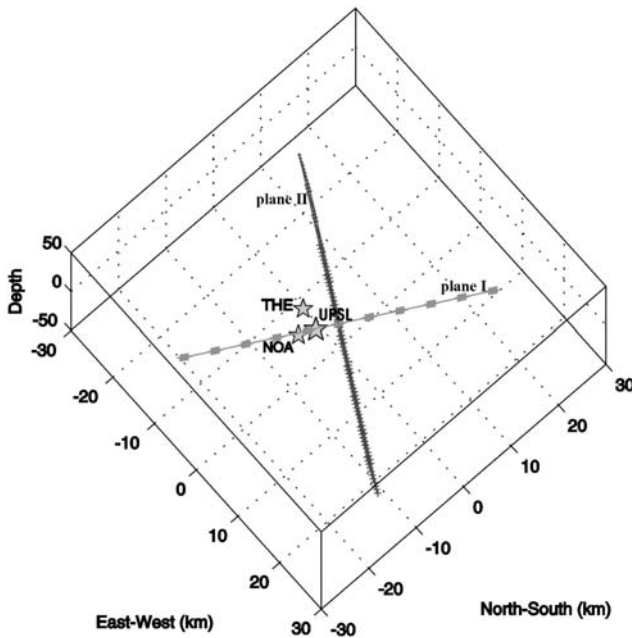
Fig. 5: Two nodal planes passing through the centroid, both according to the MT solution of this paper and the hypocenters: the one calculated in this paper - UPSL, National Observatory of Athens – NOA and Thessaloniki University – THE. Nodal plane I appears in gray line while nodal plane II, in black line.

plication of empirical relationship, according to Papazachos and Papazachou (1997), indicates a 10km fault length and 8km fault width.

The application of the moment tensor inversion method produced results slightly different than the previously published by Roumelioti et al. (2004) for the same event (strike:50°, dip: 68°, rake: -166°).

Joint knowledge of centroid, MT solution (nodal planes) and hypocenter position is a key to identify the causative fault plane. This is the nodal plane that passes through centroid (C) and includes the hypocenter (H) (Zahradnik et al., 2008). The mainshock was investigated for the mutual position of the hypocenter (H) and the centroid (C).

4. H-C Method

The method is based on relative position of hypocenter (H), centroid (C) and nodal planes. Hypocenter (nucleation point) is determined by kinematic location. Centroid (the point approximating the dominant slip region) is determined as a part of the moment tensor (MT) retrieval, C is the position of the best match between observed and synthetic seismograms. The nodal planes I and II, passing through the centroid C, are determined by the strike, dip and rake of the optimum moment tensor. Then the fault plane can be identified as the nodal plane encompassing the hypocenter (Zahradnik et al., 2008).

The H-C method was applied for the mainshock using the hypocenter, which was proposed in this paper (UPSL) but also the ones by the Greek institutes (National Observatory of Athens – NOA and University of Thessaloniki – THE). The distribution (Fig. 5) shows consistency of the hypocenters with the nodal plane I (strike:209° and dip:83°). The UPSL hypocenter and NOA hypocenter both lay in the nodal plane I, while the THE hypocenter is located closer to nodal plane I also.
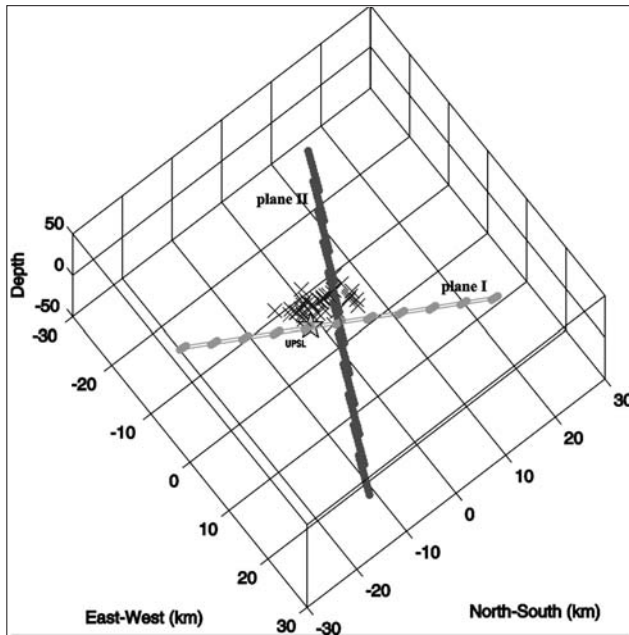
Fig. 6: Two nodal planes passing through the centroid, both according to the MT solution of this paper and the thirty eight relocated hypocenters.

Finally, the method was applied for the hypocenters produced by relocation of the combined data, from PATNET and microseismic network. Fig. 6 shows that the hypocenters distribution is consistent with nodal plane I. Furthermore, the best-fit plane for the relocated hypocenters was calculated which, pointed out a plane with strike=198° and dip=87°. This plane is in good agreement with nodal plane I.

5. Conclusions

A moderate magnitude earthquake occurred on 2 December 2002 close to the city of Vartholomio (Western Peloponnese). We located the mainshock using the available short period and broad band records. Several tests were carried out in order to decide the most appropriate crustal model and location parameters (starting depth, ratio Vp/Vs). The aftershock sequence was recorded by the permanent network PATNET and partially by a temporary microseismic network, which was installed in Vartholomio and surroundings. The aftershocks were located using the available records and a dataset of the most accurate hypocenters was relocated by double-difference method. The epicenters spatial distribution suggests a NNE-SSW trending fault of about 10km long. The cross- sections show that the hypocenters are distributed in an almost vertical plane of 8km width.

The moment tensor inversion was applied for the mainshock. The focal mechanism reveals a strike – slip fault; nodal plane I trending NNE – SSW and nodal plane II trending WNW – ESE, both dipping almost vertical. The aftershock sequence epicenters distribution favors the nodal plane I.

The H – C plot method was applied for the mainshock; the hypocenter calculated in this work as well as the hypocenters published by the Greek institutes NOA and THE favor nodal plane I. Finally, the H - C plot also indicates that the 38 events lie closer to the nodal plane I while, the distribution of the relocated hypocenters dataset fits a plane which also approximates nodal plane I.

The results of the analysis suggest that the activated fault was a nearly vertical strike - slip fault with dextral movement, trending NNE – SSW, which is in consistence with the evidence from tectonic studies in the area. The fault length was estimated to be 10km and the width up to 8km.

6. Acknowledgments

7. References

Haslinger, F., Kissling, E., Ansorge, J., Hatzfeld, D., Papadmitriou, E., Karakostas, V., Makropoulos, K., Kahle, H-G., Peter, Y., 1999. 3D crustal structure from local earthquake tomography around the Gulf of Arta (Ionian region, NW Greece). *Tectonophysics* 304, 201-218.

ITSAK, Institute of Engineering Seismology and Earthquake Engineering., 2003. The Earthquake of Vartholomio (M=5.6), 2 of December 2002. *Report in Greek,* 60pp.

Kikuchi M, Kanamori H., 1991. Inversion of complex body waves – III. *Bull. Seis. Soc. Am.* 81, 2335-2350.

Kiratzi, A., Louvari, E., 2003. Focal mechanisms of shallow earthquakes in the Aegean Sea and the surrounding lands determined by waveform modeling: a new database. *J. Geodyn*. 36, 251– 274.

Klein, F.W., 2002. User's guide to HYPOINVERSE-2000, a FORTRAN program to solve earthquake locations and magnitudes. *U. S. Geological Survey Open File Report* 02 171 Version 1.0.

Lee, W.H.K. and Lahr, J.C., 1975. A computer program for determining hypocenter, magnitude, and first motion pattern of local earthquakes Hypo71 (revised) . *US Geol. Surv. Open File Rep*. 75 (1975), p. 311.

Lee, W.H.K. and Lahr, J.C., 1972. HYPO 71: A computer program for determining hypocenter, magnitude, and first motion pattern of local earthquakes, *U.S. Geol. Surv. Open-file Rep*., p. 100.

Le Pichon, X., Chamot-Rooke, N., Lallemant, S., Noomen, R., Veis, G., 1995. Geodetic determination of the kinematics of central Greece with respect to Europe: implications for eastern Mediterranean tectonics. *J. Geophys. Res*. 100, 12675–12690.

Novotny, O., Zahradnik, J. and Tselentis, G.-A. 2001. North-western Turkey earthquakes and the crustal structure inferred from surface waves observed in Western Greece, *Bull. Seism. Soc. Am*. 91, 875 – 879.

Papazachos, B.C. and Papazachou, C.B., 1997. The earthquakes of Greece. Editions Ziti. pp.304.

Roumelioti Z., Benetatos, Ch., Kiratzi, A., Stavrakakis, G., Melis, N., 2004. A study of the 2 December 2002 (M5.5) Vartholomio (western Peloponnese, Greece) earthquake and of its largest aftershocks. *Tectonophysics* 387, 65– 79.

Sokos, E. Zahradnik, J., 2008. ISOLA a Fortran code and a Matlab GUI to perform multiple-point source inversion of seismic data*, Computers and Geosciences*, 34, 967-977.

Tselentis, G.-A., Melis, N.S., Sokos, E. and Papatsimpa, K., 1996. The Egion June 15, 1995 (6.2 ML) earthquake, Western Greece, *Pure Appl. Geophys*. 147, 83-98.

Waldhauser F., 2001. HypoDD - A program to compute double-difference hypocenter locations, *U.S. Geological. Survey open-file report*, 113pp.

Zahradnik, J and Plesinger, A., 2005. Long-period pulses in broadband records of near earthquakes. Bulletin of the Seismological Society of America. v95 i5. 1928-1939.

Zahradnik, J., Serpetsidaki, A., Sokos, E., Tselentis, G-A., 2005. Iterative deconvolution of regional

waveforms and double-event interpretation of the 2003 Lefkada earthquake, Greece. *Bull. Seis. Soc. Am.* 95, 159-172.

Zahradnik, J., Sokos, E., Tselentis, G-A., Martakis, N., 2008. Non-double-couple mechanism of moderate earthquakes near Zakynthos, Greece, April 2006; explanation in terms of complexity. *Geophysical Prospecting*, 56, 341-356.

Zahradnik, J., Gallovic, F., Sokos, E., Serpetsidaki, A. and Tselentis, G-A., 2008. Quick Fault-Plane Identification by a Geometrical Method: Application to the Mw 6.2 Leonidio Earthquake, 6 January 2008, Greece. *Seismological Research Letters* Volume 79, Number 5, p.653.

THE APRIL 2007 SWARM IN TRICHONIS LAKE USING DATA FROM A MICROSEISMIC NETWORK

Sokos E.[1], Pikoulis V.E[2], Psarakis E.Z.[2] and Lois A.[1]

[1] *University of Patras, Department of Geology, Seismological Laboratory, 26500 Patras, Greece, esokos@upatras.gr, lois@upatras.gr*

[2] *Department of Computer Engineering and Informatics, University of Patras, 26500 Patras - Greece, pikoulis@ceid.upatras.gr, psarakis@ceid.upatras.gr,*

Abstract

A series of strong earthquakes took place at the Trichonis lake area, during April 2007. Three events, with M~5.0 occurred within one day, causing damages to almost all nearby villages and especially at the small town of Thermo. The sequence lasted for more than one month with small to moderate size events. It was recorded by regional networks and results related to its time and space evolution have already been published. Just after the major events a microseismic network was deployed in the area, by the University of Patras, Seismology Laboratory. Eight stations were installed, with short period, three component sensors and portable digital recorders. The network was in operation for a period of one month and a lot of events were recorded by enough stations to provide a reliable location. We present here the analysis of these data using modern methodologies like waveform cross-correlation techniques and further relocation of the events using waveform based differential time. The results partially support the findings of the regional networks, as regards the gross characteristics of the aftershock sequence, but provide an enhanced description of it. The space time evolution of the aftershock sequence reveals the activation of more than one fault in the area and suggests the connection of the sequence with an unmapped fault.

Key words: *Trichonis Lake, seismotectonics, relocation, double-difference, clustering algorithms, graph partitioning, cross-correlation.*

1. Introduction

On April 2007 an earthquake sequence occurred at the eastern side of Trichonis Lake, in western Greece. The sequence initiated with small events on the 8th of April 2007 and two days later the three strongest events of the whole sequence occurred (April 10th at 03:17, 07:15 and 10:41 GMT) with magnitudes ranging from Mw 5.0 to Mw 5.2. The seismic activity continued for more than a month with smaller events. Research studies for this sequence have been published by Evangelidis, 2008 and Kiratzi, 2008. Both papers use regional data to study the characteristics of the seismic sequence, to correlate it with another series of earthquakes that occurred in the 70's in the same area and to identify the causative fault. This was identified by both studies to be a NNW-SSE normal fault, which bounds the south west bank of the Lake (Fig.1).

On the 11th of April 2007 - one day after the strongest events - a portable microearthquake network was deployed in the area, by the University of Patras, Seismological Laboratory. Eight digital sta-
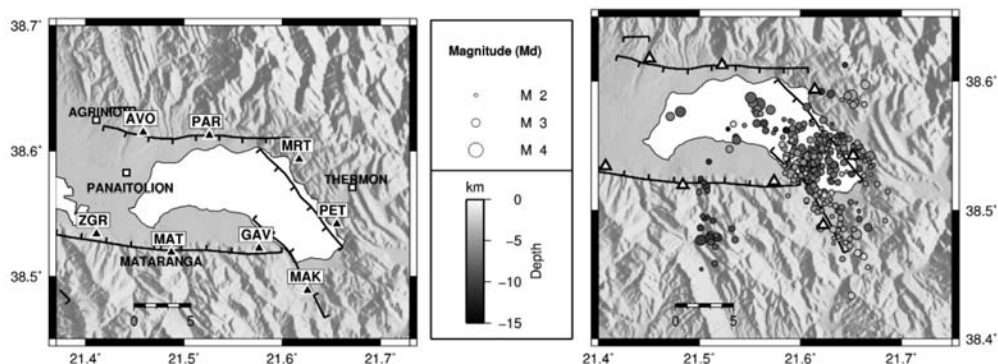
Fig. 1: (left): Simplified map showing the main faults of Trichonis graben and network configuration (right): Map of epicentres calculated using HYPOINVERSE.

tions (Fig.1), with short period sensors (0.5 to 50Hz), digital recording and GPS timing were installed. The network was kept in operation for twenty days and recorded accurately the evolution of the aftershock sequence. In this paper we present the results of the processing of these data using modern relocation techniques.

2. Geological – Tectonic Setting

The broader area of Trichonis lake is an active graben (Doutsos , 1987) with WNW-ESE strike and a length of about 30km (Fig.1). It is formed almost perpendicular to the Hellenides fold and thrust structures and is bounded by large normal faults. The main geological formations in the area are flysch and limestone; parts of Pindos and Gavrovo isopic zones. The Trichonis graben is developing in a direction almost parallel to other active structures in the area, e.g. the Corinth, Patraikos and Amvarakikos gulfs, while it lies in between them. These structures are controlled by the north-south extension, present in the area and indicated by seismicity, focal mechanisms and GPS measurements (Papazachos and Kiratzi, 1996; Cocard, 1999).

The main tectonic feature in the area is the Trichonis lake fault that bounds the graben to the south and forms a distinct topographic escarpment (Doutsos , 1987). Nevertheless this fault didn't rapture during the earthquake sequence under study, as suggested by Evangelidis, 2008 and Kiratzi et al., 2008. The causative fault of this sequence strikes NNW-SSE and controls the topography of the lake at its eastern part, probably acting as a transfer fault that links the Trichonics lake with Corinth gulf (Melis et al., 1989). Similar faults are proposed for linking Trichonis graben to Corinth Gulf and Amvarakikos Gulf e.g. Katouna fault zone (Melis et al., 1989; Doutsos and Kokkalas, 2001).

3. Data

A portable network of 8 stations was installed in the area for twenty days (11th April 2007–1st June 2007) (Fig. 1). The station spacing was chosen to be less than 10km to have reliable focal-depth estimation and in the meantime have a good azimuthal coverage of the aftershock sequence and record possible events on the main Trichonis lake fault that strikes EW. Each station was equipped with a three-component 4-Hz SIG borehole sensor, a 24-bit Earth Data recorder, and a Global Positioning System (GPS) unit. The instruments have flat transfer function for velocity in the frequency range from 0.5Hz to 50Hz. Recording was continuous with a sampling frequency of 100Hz. A special pro-

gram was developed, based on the STA/LTA (short-term average/long-term average) algorithm, to identify seismic events and store files for later processing. A minimum number of four stations was used as criterion for event selection. During the operation of the network more than 700 earthquakes were identified and seismic phases were handpicked. The initial hypocentral locations were determined using the HYPOINVERSE program (Klein, 2002). The velocity model adopted was the one proposed by Haslinger et al., 1999, which was derived by tomography studies in the broader area. From this initial catalogue, we selected 335 events having more than 12 arrivals (P and S) and epicentres within the network. The magnitudes were computed using the coda duration method (Lee et al., 1972), and computed duration magnitudes (Md) range within 1.11 and 3.2, whereas their depths vary between 1 and 15 km. (Fig.1). Although this is a high quality dataset, with small formal hypocentral errors (~1km), it is not suitable for correlation with mapped faults in the area, thus a relocation technique was designed and applied to the data, during further processing.

Nevertheless, a few important features of the aftershock sequence are evident even by applying only standard location methods. These are similar to results obtained by Evangelidis et al. (2008) and Kiratzi et al. (2008). Thus, as seen in Fig.1, the seismicity is constrained mainly in the eastern part of the lake bounded by two NW-SE normal faults while there are only a few events to the west that could be correlated to the main EW trending Trichonis lake fault. What is new and not described in previous studies, is a cluster of events south of Trichonis lake fault, with a NNW-SSE trend, located in a depth of ~10km. This cluster appeared twelve days after the main events and is formed by small magnitude events (largest magnitude was 2.7Md). It is probably related to reactivation of an older structure, due to stress transfer by the main events but this needs support by a separate study, which is beyond the scope of this paper.

4. Identification of Event Clusters and Time Differences

One of the most critical tasks involved in the relocation problem is the identification of the event clusters from a given set of events. This task is carried out in two stages.

The first one involves the comparison of all the possible pairs of seismograms of the data set in order to determine their pairwise similarities. For the comparison of individual seismograms, we use a correlation based technique (Pikoulis et al., 2006) that outperforms the classic method that is based on the maximization of the correlation coefficient. The motivation behind the development of this method was the observation that different parts of the waveforms have different impact on the value of correlation coefficient (Pikoulis et al., 2006). In particular, the contribution of each part was found to be strongly depended on its energy. Therefore, the similarity (or the dissimilarity) of the high energy waves, such as S and surface waves, will have a much greater impact on the value of correlation coefficient than the similarity of the low energy waves, such as the P wave, which is undesirable. The proposed method is applied on continuous parts of seismograms containing both P and S onsets, and it is carried out in three steps. Specifically, in the first one the optimal linear alignment of the waveforms under comparison is obtained by finding the lag that maximizes their correlation coefficient. Next, by using a sliding time window over the linearly aligned waveforms, the initial signals are broken into a sequence of equally – sized overlapping blocks. Calculating the correlation coefficient of every corresponding block pair, as well as, of a large number of bootstrapped block pairs, results in a sequence of partial correlation coefficient values. Based on the statistical properties of these values, the similarity of the waveforms at hand is to be decided. This is performed in the third and final step of the procedure. Specifically, if we consider that each sequence is a sample of values drawn from a population with a specific probability density function (pdf), and if we also assume that the histogram

of the values of the sequence is an approximation of this pdf, then our decision problem can be expressed as a typical hypothesis testing one. The outcome of the comparison stage is an undirected unweighted similarity graph, where each vertex represents a particular event of the data set, and there exists an edge between two vertices of the graph if and only if the corresponding events are characterized as similar by the above mentioned correlation based technique.

In the second stage, a clustering algorithm is needed in order to group the pairs of similar events into event clusters. In order to avoid the limitations of well known clustering algorithms such as the hierarchical methods, the k – means, the fuzzy means, and the Expectation Maximization algorithm (Everitt et al., 2001, Bardaine et al., 2006, Becker et al., 2006), we propose a fast, sequential, graph based algorithm that exploits the structure of the similarity graph and produces a single cluster in each iteration. The proposed algorithm (Pikoulis et al., 2006) emphasizes on the quality of the produced clusters by introducing a suitable measure to evaluate the participation of each object to a cluster and by expressing the overall quality of the cluster as a function of the participations of the individuals that comprise it. Each iteration is a two – step procedure. In the first step by eliminating repeatedly the vertex with the lowest degree and all the edges incident to it, an ordering of the vertices of the graph is obtained. Note that this is not the same as sorting the vertices of the graph based on their initial degrees. The elimination of a vertex (and of the edges incident to it) will only reduce the degrees of the vertices that were adjacent to it. Thus, if the vertex eliminated on a given round is part of a dense and well – separated group of vertices then, with high probability the majority of the reduced degrees will come from vertices of the same group, which, due to the assumptions had similar degrees with the eliminated vertex. As a result, the vertex that will be eliminated on the next round will most likely also belong to the same group, and this will carry on until the whole group is eliminated. Based on this, we expect the outcome of this step to be a rough grouping of the vertices, with the smallest groups located towards the beginning of the eliminated sequence and the largest ones located towards the end of it. As we go deeper in the elimination rounds, the vertices that are still remaining towards the end of the procedure should not only have had more connections in the initial graph, than the ones already eliminated, but they should also have a great number of connections among them, as it is the number of these connections that allows them to survive the elimination rounds. In this sense, the lastly eliminated vertices should not only belong to the same cluster, but they should also form the most compact (densely connected) part of it, or its core (and the seismic events they represent form the core of the corresponding group). Therefore, the algorithm decides that has reached the core of a cluster, whenever the remaining part of the graph is a clique (every pair of vertices is connected by an edge) and terminates the elimination procedure. Having the identified clique as a starting point, in the next step the algorithm involves a procedure of augmentation rounds with the purpose of gradually forming the rest of the cluster around its core. In each round, of all the vertices that have not yet been added, the vertex with the higher number of connections with the already added vertices is selected. We anticipate that the first vertices to be added will be the remaining vertices of the cluster that will frame the initial core, followed by the rest of the vertices of the graph. This is because of the starting point of the augmentation procedure and the selection criterion of the vertex which is added in each round. What remains is the determination of the particular augmentation round where the procedure of cluster formation should be stopped. In order to achieve this goal, we introduce the term of participation of a vertex to a graph and define it as the ratio of the number of the edges in the graph that are incident to that specific vertex, to the maximum possible number of such edges (which occurs if the vertex is connected to all the other vertices of the graph). We also define as a quality measure of the graph the minimum value of participation among all the vertices that belong to it. A high value of this measure ensures that every

vertex in the graph is connected to a high number of the other vertices and therefore there is a very high probability that the vertices of the graph are part of the same cluster. On the other hand, if the graph contains even as much as one vertex with few connections to the other members (an outlier), then its participation value will be low and this value will be reflected on the value of the measure. After each augmentation the algorithm calculates the value of the quality measure of the resulting graph and terminates the augmentation procedure if the value of the measure drops below a pre-selected threshold. The vertices of the identified cluster are deleted from the initial graph and the algorithm reiterates with the remaining vertices.

Finally, the computation of the time differences between events of the same cluster, is based on the maximization of a similarity measure called Enhanced Normalized Cross Correlation (ENCC) (Psarakis and Evangelidis, 2005), which constitutes an extension of the sample level correlation coefficient. The above mentioned similarity measure is a continuous function of the time lag parameter, thus leading to sub – sample accuracy. Moreover, its maximization has a closed form solution, resulting to a very low computational cost.

5. Relocation

The Double Difference (DD) relocation method proposed by Waldhauser and Ellsworth (2000), and implemented in HYPODD software (Waldhauser, 2001) was used for relocating the whole dataset. The DD method is a relative earthquake location method (e.g. Fréchet, 1985; Got et al., 1994; Roumelioti et al., 2003). It is based on the fact that when the hypocentral separation between two earthquakes is small compared to the event station distance and the scale length of the velocity heterogeneity, then the ray paths between the source region and a common station are similar along almost the entire ray path. In this case, the difference in travel times for two events observed at the same station can be attributed to the spatial offset between the events with high accuracy. This is because the absolute errors are of common origin except in the small region where the ray paths differ at the sources (Waldhauser and Ellsworth, 2000). The use of waveform cross-correlation methods improves the accuracy of the relative arrival-time readings, thus leading to highly accurate locations. According to Waldhauser and Ellsworth, 2000 the use of waveform cross-correlation methods can lead to relative locations between earthquakes, with errors of only a few meters to a few tens of meters.

As discussed above we computed cross-correlation, P-and S-wave differential travel-times for the 335 events and the defined 74 clusters. In order to access the contribution of each piece of information to final result we followed the following approach.

First we relocated the whole sequence using HYPODD clustering option and catalog absolute travel-time measurements only (CT-data). This is the most common approach when doing relocation with HYPODD and can serve as a reference point. This scheme consists of a) forming of event pairs and links to neighbors, b) formation of clusters and c) double difference relocation. Following, Waldhauser and Ellsworth, 2000, we selected only strongly connected events and this reduced our dataset by a few events. The final dataset consisted of 16576 P and 11326 S-wave phase pairs that were relocated using the conjugate gradients method (LSQR, Paige and Saunders, 1982). A pair of critical points exists when applying the above method a) which is the proper choice of damping and b) weights of data, for both of them we followed the suggestions of Waldhauser (2001). The crustal model used was again the model of Haslinger et al. (1999). In Fig. 2 the results obtained by applying HYPODD standard relocation scheme are presented.

In the next step, we implemented steps a) and b) of the scheme described in the previous paragraph by
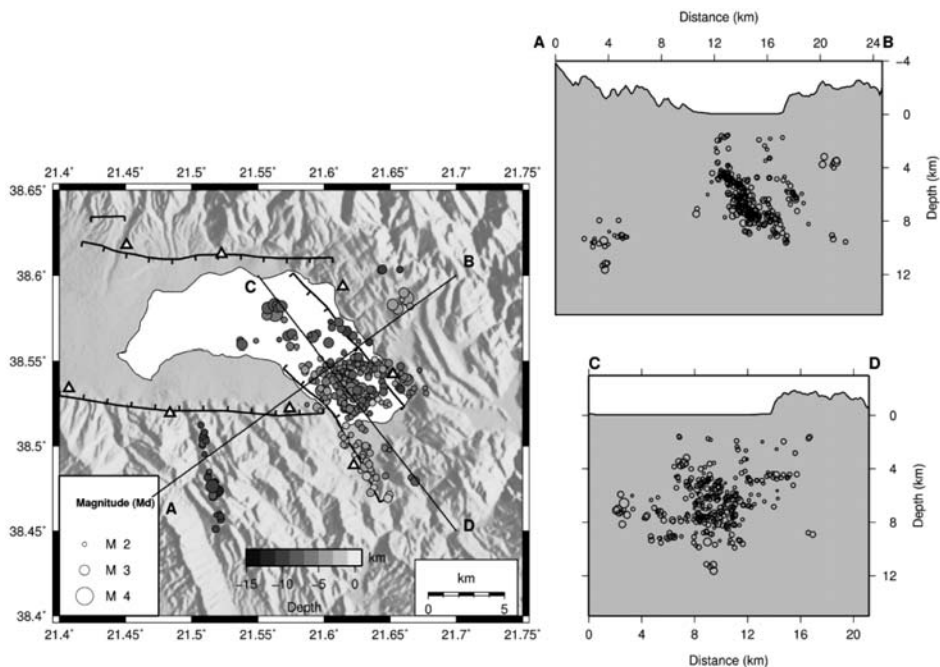
Fig. 2: Map view and cross sections of relocated epicenters applying the HYPODD relocation method. Topography is exaggerated by a factor 5.

using the procedure described in Section 4 and relocated each of the identified clusters with HYPODD using CT data only. The results are presented in Fig.3, and are comparable to the simple HYPODD clustering and relocation. Finally we added to the inversion the differential travel times, computed by using ENCC described in the last paragraph of the previous section. This resulted in a quite different view of the sequence, the main cluster of hypocenters was divided to smaller clusters that follow the causative fault both in strike and dip (Fig.4).

6. Discussion

The relocated aftershocks of Trichonis lake 2007 sequence, using data from a local microseismic network, provided a detailed view of the time-space evolution of seismicity. The sequence initiated on the 8th of April and on the 10th three moderate size events occurred (Kiratzi et al., 2008). In Fig. 5 we present in map view the evolution of the sequence during the recording period (11th of April -1st of May 2007), using the relocated data described in previous paragraphs. The main events of the sequence were not recorded by the microseismic network, thus we have included in the top left panel of Fig. 5 the location provided by Kiratzi et al. (2008) and Evangelidis et al. (2008) for the strongest one (star and square in top left panel of Fig. 5).

During the first two days, after the occurrence of the main events, the seismicity is confined in the south east part of the lake in an area of 5x5km approximately, in accordance with empirical scaling laws, (e.g. Wells and Coppersmith, 1994). There are two main clusters during this time period located at the southwest bank of the lake. The main event is located at the northwest end of the aftershock area, indicating a southward propagation of the seismicity. Furthermore the main event is located in an area free of aftershocks through the whole recording period. This is an indication of
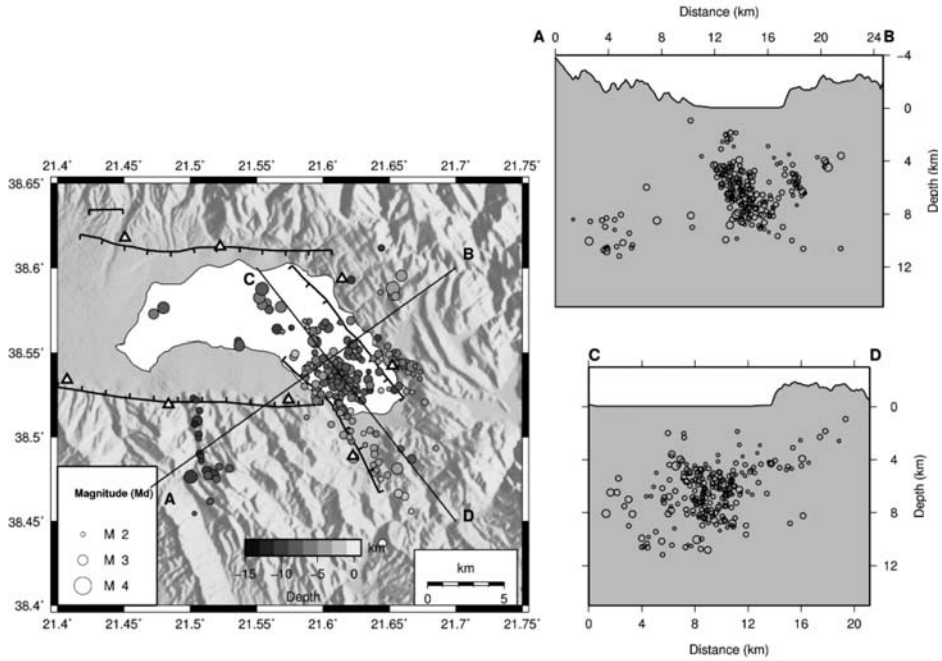
Fig. 3: Map view and cross sections of double difference relocated epicenters using our clustering scheme and CT data.
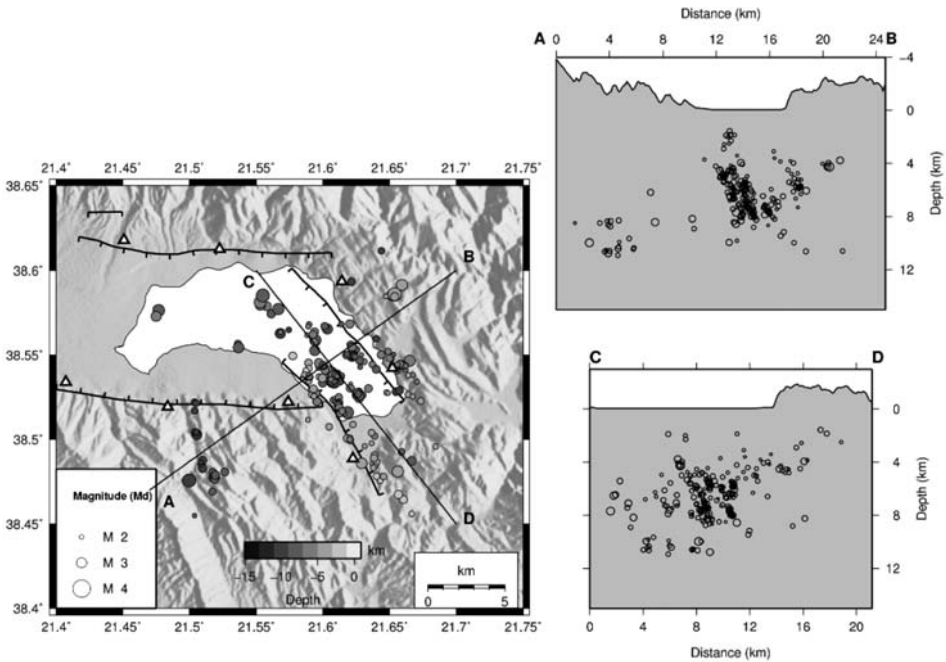
Fig. 4: Map view and cross sections of double difference relocated epicenters using our clustering scheme and both CT and CC data.
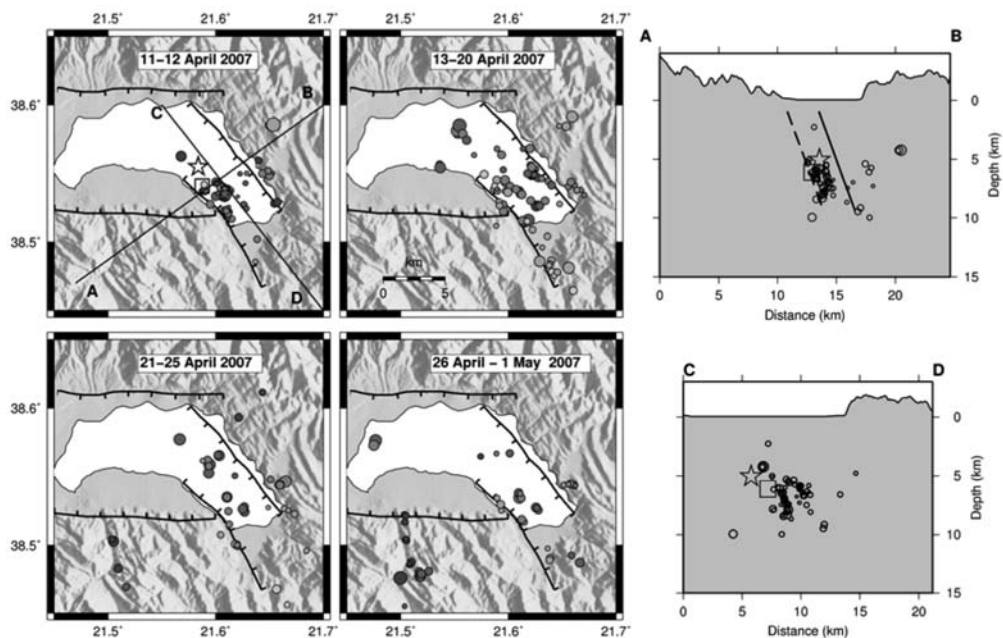
Fig. 5: Map view and cross sections of space-time evolution of aftershock sequence. Continuous line on AB cross section corresponds to mapped fault trace at the south bank of Trichonis lake, while dashed line corresponds to an inferred parallel fault, a dip of 70° was used. Star and square denote the location of main event, see text for details.

complete stress release in this part of the fault during the occurrence of the strongest events of the sequence on the 10th of April. The aftershocks depth distribution during the same time period (11th-12th of April) is depicted on the cross-sections of Fig.5. Seismicity forms a cluster at a depth of 5 to 8km comparable to the depth of the main event (Kiratzi et al., 2008, Evangelidis et al., 2008). Hypocenters in this cluster form two linear shapes that have slightly different dip. Although it is difficult to connect these with fault traces on the surface, since the true geometry of the faults closer to the surface, is not known, we can speculate about activation of two faults in the area with slightly different dip and similar strike. According to Kiratzi et al. (2008) the focal mechanisms of the strongest events had a dip of ~70°, using this dip and a linear fault geometry we can try to connect it with the depth distribution of aftershocks (Fig. 5). It is clear then that the NW-SE trending fault that bounds the south bank of Trichonis lake, cannot explain the whole aftershock distribution and we need a fault parallel to this ~3km to the west and on land. During the following days the aftershock activity started to spread in a larger area mainly towards the south and along the same NW-SE direction. An interesting feature during the last ten days of recording (21st April – 1st May) is the development of a small cluster of events south of the Trichonis lake fault. This cluster has a similar trend (NW-SE) with the main aftershock sequence and events within it are distributed at 8 to 10km depth. Since this cluster appeared a few days after the occurrence of the main events in the area, we can speculate about the possibility that is due to stress transfer. Of course a definite proof of this needs a special study which is beyond the scope of this paper.

7. Acknowledgments

8. References

Bardaine T., Gaillot P., Dudos-Sallee N., Blanco J., Senechal G. 2006. Characterization of Seismic Waveforms and Classification of Seismic Events Using Chirplet Atomic Decomposition. Example from the Lacq Gas Field (Western Pyrenees, France). *Geophys. J. Int.*, 166, pp 699-718.

Becker D., T. Meier, M. Rische, M. Bohnhoff, H.P. Harjes. 2006. Spatio – temporal microseismicity clustering in the Cretan region. *Tectonophysics*, 423, pp 3 – 16, 2006.

Cocard, M., Kahle, H.-G., Peter, Y., Geiger, A., Veis, G., Felekis, S., Paradissis, D., Billiris, H., 1999. New constraints on the rapid crustal motion of the Aegean region: recent results inferred from GPS measurements (1993–1998) across the West Hellenic Arc, Greece. *Earth and Planetary Science Letters* 172, 39–47.

Doutsos, T., Kontopoulos, N., Frydas, D., 1987. Neotectonic evolution of northwestern continental Greece. *Geol. Rundsch.* 76, 433–450.

Doutsos, T., Kokkalas, S., 2001. Stress and deformation patterns in the Aegean region. Journal of *Structural Geology* 23, 455–472.

Evangelidis C. P., Konstantinou K. I., Melis N. S., Charalambakis M., Stavrakakis G. N., 2008, Waveform relocation and focal mechanism analysis of an earthquake swarm in Trichonis lake, western Greece, *Bull. Seism. Soc. Am.* 98(2), pp. 804-811.

Everitt, B. S., Landau S., Leese M. Cluster Analysis (fourth edition). Arnold, London, 2001.

Fréchet, J., 1985. Sismogenèse et doublets sismiques. Thèse d'État, Université Scientifique et Médicale de Grenoble, 206 pp.

Got, J.-L., Fréchet, J., Klein, F.W., 1994. Deep fault plane geometry inferred from multiplet relative location beneath the south flank of Kilauea. *J. Geophys. Res.* 99, 15375–15386.

Haslinger, F., Kissling, E., Ansorge, J., Hatzfeld, D., Papadimitriou, E., Karakostas, V., Makropoulos, K., Kahle, H.G., Peter, Y., 1999. 3D crustal structure from local earthquake tomography around the Gulf of Arta (Ionian region, NW Greece). *Tectonophysics* 304, 201–218.

Kiratzi, A., Sokos, E., Ganas, A., Tselentis, A., Benetatos, C., Roumelioti, Z., Serpetsidaki, A., Andriopoulos, G., Galanis, O., Petrou, P., 2008. The April 2007 earthquake swarm near Lake Trichonis and implications for active tectonics in western Greece, *Tectonophysics* 452, 51- 65.

Klein, F.W., 2002. User's guide to HYPOINVERSE-2000, a FORTRAN program to solve earthquake locations and magnitudes. *U. S. Geological Survey Open File Report* 02- 606, Version 1.0.

Lee, W. H. K., R. E. Bennett, and K. L. Meagher, 1972. A method of estimating magnitude of local earthquakes from signal duration, *Open File Report, U. S. Geological Survey*, 28 pp.

Lee, W.H.K. and J.C. Lahr, 1975. HYPO 71: A computer program for determining hypocenter, magnitude, and first motion pattern of local earthquakes. *USGS Open file report*, p75-311.

Lee, W. H. K. and C. M. Valdes, 1985. HYP071PC: A personal computer version of the HYPO71 earthquake location program, U. S. *Geological Survey Open File Report* 85-749, 43 pp.

Lomax, A.J., 1991. User Manual for SeisGram. In Digital Seismogram Analysis and Waveform Inversion, IASPEI Soft ware Library Volume 3, W.H.K. Lee, ed., Seismological Society of America.

Melis, N.S., Brooks,M., Pearce, R.G., 1989.Amicroearthquake study in the Gulf of Patras region, west-

ern Greece, and its seismotectonic interpretation. *Geophys. J. Int.* 98, 515–524.

Paige C. C. and. Saunders M. A, 1982. LSQR: An algorithm for sparse linear equations and sparse least squares, TOMS 8(1), 43-71.

Papazachos, C.B., Kiratzi, A.A., 1996. A detailed study of the active crustal deformation in the Aegean and surrounding area. *Tectonophysics* 253, 129–153.

Pikoulis V.E., Psarakis E.Z., Sokos E.N. 2006. A New Two Step Correlation Based Technique for the Classification of Seismic Events. Poster Section of First European Conference on Earthquake Engineering and Seismology, Geneva, Sept.

Pikoulis V.E., Psarakis E.Z. and Sokos E.N. A Novel Seismic Data Processing Technique for the Event Relocation Problem. *Bulletin of the Seismological Society of America* (to be submitted).

Psarakis E. and Evangelidis G. 2005. An Enhanced Correlation-Based Method for Stereo Correspondence with Sub-Pixel Accuracy. Proc. of Inter. Conference on Computer Vision, ICCV05, pp.907-912, Beijing.

Roumelioti, Z., A. Kiratzi and N. Melis, 2003. Relocation of the July 26, 2001 Skyros island (Greece) earthquake sequence using the double-difference technique, *Physics of the Earth and Planetary Interior*, Vol. 138, 231 - 239.

Waldhauser, F., , 2001. HypoDD: A computer program to compute double-difference hypocenter locations, *U.S. Geol. Surv. open-file report*, 01-113, Menlo Park, California.

Waldhauser, F., Ellsworth, W.L., 2000. A double-difference earthquake location algorithm: method and application to the Northern Hayward fault, California. *Bull. Seismol. Soc. Am.* 90, 1353–1368.

Wells, D.L., Coppersmith, K.J., 1994. New empirical relationships among magnitude, rupture length, rupture width, rupture area, and surface displacement. *Bull. Seismol. Soc. Am.* 84, 974–1002.

DECAY PARAMETERS OF AFTERSHOCK SEQUENCES GLOBALLY DISTRIBUTED

Tsapanos, T.M.[1], Koravos, G. Ch.[1], Plessa, A.[2], Vythoulkas, N.K.[1] and Pitsonis, I.S.[1]

[1] *Aristotle University of Thessaloniki, School of Geology, Geophsical Laboratory, 54124 Thessaloniki, Greece,tsapanos@geo.auths.gr*

[2] *National Observatory of Athens, Institute of Geodynamics, 11810 Athens, a.plessa@gein.noa.gr*

Abstract

The evaluation of the parameters c and k of the decay law of the aftershocks in an earthquake sequence has been carried out in this study. For this reason 170 seismic sequences globally distributed, during the time period 1964-1986, were performed. All of them modelled well by Omori's law. We estimated that the mean global values of   and parameters   , are 0.660 ± 0.181 and -0.341 ± 0.090, respectively. The values of these parameters are also estimated for different regions of the world, west and east part of circum-Pacific rim, as well as for the Eurasia belt. The parameters c and k calculated for the various regions of the world found to be spread around the global average, although admittedly few exceptions to this generalization are also observed to exist.

Key words: *c-parameter, k-parameter, aftershocks decay laws, west and east side of Pacific rim, Eurasia belt.*

1. Introduction and data used

Aftershocks occurrence is usually attributed to the strain energy not released by main shock or its possible foreshocks. These can cause significant damage to buildings. Occasionally they can result in building collapse. This risk is highest for previously damaged buildings by the main shock. Statistical properties of aftershocks and foreshocks have been extensively studied for long time. Most of them dealt with the distribution of aftershocks and/or foreshocks in time, space and magnitude domains. The main properties of the aftershock sequences have been described by many authors (Utsu, 1961; Page, 1968; Ranalli, 1969; Kisslonger and Jones, 1991; Tsapanos, 1990a; Narteau, et al., 2002, Parsons, 2002; Felzer and Bronsky, 2006; Corral, 2007; Vinogradov, 2008, among others). Two main laws controlled for many years the distribution of the aftershock sequences: a) Omori's law and b) Bath's law.

Moment release rates during mainshocks compared with moment release rates during aftershocks sequences showed that the moment release rates of aftershock sequences are 30 times smaller than the maximum moment rate of the main shock (Kagan and Houston, 2005).

Tsapanos (1990a) listed his observations for 182 earthquake sequences, trying to establish a fresh expression for the so called Bath's law. These sequences occurred all over the world during 1964-1986. Only shallow earthquakes (h$\leq$60 km) with main shock magnitude M$\geq$7.0 are taken into ac-

count from the database of ISC global earthquake catalogue. In a previous study (Tsapanos et al., 1994) used the complete data sets for the examined aftershock sequences (with aftershock magnitude M≥4.5) and suggested that the completeness of the aftershocks is essential for such analysis. The possible incompleteness of the catalogs especially in the first time after the main shock plays a key role to the aftershock sequence processing (Lolli and Gasperini, 2006). The data of these sequences used in the present study. Distance (Utsu, 1969) and time (Tajima and Kanamori, 1985) conditions used to distinguish the aftershocks in any seismic sequence. The sequences occurred in oceans or have inadequate data for further analysis are eliminated from the present work. Only earthquake sequences occurred in the circum-Pacific rim and in the Eursia continent are finally taken into consideration, which consisted of 170 aftershock sequences.

2. Decay law of aftershocks

According to the work of Omori (1895) the aftershock rate is roughly proportional to the inverse of the time, t, elapsed after the main shock:

$$(1)$$

In eq. (1) c and k are coefficients, while time t is the time since main shock origin and n(t) is the aftershock frequency measured over a certain time interval.

Kisslinger and Jones (1991) suggested that k is dependent on the total number of aftershocks in the sequence and c on the activity in the earliest part of the sequence.

Papazachos (1975) by using data from Greece, found that the cumulative frequency distribution $N(T_i)$ of the time difference between main shock and the largest aftershock, was given by the relation:

$$(2)$$

Where c is the number of the earthquakes or the percentage of the events which occurred during the first day and k is the slope of the equation (2).

A data set of aftershocks sequences globally distributed, covered the time period 1904-1980, with main shock magnitude M≥7.4 were performed by Tsapanos et al. (1988). They found that the correlation between the probabilities N(T) of occurrence of the largest aftershock and the T (T is the time between the main shock and its largest aftershock) show the best fit (Fig. 1). The obtained values of the parameters c and k were 0.647±0.020 and -0.299±0.010, respectively.

Our data, as mentioned before, covered the circum-Pacific rim, as well as the Eurasia belt. The circum-Pacific rim separated, in two areas AREA1 and AREA2. The west side of the Pacific (AREA1) includes: Chile (1), northwest coasts of South America (2), Middle America (3), Mexico (4), west coasts of U.S.A. and Canada (5) and finally Alaska and Aleutian islands (6). The east side of Pacific (AREA2) includes: Kamchatka and Kurile islands (7), Japan (8), Taiwan (9), Marianas islands (10), Philippine islands (11), Sunda arc (12), Papua-Solomon islands (13), New Hebrides islands (14) and Fiji-Tonga and New Zealand (15). The division of the Pacific's regions is almost according to the one introduced by Tsapanos (1990b).

3. Regional values

Global average values of the parameters c and k were estimated and found that they are equal to =0.660±0.181 and =-0.341±0.090 (Fig. 2a and 2b).
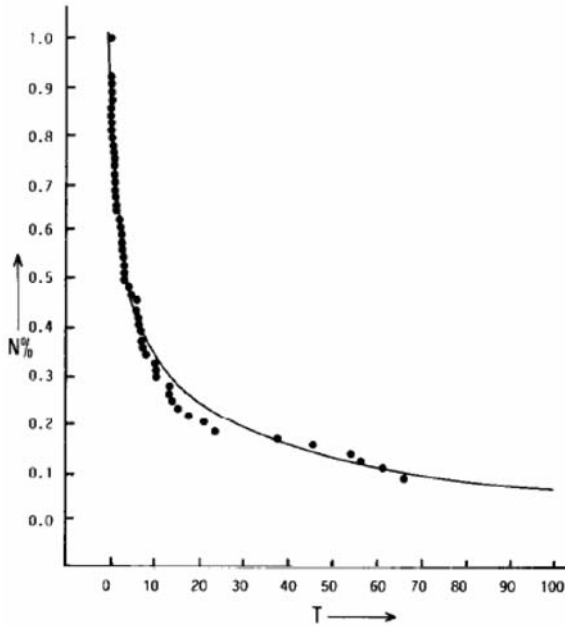
Fig. 1: Distribution of the probability (N(T)) against T, for the largest aftershocks which followed mainshocks with M≥7.4 during the period 1904-1980 (after Tsapanos et al. 1988).

(a)

(b)
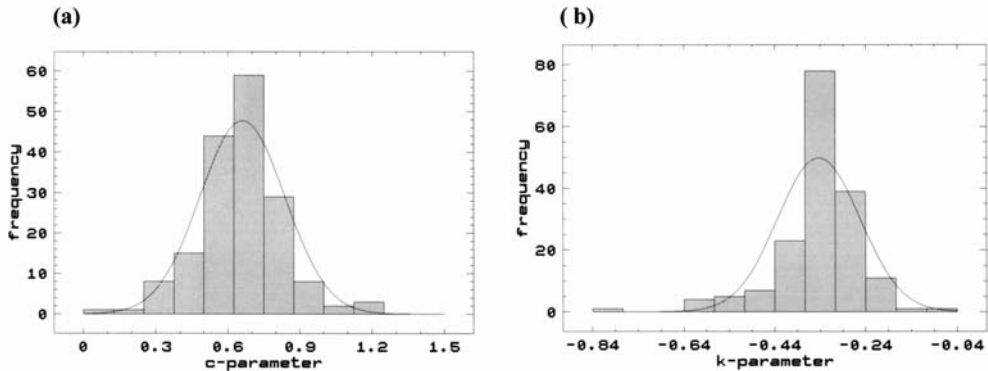
Fig. 2: The distribution of the average global values of the aftershock decay parameters: (a) c parameter and (b) k parameter.

The 170 aftershock sequences globally distributed were then separated in two groups. The first group belongs to the circum-Pacific rim, while the second one belongs to Eurasia. The obtained values of the parameters c and k are listed in Table (1).

The statistical T-test has been applied in order to verify the significance of the difference between the c-parameters of the two data groups. The results show that the parameter t (of the T-test) is equal to -1.75436 which corresponds to a probability PROB=0.0847. This means that the probability of the two groups to belong to the same population is about ≈8.5%. This result indicates that the two groups are in some sense statistically significant.

Table 1. The mean values and their standard deviation (sd) of the parameters c and k in the circum-Pacific rim and Eurasia belt.

	circum-Pacific	**Eurasia**
c-parameter+sd	0.612+0.043	0.691+0.116
k-parameter+sd	-0.319+0.007	-0.340+0.048

Table 2. Regional values and their standard deviation (sd) of the parameters c and k in the seismically active regions of the circum-Pacific belt.

Region	*c+sd*	*k+sd*
West Pacific		
Chile (1)	0.660+0.108	-0.373+0.076
NW coasts of S. America (2)	0.685+0.121	-0.321+0.057
Middle America (3)	0.550+0.073	-0.266+0.036
Mexico (4)	0.686+0.113	-0.357+0.062
W. coasts of USA & Canada (5)	0.531+0.101	-0.294+0.043
Alaska and Aleutian islands (6)	0.727+0.117	-0.348+0.042
East Pacific		
Kamchatka and Kurile islands (7)	0.728+0.163	-0.349+0.071
Japan (8)	0.620+0.160	-0.338+0.062
Taiwan (9)	0.603+0.097	-0.244+0.047
Marianas islands (10)	0.611+0.129	-0.252+0.032
Philippines islands (11)	0.695+0.112	-0.329+0.043
Sunda arc (12)	0.689+0.104	-0.316+0.048
Papua-Solomon islands (13)	0.717+0.085	-0.331+0.043
New Hebrides islands (14)	0.668+0.092	-0.354+0.062
Fiji-Kermadec-Tonga-New Zealand (15)	0.671+0.110	-0.301+0.015

 In order to study these parameters in details a further division applied. This time we divided the circum-Pacific in two sides: a) the island arcs of the east Pacific (e.g. Japan, etc) and b) the west side (American continent mainly). Regional values of the parameters c and k are calculated for the regions around the circum-Pacific rim and are listed in Table (2).

The T-test has been applied again to check the statistical significance between the data of the east and west side of the circum-Pacific belt. The t parameter (of the T-test) is equal to 1.86812 and the PROB=6.4%. From this result it can be interpreted that the mean c values of the two sides of the Pacific rim are different with a probability ≈94%.

4. Discussion and Conclusions

A first inspection to the above table (2) generally reveals that the parameters c and k have values around the average global values, although there are regions which do not follow this pattern, having values greater than or less than the global averages. Our discussion will be focused on the exceptions.

If we follow Kisslinger and Jones's (1991) suggestion that k is dependent on the total number of aftershocks in the sequence and c on the activity in the earliest part of the sequence we can lead to some conclusions about these aftershock parameters. Kagan and Houston (2005) suggested five reasons for non-zero c-parameter. It was introduced to explain, by the same authors, the seeming saturation of aftershock rate close to the origin time of a mainshock. The parameter c always found to be positive and typically ranges from 0.5 to 20 hours in empirical studies (Utsu, 1961; Reasenberg and Jones, 1989, 1994; Utsu et al. 1995) It was introduced, by the same authors, to explain the seeming saturation of aftershock rate close to the origin time of a mainshock. Shcherbakov, et al. (2006) taken into account three laws (Gutenberg & Richter, Omori's and Bath's) and suggested that the c-parameter plays the role of a characteristic time for establishment of Gutenberg-Richter scaling. This time increases systematically with a decreasing lower magnitude cutoff. The k-parameter slightly varies with the lower magnitude cutoff of the sequence.

Kamchatka and Kurile islands has the highest c value. This means that the aftershock sequences occurred in this region seem to be very active during the first times after the main shock occurrence. The value of the parameter c in Alaska and Aleutians as a whole region seems to be very active during the first times after the release of the main shock. However k parameter reveals that this is around the global value. One may argue to the results that the region is not well covered by instruments in order to record all the earthquakes. But as we mention in the present text we processing aftershocks sequences which their main shock is greater than or equal to 7.0. But Aleutians belong both in U.S.A. and Russia. The Aleutians belonged to Russia show an unusual behaviour and the c-parameter is equal to 0.827, while k-parameter is equal to -0.405. This can be interpreted that the aftershock sequences are too severe in the earliest part of sequence and their total number of the aftershocks are the highest. However this observation is not so valid, because the results came from only 4 sequences.

Papua and Solomon islands show also high activity in the early part of the aftershock sequences occurred there, while k-parameter is in accord with the global mean.

The value of c parameter (0.550) and the small number of the k-parameter (-0.266) in Middle America lead us to the conclusion the activity is not so high in the first part of the aftershock sequences in this region and the aftershock sequences released with short number of aftershocks. The same phenomenon is demonstrated in the west coast of U.S.A. and Canada as a whole region. The activity in the earliest part of aftershock sequences is the smallest among the examined regions and the total number of aftershocks in the sequence is small enough. Looking in details in this region we have one of the most studied areas of the world, California. California itself shows a total different behaviour and both parameters are in accord with the global averages (c=0.626 and k=-0.339). On the other side of American continent is the Caribbean loop which shows the same characteristics as the west coast of U.S.A. and Canada, where the activity is small the earliest part of the sequence (c=0.587) and the total number of aftershocks in a sequence is small, (k=-0.287), as well. The temporal behaviour of aftershock sequence in southern California during the time interval 1933-1988 was examined by Kisslinger and Jones (1991). They estimated the parameters c and k (with its standard errors) and they found similar values with ours, presented here.

Two regions Taiwan as well as Marianas islands exhibit values of parameter c around the global average but both have a short total number of aftershocks in a sequence, as they listed in table (2). The k-parameter in Taiwan is the shortest among the examined regions.

The tectonic setting and the mode of faulting are factors other than the fault surface properties that might control the behaviour of the sequences. Narteau et al. (2008) analyze the temporal properties of Californian mainshocks. They found that the c-parameter is a decreasing function of the magnitude of aftershocks and that it varies across different types of faulting. They also suggested that the time delay before the onset of the power -law aftershock decay rate is in average shorter for earthquake occurred in thrust than the normal faults. For earthquakes which generated in strike-slip faults this time delay takes an intermediate value.

The results illustrated here is very useful not only from theoretical point of view, but they have practical meaning, as well. Rescue teams must have knowledge about the frequency of aftershocks when they operate in collapsed structures, especially in the first hours after the main shock.

5. References

Coral, A., 2007. Statistical features of earthquake temporal occurrence. *Lect. NotesPhys*. 705, 191-221.

Felzer, K.R. and Bronsky, E.E., 2006. Decay of aftershock density with distance indicates triggering by dynamic stress. *Nature* 441, 735-738.

Kagan, Y.Y. and Houston, H, 2005. Relation between mainshock rupture process and Omori's law for aftershock moment release rate. Geophys. J. Int. 163, 1039-1048.

Kisslinger, C., L. M. and Jones, L., 1991. Properties of aftershock sequences in southern

California. *J. Geophys. Res*. 96, 11, 947-11, 958.

Lolli, B. and Gasperini, P., 2006. Comparing different models of aftershock rate decay: The role of the catalog. *Tectonophysics* 423, 43-59.

Narteau, C., Shebalin, P. and Holschneider, M., 2002. Temporal limits of the power law aftershock decay rate. *J. Geophys. Res*.107 B12, 2359.

Narteau, C., Shebalin, P. and Holschneider, M., 2008.The onset of the aftershock decay rate across different stress regimes. Geophys. Res. Abstrs. 10, EGU2008-A-05624.

Omori, F., 1895. On the aftershocks of earthquakes. *J. Coll. Sci. Imp. Univ. Tokyo* 7, 111-200.

Page, B., 1968. Aftershocks and micro-aftershocks of great Alaska earthquake of 1964. *Bull. Seism. Soc. Am*.58, 1131-1168.

Parsons, T., 2002. Global Omori law decay of triggered earthquakes: Large aftershocks outside the classical aftershock zone. *J. Geophys. Res*.107, B9, pp. ESE9.1-ESE9.20.

Ranalli, G., 1969. A statistical study of aftershock sequences. *Ann. Geofisica* 22, 359-397.

Reasenberg, P.A. and Jones, L.M., 1989. Earthquake hazard after a mainshock in California. Science 243, 1173-1176.

Reasenberg, P.A. and Jones, L.M., 1994. Earthquake aftershocks update. Science 265, 1251-1252.

Shcherbakov, R. Turcotte, D.L. and Rudle, J.B., 2006. Scaling properties of the Parkfield aftershock sequences. Bull. Seismol. Soc. Am. 96, S376-S384.

Tajima, F. and Kanamori, H., 1985. Global survey of aftershock area expansion patterns. *Phys. Earth planet. Inter*.40, 77-134.

Tsapanos, T.M., 1990a. Spatial distribution of the difference between the magnitudes of the main shock and the largest aftershock in the circum-Pacific belt. *Bull. Seism. Soc. Am.*80, 1180-1189.

Tsapanos, T.M., 1990b. B-Values of two tectonic parts in the circum-Pacific belt. *Pageoph* 134, 229-242.

Tsapanos, T.M., Karakaisis, G.F., Hatzidimitriou, P.M. and Scordilis, E.M. 1988. On the probability of the time of occurrence of the largest aftershock and the largest foreshock in seismic sequence. *Tectonophysics*149, 177-180.

Tsapanos, T.M., Moutafi, Z.D., Gabrielidis, J.N., Spyrou, T.D. and Papazachos, C.B., 1994. Properties of the globally distributed aftershock sequences" emphasis in the circum-Pacific belt. *Bulletin of the Geological Society of Greece* XXX/5, 151-158.

Utsu, T. 1961. A statistical study on the occurrence of aftershocks. *Geophys. Mag. Tokyo* 30, 521-603.

Utsu, T. 1969. Aftershocks and earthquake statistics (I). *J. Faculty Science* Hokkaido Univ., 7, 521-603.

Utsu, T., Ogata, Y. and Matsumura, R.S., 1995. The centenary of the Omori formula for a decay law of aftershocks activity, J Phys Earth 43, 1–33.

Vinogradov, S.D., 2008. Aftershock sequences as evidence for relaxation process in a region containing an earthquake source. *Izvestiya Physics of the Solid Earth* 44, 138-141.

SEMI-MARKOV MODELS FOR SEISMIC HAZARD ASSESSMENT IN CERTAIN AREAS OF GREECE

Votsi I.[1], Limnios N.[2], Tsaklidis G.[1] and Papadimitriou E.[3]

[1] *Aristotle University of Thessaloniki, Department of Mathematics, 54124 Thessaloniki, Greece,*
evotsi@math.auth.gr, tsaklidi@math.auth.gr

[2] *Université de Technologie de Compiègne, Laboratoire de Mathématiques Appliquées,*
60206 Compiègne, France, nikolaos.limnios@utc.fr

[3] *Aristotle University of Thessaloniki, Department of Geology, 54124 Thessaloniki, Greece.*
ritsa@geo.auth.gr

Abstract

The long-term probabilistic seismic hazard is studied through the application of semi-Markov model. In this model a sequence of earthquakes is considered as a Markov process and the waiting time distributions depend only on the type of the last and the next event. The principal hypothesis of the model is the property of one-step memory, according to which the probability of moving to any future state depends only on the present state. The model under consideration defines a continuous-time, discrete-state stationary process in which successive state occupancies are governed by the transition probabilities of the Markov process. The space of states is considered to be finite and the process started far in the past has achieved stationarity. Firstly, a non-parametric method is applied in order to determine the waiting times. Then, the waiting times derived by means of the exponential and Weibull distributions will be compared to each other, as well as with the actual waiting times. Thus, the probability of occurrence of the anticipated earthquakes of a specific magnitude scale is calculated. The models are applied to an historical catalogue for Northern Aegean Sea.

Key words: *Semi-Markov process, semi-Markov kernel, sojourn times, earthquakes.*

1. Introduction

Several analytical models have been proposed to represent the process of earthquake occurrence. Some of them are based on empirical observations of precursory phenomena, others on physical modelling of the earthquake process, and a third class on statistical analysis of patterns of seismicity.

Renewal models have been used for a quarter century to forecast the time of the next large earthquake on a specific fault segment, where large shocks occur repeatedly at approximately regular time intervals. The most common is the Poisson model, which assumes spatial and temporal independence of all earthquakes, including the maximum earthquake associated with a fault or within a region. In this model, it is assumed that the occurrence of one earthquake does not affect the probability of an occurrence of another earthquake in the same magnitude scale at the same location in the next unit of time. The time-independence feature characterizing the

homogeneous Poisson model, demonstrates that earthquakes are implicitly random events; however, this feature is not appealing, because almost all of our seismological instincts favour earthquake cycle models, in which strain, and hence hazard, builds up slowly from one major earthquake to the next. In this case, the probability of a large earthquake occurrence should be small immediately after a large earthquake, and then grows with time. Thus there is a need for a time-dependent "forecasting" approach to hazard assessment. The simplest time-dependent model is the non-homogeneous Poisson model. This model is not appropriate for the estimation of seismic hazard in long time intervals, because the hazard should be updated when a new earthquake occurs.

A number of statistical models that are based on other distributions have been used including Gaussian (Rikitake, 1974), Weibull (Hagiwara, 1974; Utsu, 1984; Rikitake, 1999), gamma (Udias and Rice, 1975; Utsu, 1984), double exponential (Utsu, 1972) and lognormal (Nishenko and Bouland, 1987) distributions. All these distributions have two parameters and represent the distribution of time intervals fairly well, but none of them is more consistent with the underlying process of earthquake generation. The disadvantage of these models is their lack of seismological basis. They are inadequate to characterize the occurrence of moderate to large earthquakes on a fault at specific locations. It has been noted that the occurrence of moderate to large earthquakes on a fault is non-random in space and time (Sykes, 1971 for earthquakes in subduction zones). Other stochastic models used to represent the sequences of events and probabilities of earthquake occurrence include double Poisson (Kameda and Ozaki, 1979), Markov (Veneziano and Cornell, 1974), semi-Markov (Cluff et al., 1980) and regenerative point processes (Vere-Jones and Ozaki, 1982). A model that considers the non-random character of earthquake size and recurrence time is the semi-Markov model proposed by Cluff et al. (1980). In this model a parametric method was applied for the estimates of the recurrence intervals.

However the characterisation of future earthquake occurrence is difficult because of the lack of a sufficient number of data. The application of parametric methods provides estimators with several attractive asymptotic properties but these estimators present inconvenience when the censored time or the sample size is small. Since applications of parametric methods presuppose certain conditions with respect to the sample size, non-parametric methods will be used in order overcome this difficulty and apply semi-Markov models with reliable results.

The problem of statistical inference for semi-Markov processes is of increasing interest in recent literature. There is a growing literature concerning inference problems for continuous-time semi-Markov processes. For instance, Moore and Pyke (1968) studied empirical and maximum likelihood estimators for semi-Markov kernel; Lagakos et al. (1978) obtained the non-parametric maximum likelihood estimator for the kernel of a finite state semi-Markov process with some absorbing states; Gill (1980) constructed an estimator for the kernel of a finite state semi-Markov kernel, using counting processes; Akritas and Roussas (1979) studied the asymptotic local normality; Ouhbi and Limnios (1999, 2001) studied empirical estimators for non-linear functionals of finite semi-Markov kernels.

2. Geological setting

The Aegean (Greece) and the surrounding lands, form a region of intense crustal deformation. The kinematic of the deformation is controlled by the southwestward motion of southern Aegean relative to Europe, the active Hellenic subduction in the south, the westward motion of
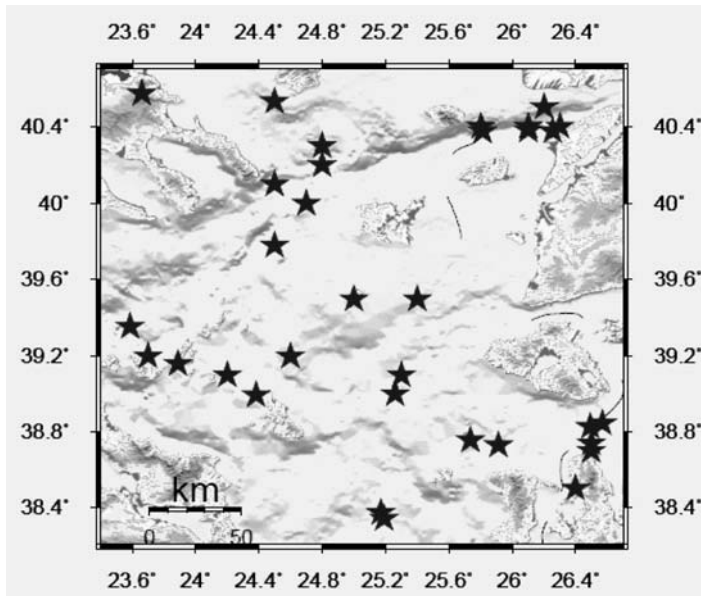
Fig.1 : Spatial distribution of Epicenters for the Earthquake Catalogue.

Anatolia in the east and the continental collision between northwestern Greece and the Apulian platform in the west. The area of northern Aegean Sea has experienced many destructive earthquakes as indicated by both instrumental data and historic information. It constitutes the northern boundary of the south Aegean plate (Papazachos et al. 1998) and is a continuation of the western part of the North Anatolian fault. Strike-slip dextral faulting dominates this region as the North Anatolian fault prolongs into the north Aegean area, where it bifurcates into two main branches of NE-SW trend. Parallel secondary faults are also recognized from seismicity and fault-plane solutions of recent strong earthquakes.

This area has frequently experienced large (M>=7.0) earthquakes, some of them occurring very close in time. The exact locations and magnitudes are of low precision before 1950, so inclusion of the events after this year is chosen. The region is bounded by latitudes 23.5 °E and 26.7ºE, longitudes 38.3°E and 40.6ºE, and the catalogue concerns earthquakes with magnitude M5.50 over the period 1950-2007. This catalogue is characterized by the desirable features of completeness, homogeneity and accuracy (Fig. 1).

Because it is implicit in the formulation that earthquakes lower the regional stress, and hence reduce the probability of immediately subsequent events, the model refers to main-sequence events only. For this reason aftershocks must be carefully identified and removed from the data before numerical fitting begins, by means of Reasenberg's (1985) declustering algorithm. The events of the catalogue are divided into three states. State 1 includes the events with magnitude $5.5 \leq M \leq 5.6$; State 2 includes events with magnitude $5.7 \leq M \leq 6$ and State 3 includes events with magnitude .

3. Methods of Estimation

3.1. Non-Parametric Method

In this section we briefly summarize the main definitions from the theory of semi-Markov

processes which are directly useful for our purposes. Let us consider a Markov renewal process (MRP), $(J,S) = (J_n, S_n)_{n \geq 0}$ defined on a probability complete space, where $(J_n)_{n \geq 0}$ is a Markov chain with values state space $E = \{1, 2, \ldots, s\}$, $(S_n)_{n \geq 0}$ are the jump times which take values in R^+, $J_0, J_1, \ldots, J_n$, are the consecutive states to be visited by the MRP and $X_0 = 0, X_1, X_2, \ldots$ defined by $X_n = S_n - S_{n-1}$ for $n \geq 1$, are the sojourn times in these states. The stochastic behaviour of the MRP is determined completely by its initial law and its semi-Markov kernel defined respectively by $P(J_0 = k) = p(k)$ and $P(J_{n+1} = j, X_{n+1} \leq x \, / \, J_0, J_1, \ldots, J_n, X_1, X_2, \ldots, X_n) = Q_{ij}(x)$ on

the event $\{J_n = i\}$, for all $x \in S$ and $j \in E$. The probabilities   are the transition probabilities of the Markov process $(J_n)_{n \geq 0}$

Let us now consider the distribution function associated with the sojourn time in state i before

going to state j and defined as

Let $N_i(t)$ be the number of visits of $(J_n)_{n \geq 0}$ to state $j \in E$ up to time t, and $N_{ij}(t)$ be the number of transitions from state i to state j up to time t, that is

and

Let us also define the distribution function   and its mean value m_i, which is the

mean sojourn time of Z in state i.

3.1.1. Empirical Estimator of the Semi-Markov Kernel

The observation of a sample path of a semi-Markov process in the time interval $[0, t]$ is described as $H_t = \{J_0, J_1, \ldots, J_{N(t)}, X_1, X_2, \ldots, X_{N(t)}\}$.

In order to estimate the semi-Markov kernel of a finite state space semi-Markov process by observing one or several sample paths in the time interval under consideration, let as define the following empirical estimator of the semi-Markov kernel:

Then   can be written as   where

,

and
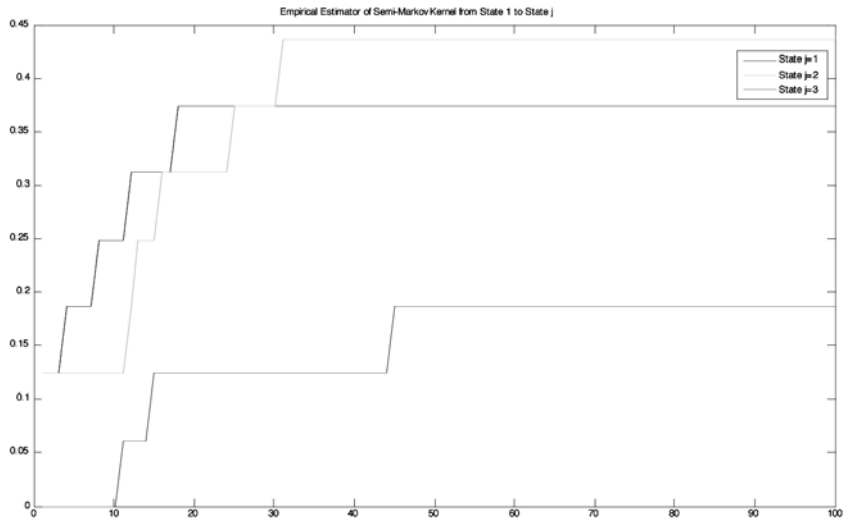
Fig. 2: Empirical Estimator for Semi-Markov Kernel from State 1 to State j, j=1, 2, 3.
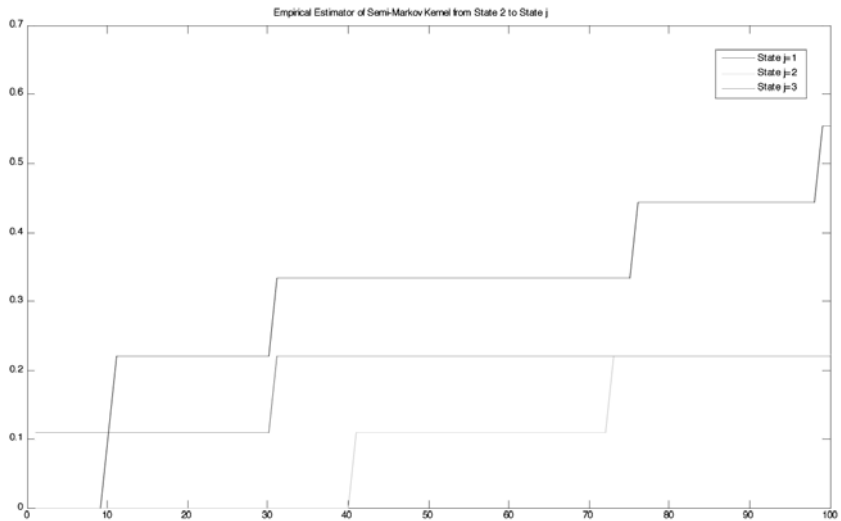
Fig. 3: Empirical Estimator for Semi-Markov Kernel from State 2 to State j, j=1, 2, 3.
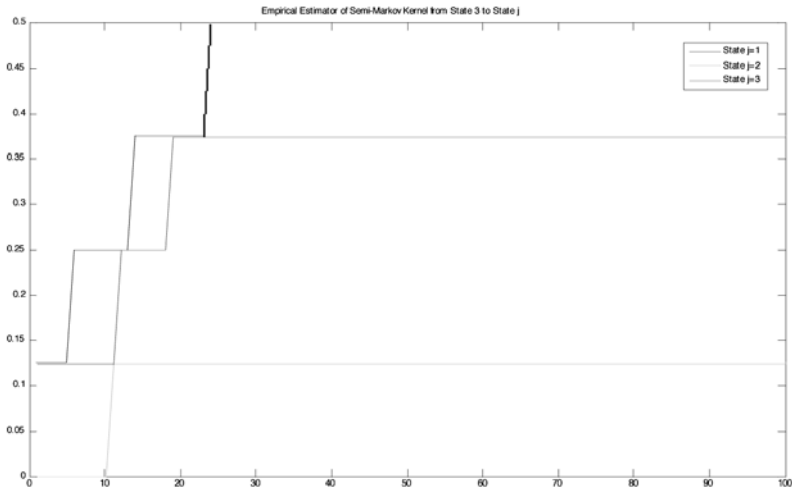
Fig. 4: Empirical Estimator for Semi-Markov Kernel from State 3 to State j, j=1, 2, 3.

Table 1.

Transitions	95% Confidence intervals for the transition probabilities	Point estimates for the transition probabilities
$1 \to 1$	$(0.3405, 0.7559)$	0.56
$1 \to 2$	$(0.2439, 0.6593)$	0.44
$2 \to 1$	$(0.3249, 0.7938)$	0.57
$2 \to 2$	$(0.2060, 0.6749)$	0.43

are the estimators of the transition probabilities and state transition functions.

In the case of two states

State 1: includes events with magnitude $5.5 \le M \le 5.7$

State 2: includes events with magnitude, $M \ge 5.8$

The point estimates and the 95% confidence intervals for the transition probabilities are presented in Table 1:

3.1.2. Empirical Estimator of Stationary Distribution for the Semi-Markov Process

Here we will assume that the embedded Markov chain (J_n) irreducible with invariant distribution v_i and that $m_i < \infty$ for all $i \in E$, where m_i is the mean sojourn time in state i. The empirical estimator for the stationary distribution of the semi-Markov process is:

,

Table 2.

State	$\hat{v}_i(T)$	$\hat{m}_i(T)$	$\hat{\pi}_i(T)$
State 1	0.4848	12.3750	0.3084
State 2	0.2727	40.4444	0.5670
State 3	0.2425	10.0000	0.1246

where   is an estimator of the stationary distribution of the embedded Markov chain and   is an estimator of the mean sojourn time in state i. The mean sojourn time in state i is

. We will use the empirical estimator of the stationary distribution of the embedded Markov chain, defined as

In Table 2 empirical estimators of the stationary distribution for the embedded Markov chain, the mean sojourn time and the stationary distribution for the semi-Markov process are presented.

3.2. Parametric Method

In order to use a parametric method of estimation and due to the small sample size, we define only two different states:
State 1: includes events with magnitude $5.5 \le M \le 5.7$
State 2: includes events with magnitude $M \le 5.8$.

We present below the numbers of observed transitions in the dataset, and the mean sojourn times in between, in months (rounded):

Number of transitions: Means of sojourn times:
                                                               .

Let us suppose that the sojourn times follow exponential distributions, namely their probability density functions are of the form

The parameters' estimation is achieved through the maximum likelihood estimation method as follows.

Table 3.

	Parameters λ_{ij}
$1 \to 1$	30.0867
$1 \to 2$	10.6667
$2 \to 1$	14.0208
$2 \to 2$	28.5722

Table 4.

Transitions	Parameters a_{ij}	Parameters λ_{ij}
$1 \rightarrow 1$	31.2758	1.0947
$1 \rightarrow 2$	9.5418	1.0000
$2 \rightarrow 1$	12.6088	1.0000
$2 \rightarrow 2$	29.0511	1.0488
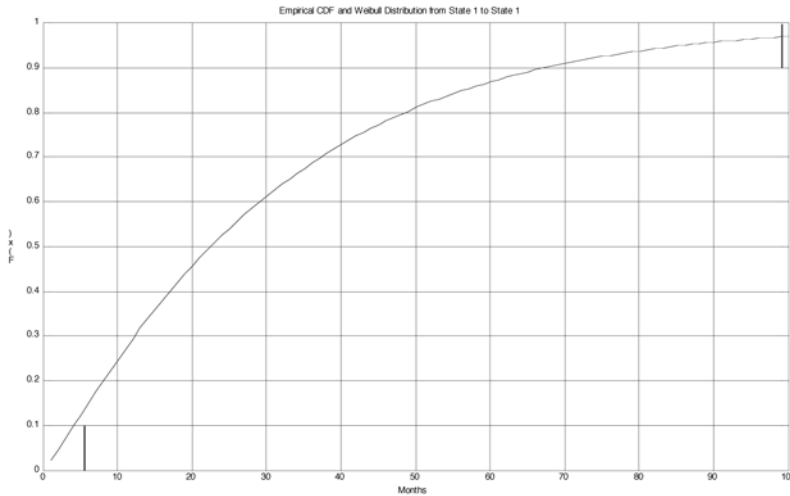
Fig. 5: Weibull Cumulative Distribution and Empirical Cumulative Distribution for Transitions from State 1 to State 1.

Supposing that the sojourn times follow Weibull distributions, their probability density functions are given by

The Weibull distribution is desirable because the associated hazard rate increases in time if λ_{ij} > 1. Actually the longer is the waiting time for transition from one state to another the higher is the probability that the transition happens. In order to estimate the parameters of the above distributions the maximum likelihood estimation method is used.

In figure 5 we present the empirical cumulative distribution and the theoretical cumulative distribution $F_{11}(t)$ of the sojourn time in state 1 before a new earthquake of the first class (i.e. state 1) occurs. Similar diagrams can be derived also for the functions $F_{12}(t)$, $F_{21}(t)$ and $F_{22}(t)$.

Assuming Weibull distributed sojourn times, the probabilities of successive earthquake occurrences in any time interval $(0, t)$, $t>0$, can be estimated using the cumulative distributions $F_{ij}(t)$. Taking into account the hazard rate functions (for the case of Weibull distribution)

we get that

for $\Delta(t)$ sufficiently small. So, the conditional probability of occurrence of an earthquake of magnitude class j, after 1 month and 6 months from the last event of magnitude class i, is given in the following tables:

Table 5.

Number of Months	Probability of next event in State 1 if last event in State 1	Probability of next event in State 1 if last event in State 2
1	0.0253	0.1076
6	0.1796	0.4378

Table 6.

Number of Months	Probability of next event in State2 if last event in State 1	Probability of next event in State 2 if last event in State 2
1	0.1318	0.0306
6	0.5546	0.2006

References

Alvarez, E. E., 2005. Estimation in Stationary Markov Renewal Processes, with Application to Earthquake Forecasting in Turkey. *Methodology and Computing in Applied Probability* 7, 119-130.

Alvarez, E. E., 2005. Smoothed nonparametric estimation in window censored semi-Markov processes. *Journal of Statistical Planning and Inference* 131, 209-229.

Anderson, A. W., Goodman, L. A., 1957. Statistical inference about Markov chains. *Ann. Math. Statist.* 28, 89-110.

Andersen, P. K., Borgan, O., Gill, R. D. & Keiding, N., 1993. *Statistical Models Based on Counting Processes.* New York: Springer.

Balakrishnan, N., Limnios, N., Papadopoulos, C., 2001. Basic probabilistic models in reliability. In: Balakrishnan, N., Rao, C. R., eds. *Handbook of Statistics* 20. Amsterdam: North-Holland.

Cluff, L. S., Patwardhan, A. S. & Coppersmith, K. J., 1980. Estimating the probability of occurrences of surface faulting earthquakes on the Wasatch fault zone, Utah. *Bulletin of Seismological Society of America* 70, 5, 1463-1478.

Console, R., Rhodes, D. A., Murru, M, Evison, F. F., Papadimitriou, E. E. & Karakostas, V. G., 2006. Comparative performance of time-invariant, long-range and short-range forecasting models on the earthquake catalogue of Greece. *Journal of Geophysical Research* 111, B09304.

Garavaglia, E., Pavani, R, 2009. About Earthquake Forecasting by Markov Renewal Processes. *Methoodol. Comput. Appl. Probab.*

Greenwood, P. E., Wefelmeyer, W., 1996. Empirical Estimators for Semi-Markov Processes. *Mathematical Methods of Statistics* 5, 299-315.

Janssen, J. Limnios, N., (eds). 1999. *Semi-Markov Models and Applications*. Dordrecht: Kluwer Academic.

Kiremidjian, A. S., Anagnos, T., 1984. Stochastic slip-predictable model for earthquake occurrences. *Bulletin of Seismological Society of America* 72, 2, 739-755.

Limnios, N., Ouhbi, B., 2006. Nonparametric estimation of some important indicators in reliability for semi-Markov processes, *Statistical Methodology* 3, 341-350.

Limnios, N., Ouhbi, B., 2003. Nonparametric reliability estimation of semi-Markov processes, *Journal of Statistical Planning and Inference* 109, 155-165.

Limnios, N., Ouhbi, B. & Sadek, A., 2005. Empirical estimator of stationary distribution for semi- Markov processes. *Communications in Statistics-Theory and Methods* 34, 287-995.

Limnios, N., Opriçan, G., 2001. Semi-Markov Processes and Reliability, Birkhäuser, Boston.

Ouhbi, B., Limnios, N., 2001. Non-parametric Estimation for Semi-Markov Processes Based on its Hazard Rate Functions. *Statistical Inference for Stochastic Processes* 2, 151-173.

Limnios, N., Ouhbi, B., 2003. Empirical estimators and related functions for semi-Markov systems. In: Linqvist, B., Doksum, K., (eds). Mathematical and Statistical Methods in Reliability. Word Scientific.

Papadimitriou, E. E., Sykes, L. R., 2001. Evolution of the stress field in the northern Aegean Sea (Greece). *Geophysical Journal International* 146, 747-759.

ΕΥΡΕΤΗΡΙΟ ΟΝΟΜΑΤΩΝ
AUTHOR INDEX

Georgiou P.: 1056
Georgoulas A.: 1074
Geraga M.: 1018, 1064
Germenis N.: 989
Gerogianni N.: 2786
Gerolymatou E.: 1438
Gialamas J.: 1777
Giannakopoulos A.: 958
Giannoulopoulos P.: 1438, 1447
Gimeno D.: 2373
Gioti Ev.: 1627
Gkadri E.: 548
Gkiolas A.: 1272
Gkiougkis I.: 1697
Golubović Deliganni M.: 1582
Gospodinov D.: 1994
Gournelos Th.: 1335, 1647
Hademenos V.: 1539
Hagiou E.: 1157
Haidarlis M.: 907
Hamdan H.: 1802
Handler R.: 299
Hatzipanagiotou K.: 876, 2501, 2540, 2617, 2712
Helly B.: 845
Iatrou M.: 1018
Ilia I.: 1590, 1688
Iliopoulos G.: 746, 781, 918
İnaner H.: 2218
Ioakim Chr.: 1035
Ioannidis N.: 1888
Janikian Z.: 939
Jenkyns H.C.: 627
Jipa–Murzea C.: 594
Kacandes G.: 2562
Kadetova A.V.: 1341
Kafkala I.G.: 2390
Kafousia N.: 627
Kalantzi F.: 1350
Kalisperi D.: 654
Kallergis G.: 1821
Kallioras A.: 69, 1697
Kalogerogiannis G.: 1149
Kamberis E.: 289, 715
Kanaris D.: 1202, 1230
Kantiranis N.: 2762
Kapetanidis V.: 2015
Karageorgiou D.E.: 1457, 1601, 2229, 2236, 2274, 2692
Karageorgiou M.M.D.: 1601, 2236, 2274
Karagianni A.: 1165
Karagianni E.: 495
Karakaisis G.F.: 46, 2026
Karakonstantis A.: 2043

Karakostas V.G.: 1984, 1994, 2053, 2064, 2075, 2093, 2114
Karalemas N.: 1707
Karamanos Ch.K.: 2053, 2075
Karapanos E.: 1716
Karastathis V.K.: 1438
Karfakis J.: 1619
Kargiotis E.: 2257
Karipi S.: 2617, 2712
Karmis P.D.: 1393, 1438, 1447, 1919
Karoutzos G.: 1165
Karydakis Gr.: 2246, 2265
Karymbalis E.: 409, 418, 1601
Kastanioti G.: 2786
Kastanis N.: 169
Katagas Ch.: 247
Kati M.: 2786
Katrivanos D.E.: 999
Katsanou K.: 1726, 1878, 2218
Katsiki P.: 2562
Katsikis J.: 2692
Katsonopoulou D.: 812
Kaviris G.: 2084
Kelepertsis A.: 1858
Kelepertzis E.: 1737
Kementzetzidou D. A.: 2053
Keupp H.: 579
Khak V.A.: 1192
Kidd W.S.F.: 309
Kilias A.: 276, 2075, 2114
Kilias S.P.: 2646
Kiratzi A.: 2135, 2144
Kitsopoulos K.: 2455, 2625
Kokinou E.: 289
Kokkalas S.: 368, 428
Kokkidis N.: 548
Kolaiti E.: 1286
Kolios N.: 2246
Kondopoulou D.: 1888, 1972
Konstantinidi–Syvridi E.: 804
Konstantopoulou G.: 1157, 1619
Kontakiotis G.: 763
Kontogianni V.: 886, 1202
Kontopoulos N.: 558, 643, 654
Koravos G.Ch.: 2193
Koroneos A.: 2606, 2680, 2752
Koskeridou E.: 613
Kosmidis E.: 1812
Kossiaris G.: 939
Kostopoulou V.: 726
Kotsovinos N.: 1074
Kougemitrou I.: 804
Kouki A.: 1169, 1177, 1184
Koukidou I.: 1747
Koukis G.: 1138, 1165, 1210, 1508,

1619
Koukoulis A.: 1457
Koukouvelas I.: 368, 1350
Koulouris S.: 1210
Koumantakis I.: 1590, 1656
Kounis G.D.: 1758, 1767, 1821
Kounis K.G.: 1758, 1767
Kourkouli P.: 1301
Kourkounis S.: 643
Koutsinos S.: 2246
Koutsios A.: 654
Koutsopoulou E.: 2635
Koutsouveli An.: 1418, 1619
Kozireva E.A.: 1341
Kozyreva E.A.: 1192
Kranis H.: 1919
Kritikou S.: 1007
Ktena S.: 1165
Ktenas D.: 548
Kurz W.: 299
Kynigalaki M.: 1202, 1619
Kyriakopoulos K.G.: 309, 663, 2327, 2361, 2726
Kyrousis I.: 1406
Lagios E.: 344, 2005
Lainas S.: 1138, 1210
Lalechos N.S.: 442
Lalechos S.N.: 442
Lambrakis N.: 1716, 1726, 1878, 2218
Lampropoulou P.: 2465
Laskaridis K.: 2475
Lasocki S.: 2114
Lazaridis A.: 1840, 2383
Lazaris S.: 2390
Lehmann P.: 1831
Leivaditi A.: 1406
Lekkas E.: 1361
Lekkas S.: 1707
Lelli M.: 1840
Lemesios I.: 1878
Leone G.: 886
Leontakianakos G.: 2485
Leptokaropoulos K.M.: 2093
Liakopoulos S.: 1438
Limnios N.: 2200
Locutura J.: 2338
Lois A.: 2183
Loukaidi V.: 737
Loupasakis C.: 1219, 1230, 1465, 1619, 1850
Lycourghiotis S.: 1029
Lykakis N.: 2646
Lykoudi E.: 1314, 1406
Lykousis V.: 1046
Magganas A.: 2786

Schütz C.: 1831
Scordilis E.M.: 46, 2026, 2154
Sdrolia S.: 845
Seeber L.: 2075
Segou M.: 2163
Serelis K.G.: 2390
Serpetsidaki A.: 2174
Siavalas G.: 2218
Sideri D.: 1850
Sifakis A.: 907
Sigalos G.: 737
Sigurdsson H.: 1056
Sikalidis C.: 2373, 2532, 2597,
    2762
Skarlatoudis A.A.: 1930
Skarpelis N.: 2417, 2510, 2553
Skianis G.Aim.: 1627, 1647
Skilodimou H.D.: 1572, 1637
Skordas K.: 1858
Smith D.C.: 804
Sofianska E.: 2657
Sokos E.: 989, 2174, 2183
Soldatos T.: 2752
Solomonidou A.: 2726
Sotiropoulos P.: 344
Sotiropoulos S.: 715
Soulios G.: 196
Soulis V.J.: 1094
Soupios P.: 654
Spanos D.: 368
Spanou N.: 1230, 1619
Spassov S.: 1972
Spry P.G.: 2406
Spyridonos E.: 1314, 1785, 2492
Spyropoulos N.: 886
St. Seymour K.: 2406
Stamatakis G.: 2739
Stamatakis M.: 2606, 2739, 2773
Stamatis G.: 1868, 1878
Stamboliadis E.: 697
Stampolidis A.D.: 1907
Stefanova M.: 2398
Stiros S.: 886, 1029
Stivanakis V.: 2465
Stoulos S.: 2680
Stoykova K.: 675
Stratikopoulos K.: 1726
Svana K.: 746
Symeonidis K.: 1286
Syrides G.: 1131
Tagkas Th.: 1149
Tarvainen T.: 2350
Tassiou S.: 1520

Theocharis D.: 821
Theodorou D.: 1335
Theodorou G.: 763
Theodosiou Ir.: 926, 939
Theodosoglou E.: 2752
Thomopoulos Ach.: 1112
Thomopoulos K.: 1064
Tombros S.F.: 2406
Tortorici G.: 400
Tortorici L.: 400
Tougiannidis N.: 2284
Tranos M.D.: 495, 2064
Triantafyllidis S.: 2417
Triantafyllou G.: 2294
Triantaphyllou M.: 475, 602, 634,
    715, 754, 763,
Trontzios G.: 2657
Tryfonas G.: 1149
Tsagas D.: 1335
Tsaklidis G.M.: 1984, 2200
Tsanakas K.: 418, 506
Tsangaratos P.: 1406, 1590, 1656,
    1688
Tsapanos T.M.: 2193
Tsaparas N.: 620
Tselentis G–A.: 2174
Tselepides V.: 379
Tsiambaos G.: 183, 1104, 1259
Tsikouras B.: 876, 2501, 2540,
    2617, 2712
Tsimas S.: 2485
Tsipoura–Vlachou M.: 663
Tsirambides A.: 2606, 2762
Tsirigotis N.: 1149
Tsobanoglou C.: 1812
Tsokas G.N.: 1907
Tsolakis E.: 763
Tsolis–Katagas P.: 856, 2635
Tsombos P.: 1438, 1447, 1486,
    1528, 1539, 1547, 1539, 1548,
    1559
Tsoukala E.: 958
Tsourlos P.: 1962
Tzamos E.: 2762
Tzanaki I.: 289
Tzanis A.: 344, 1919, 1941
Tzavidopoulos I.: 886
Tzevelekou Th.: 2465
Tziritis E.: 1858
Tzortzaki E.: 613
Vafidis A.: 1802
Vagenas N.: 1165
Vagenas S.: 1210

Vagiotou E.: 1149
Vaiopoulos D.: 1627, 1647
Vakalas I.: 675, 697
Vako E.: 1777
Valera P.: 2446, 2558
Valiakos I.: 965
Valkaniotis S.: 486, 1383
Vamvakaris D.: 495
Van Cappellen P.: 2310
Varaggouli E.: 1074
Vargemezis G.: 1953, 1962
Varnavas S.: 234
Varvarousis G.: 2229, 2265
Vasilatos Ch.: 2773
Vassiliades E.: 1520
Vassiliou E.: 1688
Vassilopoulou S.: 516
Vaxevanopoulos M.: 948
Vitsas T.: 989
Vlachopoulos I.: 1165
Vlachou–Tsipoura M.: 2773
Vogiatzis D.: 2762
Vontobel P.: 1831
Votsi I.: 2200
Voudouris K.: 1678
Voudouris P.: 685, 845, 2786
Vougioukalakis G.: 939
Voulgaris N.: 2163
Vouvalidis K.: 706, 1122
Vrettos K.: 2236
Vythoulkas N.K.: 2193
Wölfler A.: 299
Xeidakis G.: 1074
Xypolias P.: 368, 387
Zagana E.: 1726, 1878
Zambetakis–Lekkas A.: 773
Zananiri I.: 1474, 1539, 1549, 1972
Zanchetta G.: 886
Zelilidis A.: 643, 675, 697, 793
Zerefos C.S.: 2
Zervakou A.D.: 1528, 1539, 1549,
    1559
Zevgitis T.: 989
Ziannos V.: 1812
Zidianakis G.: 781
Zisi N.: 958, 1840, 2383
Zorba T.: 2752
Zoumpoulis E.: 793
Zouridakis N.: 1792
Zouros N.: 159, 896, 965
Zygouri V.: 527